

Volcanism and Evolution of the African Lithosphere



Edited by
Luigi Beccaluva,
Gianluca Bianchini,
and Marjorie Wilson



THE
GEOLOGICAL
SOCIETY
OF AMERICA®

Special Paper 478

Volcanism and Evolution of the African Lithosphere

edited by

Luigi Beccaluva
Dipartimento di Scienze della Terra
Università di Ferrara
Via Saragat 1
44100 Ferrara
Italy

Gianluca Bianchini
Dipartimento di Scienze della Terra
Università di Ferrara
Via Saragat 1
44100 Ferrara
Italy

Marjorie Wilson
School of Earth & Environment
The University of Leeds
Leeds, LS2 9JT
UK



THE
GEOLOGICAL
SOCIETY
OF AMERICA®

Special Paper 478

3300 Penrose Place, P.O. Box 9140 ■ Boulder, Colorado 80301-9140, USA

2011

Copyright © 2011, The Geological Society of America (GSA), Inc. All rights reserved. GSA grants permission to individual scientists to make unlimited photocopies of one or more items from this volume for noncommercial purposes advancing science or education, including classroom use. In addition, an author has the right to use his or her article or a portion of the article in a thesis or dissertation without requesting permission from GSA, provided the bibliographic citation and the GSA copyright credit line are given on the appropriate pages. For permission to make photocopies of any item in this volume for other noncommercial, nonprofit purposes, contact The Geological Society of America. Written permission is required from GSA for all other forms of capture or reproduction of any item in the volume including, but not limited to, all types of electronic or digital scanning or other digital or manual transformation of articles or any portion thereof, such as abstracts, into computer-readable and/or transmittable form for personal or corporate use, either noncommercial or commercial, for-profit or otherwise. Send permission requests to GSA Copyright Permissions, 3300 Penrose Place, P.O. Box 9140, Boulder, Colorado 80301-9140, USA. GSA provides this and other forums for the presentation of diverse opinions and positions by scientists worldwide, regardless of their race, citizenship, gender, religion, or political viewpoint. Opinions presented in this publication do not reflect official positions of the Society.

Copyright is not claimed on any material prepared wholly by government employees within the scope of their employment.

Published by The Geological Society of America, Inc.
3300 Penrose Place, P.O. Box 9140, Boulder, Colorado 80301-9140, USA
www.geosociety.org

Printed in U.S.A.

GSA Books Science Editors: Marion E. Bickford and Donald I. Siegel

Library of Congress Cataloging-in-Publication Data

Volcanism and evolution of the African lithosphere / edited by Luigi Beccaluva, Gianluca Bianchini, Marjorie Wilson.

p. cm. — (Special paper ; 478)

Includes bibliographical references.

ISBN 978-0-8137-2478-2 (pbk.)

1. Volcanism—Africa, Eastern. 2. Lithosphere. 3. Geodynamics—Africa, Eastern. I. Beccaluva, Luigi. II. Bianchini, Gianluca. III. Wilson, Marjorie.

QE526.2.A354V65 2011

551.21096—dc22

2011006982

Cover: (Top) Mount Meru (4566 m high), Tanzania, from the western side. Courtesy Philippe Nonnotte. (Bottom) Carbonatite lava at Oldoinyo Lengai volcano, northern Tanzania. Courtesy Alexander J. Teague.

Contents

<i>Preface and Acknowledgments</i>	v
1. Late Mesozoic to Quaternary intraplate magmatism and its relation to the Neoproterozoic lithosphere in NE Africa—New data from lower-crustal and mantle xenoliths from the Bayuda volcanic field, Sudan	1
Friedrich Lucassen, Gerhard Franz, Rolf L. Romer, and Peter Dulski	
2. Holocene opening directions along the axes of the Red Sea (Afar) and Main Ethiopian Rifts: An overview	25
V. Acocella, B. Abebe, and T. Korme	
3. The upper-mantle low-velocity anomaly beneath Ethiopia, Kenya, and Tanzania: Constraints on the origin of the African superswell in eastern Africa and plate versus plume models of mantle dynamics	37
Andrew A. Nyblade	
4. The Ethiopia Afar Geoscientific Lithospheric Experiment (EAGLE): Probing the transition from continental rifting to incipient seafloor spreading	51
Ian D. Bastow, Derek Keir, and Eve Daly	
5. Peridotite xenoliths from Ethiopia: Inferences about mantle processes from plume to rift settings	77
Luigi Beccaluva, Gianluca Bianchini, Robert M. Ellam, Claudio Natali, Alessandro Santato, Franca Siena, and Finlay M. Stuart	
6. Evolution of the lithospheric mantle beneath the East African Rift in Tanzania and its potential signatures in rift magmas	105
Sonja Aulbach, Roberta L. Rudnick, and William F. McDonough	
7. Petrology and geochemistry of alkaline lava series, Kilimanjaro, Tanzania: New constraints on petrogenetic processes	127
Philippe Nonnotte, Mathieu Benoit, Bernard Le Gall, Christophe Hémond, Joël Rolet, Joseph Cotten, Pierre Brunet, and Edikafumeni Makoba	
8. Trace-element distribution between coexisting aqueous fumarole condensates and natrocarbonatite lavas at Oldoinyo Lengai volcano, Tanzania	159
Alexander J. Teague, Jacob Hanley, Terry M. Seward, and Frederik Reutten	
9. Cameroon Line alkaline magmatism (central Africa): A reappraisal	173
Emmanuel Njonfang, Alexandre Nono, Pierre Kamgang, Vincent Ngako, and Félix M. Tchoua	
10. Mineralogical and geochemical fingerprints of mantle metasomatism beneath Nyos volcano (Cameroon volcanic line)	193
M.I. Teitchou, M. Grégoire, R. Temdjim, R.T. Ghogomu, C. Ngwa, and F.T. Aka	

11. Dolomitic volcanism in Zambia: Cr and K signatures and comparisons with other dolomitic melts from the mantle	211
D.K. Bailey and S. Kearns	
12. Post-Paleozoic magmatism in Angola and Namibia: A review	223
P. Comin-Chiaramonti, A. De Min, V.A.V. Girardi, and E. Ruberti	
13. Is the African cratonic lithosphere wet or dry?	249
Ikuo Katayama and Jun Korenaga	
14. New ^{40}Ar-^{39}Ar ages and petrogenesis of the Massif d'Ambre volcano, northern Madagascar	257
C. Cucciniello, L. Melluso, V. Morra, M. Storey, I. Rocco, L. Franciosi, C. Grifa, C.M. Petrone, and M. Vincent	
15. Metasomatism versus host magma infiltration: A case study of Sal mantle xenoliths, Cape Verde Archipelago	283
Costanza Bonadiman, Massimo Coltorti, Luigi Beccaluva, William L. Griffin, Suzanne Y. O'Reilly, and Franca Siena	
16. Magmatic evidence for African mantle propagation into the southern Tyrrhenian backarc region.	307
Teresa Trua, Michael P. Marani, and Fabiano Gamberi	

Preface and Acknowledgments

The distribution of volcanism in the African plate reflects a variety of processes, many of which are poorly understood, involving interaction between the lithosphere and the underlying convective mantle. Despite the maturity of the plate tectonic paradigm, our knowledge of the processes involved in the breakup of continents and the formation of new ocean basins remains limited. The African Rift system provides a unique natural laboratory to study the transition from continental breakup to seafloor spreading. In this respect it is important to explore the similarities among the volcanic provinces of the Saharan zone, Cameroon volcanic line, Angola and Namibia, and the East African Rift system.

This Special Paper arose out of the symposium on “Cenozoic volcanism and evolution of the African lithosphere,” held at the 33rd International Geological Congress in Oslo, Norway, in August 2008. The aim of this volume is to bring together recent and updated contributions on African volcanism (and associated xenoliths), providing multidisciplinary contexts that include volcanology, geochemistry, petrology, geophysics, and structural geology, for a better understanding of the geological evolution of the African lithosphere.

Nine of the 16 chapters in this Special Paper address volcanism and petrogenetic aspects of various African provinces, whereas the remaining contributions focus on the characteristics of mantle and crustal xenoliths and on geophysical investigation of the African lithosphere. The debate on the presence of one or more mantle plume(s) beneath the African plate is broached in several of these papers, reporting speculations on mantle dynamics and on scale length and triggering mechanisms of the convective instabilities, as well as their surface expression.

Acknowledgments

Each of the contributions in this volume has been reviewed by two or more external reviewers. We are grateful to the suggestions and criticism provided by Ulrich Achauer, Shoji Arai, Irina Artemieva, Julie Bryce, Guillaume Delpech, Damien Delvaux, Daniel Demaiffe, Stewart Fishwick, Gareth Funning, Tanya Furman, Massimo Gasparon, John Gittins, Marguerite Godard, Kathryn Goodenough, Christophe Hemond, Paul Martin Holm, Fred Jourdan, Katie Keranen, Andrey Kozhurin, Philip R. Kyle, Philip T. Leat, Anton Le Roex, Felicity E. Lloyd, Peter Maguire, Roger Mitchell, Andy Moore, Else-Ragnhild Neumann, Andy Nicol, Theo Ntaflos, Giovanni B. Piccardo, David Pyle, Nick W. Rogers, Andrew D. Saunders, Ashley Shuler, Philip Skemer, Mauro G. Spagnuolo, Robert J. Stern, Greg A. Valentine, Stephanie Werner, Anthony E. Williams-Jones, and Alan R. Woolley.

***Late Mesozoic to Quaternary intraplate magmatism and
its relation to the Neoproterozoic lithosphere in NE Africa—
New data from lower-crustal and mantle xenoliths from
the Bayuda volcanic field, Sudan***

Friedrich Lucassen*
Gerhard Franz

Fachgebiet Mineralogie-Petrologie, Technische Universität Berlin, Ackerstrasse 71-76, 13355 Berlin, Germany

Rolf L. Romer
Peter Dulski

Deutsches GeoForschungsZentrum, Telegrafenberg, 14473 Potsdam, Germany

ABSTRACT

A variety of xenoliths from the lower crust to mantle transition occur in Quaternary mafic intraplate lavas of the Bayuda volcanic field of northern Sudan. The lower-crust xenoliths include plagioclase- and garnet-bearing mafic granulite. Ultramafic garnet-bearing pyroxenite, websterite, hornblendite, and distinct peridotite xenoliths are from the upper lithospheric mantle. Sr, Nd, and Pb isotope signatures distinguish between ultramafic and granulite xenoliths. The latter show a strong compositional affinity to juvenile Neoproterozoic crust. The Pb isotope composition of the ultramafic xenoliths resembles the distinct high- μ signature ($^{206}\text{Pb}/^{204}\text{Pb} > 19.5$) of their host basanite. These xenoliths may represent cumulates of late Mesozoic to Quaternary mafic intraplate magmatism. The felsic upper crust in a schematic lithospheric profile of the Bayuda area includes predominantly granitoids, migmatites, and metasedimentary rocks that represent reworked old cratonic or juvenile Neoproterozoic rocks. The deep lower crust is represented by mafic granulite, likely cumulate rocks from Neoproterozoic juvenile magmatism. The crust-mantle transition is characterized by ultramafic cumulate rocks possibly from the late Mesozoic to Quaternary magmatism. The peridotites of the same xenolith suites represent typical lithospheric mantle with variable degrees of depletion by melt extraction.

*lucassen@gfz-potsdam.de

Lucassen, F., Franz, G., Romer, R.L., and Dulski, P., 2011, Late Mesozoic to Quaternary intraplate magmatism and its relation to the Neoproterozoic lithosphere in NE Africa—New data from lower-crustal and mantle xenoliths from the Bayuda volcanic field, Sudan, *in* Beccaluva, L., Bianchini, G., and Wilson, M., eds., *Volcanism and Evolution of the African Lithosphere: Geological Society of America Special Paper 478*, p. 1–24, doi:10.1130/2011.2478(01). For permission to copy, contact editing@geosociety.org. © 2011 The Geological Society of America. All rights reserved.

INTRODUCTION

The surface geology of NE Africa is dominated by eroded Neoproterozoic crust and younger sediments, but exposures of deep crustal sections are rare. Thus, despite the general knowledge of the compositional differences between possible lithospheric reservoirs, derived from the composition of magmatic rocks, the composition of NE African lower crust and its transition to the lithospheric mantle is essentially unknown. Xenoliths in Cenozoic alkaline magmatic rocks open a window into the makeup of the present deeper crust and upper mantle. The only studies of xenoliths from the lower crust in the region are from the Arabian plate, where juvenile Neoproterozoic crust is dominant (McGuire and Stern, 1993; Al-Mishwat and Nasir, 2004). The target area of this study, the Quaternary Bayuda volcanic field, is near the boundary between reworked Paleoproterozoic craton and Neoproterozoic juvenile crust (Fig. 1A; e.g., Abdelsalam et al., 2002). The upper felsic crust of the Bayuda region consists of abundant cratonic material reworked during the Pan-African orogeny, but hybrid granitoid and metamorphosed mafic rocks also indicate the activity of a Pan-African juvenile source (Kröner et al., 1987; Küster and Liégeois, 2001; Küster et al., 2008). Thus, the area might provide insight into formation and modification processes in the lower crust to upper mantle transition, including both juvenile and cratonic material.

The NE African lithosphere was stabilized during the Neoproterozoic, manifested in pre- Neoproterozoic ca. 920 Ma metamorphism and granitoid magmatism, Neoproterozoic island-arc formation, collision, and metamorphism ca. 800–700 Ma, and abundant postcollisional granitoids between ca. 620 and 560 Ma (e.g., Kröner et al., 1987; Stern and Kröner, 1993; Stern, 1994; Küster and Harms, 1998; Küster and Liégeois, 2001; Küster et al., 2008). The region has been a stable cratonic area since then. The first-order growth and compositional pattern of the Neoproterozoic orogen in NE Africa involve (1) reworked Paleoproterozoic basement with high-grade metamorphic rocks and granitoids at the margin of the Sahara metacraton (Abdelsalam et al., 2002) and (2) accretion of abundant Neoproterozoic juvenile island-arc material toward and on the Arabian plate (Fig. 1A; Brueckner et al., 1988, 1995; Zimmer et al., 1995; Stern and Abdelsalam, 1998; Teklay et al., 2002; Abdelsalam et al., 2002; Bailo et al., 2003; Stoeser and Frost, 2006). During the long period of relative tectonic quiescence, up to the mid-Tertiary, abundant small-scale intraplate magmatism from the Paleozoic onward records the expression of scattered local thermal disturbances in the mantle (e.g., Vail, 1989; Schandelmeyer and Reynolds, 1997). In the Tertiary, at ca. 30 Ma, a major change in the tectonic regime triggered eruption of flood basalt (e.g., Hofmann et al., 1997) in the Afar region and subsequent plate separation with ongoing rifting and ocean floor formation in the Gulf of Aden and Red Sea (Fig. 1A; e.g., Bosworth et al., 2005). Mafic intraplate magmatism of small

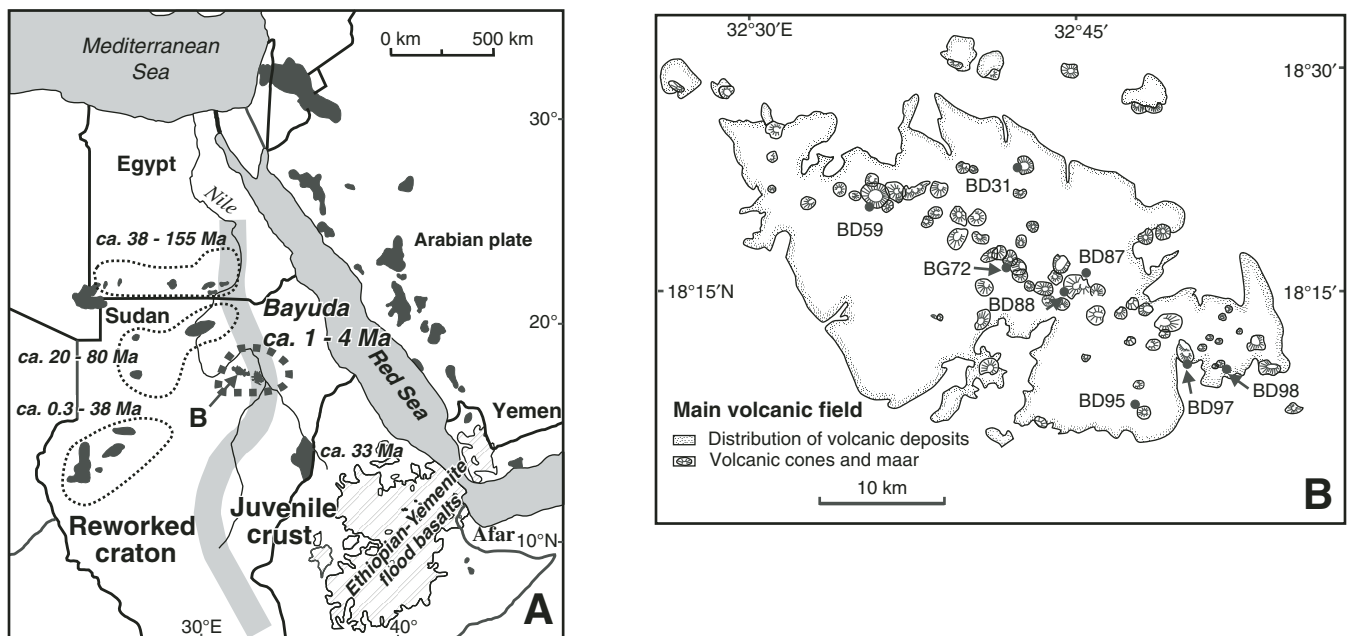


Figure 1. (A) Distribution and ages of intraplate magmatism in NE Africa and occurrences of intraplate volcanism on the western Arabian plate and the Ethiopian-Yemenite "Afar" flood basalt province (compiled from Schandelmeyer and Reynolds, 1997; Bertrand et al., 2003; Shaw et al., 2003). The Neoproterozoic basement is subdivided by the thick gray line into mainly reworked Paleoproterozoic craton (west) and mainly Neoproterozoic juvenile crust (east; e.g., Küster and Liégeois, 2001; Abdelsalam et al., 2002). (B) Enlarged map from the Bayuda main volcanic field. Sample locations of the lower crust xenoliths are indicated (Table 1). Blank areas are thin cover of sedimentary rocks or metamorphic-magmatic basement.

to moderate volume in NE Africa intensified before and after flood basalt extrusion and onset of rifting, whereas on the Arabian plate, many occurrences of intraplate magmatism postdate the onset of rifting (Fig. 1A). This widespread mafic intraplate magmatism provides information on the composition of the lithospheric mantle (e.g., Franz et al., 1999; Bertrand et al., 2003; Shaw et al., 2003; Lucassen et al., 2008a), whereas the magmatism related to the formation of the Red Sea gives insight into the convective, asthenospheric mantle (e.g., Altherr et al., 1990; Volker et al., 1993, 1997; Schilling et al., 1992).

This study presents new data on the petrology of whole-rock samples and mineral separates from a suite of xenoliths, including pressure-temperature (P - T) estimates and compositional and radiogenic isotope data that reflect the transition from the lower crust to the upper mantle beneath the Bayuda volcanic field, NE Sudan (Fig. 1). This suite consists of plagioclase-bearing granulite and—summarized as ultramafic rocks—garnet pyroxenite, hornblende, websterite, and amphibole megacrysts. The compositions of Quaternary intraplate lavas of the Bayuda volcanic field and peridotite xenoliths of the same suite have already been studied (Lucassen et al., 2008a, 2008b) and resemble characteristics of the mantle lithosphere known from NE Africa and the Arabian plate (e.g., Franz et al., 1999; Bertrand et al., 2003; Shaw et al., 2003, 2007; Lucassen et al., 2008a, 2008b). The new data set completes the section of the deep and shallower mantle lithosphere (derived from Quaternary intraplate magmas and spinel-lherzolite xenoliths, respectively) and upper crust (Neoproterozoic metamorphic and magmatic rocks), all from a restricted area with a coherent geological evolution from the Neoproterozoic onward.

BAYUDA VOLCANIC FIELD AND ITS BASEMENT

The explosive successions of Quaternary alkaline volcanism (age <1.5 Ma; Barth and Meinhold, 1979; Almond et al., 1984) from the main volcanic field in the Bayuda desert of NE Sudan (Fig. 1) bear abundant xenoliths of upper-mantle and, less commonly, lower-crust origin. Bayuda volcanism is compositionally related to the mainly alkaline province of intraplate magmatism in north Sudan and south Egypt (Fig. 1; e.g., Franz et al., 1987, 1999; Lucassen et al., 2008a). The age of some lavas is Mesozoic, but most are Paleogene to Holocene in age (Barth and Meinhold, 1979; Franz et al., 1987; Schandemeier and Reynolds, 1997; Lucassen et al., 2008a; Schandemeier and Reynolds, 1997). Alkaline magmatism north of the Bayuda field is Late Cretaceous to Paleogene (Satir et al., 1991) whereas magmatism to the east is only slightly older than that in the main volcanic field (4 Ma; Jebel Umm Arafieb; Barth and Meinhold, 1979). The magmatism is not related to a systematic fault pattern (Fig. 1).

The Bayuda desert is located at the eastern edge of the Sahara metacraton (Fig. 1; Abdelsalam et al., 2002). The latter is made up of mainly reworked Paleoproterozoic cratonic material, whereas the basement east of the inferred suture is dominated by juvenile Neoproterozoic crust. Detailed studies of granitoids and

metamorphic rocks have revealed the transition from reworked cratonic to juvenile crust toward the east (e.g., Kröner et al., 1987; Küster and Liégeois, 2001; Küster et al., 2008). Neoproterozoic metamorphism and magmatism (ca. 860–550 Ma) were preceded by ca. 920–900 Ma metamorphism and magmatism in the reworked Paleoproterozoic cratonic rocks (Küster et al., 2008). The isotopic composition of Neoproterozoic granitoids from Bayuda and surroundings indicates an origin from hybrid melts of a depleted mantle and cratonic metamorphic basement (e.g., Küster et al., 2008, and references therein). Early Paleozoic to Mesozoic anorogenic alkaline ring complexes are common in NE Africa (e.g., Vail, 1989) and occur also in the Bayuda area (Barth et al., 1983). They have not been studied in detail, and therefore their genesis is largely unknown. Except for this sporadic small-volume magmatism, the area became geologically quiet after the Neoproterozoic consolidation.

PETROGRAPHY OF THE XENOLITHS

The xenoliths samples were collected from the Bayuda volcanic field by D. Pudlo and R. Brumm in the year 1995 within the frame of the Sonderforschungsbereich (collaborative research center) 67 project hosted by Technische Universität Berlin. They occur within the deposits of the Quaternary explosive volcanism (Fig. 1B). Samples for this study were chosen after the study of thin sections from a collection of >50 pyroxenite- and >30 plagioclase-bearing xenoliths. Sample locations considered in this study are given in Figure 1B.

The xenoliths were subdivided according to their mineral paragenesis into two groups, a “granulite” and an “ultramafic” group. The granulites are plagioclase and occasionally quartz-bearing and include both garnet-free and garnet-bearing samples. Details of mineral modes and petrographic features are given in Table 1. Both groups show similar granoblastic texture with polygonal grain-shapes and common 120° grain intersections. Such textures are typical for high-temperature equilibration (upper amphibolite- to granulite-facies conditions) of rocks dominated by pyroxene or amphibole. There is no evidence for pervasive deformation after the high-temperature event, and compositional layering in some samples is the only planar texture. Textures that are younger than the formation of the dominant fabric and mineral assemblage are absent except in sample C4 (Table 1). This sample is the only one with visible, likely in situ modal metasomatism. The minerals in general show no optical zoning, and there are no traces of metamorphic or inherited magmatic growth patterns. Small, optically different rims are restricted to contacts with secondary minerals, such as the common kelyphitic rims around garnet. Weathering is restricted to hydro-oxidation around magnetite-ilmenite grains and to thin films that do not invade into the grains.

The ultramafic xenoliths are near-monomineralic aggregates of clinopyroxene or hornblende, or their mineralogy is dominated by one of the latter minerals with variable amounts of other Fe-Mg minerals. Olivine occurs in one sample only. Large single

crystals of amphibole up to 5 cm long are common in the debris of the explosive volcanism and are included in the ultramafic group. Similar clinopyroxene crystals were found but not included in the study, because clinopyroxene-dominated xenoliths were studied.

MINERAL COMPOSITIONS

Mineral analyses were obtained using an automated CAM-EBAX microprobe at Technical University Berlin (analytical procedure in Lucassen et al., 2008b). Representative analyses are listed in Table 2.

Clinopyroxene from the ultramafic and granulite xenoliths shows overlapping compositions with quadrilateral components (diopside-hedenbergite-enstatite-ferrosilite) >85–90 mol%. They are classified as augite, with ~34–44 mol% wollastonite and ~7–15 mol% ferrosilite (Fig. 2A). Compositional zoning was determined in detail for clinopyroxene from samples C27, C54, and C56 of the ultramafic group. The rims are generally <50 µm and small compared to the size of the grains, which commonly exceed 500–1000 µm. Variable, small systematic variations are restricted to these rims, whereas the cores are uniform within the small scatter between the analysis points. The depletion of Al,

TABLE 1. MINERALOGY, TEXTURES, AND PRESSURE-TEMPERATURE (*P-T*) ESTIMATES

Sample	Location	Mineralogy and textures	$T(^{\circ}\text{C})^{*}$	$T(^{\circ}\text{C})^{*}$
			$\text{Fe}^{2+} = \text{Fe}_{\text{tot}}$	$\text{Fe}^{2+}_{\text{calculated}}$
<u>Ultramafic</u>				
<u>garnet-clinopyroxenite</u>				
C36	Maar BD95	Cpx (~0.5 mm; >50–70 vol%), euhedral gt surrounded by kelyphite (10–30 vol%), sp, ilm, brown hbl (<5 vol%, sample C36 contains ~30 vol% of opaque minerals; hbl in C42 and 59); granoblastic fabric with common triple junctions between gt, cpx, sp	1030	940
C42	Maar BD95		1030	950
C59	Scoria cone BD98		1030	890
<u>Garnet-websterite</u>				
C25	Maar BG72	Cpx (60–80 vol%), variable modes opx, gt, sp (also as inclusion in gt), and ilm, minor brown hbl (C25 only); gt rimmed by kelyphite; exsolution lamellae of gt and Ti-rich sp in cpx of sample C25. Granoblastic fabric between cpx, opx, gt; also some interstitial gt between cpx in C27	890	850
C27	Scoria cone BD97		940	850
C54	Scoria cone BD98		880	850
<u>Garnet-hornblende</u>				
C19	Scoria cone BD88	Brown hbl (~1–3 mm; >90 vol%), minor cpx forms mainly on triple junctions or as inclusion in hbl; subordinate ilm; gt framed or totally displaced by kelyphite in a matrix of pl, cpx, minor opaque minerals, sp, and glass; ophitic texture of the matrix indicates former melt-pods; cpx-rims in contact with the latter have pinkish to gray pleochroism; protogranular fabric		
C39	Scoria cone BD88			
<u>Olivine-amphibole-spinel pyroxenite</u>				
C4	Scoria cone BD87	Variably cpx-rich (<50 vol%) and ol-rich (<30 vol%) layers, crosscut by hornblende veins (<30 vol%); adjacent cpx likely replaced by hbl, but grain boundaries between cpx and hbl indicate textural equilibrium; minor sp forms rounded inclusions (0.05–0.2 mm) in ol and cpx; granoblastic fabric of ol and cpx		
<u>Hornblende megacrystal</u>				
M1		Single hbl crystal (~5 × 3 × 3 cm) with small spherical inclusions (diameter <150 μm) of opaque minerals including rare sulfide; solitary and along trails		
<u>Granulite-pyroxene-plagioclase</u>				
BD59	Maar BD59	BD72 and BD88: cpx (~70–80 vol%), opx (<10 vol%), pl (<10 vol%), opaque minerals (<1 vol%, BD88; <10 vol%, BD72); BD59: pl (~90 vol%), cpx, opx (<10 vol%), opaque minerals (<1 vol%), cpx (BD59) framed by palisade textures of secondary cpx and interstitial symplectite in contact to pl; granoblastic fabric, 120° intersections		
BD72	Maar BG72			
BD88	Scoria cone BD88			
<u>Clinopyroxene-plagioclase-garnet</u>				
BD88a	Scoria cone BD88	Cpx (~40–60 vol%), pl (~20–40 vol%), gt and kelyphite (~10–30 vol%), opaque minerals (<2, BD88a <~10 vol%), kelyphite rims vary from ~20 μm to near consumption of the garnet; BD98 with subordinate qtz; granoblastic fabrics, no deformation after high- <i>T</i> equilibration	880	—
BD88b	Scoria cone BD88		860	840
BD98	Scoria cone BD88		920	890
<u>Garnet-quartz-amphibole</u>				
BD31	Maar BD31	Gt and qtz in approx. equal amounts (together <80 vol%), green hbl (<20 vol%), opaque minerals (<5 vol%); cpx at two spots in contact with hbl and qtz is largely reacted to symplectite; no kelyphite		

Note: Sample locations are given in Figure 1B. Abbreviations: cpx—clinopyroxene, opx—orthopyroxene, gt—garnet, hbl—hornblende, pl—plagioclase, sp—spinel, ilm—ilmenite, qtz—quartz.

*Temperature estimates are after Ellis and Green (1979), and Fe²⁺_{calculated} is from charge balance; all *T* values were calculated for *P* = 1.0 GPa (uncertainty in *P* of 0.5 GPa introduces an uncertainty of ~±20 °C in the *T* calculated at 10 kbar); the last digit in the *T* estimates is rounded off.

TABLE 2. ELECTRON MICROPROBE AVERAGE ANALYSES*

Clinopyroxene													
Rock:		Granulite											
Sample:		BD88a											
Position:		Core											
No. analyses:		n = 9											
SiO ₂ (wt%)		BD88a		BD88B		BD98		Ultramafic		C36			
		Rim		n = 34		Core		BD98		Core			
		n = 20		n = 34		n = 9		n = 14		n = 6			
		1sd		1sd		1sd		1sd		1sd			
TiO ₂		0.88	52.50	0.77	50.03	0.67	49.30	0.28	50.62	0.56	49.70		
Al ₂ O ₃		0.06	1.02	0.10	1.05	0.09	7.55	0.07	0.85	0.04	1.31		
Cr ₂ O ₃		0.40	6.21	0.39	6.86	0.62	0.00	0.47	6.20	0.11	7.63		
FeO		0.00	0.00	0.00	0.00	0.00	0.00	0.00	0.00	0.00	0.00		
MnO		0.24	6.32	0.32	6.39	0.48	3.79	0.13	3.50	0.14	5.69		
MgO		0.04	0.08	0.05	0.06	0.03	0.04	0.03	0.02	0.02	0.06		
CaO		0.28	12.96	0.37	12.14	0.41	13.35	0.18	14.13	0.11	12.37		
Na ₂ O		0.40	20.63	0.52	20.87	0.43	21.16	0.10	21.67	0.11	21.17		
Total		0.06	101.1	0.06	98.78	0.06	97.44	0.05	98.08	0.04	99.5		
Sample:		C42		C59		C59		C25		C25			
Position:		Core		Core		Rim		Core		Rim			
No. analyses:		n = 7		n = 35		n = 24		n = 15		n = 3			
SiO ₂		0.39	49.34	0.48	48.33	0.77	49.58	1.08	50.25	0.79	51.70		
TiO ₂		0.12	1.28	0.12	1.62	0.09	1.20	0.23	0.86	0.20	0.54		
Al ₂ O ₃		0.30	7.49	0.52	8.57	0.26	7.51	0.60	5.67	0.87	3.98		
Cr ₂ O ₃		0.00	0.00	0.00	0.00	0.00	0.00	0.00	0.19	0.04	0.16		
FeO		0.11	6.25	0.19	6.35	0.18	6.44	0.23	5.73	0.18	5.61		
MnO		0.02	0.06	0.04	0.06	0.03	0.08	0.04	0.09	0.03	0.07		
MgO		0.28	11.97	0.33	11.79	0.18	12.36	0.35	13.50	0.47	14.41		
CaO		0.26	21.21	0.49	20.51	0.49	20.57	0.64	21.97	0.27	22.05		
Na ₂ O		0.04	1.54	0.09	1.79	0.06	1.68	0.07	0.90	0.06	0.80		
Total		0.04	99.14	0.09	99.02	0.06	99.42	0.07	99.16	0.06	99.32		
Sample:		C27		C54		C54		C4		C4			
Position:		Core		Core		Rim		Core		Rim			
No. analyses:		n = 19		n = 9		n = 17		n = 8		n = 8			
SiO ₂		0.50	49.14	1.17	52.03	0.49	51.20	0.21	49.31	0.71	49.72		
TiO ₂		0.19	1.22	0.28	0.70	0.07	1.10	0.09	1.24	0.19	1.26		
Al ₂ O ₃		0.16	6.56	0.21	5.15	0.20	6.52	0.27	7.21	0.79	6.13		
Cr ₂ O ₃		0.02	0.16	0.03	0.15	0.04	0.14	0.05	0.21	0.15	0.13		
FeO		0.20	4.94	0.21	5.03	0.09	5.94	0.30	5.58	0.83	6.11		
MnO		0.04	0.06	0.04	0.09	0.03	0.12	0.05	0.14	0.02	0.15		
MgO		0.29	13.84	0.62	14.57	0.14	14.31	0.10	13.40	0.56	13.61		
CaO		0.10	22.72	0.11	20.74	0.26	19.27	0.44	21.10	0.70	21.67		
Na ₂ O		0.04	0.67	0.03	1.23	0.02	1.43	0.06	0.71	0.08	0.70		
Total		0.04	99.16	0.03	99.69	0.02	100.0	0.06	98.90	0.08	99.48		
													(Continued)

TABLE 2. ELECTRON MICROPROBE AVERAGE ANALYSES* (Continued)

Garnet Rock: Sample: No. analyses:	Kelyphite			Kelyphite			Kelyphite		
	Granulite BD88A n = 30	1sd	BD88B n = 35	1sd	BD98 n = 26	1sd	BD31 n = 33	1sd	1sd
SiO ₂	40.60	0.64	40.43	0.33	40.13	0.25	41.87	0.29	
TiO ₂	0.32	1.20	0.06	0.02	0.07	0.02	0.06	0.02	
Al ₂ O ₃	22.30	0.33	22.25	0.26	22.06	0.11	23.24	0.19	
Cr ₂ O ₃	0.00		0.00		0.00		0.00		
FeO	20.45	0.37	20.41	0.42	20.42	0.18	12.40	0.52	
MnO	0.72	0.07	0.75	0.05	0.55	0.03	0.27	0.10	
MgO	11.51	0.23	11.23	0.24	10.26	0.24	15.64	0.10	
CaO	5.49	1.04	5.48	0.09	5.98	0.08	5.69	0.21	
Total	101.4		100.6	100.0	99.47		99.17	99.27	
Rock: Ultramafic									
Sample: C36									
No. analyses:	n = 9	1sd	C42 n = 25	1sd	C59 n = 16	1sd	C25 n = 8	1sd	C27 n = 12
SiO ₂	40.74	0.34	40.62	0.34	41.20	0.57	40.16	0.31	41.33
TiO ₂	0.08	0.04	0.15	0.07	0.17	0.04	0.08	0.03	0.12
Al ₂ O ₃	22.84	0.16	22.34	0.27	22.82	0.40	22.33	0.15	23.16
Cr ₂ O ₃	0.00		0.00		0.00		0.23	0.03	0.00
FeO	15.52	0.33	16.42	0.26	17.11	0.18	17.97	0.30	16.10
MnO	0.53	0.04	0.48	0.06	0.52	0.05	0.68	0.05	0.52
MgO	14.22	0.20	13.27	0.40	13.94	0.12	12.56	0.14	14.15
CaO	5.72	0.16	5.71	0.18	5.37	0.20	6.06	0.19	5.27
Total	99.65		98.99	101.1	101.1		100.1	100.7	
Sample: C19									
No. analyses:	n = 6	1sd	C39 n = 4	1sd					
SiO ₂	39.32	0.15	40.68	0.11					
TiO ₂	0.13	0.04	0.13	0.05					
Al ₂ O ₃	21.84	0.48	22.50	0.10					
Cr ₂ O ₃	0.00		0.00						
FeO	19.71	0.78	20.23	0.14					
MnO	0.76	0.07	0.75	0.06					
MgO	10.11	0.13	10.77	0.19					
CaO	6.19	0.13	6.18	0.20					
Total	98.06		101.2						

(Continued)

TABLE 2. ELECTRON MICROPROBE AVERAGE ANALYSES* (Continued)

Hornblende													
Rock: Granulite													
Sample: BD88B													
No. analyses:													
	n = 7	1sd	BD98 n = 3	1sd	BD31 n = 20	1sd	Ultramafic C42 n = 12	1sd	C59 n = 10	1sd	C25 n = 5	1sd	1sd
SiO ₂	40.96	0.26	42.50	0.29	41.99	0.84	41.06	0.57	41.09	0.57	41.94	0.57	0.43
TiO ₂	3.68	0.05	2.78	0.18	1.47	0.20	3.41	0.07	3.43	0.09	2.63	0.09	0.43
Al ₂ O ₃	14.08	0.19	14.62	0.10	12.45	0.54	14.07	0.54	14.72	0.41	13.64	0.41	0.50
Cr ₂ O ₃	0.00		0.00		0.00		0.00		0.00		0.25		0.15
FeO	11.67	0.13	5.41	0.08	20.79	0.62	8.99	0.14	9.47	0.22	8.99	0.22	0.08
MnO	0.05	0.02	0.04	0.03	0.11	0.03	0.06	0.03	0.02	0.02	0.06	0.02	0.05
MgO	11.74	0.18	15.89	0.06	6.07	0.16	13.52	0.22	13.39	0.16	14.32	0.16	0.54
CaO	11.10	0.08	11.31	0.05	11.34	0.20	11.22	0.17	10.57	0.74	11.25	0.74	0.12
Na ₂ O	2.67	0.06	2.51	0.09	1.09	0.08	3.31	0.11	2.91	0.28	2.87	0.28	0.37
K ₂ O	1.01	0.10	0.96	0.03	1.04	0.10	0.58	0.05	1.26	0.33	0.73	0.33	0.34
Total	96.96		96.02		96.35		96.22		96.86		96.68		
Sample: C19													
No. analyses:													
	n = 17	1sd	C39 n = 9	1sd	C4 n = 24	1sd							
SiO ₂	40.68	0.43	41.71	0.53	40.79	0.62							
TiO ₂	3.59	0.24	3.45	0.25	3.16	0.71							
Al ₂ O ₃	14.32	0.38	14.11	0.52	14.25	0.30							
Cr ₂ O ₃	0.00		0.00		0.23	0.24							
FeO	11.33	0.48	11.80	0.25	9.05	1.39							
MnO	0.00	0.00	0.00	0.00	0.10	0.03							
MgO	11.42	0.25	12.24	0.37	14.11	1.09							
CaO	11.15	0.17	10.77	0.32	11.27	0.36							
Na ₂ O	2.92	0.13	2.91	0.11	2.70	0.26							
K ₂ O	0.97	0.07	0.90	0.14	1.05	0.41							
Total	96.38		97.89		96.71								
Plagioclase													
Sample: BD88A													
Position: Core													
No. analyses:													
	n = 8	1sd	BD88A Rim n = 9	1sd	BD88b Core n = 15	1sd	BD88B Rim n = 17	1sd	BD98 Core n = 9	1sd	BD98 Rim n = 14	1sd	1sd
SiO ₂	57.82	0.40	59.67	0.79	56.89	0.39	57.74	0.60	55.07	1.17	54.99	1.17	0.86
Al ₂ O ₃	26.95	0.50	26.55	0.46	27.71	0.31	27.00	0.42	27.65	0.13	27.65	0.13	0.09
FeO	0.08	0.05	0.11	0.08	0.06	0.03	0.18	0.06	0.06	0.04	0.10	0.04	0.05
CaO	9.05	0.31	8.24	0.25	9.41	0.22	8.75	0.46	9.78	0.07	9.74	0.07	0.08
Na ₂ O	6.11	0.23	6.69	0.14	6.01	0.12	6.33	0.25	5.61	0.11	5.70	0.11	0.13
K ₂ O	0.27	0.02	0.34	0.03	0.25	0.03	0.28	0.04	0.17	0.02	0.18	0.02	0.01
Total	100.31		101.62		100.35		100.3		98.36		98.38		

*1sd—1 standard deviation; all values are in wt% oxide; 0.00 indicates value below detection limit of the microprobe; kelyphite analyses are to respective garnet; n—number of analyses. Mineral analyses were obtained using an automated CAMEBAX microprobe (at Technical University Berlin) at 15 kV acceleration voltage and 20 nA sample current. Counting times have been adjusted to the respective content of the element.

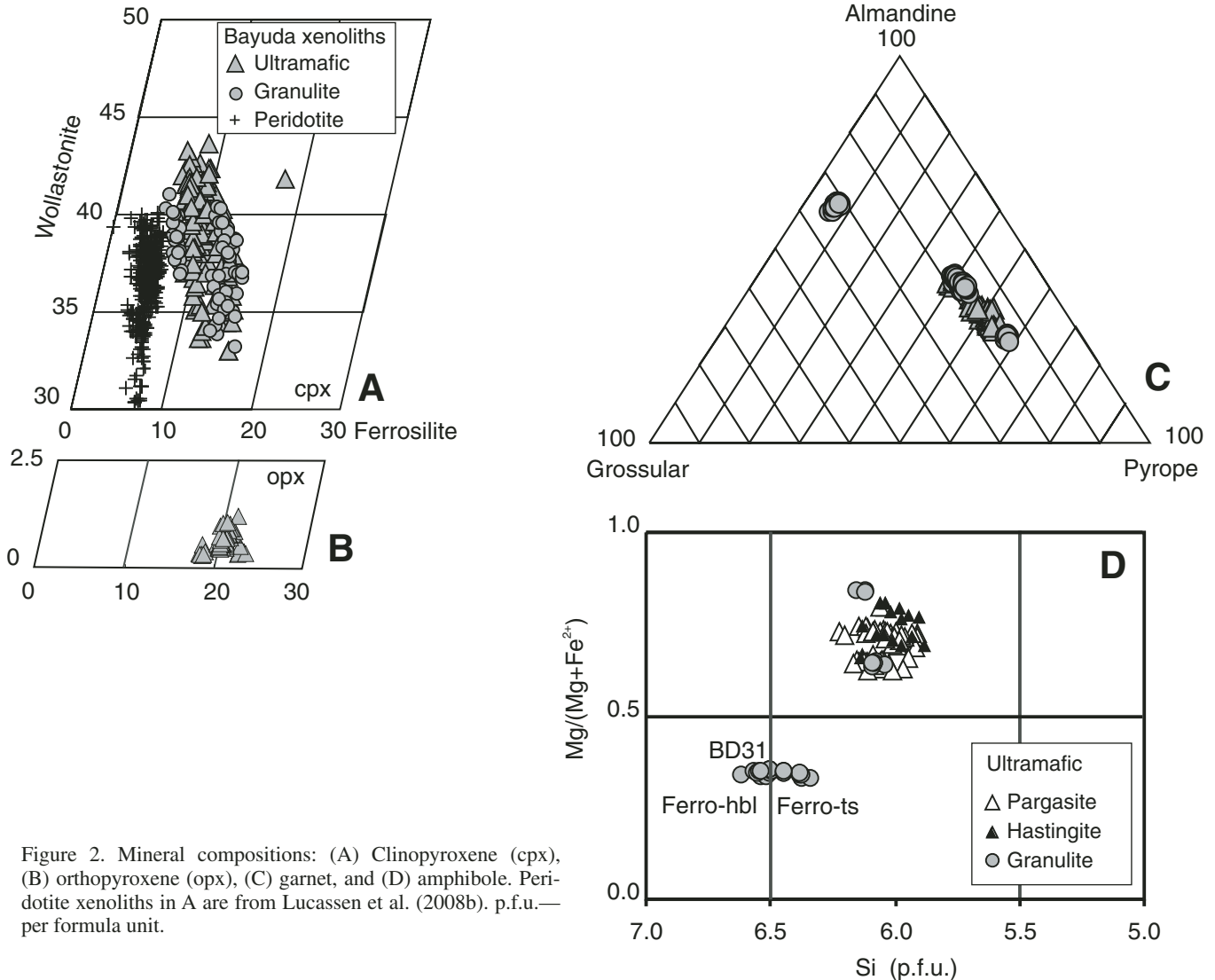


Figure 2. Mineral compositions: (A) Clinopyroxene (cpx), (B) orthopyroxene (opx), (C) garnet, and (D) amphibole. Peridotite xenoliths in A are from Lucassen et al. (2008b). p.f.u.—per formula unit.

Ti, and Na and enrichment of Mg and Si at the rim appear to be independent of the mineral in contact, which is garnet (kelyphite) and other clinopyroxene in samples C59 (Fig. DR1A¹) and C27. Clinopyroxene (sample C54) in contact with orthopyroxene shows increases in Al, Fe, and Ti and decreases in Ca, whereas at the rim of the orthopyroxene, these elements are nearly unchanged (slight increase of Al and Ca). In the granulite xenoliths, rim analyses of clinopyroxene in contact with kelyphite, plagioclase, or hornblende show generally lower Ti, Al, Fe, and Na, and higher Si, Mg, and Ca contents compared to the core. A slight increase of wollastonite and enstatite component in the outer rims is common in the ultramafic and granulite xenoliths.

Orthopyroxene was analyzed only in the garnet-websterite (samples C25, C27, and C54) of the ultramafic xenoliths, but it also occurs in the garnet-free granulite xenoliths. Orthopyroxene is enstatite with ~20 mol % ferrosilite (Fig. 2B). Compositional differences between outer rims and cores are small, e.g., Al contents at rims of C25 and C27 is ~0.02 cations per formula unit (p.f.u.) lower than at cores, whereas C54 shows a slight increase in Al at rims to garnet (Fig. DR1B [see footnote 1]).

Garnet crystals in granulite and ultramafic xenoliths do not show systematic compositional zoning. However, compositional variations at the outermost rims (which are observed in coexisting pyroxene) could be blurred by the common kelyphite rims. Garnet crystals of the ultramafic rocks and the granulites do not differ significantly, although compositions are slightly more variable in granulitic xenoliths (Fig. 2C). They have ~40–60 mol% pyrope, ~25–40 mol% almandine, ~15–20 mol% grossular, and <1.5 mol% spessartine contents. One granulite sample (BD 31)

¹GSA Data Repository item 2011166, Figure DR1: Composition of pyroxenes and Figure DR2: Normalized trace element distribution of the xenoliths, is available at <http://www.geosociety.org/pubs/ft2011.htm> or by request to editing@geosociety.org.

has a much higher almandine and grossular content. Analyses of the kelyphite rims with a defocused electron beam very closely match the compositions of the respective garnets. Calculated amounts of andradite by charge balance from electron microprobe analyses are small and not systematic in the grains or between the different types of xenoliths.

Amphibole in granulite and ultramafic xenoliths is calcic amphibole (Fig. 2D; Leake et al., 1997). In the ultramafic xenoliths, it is assigned to the subgroup titanian pargasite (samples C19, C25, C39, C42, and C59) and straddles the border to magnesio-hastingsite in the olivine pyroxenite (C4). In the granulite xenoliths, the amphibole is titanian pargasite (BD88B and BD98), or its composition plots around the border between ferrohornblende and ferrotschermakite (BD31).

The compositions of the Fe-Mg minerals clinopyroxene, garnet, and amphibole from granulite and ultramafic xenoliths overlap, respectively, except those of sample BD31. The ranges of whole-rock Mg# in both xenolith groups largely overlap (Mg# ~41–77, except the low value of ~21 from BD31; Table 3).

Plagioclase of the granulite xenoliths has ~40–49 mol% anorthite, ~50–59 mol% albite, and <~1.6 mol % K-feldspar. Compositional variations of the outermost rims are indicated by a slight increase in Na and K values (samples BD88A and BD88B).

Olivine of the olivine-spinel-pyroxenite (C4) has forsterite contents of ~70–80 mol%, with compositional variations occurring among different grains.

Oxides are spinel and ilmenite in the ultramafic and ilmenite in the granulite xenoliths. Spinel typically has ~20–35 mol% hercynite (~10 mol% in a single grain with high Cr contents of sample C4), and ~5–12 mol% magnetite, whereas chromite content is only elevated in garnet websterite C27 (~4 mol%) and olivine pyroxenite C4 (~2–3 mol%, one grain ~10 mol%). Ilmenite in the garnet pyroxenite has ~16–21 mol% geikielite and ~9–21 mol% hematite and ~16–26 mol% and ~3–8 mol% in garnet websterite, respectively. Ilmenite in granulite xenoliths BD88A and BD88B has ~12–17 mol% geikielite and ~8–12 mol% hematite and is nearly pure ilmenite (~96–98 mol%) in BD31.

CHEMICAL AND ISOTOPIC COMPOSITION

Sample Preparation and Analytical Procedure

Samples for geochemical studies were selected after petrographic examination of thin sections applying the following criteria (1) absence of magma infiltration; (2) lowest grade of alteration by weathering; and (3) sufficient material (>200 g) for bulk rock analyses. Selected samples were cleaned of any crusts of host basanite, placed in polyethylene bags, and broken into fragments <10 mm. The fragments were cleaned in distilled water to remove dust. The volumes (~50 g) used for milling in an agate box were checked for irregularities such as host rock fragments under a binocular microscope before processing. Minerals for trace-element and isotope analyses were handpicked under a binocular

microscope: five plagioclase separates of BD98, BD88, BD88b, and BD59 (clear and cloudy plagioclase in BD59) were prepared for Pb and Sr isotope analyses, and hornblende of samples C4 (additionally clinopyroxene), C39, and M1 for trace element and isotope analyses. Garnet, amphibole, and the nonmagnetic fraction of sample BD31 were separated for Sm-Nd isotopic dating.

Analytical procedures and data quality of X-ray fluorescence (XRF) (major elements), solution inductively coupled plasma-mass spectrometry (ICP-MS) (trace elements), and thermal ionization mass spectrometry (TIMS) (Sr, Nd, Pb isotope ratios) are the same as those presented by Lucassen et al. (2008a, 2008b).

Major and Trace Elements

Variable major-element compositions of the ultramafic xenoliths and MgO contents as a possible indicator of progressive magmatic differentiation or melt extraction do not define any systematic trends (Fig. 3; Table 3). Major-element contents of the granulite xenoliths show no well-defined correlation with MgO and preclude a direct genetic link of the samples by differentiation from common parent magma (Fig. 3; Table 3). Whole-rock chemistry of the near monomineralic garnet hornblende and the heterogeneous olivine-pyroxenite C4 was not measured.

Ultramafic Xenoliths

Variations of the normalized trace-element patterns are similar in garnet-pyroxenite and websterite and always similar or higher than the values of the primitive mantle (Fig. 4A; Fig. DR2A [see footnote 1]), with the exception of Rb, Ba, and K in two samples. Incompatible elements (Sr, Rb, K, Ba, Th, U, Nb, and Ta) are—in comparison with the compatible elements—variably depleted, except Cs and Pb, which are enriched. Nb, Ta, and Ti of garnet-pyroxenite C36 is enriched, probably due to accumulation of a Ti-Fe mineral, likely ilmenite. Hornblende (C19, C39), hornblende megacrystal M1, and separated hornblende from C4 are similar and show a characteristic enrichment of Sr, Pb (except C4, where Pb is partitioned into coexisting clinopyroxene), Ta, Nb, and Ba and a relative depletion of Rb and Cs (Fig. 4A; Fig. DR2A). Distribution coefficients between clinopyroxene and hornblende in C4 appear to be close to 1 for REE (rare earth elements), but different for the other trace elements (Fig. DR2A). Chondrite-normalized REE patterns of most ultramafic xenoliths are upward convex and show a relative depletion of La, Ce, and the heavy REE, except sample C54, which has a negative Eu anomaly and no depletion of heavy REE (Fig. 4B).

Granulite Xenoliths

Variable trace-element composition is in line with the variable major-element composition, e.g., plagioclase-rich BD59 and garnet-hornblende-quartz-rich BD31 (Fig. 4C; Fig. DR2B [see footnote 1]). REE patterns show variable Eu anomalies and are—in comparison with the upward convex pattern of the ultramafic xenoliths—flat or mildly LREE (light REE) depleted (Fig. 4). The REE pattern of sample BD59 reflects high plagioclase with

TABLE 3. CHEMICAL AND ISOTOPE COMPOSITION OF ULTRAMAFIC AND GRANULITE XENOLITHS

Sample: Rock:	C36 Ultramafic wr	CB42 wr	C59 wr	C25 wr	C27 wr	C54 wr	C19 hbl	C39 hbl	C4 cpx
<u>XRF (wt%)</u>									
SiO ₂	31.2	39.0	37.0	47.8	45.9	47.6			
TiO ₂	11.7	2.25	2.16	1.16	1.16	0.77			
Al ₂ O ₃	12.1	17.2	18.5	7.20	10.2	10.6			
Fe ₂ O ₃	21.2	14.1	14.9	9.71	11.1	10.2			
MnO	0.21	0.19	0.18	0.18	0.13	0.21			
MgO	11.1	12.8	12.7	14.4	18.5	15.7			
CaO	10.8	13.2	12.7	17.9	11.8	13.2			
Na ₂ O	0.65	0.87	0.95	0.61	0.21	0.95			
K ₂ O	0.03	0.04	0.05	0.00	0.01	0.06			
P ₂ O ₅	0.03	0.03	0.03	0.02	0.02	0.03			
LOI	-0.38	0.07	-0.01	0.30	0.26	0.23			
Total	98.7	99.8	99.2	99.4	99.7	99.6			
<u>ICP-MS (ppm)</u>									
Li	2.18	1.58	2.04	2.29	1.47	4.03	1.87		
Rb	1.63	0.94	1.42	0.21	0.29	0.86	9.43	3.46	0.81
Sr	62.7	69.2	78.9	42.2	28.8	51.7	541	707	87.6
Y	12.7	15.4	13.9	17.2	9.0	22.0	18.1	21.4	15.7
Zr	81.4	55.9	54.3	45.2	40.1	37.5	68.7	111.6	109.4
Nb	21.6	2.21	3.30	0.83	1.21	3.19	25.4	19.2	1.89
Mo	2.65	2.16	0.84	0.20	0.28	0.31	0.29		
Cs	0.07	0.04	0.09	0.03	0.02	0.01	0.02	0.20	0.18
Ba	10.7	8.67	13.5	3.94	2.25	10.0	248	165	12.4
La	2.56	2.29	3.01	1.95	1.64	2.49	6.56	6.82	7.82
Ce	8.35	8.44	10.0	6.84	6.28	7.54	20.2	23.4	21.1
Pr	1.47	1.59	1.74	1.30	1.20	1.38	3.30	4.33	3.15
Nd	8.40	9.17	10.0	7.70	6.67	7.96	16.7	24.4	15.3
Sm	2.59	2.97	3.22	2.84	2.21	2.90	4.57	7.63	3.95
Eu	0.99	1.18	1.27	1.07	0.77	0.76	1.62	2.73	1.30
Gd	3.03	3.53	3.66	3.81	2.60	3.73	4.87	8.11	4.11
Tb	0.47	0.57	0.55	0.61	0.39	0.68	0.70	1.09	0.63
Dy	2.80	3.48	3.36	3.79	2.28	4.38	4.13	5.58	3.51
Ho	0.56	0.67	0.62	0.72	0.43	0.95	0.76	0.90	0.67
Er	1.40	1.76	1.66	1.86	1.01	2.74	1.78	1.96	1.64
Tm	0.19	0.24	0.22	0.24	0.12	0.38	0.24	0.21	0.21
Yb	1.11	1.43	1.22	1.44	0.68	2.46	1.35	1.16	1.25
Lu	0.14	0.19	0.19	0.21	0.09	0.35	0.18	0.16	0.18
Hf	2.59	1.99	1.98	1.77	1.55	1.10	2.37	3.67	3.32
Ta	1.76	0.21	0.27	0.10	0.14	0.19	1.49	1.05	0.24
Pb	4.33	0.77	1.32	1.05	0.70	0.68	1.45	2.86	2.61
Th	0.24	0.08	0.23	0.19	0.12	0.14	0.28	0.67	0.96
U	0.10	0.06	0.07	0.06	0.03	0.09	0.06	0.15	0.21
⁸⁷ Rb/ ⁸⁶ Sr	0.075	0.039	0.052	0.014	0.029	0.048	0.050	0.014	0.027
⁸⁷ Sr/ ⁸⁶ Sr	0.703238	0.703305	0.703212	0.702922	0.702838	0.703115	0.703083	0.703070	0.703125
2σ (m)	0.000008	0.000009	0.000009	0.000011	0.000009	0.000010	0.000012	0.000006	0.000007
*	0.704555	0.704277	0.704304	0.704508	0.704721	0.705251	0.703462		
	0.000007	0.000007	0.000007	0.000009	0.000008	0.000008	0.000008		
¹⁴⁷ Sm/ ¹⁴⁴ Nd	0.187	0.196	0.194	0.223	0.200	0.220	0.165	0.189	0.156
¹⁴³ Nd/ ¹⁴⁴ Nd	0.512801	0.512806	0.512800	0.512984	0.512953	0.512902	0.512880	0.512890	0.512890
2σ (m)	0.000004	0.000005	0.000005	0.000005	0.000005	0.000005	0.000005	0.000005	0.000007
²³⁸ U/ ²⁰⁴ Pb	1.5	5.1	3.7	3.3	2.8	9.2	2.9	3.4	5.3
²³² Th/ ²⁰⁴ Pb	3.8	6.8	11.9	11.9	11.4	14.4	13.3	15.4	24.9
²⁰⁶ Pb/ ²⁰⁴ Pb	19.74	19.85	19.85	18.60	19.65	19.62	19.88	18.88	19.62
*		19.89	19.69	19.59	19.87	19.82	19.05		
²⁰⁷ Pb/ ²⁰⁴ Pb	15.64	15.70	15.68	15.56	15.65	15.67	15.64	15.58	15.63
*		15.72	15.70	15.70	15.71	15.71	15.66		
²⁰⁸ Pb/ ²⁰⁴ Pb	39.66	39.58	39.79	38.41	39.35	39.31	39.64	38.68	39.38
*		39.27	39.31	39.06	39.15	39.18	38.94		

(Continued)

TABLE 3. CHEMICAL AND ISOTOPE COMPOSITION OF ULTRAMAFIC AND GRANULITE XENOLITHS (*Continued*)

Sample Rock:	C4 Ultramafic hbl	M1 hbl	BD59 Granulite wr	BD59 pl (clear)	BD59 pl (cloud)	BD72 wr unl.	BD72 wr leach.	BD88 wr	BD88 pl
<u>XRF (wt%)</u>									
SiO ₂			53.6			41.5		47.9	
TiO ₂			0.13			6.88		1.76	
Al ₂ O ₃			26.7			7.59		7.66	
Fe ₂ O ₃			1.68			16.4		11.0	
MnO			0.02			0.18		0.19	
MgO			1.35			10.5		13.0	
CaO			10.3			14.0		16.8	
Na ₂ O			5.05			1.65		1.11	
K ₂ O			0.25			0.12		0.02	
P ₂ O ₅			0.02			0.05		0.02	
LOI			0.31			0.90		0.06	
Total			99.5			99.9		99.5	
<u>ICP-MS (ppm)</u>									
Li			1.76			4.50	3.90	3.23	
Rb	7.36	8.76	0.59			nd	nd	0.35	
Sr	356	397	924			223	197	109	
Y	19.4	14.5	0.47			12.2	10.4	20.5	
Zr	66.0	73.8	5.98			56.8	53.0	46.1	
Nb	34.8	16.1	0.16			11.7	11.2	0.74	
Mo			0.25			0.57	0.42	0.20	
Cs	0.05	0.10	0.01			0.02	0.01	0.02	
Ba	191	186	86.5			63.2	26.8	11.0	
La	8.59	4.90	1.24			4.24	2.21	1.69	
Ce	24.1	15.3	2.22			10.5	6.79	6.54	
Pr	3.70	2.59	0.26			1.64	1.24	1.38	
Nd	18.6	13.3	1.02			9.19	7.62	8.63	
Sm	4.87	3.77	0.16			3.07	2.86	3.28	
Eu	1.78	1.35	0.43			1.37	1.26	1.43	
Gd	5.37	4.12	0.14			3.80	3.54	4.47	
Tb	0.77	0.58	0.02			0.56	0.51	0.71	
Dy	4.39	3.36	0.10			3.09	2.72	4.50	
Ho	0.81	0.61	0.02			0.53	0.46	0.85	
Er	2.02	1.45	0.03			1.27	1.02	2.29	
Tm	0.25	0.17	0.01			0.15	0.12	0.29	
Yb	1.42	0.93	0.04			0.86	0.67	1.77	
Lu	0.21	0.13	0.01			0.12	0.09	0.24	
Hf	2.32	2.35	0.15			1.93	1.92	1.93	
Ta	1.54	1.01	0.04			0.80	0.79	0.09	
Pb	0.67	3.92	0.96			0.51	0.43	0.63	
Th	0.36	0.52	0.06			0.83	0.51	0.11	
U	0.08	0.11	0.02			0.22	0.13	0.03	
⁸⁷ Rb/ ⁸⁶ Sr	0.059	0.064	0.002					0.009	
⁸⁷ Sr/ ⁸⁶ Sr	0.703117	0.703143	0.703318	0.703343	0.703311		0.703716	0.703439	0.703466
2σ (m)	0.000007	0.000008	0.000009	0.000008	0.000009		0.000010	0.000008	0.000007
*			0.703429				0.705095	0.704061	
			0.000008				0.000007	0.000009	
¹⁴⁷ Sm/ ¹⁴⁴ Nd	0.158	0.172	0.096				0.227	0.230	
¹⁴³ Nd/ ¹⁴⁴ Nd	0.512912	0.512884	0.512616				0.512941	0.512968	
2σ (m)	0.000006	0.000006	0.000006				0.000004	0.000005	
²³⁸ U/ ²⁰⁴ Pb	7.6	1.9	1.0				28.1	3.0	
²³² Th/ ²⁰⁴ Pb	36.2	9.0	3.9				111.3	11.4	
²⁰⁶ Pb/ ²⁰⁴ Pb	19.68	19.93	18.43	18.23	18.23		20.37	19.04	18.43
*			19.82				19.43	19.79	
²⁰⁷ Pb/ ²⁰⁴ Pb	15.63	15.63	15.59	15.57	15.57		15.68	15.64	15.59
*			15.72				15.65	15.71	
²⁰⁸ Pb/ ²⁰⁴ Pb	39.43	39.67	38.05	37.88	37.88		40.47	38.64	38.18
*			39.12				39.31	39.10	

(Continued)

TABLE 3. CHEMICAL AND ISOTOPE COMPOSITION OF ULTRAMAFIC AND GRANULITE XENOLITHS (*Continued*)

Sample Rock:	BD88a Granulite wr	BD88b wr	BD88b pl	BD 98 wr unl.	BD 98 wr leach.	BD 98 pl	BD 31 wr unl.	BD 31 wr leach.	BD 31 unmag.
<u>XRF (wt%)</u>									
SiO ₂	42.8	42.7		47.8			50.1		
TiO ₂	5.23	6.08		0.41			2.64		
Al ₂ O ₃	12.0	17.0		17.5			11.9		
Fe ₂ O ₃	15.7	14.3		7.26			21.7		
MnO	0.22	0.13		0.12			0.44		
MgO	10.0	5.45		11.6			2.93		
CaO	12.1	10.9		12.9			8.20		
Na ₂ O	1.56	2.78		1.80			0.38		
K ₂ O	0.07	0.13		0.06			0.46		
P ₂ O ₅	0.02	0.09		0.02			0.26		
LOI	-0.20	-0.20		0.49			1.03		
Total	99.6	99.4		99.9			100.0		
<u>ICP-MS (ppm)</u>									
Li	2.77	2.44		2.67	2.26		2.74	2.25	
Rb	0.52	0.63		nd	nd		6.04	3.94	
Sr	281	588		394	396		37.4	26.5	
Y	14.9	6.83		6.47	5.56		62.6	59.2	
Zr	43.8	35.1		20.1	12.9		25.4	20.4	
Nb	4.31	6.00		0.89	0.82		11.8	11.8	
Mo	0.29	0.25		0.17	0.18		0.70	0.23	
Cs	0.03	0.01		0.01	0.01		0.05	0.02	
Ba	31.1	64.4		38.6	18.4		33.9	17.9	
La	1.39	1.76		1.74	1.34		9.70	5.19	
Ce	4.57	4.23		4.25	3.80		25.2	14.9	
Pr	0.86	0.67		0.61	0.55		3.82	2.49	
Nd	5.34	3.71		3.15	2.90		20.0	13.7	
Sm	1.99	1.22		1.05	0.98		6.82	5.18	
Eu	0.98	0.74		0.56	0.49		1.85	1.51	
Gd	2.82	1.55		1.38	1.21		9.78	8.16	
Tb	0.45	0.22		0.23	0.21		1.75	1.55	
Dy	3.03	1.46		1.40	1.26		11.7	10.9	
Ho	0.61	0.29		0.27	0.24		2.53	2.39	
Er	1.71	0.76		0.72	0.64		7.59	7.12	
Tm	0.24	0.10		0.10	0.08		1.11	1.06	
Yb	1.46	0.62		0.56	0.50		7.21	7.04	
Lu	0.22	0.08		0.08	0.07		1.10	1.06	
Hf	1.48	1.18		0.67	0.54		1.24	1.09	
Ta	0.91	0.49		0.06	0.06		0.73	0.77	
Pb	0.93	0.85		0.53	0.27		2.24	1.46	
Th	0.18	0.08		0.12	0.06		1.37	0.51	
U	0.05	0.04		0.04	0.02		0.37	0.20	
⁸⁷ Rb/ ⁸⁶ Sr	0.005	0.003						0.430	
⁸⁷ Sr/ ⁸⁶ Sr	0.703563	0.703504	0.703501		0.702898	0.702877		0.711093	0.711893
2σ (m)	0.000008	0.000008	0.000008		0.000008	0.000008		0.000014	0.000034
*	0.705144	0.704652			0.705095			0.708913	
	0.000007	0.000008			0.000010			0.000007	
¹⁴⁷ Sm/ ¹⁴⁴ Nd	0.225	0.199			0.204			0.229	
¹⁴³ Nd/ ¹⁴⁴ Nd	0.512946	0.512890			0.512970			0.512932	
2σ (m)	0.000005	0.000006			0.000008			0.000005	
²³⁸ U/ ²⁰⁴ Pb	3.7	2.8			4.7			10.6	
²³² Th/ ²⁰⁴ Pb	12.5	6.6			14.4			40.7	
²⁰⁶ Pb/ ²⁰⁴ Pb	18.95	18.69	18.55		18.74	18.74		19.08	22.71
*	19.67	19.46			18.89			20.49	
²⁰⁷ Pb/ ²⁰⁴ Pb	15.63	15.49	15.60		15.56	15.56		15.83	15.99
*	15.70	15.69			15.66			15.86	
²⁰⁸ Pb/ ²⁰⁴ Pb	38.53	40.09	38.27		38.63	38.62		38.77	42.16
*	39.06	38.99			38.80			42.96	

Note: X-ray fluorescence (XRF) data are on unleached whole rock (wr) samples in wt%. Mineral separates (hbl—hornblende; cpx—clinopyroxene; pl—plagioclase) have not been analyzed for major elements. Inductively coupled plasma–mass spectrometry (ICP-MS) analyses and isotope ratios are on leached (leach.) sample powders. Sr and Pb isotope ratios of leachates from most samples and three ICP-MS analyses on unleached (unl.) samples are also shown. Other abbreviations: unmag.—unmagnetic fraction of sample BD31; LOI—loss on ignition; nd—not detected.

*Leachate.

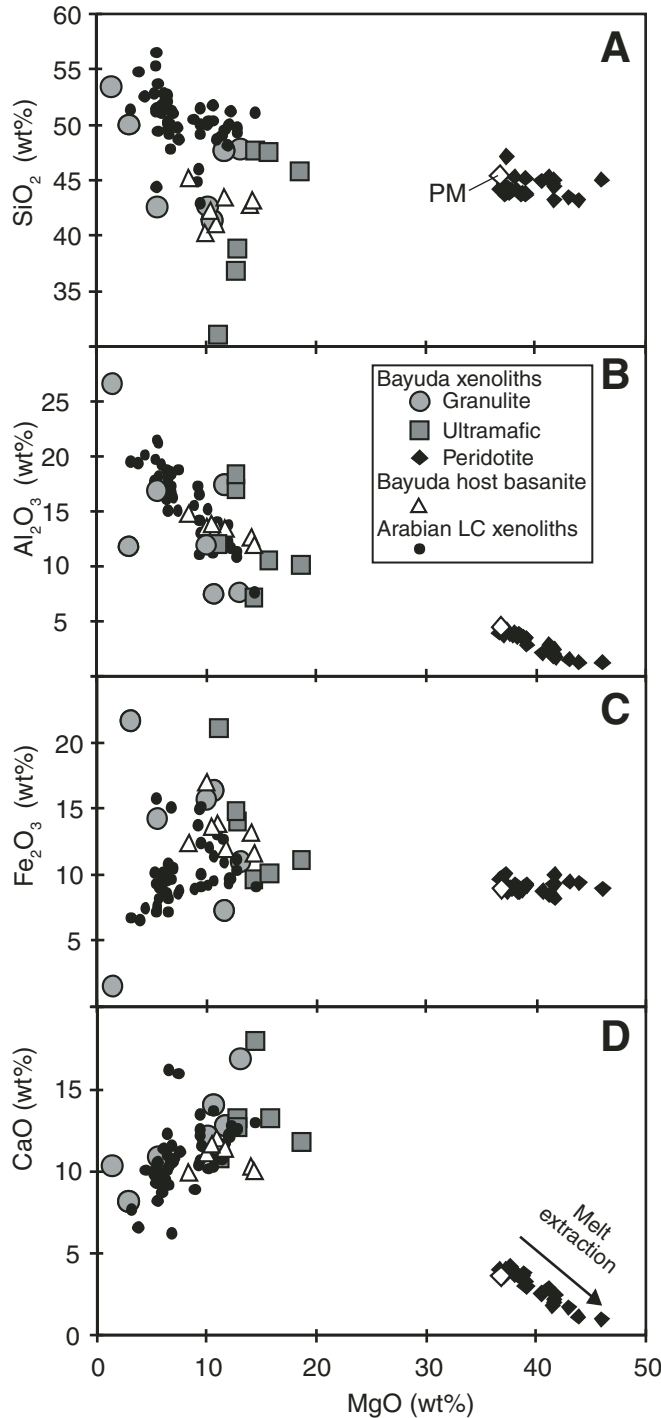


Figure 3. Major-element compositions of the Bayuda ultramafic and granulite xenoliths compared with the compositions of their host basanite (Lucassen et al., 2008a), peridotite xenoliths from the same suite (Lucassen et al., 2008b), and lower-crust (LC) xenoliths from the Arabian plate (McGuire and Stern, 1993; Al-Mishwat and Nasir, 2004). The compositions of ultramafic xenoliths and host basanite show no systematic relations with respect to MgO contents. Most Arabian meta-igneous xenoliths are compositionally more evolved than the Bayuda ultramafic and granulite xenoliths. The compositions of Bayuda peridotite xenoliths follow the melt extraction path from primitive mantle (PM; Sun and McDonough, 1989).

relative depletion of Eu, and BD31 has high garnet contents with slightly elevated HREE (heavy REE; Fig. 4D).

Sr-Nd-Pb Isotope Data

Results of Whole-Rock Leaching

Rock powders used for isotope measurements were leached in warm double-distilled 2 N HCl and mineral separates in hot 7 N HNO₃ for 30 min and washed three times with ultraclean H₂O in an ultrasonic bath. This leaching should remove possible impurities on grain boundaries and from easily soluble minerals, which could have been influenced by late-stage fluid-rock interaction or weathering. Sr and Pb isotope ratios of leached samples and leachates of selected samples are presented in Table 3 and discussed in the following. Nd isotopes in the leachates could not be determined because Nd contents were too low. This implies that the Nd isotope ratios were not changed by weathering. Three of the leached rock powders (BD72, BD98, and BD31) were also analyzed for trace elements. Leached and unleached samples do not show systematic and significant differences in their trace-element contents and patterns (Table 3; Fig. DR2). Therefore, they are not discussed separately.

The relationships between the individual samples and their leachates are described in the ⁸⁷Sr/⁸⁶Sr–Pb isotope compositional space (Fig. 5). Leachates of all but two samples show substantially more radiogenic ⁸⁷Sr/⁸⁶Sr than the leached samples and ²⁰⁶Pb/²⁰⁴Pb in the range of the host basanite. The ⁸⁷Sr/⁸⁶Sr value in the granulite rocks is slightly more radiogenic than in many samples of the ultramafic group, but the compositional range of the leachates is indistinguishable. The four feldspar separates and the respective leached samples of the granulite group have near-identical ⁸⁷Sr/⁸⁶Sr ratios. The variation of Pb isotope ratios in the leached samples is considerable, but the ranges in the leachates are small ²⁰⁶Pb/²⁰⁴Pb 19.4–19.9, ²⁰⁷Pb/²⁰⁴Pb around 15.7, and ²⁰⁸Pb/²⁰⁴Pb around 39 (Fig. 5). The Pb isotope ratios of feldspar separates are moderately (two samples) or substantially (one sample) lower than in the leached whole-rock samples; the Pb isotope compositions of feldspar and whole rock of sample BD98 are near-identical.

The leachate of sample BD31 (not shown in Fig. 5) shows relatively unradiogenic ⁸⁷Sr/⁸⁶Sr of ~0.70891, compared to 0.71109 in the leached sample. Pb isotope ratios of the leachate are more radiogenic than in the leached sample, with ²⁰⁶Pb/²⁰⁴Pb of 20.48 versus 19.08 and ²⁰⁸Pb/²⁰⁴Pb of 42.96 versus 38.77, or values are similar, with ²⁰⁷Pb/²⁰⁴Pb of 15.85 versus 15.82. Sample BD31 indicates the preferred dissolution of a Th (and minor U)–rich mineral, likely apatite, by the leaching procedure. This is supported by the radiogenic Pb isotope composition (22.71; 15.99; 42.16) of the nonmagnetic fraction, which is mostly quartz and some apatite.

Except for sample BD31, the differences in mineralogy between the samples and sample groups preclude the dominance of preferred dissolution of possible inherited high ⁸⁷Sr/⁸⁶Sr (e.g., an easily soluble high Rb/Sr mineral) or ²⁰⁶Pb/²⁰⁴Pb minerals (e.g.,

an easily soluble high U/Pb and Th/Pb mineral) in the isotope signature of the leachates. The source of the leachate signature is likely external. Infiltrating melt or fluid from the host basanite is precluded by the radiogenic Sr isotope signature and by the comparable radiogenic $^{207}\text{Pb}/^{204}\text{Pb}$ and unradiogenic $^{208}\text{Pb}/^{204}\text{Pb}$ signatures of the leachate (Fig. 5). Further, features of invading melts were not observed in the thin sections. Therefore, meteoric fluids likely imprinted their isotopic signature onto the leachates. The leaching sampled the thin coating of grains, i.e., secondary deposits on the open grain boundaries. The Pb isotope composition of the leachate is dominated by the crustal signature (average Bayuda basement: $^{87}\text{Sr}/^{86}\text{Sr}$ of 0.739 and Pb isotope composition of 19.72, 15.80, 39.61; Küster et al., 2008), likely from meteoric fluids circulating through the weathered basement. The Sr isotope signature of the leachate likely represents a mixture of crustal signature and original signature of the xenoliths (Fig. 5). The following observations support the validity of this assumption. Samples of different mineralogy, isotope composition, and possibly different age show similar leachate composition. Feldspar separates reproduce the Sr isotope compositions of the leached samples but have less radiogenic or similar Pb isotope compositions. In summary, we believe that the isotope signa-

ture of the leached whole-rock samples is representative for the unweathered samples.

Sr and Nd Isotopes

All granulite and ultramafic xenoliths have a narrow range of Sr isotope ratios near 0.7035, except sample BD31, which is more radiogenic (Table 3; Fig. 6). All xenoliths except BD31 have $^{87}\text{Rb}/^{86}\text{Sr} < 0.07$ (Table 3). Nd isotope ratios are variable between bulk solid earth and depleted-mantle composition. Sr and Nd isotopes of the ultramafic xenoliths are negatively correlated. Nd isotope ratios of all but one (BD59) sample of the granulite group are similar or slightly more radiogenic than in the ultramafic xenoliths. Sr isotope ratios of most granulite samples are more radiogenic than the ultramafic samples (Fig. 6A). Sample BD59 has a relatively unradiogenic Nd isotope ratio but the Sr isotope ratio is also unradiogenic.

Pb Isotopes

Pb isotope ratios of all but two ultramafic xenoliths plot tightly around the composition of their host basanite (Fig. 7). The two deviating samples (C39, C25; Fig. 7) have less radiogenic $^{206}\text{Pb}/^{204}\text{Pb}$ isotope ratios and plot into the compositional range of granulite xenoliths and feldspar separates of the latter.

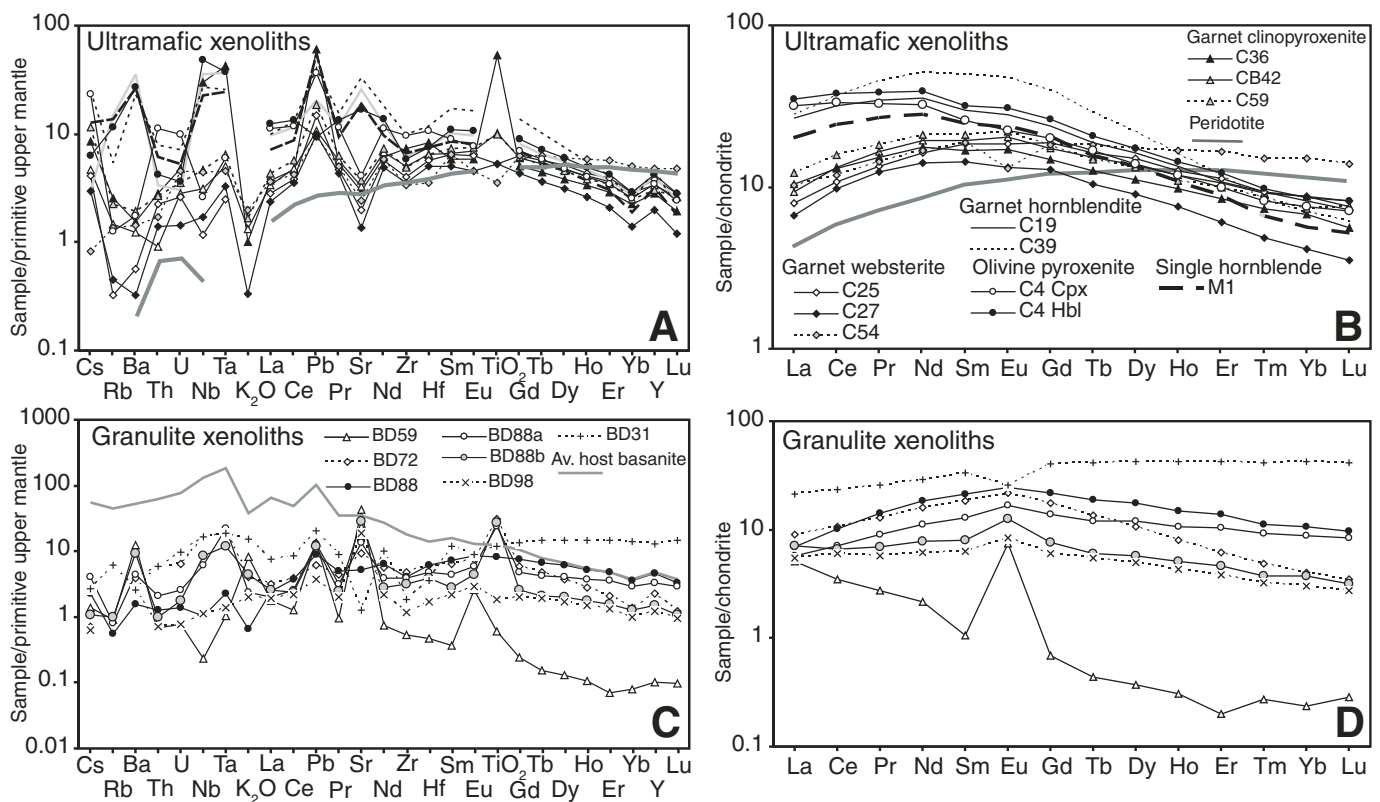


Figure 4. Trace-element composition of the ultramafic (A, B) and granulite (C, D) xenoliths. The composition of the average host basanite (C) is not related to the composition of the granulite xenoliths. (A, B) The element distribution pattern of a clinopyroxene from a typical peridotite xenolith from the same suite is shown for comparison (Lucassen et al., 2008b). Primitive mantle—Sun and McDonough (1989); C1 chondrite—McDonough and Sun (1995).

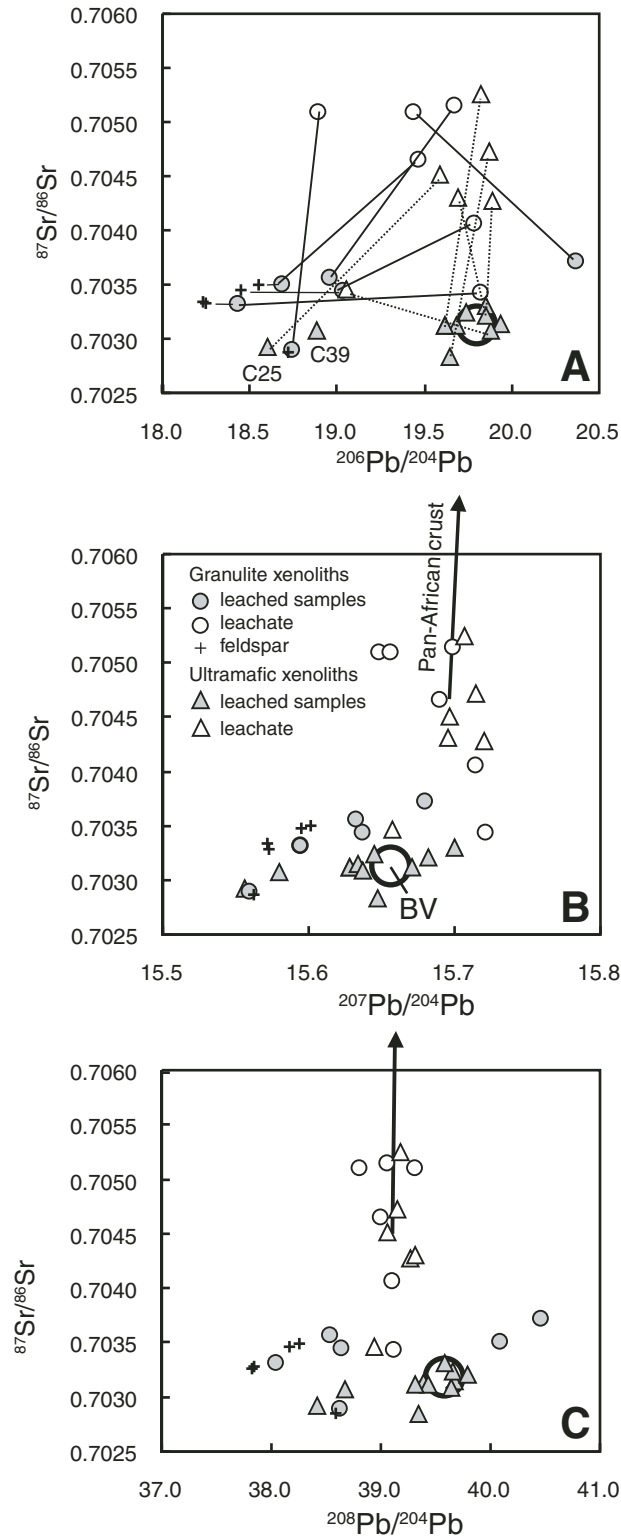


Figure 5. Sr and Pb isotope composition of leached ultramafic and granulite xenoliths, their leachate, and feldspar from granulite xenoliths compared to the composition of the host basanites (BV; Lucassen et al., 2008a). (A) Lines connect sample and respective leachate, and feldspars and respective whole-rock samples. (B, C) The composition of the average Bayuda upper Pan-African crust (Küster and Liégeois, 2001; Küster et al., 2008) is far off the diagram, indicated by the arrow between the field of leachate compositions and average Bayuda. For discussion see text.

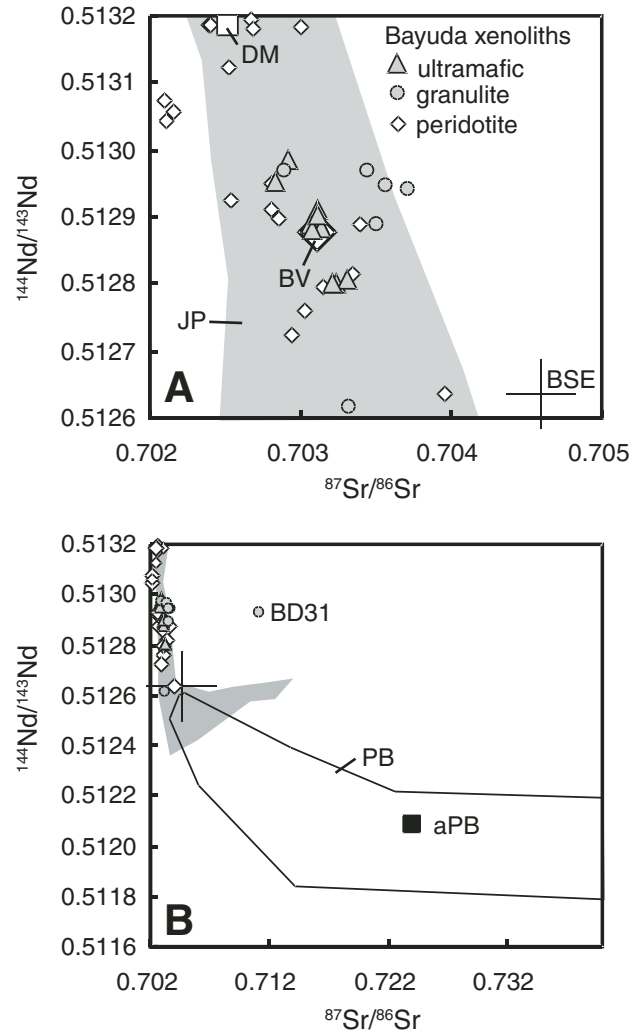


Figure 6. Present-day Sr and Nd isotope composition of (A) the Bayuda xenoliths compared to the juvenile Pan-African basement (JP), Bayuda host volcanic rocks of the xenoliths (BV), and (B) the Bayuda Neoproterozoic basement (PB; aPB—average Bayuda Neoproterozoic basement). Sample BD31 is a granulite xenolith of special composition (see text). The field of the Bayuda peridotite xenoliths and juvenile Neoproterozoic basement (gray area) extends to more radiogenic $^{144}\text{Nd}/^{143}\text{Nd}$ ratios than average depleted mantle (up to ~0.5138); the field of the Bayuda Neoproterozoic basement extends to more radiogenic $^{87}\text{Sr}/^{86}\text{Sr}$ ratios, up to ~0.8. Data sources: Juvenile Neoproterozoic basement (Brueckner et al., 1988, 1995; Zimmer et al., 1995; Stern and Abdelsalam, 1998; Teklay et al., 2002; Bailo et al., 2003); Bayuda basement (Küster and Liégeois, 1998; Küster et al., 2008); Bayuda peridotite xenoliths (Lucassen et al., 2008b); Bayuda volcanic rocks (Lucassen et al., 2008a); average depleted mantle (DM; e.g., Workman and Hart, 2005); bulk silicate earth (BSE; e.g., Zindler and Hart, 1986).

Granulite sample BD72 has a radiogenic Pb isotope composition; sample BD31 is very radiogenic in $^{207}\text{Pb}/^{204}\text{Pb}$ (~15.83); and sample BD59 has radiogenic $^{208}\text{Pb}/^{204}\text{Pb}$ at given $^{206}\text{Pb}/^{204}\text{Pb}$ values (Fig. 7). The Pb isotope ratios of all other samples from both groups are situated near the Northern Hemisphere reference line (NHRL). Isotope ratios of clinopyroxene from the matrix and hornblende from veins in sample C4 are near-identical within their error ranges (Table 3).

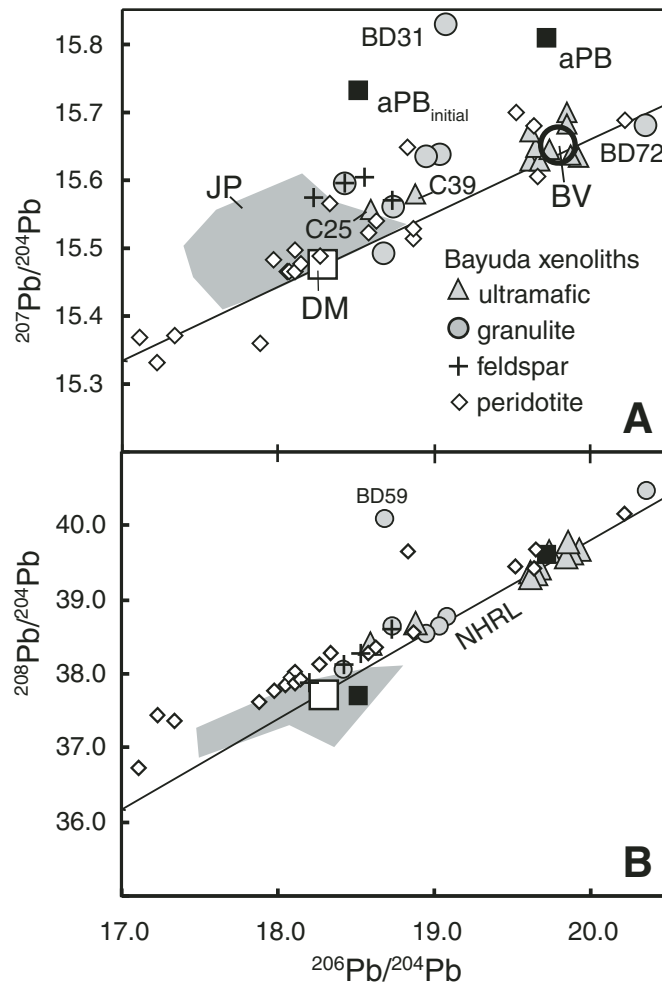


Figure 7. (A, B) Present-day whole-rock and feldspar Pb isotope composition of the Bayuda xenoliths, compared to the juvenile Neoproterozoic basement (JP) represented by ophiolite compositions (Brueckner et al., 1988, 1995; Zimmer et al., 1995), Bayuda host volcanic rocks of the xenoliths (BV), and the average Bayuda Neoproterozoic basement (aPB; aPB initial at 800 Ma; Küster et al., 2008). The initial composition of this basement could approximate the composition of Neoproterozoic U-depleted sections of reworked old cratonic crust in the deeper crust. The high $^{207}\text{Pb}/^{204}\text{Pb}$ ratio at given $^{206}\text{Pb}/^{204}\text{Pb}$ is attributed to an old, Archean? to Paleoproterozoic high- μ ($^{238}\text{U}/^{204}\text{Pb}$) component in the cratonic crust. The $^{206}\text{Pb}/^{204}\text{Pb}$ ratios of some Bayuda peridotite xenoliths are as low as ~16 (not shown) and indicate the presence of old depleted mantle (DM) in the lithosphere. For data sources, see Figure 6. NHRL—Northern Hemisphere reference line.

DISCUSSION

Thermobarometry

Interpretation of the mineral chemistry in terms of equilibrium temperatures and pressures is aimed at the comparison within the different xenoliths groups. A joint interpretation of metamorphic conditions in the granulite and ultramafic xenoliths is not possible. The granulite xenoliths likely represent Neoproterozoic crystallization conditions, whereas the ultramafic xenoliths are late Mesozoic to Quaternary (see following discussion of the isotope data). Chemical equilibrium between the minerals was likely attained at one point of their evolution. This is indicated by the fabrics and the large compositionally homogeneous cores. Compositional zoning of minerals only occurs in the small outermost rims of clinopyroxene, and compositional variations between core and outer rim in orthopyroxene are even less pronounced. Rim analyses are not available for garnet crystals, which are surrounded by a kelyphite rim. Therefore, we use only average core compositions (Table 2) for all minerals.

Temperatures are estimated from clinopyroxene-garnet thermometry (Table 1; Ellis and Green, 1979). In absence of the measured state of oxidation of Fe, we made two calculations of T : (1) assuming all Fe in the clinopyroxenes and garnets as Fe^{2+} and (2) using calculated Fe^{2+} from charge balance. Fe^{3+} in the garnet was calculated in two ultramafic xenoliths (C25 ~4%, C27 ~6% of Fe total). In clinopyroxenes, calculated Fe^{3+} is variable (ultramafic xenoliths ~7–29%, two granulite xenoliths ~5 and 7% of Fe total). Reliable pressure estimates are not possible with the mineral paragenesis, and we considered a pressure of 1.0 GPa for all temperature calculations in Table 1. The assumed error on the pressure of 0.5 GPa includes the lower crust and uppermost mantle realm and introduces an error of approximately ± 20 °C on the temperatures calculated at 1 GPa. Temperatures for the three granulite samples are 880, 860 (840 Fe^{2+} calculated), and 920 °C (890). The variation in the ultramafic xenoliths is larger, at 880–1030 °C (850–950 °C), with the lower temperatures at 880–940 °C (850 °C) in the garnet-websterites and the higher temperatures at 1030 °C (890–950 °C) in the garnet-pyroxenites.

The ultramafic xenoliths, garnet-websterite, and garnet-pyroxenite show compositional relations with the young high- μ magmatism and likely represent cumulates of the latter at the crust mantle-boundary, i.e., in the lowermost crust or uppermost mantle (see following discussion). Thermometry in the peridotite xenoliths (garnet-free spinel ilherzolite) from the same suite yielded a temperature range of 760–1190 °C (most samples between 800–960 °C; Lucassen et al., 2008b), which is similar to the temperature range in the ultramafic xenoliths (Table 1). Their pressure conditions could not be estimated, but the peridotite xenoliths include some samples with fertile compositions, and the garnet-in reaction for the given temperatures would be between ~1.5 and 1.7 GPa (e.g., Green and Ringwood, 1967; O'Neill, 1981).

Chemical Composition

Ultramafic Xenoliths

The major-element compositions of the basanites and ultramafic xenoliths are not systematically related (Fig. 3). The MgO contents and Mg# of the basanites (Mg# 54–71; average 62) and xenoliths (Mg# 51–77; average 67) are similar. The Mg contents and Mg# of the pristine basanitic melt likely were higher, considering possible olivine fractionation (Lucassen et al., 2008a). SiO_2 , Al_2O_3 , Fe_2O_3 , CaO, and TiO_2 contents of the xenoliths show considerably broader scatter than respective contents of the basanites (Fig. 3; Table 3). The high Ti and Fe and low SiO_2 contents (Table 3) of sample C36 reflect the accumulation of ilmenite. Major-element compositions of the ultramafic xenoliths are not coherent, in contrast to the peridotite xenoliths of the same suite, which document in their compositions variable proportions of melt extraction from a fertile mantle (Fig. 3; Lucassen et al., 2008b).

The trace-element abundance in the ultramafic xenoliths is variable, but the element distribution patterns of the garnet-pyroxenite and garnet-websterite are similar (Fig. 4). Those of the garnet-hornblendite, hornblende megacrystal, and hornblende-bearing pyroxenite are different, and specifically Rb, Ba, Th, U, Nb, Ta, Pb, and Sr are higher than in most pyroxenites and websterites. U, Th, and Pb are higher in the clinopyroxene than in the coexisting hornblende from veins in sample C4, which are both very similar in their isotope composition (Table 3). Trace-element patterns of ultramafic xenoliths are different from the patterns of peridotite xenoliths of the same suite, which mostly show a strong systematic depletion of the incompatible trace elements (Fig. 4). Hypothetical liquids in equilibrium with the average trace-element abundances of the pyroxenite and websterite, and with the most depleted websterite (sample C27), were calculated assuming a control of most trace elements in the ultramafic xenoliths by clinopyroxene (Fig. 8). Despite the uncertainty in the application of experimental and calculated distribution coefficients to natural systems, the calculations show that the ultramafic xenoliths are compatible with an origin from liquids similar to the host basanites.

Granulite Xenoliths

Compared to data from lower-crust xenoliths from the Arabian plate (McGuire and Stern, 1993; Al-Mishwat and Nasir, 2004), the major-element composition of the Bayuda xenoliths is less evolved (Fig. 3). The granulite xenoliths represent metamorphosed cumulates, but they are apparently not related to fractionation of any single magma.

The trace-element patterns of the granulite xenoliths (Fig. 4) are variable, and similarities between the samples are restricted to positive Pb (all samples), Sr (all samples except BD31 and 88), and Ti spikes (samples BD88a, BD88b, and BD72). High heavy REE content in BD31 is attributed to the abundant garnet. The trace-element pattern of BD59 reflects the high plagioclase contents of a cumulate. There is no relation between the trace-

element pattern of the host basanite and these granulite rocks, which crystallized in the plagioclase stability field.

Isotopic Composition: Source and Time Constraints

In NE Africa and Arabia, four regionally important compositional reservoirs have been distinguished on the base of their isotope composition. (1) Neoproterozoic reworked old cratonic crust has variable but generally unradiogenic Nd and radiogenic Sr isotope composition (Fig. 6) and a distinct Pb isotope signature (radiogenic $^{207}\text{Pb}/^{204}\text{Pb}$ at given $^{206}\text{Pb}/^{204}\text{Pb}$; Fig. 7A), the latter of which is due to the contribution of old, Paleoproterozoic or Archean high- μ sources of the craton (e.g., Kröner et al., 1987; Stern and Kröner, 1993; Stern, 1994; Küster and Harms, 1998; Küster and Liégeois, 2001; Küster et al., 2008; Stoesser and Frost, 2006). (2) The juvenile Neoproterozoic basement represents melts from the contemporaneous asthenosphere, i.e., represents isotopic compositions of depleted mantle, plus variable contributions from reworked old cratonic crust in magmatic arc settings (Figs. 6 and 7; e.g., Altherr et al., 1990; Brueckner et al., 1995; Zimmer et al., 1995; Stern and Abdelsalam, 1998; Teklay et al., 2002; Bailo et al., 2003; Stoesser and Frost, 2006). (3) The late Mesozoic and younger NE African intraplate magmatism is characterized by radiogenic Pb isotope compositions (Fig. 7) and Nd and Sr isotope compositions in

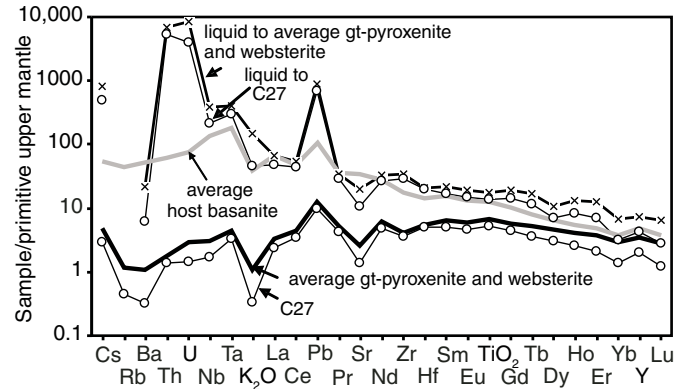


Figure 8. Trace-element content of modeled liquids in equilibrium with the average garnet pyroxenite and websterite and garnet (gt) websterite sample C27. Element distribution coefficients between clinopyroxene and basaltic liquid are from Hart and Dunn (1993) and McKenzie and O'Nions (1991). The trace-element patterns of the calculated liquids, especially of the liquid to sample C27, are similar to the patterns of the host basanite, except for some of the more incompatible elements like U and Th. The prominent U and Th peak in the calculated liquid depends (as the concentration of the other elements) on the chosen distribution coefficients: those of McKenzie and O'Nions (1991) are at the lower end of the range of published values for U and Th, which vary by up to two orders of magnitude (compilation for clinopyroxene/basalt at the Geochemical Earth Reference Model Web site <http://www.earthref.org/GERM>). Sample C36, which has >30 vol% opaque minerals and shows pronounced relative enrichment of Nb, Ta, Pb, and Ti, was excluded from the calculation of the average garnet pyroxenite and websterite.

the field of depleted mantle composition (Fig. 6), which are believed to originate from the lithospheric mantle modified during Neoproterozoic (e.g., Altherr et al., 1990; Stein et al., 1997; Bertrand et al., 2003; Shaw et al., 2003, 2007; Lucassen et al., 2008a, 2008b). Their Pb isotope composition resembles the field of high- μ ($\mu = {}^{238}\text{U}/{}^{204}\text{Pb}$) ocean-island basalts (OIB) of the focal zone type (sensu Stracke et al., 2005). (4) Composition of the present asthenospheric convective mantle is known from late Cenozoic magmatism along the divergent plate boundary along the Red Sea–Gulf of Aden rift (Fig. 1A; e.g., Altherr et al., 1990; Volker et al., 1993, 1997; Schilling et al., 1992). The isotope composition of this reservoir resembles present average depleted mantle (Figs. 6 and 7; e.g., Salters and Stracke, 2004; Workman and Hart, 2005). This reservoir did not substantially contribute to the intraplate magmatism in NE Africa (Lucassen et al., 2008a).

Ultramafic Xenoliths

Sr isotope ratios of seven samples are within the compositional range of the host basanite, and the others plot close to the basanite field (Fig. 6). The ${}^{87}\text{Sr}/{}^{86}\text{Sr}$ ratio of the xenoliths is more radiogenic than average depleted mantle (Fig. 6). The ${}^{87}\text{Rb}/{}^{86}\text{Sr}$ ratio (0.02–0.07; Table 3) in the xenoliths are similar or slightly higher than assumed for average depleted mantle (Salters and Stracke, 2004; Workman and Hart, 2005) and do not explain the observed ${}^{87}\text{Sr}/{}^{86}\text{Sr}$ by radiogenic growth after separation from depleted mantle, e.g., in Neoproterozoic (ca. 800 Ma). The ${}^{143}\text{Nd}/{}^{144}\text{Nd}$ ratios of two xenolith samples are slightly more and, for another three samples, slightly less radiogenic than the very

uniform host basanite (Figs. 6 and 9). All xenoliths show considerably less radiogenic ${}^{143}\text{Nd}/{}^{144}\text{Nd}$ than average depleted mantle. The ${}^{147}\text{Sm}/{}^{144}\text{Nd}$ ratios in the ultramafic xenoliths are higher than in the host basanite and lower, similar, or higher than in average depleted mantle, but they show no correlation with ${}^{143}\text{Nd}/{}^{144}\text{Nd}$ (Fig. 9). The ${}^{147}\text{Sm}/{}^{144}\text{Nd}$ ratio similar or higher than in average depleted mantle is mismatched with the comparable unradiogenic ${}^{143}\text{Nd}/{}^{144}\text{Nd}$. The latter requires a prolonged evolution with low ${}^{147}\text{Sm}/{}^{144}\text{Nd}$ in an enriched mantle.

Pb isotope ratios of all samples, except C25 and C39, are closely related to the radiogenic Pb isotope ratios of their host basanite (Figs. 7 and 10). U–Pb isotope ratios and μ -ratios are not related, and the data fall on the trend defined by the host basanite, which shows variable μ ratios and uniform Pb isotope compositions (Fig. 10; Table 3). The μ ratios of the ultramafic xenoliths are much too low (all but one are <8 , the ratio assumed for depleted mantle evolution) to explain the radiogenic Pb isotope composition by in situ growth at any time-scale. Again, a prolonged evolution in an enriched mantle is required. Pb isotope compositions of clinopyroxene and amphibole in sample C4 are very similar despite higher U/Pb and Th/Pb in the amphibole (Table 3). Ancient, e.g., Neoproterozoic, variations in Sm/Nd and U/Pb should cause systematic variations in the related isotope compositions. This is not the case, and we conclude that these xenoliths formed at a time close to their host basanite.

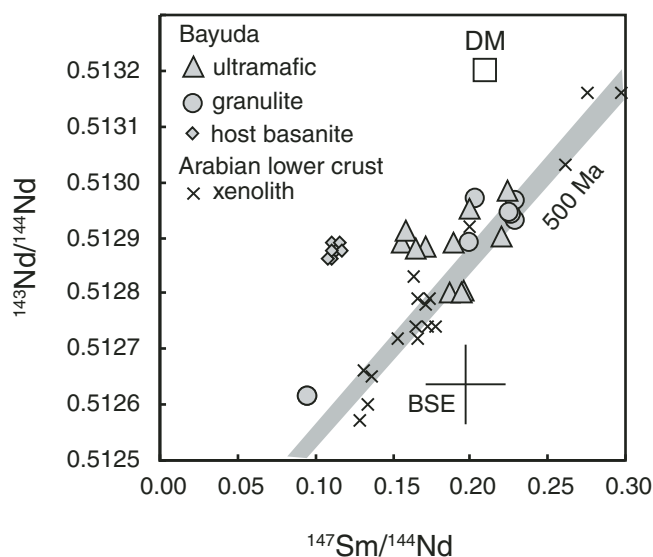


Figure 9. Relations between ${}^{147}\text{Sm}/{}^{144}\text{Nd}$ and ${}^{143}\text{Nd}/{}^{144}\text{Nd}$ of the Bayuda xenoliths and their host basanite (Lucassen et al., 2008a) compared to lower-crust xenoliths from Arabia (McGuire and Stern, 1993). The Arabian xenoliths align to a 500 Ma reference line. DM—depleted mantle; BSE—bulk silicate earth.

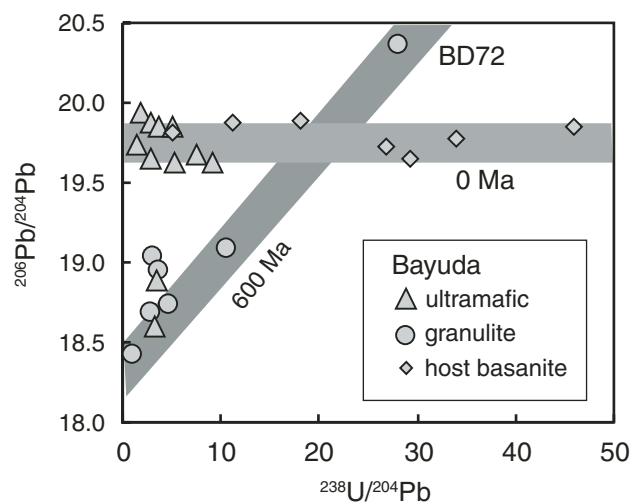


Figure 10. Relations between ${}^{238}\text{U}/{}^{204}\text{Pb}$ and ${}^{206}\text{Pb}/{}^{204}\text{Pb}$ of the Bayuda xenoliths and their host basanite (Lucassen et al., 2008a). All granulite except sample BD72 show unradiogenic ${}^{206}\text{Pb}/{}^{204}\text{Pb}$ compared to the signature of most ultramafic xenoliths and all host basanite. The ratios of some granulite xenoliths align to a 600 Ma reference line (mainly defined by sample BD72), and the high- μ Pb isotope signature of granulite BD72 could be also interpreted as a high- ${}^{238}\text{U}/{}^{204}\text{Pb}$ sample of Neoproterozoic age with an initial Pb isotope signature similar to the other granulite. The ratios of ultramafic xenoliths and host basanite are not correlated (0 Ma reference line).

Granulite Xenoliths

Sr isotope ratios in granulite xenoliths (5 of 7) are slightly more radiogenic at similar or slightly more radiogenic $^{143}\text{Nd}/^{144}\text{Nd}$ ratios (6 of 7 samples) than in host basanite and ultramafic xenoliths (Fig. 6A). The $^{207}\text{Pb}/^{204}\text{Pb}$ ratios of five granulite samples and C25 and C39 are distinctly lower than of the average reworked cratonic basement of the Bayuda area. Their Pb isotope ratios are distinctly less radiogenic than those of ultramafic xenoliths and the host basanites (Fig. 7A). They plot between the composition of the latter and the field defined by Neoproterozoic ophiolite, which plots around average depleted mantle composition (Fig. 7). Sr and Nd isotope compositions of most granulite xenoliths and Neoproterozoic juvenile basement are similar or overlap (Figs. 6 and 9). Nd isotope compositions of the granulite xenoliths and xenoliths from the juvenile Arabian lower crust overlap, but the latter show a much broader Nd isotope compositional range and a rough alignment with their $^{147}\text{Sm}/^{144}\text{Nd}$ around a 500 Ma reference line (Fig. 9; McGuire and Stern, 1993). Five granulite xenoliths have very similar high $^{147}\text{Sm}/^{144}\text{Nd}$, ranging from 0.225 to 0.229 (Fig. 9; Table 3). This range is above the value of average depleted mantle (0.214; Goldstein et al., 1984) and at odds with the low related $^{143}\text{Nd}/^{144}\text{Nd}$ ratios (~ 0.51289 – 0.51297 ; present-day depleted mantle $^{143}\text{Nd}/^{144}\text{Nd} \sim 0.5132$; Goldstein et al., 1984). Only sample BD59 has low $^{147}\text{Sm}/^{144}\text{Nd}$ (plagioclase-dominated REE pattern; garnet absent) and comparably unradiogenic $^{143}\text{Nd}/^{144}\text{Nd}$. All samples except BD31 ($^{87}\text{Rb}/^{86}\text{Sr} \sim 0.43$) show very low $^{87}\text{Rb}/^{86}\text{Sr}$ (< 0.08 ; Table 3) ratios, which are not correlated with the $^{87}\text{Sr}/^{86}\text{Sr}$ ratios. All Sr isotope ratios are considerably higher than average depleted mantle and cannot be explained by radiogenic growth from the $^{87}\text{Rb}/^{86}\text{Sr}$, not even for a Neoproterozoic age (ca. 800 Ma). The μ ratios in five of seven samples are below ~ 8 (Fig. 10; Table 3), which is the ratio assumed for the Pb isotope evolution of the depleted mantle. The $^{206}\text{Pb}/^{204}\text{Pb}$ ratios are moderately higher than in present average depleted mantle, and hence not in accordance with the low μ ratios.

Nd, Sr, and Pb isotope compositions of the granulite xenoliths indicate similarity with the composition of Neoproterozoic juvenile rocks. However, Sm/Nd, Rb/Sr, and U/Pb of the granulite xenoliths are at odds with the related isotope ratios and preclude a single-stage evolution from magmatic crystallization. Two explanations for the mismatch of elemental and isotope composition are given, both of which likely contributed to the observed variations in the isotope compositions.

The first explanation suggests that the parent-daughter pairs of the Rb-Sr, U-Pb, and Sm-Nd isotope systems were changed from variable but initially high Rb/Sr and U(Th)/Pb and low Sm/Nd ratios by depletion of the incompatible elements Rb, U, and Nd. This could have happened a considerable time (> 100 m.y.) after crystallization from Neoproterozoic juvenile magma by melt extraction from the meta-igneous rocks. The high temperatures in the lower crust required for melting were reached during several stages of metamorphism and granitoid magmatism between ca. 920 and 560 Ma in the Bayuda and

surrounding Neoproterozoic basement (e.g., Stern and Kröner, 1993; Küster and Harms, 1998; Küster and Liégeois, 2001; Küster et al., 2008). A (late) Neoproterozoic age is preferred, because the isotope compositions of these xenoliths show strong affinities to the juvenile Neoproterozoic basement. A possible Mesozoic to Holocene high-temperature regime in the lower crust would be likely linked to the small-volume high- μ intraplate magmatism. This should have compositional consequences for the intruded region. The radiogenic Pb-isotope (high- μ) signature in the granulite sample BD72 could indicate such an influence, but this sample also has high U/Pb and Th/Pb ratios, which allow an interpretation of the radiogenic Pb isotope signature by the assumption of a Neoproterozoic age of the last reset of the U-Pb system (Fig. 10).

The second explanation suggests that isotopic heterogeneity was acquired by mixing of compositionally different sources. Source contamination of magmatic arc magmas is a common phenomenon (e.g., Hildreth and Moorbath, 1988) and could occur in the mantle source of such rocks by subducted material or during magmatic evolution of the mantle-derived magma in the crust. Reworked old cratonic basement is an important constituent of the crust in the Bayuda area (Küster and Liégeois, 2001; Küster et al., 2008, and references therein). A small contribution of such basement could be inferred from the Sr-Pb isotope relation in some granulite xenoliths. The $^{87}\text{Sr}/^{86}\text{Sr}$ and $^{207}\text{Pb}/^{204}\text{Pb}$ ratios (less pronounced for other Pb isotope ratios) are correlated in the granulite xenolith whole-rock samples and related feldspars (Fig. 5). Such small contributions could induce initial isotope heterogeneity to granulite xenoliths

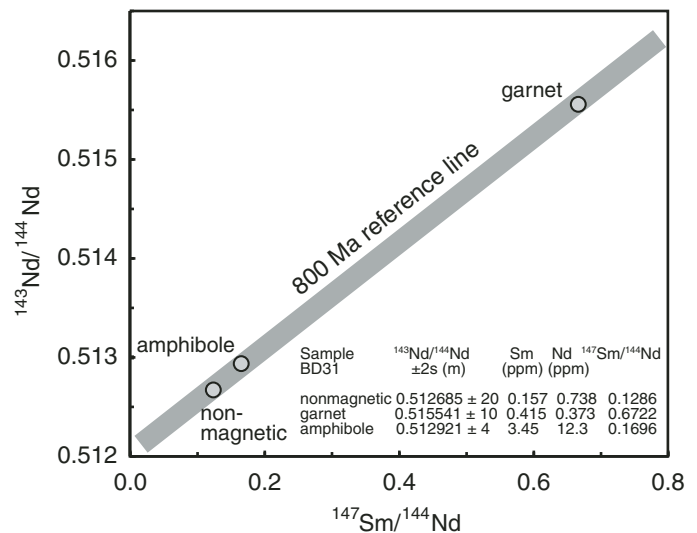


Figure 11. Sm-Nd isotope compositions of garnet, amphibole, and the nonmagnetic fraction of sample BD31. For data, see inset; Sm and Nd contents were determined by isotope dilution. The data align to a 800 Ma reference line and indicate a possible Neoproterozoic crystallization age.

during their magmatic evolution. Sample BD31 illustrates the complexity of the possible crustal interaction. Sm-Nd isotope composition of garnet, amphibole, and the nonmagnetic fraction (mainly apatite) align to a 800 Ma reference line (Fig. 11) and indicate a possible Neoproterozoic age of crystallization. The Pb isotope composition of this sample resembles the “old high- μ ” signature, i.e., the radiogenic $^{207}\text{Pb}/^{204}\text{Pb}$ of the reworked Archean (?) to Paleoproterozoic cratonic crust (Fig. 7). It also has radiogenic $^{87}\text{Sr}/^{86}\text{Sr}$ (800 Ma) of 0.7063 (Fig. 6), but the ϵ_{Nd} (800 Ma) of +2.5 indicates the contribution of juvenile material to this rock. Contamination of juvenile Neoproterozoic material would require an agent with high Sr (and Pb) and very low Nd contents and the isotope signature of the cratonic basement. Anomalous radiogenic Sr and relatively radiogenic Nd isotope ratios are known from other Neoproterozoic (meta)igneous rocks (Fig. 5B).

In summary, the isotope compositions distinguish clearly between two different xenoliths groups. The ultramafic xenoliths show a strong relation to the composition of the host basanite, and their isotope composition indicates a young evolution for the ultramafic xenoliths (latest Mesozoic or younger). The granulite xenoliths resemble the composition of juvenile Neoproterozoic crust, and their isotope compositions indicate an early Paleozoic or older compositional evolution.

Origin of the Ultramafic Xenoliths

The composition and origin of ultramafic rocks with pyroxene-dominated mineralogy in peridotite massifs and upper-mantle xenoliths suites have been investigated in field and experimental studies (e.g., Frey and Prinz, 1978; Frey, 1980; Kogiso et al., 2003; Keshav et al., 2004; Downes, 2007). High- P melting of pyroxenite was discussed as the possible source of alkaline ocean-island basalts (Frey, 1980; Kogiso et al., 2003; Keshav et al., 2004). Such melting would leave garnet-pyroxenite as residual in the source. The majority of pyroxenite in the mantle lithosphere is considered to be cumulates from basaltoid melts, however (for a recent review, see Downes, 2007).

Isotope composition does not unambiguously allow us to distinguish between a residual and cumulate origin of the pyroxenite. The major-element composition of the Bayuda ultramafic xenoliths and host basanite precludes a residue-melt relation between the xenoliths and the basanite (and other rocks of similar composition). The host basanites represent typical alkaline melts that are strongly enriched in trace elements (Fig. 5). The Mg# of the basanites is similar, or considering olivine fractionation, higher than in the ultramafic xenoliths. Experiments including variable degrees of melting of garnet-pyroxenite show however significantly lower Mg# in the melts than the pyroxenite residue (e.g., Kogiso et al., 2003, 2004; Keshav et al., 2004). The ultramafic xenoliths resemble features of cumulate xenoliths (group II xenoliths of Frey and Prinz, 1978), such as the variable and relatively low Mg num-

bers (~51–77; Table 3) and convex-upward REE distribution patterns (Fig. 4). Trace-element patterns of the ultramafic xenoliths require equilibrium with a melt reservoir strongly enriched in trace elements, comparable to the compositions of the host basanites (Fig. 8). Parent-daughter isotope ratios, e.g., those of the U-Pb isotope system, indicate a relatively young adjustment. The radiogenic Pb isotopes are distinctive in the regional compositional framework and indicate a close relationship of the ultramafic xenoliths and Mesozoic to Quaternary volcanic rocks (Lucassen et al., 2008a). In summary, we favor the interpretation of the ultramafic xenoliths as cumulates of the Mesozoic to Quaternary volcanism.

Lower Crust in the Bayuda Area as Part of the NE African Lithosphere

A tentative section through the lithosphere of the Bayuda area is based on the information from the Neoproterozoic metamorphic and magmatic rocks of the upper crust (Stern and Abdelsalam, 1998; Küster and Liégeois, 2001; Küster et al., 2008), lower-crust xenoliths from this study, intraplate magmatism (Lucassen et al., 2008a), and mantle xenoliths (Lucassen et al., 2008b), the latter two describing the mantle lithosphere (Fig. 12). The assumption of a crustal thickness of ~35 km is based on the long-term stability criteria of the Neoproterozoic erosion surface (e.g., Schandelmeier and Reynolds, 1997). The thickness of the thermal lithosphere is assumed to be ~120 km, which was proposed for the prerifting lithosphere of the Ethiopian plateau (Dugda et al., 2007). Such assumptions are reasonable considering the long period of tectonic quiescence after the Neoproterozoic orogeny in this section of the Nubian-Arabian Shield. Any thick Paleozoic and/or Mesozoic sedimentary cover, which occurs elsewhere in Africa and Arabia in intracratonic basins related to lithospheric extension (e.g., Bumby and Guiraud, 2005; Bosworth et al., 2005), is absent in the Bayuda area (Schandelmeier and Reynolds, 1997). The Bayuda area is also not affected by the formation of Cenozoic rift-related basins, which are restricted to the Red Sea rift and its margins (e.g., Bosworth et al., 2005).

Upper Crust

Reworked cratonic material dominates in the upper crust of the Bayuda and nearby areas. This basement consists of metasedimentary and meta-igneous metamorphic rocks and abundant granitoid intrusions (Küster and Liégeois, 2001; Küster et al., 2008, and references therein). Anatexis of felsic crustal rocks and granulite facies mark the peak metamorphic conditions in the midcrust during the Neoproterozoic orogen and reworked old cratonic basement with distinct isotope signatures (e.g., Kröner et al., 1987; Küster and Liégeois, 2001; Küster et al., 2008). Hybrid rocks, mixtures between cratonic and juvenile material of variable Neoproterozoic ages, are also present, especially visible in the Sr-Nd isotope signatures toward the depleted mantle array (Fig. 6B; e.g., Stern and

Abdelsalam, 1998; Küster and Liégeois, 2001; Küster et al., 2008, and references therein).

Lower Crust

Granulite-facies metamorphic conditions would be expected in the lower crust considering the abundant migmatite (and rare granulite) in the presently exposed Neoproterozoic midcrust and the abundant granite intrusions. If the granulite xenoliths are representative for the lower crust, upper and lower crust of the Bayuda area are of contrasting composition. The granulite xenoliths resemble the radiogenic isotope composition of juvenile material from Neoproterozoic ophiolite suites (Zabargad—e.g., Brueckner et al., 1988, 1995; Gabal Gerf—e.g., Zimmer et al., 1995) and other Neoproterozoic juvenile rocks (Figs. 5 and 6). Deep-seated cumulates of the juvenile contribution to the long-standing Neoproterozoic magmatism in the Bayuda area (ca. 860–590 Ma; e.g., Küster et al., 2008, and references therein) likely formed the protoliths of the granulite xenoliths. Peculiarities of the trace-element and isotope composition could be primary features from minor assimilation of cratonic crust during the magmatic evolution of the cumulate or induced by possible melt extraction after crystallization or both. Melting of lower crust

has been invoked for late Neoproterozoic alkaline postcollisional granitoids (e.g., Küster et al., 2008, and references therein), or it could be related to Paleozoic to Mesozoic alkaline ring complexes in the area (Barth et al., 1983; Vail, 1989). Melting did not change the distinctive isotope signatures of Pan-African juvenile crust, but it caused the depletion of incompatible trace elements like Rb, U, and Nd.

Lithospheric Mantle—Magmatic Evidence

A compositionally distinct type of juvenile rock occurs within the widespread, mainly Cenozoic, mafic intraplate magmatism in NE Africa and Arabia (e.g., Franz et al., 1999; Bertrand et al., 2003; Shaw et al., 2003; Lucassen et al., 2008a). The radiogenic (high- μ) Pb isotope signature of these rocks, e.g., the Bayuda host basanite (Fig. 7), is characteristic and distinct from reworked craton and juvenile Neoproterozoic crust. There is no or little influence from both types of Neoproterozoic crust in the isotope signatures in the Bayuda basanite (Figs. 5, 6, and 7) and many other NE African intraplate magmatic rocks over a large region (Fig. 1A; e.g., Lucassen et al., 2008a). The intraplate magmatic rocks are believed to represent the composition of sections in the Pan-African

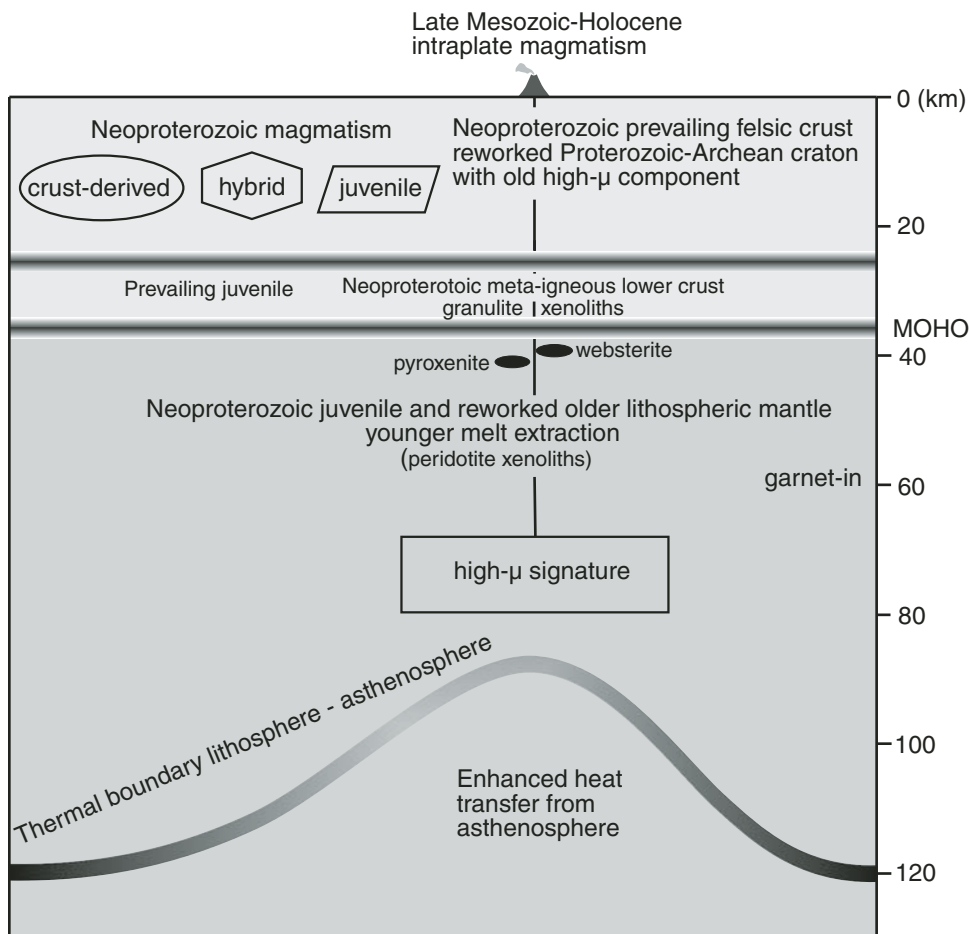


Figure 12. Lithospheric section through the Bayuda region, as derived from the composition of granulite, peridotite, and ultramafic xenoliths, the composition of the late Mesozoic–Holocene magmatism, and investigations of the surrounding basement. Sedimentary rocks are restricted to a thin cover of Nubian Sandstone Formation, which is not shown. Pyroxenite and websterite in the Bayuda xenoliths suite are interpreted as cumulates of the Mesozoic–Holocene young high- μ magmatism from lithospheric sources. Database: crust (Küster and Liégeois, 2001; Küster et al., 2008; this work); lithospheric mantle (Lucassen et al., 2008a, 2008b; this work). The garnet-in of peridotite is variable with pressure, temperature, and chemical composition; “garnet-in” is for fertile peridotite at ~900 °C (e.g., Green and Ringwood, 1967; O'Neill, 1981).

lithospheric mantle that were enriched in incompatible trace elements compared to depleted mantle, e.g., in U and Th (Stein et al., 1997; Lucassen et al., 2008a). This part of the lithospheric mantle was also separated long-term from convection and voluminous melt extraction (Fig. 11).

Lithospheric Mantle Xenoliths

Peridotite xenoliths (mainly spinel-lherzolite) occur at the Bayuda main volcanic field (Lucassen et al., 2008b) and other localities on the Arabian plate (Shaw et al., 2007). Both suites show a mantle that was reworked and formed during the Neoproterozoic and made of very similar Sr, Nd, and Pb isotope compositions (discussion in Lucassen et al., 2008b). The Bayuda peridotite xenoliths display a broad compositional variation in the lithospheric mantle above the source of their host basanite (Figs. 6 and 7). Xenolith samples with isotope compositions that require pre-Neoproterozoic strong depletion of incompatible elements, and samples with high- μ signature that require the recent activity of an enriched mantle source are found at the same locations.

The ultramafic xenoliths, with their uniform high- μ signature and geochemical features different from peridotite, likely reside in the uppermost lithospheric mantle. Mismatches between the major-element composition of intraplate volcanism and ultramafic xenoliths, geochemical features of group II xenoliths (Frey and Prinz, 1978), and high- μ isotope signatures suggest a cumulate origin related to the intraplate magmatism, which is documented since the Late Cretaceous in the region (Satir et al., 1991; Lucassen et al., 2008a). The overall volume of the cumulate in the uppermost mantle should be small, because high- μ magmatism is of minor volume and includes in the Bayuda area exclusively less evolved alkaline basalt to basanite.

Asthenosphere

Average depleted mantle (e.g., Workman and Hart, 2005), or ultra-depleted old mantle as known from the Bayuda peridotite xenoliths (Lucassen et al., 2008b), is not the major source of any intraplate magmatic rock. The composition of the convective mantle beneath Bayuda is unknown from direct evidence, but the convective mantle known from the major active tectonic element of the divergent plate boundary along the Red Sea–Gulf of Aden rift (Fig. 1A; e.g., Altherr et al., 1990; Volker et al., 1993, 1997; Schilling et al., 1992) likely extends some 600 km SE of the rift axes.

New and published data on the Bayuda lithosphere prove the validity of the concept for the Neoproterozoic lithosphere makeup on a small regional scale. The differences between reworked old cratonic and juvenile Neoproterozoic crust are preserved in the present depth profile, with juvenile material in the presumably deep-crustal cumulate section of the Neoproterozoic magmatism. Xenoliths from the mantle lithosphere indicate the preservation of old compositional features and show traces of the youngest magmatic activity.

ACKNOWLEDGMENTS

The xenoliths were collected within the framework of the Sonderforschungsbereich 67 project at the Technische Universität (TU) Berlin by Dieter Pudlo and Richard Brumm, and we acknowledge the invaluable logistical help and cooperation of the Geological Research Authorities of Sudan. Rudolf Naumann, Cathrin Schulz, and Birgit Zander (Deutsches Geoforschungszentrum) and Francois Galbert (Zentraleinrichtung Elektronenmikroskopie, TU Berlin) are thanked for their help with the analytical work, and Rosemarie Geffe (TU Berlin) is thanked for drawing Figure 12. Reviews by Daniel Demaiffe and Robert J. Stern are appreciated and improved the manuscript. This study was financed by the German Research Foundation (DFG) grant FR 557/20-1.

REFERENCES CITED

- Abdelsalam, M.G., Liégeois, J.-P., and Stern, R.J., 2002, The Saharan metacraton: Journal of African Earth Sciences, v. 34, p. 119–136, doi:10.1016/S0899-5362(02)00013-1.
- Al-Mishwat, A.T., and Nasir, S.J., 2004, Composition of the lower crust of the Arabian plate: A xenolith perspective: Lithos, v. 72, p. 45–72, doi:10.1016/j.lithos.2003.08.003.
- Almond, D.C., Kheir, O.M., and Poole, S., 1984, Alkaline basalt volcanism in the northeastern Sudan: A comparison of the Bayuda and Gedaref areas: Journal of African Earth Sciences, v. 2, p. 233–245, doi:10.1016/S0731-7247(84)80018-X.
- Altherr, R., Henjes-Kunst, F., and Baumann, A., 1990, Asthenosphere versus lithosphere as possible sources for basaltic magmas erupted during formation of the Red Sea: Constraints from Sr, Pb and Nd isotopes: Earth and Planetary Science Letters, v. 96, p. 269–286, doi:10.1016/0012-821X(90)90007-K.
- Bailo, T., Schandelmeyer, H., Franz, G., Sun, C.-H., and Stern, R.J., 2003, Plutonic and metamorphic rocks from the Kerf Suture (NE Sudan): A glimpse of Neoproterozoic tectonic evolution on the NE margin of W. Gondwana: Precambrian Research, v. 123, p. 67–80, doi:10.1016/S0301-9268(03)00044-5.
- Barth, H., and Meinhold, K.D., 1979, Mineral Prospecting in the Bayuda Desert: Hannover, Germany, Bundesanstalt für Geowissenschaften und Rohstoffe, 336 p.
- Barth, H., Besang, C., Lenz, H., and Meinhold, K.-D., 1983, Results of petrological investigations and Rb/Sr age determinations on the non-orogenic igneous ring-complexes in the Bayuda Desert, Sudan: Geologisches Jahrbuch, v. B51, p. 3–34.
- Bertrand, H., Chazot, G., Blichert-Toft, J., and Thorvald, S., 2003, Implications of widespread high- μ volcanism on the Arabian plate for Afar mantle plume and lithosphere composition: Chemical Geology, v. 198, p. 47–61, doi:10.1016/S0009-2541(02)00418-7.
- Bosworth, W., Huchon, P., and McClay, K., 2005, The Red Sea and Gulf of Aden Basins: Journal of African Earth Sciences, v. 43, p. 334–378, doi:10.1016/j.jafrearsci.2005.07.020.
- Brueckner, H.K., Zindler, A., Seyler, M., and Bonatti, E., 1988, Zabargad and the isotopic evolution of the sub-Red Sea mantle and crust: Tectonophysics, v. 150, p. 163–176, doi:10.1016/0040-1951(88)90300-9.
- Brueckner, H.K., Elhaddad, M.A., Hamelin, B., Hemming, S., Kröner, A., Reisberg, L., and Seyler, M., 1995, A Pan African origin and uplift for the gneisses and peridotites of Zabargad island, Red Sea: A Nd, Sr, Pb, and Os isotope study: Journal of Geophysical Research, v. 100, p. 22,283–22,297, doi:10.1029/95JB02247.
- Bumby, A.J., and Guiraud, R., 2005, The geodynamic setting of the Phanerozoic basins of Africa: Journal of African Earth Sciences, v. 43, p. 1–12, doi:10.1016/j.jafrearsci.2005.07.016.
- Downes, H., 2007, Origin and significance of spinel and garnet pyroxenites in the shallow lithospheric mantle: Ultramafic massifs in orogenic belts in Western Europe and NW Africa: Lithos, v. 99, p. 1–24, doi:10.1016/j.lithos.2007.05.006.

- Dugda, M.T., Nyblade, A.A., and Julia, J., 2007, Thin lithosphere beneath the Ethiopian Plateau revealed by a joint inversion of Rayleigh wave group velocities and receiver functions: *Journal of Geophysical Research*, v. 112, doi:10.1029/2006JB004918.
- Ellis, D.J., and Green, D.H., 1979, An experimental study of the effect of Ca upon garnet clinopyroxene Fe–Mg exchange equilibria: *Contributions to Mineralogy and Petrology*, v. 71, p. 13–22, doi:10.1007/BF00371878.
- Franz, G., Puchelt, H., and Pasteels, P., 1987, Petrology, geochemistry and age relations of Triassic and Tertiary volcanic rocks from SW Egypt and NW Sudan: *Journal of African Earth Sciences*, v. 6, p. 335–352, doi:10.1016/0899-5362(87)90077-7.
- Franz, G., Steiner, G., Volker, F., Puldo, D., and Hammerschmidt, K., 1999, Plume related alkaline magmatism in central Africa—The Meidob Hills (W Sudan): *Chemical Geology*, v. 157, p. 27–47, doi:10.1016/S0009-2541(98)00195-8.
- Frey, F.A., 1980, The origin of pyroxenites and garnet pyroxenites from Salt Lake Crater, Oahu, Hawaii: Trace element evidence: *American Journal of Science*, v. 280A, p. 427–449.
- Frey, F.A., and Prinz, M., 1993, Ultramafic inclusions from San Carlos, Arizona: Petrologic and geochemical data bearing on their petrogenesis: *Earth and Planetary Science Letters*, v. 38, p. 129–176, doi:10.1016/0012-821X(78)90130-9.
- Goldstein, S.L., O’Nions, R.K., and Hamilton, P.J., 1984, A Sm–Nd study of atmospheric dust and particulates from major river systems: *Earth and Planetary Science Letters*, v. 70, p. 221–236, doi:10.1016/0012-821X(84)90007-4.
- Green, D.H., and Ringwood, A.E., 1967, The stability field of aluminous pyroxene peridotite and garnet peridotite and their relevance in upper mantle structure: *Earth and Planetary Science Letters*, v. 3, p. 151–160, doi:10.1016/0012-821X(67)90027-1.
- Hart, S.R., and Dunn, T., 1993, Experimental cpx/melt partitioning of 23 trace elements: *Contributions to Mineralogy and Petrology*, v. 113, p. 1–18, doi:10.1007/BF00320827.
- Hildreth, W., and Moorbath, S., 1988, Crustal contributions to arc magmatism in the Andes of central Chile: *Contributions to Mineralogy and Petrology*, v. 98, p. 455–489, doi:10.1007/BF00372365.
- Hofmann, C., Courtillot, V., Féraud, G., Rochette, P., Yirgu, G., Ketefo, E., and Pik, R., 1997, Timing of the Ethiopian flood basalt event and implications for plume birth and global change: *Nature*, v. 389, p. 838–841, doi:10.1038/39853.
- Keshav, S., Gudfinnsson, G.H., Sen, G., and Fei, Y., 2004, High-pressure melting experiments on garnet clinopyroxenite and the alkalic to tholeiitic transition in ocean-island basalts: *Earth and Planetary Science Letters*, v. 223, p. 365–379, doi:10.1016/j.epsl.2004.04.029.
- Kogiso, T., Hirschmann, M.M., and Frost, D.J., 2003, High-pressure partial melting of garnet pyroxenite: Possible mafic lithologies in the source of ocean island basalts: *Earth and Planetary Science Letters*, v. 216, p. 603–617, doi:10.1016/S0012-821X(03)00538-7.
- Kogiso, T., Hirschmann, M.M., and Pertermann, M., 2004, High-pressure partial melting of mafic lithologies in the mantle: *Journal of Petrology*, v. 45, p. 2407–2422, doi:10.1093/petrology/egh057.
- Kröner, A., Stern, R.J., Dawoud, A.S., Compston, W., and Reischmann, T., 1987, The Pan-African continental margin in northeastern Africa: Evidence from a geochronological study of granulites at Sabaloka, Sudan: *Earth and Planetary Science Letters*, v. 85, p. 91–104, doi:10.1016/0012-821X(87)90024-0.
- Küster, D., and Harms, U., 1998, Post-collisional potassic granitoids from the southern and northwestern parts of the Late Neoproterozoic East African orogen: A review: *Lithos*, v. 45, p. 177–195, doi:10.1016/S0024-4937(98)00031-0.
- Küster, D., and Liégeois, J.-P., 2001, Isotopic and geochemical study of high-grade metamorphic lithologies from Bayuda Desert, Sudan: New insights into the Neoproterozoic evolution of the East Sahara craton: *Precambrian Research*, v. 109, p. 1–23.
- Küster, D., Liégeois, J.-P., Matukov, D., Sergeev, S., and Lucassen, F., 2008, Zircon geochronology and Sr, Nd, Pb isotope geochemistry of granitoids from Bayuda Desert and Sabaloka (Sudan): Evidence for a Bayudian event (920–900 Ma) preceding the Pan-African orogenic cycle (860–590 Ma) at the eastern boundary of the Saharan metacraton: *Precambrian Research*, v. 164, p. 16–39, doi:10.1016/j.precamres.2008.03.003.
- Leake, B.E., Woolley, A.R., Arps, C.E.S., Birch, W.D., Gilbert, M.C., Grice, J.D., Hawthorne, F.C., Kato, A., Kisch, H.J., Krivovichev, V.G., Linthout, K., Laird, J., Mandarino, J.A., Maresch, W.V., Nickel, E.H., Rock, N.M.S., Schumacher, J.C., Smith, D.C., Stephenson, N.C.N., Ungaretti, L., Whittaker, E.J.W., and Guo, Y., 1997, Nomenclature of amphiboles: Report of the Subcommittee on Amphiboles of the International Mineralogical Association, Commission on New Minerals and Mineral Names: *Mineralogical Magazine*, v. 61, p. 295–321, doi:10.1180/minmag.1997.061.405.13.
- Lucassen, F., Franz, G., Romer, R.L., Pudlo, D., and Dulski, P., 2008a, Nd, Pb, and Sr isotope composition of late Mesozoic to Quaternary intra-plate magmatism in NE-Africa (Sudan, Egypt): High- μ signatures from the mantle lithosphere: *Contributions to Mineralogy and Petrology*, v. 156, p. 765–784, doi:10.1007/s00410-008-0314-0.
- Lucassen, F., Franz, G., Romer, R.L., and Dulski, P., 2008b, Late Cenozoic xenoliths as a guide to the chemical-isotopic composition and thermal state of the upper mantle under northeast Africa: *European Journal of Mineralogy*, v. 20, p. 1079–1096, doi:10.1127/0935-1221/2008/0020-1855.
- McDonough, W.F., and Sun, S.-S., 1995, Composition of the Earth: *Chemical Geology*, v. 120, p. 223–253, doi:10.1016/0009-2541(94)00140-4.
- McGuire, A.V., and Stern, R.J., 1993, Granulite xenoliths from western Saudi Arabia; the lower crust of the late Precambrian Arabian–Nubian Shield: *Contributions to Mineralogy and Petrology*, v. 114, p. 395–408, doi:10.1007/BF01046541.
- McKenzie, D., and O’Nions, R.K., 1991, Partial melt distributions from inversion of rare earth element concentrations: *Journal of Petrology*, v. 32, p. 1021–1091.
- O’Neill, H.St.C., 1981, The transition between spinel lherzolite and garnet lherzolite, and its use as geobarometer: *Contributions to Mineralogy and Petrology*, v. 77, p. 185–194, doi:10.1007/BF00636522.
- Salter, V.J.M., and Stracke, A., 2004, Composition of the depleted mantle: *Geochemistry Geophysics Geosystems*, v. 5, doi:10.1029/2003GC000597.
- Satir, M., Moorteani, G., Fuganti, A., and Drach, V., 1991, K–Ar ages, Sr isotopic compositions and chemistry of Late Cretaceous–Tertiary basalts from the Nubian Desert (northern Sudan): *European Journal of Mineralogy*, v. 3, p. 943–955.
- Schandelmeier, H., and Reynolds, P.-O., eds., 1997, *Paleogeographic–Paleotectonic Atlas of North-Eastern Africa, Arabia, and Adjacent Areas*: Rotterdam, Balkema, 160 p.
- Schilling, J., Kingsley, R.H., Hanan, B.B., and McCully, B.L., 1992, Nd–Sr–Pb isotopic variations along the Gulf of Aden: Evidence for Afar mantle plume–continental lithosphere interaction: *Journal of Geophysical Research*, v. 97, p. 10,927–10,966, doi:10.1029/92JB00415.
- Shaw, J.E., Baker, J.A., Menzies, M.A., Thirlwall, M.F., and Ibrahim, K.M., 2003, Petrogenesis of the largest intraplate volcanic field on the Arabian plate (Jordan): A mixed lithosphere–asthenosphere source activated by lithospheric extension: *Journal of Petrology*, v. 44, p. 1657–1679, doi:10.1093/petrology/egg052.
- Shaw, J.E., Baker, J.A., Kent, J.R., Ibrahim, K.M., and Menzies, M.A., 2007, The geochemistry of the Arabian lithospheric mantle—A source for intraplate volcanism?: *Journal of Petrology*, v. 48, p. 1495–1512, doi:10.1093/petrology/egm027.
- Stein, M., Navon, O., and Kessel, R., 1997, Chromatographic metasomatism of the Arabian–Nubian lithosphere: *Earth and Planetary Science Letters*, v. 152, p. 75–91, doi:10.1016/S0012-821X(97)00156-8.
- Stern, R.J., 1994, Neoproterozoic (900–550 Ma) arc assembly and continental collision in the East African orogen: Implications for the consolidation of Gondwanaland: *Annual Review of Earth and Planetary Sciences*, v. 22, p. 319–351.
- Stern, R.J., and Abdelsalam, M.G., 1998, Formation of juvenile continental crust in the Arabian–Nubian Shield: Evidence from granitic rocks of the Nakasib suture, NE Sudan: *Geologische Rundschau*, v. 87, p. 150–160, doi:10.1007/s005310050196.
- Stern, R.J., and Kröner, A., 1993, Geochronologic and isotopic constraints on Late Precambrian crustal evolution in NE Sudan: *The Journal of Geology*, v. 101, p. 555–574, doi:10.1086/648249.
- Stoeser, D.B., and Frost, C.D., 2006, Nd, Pb, Sr, and O isotopic characterization of Saudi Arabian Shield terranes: *Chemical Geology*, v. 226, p. 163–188, doi:10.1016/j.chemgeo.2005.09.019.
- Stracke, A., Hofmann, A.W., and Hart, S.R., 2005, FOZO, HIMU, and the rest of the mantle zoo: *Geochemistry Geophysics Geosystems*, v. 6, doi:10.1029/2004GC000824.
- Sun, S.-S., and McDonough, W.F., 1989, Chemical and isotopic systematics of oceanic basalts: Implications for mantle composition and processes,

- in* Saunders, A.D., and Norry, M.J., eds., *Magmatism in Ocean Basins*: Geological Society of London Special Publication 42, p. 313–345.
- Teklay, M., Kröner, A., and Mezger, K., 2002, Enrichment from plume interaction in the generation of Neoproterozoic arc rocks in northern Eritrea: Implications for crustal accretion in the southern Arabian–Nubian Shield: *Chemical Geology*, v. 184, p. 167–184, doi:10.1016/S0009-2541(01)00359-X.
- Vail, J.R., 1989, Ring complexes and related rocks in Africa: *Journal of African Earth Sciences*, v. 8, p. 19–40, doi:10.1016/S0899-5362(89)80006-5.
- Volker, F., McCulloch, M.T., and Altherr, R., 1993, Submarine basalts from the Red Sea: New Pb, Sr, and Nd isotopic data: *Geophysical Research Letters*, v. 20, p. 927–930, doi:10.1029/93GL00050.
- Volker, F., Altherr, R., Jochum, K.-P., and McCulloch, M.T., 1997, Quaternary volcanic activity of the southern Red Sea: New data and assessment of models on magma sources and Afar plume-lithosphere interaction: *Tectonophysics*, v. 278, p. 15–29, doi:10.1016/S0040-1951(97)00092-9.
- Workman, R.K., and Hart, S.R., 2005, Major and trace element composition of the depleted MORB mantle (DMM): *Earth and Planetary Science Letters*, v. 231, p. 53–72, doi:10.1016/j.epsl.2004.12.005.
- Zimmer, M., Kröner, A., Jochum, K.P., Reischmann, T., and Todt, W., 1995, The Gabal Gerf complex: A Precambrian N-MORB ophiolite in the Nubian Shield, NE Africa: *Chemical Geology*, v. 123, p. 29–51, doi:10.1016/0009-2541(95)00018-H.
- Zindler, A., and Hart, S.R., 1986, Chemical geodynamics: *Annual Review of Earth and Planetary Sciences*, v. 14, p. 493–571, doi:10.1146/annurev.ea.14.050186.002425.

MANUSCRIPT ACCEPTED BY THE SOCIETY 9 NOVEMBER 2010

Holocene opening directions along the axes of the Red Sea (Afar) and Main Ethiopian Rifts: An overview

V. Acocella*

Dipartimento Scienze Geologiche Università Roma Tre, Largo S.L. Murialdo, 1, 00146 Roma, Italy

B. Abebe

Department of Earth Sciences, Addis Ababa University, P.O. Box 1176, Addis Ababa, Ethiopia

T. Korme

Regional Center for Mapping of Resources for Development, P.O. Box 632, 00618 Nairobi, Kenya

ABSTRACT

Assessments of the extension directions and their variations are critical for understanding rifting processes. This study provides an overview of the extension directions along the axes of the Main Ethiopian Rift and the Red Sea Rift (or propagator) of Afar, two of the three rifts meeting at the Afar triple junction. This overview is based on new and published field data on the opening direction of significant (width >0.2 m) Holocene extension fractures along the rift axis. The data show that the Red Sea propagator axis opens orthogonally, both in northern and central Afar, even though a significant strike-slip component is recognized at the rift margins in central Afar. The Main Ethiopian Rift axis also opens orthogonal to the trend of the rift, which varies between the different rift segments. Therefore, the axes of two of the three rifts meeting in Afar are characterized by orthogonal extension. However, given the variable orientations of the rift segments, the obtained opening directions are usually not uniform along the rift. Current plate-motion models suggest slightly different divergence directions, especially along the Main Ethiopian Rift, which shows a significant oblique component. The discrepancy between the data along the rift axis and those from plate-motion models suggests an across-rift strain partitioning. The observed orthogonal extension along the rift axis may be magma-induced, provided that a depth-dependent variation in the kinematics exists, at least below the Main Ethiopian Rift axis.

*acocella@uniroma3.it

INTRODUCTION

A crucial matter for understanding rifting processes and the resulting regional extension is the evaluation of fault kinematics. The extension direction may locally vary along the rift, especially if it has a complex architecture, characterized by segments with variable orientations. The overall structure of a rift is closely related to its kinematics, and both field data and models show that the higher the obliquity of the extension direction to the rift, the more complex is its deformation pattern (e.g., Taylor et al., 1994; McClay and White, 1995). Rifts with orthogonal extension are usually characterized by swarms of extensional structures with collinear configuration. Conversely, rifts with oblique extension consist of faults with a predominantly transtensive motion and en-echelon geometries that are oblique to the main rift zone (Dau-teuil and Brun, 1993; McClay and White, 1995; Tuckwell et al., 1998). Such a deformation pattern may be further complicated at triple rift junctions, where local variations in the extension direction, due to the connection between different rifts, are expected (e.g., Mouslopoulou et al., 2007, and references therein).

Magmatism may also play an important role in influencing the geometry and kinematics of a rift. In fact, the axis of a rift is the site of active extension and volcanism: Here extensional fractures and normal faults develop, and their activity is commonly accompanied by central or fissure eruptions. Different models have been proposed to explain the relationships between magmatism and tectonics along rift axes. While it has been widely accepted that extension (fracturing and faulting) enhances volcanic activity (e.g., Latin and White, 1990), recent studies suggest that a considerable part of the deformation within a rift is magma-induced (Kendall et al., 2005; Buck, 2006; Casey et al., 2006). Therefore, an assessment of the opening direction of a rift axis may be important also to evaluate the relative contributions of tectonic and magmatic processes on rift growth.

In continental crust, the relationships among rift geometry, kinematics, and magmatism can be best appreciated in the area of the Afar triple junction, which is characterized by the connection between the Aden Rift, the Red Sea Rift, and the Main Ethiopian Rift (Fig. 1; McKenzie et al., 1970). While the geometry and kinematics of the onshore and offshore portions of the oblique Aden Rift have been established (Needham et al., 1976; Stein et al., 1991; Manighetti et al., 1998, 2001; Audin et al., 2004), the current kinematics of the Red Sea Rift and Main Ethiopian Rift are less well-defined and more debated, respectively. The Red Sea Rift (or propagator; Manighetti et al., 2001, and references therein) is poorly known, except for a few selected portions, including the Dabbahu segment (the site of a recent major rifting event; e.g., Wright et al., 2006) and the Tendaho graben (Abbate et al., 1995; Acocella et al., 2008). The current opening direction of the Main Ethiopian Rift is still controversial, and an orthogonal approximately NW-SE-trending or an oblique approximately E-W-trending extension direction have both been proposed to occur in response to plate motion (see overview in Acocella and Korme, 2002).

This study considers the Holocene kinematics of the axial portions of the Red Sea propagator and the Main Ethiopian Rift, based on original (northern part of Main Ethiopian Rift) and previously collected (Red Sea propagator and part of Main Ethiopian Rift) data. The data were obtained from the opening directions of active and large (width >0.2 m) extension fractures, which have been systematically measured in the axial part of the rift. The results are largely consistent with an along-axis orthogonal opening, not necessarily coinciding with the direction of plate motion.

TECTONIC FRAMEWORK

In Afar, the Red Sea and Aden propagators (on-land continuation of the Red Sea and Aden Rifts, respectively) meet with the northern Main Ethiopian Rift (Fig. 1; McKenzie et al., 1970; Tazieff et al., 1972; Le Pichon and Francheteau, 1978; Bosworth et al., 2005). The current mean spreading rates of the Aden and northern Red Sea propagators are ~1.1 cm/yr (Vigny et al., 2007, and references therein) and ~2 cm/yr (Jestin et al., 1994), respectively, which are significantly higher than the ~2.5 mm/yr of the northern Main Ethiopian Rift (Fig. 1; Wolfenden et al., 2004, and references therein). A factor related to the development of the

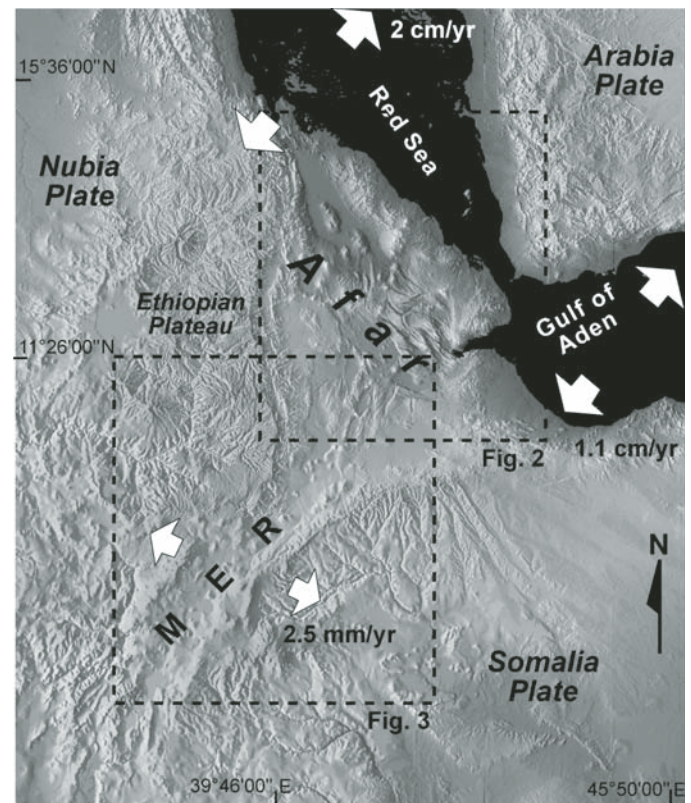


Figure 1. Digital elevation model of the investigated area, highlighting the Main Ethiopian Rift (MER) and its junction with the Red Sea and Aden Rifts in the Afar triple junction. Arrows represent directions of plate motion (after Manighetti et al., 2001, and references therein; Keir et al., 2006).

Red Sea propagator is the eastward shift and counterclockwise rotation of the Danakil microplate, over the last ~11 m.y. at least (Fig. 2; Eagles et al., 2002).

The opening direction of the offshore portion of the axis of the Aden Rift is constrained by the approximately NE-SW strike of the fracture zones dissecting the ridge (Dauteuil et al., 2001; D'Acremont et al., 2005; Manighetti et al., 1997), while the opening direction of the onshore portion is constrained by field and global positioning system (GPS) studies (Manighetti et al., 1998; Cattin et al., 2005; Vigny et al., 2007). The on-land structure of the Aden propagator consists of two NW-SE-trending rift segments that are connected by an oblique transfer zone (Manighetti et al., 2001, and references therein). Each segment consists of subvertical to riftward-dipping active normal faults and an axial portion of active tensile fracturing and volcanic activity (Needham et al., 1976; Manighetti et al., 1998).

The Red Sea propagator is characterized, to the north, by the Erta Ale Range, which separates the Ethiopian Plateau from the Danakil block (Fig. 2). The Erta Ale Range consists of an approximately NNW-SSE alignment of active volcanoes, largely shield volcanoes with basaltic composition, associated with fracturing (Barberi and Varet, 1970). To the south, the Red Sea propagator continues into central Afar, in the approximately

NW-SE-trending Tendaho graben (TG; Fig. 2), the largest basin of central Afar (Fig. 1), forming the currently active NW-SE-trending Manda Hararo Rift (MHR; Fig. 2; Tapponnier et al., 1990; Manighetti et al., 2001). A major rifting episode, associated with the emplacement of a dike that is 60 km long and up to 8 m wide, occurred in 2005 to the NW of the Dabbahu segment of the Manda Hararo Rift (Wright et al., 2006; Ayele et al., 2007).

The NNE-SSW-trending Main Ethiopian Rift intersected Afar after propagating northward over the last 11 m.y. (Wolfenden et al., 2004). The Main Ethiopian Rift progressively widens northward. This widening is associated with a decrease in the length of its rift segments, of the separation of magmatic centers, and of the effective elastic thickness of the crust (Fig. 3; Ebinger and Hayward, 1996; Hayward and Ebinger, 1996). The rift started to develop during the Miocene (Davidson and Rex, 1980; Woldegabriel et al., 1990; Chernet et al., 1998), following a broad doming centered on the present Afar depression (Almond, 1986; Ebinger et al., 1989; Collet et al., 2000; Benoit et al., 2006). During the Pliocene and Quaternary, the Main Ethiopian Rift progressively deepened, evolving through a sequence of interacting half-graben segments marking the boundary between the Nubia and Somalia Plates (Hayward and Ebinger, 1996).

The youngest part of the Main Ethiopian Rift is the axial zone, or rift axis, which coincides with the so-called Wonji fault belt, which mainly formed during the Quaternary (Fig. 3; Mohr, 1967, 1987; Boccaletti et al., 1998; Corti, 2008). Despite the

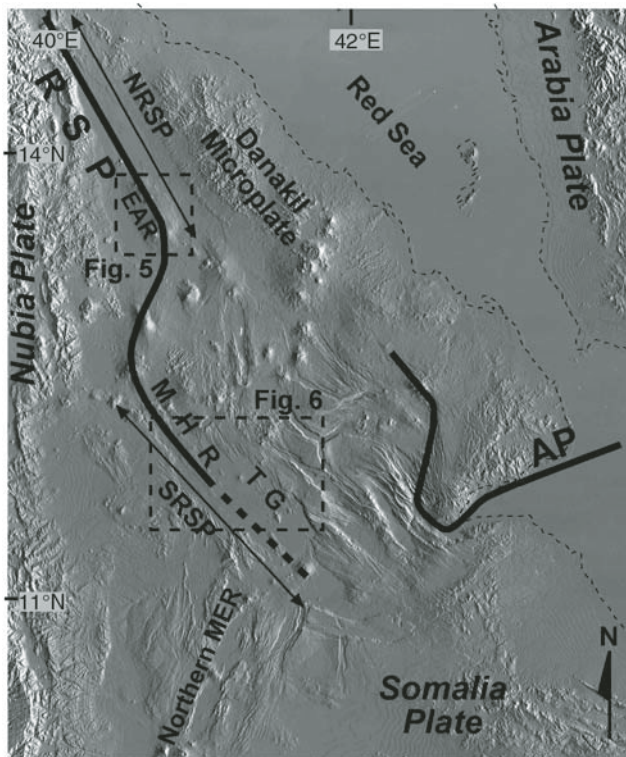


Figure 2. General structure of the Afar triple junction and the Red Sea propagator (RSP). Abbreviations: NRSP—northern Red Sea propagator; SRSP—southern Red Sea propagator; AP—Aden propagator; EAR—Erta Ale Range; MHR—Manda Hararo Rift; TG—Tendaho graben.

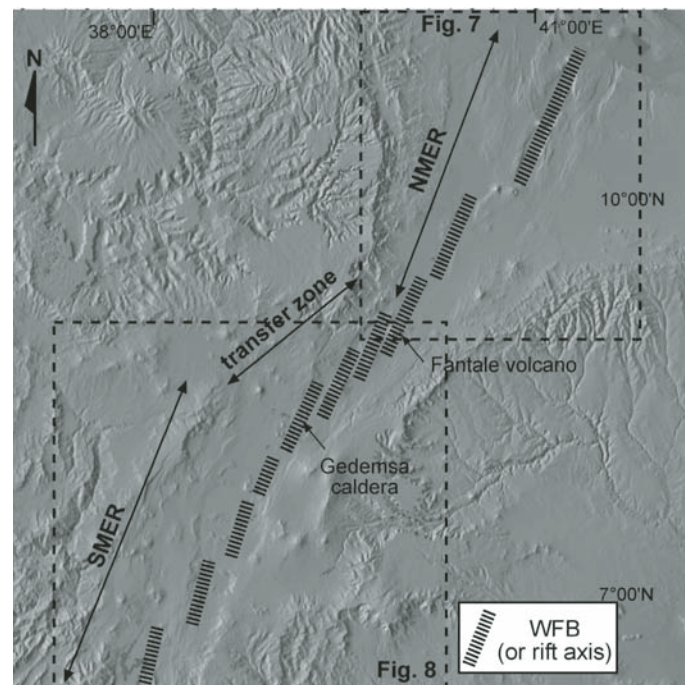


Figure 3. Schematic structure of Main Ethiopian Rift (MER), highlighting its NNE-SSW-trending northern (NMER) and southern portions (SMER), separated by the NE-SW-trending transfer zone between Gedemsa caldera and Fantale volcano. WFB—Wonji fault belt.

overall NE-SW trend of the Main Ethiopian Rift, the Wonji fault belt is characterized by active NNE-SSW-trending extension fractures and normal faults. These are often set in a right-stepping en-echelon arrangement and are associated with volcanic activity, suggesting a possible overall left-lateral component of motion along the Wonji fault belt (Bonini et al., 1997). The slightly different trends of the Wonji fault belt and the Main Ethiopian Rift margins suggest a change in the extension direction during the Quaternary (Bonini et al., 1997; Boccaletti et al., 1998). However, different types of data give different information on the opening directions of the Wonji fault belt. Fault-slip data along the rift suggest an approximately E-W extension (Bonini et al., 1997; Boccaletti et al., 1998), while structural data along the rift axis suggest an approximately NW-SE extension (Chorowicz et al., 1994; Korme et al., 1997; Acocella and Korme, 2002). GPS and EDM (electronic distance meter) data along the sides of the

rift suggest an approximately N108° extension direction (Bilham et al., 1999), while GPS data in the inner part of the rift suggest approximately NW-SE extension (Pan et al., 2002; Pizzi et al., 2006). Tension (T) axes of earthquake focal mechanisms from throughout the Main Ethiopian Rift are consistent with an approximately E-W extension (Ayele, 2000; Keir et al., 2006), in agreement with those obtained from plate motion models (Jestin et al., 1994; Chu and Gordon, 1999; Calais et al., 2006; Keir et al., 2006, and references therein).

METHODOLOGY

In order to evaluate the contemporary opening direction of the rift axis, we measured 141 opening directions of extension fractures in dated late Quaternary and, mostly, Holocene volcanic products in the axial part of the Red Sea propagator and the Main

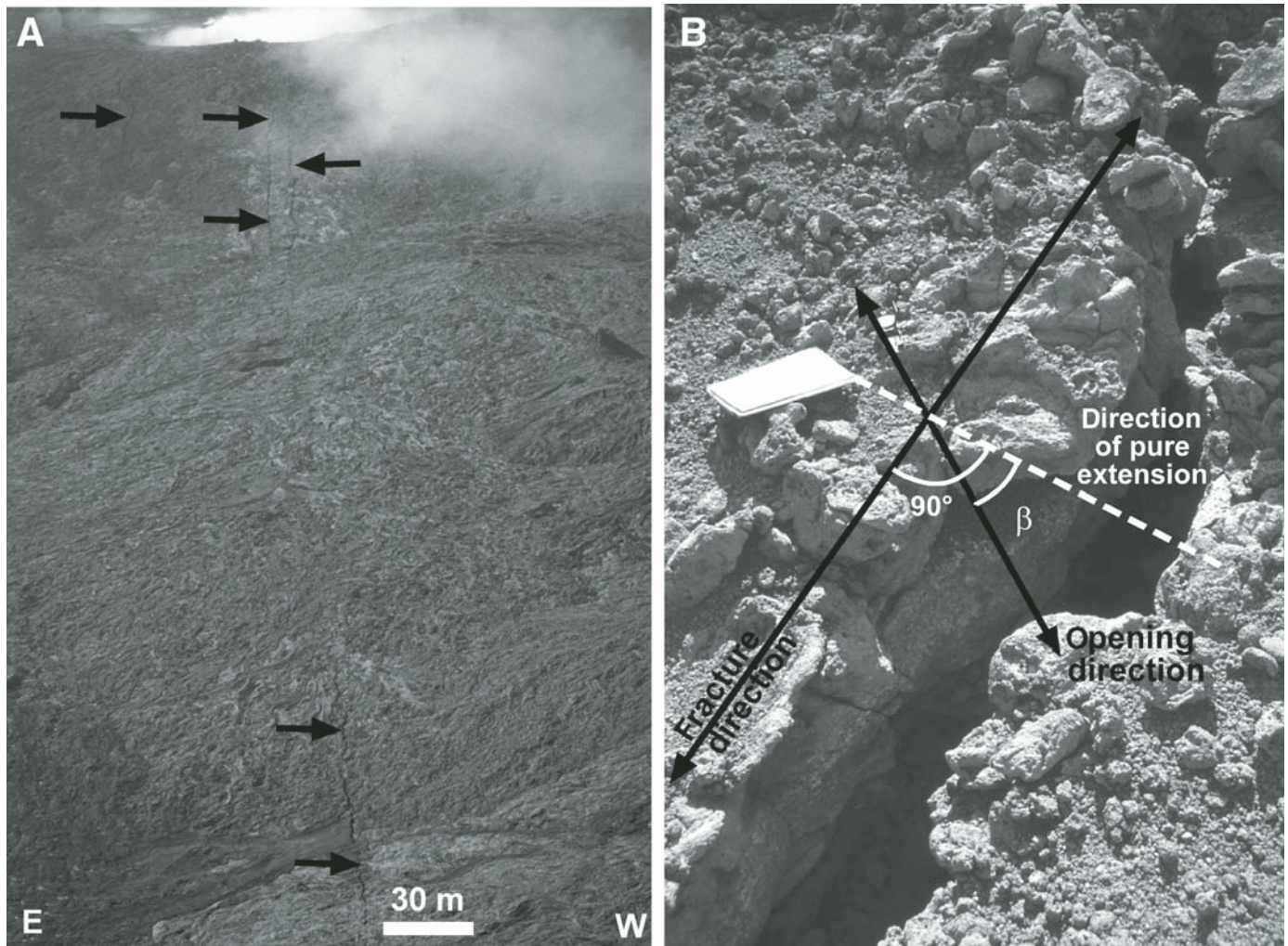


Figure 4. (A) Aerial view of extension fractures (pointed by arrows), partially covered by modern lava flows, along the axis of the Erta Ale rift; scale refers to foreground. (B) Determination of the opening direction of an extension fracture along the rift axis. The opening direction is obtained by matching pairs of asperities on the opposite walls of the fracture. This comparison to the pure opening direction (perpendicular to the strike of the fracture) allows us to determine any component of horizontal shear, expressed through the angle β .

Ethiopian Rift. The axis of the rift is defined as the zone of active volcanism and extension, not necessarily coinciding with the central portion. Volcanism is characterized by central felsic volcanoes and mafic eruptive fissures responsible for the emplacement of basaltic lava flows (Gibson, 1969; Ebinger and Casey, 2001; Williams et al., 2004). Extension is accommodated by normal faults with a tensile component (Acocella et al., 2003, and references therein) and extension fractures, where the separation between the two walls is primarily by movement normal to the failure surface. The measured extension fractures have lengths between 20 and 400 m and openings of 0.2–4 m; their maximum depth, ~700 m, is inferred from mechanical considerations (Gudmundsson, 1992; Acocella et al., 2003). This type of extension fracture is exclusively found along divergent plate boundaries, both in oceanic and continental crust. The fracture strike is consistent with that of the main deformation zone characterizing the rift axis, which supports and confirms the importance of these fractures in the opening of the rift at the surface.

All measurements were made on extension fractures in lava flows or highly welded ignimbrites. These rocks have subvertical cooling joints (Fig. 4). The extension fractures partly reactivate preexisting cooling joints during their tectonic develop-

ment. Small asperities, bounded by the joints, have formed on the opposite walls of the extension fractures. The vector of total horizontal displacement across the fractures was measured by matching associated pairs of asperities on the opposite walls of the fractures. This vector, measured with a compass, gives the opening direction of the extension fractures, as discussed in detail by Gudmundsson (1987) and Acocella et al. (2000). Any positive or negative variation of the angle β between the opening direction of the fracture and the direction orthogonal to its strike (Fig. 4) permits quantification of the amount of horizontal shear along the fracture.

The asperities along the fracture walls are sharp and have not been affected by significant erosion (e.g., Fig. 4). This, together with the predominantly Holocene age of the rocks, confirms that the fractures are active.

Because of the location (active axial zone), trend (subparallel to the rift trend), and age (mainly Holocene) of the extension fractures, the recorded opening directions are inferred to be first-order Holocene kinematic indicators of the shallow part of the rift axis. The opening directions of the extension fractures were obtained at two locations along the Red Sea propagator (Erta Ale volcano slopes and Manda Hararo Rift). Along the Main Ethiopian Rift,

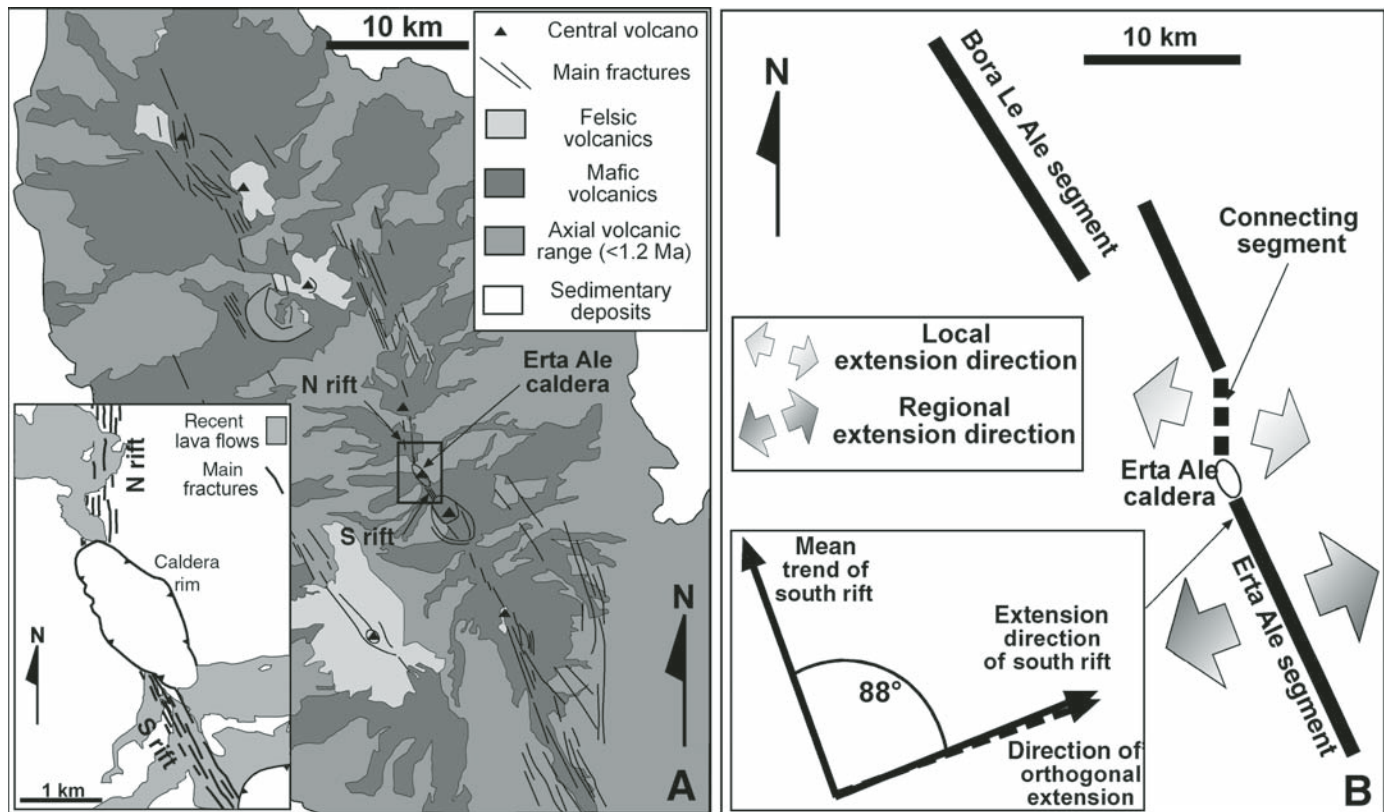


Figure 5. (A) Geology and structure of the central part of Erta Ale Range, northern Red Sea propagator (modified after Barberi and Varet, 1970); inset shows location of the north and south rift zones of Erta Ale caldera. (B) Schematic structure and kinematics of the central Erta Ale Range (same area as in A). The connecting segment (N rift of Erta Ale) is characterized by a local extension direction, different from the regional one of the Erta Ale segment (S rift of Erta Ale). Inset shows the opening direction of the S rift of Erta Ale with regard to its strike (Acocella, 2006).

the data have been collected much more regularly, with spacing less than a few tens of kilometers over a distance of ~500 km.

RESULTS

Northern Red Sea Propagator

Opening directions in the NNW-SSE-trending northern part of the Red Sea propagator have been determined previously on the slopes of Erta Ale volcano (Acocella, 2006, and references therein). Erta Ale has a northern and a southern rift zone, both a few hundred meters wide and several kilometers long, characterized by extension fractures, normal faults, and fissure volcanism (Fig. 5). The northern rift is interpreted to be a connecting segment between noncollinear NNW-SSE-trending regional rift segments; therefore, both its strike (approximately N-S) and

opening direction (approximately WNW-ESE) are local features accommodating the interaction between the main rift segments (Acocella, 2006). Conversely, the NNW-SSE-trending southern rift is one of the main regional tectonic features of the Erta Ale range (Fig. 5), which continues to the south with the same orientation for several tens of kilometers. For this reason, it is thought to be important for determining the opening direction of the axis of this portion of the rift. The 33 opening directions of extension fractures along the southern rift have a mean orientation of $N68^\circ \pm 10^\circ$, at 88° to the trend of the rift and Erta Ale Range (Fig. 5B), i.e., with a pure orthogonal opening.

Southern Red Sea Propagator

The opening directions in the NW-SE-trending southern part of the Red Sea propagator were collected in the Tendaho graben

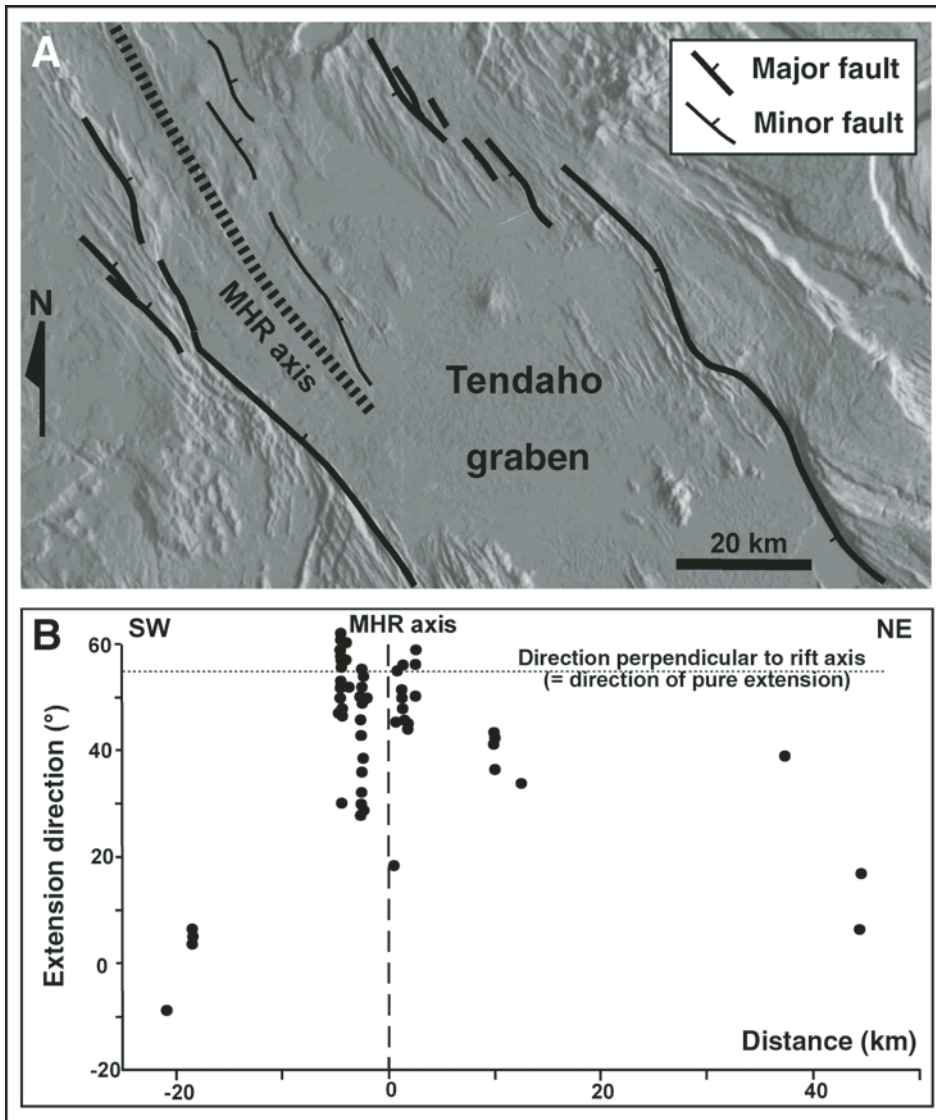


Figure 6. (A) Simplified structure of the central part of Tendaho graben (TG), reporting the largest faults (smallest-scale faults are neglected), and the location of the currently active Manda Hararo Rift (MHR). (B) Variation of the angle β across Tendaho graben with regard to the Manda Hararo Rift axis. Positive values of β imply a component of sinistral shear; negative values imply a component of dextral shear (Acocella et al., 2008).

area, mainly along the active Manda Hararo Rift (Fig. 6; Acocella et al., 2008). The 49 opening directions collected are characterized by the following behavior (Fig. 6B). In the area of the rift axis (~ 20 km wide), the opening direction has a mean $N50^\circ E \pm 15^\circ$ orientation, at $\sim 85^\circ$ to the trend of the rift. This implies an almost pure orthogonal opening, with a negligible ($\beta \sim 5^\circ$) component of sinistral shear. With increasing distance from the rift axis, the opening direction, as estimated along faults, becomes progressively more oblique to the trend of the rift, reaching an approximately N-S orientation and carrying a significant component ($\beta > 40^\circ$) of sinistral shear (Acocella et al., 2008). This result is consistent with previous data, which highlight a significant left-lateral component of slip along the NW-SE-trending faults bordering Tendaho graben (Tapponnier et al., 1990; Abbate et al., 1995). Therefore, the southern part of the Red Sea propagator is characterized, along the rift axis, by pure opening, and, toward the rift sides, by increasing left-lateral motion, suggesting an across-rift partitioning in the deformation (Acocella et al., 2008).

Northern Main Ethiopian Rift

The Main Ethiopian Rift consists of two main rift portions with an overall NNE-SSW trend separated by a major transfer zone in the Gedemsa-Fantale area, which has an overall NE-SW trend (Fig. 3). To the north and south of the transfer zone, the Main Ethiopian Rift has mean trends of $N24^\circ E$ and $N32^\circ E$, respectively.

The northern part of the Main Ethiopian Rift extends from central Afar (Tendaho graben area) to the area north of Fantale volcano, a distance of ~ 250 km (Fig. 3). This portion of the rift consists of two main offset segments, characterized by the same NNE-SSW trend, with an en-echelon dextral configuration. The segments interact, forming a transfer zone in the area of Gewane (Fig. 7).

The 12 opening directions in the northern Main Ethiopian Rift were collected in the southern rift segment, here named Kereyou-Dofan rift, after the names of its most distinctive volcano-tectonic features (Fig. 7; Wolfenden et al., 2004). These data, relative to approximately N-S to approximately

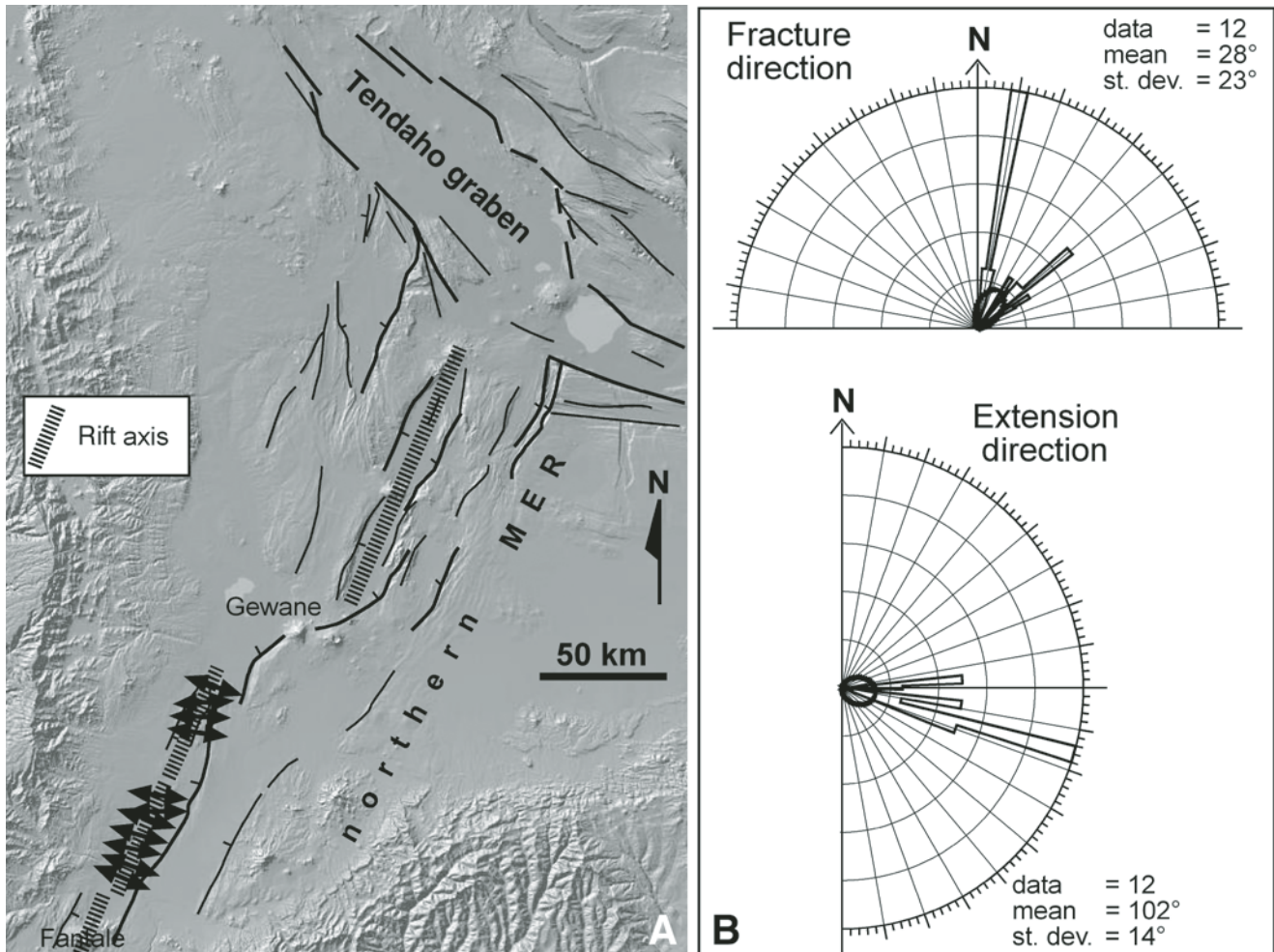


Figure 7. (A) Simplified structure of the northern Main Ethiopian Rift (MER), from Fantale volcano to the Tendaho graben area. (B) Distribution of the strike of the considered extension fractures, with a mean $N28^\circ E$ trend (above), and of their opening direction, with a mean $N102^\circ$ trend (below). st.dev.—standard deviation.

NE-SW–trending extension fractures, are consistent with a mean opening direction of $N102^\circ \pm 14^\circ$, independent of the fractures strike (Fig. 7B). This opening direction suggests mainly orthogonal opening along the northern Main Ethiopian Rift, with a minor component of sinistral shear ($\beta = 12^\circ$).

Southern Main Ethiopian Rift

The data in the southern part of the Main Ethiopian Rift were collected in the portion of rift between Gedemsa caldera, to the north, and Lake Abaya, to the south (Fig. 8A). In between the two locations, the rift has a consistent $N32^\circ E$ trend. Sixteen opening directions were measured in this portion of the Main Ethiopian Rift (Acocella and Korme, 2002), along NNE-SSW–trending extension fractures forming the Wonji fault belt. The mean strike of these fractures is $N23^\circ E$, consistent with a mean $N54^\circ W \pm 20^\circ$ opening direction, perpendicular (with a negligible scatter of $\beta = 4^\circ$) to the mean trend of the southern portion of the Main Ethiopian Rift (Fig. 8B). However, this opening direction also indicates a minor component of dextral shear (in the order of $\beta = 13^\circ$) along the NNE-SSW–trending extension fractures, in line with field observations showing that the extension fractures usually do not have pure opening (Acocella and Korme, 2002, and references therein).

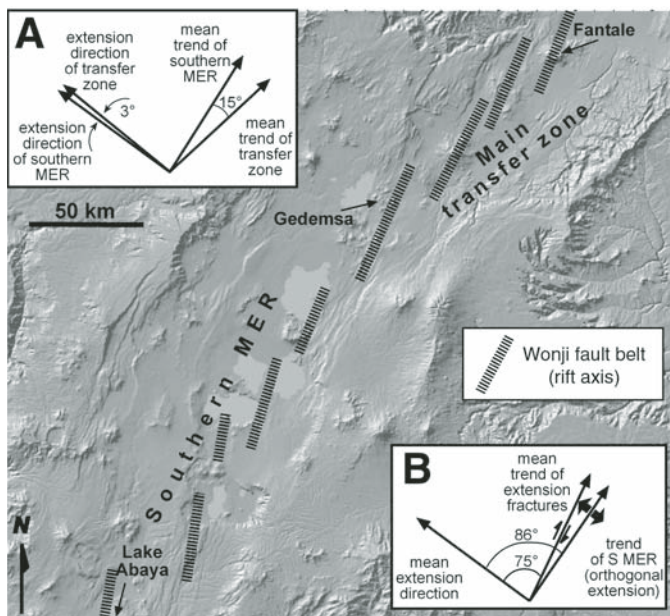


Figure 8. (A) Relationships among the trend of the southern part of the Main Ethiopian Rift (MER), the trend of the major transfer zone, and their related mean extension directions. (B) Relationships among the trend of southern Main Ethiopian Rift and Wonji fault belt and the mean extension direction of the extension fractures in the southern Main Ethiopian Rift. The angles obtained show that the southern Main Ethiopian Rift undergoes an orthogonal extension, whereas the Wonji fault belt shows a component of right-lateral shear (Acocella and Korme, 2002).

In order to further constrain the kinematics of the Main Ethiopian Rift, we also considered the opening directions obtained from the fractures along the axis (Wonji fault belt area) of the rift in the transfer zone between Fantale volcano and Gedemsa caldera. This transfer zone has a mean $N47^\circ E$ orientation. These 32 opening directions, which were collected along extension fractures with a mean $N23^\circ$ strike, have a mean trend of $N51^\circ W \pm 20^\circ$ (Acocella and Korme, 2002). This direction, similar to the previous one, is almost perpendicular to the NE-SW trend of the transfer zone, with a minor $\beta = 8^\circ$ of left-lateral shear. The $N51^\circ W$ opening direction is also almost perpendicular to the NNE-SSW trend of the southern Main Ethiopian Rift, with $\beta = 7^\circ$ of right-lateral shear. Finally, this direction implies a moderate component of dextral shear along the extension fractures (having a mean $N23^\circ E$ direction) in the axial part of the rift, with a mean value of $\beta = 16^\circ$.

DISCUSSION

Within the Red Sea propagator, the opening direction is consistently perpendicular to the trend of the rift, with negligible lateral slip ($\beta = 2^\circ$ and $\beta = 5^\circ$ in the Erta Ale and Tendaho Graben areas, respectively). However, because the directions of the rift axis in the northern and southern parts of the Red Sea propagator are slightly different, the opening directions in the two areas are not parallel (Fig. 9).

The variation in the opening direction along the axis of the northern and southern parts of the Red Sea propagator may be explained by the complexity of the area, which is characterized by the partial overlap of interacting rifts in a triple junction. In addition, across-rift variations in the opening direction, with a partitioning of the deformation, have been found in the southern part of the Red Sea propagator, in the area of Tendaho graben; these may be related to the presence of, and interaction with, the nearby Aden and Main Ethiopian Rift segments toward the center of the triple junction area (Acocella et al., 2008). Therefore, as a consequence of such a complex tectonic setting, partitioning along and across the axis of the rift may be expected.

Data along the axis of northern Main Ethiopian Rift point to an overall orthogonal extension, approximately $N102^\circ$ oriented, with a minor component ($\beta = 12^\circ$) of sinistral shear. Even though data along this portion of rift are rare, the uniformity of the opening direction independent of the strike of the fractures suggests the reliability of the estimated opening direction.

Along the axis of the southern Main Ethiopian Rift, including the area of the Gedemsa-Fantale transfer zone, extension is also orthogonal, oriented between $N54^\circ W$ and $N51^\circ W$, with a negligible ($\beta = 4^\circ$ in the southern Main Ethiopian Rift and $\beta = 8^\circ$ in the transfer zone) component of horizontal shear. However, because of their slightly different orientation (mean strike = $N23^\circ E$; Acocella and Korme, 2002) with respect to the trend of the southern part of the Main Ethiopian Rift ($N32^\circ$), the fractures along the axis of this part of the rift are associated with a slightly higher dextral shear, $\beta = 13^\circ$.

Despite the generally orthogonal extension, the opening directions collected along different portions of the Main Ethiopian Rift are not the same, due to the variable strike of the rift segments (Fig. 9). Unlike the Red Sea propagator, the variations in the opening direction along the Main Ethiopian Rift do not appear to have been influenced by the development of the triple junction. This implies that the data collected in the axial part

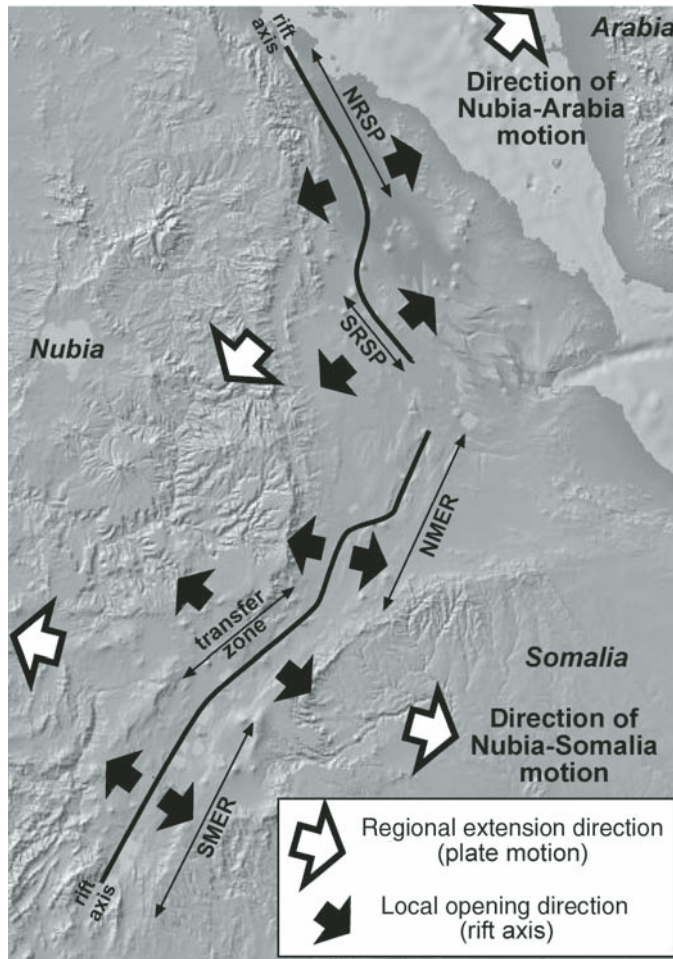
of the Main Ethiopian Rift are not the direct expression of the motion of the rigid plates along the rift sides, which rather show a kinematic consistency over thousands of kilometers (Fig. 9; Calais et al., 2006, and references therein).

More generally, there is an overall discrepancy between the opening directions along the axes of the Red Sea propagator and the Main Ethiopian Rift and the extension directions from plate-motion data at the rifts sides (Fig. 9). Along the axes of the rifts, there are at least five main domains with different, yet statistically significant, opening directions. Conversely, plate-motion data predict consistent extension directions along the sides of both rifts.

An explanation for this different behavior is that the measured opening directions may reflect local kinematics, restricted to the area of the rift axis. At the margins of the rift, other mechanisms, more directly related to regional processes, may explain any consistent motion of the diverging plates. This suggests the existence of strain partitioning across the plate boundary, in which the kinematics of the rift axis are a local feature. The partitioning may explain the change in the extension direction in different parts of the Main Ethiopian Rift, requiring orthogonal (local, along the rift axis) or oblique (regional, along the rift sides) fault slip (Chorowicz et al., 1994; Bonini et al., 1997; Korme et al., 1997; Bilham et al., 1999; Acocella and Korme, 2002; Pan et al., 2002; Calais et al., 2006; Keir et al., 2006; Pizzi et al., 2006). Such partitioning may help to explain the variations in the across-rift opening direction in the Tendaho graben (Acocella et al., 2008) and, at a larger scale, between the Red Sea propagator and the direction of plate motion. In fact, while the local opening directions along the propagator axis have a N68°E and N50°E orientation, the motion direction between Nubia and Arabia has a N40°E trend (Fig. 9).

This overview also shows that, along the axes of both the Red Sea propagator and the Main Ethiopian Rift, the opening is largely (with minor variations, as in the northern Main Ethiopian Rift) orthogonal to the trend of the rift. This implies that, regardless of any regional plate-motion direction, the active portion of a rift, that is its axis, is associated with an overall orthogonal extension. One may speculate whether this results from magmatic activity or not. In fact, there is recent and robust evidence that the deformation (extension fractures and normal faults) along the axis of the Main Ethiopian Rift and Red Sea propagator is magma-induced (Kendall et al., 2005; Buck, 2006; Casey et al., 2006; Sigmundsson, 2006; Ebinger et al., 2008). In this context, it may be postulated that the opening direction measured along the rift axis is related to the shallow emplacement of magma, commonly occurring by means of dikes (e.g., Gudmundsson, 1995, 1998). The measured opening directions at the surface may thus result from the emplacement of dikes, which are usually expected to open perpendicularly to the rift axis, regardless of any plate-motion direction.

In the Main Ethiopian Rift, the obtained opening direction of the fractures is slightly different (discrepancy of 16°) from that inferred by shear wave splitting data associated with dike



Rift axis	Trend	Open dir.	β
NRSP	N340°	N68°±10°	-2°
SRSP	N315°	N50°±15°	+5°
NMER	N24°	N102°±14°	-12°
Transfer zone	N47°	N129°±20°	-8°
SMER	N32°	N126°±20°	-4°

Figure 9. Synthesis of the collected opening directions along the northern (N) and southern (S) portions of the axis of the Red Sea propagator (RSP) and Main Ethiopian Rift (MER) (black arrows). White arrows show Nubia-Somalia (Calais et al., 2006; Keir et al., 2006) and Nubia-Arabia plate motions (Manighetti et al., 2001, and references therein). Table below summarizes the values obtained in this study.

emplacement, assuming orthogonal extension (Kendall et al., 2005). Within the rift, such an opening direction is assumed to be approximately N110°, whereas at the rift margins it increases to N125°. Therefore, if a magmatic control on the opening of the axial part of the Main Ethiopian Rift is expected, this should promote the possibility of a depth-dependent change in the kinematics of the rift. The deeper portion of the rift axis should be characterized by an extension direction consistent with plate motion, whereas the shallower portion, associated with orthogonal extension, should reflect a local variation.

CONCLUSIONS

The opening directions along the axis of the Red Sea propagator and Main Ethiopian Rift are constantly orthogonal to the trend of the rift. However, since the latter varies, the along-rift variation in the opening direction does not necessarily coincide with that inferred from plate-motion models. This discrepancy suggests the existence of an across-rift strain partitioning. The observed orthogonal extension along the rift axis may be magma-induced, provided that a depth-dependent variation in the kinematics exists, at least below the Main Ethiopian Rift axis.

ACKNOWLEDGMENTS

This study was financed with Ministero Università e Ricerca Scientifica e Tecnologica funds (F. Barberi and F. Salvini responsible). Structural analysis was performed with Daisy software (F. Salvini). A. Nicol and an anonymous reviewer provided helpful reviews.

REFERENCES CITED

- Abbate, E., Passerini, P., and Zan, L., 1995, Strike-slip faults in a rift area: A transect in the Afar Triangle, East Africa: *Tectonophysics*, v. 241, p. 67–97, doi:10.1016/0040-1951(94)00136-W.
- Acocella, V., 2006, Regional and local tectonics at Erta Ale caldera, Afar (Ethiopia): *Journal of Structural Geology*, v. 28, p. 1808–1820, doi:10.1016/j.jsg.2006.06.014.
- Acocella, V., and Korme, T., 2002, Holocene extension direction along the Main Ethiopian Rift, East Africa: *Terra Nova*, v. 14, p. 191–197, doi:10.1046/j.1365-3121.2002.00403.x.
- Acocella, V., Gudmundsson, A., and Funicello, R., 2000, Interaction and linkage of extensional fractures: Examples from the rift zone of Iceland: *Journal of Structural Geology*, v. 22, p. 1233–1246, doi:10.1016/S0191-8141(00)00031-6.
- Acocella, V., Korme, T., and Salvini, F., 2003, Formation of normal faults along the axial zone of the Ethiopian Rift: *Journal of Structural Geology*, v. 25, p. 503–513, doi:10.1016/S0191-8141(02)00047-0.
- Acocella, V., Abebe, B., Korme, T., and Barberi, F., 2008, Structure of Tendaho graben and Manda Hararo Rift: Implications for the evolution of the Red Sea propagator in central Afar: *Tectonics*, v. 27, TC4016, doi:10.1029/2007TC002236.
- Almond, D.C., 1986, Geological evolution of the Afro-Arabian dome: *Tectonophysics*, v. 131, p. 301–332, doi:10.1016/0040-1951(86)90180-0.
- Audin, L., Quidelleur, X., Coulie, E., Courtillot, V., Gilder, S., Manighetti, I., Gillot, P.Y., Tapponnier, P., and Kidane, T., 2004, Paleomagnetism and K-Ar and ⁴⁰Ar/³⁹Ar ages in the Ali Sabieh area (Republic of Djibouti and Ethiopia): Constraints on the mechanism of Aden ridge propagation into southeastern Afar during the last 10 Myr: *Geophysical Journal International*, v. 158, p. 327–345, doi:10.1111/j.1365-246X.2004.02286.x.
- Ayele, A., 2000, Normal left-oblique fault mechanisms as an indication of sinistral deformation between the Nubia and Somalia plates in the Main Ethiopian Rift: *Journal of African Earth Sciences*, v. 31, p. 359–367, doi:10.1016/S0899-5362(00)00093-2.
- Ayele, A., Jacques, E., Kassim, M., Kidane, T., Omar, A., Tait, S., Nercessian, A., de Chabaliere, J.B., and King, G., 2007, The volcano-seismic crisis in Afar, Ethiopia, starting December 2005: *Earth and Planetary Science Letters*, v. 255, p. 177–187, doi:10.1016/j.epsl.2006.12.014.
- Barberi, F., and Varet, J., 1970, The Erta Ale Volcanic Range (Danakil depression, northern Afar, Ethiopia): *Bulletin Volcanologique*, v. 34, p. 848–917, doi:10.1007/BF02596805.
- Benoit, M.H., Nyblade, A.A., and VanDecar, J.C., 2006, Upper mantle P-wave speed variations beneath Ethiopia and the origin of the Afar hotspot: *Geology*, v. 34, p. 329–332, doi:10.1130/G22281.1.
- Bilham, R., Bendick, R., Larson, K., Mohr, P., Braun, J., Tesfaye, S., and Asfaw, L., 1999, Secular and tidal strain across the Main Ethiopian Rift: *Geophysical Research Letters*, v. 26, p. 2789–2792, doi:10.1029/1998GL005315.
- Boccaletti, M., Bonini, M., Mazzuoli, R., Abebe, B., Piccardi, L., and Tortorici, L., 1998, Quaternary oblique extensional tectonics in the Ethiopian Rift (Horn of Africa): *Tectonophysics*, v. 287, p. 97–116, doi:10.1016/S0040-1951(98)80063-2.
- Bonini, M., Souriot, T., Boccaletti, M., and Brun, J.P., 1997, Successive orthogonal and oblique extension episodes in a rift zone: Laboratory experiments with application to the Ethiopian Rift: *Tectonics*, v. 16, p. 347–362, doi:10.1029/96TC03935.
- Bosworth, W., Huchon, P., and McClay, K., 2005, The Red Sea and Gulf of Aden basins: *Journal of African Earth Sciences*, v. 43, p. 334–378, doi:10.1016/j.jafrearsci.2005.07.020.
- Buck, W.R., 2006, The role of magma in the development of the Afro-Arabian rift system, in Yirgu, G., Ebinger, C.J., and Maguire, P.K.H., eds., *The Afar Volcanic Province within the East African Rift System: Geological Society of London Special Publication 259*, p. 43–54.
- Calais, E., Ebinger, C., Hartnady, C., and Nocquet, J.M., 2006, Kinematics of the East African Rift from GPS and earthquake slip vector data, in Yirgu, G., Ebinger, C.J., and Maguire, P.K.H., eds., *The Afar Volcanic Province within the East African Rift System: Geological Society of London Special Publication 259*, p. 9–22.
- Casey, M., Ebinger, C., Keir, D., Gloaguen, R., and Mohamed, F., 2006, Strain accommodation in transitional rifts: Extension by magma intrusion and faulting in Ethiopian rift magmatic segments, in Yirgu, G., Ebinger, C.J., and Maguire, P.K.H., eds., *The Afar Volcanic Province within the East African Rift System: Geological Society of London Special Publication 259*, p. 143–163.
- Cattin, R., Doubre, C., de Chabaliere, J.B., King, G., Vigny, C., Avouac, J.P., and Ruegg, J.C., 2005, Numerical modeling of Quaternary deformation and post-rifting displacement in the Asal-Ghoubbet rift (Djibouti, Africa): *Earth and Planetary Science Letters*, v. 239, p. 352–367, doi:10.1016/j.epsl.2005.07.028.
- Chernet, T., Hart, W., Aronson, J.L., and Walter, R.C., 1998, New age constraints on the timing of volcanism and tectonism in the northern Main Ethiopian Rift–southern Afar transition zone (Ethiopia): *Journal of Volcanology and Geothermal Research*, v. 80, p. 267–280, doi:10.1016/S0377-0273(97)00035-8.
- Chorowicz, J., Collet, B., Bonavia, F.F., and Korme, T., 1994, Northwest to north-northwest extension direction in the Ethiopian Rift deduced from the orientation of extension structures and fault-slip analysis: *Geological Society of America Bulletin*, v. 106, p. 1560–1570, doi:10.1130/0016-7606(1994)105<1560:NTNED>2.3.CO;2.
- Chu, D., and Gordon, R.G., 1999, Evidence for motion between Nubia and Somalia along the Southwest Indian Ridge: *Nature*, v. 398, p. 64–67, doi:10.1038/18014.
- Collet, B., Parrot, J.F., and Taud, H., 2000, Orientation of absolute African plate motion revealed by tomographic analysis of the Ethiopian dome: *Geology*, v. 28, p. 1147–1149, doi:10.1130/0091-7613(2000)28<1147:OOAAMP>2.0.CO;2.
- Corti, G., 2008, Control of rift obliquity on the evolution and segmentation of the main Ethiopian rift: *Nature Geoscience*, v. 1, p. 258–262, doi:10.1038/ngeo160.
- D’Acromont, E., Leroy, S., Beslier, M.O., Bellahsen, N., Fournier, M., Robin, C., Maia, M., and Gente, P., 2005, Structure and evolution of the eastern Gulf of Aden conjugate margins from seismic reflection data: *Geophysical Journal International*, v. 160, p. 869–890, doi:10.1111/j.1365-246X.2005.02524.x.

- Dauteuil, O., and Brun, J., 1993, Oblique rifting in a slow-spreading ridge: *Nature*, v. 361, p. 145–148, doi:10.1038/361145a0.
- Dauteuil, O., Huchon, P., Quemeneur, F., and Souriot, T., 2001, Propagation of an oblique spreading centre: The western Gulf of Aden: *Tectonophysics*, v. 332, p. 423–442, doi:10.1016/S0040-1951(00)00295-X.
- Davidson, A., and Rex, D.C., 1980, Age of volcanism and rifting in southwestern Ethiopia: *Nature*, v. 283, p. 657–658, doi:10.1038/283657a0.
- Eagles, G., Gloaguen, R., and Ebinger, C., 2002, Kinematics of the Danakil microplate: *Earth and Planetary Science Letters*, v. 203, p. 607–620, doi:10.1016/S0012-821X(02)00916-0.
- Ebinger, C.J., and Casey, M., 2001, Continental breakup in magmatic provinces: An Ethiopian example: *Geology*, v. 29, p. 527–530, doi:10.1130/0091-7613(2001)029<0527:CBIMPA>2.0.CO;2.
- Ebinger, C.J., and Hayward, N.J., 1996, Soft plates and hot spots: Views from Afar: *Journal of Geophysical Research*, v. 101, p. 21,859–21,876, doi:10.1029/96JB02118.
- Ebinger, C.J., Bechtel, T.D., Forsyth, D.W., and Bowin, C.O., 1989, Effective elastic plate thickness beneath the East African and Afar plateaus and dynamic compensation of the uplifts: *Journal of Geophysical Research*, v. 94, p. 2883–2901, doi:10.1029/JB094iB03p02883.
- Ebinger, C.J., Keir, D., Ayele, A., Calais, E., Wright, T.J., Belachew, M., Hammond, J.O.S., Campbell, E., and Buck, W.R., 2008, Capturing magma intrusion and faulting processes during continental rupture: Seismicity of the Dabbahu (Afar) rift: *Geophysical Journal International*, v. 174, p. 1138–1152, doi:10.1111/j.1365-246X.2008.03877.x.
- Gibson, I., 1969, The structure and volcanic geology of an axial portion of the Main Ethiopian Rift: *Tectonophysics*, v. 8, p. 561–565, doi:10.1016/0040-1951(69)90054-7.
- Gudmundsson, A., 1987, Geometry, formation and development of tectonic fractures on the Reykjanes Peninsula, southwest Iceland: *Tectonophysics*, v. 139, p. 295–308, doi:10.1016/0040-1951(87)90103-X.
- Gudmundsson, A., 1992, Formation and growth of normal faults at the divergent plate boundary in Iceland: *Terra Nova*, v. 4, p. 464–471, doi:10.1111/j.1365-3121.1992.tb00582.x.
- Gudmundsson, A., 1995, Infrastructure and mechanics of volcanic systems in Iceland: *Journal of Volcanology and Geothermal Research*, v. 64, p. 1–22, doi:10.1016/0377-0273(95)92782-Q.
- Gudmundsson, A., 1998, Magma chambers modeled as cavities explain the formation of rift zone central volcanoes and their eruption and intrusion statistics: *Journal of Geophysical Research*, v. 103, p. 7401–7412, doi:10.1029/97JB03747.
- Hayward, N.J., and Ebinger, C.J., 1996, Variation in the along-axis segmentation of the Afar Rift system: *Tectonics*, v. 15, p. 244–257, doi:10.1029/95TC02292.
- Jestin, F., Huchon, P., and Gaulier, J.M., 1994, The Somalia plate and the East African Rift system: Present-day kinematics: *Geophysical Journal International*, v. 116, p. 637–654, doi:10.1111/j.1365-246X.1994.tb03286.x.
- Keir, D., Ebinger, C.J., Stuart, G.W., Daly, E., and Ayele, A., 2006, Strain accommodation by magmatism and faulting as rifting proceeds to breakup: Seismicity of the northern Ethiopian Rift: *Journal of Geophysical Research*, v. 111, B05314, doi:10.1029/2005JB003748.
- Kendall, J.M., Stuart, G.W., Ebinger, C.J., Bastow, I.D., and Keir, D., 2005, Magma-assisted rifting in Ethiopia: *Nature*, v. 433, p. 146–148, doi:10.1038/nature03161.
- Korme, T., Chorowicz, J., Collet, B., and Bonavia, F.F., 1997, Volcanic vents rooted on extension fractures and their geodynamic implications in the Ethiopian Rift: *Journal of Volcanology and Geothermal Research*, v. 79, p. 205–222, doi:10.1016/S0377-0273(97)00034-6.
- Latin, D., and White, N., 1990, Generating melt during lithospheric extension: Pure shear vs. simple shear: *Geology*, v. 18, p. 327–331.
- Le Pichon, X., and Francheteau, J., 1978, A plate-tectonic analysis of the Red Sea–Gulf of Aden area: *Tectonophysics*, v. 46, p. 369–406, doi:10.1016/0040-1951(78)90214-7.
- Manighetti, I., Tapponnier, P., Courtillot, V., Gruszow, S., and Gillot, P.Y., 1997, Propagation of rifting along the Arabia–Somalia plate boundary: The Gulfs of Aden and Tadjoura: *Journal of Geophysical Research*, v. 102, p. 2681–2710, doi:10.1029/96JB01185.
- Manighetti, I., Tapponnier, P., Gillot, P.Y., Jacques, E., Courtillot, V., Armijo, R., Ruegg, J.C., and King, G., 1998, Propagation of rifting along the Arabia–Somalia plate boundary: Into Afar: *Journal of Geophysical Research*, v. 103, p. 4947–4974, doi:10.1029/97JB02758.
- Manighetti, I., Tapponnier, P., Courtillot, V., Gallet, Y., Jacques, E., and Gillot, P.Y., 2001, Strain transfer between disconnected, propagating rifts in Afar: *Journal of Geophysical Research*, v. 106, p. 13,613–13,665, doi:10.1029/2000JB000454.
- McClay, K.R., and White, M.J., 1995, Analogue modelling of orthogonal and oblique rifting: *Marine and Petroleum Geology*, v. 12, p. 137–151, doi:10.1016/0264-8172(95)92835-K.
- McKenzie, D.P., Davies, D., and Molnar, P., 1970, Plate tectonics of the Red Sea and East Africa: *Nature*, v. 226, p. 243–248, doi:10.1038/226243a0.
- Mohr, P., 1967, Major volcano-tectonic lineament in the Ethiopian Rift system: *Nature*, v. 213, p. 664–665, doi:10.1038/213664a0.
- Mohr, P., 1987, Patterns of faulting in the Ethiopian Rift Valley: *Tectonophysics*, v. 143, p. 169–179, doi:10.1016/0040-1951(87)90086-2.
- Mouslopoulou, V., Nicol, A., Little, T.A., and Walsh, J.J., 2007, Displacement transfer between intersecting regional strike-slip and extensional fault systems: *Journal of Structural Geology*, v. 29, p. 100–116, doi:10.1016/j.jsg.2006.08.002.
- Needham, H.D., Choukroune, P., Cheminee, J.L., Le Pichon, X., Francheteau, J., and Tapponnier, P., 1976, The accreting plate boundary: Ardoukoba rift (northeast Africa) and the oceanic rift valley: *Earth and Planetary Science Letters*, v. 28, p. 439–453, doi:10.1016/0012-821X(76)90205-3.
- Pan, M., Sjöberg, L.E., Asfaw, L.M., Asenjo, E., Alemu, A., and Hunegnaw, A., 2002, An analysis of the Ethiopian Rift Valley GPS campaigns in 1994 and 1999: *Journal of Geodynamics*, v. 33, p. 333–343, doi:10.1016/S0264-3707(01)00076-X.
- Pizzi, A., Coltorti, M., Abebe, B., Disperati, L., Sacchi, G., and Salvini, R., 2006, The Wonji fault belt (Main Ethiopian Rift): Structural and geomorphological constraints and GPS monitoring, in Yirgu, G., Ebinger, C.J., and Maguire, P.K.H., eds., *The Afar Volcanic Province within the East African Rift System: Geological Society of London Special Publication* 259, p. 191–207.
- Sigmundsson, F., 2006, Magma does the splits: *Nature*, v. 442, p. 251–252, doi:10.1038/442251a.
- Stein, R.S., Briole, P., Ruegg, J.C., Tapponnier, P., and Gasse, F., 1991, Contemporary Holocene and Quaternary deformation of the Asal Rift, Djibuti: Implications for the mechanics of slow spreading ridges: *Journal of Geophysical Research*, v. 96, p. 21,789–21,806, doi:10.1029/91JB02118.
- Tapponnier, P., Armijo, R., Manighetti, I., and Courtillot, V., 1990, Bookshelf faulting and horizontal block rotations between overlapping rifts in Southern Afar: *Geophysical Research Letters*, v. 17, p. 1–4, doi:10.1029/GL017i001p00001.
- Taylor, B., Crook, K., and Sinton, J., 1994, Extensional transform zones and oblique spreading centers: *Journal of Geophysical Research*, v. 99, p. 19,707–19,718, doi:10.1029/94JB01662.
- Tazieff, H., Varet, J., Barberi, F., and Giglia, G., 1972, Tectonic significance of the Afar (or Danakil) depression: *Nature*, v. 235, p. 144–147.
- Tuckwell, G.W., Bull, J.M., and Sanderson, D.J., 1998, Numerical models of faulting at oblique spreading centers: *Journal of Geophysical Research*, v. 103, p. 15,473–15,482, doi:10.1029/97JB03673.
- Vigny, C., de Chaballier, J.B., Ruegg, J.C., Huchon, P., Feigl, K.L., Cattin, R., Asfaw, L., and Kanbari, K., 2007, Twenty-five years of geodetic measurements along the Tadjoura–Asal rift system, Djibuti, East Africa: *Journal of Geophysical Research*, v. 112, B06410, doi:10.1029/2004JB003230.
- Williams, F.M., Williams, M.A.J., and Aumento, F., 2004, Tensional fissures and crustal extension rates in the northern part of the Main Ethiopian Rift: *Journal of African Earth Sciences*, v. 38, p. 183–197, doi:10.1016/j.jafrearsci.2003.10.007.
- Woldegabriel, G., Aronson, J.L., and Walter, R.C., 1990, Geology, geochronology and rift basin development in the central sector of the Main Ethiopian Rift: *Geological Society of America Bulletin*, v. 102, p. 439–458, doi:10.1130/0016-7606(1990)102<0439:GGARBD>2.3.CO;2.
- Wolfenden, E., Ebinger, C., Yirgu, G., Deino, A., and Ayalew, D., 2004, Evolution of the northern Main Ethiopian Rift: Birth of a triple junction: *Earth and Planetary Science Letters*, v. 224, p. 213–228, doi:10.1016/j.epsl.2004.04.022.
- Wright, T.J., Ebinger, C., Biggs, J., Ayele, A., Yirgu, G., Keir, D., and Stork, A., 2006, Magma maintained rift segmentation at continental rupture in the 2005 Afar dyking episode: *Nature*, v. 442, p. 291–294, doi:10.1038/nature04978.

The upper-mantle low-velocity anomaly beneath Ethiopia, Kenya, and Tanzania: Constraints on the origin of the African superswell in eastern Africa and plate versus plume models of mantle dynamics

Andrew A. Nyblade*

Department of Geosciences, Pennsylvania State University, University Park, Pennsylvania 16802, USA

ABSTRACT

To further advance our understanding of the way in which a portion of the African superswell in eastern Africa formed, and also to draw attention to the importance of eastern Africa for the plume versus plate debate about mantle dynamics, upper-mantle structure beneath eastern Africa is reviewed by synthesizing published results from three types of analyses applied to broadband seismic data recorded in Tanzania, Kenya, and Ethiopia. (1) Joint inversions of receiver functions and surface wave dispersion measurements show that the lithospheric mantle of the Ethiopian Plateau has been significantly perturbed, much more so than the lithospheric mantle of the East African Plateau. (2) Body wave tomography reveals a broad (≥ 300 km wide) and deep (≥ 400 km) low-velocity anomaly beneath the Ethiopian Plateau and the eastern branch of the rift system in Kenya and Tanzania. (3) Receiver function stacks showing Ps conversions from the 410 km discontinuity beneath the eastern branch in Kenya and Tanzania reveal that this discontinuity is depressed by 20–40 km in the same location as the low-velocity anomaly. The coincidence of the depressed 410 km discontinuity and the low-velocity anomaly indicates that the low-velocity anomaly is caused primarily by temperatures several hundred degrees higher than ambient mantle temperatures. These findings cannot be explained easily by models invoking a plume head and tail, unless there are a sufficient number of plume tails presently under eastern Africa side-by-side to create a broad and deep thermal structure. These findings also cannot be easily explained by the plate model. In contrast, the breadth and depth of the upper-mantle thermal structure can be explained by the African superplume, which in some tomographic models extends into the upper mantle beneath eastern Africa. Consequently, a superplume origin for the anomalous topography of the African superswell in eastern Africa, in addition to the Cenozoic rifting and volcanism found there, is favored.

*nyblade@psu.edu

INTRODUCTION

The African superswell is a first-order topographic feature on Earth, covering some 1×10^7 km² (Nyblade and Robinson, 1994) of the African plate. It is composed of several contiguous geographic regions, including the Ethiopian Plateau, the East African Plateau, the Southern African Plateau, and a region of elevated bathymetry in the southeastern Atlantic Ocean Basin, which together form a distinctive topographic anomaly. By removing the mean global continental elevation from the observed elevations in Africa, and by removing the age-predicted bathymetry from the observed bathymetry in the ocean basins around Africa, Nyblade and Robinson (1994) showed that the long-wavelength (i.e., more than a few hundred kilometers) anomalous topography and bathymetry associated with the African superswell is ~500 m. Many shorter-wavelength topographic and bathymetric features are superimposed on this long-wavelength swell, creating the so-called “basin and swell” landscape of Holmes (1944). It has long been argued (e.g., Holmes, 1944; King, 1962; Burke, 1996; Burke et al., 2003; Burke and Gunnell, 2008) that the shorter-wavelength “basin and swell” landscape is the most prominent topographic feature of the African continent, but Doucouré and de Wit (2003), through a statistical analysis of African topography, showed clearly that most of the “basins and swells” are second- or third-order topographic features superimposed on the first-order topographic anomaly of the superswell.

The origin of the African superswell has been debated for many years, and as yet there is no clear consensus about the geodynamic mechanisms giving rise to its defining long-wavelength topographic structure. Given the different tectonic histories of the major regions that constitute the superswell (i.e., eastern African, southern Africa, the southern Atlantic Ocean Basin), it is possible that many mechanisms may have contributed to its overall development. On the other hand, because the superswell is located above one of the largest geophysical anomalies anywhere in the lower mantle, the African superplume, several investigators have attributed the uplift of one or more parts of the superswell to lower-mantle processes that affect, and possibly extend into, the upper mantle (e.g., Lithgow-Bertelloni and Silver, 1998; Gurnis et al., 2000; Doucouré and de Wit, 2002; Benoit et al., 2006b; Huerta et al., 2009).

The origin of the African superswell is also relevant to an ongoing debate about the extent to which hotspot tectonism is caused by mantle plumes versus upper-mantle processes linked to plate motions and plate structures (e.g., the plume versus plate model debate; see Anderson, 2005, and references therein). A significant portion of the superswell in eastern Africa is considered to be a classic hotspot locale, in particular, those areas of eastern Africa affected by Cenozoic rifting, volcanism, and uplift. Resolving the uncertainties over the origin of the African superswell, therefore, has the potential to substantially improve our knowledge of mantle dynamics.

To advance further our understanding of how the portion of the African superswell in eastern Africa formed, and also to

draw attention to the importance of eastern Africa for the plume versus plate debate, in this paper, upper-mantle structure beneath eastern Africa is reviewed by synthesizing published results from data recorded on regional broadband seismic networks operated in Tanzania, Kenya, and Ethiopia between 1994 and 2002. Both lithospheric and sublithospheric mantle structure is examined by focusing on results from three types of data analyses—joint inversion of receiver functions and surface wave dispersion measurements for imaging lithospheric mantle structure, body wave tomography for imaging seismic velocity variations in the sublithospheric mantle, and receiver function stacks for imaging the mantle discontinuities around depths of 410 and 660 km. Results from these analyses, which place firm seismological constraints on the width and depth extent of the upper-mantle low-velocity anomaly beneath eastern Africa, are then used to evaluate conceptual models for the origin of plateau uplift in eastern Africa, along with the associated Cenozoic volcanism and rifting. In conclusion, the findings of the review regarding the origin of the African superswell are discussed in light of other seismic models of the African mantle and also the plume versus plate debate about mantle dynamics.

BACKGROUND

The Precambrian tectonic framework of eastern Africa consists of the Archean Tanzania craton surrounded by the Proterozoic Ruwenzori, Kibaran, Ubendian, and Mozambique belts (Fig. 1). The Cenozoic East African Rift system developed primarily within the mobile belts and forms two branches (eastern and western; Fig. 1). The eastern branch in Ethiopia divides the Ethiopian Plateau into eastern and western sections and continues southward through west-central Kenya and into northern Tanzania, transecting the northeastern corner of the East African Plateau. In Kenya, the eastern branch is locally referred to as the Kenya or Gregory Rift. The eastern branch of the East African Rift system was formed within the Mozambique belt, which runs from Ethiopia south through Kenya, Tanzania, and Mozambique, and is often interpreted as the relict of a Himalayan-type orogenic system (Burke and Şengör, 1986; Shackleton, 1986). The western branch of the East African Rift system defines the western side of the East African Plateau (Fig. 1), and was developed within the Ruwenzori, Kibaran, and Ubendian belts.

Widespread volcanic activity started in the central Ethiopian Plateau during the Oligocene (ca. 29–31 Ma) and resulted in the emplacement of thick (500–2000 m) flood basalts and rhyolites within 1–2 m.y. (Hofmann et al., 1997; Mohr and Zanettin, 1988; Mohr, 1983; Berhe et al., 1987; Baker et al., 1996; Ayalew et al., 2002; Coulié et al., 2003). Less voluminous synrift shield volcanoes formed between 30 and 10 Ma and sit on top of the flood basalts to create additional relief of 1000–2000 m (Berhe et al., 1987; Coulié et al., 2003). The Afar triple junction formed long after the eruption of the Afar flood basalt volcanism as a result of the opening of the eastern branch of the East African Rift system. In the northern parts of the Main

Ethiopian Rift, extension started ca. 11 Ma (Wolfenden et al., 2004; Chernet et al., 1998; WoldeGabriel et al., 1999), while in southwestern Ethiopia, extension started ca. 18 Ma (Ebinger et al., 2000). Uplift of the Ethiopian Plateau occurred between 20 and 30 Ma, coincident with or soon after the major flood basalt eruption (Pik et al., 2003). Volcanism and rifting in Kenya are thought to have occurred at about the same time (Ebinger et al., 1989). The earliest volcanism in Kenya started in the Turkana region of northern Kenya ca. 35–40 Ma (Furman et al., 2006; MacDonald et al., 2001). Magmatic activity in other parts of northern Kenya began ca. 30 Ma (Morley et al., 1992; Ritter and Kaspar, 1997), while volcanism started ca. 15 Ma in the

central portion of the Kenya rift, at ca. 12 Ma in southern Kenya (Morley et al., 1992; Hendrie et al., 1994; Mechie et al., 1997), and at ca. 8 Ma in northern Tanzania (Dawson, 1992; Foster et al., 1997). Volcanism in the western rift began ca. 12 Ma in the Virunga Province, ca. 8 Ma in the Kivu and Rungwe Provinces, ca. 6 Ma in the Mwenga-Kamituga Province, and ca. 2–1 Ma in the Toro-Ankolean Province (Ebinger et al., 1989; Pasteels et al., 1989; Kampunzu et al., 1998). Timing of plateau formation in East Africa remains poorly constrained, although there is evidence for localized Neogene uplift along the flanks of some rift valleys (e.g., Noble et al., 1997; van der Beek et al., 1998; Spiegel et al., 2007).

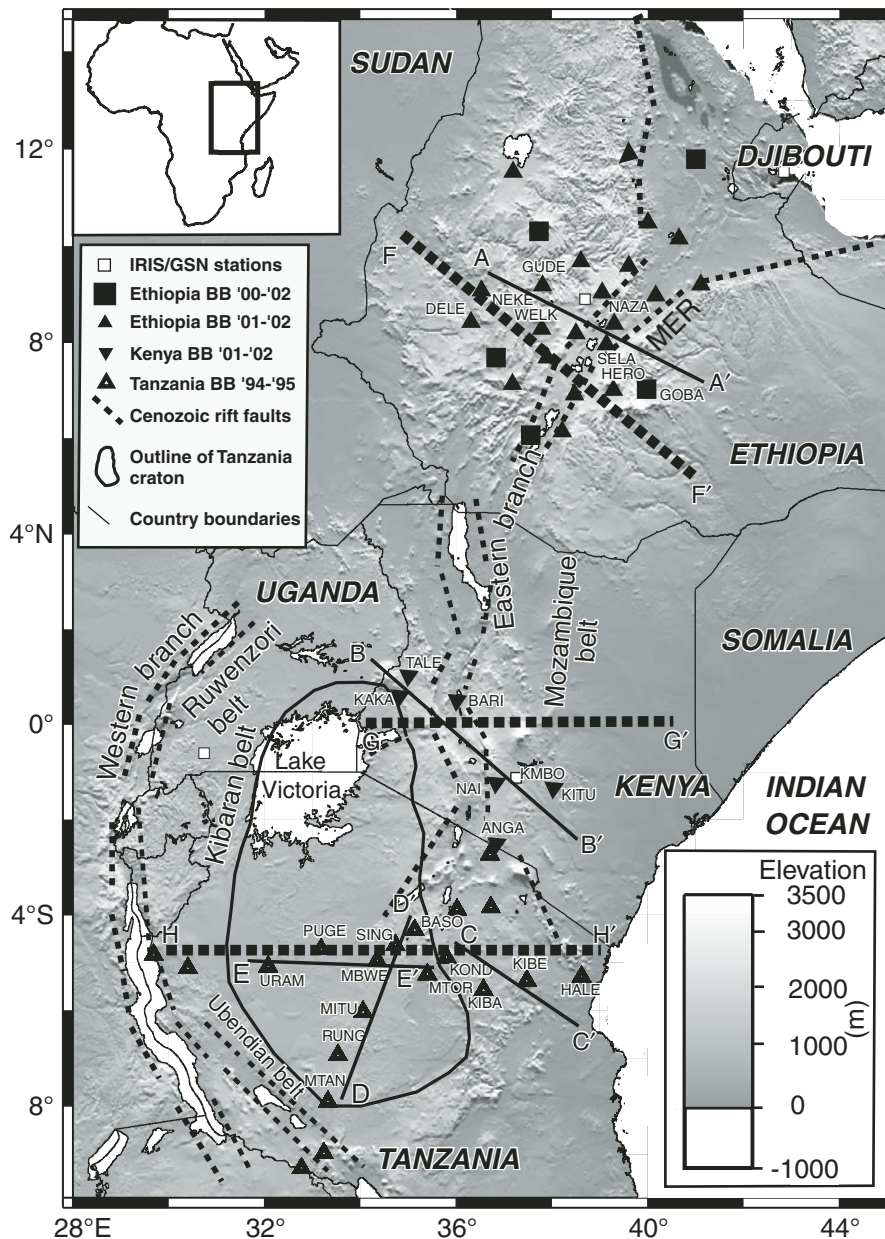


Figure 1. Map of eastern Africa showing elevation (gray scale), political boundaries, Precambrian terrains, major Cenozoic rift faults, the location of broadband (BB) seismic stations, and the location of lithospheric profiles shown in Figure 2 (profiles A–A', B–B', C–C', D–D', E–E') and cross sections shown in Figure 3 (F–F', G–G', H–H'). IRIS—Incorporated Research Institutions for Seismology; GSN—Global Seismographic Network.

Data used for the seismic analyses come primarily from three temporary deployments of broadband seismic stations in eastern Africa (Fig. 1). The 1994–1995 Tanzania broadband seismic experiment consisted of 20 stations deployed in two more-or-less linear arrays spanning Tanzania (Nyblade et al., 1996). The 2000–2002 Kenya broadband seismic experiment consisted of 10 stations deployed across central and southern Kenya, and the Ethiopia broadband seismic experiment consisted of 27 stations deployed across central and northern Ethiopia (Nyblade and Langston, 2002). In addition to these data sets, data from earthquakes recorded on the KRISP (Kenya Rift International Science Project) 1985 and 1989–1990 networks in Kenya (Green et al., 1991; Slack et al., 1994) were used, as well as data from the 2001–2003 EAGLE (Ethiopia Afar Geoscientific Lithosphere Experiment) project in Ethiopia (Bastow et al., 2005) and the permanent Global Seismic Network and Geoscope stations in the region.

LITHOSPHERIC MANTLE STRUCTURE

To image lithospheric mantle structure, the same joint inversion scheme has been applied to P-wave receiver functions and fundamental mode Rayleigh wave phase and group velocities for all three data sets by Julià et al. (2005) (Tanzania), Dugda et al. (2007) (Ethiopia), and Dugda et al. (2009) (Kenya). Receiver functions and surface wave velocities provide complementary information on Earth structure. Receiver functions are time series obtained by deconvolving the vertical component of the teleseismic P-wave coda from the corresponding radial component and can be used to resolve velocity discontinuities in the neighborhood of a seismic station (Langston, 1979; Ammon et al., 1990; Julià et al., 2000). Rayleigh wave phase and group velocities, in contrast, can be used to constrain the average shear wave velocity between the discontinuities (Julià et al., 2000).

The method developed by Julià et al. (2003) for the joint inversion was applied to the seismic data from Tanzania (Julià et al., 2005), Kenya (Dugda et al., 2009), and Ethiopia (Dugda et al., 2007). Rayleigh wave group velocities between periods of 10 and 45 s from Pasyanos (2005), and Rayleigh wave phase velocities between periods of 50 and 140 s from Weeraratne et al. (2003), were used in the joint inversion for the data from Tanzania and Kenya (Dugda et al., 2009; Julià et al., 2005). For Ethiopia, Rayleigh wave group velocities between periods of 10 and 85 s were used from Pasyanos (2005) and between periods of 90 and 175 s from the Harvard model (Larson and Ekstrom, 2001). Receiver functions were computed using seismograms from teleseismic events between distances of 30° and 95° with magnitudes greater than 5.5. The time-domain iterative deconvolution method of Ligorria and Ammon (1999) was employed to compute the receiver functions.

Results of the joint inversions to a depth of 100 km for selected stations are shown in Figure 2 to illustrate variations and similarities in lithospheric mantle velocities (i.e., shaded regions on profiles with $V_s > 4$ km/s) between the East African

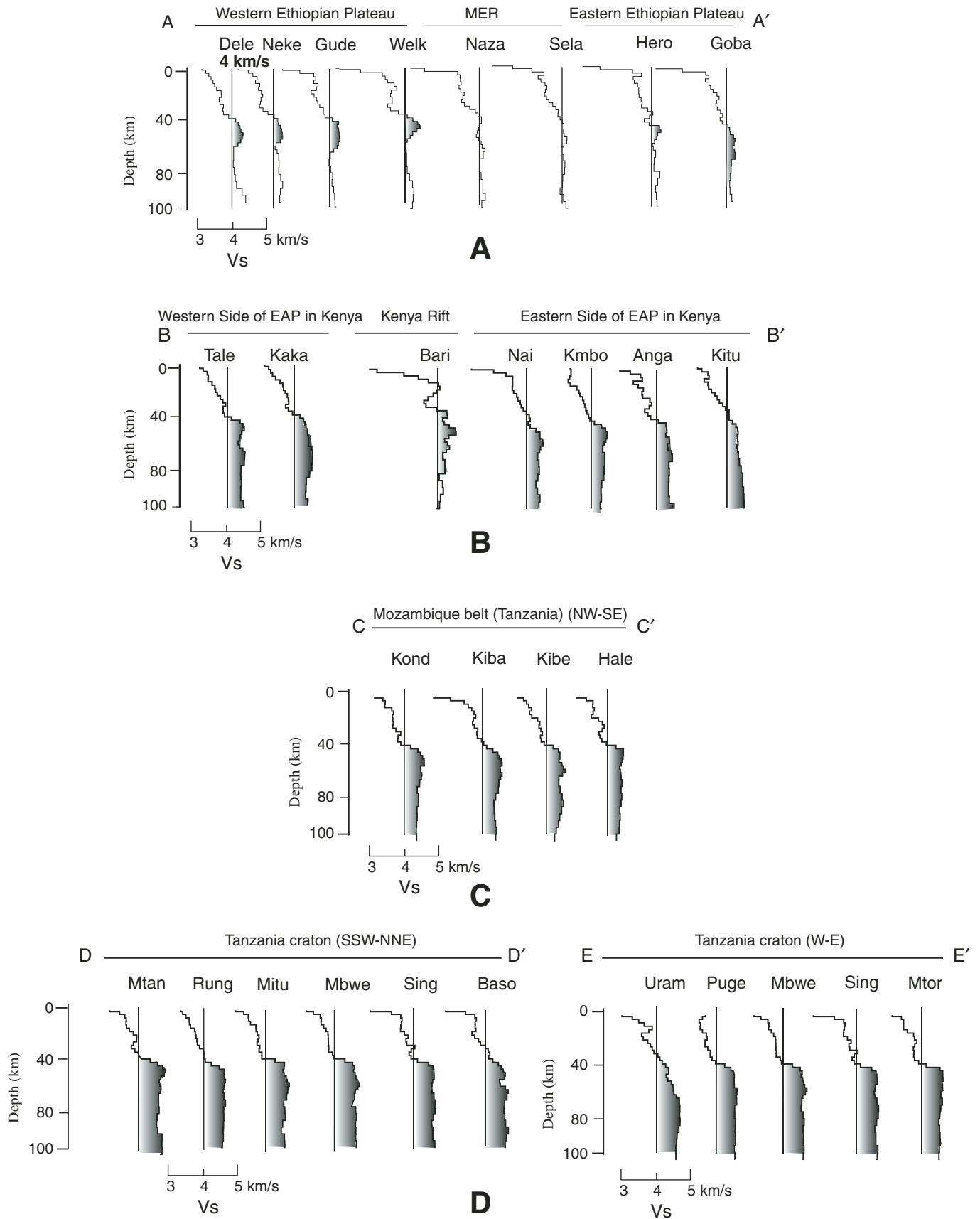
and Ethiopian Plateaus. Structure below 100 km depth is not shown because it is not as well constrained by the joint inversion as structure above ~100 km depth. From Figure 2, it can be seen that lithospheric mantle velocities beneath the Tanzania craton and Mozambique belt in Tanzania and Kenya are similar, with more or less constant shear wave velocities of 4.5–4.7 km/s from the Moho to 100 km depth. The figure suggests that the velocities in the lithosphere under the Tanzania craton might be somewhat faster than beneath the Mozambique belt, but given the uncertainties in the velocities at any one depth of 0.1–0.2 km/s, the differences between the craton and mobile belt may not be significant. Interestingly, lithospheric mantle structure under the Mozambique belt in Kenya within proximity of the Kenya Rift is similar to that in Tanzania well away from the rift, while lithospheric mantle structure beneath the Kenya Rift (station BARI, Fig. 2) is clearly perturbed.

Figure 2 also shows that there are significant differences in lithospheric mantle structure between the East African and Ethiopian Plateaus. The lithosphere under the Ethiopian Plateau is thin, extending to depths of no more than ~80–90 km. The maximum S velocity is also very low, reaching only to 4.2–4.3 km/s, compared to 4.5–4.7 km/s beneath the Mozambique belt in Tanzania and Kenya. There is little similarity between the lithosphere under the East African and Ethiopian Plateaus. The lithospheric mantle of the Ethiopian Plateau has been significantly perturbed by the hotspot activity, much more so than the lithospheric mantle of the East African Plateau (Dugda et al., 2007, 2009).

SUBLITHOSPHERIC MANTLE STRUCTURE

To image sublithospheric mantle structure, the same body wave traveltime tomography method was applied to the data sets from all three regions by Ritsema et al. (1998) (Tanzania), Benoit et al. (2006a, 2006b) (Ethiopia), and Park and Nyblade (2006) (Kenya). The teleseismic events used from each data set were distributed over a range of back azimuths, providing reasonably good azimuthal coverage. Relative traveltime delays were computed using the multichannel cross-correlation technique of VanDecar and Crosson (1990), and then values were inverted for three-dimensional wave speed models using the method of VanDecar (1991). This method incorporates three-dimensional ray tracing into a simultaneous linear inversion for slowness, near-surface corrections, and earthquake relocations and provides a conservative estimate of the structure that accounts for

Figure 2. Profiles showing one-dimensional shear wave velocity models for seismic stations in eastern Africa (from Dugda et al., 2009). The locations of the profiles and seismic stations are given in Figure 1. The thin vertical line on each model shows a reference velocity of 4 km/s. The shaded regions on each model highlight parts of the model where velocities are >4 km/s. MER—Main Ethiopian Rift; EAP—East African Plateau.



the variations in the traveltime residuals across a network. P- and S-wave models were obtained for Tanzania (Ritsema et al., 1998) and Ethiopia (Benoit et al., 2006a, 2006b), and for each region, the first-order features in the P and S models are similar. Because of limited data, only a P-wave model was obtained for Kenya (Park and Nyblade, 2006).

To evaluate model resolution, several tests were conducted for each region. Synthetic traveltime data were generated for many input models (checkerboards, slabs, spheres) by using the ray paths for the data and then inverting them using the same model parameterization and regularization parameters that were used to invert the data. Results of the synthetic tests illustrate that model resolution for each region is comparable, ~ 50 km horizontally and ~ 100 km vertically.

Figures 3 and 4 illustrate the main features of the models. In Figure 3, slices through the models at 200 km depth are shown. The models were constructed independently, and the slices have been simply assembled together to create a composite image for eastern Africa. Figure 4 shows three W-E cross sections (see Fig. 1 for locations of the cross sections). The model for Ethiopia shows a broad (>400 -km-wide) region of low seismic velocity beneath the Ethiopian Plateau. At 150–200 km depth, a region of low velocities is seen beneath the Afar Depression, the Main Ethiopian Rift, and slightly west of the rift under the western portion of the Ethiopian Plateau. Deeper in the models (>200 km depth), the center of the low-velocity structure shifts westward across the western section of the Ethiopian Plateau, offset from the strike of the Main Ethiopian Rift (Fig. 4A).

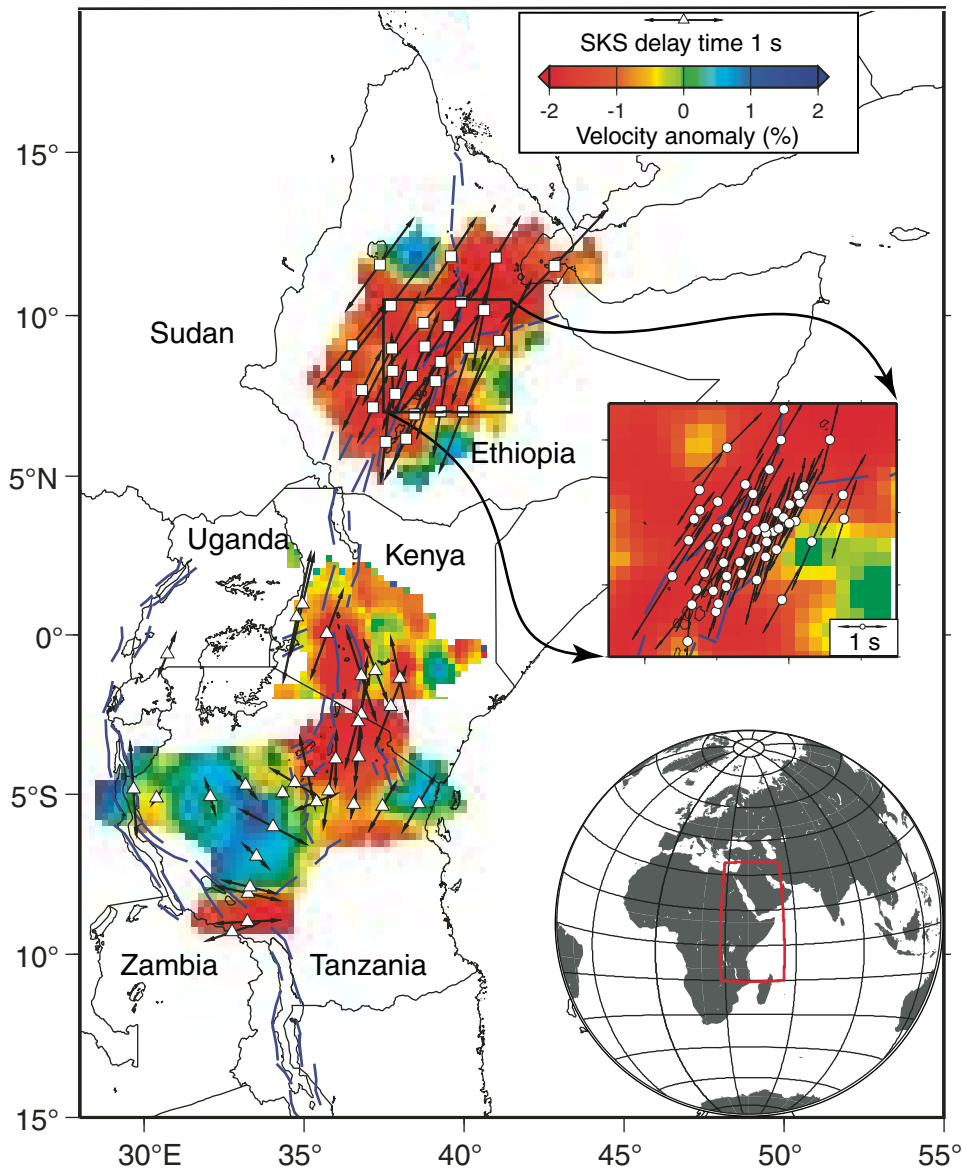


Figure 3. Map showing the location of the major rift faults (blue lines) and S-wave velocity variations at 200 km depth beneath eastern Africa from body wave tomography models for Tanzania (Ritsema et al., 1998), Kenya (Park and Nyblade, 2006), and Ethiopia (Benoit et al., 2006b). For Kenya, the P-wave velocity variations were converted to S-wave velocity variations using a Poisson's ratio of 0.295. Also shown with arrows are results from shear wave splitting measurements (Tanzania and Kenya—Walker et al., 2004; Ethiopia—Kendall et al., 2005; Gashawbeza et al., 2004). The orientation of the arrows shows the direction of fast polarization, and the length of the arrows gives delay time. The inset box shows the shear wave splitting measurements from within the Main Ethiopian Rift.

The low-velocity region in the upper mantle beneath the Ethiopian Plateau extends at least as deep as the top of the mantle transition zone over a region >400 wide (Fig. 4A). Resolution tests (Benoit et al., 2006a, 2006b) indicate that the low velocities in the transition zone cannot be attributed to the smearing of shallower (i.e., ≤ 300 km depth) structure downward into the transition zone by the inversion algorithm. Given the ~ 100 km vertical resolution of the models, the presence of low velocities at

≥ 500 km depth indicates that the low velocities extend at least to the top of the transition zone. A similar model showing a broad, low-velocity anomaly beneath Ethiopia extending into the transition zone has been reported by Bastow et al. (2008) using a larger traveltimes data set than used by Benoit et al. (2006a, 2006b).

For the Kenya model, traveltimes data from the KRISP network were used together with the data from the Kenya broadband seismic experiment. The shape of the low-velocity anomaly in the model for Kenya above 150 km depth is almost identical to that obtained by the KRISP group (Green et al., 1991; Achauer et al., 1994; Slack et al., 1994; Achauer and Masson, 2002; Davis and Slack, 2002) (Fig. 4B). The low-velocity region is characterized by steep, near-vertical sides located under the rift border faults (Fig. 4B). At depths greater than 150 km, the low-velocity region enlarges to the west and south toward the margin of the Tanzania craton, reaching a width of ~ 200 km. The low-velocity region extends to a depth of at least 300 km. Because of the smaller aperture of the Kenya network compared to the Ethiopia network, the low-velocity zone below ~ 300 km depth cannot be well imaged, thus allowing for the possibility that the anomaly could also broaden to the east at depth.

The cross section through the model for the Tanzania data set shows higher than average velocities beneath the Tanzania craton and predominantly lower than average velocities beneath the rifted mobile belts surrounding the craton (Fig. 4C). The low-velocity region under the eastern branch of the rift extends to depths greater than 400 km and laterally over a region ~ 300 km wide (Fig. 4C). The lithospheric keel beneath the craton, as defined by the relatively fast velocities, extends to a depth of ~ 200 km (the apparent continuation of fast velocities to ~ 300 km depth is likely due to limited vertical resolution). Between depths of 200 and 300 km, the low-velocity structure associated with the eastern branch extends westward under the fast structure of the cratonic lithosphere.

TRANSITION ZONE DISCONTINUITIES

To place additional constraints on the depth extent and width of the low-velocity anomalies in the sublithospheric mantle, P-wave receiver functions from all three data sets were stacked using the same procedure to image the 410 and 660 km discontinuities by Owens et al. (2000) (Tanzania), Benoit et al. (2006b) (Ethiopia), and Huerta et al. (2009) (Kenya). The receiver functions for each data set were computed using a frequency domain deconvolution method with water-level stabilization (Langston, 1979) and stacked following the method described by Owens et al. (2000). The estimated uncertainty in the depths of the discontinuities obtained is ± 10 km.

The phase transitions that nominally occur at depths of 410 and 660 km are generally interpreted as the α -spinel to β -spinel transition and the γ -spinel to perovskite + magnesiowüstite transition, respectively (Bina and Helffrich, 1994). The Clapeyron slope of these transitions is such that under warm conditions, the 410 km transition is depressed and the 660 km transition

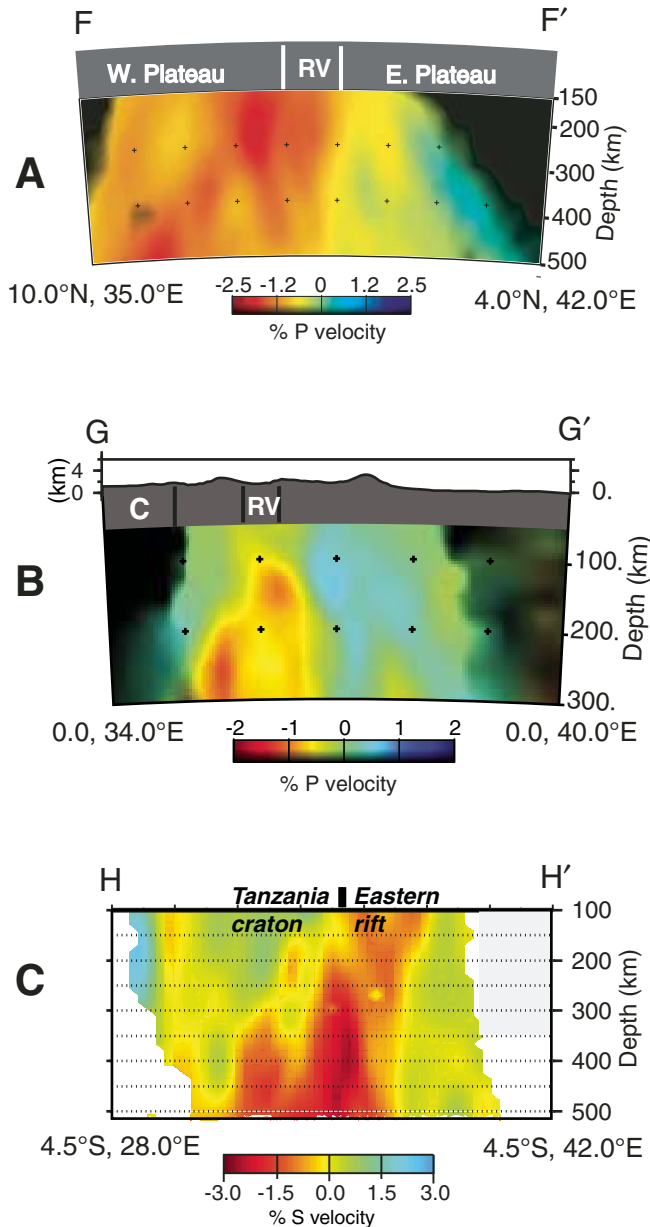


Figure 4. Cross sections through the body wave tomography models from (A) Ethiopia (Benoit et al., 2006b), (B) Kenya (Park and Nyblade, 2006), and (C) Tanzania (Ritsema et al., 1998). The locations of the cross sections are shown in Figure 1. C—craton; RV—rift valley.

is elevated, and the thickness of the transition zone decreases. Hence, if the low-velocity anomalies at depths >400 km are caused by elevated temperatures, then topography on the discontinuities can be used to verify this.

Recent studies of the phase transformations in the lower part of the transition zone, however, indicate that Ps arrivals on receiver functions around 650–700 km depth can be a combination of Ps conversions from the α -spinel to β -spinel transition and the γ -spinel to perovskite + magnesiowüstite transition and the majorite (garnet) + perovskite + magnesiowüstite transition, complicating the interpretation of seismic wave conversions from that depth interval in the transition zone (Deuss et al., 2006; Deuss, 2007; Hirose, 2002; Simmons and Gurrola, 2000; Vacher et al., 1998). The majorite-perovskite transition has a positive Clapeyron slope, and thus the transition deepens with increasing temperature, opposite to the Clapeyron slope of the olivine-perovskite transition. Because of the uncertainty in the phase transformation that dominates in regions of elevated temperatures (Hirose, 2002; Deuss, 2007), Ps conversions from around 660 km depth in the data sets from Tanzania, Kenya, and Ethiopia are not reviewed.

Data from the EAGLE project (Bastow et al., 2005) were incorporated into the receiver function stacks for Ethiopia (Benoit et al., 2006b), and in spite of the fairly dense coverage of Ps conversion points at 410 km depth from the combined data sets, a discontinuity around 410 km depth could not be imaged. The inability to resolve the 410 km discontinuity could be due to many factors. Complicated crustal and uppermost mantle structure (Dugda et al., 2005, 2007), such as sharp lateral changes in Moho depth across the rift, and large variations in surface topography (Rondenay et al., 2005) could cause wavefield scattering. The presence of melt beneath the rift (Bastow et al., 2005, 2008; Kendall et al., 2005; Keranen et al., 2009; Keir et al., 2009) could also attenuate the Ps converted phases. However, these factors would also affect Ps conversions recorded on the network in Kenya, and, as reviewed in the following paragraph, Ps conversions from the 410 km discontinuity can be well imaged beneath Kenya. Hence, these factors are probably not the reason why the 410 km discontinuity beneath Ethiopia cannot be imaged. A more likely explanation is heterogeneity within the sublithospheric mantle that scatters the wavefield, including topography on the discontinuity itself. For example, Van der Lee et al. (1994) have shown that topography on the discontinuity with an amplitude of 15–25 km (in depth) could cause inherent waveform distortion affecting the Ps conversions.

Figure 5 shows a profile that runs almost parallel to the Tanzania-Kenya border and a map of the depth to the 410 km discontinuity illustrating the major changes in the 410 km discontinuity beneath Tanzania and Kenya (Huerta et al., 2009; Owens et al., 2000). There are significant variations in the depth and characteristics of the 410 km discontinuity. Strong and coherent Ps conversions from the 410 km discontinuity can be seen. Beneath the Tanzania craton, a clear Ps arrival can be seen at a depth of ~410–420 km (Fig. 5A). Across the central portion of the profile

(beneath the rift and the volcanic fields east of the rift), this Ps arrival shifts deeper to ~430–450 km depth (Fig. 5A). In addition, in the southeast portion of the profile (beneath the coastal plains), the Ps conversion from the 410 km discontinuity shallows again to ~410–420 km depth (Fig. 5A). Figure 5B shows the spatial extent of the region where the 410 km discontinuity is 20–40 km deeper than normal. In Kenya, the region extends from under the Kenya rift to the east some 200–400 km, and in northern Tanzania, the region extends beneath the entire area where the eastern branch impinges on the eastern edge of the Tanzania craton (Fig. 5B).

DISCUSSION

The depressed 410 km discontinuity beneath the eastern branch of the rift system in Kenya and Tanzania can be readily attributed to warmer-than-average temperatures at the top of the transition zone. Using a Clapeyron slope of 2.9 MPa/K (Bina and Helffrich, 1994) for the α -spinel to β -spinel transition, the 20–40 km depression of the 410 km corresponds to a temperature increase of as much as 350 K. This increase in temperature is consistent with the velocity model of Ritsema et al. (1998) for Tanzania, which shows a 2%–3% reduction in S-wave velocities beneath the eastern branch coincident with the location of the depressed 410 km discontinuity. The depressed 410 km discontinuity in the same location as the low-velocity anomaly beneath the eastern branch cannot be explained other than by a deep (>400 km) thermal anomaly in the mantle under the rift system. The tomographic models of Ritsema et al. (1998) and Park and Nyblade (2006) indicate that the thermal anomaly extends upward at least to the base of the lithosphere regionally beneath the East African Plateau, but that the thermal anomaly has not yet significantly altered the uppermost mantle beneath areas of the East African Plateau away from the rift valleys, as illustrated by the fast (4.5–4.7 km/s) S-wave velocities between the Moho and 100 km depth (Fig. 2). It is also possible that some portion of the upper-mantle low-velocity anomaly could be caused by compositional changes.

The broad (>400-km-wide) and deep (>400 km) low-velocity anomaly beneath the Ethiopian Plateau is also indicative of a thermal anomaly similar to the one beneath the eastern branch in Tanzania and Kenya. However, in the case of Ethiopia, the thermal anomaly does extend upward to the very top of the mantle, affecting broadly the structure of the Ethiopian lithosphere, as illustrated by the slow (4.0–4.2 km/s) S-wave velocities between the Moho and 80–90 km depth (Fig. 2).

Geodynamic models for the origin of the portion of the African superplume in eastern Africa, as well as for the Cenozoic rifting and volcanism found there, must account for the broad and deep thermal structure in the upper mantle beneath eastern Africa revealed by the low-velocity anomaly and depressed 410 km discontinuity in Tanzania and Kenya. Indeed, the nature of the thermal structure, in particular its breadth and depth, places a first-order constraint on geodynamic models of the African mantle.

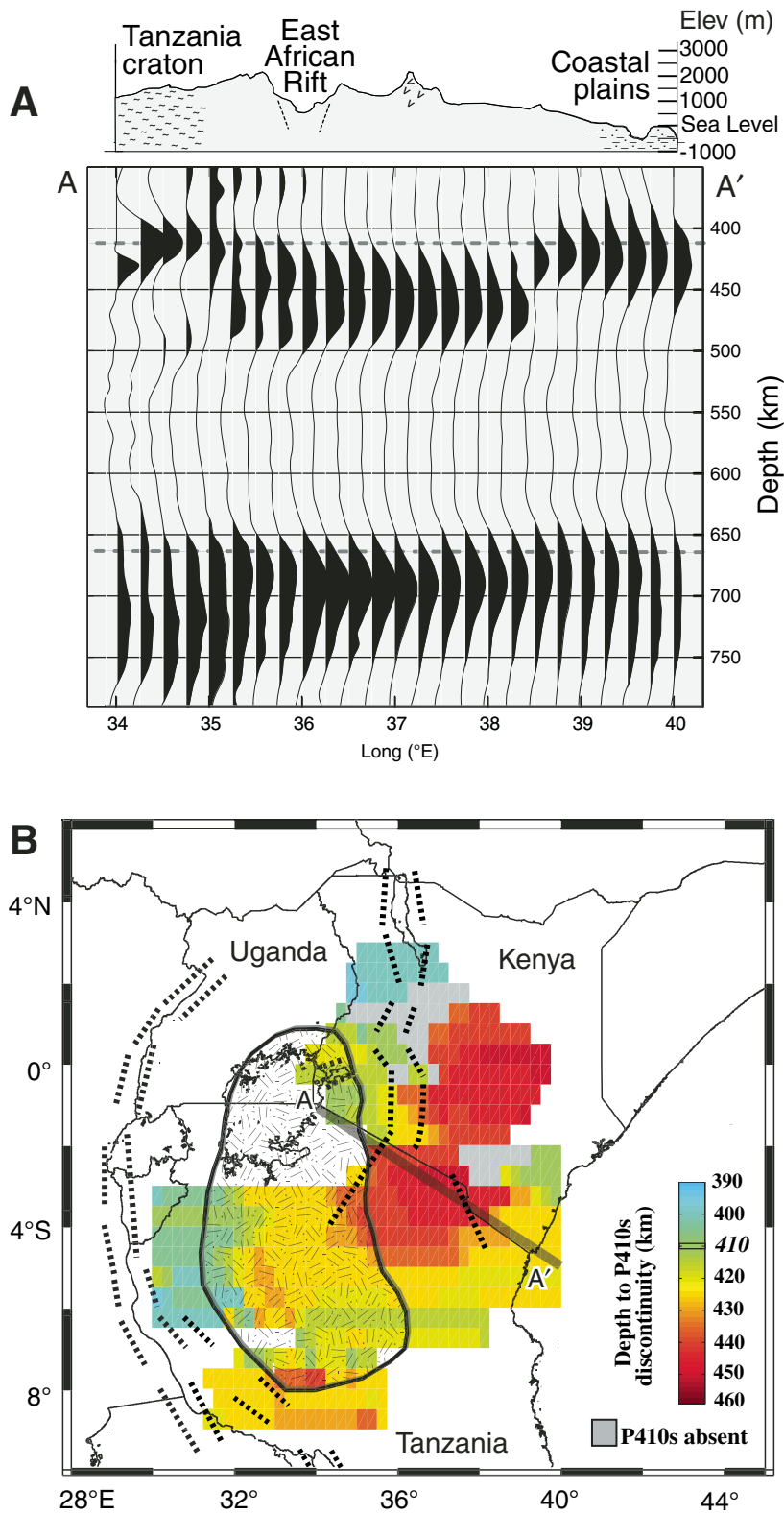


Figure 5. Results of stacking P-wave receiver functions to image Ps conversions from the 410 and 660 km discontinuities beneath the eastern branch of the rift system in Kenya and Tanzania (from Huerta et al., 2009). (A) Cross section A–A' along the Kenya–Tanzania border showing a Ps conversion from the 410 km discontinuity at the normal depth of 410 km beneath the Tanzania craton and Mozambique belt along the coastal plain. (B) Map showing the depth of the 410 km discontinuity beneath East Africa. The geology shown in the map is the same as in Figure 1. The location of the cross section in A is shown with a gray line (A–A').

The breadth and depth of the thermal structure cannot be easily explained by plume models invoking a bulbous plume head fed by a narrow plume tail. Although many authors have attributed the hotspot tectonism to one or more plume heads fed by a plume tail (e.g., Schilling et al., 1992; Marty et al., 1996; Burke, 1996; Ebinger and Sleep, 1998; Courtillot et al., 1999; Debayle et al., 2001; George et al., 1998; Pik et al., 1999, 2006; Burke and Gunnell, 2008), the thermal structure cannot be accounted for by either a narrow (~100 km diameter) plume tail or plume head that has impinged on the underside of the lithosphere (Benoit et al., 2006b). The plume tail is too narrow to account for the breadth of the thermal structure, and the plume head, once it has spread out beneath the lithosphere, is too thin to account for the depth extent of the thermal structure. For the plume model to explain the thermal structure, many plume tails would have to exist under eastern Africa sufficiently close to one another to create a composite thermal anomaly several hundred kilometers wide.

In contrast to the plume head/tail model, the breadth and depth of the thermal structure is more easily attributed to the African superplume. The African superplume is a low-velocity anomaly that extends from the core-mantle boundary beneath southern Africa at least to midmantle depths (Simmons et al., 2007), and it is often interpreted as a thermo-chemical structure. In some tomographic models, it even appears to extend into the upper mantle beneath eastern Africa (e.g., Ritsema et al., 1999; Grand et al., 1997; Grand, 2002; Trampert et al., 2004). Whether or not the superplume extends across the transition zone and into the upper mantle beneath eastern Africa is debated, but either a thermal or thermo-chemical anomaly as large as the superplume, if it extends into the upper mantle, could cause the 410 km discontinuity to be regionally depressed, as seen in Tanzania and Kenya, and could also lead to sufficient topography on the 410 km discontinuity that it might not be well imaged, as found beneath Ethiopia. The superplume structure extending into the upper mantle would also create a wide and deep low-velocity anomaly.

Given the shortcomings with the plume model, a geodynamic model for the African superswell topography in eastern Africa, and also for the Cenozoic rifting and volcanism, invoking a geodynamic connection between the lower-mantle superplume structure and the anomalous upper mantle beneath eastern Africa is favored. The geodynamic connection could be either through flow of mantle rock across the transition zone or simply by conduction of heat across the transition zone into the upper mantle (e.g., Pik et al., 2006; Burke and Torsvik, 2004). Improved seismic images of midmantle structure beneath eastern and southern Africa are needed to determine further the nature of the geodynamic connection.

The low-velocity anomaly beneath eastern Africa, as determined from the three types of seismic analyses reviewed here, is consistent with both regional (Weeraratne et al., 2003) and continental-scale surface wave tomography models (Debayle et al., 2001; Priestley et al., 2008; Pasyanos and Nyblade, 2007; Sebai et al., 2006; Montagner et al., 2007; Sicilia et al., 2008),

which also show a broad region of low shear wave velocities in the upper mantle under eastern Africa. Although estimates of seismic anisotropy from shear wave splitting have not been interpreted previously in terms of flow in the mantle (Kendall et al., 2005; Gashawbeza et al., 2004; Walker et al., 2004), they are possibly consistent with a geodynamic model for eastern Africa that attributes the upper-mantle low-velocity anomaly to flow associated with the superplume. In Figure 3, the results from shear wave splitting measurements in eastern Africa are shown. The fast polarization direction within and around the eastern branch is rift-parallel. This pattern of anisotropy has been interpreted as resulting from melt inclusions in the lithosphere aligned parallel to the rift (Kendall et al., 2005; Gashawbeza et al., 2004; Walker et al., 2004). However, the pattern of anisotropy could also indicate flow of sublithospheric mantle rock parallel to the rift. Such a flow pattern could arise from a broad upwelling of rock from the superplume flowing to the northeast under the eastern branch as it rises through the upper mantle.

The nature of the low-velocity anomaly in the upper mantle beneath eastern Africa is also important for the plume versus plate debate, as mentioned in the introduction. In the plate model, upper-mantle anomalies, such as the one beneath eastern Africa, are commonly attributed to plate motions and/or variations in lithospheric structure between regions giving rise to shallow convective flow in the sublithospheric mantle. Two candidate “plate” mechanisms for generating a low-velocity anomaly in the upper mantle beneath eastern Africa are edge-drive convection (King and Anderson, 1995, 1998; King and Ritsema, 2000; King, 2007) and small-scale convection induced by lithospheric thinning.

In one form of the edge-driven convection model, the difference in heat flux through older, thicker lithosphere (i.e., cratonic) located adjacent to the thinner, younger lithosphere (i.e., mobile belt) drives small-scale convection, drawing mantle from under the thicker lithosphere to the suture between the thicker and thinner lithosphere. As the mantle material rises and impinges on the base of the thinner lithosphere, it can cross into the melting zone and produce basaltic melt. Extensional stresses across the suture can help to focus the flow at the suture.

The application of this model to East Africa might appear to be straightforward, given the thicker lithosphere of the Archean Tanzania craton in the middle of the East African Plateau surrounded by thinner Proterozoic mobile belt lithosphere. However, as reviewed by Nyblade (2002), there are a number of reasons, based on the geological history and present-day structure of the lithosphere in eastern Africa, why edge-driven convection does not appear to be a viable model for explaining the Cenozoic extensional tectonism in eastern Africa.

The width of the low-velocity anomaly in the upper mantle beneath eastern Africa also presents a challenge for the edge-driven convection model. Beneath Kenya, the anomaly at around 400 km depth is several hundred kilometers wide and extends well to the east of the Kenya Rift (Huerta et al., 2009). Such a wide anomaly well below and to the east of the base of the ~150–200-km-thick Tanzania craton lithosphere is not consistent

with edge flow around the sides of the cratonic lithosphere. In Ethiopia, the low-velocity anomaly is also many hundreds of kilometers wide, and it maintains that width through the entire upper mantle. Such a wide and deep anomaly is not consistent with edge-flow either around the northern margin of the Tanzania craton to the south of Ethiopia or from around the northeastern margin of the Congo craton to the southwest of Ethiopia.

Another “plate” mechanism that can possibly be invoked for eastern Africa is small-scale convection induced by lithospheric thinning, which results from far-field stresses generated at the edge of the African plate (i.e., the so-called passive rift mechanism). However, given the small amount ($\leq 10\%$) of lithospheric extension in eastern Africa, it is unlikely that the convective instabilities beneath the lithosphere could extend deep into the upper mantle (e.g., Buck, 1986; Mutter et al., 1988). Thus, the depth to which the upper-mantle velocity anomaly extends is not readily explained by this model.

SUMMARY AND CONCLUSIONS

To advance further our understanding of the way in which a portion of the African superswell in eastern Africa formed, and also to draw attention to the importance of eastern Africa for the plume versus plate debate, the upper-mantle structure beneath eastern Africa was reviewed using results from seismic data recorded on regional broadband seismic networks operated in Tanzania, Kenya, and Ethiopia using three types of data analyses. (1) Joint inversions of receiver functions and surface wave dispersion measurements show that there are significant differences in lithospheric mantle structure between the East African and Ethiopian Plateaus. The lithosphere under the Ethiopian Plateau is thin, extending to depths of no more than ~ 80 – 90 km. The maximum S-wave velocity is also very low, reaching only to 4.2 – 4.3 km/s. Beneath the East African Plateau, away from the rift valleys, shear wave velocities of 4.5 – 4.7 km/s characterize the mantle lithosphere to depths of more than 100 km. The lithospheric mantle of the Ethiopian Plateau has been significantly perturbed, much more so than the lithospheric mantle of the East African Plateau. (2) Body wave tomography reveals a broad (≥ 300 -km-wide) and deep (≥ 400 km) low-velocity anomaly beneath the Ethiopian Plateau and the eastern branch of the rift system in Kenya and Tanzania. (3) Receiver function stacks of Ps conversions from the 410 km discontinuity show that this discontinuity beneath the eastern branch in Kenya and Tanzania is depressed by 20 – 40 km in the same location as the low-velocity anomaly. The coincidence of the depressed 410 km discontinuity and the low-velocity anomaly indicates that the low-velocity anomaly is caused primarily by elevated temperatures.

Results from these analyses cannot be explained by models invoking a plume head and tail, unless there are a sufficient number of plume tails presently under eastern Africa side-by-side to create a broad and deep thermal structure. The breadth and depth of the thermal structure are more easily attributed to the African superplume, which in some tomographic models extends into the

upper mantle beneath eastern Africa. If the superplume extends into the upper mantle, it could cause the 410 km discontinuity to be regionally depressed, as seen in Tanzania and Kenya, and also create a wide and deep low-velocity anomaly. Consequently, a superplume origin for the anomalous topography of the African superswell in eastern Africa, in addition to the Cenozoic rifting and volcanism found there, is favored.

The nature of the low-velocity anomaly within the upper mantle beneath eastern Africa is difficult to explain with the plate model, as illustrated for the edge-drive convection and the passive rift mechanisms. This result presents a challenge to advocates of the plate model seeking to account for deep-seated upper-mantle thermal anomalies without invoking plume-like upwellings, at least for eastern Africa.

ACKNOWLEDGMENTS

This work was funded by the National Science Foundation (grants EAR-9304555, EAR-993093, EAR-0003424, OISE-0530062). S. Fishwick and an anonymous reviewer provided constructive comments that helped to improve this paper.

REFERENCES CITED

- Achauer, U., and Masson, F., 2002, Seismic tomography of continental rifts revisited: From relative to absolute heterogeneities: *Tectonophysics*, v. 358, p. 17–37, doi:10.1016/S0040-1951(02)00415-8.
- Achauer, U., Glahn, A., Ritter, J.R.R., Maguire, P.K.H., Meyer, R.P., Davis, P., Slack, P., and Green, W.V., 1994, New ideas on the Kenya Rift based on the inversion of the combined dataset of the 1985 and 1989/90 seismic tomography experiments: *Tectonophysics*, v. 236, p. 1–4, 305–329.
- Ammon, C.J., Randall, G.E., and Zandt, G., 1990, On the nonuniqueness of receiver function inversions: *Journal of Geophysical Research*, v. 95, p. 15,303–15,318, doi:10.1029/JB095iB10p15303.
- Anderson, D.L., 2005, Scoring hotspots: The plume and plate paradigms, in Foulger, G.R., Natland, J.H., Presnall, D.C., and Anderson, D. L., eds., *Plates, Plumes, and Paradigms: Geological Society of America Special Paper 388*, p. 31–54, doi:10.1130/0-8137-2388-4.31.
- Ayalew, D., Barbey, P., Marty, B., Reisberg, L., Yirgu, G., and Pik, R., 2002, Source, genesis, and timing of giant ignimbrite deposits associated with Ethiopian continental flood basalts: *Geochimica et Cosmochimica Acta*, v. 66, no. 8, p. 1429–1448, doi:10.1016/S0016-7037(01)00834-1.
- Baker, J., Snee, L., and Menzies, M., 1996, A brief Oligocene period of flood volcanism in Yemen: *Earth and Planetary Science Letters*, v. 138, p. 39–55, doi:10.1016/0012-821X(95)00229-6.
- Bastow, I.D., Stuart, G.W., Kendall, J.-M., and Ebinger, C.J., 2005, Upper mantle seismic structure in a region of incipient continental breakup: Northern Ethiopian rift: *Journal of Geophysical Research*, v. 162, p. 479–493, doi:10.1111/j.1365-246X.2005.02666.x.
- Bastow, I.D., Nyblade, A.A., Stuart, G.W., Rooney, T.O., and Benoit, M.H., 2008, Upper mantle seismic structure beneath the Ethiopian hot spot: Rifting at the edge of the African low-velocity anomaly: *Geochimica et Cosmochimica Acta*, v. 72, p. 1029–1040, doi:10.1016/j.gca.2007.11.017.
- Benoit, M.H., Nyblade, A.A., and VanDecar, J.C., 2006a, Upper mantle P wave speed variations beneath Ethiopia and the origin of the Afar hotspot: *Geology*, v. 34, p. 329–332, doi:10.1130/G22281.1.
- Benoit, M.H., Nyblade, A.A., Owens, T.J., and Stuart, G., 2006b, Mantle transition zone structure and upper mantle S velocity variations beneath Ethiopia: Evidence for a broad, deep-seated thermal anomaly: *Geochimica et Cosmochimica Acta*, v. 70, p. 1029–1040, doi:10.1016/j.gca.2006.03.013.
- Berhe, S.M., and Desta, B., Nicoletti, M., and Teferra, M., 1987, Geology, geochronology and geodynamic implications of the Cenozoic magmatic province in W and SE Ethiopia: *Journal of the Geological Society of London*, v. 144, p. 213–226.

- Bina, C.R., and Helffrich, G., 1994, Phase transition Clapeyron slopes and transition zone seismic discontinuity topography: *Journal of Geophysical Research*, v. 99, p. 15,853–15,860, doi:10.1029/94JB00462.
- Buck, W.R., 1986, Small-scale convection induced by passive rifting: The cause for uplift of rift shoulders: *Earth and Planetary Science Letters*, v. 77, p. 362–372, doi:10.1016/0012-821X(86)90146-9.
- Burke, K., 1996, The African plate: *South African Journal of Geology*, v. 99, no. 4, p. 341–409.
- Burke, K., and Gunnell, Y., 2008, The African Erosion Surface: A Continental-Scale Synthesis of Geomorphology, Tectonics, and Environmental Change over the Past 180 Million Years: *Geological Society of America Memoir* 201, 66 p.
- Burke, K., and Şengör, A.M.C., 1986, Tectonic escape in the evolution of the continental crust, in Barazangi, M., and Brown, L., eds., *Reflection Seismology—The Continental Crust: American Geophysical Union Geodynamic Monograph* 14, p. 41–53.
- Burke, K., and Torsvik, T.H., 2004, Derivation of large igneous provinces of the past 200 m.y. from long-term heterogeneities in the deep mantle: *Earth and Planetary Science Letters*, v. 227, p. 531–538, doi: 10.1016/j.epsl.2004.09.015.
- Burke, K., Macgregor, D., and Cameron, N., 2003, African petroleum systems: Four tectonic “aces” in the past 600 million years, in Arthur, T.J., Macgregor, D.S., and Cameron, N.R., eds., *Petroleum Geology of Africa: New Themes and Developing Technologies: Geological Society of London Special Publication* 207, p. 21–60.
- Chernet, T., Hart, W.K., Aronson, J.L., and Walter, R.C., 1998, New age constraints on the timing of volcanism and tectonism in the northern Main Ethiopian Rift—southern Afar transition zone (Ethiopia): *Journal of Volcanology and Geothermal Research*, v. 80, no. 3–4, p. 267–280.
- Coulié, E., Quidelleur, X., Gillet, P.Y., Courtillot, V., Lefèvre, J.C., and Chiesa, S., 2003, Comparative K-Ar and Ar/Ar dating of Ethiopian and Yemenite Oligocene volcanism: Implications for timing and duration of the Ethiopian Traps: *Earth and Planetary Science Letters*, v. 206, p. 477–492, doi:10.1016/S0012-821X(02)01089-0.
- Courtillot, V.C.J., Manighetti, I., Tapponnier, P., and Besse, J., 1999, On causal links between flood basalts and continental breakup: *Earth and Planetary Science Letters*, v. 166, p. 177–195, doi:10.1016/S0012-821X(98)00282-9.
- Davis, P.M., and Slack, P.D., 2002, The uppermost mantle beneath the Kenya dome and relation to melting, rifting and uplift in East Africa: *Geophysical Research Letters*, v. 29, no. 7, 1117, doi:10.1029/2001GL013676.
- Dawson, J.B., 1992, Neogene tectonics and volcanicity in the North Tanzania sector of the Gregory Rift Valley: Contrasts with the Kenya sector: *Tectonophysics*, v. 204, p. 81–92, doi:10.1016/0040-1951(92)90271-7.
- Debayle, E., Levque, J.J., and Cara, M., 2001, Seismic evidence for a deeply rooted low-velocity anomaly in the upper mantle beneath the northeastern Afro/Arabian continent: *Earth and Planetary Science Letters*, v. 193, p. 423–436.
- Deuss, A., 2007, Seismic observations of transition zone discontinuities beneath hotspot locations, in Foulger, G., and Jurdy, D., eds., *Plates, Plumes, and Planetary Processes: Geological Society of America Special Paper* 430, p. 121–136, doi:10.1130/2007.2430(07).
- Deuss, A., Redfern, S.A.T., Chambers, K., and Woodhouse, J.H., 2006, The nature of the 660-kilometer discontinuity in Earth’s mantle from global seismic observations of PP precursors: *Science*, v. 311, no. 5758, p. 198–201, doi:10.1126/science.1120020.
- Doucouré, C.M., and de Wit, M.J., 2002, Temporal variation in rigidity and mechanical behaviour of old thick continental lithosphere: *South African Journal of Geology*, v. 105, p. 39–50, doi:10.2113/1050039.
- Dugda, M.T., Nyblade, A.A., Julià, J., Langston, C.A., Ammon, C.J., and Simiyu, S., 2005, Crustal structure in Ethiopia and Kenya from receiver function analysis: Implications for rift development in eastern Africa: *Journal of Geophysical Research*, v. 110, B01303, doi:10.1029/2004JB003065.
- Dugda, M.T., Nyblade, A.A., and Julià, J., 2007, Thin lithosphere beneath Ethiopia and Djibouti revealed by a joint inversion of Rayleigh wave group velocities and receiver functions: *Journal of Geophysical Research*, v. 112, B08305, doi:10.1029/2006JB004918.
- Dugda, M.T., Nyblade, A., and Julià, J., 2009, S-wave velocity structure of the crust and upper mantle beneath Kenya in comparison to Tanzania and Ethiopia: Implications for the formation of the East African and Ethiopian Plateaus: *South African Journal of Earth Science*, v. 112, p. 241–250.
- Ebinger, C., and Sleep, N., 1998, Cenozoic magmatism throughout east Africa resulting from impact of one large plume: *Nature*, v. 395, p. 788–791, doi:10.1038/27417.
- Ebinger, C.J., Bechtel, T.D., Forsyth, D.W., and Bowin, C.O., 1989, Effective elastic plate thickness beneath the East African and Afar Plateaus and dynamic compensation of the uplifts: *Journal of Geophysical Research*, v. 94, no. B3, p. 2883–2901, doi:10.1029/JB094iB03p02883.
- Ebinger, C., Yemane, T., Harding, D.J., Tesfaye, S., Kelley, S., and Rex, D.C., 2000, Rift deflection, migration, and propagation: Linkage of the Ethiopian and Eastern Rifts, Africa: *Geological Society of America Bulletin*, v. 112, p. 163–176, doi:10.1130/0016-7606(2000)112<163:RDMAPL>2.0.CO;2.
- Foster, A., Ebinger, C., Mbede, E., and Rex, D., 1997, Tectonic development of the northern Tanzanian sector of the East African Rift system: *Journal of the Geological Society of London*, v. 154, no. 4, p. 689–700, doi:10.1144/gsjgs.154.4.0689.
- Furman, T., Kaleta, K., Bryce, J., and Hanan, B., 2006, Tertiary mafic lavas of Turkana, Kenya: Constraints on East African plume structure and the occurrence of high- μ volcanism in Africa: *Journal of Petrology*, v. 47, no. 6, p. 1221–1244, doi:10.1093/petrology/egl009.
- Gashawbeza, E.M., Klemperer, S.L., Nyblade, A.A., Walker, K.T., and Keranen, K.M., 2004, Shear-wave splitting in Ethiopia: Precambrian mantle anisotropy locally modified by Neogene rifting: *Geophysical Research Letters*, v. 31, L18602, doi:10.1029/2004GL020471.
- George, R., Rogers, N., and Kelley, S., 1998, Earliest magmatism in Ethiopia: Evidence for two mantle plumes in one flood basalt province: *Geology*, v. 26, p. 923–926, doi:10.1130/0091-7613(1998)026<0923:EMIEEF>2.3.CO;2.
- Grand, S.P., 2002, Mantle shear wave tomography and the fate of subducted slabs: *Philosophical Transactions of the Royal Society of London, ser. A*, v. 360, p. 2475–2491, doi:10.1098/rsta.2002.1077.
- Grand, S.P., van der Hilst, R.D., and Widiyantoro, S., 1997, Global seismic tomography: A snapshot of convection in the Earth: *GSA Today*, v. 7, no. 4, p. 1–7.
- Green, W.V., Achauer, U., and Meyer, R.P., 1991, A three-dimensional seismic image of the crust and upper mantle beneath the Kenya Rift: *Nature (London)*, v. 354, p. 199–203.
- Gurnis, M., Mitrovica, J.X., Ritsema, J., and van-Heijst, H.-J., 2000, Constraining mantle density structure using geological evidence of surface uplift rates: The case of the African superplume: *Geochemistry Geophysics Geosystems*, v. 1, no. 7, 1020, doi:10.1029/1999GC000035.
- Hendrie, D.B., Kusznir, N.J., Morley, C.K., and Ebinger, C.J., 1994, Cenozoic extension in northern Kenya: a quantitative model of rift basin development in the Turkana region: *Tectonophysics*, v. 236, no. 1–4, p. 409–438.
- Hirose, K., 2002, Phase transitions in pyrolytic mantle around 670-km depth: Implications for upwelling of plumes from the lower mantle: *Journal of Geophysical Research, Solid Earth*, v. 107, no. B4, 2078, doi:10.1029/2001JB000597.
- Hofmann, C., Courtillot, V., Feraud, G., Rochette, P., Yirgu, G., Ketefo, E., and Pik, R., 1997, Timing of the Ethiopian flood basalt event and implications for plume birth and global change: *Nature*, v. 389, p. 838–841, doi:10.1038/39853.
- Holmes, A., 1944, *Principles of Physical Geology*: Edinburgh, Thomas Nelson and Sons Ltd., 532 p.
- Huerta, A.D., Nyblade, A., and Reusch, A., 2009, Mantle transition zone structure beneath Kenya and Tanzania: More evidence for a deep-seated thermal upwelling in the mantle: *Geophysical Journal International*, v. 177, no. 3, p. 1249–1255, doi:10.1111/j.1365-246X.2009.04092.x.
- Julià, J., Ammon, C.J., Herrmann, R.B., and Correig, A.M., 2000, Joint inversion of receiver functions and surface wave dispersion observations: *Geophysical Journal International*, v. 143, p. 99–112, doi:10.1046/j.1365-246x.2000.00217.x.
- Julià, J., Ammon, C.J., and Herrmann, R.B., 2003, Lithospheric structure of the Arabian Shield from the joint inversion of receiver functions and surface-wave group velocities: *Tectonophysics*, v. 371, p. 1–21.
- Julià, J., Ammon, C.J., and Nyblade, A.A., 2005, Evidence for mafic lower crust in Tanzania, East Africa, from joint inversion of receiver functions and Rayleigh wave dispersion velocities: *Geophysical Journal International*, v. 162, no. 2, p. 555–569, doi:10.1111/j.1365-246X.2005.02685.x.
- Kampunzu, A.B., Bonhomme, M.G., and Kanika, M., 1998, Geochronology of volcanic rocks and evolution of the Cenozoic western branch of the East African Rift system: *Journal of African Earth Sciences*, v. 26, p. 441–461, doi:10.1016/S0899-5362(98)00025-6.
- Keir, D., Bastow, I.D., Whaler, K.A., Daly, E., Cornwell, D.G., and Hautot, S., 2009, Lower crustal earthquakes near the Ethiopian rift induced by magmatic processes, *Geochemistry Geophysics Geosystems*, v. 10, Q0AB02, doi:10.1029/2009GC002382.

- Kendall, J.-M., Stuart, G.W., Ebinger, C.J., Bastow, I.D., and Keir, D., 2005, Magma-assisted rifting in Ethiopia: *Nature*, v. 433, p. 146–148, doi:10.1038/nature03161.
- Keranen, K., Klemperer, S., Julià, J., Lawrence, J., and Nyblade, A., 2009, Low lower-crustal velocity across Ethiopia: Is the Main Ethiopian Rift a narrow rift in a hot craton? *Geochemistry Geophysics Geosystems*, v. 10, Q0AB01, doi:10.1029/2008GC002293.
- King, L.C., 1962, *The Morphology of the Earth*: Edinburgh, Oliver and Boyd, 699 p.
- King, S.D., 2007, Hotspots and edge-driven convection: *Geology*, v. 35, p. 223–226, doi:10.1130/G23291A.1.
- King, S.D., and Anderson, D.L., 1995, An alternative mechanism of flood basalt formation: *Earth and Planetary Science Letters*, v. 136, p. 269–279, doi:10.1016/0012-821X(95)00205-Q.
- King, S.D., and Anderson, D.L., 1998, Edge-driven convection: *Earth and Planetary Science Letters*, v. 160, p. 289–296, doi:10.1016/S0012-821X(98)00089-2.
- King, S.D., and Ritsema, J., 2000, African hot spot volcanism: Small-scale convection in the upper mantle beneath cratons: *Science*, v. 290, no. 5494, p. 1137–1140, doi:10.1126/science.290.5494.1137.
- Langston, C.A., 1979, Structure under Mount Rainier, Washington, inferred from teleseismic body waves: *Journal of Geophysical Research*, v. 84, no. B9, p. 4749–4762, doi:10.1029/JB084iB09p04749.
- Larson, E.W.F., and Ekstrom, G., 2001, Global models of surface wave group velocity: *Pure and Applied Geophysics*, v. 158, no. 8, p. 1377–1399, doi:10.1007/PL00001226.
- Ligorria, J., and Ammon, C.J., 1999, Iterative deconvolution of teleseismic seismograms and receiver functions estimation: *Bulletin of the Seismological Society of America*, v. 89, p. 1395–1400.
- Lithgow-Bertelloni, C.A., and Silver, P.G., 1998, Dynamic topography, plate driving forces and the African superswell: *Nature*, v. 395, p. 269–272, doi:10.1038/26212.
- MacDonald, R., Rogers, N.W., Fitton, J.G., Black, S., and Smith, M., 2001, Plume-lithosphere interactions in the generation of the basalts of the Kenya Rift, East Africa: *Journal of Petrology*, v. 42, no. 5, p. 877–900, doi:10.1093/petrology/42.5.877.
- Marty, B., Pik, R., and Gezahagen, Y., 1996, Helium isotopic variations in the Ethiopia plume lavas: nature of magmatic sources and limit on lower mantle contribution: *Earth and Planetary Science Letters*, v. 144, p. 223–237, doi:10.1016/0012-821X(96)00158-6.
- Mechie, J., Keller, G.R., Prodehl, C., Khan, M.A., and Gaciri, S.J., 1997, Structure and dynamic processes in the lithosphere of the Afro-Arabian Rift system: A model for the structure, composition and evolution of the Kenya Rift: *Tectonophysics*, v. 278, p. 95–119.
- Mohr, P., 1983, Ethiopian flood basalt province: *Nature*, v. 303, p. 577–584, doi:10.1038/303577a0.
- Mohr, P., and Zanettin, B., 1988, The Ethiopian flood basalt province, in MacDougall, J.D., ed., *Continental Flood Basalts*: Dordrecht, the Netherlands, Kluwer Academic Publishers, p. 63–110.
- Montagner, J.P., Marty, B., Stutzmann, E., Sicilia, D., Cara, M., Pik, R., Leveque, J.-J., Roult, G., Beucler, E., and Debayle, E., 2007, Mantle upwellings and convective instabilities revealed by seismic tomography and helium isotope geochemistry beneath eastern Africa: *Geophysical Research Letters*, v. 34, L21303, doi:10.1029/2007GL031098.
- Morley, C.K., Wescott, W.A., Stone, D.M., Harper, R.M., Wigger, S.T., and Karanja, F.M., 1992, Tectonic evolution of the northern Kenyan Rift: *Journal of the Geological Society of London*, v. 149, p. 333–348, doi:10.1144/gsjgs.149.3.0333.
- Mutter, J.C., Buck, W.R., and Zehnder, C.M., 1988, Convective partial melting: 1. A model for the formation of thick basaltic sequences during the initiation of spreading: *Journal of Geophysical Research*, v. 93, p. 1031–1048, doi:10.1029/JB093iB02p01031.
- Noble, W.P., Foster, D.A., and Gleadow, A.J.W., 1997, The post-Pan-African thermal and extensional history of crystalline basement rocks in eastern Tanzania: *Tectonophysics*, v. 275, no. 4, p. 331–350, doi:10.1016/S0040-1951(97)00026-7.
- Nyblade, A.A., 2002, Crust and upper mantle structure in East Africa: Implications for the origin of Cenozoic rifting and volcanism and the formation of magmatic rifted margins, in Menzies, M.A., Klemperer, S.L., Ebinger, C.J., and Baker, J., eds., *Volcanic Rifted Margins*: Geological Society of America Special Paper 362, p. 15–26.
- Nyblade, A.A., and Langston, C.A., 2002, Broadband seismic experiments probe the East African Rift: *Eos (Transactions, American Geophysical Union)*, v. 83, p. 405–408, doi:10.1029/2002EO000296.
- Nyblade, A.A., and Robinson, S.W., 1994, The African superswell: *Geophysical Research Letters*, v. 21, p. 765–768, doi:10.1029/94GL00631.
- Nyblade, A.A., Vogfjord, K.S., and Langston, C.A., 1996, P wave velocity structure of Proterozoic upper mantle beneath central and southern Africa: *Journal of Geophysical Research, Solid Earth*, v. 101, no. B6, p. 13,973, doi:10.1029/96JB01483.
- Owens, T.J., Nyblade, A.A., Gurrula, H., and Langston, C.A., 2000, Mantle transition zone structure beneath Tanzania, East Africa: *Geophysical Research Letters*, v. 27, p. 827–830, doi:10.1029/1999GL005429.
- Park, Y., and Nyblade, A.A., 2006, P-wave tomography reveals a westward dipping low velocity zone beneath the Kenya Rift: *Geophysical Research Letters*, v. 33, L07311, doi:10.1029/2005GL025605.
- Pasteels, P., Villeneuve, M., De Paepe, P., and Klerkx, J., 1989, Timing of the volcanism of the southern Kivu Province: Implications for the evolution of the western branch of the East African rift system: *Earth and Planetary Science Letters*, v. 94, p. 353–363, doi:10.1016/0012-821X(89)90152-0.
- Pasyanos, M.E., 2005, A variable resolution surface wave dispersion study of Eurasia, North Africa, and surrounding regions: *Journal of Geophysical Research*, v. 110, B12301, doi:10.1029/2005JB003749.
- Pasyanos, M., and Nyblade, A., 2007, A top to bottom lithospheric study of Africa and Arabia: *Tectonophysics*, v. 444, p. 27–44, doi:10.1016/j.tecto.2007.07.008.
- Pik, R., Deniel, C., Coulon, C., Yirgu, G., and Marty, B., 1999, Isotopic and trace element signatures of Ethiopian flood basalts: Evidence for plume-lithosphere interactions: *Geochimica et Cosmochimica Acta*, v. 63, no. 15, p. 2263–2279, doi:10.1016/S0016-7037(99)00141-6.
- Pik, R., Marty, B., Carignan, J., and Lave, J., 2003, Stability of the upper Nile drainage network (Ethiopia) deduced from (U-Th)/He thermochronometry; implications for uplift and erosion of the Afar plume dome: *Earth and Planetary Science Letters*, v. 215, p. 73–88, doi:10.1016/S0012-821X(03)00457-6.
- Pik, R., Marty, B., and Hilton, D., 2006, How many mantle plumes in Africa? The geochemical point of view: *Chemical Geology*, v. 226, no. 3–4, p. 100–114, doi:10.1016/j.chemgeo.2005.09.016.
- Priestley, K., McKenzie, D., Debayle, E., and Pilidou, S., 2008, The African upper mantle and its relationship to tectonics and surface geology: *Geophysical Journal International*, v. 175, p. 1108–1126, doi:10.1111/j.1365-246X.2008.03951.x.
- Ritsema, J., Nyblade, A.A., Owens, T.J., Langston, C.L., and VanDecar, J.C., 1998, Upper mantle seismic velocity structure beneath Tanzania, East Africa: Implications for the stability of cratonic lithosphere: *Journal of Geophysical Research*, v. 103, p. 21,201–21,213, doi:10.1029/98JB01274.
- Ritsema, J., van Heijst, H.J., and Woodhouse, J.H., 1999, Complex shear wave velocity structure beneath Africa and Iceland: *Science*, v. 286, p. 1925–1928, doi:10.1126/science.286.5446.1925.
- Ritter, J.R.R., and Kaspar, T., 1997, A tomography study of the Chyulu Hills, Kenya, in Fuchs, K., Altherr, R., Müller, B., and Prodehl, C., eds., *Structure and dynamic processes in the lithosphere of the Afro-Arabian Rift System*: *Tectonophysics*, v. 278, p. 149–169.
- Rondenay, S., Bostock, M.G., and Fischer, K.M., 2005, Multichannel inversion of scattered teleseismic body waves: Practical considerations and applicability, in Levander, A., and Nolet, G., eds., *Seismic Earth: Array Analysis of Broadband Seismograms*: Washington, D.C., American Geophysical Union Geophysical Monograph 157, p. 187–204.
- Schilling, J.-G., Kingsley, R., Hanan, B., and McCully, B., 1992, Nd-Sr-Pb isotopic variations along the Gulf of Aden: Evidence for the Afar mantle plume-lithosphere interaction: *Journal of Geophysical Research*, v. 97, p. 10,927–10,966, doi:10.1029/92JB00415.
- Sebai, A., Stutzmann, E., Montagner, J.-P., Sicilia, D., and Beucler, E., 2006, Anisotropic structure of the African upper mantle from Rayleigh and Love wave tomography: *Physics of the Earth and Planetary Interiors*, v. 155, p. 48–62, doi:10.1016/j.pepi.2005.09.009.
- Shackleton, R.M., 1986, Precambrian collision tectonics in Africa, in Coward, M.P., and Reis, A.C., eds., *Collision Tectonics*: Geological Society of London Special Publication 19, p. 329–349.
- Sicilia, D., Montagner, J.-P., Cara, M., Stutzmann, E., Debayle, E., Lépine, J.-C., Lévêque, J.-J., Beucler, E., Sebai, A., Roult, G., Ayele, A., and Sholan, J.M., 2008, Upper mantle structure of shear-wave velocities and stratification of anisotropy in the Afar hotspot region: *Tectonophysics*, v. 462, p. 164–177, doi:10.1016/j.tecto.2008.02.016.
- Simmons, N.A., and Gurrula, H., 2000, Multiple seismic discontinuities near the base of the transition zone in the Earth's mantle: *Nature*, v. 405, p. 559–562, doi:10.1038/35014589.

- Simmons, N.A., Forte, A.M., and Grand, S.P., 2007, Thermochemical structure and dynamics of the African superplume: *Geophysical Research Letters*, v. 34, L02301, doi:10.1029/2006GL028009.
- Slack, P.D., Davis, P.M., Dahlheim, H.A., Glahn, A., Ritter, J.R.R., Green, W.V., Maguire, P.K.H., and Meyer, R.P., 1994, Attenuation and velocity of P-waves in the mantle beneath the East African Rift, Kenya: *Tectonophysics*, v. 236, no. 1–4, p. 331–358.
- Spiegel, C., Kohn, B., Belton, D., and Gleadow, A., 2007, Morphotectonic evolution of the central Kenya rift flanks: Implications for late Cenozoic environmental change in East Africa: *Geology*, v. 35, p. 427–430, doi:10.1130/G23108A.1.
- Trampert, J., Deschamps, F., Resovsky, J., and Yuen, D., 2004, Probabilistic tomography maps chemical heterogeneities throughout the lower mantle: *Science*, v. 306, p. 853–856, doi:10.1126/science.1101996.
- Vacher, P., Mocquet, A., and Sotin, C., 1998, Computation of seismic profiles from mineral physics: The importance of the non-olivine components for explaining the 660 km depth discontinuity: *Physics of the Earth and Planetary Interiors*, v. 106, no. 3–4, p. 275–298, doi:10.1016/S0031-9201(98)00076-4.
- VanDecar, J.C., 1991, Upper-Mantle Structure of the Cascadia Subduction Zone from Nonlinear Teleseismic Travel-Time Inversion [Ph.D. thesis]: Seattle, University of Washington, 168 p.
- VanDecar, J.C., and Crosson, R.S., 1990, Determination of teleseismic relative phase arrival times using multi-channel cross-correlation and least squares: *Bulletin of the Seismological Society of America*, v. 80, p. 150–169.
- Van der Beek, P., Mbende, E., Andriessen, P., and Delvaux, D., 1998, Denudation history of the Malawi and Rukwa Rift flanks (East Africa Rift system) from apatite fission track thermochronology: *Journal of African Earth Sciences*, v. 26, p. 363–385, doi:10.1016/S0899-5362(98)00021-9.
- Van der Lee, S., Paulssen, H., and Nolet, G., 1994, Variability of P660s phases as a consequence of topography of the 660 km discontinuity: *Physics of the Earth and Planetary Interiors*, v. 86, p. 147–164, doi:10.1016/0031-9201(94)05066-X.
- Walker, K.T., Nyblade, A.A., Klemperer, S.L., Bokelmann, G.H.R., and Owens, T.J., 2004, On the relationship between extension and anisotropy: Constraints from shear wave splitting across the East African Plateau: *Journal of Geophysical Research*, v. 109, B08302, doi:10.1029/2003JB002866.
- Weeraratne, D.S., Forsyth, D.W., Fischer, K.M., and Nyblade, A.A., 2003, Evidence for an upper mantle plume beneath the Tanzanian craton from Rayleigh wave tomography: *Journal of Geophysical Research, Solid Earth*, v. 108, no. B9, 2427, doi:10.1029/2002JB002273.
- WoldeGabriel, G., Walter, R.C., Hart, W.K., Mertzman, S.A., and Aronson, J.L., 1999, Temporal relations and geochemical features of felsic volcanism in the central sector of the Main Ethiopian Rift: *Acta Vulcanologica*, v. 11, no. 1, p. 53–67.
- Wolfenden, E., Ebinger, C., Yirgu, G., Deino, A., and Ayalew, D., 2004, Evolution of the northern Main Ethiopian Rift: Birth of a triple junction: *Earth and Planetary Science Letters*, v. 224, p. 213–228, doi:10.1016/j.epsl.2004.04.022.

MANUSCRIPT ACCEPTED BY THE SOCIETY 9 NOVEMBER 2010

The Ethiopia Afar Geoscientific Lithospheric Experiment (EAGLE): Probing the transition from continental rifting to incipient seafloor spreading

Ian D. Bastow*

Department of Earth Sciences, University of Bristol, Bristol, BS8 1RJ, UK

Derek Keir†

School of Earth and the Environment, University of Leeds, Leeds, LS2 9JT, UK

Eve Daly

Department of Earth and Ocean Sciences, National University of Ireland, Galway, Ireland

ABSTRACT

The Miocene–Holocene East African Rift in Ethiopia is unique worldwide because it subaerially exposes the transition between continental rifting and seafloor spreading within a young continental flood basalt province. As such, it is an ideal study locale for continental breakup processes and hotspot tectonism. Here, we review the results of a recent multidisciplinary, multi-institutional effort to understand geological processes in the region: the Ethiopia Afar Geoscientific Lithospheric Experiment (EAGLE). In 2001–2003, dense broadband seismological networks probed the structure of the upper mantle, while controlled-source wide-angle profiles illuminated both along-axis and across-rift crustal structure of the Main Ethiopian Rift. These seismic experiments, complemented by gravity and magnetotelluric surveys, provide important constraints on variations in rift structure, deformation mechanisms, and melt distribution prior to breakup. Quaternary magmatic zones at the surface within the rift are underlain by high-velocity, dense gabbroic intrusions that accommodate extension without marked crustal thinning. A magnetotelluric study illuminated partial melt in the Ethiopian crust, consistent with an overarching hypothesis of magma-assisted rifting. Mantle tomographic images reveal an ~500-km-wide low-velocity zone at ≥ 75 km depth in the upper mantle that extends from close to the eastern edge of the Main Ethiopian Rift westward beneath the uplifted and flood basalt-capped NW Ethiopian Plateau. The low-velocity zone does not interact simply with the Miocene–Holocene (rifting-related) base of lithosphere topography, but it provides an abundant source of partially molten material that assists extension of the seismically and volcanically active Main Ethiopian Rift to the present day.

*ian.bastow@bristol.ac.uk

†Current address: National Oceanography Centre, University of Southampton, Southampton, SO14 3ZH, UK.

Bastow, I.D., Keir, D., and Daly, E., 2011, The Ethiopia Afar Geoscientific Lithospheric Experiment (EAGLE): Probing the transition from continental rifting to incipient seafloor spreading, in Beccaluva, L., Bianchini, G., and Wilson, M., eds., *Volcanism and Evolution of the African Lithosphere*: Geological Society of America Special Paper 478, p. 51–76, doi:10.1130/2011.2478(04). For permission to copy, contact editing@geosociety.org. © 2011 The Geological Society of America. All rights reserved.

INTRODUCTION

Overview

Continental rifts mark zones of lithospheric thinning and heating in response to extension, and these zones of plate stretching may eventually become the site of continental rupture. Lithospheric thinning may induce adiabatic upwelling and melting of the asthenosphere, leading to magmatism during rifting. Magmatism is enhanced further in regions of anomalously hot mantle, such as the East African Rift (e.g., White and McKenzie, 1989; Ebinger, 2005). Fault-bounded rift systems are long, relatively narrow systems in cratonic lithosphere and wide zones of basins and ranges in collapsing orogenic belts (e.g., Buck, 1991; Hopper and Buck, 1993). The geological record shows that if tensional stresses are sufficient and sustained enough to thin and rupture the rigid 150–250-km-thick continental lithospheric plates, extension can lead to complete continental breakup and the subsequent creation of new oceanic lithosphere (e.g., Buck, 2004; Ebinger, 2005). After rupture, the now-inactive rift zone becomes a “passive margin” that subsides beneath sea level as the heat transferred from the asthenosphere to the plate during rifting finally dissipates (e.g., McKenzie, 1978; Bown and White, 1995).

Many passive margins worldwide are “magmatic margins,” characterized by thick sequences of extruded, intruded, and underplated igneous rocks emplaced prior to, or during, rifting (e.g., Coffin and Eldholm, 1994; Menzies et al., 2002). Extension is accommodated through the combined processes of faulting, ductile stretching, and magma intrusion in the form of dikes and sills (e.g., Ebinger and Casey, 2001; Buck, 2004, 2006). Pressure gradients caused by topographic relief on the lithosphere–asthenosphere boundary beneath continents may guide the distribution of melt hundreds of kilometers from the zone of mantle melting (e.g., Sleep, 1996; Ebinger and Sleep, 1998) and, as such, influence the localization of intrusive and extrusive magmatism. Despite the global abundance of ancient magmatic margins, the timing and distribution of magmatism, as well as the strain partitioning among faulting, ductile stretching, and magma intrusion are not well understood because the ocean–continent boundary is concealed by thick seaward-dipping reflectors (e.g., Mutter et al., 1982; Mutter, 1985; Holbrook and Kelemen, 1993). Additionally, many passive margins worldwide ruptured during Gondwana breakup prior to ca. 100 Ma, so the exact nature of the continent–ocean transition has to be deduced rather than directly observed.

Continental rift zones worldwide are structurally segmented along their length, but the length scales and character of the along-axis segmentation may change during rift evolution (e.g., Hayward and Ebinger, 1996; d’Acremont et al., 2005). During the initial rift stages, basin dimension scales with the mechanical thickness of the lithosphere, with long, wide basins forming in strong lithosphere (e.g., Buck, 1991; Ebinger et al., 1999). As lithospheric thinning and heating continue, strain localizes to a narrower zone in response to reduced lithospheric strength. In addition, an increase in magma intrusion may play an important

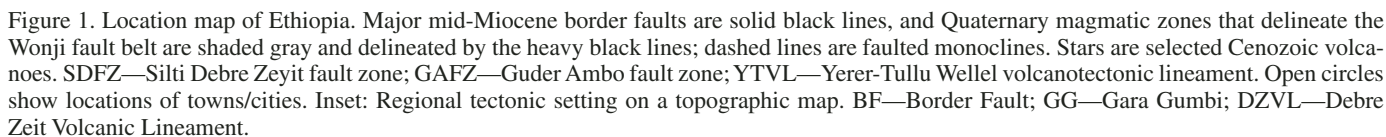
role in localizing strain as well as weakening the lithosphere by heating (Ebinger and Hayward, 1996; Pérez-Gussinyé et al., 2009), thereby significantly influencing along-axis segmentation of the rift (e.g., Ebinger and Casey, 2001; Wolfenden et al., 2004). If rifting continues to the point of continental rupture, then full oceanic spreading is established and results in the formation of new lithosphere (e.g., Kuo and Forsyth, 1988; Phipps-Morgan and Chen, 1993; Wang et al., 2009).

EAGLE (Ethiopia Afar Geoscientific Lithospheric Experiment) probed the crust and upper mantle in the seismically and volcanically active East African Rift system in Ethiopia using passive and controlled-source seismology as well as complementary geophysical techniques such as gravity and magnetotelluric surveying (e.g., Maguire et al., 2003). This synthesis of geophysical and geological results from EAGLE aims to summarize new constraints on (1) the generation and migration of melt beneath the rift, and (2) the relative importance of faulting, magma intrusion, and ductile stretching in accommodating extension during the final stages of continental breakup. The results further our understanding of both hotspot tectonism and evolution of lithospheric structure during incipient oceanic spreading and continental margin formation. We also summarize the many tectonic questions raised by the project—questions that will fuel future generations of research in East Africa.

Tectonic Setting

The term “rift valley” was first introduced by Gregory (1896) to describe the fissure in Earth’s surface into which a strip of the surface has been let down by parallel faults. When Gregory penned his famous work at the end of the nineteenth century, he also remarked that the scar in the East African landscape before him was likely an extensional feature. We now know that the Ethiopian Rift forms the third arm of the East African–Red Sea–Gulf of Aden rift–rift–rift triple junction where the Arabian, Nubian, Somali, and Danakil plates join in Afar (Fig. 1) (McKenzie and Morgan, 1969; McKenzie and Davies, 1970). Embryonic magmatic rifting of the continental lithosphere is observed to the south in northern Tanzania and southern Kenya (Maguire et al., 1994; Nyblade et al., 1996). To the northeast of the East African Rift in Ethiopia, incipient seafloor spreading is evident in the Asal Rift, which is the onshore westward extension of the Gulf of Aden spreading ridge (e.g., Ruegg and Kasser, 1987; Stein et al., 1991; De Chabali and Avouac, 1994). The Red Sea Rift arm encompasses incipient seafloor spreading in northern Afar, including the currently active Dabbahu and Ertale Rift segments. The Ethiopian Rift is the least evolved, youngest of the three rift arms and terminates at the Tendaho Goba’ad discontinuity in central Afar (e.g., Tesfaye et al., 2003; Wolfenden et al., 2005; Bellahsen et al., 2003) (Fig. 1).

The Miocene–Holocene East African Rift in Ethiopia subaerially exposes the transitional stage of rifting within a young continental flood basalt province, making it an ideal study location for continental breakup processes. In addition to



transitional rifting processes, Ethiopia is also an ideal natural laboratory for the study of hotspot tectonism. Seismic imaging reveals a broad (~500-km-wide) ~3% S-wave low-velocity anomaly that originates at the core-mantle boundary beneath southern Africa and rises toward the base of the lithosphere somewhere in the region of Ethiopia and the Red Sea–Gulf of Aden (Grand, 2002; Ritsema and Allen, 2003; Simmons et al., 2007; Li et al., 2008): the African superplume. When reviewed in light of other geophysical observations that can be used to constrain mantle convection (e.g., the global free-air gravity field, tectonic plate motions, and dynamic surface topography), the morphology and sharp velocity gradients of the African superplume are explained best by a thermochemical plume rising from the core-mantle boundary (e.g., Ni et al., 2002; Simmons et al., 2007). There is increasing evidence from global tomographic studies that low-velocity structures could be continuous across the 410 and 660 km discontinuities in the Kenya–Ethiopia region (e.g., Ritsema and Allen, 2003; Li et al., 2008; Montelli et al., 2004, 2006, and references therein; Sicilia et al., 2008), but the precise location and number of upwellings beneath East Africa remain somewhat controversial.

The timing of the widespread and voluminous volcanism in the Ethiopia–Yemen area suggests that this mantle upwelling impinged on the base of the lithosphere ca. 45 Ma, prior to the onset of rifting of Arabia from Africa at ca. 30 Ma (e.g., Wolfenden et al., 2004). The earliest Cenozoic volcanism in East Africa occurred in southwest Ethiopia and the Turkana Depression in northernmost Kenya at 40–45 Ma (e.g., Ebinger et al., 1993; George et al., 1998; Furman et al., 2006). This area had been rifted during the Mesozoic breakup of Gondwana (e.g., Hendrie et al., 1994). Approximately 2 km of basalts and subordinate rhyolites were then erupted rapidly across the Ethiopian Plateau at ca. 29–31 Ma (Baker et al., 1996; Hofmann et al., 1997) prior to or concomitant with the onset of rifting in the Red Sea and Gulf of Aden (e.g., Wolfenden et al., 2004). Additional isolated shield volcanism in the interval ca. 30–10 Ma occurred across the Ethiopian Plateau (Fig. 1) and added ~2 km of additional local relief in areas such as the Simien, Choke, and Gugufu shield volcanoes (e.g., Kieffer et al., 2004; Beccaluva et al., 2009). However, the timing of uplift in Ethiopia is controversial; commencement has been estimated at 20–30 Ma on the basis of U–Th/He thermochronometry data (Pik et al., 2003), but more recent studies indicate an episodic uplift history with ~1 km uplift being produced more recently (ca. 10 Ma–present); this is postulated to be due to foundering of the plateau lithosphere by delamination or convective removal of lithospheric mantle (e.g., Duggen et al., 2003; Molnar et al., 1993) following extensive heating and weakening since the onset of flood basalt volcanism at ca. 30 Ma (Gani et al., 2007).

Although prerift basement is rarely exposed beneath the thick Eocene–Holocene volcanic cover, the Main Ethiopian Rift is thought to have formed within the Precambrian metamorphic crustal basement of the Pan-African Mozambique belt (Kazmin et al., 1978), which exhibits N–S to NNE–SSW suture zones

(Vail, 1983; Berhe, 1990) and NW–SE-oriented strike-slip faults (Brown, 1970; Purcell, 1976). Extension in SW Ethiopia and the Turkana Depression in northern Kenya commenced by ca. 20 Ma, with the central and northern sectors of the Main Ethiopian Rift developing between 18 and 10 Ma, respectively (e.g., WoldeGabriel, 1988; Wolfenden et al., 2004). Large offset border faults formed along one or both sides of the rift (Fig. 1) and are often marked by chains of silicic centers (e.g., Chernet et al., 1998). South of ~7.5°N, a broad (~500-km-wide) faulted region extends to the west of the present-day Main Ethiopian Rift and marks the zone across which the axis of the Main Ethiopian Rift has migrated east since Oligocene times (e.g., Ebinger et al., 2000).

The distribution, kinematics, and estimated age of fault populations suggest that deformation in the Main Ethiopian Rift north of 8.5°N migrated to the center of the rift sometime in the interval 6.6–3 Ma, with an associated change from N130°E-directed extension to N105°E-directed extension (Bonini et al., 1997; Boccaletti et al., 1998; Wolfenden et al., 2004). Opening models of the East African Rift based on global positioning system (GPS) data and earthquake focal mechanisms constrain the current extension direction in the Main Ethiopian Rift to between N95°E and N110°E at rates of 4–7 mm/yr (Bilham et al., 1999; Fernandes et al., 2004; Calais et al., 2006; Stamps et al., 2008). GPS data collected during 1969–1997 from the Main Ethiopian Rift and adjacent plateaus indicate that ~80% of this present-day strain is localized within an ~30-km-wide zone within the rift valley (Bilham et al., 1999). On the strength of this evidence, Casey et al. (2006) proposed that the locus of extension in this transitional rifting environment has localized progressively since ca. 12 Ma, away from the mid-Miocene border faults, toward central en-echelon chains of eruptive magmatic centers, dikes, and small offset faults. Thus, axial magmatic emplacement, not border faulting, increasingly dominates the rifting process after the initial stages of breakup (e.g., Ebinger and Casey, 2001; Keranen et al., 2004; Rooney et al., 2005; Kurz et al., 2007; Keranen and Klemperer, 2008). Numerical modeling suggests that once an elongate zone of diking is established in the rift axis, the strong, cooled mafic intrusions function to focus extensional stress and thereby promote emplacement of new dikes into the narrow zone of intrusion (Beutel et al., 2010).

Geochemistry provides constraints on the evolving lithosphere, as well as the development of faulting and lithospheric thinning (e.g., Peccerillo et al., 2003; Ronga et al., 2010). Much of the Quaternary magmatic activity within the Main Ethiopian Rift has occurred in magmatic zones in the center of the rift north of 8.5°N in the Wonji fault belt (e.g., Mohr, 1967; Ebinger and Casey, 2001; Abebe et al., 2007), where magmas fractionate at shallow (<5 km) depths (Rooney et al., 2007). South of 8.5°N, the Wonji fault belt appears offset within the Main Ethiopian Rift toward the Somalian plate and is flanked to the west by the Silti Debre Zeyit fault zone (SDFZ, Fig. 1), in which magmas fractionate at various depths throughout the crust (Rooney et al., 2005, 2007; Rooney, 2010). These differences in magmatic

plumbing system north and south of $\sim 8.5^\circ\text{N}$ (Rooney et al., 2007), combined with structural and geochronological evidence that the $\sim 7.5^\circ\text{--}9.5^\circ\text{N}$ sector of the rift is the youngest (Bonini et al., 2005), suggest that a simple south-to-north transition from continental rifting to seafloor spreading may be inappropriate. Buck (2006) noted the straightness of the East African and Red Sea Rifts and suggested that this straightness is in part controlled by movement of melt-filled dikes through the plates. It is intriguing, therefore, to note that the Wonji fault belt is remarkably straight throughout the Main Ethiopian Rift. Its apparent offset toward the SE Ethiopian Plateau south of 8.5°N is due in part to the kink in the mid-Miocene border faults at this latitude.

The ongoing extension in the Main Ethiopian Rift continues to alter rift morphology and cause natural phenomena such as earthquakes, surface fissuring, and volcanic eruptions. Prior to the temporary deployments of dense seismic networks in Ethiopia since the turn of the millennium, assessment of seismotectonics and seismic hazard was based primarily on relatively few earthquakes ($M > 3.5$) recorded since ca. 1960 by sparse permanent stations in Ethiopia and surrounding countries, as well as from Global Seismograph Network/Global Dense Seismograph Network permanent stations (e.g., Gouin, 1979; Kebede and Kulhánek, 1994; Kebede and van Eck, 1997; Ayele and Kulhánek, 1997; Foster and Jackson, 1998; Ayele, 2000). These data show that seismic moment release over the last ~ 50 yr in the Main Ethiopian Rift accounts for less than 50% of total geodetic moment predicted from the current rate of plate opening. This lends some support to the importance of aseismic processes (e.g., diking) in accommodating strain (Hofstetter and Beyth, 2003). Localized, rift-axial brittle failure in the Main Ethiopian Rift is manifest in development of extensional fissures at the surface and associated fault growth in the upper crust (e.g., Asfaw, 1982; Acocella and Korme, 2002; Acocella et al., 2003; Williams et al., 2004; Soliva and Schultz, 2008; Kidane et al., 2009). In addition to brittle strain, magma intrusion and extrusion processes in the Main Ethiopian Rift are known to have occurred episodically since historical times to the present day (e.g., Gibson, 1969; Tadesse et al., 2003; Williams et al., 2004). Asfaw et al. (1992) postulated that deformation in the Main Ethiopian Rift occurs primarily during episodic, magma-dominated rifting episodes similar to those observed in Iceland and the subaerial Red Sea and Aden Rifts in Afar (e.g., Abdallah et al., 1979; Björnsson et al., 1977; Wright et al., 2006; Ayele et al., 2007a; Rowland et al., 2007; Hamling et al., 2009; Keir et al., 2009a; Ebinger et al., 2010).

EAGLE—THE EXPERIMENTS AND MAIN OBSERVATIONS

In this section, we review the major components of EAGLE from controlled-source profiles that probe crustal-scale structures to three-dimensional (3-D) imaging of the deeper mantle structures using passive-source seismological techniques. The passive-source seismic and geodetic experiments also constrain kinematics and dynamics of the current stage of rifting, and

along-axis variations provide clues as to temporal development. We summarize the major observations from these studies before discussing their significance in the context of continental rifting and hotspot tectonism.

Passive Seismic Networks

Based on the requirement for seismic body-wave tomography of crossing rays in the mantle to a depth of ~ 300 km beneath Ethiopia, the 29 station EAGLE phase I broadband network of 20 Güralp CMG-40TD instruments and 9 CMG-3TD instruments (e.g., Bastow et al., 2005) was designed with a nominal spacing of 40 km covering a region of the rift and its uplifted flanks measuring 250×350 km (Fig. 2). The network was centered on the Boset volcanic zone in the center of the rift, ~ 75 km SE of Addis Ababa. Seismometers recorded at 50 s.p.s. (samples per second) for 16 mo between October 2001 and February 2003. EAGLE phase I was deployed in the footprint of the broader Pennsylvania State University Ethiopia Broadband Seismic Experiment (EBSE; Fig. 2) (Nyblade and Langston, 2002; Brazier et al., 2008).

Between October 2002 and February 2003, 50 Güralp CMG-6TD instruments recording at 100 s.p.s. (Fig. 2) operated mainly in the Main Ethiopian Rift as EAGLE phase II (e.g., Keir et al., 2006b). The ~ 10 km station spacing covered regions of active seismicity and was specifically designed to: (1) improve the accuracy of hypocenter locations; (2) increase ray coverage in a joint inversion of local earthquake arrival times for locations and seismic velocity structure; and (3) provide information from which we could infer the position and depth of active faults and therefore illuminate how the locus of seismic deformation in the upper crust compares with variations in crustal structure caused by intrusion of magma. (4) The study is also valuable for future assessment of seismic hazard since it provides the first high-resolution snapshot of seismicity in the Ethiopian Rift.

The final broadband component of the EAGLE project (EAGLE phase III) recorded data between November 2002 and January 2003 (Fig. 2), during which 91 Güralp CMG-6TD broadband seismometers were deployed at 5 km intervals along the cross-rift controlled-source profile recording at 100 s.p.s. with the aim of better understanding cross-rift variations in crustal structure (Cornwell et al., 2010).

Mantle Seismic Tomography

Mantle seismic tomography is a useful tool for mapping the structure of seismic velocity anomalies and hence the morphology of upwellings and magma source zones beneath rifts (e.g., Evans and Achauer, 1993; Wang et al., 2009). Bastow et al. (2005, 2008) performed regularized nonlinear, least-squares inversion of P- and S-wave traveltimes for broadband stations in Ethiopia. These studies built on images from global tomographic studies (Ritsema and van Heijst, 2000; Grand, 2002; Li et al., 2008) and regional studies in the area (Debaille et al., 2001; Benoit et al., 2006a, 2006b; Pasyanos and Nyblade, 2007;

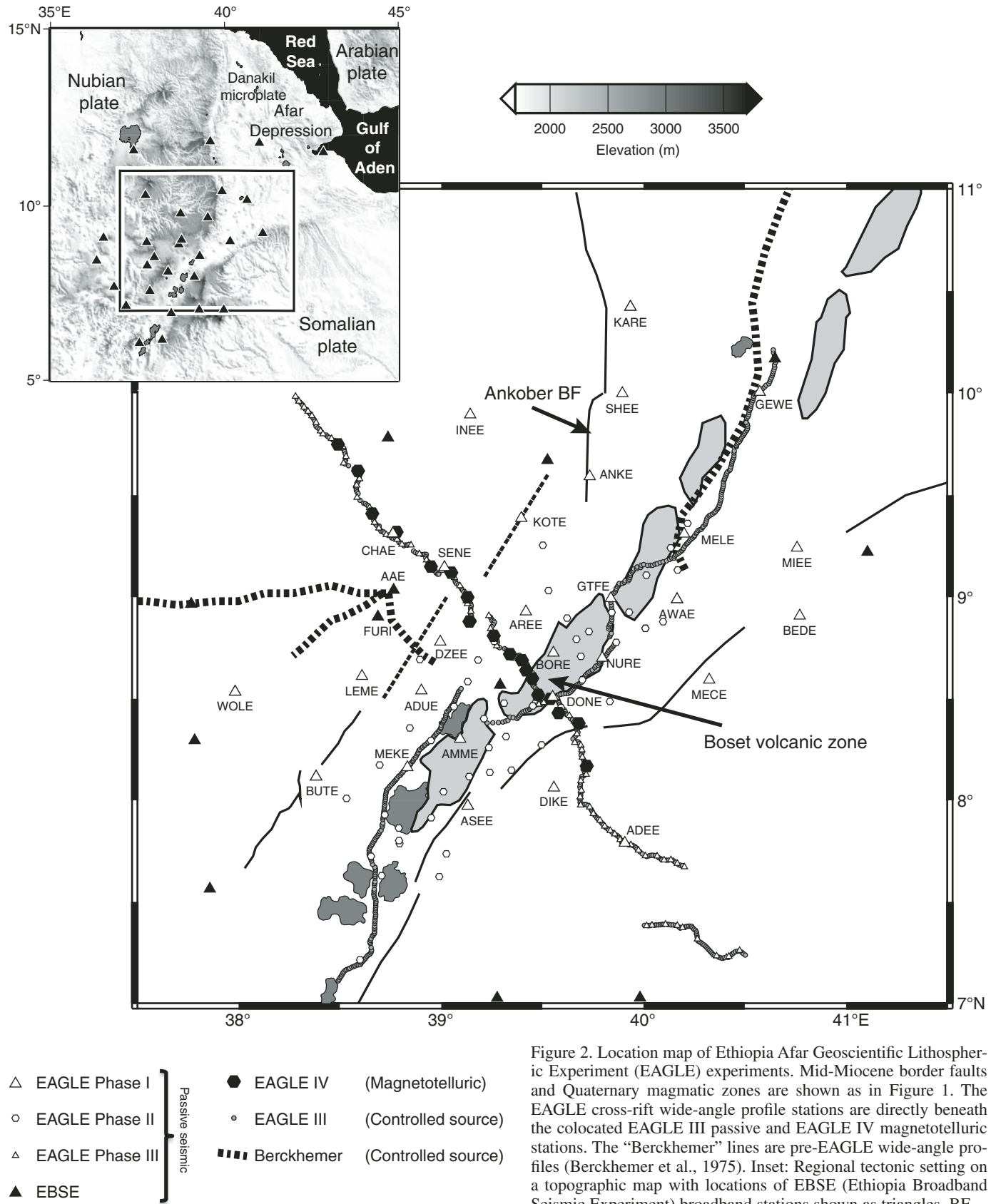


Figure 2. Location map of Ethiopia Afar Geoscientific Lithospheric Experiment (EAGLE) experiments. Mid-Miocene border faults and Quaternary magmatic zones are shown as in Figure 1. The EAGLE cross-rift wide-angle profile stations are directly beneath the colocated EAGLE III passive and EAGLE IV magnetotelluric stations. The “Berckhemer” lines are pre-EAGLE wide-angle profiles (Berckhemer et al., 1975). Inset: Regional tectonic setting on a topographic map with locations of EBSE (Ethiopia Broadband Seismic Experiment) broadband stations shown as triangles. BF—Border Fault.

Priestley et al., 2008). Bastow et al. (2008) resolved an ~500-km-wide P- and S-wave low-velocity zone at 75 to >400 km depth in the upper mantle that extends from close to the eastern edge of the Main Ethiopian Rift westward beneath the uplifted and flood basalt-capped NW Ethiopian Plateau (Figs. 3 and 4). Within the broad low-velocity region (LVR), zones of particularly low velocity are observed that have absolute delay times ($\delta t_p \sim 4$ s) indicating that the mantle beneath this region is amongst the slowest worldwide (see Poupinet, 1979). The observations are explained best by hypotheses involving high temperatures and partial melt beneath the Main Ethiopian Rift and adjacent NW Ethiopian Plateau. The S-wave model shows particularly low velocities at 75 km depth (Fig. 4B), probably indicating a larger portion of partial melt there (Bastow et al., 2005, 2008).

The lowest-velocity region appears not to be beneath southern/central Afar, but beneath the central part of the study area at ~9°N, 39°E (Figs. 3 and 4). This observation is corroborated by observations of mean relative arrival-time residuals that do not suffer the same amplitude recovery problems as tomographic inversion. The abrupt increase in velocity north of ~10.5°N coincides with an ~20 m.y. increase in the time elapsed since the onset of plate stretching in Afar compared to the northern Main Ethiopian Rift (Bastow et al., 2008).

The Main Ethiopian Rift is located toward the eastern edge of the broad low-velocity structure, not above its center. This observation, along with strong correlations between lowest-velocity zones and lithospheric structures, suggests that preexisting structural trends and Miocene-to-Holocene rift tectonics strongly control melt migration at the base of the lithosphere (e.g., Bastow et al., 2005, 2008).

Studies of Seismic Anisotropy

Measurements of seismic anisotropy from teleseismic earthquakes can be used to infer patterns of strain and flow in the mantle (e.g., Vauchez et al., 2000). The anisotropy can be due to the lattice preferred orientation (LPO) of crystals or the preferred orientation of inclusions (e.g., oriented melt pockets [OMP]) or periodic thin layering (PTL) of contrasting materials (e.g., Kendall, 2000). The resulting rock fabric produces a directional dependence in seismic velocities: seismic anisotropy. A shear wave in an isotropic medium will split into two shear waves when it encounters an anisotropic medium. The orientation of the shear waves and their difference in travel-times constrain the symmetry and magnitude of the anisotropy. Seismic anisotropy can be measured using core phases such as SKS (for a review, see, e.g., Long and Silver, 2009). Such measurements offer good lateral resolution of anisotropy (e.g., Bastow et al., 2007) but poor vertical resolution. Seismic anisotropy also affects surface waves (Figs. 5 and 6). It leads to azimuthal variations in surface-wave phase velocities, discrepancies between Love-wave- and Rayleigh-wave-derived shear-wave velocity models, and particle motion anomalies (Kirkwood and Crampin, 1981). The dispersive nature of surface-wave propagation leads to good resolution of anisotropy variation with

depth, but long wavelengths mean poor horizontal resolution compared to SKS studies. The analysis of anisotropy using a combination of seismic body and surface waves provides good vertical and horizontal resolution and offers information about length scales of anisotropy (e.g., Bastow et al., 2010). Local earthquake shear-wave splitting, if available, can also be used to constrain anisotropy above the earthquake hypocenter: typically, the upper crust in volcanic rift environments where the majority of earthquakes are relatively shallow (e.g., Barclay and Toomey, 2003; Crampin et al., 2008).

Analyses of regional surface waves in Ethiopia show sublithospheric fast shear waves coherently oriented in a northeastward direction from southern Kenya to the Red Sea (Debayle et al., 2001; Kendall et al., 2006). This parallels the trace of the deeper African superplume. The pattern of shear-wave anisotropy is more variable above depths of 150 km. Analyses of splitting in teleseismic phases (SKS) and local shear waves within the rift valley consistently parallel trends of the Quaternary magmatic zones (Kendall et al., 2005; Keir et al., 2005; Fig. 7). The magnitude of the splitting correlates with the degree of magmatism, and the polarizations of the shear waves align with magmatic segments along the rift valley (e.g., Ayele et al., 2004; Kendall et al., 2005, 2006). Analysis of surface-wave propagation across the rift valley confirms that anisotropy in the uppermost 75 km is due primarily to melt alignment (Figs. 6 and 7; Bastow et al., 2010), not LPO (flow)-type anisotropy. Away from the rift valley, the anisotropy agrees reasonably well with the preexisting Pan-African lithospheric fabric (e.g., Kendall et al., 2005; Gashawbeza et al., 2004). An exception is the region beneath the Ethiopian Plateau, where the anisotropy is variable and likely corresponds to preexisting fabric and ongoing melt-migration processes (Kendall et al., 2006).

Receiver Functions

Receiver functions can be used to capture P- to S-wave conversions at velocity contrasts in the receiver crust and mantle recorded in the P-wave coda from distant teleseismic earthquakes (e.g., Langston, 1979). They can be used to provide estimates of bulk crustal properties: crustal thickness (H) and V_p/V_s ratio (e.g., Zhu and Kanamori, 2000; Di Leo et al., 2009), which can then be related to bulk crustal composition via Poisson's ratio (e.g., Christensen, 1996; Chevrot and van der Hilst, 2000). Stuart et al. (2006) analyzed receiver functions in this way for EAGLE broadband stations, building on earlier work by Dugda et al. (2005). On the flanks of the rift, the crust on the Somalian plate to the east is 38–40 km thick. On the NW Ethiopian Plateau, the crust is thicker to the north (41–43 km) than to the south (<40 km); the thinning takes place over an off-rift upper-mantle low-velocity structure previously imaged by traveltimes tomography (Bastow et al., 2005). The crust is slightly more mafic ($V_p/V_s > 1.85$) on the NW plateau than on the SE plateau ($V_p/V_s \approx 1.80$). This could be due to either magmatic activity or different prerift crustal compositions. Regions of volcanism on the side of the rift (e.g., SDFZ, Fig. 1) are characterized by thinned crust and a

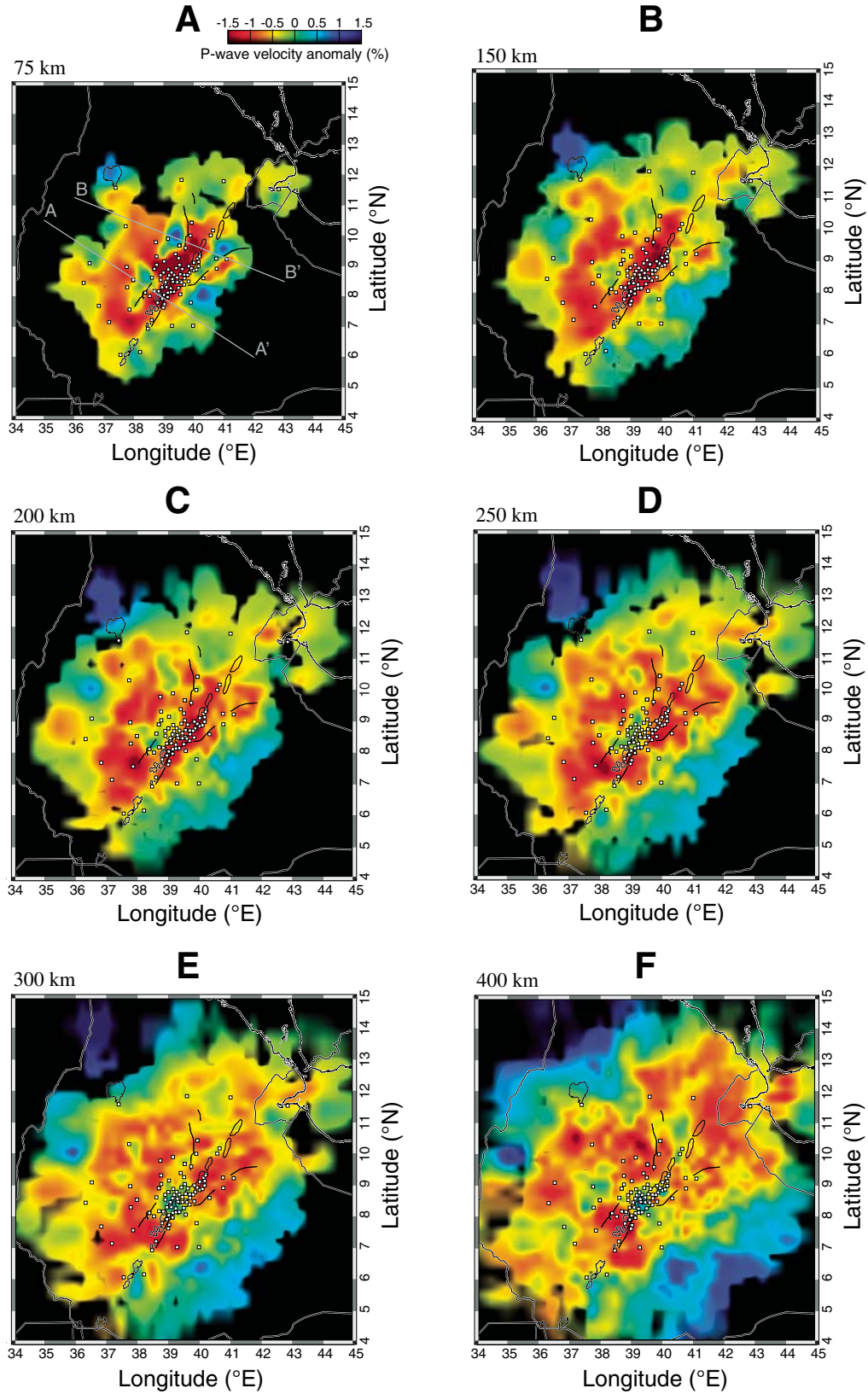


Figure 3. Depth slices through the P-wave velocity model at 75, 150, 200, 250, 300, and 400 km depth. The locations of the stations contributing to the tomographic inversions are shown by white squares. Figure is modified after Bastow et al. (2008).

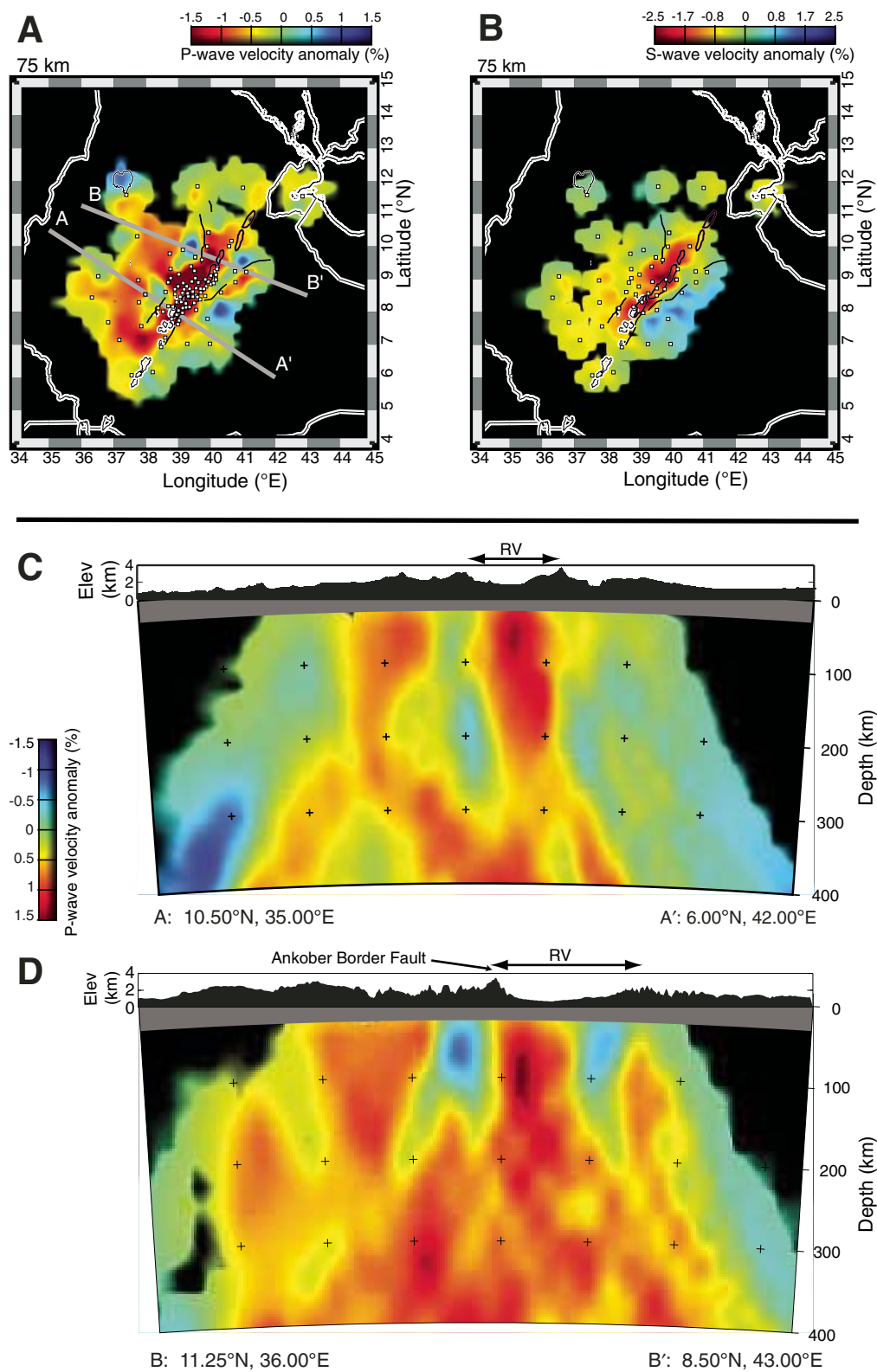


Figure 4. P- and S-wave seismic traveltime tomography for Ethiopia. (A–B) Comparison of P- and S-wave velocity models at 75 km depth. (C) A–A': Vertical cross sections through the P-wave velocity model in the continental rifting part of the study area. (D) B–B': Cross section through southernmost Afar. Orientations of the cross sections are shown as gray lines in Figures 3A and 4A. Gray bands at the top of the cross sections obscure the view of the upper 30 km of the model space, where a lack of crossing rays prevents accurate recovery of velocity structure. RV—Rift Valley. Figure is modified after Bastow et al. (2008).

V_p/V_s ratio >2.0 , indicative of partial melt within the crust. Within the rift, the V_p/V_s ratio increases to greater than 2.0 (Poisson's ratio >0.33) northward toward the Afar Depression. Such high values are once again indicative of partial melt in the crust and corroborate other geophysical evidence for increased magmatic activity as continental rifting evolves to oceanic spreading in Afar. Along the axis of the rift, crustal thickness varies from around 38 km in the south to 30 km in the north, with most of the change in Moho depth occurring just south of the Boset magmatic zone where the rift opens into the Afar Depression.

Of some debate in the receiver function literature is about the spatial extent of the underplate beneath the NW plateau. Keranen et al. (2009) argued that away from the wide-angle profile, the Moho is a sharper feature when observed with receiver functions than it appears using data from stations coincident with controlled-source wide-angle refraction Line 1 (Fig. 2). Stuart et al. (2006), in contrast, used forward modeling of receiver functions at station SENE on Line 1 (Fig. 2) and concluded that the receiver function method was sensitive to the top, not the bottom of the underplate. The spatial extent of this layer is therefore uncertain away from Line 1 on the NW plateau.

Seismicity

From October 2001 to February 2003, 1957 earthquakes occurred within the EAGLE passive network area (Fig. 8), and a selection of these was used for accurate location using a 3-D velocity model (Daly et al., 2008), focal mechanism determination (Keir et al., 2006b), and local earthquake splitting analysis (Keir et al., 2005). Border faults of the Main Ethiopian Rift are relatively inactive, except for clusters of seismicity at the intersections between the Main Ethiopian Rift and the older Red Sea and Gulf of Aden Rifts. Along the axis of the Main Ethiopian Rift, earthquakes are predominantly localized to depths of less than ~ 15 km within 20-km-wide, right-stepping, en-echelon zones of Quaternary volcanism and faulting. Seismicity in these zones is characterized by low-magnitude ($M_L \sim 1-4$) clusters (Keir et al., 2006a) coincident with Quaternary faults, fissures, and chains of eruptive centers. All but three focal mechanisms show normal dip-slip motion; the minimum compressive stress is $N103^\circ E$, perpendicular to Quaternary faults and aligned volcanic cones (Fig. 8A). The seismogenic zone lies within and above the 20-km-wide zone of dense mafic intrusions: Strain localization through magmatism in the mid-upper crust most likely controls

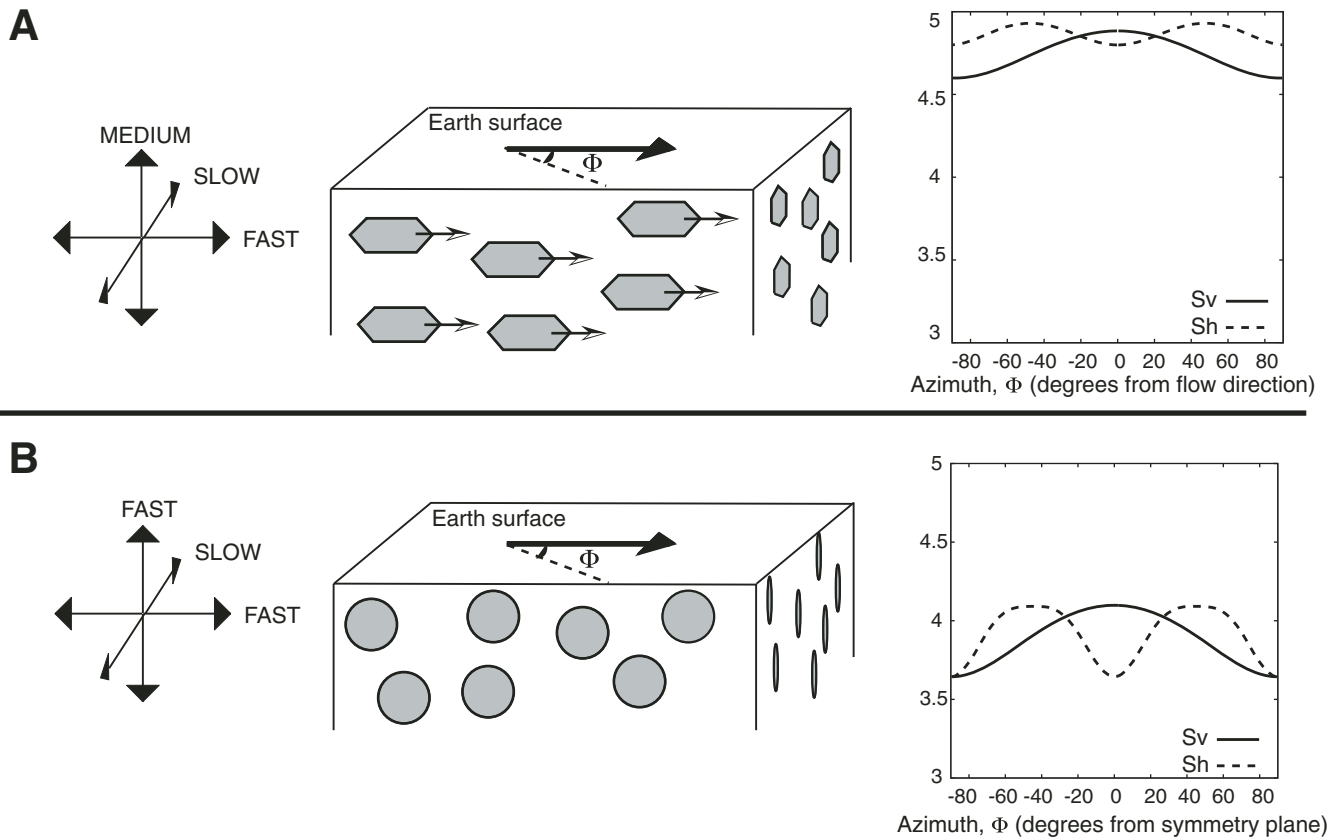


Figure 5. Mechanisms for seismic anisotropy. (A) Anisotropy due to lattice preferred orientation of upper-mantle minerals. Top left shows directions of fast, slow, and medium P-wave velocities, assuming a horizontal flow direction and a vertical flow plane as shown in the cartoon (middle). Top right shows azimuthal variations in vertically and horizontally polarized shear waves (S_v and S_h). (B) Anisotropy due to oriented melt pockets. Melt volume fraction is assumed to be 0.1%, and the melt lies in disk-like pockets (oblate spheroids) with an aspect ratio of 0.02. Figures are modified after Bastow et al. (2010).

the formation and continued growth of narrow axial rift grabens in the overlying seismogenic zone.

A minor cluster of anomalously deep (20–35 km) low-magnitude earthquakes underlies distinctive chains of aligned volcanoes on the western margin of the Main Ethiopian Rift. The cluster of deep earthquakes also coincides with a zone of particularly high conductivity (attributed to

presence of fluids such as partial melt and hydrous fluids; Whaler and Hautot, 2006; Whaler, 2006) in the lower crust, which is positioned directly above the slowest-velocity P-wave uppermost mantle (Keir et al., 2009b). These lower-crustal earthquakes are interpreted as related to either the emplacement of magma or release of fluids during magma crystallization (Keir et al., 2009b).

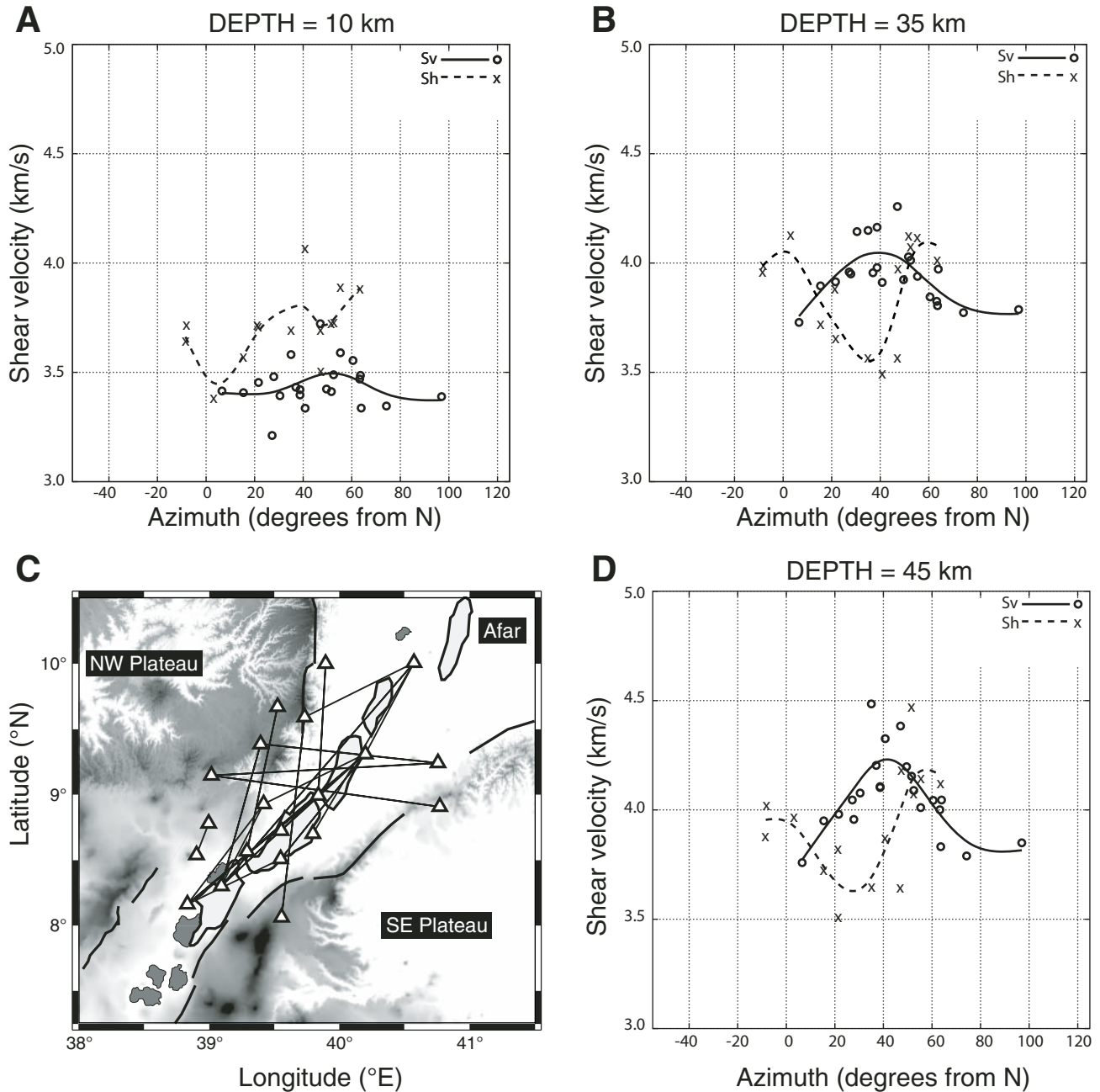


Figure 6. Surface-wave anisotropy within the Main Ethiopian Rift. Azimuthal variation in S_v and S_h wave speeds at depths of (A) 10 km, (B) 35 km, and (D) 45 km. Solid lines are natural smooth spline fits to individual measurements, and azimuth is measured clockwise from north. Estimates are made from group velocity measurements of local events and interstation phase velocity measurements. (C) Interstation paths for phase velocity measurements. Figures were modified after Bastow et al. (2010).

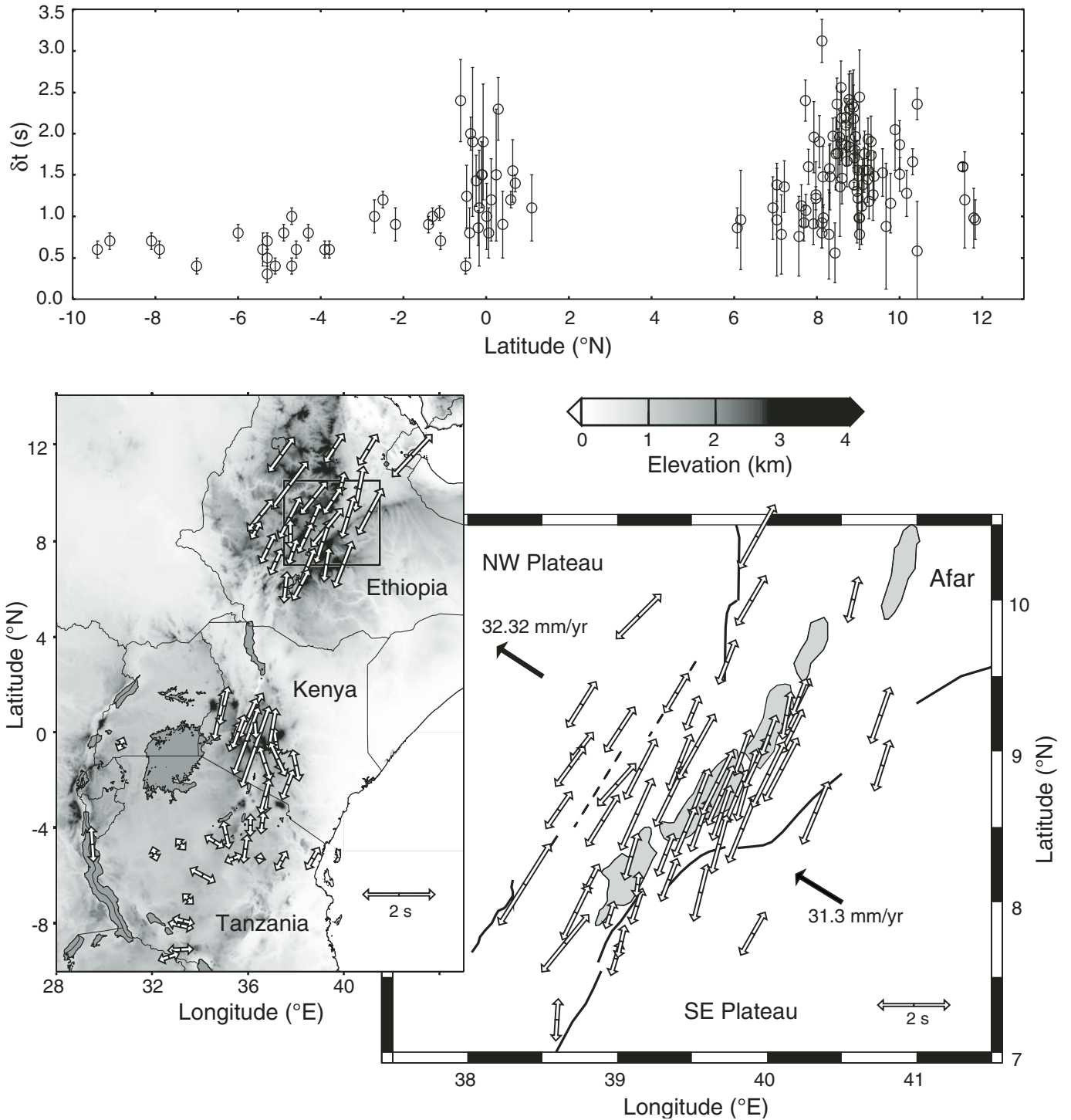
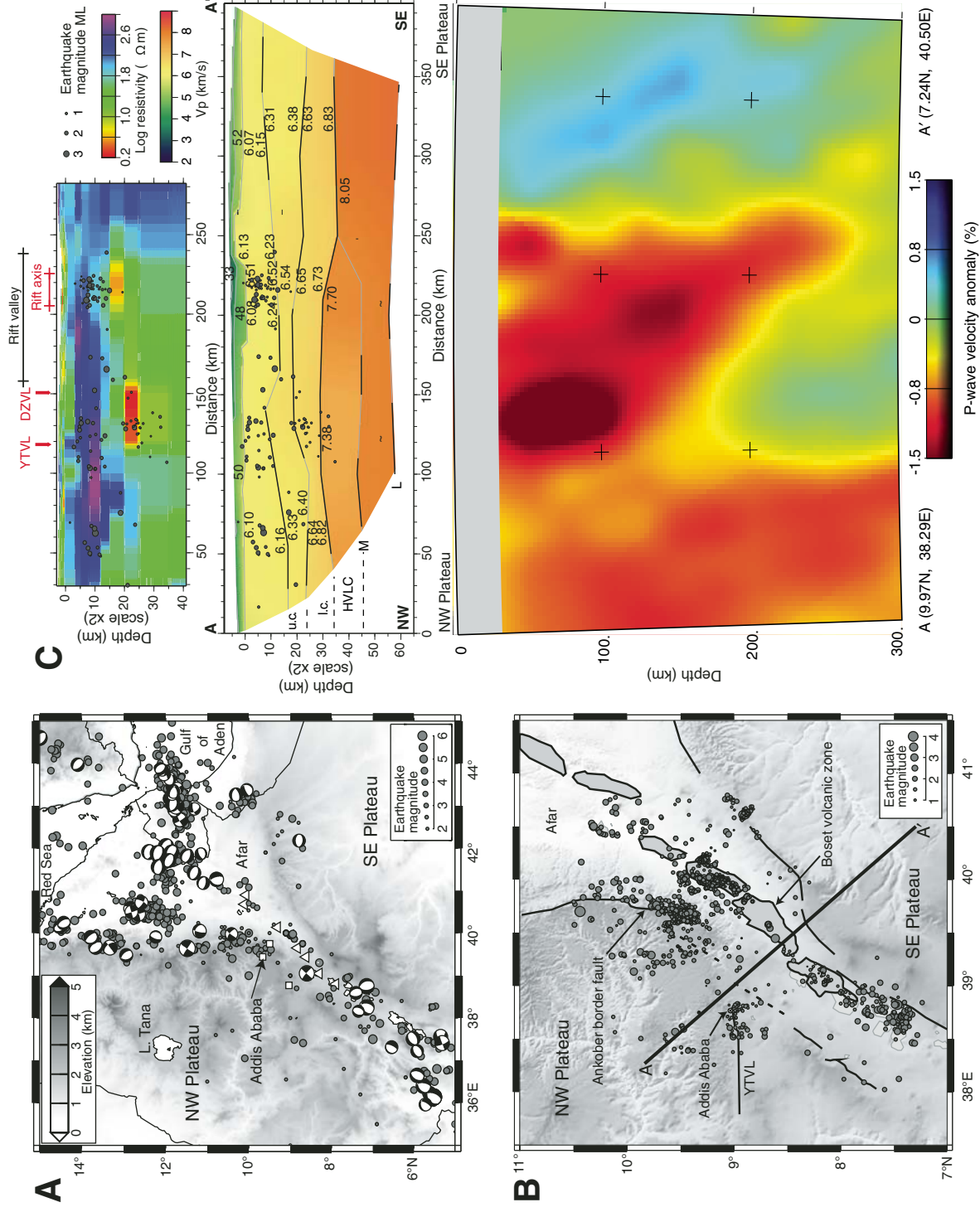


Figure 7. SKS splitting measurements along the East African Rift. Lower right shows detail from Main Ethiopian Rift. Mid-Miocene border faults and monoclines are marked with solid and dashed lines, respectively. Large arrows indicate absolute plate motion. Quaternary magmatic zones are shaded. In both maps, arrows show orientation of fast shear wave, and length of arrow is proportional to magnitude of splitting. Top figure shows SKS splitting delays (δt) as a function of latitude. Figure is modified after Kendall et al. (2006).

Figure 8. Seismicity in Ethiopia. (A) Seismic activity of the Horn of Africa since 1960. Earthquake locations and magnitudes are from Ayele and Kulhnek (1997) for the time period 1960–1997 and the National Earthquake Information Center catalogue (1997–2005). Earthquake focal mechanisms are from the Harvard Centroid Moment Tensor (CMT) catalog, Foster and Jackson (1998), Ayele and Arvidsson (1997), Ayele (2000), and Hofstetter and Beyth (2003). Quaternary volcanoes in the Main Ethiopian Rift are shown by triangles. (B) Seismicity of the Main Ethiopian Rift from October 2001 to January 2003. Earthquakes were located with the minimum one-dimensional (1-D) P-wave velocity model determined from local earthquake tomography. Only events recorded by at least four stations and located within the array of seismic stations are displayed. (C) Top: Two-dimensional (2-D) resistivity structure of the Main Ethiopian Rift crust determined using magnetotelluric data (Whaler and Hautot, 2006). Middle: The cross-rift wide-angle profile (Mackenzie et al. (2005) with hypocenters (dark gray circles) recorded during October 2001 to January 2003 and located within 50 km to either side (dashed lines) of the profile projected onto the section. Abbreviations: u.c.—upper crust; l.c.—lower crust; HVLC—high-velocity lower crust; M—Moho; L—lithosphere; YTVL—Yerer-Tullu Wellet volcanotectonic lineament. Bottom: Cross section through the P-wave velocity model of Bastow et al. (2008). Figures are modified after Keir et al. (2006b, 2009b).



Despite the focus of EAGLE on the Main Ethiopian Rift, the most significant regional seismic activity occurred during August 2002 on the western flank of the Red Sea Rift near the border between Ethiopia and Eritrea. Over a period of 2 wk following 7 August 2002, 75 earthquakes of M_L 2.1–5.6 were located using combined data from EAGLE and permanent stations in Ethiopia and Eritrea (Ayele et al., 2007b). Moment tensor inversion on a selection of data is consistent with earthquakes being 5–7 km deep and normal slip on NNW-striking faults, parallel to the predominant structures mapped at the surface. The well-constrained cluster of earthquakes, combined with macroseismic reports of ground shaking in the city of Mekele (Fig. 1), shows that the grabens on the heavily populated western Afar margin pose a significant seismic hazard. Indeed, historical records of macroseismic destruction at other localities on the western Afar margin such as Kara Kore (1961) and Ankober (Fig. 1) (1841–1842) (Gouin et al., 1979), combined with the recent study during EAGLE advise the Ethiopian government to enforce building codes for earthquake-resistant structures.

Crustal Tomography

Using the local earthquake catalog of Keir et al. (2006b), Daly et al. (2008) presented 3-D P-wave velocity and V_p/V_s models of the midcrust (Fig. 9). The models show high P-wave velocities (6.5 km/s) beneath the axis of the rift at a depth of 12–25 km, consistent with the findings of Keranen et al. (2004), who found high P-wave velocities (6.5–6.8 km/s) at 7–15 km depth using tomographic inversion of the controlled-source traveltimes data set. The presence of high V_p/V_s ratios (1.81–1.84) at 12–25 km, segmented positive Bouguer anomalies (Mahatsente, et al., 1999; Tiberi et al., 2005; Mickus et al., 2007), and coincidence with zones of surface Quaternary volcanism suggest that the higher-velocity, higher-density zones are cooled dense mafic intrusions. The high V_p/V_s values, along with other geophysical evidence, suggest that magmatic processes continue to the present day.

Controlled-Source Profiles

A major component of EAGLE was a controlled-source wide-angle experiment, which consisted of one cross-rift (Line 1) and one rift-axial (Line 2) profile (both ~400 km) and an ~100-km-diameter two-dimensional (2-D) array (Fig. 2) to provide 3-D subsurface images beneath the Boset volcano where the profiles intersected (Mackenzie et al., 2005; Maguire et al., 2006).

Twenty-three explosive charges, with an average shot size of 1100 kg, were detonated in boreholes up to 50 m deep, in two lakes, and in two quarries. Approximately 1000 single-channel “Texan” geophones spaced at ~1 km along the 400 km profiles and ~2.5 km within the 2-D array recorded the shots simultaneously with a 93 Guralp CMG-6TD three-component broadband deployment using ~5 km station spacing along Line 1 (Fig. 2). Further details of the wide-angle deployment and raw data qual-

ity are available in Mackenzie et al. (2005) and Maguire et al. (2006), but the final analyses of these data are shown here in Figure 10. Some key features of the profiles are as follows:

The 6.5 km/s high-velocity bodies in the upper crust beneath the rift axis are noted in Line 1 (Fig. 10A).

The 6.1–6.4 km/s upper crust is ~28 km thick beneath the NW and SE plateaus. It then thins to ~23 km beneath the Main Ethiopian Rift. Along Line 2 (Fig. 10B), upper-crust thickness falls to ~8 km in Afar, and the most dramatic thinning occurs across the Boset magmatic zone of the Main Ethiopian Rift.

The 6.6–7.1 km/s lower crust on Line 1 is ~14 km thick on the SE plateau and 9–12 km thick beneath the NW plateau. Lower-crustal thickness is relatively uniform at ~16–20 km along Line 2.

Beneath Line 1, the lower crust overlies an anomalous ~8–15-km-thick layer of velocity ~7.38 km/s on the NW plateau; this feature is absent from the east.

The NW plateau crust is underlain by a ~8.0 km/s mantle, while the SE plateau uppermost mantle is characterized by “normal” mantle velocities of ~8.05 km/s.

Mantle reflectors occur at 50–60 km beneath large portions of Lines 1 and 2 but shallow considerably to ~40 km beneath the northernmost part of Line 2.

The results from crustal seismic tomography using the 2-D array (Keranen et al., 2004) also indicate the presence of P-wave high-velocity bodies beneath Boset, as well as other regions of the Wonji fault belt (Fig. 11).

Gravity and Magnetotelluric Surveys

The interpretation of gravity anomalies, like other potential field data, suffers from nonuniqueness. However, in conjunction with controlled-source seismic data (which can be used to add geometric constraints during modeling), gravity data become a powerful tool for constraining the physical properties of the lithosphere. Cornwell et al. (2006) conducted a cross-rift gravity survey coincident with wide-angle Line 1 (Fig. 2). Data from 72 stations across the Main Ethiopian Rift were forward and inverse modeled for density structure to a depth of ~60 km using starting models defined by the seismic results of Mackenzie et al. (2005) and Keranen et al. (2004) (Figs. 10 and 11). The starting model provided a good first-order fit to the data, but the sensitivity of the gravity method to lateral density changes enabled improved definition of structure. Figure 12 shows the final model, which has the following salient features:

The upper-mantle density beneath the NW rift flank has to be reduced to 3290 kg/m³ to fit the observed anomaly.

An axial low-density upper-mantle or high-density lower-crustal zone is modeled as a ~50-km-wide body with a density of 3190 kg/m³.

Two high-density (3000 kg/m³) upper-crustal bodies underlie the Main Ethiopian Rift: a 20-km-wide axial body, and a 12-km-wide off-axis body, both of which are most likely to be gabbroic in composition.

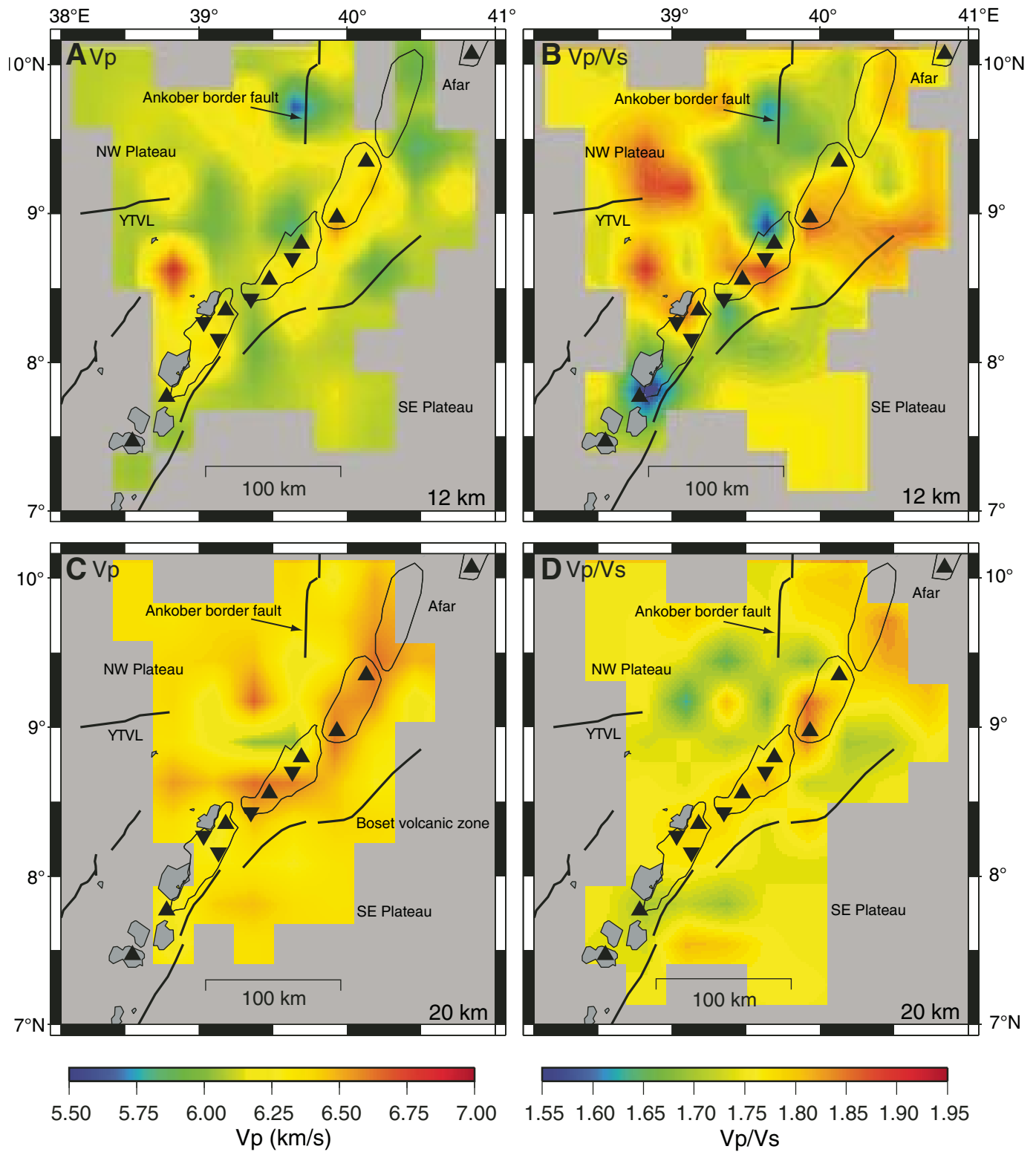


Figure 9. 12 and 20 km depth slices through the three-dimensional (3-D) P-wave velocity and V_p/V_s ratio models. YTVL—Yerer-Tullu Wellel volcanotectonic lineament. Figure is modified after Daly et al. (2008).

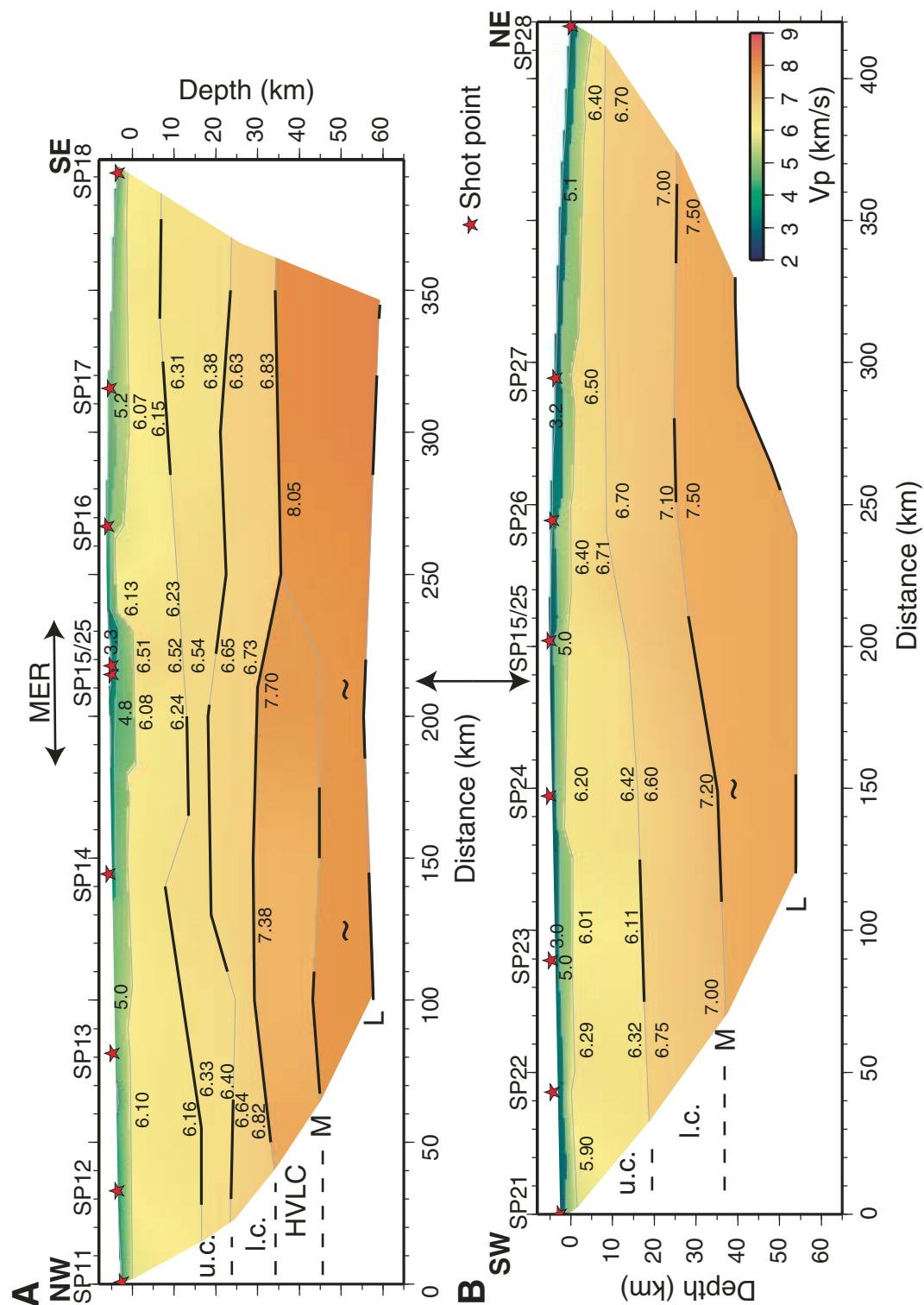


Figure 10. P-wave velocity models for (A) Line 1 and (B) Line 2. Model outlines indicate regions sampled by raypaths; P-wave velocities are in km/s; ~ indicates there is no velocity information available; the depths in these regions have been extrapolated from neighboring known velocities within the same layer. Bold lines at layer boundaries are those regions sampled by reflected rays. u.c.—upper crust; l.c.—lower crust; HVLC—high-velocity lower crust; M—Moho; L—lithospheric mantle reflector. Lines 1 and 2 are aligned at their intersection (double-headed arrow). Figures are modified after Mackenzie et al. (2005) and Maguire et al. (2006). MER—Main Ethiopian Rift.

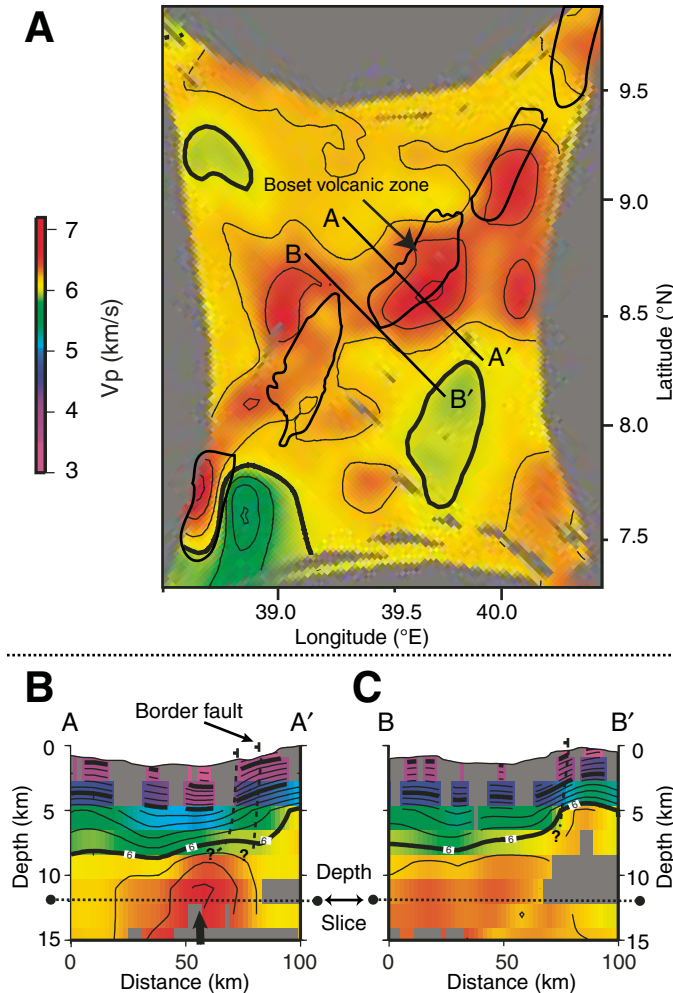


Figure 11. Controlled-source seismic tomography. (A) Horizontal slice 10 km beneath the two-dimensional (2-D) controlled-source array. The thick contour lines mark 6.0 km/s, with minor contours at 0.2 km/s intervals. High-velocity bodies (red) are interpreted as solidified magmatic intrusions beneath the rift. (B) Rift-perpendicular cross section A–A' extending through the Boset magmatic field. High-velocity (V_p) body (vertical arrow) beneath the rift valley is interpreted as a solidified mafic intrusion into Precambrian basement. (C) B–B' shows rift-perpendicular section between magmatic segments. Fault symbols and proposed subsurface continuation of faults (dashed lines) are marked. Areas of no ray coverage are gray. Figure is modified after Keranen et al. (2004).

A <10-km-wide high-density (2850 kg/m^3) body lies directly beneath Boset.

The high-velocity lower-crust/low-velocity upper-mantle low-velocity layer seen in wide-angle Line 1 is characterized by a 3170 kg/m^3 layer, which is absent from the east.

Coincident with the wide-angle Line 1 and the gravity survey (Fig. 2), Whaler and Hautot (2006) carried out a magnetotelluric profile to investigate the electrical conductivity structure of the crust beneath the Main Ethiopian Rift and adjacent plateaus. The resulting model, shown in Figure 8C, has several key features:

A shallow conductive lens at <1 km depth underlies the Boset Volcano (Fig. 1).

Deeper conductive material beneath Boset extends to at least lower-crustal depths.

A second, highly conductive layer underlies rift flank to the east of Addis Ababa at 20–25 km depth (at 120–150 km along the magnetotelluric profile).

The lowermost crust and uppermost mantle of the NW plateau, though not well resolved, is more conductive than to the SE of the Somalian plate.

DISCUSSION

In this section, we summarize the main conclusions of the EAGLE experiments and show, with reference to other studies (e.g., geochemistry and geodynamics), how they have advanced our understanding of both hotspot tectonism and continental breakup processes.

Hotspot Tectonism and the Ethiopian Low-Velocity Anomaly

The most detailed P- and S-wave seismic tomographic images to date (Figs. 3 and 4) of the upper mantle in Ethiopia are presented by Bastow et al. (2008); they corroborate a growing body of evidence that Ethiopia is underlain by a broad (~500-km-wide) low-velocity zone (e.g., Debayle et al., 2001; Grand, 2002; Ritsema and Allen, 2003; Benoit et al., 2006a, 2006b; Li et al., 2008) that connects to the deeper African superplume in the lower mantle. There is no evidence for a narrow (~100–200-km-diameter) plume tail beneath Ethiopia, as would be expected if a starting plume existed today (e.g., Hawaii; Wolfe et al., 2009), although the assumption that such a feature would be illuminated by seismic tomography proceeds on the assumption that thermal effects are the dominant cause of heterogeneity. On the contrary, absolute delay times at permanent station AAE (Fig. 2), which indicate the mantle beneath Ethiopia is amongst the slowest worldwide (e.g., Poupinet, 1979; Bastow et al., 2005, 2008), suggest strongly that high temperatures and the presence of partial melt are necessary to explain the seismic observations.

Within the broad low-velocity anomaly, the lowest-velocity zones, interpreted as zones of enhanced partial melt, are located at ~9°N in the Main Ethiopian Rift, not beneath southern Afar (Bastow et al., 2008). New experiments in Afar will illuminate the crust and mantle there and help reconcile this finding with the results of many global tomographic studies, but it is unclear whether the intense LVR has resulted from focused mantle upwelling (resulting, for example, from a steeper lithosphere–asthenosphere boundary at this latitude compared to the more extended Afar region, where melt may be less focused; e.g., Bastow et al., 2005, 2008) and/or enhanced decompressional melting at this latitude, where the Main Ethiopian Rift is younger than the East African Rift to the south and Afar to the north (which was largely formed during the rifting of Arabia from Africa at

ca. 30 Ma). Kinematic rifting models indicate that rapid lithospheric thinning can result in decompressional melting of the underlying mantle (e.g., Bown and White, 1995). Rifting over longer periods, however, greatly reduces melt volumes, as heat is lost through conduction. Such ideas, coupled with greater depletion of the subcontinental lithospheric mantle beneath Afar, could explain the seismic observations, with larger melt volumes pro-

ducing the lower velocities in the Main Ethiopian Rift (Bastow et al., 2008, 2010).

Whatever the model for rifting in Ethiopia, the results from the seismic tomography studies provide clear evidence for an abundant source of partial melt in the mantle. In the following section, we present evidence to suggest that this melt source plays a vital role in the ongoing rifting process in Ethiopia.

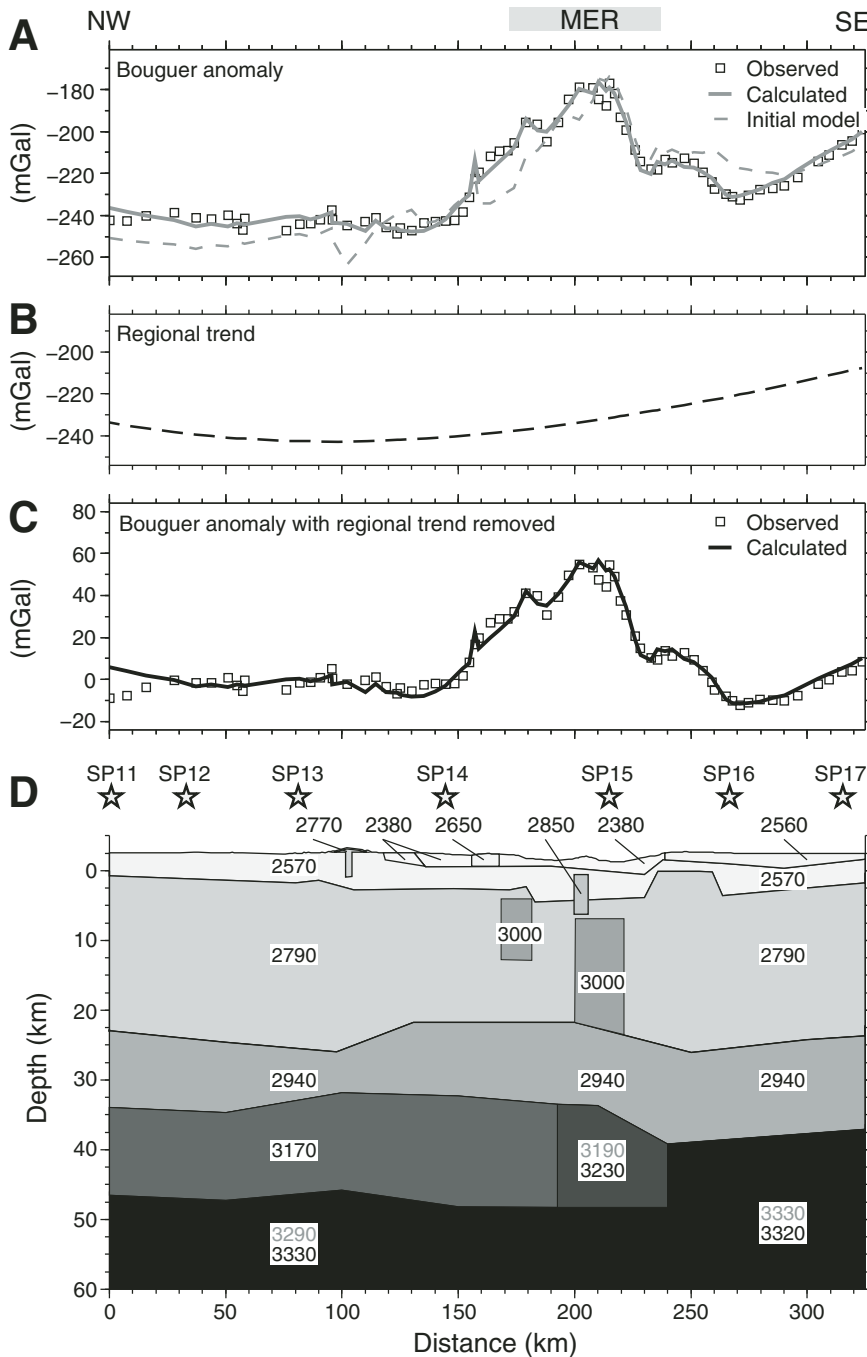


Figure 12. (A) Calculated final (solid line) and initial (dashed line) Bouguer anomaly compared with observed Bouguer anomaly (squares) along the Ethiopia Afar Geoscientific Lithospheric Experiment cross-rift profile. MER—Main Ethiopian Rift. (B) Regional long-wavelength trend from low-pass filtering (i.e., wavelengths more than ~80 km) of existing Ethiopian gravity data (e.g., Mahatsente et al., 1999; Tiberi et al., 2005). (C) Calculated Bouguer anomaly (solid line) and observed Bouguer anomaly with regional trend subtracted (squares). (D) Final density model (values in kg/m³). Where two density values are labeled for a particular layer, the upper corresponds to the calculated anomaly in A and the lower corresponds to the calculated anomaly in C. Stars are the locations of the seismic shot points. Figure is modified after Cornwell et al. (2006).

Rifting in Ethiopia: Geophysical Studies of Crustal Structure and Process

An aim central to EAGLE was to understand better how strain is partitioned between magma intrusion and fault slip along the axis of the Main Ethiopian Rift. Geodetic data indicate that ~80% of present-day strain in the Main Ethiopian Rift is accommodated within the Main Ethiopian Rift, not on mid-Miocene border faults (Bilham et al., 1999; Bendick et al., 2006). Ebinger and Casey (2001) proposed that the locus of strain since ca. 12 Ma has migrated away from mid-Miocene border faults to en-echelon chains of Quaternary magmatic segments (Figs. 1 and 2) in the Wonji fault belt. Crustal-scale imaging by EAGLE offered a unique opportunity to test this hypothesis.

The relatively unfaulked flanks of the rift zone are underlain by crust of thickness 40–45 km, and yet most of the region was below sea level in Paleocene times. Thus, much of the plateau uplift can be explained by crustal intrusion associated with the flood basaltic magmatism in Eocene–Oligocene times. Cross-rift wide-angle profiles (Fig. 10) image mafic intrusions beneath the zones of Quaternary magmatism, calibrating the crustal tomography (Fig. 11; Keranen et al., 2004; Fig. 9; Daly et al., 2008) and gravity anomaly studies (Fig. 12; Cornwell et al., 2006). Despite the relatively small reduction in crustal thickness from rift shoulders (40–48 km) to the rift axis (40–26 km), strain has localized to a zone of magma intrusion and minor faulting that is less than 20 km in width. In addition to axial magmatism, the presence of high conductivities and coincident anomalously deep earthquakes beneath chains of volcanoes near the rift margin support ongoing off-axis emplacement of magma into the lower crust (Fig. 8). These observations are consistent with those from passive margins worldwide: Magmatic margins have a narrow, relatively thick ocean-continent transition zone compared to wide, highly attenuated, amagmatic margins (e.g., Hopper and Buck, 1993).

The along-axis wide-angle seismic profile shows a south-to-north decrease in crustal thickness from ~40 km in the SW to ~26 km in the NE beneath Afar (Fig. 10N). The accompanying increase in upper-crustal V_p has been interpreted as evidence for an increased volume of intruded gabbroic material during extension toward full incipient seafloor spreading. Tomographic inversions of active and passive source seismic data by Keranen et al. (2004) and Daly et al. (2008) also have confirmed the presence of elevated seismic velocities to ~20–30 km depth beneath many areas of Quaternary volcanism in the Main Ethiopian Rift (Figs. 9 and 11). Zones of higher-velocity and higher-density (Fig. 12) anomalies correspond to the surface expression of Quaternary magmatism within the Ethiopian Rift. This, in combination with the lack of crustal thinning, suggests that an ~20–30-km-wide zone of mafic intrusions beneath the rift axis accommodates the majority of strain in the midcrust.

During Miocene–Pliocene times, large offset border faults accommodated the largest proportion of strain across the Ethiopian Rift. However, since Pliocene times, extension in the upper

crust has been accommodated by a combination of dikes and normal faults within the Main Ethiopian Rift (e.g., Keranen et al., 2004; Keir et al., 2006b). The marked coincidence between narrow, seismically active (Keir et al., 2006b) Quaternary rift-axial grabens containing aligned volcanic cones and fissural flows, and mid- to upper-crustal zones of mafic intrusions suggests that the locus of brittle failure in the upper crust is controlled by dike intrusion both within and beneath the seismogenic zone. The EAGLE results therefore point toward a model of magma-assisted rifting in Ethiopia, where magma intrusion throughout the lithosphere dominates over mechanical stretching to accommodate extension through localized axial dike (e.g., Buck, 2004, 2006).

The presence of magma in the crust beneath the regions of Quaternary rift magmatism and the uplifted rift shoulders is indicated not only by recent volcanism in the region (e.g., Rooney et al., 2005, 2007), but also by high V_p/V_s ratios in the crust. This has been observed both on the bulk crustal scale by analyses of teleseismic receiver functions (e.g., Dugda et al., 2005; Stuart et al., 2006), and also by shallower analysis of local seismicity data (e.g., Daly et al., 2008). Magnetotelluric data are more sensitive to the presence of melt than seismic methods. The high conductivity anomalies (Fig. 8C) beneath the rift axis in the upper ~2 km and at 15–20 km depth provide the most compelling geophysical evidence for the presence of partial melt in the crust beneath the rift (e.g., Whaler and Hautot, 2006).

A recurring theme amongst many EAGLE studies is the asymmetry of the Main Ethiopian Rift with respect to the underlying mantle low-velocity body (e.g., Bastow et al., 2008). Mackenzie et al. (2005), Maguire et al. (2006), Stuart et al. (2006), and Cornwell et al. (2006) all have presented evidence for the presence of a 15-km-thick high-velocity ($V_p \approx 7.38$ km/s), dense (3170 kg/m³) lower-crustal layer, which they interpreted to be underplated material emplaced at the time of continental flood basalt eruption (ca. 45–30 Ma) and modified by subsequent Miocene-to-Holocene rifting in the Main Ethiopian Rift. Recent analyses of earthquake data in Ethiopia also highlight the absence of seismicity on the Somalian plate (SE) and its relative abundance on the Nubian plate (NW; Keir et al., 2009b). In places, seismicity on the NW side of the Main Ethiopian Rift is anomalously deep and most likely caused by ongoing magmatic processes (Fig. 8). Alternatively, asymmetry in rift structure may not be due to post-ca. 45 Ma magmatism, but rather may have been caused by Paleozoic structural inheritance proposed to have exerted a major control on the location of the Main Ethiopian Rift (Bastow et al., 2008; Keranen and Klemperer, 2008; Keranen et al., 2009; Agostini et al., 2009; Cornwell et al., 2010). However, such a hypothesis is hard to test because of the paucity of basement fabrics exposed in Ethiopia (e.g., Church, 1991).

Ethiopian Lithospheric Structure

Despite the abundance of geophysical information available for Ethiopia's upper mantle (Debayle et al., 2001; Bastow et al., 2005, 2008; Benoit et al., 2006a, 2006b; Pasyanos and Nyblade,

2007; Priestley et al., 2008) and the plethora of aforementioned images of crustal structure, less is known about the deeper lithospheric structure (45–75 km) because the data/methods employed by EAGLE do not sample the range well. Teleseismic tomography has insufficient crossing rays to resolve this depth range, and it is toward the limits of the depth resolution of the wide-angle seismic profiles and the magnetotelluric survey. This depth range is important, however, because it constrains the link between surface observations of Quaternary volcanism and crustal magma intrusion and deeper sources of melt in the upper mantle that likely link to the underlying African superplume structure. The mantle reflectors identified by Maguire et al. (2006) beneath both controlled-source profiles (Fig. 10) were also noted in earlier wide-angle studies in Ethiopia (Berckhemer et al., 1975; Makris and Ginzburg, 1987) and further south in Kenya (e.g., Maguire et al., 1994). Beneath Afar, the reflector shallows by ~20 km, but it remains 10–25 km beneath the Moho throughout the study area. Several causes of mantle reflectors in the depth range 50–100 km depth are discussed by Levin and Park (2000). Maguire et al. (2006), however, believe that the reflector is a compositional or structural boundary within preexisting lithosphere, owing to the correlation of reflector depth with the amount of lithospheric extension, rather than a phase change or melt front.

SKS shear-wave splitting analyses by Kendall et al. (2005) indicate that some parts of Ethiopia are amongst the most anisotropic worldwide (δt up to ~3 s; Fig. 7). A rotation of the fast splitting direction (ϕ) within the Main Ethiopian Rift may mirror a shift from N130°E-directed extension to N110°E-directed extension at ca. 2 Ma, when crustal strain localized toward the Wonji fault belt (Wolfenden et al., 2004). Alternatively, analog modeling of deformation in Ethiopia (Corti, 2008, 2009) shows that the same evolution in structural trends since the mid-Miocene can be obtained by uniformly directed N110°E extension of the lithosphere with early border fault structural trends controlled by preexisting lithospheric structural inheritances buried beneath Cenozoic flood basalts. Either way, the SKS results provide compelling evidence to suggest that anisotropy is dominated by rifting processes. It is difficult to discriminate among anisotropy due to olivine lattice preferred orientation (LPO) associated with mantle flow, fossil anisotropy in the lithosphere, and anisotropy due to oriented melt pockets (OMP). Analyses of interstation phase velocities for Love (L_Q) and Rayleigh waves (L_R) in the Main Ethiopian Rift can be used to distinguish between different mechanisms of anisotropy (Fig. 5; e.g., Bastow et al., 2010). These analyses in Ethiopia (Fig. 6) show that anisotropy in at least the top ~45 km of the lithosphere beneath the Main Ethiopian Rift is controlled by OMP-type anisotropy (e.g., Kendall et al., 2005). Intriguingly, SKS delay times peak at ~9°N (not in Afar), where lowest velocities are thought to exist beneath Ethiopia (e.g., Bastow et al., 2008, 2010). Kendall et al. (2005) also noted that δt is higher at the rift flanks than beneath the rift axis. A factor consistent with this is the observed offset of lowest-velocity zones in the upper mantle (Bastow et al., 2005, 2008). This offset

of low-velocity anomalies away from the center of the rift toward the uplifted rift flanks (Fig. 4) indicates some linkage between the fault-controlled strain and the development of the upper-mantle along-axis segmentation (Bastow et al., 2008). Such observations show that preexisting, as well as strain (rifting)-induced, base-of-lithosphere topography may play an important role in melt transport beneath the rift system (Bastow et al., 2005, 2008). If the mantle organizes itself as it would beneath a fully developed seafloor spreading center (e.g., Kuo and Forsyth, 1988; Phipps-Morgan and Chen, 1993; Gregg et al., 2007; Wang et al., 2009), with low velocities directly beneath Quaternary volcanic centers, it is expected to do so further north into Afar (Fig. 1), where the influence of the steep base-of-lithosphere topography of the Miocene border faults is reduced as the rift progressively widens (Bastow et al., 2008).

CONCLUSIONS AND FOCUS FOR FUTURE RESEARCH

We have summarized a major geoscientific experiment in East Africa: the Ethiopia Afar Geoscientific Lithospheric Experiment, which probed crust and upper-mantle structure in a region of incipient continental breakup. Seismic tomography reveals some of the lowest-velocity mantle worldwide in a broad (~500-km-wide) upwelling beneath the Main Ethiopian Rift and uplifted Ethiopian Plateau. This anomalous body likely originated from Paleogene flood basaltic volcanism that presently sits atop the Ethiopian Plateau. We now know that this source of partial melt is playing an integral role in the breakup of the African continent in Ethiopia. Controlled-source seismic profiles, in conjunction with magnetotelluric, gravity, crustal seismic analyses, and geological observations, show that extension in the Main Ethiopian Rift is not accommodated by simple or pure shear of the lithosphere, but by a magma-assisted rifting model in which gabbroic intrusions (dikes and veins) achieve extension without marked crustal thinning. The observations from Ethiopia join a growing body of evidence from continental rifts (e.g., Thybo and Nielsen, 2009) and passive margins (e.g., White et al., 2008) that show that magma intrusion plays an important role in accommodating extension during continental breakup. A summary of the major findings and ideas we have discussed is shown in Figure 13. EAGLE has addressed many of the fundamental first-order questions about the transition from continental rifting to incipient oceanic spreading, but many questions remain, and these questions will fuel future generations of research in East Africa:

What are the causes of seismic heterogeneity in the mantle, and how can images of broad mantle upwellings be reconciled with geochemical models of mantle plumes (e.g., Ebinger and Sleep, 1998; George et al., 1998; Pik et al., 1999, 2003; Rogers et al., 2000; Rogers, 2006; Beccaluva et al., 2009; Ayalew and Gibson, 2009)?

At what stage and by what mechanism in the breakup process does the mantle organize itself into punctuated upwellings

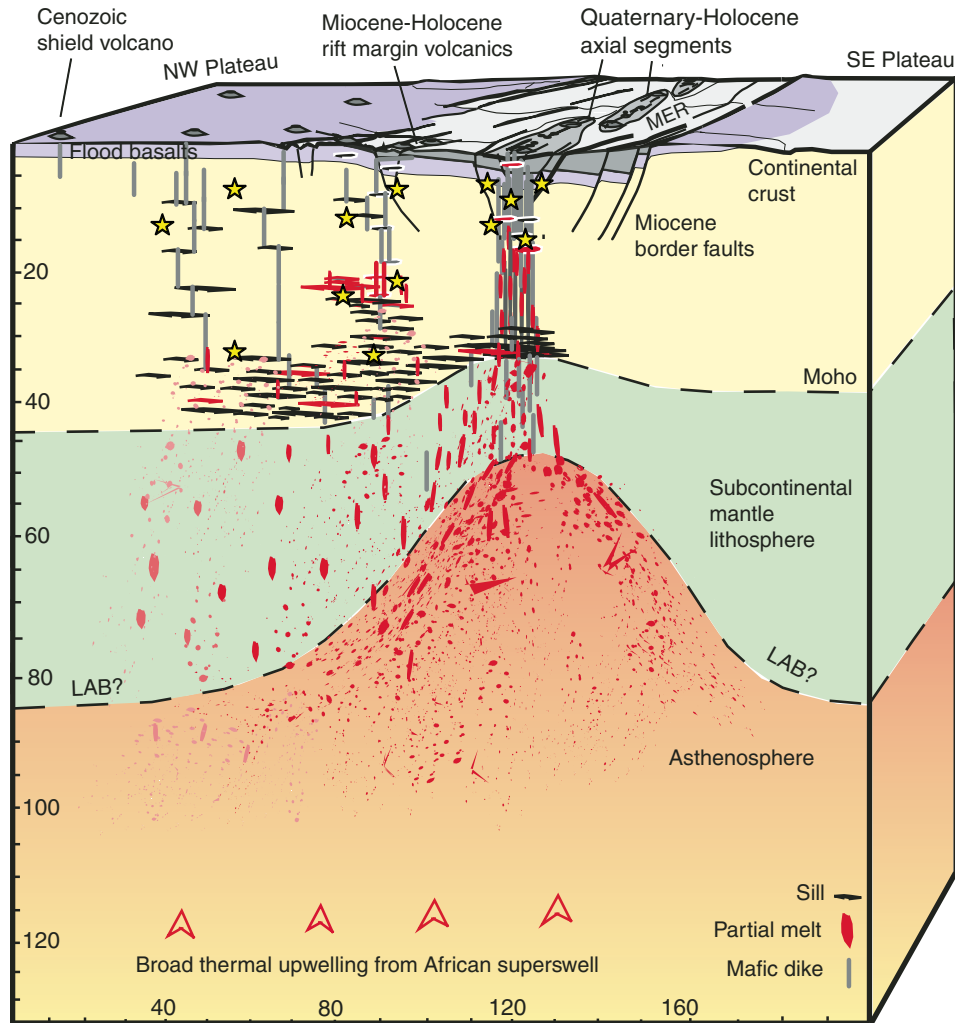


Figure 13. Conceptual model for the Main Ethiopian Rift (MER) based on the results from the Ethiopia Afar Geoscientific Lithospheric Experiment (EAGLE) project and complementary geoscientific studies. During Cenozoic times, ~2 km of flood basalts and rhyolites (purple) were erupted onto the Ethiopian Plateau, giving rise to shield volcanoes and underplate beneath the NW plateau. During the Miocene, border faults accommodated extension as rifting of the elevated plateau began. By Quaternary times, the locus of extension had then shifted to the axis of the Main Ethiopian Rift, where magma intrusion accommodated most of the extension without marked crustal thinning. Today, we see evidence of these magmatic processes in the form of magnetotellurically inferred melt zones and associated seismicity throughout the crust. Beneath the Main Ethiopian Rift, some of the lowest mantle velocities on Earth are best explained by a hypothesis of high temperatures and partial melt, which flows in a complex manner in response to the base of lithosphere topography. Deeper still, the low-velocity region is 500 km wide and likely connects across the transition zone to the deeper African superplume. LAB—lithosphere-asthenosphere boundary.

as is observed beneath a proto-seafloor spreading center (e.g., Bonatti, 1985; Wang et al., 2009)?

What is the composition and geometry, and over what time-scales is melt delivered from the upper mantle to various depths within the crust? How is strain partitioned between ductile stretching, and magma injection in the lithosphere? These questions have fundamental implications for the thermal-mechanical evolution of potential hydrocarbon passive margins and failed rifts (e.g., Thybo et al., 2009).

Does fault growth along the rift axis occur primarily during episodes of increased dike intrusion, such as is currently being observed in the subaerial Red Sea Rift in Afar (e.g., Rowland et al., 2007; Grandin et al., 2009), or does the majority of fault growth occur during amagmatic interdiking periods? Discrimination between these two end-member models has important implications for seismic hazard assessment in Ethiopia, since a model of co-diking fault growth implies that prediction of the repeat times of dike injections

is more important than an understanding of a fault-controlled seismic cycle.

ACKNOWLEDGMENTS

We thank the Ethiopia Afar Geoscientific Lithospheric Experiment (EAGLE) working group for fruitful discussions over the years since EAGLE began. Cindy Ebinger provided invaluable advice that improved the manuscript. Research staff at Addis Ababa University, especially Laike Mariam Asfaw, Bekele Abebe, Atalay Ayele, Dereje Ayalew, Gezahegn Yirgu, and Tesfaye Kidane, are gratefully acknowledged for their considerable scientific insight and invaluable support, without which the EAGLE project would not have been possible. Peter Maguire and Ullrich Achauer provided helpful reviews that improved the quality of the manuscript. IDB funded by the Leverhulme Trust. DK funded by National Environment Research Council fellowship NE/E013945/1.

REFERENCES CITED

- Abdallah, A., Courtillot, V., Kasser, M., Le Dain, A.-Y., L  pine, C., Rabineau, B., Ruegg, J.C., Taponnier, P., and Trantola, P., 1979, Relevance of Afar seismicity and volcanism to the mechanics of accreting plate boundaries: *Nature*, v. 282, p. 17–23, doi:10.1038/282017a0.
- Abebe, B., Acocella, V., Korme, T., and Ayalew, D., 2007, Quaternary faulting and volcanism in the Main Ethiopian Rift: *Journal of African Earth Sciences*, v. 48, p. 115–124, doi:10.1016/j.jafrearsci.2006.10.005.
- Acocella, V., and Korme, T., 2002, Holocene extension direction along the Main Ethiopian Rift, East Africa: *Terra Nova*, v. 14, p. 191–197, doi:10.1046/j.1365-3121.2002.00403.x.
- Acocella, V., Korme, T., and Salvini, F., 2003, Formation of normal faults along the axial zone of the Ethiopian Rift: *Journal of Structural Geology*, v. 25, p. 503–513.
- Agostini, A., Corti, G., Zeoli, A., and Mulugeta, G., 2009, Evolution, pattern, and partitioning of deformation during oblique continental rifting: Inferences from lithospheric-scale centrifuge models: *Geochemistry, Geophysics, Geosystems*, v. 10, no. 11, Q11015, doi:10.1029/2009GC002676.
- Asfaw, L., 1982, Development of earthquake-induced fissures in the Main Ethiopian Rift: *Nature*, v. 297, no. 5865, p. 393–395, doi:10.1038/297393a0.
- Asfaw, L., Bilham, R., Jackson, M., and Mohr, P., 1992, Recent inactivity in African rift: *Nature*, v. 357, no. 6378, p. 447, doi:10.1038/357447a0.
- Ayalew, D., and Gibson, S.A., 2009, Head-to-tail transition of the Afar mantle plume: Geochemical evidence from a Miocene bimodal basalt-rhyolite succession in the Ethiopian large igneous province: *Lithos*, v. 112, no. 3–4, p. 461–476, doi:10.1016/j.lithos.2009.04.005.
- Ayele, A., 2000, Normal left-oblique fault mechanisms as an indication of sinistral deformation between the Nubia and Somalia plates in the Main Ethiopian Rift: *Journal of African Earth Sciences*, v. 31, no. 2, p. 359–367, doi:10.1016/S0899-5362(00)00093-2.
- Ayele, A., and Arvidsson, R., 1997, Fault mechanisms and tectonic implication of the 1985–1987 earthquake sequence in south-western Ethiopia: *Journal of Seismology*, v. 1, no. 4, p. 383–394, doi:10.1023/A:1009774331917.
- Ayele, A., and Kulh  nek, O., 1997, Spatial and temporal variation of the seismicity in the Horn of Africa from 1960–1993: *Geophysical Journal International*, v. 130, p. 805–810, doi:10.1111/j.1365-246X.1997.tb01875.x.
- Ayele, A., Stuart, G.W., and Kendall, J.-M., 2004, Insights into rifting from shear wave splitting and receiver functions: An example from Ethiopia: *Geophysical Journal International*, v. 157, p. 354–362, doi:10.1111/j.1365-246X.2004.02206.x.
- Ayele, A., Jacques, E., Kassim, M., Kidane, T., Omar, A., Tait, S., Nercessian, A., de Chabali  r, J.-B., and King, G., 2007a, The volcano-seismic crisis in Afar, Ethiopia, starting September 2005: *Earth and Planetary Science Letters*, v. 48, p. 70–79.
- Ayele, A., Stuart, G.W., Bastow, I.D., and Keir, D., 2007b, The August 2002 earthquake sequence in north Afar: Insights into the neotectonics of the Danakil microplate: *Journal of African Earth Sciences*, v. 48, p. 70–79, doi:10.1016/j.jafrearsci.2006.06.011.
- Baker, J., Snee, L., and Menzies, M., 1996, A brief Oligocene period of flood volcanism in Yemen: *Earth and Planetary Science Letters*, v. 138, p. 39–55, doi:10.1016/0012-821X(95)00229-6.
- Barclay, A.H., and Toomey, D.R., 2003, Shear wave splitting and crustal anisotropy at the Mid-Atlantic Ridge, 35  N: *Journal of Geophysical Research*, v. 108, no. B8, p. 2378, doi:10.1029/2001JB000918.
- Bastow, I.D., Stuart, G.W., Kendall, J.-M., and Ebinger, C.J., 2005, Upper-mantle seismic structure in a region of incipient continental breakup: Northern Ethiopian Rift: *Geophysical Journal International*, v. 162, p. 479–493, doi:10.1111/j.1365-246X.2005.02666.x.
- Bastow, I.D., Owens, T.J., Helffrich, G., and Knapp, J.H., 2007, Spatial and temporal constraints on sources of seismic anisotropy: Evidence from the Scottish Highlands: *Geophysical Research Letters*, v. 34, no. 5, doi:10.1029/2006GL028911.
- Bastow, I.D., Nyblade, A.A., Stuart, G.W., Rooney, T.O., and Benoit, M.H., 2008, Upper mantle seismic structure beneath the Ethiopian hotspot: Rifting at the edge of the African low velocity anomaly: *Geochemistry, Geophysics, Geosystems*, v. 9, Q12022, doi:10.1029/2008GC002107.
- Bastow, I.D., Pilidou, S., Kendall, J.-M., and Stuart, G.W., 2010, Melt-induced seismic anisotropy and magma assisted rifting in Ethiopia: Evidence from surface waves: *Geochemistry, Geophysics, Geosystems*, v. 11, Q0AB05, doi:10.1029/2010GC003036.
- Beccaluva, L., Bianchini, G., Natali, C., and Siena, F., 2009, Continental flood basalts and mantle plumes: A case study of the northern Ethiopian Plateau: *Journal of Petrology*, v. 50, p. 1377–1403, doi:10.1093/petrology/egp024.
- Bellahsen, N., Faccenna, C., Funicello, F., Daniel, J.M., and Jolivet, L., 2003, Why did Arabia separate from Africa? Insights from 3-D laboratory experiments: *Earth and Planetary Science Letters*, v. 216, no. 3, p. 365–381, doi:10.1016/S0012-821X(03)00516-8.
- Bendick, R., McClusky, S., Bilham, R., Asfaw, L., and Klemperer, S., 2006, Distributed Nubia-Somalia relative motion and dike intrusion in the Main Ethiopian Rift: *Geophysical Journal International*, v. 165, p. 303–310, doi:10.1111/j.1365-246X.2006.02904.x.
- Benoit, M.H., Nyblade, A.A., Owens, T.J., and Stuart, G.W., 2006a, Mantle transition zone structure and upper mantle S velocity variations beneath Ethiopia: Evidence for a broad, deep-seated thermal anomaly: *Geochemistry, Geophysics, Geosystems*, v. 7, Q11013, doi:10.1029/2006GC001398.
- Benoit, M.H., Nyblade, A.A., and VanDecar, J.C., 2006b, Upper mantle P wavespeed variations beneath Ethiopia and the origin of the Afar hotspot: *Geology*, v. 34, no. 5, p. 329–332, doi:10.1130/G22281.1.
- Berckhemer, H., Baier, B., Bartlesen, H., Behle, A., Burkhardt, H., Gebrande, H., Makris, J., Menzel, H., Miller, H., and Vees, R., 1975, Deep seismic soundings in the Afar region and on the highland of Ethiopia, in Pilger, A., and R  sler, A., eds., *Afar Depression of Ethiopia*: Stuttgart, Schweizerbart, p. 89–107.
- Berhe, S.M., 1990, Ophiolites in northeast and East Africa: Implications for Proterozoic crustal growth: *Journal of the Geological Society of London*, v. 147, p. 41–57, doi:10.1144/gsjgs.147.1.0041.
- Beutel, E., van Wijk, J., Ebinger, C., Keir, D., and Agostini, A., 2010, Formation and stability of magmatic segments in the Main Ethiopian and Afar Rifts: *Earth and Planetary Science Letters*, v. 293, p. 225–235, doi:10.1016/j.epsl.2010.02.006.
- Bilham, R., Bendick, R., Larson, K., Mohr, P., Braun, J., Tesfaye, S., and Asfaw, L., 1999, Secular and tidal strain across the Main Ethiopian Rift: *Geophysical Research Letters*, v. 26, p. 2789–2792, doi:10.1029/1998GL005315.
- Bj  rnsson, A., Saemundsson, K., Einarsson, P., Tryggvason, E., and Gr  nvold, K., 1977, Current rifting episode in north Iceland: *Nature*, v. 266, no. 5600, p. 318–323, doi:10.1038/266318a0.
- Boccaletti, M., Bonini, M., Mazzuoli, R., Abebe, B., Piccardi, L., and Tortorici, L., 1998, Quaternary oblique extensional tectonics in the Ethiopian Rift (Horn of Africa): *Tectonophysics*, v. 287, no. 1–4, p. 97–116, doi:10.1016/S0040-1951(98)80063-2.
- Bonatti, E., 1985, Punctiform initiation of seafloor spreading in the Red Sea during transition from a continental to an oceanic rift: *Nature*, v. 316, no. 6023, p. 33–37, doi:10.1038/316033a0.
- Bonini, M., Souriot, T., Boccaletti, M., and Brun, J., 1997, Successive orthogonal and oblique extension episodes in a rift zone: Laboratory experiments with application to the Ethiopian Rift: *Tectonics*, v. 16, no. 2, p. 347–362, doi:10.1029/96TC03935.
- Bonini, M., Corti, G., Innocenti, F., Manetti, P., and Mazzarini, F., 2005, Evolution of the Main Ethiopian Rift in the frame of Afar and Kenya Rift propagation: *Tectonics*, v. 24, no. 1, TC1007, doi:10.1029/2004TC001680.
- Bown, J.W., and White, R.S., 1995, Effect of finite extension rate on melt generation at rifted continental margins: *Journal of Geophysical Research*, v. 100, no. B9, p. 18,011–18,029, doi:10.1029/94JB01478.
- Brazier, R.A., Miao, Q., Nyblade, A.A., Ayele, A., and Langston, C.A., 2008, Local magnitude scale for the Ethiopian Plateau: *Bulletin of the Seismological Society of America*, v. 98, no. 5, p. 2341, doi:10.1785/0120070266.
- Brown, G.F., 1970, Eastern margin of Red Sea and coastal structures in Saudi Arabia: *Philosophical Transactions of the Royal Society of London*, v. 267, p. 75–87.
- Buck, W.R., 1991, Modes of continental lithospheric extension: Pure and simple: *Journal of Geophysical Research*, v. 96, no. B12, p. 20,161–20,178, doi:10.1029/91JB01485.
- Buck, W.R., 2004, Consequences of asthenospheric variability on continental rifting, in Karner, G., Taylor, B., Driscoll, N.W., and Kohlstedt, D.L., eds., *Rheology and Deformation of the Lithosphere at Continental Margins*: New York, Columbia University Press, p. 1–30.
- Buck, W.R., 2006, The role of magma in the development of the Afro-Arabian rift system, in Yirgu, G., Ebinger, C.J., and Maguire, P.K.H., eds., *The Afar Volcanic Province within the East African Rift System*: Geological Society of London Special Publication 259, p. 43–54.
- Calais, E., Ebinger, C., Hartnady, C., and Nocquet, J., 2006, Kinematics of the East African Rift from GPS and earthquake slip vector data, in Yirgu, G., Ebinger, C.J., and Maguire, P.K.H., eds., *The Afar Volcanic Province*

- within the East African Rift System: Geological Society of London Special Publication 259, p. 9–23.
- Casey, M., Ebinger, C., Keir, D., Gloaguen, R., and Mohammed, F., 2006, Strain accommodation in transitional rifts: Extension by magma intrusion and faulting, *in* Yirgu, G., Ebinger, C.J., and Maguire, P.K.H., eds., The Afar Volcanic Province within the East African Rift System: Geological Society of London Special Publication 259, p. 143–163.
- Chernet, T., Hart, W.K., Aronson, I.L., and Walter, R.C., 1998, New age constraints on the timing of volcanism and tectonism in the northern Main Ethiopian Rift—Southern Afar transition zone (Ethiopia): *Journal of Volcanology and Geothermal Research*, v. 80, p. 267–280, doi:10.1016/S0377-0273(97)00035-8.
- Chevrot, S., and van der Hilst, R.D., 2000, The Poisson's ratio of the Australian crust: Geological and geophysical implications: *Earth and Planetary Science Letters*, v. 183, p. 121–132, doi:10.1016/S0012-821X(00)00264-8.
- Christensen, N.I., 1996, Poisson's ratio and crustal seismology: *Journal of Geophysical Research*, v. 101, no. B2, p. 3139–3156, doi:10.1029/95JB03446.
- Church, W.R., 1991, Discussion of "Ophiolites in northeast and East Africa: Implications for Proterozoic crustal growth": *Journal of the Geological Society of London*, v. 48, p. 600–606.
- Coffin, M.F., and Eldholm, O., 1994, Large igneous provinces: Crustal structure, dimensions, and external consequences: *Reviews of Geophysics*, v. 32, no. 1, p. 1–36, doi:10.1029/93RG02508.
- Cornwell, D., Mackenzie, G., England, R., Maguire, P., Asfaw, L., and Oluma, B., 2006, Northern Main Ethiopian Rift crustal structure from new high-precision gravity data, *in* Yirgu, G., Ebinger, C.J., and Maguire, P.K.H., eds., The Afar Volcanic Province within the East African Rift System: Geological Society of London Special Publication 259, p. 307–321.
- Cornwell, D.G., Maguire, P.K.H., England, R.W., and Stuart, G.W., 2010, Imaging detailed crustal structure and magmatic intrusion across the Ethiopian Rift using a dense linear broadband array: *Geochemistry, Geophysics, Geosystems*, v. 11, Q0AB03, doi:10.1029/2009GC002637.
- Corti, G., 2008, Control of rift obliquity on the evolution and segmentation of the main Ethiopian Rift: *Nature Geoscience*, v. 1, no. 4, p. 258–262, doi:10.1038/ngeo160.
- Corti, G., 2009, Continental rift evolution: From rift initiation to incipient break-up in the Main Ethiopian Rift, East Africa: *Earth-Science Reviews*, v. 96, p. 1–53, doi:10.1016/j.earscirev.2009.06.005.
- Crampin, S., Gao, Y., and Peacock, S., 2008, Stress-forecasting (not predicting) earthquakes: A paradigm shift?: *Geology*, v. 36, no. 5, p. 427–430, doi:10.1130/G24643A.1.
- d'Acremont, E., Leroy, S., Beslier, M.O., Bellahsen, N., Fournier, M., Robin, C., Maia, M., and Gente, P., 2005, Structure and evolution of the eastern Gulf of Aden conjugate margins from seismic reflection data: *Geophysical Journal International*, v. 160, no. 3, p. 869–890, doi:10.1111/j.1365-246X.2005.02524.x.
- Daly, E., Keir, D., Ebinger, C.J., Stuart, G.W., Bastow, I.D., and Ayele, A., 2008, Crustal tomographic imaging of a transitional continental rift: The Ethiopian Rift: *Geophysical Journal International*, v. 172, no. 3, p. 1033–1048, doi:10.1111/j.1365-246X.2007.03682.x.
- Debaille, E., Lévêque, J.J., and Cara, M., 2001, Seismic evidence for a deeply rooted low-velocity anomaly in the upper mantle beneath the northeastern Afro/Arabian continent: *Earth and Planetary Science Letters*, v. 193, p. 423–436, doi:10.1016/S0012-821X(01)00509-X.
- De Chabali, J.B., and Avouac, J.P., 1994, Kinematics of the Asal Rift, Djibouti, determined from the deformation of the Fieale volcano: *Science*, v. 265, p. 1677–1681, doi:10.1126/science.265.5179.1677.
- Di Leo, J., Bastow, I.D., and Helfrich, G., 2009, Nature of the Moho beneath the Scottish Highlands from a receiver function perspective: *Tectonophysics*, v. 479, p. 214–222, doi:10.1016/j.tecto.2009.08.014.
- Dugda, M.T., Nyblade, A.A., Julià, J., Langston, C.A., Ammon, C.A., and Simiyu, S., 2005, Crustal structure in Ethiopia and Kenya from receiver function analysis: *Journal of Geophysical Research*, v. 110, no. B1, doi:10.1029/2004JB003065.
- Duggen, S., Hoernle, K., and van den Bogaard, P.R., 2003, Deep roots of the Messinian salinity crisis: *Nature*, v. 422, p. 602–606, doi:10.1038/nature01553.
- Ebinger, C.J., 2005, Continental break-up: The East African perspective: *Astronomy & Geophysics*, v. 46, p. 16–21, doi:10.1111/j.1468-4004.2005.46216.x.
- Ebinger, C.J., and Casey, M., 2001, Continental breakup in magmatic provinces: An Ethiopian example: *Geology*, v. 29, p. 527–530, doi:10.1130/0091-7613(2001)029<0527:CBIMPA>2.0.CO;2.
- Ebinger, C., and Hayward, N., 1996, Soft plates and hot spots: Views from Afar: *Journal of Geophysical Research*, v. 101, no. B10, p. 21,859–21,876, doi:10.1029/96JB02118.
- Ebinger, C., and Sleep, N., 1998, Cenozoic magmatism throughout East Africa resulting from impact of a single plume: *Nature*, v. 395, p. 788–791, doi:10.1038/27417.
- Ebinger, C.J., Yemane, T., WoldeGabriel, G., Aronson, J., and Walter, R., 1993, Eocene–Recent volcanism and faulting in the southern Main Ethiopian Rift: *Journal of the Geological Society of London*, v. 150, p. 99–108, doi:10.1144/gsjgs.150.1.0099.
- Ebinger, C.J., Jackson, J.A., Foster, A.N., and Hayward, N.J., 1999, Extensional basin geometry and the elastic lithosphere: *Philosophical Transactions of the Royal Society of London*, ser. A, v. 150, p. 99–108.
- Ebinger, C.J., Yemane, T., Harding, T.J., Tesfaye, S., Kelley, S., and Rex, D.C., 2000, Rift deflection, migration, and propagation: Linkage of the Ethiopian and Eastern Rifts, Africa: *Geological Society of America Bulletin*, v. 112, no. 2, p. 163–176, doi:10.1130/0016-7606(2000)112<163:RDMAPL>2.0.CO;2.
- Ebinger, C., Ayele, A., Keir, D., Rowland, J., Yirgu, G., Wright, T., Belachew, M., and Hamling, I., 2010, Length and timescales of rift faulting and magma intrusion: The Afar rifting cycle from 2005 to present: *Annual Review of Earth and Planetary Sciences*, v. 38, p. 439–466, doi:10.1146/annurev-earth-040809-152333.
- Evans, J.R., and Achauer, U., 1993, Teleseismic tomography using the ACH method: Theory and application to continental scale studies, *in* Iyer, H., and Hirahara, K., eds., *Seismic Tomography: Theory and Practice*: New York, Chapman and Hall, p. 319–360.
- Fernandes, R.M.S., Ambroseus, B.A.C., Noomen, R., Bastos, L., Combrinck, L., Miranda, J.M., and Spakman, W., 2004, Angular velocities of Nubia and Somalia from continuous GPS data: Implications on present-day relative kinematics: *Earth and Planetary Science Letters*, v. 222, p. 197–208, doi:10.1016/j.epsl.2004.02.008.
- Foster, A., and Jackson, J., 1998, Source parameters of large African earthquakes: Implications for crustal rheology and regional kinematics: *Geophysical Journal International*, v. 134, p. 422–448, doi:10.1046/j.1365-246x.1998.00568.x.
- Furman, T., Bryce, J., Hanan, B., Yirgu, G., and Ayalew, D., 2006, Heads and tails: 30 years of the Afar plume, *in* Yirgu, G., Ebinger, C.J., and Maguire, P.K.H., eds., The Afar Volcanic Province within the East African Rift System: Geological Society of London Special Publication 259, p. 95–119.
- Gani, N.D.S., Gani, M.R., and Abdelsalam, M.G., 2007, Blue Nile incision on the Ethiopian Plateau: Pulsed plateau growth, Pliocene uplift, and hominin evolution: *GSA Today*, v. 17, no. 9, p. 4–11, doi:10.1130/GSAT01709A.1.
- Gashawbeza, E.M., Klempner, S.L., Nyblade, A.A., Walker, K.T., and Keranen, K.M., 2004, Shear-wave splitting in Ethiopia: Precambrian mantle anisotropy locally modified by Neogene rifting: *Geophysical Research Letters*, v. 31, doi:10.1029/2004GL020471.
- George, R., Rogers, N., and Kelley, S., 1998, Earliest magmatism in Ethiopia: Evidence for two mantle plumes in one continental flood basalt province: *Geology*, v. 26, p. 923–926, doi:10.1130/0091-7613(1998)026<0923:EMIEEF>2.3.CO;2.
- Gibson, I., 1969, The structure and volcanic geology of an axial portion of the Main Ethiopian Rift: *Tectonophysics*, v. 8, p. 561–565, doi:10.1016/0040-1951(69)90054-7.
- Gouin, P., 1979, *Earthquake History of Ethiopia and the Horn of Africa*: Ottawa, Ontario, International Development Research Centre (IDRC), 258 p.
- Grand, S.P., 2002, Mantle shear-wave tomography and the fate of subducted slabs: *Royal Society of London Philosophical Transactions*, ser. A, v. 360, p. 2475–2491, doi:10.1098/rsta.2002.1077.
- Grandin, R., Socquet, A., Binet, R., Klinger, Y., Jacques, E., De Chabali, J.-B., King, G.C.P., Lasserre, C., Tait, S., Tapponnier, P., Delorme, A., and Pinzuti, P., 2009, 2005 Manda Hararo-Dabbahu rifting event, Afar (Ethiopia): Constraints provided by geodetic data: *Journal of Geophysical Research*, v. 114, B08404, doi:10.1029/2008JB005843.
- Gregg, P.M., Lin, J., Behn, M.D., and Montesi, L.G.I., 2007, Spreading rate dependence of gravity anomalies along oceanic transform faults: *Nature*, v. 448, doi:10.1038/nature05962.
- Gregory, J., 1896, *The Great Rift Valley: Being the Narrative of a Journey to Mount Kenya and Lake Baringo: With Some Account of the Geology, Natural History, Anthropology and Future Prospects of British East Africa*: London, J. Murray, 423 p.
- Hamling, I., Ayele, A., Bennati, L., Calais, E., Ebinger, C., Keir, D., Lewi, E., Wright, T., and Yirgu, G., 2009, Geodetic observations of the ongoing Dabbahu rifting

- episode: New dyke intrusions in 2006 and 2007: *Geophysical Journal International*, v. 178, p. 989–1003, doi:10.1111/j.1365-246X.2009.04163.x.
- Hayward, N.J., and Ebinger, C.J., 1996, Variations in the along-axis segmentation of the Afar Rift system: *Tectonics*, v. 15, p. 244–257, doi:10.1029/95TC02292.
- Hendrie, D.B., Kusznir, N.J., Morley, C.K., and Ebinger, C.J., 1994, Cenozoic extension in northern Kenya: A quantitative model of rift basin development in the Turkana region: *Tectonophysics*, v. 236, no. 1–4, p. 409–438, doi:10.1016/0040-1951(94)90187-2.
- Hofmann, C., Courtillot, V., Feraud, G., Rochette, P., Yirgu, G., Ketefo, E., and Pik, R., 1997, Timing of the Ethiopian flood basalt event and implications for plume birth and global change: *Nature*, v. 389, p. 838–841, doi:10.1038/39853.
- Hofstetter, R., and Beyth, M., 2003, The Afar Depression: Interpretation of the 1960–2000 earthquakes: *Geophysical Journal International*, v. 155, no. 2, p. 715–732, doi:10.1046/j.1365-246X.2003.02080.x.
- Holbrook, W., and Kelemen, P., 1993, Large igneous province on the US Atlantic margin and implications for magmatism during breakup: *Nature*, v. 364, p. 433–436, doi:10.1038/364433a0.
- Hopper, J., and Buck, W.R., 1993, The initiation of rifting at constant tectonic force: The role of diffusion creep: *Journal of Geophysical Research*, v. 98, p. 16,213–16,221, doi:10.1029/93JB01725.
- Kazmin, V., Shifferaw, A., and Balcha, T., 1978, The Ethiopian basement: Stratigraphy and possible manner of evolution: *International Journal of Earth Sciences*, v. 67, p. 531–546.
- Kebede, F., and Kulháněk, O., 1994, Spatial and temporal variations of b-values along the East African Rift system and the southern Red Sea: *Physics of the Earth and Planetary Interiors*, v. 83, p. 249–264, doi:10.1016/0031-9201(94)90092-2.
- Kebede, F., and van Eck, T., 1997, Probabilistic seismic hazard assessment for the Horn of Africa based on seismotectonic regionalization: *Tectonophysics*, v. 270, p. 221–237, doi:10.1016/S0040-1951(96)00215-6.
- Keir, D., Kendall, J.-M., Ebinger, C.J., and Stuart, G.W., 2005, Variations in late syn-rift melt alignment inferred from shear-wave splitting in crustal earthquakes beneath the Ethiopian Rift: *Geophysical Research Letters*, v. 32, L23308, doi:10.1029/2005GL024150.
- Keir, D., Stuart, G.W., Jackson, A., and Ayele, A., 2006a, Local earthquake magnitude scale and seismicity rate of the northern Ethiopian Rift: *Bulletin of the Seismological Society of America*, v. 96, doi:10.1785/0120060051.
- Keir, D., Ebinger, C.J., Stuart, G.W., Daly, E., and Ayele, A., 2006b, Strain accommodation by magmatism and faulting as rifting proceeds to breakup: Seismicity of the northern Ethiopian Rift: *Journal of Geophysical Research*, v. 111, B05314, doi:10.1029/2005JB003748.
- Keir, D., Hamling, I.J., Ayele, A., Calais, E., Ebinger, C., Wright, T.J., Jacques, E., Mohamed, K., Hammond, J.O.S., Belachew, M., Baker, E., Rowland, J.V., Lewi, E., and Bennati, L., 2009a, Evidence for focused magmatic accretion at segment centers from lateral dike injections captured beneath the Red Sea Rift in Afar: *Geology*, v. 37, p. 59–62, doi:10.1130/G25147A.1.
- Keir, D., Bastow, I.D., Whaler, K.A., Daly, E., Cornwell, D.G., and Hautot, S., 2009b, Lower crustal earthquakes near the Ethiopian Rift induced by magmatic processes: *Geochemistry, Geophysics, Geosystems*, v. 10, p. 1–10, doi:10.1029/2009GC002382.
- Kendall, J.-M., 2000, Seismic anisotropy in the boundary layers of the mantle, in Karato, S., Stixrude, L., Liebermann, R.C., and Masters, T.G., eds., *Earth's Deep Interior: Mineral Physics and Tomography from the Atomic to the Global Scale*: Washington, D.C., American Geophysical Union Geophysical Monograph 117, p. 149–175.
- Kendall, J.-M., Stuart, G.W., Ebinger, C.J., Bastow, I.D., and Keir, D., 2005, Magma assisted rifting in Ethiopia: *Nature*, v. 433, p. 146–148, doi:10.1038/nature03161.
- Kendall, J.-M., Pilidou, S., Keir, D., Bastow, I., Stuart, G., and Ayele, A., 2006, Mantle upwellings, melt migration and the rifting of Africa: Insights from seismic anisotropy, in Yirgu, G., Ebinger, C.J., and Maguire, P.K.H., eds., *The Afar Volcanic Province within the East African Rift System*: Geological Society of London Special Publication 259, p. 55–72.
- Keranen, K., and Klemperer, S.L., 2008, Discontinuous and diachronous evolution of the Main Ethiopian Rift: Implications for development of continental rifts: *Earth and Planetary Science Letters*, v. 265, p. 96–111, doi:10.1016/j.epsl.2007.09.038.
- Keranen, K., Klemperer, S.L., Gloaguen, R., and EAGLE Working Group, 2004, Three-dimensional seismic imaging of a protoridge axis in the Main Ethiopian Rift: *Geology*, v. 32, p. 949–952, doi:10.1130/G20737.1.
- Keranen, K., Klemperer, S., Julia, J., Lawrence, J., and Nyblade, A., 2009, Low lower-crustal velocity across Ethiopia: Is the Main Ethiopian Rift a narrow rift in a hot craton?: *Geochemistry, Geophysics, Geosystems*, v. 10, Q0AB01, doi:10.1029/2008GC002293.
- Kidane, T., Otofuiji, Y.I., Komatsu, Y., Shibasaki, H., and Rowland, J., 2009, Paleomagnetism of the Fentale magmatic segment, Main Ethiopian Rift: New evidence for counterclockwise block rotation linked to transtensional deformation: *Physics of the Earth and Planetary Interiors*, v. 176, no. 1–2, p. 109–123, doi:10.1016/j.pepi.2009.04.006.
- Kieffer, B., Arndt, N., Lapierre, H., Bastien, F., Bosch, D., Pecher, A., Yirgu, G., Ayalew, D., Weiss, D., Jerram, D.A., Keller, F., and Meugniot, C., 2004, Flood and shield basalts from Ethiopia: Magmas from the African superswell: *Journal of Petrology*, v. 45, no. 4, p. 793–834, doi:10.1093/petrology/egg112.
- Kirkwood, S.C., and Crampin, S., 1981, Surface wave propagation in an ocean basin with an anisotropic upper mantle: Numerical modelling: *Geophysical Journal International*, v. 64, no. 2, p. 463–485, doi:10.1111/j.1365-246X.1981.tb02677.x.
- Kuo, B.Y., and Forsyth, D.W., 1988, Gravity anomalies of the ridge-transform system in the South Atlantic between 31 and 34.5°S: Upwelling centers and variations in crustal thickness: *Marine Geophysical Researches*, v. 10, no. 3, p. 205–232, doi:10.1007/BF00310065.
- Kurz, T., Gloaguen, R., Ebinger, C., Casey, M., and Abebe, B., 2007, Deformation distribution and type in the Main Ethiopian Rift (MER): A remote sensing study: *Journal of African Earth Sciences*, v. 48, no. 2–3, p. 100–114, doi:10.1016/j.jafrearsci.2006.10.008.
- Langston, C.A., 1979, Structure under Mount Rainer, Washington, inferred from teleseismic body waves: *Journal of Geophysical Research*, v. 84, p. 4749–4762, doi:10.1029/JB084iB09p04749.
- Levin, V., and Park, J., 2000, Shear zones in the Proterozoic lithosphere of the Arabian Shield and the nature of the Hales discontinuity: *Tectonophysics*, v. 323, no. 3–4, p. 131–148, doi:10.1016/S0040-1951(00)00105-0.
- Li, C., van der Hilst, R.D., Engdahl, R., and Burdick, S., 2008, A new global model for P wave speed variations in Earth's mantle: *Geochemistry, Geophysics, Geosystems*, v. 9, no. 5, p. 21, doi:10.1029/2007GC001806.
- Long, M.D., and Silver, P.G., 2009, Shear wave splitting and mantle anisotropy: Measurements, interpretations, and new directions: *Surveys in Geophysics*, v. 30, no. 4, p. 407–461, doi:10.1007/s10712-009-9075-1.
- Mackenzie, G.D., Thybo, H., and Maguire, P.K.H., 2005, Crustal velocity structure across the Main Ethiopian Rift: Results from 2-dimensional wide-angle seismic modeling: *Geophysical Journal International*, v. 162, p. 994–1006, doi:10.1111/j.1365-246X.2005.02710.x.
- Maguire, P.K.H., Swain, C.J., Masotti, R., and Khan, M.A., 1994, A crustal and uppermost mantle cross-sectional model of the Kenya rift derived from seismic and gravity data: *Tectonophysics*, v. 236, p. 217–249, doi:10.1016/0040-1951(94)90178-3.
- Maguire, P.K.H., Ebinger, C.J., Stuart, G.W., Mackenzie, G.D., Whaler, K.A., Kendall, J.-M., Khan, M.A., Fowler, C.M.R., Klemperer, S.L., Keller, G.R., Harder, S., Furman, T., Mickus, K., Asfaw, L., Ayele, A., and Abebe, B., 2003, Geophysics project in Ethiopia studies continental breakup: *Eos (Transactions, American Geophysical Union)*, v. 84, no. 35, p. 342–343, doi:10.1029/2003EO350002.
- Maguire, P., Keller, G., Klemperer, S., Mackenzie, G., Harder, S., O'Reilly, B.H.T., Asfaw, L., Khan, M., and Amha, M., 2006, Crustal structure of the northern Main Ethiopian Rift from the EAGLE controlled-source survey: a snapshot of incipient lithospheric break-up, in Yirgu, G., Ebinger, C.J., and Maguire, P.K.H., eds., *The Afar Volcanic Province within the East African Rift System*: Geological Society of London Special Publication 259, p. 269–291.
- Mahatsente, R., Jentzsch, G., and Jahr, T., 1999, Crustal structure of the Main Ethiopian Rift from gravity data: 3-dimensional modeling: *Tectonophysics*, v. 313, p. 363–382, doi:10.1016/S0040-1951(99)00213-9.
- Makris, J., and Ginzburg, A., 1987, The Afar Depression: Transition between continental rifting and sea floor spreading: *Tectonophysics*, v. 141, p. 199–214, doi:10.1016/0040-1951(87)90186-7.
- McKenzie, D., 1978, Some remarks on the development of sedimentary basins: *Earth and Planetary Science Letters*, v. 40, p. 25–32, doi:10.1016/0012-821X(78)90071-7.
- McKenzie, D.P., and Davies, D., 1970, Plate tectonics of the Red Sea and East Africa: *Nature*, v. 226, p. 243–248, doi:10.1038/226243a0.
- McKenzie, D.P., and Morgan, W.J., 1969, Evolution of triple junctions: *Nature*, v. 224, p. 125–133.

- Menzies, M., Klemperer, S., Ebinger, C., and Baker, J., 2002, Characteristics of volcanic rifted margins, *in* Menzies, M., Klemperer, S., Ebinger, C., and Baker, J., eds., *Volcanic Rifted Margins: Geological Society of America Special Paper 362*, p. 1–14.
- Mickus, K., Tadesse, K., Keller, G., and Oluma, B., 2007, Gravity analysis of the Main Ethiopian Rift: *Journal of African Earth Sciences*, v. 48, no. 2–3, p. 59–69, doi:10.1016/j.jafrearsci.2007.02.008.
- Mohr, P.A., 1967, Major volcano-tectonic lineament in the Ethiopian Rift system: *Nature*, v. 213, p. 664–665, doi:10.1038/213664a0.
- Molnar, P., England, P., and Martinod, J., 1993, Mantle dynamics, uplift of the Tibetan Plateau, and the Indian monsoon: *Reviews of Geophysics*, v. 31, p. 357–396, doi:10.1029/93RG02030.
- Montelli, R., Nolet, G., Dahlen, F.A., Masters, G., Engdahl, E.R., and Hung, S.-H., 2004, Finite-frequency tomography reveals a variety of plumes in the mantle: *Science*, v. 303, p. 338–343, doi:10.1126/science.1092485.
- Montelli, R., Nolet, G., Dahlen, F.A., and Masters, G., 2006, A catalogue of deep mantle plumes: New results from finite-frequency tomography: *Geochemistry, Geophysics, Geosystems*, v. 7, Q11007, doi:10.1029/2006GC001248.
- Mutter, J., 1985, Seaward dipping reflectors and the continent-ocean boundary at passive continental margins: *Tectonophysics*, v. 114, no. 1–4, p. 117–131, doi:10.1016/0040-1951(85)90009-5.
- Mutter, J., Talwani, M., and Stoffa, P., 1982, Origin of seaward-dipping reflectors in oceanic crust off the Norwegian margin by “subaerial seafloor spreading”: *Geology*, v. 10, no. 7, p. 353–357, doi:10.1130/0091-7613(1982)10<353:OOSRIO>2.0.CO;2.
- Ni, S., Tan, E., Gurnis, M., and Helmberger, D., 2002, Sharp sides to the African superplume: *Science*, v. 296, p. 1850–1852, doi:10.1126/science.1070698.
- Nyblade, A., and Langston, C., 2002, Broadband seismic experiments probe the East African Rift: *Eos (Transactions, American Geophysical Union)*, v. 83, p. 405–410, doi:10.1029/2002EO000296.
- Nyblade, A.A., Birt, C., Langston, C.A., Owens, T.J., and Last, R.J., 1996, Seismic experiment reveals rifting of craton in Tanzania: *Eos (Transactions, American Geophysical Union)*, v. 77, p. 517, doi:10.1029/96EO00339.
- Pasyanos, M.E., and Nyblade, A.A., 2007, A top to bottom lithospheric study of Africa and Arabia: *Tectonophysics*, v. 444, no. 1–4, p. 27–44, doi:10.1016/j.tecto.2007.07.008.
- Peccerillo, A., Barberio, M.R., Yirgu, G., Ayalew, D., Barbieri, M., and Wu, T.W., 2003, Relationships between mafic and peralkaline silicic magmatism in continental rift settings: A petrological, geochemical and isotopic study of the Gedemsa volcano, central Ethiopian Rift: *Journal of Petrology*, v. 44, no. 11, p. 2003–2032, doi:10.1093/petrology/egg068.
- Pérez-Gussinyé, M., Metois, M., Fernández, M., Vergés, J., Fulla, J., and Lowry, A.R., 2009, Effective elastic thickness of Africa and its relationship to other proxies for lithospheric structure and surface tectonics: *Earth and Planetary Science Letters*, v. 287, no. 1–2, p. 152–167, doi:10.1016/j.epsl.2009.08.004.
- Phipps-Morgan, J., and Chen, J., 1993, Dependence of ridge-axis morphology on magma supply and spreading rate: *Nature*, v. 364, p. 706–708, doi:10.1038/364706a0.
- Pik, R., Deniel, C., Coulon, C., Yirgu, G., and Marty, B., 1999, Isotopic and trace element signatures of Ethiopian flood basalts: Evidence for plume-lithosphere interactions: *Geochimica et Cosmochimica Acta*, v. 63, no. 15, p. 2263–2279, doi:10.1016/S0016-7037(99)00141-6.
- Pik, R., Marty, B., Carignan, J., and Lavé, J., 2003, Stability of the Upper Nile drainage network (Ethiopia) deduced from (U-Th)/He thermochronometry: Implications for uplift and erosion of the Afar plume dome: *Earth and Planetary Science Letters*, v. 215, p. 73–88, doi:10.1016/S0012-821X(03)00457-6.
- Poupinet, G., 1979, On the relation between P-wave travel time residuals and the age of the continental plates: *Earth and Planetary Science Letters*, v. 43, p. 149–161, doi:10.1016/0012-821X(79)90163-8.
- Priestley, K., McKenzie, D., Debayle, E., and Pilidou, S., 2008, The African upper mantle and its relationship to tectonics and surface geology: *Geophysical Journal International*, v. 175, no. 3, p. 1108–1126, doi:10.1111/j.1365-246X.2008.03951.x.
- Purcell, P.G., 1976, The Marda fault zone, Ethiopia: *Nature*, v. 261, p. 569–571, doi:10.1038/261569a0.
- Ritsema, J., and Allen, R.M., 2003, The elusive mantle plume: *Earth and Planetary Science Letters*, v. 207, p. 1–12, doi:10.1016/S0012-821X(02)01093-2.
- Ritsema, J., and van Heijst, H., 2000, New seismic model of the upper mantle beneath Africa: *Geology*, v. 28, no. 1, p. 63–66, doi:10.1130/0091-7613(2000)28<63:NSMOTU>2.0.CO;2.
- Rogers, N., 2006, Basaltic magmatism and the geodynamics of the East African Rift system, *in* Yirgu, G., Ebinger, C.J., and Maguire, P.K.H., eds., *The Afar Volcanic Province within the East African Rift System: Geological Society of London Special Publication 259*, p. 77–93.
- Rogers, N., Macdonald, R., Fitton, J.G., George, R., Smith, R., and Barreiro, B., 2000, Two mantle plumes beneath the East African Rift system: Sr, Nd and Pb isotope evidence from Kenya rift basalts: *Earth and Planetary Science Letters*, v. 176, p. 387–400, doi:10.1016/S0012-821X(00)00012-1.
- Ronga, F., Lustrino, M., Marzoli, A., and Melluso, L., 2010, Petrogenesis of a basalt-comendite-pantellerite rock suite: The Boseti volcanic complex (Main Ethiopian Rift): *Mineralogy and Petrology*, v. 98, p. 1–17, doi:10.1007/s00710-009-0064-3.
- Rooney, T.O., 2010, Geochemical evidence of lithospheric thinning in the southern Main Ethiopian Rift: *Lithos*, v. 117, p. 33–48, doi:10.1016/j.lithos.2010.02.002.
- Rooney, T.O., Furman, T., Yirgu, G., and Ayalew, D., 2005, Structure of the Ethiopian lithosphere: Xenolith evidence in the Main Ethiopian Rift: *Geochimica et Cosmochimica Acta*, v. 69, no. 15, p. 3889–3910, doi:10.1016/j.gca.2005.03.043.
- Rooney, T.O., Furman, T., Bastow, I.D., Ayalew, D., and Yirgu, G., 2007, Lithospheric modification during crustal extension in the Main Ethiopian Rift: *Journal of Geophysical Research*, v. 112, B10201, doi:10.1029/2006JB004916.
- Rowland, J.V., Baker, E., Ebinger, C.J., Keir, D., Kidane, T., Biggs, J., Hayward, N., and Wright, T.J., 2007, Fault growth at a nascent slow-spreading ridge: 2005 Dabbahu rifting episode, Afar: *Geophysical Journal International*, v. 171, no. 3, p. 1226–1246, doi:10.1111/j.1365-246X.2007.03584.x.
- Ruegg, J.C., and Kasser, M., 1987, Deformation across the Asal-Ghoubbet Rift, Djibouti, uplift and crustal extension 1979–1986: *Geophysical Research Letters*, v. 14, p. 745–748, doi:10.1029/GL014i007p00745.
- Sicilia, D., Montagner, J.P., Cara, M., Stutzmann, E., Debayle, E., Lépine, J.C., Lévêque, J.J., Beucler, E., Sebai, A., Roult, G., Ayele, A., and Sholan, J.M., 2008, Upper mantle structure of shear-waves velocities and stratification of anisotropy in the Afar Hotspot region: *Tectonophysics*, v. 462, no. 1–4, p. 164–177, doi:10.1016/j.tecto.2008.02.016.
- Simmons, N.A., Forte, A.M., and Grand, S.P., 2007, Thermochemical structure and dynamics of the African superplume: *Geophysical Research Letters*, v. 34, no. 2, doi:10.1029/2006GL028009.
- Sleep, N.H., 1996, Lateral flow of hot plume material ponded at sub-lithospheric depths: *Journal of Geophysical Research*, v. 101, p. 28,065–28,083, doi:10.1029/96JB02463.
- Soliva, R., and Schultz, R., 2008, Distributed and localized faulting in extensional settings: Insight from the north Ethiopian Rift–Afar transition area: *Tectonics*, v. 27, no. 2, TC2003, doi:10.1029/2007TC002148.
- Stamps, D., Calais, E., Saria, E., Hartnady, C., Nocquet, J., Ebinger, C., and Fernandes, R., 2008, A kinematic model for the East African Rift: *Geophysical Research Letters*, v. 35, no. 5, L05304, doi:10.1029/2007GL032781.
- Stein, R.S., Briole, P., Ruegg, J.C., Taponnier, P., and Gasse, F., 1991, Contemporary Holocene, and Quaternary deformation of the Asal Rift, Djibouti—Implications for the mechanisms of slow spreading ridges: *Journal of Geophysical Research*, v. 96, p. 21,789–21,806, doi:10.1029/91JB02118.
- Stuart, G., Bastow, I., and Ebinger, C., 2006, Crustal structure of the northern Main Ethiopian Rift from receiver function studies, *in* Yirgu, G., Ebinger, C.J., and Maguire, P.K.H., eds., *The Afar Volcanic Province within the East African Rift System: Geological Society of London Special Publication 259*, p. 253–267.
- Tadesse, S., Milesi, J.-P., and Deschamps, Y., 2003, Geology and mineral potential of Ethiopia: A note on geology and mineral map of Ethiopia: *Journal of African Earth Sciences*, v. 36, p. 273–313, doi:10.1016/S0899-5362(03)00048-4.
- Tesfaye, S., Harding, D., and Kusky, T., 2003, Early continental breakup boundary and migration of the Afar triple junction, Ethiopia: *Geological Society of America Bulletin*, v. 115, no. 9, p. 1053–1067, doi:10.1130/B25149.1.
- Thybo, H., and Nielsen, C.A., 2009, Magma-compensated crustal thinning in continental rift zones: *Nature*, v. 457, no. 7231, p. 873–876, doi:10.1038/nature07688.
- Tiberi, C., Ebinger, C., Ballu, V., Stuart, G.W., and Oluma, B., 2005, Inverse models of gravity data from the Red Sea–Aden–East African Rifts triple junction zone: *Geophysical Journal International*, v. 163, no. 2, p. 775–787, doi:10.1111/j.1365-246X.2005.02736.x.
- Vail, J.R., 1983, Pan-African crustal accretion in north-east Africa: *Journal of African Earth Sciences*, v. 1, p. 285–294, doi:10.1016/S0731-7247(83)80013-5.

- Vaucher, A., Tomassi, A., Barruol, G., and Maumus, J., 2000, Upper mantle deformation and seismic anisotropy in continental rifts: Physics and Chemistry of the Earth, v. 25, no. 2, p. 111–117, doi:10.1016/S1464-1895(00)00019-3.
- Wang, Y., Forsyth, D.W., and Savage, B., 2009, Convective upwelling in the mantle beneath the Gulf of California: *Nature*, v. 462, no. 7272, p. 499–501, doi:10.1038/nature08552.
- Whaler, K., 2006, Magnetotelluric fieldwork adventures in Africa: *Astronomy & Geophysics*, v. 47, no. 2, p. 28–37, doi:10.1111/j.1468-4004.2006.47228.x.
- Whaler, K., and Hautot, S., 2006, The electrical resistivity structure of the crust beneath the northern Ethiopian Rift, in Yirgu, G., Ebinger, C.J., and Maguire, P.K.H., eds., *The Afar Volcanic Province within the East African Rift System*: Geological Society of London Special Publication 259, p. 293–305.
- White, R.S., and McKenzie, D.P., 1989, Magmatism at rift zones: the generation of volcanic continental margins and flood basalts: *Journal of Geophysical Research*, v. 94, p. 7685–7729.
- White, R.S., Smith, L.K., Roberts, A.W., Christie, P.A.F., Kuszniir, N.J., and The iSIMM Team, 2008, Lower-crustal intrusion on the North Atlantic continental margin: *Nature*, v. 452, no. 7186, p. 460–464, doi:10.1038/nature06687.
- Williams, F., Williams, M., and Aumento, F., 2004, Tensional fissures and crustal extension rates in the northern part of the Main Ethiopian Rift: *Journal of African Earth Sciences*, v. 38, no. 2, p. 183–198, doi:10.1016/j.jafrearsci.2003.10.007.
- WoldeGabriel, G., 1988, *Volcanotectonic History of the Central Sector of the Main Ethiopian Rift: A Geochronological, Geochemical and Petrological Approach* [Ph.D. thesis]: Cleveland, Ohio, Case Western Reserve University, 410 p.
- Wolfe, C.J., Solomon, S.C., Laske, G., Collins, J.A., Detrick, R.S., Orcutt, J.A., Bercovici, D., and Hauri, E.H., 2009, Mantle shear-wave velocity structure beneath the Hawaiian hot spot: *Science*, v. 326, no. 5958, p. 1388, doi:10.1126/science.1180165.
- Wolfenden, E., Ebinger, C.J., Yirgu, G., Deino, A., and Ayalew, D., 2004, Evolution of the northern Main Ethiopian Rift: Birth of a triple junction: *Earth and Planetary Science Letters*, v. 224, p. 213–228, doi:10.1016/j.epsl.2004.04.022.
- Wolfenden, E., Ebinger, C.J., Yirgu, G., Renne, P., and Kelley, S.P., 2005, Evolution of a volcanic rifted margin: Southern Red Sea, Ethiopia: *Geological Society of America Bulletin*, v. 117, no. 7–8, p. 846–864, doi:10.1130/B25516.1.
- Wright, T.J., Ebinger, C., Biggs, J., Ayele, A., Yirgu, G., Keir, D., and Stork, A., 2006, Magma-maintained rift segmentation at continental rupture in the 2005 Afar dyking episode: *Nature*, v. 442, no. 7100, p. 291–294, doi:10.1038/nature04978.
- Zhu, L., and Kanamori, H., 2000, Moho depth variation in southern California from teleseismic receiver functions: *Journal of Geophysical Research*, v. 105, no. B2, p. 2969–2980, doi:10.1029/1999JB900322.

MANUSCRIPT ACCEPTED BY THE SOCIETY 9 NOVEMBER 2010

Peridotite xenoliths from Ethiopia: Inferences about mantle processes from plume to rift settings

Luigi Beccaluva*

Dipartimento di Scienze della Terra, Università di Ferrara, Via Saragat 1, 44100 Ferrara, Italy

Gianluca Bianchini*

*Dipartimento di Scienze della Terra, Università di Ferrara, Via Saragat 1, 44100 Ferrara, Italy, and
Istituto di Geoscienze e Georisorse (IGG), Consiglio Nazionale delle Ricerche (CNR), Via Moruzzi 1, 56124 Pisa, Italy*

Robert M. Ellam*

*Scottish Universities Environmental Research Centre (SUERC), Rankine Avenue,
Scottish Enterprise Technology Park, East Kilbride G75 0QF, UK*

Claudio Natali*

Alessandro Santato*

Franca Siena*

Dipartimento di Scienze della Terra, Università di Ferrara, Via Saragat 1, 44100 Ferrara, Italy

Finlay M. Stuart*

*Scottish Universities Environmental Research Centre (SUERC), Rankine Avenue,
Scottish Enterprise Technology Park, East Kilbride G75 0QF, UK*

ABSTRACT

A comprehensive petrological study carried out on Ethiopian mantle xenoliths entrained in Neogene–Quaternary alkaline lavas overlying the continental flood basalt area (Dedessa River–Wollega region, Injibara–Gojam region) and from the southern Main Ethiopian Rift (Mega-Sidamo region) provides an ideal means to investigate mantle evolution from plume to rift settings. Mantle xenoliths from the plateau area (Injibara, Dedessa River) range in composition from spinel lherzolite to harzburgite and olivine websterite, showing pressure-temperature (P - T) equilibrium conditions in the range 1.3–0.9 GPa and 950–1050 °C. These xenoliths show flat chondrite (ch)-normalized bulk-rock rare earth element (REE) patterns, with only few light (L) REE-enriched samples (La_N/Yb_N up to 7) in the most refractory lithotypes.

E-mails: bcc@unife.it, gianluca.bianchini@unife.it, r.ellam@suerc.gla.ac.uk, ntclcd@unife.it, alessandro.santato@unife.it, franca.siena@unife.it, f.stuart@suerc.gla.ac.uk.

Beccaluva, L., Bianchini, G., Ellam, R.M., Natali, C., Santato, A., Siena, F., and Stuart, F.M., 2011, Peridotite xenoliths from Ethiopia: Inferences about mantle processes from plume to rift settings, *in* Beccaluva, L., Bianchini, G., and Wilson, M., eds., *Volcanism and Evolution of the African Lithosphere*: Geological Society of America Special Paper 478, p. 77–104, doi:10.1130/2011.2478(05). For permission to copy, contact editing@geosociety.org. © 2011 The Geological Society of America. All rights reserved.

Clinopyroxene (cpx) REE patterns are mostly LREE depleted (La_N/Yb_N down to 0.2) or enriched (La_N/Yb_N up to 4.4). Sr-Nd isotopes of clinopyroxene mainly show compositions approaching the depleted mantle (DM) end member ($^{87}\text{Sr}/^{86}\text{Sr} < 0.7030$; $^{143}\text{Nd}/^{144}\text{Nd} > 0.5132$), or less depleted values ($^{87}\text{Sr}/^{86}\text{Sr} = 0.7033\text{--}0.7034$; $^{143}\text{Nd}/^{144}\text{Nd} = 0.5129\text{--}0.5128$) displaced toward the enriched mantle components that characterize the Afar plume signature and the related Ethiopian Oligocene continental flood basalts. The $^3\text{He}/^4\text{He}$ (R_a) values of olivines range from 6.6 to 8.9 R_a , overlapping typical depleted mantle values. These characteristics suggest that most xenoliths reflect complex asthenosphere-lithosphere interactions due to refertilization processes by mafic subalkaline melts that infiltrated and reacted with the pristine peridotite parageneses, ultimately leading to the formation of olivine-websterite domains. On the other hand, mantle xenoliths from the southern Main Ethiopian Rift (Mega-Sidamo region) consist of spinel lherzolite to harzburgites showing various degree of deformation and recrystallization, coupled with a wider range of P - T equilibrium conditions, from 1.6 ± 0.4 GPa and 1040 ± 80 °C to 1.0 ± 0.2 GPa and 930 ± 80 °C. Bulk-rock REE patterns show generally flat heavy (H) REEs, ranging from 0.1 chondritic values in harzburgites up to twice chondritic abundances in fertile lherzolites, and are variably enriched in LREE, with La_N/Yb_N up to 26 in the most refractory lithologies. The constituent clinopyroxenes have flat HREE distributions and La_N/Yb_N between 0.1 and 76, i.e., in general agreement with the respective bulk-rock chemistry. Clinopyroxenes from lherzolites have $^{87}\text{Sr}/^{86}\text{Sr} = 0.7022\text{--}0.7031$, $^{143}\text{Nd}/^{144}\text{Nd} = 0.5130\text{--}0.5138$, and $^{206}\text{Pb}/^{204}\text{Pb} = 18.38\text{--}19.34$, and clinopyroxenes from harzburgites have $^{87}\text{Sr}/^{86}\text{Sr} = 0.7027\text{--}0.7033$, $^{143}\text{Nd}/^{144}\text{Nd} = 0.5128\text{--}0.5130$, and $^{206}\text{Pb}/^{204}\text{Pb} = 18.46\text{--}18.52$. These range between the DM and high- μ (HIMU) mantle end members. The helium isotopic composition varies between 7.1 and 8.0 R_a , comparable to the xenoliths from the plateau area. Regional comparison shows that HIMU-like alkali-silicate melt(s), variably carbonated, were among the most effective metasomatizing agent(s) in mantle sections beneath the southern Main Ethiopian Rift, as well as along the Arabian rifted continental margins and the whole East African Rift system.

The different types of metasomatic agents recorded in Ethiopian mantle xenoliths from the continental flood basalt area and the rift systems clearly reflect distinct tectonomagmatic settings, i.e., plume-related subalkaline magmatism and rift-related alkaline volcanism, with the latter extending far beyond the influence of the Afar plume.

INTRODUCTION

The long-standing debate concerning the role of mantle plumes in Earth history has been mainly focused on geophysical records, tectonomagmatic evolution of large igneous provinces, and petrological and geochemical characteristics of hotspot magmas (Ernst and Buchan, 2001; Foulger et al., 2005; Foulger and Jurdy, 2007).

In this regard, one of the most significant large igneous provinces is manifested in the Oligocene Ethiopian basaltic plateau, the origin of which is commonly attributed to the activation of the current Afar plume (Hofmann et al., 1997; Pik et al., 1999, 2006; Rogers et al., 2000; Davaille et al., 2005). Further support for this genetic link has been provided by petrogenetic modeling of the northern Ethiopian continental flood basalts, which are zonally arranged (corresponding to a parallel increase in magma temperature) from low-titanium (LT) tholeiites to high- and very high-titanium (HT1 and HT2, respectively) basalts and picrites

closer to the Afar triple point, the inferred axis of the plume (Beccaluva et al., 2009).

The subsequent tectonomagmatic evolution was characterized by diachronous rifting phases accompanied by widespread Neogene–Quaternary transitional to alkaline volcanism, both on the plateau area and along the Main Ethiopian Rift (Corti, 2009). The degree to which this tectonomagmatic record is reflected by the lithospheric mantle xenoliths remains somewhat unclear, in spite of several studies from various Ethiopian locations (Bedini et al., 1997; Conticelli et al., 1999; Roger et al., 1997, 1999; Orlando et al., 2006; Ferrando et al., 2008; Ayalew et al., 2009) in which authors have inferred the pressure-temperature (P - T) equilibration conditions and metasomatic enrichments. Specifically, mantle xenoliths entrained in Neogene–Quaternary alkaline volcanic rocks from different tectonomagmatic settings (e.g., plateau vs. rift) may afford one of the best ways to obtain direct records of the processes that have affected the underlying mantle.

In this paper, we present new major- and trace-element data from both bulk rock and constituent minerals, as well as Sr, Nd, Pb, and He isotopic analyses on separated phases from two localities within the northern Ethiopia Plateau (sites of Injibara and Dedessa River) and outside the plateau, along the southern part of the Main Ethiopian Rift (site of Mega, Fig. 1). These data pro-

vide a means (1) to highlight their relationships with the plume-related continental flood basalt magmatism; (2) to assess the possible compositional and textural differences between plume- and rift-related mantle evolution; and (3) to assess the nature of the mantle metasomatic agent(s), which characterize the distinct tectonomagmatic phases.

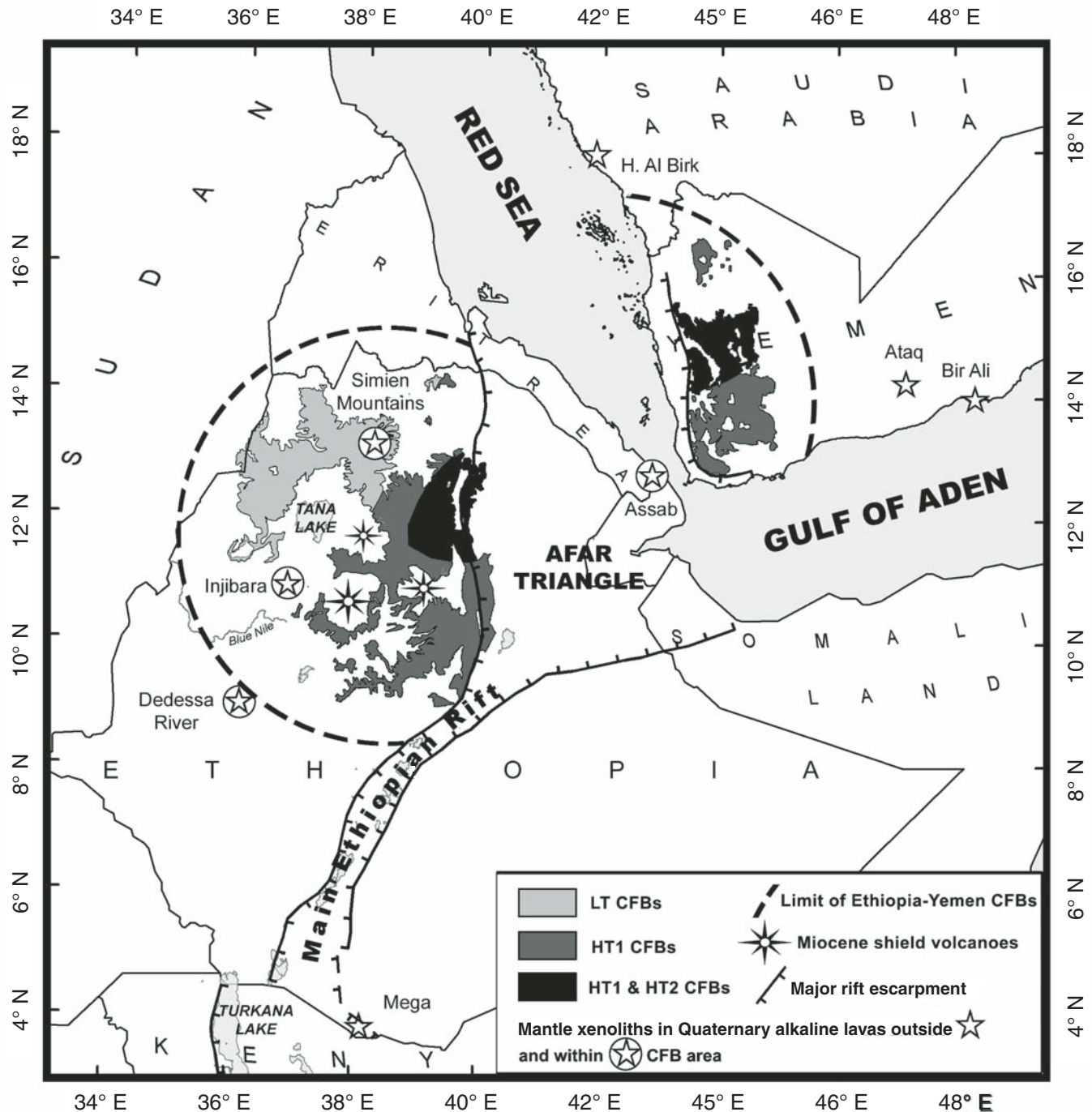


Figure 1. Sketch map of Oligocene continental flood basalts (CFBs) from the Northern Ethiopia–Yemen Province (modified after Becaluva et al., 2009). Mantle xenolith location within (circled star) and outside (star) continental flood basalt area is reported. LT—low titanium tholeiites; HT1—high titanium tholeiites; HT2—very high titanium transitional basalts and picrites.

REGIONAL DISTRIBUTION OF ETHIOPIAN MANTLE XENOLITHS

Mantle xenoliths included in Neogene–Quaternary alkaline lavas from different Ethiopian locations provide direct information on the subcontinental mantle sections across a longitudinal distance of ~1000 km (Fig. 1). Some locations are within the Northern Ethiopian Plateau (Injibara in the Gojam region and Simien Mountains) or close to its southwestern border (Dedessa River, Wollega region) and therefore may record interaction with Oligocene continental flood basalt magmatism and its causative mantle plume, which produced arching without significant thinning of the lithosphere (Bastow et al., this volume). Accordingly, geophysical data indicate under the plateau area a Moho depth of ~40 km and a total lithosphere thickness of ~100 km. Other xenolith occurrences far from the plateau (such as Mega, in the Sidamo region) are located close to the southernmost part of the Ethiopian Rift and therefore may show evidence of the subsequent lithospheric thinning and rift-related geodynamic evolution. Here, geophysical data suggest a crustal thickness of ~30 km and an attenuation of the elastic lithospheric mantle down 20 km (Bastow et al., this volume; Corti, 2009).

Mantle Xenoliths from the Plateau Area

Abundant mantle xenoliths (up to 10 cm across) included in Quaternary alkaline lavas erupted in the Northern Ethiopian Plateau area have been recorded mainly at Injibara (Gojam) and west of Nekemte along the Dedessa River (Wollega). They are mostly represented by medium-grained spinel (sp)–lherzolites, spinel–harzburgites, and spinel–olivine websterites. Similar but smaller-sized spinel–lherzolite xenoliths have been reported from a single alkali-basalt Miocene flow in the Simien Mountains (Roger et al., 1997, 1999; Ayalew et al., 2009).

The prevailing peridotite texture is protogranular, only rarely fading into transitional or porphyroclastic patches (Fig. 2A). Olivine and orthopyroxene (with scarce thin exsolution lamellae) are coarse grained (up to 3–4 mm across) with curvilinear boundaries; smaller clinopyroxene (cpx) and lobate brown spinel are generally interstitial, sometimes surrounded by reaction rims and patches. Olivine–websterites are sometimes present as centimeter-sized bands in composite xenoliths (GOJ32) or in individual samples showing coarse- to medium-grained textures. They are characterized by large undeformed orthopyroxene (opx) crystals locally including olivine (ol) and clinopyroxene relics, with interstitial smaller clinopyroxene and lobate spinel. Rare amphibole crystals are also present (GOJ12).

The same rock types and constituent minerals, including amphibole, have been reported for Injibara (Gojam) xenoliths by Conticelli et al. (1999) and Ferrando et al. (2008).

Microprobe analyses of the main mineral phases are reported in Table 1A (Injibara) and Table 1B (Dedessa). Olivine is forsteritic in composition ($\text{Fo}_{88.4}$ – $\text{Fo}_{89.9}$ in lherzolites and $\text{Fo}_{88.7}$ – $\text{Fo}_{91.2}$ in harzburgites). Lower Fo contents are present in some

clinopyroxene-poor lherzolites from Injibara (as low as ~ $\text{Fo}_{86.5}$ in GOJ19). In olivine websterites, forsterite content (down to $\text{Fo}_{83.6}$) is lower than common mantle olivine composition, suggesting peridotite–melt interactions.

Orthopyroxene composition is $\text{En}_{86.8-90.1}$ in lherzolites and $\text{En}_{87.9-90.8}$ in harzburgites, whereas it is $\text{En}_{81.4-88.8}$ in olivine websterites.

Clinopyroxene in peridotites is generally diopsidic in composition, with $\text{Wo}_{43.0}$ – $\text{Wo}_{48.7}$, $\text{En}_{45.6}$ – $\text{En}_{51.1}$, $\text{Fs}_{4.1}$ – $\text{Fs}_{6.9}$, and $\text{Mg\#} 0.88$ – 0.92 , $\text{Cr\#} 0.04$ – 0.25 , $\text{Na}_2\text{O} 1.2$ – 2.2 wt%, and $\text{TiO}_2 0.03$ – 1.0 wt%. Clinopyroxene of olivine websterites tends toward salitic composition with $\text{Wo}_{44.7-48.7}$, $\text{En}_{44.7-48.2}$, $\text{Fs}_{4.5-8.7}$, $\text{Mg\#} 0.83$ – 0.90 , $\text{Cr\#} 0.04$ – 0.07 , $\text{Na}_2\text{O} 1.34$ – 1.90 wt%, and $\text{TiO}_2 0.27$ – 0.84 wt%.

Spinel composition is $\text{Mg\#} 0.71$ – 0.80 and $\text{Cr\#} 0.07$ – 0.13 in lherzolites and $\text{Mg\#} 0.67$ – 0.76 and $\text{Cr\#} 0.09$ – 0.45 in harzburgites, whereas in olivine websterites, Mg\# varies from 0.75 to 0.79 and Cr\# varies from 0.07 to 0.09.

Application of the geothermobarometer of Brey and Köhler (1990) and Köhler and Brey (1990) using the composition of large equilibrated crystals from the samples least affected by secondary textures gives nominal equilibration temperatures and pressures in the range of 930–1050 °C and 9–12.5 kbar.

Bulk-rock major- and trace-element distributions of representative samples of Ethiopian xenoliths are reported in Table 2A (Injibara), Table 2B (Dedessa), and Figure 3, where elements classically considered indicators of mantle depletion by melt extraction, such as CaO , Al_2O_3 , and TiO_2 , decrease with increasing MgO and Ni in the most refractory parageneses.

Most xenoliths from Injibara (Gojam) are fertile lherzolites (up to 19% modal clinopyroxene), whereas xenoliths from Dedessa River (Wollega) vary in composition from lherzolites to harzburgites, approaching the theoretical mantle partial melting trends defined by Niu (1997).

Olivine websterite xenoliths from both sites plot outside the partial melting trends and are characterized by comparatively lower MgO and higher SiO_2 , modally reflected in a remarkable increase of orthopyroxene (mostly between 50% and 75%). This suggests that these mantle portions were refertilized by


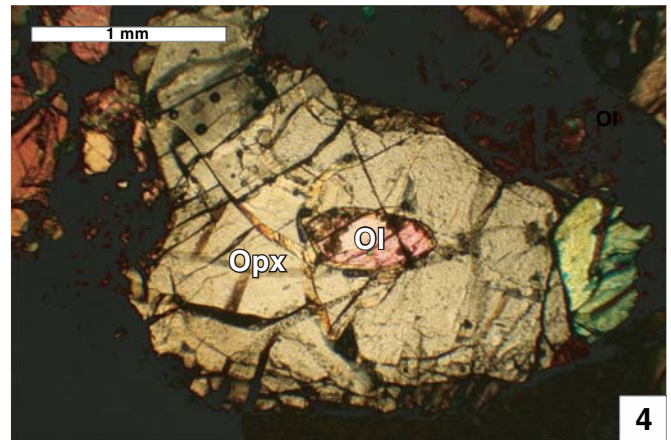
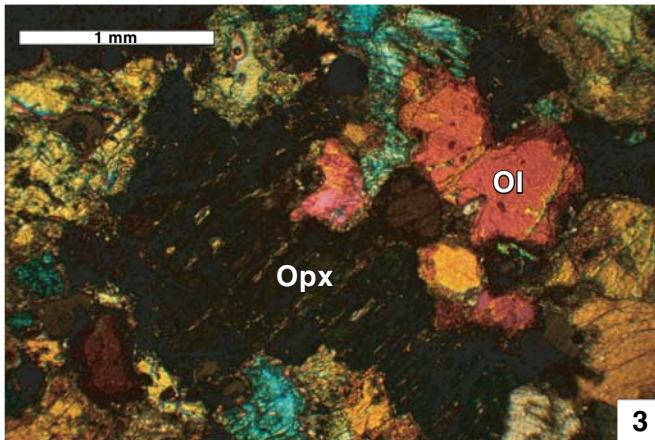
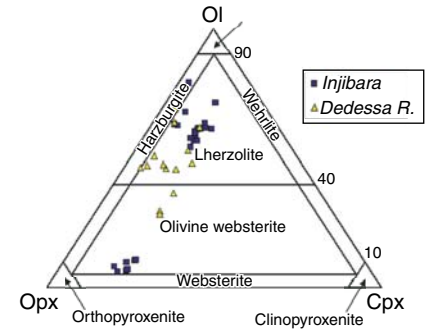
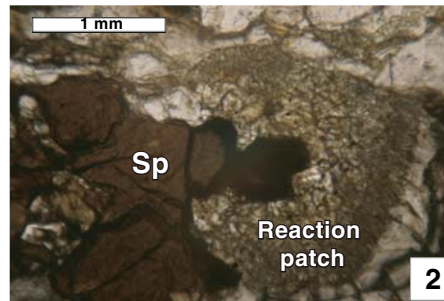
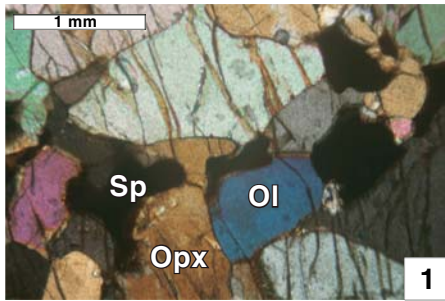


Figure 2. (A) Photomicrographs of mantle xenoliths from Northern Ethiopian Plateau area (Injibara and Dedessa River): typical four-phase protogranular texture widespread in lherzolites (1), pyrometamorphic reaction patches around spinel in harzburgite (2), and olivine–websterites characterized by crystallization of orthopyroxene replacing and growing on olivine (3 and 4). The modal composition in terms of ol–opx–cpx is also reported. (B) Photomicrographs of mantle xenoliths from the Main Ethiopian Rift (Mega): porphyroclastic textures with large kinked olivine and orthopyroxene crystals associated with undeformed smaller neoblasts (1), pyrometamorphic textures observed in the most refractory lithologies as reaction rims around spinel and pyroxenes (2), metasomatic veinlets containing green clinopyroxene (3), and reaction patches including feldspar microlites and glass (4). The modal composition in terms of ol–opx–cpx is also reported. Abbreviations: Ol—olivine, Opx—orthopyroxene, Cpx—clinopyroxene, Sp—spinel.

A



B

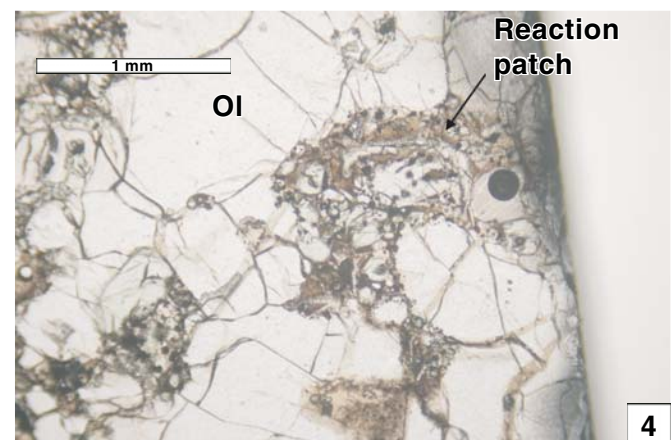
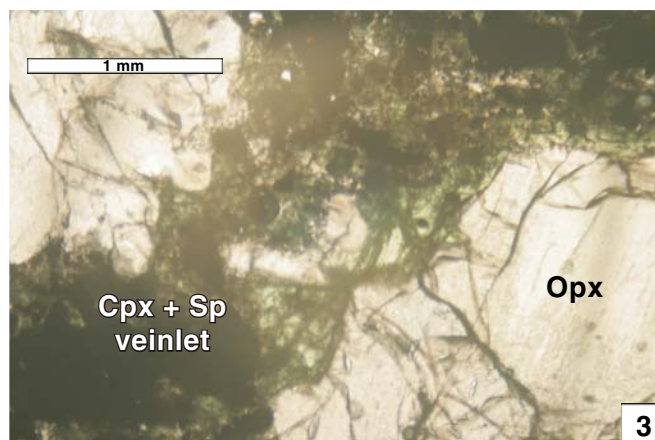
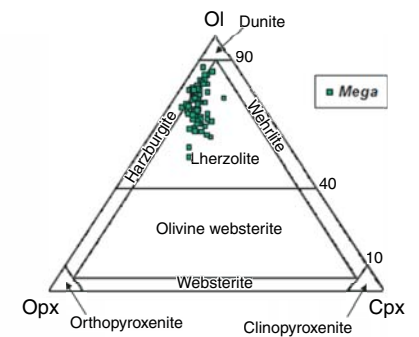
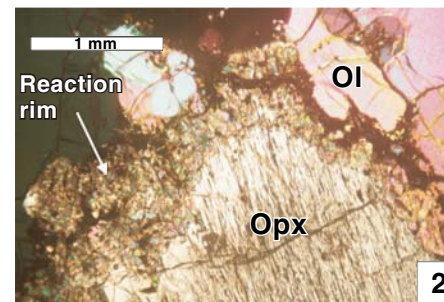
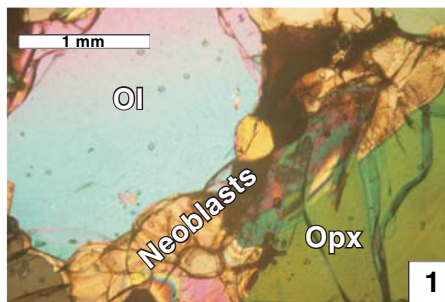


TABLE 1A. MICROPROBE MINERAL ANALYSES OF REPRESENTATIVE MANTLE XENOLITHS FROM INJIBARA

Sample:	Lh GOJ 10				Lh GOJ 16			
Mineral:	Ol	Opx	Cpx	Sp	Ol	Opx	Cpx	Sp
Avg. no. analyses	2	10	4	2	4	8	10	10
SiO ₂	41.26	55.88	52.58	0.06	41.47	56.04	52.61	0.39
TiO ₂	0.01	0.17	0.65	0.13	0.01	0.13	0.65	0.12
Al ₂ O ₃	0.01	4.14	6.95	58.42	0.01	3.99	6.63	58.47
FeO _{tot}	10.01	6.19	2.76	10.84	9.89	6.63	2.81	10.82
MnO	0.15	0.15	0.09	0.09	0.16	0.17	0.07	0.11
MgO	48.23	31.02	14.31	20.65	47.39	32.47	14.52	20.53
CaO	0.05	2.53	20.23	0.01	0.05	0.57	20.21	0.01
Na ₂ O	0.01	0.27	2.04	0.05	0.02	0.14	1.79	0.02
K ₂ O	0.02	0.01	0.01	0.03	0.02	0.01	0.02	0.01
Cr ₂ O ₃	0.01	0.31	0.79	8.18	0.03	0.25	0.69	8.47
NiO	0.37	0.07	0.05	0.35	0.35	0.10	0.06	0.37
Sum	100.13	100.73	100.41	98.44	99.41	100.51	99.99	98.95
Mg#	0.89	0.90	0.90	0.77	0.90	0.90	0.90	0.77
Cr#			0.07	0.09			0.06	0.09
Sample:	Cpx-poor Lh GOJ 4				Cpx-poor Lh GOJ 19			
Mineral:	Ol	Opx	Cpx	Sp	Ol	Opx	Cpx	
Avg. no. analyses	5	6	6	5	4	5	7	
SiO ₂	41.23	56.07	52.38	0.09	41.05	55.97	52.13	
TiO ₂	0.00	0.17	0.91	0.26	0.02	0.20	0.84	
Al ₂ O ₃	0.00	3.89	6.38	54.83	0.00	3.81	6.06	
FeO _{tot}	12.18	7.70	3.40	13.39	12.61	7.69	3.40	
MnO	0.13	0.15	0.10	0.12	0.19	0.17	0.12	
MgO	46.80	31.87	14.59	18.86	46.95	31.99	15.06	
CaO	0.05	0.64	20.70	0.00	0.06	0.63	20.74	
Na ₂ O	0.03	0.06	1.46	0.01	0.00	0.06	1.36	
K ₂ O	0.01	0.00	0.01	0.00	0.01	0.00	0.01	
Cr ₂ O ₃	0.01	0.34	0.79	11.99	0.02	0.35	0.80	
NiO	0.34	0.10	0.08	0.36	0.38	0.07	0.02	
Sum	100.80	100.99	100.72	99.55	101.31	100.93	100.51	
Mg#	0.87	0.88	0.88	0.72	0.87	0.88	0.89	
Cr#			0.08	0.13			0.08	
Sample:	Hz GOJ 33				OIWb GOJ 31C			
Mineral:	Ol	Opx	Cpx	Sp	Ol	Opx	Cpx	Sp
Avg. no. analyses	3	5	8	4	2	4	7	3
SiO ₂	41.89	57.71	54.46	0.08	41.24	54.97	51.85	0.42
TiO ₂	0.01	0.03	0.07	0.09	0.03	0.20	0.80	0.46
Al ₂ O ₃	0.03	2.18	2.88	31.61	0.09	4.40	6.55	59.66
FeO _{tot}	8.83	5.43	2.32	13.97	14.77	10.33	4.63	10.57
MnO	0.14	0.12	0.05	0.00	0.25	0.22	0.11	0.00
MgO	49.64	34.00	16.80	16.58	44.48	29.82	14.27	21.70
CaO	0.06	0.63	22.24	0.01	0.19	0.79	19.98	0.00
Na ₂ O	0.03	0.06	0.88	0.01	0.00	0.08	1.45	0.01
K ₂ O	0.01	0.01	0.01	0.00	0.01	0.02	0.01	0.01
Cr ₂ O ₃	0.04	0.48	1.09	38.33	0.06	0.30	0.67	6.97
NiO	0.39	0.13	0.05	0.18	0.17	0.10	0.05	0.50
Sum	101.06	100.78	100.68	100.68	101.31	101.24	100.32	99.81
Mg#	0.91	0.92	0.93	0.68	0.84	0.84	0.85	0.79
Cr#			0.20	0.45			0.06	0.07

Note: Lh—lherzolite, Hz—harzburgite, OIWb—olivine-websterite, Ol—olivine, Opx—orthopyroxene, Cpx—clinopyroxene, Sp—spinel, Mg#—Mg/(Mg + Fe²⁺) a.p.f.u., Cr#—Cr/(Cr + Al) a.p.f.u., avg. no. anal.—number of averaged analyses.

TABLE 1B. MICROPROBE MINERAL ANALYSES OF REPRESENTATIVE MANTLE XENOLITHS FROM DEDESSA RIVER

Sample:	Lh WOL 49				Lh WOL 8			
Mineral:	Ol	Opx	Cpx	Sp	Ol	Opx	Cpx	
Avg. no.	5	4	2	2	2	2	3	
analyses								
SiO ₂	41.54	55.65	52.20	0.16	41.04	55.11	51.39	
TiO ₂	0.01	0.15	0.61	0.19	0.05	0.17	0.63	
Al ₂ O ₃	0.02	5.06	6.96	57.65	0.03	4.92	5.91	
FeO _{tot}	10.51	6.99	3.65	12.52	11.45	7.28	3.50	
MnO	0.16	0.16	0.09	0.00	0.18	0.14	0.11	
MgO	48.01	32.24	15.23	20.69	46.75	31.49	15.14	
CaO	0.08	0.81	19.82	0.00	0.17	0.76	21.52	
Na ₂ O	0.02	0.11	1.47	0.01	0.06	0.15	0.84	
K ₂ O	0.01	0.01	0.02	0.00	0.01	0.01	0.02	
Cr ₂ O ₃	0.01	0.37	0.63	8.55	0.04	0.17	0.68	
NiO	0.35	0.09	0.04	0.42	0.30	0.05	0.09	
Sum	100.72	101.64	100.71	99.77	100.08	100.26	99.74	
Mg#	0.89	0.89	0.88	0.75	0.88	0.89	0.88	
Cr#			0.06	0.09			0.07	
Sample:	Cpx-poor Lh WOL 34				Cpx-poor Lh WOL 2			
Mineral:	Ol	Opx	Cpx	Sp	Ol	Opx	Cpx	
Avg. no.	2	2	2	2	4	3	4	
analyses								
SiO ₂	41.75	57.05	54.10	0.03	41.68	56.89	53.57	
TiO ₂	0.01	0.13	0.24	0.07	0.01	0.05	0.07	
Al ₂ O ₃	0.00	3.01	3.81	57.27	0.01	2.46	3.51	
FeO _{tot}	9.91	5.99	3.32	9.69	8.72	5.59	2.67	
MnO	0.12	0.13	0.10	0.14	0.13	0.09	0.09	
MgO	48.92	33.45	16.79	21.07	48.91	33.40	16.42	
CaO	0.07	0.99	20.23	0.01	0.11	0.98	20.26	
Na ₂ O	0.01	0.07	1.29	0.00	0.06	0.09	1.23	
K ₂ O	0.02	0.01	0.01	0.01	0.03	0.04	0.00	
Cr ₂ O ₃	0.03	0.59	1.06	11.05	0.05	0.74	1.66	
NiO	0.37	0.17	0.03	0.34	0.38	0.04	0.04	
Sum	101.21	101.59	100.96	99.33	100.08	100.37	99.48	
Mg#	0.90	0.91	0.90	0.79	0.91	0.91	0.92	
Cr#			0.16	0.11			0.24	
Sample:	Hz WOL 7				OIWb WOL 26			
Mineral:	Ol	Opx	Cpx	Sp	Ol	Opx	Cpx	Sp
Avg. no.	3	5	2	3	3	3	5	2
analyses								
SiO ₂	41.32	56.02	52.39	0.16	41.60	55.87	52.42	0.14
TiO ₂	0.01	0.14	0.65	0.18	0.01	0.15	0.63	0.15
Al ₂ O ₃	0.02	4.52	7.03	58.45	0.01	4.32	6.54	57.65
FeO _{tot}	10.64	6.68	3.18	12.15	10.31	6.76	3.30	12.48
MnO	0.17	0.14	0.06	0.00	0.19	0.14	0.07	0.00
MgO	47.86	32.28	14.72	20.48	48.60	32.76	15.04	20.49
CaO	0.09	0.68	20.00	0.01	0.05	0.70	20.40	0.00
Na ₂ O	0.01	0.10	1.78	0.00	0.01	0.09	1.49	0.00
K ₂ O	0.00	0.01	0.00	0.00	0.00	0.00	0.00	0.01
Cr ₂ O ₃	0.02	0.29	0.73	8.50	0.04	0.30	0.70	8.68
NiO	0.38	0.09	0.04	0.35	0.37	0.11	0.05	0.37
Sum	100.53	100.95	100.56	99.94	101.20	101.21	100.63	99.60
Mg#	0.89	0.90	0.89	0.75	0.89	0.90	0.89	0.75
Cr#			0.07	0.09			0.07	0.09

TABLE 1C. MICROPROBE MINERAL ANALYSES OF REPRESENTATIVE MANTLE XENOLITHS FROM MEGA

Sample: Mineral:		Lh MA 10						Lh MA 15						Cpx-poor Lh MA 9						Cpx-poor Lh MA 35					
		Ol	Opx	Cpx	Sp	2	1	Ol	Opx	Cpx	Sp	2	1	Ol	Opx	Cpx	Sp	4	3	Ol	Opx	Cpx	Sp		
Avg. no.		3	3	2	2	2	1	2	2	2	2	1	4	3	3	3	4	3	3	2	1	4	1		
analyses																									
SiO ₂		41.65	56.51	53.25	0.12		0.12	41.80	57.09	53.49		0.12	41.05	56.50	53.29		0.15			41.61	57.06	53.90	0.12		
TiO ₂		0.01	0.05	0.33	0.03		0.09	0.00	0.07	0.35		0.09	0.01	0.09	0.55		0.07			0.00	0.00	0.08	0.04		
Al ₂ O ₃		0.05	3.87	5.40	56.25		49.19	0.00	3.60	5.68		49.19	0.00	3.40	5.48		57.92		0.00	0.00	3.32	3.83	50.80		
FeO _{tot}		9.52	5.76	2.43	9.85		10.62	9.10	5.77	2.37		10.62	10.90	7.05	2.44		11.29		9.20	5.75	2.36	10.68			
MnO		0.20	0.19	0.03	0.05		0.13	0.17	0.15	0.14		0.13	0.17	0.19	0.07		0.11		0.19	0.13	0.08	0.11			
MgO		49.13	33.63	15.84	20.18		19.33	49.90	33.90	15.77		19.33	48.80	33.62	15.44		20.09		50.08	34.58	16.97	19.12			
CaO		0.06	0.64	21.18	0.01		0.00	0.03	0.51	21.02		0.00	0.03	0.38	21.77		0.01		0.06	0.53	22.35	0.00			
Na ₂ O		0.01	0.09	1.31	0.00		0.01	0.00	0.03	1.59		0.01	0.01	0.02	1.46		0.00		0.04	0.04	0.81	0.00			
K ₂ O		0.02	0.01	0.01	0.02		0.00	0.00	0.01	0.01		0.00	0.01	0.03	0.01		0.01		0.00	0.00	0.01	0.01			
Cr ₂ O ₃		0.00	0.28	0.83	12.32		19.62	0.01	0.42	1.02		19.62	0.01	0.29	0.70		10.54		0.01	0.40	0.71	18.03			
NiO		0.38	0.09	0.11	0.24		0.37	0.32	0.12	0.06		0.37	0.36	0.09	0.04		0.32		0.39	0.09	0.05	0.25			
Sum		101.02	101.12	100.71	99.09		99.48	101.33	101.67	101.49		99.48	101.34	101.66	101.25		100.51		101.59	101.90	101.15	99.17			
Mg#		0.90	0.91	0.92	0.79		0.78	0.91	0.91	0.93		0.78	0.89	0.90	0.92		0.78		0.91	0.92	0.93	0.77			
Cr#			0.09	0.13			0.21		0.11			0.21		0.08	0.11					0.11		0.19			
Sample: Mineral:		Hz MA 48						Hz MA 68						Hz MA 24						Hz MA 11					
		Ol	Opx	Cpx	Sp	3	2	Ol	Opx	Cpx	Sp	3	2	Ol	Opx	Cpx	Sp	5	3	Ol	Opx	Cpx	Sp		
Avg. no.		2	1	1	3		2	3	2	4		2	3	2	3	4		4	3	2	1	2	1		
analyses																									
SiO ₂		41.92	58.22	54.82	0.07		0.06	41.50	57.76	54.44		0.06	41.35	56.67	53.33		0.09		41.93	57.65	54.55	0.15			
TiO ₂		0.02	0.00	0.06	0.27		0.29	0.03	0.06	0.11		0.29	0.04	0.09	0.38		0.21		0.05	0.04	0.07	0.09			
Al ₂ O ₃		0.00	1.98	3.77	21.18		21.11	0.01	1.37	2.71		21.11	0.02	3.29	5.81		41.36		0.01	2.38	2.95	34.96			
FeO _{tot}		8.38	5.05	2.31	17.31		17.17	9.30	6.01	2.67		17.17	8.98	5.79	2.62		12.46		8.51	5.14	2.23	12.46			
MnO		0.14	0.13	0.11	0.31		0.30	0.18	0.15	0.09		0.30	0.08	0.13	0.07		0.11		0.14	0.12	0.01	0.17			
MgO		50.49	35.15	16.72	14.09		13.87	49.60	35.21	17.16		13.87	50.59	34.22	15.85		18.55		50.49	34.64	17.24	16.90			
CaO		0.05	0.47	20.49	0.01		0.00	0.05	0.61	20.51		0.00	0.08	0.71	19.47		0.01		0.04	0.68	22.20	0.00			
Na ₂ O		0.00	0.04	1.72	0.05		0.05	0.01	0.06	1.38		0.05	0.01	0.13	2.09		0.02		0.00	0.02	0.83	0.00			
K ₂ O		0.00	0.00	0.01	0.00		0.00	0.01	0.01	0.00		0.00	0.00	0.00	0.02		0.00		0.00	0.02	0.00	0.00			
Cr ₂ O ₃		0.03	0.46	1.57	46.51		46.91	0.00	0.40	1.64		46.91	0.05	0.55	1.59		26.98		0.03	0.50	0.97	34.72			
NiO		0.35	0.09	0.00	0.22		0.23	0.38	0.11	0.09		0.23	0.38	0.10	0.06		0.24		0.44	0.00	0.05	0.14			
Sum		101.39	101.59	100.02	100.02		99.98	101.08	101.76	100.80		99.98	101.59	101.68	101.31		100.03		101.64	101.19	101.10	99.60			
Mg#		0.91	0.92	0.93	0.65		0.64	0.90	0.92	0.93		0.64	0.91	0.92	0.93		0.77		0.91	0.92	0.93	0.72			
Cr#			0.22	0.60			0.60		0.29			0.60		0.16	0.30						0.17	0.40			

TABLE 2B. WHOLE-ROCK MAJOR- AND TRACE-ELEMENT COMPOSITION OF MANTLE XENOLITHS FROM DEDESSA RIVER

Rock type: Sample:	Lh	Lh	Lh	Lh	Lh	Lh	Cpx-poor				Lh	Lh	Lh	Lh	Lh	Lh
	WOL8	WOL13	WOL25	WOL39	WOL49	WOL51	WOL2	WOL34	WOL42	WOL7	Hz	WOL28	WOL26	WOL31	WOL41	WOL18
Major oxides (wt%)																
SiO ₂	44.59	45.78	47.44	46.68	45.27	47.13	45.72	47.92	47.77	44.86	47.50	47.57	48.48	48.89	47.49	
TiO ₂	0.14	0.16	0.10	0.18	0.28	0.08	0.03	0.05	0.06	0.04	0.05	0.19	0.26	0.26	0.86	
Al ₂ O ₃	2.46	3.04	2.13	3.10	3.97	2.01	0.92	1.10	1.13	0.97	1.00	3.27	4.06	3.33	6.66	
Fe ₂ O ₃	8.54	7.97	7.58	8.10	9.57	8.19	8.96	8.37	7.28	8.22	7.42	8.11	8.27	7.90	8.89	
Fe ₂ O ₃ _{tot}	0.14	0.13	0.12	0.12	0.14	0.12	0.12	0.12	0.12	0.12	0.11	0.12	0.13	0.12	0.15	
MnO	40.10	38.26	37.92	36.95	35.26	38.05	41.32	38.38	40.13	43.89	39.49	34.19	33.02	32.88	20.61	
MgO	2.85	2.71	2.23	2.79	3.33	1.88	0.80	0.71	0.90	0.71	0.97	3.41	2.91	3.35	12.36	
CaO	0.28	0.42	0.33	0.36	0.46	0.31	0.36	0.43	0.35	0.07	0.08	0.49	0.62	0.51	0.90	
Na ₂ O	0.04	0.18	0.18	0.18	0.24	0.15	0.16	0.20	0.17	0.05	0.06	0.23	0.32	0.29	0.40	
K ₂ O	0.02	0.03	0.03	0.03	0.05	0.02	0.03	0.03	0.02	0.03	0.05	0.03	0.06	0.05	0.03	
P ₂ O ₅	0.86	1.33	1.93	1.49	1.43	2.05	1.58	2.68	2.08	1.05	3.26	2.39	1.87	2.42	1.64	
LOI	100.00	100.00	100.00	100.00	100.00	100.00	100.00	100.00	100.00	100.00	100.00	100.00	100.00	100.00	100.00	
Sum																
Mg#	0.90	0.90	0.91	0.90	0.88	0.90	0.90	0.90	0.92	0.91	0.91	0.89	0.89	0.89	0.82	
Trace elements (ppm)																
Ni	1966	2034	2065	1961	1782	2192	2666	2478	2260	2455	2824	1938	1817	1882	268	
Co	119	122	117	111	107	121	130	129	118	119	142	111	107	107	48	
Cr	1026	1848	2380	2078	2266	1978	1967	2731	1213	2873	1556	2023	2360	1738	1340	
V	65	70	57	71	95	55	29	33	34	34	27	90	82	93	314	
Sc	9	15	13	10	14	8	5	5	10	5	10	19	18	21	49	
Sr	12	33	32	35	43	8	22	9	9	2	5	18	63	49	58	
Zr	9.22	5.39	5.50	11.1	19.0	3.65	5.64	4.19	1.64	2.75	2.50	6.12	17.0	10.7	20.0	
Hf	0.27	0.13	0.11	0.28	0.49	0.10	0.10	0.09	0.04	0.05	0.06	0.18	0.37	0.27	0.57	
Nb	0.91	1.15	1.22	1.37	2.55	0.40	0.46	0.51	0.67	0.39	1.00	0.76	4.69	2.62	1.84	
Th	0.10	0.07	0.06	0.15	0.21	0.02	0.08	0.05	0.03	0.05	0.06	0.03	0.23	0.15	0.15	
U	0.03	0.05	0.09	0.06	0.07	0.06	0.05	0.10	0.11	0.04	0.08	0.10	0.20	0.20	0.12	
Y	3.40	1.62	0.81	3.35	5.02	1.69	1.93	1.14	0.36	0.39	0.55	2.38	3.06	2.82	5.27	
La	0.85	0.58	0.69	1.25	2.27	0.41	1.40	0.92	0.30	0.36	0.51	0.31	1.84	1.20	1.42	
Ce	1.90	1.38	1.84	2.66	4.29	0.83	3.57	2.14	0.92	0.72	1.01	0.97	4.93	2.76	4.90	
Pr	0.25	0.17	0.23	0.33	0.60	0.12	0.51	0.25	0.10	0.08	0.12	0.14	0.62	0.35	0.76	
Nd	1.35	0.74	0.92	1.64	2.47	0.54	2.54	1.09	0.39	0.32	0.48	0.70	2.58	1.48	3.72	
Sm	0.39	0.19	0.17	0.40	0.67	0.16	0.56	0.23	0.08	0.06	0.09	0.23	0.55	0.35	0.98	
Eu	0.14	0.07	0.05	0.14	0.20	0.06	0.16	0.06	0.02	0.01	0.03	0.08	0.18	0.12	0.32	
Gd	0.41	0.22	0.16	0.43	0.67	0.18	0.47	0.21	0.08	0.05	0.10	0.29	0.54	0.40	0.99	
Tb	0.11	0.05	0.03	0.09	0.14	0.05	0.09	0.04	0.01	0.01	0.02	0.06	0.10	0.08	0.19	
Dy	0.66	0.27	0.14	0.60	0.82	0.32	0.45	0.21	0.07	0.05	0.08	0.40	0.53	0.46	1.02	
Ho	0.16	0.06	0.03	0.14	0.18	0.08	0.09	0.04	0.02	0.01	0.02	0.09	0.11	0.10	0.21	
Er	0.46	0.17	0.09	0.39	0.54	0.23	0.23	0.13	0.04	0.03	0.05	0.25	0.32	0.29	0.55	
Tm	0.08	0.03	0.01	0.06	0.08	0.03	0.03	0.02	0.01	0.00	0.01	0.04	0.05	0.05	0.08	
Yb	0.46	0.18	0.10	0.39	0.51	0.26	0.21	0.15	0.05	0.04	0.05	0.27	0.34	0.32	0.50	
Lu	0.07	0.03	0.02	0.06	0.08	0.04	0.03	0.02	0.01	0.00	0.01	0.04	0.05	0.05	0.07	
Ol	62	53	46	46	48	48	63	47	51	69	47	37	30	29	13	
Opx	23	31	41	38	33	41	31	46	42	27	48	44	51	52	26	
Cpx	15	16	13	16	19	11	6	7	7	4	5	19	19	19	61	

TABLE 2C. WHOLE-ROCK MAJOR- AND TRACE-ELEMENT COMPOSITION OF MANTLE XENOLITHS FROM MEGA

Rock type: Sample:	Cpx-poor																											
	Lh MA10	Lh MA15	Lh MA27	Lh MA51	Lh MA53	Lh MA56	Lh MA58	Lh MA63	Lh MA67	Lh MA8	Lh MA9	Lh MA17	Lh MA19	Lh MA32	Lh MA35	Lh MA36												
Major oxides																												
SiO ₂ (wt%)	44.71	45.37	43.58	43.95	44.11	44.06	43.46	45.98	45.49	44.60	43.37	42.88	43.42	43.89	44.42	42.85												
TiO ₂	0.09	0.12	0.13	0.13	0.08	0.08	0.06	0.13	0.09	0.10	0.08	0.11	0.03	0.06	0.02	0.04												
Al ₂ O ₃	2.82	2.77	3.03	3.26	2.66	2.83	1.68	3.28	3.11	2.59	2.30	1.75	1.46	1.74	1.81	0.90												
Fe ₂ O _{3tot}	7.09	5.85	8.47	9.26	7.36	7.65	7.19	7.16	7.35	8.36	7.74	9.26	7.27	7.52	6.97	7.53												
MnO	0.12	0.11	0.14	0.14	0.12	0.13	0.12	0.13	0.13	0.13	0.12	0.16	0.11	0.13	0.12	0.13												
MgO	41.71	41.52	41.25	39.30	42.89	42.63	44.03	39.77	40.71	41.96	44.63	43.70	46.59	45.14	44.45	47.25												
CaO	2.88	3.69	2.99	3.29	2.32	1.97	3.18	3.07	2.70	2.00	1.42	1.46	0.88	0.86	1.86	1.03												
Na ₂ O	0.27	0.37	0.29	0.30	0.22	0.29	0.19	0.28	0.24	0.20	0.20	0.07	0.12	0.42	0.13	0.16												
K ₂ O	nd	nd	nd	nd	nd	0.02	nd	nd	nd	nd	nd	0.07	nd	0.01	nd	nd												
P ₂ O ₅	0.03	0.04	0.02	0.05	0.02	0.01	0.02	0.03	0.01	0.04	0.02	0.07	0.04	0.04	0.01	0.02												
LOI	0.27	0.17	0.10	0.31	0.22	0.31	0.07	0.16	0.19	0.02	0.12	0.21	0.08	0.18	0.21	0.10												
Sum	100.00	100.00	100.00	100.00	100.00	100.00	100.00	100.00	100.00	100.00	100.00	100.00	100.00	100.00	100.00	100.00												
Mg#	0.92	0.93	0.91	0.89	0.92	0.92	0.92	0.92	0.92	0.91	0.92	0.90	0.93	0.93	0.93	0.93												
Trace elements (ppm)																												
Ni	1859	1742	1879	1836	1847	2040	1972	1655	1642	1827	2085	2002	2216	2090	1982	2165												
Co	103	97	111	106	110	113	114	94	95	112	117	114	115	117	106	121												
Cr	2314	2239	1598	2576	1714	1458	1823	2232	2542	1852	1595	1257	1653	1267	2118	1348												
V	68	77	76	75	66	53	67	81	78	60	48	26	31	34	54	23												
Sc	23	24	22	22	20	19	25	24	24	19	18	91	15	12	18	12												
Sr	5	25	3	4	5	20	6	5	nd	2	3	14	1	57	1	35												
Zr	3.17	6.65	4.26	3.52	0.90	2.19	1.10	2.96	0.76	4.52	2.17	19.6	0.95	2.05	0.91	14.7												
Hf	0.12	0.14	0.15	0.05	nd	nd	0.04	0.14	0.03	0.28	0.08	0.36	0.03	0.05	0.02	0.33												
Nb	0.94	0.49	0.13	0.56	0.21	0.97	0.13	0.28	0.10	1.09	0.47	8.45	0.20	0.10	0.35	3.13												
Th	0.03	0.03	0.05	0.02	nd	0.08	nd	0.01	nd	0.05	nd	0.26	0.02	0.18	0.04	0.08												
U	0.01	0.01	0.03	0.02	nd	0.01	nd	nd	nd	nd	nd	0.09	0.01	0.05	0.02	0.03												
Y	2.54	3.02	3.90	1.29	2.95	2.56	1.20	2.09	3.17	2.24	1.54	3.56	0.48	2.11	1.02	1.07												
La	0.33	0.57	0.23	0.43	0.13	0.52	0.06	0.08	0.03	0.16	0.09	2.84	0.10	1.41	0.21	0.79												
Ce	0.33	0.93	0.37	0.98	0.48	1.30	0.17	0.23	0.11	0.41	0.20	6.23	0.21	4.22	0.33	2.10												
Pr	0.04	0.14	0.07	0.12	0.07	0.16	0.03	0.05	nd	0.06	0.03	0.75	0.03	0.55	0.03	0.28												
Nd	0.28	0.76	0.45	0.50	0.40	0.67	0.19	0.33	0.15	0.41	0.25	3.30	0.13	2.48	0.12	1.26												
Sm	0.14	0.26	0.23	0.12	0.16	0.18	0.07	0.15	0.09	0.16	0.10	0.69	0.04	0.48	0.02	0.29												
Eu	0.05	0.08	0.08	0.04	0.06	0.07	0.03	0.06	0.02	0.06	0.03	0.19	0.01	0.14	0.01	0.09												
Gd	0.19	0.30	0.29	0.13	0.25	0.26	0.10	0.20	0.20	0.23	0.15	0.65	0.05	0.39	0.03	0.28												
Tb	0.05	0.07	0.08	0.02	0.06	0.05	0.02	0.05	0.03	0.04	0.03	0.11	0.01	0.06	0.01	0.04												
Dy	0.34	0.46	0.54	0.15	0.39	0.35	0.17	0.33	0.38	0.33	0.23	0.55	0.07	0.29	0.07	0.19												
Ho	0.08	0.10	0.12	0.03	0.09	0.08	0.04	0.08	0.07	0.07	0.05	0.11	0.02	0.06	0.02	0.03												
Er	0.24	0.28	0.35	0.09	0.28	0.24	0.12	0.23	0.28	0.24	0.16	0.30	0.05	0.15	0.06	0.08												
Tm	0.04	0.04	0.06	0.02	0.04	0.03	0.02	0.04	0.02	0.03	0.02	0.04	0.01	0.02	0.01	0.01												
Yb	0.24	0.27	0.37	0.11	0.33	0.27	0.13	0.24	0.35	0.26	0.18	0.29	0.06	0.15	0.08	0.06												
Lu	0.04	0.04	0.06	0.02	0.05	0.04	0.02	0.04	0.03	0.03	0.02	0.05	0.01	0.02	0.01	0.01												
Ol	62	60	66	61	67	66	75	52	56	63	73	78	78	75	70	84												
Opx	23	21	18	22	21	22	10	32	30	26	18	13	17	18	21	10												
Cpx	15	19	16	17	12	12	15	16	14	11	8	9	5	7	9	6												

(Continued)

TABLE 2C. WHOLE-ROCK MAJOR- AND TRACE-ELEMENT COMPOSITION OF MANTLE XENOLITHS FROM MEGA (Continued)

Rock type: Sample:	Cpx-poor														Hz	MA48	Hz	MA65	Hz	MA68
	Lh	Lh	Lh	Lh	Lh	Lh	Lh	Lh	Lh	Lh	Lh	Lh	Lh	Lh						
	MA38	MA40	MA46	MA57	MA70	MA11	MA24	MA26	MA37	MA42	MA43	MA47	MA48	MA65	MA68					
Major oxides (wt%)																				
SiO ₂	43.55	43.79	43.69	44.21	43.52	43.72	44.27	42.71	43.54	44.66	43.25	42.93	43.19	43.85	42.63	42.30				
TiO ₂	0.08	0.09	0.06	0.02	0.07	0.02	0.06	0.02	0.03	0.02	0.07	0.02	0.02	0.01	0.03	0.04				
Al ₂ O ₃	2.24	1.52	1.98	2.31	1.80	1.19	1.40	1.02	1.05	1.16	1.34	1.11	1.32	1.06	0.82	1.02				
Fe ₂ O ₃ _{tot}	8.59	7.87	7.75	6.92	7.94	7.16	8.22	9.59	7.49	6.92	9.02	6.88	7.00	7.33	6.97	8.44				
MnO	0.13	0.12	0.12	0.12	0.12	0.12	0.12	0.16	0.11	0.12	0.12	0.11	0.11	0.12	0.11	0.14				
MgO	43.14	44.99	44.48	44.65	45.23	46.73	44.73	45.38	46.86	45.99	45.19	48.00	47.16	46.63	48.88	46.51				
CaO	1.82	1.28	1.54	1.28	1.06	0.80	0.66	0.72	0.58	0.89	0.64	0.60	0.75	0.73	0.38	1.20				
Na ₂ O	0.20	0.19	0.17	0.14	0.18	0.11	0.15	0.18	0.12	0.10	0.15	0.23	0.25	0.14	0.10	0.18				
K ₂ O	nd	nd	nd	nd	nd	nd	nd	0.02	nd	nd	nd	nd	nd	nd	nd	nd				
P ₂ O ₅	0.07	0.01	0.02	0.01	0.01	0.02	0.04	0.07	0.05	0.02	0.01	0.03	0.03	0.06	0.01	0.05				
LOI	0.19	0.13	0.18	0.33	0.07	0.14	0.34	0.14	0.18	0.11	0.21	0.09	0.16	0.08	0.08	0.12				
Sum	100.00	100.00	100.00	100.00	100.00	100.00	100.00	100.00	100.00	100.00	100.00	100.00	100.00	100.00	100.00	100.00				
Mg#																				
Trace elements (ppm)																				
Ni	2107	2072	2101	2046	2115	2208	2203	2252	2291	2090	2246	2249	2201	2214	2310	2236				
Co	112	114	113	114	116	115	108	115	113	110	117	119	114	115	119	117				
Cr	2230	2412	2047	2073	1843	2204	1898	1825	2700	2241	2275	1581	2163	3056	983	2517				
V	52	46	48	45	47	33	35	26	29	40	35	30	34	34	20	27				
Sc	17	14	15	17	17	14	14	14	13	17	12	14	14	15	12	14				
Sr	12	1	5	36	6	4	4	21	5	3	nd	48	60	40	3	48				
Zr	1.81	1.54	2.49	0.53	2.10	3.30	2.48	7.38	1.99	0.97	0.84	0.82	0.65	1.67	2.24	13.2				
Hf	nd	0.05	0.07	nd	nd	0.05	0.03	0.12	0.04	0.02	0.02	0.02	0.01	0.03	0.04	0.26				
Nb	0.35	0.07	0.21	0.44	0.23	1.08	0.44	3.46	0.52	0.35	0.06	0.60	0.67	1.03	0.82	3.52				
Th	0.92	0.02	0.11	0.17	0.01	0.02	0.05	0.01	0.02	0.08	0.01	0.29	0.24	0.12	0.04	0.50				
U	0.15	0.01	nd	0.21	0.02	0.01	0.02	0.01	0.01	0.03	0.01	0.09	0.12	0.05	0.02	0.05				
Y	2.52	1.23	2.90	0.50	1.27	0.71	0.82	1.44	0.77	0.68	0.88	0.67	0.62	0.84	0.35	1.55				
La	0.89	0.17	0.37	0.20	0.30	1.09	1.04	1.06	0.19	0.40	0.10	1.81	2.10	1.07	0.28	2.18				
Ce	1.04	0.40	1.10	2.61	0.58	0.32	0.44	1.22	0.48	0.62	0.24	4.11	4.54	2.46	0.58	4.71				
Pr	0.11	0.05	0.11	0.16	0.07	0.04	0.05	0.18	0.06	0.06	0.03	0.46	0.47	0.27	0.07	0.57				
Nd	0.49	0.27	0.58	0.36	0.27	0.18	0.24	0.94	0.27	0.27	0.14	1.58	1.49	1.02	0.25	2.43				
Sm	0.16	0.09	0.17	0.04	0.07	0.04	0.05	0.24	0.05	0.05	0.04	0.20	0.16	0.14	0.05	0.52				
Eu	0.06	0.03	0.04	0.01	0.02	0.01	0.02	0.07	0.01	0.01	0.01	0.06	0.05	0.03	0.01	0.13				
Gd	0.23	0.10	0.25	0.09	0.09	0.04	0.05	0.21	0.05	0.05	0.04	0.23	0.20	0.13	0.05	0.46				
Tb	0.05	0.02	0.03	0.01	0.02	0.01	0.01	0.04	0.01	0.01	0.01	0.02	0.02	0.01	0.01	0.04				
Dy	0.34	0.11	0.36	0.04	0.12	0.03	0.05	0.19	0.04	0.04	0.05	0.08	0.05	0.05	0.03	0.29				
Ho	0.08	0.02	0.06	0.01	0.03	0.01	0.01	0.03	0.01	0.01	0.01	0.01	0.01	0.01	0.01	0.02				
Er	0.24	0.06	0.25	0.04	0.09	0.02	0.03	0.08	0.02	0.02	0.03	0.04	0.03	0.03	0.02	0.09				
Tm	0.04	0.01	0.02	0.01	0.01	nd	0.01	0.01	nd	0.00	nd	0.01	nd	nd	nd	nd				
Yb	0.28	0.06	0.30	0.05	0.10	0.03	0.04	0.07	0.02	0.03	0.03	0.04	0.04	0.03	0.02	0.06				
Lu	0.04	0.01	0.02	0.01	0.02	nd	0.01	0.01	nd	0.01	0.01	0.01	0.01	0.01	nd	nd				
Ol	71	75	73	69	75	78	72	82	79	73	77	84	81	78	87	86				
Opx	20	18	19	24	18	18	24	14	17	22	18	11	13	18	10	9				
Cpx	10	7	8	7	7	5	4	4	4	5	4	5	5	4	3	5				

Note: nd—not detected.

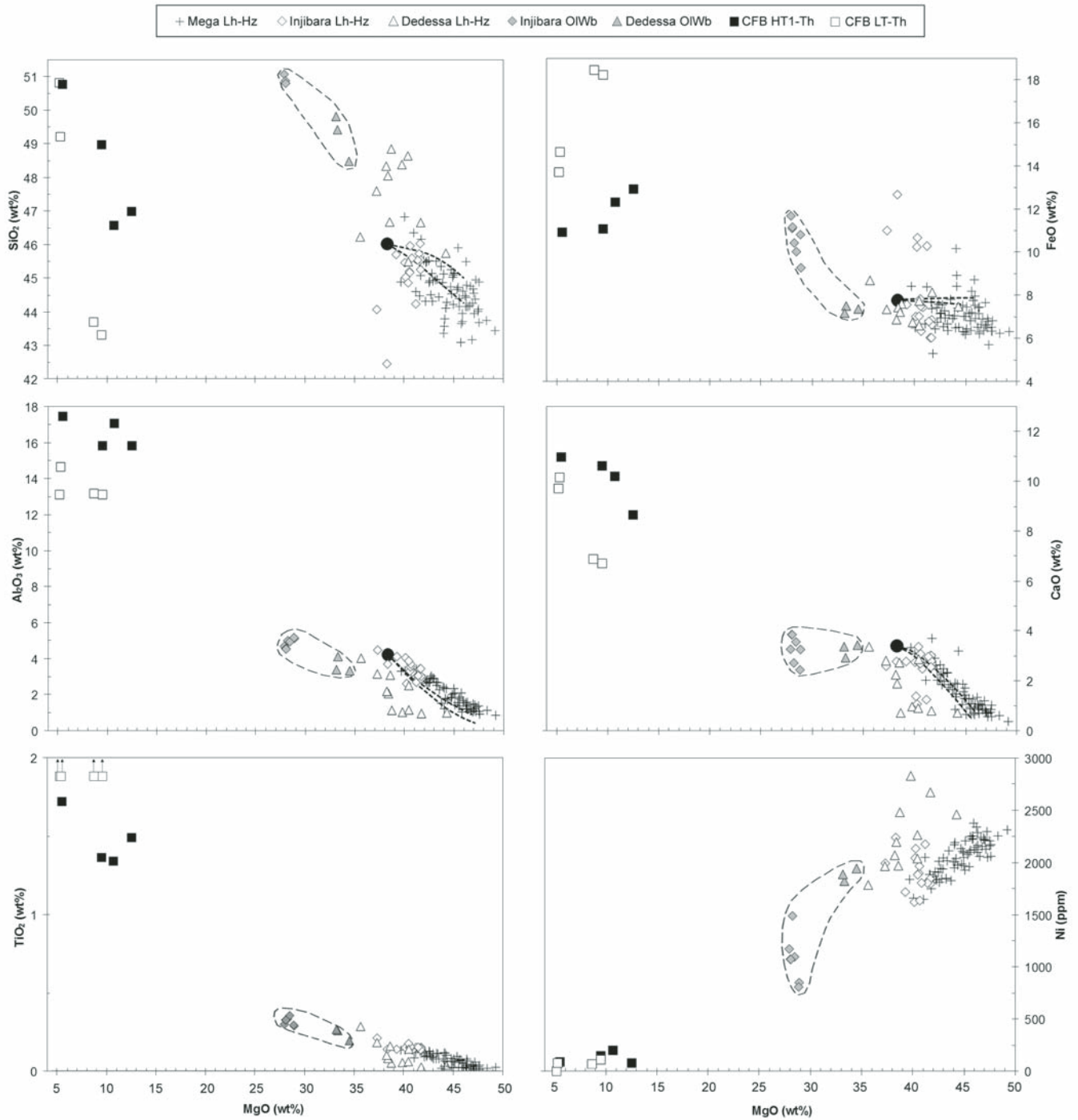


Figure 3. Variation diagrams of SiO₂, Al₂O₃, TiO₂, FeO, CaO, and Ni versus MgO (wt%) of mantle xenoliths from Ethiopia. The field of olivine-websterites (dashed line) and representative LT (low titanium tholeiites) and HT1 (high titanium tholeiites) continental flood basalts (CFBs; open and filled squares, respectively) are reported. Batch and fractional melting trends from a fertile lherzolite source (filled circle) are also reported after Niu (1997). Abbreviations: Lh—lherzolite; Hz—harzburgite; Ol—olivine; Wb—websterite.

subalkaline melts that converted olivine into orthopyroxene, consistent with the petrographical features and mineral compositional variations observed in olivine websterites. These melts could be, in principle, similar to the Oligocene continental flood basalt tholeiites (Pik et al., 1999; Beccaluva et al., 2009), reported for comparison in Figure 3, where olivine websterites may be considered reaction products, being intermediate basalts and peridotites. Moreover, the location of these mantle xenoliths close to the boundary between LT and HT1 volcanics of the Northern Ethiopian Plateau is compatible with the possible mantle refertilization by both types of lavas during their ascent to the surface.

Figure 4A reports bulk-rock chondrite (Ch)-normalized rare earth element (REE) patterns from Injibara and Dedessa River mantle xenoliths. Lherzolites display heavy (H) REE varying from ~ 3 to $1.5 \times \text{Ch}$. In particular, clinopyroxene-rich lherzolites (clinopyroxene modes between 15% and 19%) show nearly flat patterns with slight light (L) REE depletion (La_N/Yb_N down to 0.2); clinopyroxene-poor lherzolites (clinopyroxene 6%–8%) from Injibara are characterized by spoon-shaped, downward-convex patterns ($\text{La}_N/\text{Yb}_N \sim 0.4$), whereas at Dedessa River, they are LREE enriched (La_N/Yb_N up to 6); harzburgites show a continuous middle (M) REE to LREE enrichment with La_N/Yb_N up to 6.

Major- and trace-element analyses of representative clinopyroxenes from Injibara and Dedessa mantle xenoliths are reported in Table 3A. Ch-normalized REE patterns of clinopyroxenes from clinopyroxene-rich lherzolites display HREE patterns around or slightly higher than ten times those of the chondritic model, and a constant LREE depletion (La_N/Yb_N down to 0.2). Cpx in clinopyroxene-poor lherzolites show REE patterns either slightly depleted (La_N/Yb_N down to 0.3 and Tb_N/Yb_N up to 1.6) or enriched in LREE, consistent with the respective whole-rock patterns. Clinopyroxene in a single sample from Dedessa River (WOL2) represents a peculiar composition, showing an upward-convex LREE pattern with La_N/Yb_N up to 10. This is significantly different from other clinopyroxenes patterns and resembles those of clinopyroxene phenocrysts from alkaline magmas (Jeffries et al., 1995). Olivine-websterite clinopyroxenes are characterized by a generally flat pattern in M-HREEs, with a significant enrichment in La and Ce in some samples (GOJ31C and GOJ37B), in agreement with their bulk-rock REE distribution. Primitive mantle (PM)-normalized trace-element distributions of clinopyroxene (Fig. 5A) show a positive correlation between the most incompatible elements, such as Rb, Th, U, and LREE, coupled with the usual negative anomalies in Nb-Ta and Ba. On the other hand, clinopyroxene of sample WOL2 shows a remarkably enriched pattern, in addition to Ti-Zr negative anomalies, more typical of alkaline pyroxene.

Sr-Nd isotopes measured on clinopyroxene separates display different compositions depending on lithologies (Table 4; Fig. 6). Lherzolites are similar to depleted mantle, whereas clinopyroxene-poor lherzolites and harzburgites are variably displaced toward the composition of the northern Ethiopian continental flood basalt; olivine websterites plot within the continental flood basalt field. This suggests that the pristine

(depleted) lithospheric mantle beneath the plateau area was increasingly enriched from lherzolites to clinopyroxene-poor lherzolites/harzburgites and olivine websterites by melts similar in elemental and isotopic composition to tholeiitic continental flood basalt magmas that gradually modified mode and mineral composition of the peridotite matrix, ultimately leading to the olivine websterite parageneses.

Clinopyroxene from the clinopyroxene-poor lherzolite WOL2 has $^{87}\text{Sr}/^{86}\text{Sr} = 0.70332$ and $^{143}\text{Nd}/^{144}\text{Nd} = 0.51283$, i.e., it is significantly more enriched than the other mantle xenoliths of the same population, possibly reflecting metasomatic agents characterized by a different isotopic signature.

The $^3\text{He}/^4\text{He}$ ratio of olivines ranges from 6.6 to 8.9 R_a (Table 5). These values overlap the range typical of depleted mantle and show no clear signal of the high- ^3He component that characterizes both the Northern Ethiopian Plateau continental flood basalts and the subsequent alkaline volcanic cycles (Pik et al., 2006). However, they are slightly higher than $^3\text{He}/^4\text{He}$ ratios in African subcontinental mantle xenoliths from the Saharan belt (Beccaluva et al., 2007, 2008).

Mantle Xenoliths from Mega, Southern Ethiopian Rift

Abundant mantle xenoliths (up to 20 cm across) are found in Mega (Sidamo region, southern Ethiopia) Pliocene–Quaternary alkaline lavas, ~ 600 km south of the plateau, at the eastern border of the Main Ethiopian Rift where it crosses the Mesozoic–Paleogene structure of the Anza graben.

Xenoliths vary in composition from spinel-lherzolite to spinel-harzburgite. They show a wide spectrum of textures testifying to variably intense deformation events (Fig. 2B). Pure protogranular textures are rare; more common textures are transitional to porphyroclastic, which are characterized by strongly kinked large olivine and orthopyroxene crystals with unmixing lamellae, associated with undeformed smaller neoblasts mainly represented by clinopyroxene. Typical porphyroclastic textures are well represented and show more intense deformation in olivine and orthopyroxene, in turn fading in recrystallized domains where the largest porphyroclasts do not exhibit deformation and unmixing lamellae and show frequent 120° triple boundaries. Undeformed clinopyroxene neoblasts become progressively larger. This appears to delineate a rheological evolution of the mantle section with time, implying (1) upwelling and deformation of mantle material, (2) exsolution lamellae in pyroxenes, and (3) partial recrystallization under static conditions.

Evidence for modal metasomatism, though not abundant, is present, particularly in the most refractory lithologies, such as harzburgites or clinopyroxene-poor lherzolites. They consist of spongy borders in clinopyroxene, dark rims in spinel often surrounded by microcrystalline zones of olivine and clinopyroxene, as well as microgranular patches made up of olivine, dark spinel, Clinopyroxene, and yellowish glass including feldspar micro-lites. Clinopyroxene/spinel veinlets are also sometimes present in harzburgites (Fig. 2B).

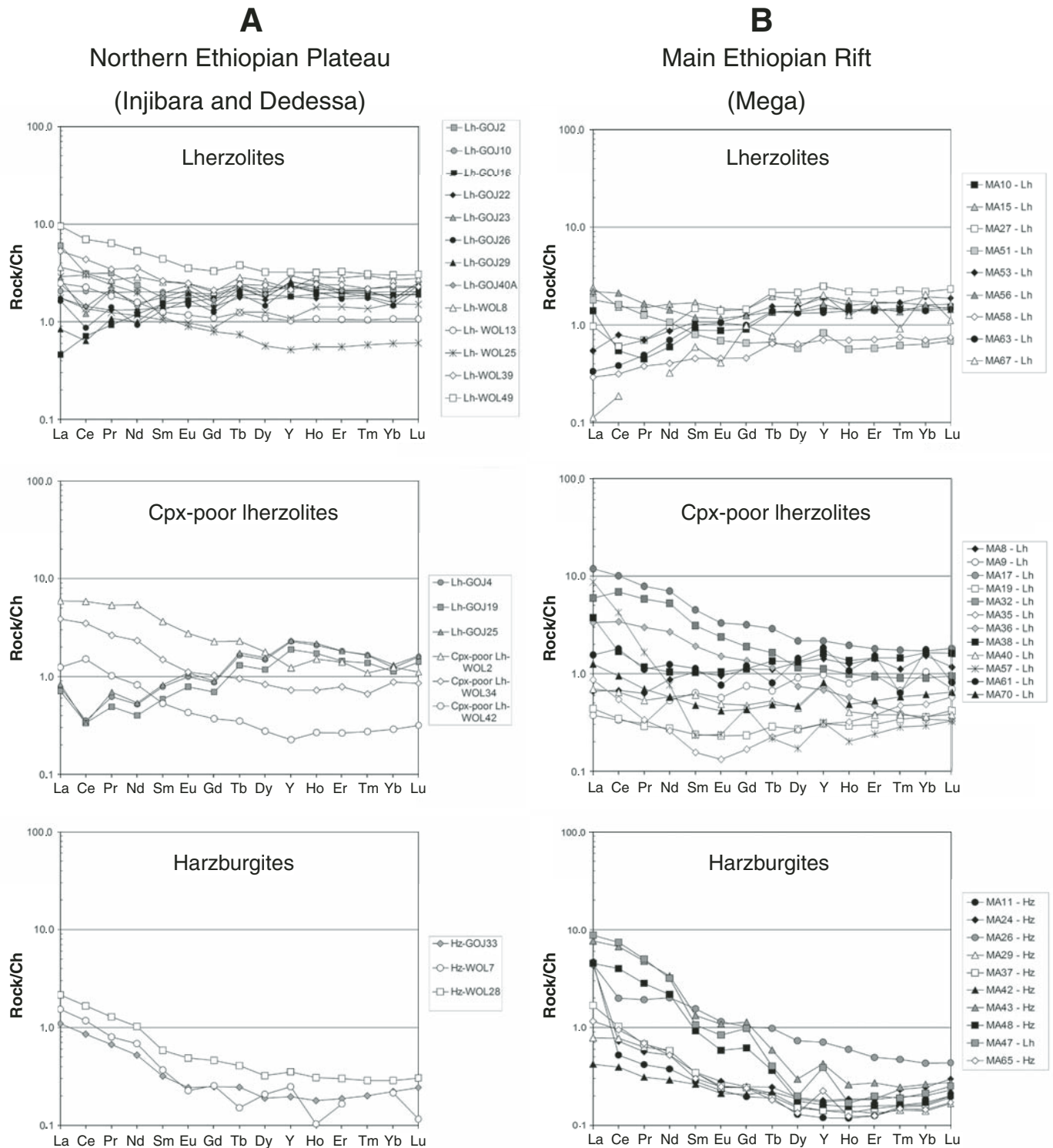


Figure 4. Chondrite (Ch)-normalized whole-rock rare earth element (REE) + Y distribution of mantle xenoliths from (A) Northern Ethiopian Plateau area (Injibara and Dedessa River) and (B) from the Main Ethiopian Rift (Mega). Normalizing factors are after McDonough and Sun (1995).

TABLE 3A. MAJOR- AND TRACE-ELEMENT CLINOPYROXENE COMPOSITION FROM DEDESSA RIVER AND INJIBARA MANTLE XENOLITHS

Rock type: Sample:	Dedessa										Injibara									
	Cpx-poor					Cpx-poor					Cpx-poor					Cpx-poor				
	Lh	Lh	Lh	Lh	OlWb	Lh	Lh	Lh	Lh	Lh	Lh	Lh	Lh	Lh	Lh	Lh	Lh	Lh	OlWb	OlWb
WOL19	WOL20B	WOL2	WOL35	WOL6	WOL4	WOL3	WOL4	WOL4	WOL4	WOL4	WOL3	WOL4	WOL4	WOL4	WOL4	WOL4	WOL4	WOL4	WOL4	WOL4
4	3	4	4	4	4	4	4	4	4	4	3	4	4	4	4	4	4	4	4	5
Avg. no.	52.99	53.57	52.99	50.57	52.78	52.61	52.13	52.13	52.13	52.13	52.13	52.13	52.13	52.13	52.13	52.13	52.13	52.13	52.13	52.13
SiO ₂ (wt%)	0.54	0.07	0.35	0.60	0.55	0.65	0.51	0.51	0.51	0.51	0.51	0.51	0.51	0.51	0.51	0.51	0.51	0.51	0.51	0.51
TiO ₂	6.28	3.51	5.18	7.34	6.23	6.63	6.22	6.36	6.36	6.36	6.22	6.36	6.36	6.36	6.36	6.36	6.36	6.36	6.36	6.36
Al ₂ O ₃	2.60	2.67	3.11	4.57	3.09	2.81	2.83	3.02	3.02	3.02	2.83	3.02	3.02	3.02	3.02	3.02	3.02	3.02	3.02	3.02
FeO _{Tot}	0.08	0.09	0.11	0.14	0.09	0.07	0.13	0.09	0.09	0.09	0.07	0.13	0.09	0.09	0.09	0.09	0.09	0.09	0.09	0.09
MnO	14.87	16.42	15.87	14.10	14.31	15.50	14.52	14.93	14.93	14.93	15.25	14.93	14.93	14.93	14.93	14.93	14.93	14.93	14.93	14.93
MgO	21.09	20.26	21.29	20.53	20.23	20.21	20.65	20.47	20.47	20.47	20.65	20.47	20.47	20.47	20.47	20.47	20.47	20.47	20.47	20.47
CaO	1.71	1.23	1.04	1.19	1.32	1.79	1.63	1.40	1.40	1.40	1.63	1.40	1.40	1.40	1.40	1.40	1.40	1.40	1.40	1.40
Na ₂ O	0.01	nd	nd	nd	0.01	0.02	0.01	0.03	0.03	0.03	0.01	0.03	0.03	0.03	0.03	0.03	0.03	0.03	0.03	0.03
K ₂ O	1.03	1.66	0.83	0.63	0.50	0.69	0.66	0.50	0.50	0.50	0.66	0.50	0.50	0.50	0.50	0.50	0.50	0.50	0.50	0.50
Cr ₂ O ₃	0.05	0.04	0.02	0.03	0.03	0.06	0.03	0.01	0.01	0.01	0.03	0.01	0.01	0.01	0.01	0.01	0.01	0.01	0.01	0.01
NiO	101.20	100.23	99.48	100.77	100.41	101.09	99.99	101.05	99.44	99.44	101.05	99.44	99.44	99.44	99.44	99.44	99.44	99.44	99.44	99.44
Sum	0.91	0.92	0.90	0.85	0.90	0.90	0.91	0.90	0.90	0.90	0.91	0.90	0.90	0.90	0.90	0.90	0.90	0.90	0.90	0.90
Mg#	0.10	0.09	0.24	0.10	0.05	0.06	0.07	0.05	0.05	0.05	0.07	0.05	0.05	0.05	0.05	0.05	0.05	0.05	0.05	0.05
Cr#																				
Avg. no.	4	2	7	4	5	4	4	4	4	4	10	2	5	3	4	6	3	6	6	6
analyses	nd	nd	2.50	0.86	0.04	nd	0.06	0.03	0.03	0.03	0.03	nd	0.06	0.10	0.03	0.04	0.02	0.03	0.03	0.03
Rb (ppm)	nd	nd	0.40	0.27	0.08	0.05	0.41	0.05	0.05	0.05	0.05	nd	0.26	0.10	0.27	0.04	0.04	0.02	0.08	0.06
Ba	nd	nd	0.65	0.36	0.10	0.03	0.04	0.01	0.01	0.01	0.01	nd	0.03	0.07	0.27	0.19	0.19	0.20	0.08	0.20
Th	nd	nd	0.15	0.09	0.04	0.01	0.02	0.01	0.01	0.01	0.01	nd	0.01	0.03	0.18	0.07	0.07	0.08	0.30	0.38
U	0.03	0.04	0.29	0.18	0.56	0.13	0.04	0.09	0.03	0.03	0.03	nd	0.02	0.08	0.11	0.12	0.09	0.11	0.19	0.19
Nb	0.32	0.03	2.90	0.18	0.03	0.01	0.01	0.01	0.01	0.01	0.01	nd	0.01	0.02	0.02	0.02	0.02	0.02	0.03	0.03
Ta	nd	nd	0.23	0.02	0.03	0.01	0.01	0.01	0.01	0.01	0.01	nd	0.01	0.01	0.01	0.01	0.01	0.01	0.01	0.01
La	1.42	0.80	32.9	8.68	1.61	0.73	1.34	0.81	0.50	0.50	0.50	nd	1.13	0.88	0.72	1.40	1.25	1.25	7.27	9.35
Ce	5.44	3.76	100	15.4	4.53	3.09	2.74	3.33	2.28	2.28	2.28	nd	4.78	2.66	3.32	3.73	3.60	3.60	9.07	11.1
Pr	0.82	0.60	14.5	1.42	0.71	0.67	0.49	0.66	0.46	0.46	0.46	nd	0.93	0.45	0.63	0.68	0.64	0.64	0.98	1.17
Sr	70.8	63.0	589	158	54.2	67.4	82.3	62.5	55.4	55.4	55.4	nd	40.0	52.6	65.5	31.7	31.6	31.6	50.2	50.8
Nd	3.92	3.36	68.5	4.74	3.86	4.11	3.30	4.16	3.18	3.18	3.18	nd	6.03	2.69	4.11	4.44	4.07	4.07	4.99	5.22
Zr	26.6	20.1	64.4	14.2	15.1	32.5	21.8	24.7	26.2	26.2	26.2	nd	35.7	20.8	31.3	52.6	53.7	53.7	27.3	34.8
Hf	0.73	0.66	1.02	0.59	0.59	1.03	0.76	0.79	0.91	0.91	0.91	nd	1.50	0.60	1.06	1.72	1.40	1.40	0.93	1.38
Sm	1.63	1.37	15.3	1.42	1.38	1.62	1.40	1.75	1.43	1.43	1.43	nd	2.49	1.00	1.79	2.06	2.00	2.00	1.62	1.82
Eu	0.66	0.57	5.02	0.54	0.60	0.71	0.64	0.77	0.60	0.60	0.60	nd	0.88	0.74	0.75	0.86	0.93	0.93	0.65	0.74
Ti	2745	2467	392	2163	3191	3671	3115	3998	2990	2990	2990	nd	3127	3372	3687	5490	4718	4601	3612	3612
Gd	1.97	1.80	10.8	1.82	1.71	2.14	2.01	2.29	2.20	2.20	2.20	nd	2.60	1.57	2.56	3.36	3.11	3.11	1.90	2.11
Tb	0.40	0.36	1.56	0.35	0.27	0.43	0.39	0.45	0.45	0.45	0.45	nd	0.48	0.31	0.50	0.67	0.73	0.73	0.32	0.42
Dy	2.64	2.39	7.50	2.39	1.78	3.08	2.63	3.02	2.86	2.86	2.86	nd	3.15	2.04	3.45	5.29	5.49	5.49	2.08	2.52
Y	15.6	13.2	30.8	13.4	9.5	17.4	14.6	17.1	16.3	16.3	16.3	nd	17.0	11.8	18.5	29.2	31.3	31.3	10.4	12.8
Ho	0.60	0.55	1.32	0.53	0.39	0.69	0.54	0.70	0.56	0.56	0.56	nd	0.68	0.44	0.72	1.15	1.25	1.25	0.43	0.52
Er	1.75	1.53	2.87	1.37	0.87	2.05	1.53	1.97	1.78	1.78	1.78	nd	1.93	1.37	2.04	3.06	3.20	3.20	1.12	1.53
Tm	0.26	0.23	0.32	0.22	0.14	0.26	0.23	0.28	0.27	0.27	0.27	nd	0.25	0.20	0.30	0.38	0.39	0.39	0.16	0.20
Yb	1.84	1.51	2.06	1.47	1.16	2.00	1.59	1.92	1.87	1.87	1.87	nd	2.00	1.51	1.90	2.38	2.56	2.56	1.03	1.31
Lu	0.26	0.27	0.24	0.22	0.13	0.26	0.18	0.28	0.26	0.26	0.26	nd	0.26	0.21	0.27	0.29	0.27	0.27	0.16	0.15

Note: Lh—hercynite, Hz—harzburgite, OlWb—olivine-websterite, Ol—olivine, Opx—orthopyroxene, Cpx—clinopyroxene, Sp—spinel, Mg#—Mg/(Mg + Fe²⁺) a.p.f.u., Cr#—Cr/(Cr + Al) a.p.f.u., avg. no. anal.—number of averaged analyses, nd—not detected.

TABLE 3B. MAJOR- AND TRACE-ELEMENT CLINOPYROXENE COMPOSITION FROM MEGA MANTLE XENOLITHS

Rock type: Sample:	Gpx-poor														Hz MA68
	Lh MA10	Lh MA15	Lh MA27	Lh MA67	Lh MA9	Lh MA17	Lh MA35	Lh MA38	Lh MA40	Hz MA11	Hz MA24	Hz MA26	Hz MA42	Hz MA47	Hz MA48
Avg. no. analyses	2	2	1	3	3	2	4	4	1	2	4	1 (microph)	7	5	1
SiO ₂ (wt%)	53.25	53.49	52.95	53.42	53.29	55.28	53.90	52.75	53.50	54.55	53.33	54.83	53.50	55.18	54.82
TiO ₂	0.33	0.35	0.43	0.37	0.55	0.08	0.08	0.41	0.50	0.07	0.38	0.04	0.62	0.04	0.06
Al ₂ O ₃	5.40	5.68	6.29	5.90	5.48	3.68	3.83	6.35	5.94	2.95	5.81	3.95	6.05	3.43	3.77
FeO _{Tot}	2.43	2.37	2.48	2.46	2.44	2.91	2.36	2.85	2.28	2.23	2.62	2.94	2.46	2.39	2.31
MnO	0.03	0.14	0.06	0.15	0.07	0.07	0.07	0.09	0.03	0.01	0.07	0.14	0.05	0.09	0.11
MgO	15.84	15.77	15.54	16.18	15.44	16.08	16.97	15.88	15.03	17.24	15.85	16.03	14.79	17.01	16.72
CaO	21.18	21.02	21.22	20.89	21.77	20.30	22.35	19.97	19.32	22.20	19.47	19.55	19.48	20.32	20.49
Na ₂ O	1.31	1.59	1.49	1.63	1.46	1.81	0.81	1.64	2.27	0.83	2.09	2.01	2.47	1.74	1.72
K ₂ O	0.01	0.01	0.02	nd	0.01	0.02	0.01	0.01	0.03	nd	0.02	0.02	0.01	nd	0.01
Cr ₂ O ₃	0.83	1.02	0.74	0.67	0.70	1.13	0.71	0.89	1.41	0.97	1.59	1.61	1.51	1.18	1.64
NiO	0.11	0.06	nd	0.07	0.04	0.01	0.05	0.05	0.06	0.05	0.06	0.09	0.04	0.06	nd
Sum	100.71	101.49	101.24	101.74	101.25	101.37	101.15	100.89	100.35	101.10	101.31	101.22	100.98	101.45	101.59
Mg#	0.92	0.93	0.92	0.93	0.92	0.91	0.93	0.92	0.92	0.93	0.93	0.91	0.92	0.93	0.93
Cr#	0.09	0.11	0.07	0.07	0.08	0.17	0.11	0.09	0.14	0.17	0.16	0.21	0.14	0.19	0.22
Avg. no. analyses	4	3	2	5	6	1	3	7	4	3	7	3	8	6	4
Rb (ppm)	0.04	0.05	0.09	nd	0.03	0.02	nd	0.03	0.10	0.03	0.03	0.04	0.03	0.02	0.19
Ba	0.11	0.08	0.89	0.02	0.03	0.63	0.20	0.50	0.62	0.04	0.15	0.12	0.14	1.03	0.96
Th	0.16	0.11	0.85	0.03	0.27	2.72	0.45	4.80	0.46	0.38	2.18	0.18	0.51	3.39	2.53
U	0.05	0.03	0.21	0.01	0.06	0.62	0.09	1.18	0.14	0.14	0.44	0.05	0.13	0.80	0.80
Nb	0.04	0.02	0.06	0.02	0.05	0.55	0.07	0.64	0.05	0.26	0.06	0.89	0.04	0.02	0.59
Ta	0.01	nd	0.01	nd	0.01	0.04	nd	0.04	0.01	0.01	0.01	0.11	nd	nd	0.03
La	1.36	1.16	4.14	0.32	1.95	33.8	1.49	10.4	3.42	4.03	5.23	11.9	3.76	33.5	37.3
Ce	2.01	4.44	5.54	0.81	4.06	72.3	1.27	10.0	7.08	7.68	8.67	40.8	8.22	78.8	90.0
Pr	0.32	0.79	0.53	0.15	0.62	9.31	0.09	0.87	0.93	0.93	1.20	6.40	0.95	7.97	9.79
Sr	49.3	86.6	64.7	26.7	46.3	648	18.5	102	84.5	119	91.5	345	77.1	504	755
Nd	2.15	4.23	3.06	1.11	3.56	40.0	0.28	3.76	4.81	4.26	6.27	32.4	4.43	25.8	34.6
Zr	16.2	26.9	19.5	5.66	24.7	154	0.30	15.6	15.3	19.9	47.1	173	14.2	5.15	14.1
Hf	0.58	0.53	1.07	0.37	0.85	2.42	0.02	0.64	0.63	0.18	0.41	2.62	0.53	0.18	0.15
Sm	1.09	1.53	1.42	0.77	1.55	8.58	0.07	1.33	1.54	0.93	1.67	8.26	1.29	2.96	3.90
Eu	0.50	0.65	0.56	0.43	0.76	2.89	0.04	0.58	0.63	0.37	0.62	3.03	0.52	0.83	1.25
Ti	1739	1679	2398	1869	3116	467	320	2120	3432	300	1953	140	3461	164	180
Gd	1.72	2.07	1.97	1.52	2.16	7.29	0.28	1.73	1.79	0.76	1.47	6.81	1.34	1.32	2.24
Tb	0.37	0.41	0.42	0.33	0.44	1.04	0.08	0.37	0.29	0.12	0.22	1.10	0.22	0.16	0.25
Dy	2.65	2.67	3.00	2.51	2.95	6.60	0.84	2.57	1.77	0.68	1.30	5.73	1.38	0.79	1.06
Y	14.7	14.1	16.0	14.6	17.1	34.0	5.64	14.3	8.26	3.41	6.75	23.1	6.80	4.24	5.33
Ho	0.59	0.58	0.70	0.57	0.69	1.30	0.22	0.59	0.36	0.12	0.27	0.98	0.28	0.15	0.18
Er	1.71	1.51	1.97	1.65	1.95	3.21	0.73	1.63	0.84	0.36	0.71	2.29	0.72	0.38	0.44
Tm	0.23	0.23	0.28	0.24	0.29	0.51	0.10	0.24	0.13	0.05	0.10	0.27	0.11	0.06	0.07
Yb	1.64	1.60	2.00	1.71	1.91	3.03	0.78	1.61	0.76	0.40	0.72	1.65	0.72	0.47	0.48
Lu	0.22	0.22	0.31	0.24	0.29	0.54	0.12	0.22	0.11	0.05	0.11	0.19	0.10	0.07	0.07

Microprobe data on the mineral phases show slight compositional differences between lherzolites and harzburgites (Table 1C). Olivine varies in composition between Fo_{88.4–91.8} in lherzolites and Fo_{89.3–91.7} in harzburgites. Orthopyroxene composition varies in the ranges En_{88.1–91.1} in lherzolites and En_{89.3–91.5} in harzburgites. Clinopyroxenes are rather homogeneous in both lherzolites and harzburgites, showing the following composi-

tional variations: Wo_{42.9–48.8}, En_{45.7–52.1}, Fs_{3.0–5.5}, Mg# 0.91–0.93, Cr# 0.07–0.29, Na₂O 0.81–2.66 wt%, and TiO₂ 0.04–0.62 wt%. Spinel composition in both lherzolites and harzburgites shows Mg# ranging from 0.64 to 0.79 and Cr# from 0.11 to 0.60.

Application of the geothermobarometer of Brey and Köhler (1990) and Köhler and Brey (1990) gives nominal *P-T* estimates spanning over a wide range that can be subdivided in two

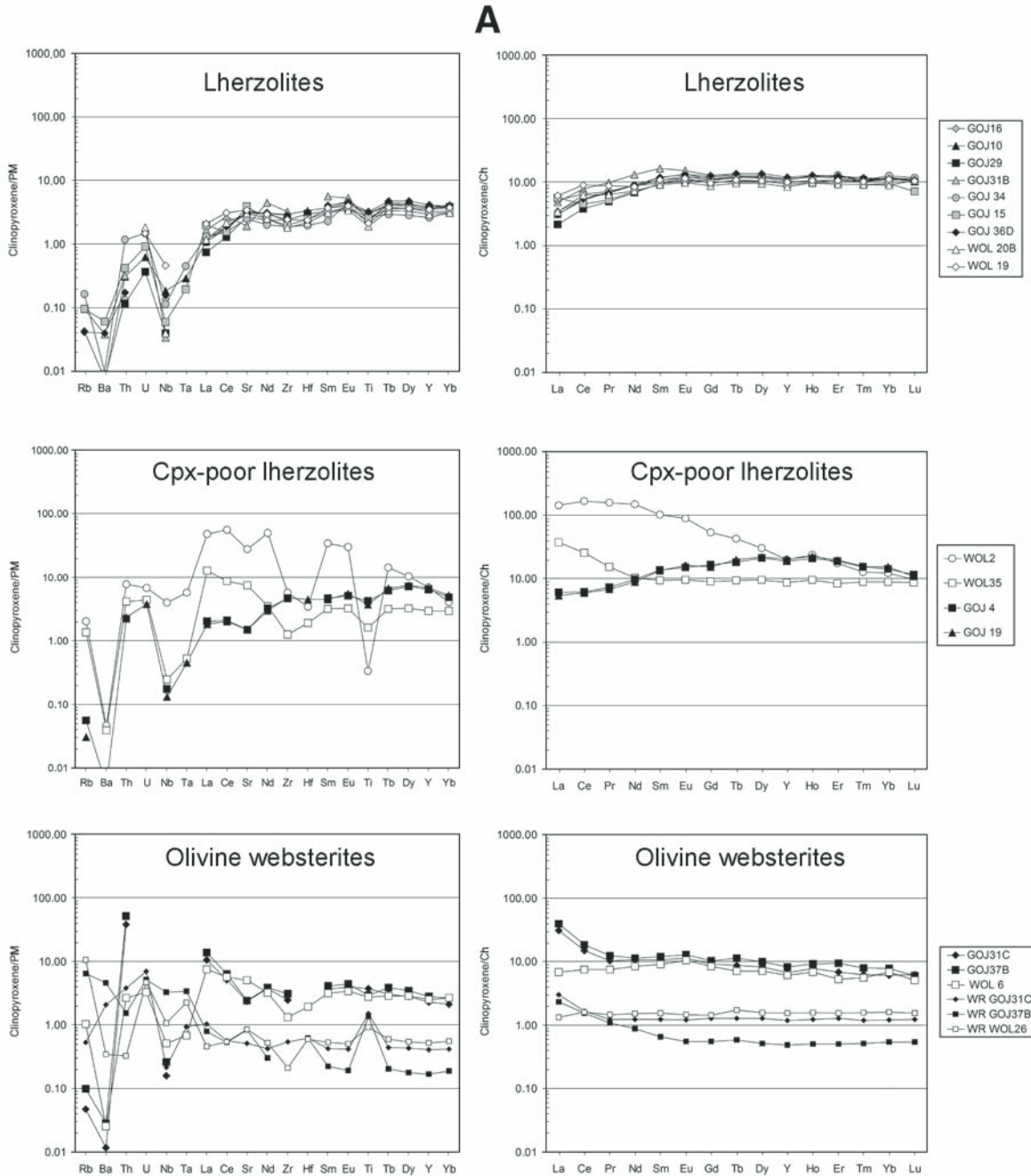


Figure 5 (Continued on following page). Chondrite (Ch)-normalized rare earth element (REE) + Y and primitive mantle (PM)-normalized incompatible element distribution of clinopyroxene from (A) Northern Ethiopian Plateau area (Injibara and Dedessa River) and (B) Main Ethiopian Rift (Mega) mantle xenoliths. Normalizing factors are after McDonough and Sun (1995) and Sun and McDonough (1989), respectively. Cpx—clinopyroxene.

clusters, 930 ± 80 °C at 1.0 ± 0.2 GPa and 1040 ± 80 °C at 1.6 ± 0.4 GPa, irrespective of the mantle lithology. This suggests that the mantle section beneath Mega has been subjected to upwelling and decompression processes during rift development still recorded by the higher P - T conditions in some xenoliths.

Mega xenoliths show a continuous bulk-rock depletion trend (Table 2C; Fig. 3) that is reflected in a decrease of the most fusible elements in parallel with clinopyroxene diminution from fertile lherzolites (16%–18% modal clinopyroxene) to harzburgites (modal clinopyroxene down to 3%).

Accordingly, the whole-rock REE distribution shows flat chondrite-normalized HREE patterns, decreasing from 2.2 chondritic abundances in the lherzolites to 0.1 chondritic abundances in the harzburgites. This is compatible with a progressive depletion of mantle material by extraction of basic melts (Fig. 4B). On the other hand, LREE/Ch patterns show variable enrichments that are best explained by metasomatism, with La_N/Yb_N varying from 0.1 to 26, and the highest ratios recorded in harzburgites. Clinopyroxenes show a REE distribution generally parallel to those of the respective bulk rock, with La_N/Yb_N ranging from 0.1

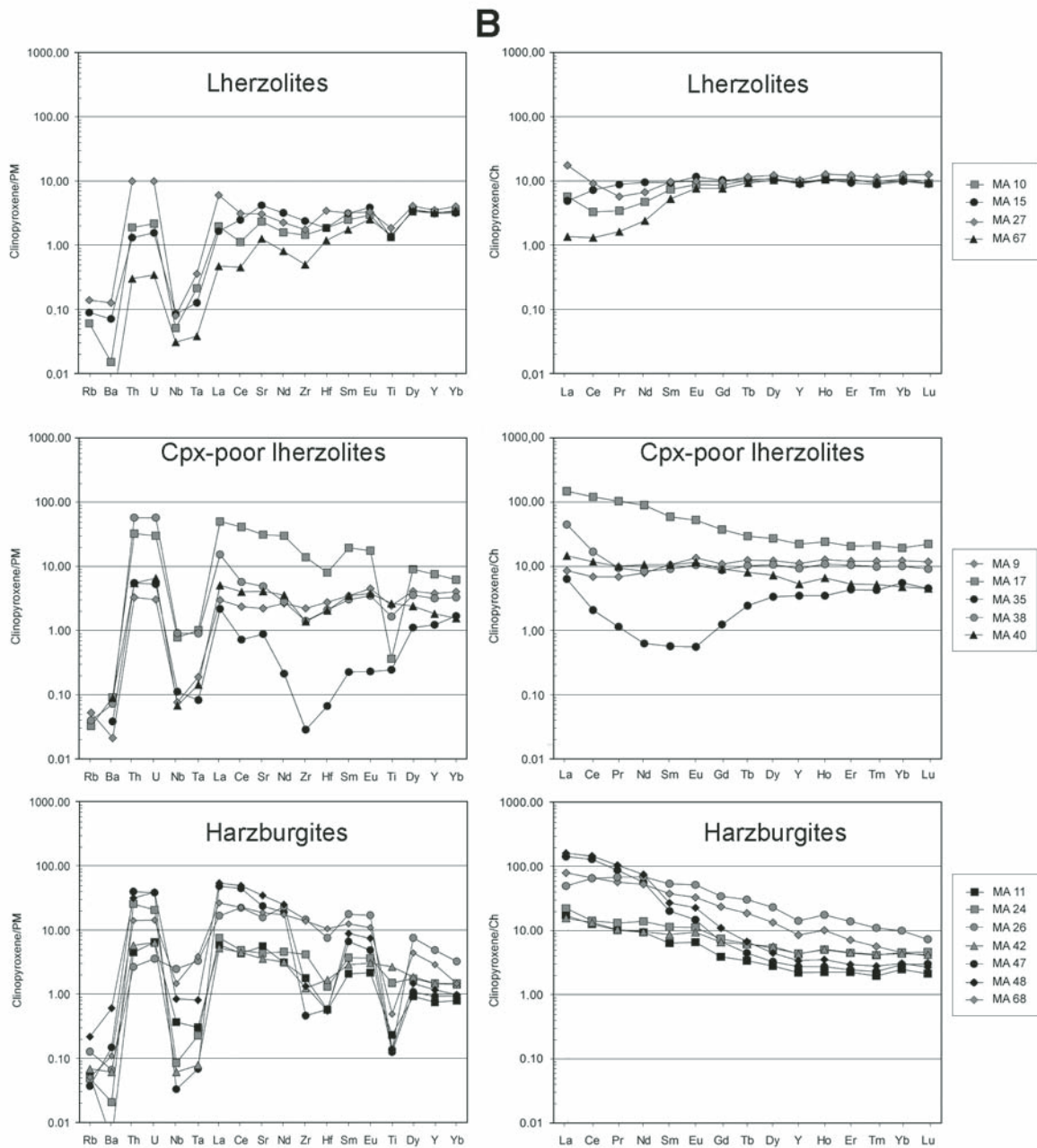


Figure 5 (Continued).

TABLE 4. Sr-Nd-Pb ISOTOPIC COMPOSITION OF CLINOPYROXENES FROM ETHIOPIAN MANTLE XENOLITHS

Sample	Rock type	Analyzed fraction	$^{87}\text{Sr}/^{86}\text{Sr}$	$^{143}\text{Nd}/^{144}\text{Nd}$	$^{206}\text{Pb}/^{204}\text{Pb}$	$^{207}\text{Pb}/^{204}\text{Pb}$	$^{208}\text{Pb}/^{204}\text{Pb}$
Mega (Sidamo)							
MA 10	Lh	Cpx	0.70262	0.51379	19.04	15.63	38.69
MA 15	Lh	Cpx	0.70240	0.51327	19.34	15.58	38.89
MA 27	Lh	Cpx	0.70220	0.51322	19.26	15.62	38.96
MA 67	Lh	Cpx	0.70301	—	—	—	—
MA 8	Cpx-poor Lh	Cpx	0.70290	0.51330	—	—	—
MA 35	Cpx-poor Lh	Cpx	0.70311	0.51366	19.02	15.59	38.65
MA 38	Cpx-poor Lh	Cpx	0.70270	0.51338	—	—	—
MA 40	Cpx-poor Lh	Cpx	0.70256	0.51301	18.51	15.53	38.09
MA 19	Cpx-poor Lh	Cpx	0.70276	0.51304	18.38	15.21	37.58
MA 11	Hz	Cpx	0.70326	0.51274	18.46	15.67	38.42
MA 24	Hz	Cpx	—	0.51278	—	—	—
MA 26	Hz	Cpx	0.70305	0.51291	—	—	—
MA 29	Hz	Cpx	0.70454	0.51219	—	—	—
MA 42	Hz	Cpx	0.70268	0.51305	—	—	—
MA 47	Hz	Cpx	0.70304	0.51289	—	—	—
MA 48	Hz	Cpx	0.70297	0.51297	18.52	15.58	38.33
MA 68	Hz	Cpx	0.70305	0.51298	—	—	—
Injibara (Gojam)							
GOJ16	Lh	Cpx	0.702414	0.513302	—	—	—
GOJ26	Lh	Cpx	0.702712	0.513259	—	—	—
GOJ31B	Lh	Cpx	0.702953	—	—	—	—
GOJ4	Cpx-poor Lh	Cpx	0.702840	0.513238	—	—	—
GOJ19	Cpx-poor Lh	Cpx	0.702895	0.513266	—	—	—
GOJ33	Hz	Cpx	0.703536	—	—	—	—
GOJ31C	OIWb	Cpx	0.703302	0.512895	—	—	—
GOJ37B	OIWb	Cpx	0.703370	0.512912	—	—	—
Dedessa (Wollega)							
WOL2	Cpx-poor Lh	Cpx	0.703320	0.512827	—	—	—

Note: Lh—Iherzolite, Hz—harzburgite, OIWb—olivine-websterite, Cpx—clinopyroxene.

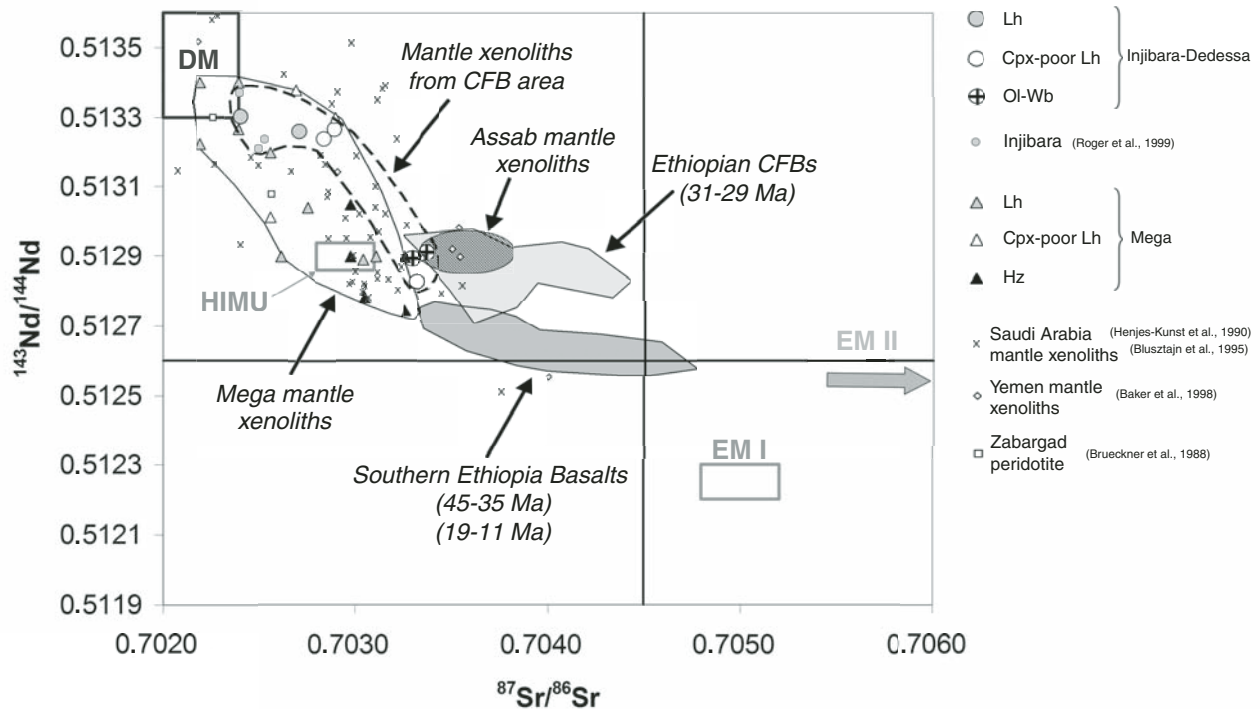


Figure 6. Sr-Nd isotopic composition of clinopyroxene from Ethiopian mantle xenoliths (this work; Roger et al., 1999). Isotopic composition of Zabargad peridotite (Brueckner et al., 1988) and mantle xenoliths from Saudi Arabia (Henjes-Kunst et al., 1990; Blusztajn et al., 1995), Yemen (Baker et al., 1998), and Assab (Teklay et al., 2010) are reported for comparison. Compositional fields of Ethiopian continental flood basalts (CFBs; Pik et al., 1999), southern Ethiopian basalts (after George and Rogers, 2002; Stewart and Rogers, 1996) are also reported. Depleted mantle (DM), high- μ (HIMU), enriched mantle (EM I and EM II) mantle end members are after Zindler and Hart (1986). Abbreviations: Lh—Iherzolite; Cpx—Clinopyroxene; Ol—olivine; Wb—websterite; Hz—harzburgite.

TABLE 5. $^3\text{He}/^4\text{He}$ COMPOSITION OF OLIVINES FROM ETHIOPIAN MANTLE XENOLITHS RELEASED BY IN VACUO CRUSHING

Sample	Rock type	Mineral	$^3\text{He}/^4\text{He}$ (R/R _a)
Mega (Sidamo)			
MA 15	Lh	OI	7.7 ± 0.3
MA 35	Cpx-poor Lh	OI	7.8 ± 0.5
MA 38	Cpx-poor Lh	OI	8.0 ± 0.8
MA 40	Cpx-poor Lh	OI	7.1 ± 0.1
MA 11	Hz	OI	7.4 ± 0.3
MA 24	Hz	OI	7.4 ± 0.2
MA 26	Hz	OI	7.2 ± 0.1
MA 68	Hz	OI	7.3 ± 0.1
Injibara (Gojam)			
GOJ31B	Lh	OI	6.9 ± 1.0
GOJ 16	Lh	OI	8.6 ± 1.7
GOJ 19	Cpx-poor Lh	OI	8.9 ± 1.6
GOJ4	Cpx-poor Lh	OI	7.3 ± 0.4
GOJ31C	OIWb	OI	7.5 ± 0.5
GOJ37B	OIWb	OI	7.8 ± 0.4
Dedessa (Wollega)			
WOL2	Hz	OI	6.6 ± 0.8

Note: Measured ratios (R) are normalized to the atmospheric ratio (R_a; 1.384 × 10⁻⁶). Uncertainties in $^3\text{He}/^4\text{He}$ are 1σ. Lh—lherzolite, Hz—harzburgite, OIWb—olivine-websterite, Cpx—Clinopyroxene; OI—olivine.

to 76 (Fig. 5B; Table 3B). Analogous bulk-rock and clinopyroxene REE patterns have been reported by Bedini et al. (1997).

Some clinopyroxenes occurring in small veinlets in the harzburgitic sample MA26 are characterized by positively fractionated MREE/HREE and an upward-convex LREE pattern, resembling magmatic pyroxenes from alkaline magmas (Jeffries et al., 1995).

Sample MA35 shows a peculiar V-shaped pattern in both bulk rock and clinopyroxene. The relative depletions in MREEs and HREEs can be attributed to a prior phase of depletion by melt extraction, whereas the marked LREE enrichment ($\text{La}_N/\text{Eu}_N = 14$) has to be related to a subsequent interaction with an alkaline metasomatic agent.

The observed petrographical, mineralogical, and geochemical features suggest that the Mega mantle section underwent percolation of alkali silicate metasomatic agents that reacted with the pristine paragenesis. These processes were most effective in harzburgites, where crystallization of clinopyroxene by this interaction leads to nearly magmatic REE compositions (Bianchini et al., 2007).

The Sr and Nd isotopic compositions of clinopyroxene separated from most of the Mega peridotite xenoliths have ranges of $^{87}\text{Sr}/^{86}\text{Sr} = 0.70220\text{--}0.70311$, $^{143}\text{Nd}/^{144}\text{Nd} = 0.51301\text{--}0.51379$ for lherzolites, and $^{87}\text{Sr}/^{86}\text{Sr} = 0.70268\text{--}0.70326$, $^{143}\text{Nd}/^{144}\text{Nd} = 0.51274\text{--}0.51305$ for harzburgites (Table 4). Noticeably, a single sample (MA29) displaying $^{87}\text{Sr}/^{86}\text{Sr} = 0.70454$ and $^{143}\text{Nd}/^{144}\text{Nd} = 0.51219$ demonstrates markedly more enrichment than the other samples.

As shown in Figure 6, the Sr-Nd isotope distribution mainly covers the compositional spectrum between the depleted mantle and the HIMU mantle end members, the latter of which represents the dominant component in the metasomatizing agents.

These agents affected preferentially the clinopyroxene-poor lherzolite/harzburgite mantle portions, confirming the higher permeability of the most refractory matrix to metasomatic agents (Toramaru and Fujii, 1986).

The anomalously high $^{143}\text{Nd}/^{144}\text{Nd}$ ratio (>0.5136) of samples MA35 and MA10 may reflect ancient melt extraction in the presence of residual garnet, leading to Sm/Nd fractionation similar to that observed in other mantle xenolith suites (Downes et al., 2003; Bianchini et al., 2007).

Pb isotopes for both lherzolites and harzburgites (Table 4) display the following compositional range: $^{206}\text{Pb}/^{204}\text{Pb} = 18.38\text{--}19.34$, $^{207}\text{Pb}/^{204}\text{Pb} = 15.21\text{--}15.67$, and $^{208}\text{Pb}/^{204}\text{Pb} = 37.58\text{--}38.96$. As observed in Figure 7, the Mega mantle xenoliths plot between depleted mantle and HIMU, thus confirming that this latter is the predominant isotopic signature of the metasomatizing agents.

It should be noted that the most elevated $^{206}\text{Pb}/^{204}\text{Pb}$ ratios have been recorded in some lherzolites that are only slightly affected by metasomatism as indicated by Sr-Nd isotopes and incompatible element patterns. As suggested by Beccaluva et al. (2008) for Gharyan (Libya) mantle xenoliths, this apparent incongruence may be attributed to the different behavior of Sm-Nd with respect to U-Th-Pb system due to the comparatively higher mobility of Pb, which is more sensitive to incipient metasomatic processes.

The helium isotopic composition varies between 7.1 and 8 R_a irrespective of the xenolith mode, overlapping the range that characterizes the xenoliths from the plateau area discussed previously (Table 5).

DISCUSSION AND CONCLUSIONS

The petrological and geochemical data on both bulk-rock and constituent minerals presented here, taken together, indicate that mantle xenolith populations from the plateau area (Injibara and Dedessa) and those from the Main Ethiopian Rift (Mega) experienced similar pre-Paleozoic depletion events (Reisberg et al., 2004) but were subsequently subjected to distinctive deformation and metasomatic/refertilization processes.

Mantle xenolith populations from both the plateau area and the rift delineate a common depletion trend from highly fertile clinopyroxene-rich spinel-lherzolites to clinopyroxene-poor spinel-lherzolites up to spinel-harzburgites. Thermobarometric estimates suggest that these mantle materials underwent reequilibration within the spinel-peridotite stability field (9–19 kbar; Green and Falloon, 2005) before their transport to the surface by Neogene–Quaternary alkaline magmas.

The pressure-temperature history prior to the eruption is more complicated. Lithospheric sections beneath the plateau show only limited evidence of rheological deformation (compatible with a long residence under relatively stable *P-T* conditions), whereas mantle domains underlying the Main Ethiopian Rift display an intense deformation history implying multistage uprising of mantle material, with partial reequilibration at shallower lithospheric levels, during the rift development (Kendall et al., 2006).

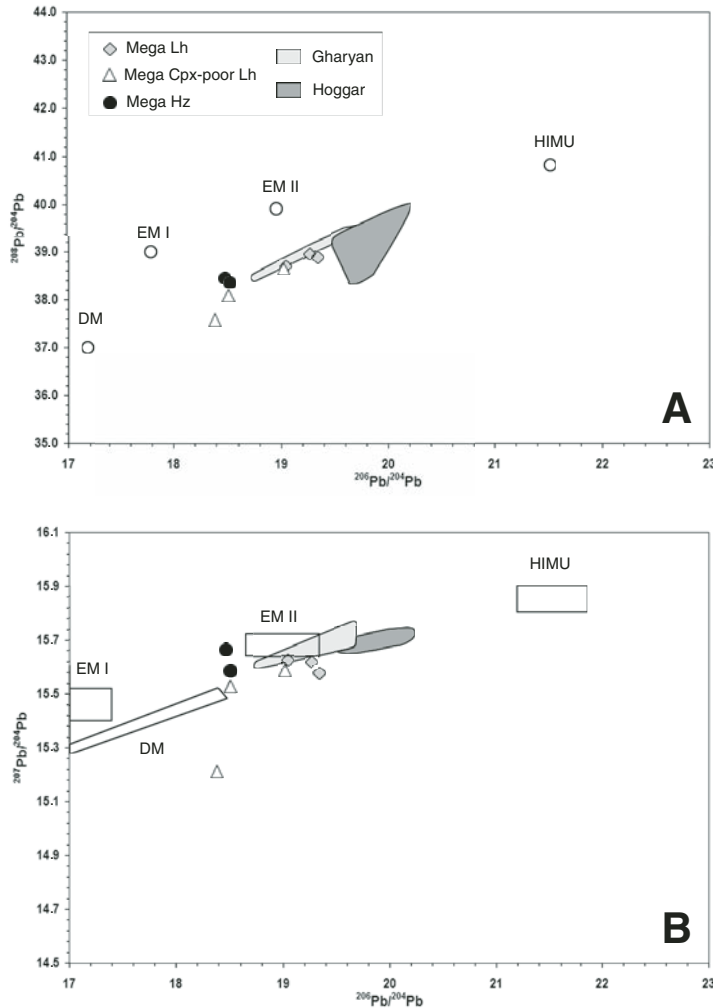


Figure 7. Pb isotopic ratios of clinopyroxene from Mega mantle xenoliths. Isotopic compositional field of mantle xenoliths from Hoggar (Algeria) and Gharyan (Libya) are reported for comparison after Beccaluva et al. (2007, 2008). Depleted mantle (DM), high- μ (HIMU), enriched mantle (EM I), and EM II are after Zindler and Hart (1986). Abbreviations: Lh—lherzolite; Cpx—Clinopyroxene; Hz—harzburgite.

Petrographical and geochemical evidence can also be used to provide insight into the metasomatic processes in mantle xenolith populations. Beneath the plateau area, these processes induced mineralogical, elemental, and isotopic variations in the pristine parageneses, lowering the Mg# of the mineral phases, causing orthopyroxene neocrystallization (at expense of olivine), and ultimately leading to widespread olivine-websterite domains; trace-element and isotopic data indicate that the causative agents were subalkaline melts closely resembling the continental flood basalt magmas related to the Afar plume (Fig. 8A). The percolation of these melts, coming from the impinging plume head, caused important asthenosphere-lithosphere interactions and thermochemical erosion of the preexisting lithosphere that was widely refertilized and rejuvenated.

On the other hand, mantle sections beneath the Main Ethiopian Rift underwent completely different metasomatic processes, particularly affecting the most refractory harzburgite domains. Modal evidences are provided by reaction textures and development of clinopyroxene veinlets. In this case, trace-element (Fig. 8B) and isotopic data indicate that the causative agents

were alkaline basic melts with a HIMU-like signature in analogy with the prevalent magmatic affinity of the Neogene–Quaternary Main Ethiopian Rift volcanism.

Moreover, the marked Zr–Ti negative anomalies observed in some of the modeled metasomatic agents may indicate a variable enrichment of carbonated components in these melts (Coltorti et al., 1999; Beccaluva et al., 2007). These features, together with xenolith deformation textures, indicate that the Mega xenoliths record mantle passive upwelling that is unrelated to the Afar plume and closely connected to the development of the Main Ethiopian Rift.

In this regard, the anomalously high $^{143}\text{Nd}/^{144}\text{Nd}$ ratios of some lherzolites may reflect a pristine residence in the garnet stability field (i.e., >20 kbar) prior to the uplift and reequilibration in the spinel-peridotite stability field. This is in agreement with seismic anisotropy data indicating mantle flow beneath the East African Rift system (Kendall et al., 2006).

Regional comparison highlights analogies and differences between Ethiopian mantle xenoliths and mantle materials from other African–Arabian occurrences. The Assab mantle xenolith

population, erupted by Quaternary alkaline volcanism along the Afar rifted margin, includes olivine websterites and pyroxenites lithologically and isotopically (Zanetti et al., 2009; Teklay et al., 2010) similar to those from Injibara and Dedessa River. This suggests a common refertilization of these mantle sections by plume-related subalkaline melts, before continental breakup and rift development.

In contrast, spinel-lherzolite xenoliths from the rifted continental margins of the Arabian Peninsula set along the Red Sea (Ottonello, 1980; Henjes-Kunst et al., 1990) and the Gulf of Aden (Baker et al., 1998) commonly show metasomatic effects by alkali silicate agents analogous to Main Ethiopian Rift xenoliths at Mega. Similar alkali silicate metasomatism with HIMU iso-

topic affinity has also been recognized all over the Saharan belt from Sudan to Morocco (Bayuda, Sudan—Lucassen et al., 2008; Gharyan—Beccaluva et al., 2008; Hoggar, Algeria—Dautria et al., 1997; Beccaluva et al., 2007; Mid Atlas, Morocco—Raffone et al., 2009).

Extending the comparison south of Main Ethiopian Rift, peridotite xenoliths from the Marsabit volcanic field (Kenya Rift) show deformation textures and alkaline metasomatism analogous to those of Mega. In this case, mantle decompression from the garnet to spinel stability field is modally recorded by rounded pyroxene-spinel symplectites (Kaesler et al., 2006).

Further south, along the Tanzanian sector of the East African Rift, peridotite xenolith populations (including lherzolites,

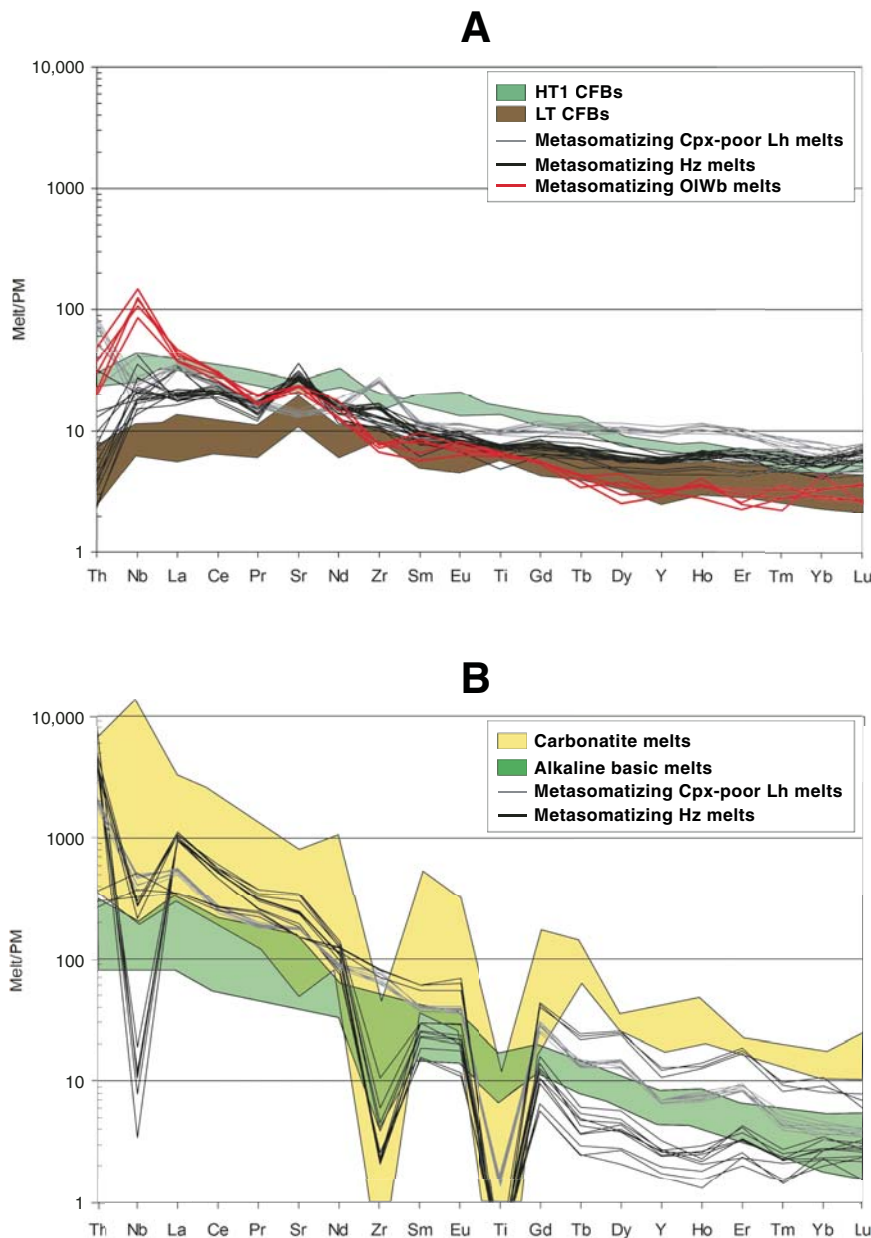


Figure 8. Primitive mantle (PM)-normalized incompatible element patterns of the calculated metasomatic agents that refertilized mantle xenoliths from Injibara and Dedessa (A) and Mega (B). Calculations were carried out on metasomatized clinopyroxenes in clinopyroxene-poor lherzolites (1 and 4), lherzolites (2), olivine-websterites (3), and harzburgites (5) using partition coefficients clinopyroxene/subalkaline basic melts (A) and clinopyroxene/alkaline basic melts (B) from GERM database (<http://earthref.org/GERM>). Compositional envelopes of LT (low titanium) and HT1 (high titanium) tholeiites from the Northern Ethiopian Plateau (after Beccaluva et al., 2009) are reported in A; compositional envelopes of alkaline basic melts (after Azzouni-Sekkal et al., 2007; Beccaluva et al., 1998; Bianchini et al., 1998; Janney et al., 2002) and carbonatites (after Coltorti et al., 1993; Nelson et al., 1998; Smithies and Marsh, 1998) from the African plate are reported in B. Normalizing factors are after Sun and McDonough (1989). Abbreviations: Lh—lherzolite; Cpx—Clinopyroxene; Ol—olivine; Wb—websterite; Hz—harzburgite; CFBs—continental flood basalts.

harzburgites, and wehrlites, sometimes garnet bearing) show widespread metasomatic evidence modally reflected in the presence of amphibole, phlogopite, apatite, and ilmenite (Pello Hill—Dawson and Smith, 1988; Labait—Dawson, 1999; Lashaine—Dawson, 2002). Detailed trace-element and isotopic studies of these xenoliths (Aulbach et al., this volume) show a wide compositional range from HIMU to extreme enriched mantle components, where HIMU-like silicate and carbonatitic agents are related to the Cenozoic rift evolution and variously overprint an ancient lithospheric mantle characterized by enriched mantle signature.

The regional distribution of mantle xenoliths from Ethiopia and the neighboring regions enables us to define the geodynamic evolution that affected the Horn of Africa from the plume-related continental flood basalt generation to the subsequent rift-related volcano-tectonic system (Fig. 9).

An impinging plume (probably triggered since the late Eocene) induced a generalized lithosphere arching and its rejuvenation by plume-related metasomatic components, leading to the generation of a compositionally and thermally zoned plume head from which Oligocene (ca. 30 Ma) continental flood basalt magmas of the Northern Ethiopian–Yemen Plateau were generated (Fig. 9A; Beccaluva et al., 2009). During this phase, plume-related subalkaline melts interacted with the pristine mantle parageneses, converting olivine to orthopyroxene, and thus leading to the olivine websterite domains seen in the Injibara and Dedessa River xenoliths; this process was coupled with incompatible element enrichment and Sr–Nd isotope variation from depleted mantle to the Afar plume signature.

Starting from the late Oligocene, the evolution is characterized by a generalized extension, radiating from the Afar triple point and leading to the gradual opening of the Red Sea and Gulf of Aden oceanic systems, as well as to the development of the Main Ethiopian Rift (Fig. 9B).

It should be noted that unlike Yemen, continental flood basalts of northern Ethiopia were overlain by huge shield volcanoes mainly of transitional-alkaline affinity ranging in age from 22 to 11 Ma (Kieffer et al., 2004). The large volumes of these lavas and the geochemical transition with the underlying continental flood basalt suggest that their generation could be related to the persistence, although vanishing with time, of the plume tail below the Northern Ethiopian Plateau. Similarly, the Miocene volcanic activity of North Sheva in the southern part of the plateau has been also related to magma generation in connection with the Afar plume head-tail transition (Ayalew and Gibson, 2009).

The lack of Miocene shield volcanoes overlying the continental flood basalts in Yemen confirms that the African–Nubian plate is relatively stable with respect to the Afar plume axis, whereas the Arabian plate progressively migrated northeastward far from the plume-tail influence (Bellahsen et al., 2003).

A generalized E–W cross section of the southernmost part of Main Ethiopian Rift (Fig. 9C) enables the data to be put into a regional perspective. Specifically, peridotite xenoliths entrained

in Pliocene–Quaternary alkaline lavas at Mega enable us to evaluate the mantle evolution in the area: (1) The pristine mantle material was variably depleted by ancient events leading to spinel-lherzolites to harzburgites characterized by depleted mantle isotopic compositions. (2) This lithospheric mantle section was subsequently affected by interaction with HIMU alkaline metasomatizing agents, coupled with deformation events possibly acquired during the development of the Main Ethiopian Rift system. These observations are in agreement with seismic anisotropy data indicating mantle flow oriented in a rift-parallel direction beneath the East African Rift system (Kendall et al., 2006).

These considerations lead to the conclusion that the geological evolution of the Horn of Africa was influenced by the activation of a deep mantle plume centered in the Afar region, which produced Oligocene continental flood basalt volcanism and extensive refertilization of the underlying lithospheric mantle by subalkaline agents. The paroxysmal plume phase was followed by a general extensional regime extending far beyond the Afar plume, during which the development of the East African Rift System was accompanied by shallow mantle upwelling events and metasomatic processes dominated by alkaline agents with HIMU affinity.

ACKNOWLEDGMENTS

The authors gratefully acknowledge the critical reading of the manuscript by G.B. Piccardo and J. Bryce. Thanks for analytical facilities are also due to R. Tassinari (X-ray fluorescence and inductively coupled plasma–mass spectrometry [ICP-MS]), R. Carampin (electron microprobe), and A. Zanetti (laser ablation ICP-MS).


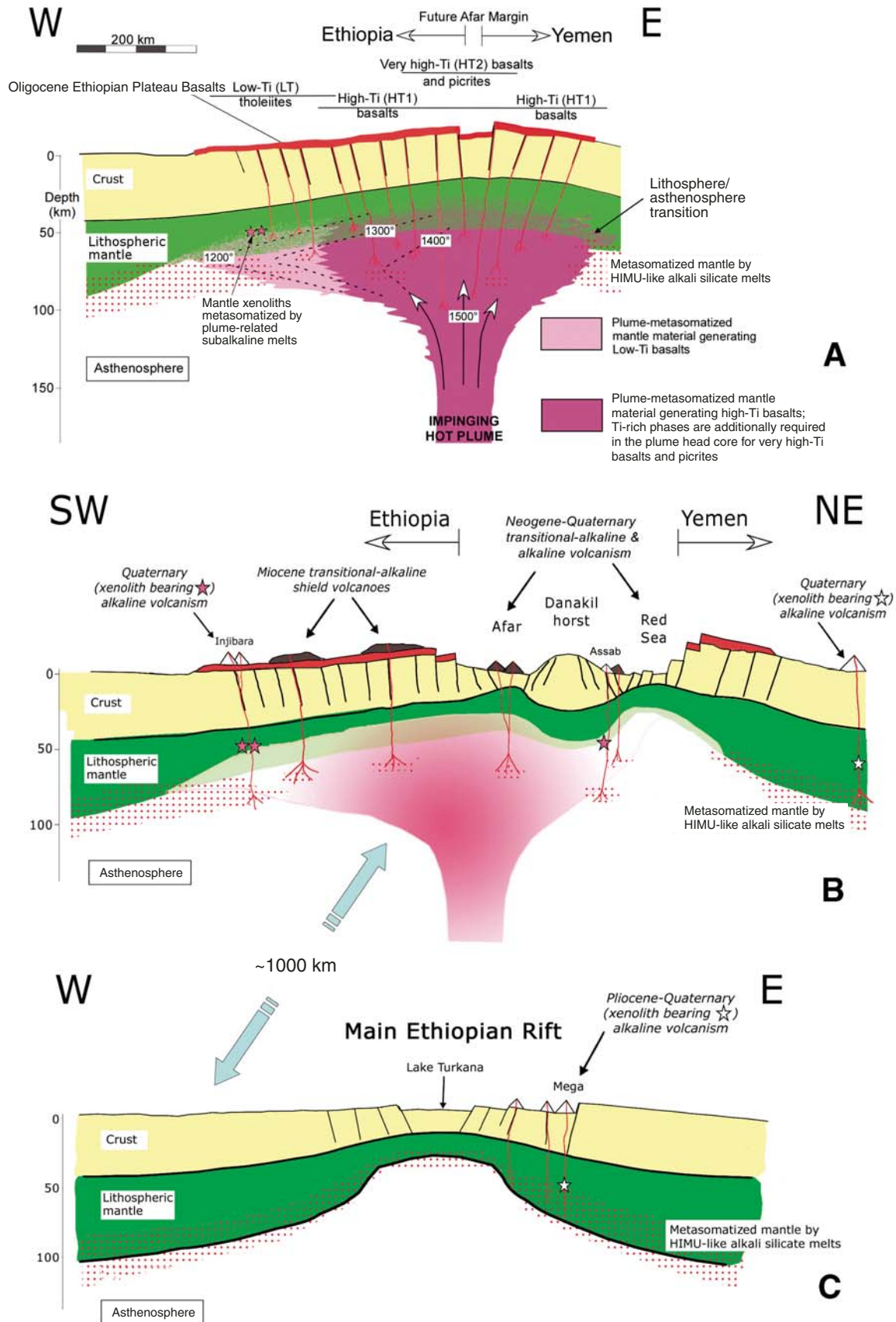


Figure 9. Schematic cross sections illustrating the tectonomagmatic evolution of the African-Arabian system from Oligocene to present. (A) The Afar plume impinged the African-Arabian lithosphere, generating the Oligocene northern Ethiopia–Yemen continental flood basalts from a thermally and compositionally zoned plume head (modified after Beccaluva et al., 2009). Lithospheric mantle sections were widely refertilized by plume-related melts (similar to LT [low titanium] and HT1 [high titanium] tholeiites), as evidenced by mantle xenoliths exhumed by alkaline Quaternary lavas at Injibara and Dedessa River. (B) The Neogene–Quaternary evolution is characterized by a generalized extensional regime, ultimately leading to the development of the Main Ethiopian Rift and the oceanic opening of the Red Sea and Gulf of Aden. This was accompanied by the gradual vanishing of the Afar plume head, as testified by the alkaline-transitional affinity of both Miocene shield volcanoes on the Northern Ethiopian Plateau, and the Neogene–Quaternary transitional to alkaline volcanism of the African-Arabian rift system. (C) An E–W section across the southernmost part of the present-day Main Ethiopian Rift. Pliocene–Quaternary alkaline lavas at the eastern border of the Main Ethiopian Rift entrained lithospheric mantle xenoliths that were metasomatized by HIMU-like alkali-silicate melts: This reflects the prevalent geochemical signature of the metasomatizing agents of the African-Arabian rift system as well as of the northern African plate.



APPENDIX: ANALYTICAL METHODS

Rock samples were selected from fresh chips and powdered in an agate mill. X-ray fluorescence (XRF) of major and trace elements (Ni, Co, Cr, V, and Sr) was analyzed on powder pellets using a wavelength-dispersive automated Philips PW 1400 spectrometer at the Department of Earth Sciences, Ferrara University, Italy. Accuracy and precision for major elements are estimated as better than 3% for Si, Ti, Fe, Ca, and K, and 7% for Mg, Al, Mn, Na; for trace elements (above 10 ppm), they are better than 10%. REEs, Sc, Y, Zr, Hf, Nb, Th, and U were analyzed by inductively coupled plasma-mass spectrometry (ICP-MS) at the Department of Earth Sciences, Ferrara University, using a Thermo-Scientific X-Series. Accuracy and precision, based on the replicated analyses of samples and standards, are estimated as better than 10% for all elements, well above the detection limit.

Mineral compositions were obtained at the CNR (Consiglio Nazionale delle Ricerche)–IGG (Istituto di Geoscienze e Georisorse) Institute of Padova with a Cameca-Camebax electron microprobe (fitted with three wavelength-dispersive spectrometers) at an accelerating voltage of 15 kV, and specimen current of 15 nA, using natural silicates and oxides as standards. In situ trace-element analyses on pyroxenes were carried out at the CNR-IGG of Pavia by laser ablation microanalysis ICP-MS, using an Elan DRC-e mass spectrometer coupled with a Q-switched Nd:YAG laser source (Quantalet Brilliant). CaO content was used as internal standard. Precision and accuracy, better than 10% for concentrations at ppm level, were assessed by repeated analyses of NIST SRM 612 and BCR-2 standards.

Sr-Nd-Pb isotopic analyses on separated (by handpicking) clinopyroxene (~200 mg) were carried out at SUERC (Scottish Universities Environmental Research Centre). Samples were digested with a mixture of HF-HNO₃-HCl and prepared as described by Hardarson et al. (1997). Sr samples were analyzed using a VG Sector 54-30 mass spectrometer in multidynamic mode using an exponential correction for mass fractionation and ⁸⁶Sr/⁸⁸Sr = 0.1194. Nd and Pb isotopes were analyzed using a Micromass IsoProbe multicollector ICP-MS. Pb was measured using the method similar to that described by Ellam (2006). NIST SRM981 gave ²⁰⁶Pb/²⁰⁴Pb = 16.940 ± 7, 15.496 ± 6, and 36.708 ± 15 (2 standard deviations [S.D.], *n* = 22). Nd was measured in multidynamic mode. Nd isotope ratios were collected as six blocks of 20 dynamic (3 mass) cycles with an on-peak zero measurement for each block determined in a blank solution of 5% (v/v) nitric acid used to make up the sample solutions. Mass bias was corrected using ¹⁴⁴Nd/¹⁴⁶Nd = 0.7219 and an exponential law. The internal laboratory Nd “standard” (JM) gave ¹⁴³Nd/¹⁴⁴Nd = 0.511481 ± 15 (*n* = 10), which is within the error of the long-term mean of 0.511499 ± 10 (all errors 2 S.D.) obtained by thermal ionization mass spectrometry (TIMS). Two determinations on the BCR-1 geostandard gave ¹⁴³Nd/¹⁴⁴Nd = 0.512615 ± 14 (2 standard error [S.E.]) and 0.512629 ± 14 (2 S.E.). Each ¹⁴³Nd/¹⁴⁴Nd measurement consumed ~150 ng of Nd.

Mineral separates for helium isotope analysis were picked under a binocular microscope and washed ultrasonically in HNO₃ and then water, prior to a final treatment with analar acetone. Helium was extracted from all minerals by in vacuo crushing and analyzed using a MAP 215-50 mass spectrometer at SUERC using procedures slightly modified from Stuart et al. (2000).

REFERENCES CITED

- Aulbach, S., Rudnick, R.L., and McDonough, W.F., 2011, this volume, Evolution of the lithospheric mantle beneath the East African Rift in Tanzania and its potential signatures in rift magmas, *in* Beccaluva, L., Bianchini, G., and Wilson, M., eds., *Volcanism and Evolution of the African Lithosphere*: Geological Society of America Special Paper 478, doi:10.1130/2011.2478(06).
- Ayalew, D., and Gibson, S.A., 2009, Head-to-tail transition of the Afar mantle plume: Geochemical evidence from a Miocene bimodal basalt-rhyolite succession in the Ethiopian large igneous province: *Lithos*, v. 112, p. 461–476, doi:10.1016/j.lithos.2009.04.005.
- Ayalew, D., Arndt, N., Bastien, F., Yirgu, G., and Kieffer, B., 2009, A new mantle xenolith locality from Simien shield volcano, NW Ethiopia: *Geological Magazine*, v. 146, p. 144–149, doi:10.1017/S0016756808005785.
- Azzouni-Sekkal, A., Bonin, B., Benhallou, A., Yahiaoui, R., and Liégeois, J.-L., 2007, Tertiary alkaline volcanism of the Atakor Massif (Hoggar, Algeria), *in* Beccaluva, L., Bianchini, G., and Wilson, M., eds., *Cenozoic Volcanism in the Mediterranean Area*: Geological Society of America Special Paper 418, p. 321–340.
- Baker, J., Chazot, G., Menzies, M., and Thirlwall, M., 1998, Metasomatism of the shallow mantle beneath Yemen by the Afar plume—Implications for mantle plumes, flood volcanism, and intraplate volcanism: *Geology*, v. 26, p. 431–434, doi:10.1130/0091-7613(1998)026<0431:MOTSMB>2.3.CO;2.
- Bastow, I.D., Keir, D., and Daly, E., 2011, this volume, The Ethiopia Afar Geoscientific Lithospheric Experiment (EAGLE): Probing the transition from continental rifting to incipient seafloor spreading, *in* Beccaluva, L., Bianchini, G., and Wilson, M., eds., *Volcanism and Evolution of the African Lithosphere*: Geological Society of America Special Paper 478, doi:10.1130/2011.2478(04).
- Beccaluva, L., Siena, F., Coltorti, M., Di Grande, A., Lo Giudice, A., Macciotta, G., Tassinari, R., and Vaccaro, C., 1998, Nephelinitic to tholeiitic magma generation in a transtensional tectonic setting: An integrated model for the Iblean volcanism, Sicily: *Journal of Petrology*, v. 39, p. 1547–1576, doi:10.1093/petrology/39.9.1547.
- Beccaluva, L., Azzouni-Sekkal, A., Benhallou, A., Bianchini, G., Ellam, R.M., Marzola, M., Siena, F., and Stuart, F.M., 2007, Intracratonic asthenosphere upwelling and lithosphere rejuvenation beneath the Hoggar swell (Algeria): Evidence from HIMU metasomatised lherzolite mantle xenoliths: *Earth and Planetary Science Letters*, v. 260, p. 482–494, doi:10.1016/j.epsl.2007.05.047.
- Beccaluva, L., Bianchini, G., Ellam, R.M., Marzola, M., Oun, K.M., Siena, F., and Stuart, F.M., 2008, The role of HIMU metasomatic components in the African lithospheric mantle: Petrological evidence from the Gharyan peridotite xenoliths, NW Libya, *in* Coltorti, M., and Grégoire, M., eds., *Metasomatism in Oceanic and Continental Lithospheric Mantle*: Geological Society of London Special Publication 293, p. 253–277.
- Beccaluva, L., Bianchini, G., Natali, C., and Siena, F., 2009, Continental flood basalts and mantle plumes: A case study of the Northern Ethiopian Plateau: *Journal of Petrology*, v. 50, p. 1377–1403, doi:10.1093/petrology/egp024.
- Bedini, R.M., Bodinier, J.-L., Dautria, J.-M., and Morten, L., 1997, Evolution of LILE-enriched small melt fractions in the lithospheric mantle: A case study from the East African Rift: *Earth and Planetary Science Letters*, v. 153, p. 67–83, doi:10.1016/S0012-821X(97)00167-2.
- Bellahsen, N., Faccenna, C., Funicello, F., Daniel, J.M., and Jolivet, L., 2003, Why did Arabia separate from Africa? Insights from 3-D laboratory experiments: *Earth and Planetary Science Letters*, v. 216, p. 365–381, doi:10.1016/S0012-821X(03)00516-8.
- Bianchini, G., Clocchiatti, R., Coltorti, M., Joron, J.L., and Vaccaro, C., 1998, Petrogenesis of mafic lavas from the northernmost sector of the Iblean District (Sicily): *European Journal of Mineralogy*, v. 10, p. 301–315.
- Bianchini, G., Beccaluva, L., Bonadiman, C., Nowell, G., Pearson, G., Siena, F., and Wilson, M., 2007, Evidence of diverse depletion and metasomatic events in harzburgite-lherzolite mantle xenoliths from the Iberian plate (Olot, NE Spain): Implications for lithosphere accretionary processes: *Lithos*, v. 94, p. 25–45, doi:10.1016/j.lithos.2006.06.008.
- Blusztajn, J., Hart, S.R., Shimizu, N., and McGuire, A.V., 1995, Trace-element and isotopic characteristics of spinel peridotite xenoliths from Saudi Arabia: *Chemical Geology*, v. 123, p. 53–65, doi:10.1016/0009-2541(95)00044-M.
- Brey, G.P., and Köhler, T., 1990, Geothermobarometry in four-phase lherzolites. II. New thermobarometers, and practical assessment of existing thermobarometers: *Journal of Petrology*, v. 31, p. 1353–1378.
- Brueckner, H.K., Zindler, A., Seyler, M., and Bonatti, E., 1988, Zabargad and the isotopic evolution of the sub-Red Sea mantle and crust: *Tectonophysics*, v. 150, p. 163–176, doi:10.1016/0040-1951(88)90300-9.
- Coltorti, M., Alberti, A., Beccaluva, L., Dos Santos, A.B., Mazzucchelli, M., Morais, E., Rivalenti, G., and Siena, F., 1993, The Tchivira-Bonga alkaline-carbonatite complex (Angola): Petrological study and

- comparison with some Brazilian analogues: *European Journal of Mineralogy*, v. 5, p. 1001–1024.
- Coltorti, M., Bonadiman, C., Hinton, R.W., Siena, F., and Upton, B.G.J., 1999, Carbonatite metasomatism of the oceanic upper mantle: Evidence from clinopyroxenes and glasses in ultramafic xenoliths of Grande Comore, Indian Ocean: *Journal of Petrology*, v. 40, p. 133–165, doi:10.1093/petrology/40.1.133.
- Conticelli, S., Sintoni, M.F., Abebe, T., Mazzarini, F., and Manetti, P., 1999, Petrology and geochemistry of ultramafic xenoliths and host lavas from the Ethiopian volcanic province: An insight into the upper mantle under eastern Africa: *Acta Vulcanologica*, v. 11, p. 143–159.
- Corti, G., 2009, Continental rift evolution: From rift initiation to incipient break-up in the Main Ethiopian Rift, East Africa: *Earth-Science Reviews*, v. 96, p. 1–53, doi:10.1016/j.earscirev.2009.06.005.
- Dautria, J.M., Dupuy, C., Takherist, D., and Dostal, J., 1992, Carbonate metasomatism in the lithospheric mantle: The peridotitic xenoliths from a melilitic district of the Sahara Basin: *Contributions to Mineralogy and Petrology*, v. 111, p. 37–52, doi:10.1007/BF00296576.
- Davaille, A., Stutzmann, E., Silveira, G., Besse, J., and Courtillot, V., 2005, Convective patterns under the Indo-Atlantic: *Earth and Planetary Science Letters*, v. 239, p. 233–252, doi:10.1016/j.epsl.2005.07.024.
- Dawson, J.B., 1999, Metasomatism and melting in spinel peridotite xenoliths from Labait, Tanzania, in Gurney, J.J., Gurney, J.L., Pascoe, M.D., and Richardson, S.H., eds., *Proceedings Volume of 7th International Kimberlite Conference*: Cape Town, Red Roof Design, p. 164–173.
- Dawson, J.B., 2002, Metasomatism and partial melting in upper mantle peridotite xenoliths from the Lashaine volcano, northern Tanzania: *Journal of Petrology*, v. 43, p. 1749–1777, doi:10.1093/petrology/43.9.1749.
- Dawson, J.B., and Smith, J.V., 1988, Metasomatized and veined upper-mantle xenoliths from Pello Hill, Tanzania—Evidence for anomalously-light mantle beneath the Tanzanian sector of the East African Rift valley: *Contributions to Mineralogy and Petrology*, v. 100, p. 510–527, doi:10.1007/BF00371380.
- Downes, H., Reichow, M.K., Mason, P.R.D., Beard, A.D., and Thirlwall, M.F., 2003, Mantle domains in the lithosphere beneath the French Massif Central: Trace element and isotopic evidence from mantle clinopyroxenes: *Chemical Geology*, v. 200, p. 71–87, doi:10.1016/S0009-2541(03)00126-8.
- Ellam, R.M., 2006, New constraints on the petrogenesis of the Nuanetsi picrite basalts from Pb and Hf isotope data: *Earth and Planetary Science Letters*, v. 245, p. 153–161, doi:10.1016/j.epsl.2006.03.004.
- Ernst, R.E., and Buchan, K.L., eds., 2001, *Mantle Plumes: Their Identification through Time*: Geological Society of America Special Paper 352, 593 p.
- Ferrando, S., Frezzotti, M.L., Neumann, E.-R., De Astis, G., Peccerillo, A., Dereje, A., Gezahegn, Y., and Teklewold, A., 2008, Composition and thermal structure of the lithosphere beneath the Ethiopian Plateau: Evidence from mantle xenoliths in basanites, Injibara, Lake Tana Province: *Mineralogy and Petrology*, v. 93, p. 47–78, doi:10.1007/s00710-007-0219-z.
- Foulger, G.R., and Jurdy, D.M., eds., 2007, *Plates, Plumes, and Planetary Processes*: Geological Society of America Special Paper 430, 997 p.
- Foulger, G.R., Natland, J.H., Presnall, D.C., and Anderson, D.L., eds., 2005, *Plates, Plumes, and Paradigms*: Geological Society of America Special Paper 388, 881 p.
- George, R.M., and Rogers, N.W., 2002, Plume dynamics beneath the African plate inferred from the geochemistry of the Tertiary basalts from southern Ethiopia: *Contributions to Mineralogy and Petrology*, v. 144, p. 286–304, doi:10.1007/s00410-002-0396-z.
- Green, D.H., and Falloon, T.J., 2005, Primary magmas at mid-ocean ridges, “hotspots,” and other intraplate setting: Constraints on mantle potential temperature, in Foulger, G.R., Natland, J.H., Presnall, D.C., and Anderson, D.L., eds., *Plates, Plumes, and Paradigms*: Geological Society of America Special Paper 388, p. 217–247.
- Hardarson, B.S., Fitton, J.G., Ellam, R.M., and Pringle, M.S., 1997, Rift relocation—A geochemical and geochronological investigation of a palaeo-rift in northwest Iceland: *Earth and Planetary Science Letters*, v. 153, p. 181–196, doi:10.1016/S0012-821X(97)00145-3.
- Henjes-Kunst, F., Altherr, F., and Baumann, A., 1990, Evolution and composition of the lithospheric mantle underneath the western Arabian peninsula: Constraints from Sr-Nd and type systematics of mantle xenoliths: *Contributions to Mineralogy and Petrology*, v. 105, p. 460–472, doi:10.1007/BF00286833.
- Hofmann, A.W., 1997, Mantle geochemistry: The message from oceanic volcanism: *Nature*, v. 385, p. 219–229, doi:10.1038/385219a0.
- Janney, P.E., Le Roex, A.P., Carlson, R.W., and Viljoen, K.S., 2002, A chemical and multi-isotope study of the Western Cape olivine melilitite province, South Africa: Implications for the sources of kimberlites and the origin of the HIMU signature in Africa: *Journal of Petrology*, v. 43, p. 2339–2370, doi:10.1093/petrology/43.12.2339.
- Jeffries, T.E., Perkins, W.T., and Pearce, N.J.G., 1995, Measurements of trace elements in basalts and their phenocrysts by laser probe microanalysis inductively coupled plasma mass spectrometry (LPMA-ICP-MS): *Chemical Geology*, v. 121, p. 131–144, doi:10.1016/0009-2541(94)00121-N.
- Kaesler, B., Kalt, A., and Pettker, T., 2006, Evolution of the lithospheric mantle beneath the Marsabit volcanic field (northern Kenya): Constraints from textural, *P-T* and geochemical studies on xenoliths: *Journal of Petrology*, v. 47, p. 2149–2184, doi:10.1093/petrology/egl040.
- Kendall, J.-M., Pilidou, S., Keir, D., Bastow, I.D., Stuart, G.W., and Ayele, A., 2006, Mantle upwellings, melt migration and rifting of Africa: Insight from seismic anisotropy, in Yirgu, G., Ebinger, C.J., and Maguire, P.K.H., eds., *The Afar Volcanic Province within the East African Rift System*: Geological Society of London Special Publication 259, p. 55–72.
- Kieffer, B., Arndt, N., Lapiere, H., Bastien, F., Bosch, D., Pecher, A., Yirgu, G., Ayalew, D., Weis, D., Jerram, D.A., Keller, F., and Meugnot, C., 2004, Flood and shield basalts from Ethiopia: Magmas from the African superwell: *Journal of Petrology*, v. 45, p. 793–834, doi:10.1093/petrology/egg112.
- Köhler, T., and Brey, G.P., 1990, Ca-exchange between olivine and clinopyroxene as a geothermobarometer calibrated from 2 to 60 kbar in primitive natural ilherzolites: *Geochimica et Cosmochimica Acta*, v. 54, p. 2375–2388, doi:10.1016/0016-7037(90)90226-B.
- Lucassen, F., Franz, G., Romer, R.L., Pudlo, D., and Dulski, P., 2008, Nd, Pb, and Sr isotope composition of late Mesozoic to Quaternary intra-plate magmatism in NE-Africa (Sudan, Egypt): High- μ signatures from the mantle lithosphere: *Contributions to Mineralogy and Petrology*, v. 156, p. 765–784, doi:10.1007/s00410-008-0314-0.
- McDonough, W.F., and Sun, S.S., 1995, Composition of the Earth: *Chemical Geology*, v. 120, p. 223–253, doi:10.1016/0009-2541(94)00140-4.
- Nelson, D.R., Chivas, A.R., Chappell, B.W., and McCulloch, M.T., 1998, Geochemical and isotopic systematics in carbonatites and implications for the evolution of ocean island sources: *Geochimica et Cosmochimica Acta*, v. 52, p. 1–17, doi:10.1016/0016-7037(88)90051-8.
- Niu, Y., 1997, Mantle melting and melt extraction processes beneath ocean ridges: Evidence from abyssal peridotites: *Journal of Petrology*, v. 38, p. 1047–1074, doi:10.1093/petrology/38.8.1047.
- Orlando, A., Abebe, T., Manetti, P., Santo, A.P., and Corti, G., 2006, Petrology of mantle xenoliths from Megado and Dilo, Kenya Rift, southern Ethiopia: *Ophiolite*, v. 32, p. 71–87.
- Ottone, G., 1980, Rare earth abundances and distribution in some spinel peridotite xenoliths from Assab (Ethiopia): *Geochimica et Cosmochimica Acta*, v. 44, p. 1885–1901, doi:10.1016/0016-7037(80)90237-9.
- Pik, R., Deniel, C., Coulon, C., Yirgu, G., and Marty, B., 1999, Isotopic and trace element signatures of Ethiopian basalts: Evidence for plume-lithospheric interactions: *Geochimica et Cosmochimica Acta*, v. 63, p. 2263–2279, doi:10.1016/S0016-7037(99)00141-6.
- Pik, R., Marty, B., and Hilton, D.R., 2006, How many mantle plumes in Africa? The geochemical point of view: *Chemical Geology*, v. 226, p. 100–114, doi:10.1016/j.chemgeo.2005.09.016.
- Raffone, N., Chazot, G., Pin, C., Vannucci, R., and Zanetti, A., 2009, Metasomatism in the lithospheric mantle beneath Middle Atlas (Morocco) and the origin of Fe- and Mg-rich wehrlites: *Journal of Petrology*, v. 50, p. 197–249, doi:10.1093/petrology/egn069.
- Reisberg, L.C., Lorland, J.-P., and Bedini, R.M., 2004, Reliability of Os model ages in pervasively metasomatised continental mantle lithosphere: A case study of Sidamo spinel peridotite xenoliths (East African Rift, Ethiopia): *Chemical Geology*, v. 208, p. 119–140, doi:10.1016/j.chemgeo.2004.04.008.
- Roger, S., Pik, R., Dautria, J.-M., Coulon, C., Yirgu, G., Ayalew, D., and Legros, P., 1997, Rifting actif ou passif en Ethiopie? Eléments de réponse apportés par l’étude des xenolithes peridotitiques de la region du lac Tana (Active or passive rifting in Ethiopia? Contribution of peridotitic xenoliths from the Lake Tana area): *Académie des Sciences Compte Rendus, Sciences de la Terre et des Planètes*, v. 324, p. 1009–1016.
- Roger, S., Dautria, J.-M., Coulon, C., Pik, R., Yirgu, G., Michard, A., Legros, P., and Ayalew, D., 1999, An insight on the nature, composition and evolution of the lithospheric mantle beneath the north-western Ethiopian Plateau:

- The ultrabasic xenoliths from the Tana Lake Province: *Acta Vulcanologica*, v. 11, p. 161–168.
- Rogers, N.W., MacDonald, R., Fitton, J.G., George, R., Smith, M., and Barreiro, B., 2000, Two mantle plumes beneath East African Rift system: Sr, Nd, and Pb isotope evidence from Kenya Rift basalts: *Earth and Planetary Science Letters*, v. 176, p. 387–400, doi:10.1016/S0012-821X(00)00012-1.
- Smithies, R.H., and Marsh, J.S., 1998, The Marinkas Quellen carbonatite complex, southern Namibia; carbonatite magmatism with an uncontaminated depleted mantle signature in a continental setting: *Chemical Geology*, v. 148, p. 201–212, doi:10.1016/S0009-2541(98)00029-1.
- Stewart, K., and Rogers, N., 1996, Mantle plume and lithosphere contributions to basalts from southern Ethiopia: *Earth and Planetary Science Letters*, v. 139, p. 195–211, doi:10.1016/0012-821X(96)00015-5.
- Stuart, F.M., Ellam, R.M., Harrop, P.J., Fitton, J.G., and Bell, B.R., 2000, Constraints on mantle plumes from the helium isotopic composition of basalts from the British Tertiary igneous province: *Earth and Planetary Science Letters*, v. 177, p. 273–285, doi:10.1016/S0012-821X(00)00050-9.
- Sun, S.S., and McDonough, W.F., 1989, Chemical and isotopic systematics of oceanic basalts: Implications for mantle composition and processes, *in* Saunders, A.D., and Norry, M.J., eds., *Magmatism in the Ocean Basins*: Geological Society of London Special Publication 42, p. 313–347.
- Teklay, M., Scherer, E.E., Mezger, K., and Danyushevsky, L., 2010, Geochemical characteristics and Sr-Nd-Hf isotope compositions of mantle xenoliths and host basalts from Assab, Eritrea: Implications for the composition and thermal structure of the lithosphere beneath the Afar Depression: *Contributions to Mineralogy and Petrology*, v. 159, p. 731–751, doi:10.1007/s00410-009-0451-0.
- Toramaru, A., and Fujii, N., 1986, Connectivity of melt phase in a partially molten peridotite: *Journal of Geophysical Research*, v. 91, p. 9239–9252, doi:10.1029/JB091iB09p09239.
- Zanetti, A., Piccardo, G.B., Raffone, N., and Vannucci, R., 2009, Trace element constraints on the evolution of the mantle column beneath the Afar region (Ethiopia): *Epitome 3*, Forum Italiano di Scienze della Terra Congress 2009: Rimini, p. 275.
- Zindler, A., and Hart, S., 1986, Chemical geodynamics: *Annual Review of Earth and Planetary Science Letters*, v. 14, p. 493–571, doi:10.1146/annurev.ea.14.050186.002425.

MANUSCRIPT ACCEPTED BY THE SOCIETY 9 NOVEMBER 2010

Evolution of the lithospheric mantle beneath the East African Rift in Tanzania and its potential signatures in rift magmas

Sonja Aulbach*
Roberta L. Rudnick
William F. McDonough

Geochemistry Laboratory, Department of Geology, University of Maryland, College Park, Maryland 20742, USA

ABSTRACT

New and published whole-rock major-element contents of xenolithic peridotites, combined with mineral trace-element, $^{87}\text{Sr}/^{86}\text{Sr}$, $^{143}\text{Nd}/^{144}\text{Nd}$, and $^3\text{He}/^4\text{He}$ isotopic compositions, are used to unravel the metasomatic history of lithospheric mantle sampled by volcanic pipes in the Tanzanian section of the East African Rift. The deepest portion of the mantle beneath Labait (craton margin) exhibits high- μ (HIMU)-like $^{87}\text{Sr}/^{86}\text{Sr}$ (0.7029), $^{143}\text{Nd}/^{144}\text{Nd}$ (0.51286), and $^3\text{He}/^4\text{He}$ (5.9), which may reflect the plume in this region. Within the Mozambique belt, recent calcio-carbonatite melt metasomatism has overprinted the mantle lithosphere signature beneath Olmani, leading to high whole-rock Ca/Al and low SiO_2 , and remarkably homogeneous $^{87}\text{Sr}/^{86}\text{Sr}$ (0.7034–0.7035) and $^{143}\text{Nd}/^{144}\text{Nd}$ (0.51281–0.51283) of clinopyroxenes. Identical Sr and Nd isotope values are also reported for clinopyroxenes from peridotite xenoliths from the northern portion of the Gregory Rift in Tanzania (Pello Hill and Eledoi), which have a strong rift magma overprint. The silicate and carbonatite metasomatic melts are likely to be related to recent plume-derived magmatism of the East African Rift, and thus $^{87}\text{Sr}/^{86}\text{Sr}$ and $^{143}\text{Nd}/^{144}\text{Nd}$ values of the clinopyroxene from these samples can be used to define the rift isotopic signature beneath northern Tanzania. Some mantle regions beneath Lashaine and Labait escaped the recent rift-related overprint and have highly variable Sr-Nd isotope systematics. Labait clinopyroxenes show a near-vertical array on a $^{87}\text{Sr}/^{86}\text{Sr}$ versus $^{143}\text{Nd}/^{144}\text{Nd}$ plot, indicating highly variable time-integrated rare earth element (REE) patterns and low time-integrated Rb/Sr. Lashaine peridotites range to much higher $^{87}\text{Sr}/^{86}\text{Sr}$ at a given $^{143}\text{Nd}/^{144}\text{Nd}$, and several plot in the right quadrants in the $^{87}\text{Sr}/^{86}\text{Sr}$ versus $^{143}\text{Nd}/^{144}\text{Nd}$ diagram, suggesting the influence of a (subducted?) Archean upper continental crust component on the lithospheric mantle beneath Lashaine. Their variable whole-rock SiO_2 and high Na_2O contents, and clinopyroxene with high Sr/Y, low Sm/Nd, and variable Zr/Sm are consistent with this interpretation.

*Present address: Institut für Geowissenschaften, Mineralogie, J.W. Goethe-Universität, Altenhöferallee 1, 60438 Frankfurt/Main, Germany; e-mail: s.aulbach@em.uni-frankfurt.de.

Aulbach, S., Rudnick, R.L., and McDonough, W.F., 2011, Evolution of the lithospheric mantle beneath the East African Rift in Tanzania and its potential signatures in rift magmas, in Beccaluva, L., Bianchini, G., and Wilson, M., eds., *Volcanism and Evolution of the African Lithosphere: Geological Society of America Special Paper 478*, p. 105–125, doi:10.1130/2011.2478(06). For permission to copy, contact editing@geosociety.org. © 2011 The Geological Society of America. All rights reserved.

Silicate lavas from the eastern branch of the East African Rift show increasingly evolved Sr and Nd isotope composition from north to south and hence increasing input of ancient metasomatized lithosphere (“EM1” and “EM2” components), similar to that beneath Lashaine and Labait, and well outside the suggested range in isotope compositions of the heterogeneous Kenya plume ($^{87}\text{Sr}/^{86}\text{Sr} = 0.7029\text{--}0.7036$; $^{143}\text{Nd}/^{144}\text{Nd} = 0.51275\text{--}0.51286$). In the western branch, the “anomalous” Sr signature identified in Lashaine peridotites is prominent in silicate lavas and may indicate that the lithospheric mantle beneath that area was similarly enriched during ancient subduction. By contrast, the Sr-Nd isotope systematics of carbonatites reflect EM1 but not EM2 inputs, suggesting that such melts in the East African Rift neither derive from nor have interacted with subduction-modified mantle regions.

INTRODUCTION

Xenolithic peridotites from the East African Rift offer a unique opportunity to investigate the effects of rifting and intrusion of sublithospheric melts on ancient subcontinental lithospheric mantle that has experienced multiple previous enrichment episodes. Based on topography and gravity data, magma generation rates and compositions, as well as the radiogenic Os isotopic composition of the rift magmas (inferred from $^{187}\text{Os}/^{188}\text{Os}$ of metasomatic xenoliths such as glimmerites and pyroxenites), the East African Rift is believed to be caused by the impingement of a plume or plumes that delivered heat and fluids to the lithospheric mantle, leading both to enrichment in magmaphile elements and eventually to thinning through either mechanical or thermal processes (Latin et al., 1993; Ebinger and Sleep, 1998; George et al., 1998; Chesley et al., 1999; Rogers et al., 2000; Vauchez et al., 2005).

Conversely, the lithosphere itself variably contributes to rift-related magmas, causing changes in trace-element and isotope compositions (e.g., Macdonald et al., 1995, 2001). Hence, trace-element and isotope compositions of inferred plume-derived basalts and carbonatites erupted through the East African Rift have been ascribed to derivation from heterogeneous lithospheric mantle or sublithospheric sources, or combinations thereof (e.g., Thompson and Gibson, 1994; Class et al., 1994; Paslick et al., 1995; Rogers et al., 2000; Macdonald et al., 2001). Peridotites from different Tanzanian xenolith localities document significant differences in the tectonothermal evolution and interaction with rift magmas at short length scales (Dawson, 1984, 2002; Dawson and Smith, 1988). These differences may reflect unrepresentative sampling by the host lava, actual compositional heterogeneity of the sampled lithosphere, or, more likely, both. Compositional heterogeneity is enhanced by the longevity of the lithosphere underlying both the exposed Tanzanian craton and adjacent reworked craton margins beneath Proterozoic mobile belts and the protracted tectonic history of the region (Rogers et al., 1992; Smith and Mosley, 1993; Chesley et al., 1999; Burton et al., 2000). Given this heterogeneity and the sampling problem, the question arises as to whether we can hope to find any correlations between the magmas erupted at the surface and the underlying lithosphere.

Here, we summarize what is known of the lithospheric mantle beneath northern Tanzania, as well as report new whole-rock major-element, mineral trace-element, and Sr-Nd-He isotope compositions from previously described peridotite xenoliths from Lashaine, Olmani, and Labait, which are located in the Gregory Rift of northern Tanzania (Rudnick et al., 1993, 1994; Lee and Rudnick, 1999; Chesley et al., 1999; Aulbach et al., 2008; Aulbach and Rudnick, 2009). We use these data to unravel the tectonothermal evolution of the lithosphere beneath Tanzania, including lithosphere formation (partial melt extraction), ancient metasomatism, and young rift-related modification. Finally, we use this amplified database to explore the relationship of these lithospheric mantle sections to the chemical composition of rift-related melts beneath different sections of the eastern and western branches of the East African Rift, from the Turkana Rift in the north to Rungwe in the south (Fig. 1).

GEOLOGY AND SAMPLES

The East African Rift system begins in the north in the Afar triple junction and traverses the Main Ethiopian Rift and the Turkana Depression before bifurcating around the Tanzanian craton into an eastern and a western branch and terminating in the south, in the Rungwe province of Tanzania (Fig. 1). Along this transect, there are the Ethiopian (Afar dome) and the East African (Kenya dome) Plateaus, which are separated by the Turkana Depression. The East African Rift’s tectonic and magmatic evolution has recently been reviewed by Furman (2007) and Dawson (2008) and is summarized here.

The Precambrian basement has apparently strongly influenced rift development and can be divided into craton, reworked craton, and mobile belt (Smith and Mosley, 1993). The Tanzanian craton is Archean in age (older than 2.6 Ga; e.g., Many et al., 2006) and is underlain by a thick lithospheric keel to depths of 150–200 km (Weeraratne et al., 2003; Chesley et al., 1999). Proterozoic mobile belts surround the craton on the south, east, and west. The Mozambique belt to the east is composed mainly of Archean crust (Möller et al., 1998; Maboko, 2000) that has been reworked in two separate collisional events. The first of these, the Usagaran orogeny, occurred at the southeastern margin of the craton and is marked by 2.0 Ga eclogite-facies rocks that have

While the oldest rift magmatism is recorded at 40–45 Ma in the northern Turkana Depression in southernmost Ethiopia, it is the 30 Ma flood basalts erupted in Ethiopia, Eritrea, and Yemen that are held to mark the onset of plume impingement. Although the exact pattern of magmatism and extension within the main Ethiopian Rift is poorly constrained, there is a general southward migration, with volcanism in central Kenya by 15 Ma and northern Tanzania by 5–8 Ma (George et al., 1998). Upon reaching the Tanzanian craton margin at ca. 10–12 Ma (Nyblade and Brazier, 2002), the rift bifurcated into the eastern branch (Gregory Rift) and western branch (Albert and Tanganyika Rifts) of the East African Rift, separated by the 1300-km-wide East African Plateau (which includes the Kenya Dome and the Tanzanian

Previous studies have been carried out on samples from the core of the Tanzanian craton (kimberlite-derived diamonds from Mwadui and eclogite xenoliths from Igwisi Hills—Jagoutz, 1988; Stachel et al., 1999; Dawson, 1994) and from several localities in the eastern branch of the East African Rift, ranging from the craton margin (Labait—Lee and Rudnick, 1999; Dawson, 1999; Chesley et al., 1999; Burton et al., 2000; Aulbach et al., 2008; Koornneef et al., 2009) to the Mozambique belt represented by reworked craton in the west (Lashaine, Olmani, Monduli, Pello Hill, Eledoi in the eastern branch—Cohen et al., 1984; Dawson and Smith, 1988; Rudnick et al., 1993, 1994; Lee et al., 2000; Burton et al., 2000; Dawson, 2002) and Proterozoic regions further to the east (Marsabit, Chyulu Hills—Henjes-Kunst and

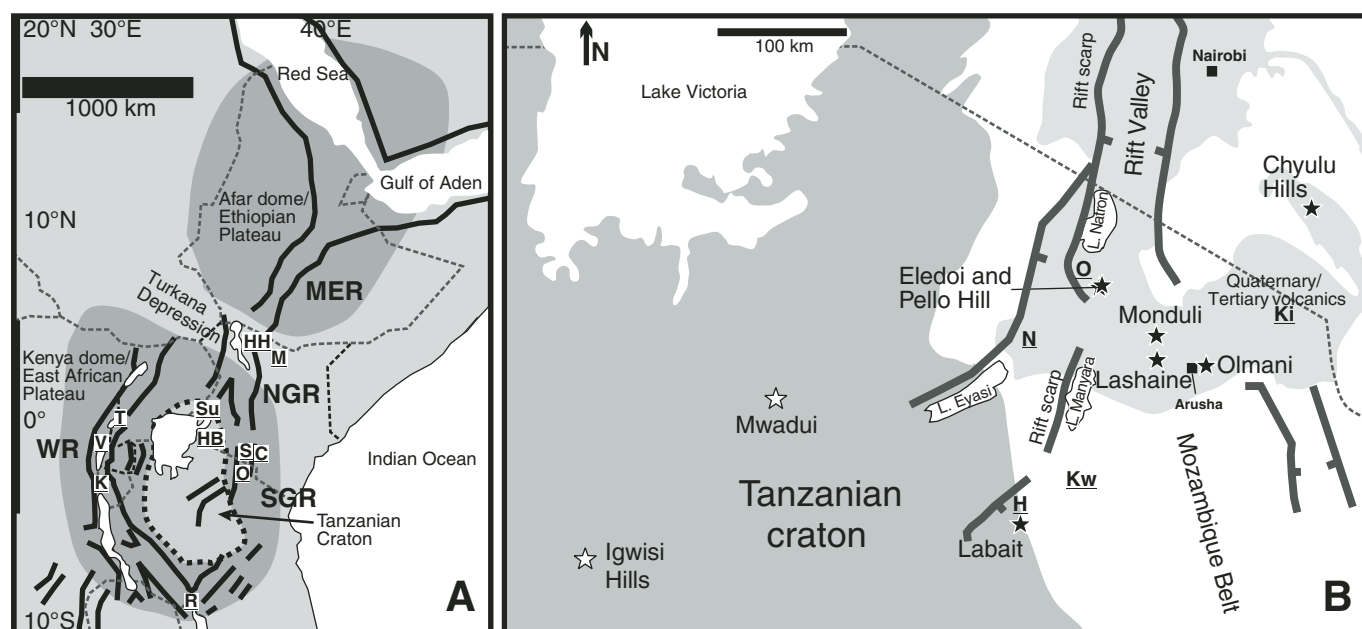


Figure 1. (A) The East African Rift system, with the Afar Dome (Ethiopian Plateau), the Kenya Dome (East African Plateau), and the Tanzanian craton outlined and with approximate political boundaries (after Kaeser et al., 2006). Large letters denote rift sections: MER—Main Ethiopian Rift, NGR—Northern Gregory Rift, SGR—Southern Gregory Rift (including S—Shombole, O—Oldoinyo Lengai, C—Chyulu Hills, Su—Sukulu, HB—Homa Bay), WR—western rift (including T—Toro Ankole, V—Virunga, K—Kivu), and R—Rungwe, at the southern junction of the eastern and western rift branches. Location of Huri Hills (HH) and Marsabit (M) mantle xenolith localities also shown. (B) Simplified map of the Kenyan and Tanzanian section of the East African Rift showing the outline of the Tanzanian craton (dark gray), Tertiary to Quaternary volcanic rocks (light gray), and location of Tanzanian xenolith localities and Chyulu Hills in Kenya (black stars), kimberlites and kimberlite-like rocks (white stars) referred to in the text, and further localities (H—Hanang, Ki—Kilimanjaro, Kw—Kwahara, N—Ngorongoro) (after Dawson and Smith, 1988).

Altherr, 1992; Kaeser et al., 2006, 2009) (Fig. 1). These studies document original lithosphere formation (from Re-Os studies) as well as a variety of metasomatic overprints that occurred during multiple stages of lithosphere evolution, including the influence of rift-related magmatism. Mantle xenoliths from the western branch are limited to pyroxenites, the origins of which were ascribed to multiple metasomatic events acting upon older protoliths (Davies and Lloyd, 1989; Link et al., 2008).

Thinning of the lithosphere within the Gregory Rift is suggested on the basis of geophysical investigations (e.g., Keller et al., 1994; Byrne et al., 1997) as well as the equilibration depths of mantle xenoliths (i.e., garnet-bearing peridotites are found only in the southern, nonrift valley localities of Lashaine and Labait). However, basalt geochemistry has been used to infer that the lithospheric mantle is at least 75 km thick beneath southernmost Kenya (le Roex et al., 2001). In the western branch of the East African Rift, mantle lithosphere is suggested to thin from north to south based on magma source mineralogy (Chakrabarti et al., 2009; Rosenthal et al., 2009).

Work in the present study was carried out on peridotite xenoliths from three Tanzanian localities, Olmani, Lashaine, and Labait. These xenoliths are generally fresh, contrary to their kimberlite-borne counterparts, and include variably refractory and metasomatized peridotites (Dawson et al., 1970; Dawson and Smith, 1973, 1988; Dawson, 1984, 1999, 2002; Cohen et al., 1984; Rudnick et al., 1993, 1994; Lee and Rudnick, 1999; Chesley et al., 1999). The Pleistocene Olmani cinder cone and the Lashaine tuff cone are located 150 km east of the Archean Tanzanian craton (Dawson et al., 1970; Jones et al., 1983; Dawson, 1984; Cohen et al., 1984; Rudnick et al., 1993, 1994), while the Labait olivine melilitite is located at the craton margin (Lee and Rudnick, 1999; Aulbach et al., 2008). Detailed sample descriptions can be found in the GSA Data Repository Appendix 1.¹

SAMPLE PREPARATION AND ANALYTICAL METHODS

Major, trace-element, and Sr and Nd isotopic compositions of Olmani peridotites as well as major-element and Os isotope data for Labait peridotites have been previously published (Rudnick et al., 1993; Lee and Rudnick, 1999; Chesley et al., 1999). Major-element concentrations for Lashaine peridotites were determined by X-ray fluorescence (XRF) in the laboratory of Bruce Chappell at the Australian National University, with the exception of Na₂O, which was determined by instrumental neutron activation analysis (INAA) in the same laboratory, as described in Rudnick et al. (1993).

Trace-element abundances in clinopyroxene (cpx) were determined using either a UP213 nm wavelength or an ArF

Excimer laser ablation unit operating at 193 nm (both from New Wave Research), coupled to an Element 2 (Thermo Finnigan MAT) magnetic sector inductively coupled plasma–mass spectrometer (ICP-MS) in the Department of Geology at the University of Maryland, or a UP213 nm wavelength laser ablation system coupled to an ELAN 6000 quadrupole ICP-MS at the University of Alberta. Conditions for analyses at the University of Maryland are the same as those reported in Aulbach et al. (2008), and analyses were carried out over the same time period (sample gas: He; laser spot sizes: ~80–100 m; laser repetition rate: 8–10 Hz; internal standard: Ti [reported in Rudnick et al., 1994]; external standard: NIST 610; data reduction: modified version of LAMTRACE by Longerich et al. (1996). Conditions for analyses at the University of Alberta are similar to those reported in Schmidberger et al. (2007) (sample gas: He; laser spot sizes: ~80–150 m; laser repetition rate: 5 Hz; internal standard: Ca [reported in Rudnick et al., 1994]; external standard: NIST 612; data reduction: GLITTER software [van Achterbergh et al., 2001]).

Clean mineral separates from two garnet-free peridotites, a garnet lherzolite, and a pyroxenite from Labait were handpicked under a binocular microscope. The samples were cleaned ultrasonically in deionized water several times, then in acetone, and allowed to air dry before a final microscopic inspection. The helium trapped in fluid inclusions was released by crushing the samples in ultrahigh vacuum, and samples were analyzed following methods described in Graham et al. (1998), using a specially designed noble gas mass spectrometer at the National Oceanic and Atmospheric Administration/Pacific Marine Environmental Laboratory (NOAA/PMEL) in Newport, Oregon.

Trace elements in clinopyroxene from Olmani and a subset of Lashaine xenoliths were analyzed over the same time period as previously reported samples from Labait (Aulbach et al., 2008). Optically pure clinopyroxene separates were cleaned in Milli-Q H₂O (18 M) in an ultrasonic bath (acids were not used because their effects on Li isotopes, which were measured from the same separate, were unknown; Aulbach et al., 2008; Aulbach and Rudnick, 2009), dissolved, and passed through columns filled with Biorad cation-exchange resin to obtain Sr and Nd fractions, which were further purified using Eichrom Sr-Spec and Ln-resin, respectively. Strontium and Nd isotope ratios were measured by thermal ionization mass spectrometry (TIMS) on the VG Sector 54 and by solution multicollector (MC) ICP-MS on the Nu Instruments, respectively, at the University of Maryland. Both solution and rock standards were analyzed to evaluate accuracy, and results agree with previously published values (Aulbach et al., 2008). The indistinguishable Sr and Nd isotope results for samples measured both in this and in an earlier study where the mineral separates were acid leached (Rudnick et al., 1993) indicate that cleaning in MQ H₂O was sufficient to remove impurities (GSA Data Repository Appendix 2 [see footnote 1]). A subset of clinopyroxene from Lashaine was analyzed by TIMS at the Australian National University in the early 1990s following the methods described in Rudnick et al. (1993).

¹GSA Data Repository Item 2011189—Appendix 1: Sample description, Appendix 2: Sr and Nd isotopic compositions, and Appendix 3: Trace-element patterns of clinopyroxenes—is available at www.geosociety.org/pubs/ft2011.htm, or on request from editing@geosociety.org or Documents Secretary, GSA, P.O. Box 9140, Boulder, CO 80301-9140, USA.

TABLE 1. MAJOR-ELEMENT CONCENTRATIONS (wt%) OF LASHAINE PERIDOTITE XENOLITHS

Sample	Rock type	SiO ₂	TiO ₂	Al ₂ O ₃	Fe ₂ O ₃	MnO	MgO	CaO	Na ₂ O	Total
89-661	Garnet lherzolite	42.38	0.08	0.70	7.53	0.09	48.07	0.94	0.21	100.0
89-662	Dunite	40.48	0.05	0.17	9.35	0.11	48.76	0.09	0.10	99.1
89-663	Harzburgite	41.11	0.10	0.68	9.94	0.11	46.34	0.35	0.11	98.7
89-664	Garnet harzburgite	41.85	0.15	0.19	9.83	0.12	47.53	0.31	0.14	100.1
89-669	Wehrlite	40.81	0.10	0.55	10.51	0.12	43.70	1.75	0.24	97.8
89-671	Dunite	40.16	0.13	0.42	12.79	0.14	46.27	0.09	0.10	100.1
89-672	Dunite	41.50	0.06	0.19	7.94	0.08	48.93	0.94	0.14	99.8
89-674	Garnet lherzolite	43.34	0.11	0.85	9.33	0.12	45.30	1.05	0.16	100.3
89-675	Garnet harzburgite	45.34	0.05	0.92	7.05	0.1	45.93	0.62	0.13	100.1
89-676	Olivine websterite	45.89	0.14	0.67	11.95	0.16	33.74	7.66	0.25	100.5
89-678	Harzburgite	41.81	0.07	0.26	9.05	0.11	48.61	0.30	0.12	100.3
89-680	Garnet harzburgite	44.28	0.03	1.22	7.35	0.1	45.93	0.81	0.14	99.9
89-719	Garnet harzburgite	43.36	0.02	1.09	7.58	0.09	47.66	0.55	0.13	100.5

RESULTS

Whole-Rock Major Elements

As previously noted (Rudnick et al., 1994), the most striking aspect of the major-element compositions for Lashaine peridotites (Table 1) are the lower contents of SiO₂ and Al₂O₃ for garnet-free peridotites (average 41.0 and 0.38 wt%, respectively), compared to garnet-bearing peridotites (average 43.4 and 0.83 wt%, respectively; Table 1; Fig. 2A). Na₂O contents in Lashaine peridotite xenoliths are high (up to 0.25 wt%) and

are positively correlated with CaO (Fig. 2B), reflecting higher modal clinopyroxene in websterites and lherzolites. Na₂O contents in most peridotites from Lashaine and Pello Hill (Dawson and Smith, 1988) are elevated at a given CaO content, compared to Olmani (Rudnick et al., 1993) and Labait xenolith suites (Lee and Rudnick, 1999).

Mineral Trace Elements

Major-element compositions for all minerals for which trace elements are reported here (Table 2) can be found in

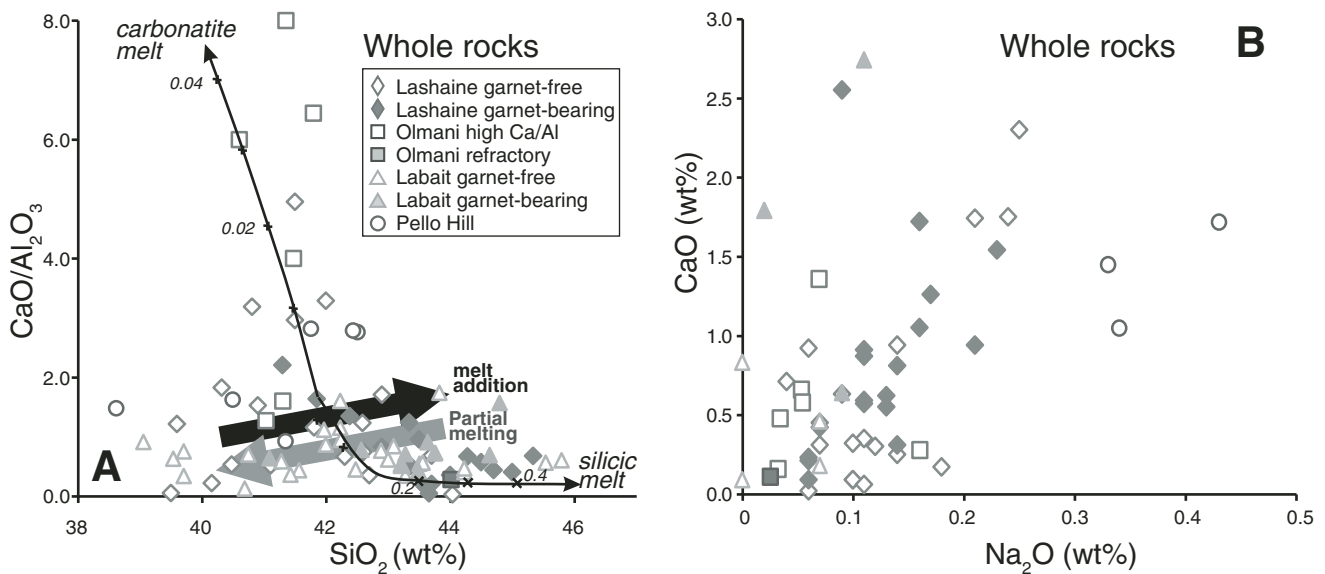


Figure 2. (A) Whole-rock SiO₂ vs. CaO/Al₂O₃ and (B) Na₂O vs. CaO contents in Lashaine peridotites (this work; Pike et al., 1980; Rhodes and Dawson, 1975) compared to those from Pello Hill (Dawson and Smith, 1988), Olmani (Rudnick et al., 1993), and Labait (Lee and Rudnick, 1999). In A, mixing lines are for depleted Lashaine peridotite 89-664 and experimental silicic and carbonatitic pelite-derived melts (Thomsen and Schmidt, 2008), and numbers in italics denote % melt in the mixture. Also shown are qualitative partial melting (gray) and melt addition trends (black).

TABLE 2. TRACE-ELEMENT ABUNDANCES IN CLINOPYROXENE (cpx) AND GARNET (ppm)

isot	89-661		1σ		89-664		1σ		89-669		1σ		89-672		1σ		89-674		1σ		89-675		1σ		89-680		1σ		89-719		1σ		TZ-2-13		1σ		89-772		1σ		89-774		1σ		89-776		1σ																																																																																																																																																																																																																																																																																																																																																																																																																																																																																																																																																																																														
	cpx Ls	gt lherz	cpx Ls	gt harz	cpx Ls	gt harz	cpx Ls	gt harz	cpx Ls	gt harz	cpx Ls	gt harz	cpx Ls	gt harz	cpx Ls	gt harz	cpx Ls	gt harz	cpx Ls	gt harz	cpx Ls	gt harz	cpx Ls	gt harz	cpx Ls	gt harz	cpx Ls	gt harz	cpx Ls	gt harz	cpx Ls	gt harz	cpx Olm dunite	gt lherz	cpx Olm dunite	gt harz	cpx Olm dunite	gt lherz	cpx Olm dunite	gt harz	cpx Olm dunite	gt lherz	cpx Olm dunite	gt harz	cpx Olm dunite	gt lherz	cpx Olm dunite	gt harz	cpx Olm dunite	gt lherz	cpx Olm dunite	gt harz	cpx Olm dunite	gt lherz	cpx Olm dunite	gt harz	cpx Olm dunite	gt lherz	cpx Olm dunite	gt harz	cpx Olm dunite	gt lherz	cpx Olm dunite	gt harz	cpx Olm dunite	gt lherz	cpx Olm dunite	gt harz	cpx Olm dunite	gt lherz	cpx Olm dunite	gt harz	cpx Olm dunite	gt lherz	cpx Olm dunite	gt harz	cpx Olm dunite	gt lherz	cpx Olm dunite	gt harz	cpx Olm dunite	gt lherz	cpx Olm dunite	gt harz	cpx Olm dunite	gt lherz	cpx Olm dunite	gt harz	cpx Olm dunite	gt lherz	cpx Olm dunite	gt harz	cpx Olm dunite	gt lherz	cpx Olm dunite	gt harz	cpx Olm dunite	gt lherz	cpx Olm dunite	gt harz	cpx Olm dunite	gt lherz	cpx Olm dunite	gt harz	cpx Olm dunite	gt lherz	cpx Olm dunite	gt harz	cpx Olm dunite	gt lherz	cpx Olm dunite	gt harz	cpx Olm dunite	gt lherz	cpx Olm dunite	gt harz	cpx Olm dunite	gt lherz	cpx Olm dunite	gt harz	cpx Olm dunite	gt lherz	cpx Olm dunite	gt harz	cpx Olm dunite	gt lherz	cpx Olm dunite	gt harz	cpx Olm dunite	gt lherz	cpx Olm dunite	gt harz	cpx Olm dunite	gt lherz	cpx Olm dunite	gt harz	cpx Olm dunite	gt lherz	cpx Olm dunite	gt harz	cpx Olm dunite	gt lherz	cpx Olm dunite	gt harz	cpx Olm dunite	gt lherz	cpx Olm dunite	gt harz	cpx Olm dunite	gt lherz	cpx Olm dunite	gt harz	cpx Olm dunite	gt lherz	cpx Olm dunite	gt harz	cpx Olm dunite	gt lherz	cpx Olm dunite	gt harz	cpx Olm dunite	gt lherz	cpx Olm dunite	gt harz	cpx Olm dunite	gt lherz	cpx Olm dunite	gt harz	cpx Olm dunite	gt lherz	cpx Olm dunite	gt harz	cpx Olm dunite	gt lherz	cpx Olm dunite	gt harz	cpx Olm dunite	gt lherz	cpx Olm dunite	gt harz	cpx Olm dunite	gt lherz	cpx Olm dunite	gt harz	cpx Olm dunite	gt lherz	cpx Olm dunite	gt harz	cpx Olm dunite	gt lherz	cpx Olm dunite	gt harz	cpx Olm dunite	gt lherz	cpx Olm dunite	gt harz	cpx Olm dunite	gt lherz	cpx Olm dunite	gt harz	cpx Olm dunite	gt lherz	cpx Olm dunite	gt harz	cpx Olm dunite	gt lherz	cpx Olm dunite	gt harz	cpx Olm dunite	gt lherz	cpx Olm dunite	gt harz	cpx Olm dunite	gt lherz	cpx Olm dunite	gt harz	cpx Olm dunite	gt lherz	cpx Olm dunite	gt harz	cpx Olm dunite	gt lherz	cpx Olm dunite	gt harz	cpx Olm dunite	gt lherz	cpx Olm dunite	gt harz	cpx Olm dunite	gt lherz	cpx Olm dunite	gt harz	cpx Olm dunite	gt lherz	cpx Olm dunite	gt harz	cpx Olm dunite	gt lherz	cpx Olm dunite	gt harz	cpx Olm dunite	gt lherz	cpx Olm dunite	gt harz	cpx Olm dunite	gt lherz	cpx Olm dunite	gt harz	cpx Olm dunite	gt lherz	cpx Olm dunite	gt harz	cpx Olm dunite	gt lherz	cpx Olm dunite	gt harz	cpx Olm dunite	gt lherz	cpx Olm dunite	gt harz	cpx Olm dunite	gt lherz	cpx Olm dunite	gt harz	cpx Olm dunite	gt lherz	cpx Olm dunite	gt harz	cpx Olm dunite	gt lherz	cpx Olm dunite	gt harz	cpx Olm dunite	gt lherz	cpx Olm dunite	gt harz	cpx Olm dunite	gt lherz	cpx Olm dunite	gt harz	cpx Olm dunite	gt lherz	cpx Olm dunite	gt harz	cpx Olm dunite	gt lherz	cpx Olm dunite	gt harz	cpx Olm dunite	gt lherz	cpx Olm dunite	gt harz	cpx Olm dunite	gt lherz	cpx Olm dunite	gt harz	cpx Olm dunite	gt lherz	cpx Olm dunite	gt harz	cpx Olm dunite	gt lherz	cpx Olm dunite	gt harz	cpx Olm dunite	gt lherz	cpx Olm dunite	gt harz	cpx Olm dunite	gt lherz	cpx Olm dunite	gt harz	cpx Olm dunite	gt lherz	cpx Olm dunite	gt harz	cpx Olm dunite	gt lherz	cpx Olm dunite	gt harz	cpx Olm dunite	gt lherz	cpx Olm dunite	gt harz	cpx Olm dunite	gt lherz	cpx Olm dunite	gt harz	cpx Olm dunite	gt lherz	cpx Olm dunite	gt harz	cpx Olm dunite	gt lherz	cpx Olm dunite	gt harz	cpx Olm dunite	gt lherz	cpx Olm dunite	gt harz	cpx Olm dunite	gt lherz	cpx Olm dunite	gt harz	cpx Olm dunite	gt lherz	cpx Olm dunite	gt harz	cpx Olm dunite	gt lherz	cpx Olm dunite	gt harz	cpx Olm dunite	gt lherz	cpx Olm dunite	gt harz	cpx Olm dunite	gt lherz	cpx Olm dunite	gt harz	cpx Olm dunite	gt lherz	cpx Olm dunite	gt harz	cpx Olm dunite	gt lherz	cpx Olm dunite	gt harz	cpx Olm dunite	gt lherz	cpx Olm dunite	gt harz	cpx Olm dunite	gt lherz	cpx Olm dunite	gt harz	cpx Olm dunite	gt lherz	cpx Olm dunite	gt harz	cpx Olm dunite	gt lherz	cpx Olm dunite	gt harz	cpx Olm dunite	gt lherz	cpx Olm dunite	gt harz	cpx Olm dunite	gt lherz	cpx Olm dunite	gt harz	cpx Olm dunite	gt lherz	cpx Olm dunite	gt harz	cpx Olm dunite	gt lherz	cpx Olm dunite	gt harz	cpx Olm dunite	gt lherz	cpx Olm dunite	gt harz	cpx Olm dunite	gt lherz	cpx Olm dunite	gt harz	cpx Olm dunite	gt lherz	cpx Olm dunite	gt harz	cpx Olm dunite	gt lherz	cpx Olm dunite	gt harz	cpx Olm dunite	gt lherz	cpx Olm dunite	gt harz	cpx Olm dunite	gt lherz	cpx Olm dunite	gt harz	cpx Olm dunite	gt lherz	cpx Olm dunite	gt harz	cpx Olm dunite	gt lherz	cpx Olm dunite	gt harz	cpx Olm dunite	gt lherz	cpx Olm dunite	gt harz	cpx Olm dunite	gt lherz	cpx Olm dunite	gt harz	cpx Olm dunite	gt lherz	cpx Olm dunite	gt harz	cpx Olm dunite	gt lherz	cpx Olm dunite	gt harz	cpx Olm dunite	gt lherz	cpx Olm dunite	gt harz	cpx Olm dunite	gt lherz	cpx Olm dunite	gt harz	cpx Olm dunite	gt lherz	cpx Olm dunite	gt harz	cpx Olm dunite	gt lherz	cpx Olm dunite	gt harz	cpx Olm dunite	gt lherz	cpx Olm dunite	gt harz	cpx Olm dunite	gt lherz	cpx Olm dunite	gt harz	cpx Olm dunite	gt lherz	cpx Olm dunite	gt harz	cpx Olm dunite	gt lherz	cpx Olm dunite	gt harz	cpx Olm dunite	gt lherz	cpx Olm dunite	gt harz	cpx Olm dunite	gt lherz	cpx Olm dunite	gt harz	cpx Olm dunite	gt lherz	cpx Olm dunite	gt harz	cpx Olm dunite	gt lherz	cpx Olm dunite	gt harz	cpx Olm dunite	gt lherz	cpx Olm dunite	gt harz	cpx Olm dunite	gt lherz	cpx Olm dunite	gt harz	cpx Olm dunite	gt lherz	cpx Olm dunite	gt harz	cpx Olm dunite	gt lherz	cpx Olm dunite	gt harz	cpx Olm dunite	gt lherz	cpx Olm dunite	gt harz	cpx Olm dunite	gt lherz	cpx Olm dunite	gt harz	cpx Olm dunite	gt lherz	cpx Olm dunite	gt harz	cpx Olm dunite	gt lherz	cpx Olm dunite	gt harz	cpx Olm dunite	gt lherz	cpx Olm dunite	gt harz	cpx Olm dunite	gt lherz	cpx Olm dunite	gt harz	cpx Olm dunite	gt lherz	cpx Olm dunite	gt harz	cpx Olm dunite	gt lherz	cpx Olm dunite	gt harz	cpx Olm dunite	gt lherz	cpx Olm dunite	gt harz	cpx Olm dunite	gt lherz	cpx Olm dunite	gt harz	cpx Olm dunite	gt lherz	cpx Olm dunite	gt harz	cpx Olm dunite	gt lherz	cpx Olm dunite	gt harz	cpx Olm dunite	gt lherz	cpx Olm dunite	gt harz	cpx Olm dunite	gt lherz	cpx Olm dunite	gt harz	cpx Olm dunite	gt lherz	cpx Olm dunite	gt harz	cpx Olm dunite	gt lherz	cpx Olm dunite	gt harz	cpx Olm dunite	gt lherz	cpx Olm dunite	gt harz	cpx Olm dunite	gt lherz	cpx Olm dunite	gt harz	cpx Olm dunite	gt lherz	cpx Olm dunite	gt harz	cpx Olm dunite	gt lherz	cpx Olm dunite	gt harz	cpx Olm dunite	gt lherz	cpx Olm dunite	gt harz	cpx Olm dunite	gt lherz	cpx Olm dunite	gt harz	cpx Olm dunite	gt lherz	cpx Olm dunite	gt harz	cpx Olm dunite	gt lherz	cpx Olm dunite	gt harz	cpx Olm dunite	gt lherz	cpx Olm dunite	gt harz	cpx Olm dunite	gt lherz	cpx Olm dunite	gt harz	cpx Olm dunite	gt lherz	cpx Olm dunite	gt harz	cpx Olm dunite

(Continued)

TABLE 2. TRACE-ELEMENT ABUNDANCES IN CLINOPYROXENE (cpx) AND GARNET (ppm) (Continued)

	89-777	89-778	89-780	1 σ	LB-2	1 σ	LB-11	1 σ	LB-12	1 σ	LB-15	1 σ	LB-22	1 σ	KAT17	1 σ	LB-2	1 σ	TZ-2-13	1 σ
	cpx Olm	cpx Olm	cpx Olm	cpx Olm	cpx Lb	sp perid	cpx Lb	cpx Lb	cpx Lb	Fe-perid	cpx Lb	Fe-perid	cpx Lb	cpx Lb	gt harz	gt harz	gt harz	gt harz	gt Ls	gt Ls
n	1	1	4	4	3	4	4	5	5	4	4	4	2	2	4	2	2	3	3	3
Sc	12	27	128	5	87	3	79	5	17	1	48	1	101	2	118	2	362	1	123	1
V	50	99	249	6	174	4	195	8	200	6	189	4	256	27	248	3	2022	5	2161	41
Mn	507	410	337	7	487	7	413	8	712	17	809	21	1047	77	2344	26	55	6	41	2
Ni	339	480	249	17	316	14	241	9	416	14	276	9	1482	320	105	8	2.1	10.7	3.5	0.1
Ga	2.2	4.3	2.6	0.1	1.9	0.2	1.0	0.1	4.7	0.3	3.7	0.2	7.9	0.2	6.9	0.2	<0.33	0	0	0
Sr	81	85	1028	27	220	21	163	20	83	6	85	1	195	27	<0.5	0.1	56.8	6.7	3.9	0.1
Y	5.9	7.3	89.7	1.8	8.5	0.2	6.5	0.1	2.0	0.3	5.2	0.2	6.2	0.7	15.1	0.1	203	12	1	0
Zr	5	36	320	9	81	5	36	2	10	1	25	3	27	1	33	2	<0.18	0	0.36	0.06
Nb	<0.08	1.06	1.39	0.23	0.37	0.02	0.22	0.02	0.23	0.02	0.25	0.02	3.59	0.86	0.14	0.01	<0.09	0.1	0.1	0.0
La	2.7	5.4	44.0	1.7	4.5	0.9	4.3	0.5	2.6	0.1	2.2	0.1	4.9	0.3	<0.05	0.4	0.2	0.2	0.0	0.0
Ce	13.6	8.0	165.1	3.1	16.1	1.6	17.2	1.5	8.2	0.4	8.2	0.0	13.5	0.2	0.4	0.0	0.2	0.0	0.0	0.0
Pr	2.3	1.3	29.7	0.4	3.1	0.3	3.0	0.2	1.2	0.1	1.5	0.1	2.3	0.1	0.2	0.0	1.5	0.0	<0.11	0.0
Nd	14.0	9.1	143.0	2.1	15.8	0.6	14.5	1.9	5.2	0.1	7.5	0.2	11.1	0.6	1.9	0.2	1.5	0.1	<0.27	0.1
Sm	3.7	2.8	36.0	0.8	4.1	0.2	3.0	0.1	1.0	0.1	2.1	0.1	3.0	0.5	1.4	0.1	0.67	0.04	<0.05	0.0
Eu	1.09	0.95	11.36	0.12	1.16	0.10	0.93	0.04	0.30	0.02	0.60	0.05	0.84	0.07	0.68	0.06	4.0	0.0	0.2	0.0
Gd	2.9	3.2	31.1	1.5	3.6	0.1	2.6	0.1	0.7	0.1	1.9	0.1	2.8	0.1	2.2	0.0	1.10	0.12	0.04	0.01
Tb	0.37	0.36	4.38	0.23	0.44	0.04	0.33	0.02	0.10	0.01	0.27	0.03	0.35	0.03	0.41	0.03	9.9	1.3	0.5	0.0
Dy	2.0	2.4	24.4	0.8	2.4	0.1	1.8	0.2	0.5	0.1	1.4	0.1	1.9	0.3	3.0	0.1	2.47	0.10	0.12	0.01
Ho	0.25	0.22	4.00	0.08	0.41	0.01	0.29	0.01	0.08	0.00	0.24	0.03	0.31	0.06	0.69	0.03	8.37	0.88	0.51	0.03
Er	0.63	0.60	9.12	0.51	0.90	0.06	0.68	0.05	0.20	0.03	0.57	0.04	0.79	0.07	1.92	0.27	8.53	0.86	0.88	0.09
Yb	0.33	<0.214	6.15	0.38	0.53	0.08	0.48	0.05	0.12	0.01	0.42	0.03	0.55	0.01	1.81	0.24	1.58	0.21	0.16	0.01
Lu	0.04	<0.047	0.73	0.05	0.07	0.01	0.06	0.01	0.02	0.00	0.05	0.01	0.07	0.02	0.33	0.02	3.7	0.2	<0.07	0.0
Hf	<0.14	0.6	3.4	0.2	2.4	0.4	0.9	0.0	0.4	0.1	1.2	0.1	1.1	0.1	1.0	0.2	<0.08	0.10	<0.02	0.0
Ta	0.01	0.22	0.06	0.01	0.06	0.01	0.06	0.01	0.03	0.01	0.05	0.01	0.21	0.11	<0.04	0.11	1.73	0.81	0.10	0.03
Pb	<0.06	<330	4.77	1.43	1.77	1.55	1.16	0.25	0.64	0.28	0.64	0.33	1.74	0.89	<0.13	0.13	<0.05	0.16	0.01	0.0
Th	0.01	0.14	0.35	0.04	0.07	0.01	0.13	0.04	0.03	0.00	0.04	0.00	0.29	0.11	<0.04	0.00	<0.04	0.02	0.02	0.00
U	0.00	0.24	0.07	0.01	0.02	0.00	0.02	0.00	<0.012	0.00	<0.014	0.00	0.04	0.03	0.01	0.00	0.00	0.00	0.00	0.00

Note: n—number of analyses; Ls—Lashaine, Olm—Olmari, Lb—Labait, isot—1 standard deviation, cpx—clinopyroxene, gt—garnet, lherz—lherzolite, harz—harzburgite, sp—spinel, perid—peridotite, gt-free p—garnet-free peridotite.

Samples cpx 89-664, 89-672, 89-680, 89-772, 89-776, and 89-777, and garnet KAT-17 were analyzed at the University of Maryland; the remaining samples were analyzed at the University of Alberta using the same isotopes except for Ni (62), Ga (69), Er (166), Yb (172), and Hf (178).

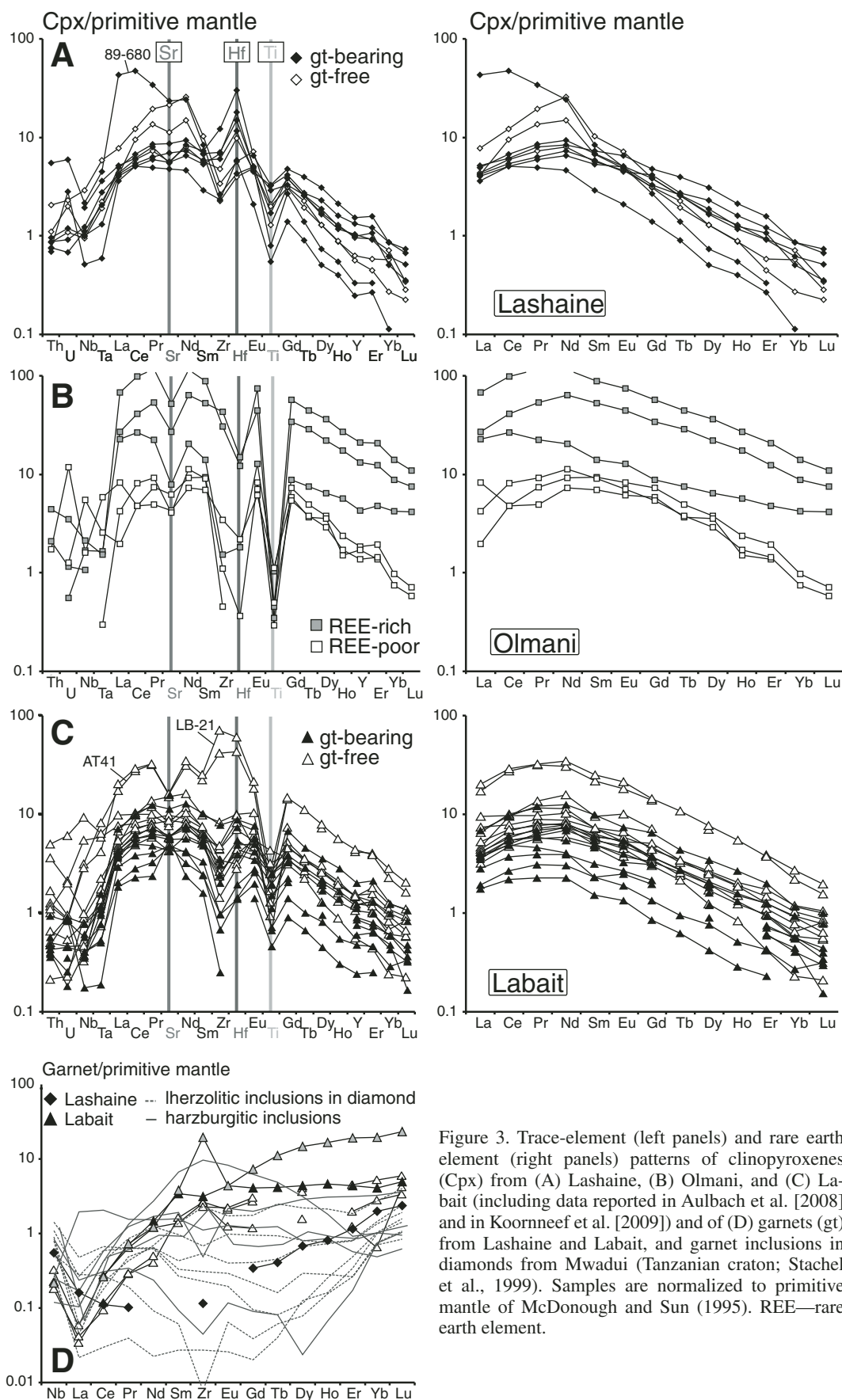


Figure 3. Trace-element (left panels) and rare earth element (right panels) patterns of clinopyroxenes (Cpx) from (A) Lashaine, (B) Olmani, and (C) Labait (including data reported in Aulbach et al. [2008] and in Koornneef et al. [2009]) and of (D) garnets (gt) from Lashaine and Labait, and garnet inclusions in diamonds from Mwadui (Tanzanian craton; Stachel et al., 1999). Samples are normalized to primitive mantle of McDonough and Sun (1995). REE—rare earth element.

Rudnick et al. (1994) (Olmani and Lashaine), Pike et al. (1980) (Lashaine), and Lee and Rudnick (1999) (Labait). These papers also explore the major-element systematics of the minerals and report calculated equilibration conditions on the basis of various thermobarometers.

Clinopyroxenes in peridotites from Lashaine have steep, heavy rare earth element (HREE)–depleted, concave-downward, primitive mantle–normalized (indicated by suffix “N”) REE patterns ($1 < \text{light [L] REE}_N < 10$, $\text{HREE}_N < 1$) (Fig. 3). Clinopyroxenes from Lashaine peridotites have high Sr_N/Y_N (up to ~ 100) values, which are due primarily to their very low abundances of HREE rather than to high Sr abundances. All but one show high Hf abundances relative to similarly compatible elements, and small negative Ti anomalies. If the unusual trace-element pattern of clinopyroxene in sample 89-680 is excluded, it is apparent that the trace-element patterns for clinopyroxene in garnet-bearing and garnet-free peridotites are generally similar, in that all show LREE enrichments and HREE depletions. However, in detail, differences are also apparent: clinopyroxenes in garnet-free peridotites have somewhat higher LREEs and other highly incompatible element abundances, lower HREE abundances, and stronger negative Ti and Zr anomalies, and all but one lack the positive Hf anomaly exhibited by clinopyroxene in garnet-bearing peridotites (GSA Data Repository Appendix 3 [see footnote 1]). Because the two varieties of peridotites are distinct in their whole-rock SiO_2 and Al_2O_3 contents (see previous), most of the differences in the clinopyroxene trace-element patterns are likely due to bulk compositional differences rather than mineral assemblage.

Clinopyroxenes in three dunites from Olmani have very high REE_N abundances (~ 10 – 100), whereas those from the other three samples (two dunites and a wehrlite) show REE_N generally < 10 . Primitive mantle–normalized trace-element patterns of the REE-rich clinopyroxenes are less fractionated than for REE-poorer clinopyroxene (Fig. 3B). One sample, with the lowest overall REE content, has $\text{La}_N/\text{Ce}_N > 1$, contrary to all other clinopyroxenes analyzed. All samples show uniformly strong negative Ti anomalies, but Zr_N and Hf_N abundances vary widely from < 1 to > 10 . As noted previously for the corresponding whole rocks (Rudnick et al., 1993), Zr/Hf_N ratios in

clinopyroxene from Olmani are mostly > 1 , which distinguishes them from clinopyroxene at other Tanzanian xenolith localities, which have ratios < 1 .

Clinopyroxene from two Labait garnet peridotites (LB-4 and LB-12) have conspicuously low middle (M) REE and HREE abundances (Fig. 3C). Clinopyroxene in garnet-free peridotite LB-21 is strongly enriched in all but the most incompatible elements and strongly resembles sample AT41 in the study of Koornneef et al. (2009). The differences between trace-element abundances in clinopyroxene from the remaining garnet-free and two garnet-bearing varieties are minor. This seems to suggest that clinopyroxene in the garnet-bearing peridotites did not equilibrate with garnet, which could indicate that the clinopyroxene is a recent addition, although in this case, one would not expect their isotopic compositions to be so heterogeneous (see following).

Garnet in Lashaine peridotite TZ-2-13 (sample originally collected by Howard Wilshire, provided to us by Tony Irving) has a U-shaped primitive mantle–normalized trace-element pattern with a trough in Pr_N (Nd, Sm, and Eu are below detection; Fig. 3D), and thus resembles some garnet inclusions in diamonds from the Mwadui kimberlite on the Tanzanian Craton (Stachel et al., 1999). Garnets from two Labait harzburgites show flat to mildly fractionated primitive mantle–normalized HREE patterns, with higher HREE abundances than seen in harzburgitic and lherzolitic garnet inclusions in diamonds from Mwadui (Stachel et al., 1999). They also lack the sinusoidal REE patterns typically seen in the inclusions. One garnet from Labait (sample LB-2) shows a distinct positive Zr anomaly.

He Isotopes

Olivines, orthopyroxene, and clinopyroxene from Labait peridotites have $^3\text{He}/^4\text{He}$ ratios ranging from 5.7 to 7.3 times atmospheric ratios (R/R_a ; Table 3; Fig. 4). While few in number, these analyses span the range of bulk compositions, from the most refractory, garnet-free peridotite (LB-14) to the most fertile peridotite (LB-45), which has a bulk composition similar to primitive mantle. The $^3\text{He}/^4\text{He}$ ratios for olivine and clinopyroxene from

TABLE 3. He CONCENTRATIONS AND ISOTOPIC COMPOSITIONS OF MINERAL SEPARATES FROM LABAIT

Sample	Rock type	Wt (mg)	R/R_a^*	2σ	$[^4\text{He}]$ (cm^3/g)
LB14 olivine	Garnet-free peridotite	690.7	5.92	0.14	2.95×10^{-8}
LB15 olivine	Pyroxenite	410.3	7.29	1.25	4.97×10^{-10}
LB15 clinopyroxene	Pyroxenite	247.6	5.82	0.22	8.81×10^{-9}
LB17 olivine	Garnet-free peridotite [†]	454.4	5.72	0.13	3.88×10^{-8}
LB45 orthopyroxene	Garnet lherzolite	501.5	7.26	0.67	8.22×10^{-10}
LB45 clinopyroxene	Garnet lherzolite	260.3	5.87	0.27	8.14×10^{-9}

*Measured $^3\text{He}/^4\text{He}$ ratios (R) relative to $^3\text{He}/^4\text{He}$ of atmospheric He (R_a), which is 1.39×10^{-6} .
[†]Includes vein.

a pyroxenite xenolith fall within the range seen in the peridotites. These values are outside those of normal MORB, ranging to lower values that are similar to those seen in some HIMU basalts (Graham et al., 1992; Parai et al., 2009).

Sr and Nd Isotopes in Clinopyroxene

Strontium isotopic compositions of clinopyroxene separates from Lashaine measured here range from 0.70411 to 0.71377 in a wehrlite and a garnet lherzolite, respectively, and $^{143}\text{Nd}/^{144}\text{Nd}$ ranges from 0.51238 to 0.51281 in a dunite and a garnet lherzolite, respectively (Table 4). None of the samples we analyzed shows the extreme isotopic compositions reported for one phlogite–garnet lherzolite by Cohen et al. (1984), but two of our samples are displaced far to the right of the “mantle array,” and one of these is in an unusual position within the upper-right quadrant of the Sr–Nd isotope plot (Fig. 5A). The compiled data set is given in GSA Data Repository Appendix 2 (see footnote 1).

Two clinopyroxene separates from Olmani are new to this study, and three additional clinopyroxenes were replicated from the original study of Rudnick et al. (1993). All clinopyroxenes show a narrow range in $^{87}\text{Sr}/^{86}\text{Sr}$ from 0.70342 to 0.70388, and $^{143}\text{Nd}/^{144}\text{Nd}$ from 0.512805 to 0.512826 (Table 4).

Strontium and Nd isotope data for clinopyroxenes from Labait peridotites were previously reported in Aulbach et al. (2008) and range from 0.70295 to 0.70558 and 0.51220–0.51288, respectively. In our discussion, we also consider the new data of Koornneef et al. (2009), which range to higher $^{143}\text{Nd}/^{144}\text{Nd}$ (up to 0.513044) but show a similar range in $^{87}\text{Sr}/^{86}\text{Sr}$.

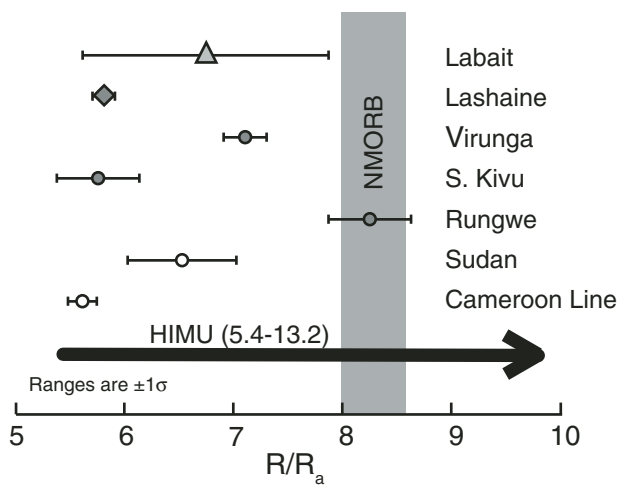


Figure 4. He isotope compositions of mineral separates from Labait compared to previously published results from other localities (after Dunai and Porcelli, 2002). HIMU—high-μ; NMORB—normal mid-ocean-ridge basalt; R: $^3\text{He}/^4\text{He}$ sample; R_a : atmospheric $^3\text{He}/^4\text{He}$.

TABLE 4. Sr AND Nd ISOTOPIC COMPOSITIONS OF MINERAL SEPARATES AND WHOLE ROCK

Sample	Rock type	Rb (ppm)	Sr (ppm)	$^{87}\text{Rb}/^{86}\text{Sr}$	$^{87}\text{Sr}/^{86}\text{Sr}$	2se/stdev	Sm (ppm)	Nd (ppm)	$^{147}\text{Sm}/^{144}\text{Nd}$	$^{143}\text{Nd}/^{144}\text{Nd}$	2se/stdev	ϵ_{Nd}
Lashaine												
89-661 cpx avg	Garnet lherzolite	0.14	165	0.0025	0.713621	0.000419	3.191	13.14	0.1468	0.512808	0.000009	3.3
89-663 cpx	Harzburgite	1.6	233	0.020	0.704030	0.000020						
89-663 opx	Harzburgite	0.0045	5.9	0.0022	0.703900	0.000020		0.623		0.512721	0.000021	1.6
89-664 wr avg	Garnet lherzolite	1.8	4.149	1.213	0.705193	0.000559	0.0495	0.336		0.512640	0.000140	0.0
89-664 cpx avg	Garnet lherzolite				0.708999	0.000018	1.78	6.831	0.1578	0.512766	0.000001	2.5
89-669 cpx avg	Wehrlite	0.29	87	0.010	0.709846	0.000207		14.8		0.512491	0.000057	-2.9
89-672 cpx avg	Dunite				0.704107	0.000031		13.5		0.512380	0.000035	-5.0
89-680 cpx avg	Garnet harzburgite				0.705196	0.000065		15.6		0.512676	0.000059	0.7
89-719	Garnet harzburgite				0.709636	0.000016						
Olmani												
89-772 cpx avg	Dunite				0.703420	0.000055		17.7		0.512826	0.000021	3.7
89-774 cpx	Dunite				0.703470	0.000010		14.0		0.512805	0.000020	3.3
89-776 cpx avg	Dunite							25.2		0.512816	0.000077	3.5
89-777 cpx avg	Wehrlite				0.703485	0.000047		57.0		0.512814	0.000044	3.4
89-778 cpx	Dunite				0.703875	0.000016		5.0		0.512811	0.000014	3.4
89-780 cpx	Dunite				0.703476	0.000015		36.3		0.512818	0.000015	3.5

Note: cpx—clinopyroxene; opx—orthopyroxene; wr—whole rock; avg—averages of several analyses, including data from Rudnick et al. (1993); se—standard error (for single analyses); stdev—standard deviation (for multiple analyses); ϵ_{Nd} is per 10,000 deviation from present-day chondrite (value of Wasserburg et al., 1981).

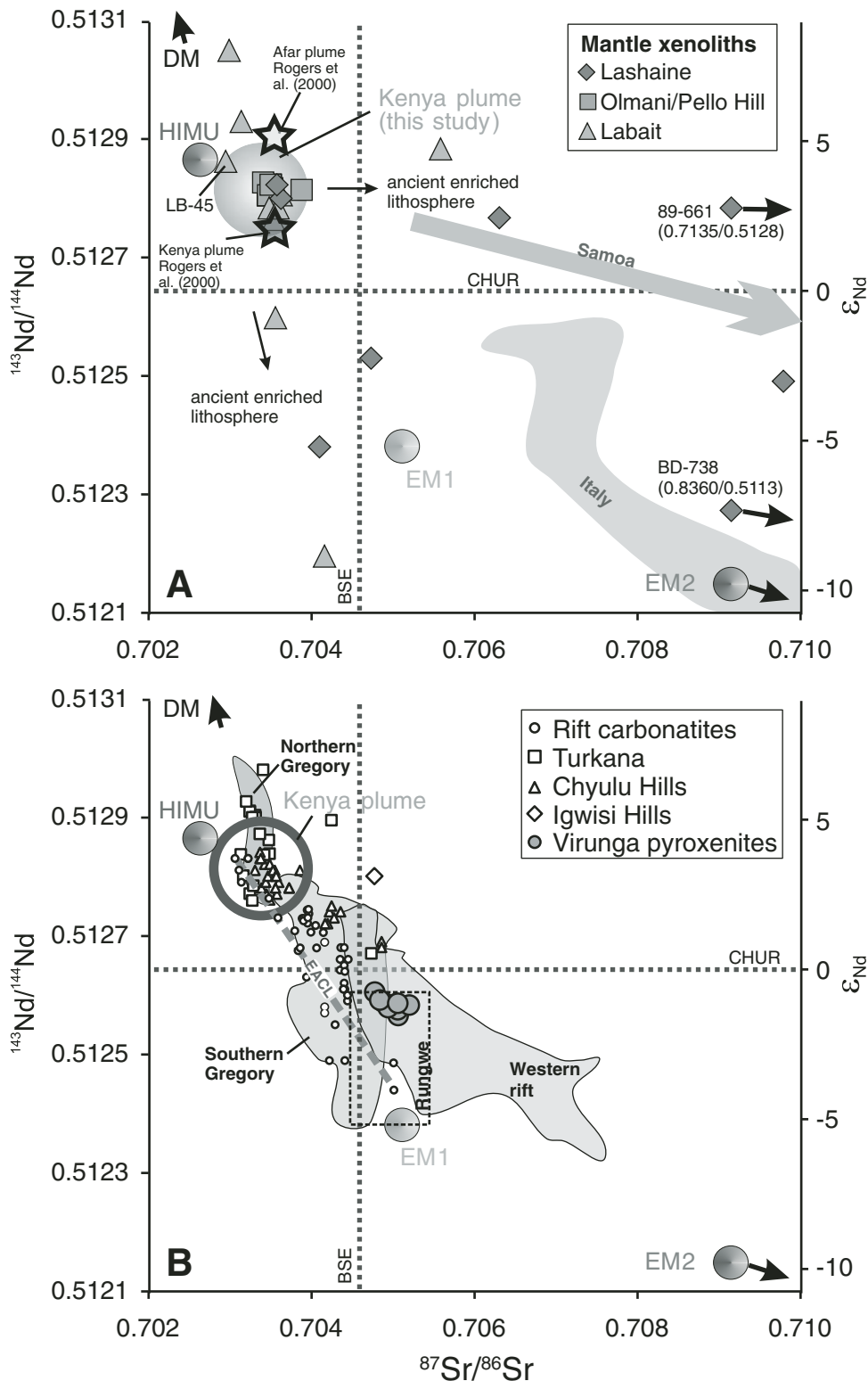


Figure 5. $^{87}\text{Sr}/^{86}\text{Sr}$ versus $^{143}\text{Nd}/^{144}\text{Nd}$ diagram (A) for clinopyroxene separates from peridotite xenoliths from Lashaine, Olmani, and Labait in the eastern branch of the East African Rift (this study; Cohen et al., 1984; Rudnick et al., 1993; Aulbach et al., 2008; Koornneef et al., 2009); Kenyan plume encompasses different estimates for the composition of the plume beneath the Kenya section of the East African Rift from Rogers et al. (2000), and based on homogeneous isotope compositions for carbonatite-metasomatized Olmani peridotites (Rudnick et al., 1993) and a heavily overprinted deep-seated peridotite from Labait (Aulbach et al., 2008). Trend and field for lavas from Samoa (Jackson et al., 2007) and Italy (Rogers et al., 1985), which are derived from subducted sediment-modified sources, are shown for comparison. Depleted mantle (DM), high- (HIMU), and enriched mantle (EM1, EM2) end members are from Zindler and Hart (1986) and Bell and Tilton (2001); bulk silicate earth (BSE) and chondritic uniform reservoir (CHUR) values (thin stippled lines) are from Bell and Tilton (2001) and Wasserburg et al. (1981), respectively. (B) Volcanic rock isotope data (at time of eruption) taken from <http://georoc.mpch-mainz.gwdg.de/georoc/>, except for Rungwe (Furman and Graham, 1994), Chyulu Hills (Späth et al., 2001), Ngorongoro Volcanic Highland (Mollet et al., 2011), Toro Ankole (Rosenthal et al., 2009), Virunga (Chakrabarti et al., 2009), and Igwisi Hills (Dawson, 1994). Silicate lavas were screened for Ce/Pb (>20) to avoid crustally contaminated samples (Hofmann et al., 1986), and for SiO_2 (50 wt%). Separate fields are shown according to rift sections (Northern Gregory, Southern Gregory, western rift) plus Rungwe; carbonatites (eastern plus western branch), Turkana lavas, Chyulu Hills lavas, and Igwisi Hills lava are shown separately. East African carbonatite line (EACL) is from Bell and Blenkinsop (1987). Whole-rock pyroxenites from Virunga in the western branch (Davies and Lloyd, 1989) are shown for comparison.

DISCUSSION

Lithosphere Formation and Modification Recorded in Mantle Samples from Tanzania

We will focus our discussion on Tanzanian xenolith localities for which both trace-element and isotopic compositions are available. Establishing the age of lithosphere formation is integral to efforts to decipher lithosphere evolution. The best tool with which to gauge the age of melt depletion, which likely gave rise to the formation of cratonic mantle lithosphere, is the Re-Os isotope system (reviewed in Rudnick and Walker, 2009). Minimum ages for Tanzanian peridotites range up to 3.2 Ga for Labait and up to 3.4 Ga for Lashaine and Olmani (Chesley et al., 1999; Burton et al., 2000). A single published Os analysis for a spinel ilmenite from Pello Hill yields a Proterozoic minimum age (1.3 Ga; Burton et al., 2000), but unpublished Os model ages for Pello Hill and Eledoi indicate that, like Olmani and Lashaine, the mantle lithosphere beneath these northern localities is Archean (J. Chesley, 1998, personal commun.). An Archean age for all of the Tanzanian localities considered here is also indicated by the very refractory nature of the peridotites, many of which have the high Fo and low Al_2O_3 and CaO contents that are characteristic of mantle xenoliths from Archean cratons (e.g., Rudnick et al., 1993, 1994; Lee and Rudnick, 1999).

Dawson (1999) remarked that each xenolith suite in Tanzania has a distinct metasomatic signature, which makes it difficult to identify spatial geochemical patterns. Moreover, there is evidence for more than one episode of mantle modification. One event was related to recent rift-related intrusion of sublithospheric melts and fluids; other episodes are older. Texturally, these multiple events are manifest in the presence of both equilibrated “old” phlogopite and unequilibrated “young” phlogopite in the same sample suite (Rudnick et al., 1994; Dawson, 2002; Koornneef et al., 2009). Melt refertilization is indicated by included minerals having higher Mg# than those occurring interstitially (Rudnick et al., 1994; Lee and Rudnick, 1999) and inclusions in diamond centers being more refractory than those occurring in diamond rims (Stachel et al., 1998). Relationships between clinopyroxene Sr and Nd isotopes and trace-element compositions reveal two types of metasomatism. The first results in relatively homogeneous isotope compositions, despite variable parent-daughter ratios, which requires that it occurred recently. The second type shows diverse $^{87}\text{Sr}/^{86}\text{Sr}$ and $^{143}\text{Nd}/^{144}\text{Nd}$ values that do not necessarily correlate with elemental abundances or parent-daughter ratios (Fig. 6). We describe each of these metasomatic types next.

Rift-Related Mantle Metasomatism

Prior work on Tanzanian xenoliths showed that the lithospheric mantle has been heated and modified recently through interaction with sublithospheric melts and fluids (Rudnick et al., 1993; Lee and Rudnick, 1999; Chesley et al., 1999; Dawson and Smith, 1988; Dawson, 2002; Aulbach et al., 2008; Koorn-

neef et al., 2009). A ca. 400 ka age for euhedral zircons from a phlogopite-rutile-orthopyroxene-chromite-sulfide vein in harzburgite suggests that this vein likely crystallized from rift-related magmas, and it documents recent metasomatism in the lithospheric mantle (Rudnick et al., 1999). Labait is located where the rift has started to propagate into the craton margin, and its xenoliths therefore testify to lithosphere modification associated with incipient extension. Iron-rich peridotites experienced strong enrichment by asthenospheric, possibly plume-derived silicate melts that added Fe, Li (Fig. 6), and radiogenic Os.

Clinopyroxenes in Olmani dunites and wehrlites are suggested to have formed via rift-related carbonatitic metasomatism (Rudnick et al., 1993). These peridotites are characterized by low Al_2O_3 and SiO_2 and high CaO contents that contrast with those of a single refractory harzburgite (Fig. 2). The clinopyroxenes from Olmani peridotites generally have strongly negative Ti_N anomalies (Fig. 3) and relatively unevolved and homogeneous Sr and Nd isotope compositions (Fig. 5). All of these features are consistent with formation of the clinopyroxene by reaction of peridotite with rift-related carbonatitic melts (Rudnick et al., 1993). The melts that gave rise to these features share similarities with silica-undersaturated, carbonate-rich lavas in the western rift of the East African Rift. The latter have been interpreted to reflect relatively recent addition of small degrees of asthenosphere-derived carbonate melts that formed during initial stretching of the mantle and solidified upon interacting with the cold lithosphere, shortly thereafter providing a low-melting-point component contributing to the formation of silica-undersaturated volcanic rocks (Rosenthal et al., 2009).

The Olmani clinopyroxenes have highly variable REE contents but similar $(\text{La}/\text{Yb})_N$ values (2.0–5.6), which are typically lower than those of clinopyroxene in SiO_2 -poor garnet-free peridotites from Lashaine (4.9–35.2; Fig. 3). Lithium enrichment appears to be a hallmark of the recent rift-related metasomatism both by silicate melt beneath Labait and carbonatite melt beneath Olmani. Overprinting of the lithosphere by rift magmas is accompanied by evidence for deep lithospheric heating at the margin and within the center of the Tanzanian craton (Labait and Igwisi Hills, respectively). This heating is consistent with the formation of symplectites surrounding garnets (Dawson, 1994; Lee and Rudnick, 1999) and enhanced Zr concentrations on the rims of recent rutiles in veins from peridotites from Labait (Watson et al., 2006). Other manifestations of rift-related metasomatism are the presence of pyroxenite xenoliths (e.g., Davies and Lloyd, 1989) and of veins in peridotite xenoliths (e.g., Rudnick et al., 1999) from the craton margin and mobile belt, both in the eastern and western branches of the East African Rift (Oldoinyo Lengai, Marsabit, Toro Ankole, Virunga; Davies and Lloyd, 1989; Dawson and Smith, 1992; Link et al., 2008; Kaeser et al., 2009). Finally, the relatively uniform and low $^3\text{He}/^4\text{He}$ ratios of Labait xenoliths, including a pyroxenite and the fertile, deepest sample (LB-45), which shows the greatest overprinting by rift basalts, suggest that the He isotopic signature of the lithosphere beneath Labait has been overprinted by the rift fluids and magmas.

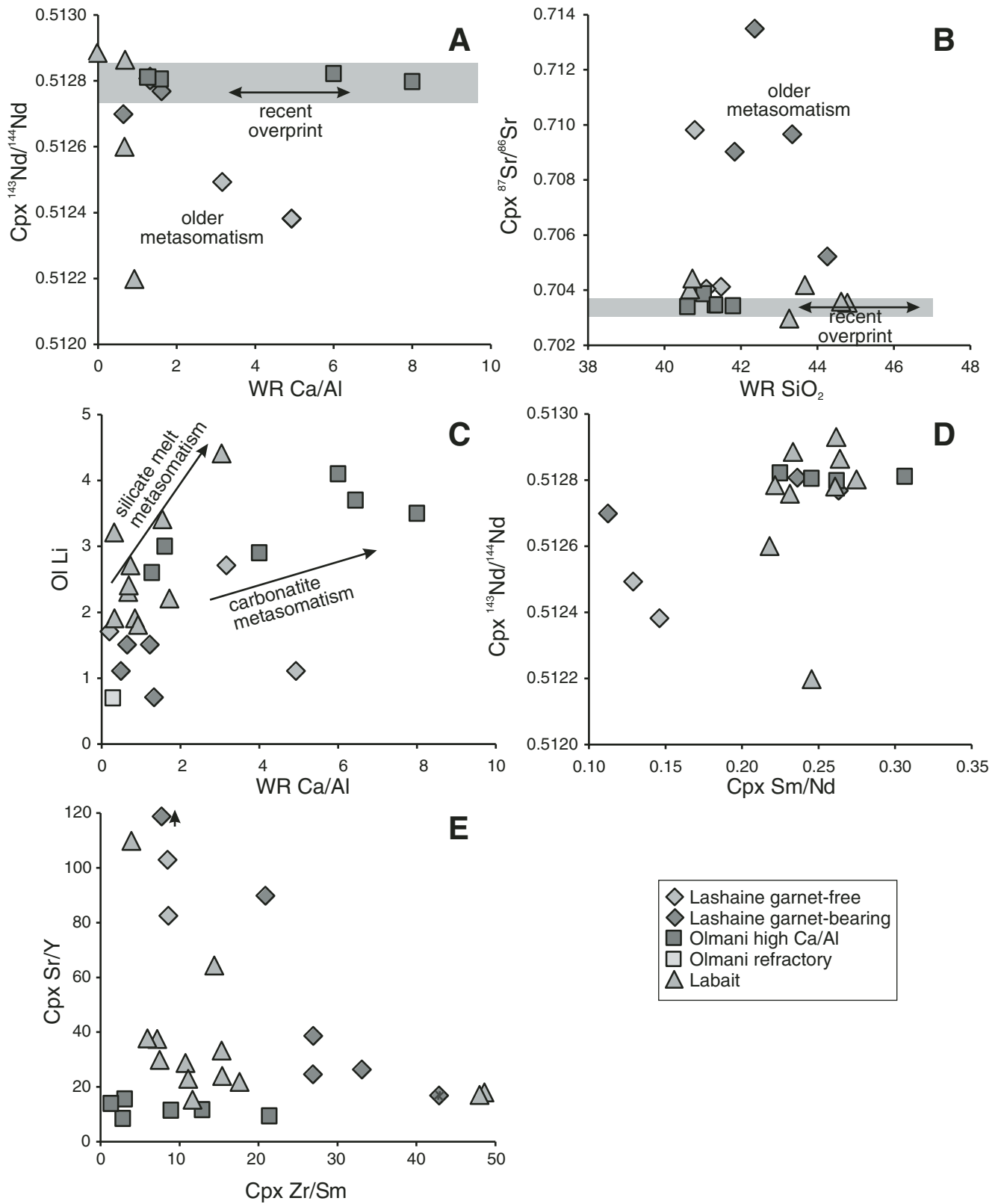


Figure 6. (A–E) Major-element, trace-element, and isotopic compositions of peridotites from Tanzania (data from Cohen et al., 1984; Rudnick et al., 1993; Aulbach et al., 2008; Aulbach and Rudnick, 2009; Koornneef et al., 2009; this study). Arrows in A and B show qualitative recent and older metasomatism trends, arrows in C show qualitative carbonatite and silicate melt enrichment trends. Gray bands in A and B show suggested range of isotope compositions of the heterogeneous Kenyan plume (see Fig. 5). WR—whole rock; Cpx—clinopyroxene; Ol—olivine.

Prerifting Mantle Metasomatism

Inclusions in diamonds from the 40–53 Ma Mwadui kimberlite cluster in the central Tanzanian craton attest to prerifting metasomatism, since the kimberlites predate earliest plume impingement in the Gregory Rift section of the East African Rift. Studies of these inclusions have revealed the mantle lithosphere to be unusually fertile at the time of, or refertilized during, diamond formation, leading to high TiO_2 in garnets and K_2O in clinopyroxene (even if a pressure dependence is considered), a high ratio of lherzolitic to harzburgitic garnet inclusions, and high FeO contents of inclusions near the rim of the diamond compared to those occurring in diamond centers (Stachel et al., 1998). The trace-element contents of these inclusions reflect LREE and MREE enrichment (Stachel et al., 1999).

Unlike inclusions in diamonds, xenoliths can be modified by metasomatic processes up to the time of entrainment in the host magma (see previous section). However, garnet in a Lashaine SiO_2 -rich peridotite has a U-shaped trace-element pattern that is similar to those of garnet inclusions in diamonds from the ca. 50 Ma Mwadui kimberlites. This pattern is distinct from those of garnets in deep, hot, and metasomatized Labait peridotites (Fig. 3D; Koornneef et al., 2009). The similarity of the Lashaine garnet and the diamond inclusion garnets points to the antiquity of the metasomatic signature in Lashaine garnet-bearing peridotites. Thus, portions of the refractory lithospheric mantle escaped the rift-related overprint. The timing of metasomatism is best documented by radiogenic isotopes, as discussed in the next section.

Ancient LREE enrichment and low Rb/Sr preserved in refractory peridotite. Clinopyroxenes in spinel peridotites and garnet-free harzburgites, the most refractory samples from Labait and Lashaine, have highly variable Sr and Nd isotope compositions that are distinct from those of rift-related volcanic rocks (Fig. 5). Clinopyroxene in refractory Labait spinel peridotite LB-31 and Lashaine dunite 89-672 have unradiogenic Nd (ϵ_{Nd} 8.6 and 5.0, respectively) and moderately radiogenic Sr (0.7042 and 0.7041) that is similar to enriched mantle 1 (EM1), which is likely due to LREE enrichment prior to any plume-related overprints. Clinopyroxene from spinel peridotite LB-31 has a depleted mantle Nd model age (T_{DM}) of 2.15 ± 0.34 Ga ($^{147}\text{Sm}/^{144}\text{Nd}$ calculated from $\text{Sm} = 3.17$ ppm, $\text{Nd} = 12.88$ ppm [Table 2]; error calculated assuming 10% uncertainty on Sm/Nd; depleted mantle [DM] values are from Michard et al., 1985). Similar isotope systematics and model ages (based on the same model for DM) for clinopyroxene from Labait xenoliths have recently been reported (Koornneef et al., 2009). These point to low time-integrated Sm/Nd of the source and may indicate that the metasomatic enrichment occurred sometime in the Paleoproterozoic.

Sediment-derived silicic to carbonate melt metasomatism?

The SiO_2 contents of less-refractory garnet lherzolites from Lashaine are higher than those of garnet-free peridotites (Fig. 2), and clinopyroxene Sr/Y ratios are generally elevated in all lithologies, but they are not unusual compared to those in fertile lher-

zolites from Labait. Hence, the silica-rich Lashaine garnet lherzolites could have been refertilized during recent silicate melt metasomatism, similar to Labait peridotites. However, olivines in Lashaine garnet-bearing peridotites are Li-poor (1.7 ppm) compared to recently silicate melt-metasomatized samples from Labait (average 3.1 ppm; Aulbach et al., 2008).

In contrast to silica-rich peridotites, several low SiO_2 peridotites from Lashaine have distinctly high $\text{CaO}/\text{Al}_2\text{O}_3$ (Fig. 2), similar to Olmani peridotites, which have previously been ascribed to carbonatite metasomatism (Rudnick et al., 1993). Again, low Li contents in high- $\text{Ca}/\text{Al}_2\text{O}_3$ Lashaine peridotites, compared to the high Li in recently carbonatite melt-metasomatized samples from Olmani (average 3.3 ppm; Aulbach and Rudnick, 2009), preclude a temporal relationship. In addition, the unusually radiogenic $^{87}\text{Sr}/^{86}\text{Sr}$ ratio relative to $^{143}\text{Nd}/^{144}\text{Nd}$ of clinopyroxene in many Lashaine peridotites (and in one Labait peridotite) is distinct from the relatively unradiogenic and uniform $^{87}\text{Sr}/^{86}\text{Sr}$ inferred for the plume (Fig. 5). Collectively, this evidence suggests that recent silicate- or carbonatite-melt metasomatism is not responsible for the observed trace-element and isotope systematics of silica-rich and high- $\text{Ca}/\text{Al}_2\text{O}_3$ peridotites from Lashaine. Therefore, we next consider a scenario of older metasomatism involving recycled components.

The unusual Sr-Nd isotope compositions recorded in many Lashaine peridotites, which plot in the upper- and lower-right quadrants of the Sr-Nd isotope diagram, toward the far right of primitive mantle $^{87}\text{Sr}/^{86}\text{Sr}$ (Fig. 5), may point to the presence of an ancient continental crust component in the lithospheric mantle, as previously argued (Rudnick et al., 1994), possibly introduced by means of subduction of ancient seafloor sediments (e.g., Zindler and Hart, 1986). Samples in the right quadrants have isotope characteristics similar to volcanic rocks from central Italy and Samoa, which have been ascribed to a subducted sediment-modified mantle source (Rogers et al., 1985; Jackson et al., 2007) (Fig. 5A). The samples plotting in the upper-right quadrant are more problematic to explain. They require high time-integrated Rb/Sr and Sm/Nd, which are unusual features in any common rock type. It is unlikely that they represent mixtures between an extreme component like that seen in BD-738 and rift basalts, because the amount of basalt required to produce this mixture would be very large (tens of percent), which is not consistent with the modal mineralogy observed in the samples. However, a relatively small amount of Sr- and Nd-rich carbonatite having an isotopic composition similar to the Olmani peridotites, mixed with the BD-738 peridotite could produce these unusual compositions. The conspicuously low Li contents in Lashaine peridotites compared to other sample localities suggest either that Li was not added by the metasomatic process, or that it has been subsequently removed.

Melting of carbonated metapelite can produce a spectrum of melts from silicic to carbonatitic (Thomsen and Schmidt, 2008) and may be able to explain the crustal-like $^{87}\text{Sr}/^{86}\text{Sr}$ signature seen in BD-738. The high Sr/Y and Na_2O contents and low Sm/Nd

observed for both high-CaO/Al₂O₃ and high-SiO₂ Lashaine peridotites qualitatively require separation of the metasomatic melt from a garnet-rich and clinopyroxene-poor source. This is observed for phase relations in subducted sediment at high pressure, where the garnet phase volume expands at the expense of clinopyroxene (Thomsen and Schmidt, 2008). Interestingly, clinopyroxenes in Lashaine peridotites show marked negative trends of Sr/Y with Zr/Sm (Fig. 6E) and Sm/Nd (not shown), which would be compatible with increasing carbonatite component, with fractionated LREE/(HREE + Y) and carrying little Zr (plus other high field strength elements [HFSEs]), in an evolving melt.

Lower-crustal xenoliths from Labait, Lashaine, and Naibor Soito (just south of Pello Hill) are, without exception, Archean in age (Mansur, 2008). There is no evidence within the crust for post-Archean magmatic additions to the lithosphere in this region until the onset of rift magmatism. Therefore, if the signatures in the Lashaine peridotites reflect crustal subduction into the mantle, it probably occurred in the Archean, consistent with the highly evolved ⁸⁷Sr/⁸⁶Sr ratios observed for many Lashaine samples. Equilibrated phlogopite, possibly precipitated during reaction of slab-derived fluid with peridotite, is observed in some samples (Cohen et al., 1984; Dawson, 2002). The most isotopically extreme example of these is BD-738, which has a ⁸⁷Sr/⁸⁶Sr of 0.83 (Cohen et al., 1984). Assuming a bulk rock with 5 vol% phlogopite, 7 vol% garnet, and 7 vol% clinopyroxene (B. Dawson, 2000, personal commun.), and using the observed Rb-Sr elemental compositions (Cohen et al., 1984) and an initial ⁸⁷Sr/⁸⁶Sr for Archean carbonates of 0.7030 (Veizer et al., 1989), this sample would evolve to a ⁸⁷Sr/⁸⁶Sr of only 0.724 after 3 b.y. However, if the initial phlogopite mode was slightly higher (i.e., 8 vol%), the assemblage could generate ⁸⁷Sr/⁸⁶Sr of 0.832 within 3 b.y.

Lithospheric Mantle Contributions to Rift Melts

As discussed already (“Rift-related mantle metasomatism” section), some mantle xenoliths from Tanzania show the chemical and isotopic signatures of recent overprinting by rift-related magmas. Conversely, these magmas show evidence of interaction with the subcontinental lithospheric mantle. In East Africa, small-volume, silica-poor, highly alkaline rock types such as nephelinites, basanites, melilitites, and carbonatites predominate in the craton, whereas in the mobile belt, alkali olivine basalts and tholeiites with higher SiO₂ contents are suggested to be more prevalent, the latter of which are associated with progressively shallower, more voluminous melting (Rogers et al., 2000; Macdonald et al., 2001). This appears reasonable given that the lithospheric mantle beneath the East African Rift, though metasomatized, is still relatively infertile (exemplified by low CaO and Al₂O₃ contents shown in Fig. 2) and cannot give rise to tholeiitic basalts. However, it can generate low-volume silica-undersaturated potassic melts fed by phlogopite- and carbonate-rich metasomatic vein assemblages that form during incipient rifting in continental settings (e.g., Tappe et al., 2007, 2008; Rosenthal et al., 2009). Figure 7 shows that there is no isotopic distinction

between the highly alkaline and tholeiitic basalts from the southern Gregory Rift, despite the reported correlation of setting and chemical composition for rift-related magmas. This may indicate that they share a range of sources from convecting mantle/plume to lithospheric mantle.

For the following analysis, it is important to consider that lithospheric mantle that has been strongly refertilized by rift melts, similar to fertile Labait peridotite LB-45, which has a major-element composition approaching that of primitive mantle, may produce melts that reflect plume geochemistry without directly being plume-derived melts (Bell and Tilton, 2001;

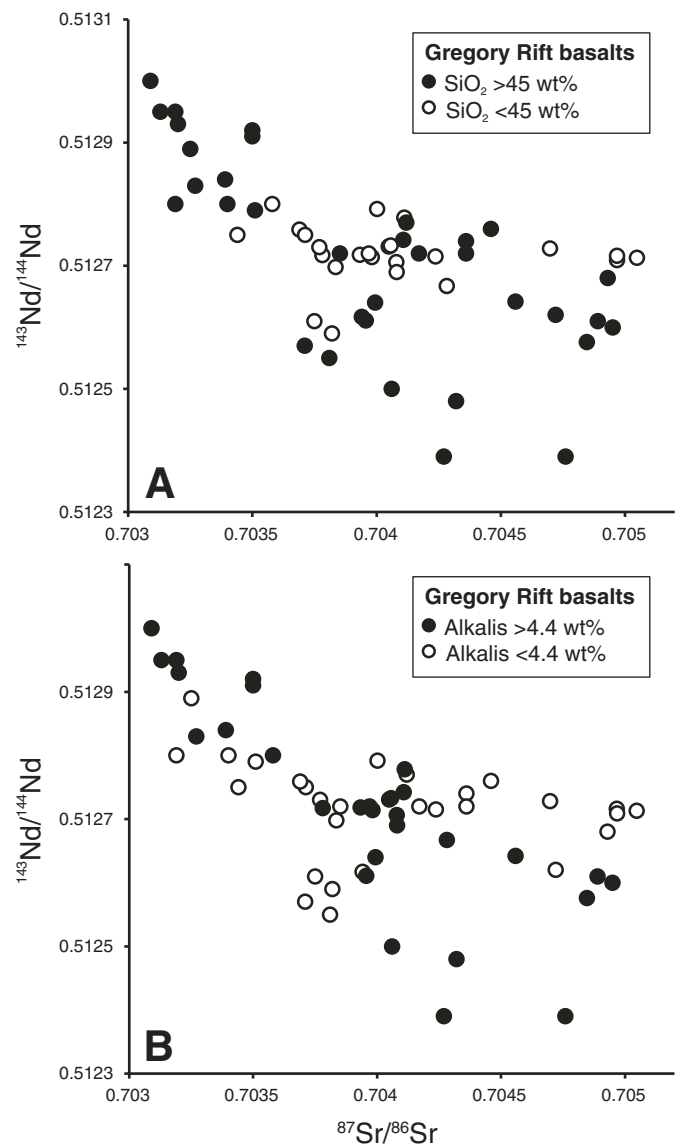


Figure 7. Sr-Nd isotope compositions for lavas from the eastern branch of the East African Rift distinguished by (A) SiO₂-content (cut-off 45 wt%) and (B) alkali content (K₂O+Na₂O, cut-off 4.4 wt%), with the cut-off corresponding to approximately the median content for the data set (references as in Fig. 5).

Späth et al., 2001). Since the isotopic maturation after young rift-related metasomatism is minimal (see, for example, carbonatite-metasomatized peridotites from Olmani), a direct versus indirect plume contribution cannot be distinguished with our data, and only contributions from lithospheric regions with large time-integrated parent-daughter fractionations can be discerned. Furthermore, Pb isotope data might not distinguish well between lithosphere settings (Macdonald et al., 2001), and such data are less commonly available for mantle xenoliths than Sr and Nd isotope data. Therefore, we will focus on the latter in the following discussion, which aims to identify lithospheric mantle signatures in rift melts and address whether they are acquired in situ upon percolation of the melt through the lithosphere or whether they are inherited from a sublithospheric source.

Sr-Nd Isotopic Composition(s) of the “Kenya Plume”

In order to identify the imprint of lithospheric mantle on rift-related melts, it is necessary to constrain the composition of the plume(s) beneath the East African Rift that feeds the wide variety of melts. The presence of one (Ebinger and Sleep, 1998; Morley, 1994) or two thermal anomalies (i.e., the Kenya and the Afar plumes: George and Rogers, 2002; Rogers et al., 2000; Debayle et al., 2001; Nyblade et al., 2000; Montelli et al., 2004) beneath the East African Rift has been suggested based on geochemical, geophysical, and modeling results. Alternatively, a single plume with several plume stems containing domains of isotopically distinct materials may feed the magmatism in the Afar and the Gregory Rifts (Furman et al., 2006). The isotopically distinct western rift magmatism may also require a heterogeneous (Kenya) plume beneath the Tanzanian craton (Chakrabarti et al., 2009). Here, we focus on contributions from sublithospheric and lithospheric mantle sources beneath the northern and southern Gregory Rift (which together form the eastern branch), the western branch, and Rungwe at the southern confluence of the two branches.

To the north, the Afar plume is suggested to have $^{87}\text{Sr}/^{86}\text{Sr}$ of 0.7035 and $^{143}\text{Nd}/^{144}\text{Nd}$ of 0.5129 (Rogers et al., 2000), whereas to the south, various compositional estimates exist for the Kenyan-Tanzanian plume. Consistent with the HIMU signatures seen in widespread African volcanism (Janney et al., 2002), Oldoinyo Lengai volcano and lavas from the Ngorongoro Volcanic Highland in northern Tanzania show both HIMU and EMI signatures, which have been ascribed to mixtures of anciently metasomatized EMI-like lithosphere and plume-derived HIMU-like melts (Bell and Simonetti, 1996; Mollel et al., 2009, 2011). Tertiary (23–20 Ma) melts in the Turkana Depression of northern Kenya and volcanic rocks in southern Ethiopia also have HIMU characteristics (Furman et al., 2006), as do younger volcanic rocks in the Huri Hills volcanic field (Class et al., 1994).

The HIMU signature has been suggested to be due to “conditioning” of the lithospheric mantle by ocean-island basalt (OIB)-like melts billions of years ago (Paslick et al., 1995; Pik et al., 2006). However, a HIMU signature is identified in the Sr-Nd isotope composition of a fertile lherzolite from Labait (LB-45: $^{87}\text{Sr}/^{86}\text{Sr} = 0.7029$, $^{143}\text{Nd}/^{144}\text{Nd} = 0.51286$; Aulbach et al., 2008),

which is derived from the lithosphere-asthenosphere boundary, where it experienced significant refertilization from plume-derived melts (Lee and Rudnick, 1999; Chesley et al., 1999; Aulbach et al., 2008). This suggests that HIMU-like Sr-Nd isotope compositions in the lithospheric mantle may stem from recent addition of and interaction with magmas from the Kenya plume. This is consistent with a model of thermal reactivation and incorporation of lithosphere into the plume (Rogers et al., 2006). At Turkana, the depth of melting exceeds the lithospheric thickness, therefore also clearly arguing against a (purely) lithospheric source of the HIMU signature (Furman et al., 2006).

Moreover, a HIMU composition for the rift magmas can be inferred from the low R/R_a ratios of the Tanzanian peridotite xenoliths (Porcelli et al., 1986; this work), because HIMU lavas typically have lower R/R_a values than those of MORB (Fig. 4; Graham et al., 1992; Hanyu and Kaneoka, 1997). Finally, if the HIMU source resided in the lithosphere and was due to ancient addition of OIB-like melts, the question arises as to why so few lithospheric mantle xenoliths show this signature. Indeed, the Sr-Nd isotope signatures of peridotite xenoliths from Labait range from DM- to EM1-like, whereas Lashaine samples range widely from EM1-like to unusually high $^{87}\text{Sr}/^{86}\text{Sr}$ compositions (Fig. 5). The various arguments outlined here imply a recent, ultimately sublithospheric origin for the HIMU component.

The HIMU-like composition of deep Labait peridotite LB-45 ($^{87}\text{Sr}/^{86}\text{Sr} = 0.7029$, $^{143}\text{Nd}/^{144}\text{Nd} = 0.51286$, $^3\text{He}/^4\text{He} = 5.9$, $^7\text{Li} = 4.9$) is different from the common rift end member in Sr-Nd isotope space ($^{87}\text{Sr}/^{86}\text{Sr} = 0.7035$, $^{143}\text{Nd}/^{144}\text{Nd} = 0.51275$) that has been identified for Tertiary to Holocene magmas from the axial Gregory Rift, which has been suggested to reflect the plume composition (Rogers et al., 2000; Fig. 5). This is, in turn, different from the remarkably homogeneous $^{87}\text{Sr}/^{86}\text{Sr}$ (0.7034–0.7039) and $^{143}\text{Nd}/^{144}\text{Nd}$ (0.51280–0.51284) values seen in the Olmani dunites and wehrlites (Rudnick et al., 1993), as well as the strongly rift-overprinted hydrous peridotites from Pello Hill and Eledoi (Dawson and Smith, 1988; Cohen et al., 1984).

The suggested spread in estimates for the isotope composition of the Kenya plume may indicate that the plume has small but significant heterogeneity in its Sr-Nd isotope characteristics, including a small EM1 component that was present in the plume source and not acquired during percolation through the subcontinental lithospheric mantle, as suggested previously (Aulbach et al., 2008). Compositional variation in a single plume is reported for Hawaii and other oceanic intraplate magmatism (Hofmann, 2005, and references therein) and has also been inferred for the Afar plume to the north (Furman et al., 2006) and for the western branch of the East African Rift (Chakrabarti et al., 2009). If, as suggested here, the Kenya plume is heterogeneous in Sr and Nd isotope compositions, encompassing the range between HIMU and HIMU plus EM1 (circle in Fig. 5), then rift melt compositions falling outside this limited range of isotope ratios (data compiled from <http://georoc.mpch-mainz.gwdg.de/georoc/> and literature cited in the caption to Fig. 5) must reflect contamination by lithospheric mantle (since crustally contaminated samples were

screened out of our compilation using Ce/Pb as a discriminant; Hofmann et al., 1986). Conversely, lithospheric mantle samples with compositions outside this plume range were not severely overprinted by plume material.

Silicate Lavas

As outlined in the previous section, there is no evidence for strongly heterogeneous source material feeding the magmas of the Gregory Rift. Therefore, the isotopic diversity (e.g., HIMU and EM components) seen in rift volcanic rocks has been ascribed to a lithospheric mantle overprint of sublithospheric melts (e.g., Norry et al., 1980; Davies and Macdonald, 1987; Class et al., 1994; Paslick et al., 1995; Bell and Simonetti, 1996; Kalt et al., 1997; Rogers et al., 2000; Macdonald et al., 2001; Clément et al., 2003). It is shown next that lithospheric signatures within rift magmas show geographic variations, as summarized in Furman (2007).

Turkana is a low-standing area of high lithospheric extension sitting between two topographic highs that may be surface expressions of one or more mantle plumes (Furman et al., 2006). At Turkana, Tertiary volcanic rocks exhibit a wider range of radiogenic isotope compositions than Quaternary volcanic rocks. The latter are compositionally similar to the Afar lavas and have HIMU characteristics. Most Turkana Sr-Nd isotope compositions fall into the suggested field of the heterogeneous Kenya plume composition, with a few samples possibly showing the influence of lithospheric mantle or depleted mantle (Fig. 5G; Furman et al., 2006).

The majority of lavas from the northern Gregory Rift have Sr-Nd isotope compositions falling between those of the Kenyan plume and depleted mantle and showing significant overlap with lavas from the Turkana Depression (Fig. 5B). They erupted after prolonged rift activity, predominantly in an axial rift setting, and therefore likely sampled more of the ambient upper mantle and less of the lithospheric mantle. By contrast, the Sr-Nd isotope systematics of most lavas from the southern Gregory Rift trend strongly toward EM1 and, to a lesser degree, toward “anomalously” high $^{87}\text{Sr}/^{86}\text{Sr}$ decoupled from $^{143}\text{Nd}/^{144}\text{Nd}$, including the host melilitite of the Labait xenoliths (Aulbach et al., 2008) (Fig. 5B). The compositions of these lavas likely reflect a significant contribution from lithospheric mantle, similar to that identified beneath Lashaine and Labait (Fig. 5A) and in a single measured Quaternary kimberlite from the Igwisi Hills in the Tanzanian craton. This is consistent with their location in the southern portion of the young Gregory Rift (5 Ma; Dawson, 1992), where the lithospheric mantle is relatively thick (Henjes-Kunst and Altherr, 1992; Rudnick et al., 1994; Ritsema et al., 1998; Lee and Rudnick, 1999; Kaeser et al., 2006). Lavas from Chyulu Hills, east of the southern Gregory Rift valley, overlap both the plume-like Sr-Nd isotope compositions of the northern Gregory Rift and the more enriched compositions seen in lavas from the southern Gregory Rift (Fig. 5B).

Lavas from Rungwe, Tanzania, at the southern terminus of the East African Rift, are not particularly potassic, but they are silica undersaturated (Furman, 1995, 2007). Their Sr-Nd isotope compositions reveal an even stronger influence of ancient LREE-enriched lithosphere than in the southern Gregory Rift.

Like Rungwe, the distinct volcanic provinces of the western branch (Toro-Ankole, Virunga, Kivu) erupt mainly silica-undersaturated lavas with high incompatible element concentrations (Furman, 2007, and references therein; Chakrabarti et al., 2009; Rosenthal et al., 2009). Contrary to the Gregory Rift, there is no identifiable southward age progression, but a systematic decrease in K_2O and CO_2 from north to south is consistent with progressively thinner lithosphere (Furman and Graham, 1999; Rosenthal et al., 2009). Chakrabarti et al. (2009) advocated the presence of a heterogeneous plume source that is tapped at various depths, giving rise to the geochemical diversity of western rift lavas. In contrast, Rogers et al. (1992, 1998) suggested that western rift magmas are derived entirely from the lithospheric mantle, which formed in the Archean and experienced 0.5 Ga and 1 Ga enrichment events. Similarly, western rift kamafugites (silica-undersaturated, Ca-rich rocks), which represent the earliest rift magmas erupted on thick continental lithosphere, are suggested to be derived from a veined lithospheric mantle source with contributions from older Mica-Amphibole-Rutile-Ilmenite-Diopside (MARID)-type and young carbonate-rich metasomes (Rosenthal et al., 2009). The wide range of chemical and isotopic characteristics of Miocene to Holocene mafic lavas from the Kivu volcanic province also bears evidence of a source region with distinct enrichment histories resulting in a heterogeneous lithospheric mantle (Furman and Graham, 1999). The only xenoliths described from western rift volcanic rocks are pyroxenites from Virunga and Toro Ankole that have a narrow range of enriched Sr-Nd isotope compositions, and compositions that overlap those of their host rocks, but for which relationships to rift-related magmatism are unclear (Davies and Lloyd, 1989; Link et al., 2008).

Of all the East African Rift lavas considered, those from the western rift show the strongest variability in Sr-Nd isotope space, many lying far outside the field of proposed intrinsic plume heterogeneity and trending strongly toward high $^{87}\text{Sr}/^{86}\text{Sr}$ compositions seen in Lashaine peridotites (Fig. 5B). Thus, western rift lavas manifest contributions from lithospheric mantle that may resemble that beneath Lashaine (Fig. 5A), which lies nearly 1000 km further east and is inferred to have been subduction-modified in the Archean (see “Prerifting Mantle Metasomatism” section). We therefore suggest that the western rift, though situated in Proterozoic mobile belts (Kokonyangi et al., 2007), like Lashaine, is underlain by cratonic lithosphere that was modified during accretionary processes.

Carbonatite Lavas

The high Sr and Nd concentrations in carbonatites ensure that they are buffered against contaminants (Bell and Blenkinsop, 1987) and can themselves act as powerful metasomatic agents in the mantle, as exemplified at Olmani (Rudnick et al., 1993). In addition, their low viscosity and rapid ascent to the surface do not allow much time for interaction with the crust (tens of years; Williams et al., 1986). In terms of the evolution of rift-related melts, small-volume, volatile-rich magmas, such as carbonatites, have been linked to incipient rifting and faulting, giving way to

larger-volume, silicate-dominated melts as rifting continues (e.g., Bell and Tilton, 2001). The Sr-Nd isotope compositions of East African Rift carbonatites (113 Ma and younger) form a linear array between HIMU and EM1 components (Fig. 5) that is termed the East African carbonatite line (EACL), which reflects mixtures of plume and enriched mantle sources (Bell and Blenkinsop, 1987; Bell and Simonetti, 1996). Individual carbonatite complexes do not show this trend and likely have small, isotopically distinct lithospheric mantle sources that cannot be described purely in terms of components in OIBs, such as HIMU and EM1 (Kalt et al., 1997). By contrast, Bell and Tilton (2001) suggested that the broad-scale mixing between HIMU and EM1 in carbonatites may reflect streaks in the convecting mantle.

For a comparison of the Sr-Nd isotope characteristics of carbonatites to those of xenoliths from the East African Rift, we exclude older complexes from the southern East African Rift (Malawi and Zambia), which, owing to their strongly enriched character, quickly acquire distinct compositions due to in situ decay that cannot be confidently corrected for (Kalt et al., 1997). The most striking observation from Figure 5 is that, contrary to many small-volume silicate melts, such as those from the western rift, carbonatites have virtually no high $^{87}\text{Sr}/^{86}\text{Sr}$ component. The absence of this signature in carbonatites may indicate that, in the East African Rift, carbonatites were not derived from ancient subduction-modified lithospheric mantle. Moreover, any interaction that occurred between carbonatites and this ancient lithosphere resulted in complete overprinting of the lithosphere (e.g., Olmani, which is geographically close to Lashaine, which has the most extreme $^{87}\text{Sr}/^{86}\text{Sr}$). Thus, an unradiogenic Sr component in asthenosphere-derived carbonate melts that were recently added would swamp the signal of radiogenic Sr resulting from ancient metasomatism, as has been postulated for silica-undersaturated lavas from the western rift (Rosenthal et al., 2009).

SUMMARY AND CONCLUSIONS

We used chemical and isotopic characteristics of whole rocks and clinopyroxene from peridotite xenoliths from northern Tanzania to unravel the plume-related and preplume history of the lithospheric mantle beneath the Tanzanian craton margin (Labait) and the rifted, reworked craton beneath the Mozambique belt (Lashaine and Olmani). The lithospheric mantle beneath Tanzania has affinities to three major mantle components identified by Zindler and Hart (1986): (1) a heterogeneous component close to HIMU, associated with recent intrusion of plume-related silicate and carbonatite melts in the deep lithosphere over a geographically wide region (e.g., Labait, Olmani, Pello Hill, and Eledoi), (2) an EM1-like component, likely reflecting old LREE enrichment, which is preserved in refractory mantle samples from Lashaine and Labait, and (3) an EM2-like component reflecting the presence of old recycled continental crustal material identified in the mantle lithosphere underlying Lashaine and Labait.

The Sr-Nd isotopic composition of the plume component is inferred to be heterogeneous and to range from 0.7029 to 0.7036

and 0.51275–0.51286, respectively, as reflected in isotope trends for rift-related magmas (Rogers et al., 2000), and in heavily melt-metasomatized samples from the lithospheric mantle beneath Labait, Pello Hill, Eledoi, and Olmani. Rift-related melts with lower $^{143}\text{Nd}/^{144}\text{Nd}$ and higher $^{87}\text{Sr}/^{86}\text{Sr}$ values than typical of plume compositions are inferred to have interacted with or be derived from ancient metasomatized lithospheric mantle sources such as those preserved beneath Labait and Lashaine that have EM1 or EM2 affinities. Silicate lavas from the southern Gregory Rift, where rifting is recent, show a stronger input of EM1 and EM2 components than lavas from the northern Gregory Rift in Tanzania and the Turkana Depression, where rifting commenced earlier. The strongest lithospheric mantle signature is seen in silicate lavas from the western branch, similar to that recognized in peridotites from Lashaine, where “anomalous” Sr is attributed to ancient subduction. In contrast, the Sr-Nd isotope systematics of rift carbonatites are inconsistent with an EM2 contribution, which indicates that carbonatite melts in the East African Rift are either not derived from or were not affected by subduction-modified regions of the lithospheric mantle.

ACKNOWLEDGMENTS

Barry Dawson provided information regarding field logistics and has always shared his impressive knowledge of Tanzanian xenoliths and lavas; he has been a constant source of inspiration and a wonderful role model for how science should be done. David Graham generously provided the He isotope data reported here. John Lupton is thanked for access to the noble gas laboratory in Newport, Oregon, which is supported by the National Oceanic and Atmospheric Administration (NOAA) Vents Program. We thank Bruce Chappell, Australian National University, for providing excellent quality X-ray fluorescence (XRF) and INAA data so long ago. Tony Irving is thanked for providing sample TZ-2-13 from the Basaltic Volcanism Study Project. At the University of Maryland, Jay Kaufman, Igor Puchtel, and Rich Walker are thanked for sharing their expertise in the isotope geochemistry laboratory and with the thermal ionization mass spectrometer, and Richard Ash is thanked for assistance on the Element2. Tony Simonetti assisted with trace-element analyses at the University of Alberta. We thank the editors for their invitation to contribute to this Special Paper and the reviewers, Tanya Furman and Nick Rogers, for incisive and constructive criticisms that considerably improved the manuscript. This work was supported by the National Science Foundation (grants EAR 9506510, 03037255, and 0609689) and was carried out while Aulbach was the recipient of a Feodor-Lynen fellowship from the Alexander-von-Humboldt Foundation.

REFERENCES CITED

- Aulbach, S., and Rudnick, R.L., 2009, Origins of non-equilibrium Li isotopic fractionation in xenolithic peridotite minerals: Examples from Tanzania: *Chemical Geology*, v. 258, p. 17–27, doi:10.1016/j.chemgeo.2008.07.015.

- Aulbach, S., Rudnick, R.L., and McDonough, W.F., 2008, Li-Sr-Nd isotope signatures of the plume and cratonic lithospheric mantle beneath the margin of the rifted Tanzanian craton (Labait): Contributions to Mineralogy and Petrology, v. 155, p. 79–92, doi:10.1007/s00410-007-0226-4.
- Bell, K., and Blenkinsop, J., 1987, Nd and Sr isotopic compositions of East African carbonatites: Implications for mantle heterogeneity: Geology, v. 15, p. 99–102, doi:10.1130/0091-7613(1987)15<99:NASICO>2.0.CO;2.
- Bell, K., and Simonetti, A., 1996, Carbonatite magmatism and plume activity: Implications from the Nd, Pb and Sr isotope systematics of Oldoinyo Lengai: Journal of Petrology, v. 37, p. 1321–1339, doi:10.1093/ptrology/37.6.1321.
- Bell, K., and Tilton, G.R., 2001, Nd, Pb and Sr isotopic compositions of East African carbonatites: Evidence for mantle mixing and plume inhomogeneity: Journal of Petrology, v. 42, p. 1927–1945, doi:10.1093/ptrology/42.10.1927.
- Burton, K.W., Schiano, P., Birck, J.L., Allegre, C.J., Rehkämpfer, M., Halliday, A.N., and Dawson, J.B., 2000, The distribution and behaviour of rhenium and osmium amongst mantle minerals and the age of the lithospheric mantle beneath Tanzania: Earth and Planetary Science Letters, v. 183, p. 93–106, doi:10.1016/S0012-821X(00)00259-4.
- Byrne, G.F., Jacob, A.W.B., Mechie, J., and Dindi, E., 1997, Seismic structure of the upper mantle beneath the southern Kenya Rift from wide-angle data: Tectonophysics, v. 278, p. 243–260, doi:10.1016/S0040-1951(97)00106-6.
- Chakrabarti, R., Basu, A.R., Santo, A.P., Tedesco, D., and Vaselli, O., 2009, Isotopic and geochemical evidence for a heterogeneous mantle plume origin of the Virunga volcanics, western rift, East African Rift system: Chemical Geology, v. 259, p. 273–289, doi:10.1016/j.chemgeo.2008.11.010.
- Chesley, J.T., Rudnick, R.L., and Lee, C.T., 1999, Re-Os systematics of mantle xenoliths from the East African Rift: Age, structure, and history of the Tanzanian craton: Geochimica et Cosmochimica Acta, v. 63, p. 1203–1217, doi:10.1016/S0016-7037(99)00004-6.
- Class, C., Altherr, R., Volker, F., Eberz, G., and McCulloch, M.T., 1994, Geochemistry of Pliocene to Quaternary alkali basalts from the Hurri Hills, northern Kenya: Chemical Geology, v. 113, p. 1–22, doi:10.1016/0009-2541(94)90002-7.
- Clément, J.-P., Caroff, M., Hémond, C., Tiercelin, J.-J., Bollinger, C., Guillou, H., and Cotten, J., 2003, Pleistocene magmatism in a lithospheric transition area: Petrogenesis of alkaline and peralkaline lavas from the Baringo–Bogoria Basin, central Kenya Rift: Canadian Journal of Earth Sciences, v. 40, p. 1239–1257, doi:10.1139/e03-046.
- Cohen, R.S., O’Nions, R.K., and Dawson, J.B., 1984, Isotope geochemistry of xenoliths from East Africa: Implications for development of mantle reservoirs and their interaction: Earth and Planetary Science Letters, v. 68, p. 209–220, doi:10.1016/0012-821X(84)90153-5.
- Collins, A.S., Reddy, S.M., Buchan, C., and Mruma, A., 2004, Temporal constraints on Palaeoproterozoic eclogite formation and exhumation (Usagaran orogen, Tanzania): Earth and Planetary Science Letters, v. 224, p. 175–192, doi:10.1016/j.epsl.2004.04.027.
- Davies, G.R., and Lloyd, F.E., 1989, Pb-Sr-Nd isotope and trace element data bearing on the origin of the potassic subcontinental lithosphere beneath south-west Uganda, in Saunders, A.D., and Norry, M.J., eds., Kimberlites and Related Rocks, Volume 2: Geological Society of Australia Special Publication 14, p. 784–794.
- Davies, G.R., and Macdonald, R., 1987, Crustal influences in the petrogenesis of the Naivasha basalt-comendite complex: Combined trace element and Sr Nd-Pb constraints: Journal of Petrology, v. 28, p. 1009–1031.
- Dawson, J.B., 1984, Contrasting types of mantle metasomatism?, in Kornprobst, J., ed., Kimberlites II; the Mantle and Crust-Mantle Relationships: Amsterdam, Elsevier, p. 289–294.
- Dawson, J.B., 1992, Neogene tectonics and volcanicity in the North Tanzania sector of the Gregory Rift Valley—Contrasts with the Kenya sector: Tectonophysics, v. 204, p. 81–92, doi:10.1016/0040-1951(92)90271-7.
- Dawson, J.B., 1994, Quaternary kimberlitic volcanism on the Tanzania craton: Contributions to Mineralogy and Petrology, v. 116, p. 473–485, doi:10.1007/BF00310913.
- Dawson, J.B., 1999, Metasomatism and melting in spinel peridotite xenoliths from Labait, Tanzania, in Gurney, J.J., Gurney, J.L., Pascoe, M.D., and Richardson, S.H., eds., The P.H. Nixon Volume: Proceedings of the 7th International Kimberlite Conference: Cape Town, Red Roof Design, p. 164–173.
- Dawson, J.B., 2002, Metasomatism and partial melting in upper-mantle peridotite xenoliths from the Lashaine Volcano, northern Tanzania: Journal of Petrology, v. 43, p. 1749–1777, doi:10.1093/ptrology/43.9.1749.
- Dawson, J.B., 2008, The Gregory Rift Valley and Neogene–Recent Volcanoes of Northern Tanzania: Geological Society of London Memoir 33, 102 p.
- Dawson, J.B., and Smith, J.V., 1973, Alkalic pyroxenite xenoliths from the Lashaine volcano, northern Tanzania: Journal of Petrology, v. 14, p. 113–131.
- Dawson, J.B., and Smith, J.V., 1988, Metasomatized and veined upper-mantle xenoliths from Pello Hill, Tanzania—Evidence for anomalously-light mantle beneath the Tanzanian sector of the East African Rift valley: Contributions to Mineralogy and Petrology, v. 100, p. 510–527, doi:10.1007/BF00371380.
- Dawson, J.B., and Smith, J.V., 1992, Olivine-mica pyroxenite xenoliths from northern Tanzania: Metasomatic products of upper-mantle peridotite: Journal of Volcanology and Geothermal Research, v. 50, p. 131–142.
- Dawson, J.B., Powell, D.G., and Reid, A.M., 1970, Ultrabasic xenoliths and lava from the Lashaine volcano, northern Tanzania: Journal of Petrology, v. 11, p. 519–548.
- Debayle, E., Leveque, J.J., and Cara, M., 2001, Seismic evidence for a deeply rooted low-velocity anomaly in the upper mantle beneath the northeastern Afro/Arabian continent: Earth and Planetary Science Letters, v. 193, p. 423–436, doi:10.1016/S0012-821X(01)00509-X.
- Dunai, T.J., and Porcelli, D., 2002, Storage and transport of noble gases in the subcontinental lithosphere: Reviews in Mineralogy and Geochemistry, v. 47, p. 371–409, doi:10.2138/rmg.2002.47.10.
- Ebinger, C.J., and Sleep, N.H., 1998, Cenozoic magmatism throughout East Africa resulting from impact of a single plume: Nature, v. 395, p. 788–791, doi:10.1038/27417.
- Ebinger, C.J., Deco, A.L., Drake, R.E., and Tesha, A.L., 1989, Chronology of volcanism and rift basin propagation: Rungwe Volcanic Province, East Africa: Journal of Geophysical Research, v. 94, p. 15,785–15,803.
- Fritz, H., Tenczer, V., Hauzenberger, C., Wallbrecher, E., and Muhongo, S., 2009, Hot granulite nappes—Tectonic styles and thermal evolution of the Proterozoic granulite belts in East Africa: Tectonophysics, v. 477, p. 160–173, doi:10.1016/j.tecto.2009.01.021.
- Furman, T., 1995, Melting of metasomatized subcontinental lithosphere: Under-saturated mafic lavas from Rungwe, Tanzania: Contributions to Mineralogy and Petrology, v. 122, p. 97–115, doi:10.1007/s004100050115.
- Furman, T., 2007, Geochemistry of East African Rift basalts: An overview: Journal of African Earth Sciences, v. 48, p. 147–160, doi:10.1016/j.jafrearsci.2006.06.009.
- Furman, T., and Graham, D., 1994, Chemical and isotopic variations in volcanic rocks from the Rungwe Province: Constraints on the development and scales of source heterogeneity beneath the African western rift: Mineralogical Magazine, v. 58A, p. 297–298, doi:10.1180/minmag.1994.58A.1.156.
- Furman, T., and Graham, D., 1999, Erosion of lithospheric mantle beneath the East African Rift system: Geochemical evidence from the Kivu volcanic province: Lithos, v. 48, p. 237–262, doi:10.1016/S0024-4937(99)00031-6.
- Furman, T., Kaleta, K.M., Bryce, J.G., and Hanan, B.B., 2006, Tertiary mafic lavas of Turkana, Kenya: Constraints on East African plume structure and the occurrence of high-volcanism in Africa: Journal of Petrology, v. 47, p. 1221–1244, doi:10.1093/ptrology/eg1009.
- George, R., and Rogers, N.W., 2002, Plume dynamics beneath the African plate inferred from the geochemistry of the Tertiary basalts of southern Ethiopia: Contributions to Mineralogy and Petrology, v. 144, p. 286–304, doi:10.1007/s00410-002-0396-z.
- George, R., Rogers, N., and Kelley, S., 1998, Earliest magmatism in Ethiopia: Evidence for two mantle plumes in one flood basalt province: Geology, v. 26, p. 923–926, doi:10.1130/0091-7613(1998)026<0923:EMIEEF>2.3.CO;2.
- Graham, D.W., Humphris, S.E., Jenkins, W.J., and Kurz, M.D., 1992, Helium isotope geochemistry of some volcanic rocks from Saint Helena: Earth and Planetary Science Letters, v. 110, p. 121–131, doi:10.1016/0012-821X(92)90043-U.
- Graham, D.W., Larsen, L.M., Hanan, B.B., Storey, M., Pedersen, A.K., and Lupton, J.E., 1998, Helium isotope composition of the early Iceland mantle plume inferred from the Tertiary picrites of West Greenland: Earth and Planetary Science Letters, v. 160, p. 241–255, doi:10.1016/S0012-821X(98)00083-1.
- Hanyu, T., and Kaneoka, I., 1997, The uniform and low $^3\text{He}/^4\text{He}$ ratios of HIMU basalts as evidence for their origin as recycled materials: Nature, v. 390, p. 273–276, doi:10.1038/36835.

- Henjes-Kunst, F., and Altherr, R., 1992, Metamorphic petrology of xenoliths from Kenya and northern Tanzania and implications for geotherms and lithospheric structures: *Journal of Petrology*, v. 33, p. 1125–1156.
- Hofmann, A.W., 2005, Sampling mantle heterogeneity through oceanic basalts: Isotopes and trace elements, in Carlson, R.W., Holland, H.D., and Turekian, K.K., eds., *Treatise on Geochemistry: The Mantle and Core*: Amsterdam, Elsevier, p. 1–38.
- Hofmann, A.W., Jochum, K.P., Seufert, M., and White, W.M., 1986, Nb and Pb in oceanic basalts: New constraints on mantle evolution: *Earth and Planetary Science Letters*, v. 79, p. 33–45, doi:10.1016/0012-821X(86)90038-5.
- Jackson, M.G., Hart, S.R., Koppers, A.A.P., Staudigel, H., Konter, J., Blusztajn, J., Kurz, M., and Russell, J.A., 2007, The return of subducted continental crust in Samoan lavas: *Nature*, v. 448, p. 684–687, doi:10.1038/nature06048.
- Jagoutz, E., 1988, Nd and Sr systematics in an eclogite xenolith from Tanzania: evidence for frozen mineral equilibria in the continental lithosphere: *Geochimica et Cosmochimica Acta*, v. 52, p. 1285–1293, doi:10.1016/0016-7637(88)90282-7.
- Janney, P.E., Le Roex, A.P., Carlson, R.W., and Viljoen, K.S., 2002, A chemical and multi-isotope study of the Western Cape olivine melilitite province, South Africa: implications for the sources of kimberlites and the origin of the HIMU signature in Africa: *Journal of Petrology*, v. 43, p. 2339–2370, doi:10.1093/petrology/43.12.2339.
- Johnson, P.R., Abdelsalam, M.G., and Stern, R.J., 2003, The Bi'r Umq-nakasib suture zone in the Arabian-Nubian Shield: A key to understanding crustal growth in the east African orogen: *Gondwana Research*, v. 6, p. 523–530, doi:10.1016/S1342-937X(05)71003-0.
- Jones, A.P., Smith, J.V., and Dawson, J.B., 1983, Glasses in mantle xenoliths from Olmani, Tanzania: *The Journal of Geology*, v. 91, p. 167–178, doi:10.1086/628754.
- Kaerer, B., Kalt, A., and Pettke, T., 2006, Evolution of the lithospheric mantle beneath the Marsabit volcanic field (northern Kenya): Constraints from textural, *P-T* and geochemical studies on xenoliths: *Journal of Petrology*, v. 47, p. 2149–2184, doi:10.1093/petrology/egl040.
- Kaerer, B., Olker, B., Kalt, A., Altherr, R., and Pettke, T., 2009, Pyroxenite xenoliths from Marsabit (northern Kenya): Evidence for different magmatic events in the lithospheric mantle and interaction between peridotite and pyroxenite: *Contributions to Mineralogy and Petrology*, v. 157, p. 453–472, doi:10.1007/s00410-008-0345-6.
- Kalt, A., Hegner, E., and Satir, M., 1997, Nd, Sr and Pb isotopic evidence for diverse lithospheric mantle sources of East African Rift carbonatites: *Tectonophysics*, v. 278, p. 31–45, doi:10.1016/S0040-1951(97)00093-0.
- Keller, G.R., Mechie, J., Braile, L.W., Mooney, W.D., and Prodehl, C., 1994, Seismic structure of the uppermost mantle beneath the Kenya Rift: *Tectonophysics*, v. 236, p. 201–216, doi:10.1016/0040-1951(94)90177-5.
- Kokonyangi, J.W., Kampunzu, A.B., Armstrong, R.A., Arima, M., Yoshida, M., and Okudaria, T., 2007, U-Pb SHRIMP dating of detrital zircons from the Znlo group (Kibaran belt): Implications for the source of sediments and Mesoproterozoic evolution of central Africa: *The Journal of Geology*, v. 115, p. 99–113, doi:10.1086/509270.
- Koornneef, J.M., Davies, G.R., Dopp, S., Vukmanovic, Z., Nikogosian, I.K., and Mason, R.D., 2009, Nature and timing of multiple metasomatic events in the sub-cratonic lithosphere beneath Labait, Tanzania: *Lithos*, v. 112, no. S2, p. 896–912, doi:10.1016/j.lithos.2009.04.039.
- Latin, D., Norry, M.J., and Tarzey, R.J.E., 1993, Magmatism in the Gregory Rift, East Africa—Evidence for melt generation by a plume: *Journal of Petrology*, v. 34, p. 1007–1027.
- Lee, C.-T., and Rudnick, R.L., 1999, Compositionally stratified cratonic lithosphere: Petrology and geochemistry of peridotite xenoliths from the Labait Volcano, Tanzania, in Gurney, J.J., Gurney, J.L., Pascoe, M.D., and Richardson, S.H., eds., *The P.H. Nixon Volume: Proceedings of the 7th International Kimberlite Conference: Cape Town, Red Roof Design*, p. 503–521.
- Lee, C.-T., Rudnick, R.L., McDonough, W.F., and Horn, I., 2000, Petrologic and geochemical investigation of carbonates in peridotite xenoliths from northeastern Tanzania: *Contributions to Mineralogy and Petrology*, v. 139, p. 470–484, doi:10.1007/s004100000144.
- Le Roex, A.P., Spaeth, A., and Zartman, R.E., 2001, Lithospheric thickness beneath the southern Kenya Rift: implications from basalt geochemistry: *Contributions to Mineralogy and Petrology*, v. 142, p. 89–106, doi:10.1007/s004100100273.
- Link, K., Barifaijo, E., Tiberindwa, J., and Foley, S.F., 2008, Veined pyroxenite xenoliths from the kamafugites in the Toro-Ankole region of western Uganda: A window to a rift-related mantle, in 9th International Kimberlite Conference Extended Abstracts: Frankfurt, Germany, abs. 9IKC-00403.
- Maboko, M.A.H., 2000, Nd and Sr isotopic investigation of the Archean-Proterozoic boundary in north eastern Tanzania: constraints on the nature of Neoproterozoic tectonism in the Mozambique belt: *Precambrian Research*, v. 102, p. 87–98, doi:10.1016/S0301-9268(00)00060-7.
- Macdonald, R., 2002, Magmatism of the Kenya Rift Valley: A review: *Transactions of the Royal Society of Edinburgh, Earth Sciences*, v. 93, p. 239–253, doi:10.1017/S0263593300000420.
- Macdonald, R., Davies, G.R., Upton, B.G.J., Dunkley, P.N., Smith, M., and Leat, P.T., 1995, Petrogenesis of Silali volcano, Gregory Rift, Kenya: *Journal of the Geological Society of London*, v. 152, p. 703–720, doi:10.1144/gsjgs.152.4.0703.
- Macdonald, R., Rogers, N.W., Fitton, J.G., Black, S., and Smith, M., 2001, Plume-lithosphere interactions in the generation of the basalts of the Kenya Rift, East Africa: *Journal of Petrology*, v. 42, p. 877–900, doi:10.1093/petrology/42.5.877.
- Mansur, A., 2008, Composition, Age, and Origin of Lower Crust in Northern Tanzania [M.S. thesis]: College Park, University of Maryland, 149 p.
- Manya, S., Kobayashi, K., Maboko, J.A.H., and Nakamura, E., 2006, Ion microprobe zircon U-Pb dating of the late Archaean metavolcanics and associated granites of the Musoma-Mara greenstone belt, northeast Tanzania: implications for the geological evolution of the Tanzania craton: *Journal of African Earth Sciences*, v. 45, p. 355–366, doi:10.1016/j.jafrearsci.2006.03.004.
- McDonough, W.F., and Sun, S.-S., 1995, The composition of the Earth: *Chemical Geology*, v. 120, p. 223–253, doi:10.1016/0009-2541(94)00140-4.
- Michard, A., Guriet, P., Soudant, M., and Albarède, F., 1985, Nd isotopes in French Phanerozoic shales: External vs. internal aspects of crustal evolution: *Geochimica et Cosmochimica Acta*, v. 49, p. 601–610, doi:10.1016/0016-7637(85)90051-1.
- Mollet, G.F., Swisher, C.C., III, McHenry, L.J., Feigenson, M.D., and Carr, M.J., 2009, Petrogenesis of basalt–trachyte lavas from Olmoti Crater, Tanzania: *Journal of African Earth Sciences*, v. 54, p. 127–143, doi:10.1016/j.jafrearsci.2009.03.008.
- Mollet, G.F., Swisher, C.C., III, Feigenson, M.D., and Carr, M.J., 2011, Petrology, geochemistry, and age of Satiman, Lemagurur, and Oldeani: Sources of the volcanic deposits of the Laetoli area, in Harrison, T., ed., *Paleontology and Geology of Laetoli: Human Evolution in Context 1*: Dordrecht, the Netherlands, Springer, p. 99–119, doi:10.1007/978-90-481-9956-3_5.
- Möller, A., Appel, P., Mezger, K., and Schenk, V., 1995, Evidence for a 2 Ga subduction zone: Eclogites in the Usagaran belt of Tanzania: *Geology*, v. 23, p. 1067–1070, doi:10.1130/0091-7613(1995)023<1067:EFAGSZ>2.3.CO;2.
- Möller, A., Mezger, K., and Schenk, V., 1998, Crustal age domains and the evolution of the continental crust in the Mozambique belt of Tanzania: Combined Sm-Nd, Rb-Sr, and Pb-Pb isotopic evidence: *Journal of Petrology*, v. 39, p. 749–783, doi:10.1093/petrology/39.4.749.
- Montelli, R., Nolet, G., Dahlen, F.A., Masters, G., Engdahl, E.R., and Hung, S.-H., 2004, Finite-frequency tomography reveals a variety of plumes in the mantle: *Science*, v. 303, p. 338–343, doi:10.1126/science.1092485.
- Morley, C.K., 1994, Interaction of deep and shallow processes in the evolution of the Kenya Rift: *Tectonophysics*, v. 236, p. 81–91, doi:10.1016/0040-1951(94)90170-8.
- Norry, M.J., Truckle, P.H., Lippard, S.J., Hawkesworth, C.J., Weaver, S.D., and Marriner, G.F., 1980, Isotopic and trace element evidence from lavas, bearing on mantle heterogeneity beneath Kenya: *Philosophical Transactions of the Royal Society of London, ser. A*, v. 279, p. 259–271.
- Nyblade, A.A., and Brazier, R.A., 2002, Precambrian lithospheric controls on the development of the East African Rift system: *Geology*, v. 30, p. 755–758, doi:10.1130/0091-7613(2002)030<0755:PLCOTD>2.0.CO;2.
- Nyblade, A.A., Owens, R.J., Gurrola, H., Ritsema, J., and Langston, C.A., 2000, Seismic evidence for a deep upper mantle thermal anomaly beneath East Africa: *Geology*, v. 28, p. 599–602, doi:10.1130/0091-7613(2000)28<599:SEFADU>2.0.CO;2.
- Parai, R., Mukhopadhyay, S., and Lassiter, J.C., 2009, New constraints on the HIMU mantle from neon and helium isotopic compositions of basalts from the Cook–Austral Islands: *Earth and Planetary Science Letters*, v. 277, p. 253–261, doi:10.1016/j.epsl.2008.10.014.
- Paslick, C., Halliday, A., James, D., and Dawson, J.B., 1995, Enrichment of the continental lithosphere by OIB melts: Isotopic evidence from the volcanic province of northern Tanzania: *Earth and Planetary Science Letters*, v. 130, p. 109–126, doi:10.1016/0012-821X(95)00002-T.

- Pik, R., Marty, B., and Hilton, D.R., 2006, How many mantle plumes in Africa? The geochemical point of view: *Chemical Geology*, v. 226, p. 100–114, doi:10.1016/j.chemgeo.2005.09.016.
- Pike, J.E.N., Meyer, C.E., and Wilshire, H.G., 1980, Petrography and chemical composition of a suite of ultramafic xenoliths from Lashaine, Tanzania: *The Journal of Geology*, v. 88, p. 343–352, doi:10.1086/628512.
- Porcelli, D.R., O'Nions, R.K., and O'Reilly, S.Y., 1986, Helium and strontium isotopes in ultramafic xenoliths: *Chemical Geology*, v. 54, p. 237–249, doi:10.1016/0009-2541(86)90139-7.
- Rhodes, J.M., and Dawson, J.B., 1975, Major and trace element chemistry of peridotite inclusions from the Lashaine volcano, Tanzania, in Ahrens, L.H., Dawson, J.B., Duncan, A.R., and Erlank, A.J., eds., *Physics and Chemistry of the Earth*, v. 9, p. 545–557.
- Ritsema, J., Nyblade, A.A., Owens, T.J., Langston, C.A., and Vandecar, J.C., 1998, Upper mantle seismic velocity structure beneath Tanzania, East Africa: Implications for the stability of cratonic lithosphere: *Journal of Geophysical Research*, v. 103, p. 21,201–21,213, doi:10.1029/98JB01274.
- Rogers, N.W., Hawkesworth, C.J., Parker, R.J., and Marsh, J.S., 1985, The geochemistry of potassic lavas from Vulsini, central Italy, and implications for mantle enrichment processes beneath the Roman region: *Contributions to Mineralogy and Petrology*, v. 90, p. 244–257, doi:10.1007/BF00378265.
- Rogers, N.W., De Mulder, M., and Hawkesworth, C.J., 1992, An enriched mantle source for potassic basanites: Evidence from Karisimbi volcano, Virunga volcanic province, Rwanda: *Contributions to Mineralogy and Petrology*, v. 111, p. 543–556, doi:10.1007/BF00320908.
- Rogers, N.W., James, D., Kelley, S.P., and DeMulder, M., 1998, The generation of potassic lavas from the eastern Virunga province, Rwanda: *Journal of Petrology*, v. 39, p. 1223–1247, doi:10.1093/petrology/39.6.1223.
- Rogers, N.W., Macdonald, R., Fitton, J.G., George, R., Smith, M., and Barreiro, B., 2000, Two mantle plumes beneath the East African Rift system: Sr, Nd, and Pb isotope evidence from Kenya Rift basalts: *Earth and Planetary Science Letters*, v. 176, p. 387–400, doi:10.1016/S0012-821X(00)00012-1.
- Rogers, N.W., Thomas, L.E., Macdonald, R., Hawkesworth, C.J., and Mokedem, F., 2006, ^{238}U – ^{230}Th disequilibrium in recent basalts and dynamic melting beneath the Kenya Rift: *Chemical Geology*, v. 234, p. 148–168, doi:10.1016/j.chemgeo.2006.05.002.
- Rosenthal, A., Foley, S.F., Pearson, D.G., Nowell, G.M., and Tappe, S., 2009, Petrogenesis of strongly alkaline primitive volcanic rocks at the propagating tip of the western branch of the East African Rift: *Earth and Planetary Science Letters*, v. 284, p. 236–248, doi:10.1016/j.epsl.2009.04.036.
- Rudnick, R.L., and Walker, R.J., 2009, Interpreting ages from Re–Os isotopes in peridotites: *Lithos*, v. 112, no. S2, p. 1083–1095, doi:10.1016/j.lithos.2009.04.042.
- Rudnick, R.L., McDonough, W.F., and Chappell, B.W., 1993, Carbonatite metasomatism in the northern Tanzanian mantle: Petrographic and geochemical characteristics: *Earth and Planetary Science Letters*, v. 114, p. 463–475, doi:10.1016/0012-821X(93)90076-L.
- Rudnick, R.L., McDonough, W.F., and Orpin, A., 1994, Northern Tanzanian peridotite xenoliths: A comparison with Kaapvaal peridotites and inferences on metasomatic interactions, in Meyer, H.O.A., and Leonardos, O., eds., *Kimberlites, Related Rocks and Mantle Xenoliths, Volume I* (Proceedings of the 5th International Kimberlite Conference): Brasilia, Companhia de Pesquisa de Recursos Minerais, p. 336–353.
- Rudnick, R.L., Ireland, T.R., Gehrels, G., Irving, A.J., Chesley, J.T., and Hanchar, J.M., 1999, Dating mantle metasomatism: U–Pb geochronology of zircons in cratonic mantle xenoliths from Montana and Tanzania, in Gurney, J.J., Gurney, J.L., Pascoe, M.D., and Richardson, S.H., eds., *The P.H. Nixon Volume: Proceedings of the 7th International Kimberlite Conference*: Cape Town, Red Roof Design, p. 728–735.
- Schmidberger, S.S., Simonetti, A., Heaman, L.M., Creaser, R.A., and Whiteford, S., 2007, Lu–Hf, in-situ Sr and Pb isotope and trace element systematics for mantle eclogites from the Diavik diamond mine: Evidence for Paleoproterozoic subduction beneath the Slave craton, Canada: *Earth and Planetary Science Letters*, v. 254, p. 55–68, doi:10.1016/j.epsl.2006.11.020.
- Smith, M., and Mosley, P., 1993, Crustal heterogeneity and basement influence on the development of the Kenya Rift, East Africa: *Tectonics*, v. 12, p. 591–606, doi:10.1029/92TC01710.
- Sommer, H., Kroener, A., Hauzenberger, C.A., Huhongo, S., and Wingate, M.T.D., 2003, Metamorphic petrology and zircon geochronology of high-grade rocks from the central Mozambique belt of Tanzania: crustal recycling of Archean and Palaeoproterozoic materials during the Pan-African orogeny: *Journal of Metamorphic Geology*, v. 21, p. 915–934, doi:10.1111/j.1525-1314.2003.00491.x.
- Späth, A., le Roex, A.P., and Opiyo-Akech, N., 2001, Plume-lithosphere interaction and the origin of continental rift-related alkaline volcanism—The Chyulu Hills volcanic province, southern Kenya: *Journal of Petrology*, v. 42, p. 765–787, doi:10.1093/petrology/42.4.765.
- Stachel, T., Harris, J.W., and Brey, G.P., 1998, Rare and unusual mineral inclusions in diamonds from Mwadui, Tanzania: *Contributions to Mineralogy and Petrology*, v. 132, p. 34–47, doi:10.1007/s004100050403.
- Stachel, T., Harris, J.W., and Brey, G.P., 1999, REE patterns of peridotitic and eclogitic inclusions in diamonds from Mwadui (Tanzania), in Gurney, J.J., Gurney, J.L., Pascoe, M.D., and Richardson, S.H., eds., *The P.H. Nixon Volume: Proceedings of the 7th International Kimberlite Conference*: Cape Town, Red Roof Design, p. 829–835.
- Tappe, S., Foley, S.F., Stracke, A., Romer, R.L., Kjarsgaard, B.A., Heaman, L.M., and Joyce, N., 2007, Craton reactivation on the Labrador Sea margins: $^{40}\text{Ar}/^{39}\text{Ar}$ age and Sr–Nd–Hf–Pb isotope constraints from alkaline and carbonatite intrusives: *Earth and Planetary Science Letters*, v. 256, p. 433–454, doi:10.1016/j.epsl.2007.01.036.
- Tappe, S., Foley, S.F., Kjarsgaard, B.A., Romer, R.L., Heaman, L.M., Stracke, A., and Jenner, G.A., 2008, Between carbonatite and lamproite—Diamondiferous Torngat ultramafic lamprophyres formed by carbonate-fluxed melting of cratonic MARID-type metasomes: *Geochimica et Cosmochimica Acta*, v. 72, p. 3258–3286, doi:10.1016/j.gca.2008.03.008.
- Thompson, R.N., and Gibson, S.A., 1994, Magmatic expression of lithospheric thinning across continental rifts: *Tectonophysics*, v. 233, p. 41–68, doi:10.1016/0040-1951(94)90219-4.
- Thomsen, T.B., and Schmidt, M.W., 2008, Melting of carbonated pelites at 2.5–5.0 GPa, silicate–carbonatite liquid immiscibility, and potassium–carbon metasomatism of the mantle: *Earth and Planetary Science Letters*, v. 267, p. 17–31, doi:10.1016/j.epsl.2007.11.027.
- van Achterbergh, E., Ryan, C.G., Jackson, S.E., and Griffin, W.L., 2001, Data reduction software for LA-ICP-MS: Appendix, in Sylvester, P.J., ed., *Laser ablation-ICP-mass spectrometry in the Earth Sciences: Principles and applications*: Mineralogical Association of Canada, Short Course Series, v. 29, p. 239–243.
- Vauchez, A., Dineur, F., and Rudnick, R., 2005, Microstructure, texture and seismic anisotropy of the lithospheric mantle above a mantle plume: Insights from the Labait volcano xenoliths (Tanzania): *Earth and Planetary Science Letters*, v. 232, p. 295–314, doi:10.1016/j.epsl.2005.01.024.
- Veizer, J., Hoefs, J., Lowe, D.R., and Thurston, P.C., 1989, Geochemistry of Precambrian carbonates: II. Archean greenstone belts and Archean sea water: *Geochimica et Cosmochimica Acta*, v. 53, p. 859–871, doi:10.1016/0016-7037(89)90031-8.
- Wasserburg, G.J., Jacobsen, S.B., DePaolo, D.J., McCulloch, M.T., and Wen, T., 1981, Precise determination of Sm/Nd ratios, Sm and Nd isotopic abundances in standard solutions: *Geochimica et Cosmochimica Acta*, v. 45, p. 2311–2323, doi:10.1016/0016-7037(81)90085-5.
- Watson, E.B., Wark, D.A., and Thomas, J.B., 2006, Crystallization thermometers for zircon and rutile: *Contributions to Mineralogy and Petrology*, v. 151, p. 413–433, doi:10.1007/s00410-006-0068-5.
- Weeraratne, D.S., Forsythe, D.W., Fischer, K.M., and Nyblade, A.A., 2003, Evidence for an upper mantle plume beneath the Tanzanian craton from Rayleigh wave tomography: *Journal of Geophysical Research*, v. 108, no. B9, p. 2427, doi:10.1029/2002JB002273.
- Williams, R.W., Gill, J.B., and Bruland, K.W., 1986, Ra–Th disequilibria systematics: Timescale of carbonatite magma formation at Oldoinyo Lengai volcano, Tanzania: *Geochimica et Cosmochimica Acta*, v. 50, p. 1249–1259, doi:10.1016/0016-7037(86)90408-4.
- Zindler, A., and Hart, S., 1986, Chemical geodynamics: *Annual Review of Earth and Planetary Sciences*, v. 14, p. 493–571, doi:10.1146/annurev.earth.14.050186.002425.

Petrology and geochemistry of alkaline lava series, Kilimanjaro, Tanzania: New constraints on petrogenetic processes

**Philippe Nonnotte
Mathieu Benoit*
Bernard Le Gall
Christophe Hémond
Joël Rolet
Joseph Cotten**

*Institut Universitaire Européen de la Mer, Université de Brest, Centre National de la Recherche Scientifique,
UMR 6538 Domaines Océaniques, Place N. Copernic, 29280 Plouzané, France*

Pierre Brunet

*Observatoire Midi Pyrénées, Université Paul Sabatier, Centre National de la Recherche Scientifique,
UMR 5563 Géosciences Environnement Toulouse, 14 av. Edouard Belin, 31400 Toulouse, France*

Edikafumeni Makoba

Department of Geology, University of Dar Es Salaam, P.O. Box 35052, Dar Es Salaam, Tanzania

ABSTRACT

New major-element, trace-element, and isotopic (Nd, Sr) analyses of undersaturated alkaline lavas from the Kilimanjaro volcano (north Tanzania) are presented. These data concern 54 samples, ranging from basanites to phonolites, collected during a 1 mo field trip in March 2005. The three main cones of Kilimanjaro were sampled, Shira, Mawenzi, and Kibo, together with numerous parasitic cones located on a SE lineament on the main edifice. On the basis of both spatial distribution and major- and trace-element characteristics of analyzed samples, the previous classification of Kilimanjaro lavas is simplified into five groups: Shira, Mawenzi, Kibo 1, Kibo 2, and parasitic activity, each of which has distinct petrological and geochemical features. The major- and trace-element characteristics of the rare primitive lavas erupted on the volcano yield the ubiquitous signature of amphibole within the magma source. We propose that Kilimanjaro melts originated from the partial melting of lithospheric mantle. Combined modeling of trace-element behavior during partial melting + fractional crystallization and isotopic constraints allow us to propose a schematic model of melt genesis under the Kilimanjaro area. Thermal heating of the

*Current address: Observatoire Midi Pyrénées, Université Paul Sabatier, Centre National de la Recherche Scientifique, UMR 5563 Géosciences Environnement Toulouse, 14 av. Edouard Belin, 31400 Toulouse, France.

Nonnotte, P., Benoit, M., Le Gall, B., Hémond, C., Rolet, J., Cotten, J., Brunet, P., and Makoba, E., 2011, Petrology and geochemistry of alkaline lava series, Kilimanjaro, Tanzania: New constraints on petrogenetic processes, *in* Beccaluva, L., Bianchini, G., and Wilson, M., eds., *Volcanism and Evolution of the African Lithosphere: Geological Society of America Special Paper 478*, p. 127–158, doi:10.1130/2011.2478(07). For permission to copy, contact editing@geosociety.org. © 2011 The Geological Society of America. All rights reserved.

ancient continental lithosphere by an upwelling plume triggered partial melting in parts of the lithosphere where amphibole was present and led to the Shira volcanic episode. Then, during a time span of ~1 m.y., the depleted lithosphere was progressively infiltrated by plume melts that resulted in crystallization of a new generation of metasomatic amphibole. Finally, this rejuvenated lithosphere underwent partial melting, leading to the magmas that formed the main edifice (Mawenzi and Kibo), and leading to a progressive depletion of the source with time. An active contribution of true asthenospheric melts during the last magmatic events of the volcano cannot be excluded, but further detailed isotopic investigations are needed to test the model.

INTRODUCTION

Numerous occurrences of abundant differentiated alkaline rocks, and particularly of phonolites, have been described, either (1) on intra-oceanic islands, e.g., Ua Pou in the Marquesas Archipelago (Legendre et al., 2005), and Tristan da Cunha (Le Roex et al., 1990) and Fernando de Noronha (Weaver, 1990) in the Atlantic, or (2) in intraplate continental settings, e.g., Mount Erebus in Antarctica (Goldich et al., 1975; Kyle et al., 1992), Mount Kenya (Price et al., 1985), and the Kenya Rift, Kenya, where plateau-type flood phonolitic lava flows are common (Lippard, 1973; Goles, 1976; Hay and Wendlandt, 1995; Hay et al., 1995). Whether from intra-oceanic or intracontinental settings, the origin of these phonolites is still a matter of debate. The bimodal distribution of the corresponding alkaline magmatic series (characterized by the absence or paucity of intermediate lavas, referred to as the “Daly gap”), in addition to the huge volume of phonolites erupted in several locations (Ua Pou, Kenya Plateau), has been explained by the derivation of these lavas from partial melting of mantle-derived basaltic material at depth (Hay and Wendlandt, 1995; Hay et al., 1995; Kaszuba and Wendlandt, 2000) or basaltic materials at depth (Legendre et al., 2005). On the contrary, the almost continuous series ranging from basanites to phonolites through phono-tephritic and tephri-phonolitic lavas, which are observed in Tristan Da Cunha, Fernando de Noronha, Mount Erebus, and Mount Kenya, have been explained by the derivation of phonolites from associated mafic magmas by fractional crystallization processes, possibly coupled with crustal assimilation (Price et al., 1985; Le Roex et al., 1990; Weaver, 1990; Kyle et al., 1992).

The aim of this study is to examine the origin and evolution of the alkaline lavas, and particularly those of the abundant phonolites, at Kilimanjaro volcano (Tanzania) in the East African Rift system. Previous studies have mainly examined the lavas at Kilimanjaro from the point of view of their emplacement and volcano-stratigraphic relationships (Downie et al., 1956, 1965; Downie and Wilkinson, 1972). We present new data on the whole-rock major- and trace-element and isotope geochemistry of lavas and intrusive rocks sampled on the southern flank of Kilimanjaro. These data are discussed in order (1) to better constrain the nature of the mantle sources and primitive magmas, and (2) to investigate the petrogenetic relationships among

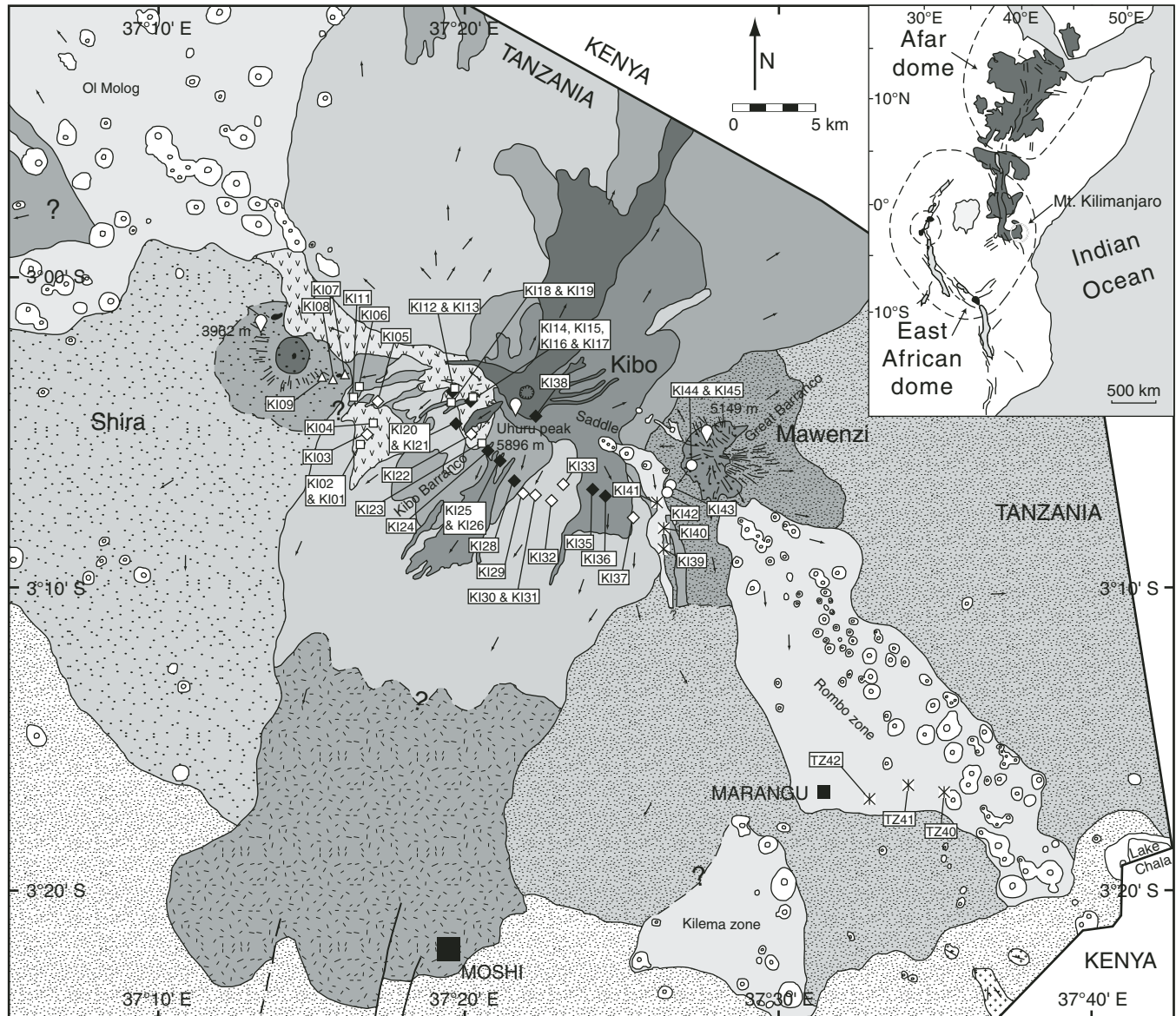
mafic, intermediate, and highly differentiated rocks sampled in the most representative volcanic formations.

GEOLOGICAL FRAMEWORK AND VOLCANIC HISTORY

Kilimanjaro is Africa's highest mountain, culminating at 5895 m, and it constitutes the most prominent volcanic construction of the East African Rift as a whole. This huge volcanic edifice belongs to the volcanic province associated with the north Tanzanian divergence (Dawson, 1992), a sector where the eastern branch of the East African Rift diverges southward from a single and narrow N-S-trending volcanic rift valley, in southern Kenya, to form a 400-km-wide three-arm rift system approaching the Tanzanian craton (Ebinger et al., 1997). In association with this significant change in the rifting morphology, a transverse volcanic chain, trending N80°E over more than 200 km, developed with the emplacement of major volcanic edifices such as the Ngorongoro crater, Mount Meru, and Kilimanjaro. Kilimanjaro is located in a key area of this system, where the N80°E-trending volcanic chain intersects a first-order NW-SE basement discontinuity. The latter might have played an important role in the propagation of rifting southward along the Pangani Rift arm (Le Gall et al., 2008).

Kilimanjaro is a 40 × 60 km elliptic edifice, consisting of three major eruptive centers located along a N110°E-trending axis: From W to E, they are the Shira, Kibo, and Mawenzi vents (Fig. 1). The chronology of volcanic activity, discussed by Nonnotte et al. (2008), is polyphased and involves the migration of eruptive processes from one center to another. Shira is the oldest vent, with activity from ca. 2.5 Ma to 1.9 Ma. The latest phases of activity in this center are characterized by the emplacement of a dense radial dike swarm and by the collapse of the northern part of the edifice. Kilimanjaro then recorded a 1-m.y.-long period of quiescence, before the migration of the volcanic activity toward

Figure 1. Simplified geological map of the three volcanic centers of Kilimanjaro (modified after Nonnotte et al., 2008), with the locations of the analyzed samples and their petrological and geochemical affinities. The insert shows the location of the Kilimanjaro volcano along the eastern arm of the East African Rift system.



Geological formations

Kibo

- Inner Crater Group
- Caldera Rim Group
- Lent Group
- Rhomb Porphyry Group
- Lava Tower Group
- Kibo lahar (rich in Rhomb Porphyry Group fragments)

Mawenzi

- Mawenzi Eruptive Center
- Neumann Tower–Mawenzi Group
- Mawenzi undifferentiated lavas

Shira

- Platzkegel agglomerates and lavas
- Shira Ridge Group
- Shira undifferentiated lavas

Parasitic activity

- Eruptive center
- Undifferentiated lavas
- Dike swarm
- Intrusion
- Superficial deposits and Meru lahar
- Precambrian basement
- Foliation
- Fault
- Direction of flow in lavas

Petrological and geochemical groups

- ◆ Kibo 1 porphyritic: Rhomb Porphyry Group + Caldera Rim Group
- ◇ Kibo 1 aphyric: Lent Group + Inner Crater Group
- Kibo 2: Lava Tower Group
- △ Shira: Shira Ridge Group
- Mawenzi: Neumann Tower–Mawenzi Group + Mawenzi eruptive center
- ✱ Parasitic activity
- Location of analyzed sample

KI38

Kibo and Mawenzi centers, which present the first evidence of eruption at around 1 Ma (Baker *et al.*, 1971) and 0.95 Ma, respectively (Bagdasaryan *et al.*, 1973). The eruptions appear to have been continuous in these two vents, but activity ceased in Mawenzi at ca. 0.45 Ma, whereas it continues in Kibo until present day, with edifice construction of the present summit cone and crater between 0.27 and 0.17 Ma (Wilkinson *et al.*, 1986; Nonnotte *et al.*, 2008). The youngest evidence of volcanic activity in the Kilimanjaro area (ca. 0.2 Ma to present), and in the volcanic province associated with the North Tanzanian divergence, is seen in the emplacement of numerous Strombolian-type tuff cones forming several parasitic belts above deep-seated fractures on the NW and SE slopes of Kilimanjaro.

MAIN VOLCANIC UNITS AND PETROGRAPHY

The main volcanic units are presented in the simplified geological map (Fig. 1). The composition of each volcanic unit is homogeneous, whatever its spatial distribution, which is often large due to flank eruptions. The petrographic features of the different sampled units are shown in Table 1 and are illustrated in Plate 1 by photomicrographs of typical samples. The lava classification is based on major-element compositions plotted in the total alkali–silica (TAS) diagram of Le Maitre *et al.* (1989) (Fig. 2). The lithological units defined by Downie and Wilkinson (1972) have been simplified into five groups: Shira, Mawenzi, Kibo 1, Kibo 2, and parasitic activity.

Shira

The western vent of Shira is made up of mainly mafic and undersaturated lavas with a considerable amount of pyroclastic material. The center of the collapsed caldera is occupied by a small conical hill composed of a heterogeneous assemblage of basaltic tuffs and thin lava flows, intruded by later-stage nepheline monzodiorite dikes (Downie and Wilkinson, 1972). This structure, called the Platzkegel agglomerate, can be interpreted as a vent infilling. Sampled lavas from Shira come from the Shira Ridge Group, composed mainly of pyroclastic materials of basaltic-basanitic compositions crosscut by an important subvertical radial dike swarm of similar composition. Basanitic samples are porphyritic with olivine, clinopyroxene, plagioclase, and Fe–Ti–oxide phenocrysts. The basanitic dikes differ from the lavas only by their doleritic texture (sample 05KI07B). Sample 05KI07C is a trachybasalt sampled from a pyroclastic block that displays the same texture and phenocrysts as the basanitic lavas and dikes, but has scarce nepheline microcrysts in its groundmass.

Mawenzi

The unusual tower-shape morphology of the Mawenzi eastern center results from a dense radial mafic dike swarm (>500 intrusions), deeply eroded, which crosscuts all the other formations. The older Mawenzi Eruptive Center formation is a pile of

pyroclastic breccias and blocky lava flows. Lava and dike samples from the Neumann Tower–Mawenzi Group and Mawenzi Eruptive Center show homogeneous compositions plotting in the trachybasalt field of the TAS diagram (Fig. 2). Trachybasaltic lavas are porphyritic with olivine, clinopyroxene, orthopyroxene, plagioclase, and Fe–Ti–oxide phenocrysts, which are also found as groundmass phases. Nepheline may occur as groundmass microcrysts, but it remains very scarce. The Mawenzi dikes differ only from the other facies by their doleritic texture.

Kibo

The Kibo central edifice forms the main peak of Kilimanjaro (Uhuru Peak, 5895 m). It typically presents a cone-shaped morphology, towering over the Saddle plateau between Kibo and Mawenzi peaks. Due to its longer activity and lesser erosion, its volcanic stratigraphy is more completed and complicated than that of the two other centers. As a general feature, Kibo erupted mainly silica-undersaturated but highly differentiated lava flows, and lesser amounts of pyroclastic breccias of similar composition, from its present summit cone or flank vents.

The oldest rocks sampled from Kibo belong to the Lava Tower Group, the lavas of which range from phono-tephrite to tephri-phonolite (Kibo 2). These lavas are highly porphyritic with nepheline, olivine, Fe–Ti–oxide, and apatite phenocrysts, and they are characterized by (>10 mm) tabular phenocrysts of plagioclase. Clinopyroxene and sanidine microcrysts occur in relatively small amounts, except in samples 05KI11 and 05KI23, where K-feldspar laths are abundant.

The Rhomb Porphyry Group is the most distinctive formation of Kibo. It is composed of porphyritic tephri-phonolite to phonolite lavas with phenocrysts (30–40 mm long) of anorthoclase with reaction rims. These lavas also contain olivine, Fe–Ti oxide and apatite. Sanidine and nepheline occur only as relatively abundant microcrysts in the groundmass.

The Lent Group, which overlies the former lavas, erupted from several flank vents. The lava flows present at their base a glassy horizon, ~30 cm thick on average. Although it is the most widely distributed formation, its lavas are rather homogeneous. They include aphyric phonolites and tephri-phonolites with rare and small phenocrysts of clinopyroxene, amphibole (kaersutite), olivine, and Fe–Ti oxides. Sanidine and nepheline occur in the glassy groundmass.

In the overlying formation of the Caldera Rim Group, features similar to those of Rhomb Porphyry Group lavas are observed. The Caldera Rim Group lavas are highly porphyritic tephri-phonolites to phonolites that contain large phenocrysts of anorthoclase with reaction rims. Olivine, scarce clinopyroxene (sample 05KI37), Fe–Ti oxides, apatite, and nepheline occur as phenocrysts. Sanidine occurs only as laths in the groundmass. The occurrence of nepheline phenocrysts in these lavas is the most distinctive petrographic character allowing us to differentiate them from the phonolites of the Rhomb Porphyry Group. The Caldera Rim Group formation principally erupted from the

TABLE 1. SUMMARY OF THE PETROGRAPHIC CHARACTERISTICS OF THE MAIN VOLCANIC FORMATIONS OF KILIMANJARO

Eruptive vent	Geological formation	TAS	Textures								Mineral paragenesis							Remarks					
			Microcrystalline	Hyaline	Doleritic	Porphyritic	Megaphenocrysts (>10 mm)	Aphyric	Microilitic	Microgranular	Equant	Fluidal	Vesicular	Olivine	Clinopyroxene	Orthopyroxene	Amphibole		Plagioclase or anorthoclase	Sanidine	Nepheline	Fe-Ti oxide	Apatite
Shira	Shira Ridge Group	Basanite											X	X	X		X		+	+	X	+	Very scarce nepheline
Shira	Shira Ridge Group	Trachybasalt											X	X	X		X		+	+	X		
Shira	Shira Ridge Group	Basanite											X	X	X		X		+	+	+	+	
Kibo	Lava Tower Group	Tephri-phonolite											X	+	X		X		+	+	X	X	Tabular Na-feldspar
Kibo	Lava Tower Group	Phono-tephrite											X	+	X		X			X	X	X	Tabular Na-feldspar
Kibo	Rhomb Porphyry Group	Phonolite											X		X		X		+	+	X	X	Na-feldspars with reaction rims
Kibo	Lent Group	Phonolite											X	X		X		+	+	+	+	+	Na-feldspars with reaction rims
Kibo	Caldera Rim Group	Phonolite											X		X		X		+	X	X	X	Na-feldspars with reaction rims
Kibo	Caldera Rim Group	Tephri-phonolite											X		X		X		+	X	X	X	Na-feldspars with reaction rims
Kibo	Caldera Rim Group	Phonolite											X		X		X		+	+	X	+	Na-feldspars with reaction rims
Kibo	Inner Crater Group	Phonolite											+	+				+	+	+	X	+	Na-feldspars with reaction rims
Mawenzi	Neumann Tower-Mawenzi Group	Trachybasalt											X	X	X		X		+	+	X	+	Groundmass rich in glass, very scarce nepheline
Mawenzi	Mawenzi Eruptive Center	Trachybasalt											X	X	X		X		+	+	X	+	Very scarce nepheline
Saddle	Parasitic activity	Foidite											X	X					+	+	+	+	Very abundant nepheline
Saddle	Parasitic activity	Tephrite											X	X		X		+	+	X	+	Abundant nepheline	
Rombo zone	Parasitic activity	Picrobasalt											X	X	X		+		+	+	+	+	Cumulative facies
Rombo zone	Parasitic activity	Basalt											X	X	X		+			+	+	+	
Rombo zone	Parasitic activity	Basanite											X	X	X		+		+	+	+	+	Amphibole can occur in few samples

Notes: X indicates minerals occurring as phenocrysts and microcrysts in the groundmass, + indicates minerals occurring only as microcrysts in the groundmass. TAS—intrusive lithologies and lavas are named using the total alkali–silica (TAS) discrimination diagram of Le Maitre et al. (1989)

Notes: X indicates minerals occurring as phenocrysts and microcrysts in the groundmass, + indicates minerals occurring only as microcrysts in the groundmass. TAS—intrusive lithologies and lavas are named using the total alkali-silica (TAS) discrimination diagram of Le Maitre et al. (1989).

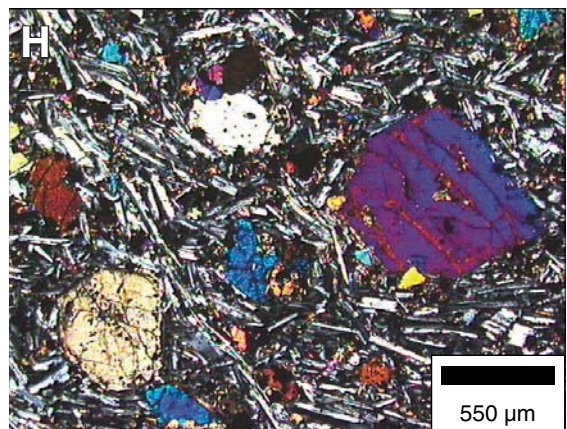
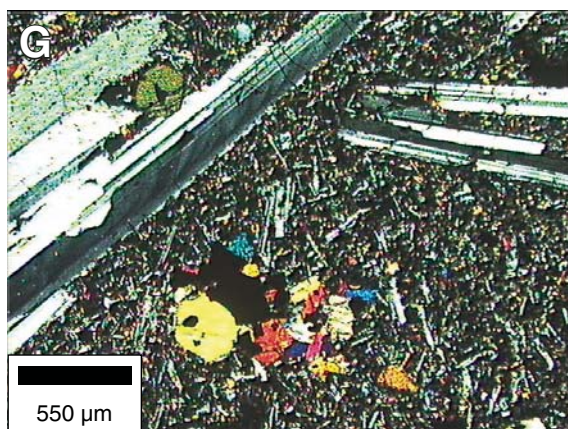
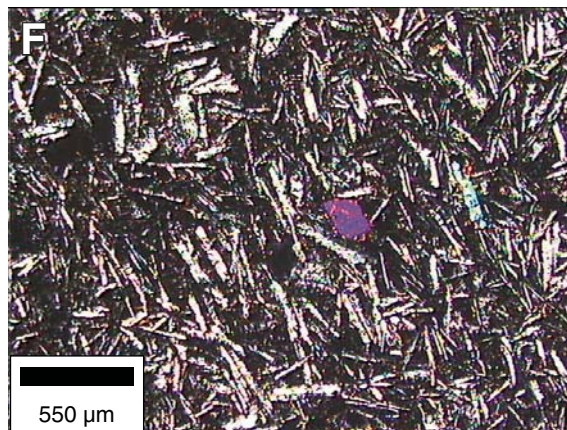
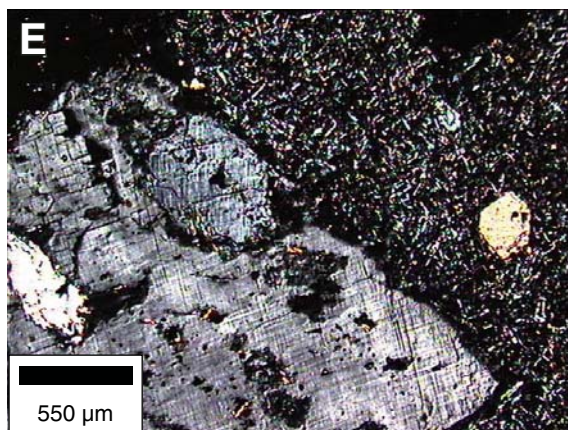
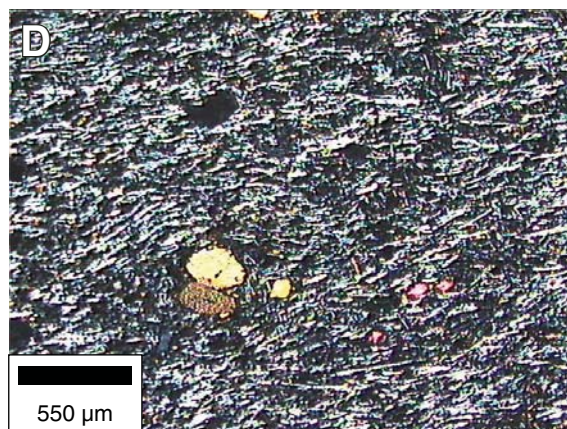
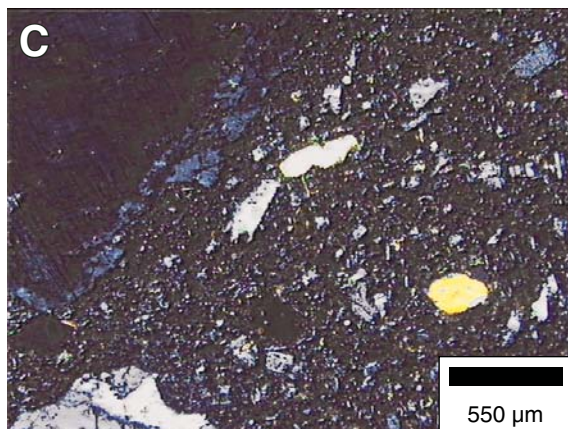
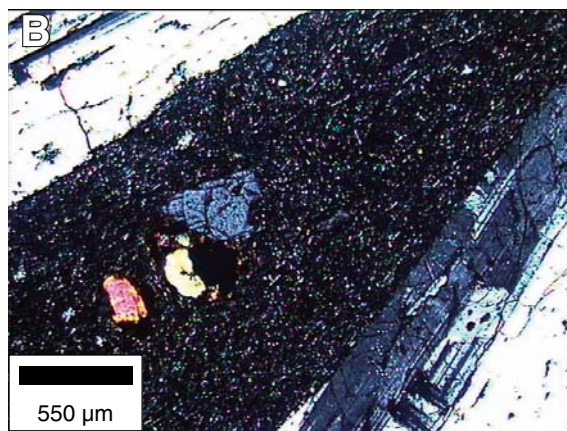
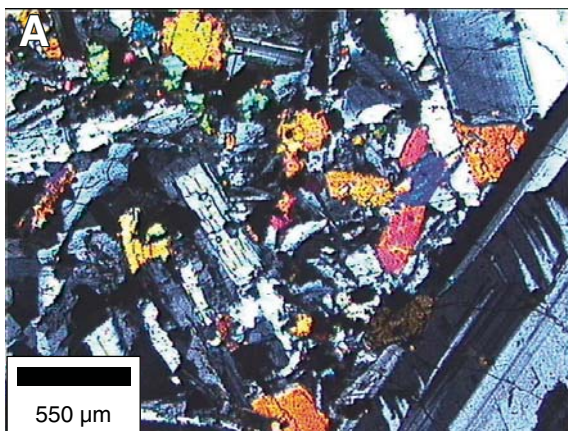


Plate 1. Photomicrographs of intrusive lithologies and lavas from the main volcanic formations of Kilimanjaro. (A) Intrusive basanitic 05KI08B sample with doleritic texture from Shira Ridge Group. (B) Phono-tephrite 05KI15 from Lava Tower Group with tabular phenocrysts of plagioclase. (C) Phonolite 05KI20 from Rhomb Porphyry Group with phenocrysts (30–40 mm long) of anorthoclase (upper-left corner) and olivine phenocrysts in a fine crystallized groundmass of nepheline microcrysts and sanidine microliths. (D) Aphyric phonolite 05KI33 from Lent Group with microcrysts of amphibole in a microlithic groundmass of sanidine. (E) Tephri-phonolite 05KI35 from Caldera Rim Group with megaphenocrysts of anorthoclase and scarce nepheline phenocrysts. (F) Aphyric phonolite 05KI22 from Inner Crater Group with olivine microcrysts in a well-crystallized groundmass of sanidine microliths. (G) Intrusive trachybasalt 05KI45 with finely crystallized groundmass from the dike swarm of the Neumann Tower–Mawenzi Group. (H) Cumulative basalt 03TZ41B from parasitic activity sampled in the Rombo zone with olivine and zoned clinopyroxene phenocrysts. All the microphotographs were taken in polarized light at 40× magnification.

present crater of Kibo. Glassy porphyritic samples 05KI38B and 05KI38C, collected at Stella Point on the summit crater rim, present the same petrographic characteristics as the “kenytes” described from the summit of Mount Kenya (Baker, 1967; Price et al., 1985).

We sampled only one lava flow from the latest formation erupted from the summit crater of Kibo, the Inner Crater Group (sample 05KI22), which spreads mainly over the northern

flanks of the edifice and fills up the present caldera floor. Inner Crater Group lavas are almost totally aphyric phonolites with K-feldspar, nepheline, Fe-Ti oxides, olivine, Clinopyroxene, and apatite microcrysts. However, some flows contain rare aegirine phenocrysts (Downie and Wilkinson, 1972).

The Rhomb Porphyry Group–Caldera Rim Group and the Lent Group–Inner Crater Group are referred hereafter to Kibo 1 porphyritic and Kibo 1 aphyric units, respectively.

Parasitic Vents

On the Saddle plateau and on the NW and SE slopes of Kilimanjaro, the eruption of a large number of Strombolian tuff cones marked the latest phases of volcanic activity on Kilimanjaro. This so-called parasitic activity is expressed by the emplacement of hundreds of pyroclastic deposits and lava flows ranging from picobasalts to trachybasalts with subordinate clinopyroxene-rich basanites and foidites (nephelinites). Two areas were sampled: the parasitic vents from the saddle plateau and the SE lower slope of Kilimanjaro near Marangu in the Rombo area (Fig. 1).

Parasitic volcanic activity on the Saddle plateau resulted in the emplacement of basanites, tephrites, and nephelinites. The basanites are porphyritic with olivine, clinopyroxene, Fe-Ti oxides, and associated scarce phenocrysts of amphibole (kaersutite) set in a groundmass containing plagioclase, nepheline, and apatite. Sample 05KI41B is a tephrite showing a low normative olivine content (<10%). However, it presents the same

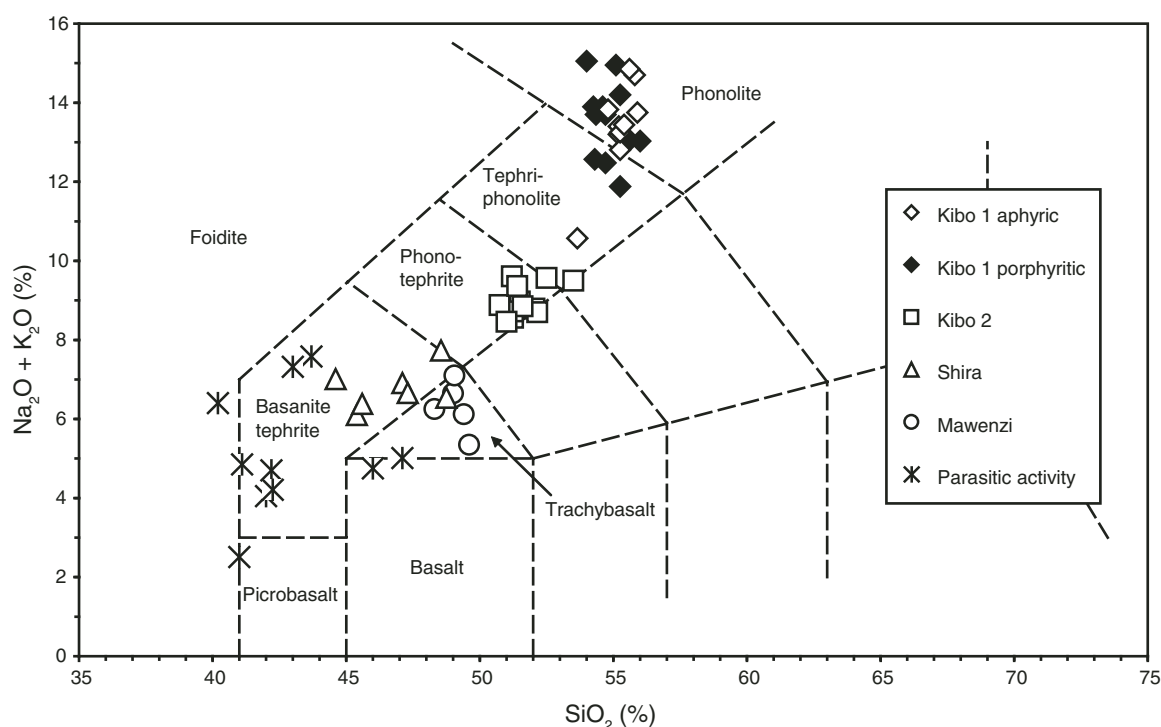


Figure 2. Total alkali-silica (TAS) diagram for lavas erupted on the three centers and from the parasitic centers of Kilimanjaro. The fields are from Le Maitre et al. (1989).

mineralogy as the basanites, but with a larger amount of nepheline phenocrysts. Sample 05KI40 is a nephelinite with olivine and clinopyroxene phenocrysts set in a groundmass rich in nepheline microcrysts associated with Fe-Ti oxides and apatite microcrysts. The Strombolian-type tuff cones of the Rombo area show compositions ranging from picrobasalt to basalt and basanite. In all these lavas, olivine and clinopyroxene phenocrysts coexist with plagioclase, Fe-Ti oxide, and apatite microcrysts in their groundmass. Rare orthopyroxene crystals occur in basaltic lavas. Typically, it appears in this group that all lavas are composed of a groundmass that is well and finely crystallized with large amounts of Fe-Ti-oxide microcrysts.

SAMPLING AND ANALYTICAL TECHNIQUES

Sampling Strategy

In total, 54 samples from the three eruptive centers were examined. Despite the restricted geographical location of this sampling on the southern side of Kilimanjaro, the selected rocks are assumed to be representative of each individual formation for several reasons: (1) the southern flank of Kilimanjaro is the only area where we can observe the entire magmatic succession because of its exposure by erosion and volcanic collapse, (2) no other specific lava formations have been mapped on the northern flank of the volcano (Downie et al., 1965), and (3) as mentioned already, the lavas from the three centers of Kilimanjaro show rather homogeneous compositions within each individual formation. The most important limitation during our sampling was the tropical vegetation, which covers all the outcrops on the lower slopes of the edifice, except in some locations of the Marangu area (Rombo zone parasitic vents; Fig. 1). Therefore, our sampling was scarce below the altitude of 3000 m, which is the upper limit of the dense tropical vegetation. The same limitation was encountered by previous authors during their mapping of the edifice (Downie et al., 1956, 1965; Downie and Wilkinson, 1972). All the collected samples were analyzed for major elements by inductively coupled plasma-atomic emission spectrometry (ICP-AES). Trace-element data were obtained by ICP-mass spectrometry (MS) on 52 samples (Table 2). Sr and Nd isotopic ratios were measured on 40 selected samples (Table 3).

Major and Trace Elements

Samples were selected for their freshness after removal of the weathered parts, i.e., altered rims, vesicles with their filling (zeolites, phyllites). Samples were then powdered first in a crusher and then in an agate grinder for 15–20 min.

Whole-rock major elements were measured on the ISA Jobin-Yvon® JY70 ICP-AES at UMR 6538 Domaines Océaniques (Brest, France). A detailed description of the analytical procedure is given by Cotten et al. (1995). Major elements were determined from an H_3BO_3 solution (boron being used as inter-

nal standard for ICP-AES analysis). For major elements, relative standard deviation is 1% for SiO_2 and 2% for the other major elements, except for low values (<0.50 wt%), for which the absolute standard deviation is ± 0.01 wt%.

Whole-rock trace-element analyses were performed on a high resolution ICP-MS Thermo Electron™ Element II at IUEM (European Institute for Marine Studies, Brest, France). Samples were dissolved with a mixture of $HF-HNO_3$ for 48 h at 95 °C, and then dried at the same temperature until the complete evaporation of acids was achieved. Dry samples were then dissolved in a 40 mL HCl solution. An aliquot of 150 μg of these solutions was spiked with 10 μg of an artificial solution enriched in Tm ([Tm] ~ 77.9 ppb; Barrat et al., 1996) and then evaporated to dryness. The samples were then dissolved in diluted HNO_3 , and all the trace elements were determined from this final solution. The detailed analytical procedure and the calculation method for concentrations are given in Barrat et al. (1996). Standard deviation was $<2\%$ for Sr and most of the rare earth elements (REEs; except for Pr, Eu, Gd, and Yb, which were 2.7%, 4.1%, 3.2%, and 5.4%, respectively), and most of the metals were measured with a standard deviation $<4\%$. However, the standard deviation was higher for elements such as Nb, Ta, and Cs (around 12%) due to ionization difficulties in the Ar plasma. International standards BHVO-2 and WSE were run regularly to check the measurements and to control the instrumental drift.

Isotopic Analyses

Sr and Nd separation was performed on an aliquot of the previous HCl solution (selected volume depending on the Nd concentration of each sample) for 17 samples (see Table 3 for details). This aliquot was dried until total evaporation was achieved and dissolved again prior to the elution. Others samples were directly processed using $HF-HNO_3$ digestions. Chemical separation for Sr and REEs was performed on cationic DOWEX® AG50X8 columns for part of the samples and on combined Sr-Spec/Thru-Spec columns for the other part (Table 3). For samples that followed the DOWEX procedure, the Sr cut was processed again through the same column to efficiently separate Sr from Rb and Ca. Nd was further eluted on LnSpec Eichrom resin. Isotopic measurements were conducted on a Thermo Electron™ Triton T1 at the IUEM for all Nd measurements; Sr was measured on Triton T1 (IUEM) and on Finnigan Mat 261 at Observatoire Midi Pyrénées, Toulouse, France. Sr was run on a single W filament with Ta activator, while Nd was run on a Re double filament. The NBS 987 (for Sr) and La Jolla (for Nd) standards were run regularly to check the measurements: average value $^{87}Sr/^{86}Sr = 0.710248 \pm 0.000020$ ($n = 17$, Triton mass spectrometer), average value $^{87}Sr/^{86}Sr = 0.710246 \pm 0.000012$ ($n = 23$, Mat 261 mass spectrometer), and average value $^{143}Nd/^{144}Nd = 0.511853 \pm 0.000010$ ($n = 16$, Triton mass spectrometer). Blanks were <650 pg for Sr and <350 pg for Nd.

TABLE 2. MAJOR-ELEMENT (%) AND TRACE-ELEMENT (ppm) ANALYSES OF KILIMANJARO SAMPLES

Sample:		05KI01	05KI02	05KI03A	05KI04	05KI05A	05KI05B	05KI06
Eruptive vent:		Kibo	Kibo	Kibo	Kibo	Kibo	Kibo	Kibo
Geological formation:		Lava Tower Group	Lava Tower Group	Lent Group	Lava Tower Group	Lent Group	Lent Group	Lava Tower Group
Geographic coordinates (WGS84)	Latitude (°S):	03°05'33"	03°05'20"	03°05'13"	03°04'55"	03°04'02"	03°04'02"	03°03'24"
	Longitude (°E):	37°16'11"	37°16'28"	37°16'32"	37°16'39"	37°16'39"	37°16'39"	37°16'03"
	Altitude (m)	3123	3326	3450	3601	3865	3865	3796
TAS:		Phono-tephrite	Phono-tephrite	Phonolite	Phono-tephrite	Phonolite	Tephri-phonolite	Phono-tephrite
Major elements (wt%) ICP-AES	SiO ₂	52.05	52.15	55.90	51.50	55.80	53.65	51.25
	TiO ₂	1.62	1.53	0.92	1.98	0.87	0.90	1.94
	Al ₂ O ₃	19.00	19.40	18.90	18.55	18.70	18.95	17.30
	Fe ₂ O ₃ *	8.07	7.61	6.14	8.80	6.10	6.29	10.50
	MnO	0.20	0.19	0.19	0.19	0.19	0.20	0.27
	MgO	1.42	1.35	0.82	1.97	0.79	0.81	1.58
	CaO	4.24	4.30	1.88	5.80	1.80	1.88	3.80
	Na ₂ O	5.20	5.20	7.75	5.77	8.60	4.97	4.88
	K ₂ O	3.59	3.50	6.00	3.20	6.10	5.60	3.68
	P ₂ O ₅	0.71	0.66	0.27	0.88	0.25	0.26	0.90
	LOI	2.97	3.48	0.78	0.74	0.01	5.52	3.03
	Total	99.07	99.37	99.55	99.38	99.21	99.03	99.13
	Mg#	0.35	0.35	0.35	0.41	0.34	0.30	0.31
Trace elements (ppm) ICP-MS	Li	19.1	20.7	37.9	7.4	44.3	57.4	18.9
	Sc	5.6	4.7	6.0				
	V	18	16	2	41	1	2	19
	Cr	1.20	0.14	3.23	1.33		0.31	0.39
	Co	9.3	9.0	3.0	13.9	2.3	2.9	10.6
	Ni	2.5	0.3	2.4	1.8	0.1		0.4
	Rb	95	91	285	126	198	211	97
	Sr	1189	1200	108	1202	93	282	949
	Y	54.2	46.7	62.9	44.5	59.1	59.2	74.3
	Zr	861	717	1879	636	1407	1983	1028
	Nb	272	175	501	183	352	519	249
	Cs	0.5	1.1	2.6	0.9	2.9	7.2	0.6
	Ba	1299	1182	504	942	480	511	1456
	La	140	123	189	125	179	192	177
	Ce	272	231	338	241	305	339	348
	Pr	29.6	24.7	34.9	25.7	33.6	35.0	38.5
	Nd	105	88.0	109	94.2	105	103	139
	Sm	18.6	15.0	16.5	16.0	15.9	16.4	24.4
	Eu	5.6	4.7	3.2	4.5	3.1	3.5	6.9
	Gd	15.8	12.6	10.8	13.9	9.7	13.1	21.0
	Tb	2.1	1.7	1.8	1.7	1.7	2.1	2.9
	Dy	11.1	9.2	10.8	9.1	10.4	10.6	15.3
	Ho	2.1	1.7	2.1	1.7	2.1	2.1	2.7
	Er	5.4	4.4	6.1	4.4	6.0	6.4	7.1
	Yb	4.9	3.9	6.5	3.6	6.3	6.8	6.3
	Lu	0.65	0.53	0.91	0.49	0.88	0.85	0.86
	Hf	18.1	14.4	35.6	13.3	26.9	37.2	21.6
	Ta	13.3	6.1	26.7	9.9	14.1	26.0	10.1
	Pb	7.9	2.4	14.5	3.2	12.7	12.8	2.6
	Th	26.5	19.9	3.5	25.2	5.0	32.8	21.7
	U	4.7	4.1	10.5	3.8	9.4	9.9	5.7

(Continued)

TABLE 2. MAJOR-ELEMENT (%) AND TRACE-ELEMENT (ppm) ANALYSIS OF KILIMANJARO SAMPLES (Continued)

Sample:		05KI07A	05KI07B	05KI07C	05KI08A	05KI08B	05KI09A	05KI09B
Eruptive vent:		Shira	Shira	Shira	Shira	Shira	Shira	Shira
Geological formation:		Shira Ridge Group	Shira Ridge Group	Shira Ridge Group	Shira Ridge Group	Shira Ridge Group	Shira Ridge Group	Shira Ridge Group
Geographic coordinates (WGS84)	Latitude (°S):	03°03'14"	03°03'14"	03°03'14"	03°03'14"	03°03'14"	03°03'22"	03°03'22"
	Longitude (°E):	37°15'27"	37°15'27"	37°15'27"	37°15'20"	37°15'20"	37°15'20"	37°15'20"
	Altitude (m):	3763	3763	3763	3776	3776	3782	3782
TAS:		Basanite	Basanite	Trachybasalt	Basanite	Basanite	Basanite	Basanite
Major elements (wt%) ICP-AES	SiO ₂	47.10	47.30	48.75	48.55	44.60	45.40	45.60
	TiO ₂	2.49	2.53	2.15	1.99	2.32	2.29	2.29
	Al ₂ O ₃	16.95	17.35	16.90	17.00	16.75	16.05	16.50
	Fe ₂ O ₃ *	13.06	13.00	12.25	12.50	13.05	13.10	13.05
	MnO	0.21	0.21	0.20	0.20	0.21	0.20	0.20
	MgO	3.68	3.95	4.08	4.32	5.20	5.44	5.00
	CaO	7.62	8.00	7.42	6.75	9.10	9.00	8.65
	Na ₂ O	4.85	4.66	4.38	5.27	5.10	4.27	4.49
	K ₂ O	2.07	2.01	2.17	2.47	1.92	1.84	1.90
	P ₂ O ₅	0.70	0.64	0.62	0.75	0.71	0.62	0.65
	LOI	0.73	0.18	0.42	0.07	0.78	1.28	1.32
	Total	99.46	99.83	99.34	99.81	99.74	99.49	99.61
	Mg#	0.41	0.43	0.49	0.51	0.50	0.51	0.49
Trace elements (ppm) ICP-MS	Li	12.8	15.8	13.9	14.2	9.3	10.0	11.2
	Sc	15.2	15.6	14.4	14.0	14.7	21.0	19.5
	V	225	236	186	209	227	281	299
	Cr	17.2	20.7	17.4	27.1	33.9	52.2	42.6
	Co	53.8	51.6	36.0	40.7	42.7	51.5	55.1
	Ni	29.6	32.3	24.8	30.3	47.2	54.0	53.6
	Rb	71	56	64	60	90	48	71
	Sr	970	1011	843	843	989	867	980
	Y	38.9	35.2	35.9	31.9	26.0	30.4	34.1
	Zr	353	311	319	306	297	285	317
	Nb	143	117	51	123	109	127	110
	Cs	0.9	0.7	0.9	0.6	0.6	0.4	0.5
	Ba	909	856	800	858	806	775	875
	La	90.9	82.3	93.4	83.2	73.8	79.1	90.2
	Ce	174	161	157	157	145	155	173
	Pr	19.2	17.3	18.2	17.0	15.2	16.5	18.7
	Nd	71.0	64.6	62.7	62.9	54.8	62.1	69.0
	Sm	12.2	11.3	10.7	10.6	9.5	11.5	12.4
	Eu	3.2	3.2	3.0	2.9	2.7	3.3	3.6
	Gd	11.6	10.3	8.6	9.0	8.0	9.6	10.1
	Tb	1.5	1.4	1.3	1.2	1.1	1.2	1.3
	Dy	7.8	7.1	6.7	6.2	5.1	6.2	6.8
	Ho	1.5	1.3	1.3	1.1	1.0	1.1	1.2
	Er	3.9	3.5	3.5	3.1	2.5	3.0	3.3
	Yb	3.5	3.1	3.0	2.9	2.1	2.5	2.7
	Lu	0.48	0.43	0.39	0.40	0.28	0.35	0.37
	Hf	7.8	6.9	6.6	6.9	6.1	6.6	6.9
	Ta	7.4	4.9	1.2	6.0	5.1	5.9	4.1
	Pb	5.6	5.1	7.8	7.3	4.2	5.6	7.0
	Th	16.1	10.7	2.7	3.4	9.5	6.5	4.6
	U	2.7	2.3	2.1	2.1	1.6	1.7	2.0

(Continued)

TABLE 2. MAJOR-ELEMENT (%) AND TRACE-ELEMENT (ppm) ANALYSIS OF KILIMANJARO SAMPLES (*Continued*)

Sample:		05KI11	05KI12	05KI13	0KI14	05KI15	05KI16	05KI17
Eruptive vent:		Kibo	Kibo	Kibo	Kibo	Kibo	Kibo	Kibo
Geological formation:		Lava Tower Group	Caldera Rim Group	Lava Tower Group	Lava Tower Group	Lava Tower Group	Lava Tower Group	Caldera Rim Group
Geographic coordinates (WGS84)	Latitude (°S):	03°03'32"	03°03'48"	03°03'55"	03°04'01"	03°04'04"	03°04'04"	03°04'05"
	Longitude (°E):	37°15'53"	37°19'01"	37°19'16"	37°19'43"	37°19'40"	37°19'38"	37°19'38"
	Altitude (m):	3750	4510	4555	4655	4622	4628	4642
TAS:		Tephri-phonolite	Phonolite	Phono-tephrite	Phono-tephrite	Phono-tephrite	Phono-tephrite	Phonolite
Major elements (wt%) ICP-AES	SiO ₂	53.50	54.35	51.25	50.74	51.60	51.20	54.70
	TiO ₂	1.67	0.94	2.01	1.97	1.87	1.88	0.97
	Al ₂ O ₃	17.95	19.50	18.50	18.30	18.58	18.50	19.90
	Fe ₂ O ₃ *	8.60	5.55	9.16	8.80	8.70	8.55	5.58
	MnO	0.23	0.18	0.19	0.18	0.20	0.19	0.17
	MgO	1.47	1.09	2.10	2.02	1.67	1.90	1.06
	CaO	4.26	2.37	5.70	5.65	5.78	5.56	2.50
	Na ₂ O	5.85	8.25	5.50	5.57	5.60	6.12	8.56
	K ₂ O	3.65	5.45	3.22	3.31	3.25	3.49	5.14
	P ₂ O ₅	0.74	0.57	0.85	0.84	0.87	0.81	0.56
	LOI	1.10	0.73	0.71	1.80	1.80	1.62	0.31
	Total	99.02	98.98	99.19	99.19	99.92	99.82	99.45
	Mg#	0.36	0.44	0.43	0.43	0.39	0.42	0.43
Trace elements (ppm) ICP-MS	Li	11.8	32.3	17.6	17.8	16.0	18.8	32.9
	Sc	5.8	3.2	7.7	7.1	6.4	6.8	3.5
	V	17	8	48	42	28	33	8
	Cr	0.13		0.83	1.21	0.21	0.21	0.14
	Co	8.6	4.6	17.1	15.9	13.4	14.1	4.9
	Ni	0.2	0.3	2.2	2.5	0.7	1.1	0.2
	Rb	90	171	88	79	90	80	172
	Sr	1048	633	1112	1022	1121	1028	753
	Y	50.9	44.7	52.5	48.1	49.6	49.6	46.0
	Zr	769	1433	764	708	716	733	1409
	Nb	247	402	164	214	171	140	420
	Cs	1.4	2.5	0.9	1.0	1.0	1.0	2.4
	Ba	1239	1020	1065	964	933	980	1114
	La	133	162	146	134	131	135	164
	Ce	259	296	281	254	254	259	291
	Pr	27.9	30.2	29.6	27.6	28.1	27.4	30.0
	Nd	99.1	94.2	105.9	96.9	98.9	96.7	94.6
	Sm	17.6	14.1	18.2	16.4	16.5	16.3	14.2
	Eu	5.3	3.8	5.0	4.7	4.8	4.4	4.1
	Gd	14.3	9.4	14.9	14.2	13.5	13.5	12.3
	Tb	2.0	1.4	2.1	1.9	2.0	1.8	1.8
	Dy	10.3	8.3	10.5	9.5	9.8	9.6	8.6
	Ho	2.0	1.6	2.0	1.7	1.7	1.8	1.6
	Er	5.2	4.5	5.1	4.7	4.7	4.7	4.8
	Yb	4.4	4.6	4.4	3.9	4.1	4.0	4.7
	Lu	0.59	0.64	0.59	0.53	0.53	0.54	0.61
	Hf	16.7	26.6	15.5	14.0	13.9	14.3	25.4
	Ta	9.5	23.1	5.8	11.2	8.9	5.1	20.7
	Pb	2.5	7.2	4.2	4.5	3.8	3.4	6.4
	Th	25.9	4.7	21.7	22.2	17.0	8.7	44.1
	U	4.1	9.2	4.5	3.6	4.0	4.3	8.3

(Continued)

TABLE 2. MAJOR-ELEMENT (%) AND TRACE-ELEMENT (ppm) ANALYSIS OF KILIMANJARO SAMPLES (Continued)

Sample:		05KI18	05KI19	05KI20	05KI21	05KI22	05KI23	05KI24
Eruptive vent:		Kibo	Kibo	Kibo	Kibo	Kibo	Kibo	Kibo
Geological formation:		Lava Tower Group	Lava Tower Group	Rhomb Porphyry Group	Rhomb Porphyry Group	Inner Crater Group	Lava Tower Group	Caldera Rim Group
Geographic coordinates (WGS84)	Latitude (°S):	03°03'58"	03°03'56"	03°04'33"	03°04'11"	03°05'03"	03°05'43"	03°05'56"
	Longitude (°E):	37°19'03"	37°19'02"	37°19'16"	37°19'23"	37°19'27"	37°20'00"	37°20'13"
	Altitude (m):	4546	4506	4371	4410	4350	4051	4211
TAS:		Phono-tephrite	Phono-tephrite	Phonolite	Phonolite	Phonolite	Tephri-phonolite	Phonolite
Major elements (wt%) ICP-AES	SiO ₂	51.40	51.00	55.60	56.00	54.80	52.50	54.60
	TiO ₂	1.93	1.90	1.00	1.01	1.13	1.97	0.86
	Al ₂ O ₃	18.70	19.67	19.50	19.55	18.80	16.70	19.95
	Fe ₂ O ₃ *	8.98	8.90	5.05	5.10	6.35	10.55	4.91
	MnO	0.19	0.19	0.17	0.17	0.19	0.24	0.19
	MgO	1.96	1.97	0.99	1.00	1.12	1.83	0.94
	CaO	5.60	5.50	2.40	2.49	2.27	4.39	1.98
	Na ₂ O	6.00	5.38	8.07	8.03	7.75	5.62	8.60
	K ₂ O	3.36	3.08	4.98	5.00	6.08	3.95	5.30
	P ₂ O ₅	0.80	0.78	0.46	0.48	0.33	0.89	0.54
	LOI	0.47	1.50	0.59	0.40	1.04	0.87	1.21
	Total	99.39	99.27	98.81	99.23	99.86	99.51	99.08
Trace elements (ppm) ICP-MS	Mg#	0.42	0.42	0.44	0.44	0.41	0.36	0.43
	Li	16.9	15.8	28.0	30.4	38.2	19.0	30.0
	Sc	7.2	7.7	4.4	4.2	6.4	11.0	1.9
	V	43	47	15	11	6	35	7
	Cr	0.21	2.96		0.06			0.12
	Co	16.5	18.7	5.4	4.6	4.6	16.3	3.9
	Ni	1.9	4.1		0.3		11.2	
	Rb	92	98	173	149	202	99	176
	Sr	1106	1212	753	592	151	783	833
	Y	50.1	53.7	55.0	48.0	56.4	71.2	38.1
	Zr	746	820	1410	1341	1757	974	1307
	Nb	175	271	505	397	493	327	407
	Cs	1.1	1.1	2.3	1.9	2.2	1.0	2.4
	Ba	1030	1126	1078	893	547	1455	1163
	La	139	150	179	152	174	175	158
	Ce	269	286	328	283	321	342	280
	Pr	28.7	31.0	32.9	28.2	31.9	37.9	27.2
	Nd	102	112	106	89.9	103	139	84.3
	Sm	17.7	18.9	17.9	14.0	16.4	25.3	12.6
	Eu	4.8	5.3	4.9	3.8	3.2	7.2	3.5
	Gd	14.3	15.3	13.5	11.2	13.6	20.3	10.4
	Tb	1.9	2.1	2.0	1.7	1.9	2.8	1.4
	Dy	10.0	10.9	10.6	8.9	10.5	14.6	7.0
	Ho	1.9	2.0	2.1	1.7	2.1	2.8	1.3
	Er	5.0	5.5	5.9	4.9	5.9	7.3	3.8
	Yb	4.3	4.7	6.2	5.0	6.2	6.4	3.8
	Lu	0.58	0.63	0.83	0.68	0.86	0.88	0.52
	Hf	15.3	17.1	29.8	26.0	33.4	22.2	24.0
	Ta	6.6	14.1	25.9	17.8	19.7	17.6	22.2
	Pb	3.7	4.2	10.3	4.5	20.6	32.1	5.4
	Th	14.8	43.8	64.7	46.9	39.4	29.8	51.8
	U	4.1	4.8	8.9	8.1	10.1	5.3	8.9

(Continued)

TABLE 2. MAJOR-ELEMENT (%) AND TRACE-ELEMENT (ppm) ANALYSIS OF KILIMANJARO SAMPLES (Continued)

Sample:		05KI25	05KI26	05KI28	05KI29	05KI30	05KI31	05KI32
Eruptive vent:		Kibo	Kibo	Kibo	Kibo	Kibo	Kibo	Kibo
Geological formation:		Caldera Rim Group	Caldera Rim Group	Rhomb Porphyry Group	Lent Group	Lent Group	Lent Group	Lent Group
Geographic coordinates (WGS84)	Latitude (°S):	03°06'04"	03°06'05"	03°06'44"	03°06'49"	03°06'58"	03°07'08"	03°07'10"
	Longitude (°E):	37°20'24"	37°20'32"	37°21'14"	37°21'19"	37°21'27"	37°21'45"	37°22'14"
	Altitude (m):	4125	4098	4035	4027	4036	4062	4103
TAS:		Phonolite	Phonolite	Tephri-phonolite	Phonolite	Phonolite	Phonolite	Phonolite
Major elements (wt%) ICP-AES	SiO ₂	54.00	54.25	55.25	55.20	55.20	55.25	55.60
	TiO ₂	0.86	0.80	1.04	1.00	1.01	1.03	1.03
	Al ₂ O ₃	20.00	20.20	19.70	18.80	18.70	19.00	19.10
	Fe ₂ O ₃ *	4.95	4.55	5.15	6.23	6.26	6.37	5.35
	MnO	0.19	0.17	0.18	0.19	0.19	0.19	0.19
	MgO	0.96	0.84	1.08	0.98	0.93	0.94	0.94
	CaO	2.01	1.86	2.61	2.12	1.95	1.91	1.93
	Na ₂ O	9.15	8.70	7.10	7.40	7.60	7.61	9.00
	K ₂ O	5.90	5.20	4.78	5.80	5.80	5.20	5.85
	P ₂ O ₅	0.53	0.49	0.47	0.30	0.30	0.30	0.29
	LOI	1.19	2.27	1.89	1.06	0.48	0.09	0.35
	Total	99.74	99.33	99.25	98.08	98.42	97.89	99.63
Trace elements (ppm) ICP-MS	Mg#	0.43	0.42	0.41	0.38	0.37	0.37	0.41
	Li	32.5	31.0	33.6	43.6	42.7	39.9	38.0
	Sc	2.1	4.7	4.7	7.3	6.6	6.6	6.3
	V	7	5	12	3	3	4	3
	Cr				0.14			0.13
	Co	3.7	3.9	5.0	4.1	3.8	3.8	3.3
	Ni							0.1
	Rb	169	168	163	228	230	230	205
	Sr	818	988	670	116	108	112	99
	Y	38.6	38.4	53.5	65.1	61.0	63.9	56.0
	Zr	1347	1327	1405	2024	1852	1909	1704
	Nb	421	423	448	576	503	519	481
	Cs	2.1	2.1	2.0	3.1	2.9	2.9	2.7
	Ba	1123	1344	1039	498	477	491	431
	La	161	168	174	200	181	190	166
	Ce	291	288	318	365	333	346	310
	Pr	27.5	28.0	31.8	36.3	34.1	35.0	31.1
	Nd	86.3	87.3	102	115	107	111	98.5
	Sm	13.2	12.9	16.1	18.4	17.2	17.6	15.4
	Eu	3.5	4.0	4.5	3.5	3.3	3.4	3.0
	Gd	10.2	10.1	12.4	16.0	14.0	15.2	13.0
	Tb	1.4	1.4	1.9	2.2	2.1	2.2	2.0
	Dy	7.3	7.3	10.1	11.9	10.8	11.2	9.8
	Ho	1.4	1.4	2.0	2.3	2.1	2.2	1.9
	Er	4.0	4.0	5.6	6.8	6.2	6.3	5.7
	Yb	4.0	4.1	5.6	6.8	6.5	6.8	5.9
	Lu	0.53	0.56	0.81	0.98	0.90	0.93	0.82
	Hf	24.9	26.2	27.8	38.1	35.6	36.8	32.3
	Ta	19.1	22.5	25.3	25.8	22.0	26.8	22.0
	Pb	5.9	15.1	4.8	13.4	12.4	12.8	11.3
	Th	66.1	61.3	55.4	61.8	75.6	78.7	70.0
	U	9.1	9.2	8.3	12.9	11.0	11.6	10.8

(Continued)

TABLE 2. MAJOR-ELEMENT (%) AND TRACE-ELEMENT (ppm) ANALYSIS OF KILIMANJARO SAMPLES (*Continued*)

Sample:		05KI33	05KI35	05KI36	05KI37	05KI38B	05KI38C	05KI39
Eruptive vent:		Kibo	Kibo	Kibo	Kibo	Kibo	Kibo	Saddle
Geological formation:		Lent Group	Caldera Rim Group	Caldera Rim Group	Lent Group	Caldera Rim Group	Caldera Rim Group	Parasitic activity
Geographic coordinates (WGS84)	Latitude (°S):	03°06'30"	03°06'56"	03°07'13"	03°07'33"	Stella Point	Stella Point	03°08'02"
	Longitude (°E):	37°22'44"	37°23'48"	37°24'18"	37°25'17"			37°26'09"
	Altitude (m):	4407	4258	4172	4043	5795	5795	3848
TAS:		Phonolite	Tephri-phonolite	Tephri-phonolite	Phonolite	Phonolite	Phonolite	Tephrite
Major elements (wt%) ICP-AES	SiO ₂	55.25	54.70	54.30	55.40	55.10	55.25	43.70
	TiO ₂	1.01	0.95	0.95	0.92	0.81	0.89	3.28
	Al ₂ O ₃	18.74	19.96	19.55	18.85	20.55	20.15	14.60
	Fe ₂ O ₃ *	6.25	5.62	5.50	6.20	4.63	5.10	14.40
	MnO	0.19	0.18	0.18	0.20	0.18	0.20	0.26
	MgO	0.92	1.04	1.08	0.88	0.87	0.95	4.83
	CaO	1.93	2.56	2.57	1.86	2.00	1.98	9.80
	Na ₂ O	7.60	7.33	7.50	7.70	9.50	8.80	5.30
	K ₂ O	5.65	5.15	5.07	5.74	5.45	5.40	2.28
	P ₂ O ₅	0.29	0.54	0.52	0.25	0.52	0.55	1.35
	LOI	0.64	1.65	1.23	0.83	0.07	0.48	0.15
	Total	98.47	99.68	98.45	98.83	99.68	99.75	99.95
	Mg#	0.37	0.38	0.39	0.36	0.43	0.42	0.45
Trace elements (ppm) ICP-MS	Li	42.2	35.8	32.7	52.1	31.9	32.6	14.9
	Sc	6.2	3.7	3.5	6.2	1.8	2.1	14.4
	V	2	6	7	2	8	9	221
	Cr		4.27	0.19	0.56		0.98	21.3
	Co	3.7	5.4	4.5	3.3	3.8	4.1	40.4
	Ni		3.5	0.1	0.2	0.3	0.8	18.6
	Rb	240	193	167	230	155	157	68
	Sr	112	846	718	110	977	828	1422
	Y	63.5	54.9	46.6	63.8	38.2	38.2	41.6
	Zr	2012	1656	1418	1986	1261	1319	541
	Nb	568	498	412	532	389	405	236
	Cs	3.1	2.5	2.2	2.9	2.0	2.0	0.7
	Ba	495	1239	1038	457	1276	1130	1176
	La	196	199	171	197	156	158	173
	Ce	362	355	305	356	279	281	322
	Pr	35.7	35.2	30.7	35.1	27.9	26.7	34.3
	Nd	113	112	96.8	112	86.6	84.7	122
	Sm	18.0	17.7	14.4	17.3	12.4	12.7	19.9
	Eu	3.3	4.7	3.7	3.3	3.8	3.5	5.4
	Gd	14.2	13.9	12.9	15.4	7.9	12.4	15.5
	Tb	2.1	2.0	1.7	2.2	1.2	1.4	1.9
	Dy	11.7	10.6	8.6	11.3	7.0	7.1	9.0
	Ho	2.3	2.0	1.6	2.2	1.3	1.4	1.5
	Er	6.6	5.7	4.7	6.5	3.8	0.8	3.9
	Yb	7.0	5.7	4.7	6.7	3.9	3.7	3.0
	Lu	0.99	0.81	0.64	0.94	0.53	0.53	0.40
	Hf	38.3	31.8	25.8	37.8	22.9	23.4	11.1
	Ta	30.7	23.4	16.9	25.1	20.6	16.7	11.0
	Pb	14.6	8.7	6.6	13.4	6.7	23.0	18.9
	Th	60.8	46.5	15.9	77.9	5.6	56.1	33.9
	U	11.7	10.1	9.8	13.2	8.7	8.4	4.1

(Continued)

TABLE 2. MAJOR-ELEMENT (%) AND TRACE-ELEMENT (ppm) ANALYSIS OF KILIMANJARO SAMPLES (*Continued*)

Sample:		05KI40	05KI41A	05KI41B	05KI42	05KI43A	05KI43B	05KI44
Eruptive vent:		Saddle	Saddle	Saddle	Mawenzi	Mawenzi	Mawenzi	Mawenzi
Geological formation:		Parasitic activity	Parasitic activity	Parasitic activity	Neumann Tower–Mawenzi Group	Neumann Tower–Mawenzi Group	Neumann Tower–Mawenzi Group	Mawenzi Eruptive Center
Geographic coordinates (WGS84)	Latitude (°S):	03°07'49"	03°07'21"	03°07'21"	03°06'54"	03°06'38"	03°06'38"	03°06'02"
	Longitude (°E):	37°26'04"	37°26'01"	37°26'01"	37°26'10"	37°26'11"	37°26'11"	37°26'40"
	Altitude (m):	3909	4031	4031	4139	4197	4197	4422
TAS:		Foidite	Basanite	Tephrite	Trachybasalt	Trachybasalt	Trachybasalt	Trachybasalt
Major elements (wt%) ICP-AES	SiO ₂	40.20	41.10	43.00	49.60	49.40	48.30	49.00
	TiO ₂	4.30	3.60	3.38	3.07	3.45	3.18	2.97
	Al ₂ O ₃	13.35	12.22	14.10	14.75	15.55	16.45	16.90
	Fe ₂ O ₃ *	14.20	13.05	14.20	13.10	13.35	12.20	11.70
	MnO	0.21	0.19	0.25	0.17	0.17	0.17	0.17
	MgO	7.55	10.75	5.93	5.20	4.69	4.08	3.23
	CaO	12.80	12.80	10.30	7.50	7.30	7.60	7.50
	Na ₂ O	4.42	3.45	5.12	3.50	4.05	4.05	4.35
	K ₂ O	1.98	1.40	2.20	1.85	2.07	2.20	2.30
	P ₂ O ₅	0.86	0.64	1.23	0.55	0.57	0.70	0.80
	LOI	0.04	0.23	0.09	0.19	–0.57	0.66	0.55
	Total	99.91	99.43	99.80	99.48	100.03	99.59	99.47
Trace elements (ppm) ICP-MS	Mg#	0.57	0.67	0.51	0.53	0.50	0.49	0.44
	Li	6.7	6.3	7.7	10.9	13.1	8.9	13.6
	Sc	33.1	41.7	18.2	26.8	23.8	14.7	14.8
	V	394	376	236	287	299	366	213
	Cr	97.7	400	67.3	137	38.4	37.9	19.3
	Co	61.4	70.9	42.8	61.2	51.1	35.3	36.8
	Ni	73.9	217.4	41.7	103.8	36.7	30.0	22.7
	Rb	58	45	57	47	41	50	53
	Sr	1109	973	1325	686	737	1192	1090
	Y	34.0	31.8	38.9	39.8	34.6	32.6	41.8
	Zr	447	346	484	383	375	323	443
	Nb	108	163	157	92	97	73	127
	Cs	0.6	0.4	0.7	0.4	0.2	0.6	0.5
	Ba	907	745	1066	790	830	822	1037
	La	119	105	152	70.9	67.8	69.9	90.6
	Ce	230	205	284	142	138	136	184
	Pr	25.2	22.5	30.3	16.1	15.4	15.2	20.3
	Nd	94.2	83.3	108	63.2	60.1	57.2	77.6
	Sm	15.9	14.5	17.8	12.6	11.5	10.8	14.8
	Eu	4.5	4.1	5.1	3.7	3.5	3.2	4.3
	Gd	14.7	12.0	16.2	11.2	9.9	9.4	12.4
	Tb	1.7	1.5	1.8	1.5	1.4	1.3	1.6
	Dy	7.5	7.0	8.2	8.2	7.2	6.4	8.6
	Ho	1.3	1.2	1.4	1.5	1.3	1.2	1.6
	Er	3.0	2.9	3.6	3.9	3.4	3.0	4.0
	Yb	2.1	2.1	2.7	3.2	2.8	2.4	3.3
	Lu	0.28	0.28	0.36	0.44	0.38	0.32	0.44
	Hf	9.1	7.7	9.5	9.3	8.8	7.4	9.8
	Ta	3.5	9.7	6.0	4.6	5.4	3.2	6.4
	Pb	6.7	3.6	8.3	11.9	18.1	5.5	8.6
	Th	11.6	24.1	20.4	15.1	12.1	4.4	14.1
	U	3.1	2.6	3.9	1.7	1.2	1.2	2.2

(Continued)

TABLE 2. MAJOR-ELEMENT (%) AND TRACE-ELEMENT (ppm) ANALYSIS OF KILIMANJARO SAMPLES (*Continued*)

Sample:		05KI45	03TZ40	03TZ41A	03TZ41B	03TZ42A	03TZ42B
Eruptive vent:		Mawenzi	Rombo Zone	Rombo Zone	Rombo Zone	Rombo Zone	Rombo Zone
Geological formation:		Mawenzi Eruptive Center	Parasitic activity	Parasitic activity	Parasitic activity	Parasitic activity	Parasitic activity
Geographic coordinates (WGS84)	Latitude (°S):	03°06'02"	03°16'29"	03°16'34"	03°16'34"	03°17'14"	03°17'14"
	Longitude (°E):	37°26'52"	37°36'56"	37°34'53"	37°34'53"	37°33'05"	37°33'05"
	Altitude (m):	4490					
TAS:		Trachybasalt	Picrobasalt	Basalt	Basalt	Basanite	Basanite
Major elements (wt%) ICP-AES	SiO ₂	49.05	41.00	46.00	47.10	42.00	42.20
	TiO ₂	3.17	3.20	3.29	3.12	3.49	3.54
	Al ₂ O ₃	16.60	11.80	13.90	15.22	11.65	11.75
	Fe ₂ O ₃ *	12.32	13.15	14.00	12.90	13.70	13.70
	MnO	0.18	0.18	0.18	0.17	0.17	0.17
	MgO	3.17	12.90	7.72	5.64	12.25	12.05
	CaO	7.60	11.90	9.10	7.60	10.80	11.00
	Na ₂ O	4.75	1.63	3.36	3.37	2.80	3.28
	K ₂ O	2.35	0.88	1.39	1.64	1.25	1.42
	P ₂ O ₅	0.77	0.50	0.67	0.56	0.55	0.56
	LOI	-0.35	2.11	-0.47	2.13	0.55	-0.25
	Total	99.61	99.25	99.14	99.45	99.21	99.42
Trace elements (ppm) ICP-MS	Mg#	0.42	0.70	0.58	0.52	0.69	0.69
	Li	8.9			9.9		5.2
	Sc	14.7			23.1		30.2
	V	206			291		336
	Cr	9.61			91.0		446
	Co	29.9			49.6		80.1
	Ni	14.6			40.7		331.6
	Rb	42			41		39
	Sr	926			754		934
	Y	37.2			34.0		27.7
	Zr	382			367		319
	Nb	85			97		131
	Cs	0.5			0.4		0.4
	Ba	846			661		689
	La	75.2			69.6		77.0
	Ce	144			143		155
	Pr	16.4			15.9		17.2
	Nd	63.3			61.0		66.8
	Sm	11.9			11.7		12.6
	Eu	3.5			3.5		3.8
	Gd	11.2			10.5		11.1
	Tb	1.4			1.4		1.4
	Dy	7.2			7.0		6.4
	Ho	1.3			1.3		1.1
	Er	3.4			3.2		2.5
	Yb	2.7			2.6		1.8
	Lu	0.37			0.35		0.23
	Hf	8.3			8.7		7.9
	Ta	4.3			4.8		7.3
	Pb	7.1			7.1		4.6
	Th	11.0			8.3		9.0
	U	1.7			1.6		2.0

Notes: Major-element data were measured by inductively coupled plasma–atomic emission spectrometry (ICP-AES), and trace-element concentrations were measured by inductively coupled plasma–mass spectrometry (ICP-MS) at UMR 6538 (Brest, France). LOI—loss on ignition. Mg# = 100 Mg/(Mg + Fe²⁺), where Mg and Fe²⁺ are expressed in number of cations per formula unit. Mg# was calculated using Fe₂O₃/FeO recommended by Middlemost (1989). TAS—intrusive lithologies and lavas were named using the total alkali–silica (TAS) discrimination diagram of Le Maitre et al. (1989).

TABLE 3. Sr AND Nd ISOTOPIC COMPOSITIONS OF SAMPLES FROM KILIMANJARO

Samples	Eruptive vent	Geological formation	Geochemical group	TAS	TIMS/Procedure for Sr-REE elution	$^{87}\text{Sr}/^{86}\text{Sr}$	Instrumental standard deviation (1 σ)	$^{143}\text{Nd}/^{144}\text{Nd}$	Instrumental standard deviation (1 σ)
05K101	Kibo	Lava Tower Group	Kibo 2	Phono-tephrite	MAT 261/Sr-Spec_Thru-spec	0.703680	0.000008	0.512782	0.000003
05K102	Kibo	Lava Tower Group	Kibo 2	Phono-tephrite	MAT 261/Sr-Spec_Thru-spec	0.703689	0.000007	0.512789	0.000003
05K103A	Kibo	Lent Group	Kibo 1 aphyric	Phonolite	Triton/aliquot. DOWEX® AG50X8	0.704012	0.000002	0.512681	0.000004
05K104	Kibo	Lava Tower Group	Kibo 2	Phono-tephrite	Triton/aliquot. DOWEX® AG50X8	0.703261	0.000004	0.512775	0.000002
05K105A	Kibo	Lent Group	Kibo 1 aphyric	Phonolite	Triton/aliquot. DOWEX® AG50X8	0.704017	0.000003	0.512694	0.000003
05K106	Kibo	Lava Tower Group	Kibo 2	Phono-tephrite	MAT 261/Sr-Spec_Thru-spec	0.703706	0.000006	0.512783	0.000003
05K107B	Shira	Shira Ridge Group	Shira	Basanite	MAT 261/Sr-Spec_Thru-spec	0.705007	0.000007	0.512533	0.000003
05K107C	Shira	Shira Ridge Group	Shira	Trachybasalt	Triton/aliquot. DOWEX® AG50X8	0.705856	0.000003	0.512444	0.000002
05K108A	Shira	Shira Ridge Group	Shira	Basanite	MAT 261/Sr-Spec_Thru-spec	0.705309	0.000006	0.512463	0.000003
05K108B	Shira	Shira Ridge Group	Shira	Basanite	Triton/aliquot. DOWEX® AG50X8	0.703816	0.000002	0.512655	0.000004
05K109A	Shira	Shira Ridge Group	Shira	Basanite	MAT 261/Sr-Spec_Thru-spec	0.704028	0.000007	0.512593	0.000004
05K111	Kibo	Lava Tower Group	Kibo 2	Tephri-phonolite	MAT 261/Sr-Spec_Thru-spec	0.703707	0.000006	0.512782	0.000003
05K112	Kibo	Caldera Rim Group	Kibo 1 porphyritic	Phonolite	Triton/aliquot. DOWEX® AG50X8	0.703745	0.000002	0.512745	0.000004
05K114	Kibo	Lava Tower Group	Kibo 2	Phono-tephrite	Triton/aliquot. DOWEX® AG50X8	0.703835	0.000003	0.512773	0.000002
05K117	Kibo	Caldera Rim Group	Kibo 1 porphyritic	Phonolite	Triton/aliquot. DOWEX® AG50X8	0.703763	0.000004	0.512741	0.000002
05K118	Kibo	Lava Tower Group	Kibo 2	Phono-tephrite	MAT 261/Sr-Spec_Thru-spec	0.703825	0.000006	0.512767	0.000003
05K120	Kibo	Rhomb Porphyry Group	Kibo 1 porphyritic	Phonolite	MAT 261/Sr-Spec_Thru-spec	0.703673	0.000009	0.512744	0.000004
05K121	Kibo	Rhomb Porphyry Group	Kibo 1 porphyritic	Phonolite	MAT 261/Sr-Spec_Thru-spec	0.703728	0.000007	0.512714	0.000005
05K122	Kibo	Inner Crater Group	Kibo 1 aphyric	Phonolite	MAT 261/Sr-Spec_Thru-spec	0.704011	0.000007	0.512679	0.000003
05K123	Kibo	Lava Tower Group	Kibo 2	Tephri-phonolite	Triton/aliquot. DOWEX® AG50X8	0.703837	0.000003	0.512755	0.000002
05K124	Kibo	Caldera Rim Group	Kibo 1 porphyritic	Phonolite	Triton/aliquot. DOWEX® AG50X8	0.703641	0.000004	0.512774	0.000004

(Continued)

TABLE 3. Sr and Nd isotopic compositions of samples from Kilimanjaro (Continued)

Samples	Eruptive vent	Geological formation	Geochemical group	TAS	TIMS/Procedure for Sr-REE elution	$^{87}\text{Sr}/^{86}\text{Sr}$	Instrumental standard deviation (1 σ)	$^{143}\text{Nd}/^{144}\text{Nd}$	Instrumental standard deviation (1 σ)
05K125	Kibo	Caldera Rim Group	Kibo 1 porphyritic	Phonolite	MAT 261/Sr-Spec_Thru-spec	0.703657	0.000007	0.512766	0.000003
05K128	Kibo	Rhomb Porphyry Group	Kibo 1 porphyritic	Tephri-phonolite	MAT 261/Sr-Spec_Thru-spec	0.703725	0.000007	0.512726	0.000004
05K129	Kibo	Lent Group	Kibo 1 aphyric	Phonolite	Triton/aliquot. DOWEX® AG50X8	0.704008	0.000003	0.512685	0.000003
05K130	Kibo	Lent Group	Kibo 1 aphyric	Phonolite	Triton/aliquot. DOWEX® AG50X8	0.704030	0.000003	0.512672	0.000004
05K131	Kibo	Lent Group	Kibo 1 aphyric	Phonolite	MAT 261/Sr-Spec_Thru-spec	0.704014	0.000007	0.512677	0.000003
05K132	Kibo	Lent Group	Kibo 1 aphyric	Phonolite	Triton/aliquot. DOWEX® AG50X8	0.704069	0.000004	0.512675	0.000003
05K133	Kibo	Lent Group	Kibo 1 aphyric	Phonolite	MAT 261/Sr-Spec_Thru-spec	0.704024	0.000007	0.512679	0.000006
05K136	Kibo	Caldera Rim Group	Kibo 1 porphyritic	Tephri-phonolite	MAT 261/Sr-Spec_Thru-spec	0.703768	0.000007	0.512739	0.000005
05K137	Kibo	Lent Group	Kibo 1 aphyric	Phonolite	Triton/aliquot. DOWEX® AG50X8	0.704058	0.000004	0.512680	0.000005
05K138B	Kibo	Caldera Rim Group	Kibo 1 porphyritic	Phonolite	Triton/aliquot. DOWEX® AG50X8	0.703647	0.000003	0.512782	0.000002
05K139	Saddle	Parasitic activity	Parasitic activity	Basanite	MAT 261/Sr-Spec_Thru-spec	0.703645	0.000007	0.512713	0.000002
05K140	Saddle	Parasitic activity	Parasitic activity	Foidite	MAT 261/Sr-Spec_Thru-spec	0.703703	0.000007	0.512759	0.000003
05K141A	Saddle	Parasitic activity	Parasitic activity	Basanite	MAT 261/Sr-Spec_Thru-spec	0.703521	0.000007	0.512748	0.000003
05K141B	Saddle	Parasitic activity	Parasitic activity	Tephrite	Triton/aliquot. DOWEX® AG50X8	0.703624	0.000002	0.512711	0.000003
05K142	Mawenzi	Neumann Tower-Mawenzi Group	Mawenzi	Trachybasalt	MAT 261/Sr-Spec_Thru-spec	0.704616	0.000008	0.512510	0.000003
05K143A	Mawenzi	Neumann Tower-Mawenzi Group	Mawenzi	Trachybasalt	MAT 261/Sr-Spec_Thru-spec	0.704333	0.000006	0.512502	0.000004
05K143B	Mawenzi	Neumann Tower-Mawenzi Group	Mawenzi	Trachybasalt	Triton/aliquot. DOWEX® AG50X8	0.703807	0.000003	0.512610	0.000002
05K144	Mawenzi	Mawenzi Eruptive Center	Mawenzi	Trachybasalt	MAT 261/Sr-Spec_Thru-spec	0.703677	0.000006	0.512618	0.000003
05K145	Mawenzi	Mawenzi Eruptive Center	Mawenzi	Trachybasalt	Triton/aliquot. DOWEX® AG50X8	0.703792	0.000002	0.512610	0.000002
03TZ41B	Rombo zone	Parasitic activity	Parasitic activity	Basalt	Triton/aliquot. DOWEX® AG50X8	0.704143	0.000004	0.512579	0.000003
03TZ42B	Rombo zone	Parasitic activity	Parasitic activity	Basanite	Triton/aliquot. DOWEX® AG50X8	0.703690	0.000003	0.512726	0.000003

Notes: Isotopic measurements were performed on a Thermo ElectronTM Triton at the IUEM (European Institute for Marine Studies, Brest, France) for all Nd measurements. Sr values were measured on Triton and Finnigan Mat 261 at Observatoire Midi Pyrénées, Toulouse, France. The NBS 987 (for Sr) and La Jolla (for Nd) standards were run regularly to check the measurements: average value $^{87}\text{Sr}/^{86}\text{Sr} = 0.710248 \pm 0.000020$ (n = 17; Triton mass spectrometer); average value $^{87}\text{Sr}/^{86}\text{Sr} = 0.710246 \pm 0.000012$ (n = 23; Mat 261 mass spectrometer); average value $^{143}\text{Nd}/^{144}\text{Nd} = 0.511853 \pm 0.000010$ (n = 16; Triton mass spectrometer). Blanks were <650 pg for Sr and <350 pg for Nd. All the experimental $^{87}\text{Sr}/^{86}\text{Sr}$ and $^{143}\text{Nd}/^{144}\text{Nd}$ values, measured during several analytical sessions, were corrected using the measured average values for NBS987 and La Jolla standards. TAS—intrusive lithologies and lavas were named using the total alkali-silica (TAS) discrimination diagram of Le Maitre et al. (1989). REE—rare earth element; TIMS (thermal ionization mass spectrometer); model of mass spectrometer used for Sr isotopic ratios measurements.

MAJOR-ELEMENT DATA

Kilimanjaro lavas are strongly silica-undersaturated, especially those from Kibo 1 (average normative nepheline [Ne] content ~19%) compared to intermediate lavas from Kibo 2 (average Ne content ~5%). Mafic facies from Shira and parasitic activity samples also show high Ne contents (average values of ~9% and 13%, respectively) in comparison to the rocks of Mawenzi, which are weakly silica-undersaturated, with an average Ne content of ~2%. Only two samples (05KI40 and 05KI41) from the saddle parasitic vents bear normative leucite (9.18% and 6.49%, respectively). Given their MgO values, ranging from 0.79% to 5.44% (basanite 05KI09A from Shira), none of the studied samples from the three main Kilimanjaro eruptive centers, including the mafic lavas from Shira and Mawenzi, can be considered to be a primary magma. Only the lavas from the parasitic vents of the Saddle and Rombo zone have MgO >10% (05KI41A, 03TZ40, 03TZ42A, and 03TZ42B), but these high contents may be related to the accumulation of olivine and clinopyroxene phenocrysts in these lavas.

Several groups of lavas can be distinguished in the TAS diagram (Fig. 2; Le Maitre et al., 1989). Lavas erupted from Shira, Mawenzi, and parasitic centers are mafic, with $40\% < \text{SiO}_2 < 50\%$ and $\text{Na}_2\text{O} + \text{K}_2\text{O} < 8\%$. All the Mawenzi samples are trachybasalts, whereas the Shira lavas are basanitic, except sample 05KI07C, which is trachybasaltic. In comparison, the samples erupted in the latest parasitic centers show a wide range of compositions. They plot within various fields (basalt, picrobasalt, basanite-tephrite, and foidite) and show SiO_2 contents <47%. Lavas erupted from Kibo have evolved compositions, with $\text{Na}_2\text{O} + \text{K}_2\text{O} > 8\%$ and $\text{SiO}_2 > 52\%$, and are phono-tephrite, tephri-phonolite, and phonolite. However, samples from the oldest volcanic formation of Kibo (Lava Tower Group) are intermediate phono-tephritic lavas, except samples 05KI11 and 05KI23, which plot at the boundary of the tephri-phonolitic field. A majority of lavas from the younger Kibo formations (Rhomb Porphyry Group, Lent Group, Caldera Rim Group, and Inner Crater Group) are phonolites, with the exception of four samples, which are less evolved tephri-phonolites. On the basis of the TAS diagram, as well as other major-elements diagrams (Fig. 3), we distinguished the intermediate lavas of the Lava Tower Group from the evolved phonolites and tephri-phonolites (other Kibo lava formations) in two groups called Kibo 2 and Kibo 1, respectively. Kibo 1 porphyritic and aphyric lavas are plotted using different symbols in the figures.

Selected major-element plots against SiO_2 are shown in Figure 3. Increasing SiO_2 values from 40.2% to 56.0% correlate with (1) a decrease in TiO_2 from 4.30% to 0.80%, and in CaO from 12.8% to 1.80%, and (2) an increase in Na_2O from 1.63% to 9.50%. On these three diagrams, it clearly appears that lavas from Kibo define isolated groups that do not overlap with the mafic facies from Shira, Mawenzi, and parasitic centers. Kibo 1 and Kibo 2 lava groups do not overlap, with the exception of sample 05KI05B in the Na_2O versus SiO_2 diagram, but the distinction between aphyric and porphyritic lavas of Kibo 1 is not

shown precisely. The TiO_2 versus SiO_2 diagram also shows that lavas from Mawenzi present a higher TiO_2 content compared to the lavas from Shira, at equivalent SiO_2 contents. Concentrations of P_2O_5 are scattered, but they show a rough negative correlation with SiO_2 in the lavas from Kibo, with a decrease from ~1% to 0.25%. A slight increase in the concentration of P_2O_5 with SiO_2 can be observed between mafic facies and intermediate lavas from the Kibo 2 group. This plot also shows clearly the differences between lavas from Kibo 2 and Kibo 1, as well as the separation between porphyritic and aphyric lavas of Kibo 1: porphyritic lavas contain ~0.5% P_2O_5 , and aphyric samples contain 0.25% P_2O_5 . This difference in the P_2O_5 content, for equivalent SiO_2 concentrations, in Kibo 1 lavas can be related to the presence of numerous apatite phenocrysts in the porphyritic facies, while apatite is present as less abundant microcrysts in aphyric lavas.

TRACE-ELEMENT DATA

The trace-element data of the different groups of lava are shown in Table 2, as well as in primitive mantle-normalized diagrams (Sun and McDonough, 1989; Fig. 4) and plots of selected element contents versus SiO_2 (Fig. 5). Considering Kilimanjaro as a whole, the level of trace-element concentrations is characteristic of enriched lavas, typically related to intraplate continental and oceanic-island volcanic activities.

Looking in detail at the trace-element patterns, each petrographic group is clearly distinct from the other, and the groups follow the petrologic classification established in the previous sections.

Primitive Mantle–Normalized Diagrams

Shira lavas are characterized by a significant heavy (H) REE depletion, relative Ti, Sr, and K negative anomalies, and slight Zr and Hf depletions. Th concentrations are highly variable, in comparison to Ba and U. One sample has a different pattern (05KI07C) and displays Nb, Ta, and Th negative anomalies. In terms of overall trace-element levels, Nb and Th concentrations can reach 100–190 times those of the primitive mantle (PM). Besides 05KI07C, Shira patterns are rather parallel, defining a consistent group within Kilimanjaro volcanics.

Mawenzi lavas have more homogeneous patterns, partly because only a few samples were collected on this volcano. Li, Ti, Sr, K, U, Rb, and Cs show negative anomalies, and there are variable positive Pb anomalies. The Zr and Hf depletion observed in Shira lavas is no longer present in these lavas. HREEs are also fractionated, and overall REE concentrations are close to those of Shira lavas.

Kibo 2 lavas display more contrasted patterns, characterized by marked Ti, Sr, and K negative spikes and variable Li and Pb negative anomalies. On the left side of the diagram, the most incompatible trace elements display higher concentrations than those of Shira and Mawenzi lavas, with typical values (Nb, Ta, Th) reaching 100–460 times PM. The range of Th, Nb, and Ta

concentrations is rather large in comparison to the neighboring elements (U, Ba, Rb, Cs). Moreover, the Nb/Ta ratios are variable, ranging from 1.06 to 1.64. One sample differs from the rest (05KI23) by its higher trace-element concentrations and marked positive Pb anomaly.

Kibo 1 lavas display the most extreme trace-element characteristics. The samples have strong negative Sr, Ti, K, and Ba anomalies. Negative Sr and Ba anomalies can be very significant for some of the samples (typically those with feldspar phenocrysts). The other characteristics are a systematic positive Li anomaly, variable Pb concentrations with both positive and negative anomalies, a large range of Th contents, and a relatively flat HREE pattern. The most noticeable feature is the level of concentrations reached by some of the most incompatible elements (Th, U, Nb, Ta), up to 900 times PM. With the exception of Ti, these lavas display the most enriched trace-element concentrations of the whole volcano.

Parasitic vent samples display very heterogeneous patterns, consistent with the polygenic characteristics of these magmas, and the fact that they have different localities. Their trace-element patterns may be interpreted with regards to (1) their petrologic affinities and (2) their geographic locations. Apart from this, there are some common features shared by all these lavas: i.e., relative Rb, Cs, K, and Li depletions, systematic Zr and Hf negative anomalies, highly variable Th, U, Nb, Ta, Pb, P, and light (L) REE enrichment, and a pronounced HREE fractionation.

Trace Element versus SiO_2

Using SiO_2 as a differentiation index, selected trace-element variations allow us to distinguish several tendencies within the Kilimanjaro lavas. LREE and HREE concentrations do not show the same behavior within the different groups: Whereas Yb concentrations systematically increase with SiO_2 , La concentrations

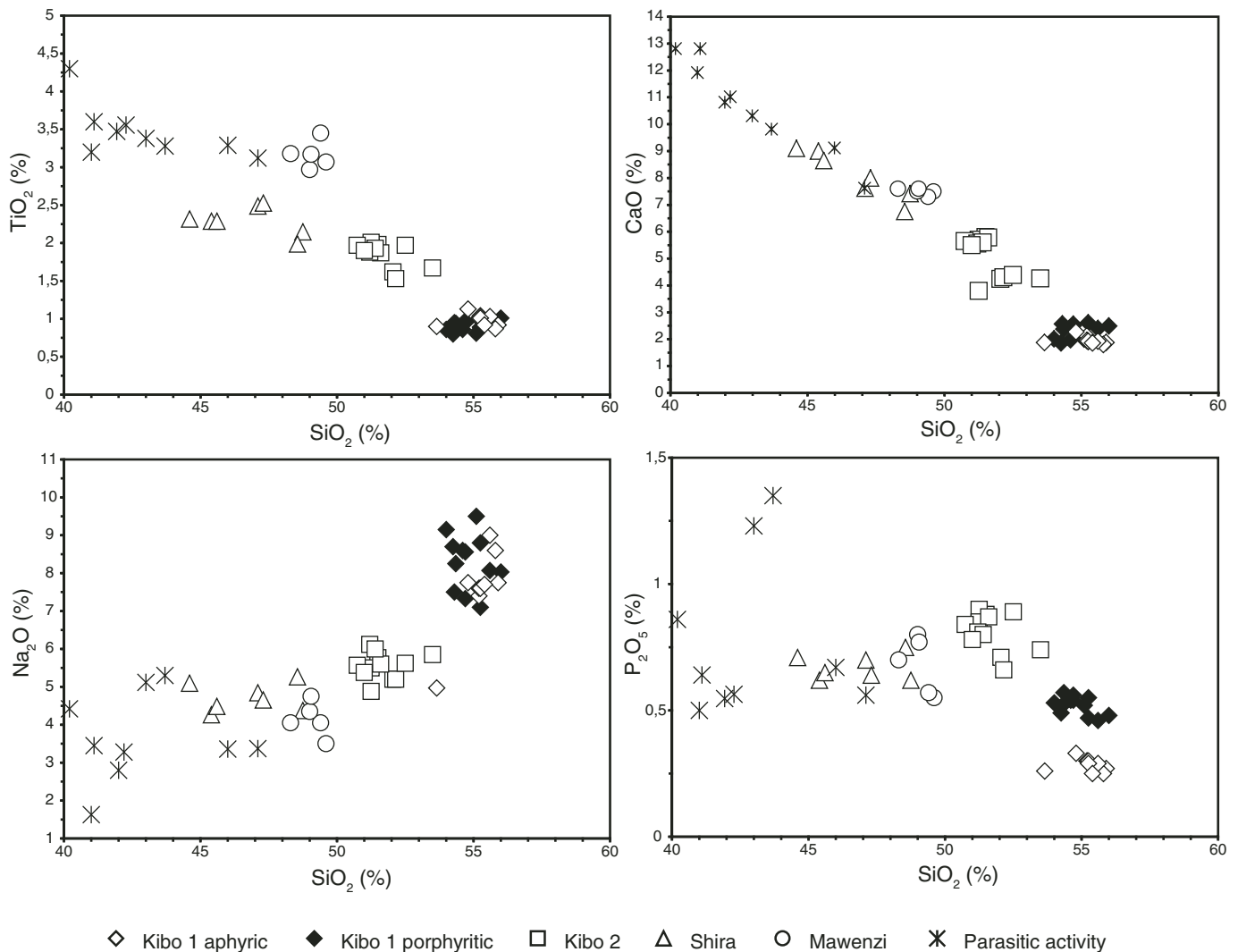


Figure 3. Variation of TiO_2 , CaO , Na_2O , and P_2O_5 (wt %) versus SiO_2 for the lavas of Kilimanjaro. SiO_2 is used as an index of differentiation.

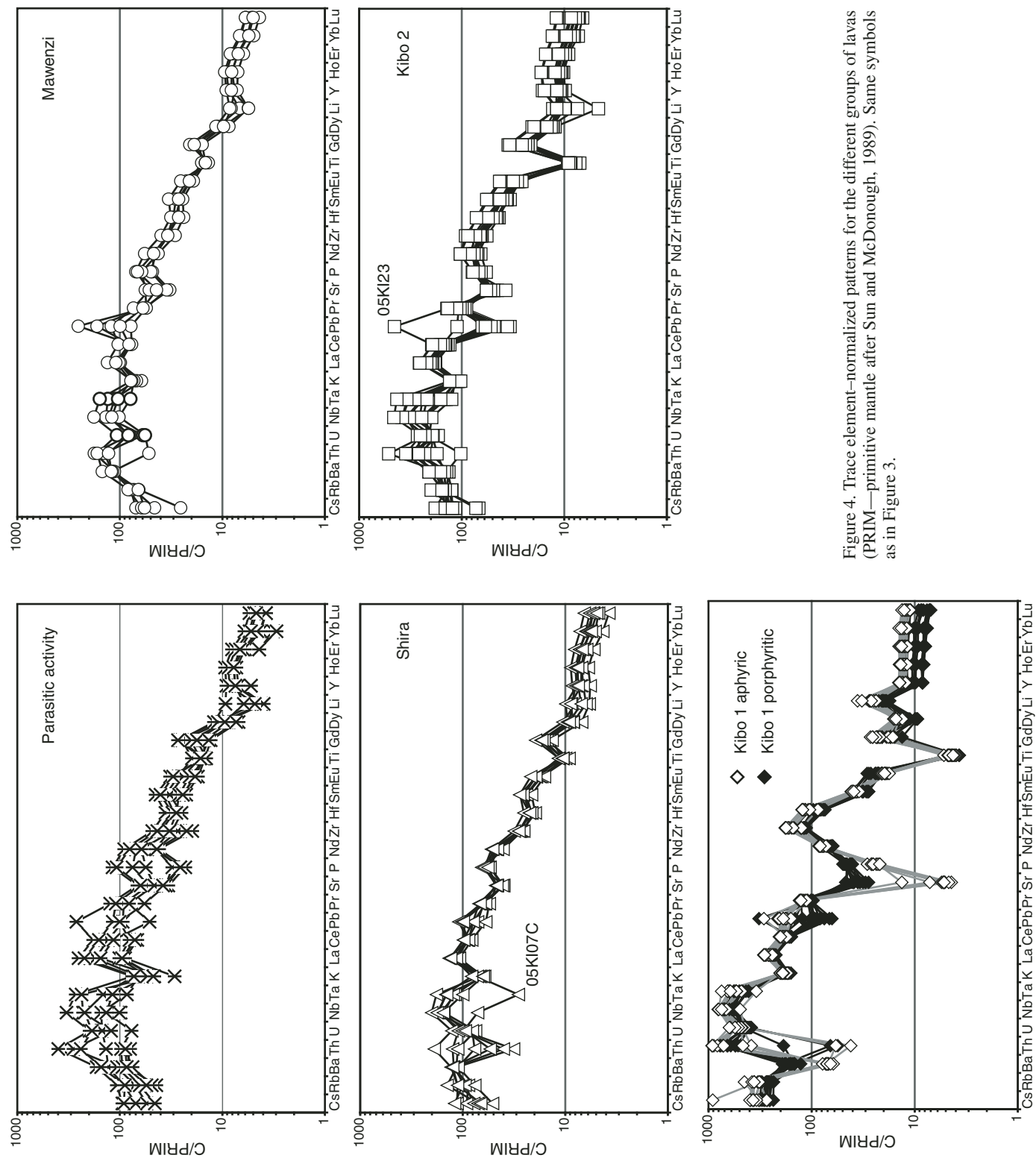


Figure 4. Trace element-normalized patterns for the different groups of lavas (PRIM—primitive mantle after Sun and McDonough, 1989). Same symbols as in Figure 3.

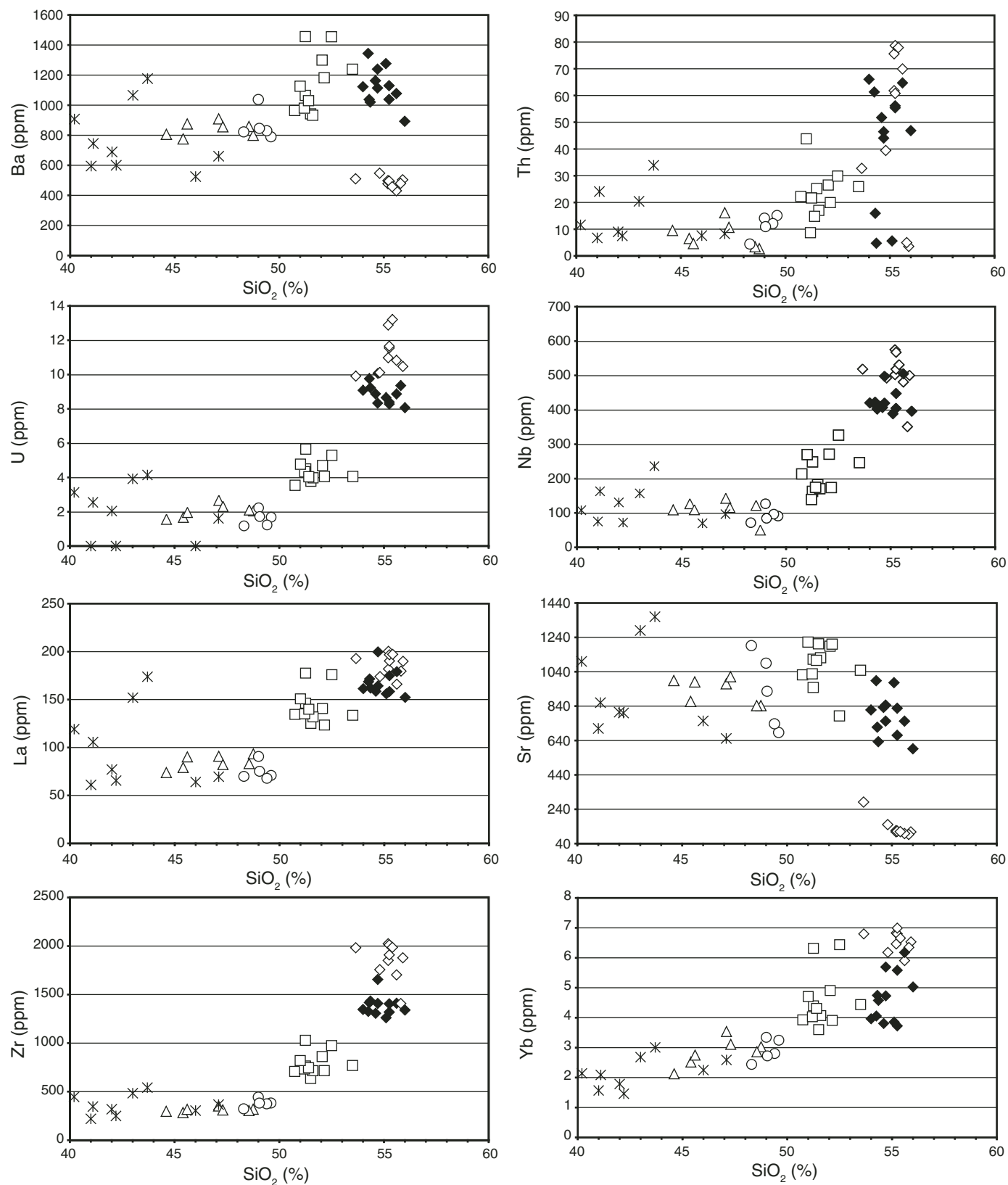


Figure 5. Selected trace-element concentrations plotted against SiO_2 . Same symbols as in Figure 3.

are very scattered within the parasitic vent group, where La can reach the level of concentrations of the samples from the Kibo 1 group but also increases linearly with SiO_2 in the other groups. In contrast, Kibo 1 and Kibo 2 lavas have rather homogeneous La concentrations but variable Yb. This last feature seems to be related to the porphyritic character of the lavas.

In Shira and Mawenzi lavas, Zr, Nb, Th, and U have the same range of concentrations, independent of SiO_2 values. All these element concentrations increase for more fractionated lavas (i.e., $\text{SiO}_2 > 50\%$). However, Zr, Nb, and U do not behave like Th or even Sr. Whereas the former systematically increase with SiO_2 , Ba, Th, and Sr are more scattered, defining two different groups. This also may be related to the porphyritic character of the lavas, but the groups defined in the Kibo 1 lavas are not the same whether we consider Sr-Ba on one side, or Th on the other side.

In terms of overall trace-element enrichment, Shira and Mawenzi lavas have a very similar range of concentrations, although they display different patterns. Parasitic activity and Kibo 2 lavas also display similar patterns and ranges of concentrations. However, parasitic activity samples have contrasted

ranges of concentrations, while Kibo 2 lavas are more homogeneous. Kibo 1 lavas show the more enriched and fractionated trace-element features.

ISOTOPIC COMPOSITIONS

The Sr and Nd isotopic compositions of 40 samples from Kilimanjaro are presented in Table 3 and have been plotted on a $^{143}\text{Nd}/^{144}\text{Nd}$ versus $^{87}\text{Sr}/^{86}\text{Sr}$ diagram (Fig. 6).

With the exception of samples 05KI07B, 05KI07C, and 05KI08A, and despite their intermediate to differentiated character, Kilimanjaro samples fall in the most depleted part of the field defined by North Tanzania lavas (Paslick et al., 1995, 1996). Our data are consistent with Sr and Nd isotopic compositions measured for Chyulu Hills (Späth et al., 2001) and for Kenya Rift lavas (Le Roex et al., 2001; MacDonald et al., 2001; Clément et al., 2003), without reaching the most Sr and Nd depleted signatures observed for these lavas. They plot on, or close to, the East African carbonatite line (EACL) defined by Bell and Blenkinshop (1987) on the basis of Sr-Nd isotopic variations in recent carbonatite lavas. This EACL has been interpreted as a mixing

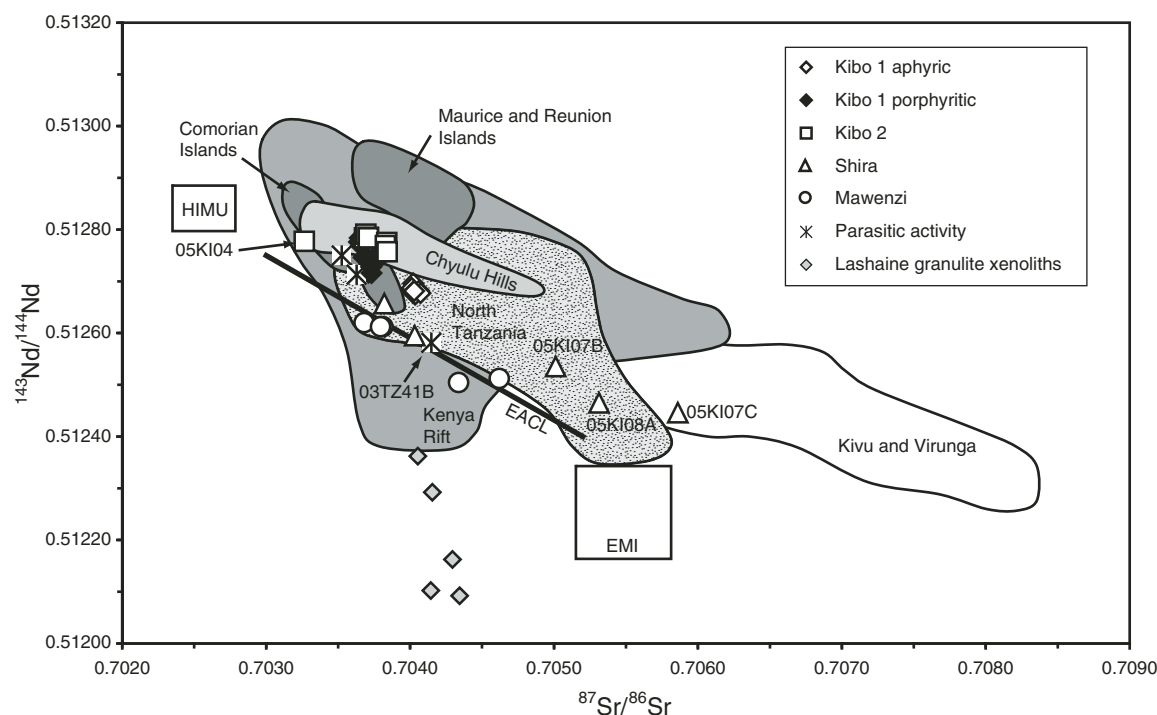


Figure 6. $^{143}\text{Nd}/^{144}\text{Nd}$ versus $^{87}\text{Sr}/^{86}\text{Sr}$ correlation diagram for lavas erupted from the different centers of Kilimanjaro (Shira, Mawenzi, Kibo, and parasitic vents) together with lavas from volcanic provinces associated with the East African Rift system and Indian Ocean ocean-island basalt (OIB). High U/Pb (HIMU) and enriched mantle (EMI)—mantle end members from Zindler and Hart (1986), EACL—East African carbonatite line defined by Bell and Blenkinshop (1987). Sources of data: Lashaine granulite xenoliths (Cohen et al., 1984), North Tanzania (Paslick et al., 1995, 1996), Chyulu Hills (Späth et al., 2001), Kenya Rift (Le Roex et al., 2001; MacDonald et al., 2001; Clément et al., 2003), Kivu and Virunga volcanic province (western arm; De Mulder et al., 1986; Rogers et al., 1992; Furman and Graham, 1999), Comorian Islands (Class and Goldstein, 1997; Class et al., 1998; Späth et al., 1996), Maurice and Reunion Islands (Hamelin et al., 1986; Mahoney et al., 1989; Peng and Mahoney, 1995; Paul et al., 2005; Newsom et al., 1986; Fisk et al., 1988; Albarède et al., 1997; Fretzdorff and Haase, 2002; Luais, 2004).

trend between two end-member mantle types with compositions similar to well-known ocean-island basalt (OIB) sources (Bell and Blenkinsop, 1987; Bell and Tilton, 2001): the HIMU (high U/Pb) and enriched mantle (EMI) components (Zindler and Hart, 1986). When compared to the Indian ocean OIB, the majority of Kilimanjaro samples display $^{87}\text{Sr}/^{86}\text{Sr}$ and $^{143}\text{Nd}/^{144}\text{Nd}$ ratios close to the Comores Archipelago (Späth et al., 1996; Class et al., 1998). However, they present a very distinctive signature, with lower $^{143}\text{Nd}/^{144}\text{Nd}$ for the same range of $^{87}\text{Sr}/^{86}\text{Sr}$, compared to the Indian ocean OIB of Maurice and Reunion Island fields (Hamelin et al., 1986; Newsom et al., 1986; Fisk et al., 1988; Mahoney et al., 1989; Peng and Mahoney, 1995; Albarède et al., 1997; Fretzdorff and Haase, 2002; Luais, 2004; Paul et al., 2005).

As a whole, Kilimanjaro samples (except the three samples mentioned before) are characterized by a restricted range in Sr isotopic compositions ($^{87}\text{Sr}/^{86}\text{Sr} = 0.703261\text{--}0.704616$) with more scattered Nd isotopic signatures ($^{143}\text{Nd}/^{144}\text{Nd} = 0.512502\text{--}0.512789$).

The Shira samples, despite their rather homogeneous composition, display a large range of isotopic signatures: from $^{87}\text{Sr}/^{86}\text{Sr} = 0.703816$ and $^{143}\text{Nd}/^{144}\text{Nd} = 0.512655$ to $^{87}\text{Sr}/^{86}\text{Sr} = 0.705856$ and $^{143}\text{Nd}/^{144}\text{Nd} = 0.512444$, the latter being the most enriched sample of our data set. It is noteworthy that all these samples come from a restricted area: 05KI07B and 05KI07C, and 05KI08A and 05KI08B. The Sr isotopic composition of 05KI07C ($^{87}\text{Sr}/^{86}\text{Sr} = 0.705856$; Table 3) may give us a constraint on the nature of the assimilated material, since crustal assimilation can be reasonably suspected to be responsible for displacement to such high $^{87}\text{Sr}/^{86}\text{Sr}$ ratios (Furman, 2007; see following discussion).

Similarly, the Mawenzi samples show scattered Sr and Nd isotopic compositions (from $^{87}\text{Sr}/^{86}\text{Sr} = 0.703677$ and $^{143}\text{Nd}/^{144}\text{Nd} = 0.512618$ to $^{87}\text{Sr}/^{86}\text{Sr} = 0.704616$ and $^{143}\text{Nd}/^{144}\text{Nd} = 0.512510$), although they fall in the North Tanzanian field. Moreover, they have systematically lower $^{143}\text{Nd}/^{144}\text{Nd}$ ratios compared to the majority of our samples, plotting on or below the EACL (Fig. 6).

Samples with the highest $^{143}\text{Nd}/^{144}\text{Nd}$ belong to the Kibo 2 and Kibo 1 porphyritic groups, and these plot clearly on the field defined by Chyulu Hills lavas (Späth et al., 2001). It is worth noting that only sample 05KI04 plots away from the North Tanzanian field, having low $^{87}\text{Sr}/^{86}\text{Sr} = 0.703261$ and $^{143}\text{Nd}/^{144}\text{Nd} = 0.512775$. This sample displays lower Sr isotopic ratios than those of the other Kibo 2 samples, for similar $^{143}\text{Nd}/^{144}\text{Nd}$ ratios. Similar signatures have been reported for nearby Chyulu Hills lavas. Furthermore, Kibo 1 porphyritic and aphyric lavas display distinctive isotopic signatures: Kibo 1 aphyric lavas have systematically lower Nd ratios (0.512672–0.512694) and higher Sr ratios (0.704008–0.704069) than Kibo 1 porphyritic lavas (respectively, 0.512714–0.512782 for Nd and 0.703641–0.703768 for Sr). It is worth noting that these lavas, which are clearly evolved in terms of petrology, display the most primitive Nd values.

Lavas erupted from the parasitic vents display a restricted range of isotopic signatures, except for one sample (03TZ41B), located in the Marangu region (Rombo zone, Fig. 1). All the other

samples plot clearly within the range of the majority of Kilimanjaro lavas ($^{87}\text{Sr}/^{86}\text{Sr} = 0.703261\text{--}0.704616$ and $^{143}\text{Nd}/^{144}\text{Nd} = 0.512502\text{--}0.512789$). The basalt 03TZ41B falls close to the Mawenzi samples, with $^{143}\text{Nd}/^{144}\text{Nd} = 0.512579$ for $^{87}\text{Sr}/^{86}\text{Sr} = 0.704143$, and is also significantly more evolved than the other parasitic activity samples ($\text{SiO}_2 = 47.1\%$).

PETROGENETIC PROCESSES

The genesis of alkaline lavas is still a matter of debate, especially in continental rift settings. This debate is intrinsically linked to the active or passive rifting models applied to the investigated magmatic extensional provinces. In the first case, melts are the direct expression of an asthenospheric mantle plume, as documented in intraplate oceanic islands (McKenzie and Bickle, 1988; Arndt and Christensen, 1992). The origin of alkaline magmas in passive rift frameworks is more complex because it involves hydrous melting of the lithospheric mantle, probably triggered at depth by the thermal effects of a hotspot (Nyblade and Robinson, 1994; Ebinger and Sleep, 1998). Hydrous melting of the lithospheric mantle becomes plausible only if hydrous phases, such as amphibole or phlogopite, occur within the source material (McKenzie, 1989; Gallagher and Hawkesworth, 1992; Turner et al., 1996; Class and Goldstein, 1997; Le Roex et al., 2001).

The East African Rift provides a unique setting where the transition from (1) rift-axis basaltic volcanics with typical plume-like isotopic compositions (Barrat et al., 1998; Rogers et al., 2000) to (2) more differentiated alkaline lavas allows us to further discuss the respective contributions of lithospheric and asthenospheric melting processes for magma genesis (Pik et al., 1999; Furman et al., 2004; Furman, 2007). In the case of the North Tanzanian divergence, the occurrence of large volcanoes over a continental crust of normal thickness (~40 km) (Birt et al., 1997; Last et al., 1997) may favor the location of the melting zone in the lithosphere. The geochemical study of young (1 Ma) primitive alkaline lavas from the Chyulu Hills chain, NE of the North Tanzanian divergence, suggests that melting occurred in the lithosphere, involving source material containing residual amphiboles directly linked to metasomatism of the lithospheric mantle by melts coming from the plume located underneath (Späth et al., 2000, 2001).

Effect of Crustal Assimilation: Coupled Isotopic and Trace-Element Constraints

The Sr and Nd isotopic compositions measured for Kilimanjaro lavas, including the evolved ones, show clearly that these lavas have been only weakly contaminated by the lower African continental crust (Fig. 6). In comparison, the Kenya Rift data show two trends: (1) toward very low Nd isotopic ratios, with isotopic composition close to the Tanzanian granulitic xenoliths (Cohen et al., 1984), suggesting that assimilation of lower crust has occurred; and (2) toward very Sr radiogenic values,

suggesting the assimilation of an upper-crustal component (Rollinson, 1993). This last case seems more relevant for some of the samples considered here. However, both contaminants were tested in the following simulations.

In Kilimanjaro lavas, we can distinguish two types of behaviors for the different groups of lavas, illustrated in Figures 7A and 7B.

Their isotopic signatures either correlate with SiO_2 (Shira, Mawenzi) and $[\text{Gd}]_N/[\text{Yb}]_N$ ratios, or they are fairly homogeneous within one group (Kibo 1, Kibo 2, parasitic activity).

As far as Sr and Nd isotopic ratios are concerned, parasitic activity and Kibo 1 and Kibo 2 lavas may be related to the same source, the latter being the fractionated end member of the former. In this case, a simple fractional crystallization process or a little AFC (assimilation and fractional crystallization) link these lavas at various stages of the volcano history. However, the average Sr and Nd isotopic signatures of both parasitic activity and Kibo 1 and 2 are slightly different: The simple fact that Kibo 2 lavas have more primitive Nd than parasitic activity samples contradicts an AFC process, keeping in mind that parasitic activity lava signatures may not be representative of all the isotopic spectrum below Kilimanjaro.

We performed AFC modeling with assimilation of either a deep (granulitic) or a shallow (felsic) crustal component (Figs. 7C and 7D). As starting material, we used two basanitic melts, one close to the most primitive parasitic activity basanites and one slightly more depleted in terms of isotopic compositions. Both modeled basanites experience felsic and granulitic assimilation (trend C to J in Figs. 7C and 7D).

Using Cohen et al. (1984) and Rudnick and Fountain (1995) data for a lower-crustal signature, it is possible to fit the Kibo 1 and Kibo 2 signatures, starting for a isotopic primitive basanitic melt and using a ratio R_a (mass assimilated divided by mass crystallized) of 0.8. Starting with the same material and assimilating a felsic crustal component, we can hardly fit the Shira signature, as extreme degrees of fractionation are required. On the opposite, the Mawenzi group may be linked to Kibo groups by this process. Regarding the Shira group, we tested different parameters for the AFC model, and the best fit was obtained using a highly REE fractionated, Sr radiogenic, crustal component (see parameter in Fig. 7 caption), with R_a of 0.9, starting from a parental melt characterized by a composition close to the parasitic activity ones.

Looking carefully at the modeled AFC curves and the positions of the Kilimanjaro lavas, one should mention that in Figures 7C and 7D both Kibo 1 and 2 and Mawenzi/Shira partly fall between their respective upper- and lower-crustal assimilation trends. This may indicate that fractionation—and therefore assimilation—occurs in different magmatic chambers at various depths beneath Kilimanjaro.

Finally, the AFC modeling suggests two opposite hypotheses for the origin of the Kilimanjaro lava signatures:

1. All lavas have a unique source, partly illustrated by the parasitic activity position in Figure 7. Kibo 1 and 2 lavas can be directly linked to the parasitic activity ones by simple fractional

crystallization, and Mawenzi can be linked to Shira by AFC with assimilation of both lower- and upper-crustal components. In this case, it is difficult to explain the fact that some of the Kibo 2 signatures are more primitive than the parasitic activity ones, although the parasitic activity signatures may not be representative of the whole spectrum of the Kilimanjaro source.

2. Shira group is clearly linked to the parasitic activity magmatic source by AFC process of both lower- and upper-crustal components. Kibo 1 and 2 are related to a more isotopic depleted source and have experienced AFC process of a dominant lower-crustal component. Mawenzi can be either related to the same Shira or Kibo source, with assimilation of an upper-crustal component. According to the timing of these lava eruptions, we are tempted to relate them to the Kibo event, since the feeding of two adjoining volcanoes by two magmatic sources seems extraneous.

These considerations are model-dependent and may vary with different sources, Ma/Mc (mass assimilated divided by mass crystallized), and fractional crystallization paths. However, SiO_2 -isotope correlations remain a good proxy for the AFC process, as for Shira/Mawenzi lavas. Kibo melt signatures are then better explained by simple fractional crystallization. In both cases, the AFC or simple fractional crystallization processes reveal that Shira and Kibo lavas do not share the same source and have not assimilated the same components.

Finally, one may note that AFC is an efficient process by which to wipe out the primary HREE depletion. Although this depletion is clearly marked for basanitic lavas, HREE patterns become flat as fractionation occurs. AFC modeling shows that this tendency may be related to continental material assimilation, the alternative hypothesis being massive crystallization of feldspars.

In the following section, sample characteristics are discussed in terms of melting and simple fractionation processes, i.e., the effects of AFC on REE fractionation are not considered. However, variations from one group to the other are not discussed in terms of fractionation, since too many parameters have to be taken into account: Fractionation modes can change, multiple crystallization stages may happen in several magma chambers, at different depths within the crust, and AFC is a predominant process for Shira and Mawenzi lavas.

Partial Melting and Source Composition

Source and partial melting hypotheses are essentially relevant for “not-too-much” fractionated melts. In the case of Kilimanjaro, the only melts that can be considered as truly “primitive” are the parasitic activity lavas and some Shira lavas. Parasitic activity samples display clear HREE depletion, high Mg#, and pristine isotopic compositions. Furthermore, their clear Zr, Hf, and Ti negative anomalies make them good candidates to test the hypothesis that Späth et al. (2001) proposed for the Chyulu Hills volcanic chain. Although Shira basanites are primitive, they have certainly experienced AFC processes, which have wiped out part of their pristine isotope and trace-element characteristics.

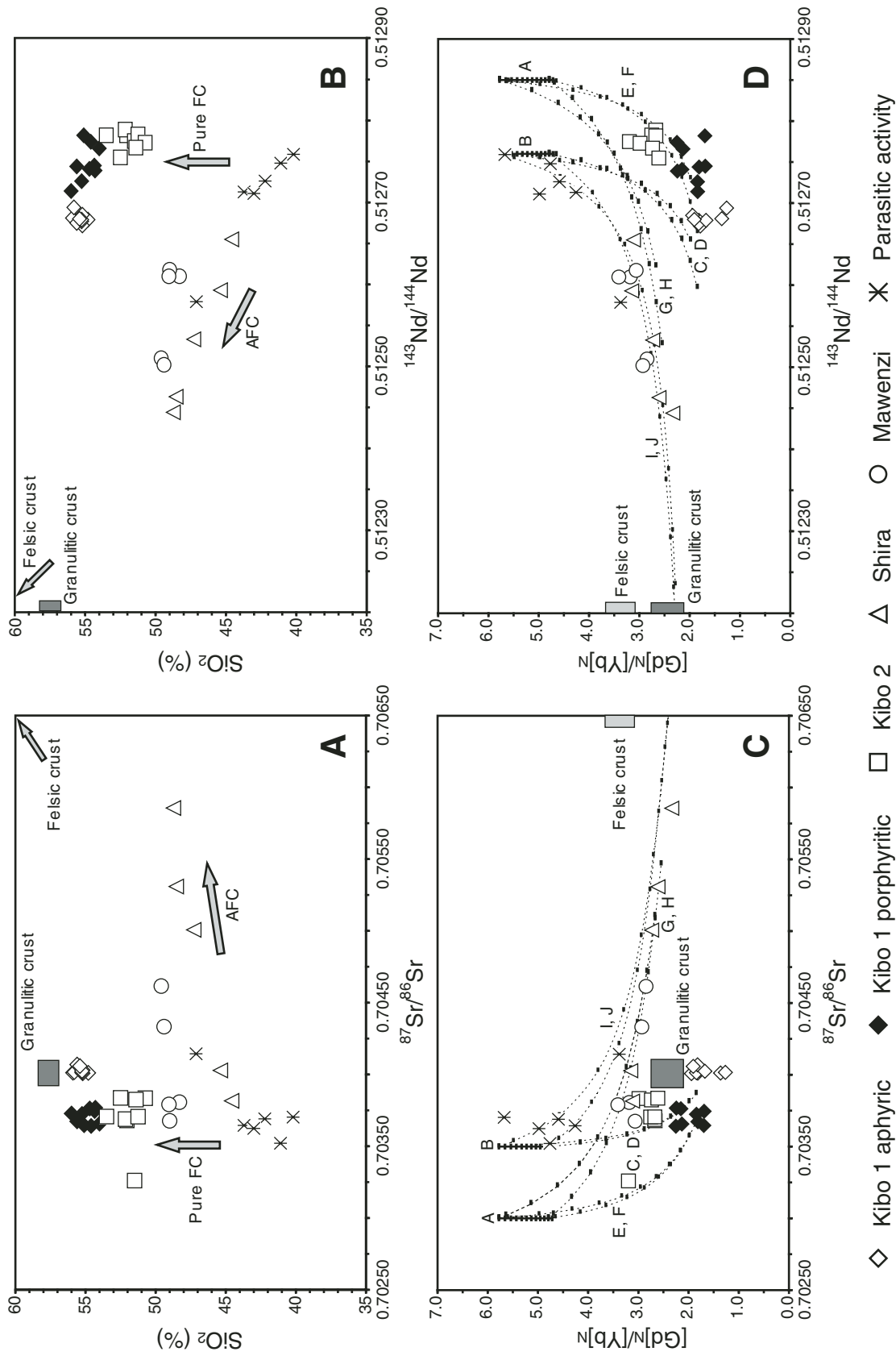


Figure 7. SiO_2 (%) and $[\text{Gd}]_{\text{N}}/[\text{Yb}]_{\text{N}}$, primitive mantle-normalized values (Sun and McDonough, 1989) plotted as a function of $^{87}\text{Sr}/^{86}\text{Sr}$ (A, C) and $^{143}\text{Nd}/^{144}\text{Nd}$ (B, D). The positions of the Tanzanian granulitic lower crust (Cohen et al., 1984; Rudnick and Fountain, 1995) and the estimated upper felsic crust are reported in all plots. AFC (assimilation and fractional crystallization) trends are plotted in C and D, as well as partial melting paths (see Fig. 8 legend for melting path details). Source compositions correspond respectively to accumulated fractional melting in the amphibole-garnet facies of a peridotite (I) with melting mode (olivine-orthopyroxene-clinopyroxene-garnet-amphibole) 5-5.4-33-6.6-5 and (2) source mode 53-22-15.5-4.5-5 for Kibo and parasitic vent trends (A, B) with initial isotopic compositions 0.512850/0.703 (A) and 0.512760/0.7035 (B). Tick marks indicate the % of melt produced, from 1% to 6%. AFC curves are reported for those melting end members used as starting compositions. C-D and E-F trends correspond to AFC processes with assimilation of a lower, granulitic crust ($[\text{Gd}]_{\text{N}}/[\text{Yb}]_{\text{N}} = 2.07$ and $^{143}\text{Nd}/^{144}\text{Nd} = 0.51209 - 0.704093$; Cohen et al., 1984) with R (mass assimilated versus mass crystallized) of 0.8. G-H and I-J trends are calculated using a contaminant with the following characteristics: $[\text{Gd}]_{\text{N}}/[\text{Yb}]_{\text{N}} = 3.2$, $^{143}\text{Nd}/^{144}\text{Nd} = 0.51209 - 0.707$, and $R_a = 0.9$. All the AFC curves show tick marks that correspond respectively to 1-5-10-15-20-25-30-40-45% of fractional crystallization. FC—pure fractional crystallization.

Furthermore, in our case, additional difficulties exist because of (1) the apparent lack of cogenetic primitive melts, and (2) the significant time interval between the emplacement of the oldest (Shira) and youngest (parasitic activity) basanites. This temporal gap, combined with the spatial distribution of analyzed lavas, which further display contrasted isotopic compositions, allows us to infer that the source(s) below the whole Kilimanjaro edifice is (are) either heterogeneous at a small/medium scale, or has changed through time. Furthermore, some lavas also display a crustal assimilation imprint that obliterates their original trace-element/isotopic signatures.

Besides Kibo, all the studied lavas show similar trace-element patterns, hence suggesting that, even if their sources are isotopically heterogeneous, their mineralogy and the melting process may be quite similar. Furthermore, the roughly similar trace-element patterns of the different lava groups provide indirect evidence for a persistent residual mineralogy of their source during the melting process (Späth et al., 2001). In order to estimate the source composition, we select sample 03TZ42A, which is olivine rich ($Mg\# = 0.69$). The olivine fractionation effect on its trace-element content is therefore balanced by the occurrence of numerous olivine phenocrysts within the lava. Therefore, we did not correct the trace-element content for crystallization of olivine prior to the calculation of the source composition. The specific trace-element features of this melt include: (1) a clear large ion lithophile element (LILE; Cs, Rb, Ba) and Th depletion, (2) a strong Nb, Ta, and LREE enrichment, (3) marked K, P, and Li negative anomalies, and finally (4) slight Zr, Hf and Ti negative anomalies. These features have been used by several authors to propose amphibole as a phase contributing to the melt fraction, but one that was not totally consumed during melting (Francis and Ludden, 1990, 1995; Class and Goldstein, 1997; Le Roex et al., 2001; Späth et al., 2001).

A detailed comparison between our primary melt composition and that of Späth et al. (2001) for the Chyulu Hills lavas shows that they share almost all the trace-element characteristics used by these authors to demonstrate the occurrence of residual amphibole during the lithospheric mantle melting process, while no feature demonstrates that of phlogopite. It is beyond the scope of this paper to perform a detailed direct and reverse partial melting modeling exercise on the basis of Kilimanjaro lava analyses, since the majority of them have undergone extreme fractional crystallization effects. Moreover, some of them have also experienced AFC processes.

In the following paragraphs, different grids relevant to various melting trends are discussed in order to address the issue about compositions of melts during melting and crystallization processes. We consider that lithospheric partial melting occurs in the stability domains of both garnet and amphibole. These two last assumptions are required to explain (1) the relative depletion of Cs, Rb, Zr, Hf, and K, and (2) the clear HREE fractionation. In the following, we test the melting of two different sources that display the same starting mineralogy, but that differ by their trace-element contents (corresponding to the original source of

03TZ42A before melting at different rates of 1% and 5%, referred to as primitive and depleted, respectively, in Figs. 8A and 8B).

We use the accumulated fractional melting equation from O'Hara (1977) and test the corresponding melting paths, considering variable amounts of residual garnet and variable contributions of amphibole to the melt fraction.

Origin of Basanites

AFC modeling has shown that basanites from Shira and parasitic activity samples may share the same source material. However, Shira basanites display lower Ti/Gd ratios compared to parasitic activity lavas. Two possible explanations are suggested by Figure 8A plots. They imply that either massive crystallization of Fe-Ti oxides occurred prior to emplacement of the Shira basanitic melts, or that oxides behaved as residual minerals in the source of the Shira basanites. Since the latter is not noticeably depleted in Cr, the second hypothesis seems more relevant. It is worth noting that basanites from Shira are different from parasitic activity basanites in terms of Ce/K ratios. However, parasitic vent lavas display a large spectrum of compositions, from primitive to depleted, according to the melting paths. This is consistent with the localized and volumetrically restricted characters of these melts, which may sample small volumes of the lithospheric mantle and ascend rapidly up to the surface.

Fractional Crystallization from Basanites to Phono-Tephrites

The fact that a continuous evolution from basanite to phonolite occurs within the Kilimanjaro edifice allows us to infer that these magmas have followed a similar fractional crystallization sequence, whether or not they are cogenetic (Price et al., 1985; Le Roex et al., 1990; Weaver, 1990; Kyle et al., 1992; Ablay et al., 1998). In Figures 8A and 8B, we reported fractionation trends corresponding to the evolution from basanites to tephrites and phono-tephrites and within phono-tephrites and phonolites (Le Roex et al., 1990). The main effect on trace-element abundances is related to fractionation of (1) apatite, which traps REEs and P, and fractionates U from Th (not shown), (2) Fe-Ti oxides, which causes a strong Ti depletion, and (3) plagioclase/feldspar, which can explain the low Dy/Yb ratios (this feature is potentially related to massive assimilation of the country-rock during AFC process).

Fractionation within the phono-tephrite (Kibo 2) and phonolitic (Kibo 1) series is partly counterbalanced by the variable amount of phenocrysts within the lavas. The occurrence of minor to major xenocrysts is not modeled in Figures 8A and 8B, but this may not drastically change the accumulation trends. The variable amount of pheno/xenocrysts is particularly critical for Sr, K, and Ba in aphyric phonolites (Figs. 4 and 5) and porphyritic phonolites (plagioclase and K-feldspar accumulation). Fe-Ti oxides have been removed from the magmas before phono-tephrite and phonolite fractionation episodes, because their fractionation commonly occurs at the tephritic/trachyandesitic stage of evolution

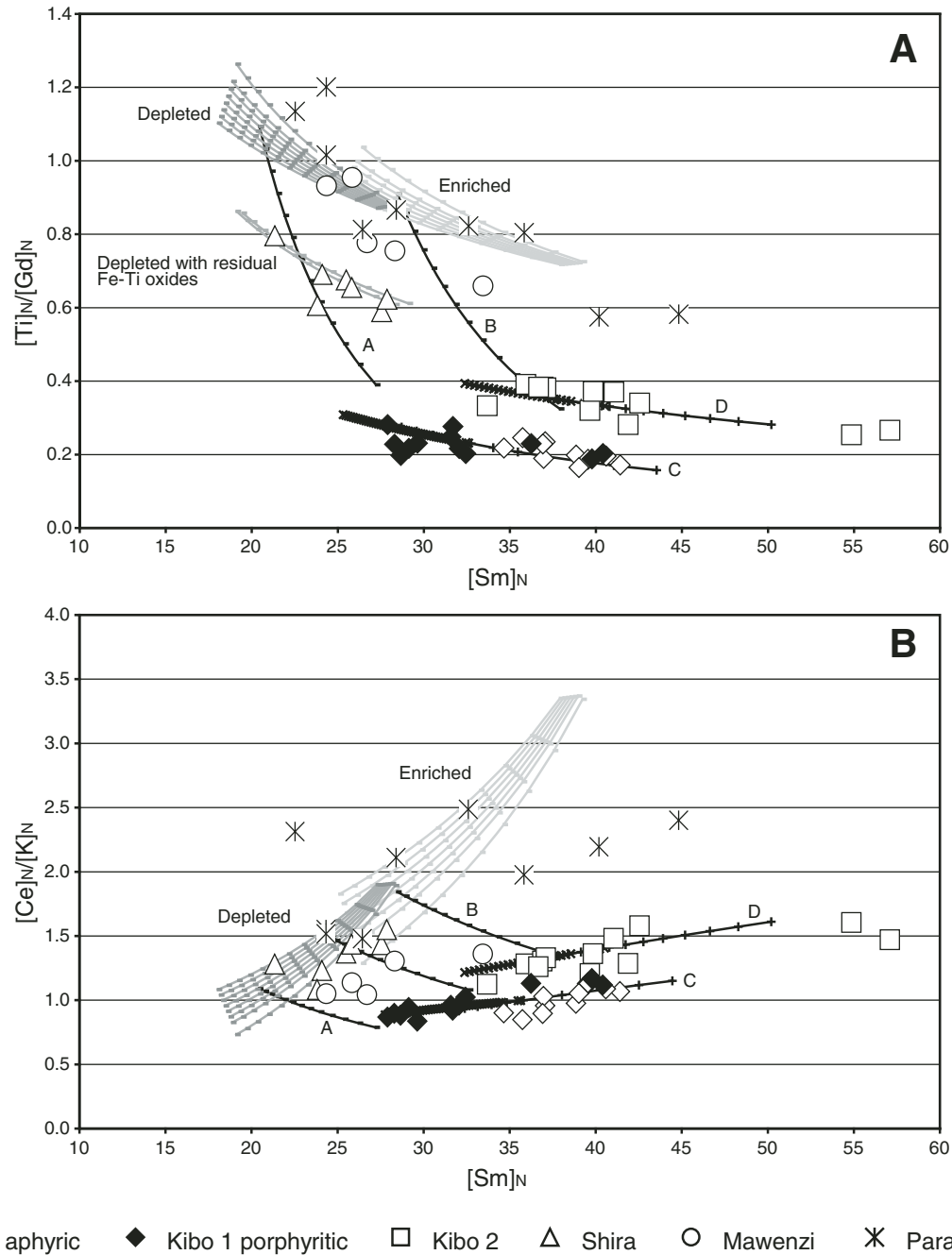


Figure 8. (A) $[Ti]_N/[Gd]_N = f[Sm]_N$, (B) $[Ce]_N/[K]_N = f[Sm]_N$, primitive mantle-normalized values (Sun and McDonough, 1989). Modeled curves: The source was inversely calculated from 03TZ42A basaltite, considering 1% and 5% partial melting. Melting mode is 5% ol + 5.4% opx + 33% cpx + 6.6% gt + 5% amph, and source mode is 53% ol + 22% opx + 15% cpx + 5% gt + 5% amph. This calculation gives two different source compositions, labeled depleted (dark gray) and enriched source (light gray). Several trends of partial melting/fractional crystallization are superimposed on the data. Partial melting was computed using O'Hara equations for accumulated fractional melting (O'Hara, 1977). The dark- and light-gray lines correspond respectively to amounts of residual garnet and amphibole involved (mode). The amount of residual garnet decreases from right (5%) to left (1%), with the exception for the primitive grid, where we chose 0.8% to fit Shira's compositions. The percentage of amphibole participating in the melting process decreases from 8% to 4% in each grid, from right to the left. Trends labeled A correspond to fractional crystallization from basaltite to phono-tephrite (5% increments) with the following abundances: 3.5 ol + 2 amph + 12 cpx + 15 plg + 2 apat + 5.5 $Ox_{(Fe-Ti)}$. Trend D illustrates evolution within phono-tephrite (5% increments) considering the following mineralogical mode 1 amph + 1 cpx + 14 plg + 15 K-felds + 1 apat + 2 $Ox_{(Fe-Ti)}$ (adapted from Le Roex et al., 1990). Partition coefficients are from Caroff et al. (1993) and references therein, and from Ablay et al. (1998). The melting path fitting Shira's basaltites was calculated with different residual source mineralogy (1.2% residual Fe-Ti oxides).

of alkaline series. Considering the mineralogical assemblage thought to crystallize from phono-tephrite to phonolite (Le Roex et al., 1990; Ablay et al., 1998), it is almost impossible to draw an evolution trend from Kibo 2 to Kibo 1 magmas. Therefore, we propose that the phono-tephritic magmas did not reach the surface at the time Kibo 1 lavas were erupted. Taking into account the limited assumptions we can make from evolved lava compositions, Kibo 1 and Kibo 2 lavas appear to have originated from different batches of magma, derived from a different source, or alternatively from the same source that has experienced variable degrees of melting.

Isotopic and Trace-Element Constraints on Kilimanjaro Edifice Construction

The isotopic signatures of Kibo 1 and Kibo 2 lavas are close in a Nd-Sr diagram. The porphyritic phonolites from Kibo 1 show only a slight shift toward enriched signatures, which can be related either to their mantle source or crustal assimilation. On the other hand, the progressive temporal depletion of the source beneath Kilimanjaro seems to be a reasonable explanation for the apparent trace-element depletion of phonolites (Kibo 1) compared to phono-tephrites (Kibo 2). This hypothesis is consistent with the time gap between Kibo 2 and Kibo 1 magmatic events (Baker et al., 1971; Bagdasaryan et al., 1973; Wilkinson et al., 1986; Nonnotte et al., 2008). Moreover, it is worth noting that Mawenzi trachybasalts fall on the continuation of the fractionation trends (Figs. 8A and 8B) defined by contemporaneous Kibo 2 phono-tephrites, although these two groups show different isotopic signatures.

Nd and Sr isotopic signatures versus time display some remarkable features. The first Shira edifice, despite the large range of isotopic compositions certainly related to crustal contamination, has the more enriched isotopic signatures. During the main building period of Kilimanjaro, there remains a significant difference between Mawenzi and Kibo magmatic sources: Whether Kibo lavas have relative depleted signatures, those from Mawenzi still display enriched, crust-contaminated isotopic ratios. This is also the period where the most depleted isotopic compositions are found, within the Kibo 2 lavas.

Later on, as the activity focused on the Kibo volcanic cone, the aphyric Kibo 1 unit erupted with intermediate, but very homogeneous, isotopic signatures between Mawenzi and Kibo 2. Finally, the porphyritic Kibo 1 unit was emplaced, displaying similar depleted signatures compared to those of Kibo 2 lavas.

To conclude, trace-element modeling and isotopic signatures both suggest a progressive depletion of the source beneath the Kilimanjaro area, from the Shira main volcanic episode to the late phonolitic event building the Kibo cone. This depletion particularly affected an amphibole-bearing lithospheric mantle, in the amphibole-garnet facies.

Indeed, two questions remain unsolved: (1) Are the hydrous minerals present in the lithospheric mantle beneath this zone related either to an ancient metasomatism of the African litho-

sphere (Cohen et al., 1984; Paslick et al. 1995; Lee et al., 2000; Burton et al., 2000), or to the recent activity of a plume beneath eastern Africa (Späth et al., 2001), or both? (2) Is there any occurrence of true asthenospheric melts?

Isotopic Signature Modeling

Decoupling of trace-element enrichment and depleted isotopic compositions has been used by several authors (Clague and Frey, 1982; Späth et al., 2001) to emphasize that the metasomatic event that affected the lithospheric mantle, and therefore triggered its melting, was contemporaneous with the activity of the plume. Alternatively, isotopic data on mantle xenoliths from Kenya and Tanzania have yielded old (Proterozoic) ages (Cohen et al., 1984; Burton et al., 2000). In case of an old lithospheric metasomatic event, a rough calculation of the initial source Nd isotopic composition (using the calculated trace-element composition of the source and an age of 2 Ga) indicates clear mantle signatures (around 0.5108 compared to 0.51006 for the CHUR [CHondritic Uniform Reservoir]). On the other hand, the effects of mixing plume-derived melts with an old refractory lithospheric mantle, which has developed its own radiogenic signature, are difficult to estimate. Refractory lithospheric mantle, isolated from a chondritic reservoir at 2 Ga, with a $^{147}\text{Sm}/^{144}\text{Nd}$ ratio of 0.003 gives a $(^{143}\text{Nd}/^{144}\text{Nd})_i$ value of 0.51303. Taking reasonable assumptions for the plume melts ($[\text{Nd}] = 60$ ppm, $^{143}\text{Nd}/^{144}\text{Nd} = 0.5126$), 10% plume melts would be needed to change the $^{143}\text{Nd}/^{144}\text{Nd}$ of the mantle source to fit the observed isotopic signatures. Furthermore, the complex geodynamic history of this part of the African continent, involving successive Precambrian orogenic events and a number of younger extensional processes (Karoo, Cenozoic), may be used as an indirect argument to support the “young metasomatism” hypothesis.

One plausible explanation reconciling trace-element and isotopic signatures may be that during the Shira magmatic episode (2–3 Ma), heating of the lithospheric mantle by the plume triggered the melting of an ancient, amphibole-rich, metasomatized source, hence producing the Shira basanites. Further temporal infiltration of plume melts led to a progressive change of the composition of the source (metasomatic crystallization of amphibole at greater depths). Then, after a time gap corresponding to further addition of plume melts into the lithosphere, thermal heating by the plume head triggered the melting of this rejuvenated lithosphere. Lithosphere metasomatic process might explain the time gap between the end of the Shira episode and the main edifice-building stage of Mawenzi and Kibo cones. In addition, the existence of a mixing trend between Kibo 1 aphyric and porphyritic phonolites may be related to the arrival into the Kibo magma chamber of enriched plume-derived asthenospheric melts, incorporating previously crystallized minerals left behind by Kibo 2 melts. However, we cannot totally discard the hypothesis of massive crustal contamination for Kibo 1 aphyric phonolites. Parasitic vents can be related to a late reactivation of sublithospheric mantle, since

they have compositions close to the source compositions of the Shira lavas.

CONCLUSIONS

Kilimanjaro is a polyphased volcano that displays various petrological lithofacies showing contrasted trace elements and isotopic signatures. However, those features are not randomly distributed for the three major edifices: They are related to time, source compositions, and fractionation processes such as fractional crystallization, assimilation of the lower and upper crust, and magma pooling at various levels within the continental crust. Based on interpretation and modeling of both isotopes and trace-element signatures, we proposed that Kilimanjaro volcanics originated within the lithosphere. Melting of the latter was at first triggered by conductive heating of fertile remnant portions of the lithosphere during impingement of a plume head. After a significant time gap corresponding to progressive infiltration of plume melt in the lithosphere, a second melting episode generated melts that participated in the construction of the main cone. There is no clear evidence for the participation of “true” asthenospheric melts in construction of the Kilimanjaro edifice, although we cannot totally rule out this hypothesis, on the basis of our data set.

ACKNOWLEDGMENTS

Research authorization was provided by the Tanzania Commission for Science and Technology and by Tanzania National Parks. We are indebted to the authorities of Kilimanjaro National Park and to J. Wakibara for their help organizing our fieldwork in the Marangu area. We thank S. Muhongo (University of Dar Es Saalam) and the French Embassy for their support. This chapter was greatly improved by the critical reviews of A. Le Roex and P. Kyle. Many thanks are due to R.C. Maury, M. Grégoire, and G. Ceuleneer for their constructive comments and corrections on a preliminary version of the article. All the team is particularly indebted to our Chagga guides, R. Mtuy and S. Gaudence, and to all the porters who guided us up to the Kilimanjaro summit. Special thanks are due to B. Doerler for climbing with us on the “White Mountain.” We thank C. Bollinger, D. Hureau, and J.P. Oldra for their great help during the data acquisition processes in Brest. This study was supported by the DyETI program of CNRS-INSU (Centre National de la Recherche Scientifique–Institut National des Sciences de l’Univers) and by a grant from SUCRI (Service Universitaire de Coopération et des Relations Internationales, University of Brest).

REFERENCES CITED

- Ablay, G.J., Carrol, M.R., Palmer, M.R., Marti, J., and Sparks, R.S., 1998, Basanite-phonolite lineage of the Teide–Pico Viejo volcanic complex, Tenerife, Canary Islands: *Journal of Petrology*, v. 39, p. 905–936, doi:10.1093/petrology/39.5.905.
- Albarède, F., Luais, B., Fitton, J.G., Semei, M.P., Kaminski, E., Upton, B.G.J., Bachelery, P., and Cheminée, J.L., 1997, The geochemical regimes of Piton de la Fournaise volcano (Réunion) during the last 530,000 years: *Journal of Petrology*, v. 38, p. 171–201, doi:10.1093/petrology/38.2.171.
- Arndt, N.T., and Christensen, U., 1992, The role of lithospheric mantle in continental flood volcanism: Thermal and geochemical constraints: *Journal of Geophysical Research*, v. 97, no. B7, p. 10,967–10,981, doi:10.1029/92JB00564.
- Bagdasaryan, G.P., Gerasimovskiy, V.I., Polyakov, A.I., and Gukasyan, R.K., 1973, Age of volcanic rocks in the rift zones of East Africa: *Geochemistry International*, v. 10, p. 66–71.
- Baker, B.H., 1967, Geology of the Mount Kenya Area: Geological Survey of Kenya Report 79, 78 p.
- Baker, B.H., Williams, L.A.J., Miller, J.A., and Fitch, F.J., 1971, Sequence and geochronology of the Kenya Rift volcanics: *Tectonophysics*, v. 11, p. 191–215, doi:10.1016/0040-1951(71)90030-8.
- Barrat, J.-A., Keller, F., Amossé, J., Taylor, R.N., Nesbitt, R.W., and Hirata, T., 1996, Determination of rare earth elements in sixteen silicate reference samples by ICP-MS after Tm addition and ion exchange separation: *Geo-standards Newsletter*, v. 20, p. 133–139, doi:10.1111/j.1751-908X.1996.tb00177.x.
- Barrat, J.-A., Fourcade, S., Jahn, B.M., Cheminée, J.L., and Capdevila, R., 1998, Isotope (Sr, Nd, Pb, O) and trace element geochemistry of volcanics from the Erta’ Ale range (Ethiopia): *Journal of Volcanology and Geothermal Research*, v. 80, p. 85–100, doi:10.1016/S0377-0273(97)00016-4.
- Bell, K., and Blenkinsop, J., 1987, Nd and Sr isotopic compositions of East African carbonatites: Implications for mantle heterogeneity: *Geology*, v. 15, p. 99–102, doi:10.1130/0091-7613(1987)15<99:NASICO>2.0.CO;2.
- Bell, K., and Tilton, G.R., 2001, Nd, Pb and Sr isotopic compositions of East African carbonatites: Evidence for mantle mixing and plume inhomogeneity: *Journal of Petrology*, v. 42, no. 10, p. 1927–1945, doi:10.1093/petrology/42.10.1927.
- Birt, C.S., Maguire, P.K., Khan, M.A., Thybo, H., Keller, G.R., and Patel, J., 1997, The influence of pre-existing structures on the evolution of the southern Kenya Rift Valley—Evidence from seismic and gravity studies: *Tectonophysics*, v. 278, p. 211–242, doi:10.1016/S0040-1951(97)00105-4.
- Burton, K.W., Schiano, P., Birck, J.L., Allègre, C.J., Rehkämer, M., Halliday, A.N., and Dawson, J.B., 2000, The distribution and behaviour of rhenium and osmium amongst mantle minerals and the age of the lithospheric mantle beneath Tanzania: *Earth and Planetary Science Letters*, v. 183, p. 93–106, doi:10.1016/S0012-821X(00)00259-4.
- Caroff, M., Maury, R.C., Leterrier, J., Joron, J.L., Cotton, J., and Guille, G., 1993, Trace element behaviour in the alkali basalt-comenditic trachyte series from Mururoa Atoll, French Polynesia: *Lithos*, v. 30, p. 1–22, doi:10.1016/0024-4937(93)90002-T.
- Clague, D.A., and Frey, F.A., 1982, Petrology and trace element geochemistry of the Honolulu volcanics, Oahu: Implications for the oceanic mantle below Hawaii: *Journal of Petrology*, v. 23, p. 447–504.
- Class, C., and Goldstein, S.L., 1997, Plume-lithosphere interactions in the ocean basins: Constraints from the source mineralogy: *Earth and Planetary Science Letters*, v. 150, p. 245–260, doi:10.1016/S0012-821X(97)00089-7.
- Class, C., Goldstein, S.L., Altherr, R., and Bachélery, P., 1998, The process of plume-lithosphere interactions in the ocean basins—The case of Grande Comore: *Journal of Petrology*, v. 39, p. 881–903, doi:10.1093/petrology/39.5.881.
- Clément, J.P., Caroff, M., Hémond, C., Tiercelin, J.J., Bollinger, C., Guillou, H., and Cotten, J., 2003, Pleistocene magmatism in a lithospheric transition area: Petrogenesis of alkaline and peralkaline lavas from the Baringo-Bogoria Basin, central Kenya Rift: *Canadian Journal of Earth Sciences*, v. 40, p. 1239–1257, doi:10.1139/e03-046.
- Cohen, R.S., O’Nions, R.K., and Dawson, J.B., 1984, Isotope geochemistry of xenoliths from East Africa: Implications for development of mantle reservoirs and their interaction: *Earth and Planetary Science Letters*, v. 68, p. 209–220, doi:10.1016/0012-821X(84)90153-5.
- Cotten, J., Le Dez, A., Bau, M., Caroff, M., Maury, R.C., Dulski, P., Fourcade, S., Bohn, M., and Brousse, R., 1995, Origin of anomalous rare-earth element and yttrium enrichments in subaerially exposed basalts: Evidence from French Polynesia: *Chemical Geology*, v. 119, p. 115–138, doi:10.1016/0009-2541(94)00102-E.
- Dawson, J.B., 1992, Neogene tectonics and volcanicity in the North Tanzania sector of the Gregory Rift Valley: Contrasts with the Kenya sector: *Tectonophysics*, v. 204, p. 81–92, doi:10.1016/0040-1951(92)90271-7.
- De Mulder, M., Hertogen, J., Deutsch, S., and André, L., 1986, The role of crustal contamination in the potassic suite of Karisimbi volcano (Virunga), African

- Rift Valley: Chemical Geology, v. 57, p. 117–136, doi:10.1016/0009-2541(86)90097-5.
- Downie, C., and Wilkinson, P., 1972, The Geology of Kilimanjaro: Sheffield, UK, Department of Geology, The University of Sheffield, 253 p.
- Downie, C., Humphries, D.W., Wilcockson, W.H., and Wilkinson, P., 1956, Geology of Kilimanjaro: Nature, v. 178, p. 828–830, doi:10.1038/178828a0.
- Downie, C., Humphries, D.W., Moore, L.R., Neves, R., Wilcockson, W.H., Wilkinson, P., Guest, N.J., Leedal, G.P., Sampson, D.N., Hartley, E.W., Orridge, G.R., Empson, H.E., and Pallister, J.W., 1965, Quarter Degree Sheets 42, 56 and 57, Kilimanjaro-Moshi and Explanatory Notes: Dodoma, Tanzanian Geological Survey, scale 1:125,000.
- Ebinger, C., and Sleep, N.H., 1998, Cenozoic magmatism throughout East Africa resulting from impact of a single plume: Nature, v. 395, p. 788–791, doi:10.1038/27417.
- Ebinger, C.J., Poudjom Djomani, Y., Mbende, E., Foster, A.N., and Dawson, J.B., 1997, Rifting Archean lithosphere: Eyasi-Manyara-Natron Rifts, East Africa: Journal of the Geological Society of London, v. 154, p. 947–960, doi:10.1144/gsjgs.154.6.0947.
- Fisk, M.R., Upton, B.G.J., Ford, C.E., and White, W.M., 1988, Geochemical and experimental study of the genesis of magmas of Reunion island, Indian Ocean: Journal of Geophysical Research, v. 93B, p. 4933–4950, doi:10.1029/JB093iB05p4933.
- Francis, D., and Ludden, J., 1990, The mantle source for olivine nephelinite, basanite and alkaline olivine basalt at Fort Selkirk, Yukon, Canada: Journal of Petrology, v. 31, p. 371–400.
- Francis, D., and Ludden, J., 1995, The signature of amphibole in mafic alkaline lavas, a study in the northern Canadian Cordillera: Journal of Petrology, v. 36, p. 1171–1191.
- Fretzdorff, S., and Haase, K.M., 2002, Geochemistry and petrology of lavas from the submarine flanks of Reunion island (Western Indian Ocean): Implications for magma genesis and the mantle source: Mineralogy and Petrology, v. 75, p. 153–184, doi:10.1007/s007100200022.
- Furman, T., 2007, Geochemistry of East African Rift basalts: An overview: Journal of African Earth Sciences, v. 48, p. 147–160, doi:10.1016/j.jafrearsci.2006.06.009.
- Furman, T., and Graham, D., 1999, Erosion of lithospheric mantle beneath East African Rift system: Geochemical evidence from the Kivu volcanic province: Lithos, v. 48, p. 237–262, doi:10.1016/S0024-4937(99)00031-6.
- Furman, T., Bryce, J.G., Karson, J., and Iotti, A., 2004, East African Rift system (EARS) plume structure: Insights from Quaternary mafic lavas of Turkana, Kenya: Journal of Petrology, v. 45, p. 1069–1088, doi:10.1093/petrology/egh004.
- Gallagher, K., and Hawkesworth, C., 1992, Dehydration melting and the generation of continental flood basalts: Nature, v. 358, p. 57–59, doi:10.1038/358057a0.
- Goldich, S.S., Treves, S.B., Suhr, N.H., and Stuckless, J.S., 1975, Geochemistry of the Cenozoic volcanic rocks of Ross island and vicinity, Antarctica: The Journal of Geology, v. 83, p. 415–435, doi:10.1086/628120.
- Goles, G.G., 1976, Some constraints on the origin of phonolites from the Gregory Rift, Kenya, and interferences concerning basaltic magmas in the rift system: Lithos, v. 9, p. 1–8, doi:10.1016/0024-4937(76)90051-7.
- Hamelin, B., Dupré, B., and Allègre, C.J., 1986, Pb-Sr-Nd isotopic data in Indian Ocean ridges: New evidence of large-scale mapping of mantle heterogeneities: Earth and Planetary Science Letters, v. 76, p. 288–298, doi:10.1016/0012-821X(86)90080-4.
- Hay, D.E., and Wendlandt, R.F., 1995, Origin of Kenya Rift plateau-type flood phonolites: Integrated petrologic and geophysical constraints on the evolution of the crust and upper mantle beneath the Kenya Rift: Journal of Geophysical Research, v. 100, no. B7, p. 10,549–10,557, doi:10.1029/94JB03036.
- Hay, D.E., Wendlandt, R.F., and Wendlandt, E.D., 1995, The origin of Kenya Rift plateau-type phonolites: Evidence from geochemical studies for fusion of lower crust modified by alkali basaltic magmatism: Journal of Geophysical Research, v. 100, no. B1, p. 411–422, doi:10.1029/94JB02159.
- Kaszuba, J.P., and Wendlandt, R.F., 2000, Effect of carbon dioxide on dehydration melting reactions and melt compositions in the lower crust and the origin of alkaline rocks: Journal of Petrology, v. 41, p. 363–386, doi:10.1093/petrology/41.3.363.
- Kyle, P.R., Moore, J.A., and Thirlwall, M.F., 1992, Petrologic evolution of anorthoclase phonolite lavas at Mount Erebus, Ross Island, Antarctica: Journal of Petrology, v. 33, p. 849–875.
- Last, R.J., Nyblade, A.A., and Langston, C.A., 1997, Crustal structure of the East African plateau from receiver functions and Rayleigh wave phase velocities: Journal of Geophysical Research, v. 102, no. B11, p. 24,469–24,483, doi:10.1029/97JB02156.
- Lee, C.-T., Rudnick, R.L., McDonough, W.F., and Horn, I., 2000, Petrologic and geochemical investigation of carbonates in peridotite xenoliths from northeastern Tanzania: Contributions to Mineralogy and Petrology, v. 139, p. 470–484, doi:10.1007/s004100000144.
- Le Gall, B., Nonnotte, P., Rolet, J., Benoit, M., Guillou, H., Mousseau-Nonnotte, M., Albaric, J., and Deverchère, J., 2008, Rift propagation at craton margin. Distribution of faulting and volcanism in the North Tanzanian divergence (East Africa) during Neogene times: Tectonophysics, v. 448, p. 1–19, doi:10.1016/j.tecto.2007.11.005.
- Legendre, C., Maury, R.C., Caroff, M., Guillou, H., Cotten, J., Chauvel, C., Bollinger, C., Hémond, C., Guille, G., Blais, S., Rossi, P., and Savanier, D., 2005, Origin of exceptionally abundant phonolites on Ua Pou island (Marquesas, French Polynesia): Partial melting of basanites followed by crustal contamination: Journal of Petrology, v. 46, no. 9, p. 1925–1962, doi:10.1093/petrology/egi043.
- Le Maitre, R.W., Bateman, P., Duddick, A., Keller, J., Le Bas, M.J., Sabine, P.A., Schmid, R., Sorensen, H., Streckeisen, A., Woolley, A.R., and Zanettin, B., 1989, A Classification of Igneous Rocks and Glossary of Terms: Oxford, UK, Blackwell, 193 p.
- Le Roex, A.P., Cliff, R.A., and Adair, B.J.I., 1990, Tristan da Cunha, South Atlantic: Geochemistry and petrogenesis of a basanite-phonolite lava series: Journal of Petrology, v. 31, p. 779–812.
- Le Roex, A.P., Späth, A., and Zartman, R.E., 2001, Lithospheric thickness beneath the southern Kenya Rift: Implications from basalt geochemistry: Contributions to Mineralogy and Petrology, v. 142, p. 89–106, doi:10.1007/s004100100273.
- Lippard, S.J., 1973, The petrology of phonolites from the Kenya Rift: Lithos, v. 6, p. 217–234, doi:10.1016/0024-4937(73)90083-2.
- Luais, B., 2004, Temporal changes in Nd isotopic composition of Piton de la Fournaise magmatism (Réunion Island, Indian Ocean): Geochemistry Geophysics Geosystems, v. 5, doi:10.1029/2002GC000502.
- MacDonald, R., Rogers, N.W., Fitton, J.G., Black, S., and Smith, M., 2001, Plume-lithosphere interactions in generation of the basalts of the Kenya Rift, East Africa: Journal of Petrology, v. 42, no. 5, p. 877–900, doi:10.1093/petrology/42.5.877.
- Mahoney, J.J., Natland, J.H., White, W.M., Poreda, R.J., Bloomer, S.M., Fisher, R.L., and Baxter, A.N., 1989, Isotopic and chemical provinces of the Western Indian Ocean spreading centers: Journal of Geophysical Research, v. 94, p. 4033–4052, doi:10.1029/JB094iB04p4033.
- McKenzie, D., 1989, Some remarks on the movement of small melt fractions in the mantle: Earth and Planetary Science Letters, v. 95, p. 53–72, doi:10.1016/0012-821X(89)90167-2.
- McKenzie, D., and Bickle, J., 1988, The volume and composition of melt generated by extension of the lithosphere: Journal of Petrology, v. 29, no. 3, p. 625–679.
- Middlemost, E.A.K., 1989, Iron oxidation ratios, norm and the classification of volcanic rocks: Chemical Geology, v. 77, p. 19–26, doi:10.1016/0009-2541(89)90011-9.
- Newsom, H.E., White, W.M., Jochum, K.P., and Hofmann, A.W., 1986, Siderophile and chalcophile element abundances in oceanic basalts, Pb isotope evolution and growth of the Earth's core: Earth and Planetary Science Letters, v. 80, p. 299–313, doi:10.1016/0012-821X(86)90112-3.
- Nonnotte, P., Guillou, H., Le Gall, B., Benoit, M., Cotten, J., and Scaillet, S., 2008, New K-Ar age determinations of Kilimanjaro volcano in the North Tanzanian diverging rift, East Africa: Journal of Volcanology and Geothermal Research, v. 173, p. 99–112, doi:10.1016/j.jvolgeores.2007.12.042.
- Nyblade, A.A., and Robinson, S.W., 1994, The African superswell: Geophysical Research Letters, v. 21, p. 765–768, doi:10.1029/94GL00631.
- O'Hara, M.J., 1977, Geochemical evolution during fractional crystallization of a periodically refilled magma chamber: Nature, v. 266, p. 503–507, doi:10.1038/266503a0.
- Paslick, C.R., Halliday, A.N., James, D., and Dawson, J.B., 1995, Enrichment of the continental lithosphere by OIB melts: Isotopic evidence from the volcanic province of northern Tanzania: Earth and Planetary Science Letters, v. 130, p. 109–126, doi:10.1016/0012-821X(95)00002-T.
- Paslick, C.R., Halliday, A.N., Lange, R.B., James, D., and Dawson, J.B., 1996, Indirect crustal contamination: Evidence from isotopic and chemical disequilibria in minerals from alkali basalts and nephelinites from northern

- Tanzania: Contributions to Mineralogy and Petrology, v. 125, p. 277–292, doi:10.1007/s004100050222.
- Paul, D., White, W.M., and Blichert-Toft, J., 2005, Geochemistry of Mauritius and the origin of rejuvenescent volcanism on ocean island volcanoes: Geochemistry Geophysics Geosystems, v. 6, doi:10.1029/2004GC000883.
- Peng, Z.X., and Mahoney, J.J., 1995, Drillhole lavas from the northwestern Deccan Traps and the evolution of Reunion hotspot mantle: Earth and Planetary Science Letters, v. 134, p. 169–185, doi:10.1016/0012-821X(95)00110-X.
- Pik, R., Deniel, C., Coulon, C., Yirgu, G., and Marty, B., 1999, Isotopic and trace element signatures of Ethiopian flood basalts: Evidence for plume-lithosphere interactions: Geochimica et Cosmochimica Acta, v. 63, no. 15, p. 2263–2279, doi:10.1016/S0016-7037(99)00141-6.
- Price, R.C., Johnson, R.W., Gray, C.M., and Frey, F.A., 1985, Geochemistry of phonolites and trachytes from the summit region of Mt. Kenya: Contributions to Mineralogy and Petrology, v. 89, p. 394–409, doi:10.1007/BF00381560.
- Rogers, N., De Mulder, M., and Hawkesworth, C., 1992, An enriched mantle source for potassic basanites: Evidence from Karisimbi volcano, Virunga volcanic province, Rwanda: Contributions to Mineralogy and Petrology, v. 111, p. 543–556, doi:10.1007/BF00320908.
- Rogers, N., MacDonald, R., Fitton, J.G., George, R., Smith, M., and Barreiro, B., 2000, Two mantle plume beneath East African Rift system: Sr, Nd and Pb isotope evidence from Kenya Rift basalts: Earth and Planetary Science Letters, v. 176, p. 387–400, doi:10.1016/S0012-821X(00)00012-1.
- Rollinson, H.R., 1993, Using Geochemical Data: Evaluation, Presentation, Interpretation: Essex, UK, Pearson Education, 352 p.
- Rudnick, R.L., and Fountain, D.M., 1995, Nature and composition of continental crust: A lower crustal perspective: Reviews of Geophysics, v. 33, p. 267–309, doi:10.1029/95RG01302.
- Späth, A., Le Roex, A.P., and Duncan, R.A., 1996, The geochemistry of lavas from the Comores Archipelago, Western Indian Ocean: Petrogenesis and mantle source region characteristics: Journal of Petrology, v. 37, no. 4, p. 961–991, doi:10.1093/petrology/37.4.961.
- Späth, A., Le Roex, A.P., and Opiyo-Akech, N., 2000, The petrology of Chyulu Hills volcanic Province, Southern Kenya: Journal of African Earth Science, v. 31, no. 2, p. 337–358.
- Späth, A., Le Roex, A.P., and Opiyo-Akech, N., 2001, Plume-lithosphere interaction and the origin of continental rift-related alkaline volcanism—The Chyulu Hills volcanic province, southern Kenya: Journal of Petrology, v. 42, no. 4, p. 765–787, doi:10.1093/petrology/42.4.765.
- Sun, S.S., and McDonough, W.F., 1989, Chemical and isotopic systematics of oceanic basalts: Implications for mantle composition and processes, *in* Saunders, A.D., and Norry, M.J., eds., Magmatism in the Ocean Basins: Geological Society of London Special Publication 42, p. 313–345.
- Turner, S., Hawkesworth, C., Gallagher, K., Stewart, K., Peate, D., and Mantovani, M., 1996, Mantle plumes, flood basalts, and thermal models for melt generation beneath continents: Assessment of a conductive heating model and application to the Paraná: Journal of Geophysical Research, v. 101, no. B5, p. 11,503–11,518, doi:10.1029/96JB00430.
- Weaver, B.L., 1990, Geochemistry of highly-undersaturated ocean island basalt suites from the South Atlantic Ocean: Fernando de Noronha and Trindade Islands: Contributions to Mineralogy and Petrology, v. 105, p. 502–515, doi:10.1007/BF00302491.
- Wilkinson, P., Mitchell, J.G., Cattermole, P.J., and Downie, C., 1986, Volcanic chronology of the Meru-Kilimanjaro region, northern Tanzania: Journal of the Geological Society of London, v. 143, p. 601–605, doi:10.1144/gsjgs.143.4.0601.
- Zindler, A., and Hart, S., 1986, Chemical geodynamics: Annual Review of Earth and Planetary Sciences, v. 14, p. 493–571, doi:10.1146/annurev.ea.14.050186.002425.

MANUSCRIPT ACCEPTED BY THE SOCIETY 9 NOVEMBER 2010

Trace-element distribution between coexisting aqueous fumarole condensates and natrocarbonatite lavas at Oldoinyo Lengai volcano, Tanzania

Alexander J. Teague*

*Department of Earth Sciences, University of Bristol, Wills Memorial Building, Queen's Road, Bristol BS8 1RJ, UK, and
Institute for Mineralogy and Petrology, ETH Zurich, CH-8092 Zürich, Switzerland*

Jacob Hanley

*Department of Geology, Saint Mary's University, 923 Robie Street, Halifax, Nova Scotia, B3H3C3, Canada, and
Institute for Mineralogy and Petrology, ETH Zurich, CH-8092 Zürich, Switzerland*

Terry M. Seward

Institute for Mineralogy and Petrology, ETH Zurich, CH-8092 Zürich, Switzerland

Frederik Reutten

Laboratory of Inorganic Chemistry, Department of Chemistry, ETH Zurich, CH-8093 Zürich, Switzerland

ABSTRACT

Fieldwork was conducted in the active north crater of Oldoinyo Lengai volcano, Tanzania. Gases, aqueous fumarole condensates, and freshly erupted natrocarbonatite lavas were collected from several hornitoes associated with the same eruptive center and are considered to represent genetically related products of the same shallow magma chamber. Apparent trace-metal mineral-mineral partition coefficients were derived for the major carbonate phases, gregoryite and nyerereite, and several accessory phases within the fresh lava samples. Trace metals display an affinity for the accessory minerals.

Textural information suggests that fluorite and coexisting sylvite are also present interstitially as quenched immiscible salt melts, and that any trace metals present may be scavenged from the carbonatite by the immiscible separation of these salt phases. Gas condensate analyses from the fumaroles associated with the eruption reveal further partitioning of trace elements into the vapor phase. Chalcophile

*alex.teague@bristol.ac.uk

Teague, A.J., Hanley, J., Seward, T.M., and Reutten, F., 2011, Trace-element distribution between coexisting aqueous fumarole condensates and natrocarbonatite lavas at Oldoinyo Lengai volcano, Tanzania, in Beccaluva, L., Bianchini, G., and Wilson, M., eds., *Volcanism and Evolution of the African Lithosphere: Geological Society of America Special Paper 478*, p. 159–172, doi:10.1130/2011.2478(08). For permission to copy, contact editing@geosociety.org. © 2011 The Geological Society of America. All rights reserved.

elements show particularly high volatility, and this implies either gas release prior to sulfide formation or the decomposition of sulfides prior to eruption.

The strong partitioning of metals into the halogenide and vapor phases has broad implications for the mobility of trace elements in the mantle source, the genesis of exotic mineralization associated with other carbonatites, and the ability of fumarole condensates to carry a direct chemical signature from their parent magma.

INTRODUCTION

Our knowledge regarding the behavior of trace elements in natural systems has been obtained through the experimental determination of crystal-melt and crystal-crystal partition coefficients in anhydrous or fluid undersaturated systems as well as from analytical studies of element partitioning between/amongst phases in rocks and hydrothermal mineral assemblages. Aqueous fluids are essential agents of mass transfer during magmatic-hydrothermal events, and while both fluids and vapors have been demonstrated to be carriers of metals in ore-forming environments (Barnes, 1997; Symonds et al., 1987; Wahrenberger et al., 2002; Williams-Jones et al., 2002), only recently have low-density vapor-like fluids and gases been clearly identified as important metal carriers. Fluid inclusion studies, for example, have demonstrated the partitioning of specific metals into low-density volatile-rich fluids in magmatic-hydrothermal systems (e.g., Audetat et al., 2000; Heinrich et al., 1999). While the database for trace-element distribution between melts or brines and vapor-like fluids formed by phase separation in plutonic igneous systems is growing rapidly, very limited data are available for metal partitioning into exsolved vapors and associated phases (either other aqueous liquids, melts, or solids) in volcanic systems.

Owing to the ubiquity of silicate magmatism, all previous studies on trace elements in volcanic gases have focused on the gases exsolved from silicate volcanoes (Allard et al., 2000; Gauthier and Le Cloarec, 1998; Gemmell, 1987; Miller et al., 1990; Stoiber and Rose, 1970; Symonds et al., 1987, 1992, 1996; Taran et al., 2001; Wahrenberger et al., 2002; Williams-Jones et al., 2002). Due to the difficulties of sampling gases from actively erupting volcanoes, such studies have analyzed condensates collected from fumaroles degassing during periods of quiescence. Thus, the composition of these gases must be recognized as a mixture of exsolved magmatic end-member fluids with possible meteoric and/or hydrothermal contributions, modified by the interaction with wall rocks upon their ascent to the surface. However, while isotopic studies in particular have characterized the relative contributions of these various end-member fluids to a volcanic gas (e.g., Brombach et al., 2003; Chiodini et al., 2000; Giggenbach, 1992; Goff and McMurtry, 2000), there is particular interest in the degree to which the bulk and trace chemistry of a fumarolic vapor may show (preserve) the nature of the magmatic source.

There is a paucity of data in this respect, and those available tend to consider the fluids (liquids or vapors or both) in isolation

from the source rocks and/or magmas. Mainly, this is due to the extreme difficulty in acquiring natural samples that adequately preserve coexisting crystals, melts, fluids, and gases at, or close to, equilibrium conditions. Very few studies have attempted to establish the partitioning behavior of trace elements in a *natural* rock-fluid-vapor system. Möller et al. (2003) examined the partitioning behavior of rare earth elements (REEs) and yttrium between high-temperature fluids and associated host rocks from the Larderello geothermal field, Tuscany. Fractionation of REEs into the fluid (normalized to Ca, the dominant cation) was observed and suggested to be largely insensitive to ligand availability. The chemistry of these fluids is also recognized to be dominated by rock-fluid interactions rather than reflecting the nature of the magmatic source. On the other hand, the few available experimental studies (Candela and Holland, 1984; Pokrovski et al., 2008; Rempel et al., 2009; e.g., Simon et al., 2005, 2006) have demonstrated that trace-element partitioning into aqueous fluids and vapors tends to be ligand dependent. Trace-element partitioning has also been studied in carbonatite systems, both on naturally occurring fluid inclusions, experimentally (Wendlandt and Harrison, 1979), and also with respect to sublimate encrustations forming on the natrocarbonatites of Oldoinyo Lengai (Gilbert and Williams-Jones, 2008). Both studies noted the affinity of REEs for a CO₂-dominated vapor phase.

The present study characterizes the distribution of trace elements, including some ore metals, in coexisting solid, vapor, and melt phases sampled from the Oldoinyo Lengai volcano in northern Tanzania. The study is unique for two reasons: First, gases could be collected from fumaroles degassing within ~10 m of an actively erupting magma vent, thereby potentially minimizing interaction of the pristine magmatic vapor with wall rocks or other fluid end members. Second, the sample suite consists of freshly erupted lavas, gas condensates, and immiscible halide melts within the lava matrix, postulated to represent the dry analogue of the intermediary saline fluids or brines seen in “wet” magmas.

The partitioning of elements between crystalline silicate phases in the silicate magmas from Oldoinyo Lengai was reported by Dawson et al. (1994). Additionally, while the immiscible salt quenches in erupted Lengai carbonatites have previously been reported by Peterson (1990) and Mitchell (1997), these studies have focused on the implications for natrocarbonatite petrogenesis rather than its possible role as intermediaries between magma and fumarole chemistry. Trace-element studies of the natrocarbonatites have only considered the bulk rock, while fluid

inclusions have only been characterized in ore-hosting, *calcium* carbonatite bodies (e.g., Bühn and Rankin, 1999; Bühn et al., 2002; Samson et al., 1995b; Williams-Jones and Palmer, 2002).

SAMPLE COLLECTION AND PREPARATION

Fieldwork was conducted in the active north crater of Oldoinyo Lengai during October 2003. Oldoinyo Lengai is the world's only active carbonatite volcano and is characterized by an extremely alkali chemistry (e.g., Dawson, 1962b; Dawson et al., 1990; Keller and Krafft, 1990). Fresh natrocarbonatite lavas were collected within 1–2 h of eruption from the central hornito, T56B, which at the time of sampling was undergoing lava fountaining and sporadic effusive activity. Lava samples were collected from still-hot lava flows (Fig. 1) at temperatures

above 300 °C and placed directly into sealed glass jars containing a sealed portion of silica gel. Within a few days of sampling, lava samples were immediately transferred to vacuum desiccators to prevent hygroscopic absorption of atmospheric H₂O.

Gas samples were collected from fumaroles degassing from vents ~10–15 m from the active center. It was hoped that these gases would represent near-pristine magmatic composition due to their close proximity to the actively erupting hornito (T56B) and closely associated, partially enclosed magma pools (particularly T48). Silica glass tubes were inserted to a depth of ~1 m into the fumarole and sealed in with loose material from around the vent. The gases focused through the tubes were sampled in various ways dependent on the desired analyses. After entering the tubes, the gases passed through two water/ice-cooled condensate flasks in series. The aqueous condensates formed in these flasks also acquired much of the halogen, sulfur, and trace metal load of the gas and were ideal for the analysis of trace elements. Additionally, the residual gases, now dried and depleted of halogenated and sulfur-based acids, were passed across a set of adsorbent cartridges packed with a variety of activated carbon-based, molecular sieve-type adsorbents for the collection of trace organic constituents (Schwandner et al., 2004). Bulk gas samples from the fumarole were taken using the alkali absorption bottle method (Giggenbach and Goguel, 1989).

ANALYTICAL METHODS

Lavas

Major and trace elements in the quenched natrocarbonatite lavas were determined on glass disks by wavelength-dispersive X-ray fluorescence spectrometry (WD-XRF). The instrument used was an Axios, PANalytical (ETH Zurich). Individual mineral grains in polished blocks of the natrocarbonatite were analyzed by electron microprobe (EMP) for major and minor elements. The instrument used was a JEOL JXA-8200 (ETH Zurich). Data quantification was done using a standard PZAF correction. Back-scattered electron imaging and X-ray mapping of the lava samples were also conducted by EMP.

The trace-element contents of carbonate phenocrysts (gregoryite, nyerereite), sulfide microcrysts, halide melts (CaF, KCl), and aqueous fumarole condensates were determined by laser ablation–inductively coupled plasma–mass spectrometry (LA-ICP-MS; ETH Zurich). The instrument used was a Perkin-Elmer Elan 6100 (quadrupole) ICP-MS operated in dual detector mode at conditions similar to those reported by Pettke et al. (2004). Aerosols were generated using a pulsed beam (5–10 Hz; 20–50 µm pit diameter) from a GEOLAS Ar-F Excimer laser (193 nm) operated at 50–60 mJ output energy with an energy-homogenized beam profile (Gunther et al., 1997). Sample aerosols were carried into the ICP-MS in an Ar-He gas mixture (He 1.15 L/min; Ar 0.8 L/min). Isotopes were measured at a dwell time of 10 ms. Oxide production rates were maintained below 0.4%. Quantification of the raw LA-ICP-MS data was

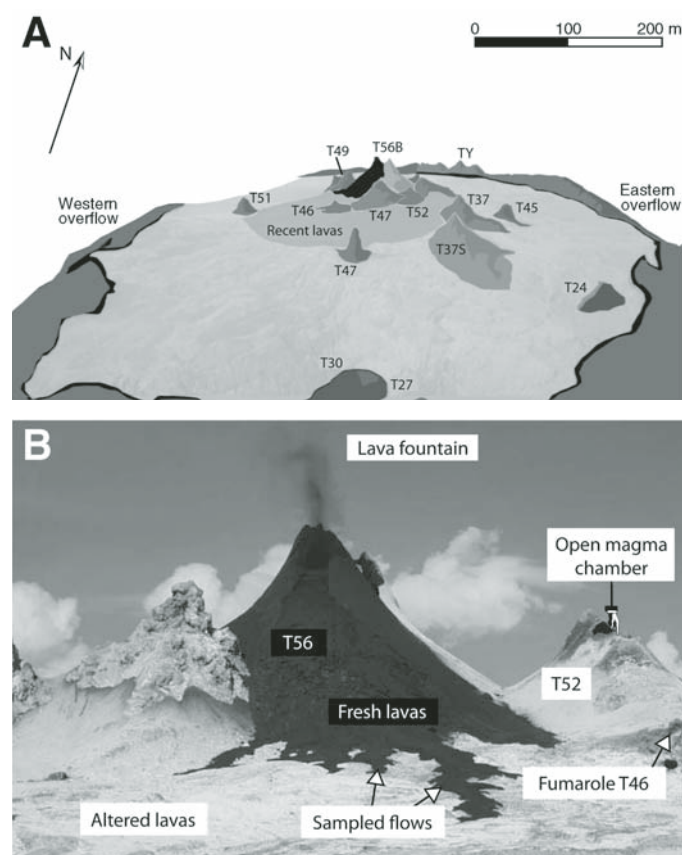


Figure 1. (A) Graphical representation of the eruptive north crater of Oldoinyo Lengai in September 2003 showing the major hornitos and other relevant features. (B) Photograph of the active center of the crater, looking east. Lava samples were collected from fresh natrocarbonatite flows, while gas samples were taken as condensates from two fumaroles located near the magma chamber(s). T46 can be seen to the right of the picture. T52 is out of sight, obscured by the hornito T48 and is situated on its far flank. The hornito T56 can clearly be seen in eruption, while T48 could be heard to contain an active lava lake, though this was considered too hazardous to explore fully. Erupting hornito T56 ~30 m in height.

performed with the software LAMTRACE (Longerich et al., 1996), with the international reference standard SRM 610 (NIST) from ETH Zurich used to calibrate analyte sensitivities. This reference standard is a silicate glass, and we are conscious of the fact that it is not matrix-matched to the samples. For phenocrysts, the concentrations of Ca or Na, determined by electron probe microanalysis, were used for internal standardization. Routine analyses of other glass standards and trace-element doped minerals by this method yielded concentrations within 5% (relative) of the expected values. Salt melt phases and sulfides were too small to analyze as homogeneous phases owing to the small size of the grains relative to the size of the laser pit. Thus, these were treated as melt or mineral inclusions within a host phase (either carbonate matrix or carbonate phenocryst) and quantified using the method described for silicate melt inclusions of Halter et al. (2002). The concentrations of Ca, K, or Mn in both host and "included" phase, determined by electron probe microanalysis, were used for internal standardization and signal deconvolution (separation of inclusion signal from mixed inclusion + host signal). Uncertainties for element concentrations in included phases by this method are in the range of 10%–20% relative (i.e., 10–20 ppm uncertainty on a concentration of 100 ppm) for trace elements that are highly to moderately compatible or incompatible in the included phase relative to the host.

It is important to note that the hygroscopic nature of the natrocarbonatite rocks makes comprehensive analyses extremely difficult. Polished blocks and thin sections deteriorate rapidly upon exposure to moisture in the atmosphere. The increasing water content of the samples not only diminishes the accuracy of the data with increasing analytical time (because the internal standardization loses robustness) but it also causes the image quality to deteriorate as the top surface of the sample starts to lose smoothness. These problems, combined with the similarities in optical properties of several of the various phases in reflected and transmitted light, led to difficulties in identifying target grains for LA-ICP-MS measurements. In the worst cases, some phases were identified after sampling on the basis of their trace-element pattern. It is recommended that future studies attempt to address the problem of sample deterioration via a unique sample preparation method (i.e., embed sample in water-tight casing prior to ablation), a different optical setup, or the use of colored dyes to identify the various phases of interest prior to analysis.

Fumarole Condensates

The fumarole condensates were analyzed by solution ICP-MS at ETH Zurich. A solution consisting of 2 ml HNO₃ and 2 ml H₂O₂ was added to a 50 ml aliquot of the condensate, and the mixture was microwave heated in a Teflon-lined autoclave for 20 min. After the sample had been allowed to cool to room temperature, it was filtered, and a 2 ml aliquot was diluted to 50 ml with ultrapure water and analyzed using an Elan 6100 (Perkin Elmer Instruments/Sciex) ICP-MS running with a dynamic reaction cell (DRC). Note that colloidal sulfur present in some

fumarole condensates is likely to adsorb trace metals. Sample treatment prior to filtration was intended to convert all sulfur into dissolved SO₄²⁻ and dissolve any adsorbed metals or fine precipitates. Simple filtration to remove particulate matter prior to analysis may thus give erroneously low values for trace metals.

Bulk abundances of some elements in fumarole condensates not analyzed by solution ICP-MS were determined by laser-ablation ICP-MS analysis of solution-filled microcapillary tubes. Analytical conditions and quantification methods for the microcapillary tubes were similar to those reported for mineral grain and inclusion analyses but utilized the concentration of Na from solution ICP-MS analyses as an internal standard. Routine analysis of microcapillary tubes filled with trace-element reference solutions yielded values within 5% (relative) of the expected concentrations.

Organic Compounds

Adsorbent cartridges were analyzed for organic compounds by combined gas chromatography–mass spectrometric (GC-MS) techniques. The cartridges were thermally desorbed under a helium stream onto a solid phase micro-extraction (SPME) needle and transferred to an HP5980 GC, where they were cryotrapped (frozen onto a short loop at the start of the column using liquid nitrogen) onto a 50 m DB5 column. Cartridges were also taken of ambient air on the windward side of the crater (air blanks) and during laboratory analysis (system blanks). Where reported, all compounds were found to be below detection within both sets of blanks.

TABLE 1. POSITIVELY IDENTIFIED SPECIES FROM GAS CHROMATOGRAPHY-MASS SPECTROMETRY ANALYSES

Name	Formula	Name	Formula
Carbonyl sulfide	COS	Pyrrole*	C ₄ H ₅ N
Ethanol*	C ₂ H ₅ O	Methyl heptane	C ₈ H ₁₈
Ethanol 2-methoxy acetate*	C ₅ H ₁₀ O ₃	Toluene	C ₇ H ₈
Methyl pentanal*	C ₆ H ₁₂ O	Methylthiophene*	C ₅ H ₆ S
Isoprene*	C ₅ H ₈	Trimethyl cyclopentane	C ₈ H ₁₆
Carbon disulfide	CS ₂	Octene	C ₈ H ₁₆
Dimethylsulfone*	C ₂ H ₆ O ₂ S	Octane	C ₈ H ₁₈
Hexane	C ₆ H ₁₄	Pentanenitrile, 4-methyl*	C ₆ H ₁₁ N
Butanone*	C ₄ H ₈ O	Chlorobenzene†	C ₆ H ₅ Cl
Acetic acid*	C ₂ H ₄ O ₂	Dimethylbenzene	C ₈ H ₁₀
Methylbutanal*	C ₅ H ₁₀ O	Ethylbenzene	C ₈ H ₁₀
Furan-2-methyl*	C ₅ H ₆ O	2-azetidine 4-phenyl*	C ₉ H ₉ NO
Benzene	C ₆ H ₆	Trimethylbenzene	C ₉ H ₁₂
Methyl hexane	C ₇ H ₁₄	Benzaldehyde*	C ₇ H ₆ O
Pentane 3-methyl	C ₆ H ₁₄	Dimethyltrisulfide*	C ₂ H ₆ S ₃
Thiophene*	C ₄ H ₄ S	Phenol*	C ₆ H ₆ O
Bicyclohexane	C ₆ H ₁₀	Dichlorobenzene†	C ₆ H ₄ Cl ₂
Heptane	C ₇ H ₁₆	Benzonitrile	C ₇ H ₅ N
		M-phenethyl*	
Methylcyclohexane	C ₇ H ₁₄	Tetramethoxypropane*	C ₇ H ₁₆ O ₄
Dimethyldisulfide*	C ₂ H ₆ S ₂	Hexanal, 5-methyl*	C ₇ H ₁₄ O

Note: Compounds are a mixture of: high-temperature species thought to represent abiotic synthesis; species considered to be an artifact of biological activity (marked *); and halocarbons (†).

RESULTS AND DISCUSSION

Organic Compounds

The organic chemistry of the Lengai gases appears to be a mixture of medium- to high-temperature species common to those reported at silicate volcanoes (Capaccioni et al., 1995; Isidorov et al., 1990; Schwandner et al., 2004; Stoiber et al., 1971), and low-temperature, oxidized compounds typical of bacterial respiratory products (see Table 1). This apparent contamination of the samples is considered to have occurred *in situ*, since the fumaroles are colonized by abundant bacteria. Despite this contamination, the sampling technique is preferred because it allows for the positive identification of some inorganic components that are often missed by standard procedures. For instance, carbonyl sulfide (COS), a potentially important metal-complexing ligand (Operti and Rabazzana, 2006) and prebiotic mediator (Leman et al.,

2004), has seldom actually been seen in fumarolic gases, though it is predicted to be thermodynamically stable at certain conditions consistent with those in the fumaroles (e.g., Symonds et al., 1994). Qualitative GC-MS analyses indicate that this compound is present in the Lengai gases, and we propose that it may go on to play an important role in the transport of trace metals and the catalysis of organic reactions. Other species, more characteristic of the high-temperature reactions expected at fumarolic conditions, are also present (e.g., benzene, toluene, medium- to long-chain alkanes). Representative chromatograms and mass spectra are shown in Figure 2.

Lavas

The lavas collected in October 2003 are broadly similar in their chemical and petrological characteristics to those described by Dawson (1962a, 1962b) and Keller and Krafft (1990). Tables 2

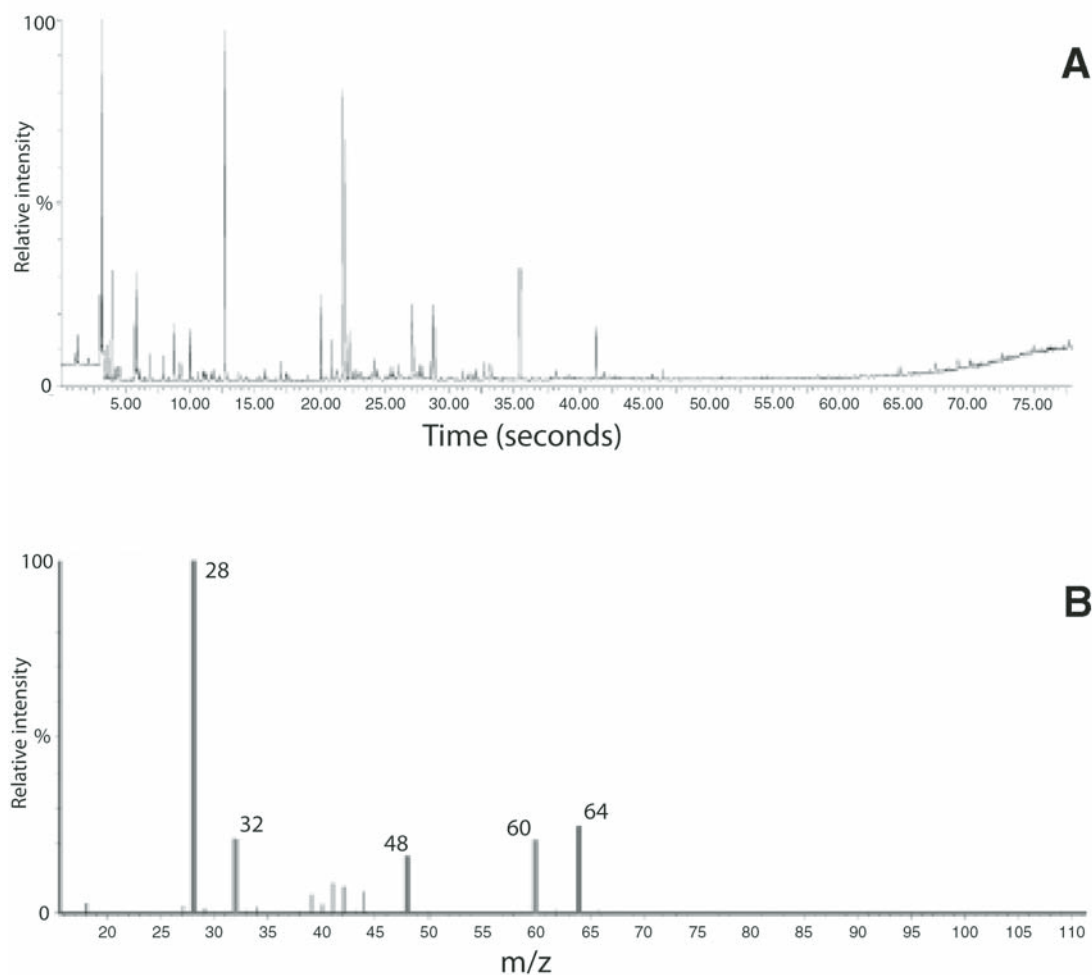


Figure 2. (A) A typical chromatographic trace from a sample taken at fumarole T46. The most prominent peaks are silanes, the product of column bleed during analysis, while most compounds of interest are present in the fine structure. (B) Mass spectra identified as carbonyl sulfide. The diagnostic mass fragments for the compound, 32 + 60, are seen co-eluting with N_2 (28), CO_2 (48), and SO_2 (64). m/z—mass/charge.

and 3 display the XRF and electron microprobe analyses, respectively. Backscattered electron images of the lavas show complex textural intergrowths that allow the paragenetic relationships between the various phases present in the lavas to be deciphered (see Fig. 3).

Maps of $K\alpha$ X-ray peak intensity distribution for Na, K, Ca, F, O, Cl, P, and S (Fig. 4) illustrate the most salient features. Phenocrysts of gregoryite and nyerereite coexist within a ground-mass of gregoryite microlites, accessory sulfides, rare wollastonite, and quenched interstitial fluorite, sylvite, and carbonate liquid. The fluorite can be seen forming dendritic quench textures with a carbonate phase, which, from the elemental mapping, is interpreted to be gregoryite. Fluorite is also present as inclusions within the gregoryite phenocrysts (visible as fluorine-rich spots within the gregoryite), indicating that the gregoryite included immiscible fluoride-rich melt blebs at the time of its growth. The fluorite remained liquid until quenched alongside the residual

carbonatite melt upon eruption. If these quench textures are truly representative of an immiscible fluoride melt, then this would represent the first volcanic setting where such a melt has been observed (the first plutonic setting being in mantle xenoliths from New Zealand; Klemme, 2004). The sylvite also displays clear evidence of immiscibility, occurring as quenched blebs within the interstices from which the fluorite dendrites can often be seen to radiate. These halide phases are texturally similar to those

TABLE 2. X-RAY FLUORESCENCE ANALYSES OF BULK LAVAS

	1	2
Major oxide (wt%)		
SiO ₂	b.d.	b.d.
TiO ₂	0.01	0.01
Al ₂ O ₃	<0.01	<0.01
Fe ₂ O ₃	0.57	0.60
MnO	0.39	0.40
MgO	0.16	0.16
CaO	18.82	19.54
Na ₂ O	29.29	30.02
K ₂ O	6.49	6.65
P ₂ O ₅	1.30	1.32
SrO	1.66	1.73
BaO	0.82	0.83
SO ₃	6.34	6.37
CO ₂ (calc)	34.09	34.06
CO ₂ (diff)	34.14	32.38
Total	99.95	101.68
Trace element (ppm)		
Nb	6.7	7.8
Zr	b.d.	b.d.
Y	4.5	4.2
U	b.d.	b.d.
Rb	154.9	158.7
Th	b.d.	b.d.
Pb	106.3	110.4
Ga	6.5	8.8
Zn	137	145.4
Cu	29.3	34.8
Ni	10.5	16.3
Co	1.2	b.d.
Cr	b.d.	b.d.
V	94	93.2
Ce	528.4	554.4
Nd	54.5	57.4
La	537.6	561.9
Sc	2.8	1.8

Note: b.d.—below detection.

TABLE 3. MICROPROBE ANALYSES OF NYEREREITE, GREGORYITE, SYLVITE, AND FLUORITE

Nyerereite (25 analyses)	Avg. wt%	
	CaO	23.02
	SrO	1.65
	BaO	0.60
	Na ₂ O	22.40
	K ₂ O	6.47
	P ₂ O ₅	0.18
	F	0.31
	Cl	0.32
	SO ₃	1.65
	CO ₂ (calc)	37.97
	Total	94.25
Gregoryite (24 analyses)	Avg. wt%	
	CaO	6.29
	SrO	1.65
	BaO	0.60
	Na ₂ O	41.88
	K ₂ O	2.69
	P ₂ O ₅	1.12
	F	0.01
	Cl	0.64
	SO ₃	3.55
	CO ₂ (calc)	36.32
	Total	93.59
Sylvite (13 analyses)	Avg. wt%	
	Ca	0.25
	K	45.68
	Na	6.45
	Sr	0.07
	Cl	47.32
	F	0.01
	P	0.01
	S	0.20
	Total	100.01
Fluorite (6 analyses)	Avg. wt%	
	Ca	44.3
	K	3.67
	Na	11.28
	Sr	2.26
	Cl	1.88
	F	34.41
	P	0.23
	S	2.48
	Total	100.52

reported by Peterson (1990), and Mitchell (1997), and also bear a resemblance to immiscible chlorides and carbonates hosted in Siberian kimberlites reported by Kamenetsky et al. (2006).

The sulfides exist primarily as euhedral microlites, though they are also evident as minor inclusions within the gregoryite. The silicates exist solely as microphenocrysts.

Lava Trace-Element Partitioning

The microbeam analytical techniques allow for in situ estimates of the magnitude of distribution (partition) coefficients

for trace elements between the two primary carbonate minerals, gregoryite and nyerereite, and in several of the interstitial phases. Gregoryite, nyerereite, and four accessory phases were considered, i.e., fluorite (CaF_2), sylvite (KCl), a Mn-rich sulfide phase, which we will refer to as alabandite (MnS), and a (K, Fe)-sulfide similar to that described by Mitchell (1997). These phases were analyzed for a variety of trace elements by LA-ICP-MS (analyses given in Table 4). Trace-element abundance patterns for the alabandite, (K, Fe)-sulfide, and fluorite relative to the carbonate minerals are shown in Figure 5. Trace elements in the KCl were routinely found to be below detection limits, although the previously mentioned problems related to sample preservation during analysis prevented robust analysis of pure volumes of this mineral.

The natrocarbonatites are characterized by high light (L) REE, large ion lithophile element (LILE), and high field strength element (HFSE) abundances. Even low abundances of such carbonatite melts, formed within a rock-forming environment by metasomatic enrichment or through unmixing, would likely scavenge the LREE, Nb, Th, U, Ba, Rb, and Sr from the parental or host silicate melt. However, within the system studied, these trace elements as well as the metals exhibit strong partitioning into the fluoride phase relative to the carbonate phases, and then, even more extremely for some metallic elements, partitioning into the sulfides relative to the fluoride phase. In the case of the fluoride melt phase, if such melts are indeed a relatively common occurrence within the mantle as postulated by Klemme (2004), then the generation of relatively minor amounts could significantly deplete the source region with respect these trace elements.

Trace-element partition coefficients between the two major phases, gregoryite and nyerereite, are shown in Figure 6. Alkalies, alkali earth, and rare earth elements all tend to fractionate into the nyerereite, whereas most other elements and particularly transition metals favor the gregoryite.

Gas-Lava Distribution

The measured gas temperatures of 169–195 °C show that considerable cooling has taken place since their original exsolution stage from a magma that has an eruption temperature of ~550 °C. A single, uncontaminated bulk gas analysis is presented in Table 5. For a more complete discussion of the bulk and noble gas analyses of the fumaroles, see Teague et al. (2008). Trace-element concentrations from two gas condensates are displayed in Table 6. High Na, K, Ca, Sr, Ba, and Mn in the condensates reflect the major- and minor-element chemistry of the carbonatite magmas. The availability of Cl, F, and various sulfur species within the bulk gases would seem to provide sufficient complexing ligands for the transport of these components from the magmas. Anomalously high levels of Ni are also observed in the gas condensates. It is important to note that Ni is only present in trace concentrations in the bulk carbonatites and is essentially missing in the sulfide phases. By normalizing the metal content of both the lavas and the fumarole gases to a common cation,

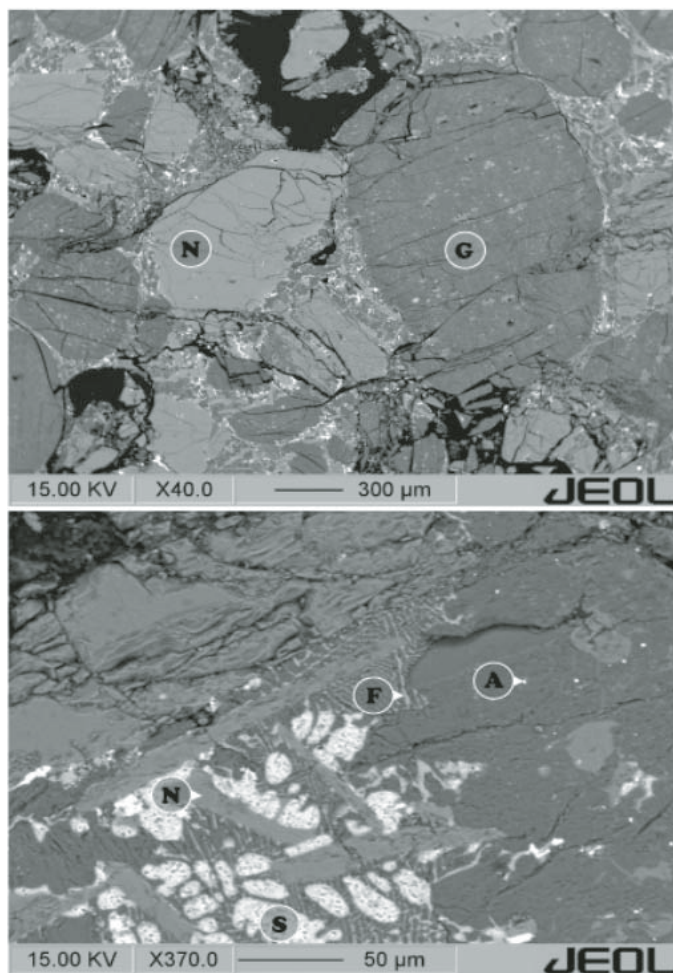


Figure 3. Backscattered-electron images of a polished block of natrocarbonatite lava. The lavas are composed of phenocrysts of (paler) nyerereite (N) and (darker) gregoryite (G). The nyerereite is generally well-formed lath-shaped crystals, free of inclusions. Gregoryite tends to be rounded and often displays exsolution of nyerereite in the cores as well as other inclusions. The fine matrix consists of microcrysts of both gregoryite and nyerereite, as well as abundant accessory minerals such as apatite, alabandite (A), fluorite (F), and sylvite (S). The bright patches seen in the interstices are typically areas of sylvite concentration. Tiny bright specks of alabandite are also seen as inclusions in the gregoryite phenocrysts.

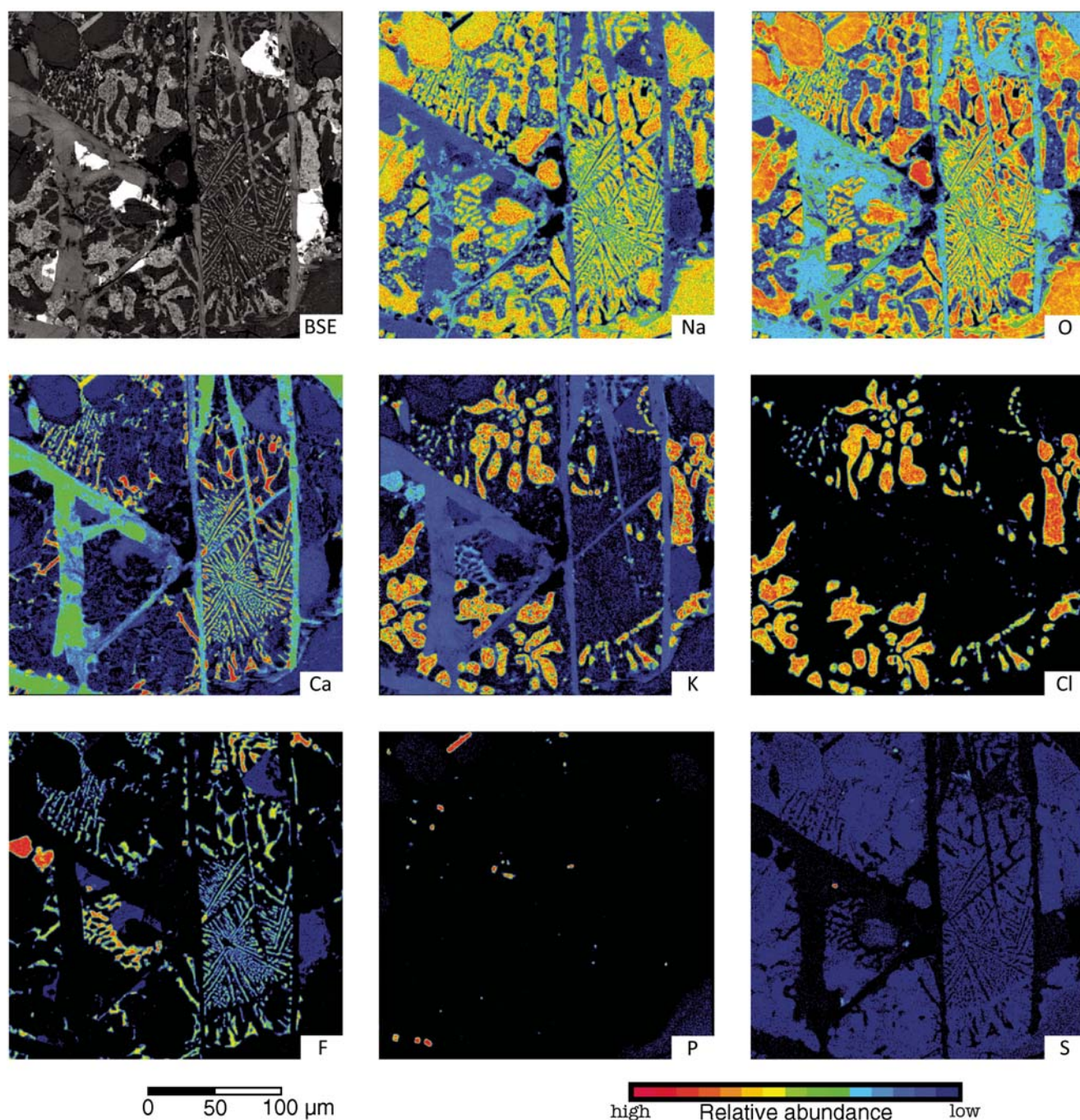


Figure 4. Trace-element maps of a single area within the natrocarbonatite lavas. Together, these elements illustrate the major features of the natrocarbonatites. BSE—Backscattered-electron image of the region of interest. Na—Rounded phenocrysts of gregoryite together with quenched gregoryite in the groundmass. O—Primarily seen only in the carbonate phases. Ca—Lath-shaped phenocrysts of nyerereite and dendritic fluorite in the interstices. K—Immiscible blebs of sylvite coexisting with fluorite in the matrix. Cl—The correlation with potassium is conclusive evidence for the presence of sylvite. F—The quench texture of the fluorite is clear. Two crystals of an Mg-fluoride phase (first reported by Keller and Krafft, 1990) as sellaite are visible in the top-left corner. The clear presence of K in the grain (see image above) suggests that it may, however, be a potassium-bearing analogue of neighborite (NaMgF_3). P—Accessory apatites. S—Bright specks of accessory alabandite are the primary sulfur phase, but it is also present in low levels throughout the sample, particularly within the gregoryite.

TABLE 4A. TRACE-ELEMENT CONCENTRATIONS FROM FUSED GLASS PELLETS FROM POWDERED BULK NATROCARBONATITE LAVAS, MEASURED BY LA-ICP-MS

Sample ID	Sc	V	Cr	Co	Ni	Cu	Zn	As	Rb
Lav2	<0.1	18.8	<2.1	<0.1	<2.5	<0.2	82.4	7.9	93.8
Lav2	<0.1	26.6	12.7	0.5	<2.3	<0.2	88.9	7.7	90.4
Lav2	<0.1	31.4	12.8	<0.1	<1.8	1.9	633.7	8.1	89.1
Inc2	<0.1	28.2	<2.3	0.4	<2.2	<0.3	73.3	7.3	92.5
Inc3	<0.1	42.3	<1.9	0.7	<2.1	<0.2	77.17	7.2	90.3
Inc4	<0.1	30.9	<1.3	0.6	<1.4	1.5	73.6	8.3	97.2
Sample ID	Sr	Nb	Mo	Sn	Sb	Ba	La	Ce	Nd
Lav2	8086.3	25.3	21.0	10.5	<0.1	4256.8	328.6	362.6	72.3
Lav2	8072.9	24.3	23.9	9.5	0.6	4205.5	329.0	360.9	75.1
Lav2	7971.7	25.5	21.5	9.3	<0.1	4203.9	325.1	358.4	70.6
Inc2	8291.6	25.8	20.7	7.8	0.7	4423.1	335.1	378.8	75.0
Inc3	8644.7	26.6	22.5	5.9	<0.1	4342.8	331.0	378.7	80.9
Inc4	8717.8	25.1	24.6	3.9	0.5	4350.4	319.6	376.4	69.7
Sample ID	Eu	Tb	Yb	Lu	Ta	Au*	Pb	Th	U
Lav2	1.1	<0.1	<0.2	<0.1	<0.1	8.6	55.8	2.6	6.0
Lav2	1.2	0.2	<0.1	<0.1	<0.1	9.1	55.8	2.2	6.2
Lav2	1.0	0.2	<0.1	<0.1	<0.1	9.1	57.9	2.4	6.0
Inc2	0.9	0.1	<0.1	<0.1	<0.1	7.1	55.9	2.6	6.7
Inc3	1.0	0.3	<0.1	<0.1	<0.1	6.4	55.9	2.4	7.0
Inc4	1.1	0.1	0.2	<0.1	0.1	4.9	63.5	2.4	6.6

Note: All values are in ppm. LA-ICP-MS—laser ablation—inductively coupled plasma—mass spectrometry.

*Au is probably the result of contamination from platinum crucibles.

TABLE 4B. TRACE-ELEMENT CONCENTRATIONS OF INDIVIDUAL MAJOR MINERAL PHASES DERIVED BY LA-ICP-MS

Mineral	Na ₂ O	MgO	Al ₂ O ₃	K ₂ O	CaO	TiO ₂	Mn	Fe	Sc
Nyerereite	22.40	0.03	<0.01	5.90	23.60	<0.01	0.1	0.0	0.1
Gregoryite	41.90	0.06	<0.01	3.10	8.40	<0.01	0.1	0.2	0.3
Mineral	V	Cr	Co	Ni	Cu	Zn	As	Rb	Sr
Nyerereite	6.4	0.3	0.0	0.7	0.5	2.2	1.9	108.7	12,057.2
Gregoryite	43.1	5.9	0.3	5.2	2.1	10.9	12.5	42.5	4518.5
Mineral	Nb	Mo	Sn	Sb	Ba	La	Ce	Nd	Eu
Nyerereite	1.2	0.7	1.4	0.0	3282.7	210.9	274.8	55.6	0.7
Gregoryite	6.4	4.6	2.6	0.1	1970.9	103.7	128.8	23.9	0.2
Mineral	Tb	Yb	Lu	Ta	Au	Pb	Th	U	
Nyerereite	0.1	b.d.	b.d.	b.d.	0.01	4.8	0.2	0.4	
Gregoryite	0.03	0.4	0.1	b.d.	0.3	1.9	0.2	1.3	

Note: Oxide values are in wt%, element values are in ppm. LA-ICP-MS—laser ablation—inductively coupled plasma—mass spectrometry; b.d.—below detection.

such as Na (Fig. 7), it can be seen that considerable fractionation into the gas phase is displayed by Ni and to a lesser extent by Sc, Co, and other chalcophile elements that are concentrated in the alabandite. Thus, it is suggested that the gases exsolve from the magma prior to the crystallization of sulfides, which should effectively store these chalcophile elements in the lavas once it starts to crystallize.

The actual speciation of the volatile metals has been addressed by various authors (e.g., Symonds et al., 1992; Wahrenberger et al., 2002), though not in a carbonatite system. The behavior of Ni in the Lengai gases is particularly interesting. Limited experimental thermodynamic data suggest that CO is one of the more likely complexing ligands responsible for Ni transport (Blomberg et al., 1991; Hummel and Curti, 2003). With CO reported at levels of ~0.1 mol% in the Lengai vapors (Oppenheimer et al.,

2002), we suggest that these gases represent an ideal environment for the volatile transport of Ni as some carbonic species.

Our results also broadly support the work of Gilbert and Williams-Jones (2008); measurable concentrations of La and Ce in our fumarole condensates mirror the dominance of the LREEs within their high-temperature sublimate encrustations. However, our data also imply that neither La nor Ce is preferentially fractionated into the vapor phase relative to Ca, K, or Na (and may even display a mildly refractory nature), and we suggest that additional processes during sublimation rather than volatilization may account for the higher REE contents of their samples. Alternatively, this could simply be explained by the higher temperature of the fumaroles during their sampling campaign, allowing for a greater mobilization of metals within the volatile phase.

TABLE 4C. TRACE-ELEMENT CONCENTRATIONS FROM ACCESSORY PHASES IN NATROCARBONATITE LAVAS, MEASURED BY LA-ICP-MS

Mineral	V	Cr	Mn	Fe	Co	Ni	Cu	Zn	As
K, Fe-sulfide	130	b.d.	44,931	443,000	20	b.d.	259	1033	b.d.
	19	b.d.	11,090	443,000	25	b.d.	36	256	b.d.
	32	b.d.	28,563	443,000	16	b.d.	178	337	b.d.
Alabandite	88	b.d.	630,000	87,790	b.d.	b.d.	8	275	b.d.
	131	b.d.	630,000	90,271	b.d.	b.d.	46	300	b.d.
	115	b.d.	630,000	74,905	b.d.	b.d.	b.d.	195	b.d.
	73	b.d.	630,000	97,353	b.d.	b.d.	22	429	b.d.
Fluorite	9	b.d.	b.d.	b.d.	b.d.	b.d.	b.d.	7	11
	11	b.d.	b.d.	b.d.	b.d.	b.d.	b.d.	13	14
	9	b.d.	b.d.	b.d.	b.d.	b.d.	b.d.	b.d.	38
Mineral	Rb	Sr	Nb	Mo	Sn	Sb	Ba	La	Ce
K, Fe-sulfide	4170	2117	6	273	b.d.	b.d.	1021	63	59
	823	4340	23	372	b.d.	b.d.	1619	116	178
	2066	1566	5	118	b.d.	b.d.	755	42	39
Alabandite	b.d.	b.d.	57	5	b.d.	4	b.d.	1553*	2117*
	b.d.	b.d.	132	b.d.	b.d.	b.d.	b.d.	92	152
	b.d.	303	112	24	b.d.	b.d.	b.d.	86	140
	37	b.d.	77	17	b.d.	b.d.	b.d.	1930*	2428*
Fluorite	239	b.d.	17	5	13	b.d.	4673	1514	2022
	204	b.d.	10	6	20	b.d.	4173	1357	1753
	235	b.d.	34	5	17	0	4206	1038	1368
Mineral	Nd	Eu	Tb	Yb	Ta	Au	Pb	Th	U
K, Fe-sulfide	9	b.d.	b.d.	b.d.	1	b.d.	1898	b.d.	b.d.
	20	b.d.	b.d.	b.d.	b.d.	b.d.	32	1	2
	11	b.d.	b.d.	3	b.d.	b.d.	75	1	1
Alabandite	360*	3	1	b.d.	b.d.	b.d.	290	12	10
	b.d.	b.d.	1	b.d.	b.d.	b.d.	126	2	31
	26	b.d.	b.d.	5	b.d.	b.d.	b.d.	2	19
	466*	2	1	b.d.	b.d.	b.d.	b.d.	6	15
Fluorite	408	5	1	b.d.	b.d.	b.d.	29	27	12
	360	b.d.	1	b.d.	b.d.	b.d.	16	13	7
	280	b.d.	0	b.d.	b.d.	b.d.	15	9	11

Note: All values are in ppm. LA-ICP-MS—laser ablation—inductively coupled plasma—mass spectrometry; b.d.—below detection.

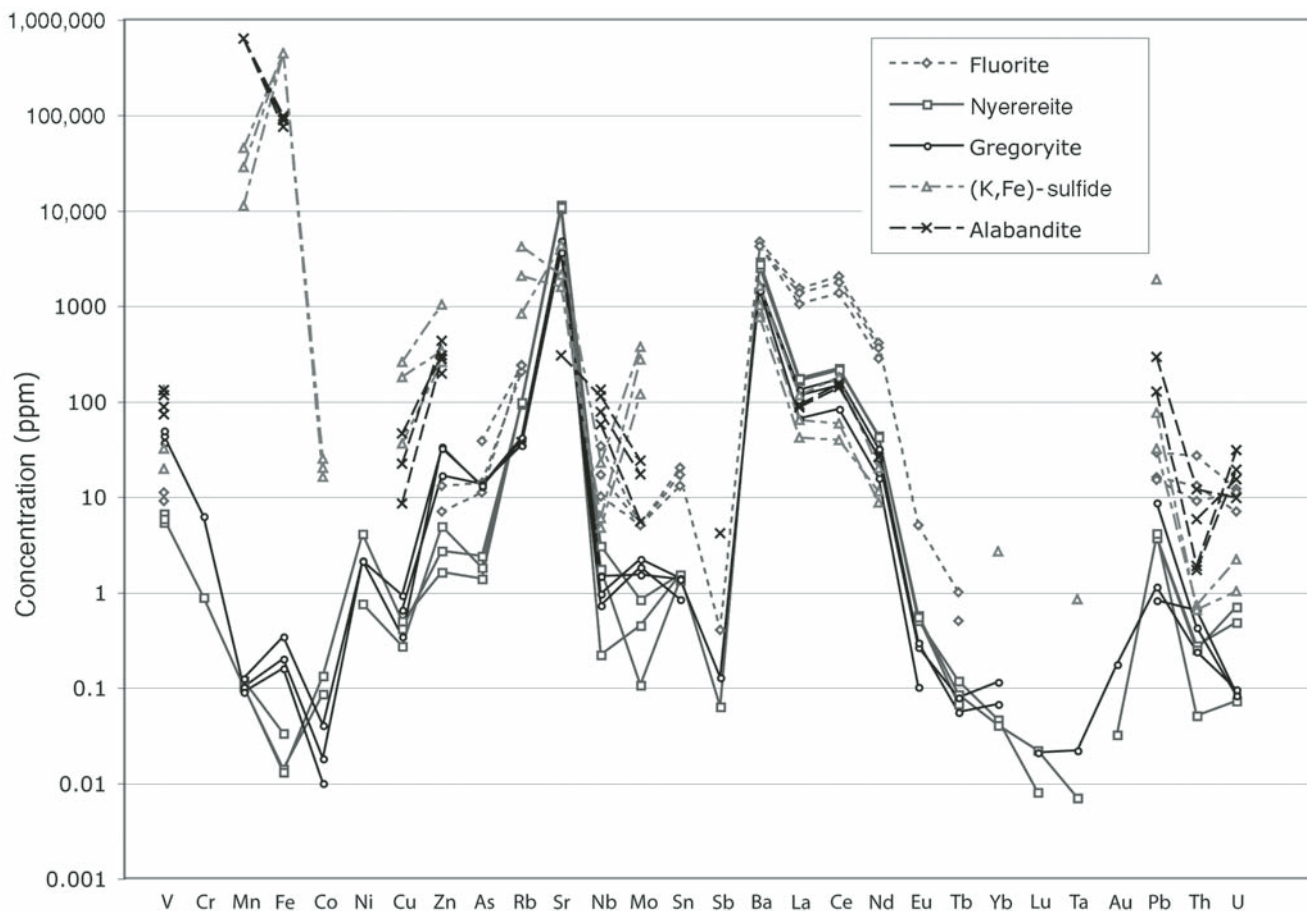


Figure 5. Trace-element patterns in nyerereite, gregoryite, (K,Fe)-sulfide, alabandite, and fluorite. All can be seen to follow the same general trend echoing the overall abundances of trace elements in the lavas. Minor partitioning between the two carbonate phases and a distinct partitioning favoring both sulfide phases can be observed. Chalcophile elements such as transition metals and Pb heavily favor the sulfide phases, and, though less pronounced, there is also a fractionation of elements into the fluorite, particularly by the rare earth elements. Interestingly, the (K,Fe)-sulfide is also able to accommodate appreciable amounts of large ion lithophile elements such as Rb and Sr.

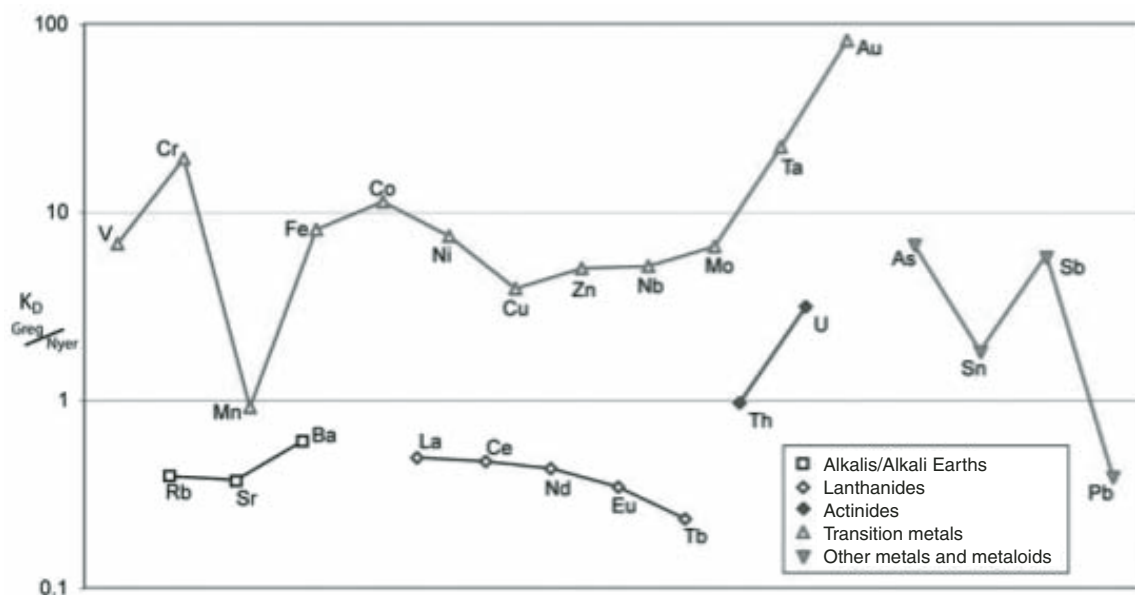


Figure 6. Mineral-mineral partition coefficients for all trace elements analyzed in gregoryite and nyerereite. With the exception of the alkalis, alkali earth elements, and light/medium rare earth elements, most trace metals favor gregoryite over nyerereite.

TABLE 5. A SINGLE BULK GAS ANALYSIS FROM OLDIOYNO LENGAI

Sample	Fumarole	Temp (°C)	H ₂ O	CO ₂	S ₁	H ₂	HCl	HF	Ar	O ₂	N ₂
B108	T46	194.7	353,012	487,251	12,186	6843	17,485	3367	588	102	44,962

Note: Values are in mmol⁻¹/mol.

TABLE 6. TRACE-ELEMENT CONCENTRATIONS MEASURED IN AQUEOUS CONDENSATES COLLECTED FROM FUMAROLAS ON TWO HORNITOES, T46 AND T52, OLDIOYNO LENGAI

	T46	T52		T46	T52
Li	7.9	10.8	Sn	<0.1	b.d.
B	13,201.7	12,724.1	Sb	<0.1	0.2
Na	10,959.8	11,100.0	Te	b.d.	b.d.
Mg	184.2	309.5	Cs	<0.1	<0.1
Al	11.0	7.6	Ba	316.2	383.7
Si	7829.3	8937.4	La	4.8	1.7
K	2021.0	1320.0	Ce	5.6	8.8
Ca	35,658.0	14,682.0	Pr	0.3	0.1
Sc	3.9	4.1	Nd	0.6	0.2
Ti	10.9	15.5	Sm	<0.1	<0.1
V	1.1	1.3	Eu	0.1	0.1
Cr	7.9	16.9	Gd	0.1	0.1
Mn	346.0	403.0	Tb	b.d.	b.d.
Fe	19.6	4.5	Dy	<0.1	b.d.
Co	16.8	13.7	Ho	b.d.	b.d.
Ni	748.7	549.7	Er	b.d.	b.d.
Cu	1.0	1.2	Tm	b.d.	b.d.
Zn	4.3	3.0	Yb	b.d.	b.d.
Ga	0.1	0.1	Lu	b.d.	b.d.
As	9.0	4.8	W	0.1	0.2
Rb	1.3	1.5	Pt	<0.1	<0.1
Sr	541.2	1003.4	Au	<0.1	b.d.
Zr	0.4	0.2	Tl	0.1	0.1
Mo	22.3	21.0	Pb	0.8	0.2
Ag	1.3	0.7	Bi	0.1	b.d.
Y	0.1	0.1	Th	<0.1	<0.1
Cd	b.d.	b.d.	U	0.1	<0.1
In	b.d.	b.d.			

Note: All concentrations are given in ppb; b.d.—below detection.

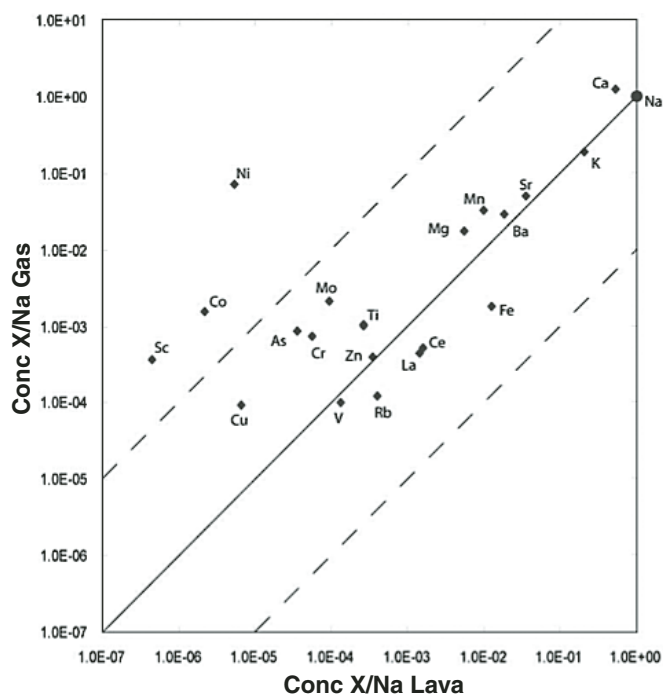


Figure 7. Trace elements in the gas condensates versus their concentration in the bulk rock analysis, normalized to Na. Alkali earth and rare earth elements show little relative fractionation. Fe is mildly refractory, though other transition metals seem to have a moderate affinity for the vapor phase. Sc, Co, and particularly Ni are seen to fractionate heavily into the vapor. Solid line denotes no relative fractionation. Dashed lines delineate fractionation factors of 100 and 0.01, respectively.

The results of this study have broad implications. Natrocarbonatites have only been described at two localities, Lengai and (inferred from calcite pseudomorphs) at her sister volcano, Kerimasi (Hay, 1983), but it has been widely postulated that alkaline eruptive products may typify much extrusive carbonatite volcanism. However, only the calcium carbonatite intrusives are capable of being preserved in the rock record (e.g., Hay, 1983; Le Bas and Aspden, 1981). If this is valid, then the extreme affinity for the vapor displayed by certain elements (e.g., Ni and other chalcophile metals) might help to explain the genesis of the exotic styles of mineralization commonly associated with carbonatite crustal complexes (e.g., Andreeva et al., 1998; Doroshkevich and Ripp, 2004; Grice et al., 2007; Samson et al., 1995a).

ACKNOWLEDGMENTS

We would like to thank Christoph Heinrich and Detlef Günther for the use of their laboratories. Eric Ruesser and Lydia Zhender are kindly thanked for their assistance on the electron microprobe and X-ray fluorometer (XRF), respectively. We thank Andy Gize and Keith Hall for their help with the gas chromatography–mass spectrometry (GC-MS) analyses of organics. Tanzanature Safaris, Everett Aviation, and the Maasai of Engare Sero provided excellent logistical support. Nicole Keller was the best field assistant one could hope for. We thank David Pyle and Anthony Williams-Jones for their well-considered and constructive reviews, and Gianluca Bianchini for his friendly editorial handling of the manuscript. The work benefited greatly from the efforts of Fred Deakin, Nick Franglen, and their experiment no. 6. Lastly, AJT thanks Lily, for putting everything into perspective. The project was funded by an ETH research grant to TMS.

REFERENCES CITED

- Allard, P., Aiuppa, A., Loyer, H., Carrot, F., Gaudry, A., Pinte, G., Michel, A., and Dongarra, G., 2000, Acid gas and metal emission rates during long-lived basalt degassing at Stromboli volcano: *Geophysical Research Letters*, v. 27, p. 1207–1210, doi:10.1029/1999GL008413.
- Andreeva, I.A., Naumov, V.B., Kovalenko, V.I., and Kononkova, N.N., 1998, Fluoride-sulfate and chloride-sulfate salt melts of the carbonatite-bearing complex Mushugai-Khuduk, southern Mongolia: *Petrology*, v. 6, p. 284–292.
- Audet, A., Gunther, D., and Heinrich, C.A., 2000, Magmatic-hydrothermal evolution in a fractionating granite: A microchemical study of the Sn-W-F-mineralized Mole Granite (Australia): *Geochimica et Cosmochimica Acta*, v. 64, p. 3373–3393, doi:10.1016/S0016-7037(00)00428-2.
- Barnes, H.L., 1997, *Geochemistry of Hydrothermal Ore Deposits*, 3rd edition: New York, Wiley, 972 p.
- Blomberg, M.R.A., Siegbahn, P.E.M., Lee, T.J., Rendell, A.P., and Rice, J.E., 1991, Binding energies and bond distances of Ni(CO)_x, x=1–4: An application of coupled-cluster theory: *The Journal of Chemical Physics*, v. 95, p. 5898–5905, doi:10.1063/1.461611.
- Brombach, T., Caliro, S., Chiodini, G., Fiebig, J., Hunziker, J.C., and Raco, B., 2003, Geochemical evidence for mixing of magmatic fluids with seawater, Nisyros hydrothermal system, Greece: *Bulletin of Volcanology*, v. 65, p. 505–516, doi:10.1007/s00445-003-0278-x.
- Bühn, B., and Rankin, A.H., 1999, Composition of natural, volatile-rich Na-Ca-REE-Sr carbonatitic fluids trapped in fluid inclusions: *Geochimica et Cosmochimica Acta*, v. 63, p. 3781–3797, doi:10.1016/S0016-7037(99)00180-5.
- Bühn, B., Rankin, A.H., Schneider, J., and Dulski, P., 2002, The nature of orthomagmatic, carbonatitic fluids precipitating REE, Sr-rich fluorite: Fluid-inclusion evidence from the Okorusu fluorite deposit, Namibia: *Chemical Geology*, v. 186, p. 75–98, doi:10.1016/S0009-2541(01)00421-1.
- Candela, P.A., and Holland, H.D., 1984, The partitioning of copper and molybdenum between silicate melts and aqueous fluids: *Geochimica et Cosmochimica Acta*, v. 48, p. 373–380, doi:10.1016/0016-7037(84)90257-6.
- Capaccioni, B., Martini, M., and Mangani, F., 1995, Light hydrocarbons in hydrothermal and magmatic fumaroles: Hints of catalytic and thermal reactions: *Bulletin of Volcanology*, v. 56, p. 593–600.
- Chiodini, G., Allard, P., Caliro, S., and Parello, F., 2000, ¹⁸O exchange between steam and carbon dioxide in volcanic and hydrothermal gases: Implications for the source of water: *Geochimica et Cosmochimica Acta*, v. 64, p. 2479–2488, doi:10.1016/S0016-7037(99)00445-7.
- Dawson, J.B., 1962a, Sodium carbonate lavas from Oldoinyo Lengai, Tanzania: *Nature*, v. 195, p. 1075–1076, doi:10.1038/1951075a0.
- Dawson, J.B., 1962b, The geology of Oldoinyo Lengai: *Bulletin of Volcanology*, v. 24, p. 349–387, doi:10.1007/BF02599356.
- Dawson, J.B., Pinkerton, H., Norton, G.E., and Pyle, D.M., 1990, Physicochemical properties of alkali carbonatite lavas: Data from the 1988 eruption of Oldoinyo Lengai, Tanzania: *Geology*, v. 18, p. 260–263, doi:10.1130/0091-7613(1990)018<0260:PPOACL>2.3.CO;2.
- Dawson, J.B., Smith, J.V., and Steele, I.M., 1994, Trace-element distribution between coexisting perovskite, apatite and titanite from Oldoinyo Lengai, Tanzania: *Chemical Geology*, v. 117, p. 285–290, doi:10.1016/0009-2541(94)90132-5.
- Doroshkevich, A.G., and Ripp, G.S., 2004, Estimation of the conditions of formation of REE-carbonatites in western Transbaikalia: *Geologiya i Geofizika*, v. 45, p. 492–500.
- Gauthier, P.J., and Le Cloarec, M.F., 1998, Variability of alkali and heavy metal fluxes released by Mt. Etna volcano, Sicily, between 1991 and 1995: *Journal of Volcanology and Geothermal Research*, v. 81, p. 311–326, doi:10.1016/S0377-0273(98)00002-X.
- Gemmell, J.B., 1987, Geochemistry of metallic trace elements in fumarolic condensates from Nicaraguan and Costa Rican volcanoes: *Journal of Volcanology and Geothermal Research*, v. 33, p. 161–181, doi:10.1016/0377-0273(87)90059-X.
- Giggenbach, W.F., 1992, Isotopic shifts in waters from geothermal and volcanic systems along convergent plate boundaries and their origin: *Earth and Planetary Science Letters*, v. 113, p. 495–510, doi:10.1016/0012-821X(92)90127-H.
- Giggenbach, W.F., and Goguel, R.L., 1989, *Methods for the Collection and Analysis of Geothermal and Volcanic Water and Gas Samples*: Petone, New Zealand, Department of Scientific and Industrial Research, Chemistry Division, 81 p.
- Gilbert, C.D., and Williams-Jones, A.E., 2008, Vapour transport of rare earth elements (REE) in volcanic gas: Evidence from encrustations at Oldoinyo Lengai: *Journal of Volcanology and Geothermal Research*, v. 176, p. 519–528, doi:10.1016/j.jvolgeores.2008.05.003.
- Goff, F., and McMurtry, G.M., 2000, Tritium and stable isotopes of magmatic waters: *Journal of Volcanology and Geothermal Research*, v. 97, p. 347–396, doi:10.1016/S0377-0273(99)00177-8.
- Grice, J.D., Maisonneuve, V., and Leblanc, M., 2007, Natural and synthetic fluoride carbonates: *Chemical Reviews*, v. 107, p. 114–132, doi:10.1021/cr050062d.
- Gunther, D., Frischknecht, R., and Heinrich, C.A., 1997, Capabilities of a 193 nm ArF excimer laser for LA-ICP-MS microanalysis of geological materials: *Journal of Analytical Atomic Spectrometry*, v. 12, p. 939–944, doi:10.1039/a701423f.
- Halter, W.E., Pettke, T., Heinrich, C.A., and Rothen-Rutishauser, B., 2002, Major to trace element analysis of melt inclusions by laser-ablation ICP-MS: Methods of quantification: *Chemical Geology*, v. 183, p. 63–86, doi:10.1016/S0009-2541(01)00372-2.
- Hay, R.L., 1983, Natrocarbonatite tephra of Kerimasi volcano, Tanzania: *Geology*, v. 11, p. 599–602, doi:10.1130/0091-7613(1983)11<599:NTOKVT>2.0.CO;2.
- Heinrich, C.A., Gunther, D., Audetat, A., Ulrich, T., and Frischknecht, R., 1999, Metal fractionation between magmatic brine and vapor, determined by microanalysis of fluid inclusions: *Geology*, v. 27, p. 755–758, doi:10.1130/0091-7613(1999)027<0755:MFBMBA>2.3.CO;2.
- Hummel, W., and Curti, E., 2003, Nickel aqueous speciation and solubility at ambient conditions: A thermodynamic elegy: *Monatshefte für Chemie (Chemical Monthly)*, v. 134, p. 941–973.

- Isidorov, V.A., Zenkevich, I.G., and Ioffe, B.V., 1990, Volatile organic compounds in Solfataric gases: *Journal of Atmospheric Chemistry*, v. 10, p. 329–340, doi:10.1007/BF00053867.
- Kamenetsky, V.S., Kamenetsky, M.B., Sharygin, V.V., Faure, K., and Golovin, A.V., 2006, Chloride and carbonate immiscible liquids at the closure of the kimberlite magma evolution (Udachnaya-East Kimberlite, Siberia): *Chemical Geology*, v. 237, p. 384–400, doi:10.1016/j.chemgeo.2006.07.010.
- Keller, J., and Krafft, M., 1990, Effusive natrocarbonatite activity of Oldoinyo Lengai, June 1988: *Bulletin of Volcanology*, v. 52, p. 629–645, doi:10.1007/BF00301213.
- Klemme, S., 2004, Evidence for fluoride melts in Earth's mantle formed by liquid immiscibility: *Geology*, v. 32, p. 441–444, doi:10.1130/G20328.1.
- Le Bas, M.J., and Aspden, J.A., 1981, The comparability of carbonatitic fluid inclusions in ijolites with natrocarbonatite lava: *Bulletin Volcanologique*, v. 44, p. 429–438, doi:10.1007/BF02600574.
- Leman, L., Orgel, L., and Ghadiri, M.R., 2004, Carbonyl sulfide-mediated prebiotic formation of peptides: *Science*, v. 306, p. 283–286, doi:10.1126/science.1102722.
- Longerich, H.P., Jackson, S.E., and Gunther, D., 1996, Laser ablation inductively coupled plasma mass spectrometry transient signal data acquisition and analyte concentration calculation: *Journal of Analytical Atomic Spectrometry*, v. 11, p. 899–904, doi:10.1039/ja9961100899.
- Miller, T.L., Zoller, W.H., Crowe, B.M., and Finnegan, D.L., 1990, Variations in trace metal and halogen ratios in magmatic gases through an eruptive cycle of the pu'u o'o vent, Kilauea, Hawaii: July–August 1985: *Journal of Geophysical Research*, v. 95, p. 12,607–12,615, doi:10.1029/JB095iB08p12607.
- Mitchell, R.H., 1997, Carbonate-carbonate immiscibility, neighborite and potassium iron sulphide in Oldoinyo Lengai natrocarbonatite: *Mineralogical Magazine*, v. 61, p. 779–789, doi:10.1180/minmag.1997.061.409.03.
- Möller, P., Dulski, P., and Morteani, G., 2003, Partitioning of rare earth elements, yttrium, and some major elements among source rocks, liquid and vapor of Larderello-Travale geothermal field, Tuscany (central Italy): *Geochimica et Cosmochimica Acta*, v. 67, p. 171–183, doi:10.1016/S0016-7037(02)01054-2.
- Operti, L., and Rabazzana, R., 2006, Gas-phase ion chemistry in organometallic systems: *Mass Spectrometry Reviews*, v. 25, p. 483–513, doi:10.1002/mas.20075.
- Oppenheimer, C., Burton, M.R., Durieux, J., and Pyle, D.M., 2002, Open-path Fourier transform spectroscopy of gas emissions from Oldoinyo Lengai volcano, Tanzania: *Optics and Lasers in Engineering*, v. 37, p. 203–214, doi:10.1016/S0143-8166(01)00095-1.
- Peterson, T.D., 1990, Petrology and genesis of natrocarbonatite: *Contributions to Mineralogy and Petrology*, v. 105, p. 143–155, doi:10.1007/BF00678981.
- Pettke, T., Heinrich, C.A., Ciocan, A.C., and Gunther, D., 2004, Quadrupole mass spectrometry and optical emission spectroscopy: Detection capabilities and representative sampling of short transient signals from laser-ablation: *Journal of Analytical Atomic Spectrometry*, v. 9, p. 1149–1155.
- Pokrovski, G.S., Borisova, A.Y., and Harrichoury, J.-C., 2008, The effect of sulfur on vapor-liquid fractionation of metals in hydrothermal systems: *Earth and Planetary Science Letters*, v. 266, p. 345–362, doi:10.1016/j.epsl.2007.11.023.
- Rempel, K.U., Williams-Jones, A.E., and Migdisov, A.A., 2009, The partitioning of molybdenum(VI) between aqueous liquid and vapour at temperatures up to 370°C: *Geochimica et Cosmochimica Acta*, v. 73, p. 3381–3392, doi:10.1016/j.gca.2009.03.004.
- Samson, I.M., Liu, W., and Williams-Jones, A.E., 1995a, The nature of orthomagmatic hydrothermal fluids in the Oka carbonatite, Quebec, Canada—Evidence from fluid inclusions: *Geochimica et Cosmochimica Acta*, v. 59, p. 1963–1977, doi:10.1016/0016-7037(95)00120-4.
- Samson, I.M., Williams-Jones, A.E., and Liu, W., 1995b, The chemistry of hydrothermal fluids in carbonatites: Evidence from leachate and SEM-decrepitate analysis of fluid inclusions from Oka, Quebec, Canada: *Geochimica et Cosmochimica Acta*, v. 59, p. 1979–1989, doi:10.1016/0016-7037(95)00121-2.
- Schwandner, F.M., Seward, T.M., Gize, A.P., Hall, P.A., and Dietrich, V.J., 2004, Diffuse emission of organic trace gases from the flank and crater of a quiescent active volcano (Vulcano, Aeolian Islands, Italy): *Journal of Geophysical Research*, ser. D, Atmospheres, v. 109, p. 20.
- Simon, A.C., Frank, M.R., Pettke, T., Candela, P.A., Piccoli, P.M., and Heinrich, C.A., 2005, Gold partitioning in melt-vapor-brine systems: *Geochimica et Cosmochimica Acta*, v. 69, p. 3321–3335, doi:10.1016/j.gca.2005.01.028.
- Simon, A.C., Pettke, T., Candela, P.A., Piccoli, P.M., and Heinrich, C.A., 2006, Copper partitioning in a melt-vapor-brine-magnetite-pyrrhotite assemblage: *Geochimica et Cosmochimica Acta*, v. 70, p. 5583–5600, doi:10.1016/j.gca.2006.08.045.
- Stoiber, R.E., and Rose, W.I., 1970, The geochemistry of Central American volcanic gas condensates: *Geological Society of America Bulletin*, v. 81, p. 2891–2912, doi:10.1130/0016-7606(1970)81[2891:TGOCAV]2.0.CO;2.
- Stoiber, R.E., Leggett, D.C., Jenkins, T.F., Murrmann, R.P., and Rose, W.I., 1971, Organic compounds in volcanic gas from Santiaguito volcano, Guatemala: *Geological Society of America Bulletin*, v. 82, p. 2299–2302, doi:10.1130/0016-7606(1971)82[2299:OCIVGF]2.0.CO;2.
- Symonds, R.B., Rose, W.I., Reed, M.H., Lichte, F.E., and Finnegan, D.L., 1987, Volatilization, transport and sublimation of metallic and non-metallic elements in high temperature gases at Merapi volcano, Indonesia: *Geochimica et Cosmochimica Acta*, v. 51, p. 2083–2101, doi:10.1016/0016-7037(87)90258-4.
- Symonds, R.B., Reed, M.H., and Rose, W.I., 1992, Origin, speciation and fluxes of trace-element gases at Augustine volcano, Alaska: Insights into magma degassing and fumarolic processes: *Geochimica et Cosmochimica Acta*, v. 56, p. 633–657, doi:10.1016/0016-7037(92)90087-Y.
- Symonds, R.B., Rose, W.I., Bluth, G.J.S., and Gerlach, T.M., 1994, Volcanic gas studies—Methods, results and applications, in Carroll, M.R., and Holloway, J.R., eds., *Volatiles in Magmas*: Mineralogical Society of America, Reviews in Mineralogy, v. 30, p. 1–66.
- Symonds, R.B., Yoshihiko, M., and Briggs, P.H., 1996, Long-term geochemical surveillance of fumaroles at Showa-Shinzan dome, Usu volcano, Japan: *Journal of Volcanology and Geothermal Research*, v. 73, p. 177–211, doi:10.1016/0377-0273(96)00029-7.
- Taran, Y.A., Bernard, A., Gavilanes, J.C., Lunezheva, E., Cortes, A., and Armienta, M.A., 2001, Chemistry and mineralogy of high-temperature gas discharges from Colima volcano, Mexico: Implications for magmatic gas-atmosphere interaction: *Journal of Volcanology and Geothermal Research*, v. 108, p. 245–264, doi:10.1016/S0377-0273(00)00289-4.
- Teague, A.J., Seward, T.M., and Harrison, D., 2008, Mantle-derived noble gases at Oldoinyo Lengai volcano, Tanzania: *Journal of Volcanology and Geothermal Research*, v. 175, p. 386–390, doi:10.1016/j.jvolgeores.2008.04.001.
- Wahrenberger, C., Seward, T.M., and Dietrich, V., 2002, Volatile trace element transport in high temperature gases from Kudriavsky volcano (Iturup, Kurile Islands, Russia), in Hellmann, R., and Wood, S.A., eds., *Water-Rock Interactions, Ore Deposits, and Environmental Geochemistry: A Tribute to David A. Crerar*: Geochemical Society Special Publication 7, p. 307–327.
- Wendlandt, R.F., and Harrison, W.J., 1979, Rare earth partitioning between immiscible carbonate and silicate liquids and CO₂ vapor: Results and implications for the formation of light rare earth-enriched rocks: *Contributions to Mineralogy and Petrology*, v. 69, p. 409–419, doi:10.1007/BF00372266.
- Williams-Jones, A.E., and Palmer, D.A.S., 2002, The evolution of aqueous-carbonic fluids in the Amba Dongar carbonatite, India: Implications for fenitisation: *Chemical Geology*, v. 185, p. 283–301, doi:10.1016/S0009-2541(01)00409-0.
- Williams-Jones, A.E., Migdisov, A.A., Archibald, S.M., and Xiao, Z., 2002, Vapor-transport of ore metals, in Hellmann, R., and Wood, S.A., eds., *Water-Rock Interactions, Ore Deposits, and Environmental Geochemistry: A Tribute to David A. Crerar*: Geochemical Society Special Publication 7, p. 279–305.

Cameroon Line alkaline magmatism (central Africa): A reappraisal

Emmanuel Njonfang*

Laboratoire de Géologie, Ecole Normale Supérieure, Université de Yaoundé I, B.P. 47, Yaoundé, Cameroon

Alexandre Nono

Département des Sciences de la Terre, Faculté des Sciences, Université de Dschang, B.P. 67, Dschang, Cameroon

Pierre Kamgang

Département des Sciences de la Terre, Faculté des Sciences, Université de Yaoundé I, B.P. 812, Yaoundé, Cameroon

Vincent Ngako

Mega Uranium Corporation Cameroon PLC, P.O. Box 14055, Yaoundé, Cameroon

Félix M. Tchoua

Département des Sciences de la Terre, Faculté des Sciences, Université de Yaoundé I, B.P. 812, Yaoundé, Cameroon

ABSTRACT

Alkaline magmatism along the Cameroon Line has been active for at least 67 m.y. and is currently defined by an almost SW-NE geological lineament (mean value: N30°E). Available petrological, geochemical, and structural data obtained over the last 20 yr lead us to reappraise its mechanism of emplacement. Known as the second most important geological curiosity in Africa, after the East African Rift system, it displays a continental part and an oceanic part, a unique feature in Africa and even in the world. The continental part contains both plutonic and volcanic massifs, and the oceanic part consists only of volcanic massifs. Plutonic rocks as a whole define a complete series of gabbro-diorite-monzonite-syenite-granite type, whereas volcanic rocks display abundant basic (basalt-hawaiite) and felsic (trachyte-phonolite-rhyolite) lavas with very few intermediate ones (mugearite-benmoreite). The formerly entire alkaline nature of these rocks is here ruled out by the discovery of volcanoes with geochemically transitional affinities in some areas of the continental sector. On the other hand, new K-Ar and $^{40}\text{Ar}/^{39}\text{Ar}$ dates confirm the absence of any age migration associated with the SW-NE linear trend. This lack of steady time-space migration and

*enjonfang@yahoo.fr; enjonfang@uyl.uninet.cm.

the SW-NE trend have also been observed in the magmatic provinces of Nigeria and Benue Trough, which share similar geochemical features with the Cameroon Line, and along the NE-SW major igneous lineaments in South Africa. The mechanism of such episodic emplacement of alkaline magmatism can be better explained in terms of complex interactions between hotspots and lithospheric fractures during African plate motion.

INTRODUCTION

The Cameroon Line forms one of the major geological lineaments of the African plate and continent (Fig. 1). It is made up of a continental part and an oceanic part, making it a unique feature in Africa and even in the world (Déruelle et al., 1991, 2007). The continental part includes both plutonic complexes and volcanic massifs, the plutonic complexes (>60) being of small size (mostly 5–10 km in diameter). The oceanic part is entirely volcanic and consists of four well-studied islands (Bioko, Principe, São Tomé, and Annobon) and two recently discovered large seamounts (Burke, 2001) between Bioko and Principe and between Principe and São Tomé. The different massifs were emplaced into North Equatorial Pan-African fold belts and/or Tertiary sandstones (Moreau et al., 1987). The line strikes almost SW-NE, forming a swell-and-basin structure (Fig. 1), where the six islands and the four central volcanoes of Mount Cameroon, Manengouba, Bambouto-Bamenda, and Oku represent swells (Burke, 2001); this recalls the horst-and-graben structure of the whole Cameroon Line (Déruelle et al., 1991). The swell-and-basin structures appear to be characteristic features of western and central Africa topography (Poudjom Djomani et al., 1997; Burke, 2001) and the Great Lakes of East Africa (Ebinger et al., 1989).

The alignment of these magmatic manifestations (67 Ma to present) remains a source of controversy in terms of mechanism of emplacement. A hotspot mechanism is generally the common explanation of such alignments, as has been well established for the Hawaiian Islands. For Lee et al. (1994), the Cameroon Line originates from a sublithospheric enriched “hot zone” periodically fed by melted deep mantle plumes, and this zone of hotter mantle represents reactivated mantle previously enriched during the opening of the South Atlantic in the Mesozoic. Other viewpoints include rejuvenation of Precambrian faults (Moreau et al., 1994) and hot line or thermally anomalous linear zone in Earth’s mantle (Meyers et al., 1998). On the basis of reliable $^{40}\text{Ar}/^{39}\text{Ar}$ dates, Marzoli et al. (1999) concluded that the Cameroon volcanic line as a whole may not be interpreted as the surface expression of simple hotspot magmatism, confirming earlier conclusions of, e.g., Fitton and Dunlop (1985) and Fitton (1987), drawn from a more restricted database. Our purpose is to show that Cameroon Line magmatism (Central Africa) and its northward related structure in West Africa up to Aïr in Niger can be interpreted as a result of complex interactions between hotspots and Precambrian faults. To prepare the groundwork for this, we present the main available new data and corresponding

features along the whole structure since the reviews made by Fitton (1987) and Déruelle et al. (1991).

GEOLOGY

Magmatism along the Cameroon Line includes both plutonic complexes and volcanic massifs (Fig. 2).

Plutonic Rocks

Plutonic complexes are predominantly made up of granites or syenites, with which subordinate intermediate and basic rocks are sometimes associated (e.g., Njonfang et al., 1992). Volcanic rocks are commonly associated with the plutonic rocks, the whole being referred to as plutonic-volcanic complexes. More than 60 such complexes are identified, but less than 20% have been studied to date. On the basis mainly of their petrographic composition and distribution, the six more representative and best studied complexes are presented here. These are Nda Ali, Pandé, Nigo, Mboutou, Kokoumi, and Ntumbaw.

The Nda Ali subvolcanic complex (SW Cameroon) rises to a height of 1000 m above the Mamfé Plain (150–200 m). It is located at the intersection of two NW- and NE-trending fracture systems and extends between $5^{\circ}32'\text{N}$ and $5^{\circ}37'\text{N}$ and $9^{\circ}27'\text{E}$ and $9^{\circ}33'\text{E}$. The complex is hook-shaped (16×13 km) with a core of plutonic rocks and a border of volcanic rocks. It is mainly intruded into a granitic basement in the southwest and Cretaceous sandstones; these are covered with trachytic lavas. Hornfels indicating the contacts are observed in some rivers (Njonfang and Moreau, 1996) (Fig. 3A). The plutonic rocks form a gabbro-diorite-monzonite-syenite alkaline suite, where alkaline syenites (coarse to fine grained) predominate over gabbros, which show magmatic layering (making up ~5% of the surface area of plutonic rocks), and subordinate intermediate rocks (diorite and monzonite). Layering in gabbros (up to 1 cm thick) is marked by alternation of plagioclase-rich layers with clinopyroxene- or amphibole-rich ones. Syenites always display miarolitic cavities (up to 3%). Coarse- to medium-grained types correspond to alkali syenites, while fine-grained types are quartz-syenites in the Streckeisen classification (1976). Volcanic rocks are mainly alkali trachytes, with small amounts of tephri-phonolite, nepheline phonolite, and dikes of phonolite and basanite. Plagioclase is the main feldspar in basic rocks; it coexists with alkali feldspars in intermediate rocks and becomes scarce in syenites, where alkali feldspar predominates. Alkali feldspar is always perthitic

with albite exsolution at some edges and locally shows the catastrophic coarsening of Parsons (1978).

The Pandé subvolcanic complex (Tikar Plain, Cameroon; Njonfang and Moreau, 2000) is a small (4.9×3.4 km), egg-shaped complex striking W-E and rising to 1231 m. It also has both plutonic and volcanic rocks (Fig. 3B). Plutonic rocks form a syenite-granite peralkaline suite with syenites (coarse to fine grained) predominating over granite (fine grained). Rocks are rich in miarolitic cavities (3.0%–5.5%). Two volcanic sequences

(trachyte-rhyolite and trachyte) predate and postdate the plutonites; they respectively occupy the eastern border and the core of the pluton, and the second sequence trachyte (T2) contains xenoliths of syenites. Trachytes of the first sequence (T1) are overlain by a thick rhyolitic flow and are rather rich in xenoliths of the Pan-African granitic basement. Both sequences are also peralkaline. Trachyte is more abundant, even in the trachyte-rhyolite sequence. Aegirine is ubiquitous, whereas arfvedsonite occurs only in coarse- to medium-grained syenites and in rhyolite; both

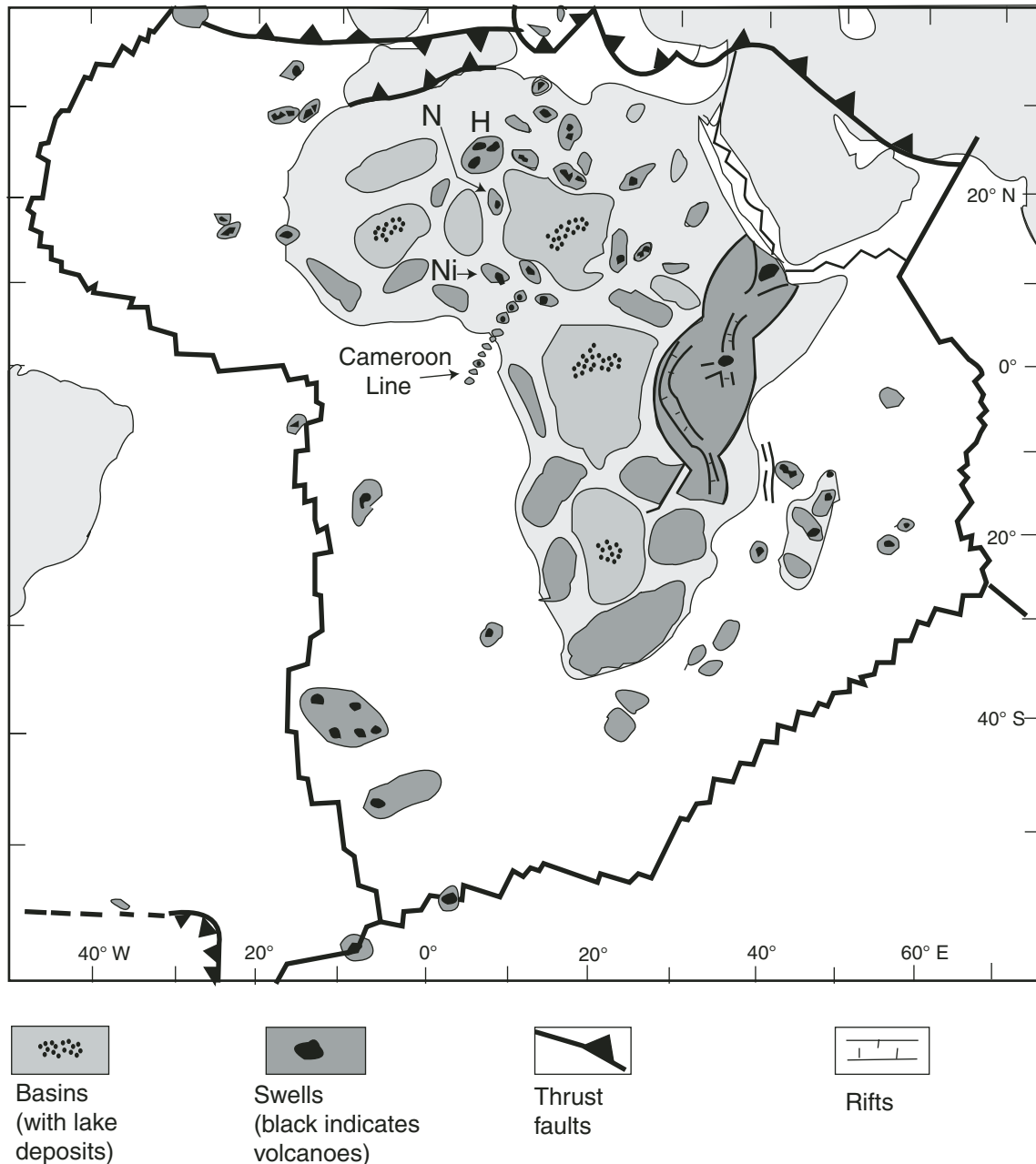


Figure 1. Basins and swells of the African plate (after Burke, 2001) showing the location of the Hoggar (H), Niger (N), and Nigeria (Ni) swells and the Cameroon Line trend. Key: dashed line—supposed prolongation of fault; zigzagging solid line—oceanic limit of the African plate (Mid-Atlantic Ridge and Mid-Indian Ridge).

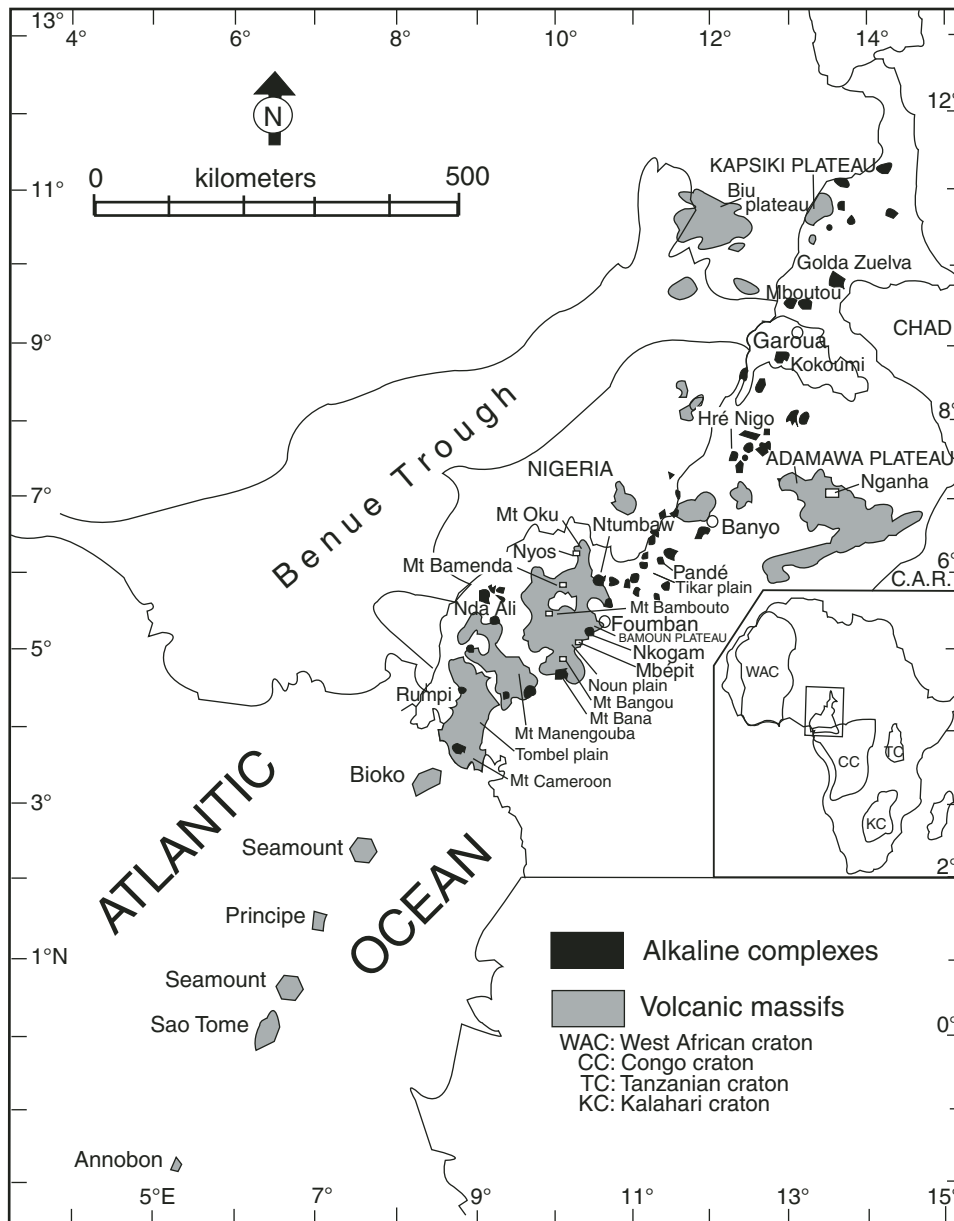


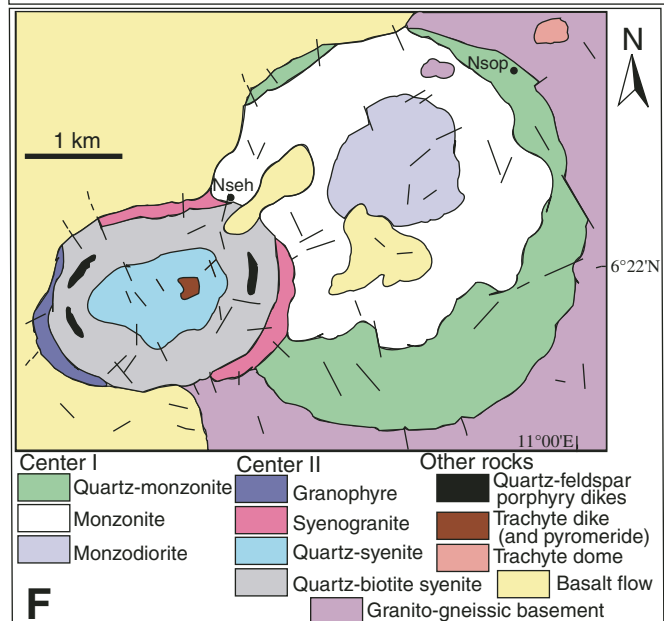
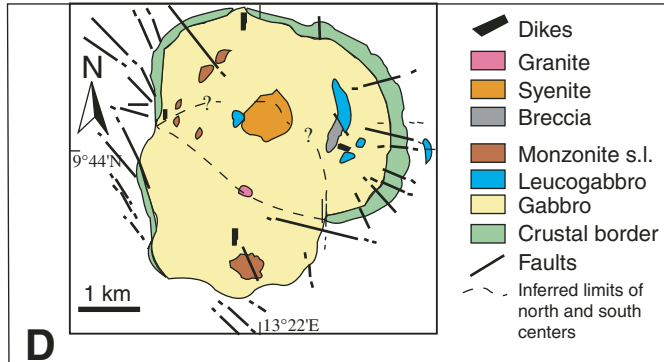
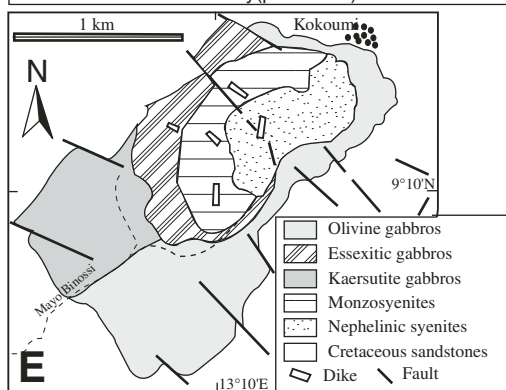
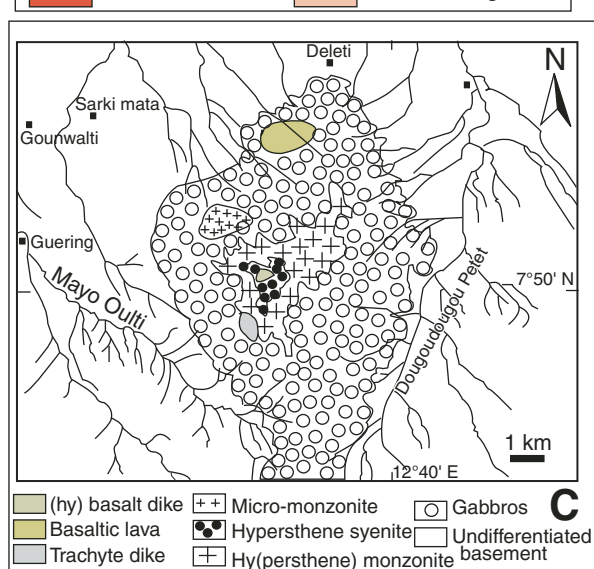
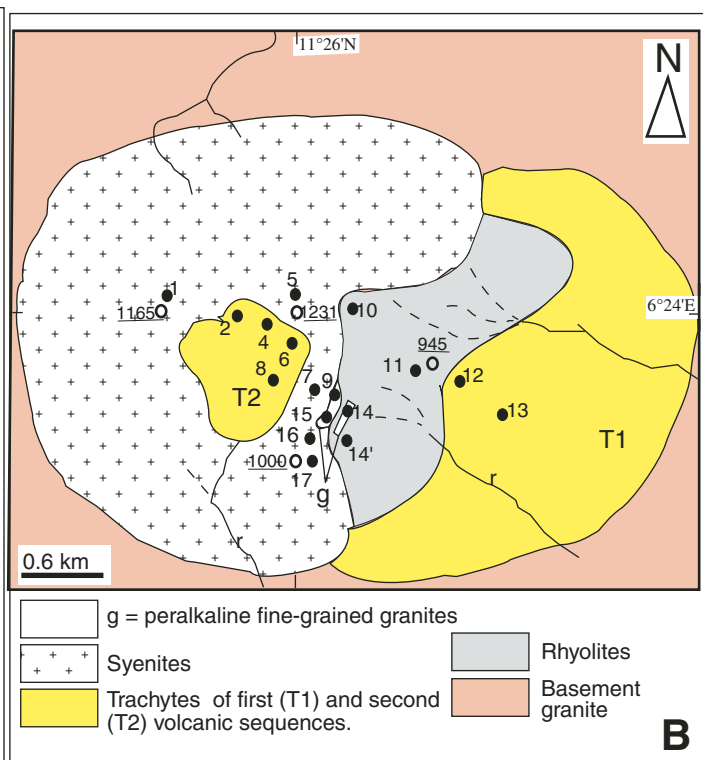
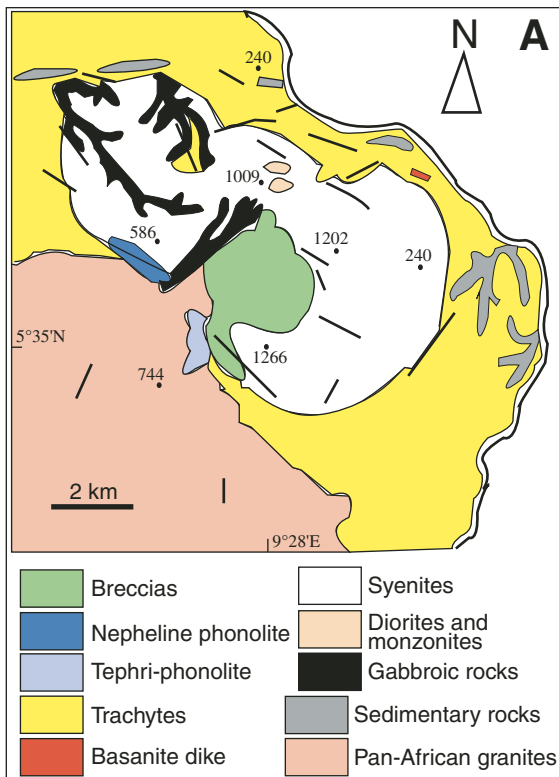
Figure 2. Map of Cameroon showing the distribution of the Cameroon Line magmatism. Locations of seamounts are after Burke (2001). C.A.R.—Central African Republic. Inset: Cameroon in Africa.

are symptomatic of peralkalinity. Where they coexist, pyroxene crystallized subsequent to amphibole. Detailed mafic mineralogy (Njonfang and Moreau, 2000) shows overlaps in plutonic and volcanic pyroxene trends that indicate their crystallization from magmas of the same composition.

The Hossere Nigo or Nigo complex (NW Adamawa, Cameroon) rises 900 m above the surrounding surface of Pan-African basement and has a diameter of ~7 km. It is a dominantly gabbroic ring structure with a core of hypersthene-bearing monzonitic to syenitic intrusive bodies (Kamdern et al., 2002). It then differs from the previously described complexes by the predominance of basic rocks (Fig. 3C). Gabbros include olivine gabbro, troctolite, and anorthosite. Volcanic rocks include few basaltic and trachytic dikes crosscutting the plutonic complex.

The Mboutou complex (North Cameroon) is located at 9°44'N, 13°22'E and has a diameter of 5.5 km; it is also predominantly gabbroic. Two overlapping centers occur, and the south center was emplaced later than the north center (Fig. 3D). The whole forms a gabbro-syenite-granite suite where gabbros are principally cumulates. Three types are recognized: titanomagnetite and ilmenite

Figure 3. Geological maps of principal types of plutonic complexes of the Cameroon Line: (A) Nda Ali (after Njonfang and Moreau, 1996); (B) Pandé (after Njonfang and Moreau, 2000). Numbers in small font represent altitude in meters. In B, the larger numbers are sample numbers. (C) Nigo (after Kamdem et al., 2002); (D) Mboutou (after Jacquemin et al., 1982) (s.l.—sensu lato); (E) Kokoumi (after Ngounouno et al., 2001); and (F) Ntumbaw (after Ghogomu et al., 1989). Lines in F represent faults.



cumulates (melagabbros), layered olivine and clinopyroxene gabbros, and plagioclase cumulates (noritic leucogabbros). They are intruded by monzogabbros, monzodiorites (microdiorite and quartz syenodiorite), and quartz syenite in the north center and hypersolvus granite in the south center (Jacquemin et al., 1982; Parsons et al., 1986). Olivine occurs only in the layered melagabbros and gabbros and never coexists with orthopyroxene, which occurs only in leucogabbros and quartz-syenodiorites. Minor volcanic (hawaiites and potassic benmoreites) and subvolcanic (alkaline dolerites) dikes complete the magmatic sequence.

The Kokoumi complex (Benue Trough, North Cameroon), located at 9°10'N, 13°09'E, is NE-SW elongated, small in size ($<2.5 \times 1.5$ km), and entirely undersaturated. It forms a gabbro-nepheline monzosyenite-nepheline syenite series cut by lamprophyric (monchiquites and camptonites) and trachytic dikes (Ngounouno et al., 2001) (Fig. 3E). The whole is intrusive into sandstones of Albian–Aptian age (Montigny et al., 2004). Gabbros include olivine-, nepheline-, and kaersutite-bearing gabbros. Monchiquites contain carbonate ocelli, and trachyte lacks ferromagnesian minerals. Nepheline syenites contain aegirine-augite, F-arfvedsonite, and aenigmatite.

The Ntumbaw complex (NW Cameroon), situated at 6°22'N, 10°54'E, occupies an area of ~ 12 km². This complex is unique because it is mainly composed of intermediate rocks (Fig. 3F). These rocks are distributed between two centers, C1 and C2 (Ghogomu et al., 1989). C1, the older of the two, occupies two-thirds of the complex and includes monzodiorite, monzonite, and quartz monzonite. Basalt dikes and frequent quartz veins also occur. C2 is composed of more differentiated rocks: syenites (quartz-syenite and biotite-quartz-syenite) and subordinate syenogranite. It is cut by few dikes (quartz-feldspar porphyry and trachyte). The complex intrudes a granitic-gneissic basement and is partly masked by late basalt flows of Ntumbaw.

Volcanic Rocks

The volcanic rocks of the Cameroon Line are more varied, ranging from basalts, basanites, and/or nephelinites to trachytes, rhyolites, and/or phonolites in a given massif, except at the continent-ocean boundary, where Bioko and Mount Cameroon are mainly basaltic and Etindé is nephelinitic.

In the continental sector, Kapsiki volcanism (Kapsiki Plateau, northernmost Cameroon), made up of basalts and hawaiites as mafic lavas and phonolites, trachytes, and rhyolites as felsic lavas (Ngounouno et al., 2000), forms a typical bimodal lava series. The plateau has a granitic-gneissic Precambrian basement locally covered with continental sediments of Lower Cretaceous age. Volcanism is represented by 30 trachytic and rhyolitic plugs (or groups of plugs) and basaltic necks and flows. The plugs are 10–1000 m high and range from 50 to 500 m in diameter, whereas exposures of basalts are mostly small outpourings (less than 20 m high and 50 m in diameter) (Ngounouno et al., 2000). Basalts include porphyritic types with phenocrysts of olivine up to 3 mm and ankaramite types with ~ 10 vol% clinopyroxene (up to

10 mm) and 5 vol% olivine phenocrysts. Trachytes and rhyolites are alkaline to peralkaline with normative acmite up to 1.2% and 1.7%, respectively.

Volcanic massifs displaying a complete range from basic to felsic rocks also exist along the Cameroon Line, and are here represented by the Nganha (Adamawa Plateau) and Bamenda-Bambouto (West Cameroon Highlands) massifs. They are characterized by the great abundance of mafic and felsic lavas relative to the relatively rare occurrence of intermediate (mugearite and benmoreite) lavas.

The Nganha volcano (Adamawa Plateau, Cameroon), located between 7°18'N and 7°25'N and 13°55'E and 14°05'E, contains a broad range of rock types (Fig. 4A), from ankaramites to trachytes and phonolites, with mafic lavas covering ~ 87 vol% of the total area (Nono et al., 1994). The volcano has a Pan-African basement made up of granites and syenites. Basaltic flows first occurred, followed by phonolitic and trachytic lavas. Xenocrysts of alkali feldspar are common in kaersutite-bearing ankaramites. Basalts usually contain more clinopyroxene than olivine phenocrysts, except where plagioclase phenocrysts occur. Hawaiites and mugearites are characterized by very low phenocryst contents. Mugearites contain abundant Fe-Ti oxides (up to 20 vol%). Benmoreite has euhedral phenocrysts of augite that contain numerous inclusions of biotite and titanomagnetite. The felsic lavas are divided into four types: phonolites, peralkaline phonolites, richterite-bearing trachytes, and arfvedsonite-bearing trachytes. Arfvedsonite-bearing trachytes are more abundant than richterite-bearing ones. Phonolites display modal feldspathoids (hauyne, nosean, or sodalite), and peralkaline phonolites do not contain any of the typical minerals (eudialyte, mosandrite, etc.) that characterize agpaite phonolites (Edgar, 1974). Furthermore, sphene is present, whereas it is systematically absent in agpaite phonolites (Nono et al., 1994).

The Bamenda Mountains (Kamgang et al., 2007, 2008), situated between 5°40'N and 6°10'N and 10°00'E and 10°30'E, constitute one of the most important volcanoes of the Cameroon Line in NW Cameroon. They are mainly made up of mafic and felsic lavas with very small amounts of intermediate compositions (mugearite and benmoreite). Felsic lavas cover ~ 85 vol% of the volcano and lie on a granitic-gneissic Pan-African basement (Nzolang, 2005). Mafic lavas include abundant basanites, alkaline basalts, and hawaiites. Basanites consist of olivine and/or pyroxene phenocrysts in a matrix where nepheline is associated with plagioclase, clinopyroxene, and Fe-Ti oxides. Basalts and hawaiites are rich in olivine and clinopyroxene phenocrysts, whereas in mugearites, phenocrysts of plagioclase dominate and olivine becomes scarce. Benmoreites are almost aphyric (rare microphenocrysts of sanidine and opaque minerals). Trachytes are the predominating felsic lavas, with minor amounts of rhyolites. Both are aphyric to porphyritic, alkaline to peralkaline in nature. Sanidine and/or quartz are the main phenocrysts; some trachyte samples contain olivine. Amphibole is common in the matrix of these felsic lavas, and aenigmatite occurs in peralkaline varieties. Pyroxene composition is restricted to diopside in

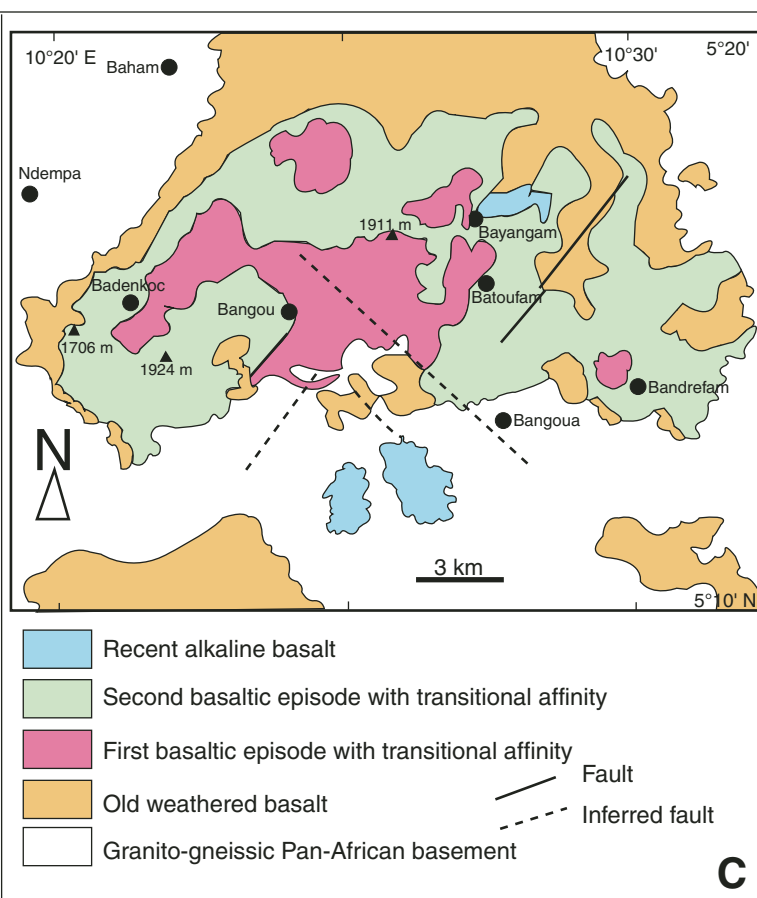
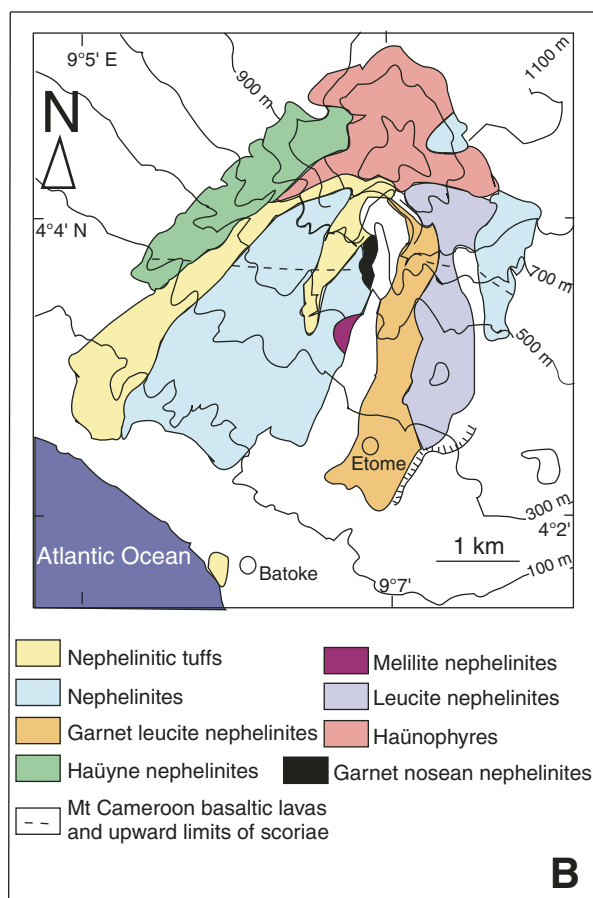
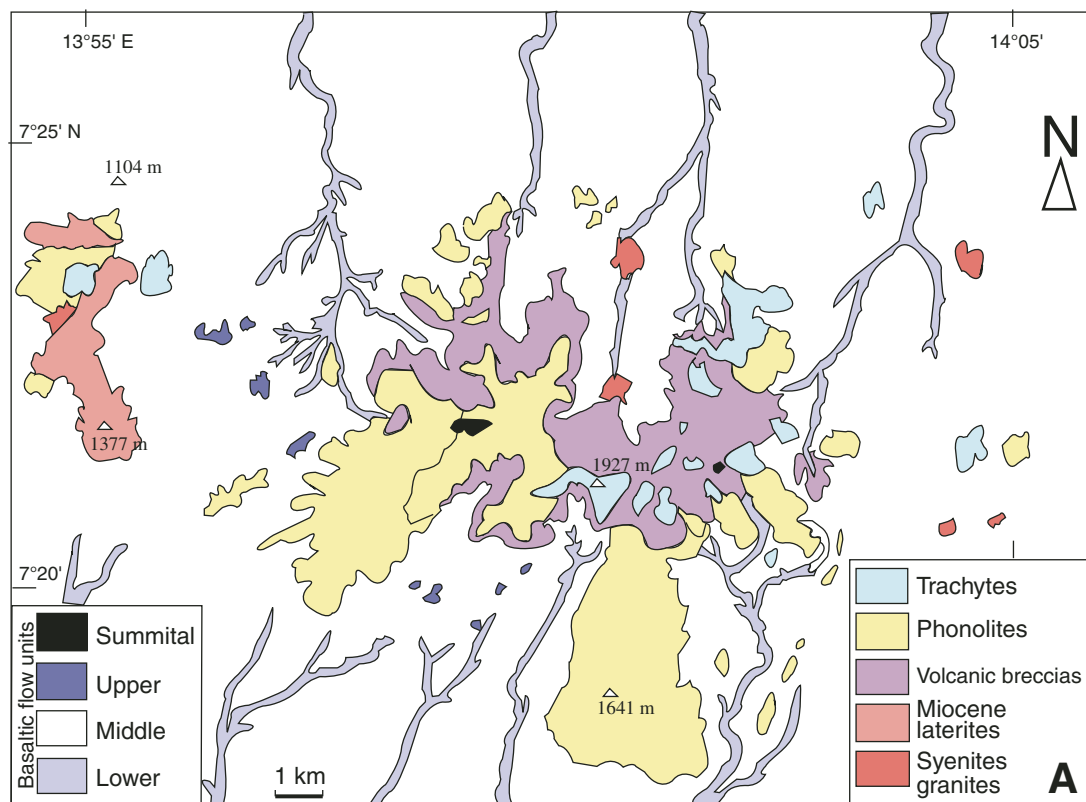


Figure 4. Geological maps of three different types of volcanic massifs of the continental sector of the Cameroon Line: (A) Nghanha (after Nono et al., 1994); (B) Etindé (after Nkoumbou et al., 1995); and (C) Bangou (after Fosso et al., 2005).

basaltic lavas and varies in felsic lavas from diopside to aegirine (in the classification of Morimoto et al., 1988). Amphibole composition varies from richterite to arfvedsonite. Anorthoclase mainly occurs in benmoreite. Compared with the Nganha massif, the Bamenda Mountains differ by the presence of significant volumes of ignimbritic flows (still to be studied), mostly rhyolitic in composition (Figs. 5A and 5B) and the late emplacement of mafic lavas over felsic ones.

The Bambouto volcano occurs as the SW prolongation of the Bamenda Mountains, and both, together with Mount Oku located to the NE, form the West Cameroon Highlands (Fig. 2). This volcano is located between 5°2'7"N and 5°48'N and 9°57'E and 10°15'E, culminating at 2740 m above sea level, where two collapse calderas (Tchoua, 1973; Youmen, 1994) are encountered. Lavas form a complete compositional series from abundant basanite, alkaline basalts, and hawaiiite through scarce mugearites and benmoreite to less abundant trachyte and phonolite, including phono-tephrite (Nkouathio et al., 2008). The most recent sequence of emplacement (Kagou Dongmo et al., 2010) indicates that mugearite flows are older, followed by rhyolite, trachytic ignimbrites, and trachytes, whereas mafic lavas are younger. Basanites and basalts are porphyritic to aphyric. They contain large subhedral phenocrysts of olivine, clinopyroxene, and scarce phenocrysts and microphenocrysts of plagioclase and Fe-Ti oxides (71–19 mol% ulvöspinel). Hawaiiite, phono-tephrite, and mugearite contain mainly phenocrysts and microphenocrysts of plagioclase associated with variable amounts of clinopyroxene, amphibole (edenite and kaersutite), and Fe-Ti oxides (titanomagnetite with 57–41 mol% ulvöspinel, and ilmenite). The same minerals occur in mugearites as matrix phases embedded in the groundmass (5%–15% glass) with scarce alkali feldspar. Benmoreite, trachyte, and phonolite tend to have a trachytic texture. Feldspars (anorthoclase and alkali feldspar) constitute the main phenocrysts in a microlitic matrix of alkali feldspar, plagioclase, clinopyroxene, and titanomagnetite (94–25 mol% ulvöspinel). In some phonolite samples, scarce nepheline and sodalite are observed; however, these are locally completely pseudomorphed by alteration products. As in the Bamenda Mountains, ignimbrites are also very common and widespread in the Bambouto volcano. They are of trachytic or, more rarely, rhyolitic composition (Nono et al., 2004). The presence within these ignimbrites of subangular and rounded fragments of scoria (Fig. 5C) led Nono et al. (2004) to conclude the existence of an initial strombolian phase in the chronostratigraphy of these volcanoes. More recently, important Quaternary scoria deposits have been discovered (Kagou Dongmo et al., 2006) north of the Bambouto caldera (Fig. 5D).

Mount Cameroon (4°20'N, 9°17'E), the only currently active volcano of the Cameroon Line (last eruption in 2000), is also one of the most studied (Dérulle et al., 1991, and references therein; Dérulle et al., 2000, 2001; Suh et al., 2003, 2008; Ngounouno et al., 2006; Ngounouno and Dérulle, 2007; Yokoyama et al., 2007). It is a huge stratovolcano, 4095 m above sea level, with a volume of ~1200 km³ (Suh et al., 2003), made up of lava flows

and pyroclastic deposits built on a crystalline basement of Paleozoic age. Recent field studies have led to the discovery of camptonites on its southern flank, mainly as loose blocks in the bed of a stream (Ngounouno et al., 2006) and of xenoliths of wehrlites in some pyroclastic deposits (Ngounouno and Dérulle, 2007).

On the southwestern flank of the huge stratovolcano, a steep-sided volcano with the highest peak at 1713 m above sea level, flanked by two other summits, is known as Etinde volcano. It represents the only feldspathoid-rich series of the Cameroon Line, with a total volume (lava flows and tuffs) of ~2.5 km³. Nkounbou et al. (1995) showed that it is unrelated to the Mount Cameroon lavas, and its abundant presence as xenoliths in those lavas indicates that it is older. Rocks are mainly melanephelinites and nephelinites *sensu stricto* (Fig. 4B). Numerous and varied nephelinites are distinguished based on the presence of one or more of the following mineral species: aenigmatite, nosean, melilite, hyalophane, melanite garnet, leucite, and hauyne. For example, hauynophyres have hauyne/(hauyne + leucite + nepheline) > 0.6, and leucite nephelinites have leucite/(leucite + nepheline) = 0.5 ± 0.1. Other types are: hauyne nephelinites, melilite nephelinites, Sr-melilite nephelinites, garnet melilite-bearing nephelinites, and leucite melilite-bearing nephelinites. Ijolites and melteigites are found as xenoliths (10 cm) in garnet and hauyne nephelinites, whereas nephelinites *sensu stricto* and hauynophyre xenoliths occur in melilite nephelinites.

In the oceanic sector, the four previously known islands (Dérulle et al., 1991, and references therein; Lee et al., 1994) consist of basanite to hypersthene-normative basalt, tristanite, and trachyte in Annobon; basalt to trachyte and phonolite with no compositional gap in São Tomé; nephelinite, basanite, tristanite, trachyphonolite, and alkali basalt in Príncipe; and basanite to hypersthene-basalt in Bioko. Hyaloclastite breccias are the oldest rocks of Príncipe and Annobon Islands, whereas conglomerates, sandstones, and shales constitute the basement rocks of São Tomé. Two large seamounts (Fig. 2) between Bioko and Príncipe and between Príncipe and São Tomé, respectively, were recently discovered (Burke, 2001), but there was no detail provided about their shape and petrography.

Another characteristic of Cameroon alkaline magmatism is that some mafic lavas are rich in ultramafic xenoliths (Lee et al., 1996; Aka et al., 2004). These occur in both the continental sector, e.g., in Oku and Nyos (Nana et al., 2001; Temdjim et al., 2004), and in the oceanic sector, as in São Tomé (Caldeira and Munhá, 2002). Their nature is varied (Fig. 6), including, from NE to SW: spinel lherzolite from Liri, south of Kapsiki Plateau (Ngounouno et al., 2008), spinel lherzolites and dunites in the Adamawa Plateau (Lee et al., 1996, and reference therein); spinel lherzolites, harzburgites, and websterites in the Nyos Plain, SW of Mount Oku (Temdjim et al., 2004), renowned since the lake Nyos emitted lethal gas that killed 1746 persons in 1986 (Kling et al., 1987); only lherzolites in the Kumba Plain, NE of Mount Cameroon (Teitchou et al., 2007); wehrlites, dunite, and pyroxenites (clino-) of Mount Cameroon (Dérulle et al., 2001; Wandji et al., 2009); and spinel lherzolites, harzburgites, and dunites and



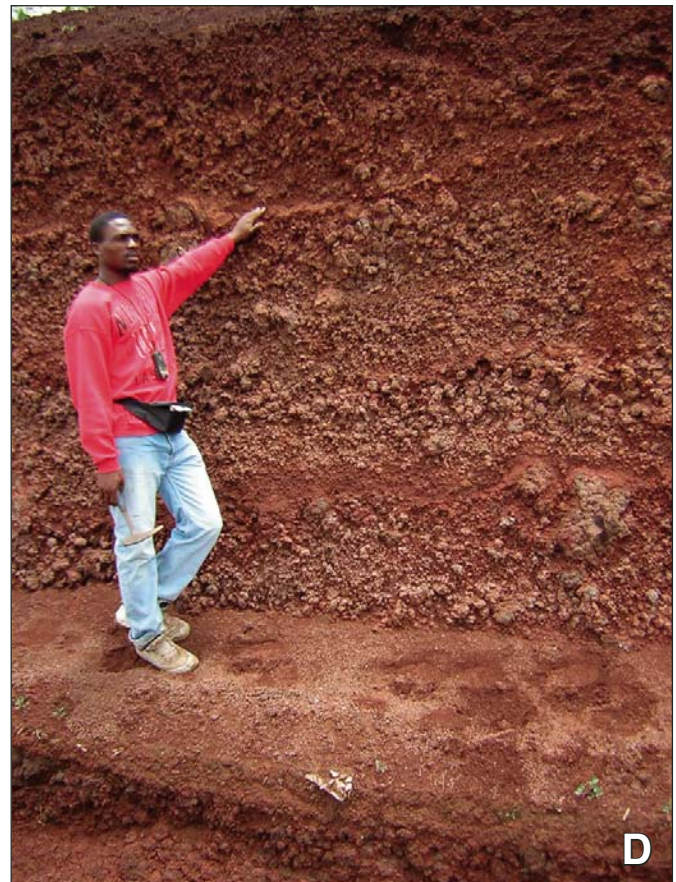
A pyroclastic landscape of the Bamenda Mountains



Detail of a pyroclastic block of A



Scoria fragments in a Mt. Bambouto ignimbritic flow



A Quaternary scoria deposit of Mt. Bambouto

Figure 5. Field photographs showing some features of pyroclastic deposits from Bamenda and Bambouto volcanoes. (A) A pyroclastic landscape of the Bamenda Mountains. (B) Detail of a pyroclastic block from A. The pen is 14.2 cm long. (C) Scoria fragments in a Mount Bambouto ignimbritic flow. The coin is 2.3 cm in diameter. (D) Vertical view of a Quaternary scoria deposit of Mount Bambouto. The man is 1.75 m tall.

pyroxenites (ortho- and clino-) from São Tomé Island (Caldeira and Munhá, 2002).

GEOCHEMISTRY

As can be seen from the various petrographic types described already, Cameroon alkaline magmatism is typically bimodal when a complex or massif is considered but as a whole forms a continuous series from less differentiated to more differentiated magmas, although these are unequally distributed in the field. This is chemically marked in the total alkali–silica (TAS) diagram by the large range of SiO_2 contents (40–76 wt%), with very few lavas of intermediate composition (51–58 wt%) and the absence of discrimination between oceanic and continental basaltic lavas (Fig. 7A). However, continental rocks mostly follow a SiO_2 -saturated to SiO_2 -oversaturated trend, whereas oceanic rocks mainly follow a SiO_2 -undersaturated one. Few exceptions to this general rule are observed, and these are principally in the continental sector, such as the Kokoumi complex and the Etindé volcano (Figs. 7B and 7C). Since the entirely alkaline nature of this magmatism was established by Déruelle et al. (1991, and references therein), many lavas with transitional affinities ($\text{Y/Nb} \geq 0.9$; Pearce and Cann, 1973) have been described in the continental sector (Moundi et al., 1996, 2007; Marzoli et al., 2000; Fosso et al., 2005; Kuepou et al., 2006). They are generally less represented in a given massif but constitute the main volcanic products of the Bangou massif (Fosso et al., 2005) and the Bamoun Plateau (Moundi et al., 2007), both in western Cameroon. The Bangou massif is characterized by two episodes of lavas with transitional affinities and the rather sporadic presence of alkaline basalts (Fig. 4C). However, as emphasized by Déruelle et al. (2007), pigeonite, a mineral symptomatic of transitional lavas, never occurs in those lavas. Indeed,

the transitional affinity is only based on geochemical discrimination diagrams (Figs. 8A–8D). On the Dy/Yb versus La/Yb diagram (Fig. 8D), these transitional lavas clearly occur as products of high melting ($>12\%$) of garnet peridotite, whereas the alkaline ones are derived from lower melting ($\leq 10\%$).

Petrological and geochemical data all along the magmatic complexes and massifs are consistent with their mantle origin and their having experienced more or less crustal contamination during ascent. The mantle origin is petrographically evidenced by the occurrence of peridotite xenoliths in some basaltic lavas. Geochemically, the Sr_i ($^{87}\text{Sr}/^{86}\text{Sr}$ initial ratios) values in basaltic rocks range between 0.7030 and 0.7051, suggesting zero to very little crustal contamination of initial mantle magma; this is consistent with the relatively high values (-2.77 – 7.35 ; Fig. 9) of ϵ_{Nd} (Lee et al., 1994; Marzoli et al., 2000; Rankenburg et al., 2005; Yokoyama et al., 2007; Kamgang et al., 2008; Nkouathio et al., 2008). The few $^{206}\text{Pb}/^{204}\text{Pb}$ ratios available (Déruelle et al., 2007; Nkouandou et al., 2008; Kamgang et al., 2008) vary between 19.0 and 20.2, which are close to those of the recently redefined Focal Zone (FOZO) reservoir (19.3–20.5; Stracke et al., 2005). Crustal contamination has affected SiO_2 -saturated to SiO_2 -oversaturated felsic lavas, and, in general, rhyolites appear to be more contaminated than trachytes, since their Sr_i is higher (0.710–0.715 vs. 0.7045–0.7115) (Nono et al., 1994; Marzoli et al., 1999; Ngounouno et al., 2000). Mugearites and benmoreites appear to be products of mixing between basaltic and evolved magmas (Déruelle et al., 2007). The variable nature of xenoliths (dunites, lherzolites, harzburgites, wehrlites, and websterites) entrained in alkaline basalts and pyroclastic deposits is consistent with the heterogeneity of mantle beneath Cameroon Cenozoic to Holocene magmatism. Indeed, volcanic products display geochemical data consistent with a major role for the FOZO component and varied contribution of depleted mantle (DMM) and enriched mantle (EM) components (Nkouathio et al., 2008).

Another important characteristic of the Cameroon alkaline magmatism is the similar trends (Fig. 10) displayed by SiO_2 -undersaturated and SiO_2 -oversaturated felsic rocks in the evolution of pyroxene (Njonfang and Nono, 2003). This indicates that they are cogenetic, as already established for many subvolcanic alkaline igneous complexes with coexisting SiO_2 -undersaturated and SiO_2 -oversaturated felsic rock types (Chen et al., 1994).

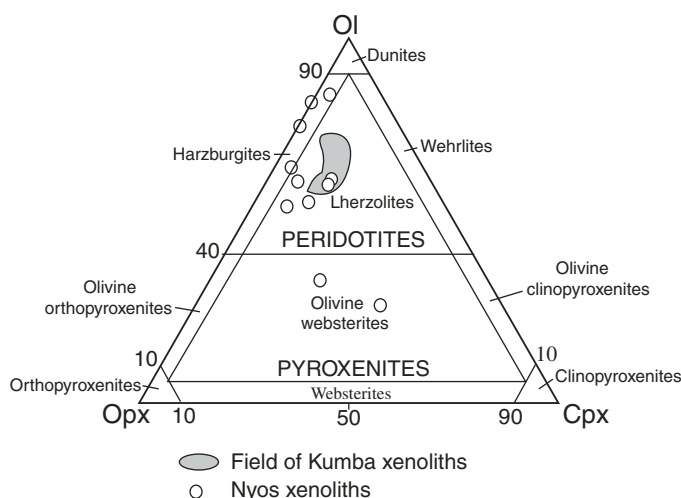
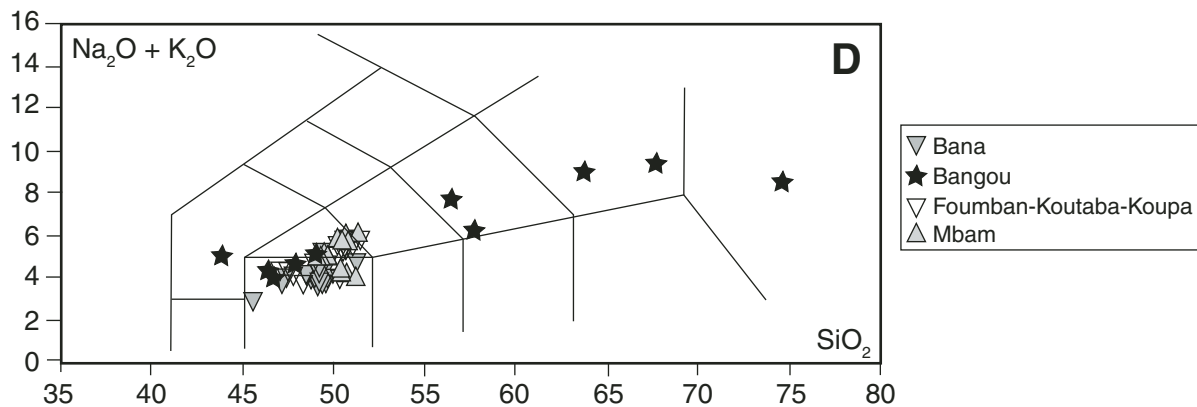
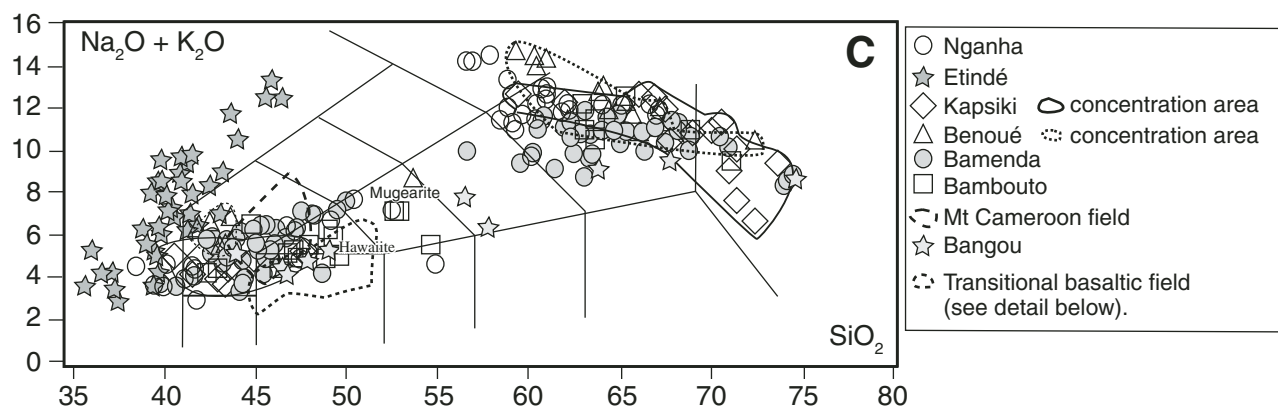
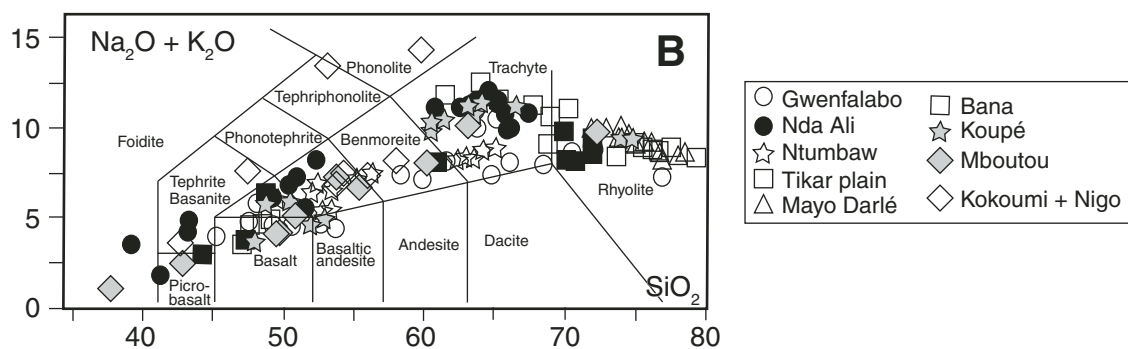
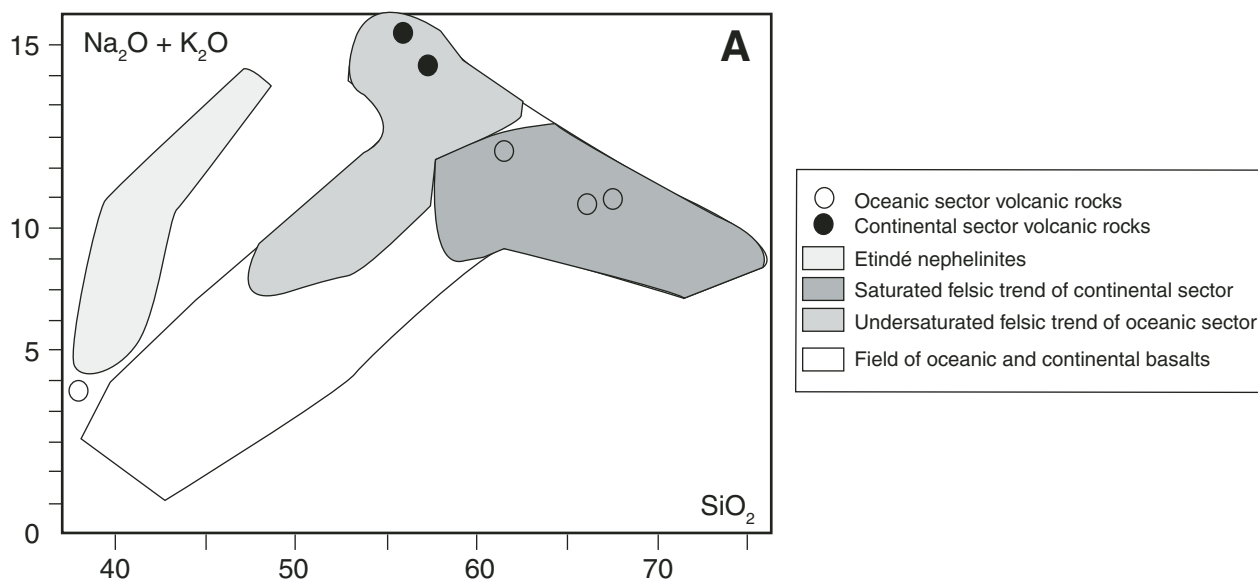


Figure 6. Plot of few Cameroon Line ultramafic xenoliths in the olivine-orthopyroxene-clinopyroxene (Ol-Opx-Cpx) modal diagram. Note the various natures of the xenoliths. Data sources: Temdjim et al. (2004) and Teitchou et al. (2007).

Figure 7. $(\text{Na}_2\text{O} + \text{K}_2\text{O})$ vs. SiO_2 diagrams (in wt%) showing the trends of Cameroon Line magmatism, both in the continental and oceanic sectors: (A) General evolution of volcanic rocks (after Fitton, 1987). (B) Plots of plutonic rocks (data from Njonfang et al., 1992; Ngounouno et al., 2001; Kamdem et al., 2002; Njonfang and Nono, 2003). (C) Plots of volcanic rocks from continental massifs (data from Njonfang et al., 1992; Nono et al., 1994; Nkoumbou et al., 1995; Ngounouno et al., 2000, 2003; Fosso et al., 2005; Kuepou et al., 2006; Moundi et al., 2007; Kamgang et al., 2008). The field of lavas with transitional affinities is delineated for comparison. (D) Plots of transitional lavas of the Cameroon Line magmatism, showing detail of basaltic transitional lavas. The different fields are after Le Bas et al. (1986).



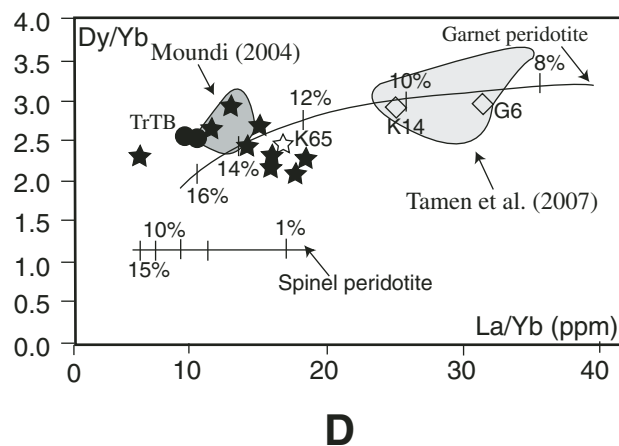
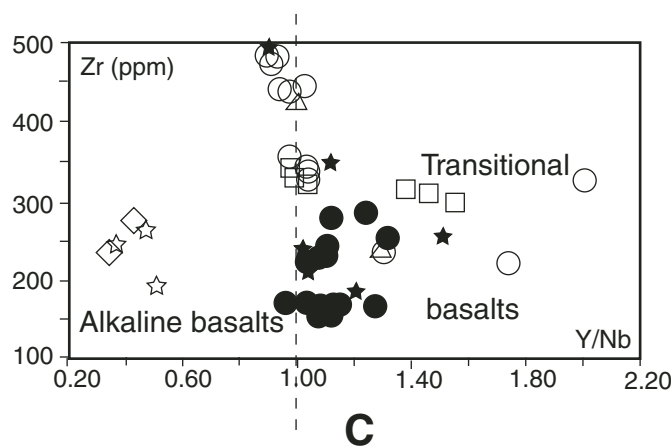
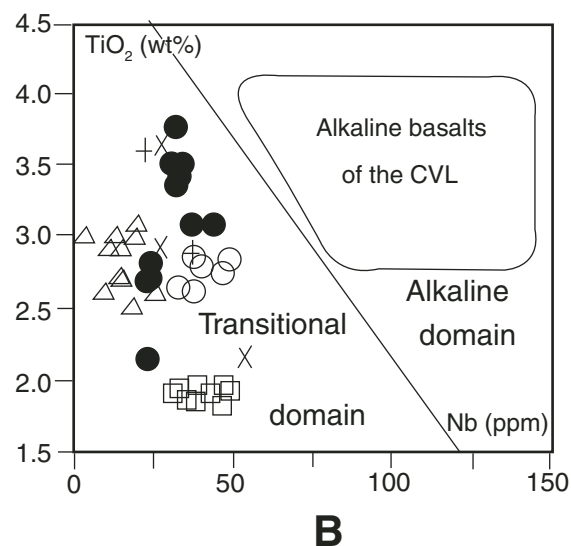
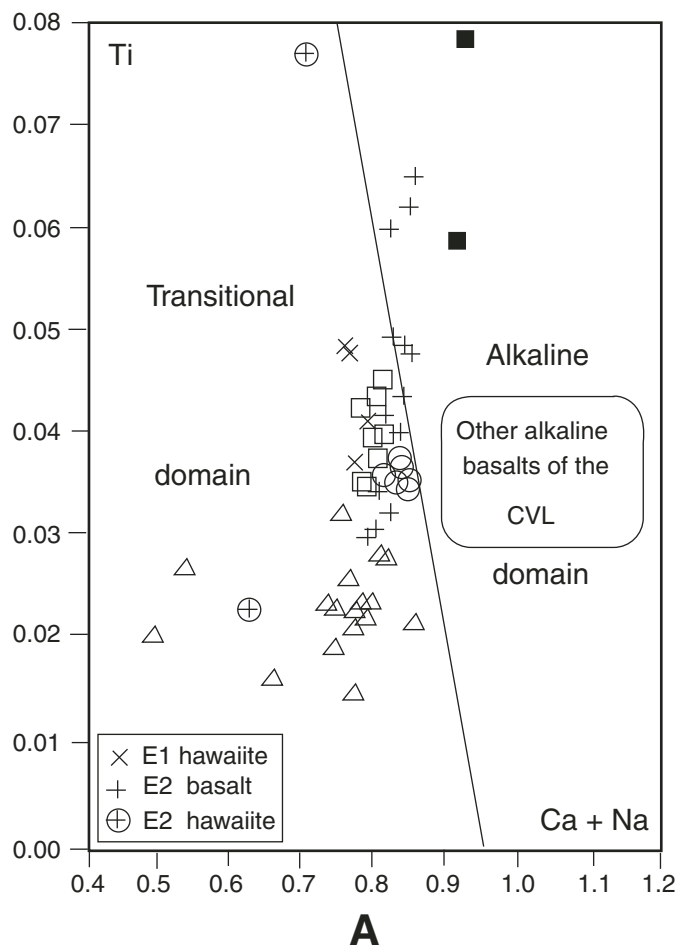


Figure 8. Plots of transitional lavas of the Cameroon Line in discrimination diagrams: (A) Clinopyroxenes from Mount Bangou and Bamoun Plateau in the diagram of Leterrier et al. (1982). Mount Bangou: E1—first episode, E2—second episode, filled squares—alkaline basalts (after Fosso et al., 2005); Bamoun Plateau: basalts of Fouban—triangles, Kouataba—empty squares, Mbam massif—empty circles (after Moundi et al., 2007). Fields of other alkaline basalts of the Cameroon volcanic line (CVL) are shown for comparison (after Moundi et al., 2007). (B) TiO_2 (wt%) vs. Nb (ppm) diagram of Middlemost (1975) for Mount Bangou and Bamoun Plateau lavas (symbols as in A) and Mount Bana (filled circles). Data for Mount Bana are from Kuepouo et al. (2006). Field of alkaline basalts of the CVL is after Moundi et al. (2007). (C) Zr (ppm) vs. Y/Nb diagram of Pearce and Cann (1973): Mount Bana: filled circles—transitional tholeiitic basalts, empty diamonds—basanites, empty stars—hawaiites; Mount Bangou—filled stars (data from Fosso et al., 2005); Bamoun Plateau—same symbols as in A (data from Moundi et al., 2007). (D) La/Yb vs. Dy/Yb diagram showing degrees of melting curves for garnet peridotite and spinel peridotite (Thirlwall et al., 1994; Bogaard and Wömer, 2003). Mount Bana (Kuepouo et al., 2006) and Mount Bangou (data from Fosso et al., 2005) symbols are as in C. Fields labeled Moundi (2004) and Tamen et al. (2007) are that of Bamoun Plateau (transitional lavas) and Kumba graben (alkaline lavas) of the Cameroon volcanic line, respectively. Note the good fit with the garnet peridotite melting curve for both groups and the higher degree of melting for transitional lavas. TrTB—transitional tholeiitic basalts.

Fitton (1987) demonstrated that, in the Cameroon volcanic line, SiO_2 -oversaturated rocks were derived by contamination of SiO_2 -undersaturated magma by siliceous country rocks. However, the fact that trachytes from Nganha and Kapsiki have similar Sr_i (0.7084 and 0.7082, respectively) but different pyroxene trends (Fig. 10) suggests that factors other than crustal contamination played an important role, namely, oxygen fugacity and peralkalinity of the evolved liquids. Njonfang and Nono (2003) showed that pyroxene trends, considered since Larsen (1976) as symptomatic of SiO_2 -undersaturated or SiO_2 -oversaturated magmas, can be obtained in both magma types. For example, the pyroxene trend of phonolites from Nganha volcano, characteristic of SiO_2 -undersaturated complexes (Larsen, 1976), is similar to the pyroxene trend of some quartz-normative trachytes from Kapsiki Plateau (Ngounouno et al., 2000) and clearly distinct from that of the Bambouto phonolite, the latter straddling the hedenbergite trend before Na-enrichment (Fig. 10).

The role of $f\text{O}_2$ was tested through detailed study of pyroxene structural formulae (Njonfang and Nono, 2003). That study revealed the presence of both Zr- and/or Ti-bearing aegirinic pyroxenes and aegirine-rich pyroxenes (Table 1), which are symptomatic of changing crystallization conditions during evolution. The Zr- and/or Ti-bearing pyroxenes are characterized by high Na contents without Fe^{3+} correlation and are known to occur under low $f\text{O}_2$ (Nash and Wilkinson, 1970; Mitchell and Platt, 1978; Nielsen, 1979; Jones and Peckett, 1980; Duggan, 1988). The more common aegirine-rich pyroxenes are marked by enrichment both in Na and Fe^{3+} and strong depletion in Ca and Fe^{2+} , with Na/Fe^{3+} ratios almost equal to 1.0; they crystallize under $f\text{O}_2$ above quartz-magnetite-fayalite (QMF) buffer

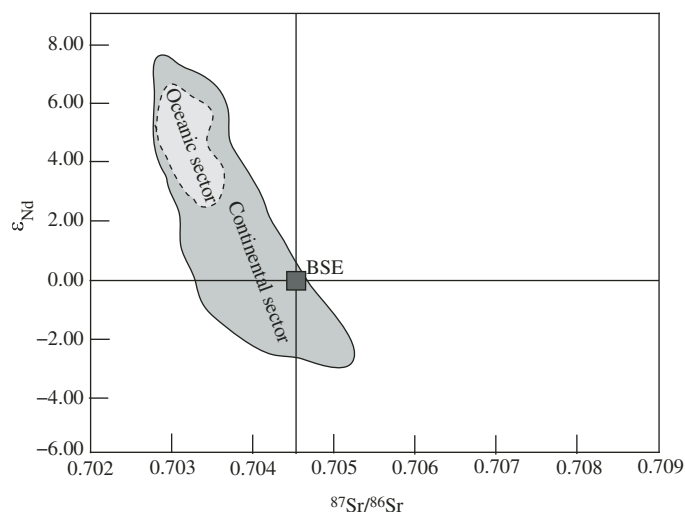


Figure 9. ϵ_{Nd} vs. $^{87}\text{Sr}/^{86}\text{Sr}$ diagram showing the fields of isotopic composition along the Cameroon volcanic line. Field of oceanic sector is defined after data plots from Lee et al. (1994); field of continental sector is defined after data plots from Marzoli et al. (2000, and references therein), Yokoyama et al. (2007), Kamgang et al. (2008), Nkouandou et al. (2008), and Nkouathio et al. (2008). BSE—bulk silicate earth.

(Nash and Wilkinson, 1970; Stephenson and Upton, 1982) and probably up to nickel-nickel-oxide (NNO) buffer (Salviulo et al., 2000). Evidence of the peralkaline affinity of the melt from which the felsic rocks crystallized includes: the MgO-poor contents ($\text{MgO} < 0.9 \text{ wt\%}$) in whole-rocks, their high Zr contents

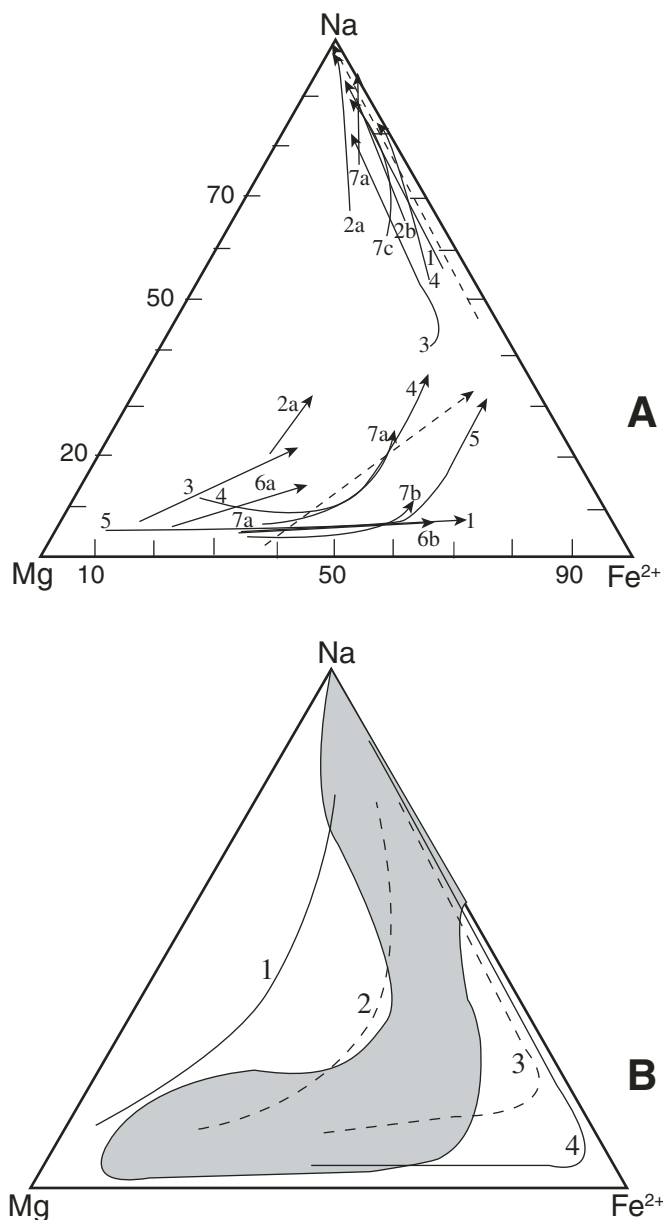


Figure 10. (A) Na-Mg- Fe^{2+} ternary diagram showing pyroxene trends of felsic rocks from some Cameroon alkaline plutonic and volcanic massifs: 1—Kapsiki rhyolites, 2—Kapsiki trachytes, 3—Nganha phonolites, 4—Nganha trachytes, 5—Bambouto phonolites, 6—Bambouto Ne-normative trachytes, 7—Nda Ali syenites, discontinuous arrows—Rumpi rhyolites. (B) Field of the Cameroon Line alkali pyroxenes (gray): Some fairly defined alkali pyroxene trends are reported for comparison. 1—Auvergne, France; 2—Chambe complex, Malawi; 3—Main complex, Malawi; 4—Ilimaussaq intrusions, Greenland. Figure is redrawn from Njonfang and Nono (2003).

TABLE 1. REPRESENTATIVE ANALYSES OF Na-PYROXENES FROM CAMEROON LINE MAGMATISM

Massif:	Kapsiki Plateau				Nganha		Pandé		Granite		Nda Ali	
Rock type:	Trachyte				Trachyte		Qtz syen.		Mpd15		Qtz syen.	
Sample:	Tm121				N105		Mpd17		10i		Na61	
Analysis no.:	1	2	3	4	5m	6m	7	8	9b	10i	11c	12
SiO ₂ (wt%)	51.80	52.05	51.67	51.40	52.43	51.42	51.28	52.42	52.21	53.19	54.34	51.83
TiO ₂	6.06	6.20	4.05	5.19	2.33	4.14	0.19	5.95	5.12	1.15	2.67	6.48
Al ₂ O ₃	0.00	0.41	0.56	0.19	0.32	0.24	0.29	0.10	0.01	0.15	0.17	0.24
FeO*	23.44	23.45	23.25	23.30	25.84	24.93	29.98	25.40	25.91	29.27	23.55	22.45
MnO	1.55	2.14	1.86	1.42	3.48	2.35	0.25	0.64	0.54	0.89	0.66	1.33
MgO	0.41	0.13	0.39	0.55	0.20	0.01	0.00	0.02	0.00	0.03	1.18	0.36
CaO	1.02	0.49	1.37	1.14	3.20	2.63	0.63	3.34	1.39	0.58	5.81	0.54
Cr ₂ O ₃	nd	nd	nd	nd	0.00	0.12	nd	nd	nd	nd	0.00	0.00
Na ₂ O	13.11	13.01	11.76	12.67	10.72	12.29	13.22	12.02	13.07	13.72	11.38	13.36
K ₂ O	0.04	0.09	0.24	0.07	0.00	0.06	0.00	0.02	0.00	0.04	0.00	0.00
ZrO ₂	1.46	2.80	3.78	1.42	nd	nd	nd	nd	nd	nd	nd	nd
Total	98.95	98.63	98.93	97.35	98.52	98.19	95.84	99.91	98.24	99.03	99.76	96.59
Si	1.972	2.026	2.014	1.984	2.024	1.968	1.984	1.983	1.989	1.992	2.034	1.995
^{iv} Al	0.000	0.000	0.000	0.009	0.000	0.011	0.013	0.004	0.000	0.007	0.000	0.005
^{iv} Fe ³⁺	0.028	0.000	0.000	0.007	0.000	0.021	0.003	0.013	0.011	0.001	0.000	0.000
^v Al	0.000	0.019	0.026	0.000	0.015	0.000	0.000	0.000	0.000	0.000	0.008	0.006
Ti	0.173	0.182	0.119	0.157	0.068	0.119	0.006	0.169	0.147	0.032	0.075	0.188
Cr	nd	nd	nd	nd	0.000	0.004	nd	nd	nd	nd	0.000	0.000
^v Fe ³⁺	0.623	0.446	0.466	0.639	0.605	0.704	0.080	0.559	0.683	0.916	0.600	0.621
Fe ²⁺	0.093	0.189	0.259	0.106	0.229	0.073	0.887	0.232	0.132	0.000	0.137	0.102
Mn	0.050	0.071	0.061	0.047	0.114	0.076	0.008	0.021	0.017	0.028	0.021	0.043
Mg	0.023	0.008	0.023	0.032	0.012	0.001	0.000	0.001	0.000	0.002	0.066	0.021
Ca	0.043	0.020	0.057	0.047	0.132	0.108	0.026	0.135	0.057	0.023	0.233	0.022
Na	0.967	0.982	0.889	0.948	0.802	0.912	0.992	0.882	0.965	0.997	0.826	0.007
K	0.002	0.005	0.012	0.003	0.000	0.003	0.000	0.001	0.000	0.002	0.000	0.000
Zr	0.027	0.053	0.072	0.027	nd	nd	nd	nd	nd	nd	nd	nd
Ae+Di+Hd (a.p.f.u.)	0.665	0.466	0.513	0.686	0.737	0.812	0.106	0.652	0.697	0.916	0.715	0.621
NAT	0.000	0.182	0.119	0.135	0.068	0.087	0.000	0.152	0.135	0.024	0.075	0.145
FM-NAZ	0.000	0.053	0.072	0.012	0.023	0.001	0.443	0.009	0.000	0.006	0.034	0.000

Note: Alk. syen.—alkaline syenite, Qtz syen.—quartz syenite, FeO*—total iron, m—microlite, b—border, i—intermediate area, c—core of crystal; Ae—NaFe³⁺Si₂O₆, Di—diopside, Hd—hedenbergite, NAT—NaTi_{0.5}(FM)_{0.5}Si₂O₆, FM—Fe²⁺ + MgO + Mn, FM-NAZ—NaZr_{0.5}(FM)_{0.5}Si₂O₆, nd—not determined, a.p.f.u.—atoms per formula unit.

(up to 2140 ppm), the ubiquity of aegirine and/or sodic amphibole in all massifs and complexes, and the presence of modal zircon only in some peralkaline granites. High-Zr abundances in the Cameroon felsic rocks are not consistent with an origin by assimilation of partially melted crustal materials, because relatively low-Zr content would result from assimilation of crustal materials (Watson, 1979).

SPATIAL-TEMPORAL EVOLUTION OF CAMEROON ALKALINE MAGMATISM

The distribution of alkaline magmatism in Cameroon follows an overall linear chain trending almost SW-NE from the oceanic to the continental sectors, defining the so-called and well-renowned Cameroon Line (Fitton, 1987; Déruelle et al., 1991). While this chain recalls that of the Hawaiian and Emperor Islands, which originated from the Pacific plate motion over a hotspot, it differs in the lack of the systematic age migration that is known to be symptomatic of such a set-

ting. The oldest age for alkaline plutonic rocks (67 ± 2 Ma) in Cameroon was obtained on the Golda Zuelva granite in the NE, and the youngest (10.8 ± 0.5 Ma) ages comes from a Mount Rumpi gabbro in the SW (Fig. 11). The oldest volcanic ages (K-Ar) so far obtained (46.7 ± 1.1 Ma and 45.5 ± 1.1 Ma) are in an olivine basalt from the Bamoun Plateau (Moundi et al., 2007) and the Mbépit rhyolites in the Noun Plain (Wandji et al., 2008), next to the Bamoun Plateau (Fig. 2), respectively. The transitional lavas from the Bamoun Plateau give a K-Ar age of 51.8 ± 1.2 Ma (Moundi et al., 2007), and those of Mount Bangou give a K-Ar age of 44.5 ± 1 Ma (Fosso et al., 2005). Another striking point is the SW younging of the earliest exposed volcanic rocks in the oceanic sector from Principe (31 Ma) to São Tomé (13 Ma) and Annobon (4.8 Ma) Islands, consistent with the suggested motion of the African plate over this period of time, and the fact that all three of these islands have been active in the past 5 m.y. (Lee et al., 1994). Aka et al. (2004) showed that Quaternary volcanism (≤ 6 Ma) have been synchronous along the whole Cameroon Line.

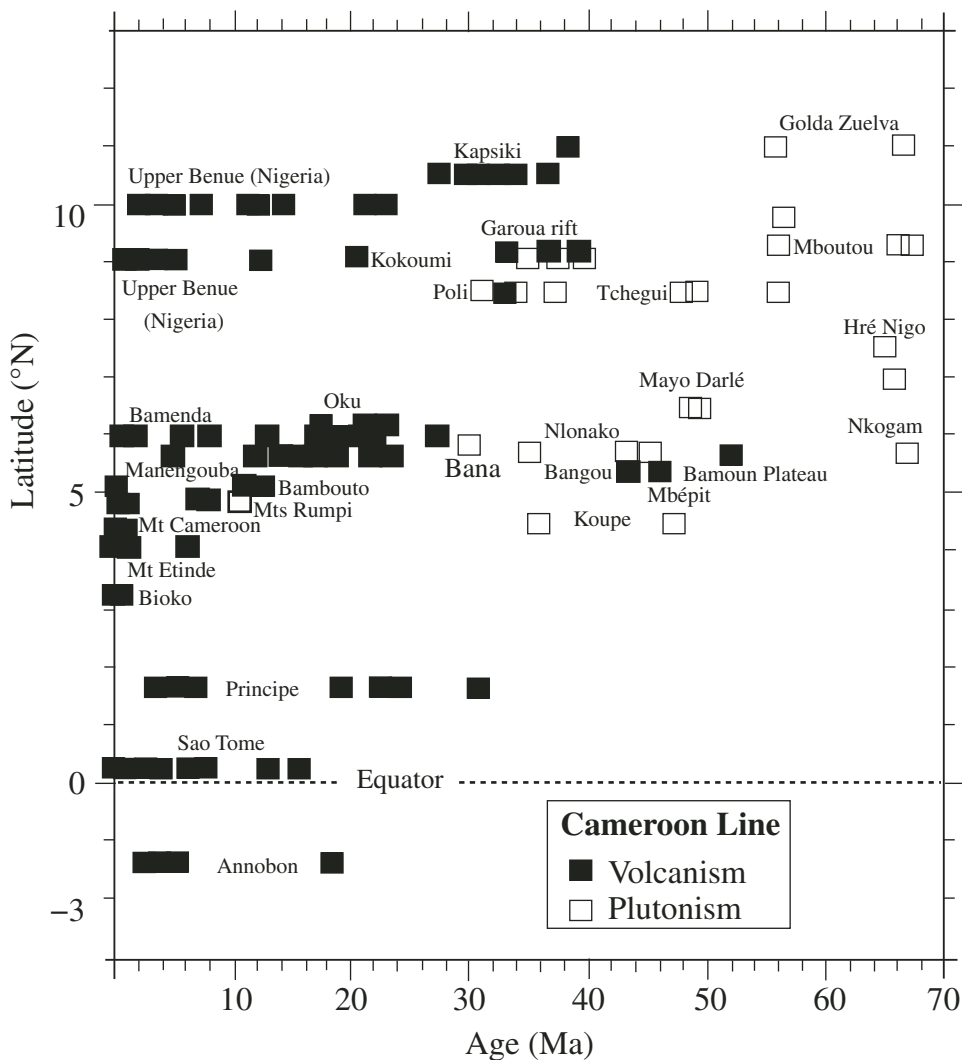


Figure 11. Age distribution of plutonic and volcanic rocks from the Cameroon Line. Data are from Déruelle et al. (2007, and references therein), Kamdem et al. (2002), Moundi et al. (2007), Kamgang et al. (2007, 2008), Wandji et al. (2008), and Nkouathio et al. (2008).

At a continental scale, the distribution of alkaline complexes in west-central Africa is consistent with two trends. (1) There is a time-space link among the magmatic alkaline provinces from 407 ± 8 Ma in Aïr (north Niger) (Moreau et al., 1994) and 330–260 Ma in Damagaram-Mounio (south Niger) through 213–141 Ma in Jos Plateau (northern Nigeria) (Bowden et al., 1976) and 147–49 Ma in the Benue Trough (southern Nigeria) (Coulon et al., 1996) to 67 Ma to present day in Cameroon (Kamdem et al., 2002). The migration follows a N-S trajectory from Aïr in Niger to Jos Plateau in Nigeria, changing southeastward toward Cameroon. (2) Parallel NE-SW trends are seen from Nigeria to Cameroon through the Benue Trough, with only the ages of Younger Granites of Nigeria becoming steadily younger from NE to SW over a distance of 420 km (see Fig. 4; Ngako et al., 2006). A similar N-S trend, followed by a NE-SW trend, links the N-S East African Rift System to the NE-SW major igneous lineaments in South Africa (Scholz et al., 1976; Modisi et al., 2000; Kinabo et al., 2007; Moore et al., 2008). The relevant interprovince time-space migration from Niger to Cameroon (410 Ma–Holocene over a distance of ~1650 km) cannot be explained by simple motion of a plate above one stationary hotspot, because hotspots older than 150 Ma do not in general have an active trace (Duncan and Richards, 1991; Courtillot et al., 1999), and 1650 km is three times the postulated diameter for the St. Helena plume (Wilson, 1992). A similar conclusion has been drawn for the NE-SW alignment of alkaline pipes without systematic age migration in South Africa (Moore et al., 2008).

The lack of a steady time-space migration despite the clear SW-NE trend for the Cameroon alkaline complexes and volcanic massifs, added to the observations presented herein, was recently explained in terms of complex interactions between hotspots and Precambrian faults (Ngako et al., 2006), since each trend is parallel to a shear or fracture zone: N-S Raghane shear zone for the Aïr area, NE-trending wrench fault for Jos Plateau, NE-trending dextral shear zone for the Benue Trough, and NE-trending sinistral fault oblique to the Central African shear zone or fracture zones directed N70°E for the Cameroon Line. In the detail, from the model of Hieronymus and Berkovici (2000) attributing the multiple lines of volcanoes to interaction of flexural, membrane, and tectonic stresses, Ngako et al. (2006) explained the parallel NE-SW magmatic lineaments between Nigeria, Benue Trough, and Cameroon Line, having overlapping ages from one lineament to another, as follows: the NE-SW-trending Younger Granites of Nigeria initiated at time of plate motion change (N to NE), marked by a change in the tectonic stress field as already mentioned by Demaiïfe and Moreau (1996). They were emplaced following some local perturbations, and the formation of a small sublithospheric melting anomaly. Here, melt migration may have been aided by tectonic and flexural stresses, such that the complexes are limited in extent to the melting region of the plume. Membrane stresses perpendicular to the axis of the Younger Granites trend interacted with the flexural stresses to generate the NE-SW Benue Trough and Cameroon Line trends. This mechanism of emplacement is consistent with the concept developed

by Bailey (1992, 1993) to explain the episodic nature of alkaline volcanism across the entire African continent.

CONCLUSION AND PERSPECTIVES

Cameroon Line magmatism is the second most important geological curiosity in Africa, after the East African Rift system. Its mechanism of emplacement and petrogenesis must take into account the fact that it is associated with overall N-S-trending west-central African magmatism, but that the Cameroon Line itself trends NE-SW, parallel to the Benue Trough and Jos Plateau magmatism. Given the similarity of this overall structure with that of the East African Rift system and its NE-SW prolongation in South Africa, a mechanism of episodic emplacement of alkaline magmatism through the entire African continent can better be explained in terms of complex interactions between hotspots and Precambrian faults, that is, on the one hand, mantle plumes acting in succession, and on the other hand, lithospheric fractures that induce oblique alignments of new magmatic complexes.

The structural control of the emplacement of Cameroon Line alkaline magmatism is also suggested or enhanced by the clear parallelism between alignment of alkaline complexes and Central Cameroon shear zone strike (a major Pan-African structure of the continent) in the Tikar Plain (Ngako et al., 2006). Given the mineral deposit potentials of shear zones and associated magmatic rocks, which have been well established worldwide, research toward a better understanding of both the shear zone structure (Njonfang et al., 2006, 2008) and those complexes needs to be undertaken. Methods of modern petrology and structural geology are needed here.

ACKNOWLEDGMENTS

The authors sincerely thank Andy Moore from Botswana and Kathryn Goodenough from Edinburgh for the contribution of their comments to the improvement of this new version.

REFERENCES CITED

- Aka, F.T., Nagao, K., Kusakabe, M., Sumino, H., Tanyileke, G., Ateba, B., and Hell, J., 2004, Symmetrical helium isotope distribution on the Cameroon volcanic line, West Africa: *Chemical Geology*, v. 203, p. 205–223, doi:10.1016/j.chemgeo.2003.10.003.
- Bailey, D.K., 1992, Episodic alkaline igneous activity across Africa: Implications for the causes of continental break-up, in Storey, B.C., Alabaster, T., and Pankhurst, R.J., eds., *Magmatism and the Causes of Continental Break-Up*: Geological Society of London Special Publication 68, p. 91–98.
- Bailey, D.K., 1993, Petrogenetic implications of the timing of alkaline, carbonate and kimberlite igneous activity in Africa: *South African Journal of Geology*, v. 96, p. 67–74.
- Bogaard, P.J.F., and Wörner, G., 2003, Petrogenesis of basanitic to tholeiitic volcanic rocks from the Miocene Vogelsberg, central Germany: *Journal of Petrology*, v. 44, p. 569–602, doi:10.1093/petrology/44.3.569.
- Bowden, P., van Breemen, O., Hutchinson, J., and Turner, J.C., 1976, Palaeozoic and Mesozoic age trends for some ring complexes in Niger and Nigeria: *Nature*, v. 259, p. 297–299, doi:10.1038/259297a0.
- Burke, K., 2001, Origin of the Cameroon Line of volcano-capped swells: *Journal of Geology*, v. 109, p. 349–362, doi:10.1086/319977.

- Caldeira, R., and Munhá, J.M., 2002, Petrology of ultramafic nodules from São Tomé Island, Cameroon volcanic line (oceanic sector): *Journal of African Earth Sciences*, v. 34, p. 231–246, doi:10.1016/S0899-5362(02)00022-2.
- Chen, J., Henderson, C.M.B., and Foland, A., 1994, Open-system, subvolcanic magmatic evolution: Constraints on the petrogenesis of the Mont Brome alkaline complex, Canada: *Journal of Petrology*, v. 35, p. 1127–1153.
- Coulon, C., Vidal, P., Dupuy, C., Baudin, P., Popoff, M., Maluski, H., and Hermitte, D., 1996, The Mesozoic to early Cenozoic magmatism of the Benue Trough (Nigeria): Geochemical evidence for the involvement of the St. Helena plume: *Journal of Petrology*, v. 37, p. 1341–1358, doi:10.1093/petrology/37.6.1341.
- Courtillet, V., Jaupart, C., Manighetti, I., Tapponnier, P., and Besse, J., 1999, On causal links between flood basalts and continental breakup: Earth and Planetary Science Letters, v. 166, p. 177–195, doi:10.1016/S0012-821X(98)00282-9.
- Demaiffe, D., and Moreau, C., 1996, Crustal growth in Aïr (Niger, West Africa): Significance of the Palaeozoic anorthosite-bearing anorogenic complexes, in Demaiffe, D., ed., *Petrology and Geochemistry of Magmatic Suites of Rocks in the Continental and Oceanic Crusts*: Brussels, Belgium, Université Libre de Bruxelles, p. 35–49.
- Déruelle, B., Moreau, C., Nkoubou, C., Kambou, R., Lissom, J., Njonfang, E., Ghogomu, R.T., and Nono, A., 1991, The Cameroon Line: A review, in Kampunzu, A.B., and Lubala, R.T., eds., *Magmatism in Extensional Structural Settings: The Phanerozoic African Plate*: Berlin, Springer, p. 274–327.
- Déruelle, B., Bardintzeff, J.-M., Cheminée, J.-L., Ngounouno, I., Lissom, J., Nkoubou, C., Etamé, J., Hell, J.V., Tanyileke, G., N'ni, J., Ateba, B., Ntepe, N., Nono, A., Wandji, P., Fosso, J., and Nkouathio, D.G., 2000, Eruptions simultanées de basalte alcalin et de hawaïte au mont Cameroun (28 mars–17 avril 1999): *Comptes Rendus de l'Académie des Sciences de Paris*, v. 331, p. 525–531.
- Déruelle, B., Ngounouno, I., and Bardintzeff, J.-M., 2001, Wherlites et pyroxénites en nodules dans les basaltes du Mt. Cameroun: Évidence d'un métasomatisme mantellique: *Journal de la Société Géoscience de l'Afrique*, v. 1, p. 90–91.
- Déruelle, B., Ngounouno, I., and Demaiffe, D., 2007, The “Cameroon Hot Line” (CHL): A unique example of active alkaline intraplate structure in both oceanic and continental lithospheres: *Comptes Rendus Geoscience*, v. 339, p. 589–600, doi:10.1016/j.crte.2007.07.007.
- Duggan, M.B., 1988, Zirconium-rich sodic pyroxene in felsic volcanics from the Warrumbungle volcano, central New South Wales, Australia: *Mineralogical Magazine*, v. 52, p. 491–496, doi:10.1180/minmag.1988.052.367.07.
- Duncan, R.A., and Richards, M.A., 1991, Hotspots, mantle plumes, flood basalts, and true polar wander: *Reviews of Geophysics*, v. 29, p. 31–50, doi:10.1029/90RG02372.
- Ebinger, C.J., Bechtel, T.D., Forsyth, D.W., and Bowin, C.O., 1989, Effective elastic plate thickness beneath the East African and Afar Plateaus and dynamic compensation of the uplifts: *Journal of Geophysical Research*, v. 94, p. 2883–2901, doi:10.1029/JB094iB03p02883.
- Edgar, A.D., 1974, On the use of the term “agpaitic”: *Mineralogical Magazine*, v. 39, p. 729–730, doi:10.1180/minmag.1974.039.306.18.
- Fitton, J.G., 1987, The Cameroon Line: West Africa: A comparison between oceanic and continental alkaline volcanism, in Fitton, J.G., and Upton, B.G.J., eds., *Alkaline Igneous Rocks*: Geological Society of London Special Publication 30, p. 273–291.
- Fitton, J.G., and Dunlop, H.M., 1985, The Cameroon Line, West Africa, and its bearing on the origin of oceanic and continental alkali basalts: *Earth and Planetary Science Letters*, v. 72, p. 23–38, doi:10.1016/0012-821X(85)90114-1.
- Fosso, J., Ménard, J.-J., Bardintzeff, J.-M., Wandji, P., Tchoua, F.M., and Bellon, H., 2005, Les laves du mont Bangou: Une première manifestation volcanique éocène, à affinité transitionnelle, de la Ligne du Cameroun: *Comptes Rendus Geoscience*, v. 337, p. 315–325, doi:10.1016/j.crte.2004.10.014.
- Ghogomu, R.T., Moreau, C., Brown, W., and Rocci, G., 1989, The Ntumbaw Complex, NW Cameroon: An atypical anorogenic ring-complex of intermediate composition: *Journal of African Earth Sciences*, v. 8, p. 1–9, doi:10.1016/S0899-5362(89)80004-1.
- Hieronymus, C.F., and Berkovici, D., 2000, Non-hotspot formation of volcanic chains: Control of tectonic and flexural stresses on magma transport: *Earth and Planetary Science Letters*, v. 181, p. 539–554, doi:10.1016/S0012-821X(00)00227-2.
- Jacquemin, H., Sheppard, S.M.F., and Vidal, P., 1982, Isotopic geochemistry (O, Sr, Pb) of the Golda Zuelva and Mboutou anorogenic complexes, North Greenland: Mantle origin with evidence for crustal contamination: *Earth and Planetary Science Letters*, v. 61, p. 97–111, doi:10.1016/0012-821X(82)90042-5.
- Jones, A.P., and Peckett, A., 1980, Zirconium-bearing aegirines from Motzfeldt, South Greenland: Contributions to Mineralogy and Petrology, v. 75, p. 251–255, doi:10.1007/BF01166764.
- Kagou Dongmo, A., Nkouathio, D., Nono, A., Kwekam, M., Tematio, P., Wandji, P., Tchoua, F., Pouclet, A., and Bourdier, J.-L., 2006, Discovery of Strombolian cone at Totap-Tapsetsa, north-east slope of Mount Bambouto: Implications in the petrogenesis and the volcanic activity of Bambouto volcanoe (Cameroon line), in Abstracts, Cities on Volcanoes 4, 23–27 January 2006: Quito.
- Kagou Dongmo, A., Nkouathio, D.G., Pouclet, A., Bardintzeff, J.-M., Wandji, P., Nono, A., and Guillou, H., 2010, The discovery of late Quaternary basalt on Mount Bambouto: Implications for recent widespread volcanic activity in the southern Cameroon Line: *Journal of African Earth Sciences*, v. 57, p. 96–108, doi:10.1016/j.jafrearsci.2009.07.015.
- Kamdern, J.B., Kraml, M., Keller, J., and Henjes-Kurst, F., 2002, Cameroon Line magmatism: Conventional K/Ar and single-crystal laser $^{40}\text{Ar}/^{39}\text{Ar}$ ages of rocks and minerals from Hossere Nigo anorogenic complex, Cameroon: *Journal of African Earth Sciences*, v. 35, p. 99–105, doi:10.1016/S0899-5362(02)00002-7.
- Kamgang, P., Njonfang, E., Chazot, G., and Tchoua, F., 2007, Géochimie et géochronologie des laves felsiques des Monts Bamenda (ligne volcanique du Cameroun): *Comptes Rendus Geoscience*, v. 339, p. 659–666, doi:10.1016/j.crte.2007.07.011.
- Kamgang, P., Chazot, G., Njonfang, E., and Tchoua, F., 2008, Geochemistry and geochronology of mafic rocks from Bamenda Mountains (Cameroon): Source composition and crustal contamination along the Cameroon volcanic line: *Comptes Rendus Geoscience*, v. 340, p. 850–857, doi:10.1016/j.crte.2008.08.008.
- Kinabo, B.D., Atekwana, E.A., Hogan, J.P., Modisi, M.P., Wheaton, D.D., and Kampunzu, A.B., 2007, Early structural development of the African rift zone, NW Botswana: *Journal of African Earth Sciences*, v. 48, p. 125–136, doi:10.1016/j.jafrearsci.2007.02.005.
- Kling, G.W., Claris, M.A., Compton, H.R., Devine, J.D., Evans, W.C., Humphrey, A.M., Koenigsberg, E.J., Lookwood, J.P., Tuttle, M.L., and Wagner, G.N., 1987, The 1986 lake Nyos gas disaster in Cameroon, West Africa: *Science*, v. 236, p. 169–175, doi:10.1126/science.236.4798.169.
- Kuepouo, G., Tchouankoué, J.P., Nagao, T., and Sato, H., 2006, Transitional tholeiitic basalts in the Tertiary Bana volcano-plutonic complex, Cameroon Line: *Journal of African Earth Sciences*, v. 45, p. 318–332, doi:10.1016/j.jafrearsci.2006.03.005.
- Larsen, L.M., 1976, Clinopyroxenes and coexisting mafic minerals from the alkaline Ilímaussaq intrusion, South Greenland: *Journal of Petrology*, v. 17, p. 258–290.
- Le Bas, M.J., Le Maître, R.W., Streckeisen, A., and Zanettin, B., 1986, A chemical classification of volcanic rocks based on the total alkali silica diagram: *Journal of Petrology*, v. 27, p. 745–750.
- Lee, D.C., Halliday, A.N., Fitton, G.J., and Poli, G., 1994, Isotopic variations with distance and time in the volcanic islands of the Cameroon Line: Evidence of the mantle plume origin: *Earth and Planetary Science Letters*, v. 123, p. 119–138, doi:10.1016/0012-821X(94)90262-3.
- Lee, D.C., Halliday, A.N., Davies, G.R., Essene, E.J., Fitton, J.G., and Temdjim, R., 1996, Melt enrichment of shallow depleted mantle: A detailed petrological, trace element and isotopic study of mantle-derived xenoliths and megacrysts from the Cameroon Line: *Journal of Petrology*, v. 37, p. 415–441, doi:10.1093/petrology/37.2.415.
- Leterrier, J., Maury, J.C., Thonon, P., Girard, D., and Marchal, M., 1982, Clinopyroxene as a method of identification of the magmatic affinities of paleo-volcanic series: *Earth and Planetary Science Letters*, v. 59, p. 139–154, doi:10.1016/0012-821X(82)90122-4.
- Marzoli, A., Renne, P.R., Piccirillo, E.M., Castorina, F., Bellieni, G., Melfi, A.J., Nyobe, J.B., and N'ni, J., 1999, Silicic magmas from the continental Cameroon volcanic line (Oku, Bambouto and Ngaoundere): $^{40}\text{Ar}/^{39}\text{Ar}$ dates, petrology, Sr-Nd-O isotopes and their petrogenetic significance: *Contributions to Mineralogy and Petrology*, v. 135, p. 133–150, doi:10.1007/s004100050502.
- Marzoli, A., Piccirillo, E.M., Renne, P.R., Bellieni, G., Iacumin, M., Nyobe, J.B., and Tongwa, A.T., 2000, The Cameroon volcanic line revisited:

- Petrogenesis of continental basaltic magmas from lithospheric and asthenospheric mantle sources: *Journal of Petrology*, v. 41, p. 87–109, doi:10.1093/petrology/41.1.87.
- Meyers, J.B., Rosendahl, B.R., Harrison, C.G.A., and Ding, Z.-D., 1998, Deep-imaging seismic and gravity results from offshore Cameroon volcanic line and speculation of African hot-lines: *Tectonophysics*, v. 284, p. 31–63, doi:10.1016/S0040-1951(97)00173-X.
- Middlemost, E.A.K., 1975, The basalt clan: *Earth-Science Reviews*, v. 11, p. 337–364, doi:10.1016/0012-8252(75)90039-2.
- Mitchell, R.H., and Platt, K.G., 1978, Mafic mineralogy of ferroaugite syenite from the Coldwell alkaline complex, Ontario, Canada: *Journal of Petrology*, v. 19, p. 627–651.
- Modisi, M.P., Atekwana, E.A., Kampunzu, A.B., and Nqwisany, T.H., 2000, Rift kinematics during the incipient stages of continental fragmentation: Evidence from the nascent Okavango Rift, NW Botswana: *Geology*, v. 28, p. 939–942, doi:10.1130/0091-7613(2000)28<939:RKDTIS>2.0.CO;2.
- Montigny, R., Ngounouno, I., and Déruelle, B., 2004, Âges K-Ar des roches magmatiques du fossé de Garoua (Cameroun): Leur place dans le cadre de la "Ligne du Cameroun": *Comptes Rendus Geoscience*, v. 336, p. 1463–1471, doi:10.1016/j.crte.2004.08.005.
- Moore, A., Blenkinsop, T., and Cotterill, F., 2008, Controls on post-Gondwana alkaline volcanism in southern Africa: *Earth and Planetary Science Letters*, v. 268, p. 151–164, doi:10.1016/j.epsl.2008.01.007.
- Moreau, C., Regnault, J.-M., Déruelle, B., and Robineau, B., 1987, A new tectonic model for the Cameroon Line, Central Africa: *Tectonophysics*, v. 139, p. 317–334.
- Moreau, C., Demaiffe, D., Bellion, Y., and Boullier, A.M., 1994, A tectonic model for the location of Palaeozoic ring complexes in Aïr (Niger, West Africa): *Tectonophysics*, v. 234, p. 129–146, doi:10.1016/0040-1951(94)90208-9.
- Morimoto, N., Fabriès, J., Ferguson, A.K., Ginzburg, I.V., Ross, M., Seifert, F.A., and Zussman, J., 1988, Nomenclature of pyroxenes: *Mineralogical Magazine*, v. 52, p. 535–550, doi:10.1180/minmag.1988.052.367.15.
- Moundi, A., 2004, Les Basaltes des Plateaux du Plateau Bamoun: Pétrologie, Géochimie et Géochronologie—Implications sur les Sources des Magmas, Leurs Contextes et Évolutions Géodynamiques [Doctorat d'État thesis]: Yaoundé, Cameroon, Université de Yaoundé I, 259 p.
- Moundi, A., Ménard, J.-J., Reusser, E., Tchoua, M.F., and Dietrich, V.J., 1996, Découverte de basaltes transitionnels dans le secteur continental de la Ligne du Cameroun (massif du Mbam, Ouest-Cameroun): *Comptes Rendus de l'Académie des Sciences de Paris*, v. 322, p. 831–837.
- Moundi, A., Wandji, P., Bardintzeff, J.-M., Ménard, J.-J., Okomo Atouba, L.C., Reusser, E., Bellon, H., and Tchoua, M.F., 2007, Les basaltes éocènes à affinité transitionnelle du plateau Bamoun, témoins d'un réservoir mantellique enrichi sous la ligne volcanique du Cameroun: *Comptes Rendus Geoscience*, v. 339, p. 396–406, doi:10.1016/j.crte.2007.04.001.
- Nana, R., Dietrich, V.J., Tchoua, F.M., and Reusser, E., 2001, Pétrologie des péridotites en enclaves dans les basaltes récents de la région de Nyos (Ligne du Cameroun), in *Proceedings of the 12th Geological Society of Africa Conference*, Yaoundé, Cameroon: *Journal of Geoscience Society of Cameroon Special Publication 1*, p. 83–84.
- Nash, W.P., and Wilkinson, J.F.G., 1970, Shonkin Sag laccolith, Montana. 1. Mafic minerals and estimates of temperature, pressure, oxygen fugacity and silica activity: *Contributions to Mineralogy and Petrology*, v. 25, p. 241–269, doi:10.1007/BF00399286.
- Ngako, V., Njonfang, E., Aka Tongwa, F., Affaton, P., and Nnange Metuk, J., 2006, The north-south Paleozoic to Quaternary trend of alkaline magmatism from Niger-Nigeria to Cameroon: Complex interaction between hotspots and Precambrian faults: *Journal of African Earth Sciences*, v. 45, p. 241–256, doi:10.1016/j.jafrearsci.2006.03.003.
- Ngounouno, I., and Déruelle, B., 2007, Pétrologie des xénolites de wehrlites et clinopyroxénites du Mont Cameroun: Évidence d'un métasomatisme mantellique: *Journal of the Cameroon Academy of Sciences*, v. 7, p. 35–46.
- Ngounouno, I., Déruelle, B., and Demaiffe, D., 2000, Petrology of the bimodal Cenozoic volcanism of the Kapsiki Plateau (northernmost Cameroon, Central Africa): *Journal of Volcanology and Geothermal Research*, v. 102, p. 21–44, doi:10.1016/S0377-0273(00)00180-3.
- Ngounouno, I., Moreau, C., Déruelle, B., Demaiffe, D., and Montigny, R., 2001, Pétrologie du complexe alcalin sous-saturé de Kokoumi (Cameroun): *Bulletin de la Société Géologique de France*, v. 172, p. 675–686, doi:10.2113/172.6.675.
- Ngounouno, I., Déruelle, B., Demaiffe, D., and Montigny, R., 2003, Petrology of Cenozoic volcanism in the Upper Benue valley, northern Cameroon (Central Africa): *Contributions to Mineralogy and Petrology*, v. 145, p. 87–106, doi:10.1007/s00410-002-0438-6.
- Ngounouno, I., Déruelle, B., Montigny, R., and Demaiffe, D., 2006, Les camptonites du Mont Cameroun, Afrique: *Comptes Rendus Géosciences*, v. 338, p. 537–544.
- Ngounouno, I., Nguindama, D., Kamgang, P., and Déruelle, B., 2008, Petrology of spinel lherzolite xenoliths in alkali basalts from Liri, south of Kapsiki Plateau (northernmost Cameroon hot line): *Journal of Cameroon Academy of Sciences*, v. 8, p. 31–42.
- Nielsen, T.F.D., 1979, The occurrence and formation of Ti-aegirine in peralkaline syenites: An example from the Tertiary ultramafic alkaline Gardiner complex, East Greenland: *Contributions to Mineralogy and Petrology*, v. 69, p. 235–244, doi:10.1007/BF00372325.
- Njonfang, E., and Moreau, C., 1996, The mineralogy and geochemistry of a subvolcanic alkaline complex from the Cameroon Line: The Nda Ali massif, southwest Cameroon: *Journal of African Earth Sciences*, v. 22, p. 113–132, doi:10.1016/0899-5362(96)00126-1.
- Njonfang, E., and Moreau, C., 2000, The mafic mineralogy of the Pandé massif, Tikar Plain, Cameroon: Implications for a peralkaline affinity and emplacement from highly evolved alkaline magma: *Mineralogical Magazine*, v. 64, p. 525–537, doi:10.1180/002646100549409.
- Njonfang, E., and Nono, A., 2003, Clinopyroxene from some felsic alkaline rocks of the Cameroon Line, Central Africa: Petrological implications: *European Journal of Mineralogy*, v. 15, p. 527–542, doi:10.1127/0935-1221/2003/0015-0527.
- Njonfang, E., Kamgang, P., Ghogomu, T.R., and Tchoua, F.M., 1992, The geochemical characteristics of some plutonic-volcanic complexes along the southern part of the Cameroon Line: *Journal of African Earth Sciences*, v. 14, p. 255–266, doi:10.1016/0899-5362(92)90102-1.
- Njonfang, E., Ngako, V., Kwékam, M., and Affaton, P., 2006, Les orthogneiss calco-alcalins de Fouban-Bankim: Témoins d'une zone interne de marge active panafricaine en cisaillement: *Comptes Rendus Geoscience*, v. 338, p. 606–616, doi:10.1016/j.crte.2006.03.016.
- Njonfang, E., Ngako, V., Moreau, C., Affaton, P., and Diot, H., 2008, Restraining bends in high temperature shear zones: The "Central Cameroon shear zone," Central Africa: *Journal of African Earth Sciences*, v. 52, p. 9–20, doi:10.1016/j.jafrearsci.2008.03.002.
- Nkouandou, O.F., Ngounouno, I., Déruelle, B., Ohnenstetter, D., Montigny, R., and Demaiffe, D., 2008, Petrology of the Mio-Pliocene volcanism to the north and east of Ngaoundéré (Adamawa, Cameroon): *Comptes Rendus Geoscience*, v. 340, p. 28–37, doi:10.1016/j.crte.2007.10.012.
- Nkouathio, D.G., Kagou Dongmo, A., Bardintzeff, J.M., Wandji, P., Bellon, H., and Poulet, A., 2008, Evolution of volcanism in graben and horst structures along the Cenozoic Cameroon Line (Africa): Implications for tectonic evolution and mantle source composition: *Mineralogy and Petrology*, v. 94, p. 287–303, doi:10.1007/s00710-008-0018-1.
- Nkoumbou, C., Déruelle, B., and Velde, D., 1995, Petrology of Mt. Etinde nephelinites series: *Journal of Petrology*, v. 36, p. 373–395.
- Nono, A., Déruelle, B., Demaiffe, D., and Kambou, R., 1994, Tchabal Nganha volcano in Adamawa (Cameroon): Petrology of a continental alkaline lava series: *Journal of Volcanology and Geothermal Research*, v. 60, p. 147–178, doi:10.1016/0377-0273(94)90066-3.
- Nono, A., Njonfang, E., Kagou Dongmo, A., Nkouathio, D.G., and Tchoua, F.M., 2004, Pyroclastic deposits of the Bambouto volcano (Cameroon Line, Central Africa): Evidence of a Strombolian initial phase: *Journal of African Earth Sciences*, v. 39, p. 409–414, doi:10.1016/j.jafrearsci.2004.07.026.
- Nzolang, C., 2005, Crustal Evolution of the Precambrian Basement in West Cameroon: Inference from Geochemistry, Sr-Nd and Experimental Investigation of Some Granitoids and Metamorphic Rocks [Ph.D. thesis]: Niigata, Japan, Graduate School of Science and Technology, Niigata University, 207 p.
- Parsons, I., 1978, Feldspars and fluids in cooling plutons: *Mineralogical Magazine*, v. 42, p. 1–17.
- Parsons, I., Brown, W.L., and Jacquemin, H., 1986, Mineral chemistry and crystallization at the Mboutou layered gabbro-syenite-granite complex, North Cameroon: *Journal of Petrology*, v. 27, p. 1305–1329.
- Pearce, J.A., and Cann, J.R., 1973, Tectonic setting of basic volcanic rocks determined using trace element analyses: *Earth and Planetary Science Letters*, v. 19, p. 290–300, doi:10.1016/0012-821X(73)90129-5.

- Poudjom Djomani, Y.H., Diamant, M., and Wilson, M., 1997, Lithospheric structure across the Adamawa Plateau (Cameroon) from gravity studies: *Tectonophysics*, v. 273, p. 317–327, doi:10.1016/S0040-1951(96)00280-6.
- Rankenburg, K., Lassister, J.C., and Brey, G., 2005, The role of continental crust and lithospheric mantle in the genesis of Cameroon volcanic line lavas: Constraints from isotopic variations in lavas and megacrysts from the Bui and Jos Plateaux: *Journal of Petrology*, v. 46, p. 169–190, doi:10.1093/petrology/egh067.
- Salviulo, G., Secco, L., Marzoli, A., Piccirillo, E.M., and Nyobé, J.B., 2000, Ca-rich pyroxene from basic to silicic volcanic rocks from the Cameroon volcanic line (West-Africa): Crystal chemistry and petrological relationships: *Mineralogy and Petrology*, v. 70, p. 73–88, doi:10.1007/s007100070014.
- Scholz, C.H., Kocynski, T.A., and Hutchins, D.G., 1976, Evidence for incipient rifting in southern Africa: *Geophysical Journal International*, v. 44, p. 135–144, doi:10.1111/j.1365-246X.1976.tb00278.x.
- Stephenson, D., and Upton, B.G.J., 1982, Ferromagnesian silicates in a differentiated alkaline complex: Kûngnat Fjeld, South Greenland: *Mineralogical Magazine*, v. 46, p. 283–300, doi:10.1180/minmag.1982.046.340.02.
- Stracke, A., Hofmann, A.W., and Hart, S.R., 2005, FOZO, HIMU, and the rest of the mantle zoo: *Geochemistry Geophysics Geosystems*, v. 6, doi:10.1029/2004GC000824.
- Streckeisen, A.L., 1976, To each plutonic rock its proper name: *Earth-Science Reviews*, v. 12, p. 1–33, doi:10.1016/0012-8252(76)90052-0.
- Suh, C.E., Sparks, R.S.J., Fitton, J.G., Ayonghe, S.N., Annen, C., Nana, R., and Luckmen, A., 2003, The 1999 and 2000 eruptions of Mount Cameroon: Eruption behaviour and petrochemistry of lava: *Bulletin of Volcanology*, v. 65, p. 267–281, doi:10.1007/s00445-002-0257-7.
- Suh, C.E., Luhr, J.F., and Njome, M.S., 2008, Olivine-hosted glass inclusions from scoria erupted in 1954–2000 at Mount Cameroon volcano, West Africa: *Journal of Volcanology and Geothermal Research*, v. 169, p. 1–33, doi:10.1016/j.jvolgeores.2007.07.004.
- Tamen, J., Nkoumbou, C., Mouafo, L., Reusser, E., and Tchoua, M.F., 2007, Petrology and geochemistry of monogenic volcanoes of Barombi Koto volcanic field (Kumba graben, Cameroon volcanic line): Implications for mantle source characteristics: *Comptes Rendus Geoscience*, v. 339, p. 799–809, doi:10.1016/j.crte.2007.09.007.
- Tchoua, F.M., 1973, Sur l'existence d'une phase initiale ignimbritique dans le volcanisme des monts Bambouto (Cameroun): *Comptes Rendus de l'Académie des Sciences Paris*, v. 276, p. 2863–2866.
- Teitchou, M.I., Grégoire, M., Dantas, C., and Tchoua, F.M., 2007, Le manteau supérieur à l'aplomb de la plaine de Kumba (ligne du Cameroun), d'après les enclaves de péridotites à spinelles dans les laves basaltiques: *Comptes Rendus Geoscience*, v. 339, p. 101–109, doi:10.1016/j.crte.2006.12.006.
- Temdjim, R., Boivin, P., Chazot, G., Robin, C., and Rouleau, E., 2004, L'hétérogénéité du manteau supérieur à l'aplomb du volcan de Nyos (Cameroun) révélée par les enclaves ultrabasiques: *Comptes Rendus Geoscience*, v. 336, p. 1239–1244, doi:10.1016/j.crte.2004.07.005.
- Thirlwall, F.M., Upton, B.G.J., and Jenkins, C., 1994, Interaction between continental lithosphere and Iceland plume—Sr-Nd-Pb isotope geochemistry of Tertiary basalts, NE Greenland: *Journal of Petrology*, v. 35, p. 839–879.
- Wandji, P., Tchokona Seuwi, D., Bardintzeff, J.-M., Bellon, H., and Platevoet, B., 2008, Rhyolites of the Mbépité Massif in the Cameroon volcanic line: An early extrusive volcanic episode of Eocene age: *Mineralogy and Petrology*, v. 94, p. 271–286, doi:10.1007/s00710-008-0013-6.
- Wandji, P., Tsafack, J.P.F., Bardintzeff, J.-M., Nkouathio, D.G., Kagou Dogmo, A., Bellon, H., and Guillou, H., 2009, Xenoliths of dunites, wehrlites and clinopyroxenites in the basanites from Batoke volcanic cone (Mount Cameroon, Central Africa): Petrogenetic implications: *Mineralogy and Petrology*, v. 96, p. 81–98, doi:10.1007/s00710-008-0040-3.
- Watson, E.B., 1979, Zircon saturation in felsic liquids: Experimental results and application to trace element geochemistry: *Contributions to Mineralogy and Petrology*, v. 70, p. 407–419, doi:10.1007/BF00371047.
- Wilson, M., 1992, Magmatism and continental rifting during the opening of the South Atlantic Ocean: A consequence of Lower Cretaceous super-plume activity?, in Storey, B.C., Alabaster, T., and Pankhurst, R.J., eds., *Magmatism and the Causes of Continental Break-Up*: Geological Society of London Special Publication 68, p. 241–255.
- Yokoyama, T., Aka, F.T., Kusakabe, M., and Nakamura, E., 2007, Plume-lithosphere interaction beneath Mt. Cameroon volcano, West Africa: Constraints from ^{238}U - ^{230}Th - ^{226}Ra and Sr-Nd-Pb isotope systematics: *Geochimica et Cosmochimica Acta*, v. 71, p. 1835–1854, doi:10.1016/j.gca.2007.01.010.
- Youmen, D., 1994, Evolution Volcanologique, Pétrologique et Temporelle de la Caldera des Monts Bambouto (Cameroun) [Ph.D. thesis]: Kiel, Germany, Universität Kiel, 294 p.

MANUSCRIPT ACCEPTED BY THE SOCIETY 9 NOVEMBER 2010

Mineralogical and geochemical fingerprints of mantle metasomatism beneath Nyos volcano (Cameroon volcanic line)

M.I. Teitchou

*Institut de Recherches Géologiques et Minières, IRGM/ARGV Ekona, B.P. 370 Buéa, Cameroon, and
Département des Sciences de la Terre, Université de Yaoundé-1, B.P. 812 Yaoundé, Cameroon*

M. Grégoire*

*GET–UMR 5562 (Géosciences-Environnement-Toulouse–Unité Mixte de Recherche 5562), Observatoire Midi Pyrénées,
Université de Toulouse-3, 14, avenue Édouard-Belin, 31400 Toulouse, France*

R. Temdjim

R.T. Ghogomu

Département des Sciences de la Terre, Université de Yaoundé-1, B.P. 812 Yaoundé, Cameroon

C. Ngwa

F.T. Aka

Institut de Recherches Géologiques et Minières, IRGM/ARGV Ekona, B.P. 370 Buéa, Cameroon

ABSTRACT

Basaltic lavas of Nyos volcano (Cameroon) mostly contain mantle peridotite xenoliths consisting of spinel-bearing lherzolites and harzburgites. Based on the trace-element patterns, especially rare earth element (REE) patterns, two groups of samples have been distinguished: group 1 samples are characterized by spoon-shaped REE patterns, and group 2 samples show light (L) REE-enriched patterns. Mineralogical characteristics together with major- and trace-element compositions point to a low degree of partial melting (less than 5%) and metasomatic processes. The latter mechanism explains in particular the LREE content of bulk rocks and clinopyroxenes and the occurrence of hydrous minerals in some samples. All the metasomatic features observed in both groups of samples are related to more or less alkaline—and carbonated—mafic silicate melts. These melts are related to the magmatic activity of the Cameroon volcanic line, leading in particular to the eruption of the host lava xenoliths.

*michel.gregoire@ctp.obs-mip.fr

Teitchou, M.I., Grégoire, M., Temdjim, R., Ghogomu, R.T., Ngwa, C., and Aka, F.T., 2011, Mineralogical and geochemical fingerprints of mantle metasomatism beneath Nyos volcano (Cameroon volcanic line), in Beccaluva, L., Bianchini, G., and Wilson, M., eds., *Volcanism and Evolution of the African Lithosphere: Geological Society of America Special Paper 478*, p. 193–210, doi:10.1130/2011.2478(10). For permission to copy, contact editing@geosociety.org. © 2011 The Geological Society of America. All rights reserved.

INTRODUCTION

Lake Nyos ($6^{\circ}26'N$, $10^{\circ}18'E$) is located in NW Cameroon, approximately 250 km from Mount Cameroon. It fills a phreatomagmatic crater of Oligocene age (Temdjim and Tchoua, 1991), which belongs to the Cameroon volcanic line (Fig. 1A), a huge tectonomagmatic feature characterized by an alignment of oceanic and continental volcanoes, grabens, and anorogenic plutons trending on average $N30^{\circ}E$ and extending for

more than 1600 km from the Atlantic island of Pagalu through the Gulf of Guinea into the African continent (Moreau et al., 1987; Déruelle et al., 1991, 2007; Lee et al., 1996; Meyers et al., 1998; Rankenburg et al., 2004, and references therein). The origin of the Cameroon volcanic line is still a subject of controversy. Recent models suggest either (1) an Oligocene to Quaternary NE-SW-extending hot line, within which distinct thermal anomalies were responsible for the Cameroon volcanic line oceanic and continental magmatism during the

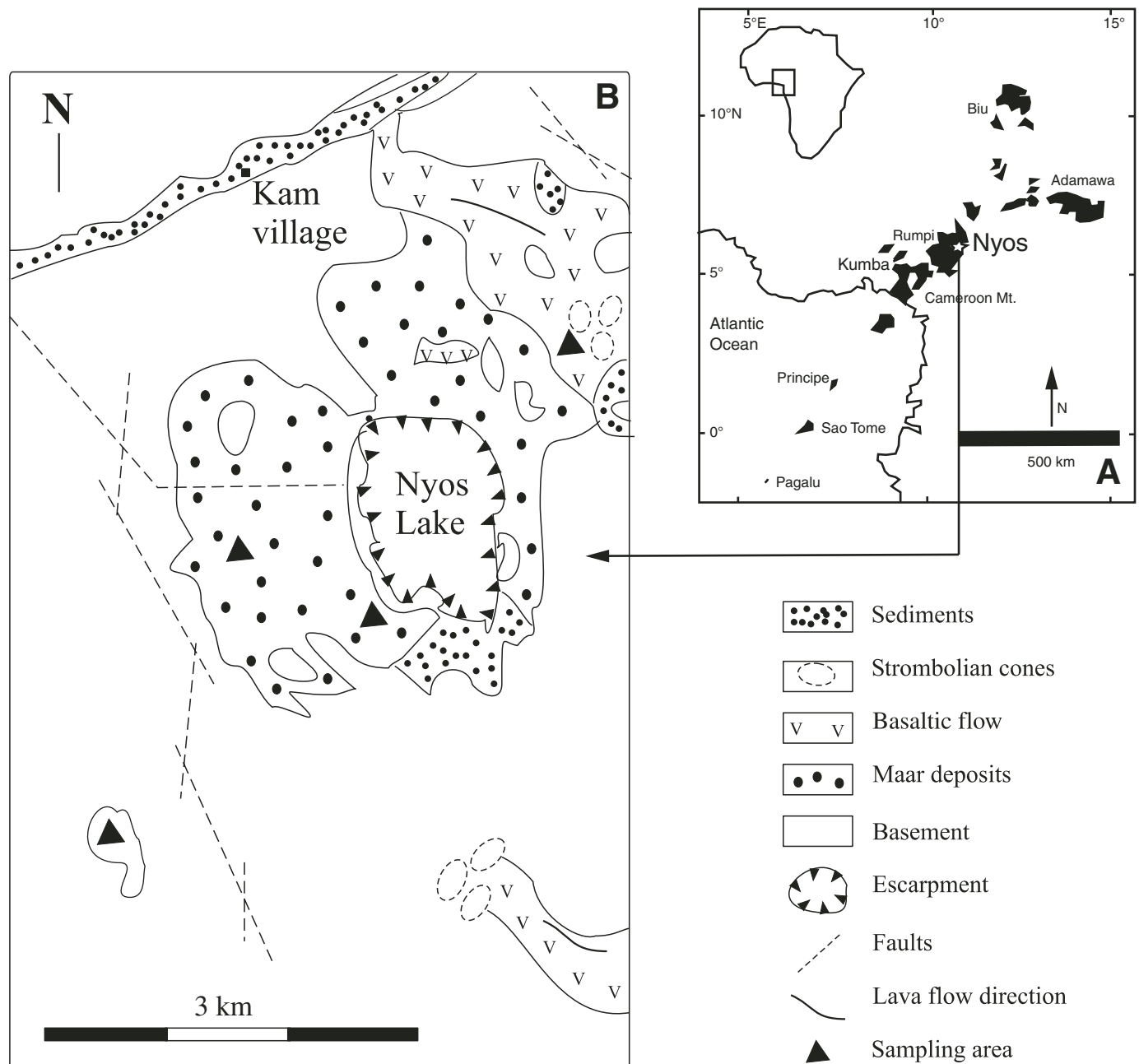


Figure 1. (A) Localization of the Cameroon volcanic line and (B) geological map of the Lake Nyos volcanic unit area.

NE movement of the African plate (Halliday et al., 1988; Lee et al., 1996; Meyers et al., 1998; Marzoli et al., 2000), or (2) a huge lithospheric crack tapping a hot, deep asthenospheric zone (Montigny et al., 2004). The Cameroon volcanic line has also been described as a paradigm of active hot lines on Earth, similar to those of the Easter chain in the Pacific Ocean (Déruelle et al., 2007).

Lake Nyos is mostly known since 1986 following an event where the lake emitted CO₂, killing ~2000 inhabitants (Kling et al., 1987) from the nearby villages of Kam and Subum. Alkaline basaltic volcanic deposits from Lake Nyos contain numerous mantle xenoliths. These xenoliths are mostly type I mantle xenoliths in the sense of Frey and Prinz (1978). They have been subdivided in two types: (1) peridotites consisting of lherzolites, harzburgites, and rare wehrlites, and (2) olivine-bearing websterites (Temdjim et al., 2004; Teitchou, 2008).

Previous studies focused on Nyos peridotite xenoliths have demonstrated several items of interest:

(1) There is evidence of a mantle metasomatic event superimposed on a previous partial melting event (Nana, 2001; Temdjim et al., 2004), which Lee et al. (1996) related to the earliest stage of the breakup of Pangea.

(2) Diapiric structures occur beneath the Cameroon volcanic line (Nana, 2001; Teitchou et al., 2007). Implications of mantle peridotites concerning the assessment of volcanic hazards have also been proposed (Nana et al., 1996).

(3) The upper mantle beneath Nyos volcano is heterogeneous (Temdjim et al., 2004; Teitchou et al., 2007) in terms of rock types (lherzolites, harzburgites, and websterites), mineral paragenesis (occurrence of amphibole), and chemical composition (quite variable rare earth element [REE] patterns). Temdjim et al. (2004) suggested that these heterogeneities may be the consequences of the recent tectonovolcanic activities that generated the Cameroon volcanic line.

The present work aims to demonstrate that upper-mantle heterogeneities occurring beneath Nyos volcano result from early partial melting processes followed by interactions between depleted peridotites and alkaline melts, leading to mineralogical and chemical enrichment processes.

GEOLOGICAL SETTING

The Lake Nyos volcanic unit (Fig. 1B) constitutes the lower part of the four massifs (Babanki, Oku, Nkambe, and Nyos) forming Mount Oku (Cameroon volcanic line). The Lake Nyos volcanic unit, mostly consisting of lava flows and maar deposits, occurs unconformably on Pan-African metamorphic formations that mostly consist of biotite-bearing gneisses intruded by granitoids. Petrochemical data (Nana, 2001) show that alkaline lavas of the Lake Nyos volcanic unit are essentially basaltic in composition and made of basalts, hawaiites, basanites, and mugearites. They display moderate magnesium numbers and originated by low degrees of partial melting of lower asthenospheric mantle sources, similar to most other lavas from the continental volcanic plains of the Cameroon volcanic line (Marzoli et al., 2000; Teitchou, 2008). The lavas are sodic with alkaline affinity and display characteristics close to those of ocean-island basalt (OIB) and high U/Pb (HIMU) components.

XENOLITH PETROGRAPHY

Type I peridotite xenoliths from Lake Nyos volcanic unit are found in recent lava flows and maar pyroclastic deposits. These xenoliths can be enclosed in stratified deposits or in base surge ejecta. Sometimes, they can form the core of basaltic bombs or even be bombs by themselves. The contact with the host lavas is commonly sharp. Unbroken bombs can be spherical, angular, or ovoid. Xenolith size ranges in diameter from few millimeters to more than 10 cm.

Modal compositions of the investigated peridotites (Table 1) were determined by mineral point counting under an optical microscope (1000 points per thin section, two thin sections per sample), image analysis (images of two thin sections per sample), and chemical composition analysis, when possible. In that latter case, we used major-element compositions of bulk rocks and constituent minerals and the petrologic mixing software PET-MIX (Wright and Doherty, 1970) based on the reference model of Le Maître (1979). Modal compositions allow us to distinguish lherzolites, harzburgites, and one wehrlite (Fig. 2).

TABLE 1. MODAL COMPOSITIONS OF THE INVESTIGATED NYOS MANTLE PERIDOTITES (IN vol%)

Sample	Olivine	Orthopyroxene	Clinopyroxene	Spinel	Amphibole	Phlogopite
NK01	67	22	8	3	—	—
NK02	80	19	1	trace	1	—
NK04	73	20	2	3	—	2
NK05	71	16	9	4	—	—
NK07	67	17	11	5	—	—
NK08	63	—	37	—	—	—
NK09	60	19	8	3	—	—
NK10a	70	22	4	4	—	—
NK10b	73	21	3	3	—	—
NK11	69	22	8	1	—	—
NK13	63	25	10	2	—	—
NK14	66	18	15	trace	—	—
NK15	65	29	3	2	—	—

Note: See text for explanation.

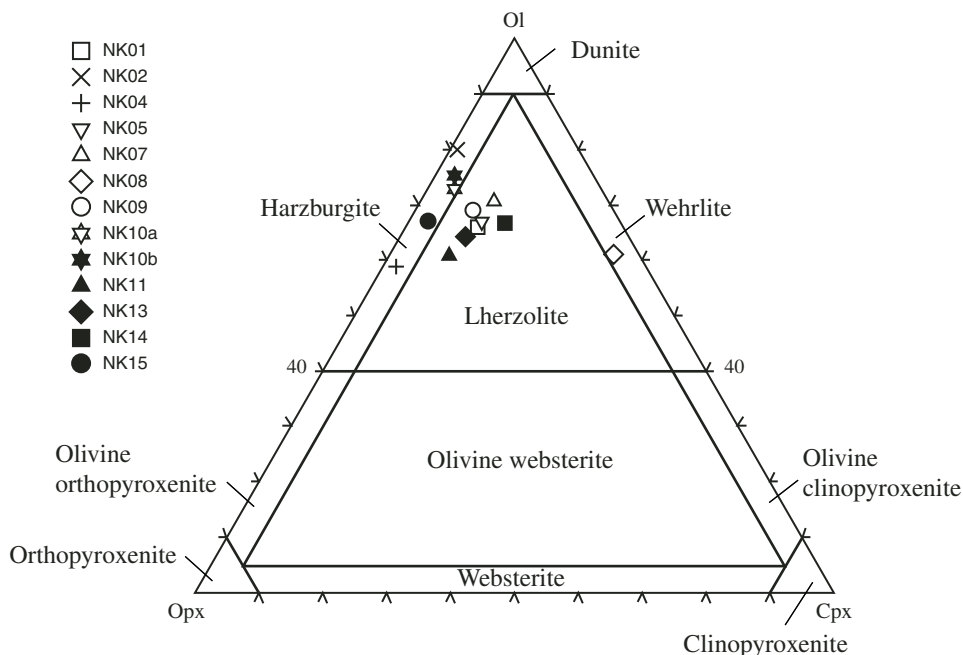


Figure 2. Modal composition of the studied Nyos xenoliths. Classification is after Streckeisen (1976). Ol—olivine; Opx—orthopyroxene; Cpx—clinopyroxene.

Spinel lherzolites (samples NK01, NK05, NK07, NK09, NK11, NK13, and NK14) are the most abundant type of xenoliths of the Lake Nyos volcanic unit (more than 60% of collected samples) and are composed of olivine (55%–70%), orthopyroxene (7%–30%), clinopyroxene (6%–20%), and up to 6% spinel. Harzburgites (samples NK02, NK04, NK10a, NK10b, and NK15) are less abundant (30%) and are composed of olivine (71%–83%), orthopyroxene (10%–20%), clinopyroxene (2%–4%), and up to 4% spinel. Finally, sample NK08 is a spinel-free wehrlite (olivine 63%, clinopyroxene 37%). Most of the lherzolites and all the harzburgites have typical mantle porphyroclastic and protogranular textures, respectively (Fig. 3). The lherzolite NK14 has a transitional porphyroclastic to equigranular texture and displays pyroxene–Cr spinel symplectites, whereas the wehrlite NK08 is the only sample that displays a cumulative texture, mostly consisting of subeuhedral olivines associated with interstitial anhedral clinopyroxenes, commonly poikilitic (Fig. 3).

ANALYTICAL METHODS

Major and trace elements of minerals were analyzed at the Observatoire Midi-Pyrénées, CNRS-UMR 5563 (Centre National de la Recherche Scientifique–Unité Mixte de Recherche 5563) (Laboratoire des Mécanismes de Transfert en Géologie) of University Paul Sabatier (Toulouse III, France). Major-element compositions of minerals were determined with the CAMECA SX50 electron microprobe and a standard program: beam current of 20 nA and acceleration voltage of 15 kV, 10–30 s/peak, 5–10 s/background counting times, and natural and synthetic minerals as standards. Nominal concentrations were subsequently corrected using the PAP data reduction method

(Pouchou and Pichoir, 1984). The theoretical lower detection limits are ~100 ppm (0.01%). The concentrations of rare earth elements and other trace elements (La, Ce, Pr, Nd, Sm, Eu, Gd, Tb, Dy, Ho, Er, Yb, Lu, Rb, Ba, Th, Sr, Zr, Ti, Y, Ni, V, and Sc) in clinopyroxenes and amphiboles were analyzed in situ on 100–120-mm-thick polished sections with a Perkin-Elmer Elan 6000 inductively coupled plasma–mass spectrometer (ICP-MS) instrument coupled to a CETAC laser-ablation module that uses a 266 nm frequency-quadrupled Nd-YAG laser. The NIST 610 and 612 glass standards were used to calibrate relative element sensitivities for the analyses. The analyses were normalized using CaO values determined by electron microprobe. The analyses were performed on intercleavage area from the cores of the freshest clinopyroxene and amphibole grains in order to get homogeneous results unaffected by alteration or exsolution processes. A beam diameter of 50–100 μm and a scanning rate of 20 $\mu\text{m/s}$ were used. The typical relative precision and accuracy for laser analysis range from 1% to 10%. Typical theoretical detection limits range from 10 to 20 ppb for REEs, Ba, Rb, Th, Sr, Zr, and Y; 100 ppb for Sc and V; and 2 ppm for Ti and Ni (for more details, see Dantas et al., 2007).

Major-element compositions were analyzed with an X-ray fluorescence (XRF) technique (Philips 2400) and measured on fused disks at Saint-Etienne Mining School, France. Trace-element compositions of five peridotites were determined by solution ICP-MS (at UMR 5563). Before analysis, the ground rock powders (~100 mg) were dissolved in HF–HNO₃ mixtures. Dried samples were taken up in HNO₃ and diluted to 1:1000 in 2% HNO₃. Reference sample BEN was used for calibration. Chemical blanks and two reference materials (UB-N, JP-1) were run on the ICP-MS with each sample batch.

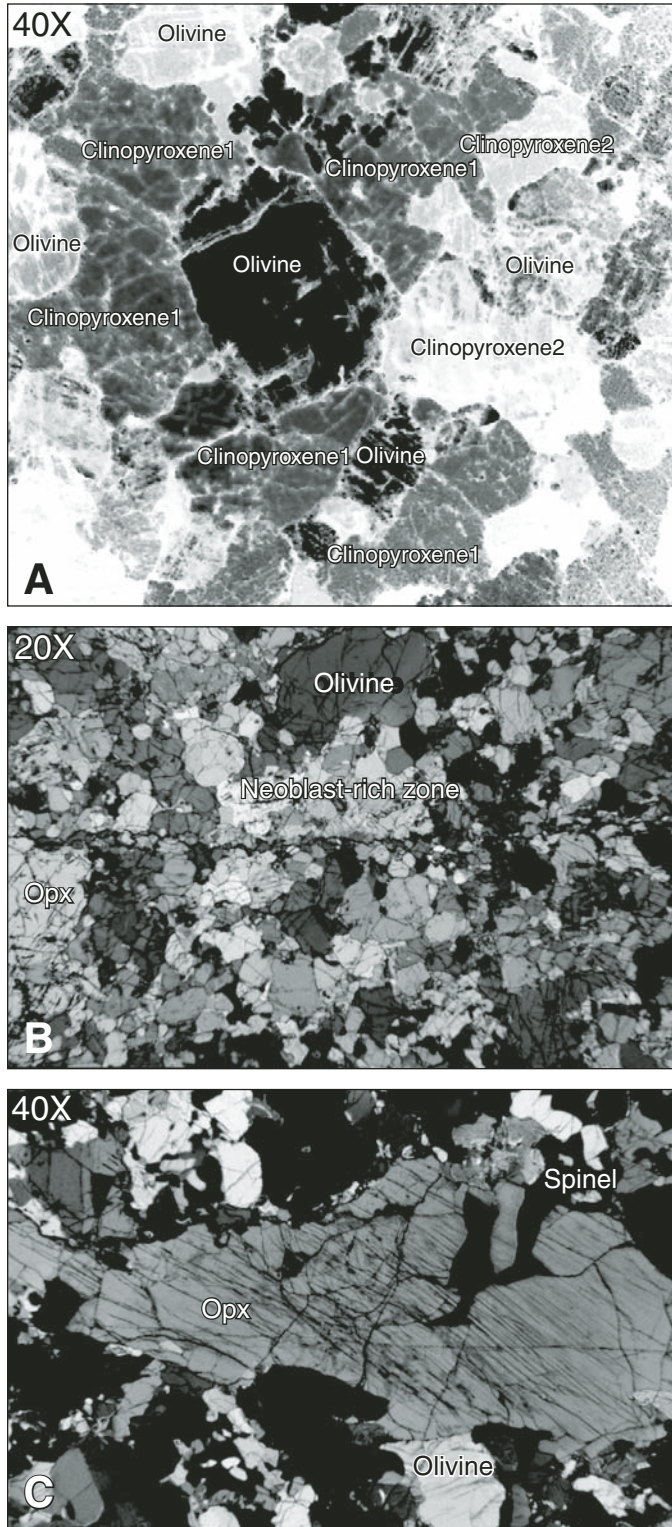


Figure 3. Microphotographs of (A) typical cumulative texture of wehrlite NK08 (inverted colors) showing subeuhedral olivines included into large poikilitic clinopyroxenes; (B) a neoblast-rich zone consisting of olivine and orthopyroxene (Opx) associated with olivine and orthopyroxene porphyroclasts in a porphyroclastic harzburgite; and (C) a large orthopyroxene porphyroclast in the same harzburgite.

MINERAL CHEMISTRY

All the Nyos peridotites display olivine, orthopyroxene, and clinopyroxene, whereas spinel occurs in all lherzolites and harzburgites but not in the wehrlite. Disseminated dark pargasitic amphibole and brown phlogopite laths are only observed in samples NK02 and NK04, respectively.

Major-Element Distribution

We provide representative analyses of selected minerals in Tables 2A–2E.

Olivine compositions in lherzolites and harzburgites range between Fo_{87} and Fo_{91} (mol%). The more magnesian ones occur in harzburgites (Fo_{87-91}). Harzburgites and lherzolites have high NiO content (0.15–0.45 wt %), similar to most mantle xenoliths worldwide, as well as ophiolitic and abyssal peridotites (e.g., Jagoutz et al., 1979; Bonatti and Michael, 1989; Nixon, 1987; Grégoire et al., 2000, 2003), while their CaO content is low, ranging from 0.05 to 0.15 wt%. On the other hand, the wehrlite NK08 contains olivines characterized by much lower Fo contents (Fo_{79}) but higher CaO (0.25 wt%).

Orthopyroxenes of lherzolites and harzburgites are enstatites ($En_{90-86.50}$) with narrow variation of Mg# ($= 100 \times Mg/[Mg + Fe_{total}]$, ranging from 88.10 to 90.90). Orthopyroxenes of Nyos peridotites are similar to those described by Caldeira and Munhá (2002) in mantle samples from São Tomé Island and from Mandara massifs, located in the oceanic and continental sectors of the Cameroon volcanic line, respectively (Tamen, 1998).

Clinopyroxenes of Nyos peridotites are diopsides ($En_{48.40-41} - Fs_{11.50-4.85} - Wo_{47.50-46.15}$) rich in Cr_2O_3 (from 0.60 to 1.10 wt%, but in the wehrlite 0.15 wt %) and Al_2O_3 (3.20–8.10 wt%). Mg# and Al_2O_3 content of clinopyroxenes from the wehrlite are respectively lower (Mg# 78.10 vs. 87.50–91) and higher (Al_2O_3 8.10% vs. 3.20–6%) compared to those of clinopyroxenes from lherzolites and harzburgites. Clinopyroxenes of Nyos lherzolites and harzburgites have low TiO_2 contents (0.20–0.50 wt%), whereas TiO_2 content of wehrlitic clinopyroxene is higher (1.75 wt%). Clinopyroxenes of Nyos peridotites are similar to those of peridotite xenoliths from Lake Nji, located in the volcanic area of Mount Oku (Princivalle et al., 2000), which belongs to the continental sector of Cameroon volcanic line.

Spinels of Nyos harzburgites and lherzolites display Mg# ($= 100 \times Mg/[Mg + Fe^{2+}]$) and Cr# ($= 100 \times Cr/[Cr + Al]$) ranging from 55 to 76 and from 12 to 39, respectively. TiO_2 contents are very low (<0.15 wt%) in most of the samples but slightly higher in the lherzolite NK14 and the harzburgite NK04 (TiO_2 0.35 and 0.55 wt%, respectively). Spinels of Nyos volcanic unit are similar to those of mantle xenoliths from the Adamawa area, located on the continental part of the Cameroon volcanic line (Girod et al., 1984).

Sample NK02 contains a calcic amphibole ($Ca/Na > 1$; $Ca + Na > 1.34$, and $Na < 0.67$; $Al^{IV} > Fe^{3+}$) corresponding to a pargasite (Leake, 1978). Nyos pargasitic amphibole is magnesian

TABLE 2A. REPRESENTATIVE MICROPROBE ANALYSES OF CORES OF OLIVINES

	Group 1	Group 1	Group 1	Group 1	Group 1	Group 1	Group 1	Group 1	Group 2	Group 2	Group 2
	Lherzolite	Lherzolite	Lherzolite	Lherzolite	Harzburgite	Lherzolite	Harzburgite	harzburgite	harzburgite	Lherzolite	Wehrlite
Olivine:	NK01	NK05	NK07	NK09	NK10	NK11	NK15	NK02	NK04	NK14	NK08
SiO ₂ (wt%)	40.90	41.10	41.71	40.82	41.03	41.44	41.64	41.29	40.51	40.87	38.95
TiO ₂	0.03	—	—	—	0.01	—	—	—	0.03	—	0.01
Al ₂ O ₃	—	—	—	—	—	—	—	—	—	—	—
Cr ₂ O ₃	0.04	0.01	0.01	0.03	0.01	0.02	—	0.02	—	0.02	0.03
FeO _{total}	10.10	9.90	9.95	9.66	9.66	9.84	9.95	9.58	12.20	12.57	19.86
MnO	0.13	0.15	0.13	0.1	0.13	0.12	0.19	0.15	0.16	0.19	0.30
MgO	49.59	50.08	49.49	49.87	49.94	49.19	49.48	49.81	47.62	47.38	41.81
CaO	0.09	0.09	0.12	0.06	0.11	0.11	0.06	0.09	0.07	0.09	0.26
NiO	0.36	0.37	0.39	0.32	0.29	0.25	0.38	0.32	0.45	0.17	0.04
Total	101.23	101.66	101.79	100.85	101.17	100.98	101.71	101.26	101.04	101.29	101.25
Mg#	89.75	90.02	89.86	90.20	90.21	89.91	89.86	90.26	87.43	87.04	78.95

TABLE 2B. REPRESENTATIVE MICROPROBE ANALYSES OF CORES OF ORTHOPYROXENES

Orthopyroxene:	NK01	NK05	NK07	NK09	NK10	NK11	NK15	NK02	NK04	NK14
SiO ₂ (wt%)	55.43	55.36	57.10	56.48	55.70	56.06	56.62	56.76	55.93	54.56
TiO ₂	0.06	0.04	0.01	0.05	0.04	—	0.06	0.01	0.04	0.13
Al ₂ O ₃	4.34	4.46	3.74	3.65	3.75	3.66	3.79	3.23	2.43	3.91
Cr ₂ O ₃	0.40	0.46	0.29	0.33	0.39	0.35	0.40	0.46	0.40	0.47
FeO _{total}	6.53	6.44	6.59	6.58	6.22	6.51	6.39	5.99	7.81	7.83
MnO	0.13	0.13	0.12	0.13	0.17	0.10	0.16	0.11	0.12	0.21
MgO	33.44	33.34	33.76	33.61	34.02	33.33	33.63	33.8	32.95	32.44
CaO	0.76	1.32	0.76	0.60	0.57	0.74	0.63	0.77	0.85	0.81
Na ₂ O	—	0.01	—	—	—	—	—	—	—	—
K ₂ O	—	0.01	—	0.01	0.01	—	—	—	—	—
Total	101.19	101.74	102.37	101.45	100.98	100.76	101.66	101.13	100.63	100.51
Mg#	90.13	90.21	90.13	90.11	90.70	90.12	90.36	90.96	88.27	88.08

TABLE 2C. REPRESENTATIVE MICROPROBE ANALYSES OF CORES OF CLINOPYROXENES

Clinopyroxene:	NK01	NK05	NK07	NK09	NK10	NK11	NK15	NK02	NK04	NK14	NK08
SiO ₂ (wt%)	52.19	52.43	52.47	52.26	51.74	52.45	53.45	52.46	52.90	52.13	47.68
TiO ₂	0.25	0.20	0.30	0.27	0.41	0.32	0.31	0.25	0.22	0.50	1.77
Al ₂ O ₃	5.34	5.37	5.67	5.13	5.98	5.70	5.13	4.40	3.22	4.54	8.10
Cr ₂ O ₃	0.72	0.66	0.79	0.63	0.85	0.81	0.78	1.26	0.71	1.10	0.14
FeO _{total}	3.07	3.10	3.17	2.96	2.84	3.08	2.78	3.07	3.36	4.05	6.67
MnO	0.10	0.07	0.10	0.093	0.08	0.043	0.09	0.10	0.07	0.13	0.16
MgO	16.11	16.28	15.75	16.05	15.12	15.68	15.84	16.19	16.61	15.90	13.35
CaO	22.05	21.69	21.65	21.94	21.56	21.53	21.67	21.70	23.15	21.69	21.50
Na ₂ O	0.88	1.09	1.02	1.07	—	1.11	1.24	0.81	0.43	0.90	0.63
K ₂ O	—	0.01	—	—	—	0.01	0.01	0.02	0.04	0.01	—
Total	100.72	100.89	100.92	100.62	98.58	100.73	101.31	100.24	100.72	100.94	99.98
Mg#	90.33	90.35	89.86	92.97	90.47	90.07	91.03	90.38	89.79	87.50	78.10

TABLE 2D. REPRESENTATIVE MICROPROBE ANALYSES OF CORES OF SPINELS

Spinel:	NK01	NK05	NK07	NK09	NK10	NK11	NK15	NK02	NK04	NK14
SiO ₂ (wt%)	0.05	0.03	0.04	0.03	0.02	0.04	0.03	0.05	0.06	0.07
TiO ₂	0.03	0.03	0.06	0.03	0.03	0.04	0.06	0.04	0.36	0.53
Al ₂ O ₃	55.08	55.67	54.91	55.48	55.32	55.21	54.82	38.46	35.63	31.79
Cr ₂ O ₃	11.64	11.30	11.49	11.47	11.94	11.32	12.43	27.99	27.15	29.85
Fe ₂ O ₃	3.78	3.98	3.99	3.08	3.01	3.42	2.25	6.49	6.54	8.94
FeO	9.76	9.20	9.32	9.47	9.39	9.36	9.37	9.38	15.11	14.11
MnO	0.12	0.11	0.11	0.10	0.07	0.11	0.11	0.16	0.16	0.18
MgO	20.13	20.63	20.40	20.28	20.39	20.26	20.09	17.52	14.54	15.20
ZnO	0.08	—	—	—	—	—	0.06	—	0.24	—
NiO	0.36	0.43	0.34	0.33	0.28	0.41	0.37	0.18	0.27	0.26
Total	101.03	101.39	100.67	100.26	100.44	100.16	99.57	100.26	100.06	100.91
Mg#	73.16	74.20	73.80	74.70	75.07	74.38	75.86	67.23	55.25	55.01
Cr#	12.42	11.99	12.31	12.18	12.65	12.09	13.21	32.81	33.82	38.65

TABLE 2E. REPRESENTATIVE MICROPROBE ANALYSES OF CORES OF AMPHIBOLES AND PHLOGOPITES

Amphibole	NK02	Phlogopite	NK04
SiO ₂ (wt%)	43.74	SiO ₂ (wt%)	38.62
TiO ₂	1.40	TiO ₂	2.92
Al ₂ O ₃	13.56	Al ₂ O ₃	15.84
Cr ₂ O ₃	2.10	Cr ₂ O ₃	0.92
FeO _{total}	4.07	FeO _{total}	4.59
		ZnO	0.03
MnO	0.07	MnO	0.05
MgO	17.43	MgO	22.20
CaO	11.07	CaO	0.01
Na ₂ O	3.09	Na ₂ O	0.54
K ₂ O	1.15	K ₂ O	9.45
		BaO	0.29
NiO	0.08	NiO	0.23
Total	97.75	Total	95.69
Mg#	88.42	Mg#	89.61

(Mg# 88.4) and aluminous (Al₂O₃ 13.55 wt%) and displays slightly high TiO₂ (1.40 wt%), Na₂O (3.10 wt%), Cr₂O₃ (2.10 wt%), and low K₂O (1.15 wt%) contents.

Phlogopite (Fe/[Fe + Mg] = 0.10 and Mg# 89.60) occurring in harzburgite NK04 has high TiO₂ (~3 wt%) and low Cr₂O₃ (<1 wt%) contents.

Trace-Element Distribution

Laser ablation (LA) ICP-MS analyses of mineral phases are given in Tables 3A and 3B. Clinopyroxene and amphibole

are rich in incompatible trace elements, while phlogopite is REE-poor.

Clinopyroxene

Transition trace-element concentrations of clinopyroxene (Sc: 55–74 ppm; V: 135–255 ppm; Ni: 228–276 ppm) are relatively similar and homogeneous in lherzolites and harzburgites, while wehrlitic clinopyroxenes have higher V (295 ppm), lower Ni (102 ppm), and similar Sc (70 ppm) contents. Ti content yields the broadest variation range, varying from 460 ppm in the amphibole-bearing harzburgite NK02 to 10,465 ppm in wehrlite NK08.

When normalized to estimated primitive mantle values (McDonough and Sun, 1995), clinopyroxenes from the investigated Nyos mantle xenoliths display two distinct types of REE patterns, which allow a subdivision of the peridotite xenoliths into two groups (Fig. 4A):

(1) Group 1 clinopyroxenes display spoon-shaped patterns corresponding to a heavy (H) REE enrichment over middle (M) REEs and light (L) REEs: [La/Sm]_N = 0.08–5.50, [Sm/Yb]_N = 0.47–1.17, and [La/Yb]_N = 0.03–6.45. Corresponding rocks are the porphyroclastic lherzolites and the three harzburgites NK02 (amphibole-bearing), NK10, and NK15.

(2) Group 2 clinopyroxenes display LREE-enriched patterns: [La/Sm]_N = 0.73–1.35; [Sm/Yb]_N = 3–6.25, and [La/Yb]_N = 3.25–4.5. The clinopyroxenes of group 2 also show a significant HREE fractionation, as evidenced by their [Dy/Lu]_N ratios, which range from 1.6 to 3 (group 1 ratios

TABLE 3A. REPRESENTATIVE CLINOPYROXENE TRACE-ELEMENT ANALYSES (LA-ICP-MS) OF NYOS PERIDOTITES (VALUES IN ppm)

Clinopyroxene:	Group 1 Amp- harzburgite	Group 1 Harzburgite	Group 1 Harzburgite	Group 1 Lherzolite	Group 1 Lherzolite	Group 1 Lherzolite	Group 1 Lherzolite	Group 2 Lherzolite	Group 2 Phl- harzburgite	Group 2 Wehrlite
Sample:	NK02	NK10	NK15	NK01	NK05	NK09	NK11	NK14	NK04	NK08
Sc	66.35	61.48	73.91	61.72	60.97	57.78	58.04	55.11	55.56	69.58
Ti	461.98	1608.62	2006.41	1702.56	1643.34	1799.66	1847.82	3563.77	1182.25	10,465.00
V	151.82	229.97	254.97	230.11	218.95	226.07	228.39	248.55	134.55	295.46
Ni	228.38	289.01	256.10	276.37	249.36	272.56	271.42	247.02	247.58	101.95
Rb	0.77	2.94	0.77	2.88	3.27	2.39	3.75	3.16	1.18	1.39
Sr	147.23	18.53	6.23	20.03	20.18	12.17	11.86	125.28	102.61	98.73
Y	13.40	15.40	16.08	16.21	16.31	14.72	18.32	15.11	10.11	10.29
Zr	19.32	12.12	7.41	12.17	12.92	9.32	13.56	56.22	108.46	78.05
Nb	0.37	0.21	0.08	0.25	0.20	0.13	0.21	0.59	0.17	0.94
Ba	7.37	26.40	2.82	26.53	33.26	20.66	34.77	29.32	9.13	5.79
La	13.26	1.67	0.09	1.70	1.44	0.26	0.51	9.43	8.04	6.15
Ce	22.05	2.37	0.29	2.47	1.83	0.68	0.96	23.18	30.15	17.46
Pr	2.01	0.25	0.09	0.24	0.20	0.16	0.12	3.28	5.53	2.93
Nd	6.90	1.48	1.07	1.31	1.04	1.37	1.18	15.12	28.22	15.80
Sm	1.51	0.82	0.71	0.72	0.66	0.81	0.78	4.34	6.94	4.99
Eu	0.51	0.40	0.41	0.38	0.35	0.40	0.43	1.42	1.71	1.68
Gd	1.71	1.55	1.69	1.63	1.51	1.55	1.85	3.81	4.27	4.75
Dy	2.13	2.20	2.42	2.29	2.25	2.13	2.50	3.51	3.77	4.28
Ho	0.47	0.52	0.58	0.55	0.55	0.50	0.58	0.70	0.62	0.75
Er	1.35	1.59	1.65	1.65	1.64	1.49	1.66	1.78	1.46	1.63
Yb	1.40	1.58	1.58	1.58	1.57	1.50	1.59	1.59	1.21	1.28
Lu	0.20	0.22	0.22	0.22	0.21	0.21	0.23	0.22	0.15	0.14
Hf	0.45	0.50	0.47	0.51	0.54	0.49	0.65	1.31	2.93	3.59
Ta	0.01	0.02	–	0.03	0.03	0.01	0.02	0.07	0.03	0.14
Th	0.34	0.26	0.03	0.34	0.37	0.08	0.22	0.81	0.38	0.21
U	0.23	0.16	0.03	0.16	0.22	0.10	0.17	0.27	0.07	0.08

Note: LA-ICP-MS—laser-ablation—inductively coupled plasma—mass spectrometry.

TABLE 3B. REPRESENTATIVE AMPHIBOLE AND PHLOGOPITE TRACE-ELEMENT ANALYSES OF NYOS PERIDOTITES (IN ppm)

	Group 1 Amp harzburgite NK02	Group 2 Phl harzburgite NK04
Sc	43.78	8.79
Ti	2132.40	17,412.84
V	207.71	212.70
Ni	295.63	1333.66
Rb	3.03	360.97
Sr	136.21	137.34
Y	13.50	0.23
Zr	32.43	17.94
Nb	9.06	8.75
Ba	31.24	2973.66
La	12.08	—
Ce	20.30	0.32
Pr	2.09	—
Nd	7.18	0.21
Sm	1.49	0.45
Eu	0.52	0.12
Gd	1.71	0.10
Dy	2.06	—
Ho	0.45	—
Er	1.35	0.03
Yb	1.40	0.05
Lu	0.21	—
Hf	0.81	0.54
Ta	0.41	0.58
Th	0.45	0.05
U	0.16	0.05

are 1–1.1). The samples making up this group are the lherzolite NK14, the phlogopite-bearing harzburgite NK04, and the wehrlite NK08.

Nearly all Nyos clinopyroxenes display deep negative Nb, Ta, and Ti anomalies and positive U anomalies (Fig. 4B). The group 2 clinopyroxenes are also characterized by negative Sr anomalies and by a higher $[Th/U]_N$ ratio than those of group 1 clinopyroxenes, ranging from 0.7 to 1.4 and from 0.2 to 0.5, respectively.

Amphibole and Phlogopite

Transitional trace-element contents of pargasitic amphibole are significant (Sc 44 ppm; V 208 ppm; Ni 296 ppm), while that of Ti (2132 ppm) is high, similar to those of other incompatible trace elements. REEs are enriched when compared to the estimated primitive mantle values of McDonough and Sun (1995). Amphibole (Fig. 5A) displays a LREE-enriched REE pattern: $[La/Sm]_N = 5.08$; $[Sm/Yb]_N = 1.16$, and $[La/Yb]_N = 5.89$, and its multi-trace-element pattern (Fig. 5B) is characterized by moderate negative Ti and Zr anomalies. The Nyos mantle amphibole is similar to those occurring in mantle xenoliths from Orania in Algeria (Zerka, 2004).

Phlogopite commonly displays high Ti (17,413 ppm), Ni (1334 ppm), V (213 ppm), Ba (2974 ppm), and Rb (361 ppm) contents. Phlogopites are low in REEs (less than 1% of the estimated primitive mantle values). Phlogopite multi-trace-element pattern (Fig. 5C) is characterized

by negative Th and Sr anomalies and positive U, Nb, and Ti anomalies.

BULK-ROCK GEOCHEMISTRY

Major Elements

The Nyos mantle xenoliths (three group 1 lherzolites [NK01, NK05, NK11], one group 1 anhydrous harzburgite [NK10], and the group 2 phlogopite-bearing harzburgite [NK04]) have generally homogeneous major-element compositions. Their $Mg\#$ ($100 \times Mg/[Mg + Fe_{total}]$) values vary from 87.40 to 89.60 (Table 4). The phlogopite-bearing harzburgite NK04 displays the lowest $Mg\#$, while that of the anhydrous harzburgite NK10 is close to those of the three lherzolites (88.95 vs. 89–89.60). These four samples are relatively fertile, with high Al_2O_3 and CaO contents (2.7–3.1 wt% and 2.4–2.7 wt%, respectively) and $Mg\#$ values close to 89. All samples display K_2O , Na_2O , and P_2O_5 contents close to or below the detection limits, while their TiO_2 content is very low (<0.2 wt%). The phlogopite-bearing harzburgite NK04 is the only sample displaying a K_2O content above the detection limit (K_2O : 0.03 wt%). This sample is also characterized by the lowest Al_2O_3 (<2 wt%) and CaO (<1 wt%) contents.

Trace-Element Distribution

The analyzed lherzolites and harzburgites (Table 4) are characterized by REE contents that plot on both sides of the values of the primitive mantle in Figure 6. Two types of REE patterns are observed:

(1) The three group 1 lherzolites and the harzburgite NK10 display “spoon-shaped” REE patterns (Fig. 6A) characterized by Pr–Nd and MREE depletion compared to La–Ce and HREE: $[La/Sm]_N = 1.37$ –2.53; $[Sm/Yb]_N = 0.33$ –0.47, and $[La/Yb]_N = 0.46$ –1.28. Their multi-trace-element patterns (Fig. 6B) are similar and characterized by negative Nb, Ti, and Sr anomalies and positive U anomalies.

(2) The phlogopite-bearing harzburgite NK04 displays an “S-shaped” REE pattern (Fig. 7) characterized by LREE enrichment over MREEs and HREEs: $[La/Sm]_N = 1.34$; $[Sm/Yb]_N = 2.46$, and $[La/Yb]_N = 3.30$. The multi-trace-element pattern (Fig. 6B) shows a negative Sr anomaly.

Bulk Rocks/Clinopyroxene Comparison

The phlogopite-bearing harzburgite NK04 (group 2 samples) and its clinopyroxene display REE patterns with a similar shape for LREEs and MREEs but not for HREEs. They are both enriched in LREEs and MREEs compared to HREEs, which are nearly constant in bulk rock but decrease from Ho to Lu in clinopyroxene (Fig. 6A). Multi-trace-element patterns of clinopyroxene and bulk rock exhibit differences in Rb, Ba, Zr, Hf, and Ti, probably related to the occurrence of phlogopite in this sample (Fig. 6B).

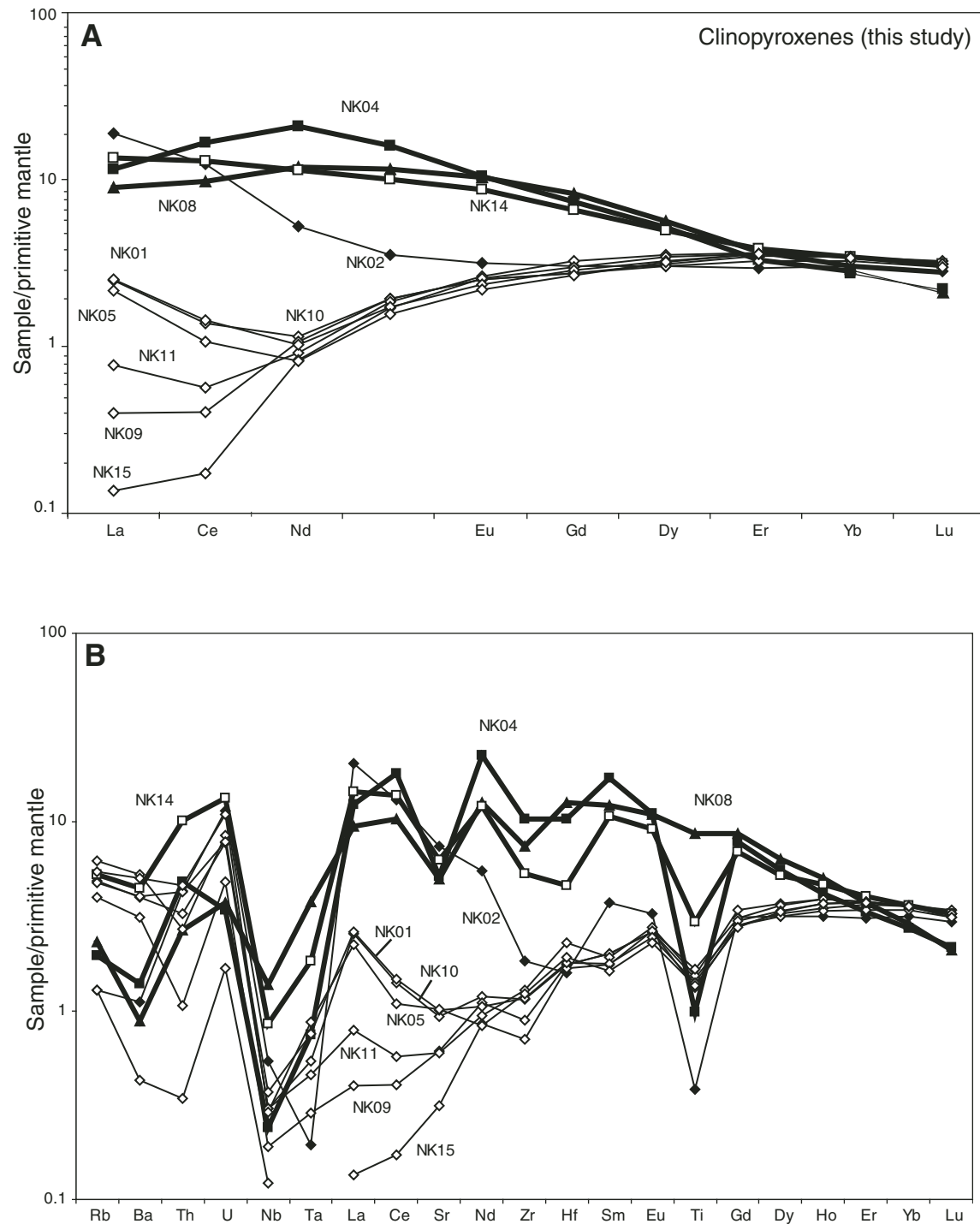


Figure 4. (A) Rare earth element (REE) patterns of clinopyroxenes of the Nyos peridotites. (B) Extended incompatible trace-element patterns of clinopyroxenes of the Nyos peridotites. Normalization is to the estimated primitive mantle values of McDonough and Sun (1995).

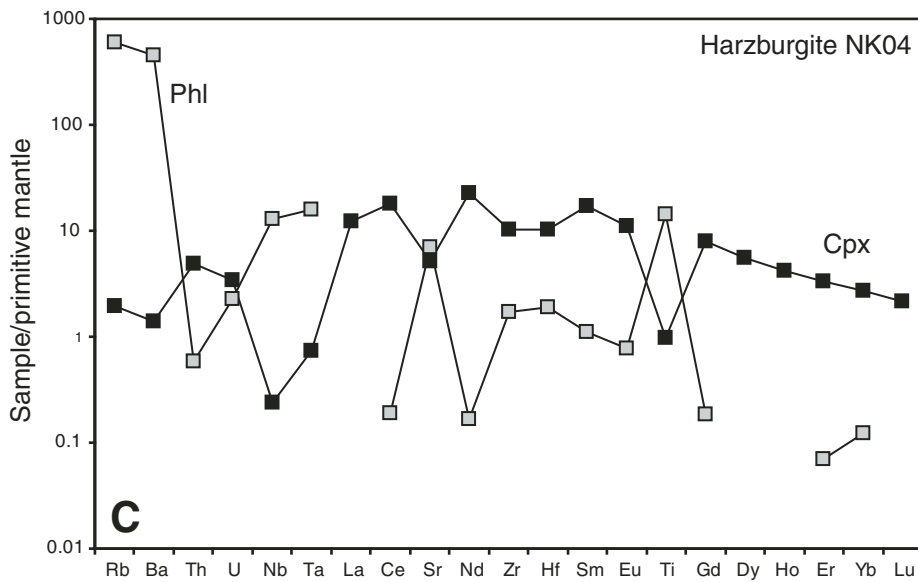
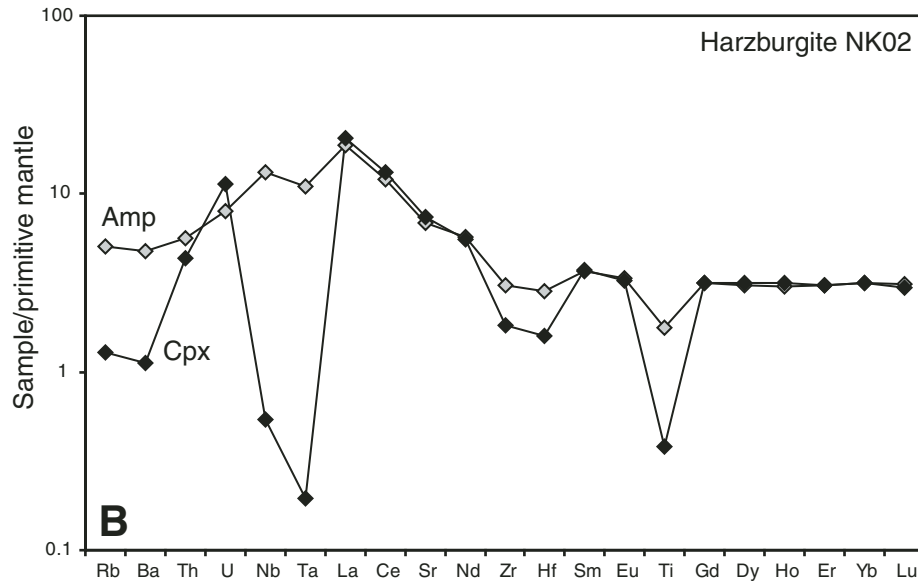
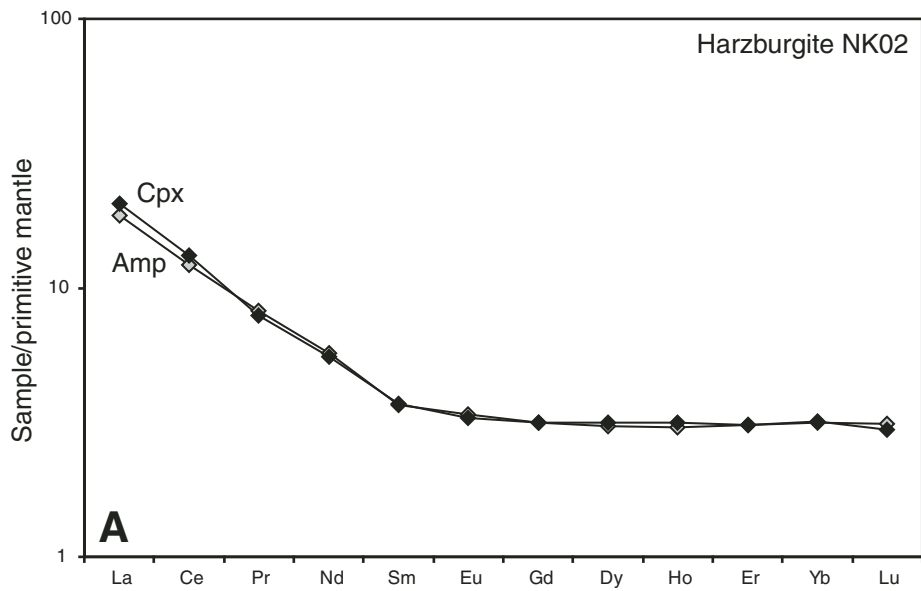


Figure 5. (A) Rare earth element (REE) patterns of amphibole (Amp) of Nyos harzburgite NK02 compared to that of the coexisting clinopyroxene (Cpx). (B) Extended incompatible trace-element patterns of amphibole of Nyos harzburgite NK02 compared to that of the coexisting clinopyroxene. (C) Extended incompatible trace-element patterns of phlogopite (Phl) of Nyos harzburgite NK04 compared to that of the coexisting clinopyroxene. Normalization is to the estimated primitive mantle values of McDonough and Sun (1995).

DISCUSSION

The spinel lherzolites and harzburgites of both groups (1 and 2) display textural, modal, and chemical characteristics of typical mantle rocks equilibrated in the spinel peridotite facies. The temperature estimate made by Teitchou (2008) using clinopyroxene-orthopyroxene thermometers of Wells (1977) and Brey and Köhler (1990) ranges from 930 to 1025 °C for the Group 1 xenoliths, while it is close to 900 °C for the phlogopite-bearing group 2 harzburgite NK04 and close to 1000 °C for the group

2 lherzolite NK14. On the other hand, no temperature estimate could be made for the cumulative wehrlite NK08.

Origin of the Wehrlite

The trace-element characteristics of the clinopyroxene of the cumulative wehrlite (NK08) are similar to those of samples NK04 and NK14, as attested by the classification of these three samples in the same group. Nevertheless, the major-element features of olivine and clinopyroxene of the wehrlite appear to be significantly different than those of their equivalents in the two other group 2 peridotites. They are indeed less magnesian (Mg# olivine: 79 vs. 87–87.50; Mg# clinopyroxene: 78.10 vs. 87.50–89.80), the olivine is higher in CaO (0.26 versus 0.07–0.09), and the clinopyroxene displays much higher Al_2O_3 (8.10 vs. 3.20–4.50) and TiO_2 (1.77 vs. 0.20–0.50) contents and a lower Cr_2O_3 content (0.15 vs. 0.60–1.25). Those characteristics are in agreement with the fact that the lherzolite NK14 and the phlogopite-bearing harzburgite NK04 are metasomatized mantle peridotites (see following), whereas the wehrlite NK08 is a magmatic cumulate. Finally, such characteristics point out that the metasomatic melt that has affected samples NK04 and NK14 is also probably the parental melt of the wehrlite cumulate.

Group 1 and Group 2 Spinel-Bearing Mantle Peridotites

Partial Melting Features

The harzburgites and lherzolites of the group 1 peridotites from the Nyos Plain display characteristics of residues from a partial melting event, including high Mg number of olivine and pyroxenes and high Cr_2O_3 content of spinel. The HREE patterns of the group 1 clinopyroxenes showing spoon-shaped REE patterns are also in agreement with such a process (Fig. 4A). The modal compositions of harzburgites are in agreement with high depletion, but the minor- and major-element compositions of mineral phases and bulk rocks indicate that the difference in the degree of depletion between lherzolites and harzburgites is not so great. In order to estimate the degree of partial melting experienced by the Nyos upper mantle, we used two methods: (1) First, we estimated the degree of partial melting by using the Cr# of spinel following the method of Hellebrand et al. (2001), calibrated for Cr# values ranging between 0.10 and 0.60, a range similar to that of our samples. The results mostly range from 2% to 4% in most of the samples, except the hydrous mineral-bearing samples (NK02 and NK04: 12%–14%) and the lherzolite NK14 (~14%). (2) Second, we compared the REE contents of the clinopyroxenes with those computed using a model of fractional melting for a primitive spinel-peridotite mantle source, based on the method described by Johnson et al. (1990) (Fig. 7). The starting composition and melting modes are those given by Hellebrand et al. (2001). In Figure 7, the REEs of most of the Nyos mantle clinopyroxenes from Gd to Yb are in good agreement with the partial melting model, whereas those of the group 2 samples, consisting of the phlogopite-bearing harzburgite (NK04), the lherzolite

TABLE 4. BULK ROCK MAJOR-ELEMENT DATA (X-RAY FLUORESCENCE) AND TRACE-ELEMENT DATA (LA-ICP-MS) OF NYOS PERIDOTITES

	Group 1	Group 1	Group 1	Group 1	Group 2
	Lherzolite	Lherzolite	Lherzolite	Harzburgite	Phl- harzburgite
	NK01	NK05	NK11	NK10	NK04
SiO ₂	43.59	43.74	45.40	44.10	45.94
TiO ₂	0.07	0.07	0.08	0.08	0.11
Al ₂ O ₃	2.70	2.77	3.09	2.89	1.68
Fe ₂ O ₃	8.93	8.50	8.38	9.12	10.32
MnO	0.14	0.14	0.14	0.15	0.16
MgO	40.91	41.29	40.31	41.16	40.18
CaO	2.63	2.64	2.39	2.72	0.94
Na ₂ O	—	—	—	—	—
K ₂ O	—	—	—	—	0.03
P ₂ O ₅	0.02	0.02	0.01	0.02	0.03
Total	99.00	99.17	99.79	100.23	99.39
Mg#	89.09	89.64	89.56	88.95	87.41
Sc	14.35	15.02	17.00	18.84	11.30
Ti	431.64	413.66	485.60	455.62	641.47
V	64.80	66.60	68.80	70.70	37.90
Cr	2844.20	2652.80	2910.00	2972.50	2934.20
Co	110.30	110.20	102.40	109.70	123.00
Ni	2145.60	2238.90	2040.70	2181.70	1983.20
Cu	15.60	5.9	2.70	16.60	24.20
Zn	53.20	46.00	48.90	63.30	64.50
Ga	1.32	1.61	1.80	1.88	1.92
Rb	0.06	0.04	0.032	0.07	3.29
Sr	2.98	1.32	0.50	3.14	4.34
Zr	1.18	0.64	0.84	1.28	6.55
Nb	0.15	—	—	—	0.19
Ba	2.96	1.09	1.37	3.76	31.37
La	0.45	0.23	0.20	0.60	0.59
Ce	0.59	0.32	0.31	0.87	1.50
Pr	0.07	0.04	0.04	0.11	0.24
Nd	0.35	0.24	0.22	0.49	1.13
Sm	0.11	0.10	0.09	0.16	0.28
Eu	0.05	0.05	0.04	0.07	0.08
Gd	0.23	0.21	0.23	0.26	0.20
Tb	0.04	0.04	0.05	0.05	0.03
Dy	0.32	0.31	0.37	0.40	0.19
Ho	0.08	0.08	0.09	0.09	0.04
Er	0.24	0.23	0.28	0.31	0.11
Tm	0.04	0.03	0.04	0.04	0.02
Yb	0.25	0.25	0.30	0.32	0.12
Lu	0.04	0.04	0.05	0.05	0.02
Th	0.04	0.04	—	0.04	0.04
U	0.01	0.02	0.01	0.02	0.02

Note: LA-ICP-MS—laser-ablation—inductively coupled plasma—mass spectrometry.

NK14, and the wehrlite NK08, are not. The estimated degrees of melting using the HREEs (Gd–Yb), which are the least subject to metasomatism, range from 1% to ~5% (Fig. 7). It finally appears that the upper mantle beneath Nyos represented by the group 1 peridotites has probably undergone a partial melting event of low

degree (less than 5% of melting). The high values given by the spinels of the two harzburgites showing amphibole (NK02) or phlogopite (NK04) as well as by the spinels of lherzolite NK14 are highly questionable, because these three samples have been hardly affected by metasomatic processes, as evidenced by the

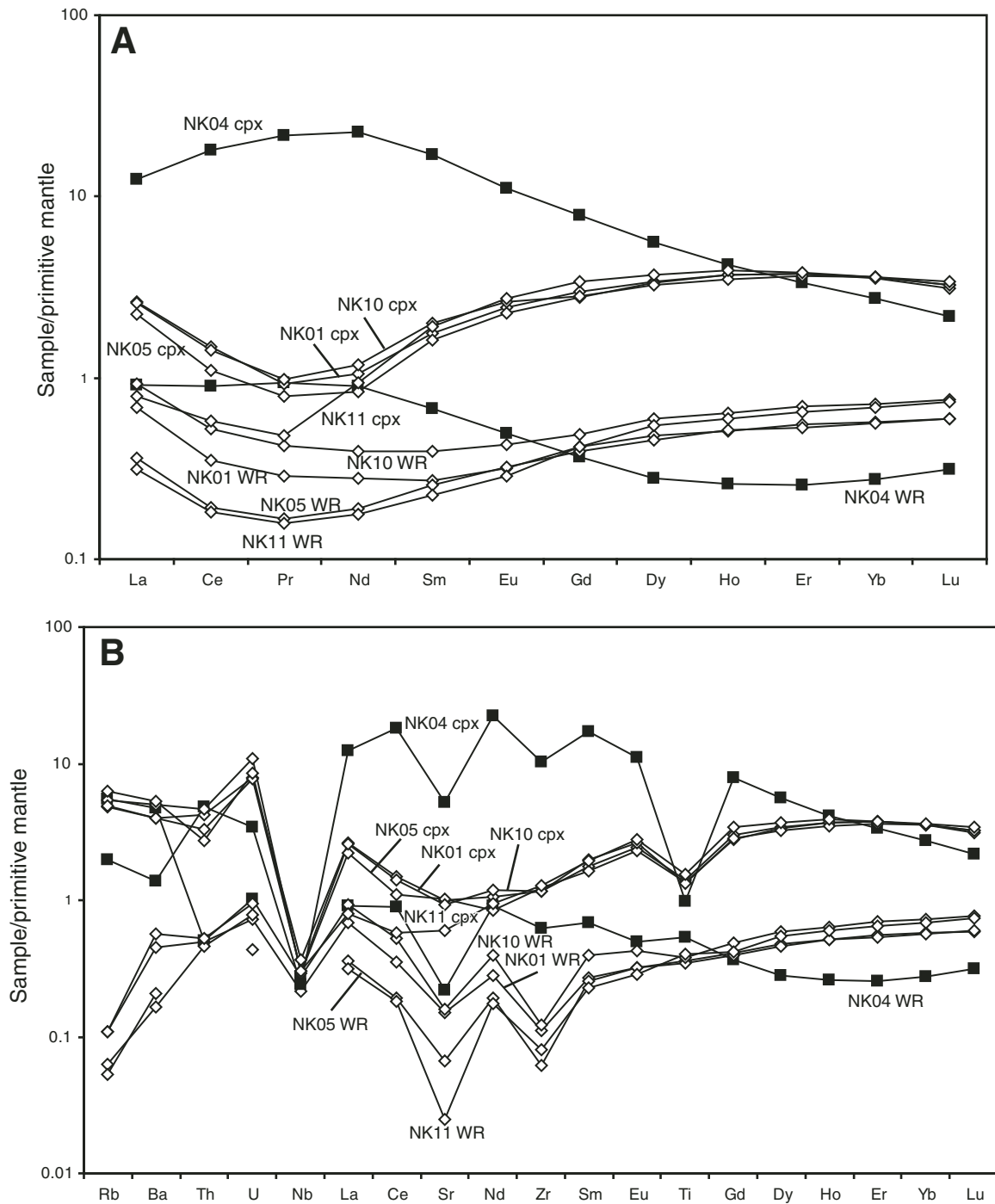


Figure 6. (A) Bulk rock rare earth element (REE) patterns of the Nyos mantle peridotites compared to those of their clinopyroxenes (cpx). (B) Bulk rock extended incompatible trace-element patterns of the Nyos peridotites compared to those of their clinopyroxenes. Normalization is to the estimated primitive mantle values of McDonough and Sun (1995). WR—whole rock.

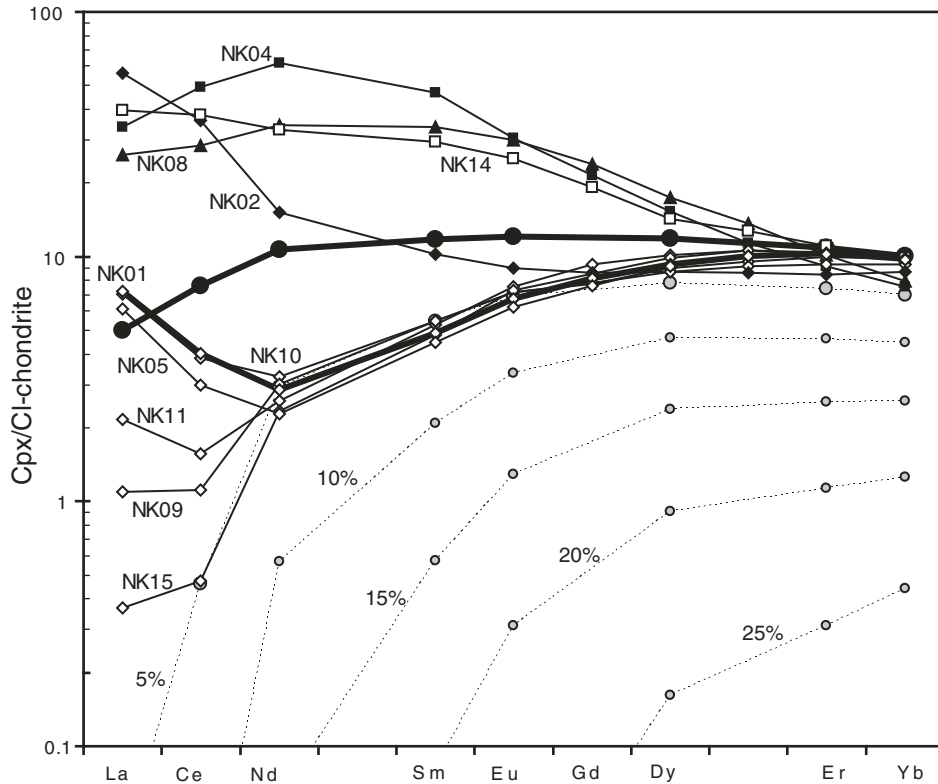


Figure 7. Nonmodal partial melting modeling for the rare earth elements (REEs) in clinopyroxenes from the Nyos mantle peridotites. The data are normalized to the CI-chondrite (carbonaceous chondrite of class CI) of McDonough and Sun (1995). Most clinopyroxenes display heavy (H) REE contents that are in agreement with a partial melting degree of ~1%–5%, except for samples NK08, NK14, and NK04, for which REE content cannot be accounted by a partial melting model (see text for further explanations).

occurrence of amphibole and phlogopite in two of them and also by their clinopyroxene REE- and trace-element patterns. Moreover, the method of Hellebrand et al. (2001) is applicable only to anhydrous peridotites. Nevertheless, the amphibole-bearing harzburgite NK02 gives a similar value as the anhydrous group 1 peridotites when the estimate is made by using the REE of clinopyroxenes (Fig. 7). Regarding the group 2 peridotites, the REE patterns of clinopyroxene are not in agreement with an origin as residues of partial melting.

Metasomatic Features

Beside the evidence for partial melting processes, all the studied Nyos spinel-bearing peridotite xenoliths display evidence for mantle metasomatism. This is supported by the concomitant increase of the Na_2O and Cr_2O_3 contents of clinopyroxenes of harzburgites and lherzolites (Fig. 8) and the REE (spoon-shaped and LREE-enriched) as well as the extended trace-element patterns of the two groups of clinopyroxenes. It has to be noticed that the Na_2O and Cr_2O_3 contents of the investigated clinopyroxenes never reach (by far) the high values found by Ikehata and Arai (2004) in the kosmochlor-bearing diopsides from type I mantle peridotite xenoliths from New Zealand that have been metasomatized by a carbonatitic melt. The selective enrichments in the most incompatible elements, LREEs (and in some samples of MREEs), in bulk rocks and clinopyroxenes, as well as the crystallization of mantle amphiboles and phlogopites, are generally considered to be a result of

interactions between melts or fluids and the surrounding mantle rocks (e.g., O'Reilly and Griffin, 1988; Coltorti et al., 1999; Van Acherbergh et al., 2001; Grégoire et al., 2003, 2005). Thus, it appears that the studied mantle xenoliths from Nyos, a volcanic plain of the Cameroon volcanic line, record two main petrogenetic processes: partial melting and metasomatism.

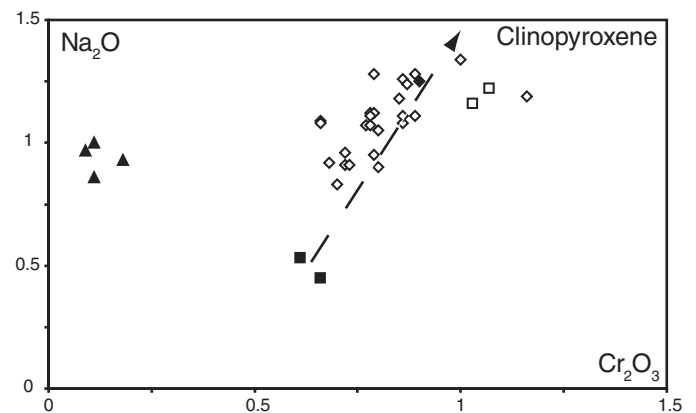


Figure 8. Diagram Na_2O versus Cr_2O_3 (wt%) of the clinopyroxenes of the peridotites from Nyos, highlighting a trend between lherzolites and harzburgites. Diamonds—group 1 samples (black diamond—amphibole-bearing harzburgite NK02); squares—group 2 samples (black square—phlogopite-bearing harzburgite NK04); triangles—wehrlite NK08.

The clinopyroxenes from the group 1 and group 2 mantle peridotites from Nyos display REE and extended trace-element patterns similar to those of the mantle spinel peridotite xenoliths entrained by the alkaline lavas from Spitsbergen and from Oman occurring in similar extensional (rifting) continental settings (Ionov *et al.*, 2002; Grégoire *et al.*, 2009) (Figs. 9 and 10). Ionov *et al.* (2002) and then Grégoire *et al.* (2009) proposed a two-stage evolution model to explain the history of their xenolith collections. First, partial melting of a more or less fertile peri-

dotitic mantle forms residues characterized by LREE-depleted patterns. These melting residues are subsequently metasomatized by OIB-like carbonate-rich mafic silicate melts (Ionov *et al.*, 2002; Grégoire *et al.*, 2009). This metasomatic event leads to enrichment in the most incompatible elements, especially LREEs (\pm MREEs) of the clinopyroxenes (Fig. 9). If we compare the Spitsbergen and Oman mantle clinopyroxenes with the studied Nyos mantle clinopyroxenes, the latter display very similar REE and incompatible trace-element patterns (Figs. 9 and 10),

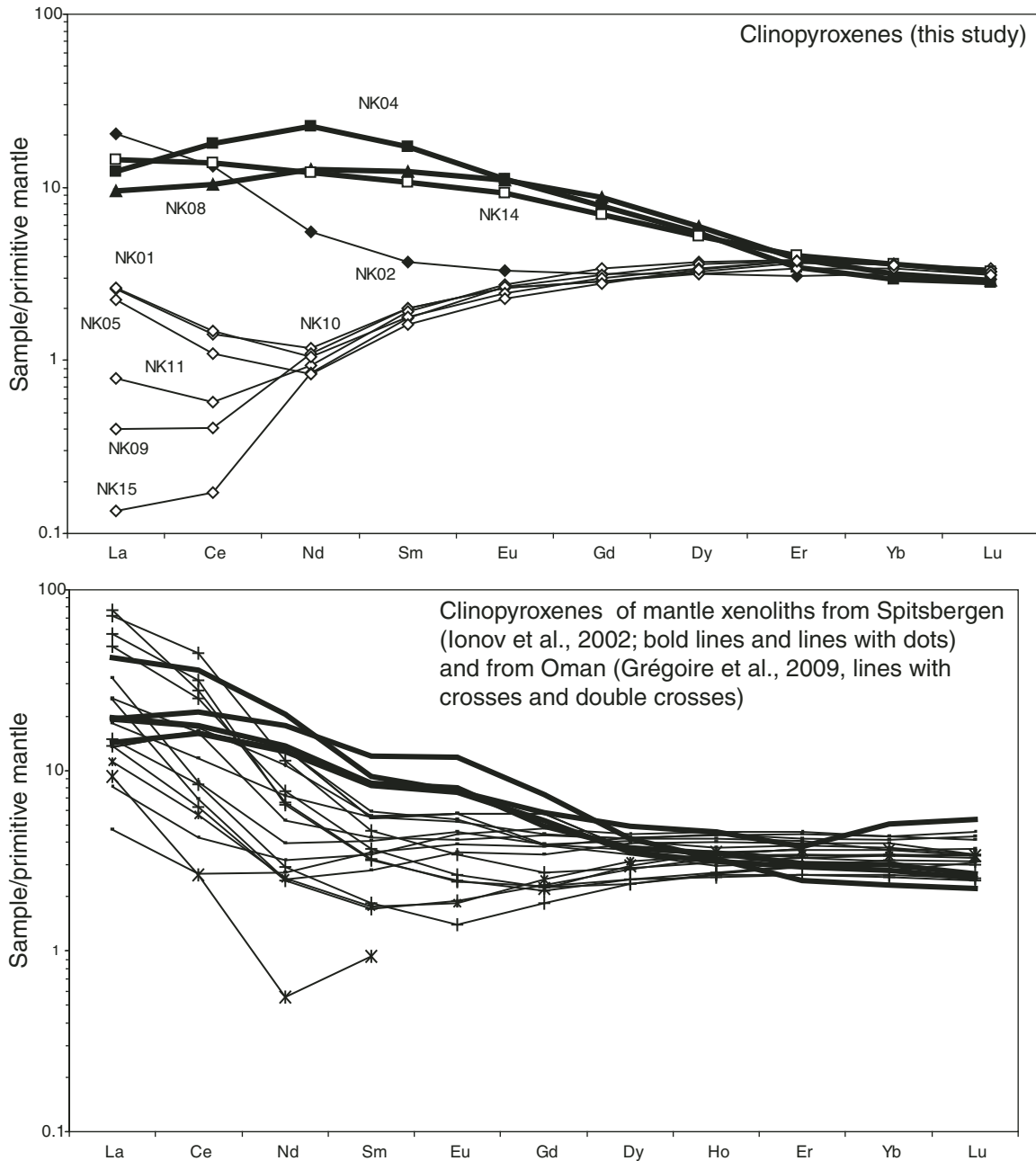


Figure 9. Rare earth element patterns of clinopyroxenes of the Nyos peridotites compared to those of Spitsbergen mantle peridotites (Ionov *et al.*, 2002) and Oman (Grégoire *et al.*, 2009).

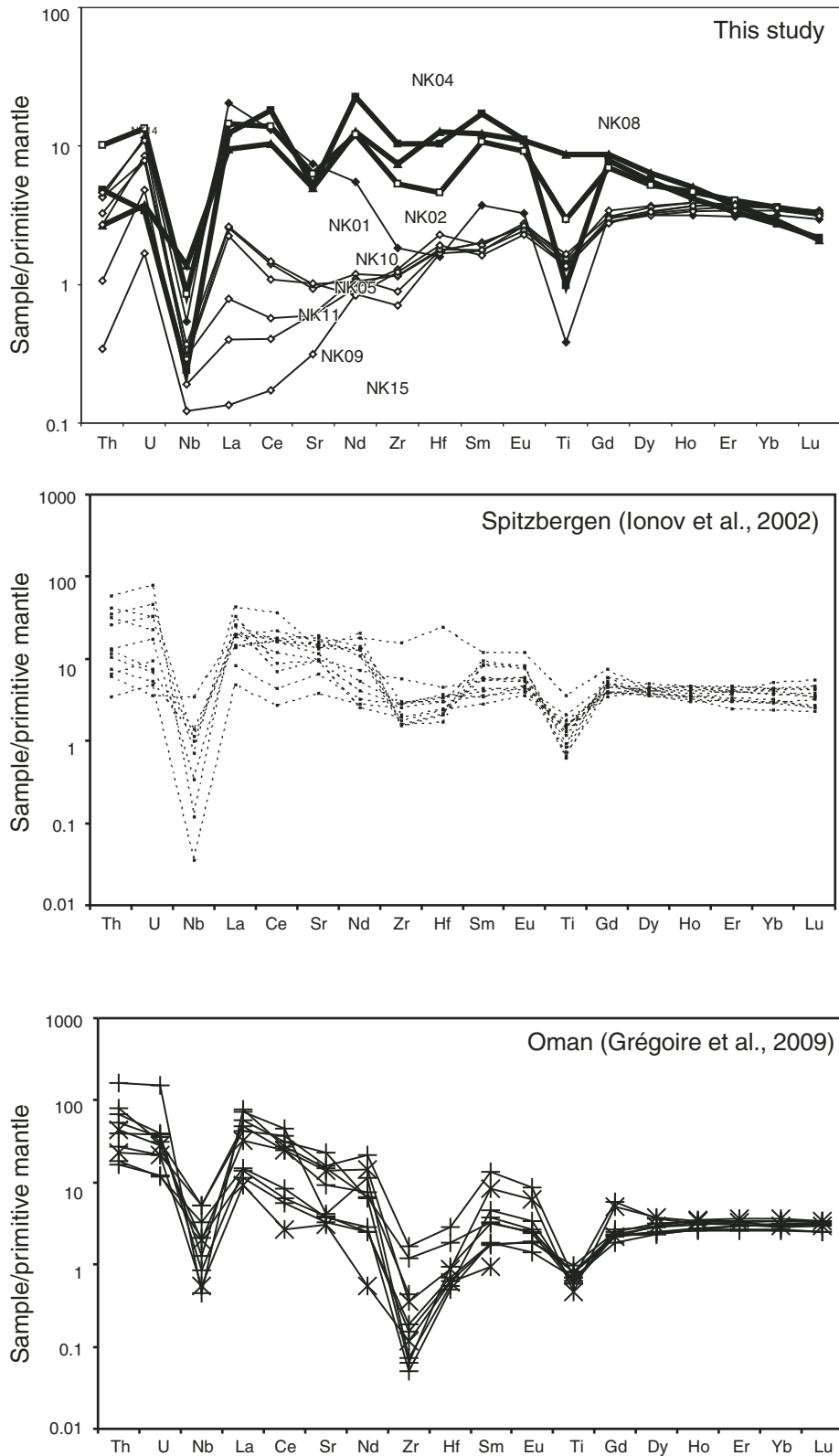


Figure 10. Extended incompatible trace-element patterns of clinopyroxenes of the Nyos peridotites compared to those of Spitzbergen mantle peridotites (Ionov et al., 2002) and Oman (Grégoire et al., 2009).

and therefore it is plausible that the metasomatic agents are similar in composition in the three cases: an OIB-like carbonate-rich mafic silicate melt. Finally, the two-step evolution model can be invoked to explain the trace-element compositions of group 1 samples from the present study. In such a model, they are affected in a first stage by partial melting degrees lower than 5%. Later, in a second stage, the resulting melting residues undergo a metasomatic event, leading to the re-enrichment in the most incompatible elements and LREEs (\pm MREEs) of both clinopyroxenes and bulk rocks. The metasomatic agent is probably a carbonate-rich mafic silicate melt enriched in highly incompatible trace elements and characterized by low abundances of Nb, Ta, and Ti. A similar two-step model has been already proposed by Temdjim et al. (2004) based on the study of some other mantle peridotite xenoliths from the Nyos Plain, but they did not give an estimate of the degree of partial melting, since they only propose a high degree of partial melting, not in agreement with our results. On the other hand, Lee et al. (1996) described some Nyos perido-

tites displaying clinopyroxenes with spoon-shaped REE patterns similar to those of our group 1 xenoliths.

It appears when we look at the group 2 spinel-bearing peridotites (Iherzolite NK14 and phlogopite-bearing harzburgite NK04) that their REE and extended trace-element patterns of both clinopyroxenes and bulk rock (NK04) are not in agreement with an origin as residues of partial melting. This kind of pattern is better explained by metasomatic processes related to the circulation of a high volume of a melt (or a fluid) within the upper mantle (e.g., Grégoire et al., 2002; Ionov et al., 2002). In order to assess if the metasomatic agent could have a link with the alkaline volcanic activity characterizing the plains of the Cameroon volcanic line and responsible for the uplift of the mantle xenoliths, we calculated the theoretical melts in equilibrium with the group 2 clinopyroxenes, as well as those in equilibrium with the clinopyroxene phenocrysts of some alkaline mafic lavas from the Kumba Plain (Cameroon volcanic line), and compared the results. For that calculation, we used the clinopyroxene/basanite

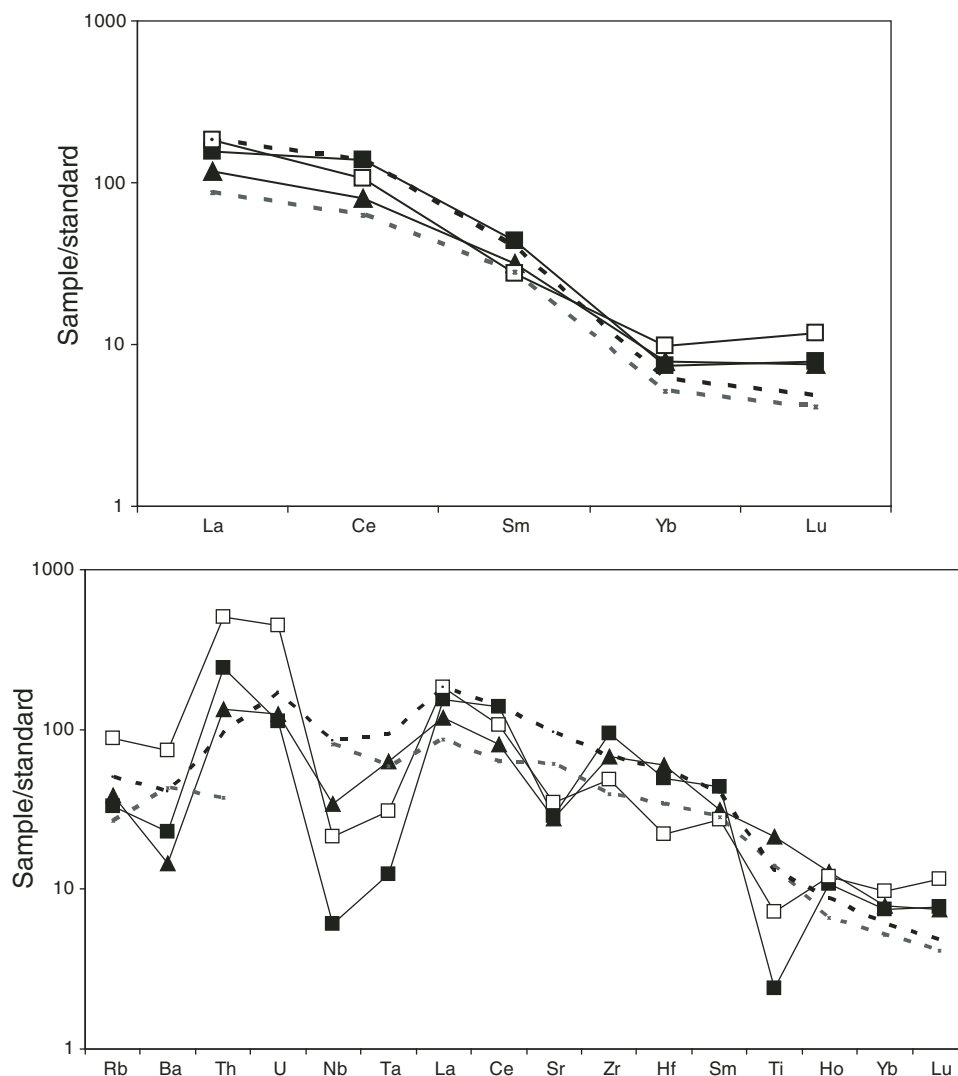


Figure 11. Rare earth element and extended incompatible trace-element patterns of the hypothetical melts in equilibrium with clinopyroxenes from group 2 peridotites from Nyos (NK04—phlogopite-bearing harzburgite; NK14—porphyroclastic to equigranular Iherzolite; and NK08—wehrlite, same symbols as in Fig. 4), compared to those of the hypothetical melts in equilibrium (dashed lines) with the clinopyroxene megacrysts of some lavas from the Kumba Plain (a plain from the Cameroon volcanic line located not far from Nyos, samples MC4 and T14; Teitchou, 2008). Normalizing values are from McDonough and Sun (1995) and clinopyroxene/basanite partition coefficients at 0.5 GPa are from Adam and Green (2003).

partition coefficients at 0.5 GPa from Adam and Green (2003) and clinopyroxenes of some lavas from the Kumba Plain, which is close to the Nyos Plain, because no in situ analyses were available for Nyos lavas. The link is clearly evidenced by the similarity of the REE and trace-element patterns of the calculated liquids in equilibrium with the clinopyroxenes of our group 2 samples with those in equilibrium with clinopyroxene phenocrysts occurring in some lavas from the Kumba Plain (Fig. 11; samples T14 and MC4 from Teitchou, 2008). Finally, it is possible to propose that the metasomatic agent that has circulated at depth within the group 2 Nyos mantle peridotites was probably an alkaline mafic silicate melt similar to some of the alkaline magmas linked to the activity of the Cameroon volcanic line.

In the diagram Na_2O versus Cr_2O_3 (Fig. 8), the two groups of samples (except the wehrlite) define the same trend of increasing Na_2O content at increasing Cr_2O_3 content, highlighting a common metasomatic history, and such a positive correlation is typical of metasomatic processes (e.g., Grégoire et al., 2003; Delpech et al., 2004). On the other hand, different hydrous minerals appear in the two groups of spinel-bearing peridotites: amphibole in group 1 and phlogopite in group 2. Those amphiboles and phlogopites display similar compositional characteristics compared to those of their equivalents in the mantle peridotites from the Kerguelen Islands, which are related to the metasomatism of mantle peridotites by alkaline to high-alkaline carbonate-rich mafic silicate melts (Grégoire et al., 2000).

Finally, it is possible to propose that the agents responsible for the metasomatic (and magmatic, for the wehrlite NK08) characteristics of group 1 and group 2 Nyos peridotites are probably similar and correspond to more or less alkaline and carbonate-rich mafic silicate melts related to the magmatic activity leading to the eruption of the alkaline lavas of the Cameroon volcanic line. Group 2 xenoliths are relatively Fe-rich, which is not typical for normal lithospheric mantle. Fe-rich mantle here is probably related to circulation within the depleted mantle of a large volume of these more or less alkaline and carbonate-rich mafic silicate melts.

CONCLUSION

The Nyos spinel peridotites studied here represent fragments of upper mantle affected by partial melting and metasomatism. The study of these peridotites reveals a complex evolution of the Nyos upper mantle that involved at least two stages. The first stage was due to relatively low degrees of partial melting (less than 5%), which produced moderately depleted lherzolites and harzburgites from a fertile, probably lherzolitic, upper mantle. Later on, metasomatic agents circulated within this previously depleted upper mantle, leading to chemical and mineralogical modifications, such as incompatible trace-element enrichment, especially LREEs, both in bulk rocks and clinopyroxenes, as well as crystallization of amphibole and phlogopite in some samples. We propose that the metasomatic agents are similar in affinity, corresponding to more or less alkaline and carbonate-rich mafic

silicate melts. Within the lithosphere, a similar melt crystallized a wehrlite characterized by a cumulative texture. This magmatic activity at depth within the Nyos lithosphere is genetically linked to the alkaline volcanic activity observed within the plains located along the Cameroon volcanic line, such as Nyos and Kumba, i.e., volcanic activity responsible for the sampling of the peridotite xenoliths. Finally, our model may also explain the characteristics of the mantle peridotites from Nyos studied before by Lee et al. (1996), Nana et al. (1996), and Temdjim et al. (2004).

ACKNOWLEDGMENTS

This work was supported by a French government scholarship and the Institute of Geological and Mining Research (IRGM), Cameroon. P. de Parseval, F. Candaudap, and C. Boucayrand are thanked for their help during data acquisition. We thank T. Ntafflos and an anonymous reviewer for their constructive reviews, and G. Bianchini for his excellent editorial work.

REFERENCES CITED

- Adam, J., and Green, T., 2003, The influence of pressure, mineral composition and water on trace element partitioning of clinopyroxene, amphibole and basaltic melts: *European Journal of Mineralogy*, v. 15, p. 831–841, doi:10.1127/0935-1221/2003/0015-0831.
- Bonatti, E., and Michael, J., 1989, Mantle peridotite from continental rifts to ocean basin to subduction zones: *Earth and Planetary Science Letters*, v. 91, p. 297–311, doi:10.1016/0012-821X(89)90005-8.
- Brey, G.P., and Köhler, T., 1990, Geothermobarometry in four phase lherzolites: II. New thermobarometers, and practical assessment of existing thermobarometers: *Journal of Petrology*, v. 31, p. 1353–1378.
- Caldeira, R., and Munhá, J.M., 2002, Petrology of ultramafic nodules from São Tomé Island, Cameroon volcanic line (oceanic sector): *Journal of African Earth Sciences*, v. 34, p. 231–246, doi:10.1016/S0899-5362(02)00022-2.
- Coltorti, M., Bonadiman, C., Hinton, R.W., Siena, F., and Upton, B.G.J., 1999, Carbonatite metasomatism of the oceanic upper mantle: Evidence from clinopyroxenes and glasses in ultramafic xenoliths of Grande Comores, Indian Ocean: *Journal of Petrology*, v. 40, p. 133–165, doi:10.1093/petrology/40.1.133.
- Dantas, C., Ceuleneer, G., Grégoire, M., Python, M., Frey, R., Warren, J., and Dick, H.B.J., 2007, Pyroxenites dredged along the South-West Indian Ridge, 9°–16°E: Cumulates from incremental melt fractions produced at the top of a cold melting regime: *Journal of Petrology*, v. 48, p. 647–660, doi:10.1093/petrology/egl076.
- Delpech, G., Grégoire, M., O'Reilly, S.Y., Moine, B.N., Michon, G., and Giret, A., 2004, Feldspar from carbonate rich silicate metasomatism in the shallow oceanic mantle under Kerguelen Islands (south Indian Ocean): *Lithos*, v. 23, p. 1213–1245.
- Dérulle, B., Moreau, C., Nkumbou, C., Kambou, R., Lissom, J., Njonfang, E., Ghogomu, R.T., and Nono, A., 1991, The Cameroon Line: A review, in Kampunzu, A.B., and Lubala, R.T., eds., *Magmatism in an Extensional Structure Setting*: Heidelberg, Springer-Verlag, p. 274–328.
- Dérulle, B., Ngounouno, I., and Demaiffe, D., 2007, The “Cameroon hot line” (CHL): A unique example of active alkaline intraplate structure in both oceanic and continental lithospheres: *Comptes Rendus Geoscience*, v. 339, p. 589–600, doi:10.1016/j.crte.2007.07.007.
- Frey, F.A., and Prinz, M., 1978, Ultramafic inclusions from San Carlos, Arizona: Petrologic and geochemical data bearing on their petrogenesis: *Earth and Planetary Science Letters*, v. 38, p. 129–176, doi:10.1016/0012-821X(78)90130-9.
- Girod, M., Dautria, J.-M., Ball, E., and Soba, D., 1984, Estimation de la profondeur du Moho, sous le massif volcanique de l'Adamaoua (Cameroun), à partir de l'étude d'enclaves de lherzolite: *Comptes Rendus de l'Académie des Sciences*, v. 298, p. 699–704.
- Grégoire, M., Moine, B.N., O'Reilly, S.Y., Cottin, J.Y., and Giret, A., 2000, Trace element residence and partitioning in mantle xenoliths

- metasomatized by highly alkaline, silicate and carbonate rich melts (Kerguelen Islands, Indian Ocean): *Journal of Petrology*, v. 41, p. 477–509, doi:10.1093/petrology/41.4.477.
- Grégoire, M., Bell, D.R., and Le Roex, A.P., 2002, Trace element geochemistry of phlogopite-rich mafic mantle xenoliths: Their classification and their relationship to phlogopite-bearing peridotite and kimberlites revisited: *Contributions to Mineralogy and Petrology*, v. 142, p. 603–625, doi:10.1007/s00410-001-0315-8.
- Grégoire, M., Bell, D.R., and Le Roex, A.P., 2003, Garnet lherzolites from the Kaapvaal craton South Africa: Trace element evidence for a metasomatic history: *Journal of Petrology*, v. 44, p. 629–657, doi:10.1093/petrology/44.4.629.
- Grégoire, M., Tinguely, C., Bell, D.R., and Le Roex, A.P., 2005, Spinel lherzolite xenoliths from the Premier kimberlite (Kaapvaal craton, South Africa): Nature and evolution of the shallow upper mantle beneath the Bushveld complex: *Lithos*, v. 84, p. 185–205, doi:10.1016/j.lithos.2005.02.004.
- Grégoire, M., Langlade, J.A., Delpech, G., Dantas, C., and Ceuleneer, G., 2009, Nature and evolution of the lithospheric mantle beneath the passive margin of east Oman: Evidence from mantle xenoliths sampled by Cenozoic alkaline lavas: *Lithos*, v. 112, p. 203–216.
- Halliday, A.N., Dickin, A.P., Fallick, A.F., and Fitton, J.G., 1988, Mantle dynamics: A Nd, Sr, Pb and O study of the Cameroon Line volcanic chain: *Journal of Petrology*, v. 29, p. 181–211.
- Hellebrand, E., Snow, J.E., Dick, H.J.B., and Hoffman, A.W., 2001, Coupled major and trace elements as indicators of the extent of melting in mid-ocean ridge peridotites: *Nature*, v. 410, p. 677–681, doi:10.1038/35070546.
- Ikehata, K., and Arai, S., 2004, Metasomatic formation of kosmochlor-bearing diopside in peridotite xenoliths from North Island, New Zealand: *The American Mineralogist*, v. 89, p. 1396–1404.
- Ionov, D.A., Bodinier, J.-L., Mukasa, S.B., and Zanetti, A., 2002, Mechanism and sources of mantle metasomatism: Major and trace element compositions of peridotite xenoliths from Spitsbergen in the context of numerical modelling: *Journal of Petrology*, v. 43, p. 2219–2259, doi:10.1093/petrology/43.12.2219.
- Jagoutz, E., Palme, H., Baddenhauser, H., Blum, K., Cendales, M., Dreibus, G., Spettel, B., Lorenz, V., and Wänke, H., 1979, The abundance of major, minor and trace elements in the Earth as derived from primitive ultramafic nodules: Houston, Lunar and Planetary Institute, Lunar and Planetary Science Conference X, p. 2031–2050.
- Johnson, K.T.M., Dick, H.J.B., and Shimizu, N., 1990, Melting in the oceanic mantle: An ion microprobe study of diopsides in abyssal peridotites: *Journal of Geophysical Research*, v. 95, p. 2661–2678, doi:10.1029/JB095iB03p02661.
- Kling, G.W., Clark, M.A., Compton, H.R., Devine, J.D., Evans, W.C., Humphrey, A.M., Koenigsberg, E.J., Lookwood, J.P., Tuttle, M.L., and Wagner, G.N., 1987, The 1986 Lake Nyos gas disaster in Cameroon, West Africa: *Science*, v. 236, p. 169–175, doi:10.1126/science.236.4798.169.
- Leake, B.E., 1978, Nomenclatures of amphiboles: *The American Mineralogist*, v. 63, p. 1023–1052.
- Lee, D.C., Halliday, A.N., Gareth, R.D., Essene, E.J., Fitton, J.G., and Temdjim, R., 1996, Melt enrichment at shallow depleted mantle: A detailed petrological, trace element and isotopic study of mantle-derived xenoliths and megacrysts from the Cameroon Line: *Journal of Petrology*, v. 37, p. 415–441, doi:10.1093/petrology/37.2.415.
- Le Maitre, R.W., 1979, A new generalised petrological mixing model: *Contributions to Mineralogy and Petrology*, v. 71, p. 133–137, doi:10.1007/BF00375429.
- Marzoli, A., Picirillio, E.M., Renne, P.R., Bellieni, G., Iacumin, M., Nyobe, J.B., and Tongwa, A.F., 2000, The Cameroon volcanic line revisited: Petrogenesis of continental basaltic magmas from lithospheric and asthenospheric mantle sources: *Journal of Petrology*, v. 41, p. 87–109, doi:10.1093/petrology/41.1.87.
- McDonough, W.F., and Sun, S.-s., 1995, The composition of the Earth: *Chemical Geology*, v. 120, p. 223–253, doi:10.1016/0009-2541(94)00140-4.
- Meyers, J.B., Rosendahl, B.R., Harrison, C.G.A., and Zan-Dong Ding, 1998, Deep-imaging seismic and gravity results from the offshore Cameroon volcanic line, and speculation of African hotlines: *Tectonophysics*, v. 284, p. 31–63, doi:10.1016/S0040-1951(97)00173-X.
- Montigny, R., Ngounouno, I., and Déruelle, B., 2004, Ages K-Ar des roches magmatiques du fossé de Garoua (Cameroun): Leur place dans le cadre de la «Ligne du Cameroun»: *Comptes Rendus Geoscience*, v. 336, p. 1463–1471, doi:10.1016/j.crte.2004.08.005.
- Moreau, C., Regnault, T.M., Déruelle, B., and Robineau, B., 1987, A new tectonic model for Cameroon Line, Central Africa: *Tectonophysics*, v. 141, p. 317–334, doi:10.1016/0040-1951(87)90206-X.
- Nana, R., 2001, *Pétrologie des Péridotites en Enclaves dans les Basaltes Alcalins Récents de Nyos: Apport à la Connaissance du Manteau Supérieur de la Ligne du Cameroun* [Ph.D. thesis]: Yaoundé, Cameroon, Université de Yaoundé I, 250 p.
- Nana, R., Nkoumbou, C., Tchouankoue, J.-P., Tabod, C., and Tchoua, F.M., 1996, Preliminary studies of some peridotite xenoliths from Nyos volcano (Cameroun): Implications for the evaluation of volcanic hazards: *Current Research on Volcanic Lakes*, v. 9, p. 21–24.
- Nixon, P.H., 1987, *Mantle Xenoliths*: Chichester, UK, J. Wiley and Sons, 844 p.
- O'Reilly, S.Y., and Griffin, W.L., 1988, Mantle metasomatism beneath Victoria, Australia: I. Metasomatic processes in Cr-diopside lherzolites: *Geochimica et Cosmochimica Acta*, v. 52, p. 433–447, doi:10.1016/0016-7037(88)90099-3.
- Pouchou, J.L., and Pichoir, F., 1984, A new model for quantitative X-ray microanalysis: Part I. Application to the analysis of homogeneous samples: *Recherche Aérospatiale*, v. 5, p. 13–38.
- Princivalle, F., Salviolo, G., Marzoli, A., and Piccirillo, E.M., 2000, Clinopyroxene of spinel-peridotite xenoliths from Lake Nji (Cameroon volcanic line, W Africa): Crystal chemistry and petrological implications: *Contributions to Mineralogy and Petrology*, v. 139, p. 503–508, doi:10.1007/s004100000151.
- Rankenburg, K., Lassiter, J.C., and Brey, G., 2004, Origin of megacrysts in volcanic rocks of the Cameroon volcanic chain—Constraints on magma genesis and crustal contamination: *Contributions to Mineralogy and Petrology*, v. 147, p. 129–144, doi:10.1007/s00410-003-0534-2.
- Streckeisen, A., 1976, To each plutonic rock its proper name: *Earth-Science Reviews*, v. 12, p. 1–33, doi:10.1016/0012-8252(76)90052-0.
- Tamen, J., 1998, *Contribution à l'Étude Géologique du Plateau Kapsiki (Extrême-Nord, Cameroun): Volcanologie, Pétrologie et Géochimie* [Ph.D. thesis]: Yaoundé, Cameroon, Université de Yaoundé I, 127 p.
- Teitchou, M.I., 2008, *Volcanologie, Pétrologie et Géochimie Comparées de Quelques Plaines Continentales de la Ligne du Cameroun: Cas de Kumba, Tombel, Noun et Nyos* [Ph.D. thesis]: Yaoundé, Cameroon, Université de Yaoundé I, 206 p.
- Teitchou, M.I., Grégoire, M., Dantas, C., and Tchoua, F.M., 2007, Le manteau supérieur à l'aplomb de la plaine de Kumba (ligne du Cameroun), d'après les enclaves de péridotites à spinelles dans les laves basaltiques: *Comptes Rendus Geoscience*, v. 339, p. 101–109, doi:10.1016/j.crte.2006.12.006.
- Temdjim, R., and Tchoua, F.M., 1991, Cadre géologique de la région du lac Nyos: *Revue de Géographie du Cameroun*, v. 10, p. 32–38.
- Temdjim, R., Boivin, P., Chazot, G., Robin, C., and Rouleau, E., 2004, L'hétérogénéité du manteau supérieur à l'aplomb du volcan de Nyos (Cameroun) révélée par les enclaves ultrabasiques: *Comptes Rendus Geoscience*, v. 336, p. 1239–1244, doi:10.1016/j.crte.2004.07.005.
- Van Acherbergh, E., Griffin, W.L., and Stiefenhofer, J., 2001, Metasomatism in mantle xenoliths from the Letlhakane kimberlites: Estimation of element fluxes: *Contributions to Mineralogy and Petrology*, v. 141, p. 397–414, doi:10.1007/s004100000236.
- Wells, P.R.A., 1977, Pyroxene thermometry in simple and complex systems: *Contributions to Mineralogy and Petrology*, v. 62, p. 129–139, doi:10.1007/BF00372872.
- Wright, T.L., and Doherty, P.C., 1970, A linear programming and least squares computer method for solving petrologic mixing problems: *Geological Society of America Bulletin*, v. 81, p. 1995–2008, doi:10.1130/0016-7606(1970)81[1995:ALPALS]2.0.CO;2.
- Zerka, M., 2004, *Le Manteau sous la Marge Maghrébine: Relations «Infiltrations-Réactions-Cristallisations» et Cisaillements Lithosphériques dans les Enclaves Ultramafiques du Volcanisme Alcalin Plio-Quaternaire d'Oranie, Exemple des Complexes d'Aïn-Temouchent et de la Basse Tafna (Algérie Nord-Occidentale)* [Doctorat d'Etat]: Oran, Algeria, Université d'Oran, 345 p.

Dolomitic volcanism in Zambia: Cr and K signatures and comparisons with other dolomitic melts from the mantle

**D.K. Bailey
S. Kearns**

Department of Earth Sciences, University of Bristol, Bristol BS8 1RJ, UK

ABSTRACT

Volcaniclastic carbonatites in southeast Zambia contain dolomitic melt lapilli, in which high-Cr chromite phenocrysts indicate direct eruption from the mantle. There are no lava flows. Vent tuffisite, with dolomite lapilli in a matrix of dolomite + iron oxides, provides the least contaminated samples of primary erupted material. This tuffisite has high trace-element levels typical of carbonatite, but its high Cr and Ni make it exceptional. Fragmental phlogopite, sanidine, and orthoclase are indicators of potassium (K) mineralization in deeper parts of the conduit. This was the only known case of dolomite eruption directly from source until 2005, when dolomite volcanism in Spain and France provided the first opportunity for comparing these characteristics. Eruptions are fragmental: typically with rounded lapilli of low-Fe, high-Mn dolomite. Outstanding common features are euhedral chrome spinels, and a high-temperature, platy habit of the dolomite crystals. In all cases, the sparse interstitial residuum between the dolomite plates is potassic, and in Spain and France, the Cr spinels are zoned to high-Ti rims, analogous to those in high-temperature kimberlites. Experiments have long predicted that dolomite should be the initial melt from carbonated mantle below 70 km: In Spain and France, the eruptions carry mantle xenoliths, and in all three provinces, the dolomite volcanic rocks have $Mg\# > 0.65$, indicative of primary magmas. Thus, for the first time, fresh constraints are emerging from a multicomponent natural system. Bearing in mind the differences between the European (Cenozoic) and Zambian (Cretaceous) provinces (including lithosphere structures, history, and tectonics), their common features indicate that dolomite melts in the mantle are in equilibrium with chromite, and contain K-Al-Si melts (without Na). The Zambian vents are part of the large, classic Chilwa carbonatite province, which was first described in Malawi and Mozambique, where, around the intrusions, K-metasomites typically exceed carbonatite in amount. When this K is included in the eruptive budget, the total introduced material invites comparison with high-K carbonate melts formed at high pressure, e.g., carbonatitic fluid inclusions in diamonds that were trapped in the diamond stability field are dolomitic

and characterized by high-K contents. Intrusive and volcanic carbonatites show a bimodal distribution in Sr-Nd isotopes, similar to group 1 and 2 kimberlites, respectively. Diamond inclusions span the same range. Together with the indications of a deep mantle source for the volcanic facies at Rufunsa, this raises the possibility that the Chilwa complexes may be highlighting a key aspect of carbonatite activity in which potassium has a special role.

INTRODUCTION

Carbonatite of dolomitic composition has been known from the earliest accounts, e.g., rauhaugite in the Fen complex (Brögger, 1921). In intrusive complexes, it takes various forms, from large plugs to sheets and veins, originating in a variety of ways, from primary injection (e.g., cone sheets) to replacement of earlier rocks (reviewed in Bailey, 1993). One widely held view is that magnesio- and ferro-carbonatites are later differentiation products from parental calcio-carbonatite. Harmer and Gittins (1997) proposed the reverse to be true, arguing that calcio-carbonatite is a differentiate from magnesio-carbonatite that has moved to crustal levels from its mantle source. Volcaniclastic magnesio-carbonatite was first described from the Rufunsa province, Zambia (Bailey, 1960; summarized in Bailey, 1966), where melt lapilli containing chromite indicated eruption directly from the mantle (Bailey, 1989). This was the only case of dolomite volcanism in the worldwide compilation of carbonate volcanoes (Woolley and Church, 2005) until 2004, when dolomite eruptives were found in Spain (Bailey et al., 2005) and France (Bailey et al., 2006). Hence, the Rufunsa volcaniclastic rocks provide an initial basis for characterization of primary dolomitic carbonatite, especially where any new cases have equivocal field and petrological relations.

A further aim of the present contribution is to examine the role of potassium (K) and consider possible links with high-K ultramafic magmatism.

GEOLOGICAL RELATIONS

The Rufunsa province is in SE Zambia, and it marks the complex intersection of the mid-Zambesi and Luangwa Rifts. Summaries of the tectonics and geology are already available (Bailey, 1961, 1966, 1990). Activity started in the Early Cretaceous (110 Ma) and constituted an extension of the classic Chilwa igneous province, Malawi (named from the first carbonatite to be recorded in Africa; Dixey et al., 1937). Mid-Cretaceous erosion exposed the Rufunsa centers as subvolcanic complexes, which in the Late Cretaceous (85 Ma) were penetrated by the dolomitic volcaniclastic rocks that form the central topic of this paper. This later activity is best displayed in the southern part of the area at Mwambuto and Chasweta, shown in Figure 1. At both centers, an older carbonatite plug is pierced by dolomitic diatremes, with intrusive tuffisites and extrusive

tuffs and agglomerates. No lavas have been found. The only associated silicate rocks are composed of orthoclase in the form of coarse-grained feldspathic breccias, and fine-grained metasomatized mudstones, best exemplified at Mwambuto (Fig. 1), where deeper erosion shows these forming concentric rings around the magnesio-carbonatite plug.

No magmatic silicate rocks are found at present exposure levels. Xenoliths of such rocks are also absent from the widespread agglomerates at Chasweta, which contain other accidental fragments from the vent walls (gneiss, dolerite, and varieties of carbonatites and K-metasomites). Hence, there are no observational grounds to infer subsurface alkaline intrusions, nor Na metasomites. None of the sodic minerals typical of the classic carbonatite association, e.g., Na pyriboles, has been observed in the Rufunsa rocks, where sanidine megacrysts are the only mineral with significant Na (~5% Na₂O; Liyungu, 1992).

Tuffisites in the main vent at Chasweta provided the first examples of dolomitic melt droplets containing Mg chromite (Bailey, 1989), and the Mwambuto rocks also have this assemblage. Quenching of the melt droplets, and the mineral compositions, was shown to be consonant with eruption in fast-moving streams through the vent (Bailey, 1989, 1993).

PETROLOGY AND MINERAL PARAGENESIS

Tuffisite samples in the Chasweta vent are red-brown, with variable contents of accidental clasts and pale grains (up to 3 mm), most of rounded melt lapilli. In outcrop, there are small areas with a green coloration in the matrix where phlogopite is abundant.

Tuffisite Matrix

Figure 2 shows a specimen of very fine-grained vent tuffisite (groundmass ~5 μ m) dominantly composed of dolomite and iron oxide/hydroxide, giving the red-brown color. This pigment consists of minute flakes, mainly hematite; in the subsequent text, "iron oxide" will be used to indicate this ultrafine red iron oxide/hydroxide in tuff matrices. The same fine-grained, red-stained carbonate forms the matrix in extrusive, subaerial tuffs and agglomerates, being part of the residuum of the transporting medium that was left after posteruptive volatile losses. Most of the pale grains are accidental clasts (chiefly quartz) from the country rocks.

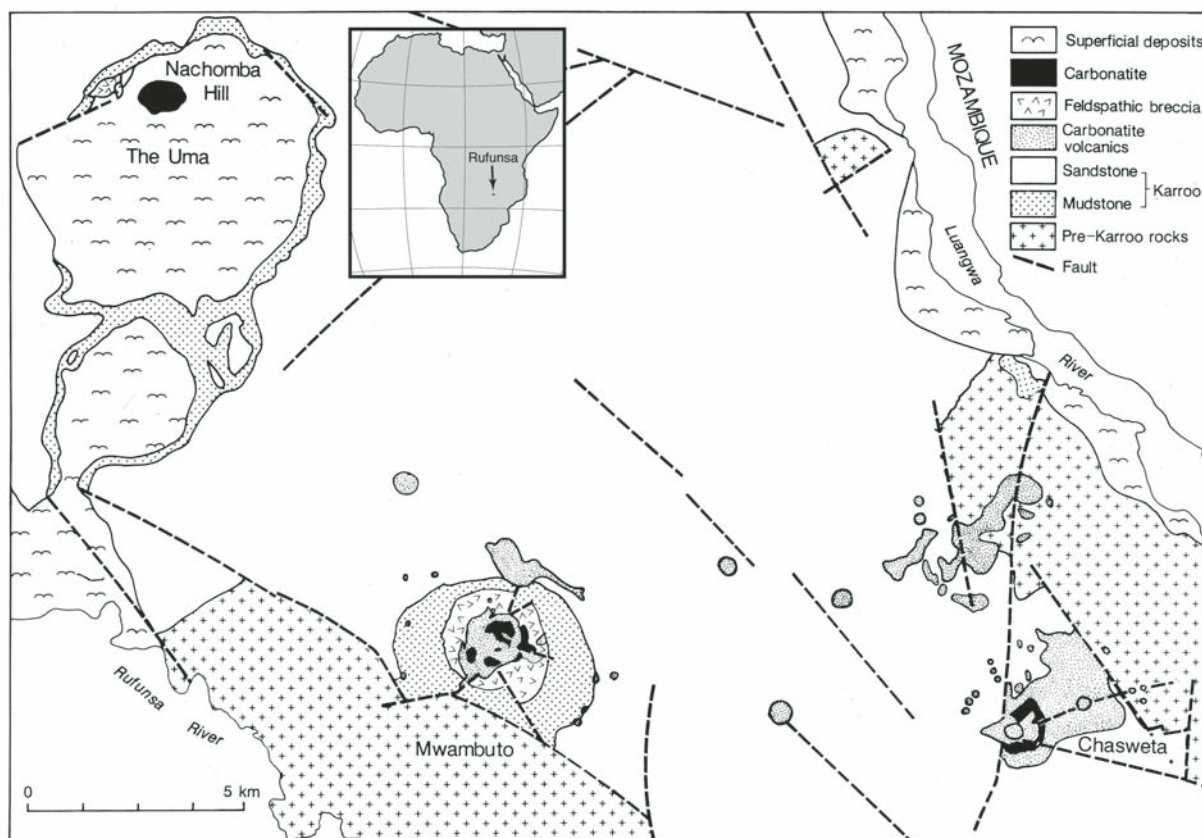


Figure 1. Simplified geological map of carbonatites in the Rufunsa province, Zambia, with inset showing location in Africa. Late Cretaceous volcanism is best displayed at Mwambuto and Chasweta. Coordinates for Chasweta are 15°21'S, 30°17'E.

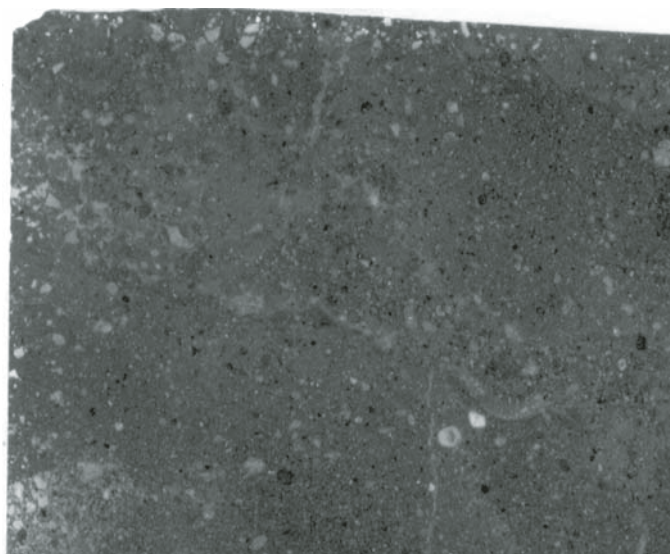


Figure 2. Vent tuffsite in thin section, Chasweta main vent, showing the very fine grain size (largest grains <1 mm). Image represents an area 1 cm across.

Melt Lapilli

Coarse pale lapilli in the Chasweta tuffsites were those first recognized to be as quenched melt (Bailey, 1989), largely aggregates of dolomite blades (~90 µm). Although these may be found in most volcanoclastic rocks of Chasweta, they are most abundant in the vent tuffsites. Many of these melt droplets have nuclei of earlier mineral grains and are essentially tiny autoliths (analyses of typical minerals are presented in Bailey, 1989). The sample in Figure 2 is essentially composed of very fine-grained material (lacking in coarser lapilli) for which a new whole-rock analysis is given in Table 1 (analysis 1).

Mineral paragenesis in the melt droplets is quite different from that which is normal in carbonatite. Along with the very distinctive high-Sr, high-Mn, and low-Fe dolomite, the only other unequivocally intrinsic mineral is zoned, euhedral, high-Cr magnesio-chromite. This is in stark contrast to normal carbonatite, where magnetite is the ubiquitous spinel, and in which Cr is typically below detection, in keeping with the general observation of low Cr in intrusive carbonatites (Woolley and Kempe, 1989; Nelson et al., 1988; Le Bas, 1999). Apatite,

TABLE 1. MAJOR ELEMENTS IN ZAMBIAN CARBONATITES

Oxide (wt%)	1	2	3	4	5	6	7	8	9	10
SiO ₂	21.59	N.D.	2.91	1.79	40.30	3.63	2.57	9.1	13.6	8.4
TiO ₂	0.30	0.012	0.03	0.06	1.15	0.33	0.72	3.1	4.6	0.7
Al ₂ O ₃	2.74	0.05	0.08	0.33	12.23	0.99	0.38	0.5	0.8	0.7
Fe ₂ O ₃ *	5.17	0.759	3.34	1.40	16.59	6.73	5.42	14.4	21.45	6.7
MnO	1.10	1.517	1.59	1.55	0.67	0.96	N.D.	N.D.	N.D.	N.D.
MgO	12.14	19.56	8.13	18.21	14.92	15.06	15.12	8.8	13.2	28.7
CaO	20.21	31.86	42.82	28.42	N.D.	30.12	21.6	13.7	20.5	23.2
Na ₂ O	0.09	0.086	0.01	d.l.	d.l.	0.29	4.93	1.5	2.2	9.1
K ₂ O	1.22	0.276	0.03	0.20	9.30	0.28	7.01	13.9	20.7	16.4
P ₂ O ₅	1.03	0.397	0.29	N.D.	N.D.	1.9	N.D.	1.6	2.4	2.6
LOI	30.2	N.D.	N.D.	N.D.	N.D.	N.D.	N.D.	N.D.	N.D.	N.D.
CO ₂	29.38	N.D.	40.47	N.D.	N.D.	36.81	N.D.	33	N.D.	N.D.
Total	95.79	54.47	99.6	52.39	96	97.47	57.36	99.6	99.45	99.3
Mg#	0.82						0.86			

Note: Columns: 1—vent tuffsite (233), Chasweta, Zambia (AES—atomic emission spectroscopy); 2—nitric acid leachate from sample 1 (AES); 3—intrusive carbonatite, Chasweta, Zambia (XRF—X-ray fluorescence); 4—line analyses across melt droplets (EPM—electron microprobe: avg. 65 points); 5—point from column 4 minus dolomite composition (normalized to 96); 6—average magnesio-carbonatite (Woolley and Kempe, 1989); 7—experimental melt (Thibault et al., 1992); 8—analysis 9 recalculated with 33% CO₂; 9—diamond inclusion end member (carbonatitic: Schrauder, and Navon, 1994); 10—diamond inclusion end member (carbonatitic: Klein-Ben David et al., 2009). N.D.—not determined; LOI—loss on ignition; d.l.—below detection limit; Mg#—Mg number. Microprobe analyses were performed on a Cameca SX100 microprobe operating at 20 kV and 10 nA employing a PAP matrix correction and using silicate and oxide standards.

*Total Fe as Fe₂O₃.

the other common accessory mineral in carbonatites, has not been found in Chasweta melt droplets.

Other forms of lapilli in the vent tuffsites have subsequently come to light, especially with advances in scanning electron microprobe (SEM) techniques, which have revealed abundant rounded lapilli that are almost indistinguishable from the enclosing fine red matrix (as in Fig. 2). These are homogeneous dolomite droplets (Fig. 3A) marking the final stages of melt fragmentation and quenching in the eruptive column. For comparison, a dolomite lapillus from Spain is shown in Figure 3B. Phase equilibrium studies on dolomite melting would require quenching deeper in the pipe (for discussion, see Bailey, 1993). These ultrafine lapilli provide the nearest approach to the final melt composition in the eruptions (Table 1, analysis 4).

Debris in the Matrix

Compared with most of the subaerial tuffs and agglomerates, the tuffsites contain less accidental debris, presumably because they were formed during the less violent, waning phases of activity. As might be anticipated, accidental debris includes grains of quartz (mainly from the immediate country rock sandstones), altered feldspar, and metamorphic micas from the underlying basement, together with recognizable orthoclase-rock fragments (K-metasomites) from the older plug. Optically, quartz grains are the most common, but the overall amounts are difficult to estimate because of the fine grain size. Most of the whole-rock analysis may be accounted for by the cognate constituents, as detailed in the following section, but there is an excess of SiO₂, ~10%–15%, which may be a measure of the amount of quartz debris, some of which could be in the ultrafine size range.

Two unexpected constituents are sanidine and phlogopite. Broken crystals of sanidine (Or_{75–85}) have compositions in the same range as megacrysts in the most easterly satellite vent of Chasweta, which will be referred to further in the later section on K activity.

In the pipe rock, phlogopite is widespread in two forms. In the matrix, as fine-grained flakes and clusters, it may be so abundant as to impart a greenish tint to the rock. Larger flakes have significant Cr contents (Bailey, 1989), with most compositions falling in the phlogopite range spanned by kimberlite groundmasses to those from mantle xenoliths (Bailey and Collier, 2000). These frequently have inclusions of euhedral chromite. Such phlogopite is absent from the fine-grained melt lapilli, but it is present in some coarser lapilli.

No phlogopite has been observed in the earlier intrusive carbonatite plug, nor, indeed, in the other central intrusive plugs at Mwambuto and Nachomba (Fig. 1).

CHEMISTRY

Major-Element Compositions

All vent tuffsite samples examined to date are more than 50% acid soluble, with almost all of the Ca, Mg, and Mn, and very little else, being taken into the leach fraction (Table 1, analyses 1 and 2). CO₂ analysis confirms carbonates in excess of 50%, leaving the major noncarbonate constituents as Fe oxides and silica, with other oxides amounting to <10%. Apart from silica, the whole-rock analysis (Table 1, analysis 1) is largely explicable in terms of observed constituents, chiefly dolomite and iron oxide, plus a small quantity of K-feldspar and phlogopite (contributing

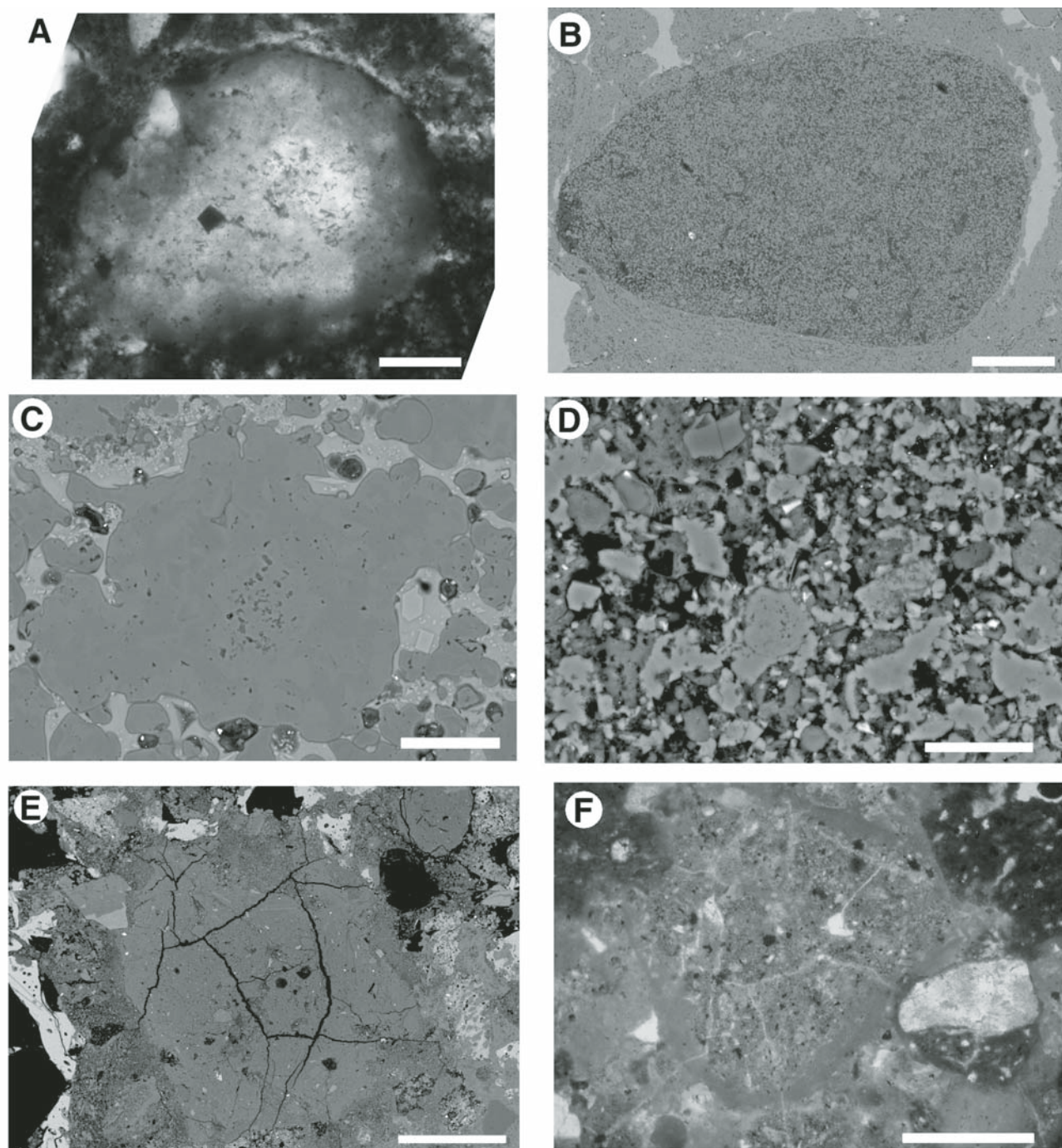


Figure 3. Showing a range of examples with potassic residua. (A) Photomicrograph of dolomite lapillus with euhedral chromite (dark), in vent tuffisite, Chasweta volcano, Zambia. The lighter region marks the central area tangentially intersected at the thin-section surface. Gray flecks in this region are potassic residua enclosed in dolomite plates. Scale bar: 100 μm . (B) Scanning electron microscope (SEM) backscattered electron (BSE) image of lapillus in extrusive dolomite lapilli tuff (CR 10 in Table 4) from Calatrava, Spain. Lapillus is a decussate mesh of pale dolomite plates enclosing the gray potassic residuum, which also forms the larger patch at the western end. Scale bar: 100 μm . (C) SEM BSE image of a coalesced aggregate of dolomite globules (gray) in nepheline glass (pale) in a pyroclastic eruption in Limagne, France (A3.1 in Table 4). This is an example where the immiscible globules coalesced, producing a larger mass with darker flecks of potassic residua in the central region. Scale bar: 50 μm . (D) SEM BSE image of the fine-grained groundmass of the pyroclastic eruption in Limagne, France (A3.1 in Table 4), consisting of dolomite plates (pale) with darker interstitial potassic residuum. Scale bar: 20 μm . (E) SEM BSE image of a fragment of the potassic residuum in the pyroclastic eruption in Limagne, France (A3.1 in Table 4). These may be readily discerned by their distinctive pattern of irregular cracks (shrinkage?) not seen in other fragment types. Fragments are surrounded by a mix of dolomite (gray) and glass (white), some of which is enclosed in the northern margin. Scale bar: 500 μm . (F) Photomicrograph of another fragment of the potassic residuum in the pyroclastic eruption in Limagne, France (A3.1 in Table 4). Fragment is marked by the pattern of irregular cracks, and rimmed by a narrow jacket of dense fine-grained dolomite. Note surrounding glass fragments (dark) partly enclosed in the potassic fragment. Scale bar: 500 μm .

to the K, Al, and Si content). High levels of carbonatitic trace elements are also consistent with little input from the accidental debris to the bulk composition.

Contamination of the tuffisite matrix from the older carbonatite complex lining the vent obviously needs consideration. Some K-feldspar, and traces of magnetite and apatite, may be attributable to this source, but because the vent rock is essentially dolomitic, while the earlier intrusion is calcitic, the contribution must be small. High Ba in the whole-rock analysis is proportionally matched by S, and some barite could come from the older complex, but some is disseminated as fine grains, and may be intrinsic.

Analysis of the ultrafine melt droplets is obviously a desirable adjunct to the whole-rock composition, but clean separation is not possible. Droplets can be analyzed by averaging lines of electron microprobe (EMP) point analyses. One of these (Table 1, analysis 4) is similar to probe analyses of single grains of melt dolomite, and thus could serve as a useful approximation to the dolomite melt fraction of the total eruptive package, possibly providing a pivot for discussion of the whole rock (Table 1, analysis 1). Iron-oxide levels in the whole-rock samples are too high (5%–12%) to be plausibly explained by assimilation of any known rocks that might have been traversed on the way to the surface, and is presumably largely from source. Intimate association with the matrix dolomite indicates that it is part of the residuum from release of volatiles during the closing stages of eruption.

Acid-soluble fractions of pipe tuffisite (50%–65%) provide another insight, an example of which is shown in Table 1 (analysis 2): Its composition is essentially high-Mn, low-Fe dolomite similar to that of most melt droplets. The earlier intrusive calcio-carbonatite contains much less Mg (Table 1, analysis 3, representing the upper Mg levels), implying that this is not a major contaminant in the pipe rock, and that the matrix dolomite is cognate. As will be seen from the trace elements (Table 2), the insoluble fraction of the whole rock must carry a substantial proportion of those elements characteristic of carbonatite, but the insoluble contribution from the older calcio-carbonatite must also be small, so that much of the trace-element content must be intrinsic to the vent rocks. Because much of the matrix is dolomite and iron oxides, the conclusion is that the bulk of the vent tuffisite at Chasweta represents the primary eruptive load.

TABLE 2. TRACE ELEMENTS IN SAMPLES 1–3 (TABLE 1)

Element (ppm)	1	2	3
Ba	19,034	2198	448
Th	225	12	68
Rb	43	3	3
Nb	573	0.1	1320
La	1666	160	434
Sr	8110	3627	1524
Sm	79	20	76
Yb	5	3	5
Ni	115	142	73
Cr	223	84	12
La/Yb	333	53	87

Trace Elements

Probably the most striking feature of the trace elements is the high levels of Ni and Cr in the tuffisites, which distinguish them from all intrusive carbonatites in the province, and from carbonatites generally (Woolley and Kempe, 1989; Nelson et al., 1988; Le Bas, 1999). Values in Table 2 show Cr to be a particularly powerful discriminant between tuffisite (analysis 1) and the earlier intrusion (analysis 3). Chromite is clearly the main Cr source, but nearly all the Ni is in the soluble fraction (Table 2, analysis 2), giving a positive Ni spike on the incompatible element profile for this fraction. The soluble fraction is almost entirely Mn-dolomite (Table 1, analysis 2), and the same distribution pattern for Ni is found in volcanic dolomites of Spain and France.

Carbonatites have yielded the highest levels of incompatible elements among igneous rocks, but because most of the data are from intrusions (with their possible differentiation histories at high levels within the crust), direct eruptions from the mantle have special value as indicators of primary levels. Rare earth elements (REEs) are most widely used as a comparative measure of incompatible element levels (Nelson et al., 1988; Le Bas, 1999), and values for some Chasweta samples are shown in Table 3 and Figure 4. Heavy (H) REEs are essentially similar in the vent tuffisite and the older intrusive carbonatite, but it is noticeable that the light (L) REEs are significantly higher in the primary volcanic material. The intrusive carbonatite (analysis 3) provides a convenient standard of reference for the trace elements because it lies midway between the average that can be calculated from the wide range given by Nelson et al. (1988) and the average carbonatite (calcio- and magnesio-) of Woolley and Kempe (1989). Furthermore, the Chasweta intrusive carbonatite profile provides another useful reference because it is virtually identical to that given by the sample with the highest LREE from diamond inclusions (Schrauder et al., 1996; Table 3, jwn 87a). Schrauder et al. (1996) refer to these as carbonatitic, showing them to have REE profiles higher than lamproites, and, for most inclusions, kimberlites also (Schrauder et al., 1996; Fig. 4). The REE profile for

TABLE 3. RARE EARTH ELEMENTS (REEs) IN SAMPLES 1–3 (TABLE 1)

Element (ppm)	1	2	3
La	1666	160	434
Ce	2592	253	879
Pr	213	34	119
Nd	710	122	509
Pm	N.D.	N.D.	N.D.
Sm	79	20	76
Eu	28	7.01	23
Gd	82	17	52
Tb	5.30	2.04	5.65
Dy	30	10	23
Ho	3.68	1.62	3.40
Er	8.64	4.55	7.69
Tm	0.86	0.59	0.91
Yb	5.26	3.28	4.69
Lu	0.79	0.47	0.64
Y	63	48	64

Note: N.D.—not determined.

the acid-soluble fraction of the vent tuffsite is notable for being significantly lower than that of the whole rock (and the intrusive carbonatite; Fig. 4) but also because it is relatively lower in LREEs (see La/Yb in Table 2). Hence, there is significant trace-element separation between the soluble and insoluble fractions of the rock.

Other elements typical of carbonatite, such as Nb, are predictably separated because they are normally in insoluble minerals. This may be seen in Table 2 and Figure 5, where a selection of trace elements, covering a range of compatibility, is compared. Together with REEs and major elements, the overall pattern is one of separation of LREE, Nb, Th, along with Fe and Cr, into the insoluble fraction, indicating that this is an essential part of the eruptive load.

POTASSIUM IN CARBONATITE

Strung along the rifts of southern Malawi and the lower Zambesi (Mozambique) to Rufunsa, Zambia, over a distance of ~1000 km, there are at least 25 carbonatite complexes of Early Cretaceous age, constituting the Chilwa province. From the very first account, the large amounts of associated orthoclase rocks were made clear by Dixey et al. (1937). In this first description of carbonatites in Africa, they were also specific about the relation of the orthoclase rocks and the carbonatites: "Their intimate relations with the 'magmatic limestones' seems to imply a common source and almost simultaneous actions for the solutions or magma supplying both the potash and calcium carbonates of the vents" (p. 44).

Subsequent studies (Bailey, 1960; Garson, 1965) led to the same conclusion, and indeed, in his detailed descriptions of the Malawi complexes, Garson was even more specific, attributing

the feldspathization directly to carbonate emplacement, including explicitly the magnesio-carbonatites at Kangankunde (Garson, 1965, p. 52), e.g., highlighting the feature of narrow veins of magnesio-carbonatite producing K-feldspathization along the margins. In his summary, he says the feldspathization "can be directly attributed to emanations from carbonatitic rocks" (Garson, 1965, p. 96).

High-K activity is one of the striking features of the Rufunsa province, being seen most spectacularly in its power to metasomatize any earlier lithology to orthoclase rock (Bailey, 1966). The extent and intensity are best seen around the Mwambuto complex (Fig. 1), which is more deeply eroded than Chasweta. Here, the earlier carbonatite plug (diameter 1.2 km) is ringed by feldspathic breccia and by Mesozoic mudstone that has been transformed into K-feldspar (diameter 2.5 km). Hence, at this level, the areal proportions of carbonatite and K-feldspar rock is ~1:4, suggesting that the K_2O released into the country rocks is equivalent to ~50% of the mass of the remaining intrusive carbonatite. In many Chilwa centers, the proportions of carbonatite to orthoclase rock are of similar order, while in others, the area of orthoclase rock far exceeds that of carbonatite in the complex, e.g., Kangankunde, Malawi. Probably the closest analogy to the Rufunsa vents in the Chilwa province is Muambe, in Mozambique, where there is a large central carbonatite intrusion encircled by a ridge of feldspathic rocks, 5 km in diameter. Only K-metasomatism is reported. Like the Rufunsa complexes, Muambe is at a high level, with Mesozoic country rocks. Details are limited, but a map, and brief review, with references, is given in Woolley (2001).

Not only is potassium high in proportion to carbonatite, but it was partitioned into an exceedingly mobile phase. In all the Chilwa vents, K release was followed or accompanied by carbonatite emplacement.

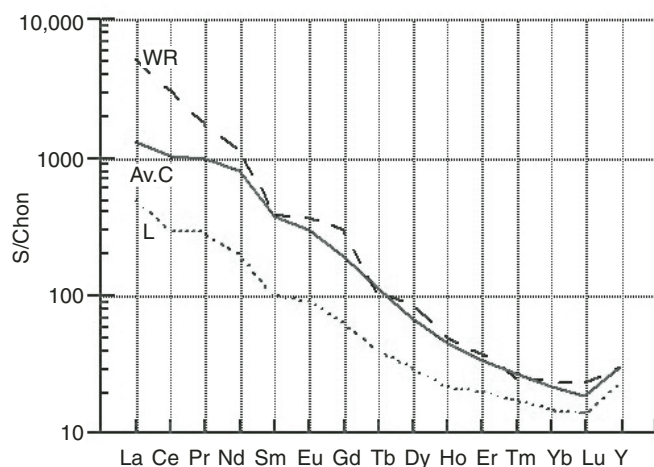


Figure 4. Chondrite-normalized rare earth element profiles (Table 3) of vent tuffsite (whole rock [WR]—long dashes; acid leachate [L]—short dashes) compared with intrusive carbonatite (Av.C—single line). The intrusive carbonatite profile is a good representative of average carbonatite, and carbonatitic inclusions in diamond (see text). Values are normalized to chondrite (Nakamura, 1974).

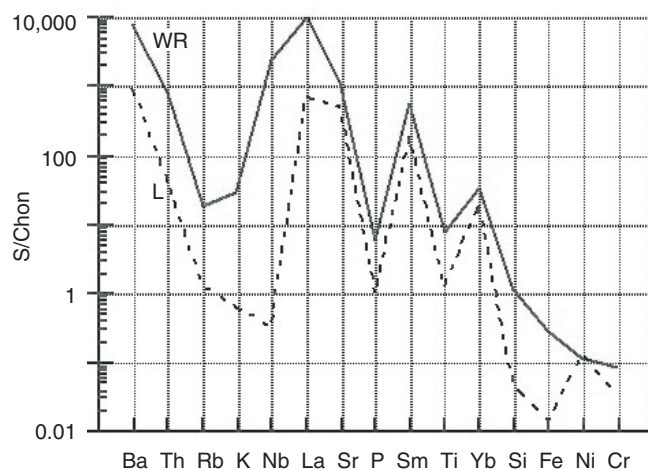


Figure 5. Comparison of a range of elements (Table 2) of different compatibilities, for the vent tuffsite (WR, single line) and acid leachate (L, short dashes), showing the separation discussed in the text. Values are normalized to chondrite (McDonough and Sun, 1995).

Na-Fe metasomatism (classic fenitization, sometimes linked with the associated alkali silicate magmatism) is also found around many of the intrusions in the Malawi part of the Chilwa province, where the two forms of alkali metasomatism were compared by Woolley (1982). Na-Fe metasomatism is absent from Rufunsa (as is alkali silicate magmatism). Throughout the Chilwa province, a unanimity emerges from the most detailed field studies (at centers hundreds of kilometers apart) showing an intimate link between abundant K activity and carbonatite (with or without Na-Fe metasomatism). The diatremic mode of eruption, and the paucity of silicate magmas, together with the vast amounts of K suggest that this province represents a distinctive form of carbonatite magmatism.

Because carbonatites are such unusual rocks, they tend to take center stage in the description of a complex or province, and the other components may pale in significance. When considering the carbonatite intrusions in the Chilwa province, for instance, the ubiquitous orthoclase rocks may be recognized as an essential part of the activity, but their status as the major constituent of most complexes has tended to evoke little, if any, comment. Hence, although Chilwa is rightly regarded as a classic African carbonatite province, it is equally an outstanding example of intense and extensive K-metasomatism (and rheomorphism). It is in this context that the Rufunsa carbonatites should be viewed.

Rufunsa volcanoclastic rocks are exceptional in the Chilwa province because they provide sections near the original surface, with present erosion levels revealing parts of the volcanic pile. Because the tuffisites were emplaced through earlier intrusive carbonatite plugs by fast-moving streams, evidence of near-surface K-metasomatism is not available. Evidence from deeper in the complex is provided by the xenocrysts of phlogopite and sanidine in the agglomerate and tuffs. Sanidine has the same composition range as sanidine megacrysts in the most easterly satellite vent of the Chasweta volcano (Fig. 1). These megacrysts are enclosed in highly rounded fragments, consisting of fine-grained orthoclase (plate IV in Bailey, 1960; Liyungu, 1992) within a sparse carbonate matrix. This vent agglomerate is similar to some described and figured by Dixey et al. (1937, their plate V, fig. i), and it also points to possible connections with the coeval carbonatite-trachyte complex of Cone Negose (Woolley, 2001) ~100 km to the SE in Mozambique, along the extension of the Rufunsa line. Late Cretaceous ages (85 Ma) indicate sanidine megacryst formation just prior to the carbonatite volcanism that brought them to the surface (Liyungu, 1992). They represent part of a growing body of evidence linking sanidine megacryst formation with carbonatite activity (Stoppa and Cundari, 1998; Riley et al., 1999, and references therein).

Deep K-metasomes are a possible source of these xenocrysts, and the fine-grained orthoclase in the satellite vent is indistinguishable from that in the aureoles around the older intrusions. Despite the differences in eruption dynamics between the intrusive and extrusive activity, the products are similar, recording K-metasomatism with carbonatite.

CARBONATITE MELTS AND HIGH-K ACTIVITY

Experimental High-K Carbonate Melts

Experimental studies have long pointed to the generation of carbonatite and kimberlite by initial, small fraction melting along the “kimberlite” solidus, with dolomite as the first melt below ~70 km, as shown in Figure 6 (see Wyllie and Lee [1999] for a review of melting in the mantle at high pressures). Many experiments have focused on conditions where Na would be the dominant alkali (e.g., amphibole in the source peridotite), but some have looked at peridotite melting where K may have a major role (for review, see Sweeney, 1994). Carbonate melts with high K levels were reported by Thibault et al. (1992) from experiments on carbonate phlogopite lherzolite (at 30 kbar); their dolomitic melt composition is listed here in Table 1 (analysis 7). Sweeney (1994) considered his high-K melt (with 5.35 wt% K_2O ; using a different method, at 32 kbar) to be close to that of Thibault et al. (1992). Similar dolomite melts were obtained at higher pressures (40–60 kbar; Foley et al., 2009) with K_2O as high as 13.74 wt%. These three experimental melts contain substantial Na_2O (2.1 wt%–4.93 wt%) and low Al_2O_3 (0.38 wt%–1.93 wt%), i.e., compositions quite different from the residual melts in

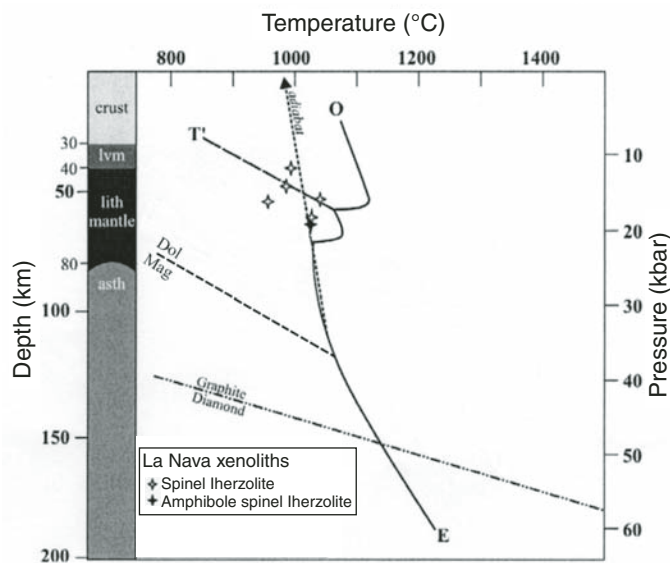


Figure 6. Pressure-temperature diagram based on data from Calatrava, Spain, showing the temperature and pressure recorded in mantle xenoliths (stars—lherzolites: +—amphibole spinel lherzolite) in relation to the peridotite solidus. O-E is $H_2O + CO_2$ peridotite solidus; T'-OE is decarbonation boundary (Olafsson and Eggler, 1983). The origin of the adiabat was chosen to show a possible eruption path from the dolomite stability region, but the range of melt types, and the bimodal distribution of Sr-Nd isotopes (Fig. 8), suggests that more than one source depth may have been sampled. Published lithosphere structure of Calatrava volcanic province (after López-Ruiz et al., 1993) is shown in left margin: lvm—low-velocity mantle; lith mantle—lithospheric mantle; asth—asthenosphere; Dol—dolomite; Mag—magnetite (G. Rosatelli, 2005, personal commun.).

natural volcanic dolomites (Table 1, analysis 5; Table 4, analyses 3 and 4), where $\text{Al}_2\text{O}_3 > \text{K}_2\text{O}$, and Na_2O is negligible. Hence, although the experiments show that K-rich dolomite melts may form from K-bearing peridotite, these are not directly comparable with volcanic samples. These differences are highlighted by samples in France (Fig. 3C), where immiscible dolomite globules, with the K-Al-Si residuum, are enclosed in nephelinite glass containing 5.28 wt% Na_2O , with only 2.08 wt% K_2O (Bailey et al., 2006). As pointed out in the following section, the volcanism in Zambia, Spain, and France has the hallmarks of primary melts, from mantle depths where dolomite is the expected first melt at the solidus (Fig. 6).

Natural High-K Melts

Samples Preserved by Rapid Quenching

Although the ultrafine lapilli in the Chasweta vent are largely dolomite and iron oxides, another minor constituent is revealed by EMP multipoint line analyses, which consistently give small amounts of K, Al, and Si. Dolomite lapilli tuffs in Spain and France (Fig. 3) are coarser grained, and between the dolomite blades, there is a distinct interstitial phase composed of the same three elements. In these rocks, there are also small discrete grains

of the same composition (Figs. 3E and 3F; Table 4, analyses 3 and 4). Many of the French pyroclastic rocks have abundant fragments of nephelinite glass enclosing immiscible dolomite melt globules, where the larger examples also contain small amounts of a K-Al-Si residuum (Fig. 3C). These globules were at the same temperature as the nephelinite melt ($\sim 1100^\circ\text{C}$, from experimental evidence; see Lloyd, 1985, and references therein), indicating high-temperature separation of these residua. Hence, in all three known provinces, the dolomite volcanism is characterized by the presence of euhedral chromite, and K-Al-Si residua.

Compared with Spain and France, the Zambian samples have chromite much richer in Cr, and the residuum has a higher proportion of K, possibly reflecting a deeper source in cratonic mantle. The composition of the residuum in the fine-grained lapilli is given in Table 1 (analysis 5) and is essentially “phlogopite + iron oxide,” which would accord with the abundance of very fine phlogopite as the green matrix constituent in some vent specimens.

Bearing in mind the differences between the European (Cenozoic) and Zambian (Cretaceous) provinces (including lithosphere structures, history, and tectonics), their common features indicate that dolomite melts in the mantle are in equilibrium with chromite, and contain K-Al-Si (with no record of Na). In addition to the hallmark chromite, it should be noted that: (1) in Spain and France, there are mantle xenoliths in the eruptions (see Fig. 6); and (2) in Zambia, Spain, and France, the dolomite volcanic rocks have $\text{Mg\#} > 0.65$, thereby meeting the foremost criterion proposed by Eggler (1989) for primary carbonatite magmas (Tables 1 and 4). The lowest Mg\# in samples from Zambia is 0.74.

Inclusions in Diamonds

As cited in Schrauder and Navon (1994), diamond should be the best sampling device for transporting trapped mantle fluids to the surface, of which they provided “the first direct evidence,” ranging from hydrous siliceous inclusions to carbonatitic melts (all of which are designated “fluid” inclusions by the authors). Compositions vary linearly through this range, and all are rich in K_2O (Table 1, analysis 9). Inclusions were trapped in the diamonds as they grew, and Schrauder and Navon (1994) deduced that the range from carbonatitic melt to hydrous fluid marks a progression with time.

When the chromite in the Rufunsa melt droplets was first described (Bailey, 1989), it was noted that the composition was in the range reported from mantle xenoliths in kimberlite, and attention was drawn to the overall composition similarities between the Rufunsa rock suite and the carbonate-rich inclusions in diamonds, which were being broadly characterized at that time (Navon et al., 1988). Chromite phenocryst cores have Cr_2O_3 contents between 50 wt% and 60 wt%, putting them in the range that characterizes diamond-bearing kimberlites and lamproites, close to the very tight field of chromite inclusions in diamonds (around 60% Cr_2O_3), and thus in the upper range of chromites in diatreme eruptions (Fipke et al., 1995). Now that

TABLE 4. DOLOMITIC PYROCLASTIC ROCKS IN SPAIN AND FRANCE, WHOLE ROCKS AND K-AL-SI RESIDUA

Oxide (wt%)	France A3.1 WR	Spain CR10 WR	CR10 K-Al-Si fragment	A3.1 K-Al-Si fragment
SiO_2	35.9	16.82	48.35	56.67
TiO_2	1.31	0.34	1.79	0.65
Al_2O_3	9.33	2.82	15.31	18.40
Fe_2O_3	7.24*	1.47	N.D.	N.D.
FeO	4.91†	0.20	8.31	6.20
MnO	0.13	0.02	0.07	0.04
MgO	7.38	14.34	3.74	4.42
CaO	14.10	24.53	0.72	0.57
Na_2O	1.34	0.15	0.15	0.39
K_2O	1.43	0.73	3.68	4.65
P_2O_5	0.43	0.08	0.07	0.19
CO_2	18.10	35.2	N.D.	N.D.
$\text{H}_2\text{O}+$	4.01	1.55	N.D.	N.D.
Sum	101	98.20	82.42	92.55
$\text{Al}_2\text{O}_3/\text{K}_2\text{O}$	6.52	3.9	4.16	3.96
Mg#	0.66	0.94		

Note: Columns: 1—Limagne, France, A3.1, mixed eruption of dolomite-nephelinite (whole-rock [WR] analysis, X-ray fluorescence [XRF], Natural History Museum, London). 2—Calatrava, Spain, CR10, dolomite lapilli tuff (whole-rock analysis, XRF, Natural History Museum, London). 3—Calatrava, Spain (CR10), K-Al-Si fragment in rock sample shown in column 2 (electron microprobe [EMP] analysis, University of Bristol). 4—Limagne, France (A3.1), K-Al-Si fragment in rock sample shown in column 1. See Figures 3E and 3F (EMP analysis, University of Bristol). N.D.—not determined.

*Total Fe as Fe_2O_3 (XRF).

†Separate determinations: FeO, $\text{H}_2\text{O}+$.

major oxides and trace elements are available for the melt and fluid inclusions in diamonds, comparisons with Rufunsa can be explored further.

Schrauder et al. (1996) specifically noted that the incompatible trace-element profiles of the diamond inclusions are closest to average carbonatite, when compared with other igneous rocks. Comparisons with Rufunsa primary volcanics are therefore shown in Figure 7. As noted previously, the REE profile for the diamond inclusions with highest LREEs is virtually identical with that of the intrusive carbonatite at Chasweta (Table 3, analysis 3), and the same applies to Sr, while Ba is similar to average carbonatite. The intrusive carbonatite is not shown in Figure 7 because for many elements, it is too close to the diamond inclusion, but for Fe, Ni, and Cr, it is significantly lower. Where the Rufunsa primary volcanics are exceptional is in their high contents of Fe, Ni, and Cr, the last two of which signal a critical difference from typical carbonatite. Whereas Cr in the tuffsite is higher than in the diamond inclusion, Cr in the intrusive (like average carbonatite) material is an order of magnitude lower. Lack of Cr in intrusive carbonatites could be attributed to loss of high-density grains, e.g., chromite phenocrysts, from low-viscosity melts as their ascent rates declined before their eventual emplacement in the crust.

Major elements in the diamond inclusions are given by Schrauder and Navon (1994) on a $\text{CO}_2\text{-H}_2\text{O}$ free basis, with oxides of Si, Al, Ti, Fe, Ca, Mg, K, and Na, normalized to 99.45%, as given in Table 1 (analysis 9). In this form, however, direct comparison with carbonatites in the table is cumbersome. So, for convenience, the analysis of the carbonatitic inclusions (analysis 9) has been recast to bring it closer to a carbonatite composition by assignment of 33% CO_2 , with the other oxides normalized to 67% (analysis 8). When the inclusion carbonatite

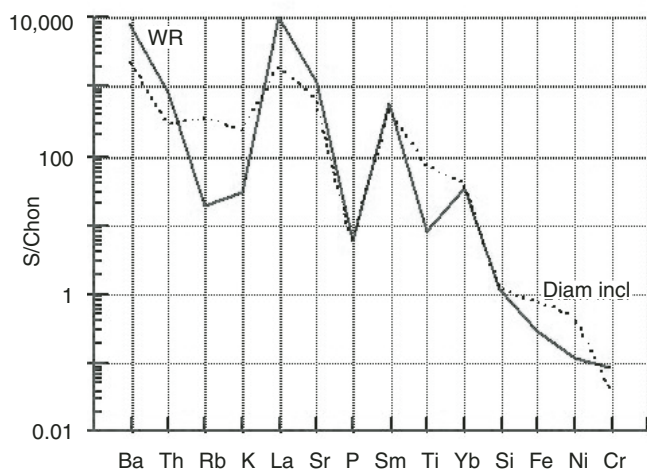


Figure 7. Comparison of a range of elements, of different compatibilities, for the vent tuffsite (WR [whole rock], single line) and carbonatitic inclusions in diamond (Diam incl, short dashes). Values are normalized to chondrite (McDonough and Sun, 1995).

(analysis 8), or the experimental melt (analysis 7), is compared with natural magnesio-carbonatite, the most obvious mismatch is in alkalis (Table 1, analysis 6). However, in most complexes, of course, carbonatite alone does not cover the whole eruptive budget, so that simple comparison of the carbonatite with any mantle melt is not possible. As pointed out earlier, for the Rufunsa complexes, the budget would need to include abundant K, fixed in the metasomatic aureoles (>10% of the preserved material). No explanation for the deficiency in Na is available, but its absence in the volcanic dolomites may be a further indication that richness in K is an integral part of magnesio-carbonatite activity, witnessed in Kangankunde, Malawi (Garson, 1965). Another indicator, of course, in Rufunsa, is the evidence of subvolcanic K activity, revealed in the xenocrysts of phlogopite and sanidine, and by the satellite vent filled with orthoclase rock and sanidine megacrysts. Pyroclastic deposits in Spain also carry ultrapotassic silicate melt lapilli (Bailey and Kearns, 2008).

A final point may be made relating to the range of diamond inclusions, from carbonatitic to hydrous (siliceous). Schrauder and Navon (1994) concluded that these are sequential in formation, which would also accord with a late flux of siliceous fluids observed in most Chilwa complexes (Bailey, 1966).

Discussion of possible connections with diamond inclusions is given added relevance when Rufunsa is seen in its wider geological context, because kimberlite and lamproite pipes constitute the only other igneous activity in this period along the Luangwa-mid-Zambesi Rift zone, most strikingly exemplified at Katete,

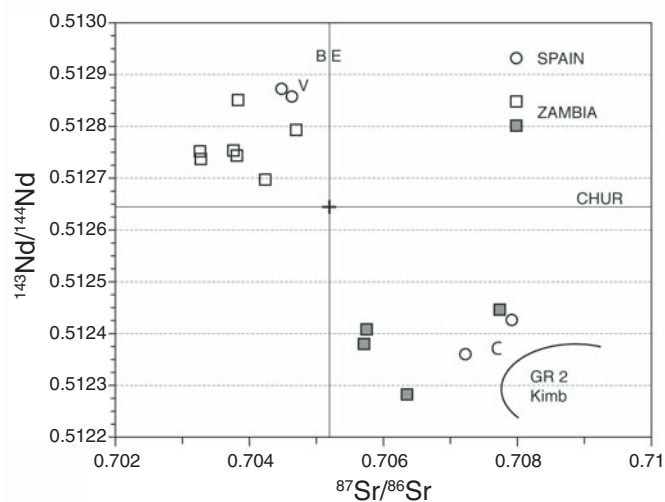


Figure 8. Sr-Nd isotopes. All Zambian samples are carbonates. Those in the enriched quadrant are extrusive dolomites (solid boxes) of Late Cretaceous age (ca. 85 Ma), while the others are intrusive (open boxes) of Early Cretaceous age (ca. 110 Ma); the latter are analogous to South African group 1 kimberlites (which fall in the depleted quadrant, i.e., in the same region). Group 2 kimberlites (GR 2 Kimb) are shown in the enriched quadrant. Samples from Calatrava, Spain, shown by circles, include volcanic carbonates and leucites (C), and other silicate melts (V). BE—bulk earth; CHUR—chondritic uniform reservoir.

Zimbabwe, where carbonatite and kimberlite were erupted in the same area (Lee, 1974). In this context, it may be noted that there are parallels in the Sr-Nd isotopes, where for Rufunsa and Spain, there is a bimodal distribution similar to group 1 and 2 kimberlites (Fig. 8).

In Spain, melilitite and nephelinite melts plot in the depleted quadrant (V; with group I kimberlites), while leucitites and volcanic carbonates (C) plot in proximity to group 2 kimberlites. In Rufunsa, the dolomite volcanics fall in the enriched quadrant, whereas the intrusive carbonatites plot in the depleted quadrant, close to bulk earth. Dolomites in the Limagne volcanism (Bailey et al., 2006) have $^{86}\text{Sr}/^{87}\text{Sr}$ ratios around 0.707 (Chazot, 2005, personal commun.), while the silicate lavas in Auvergne fall in the depleted quadrant. Diamond inclusions show Sr-Nd isotopes ranging from the depleted into the enriched quadrant, to group 2 kimberlites and beyond: This is considered to be a mixing array between two end members (Klein-Ben David et al., 2008). Other cases of alkaline/carbonatite magmatism showing bimodal arrays may be seen in the literature but seem to have passed without comment.

Diamonds from which inclusion data are available are from different source regions, widely separated in space and time but with similar inclusion compositions (e.g., Klein-Ben David et al., 2009). High potassium is a common feature of the carbonatitic inclusions, so that where carbonatite eruption is accompanied by high-K activity, with little or no associated silicate magmatism (as in the Chilwa province), the question of possible links still needs to be addressed, especially because the inclusions provide the only natural examples of high-K carbonate melts. The hope here is that by opening the enquiry, further exploration of possible connections will continue as knowledge advances on both fronts.

ACKNOWLEDGMENTS

New samples of tuffisite were collected by A.K. Liyungu, Geological Survey of Zambia, whose continuing collaboration is hereby acknowledged. Whole-rock analyses (X-ray fluorescence) were conducted by the Natural History Museum, London, UK, and by the University of Nottingham, courtesy of Teal Riley and Tim Brewer. Wet chemistry was carried out in the University of Bristol by Chung Choi and Tony Kemp, and CO_2 determinations were made by Richard Brooker. Gianluca Bianchini, Felicity Lloyd, and Alan Woolley provided constructive comments to benefit the original text.

REFERENCES CITED

- Bailey, D.K., 1960, Carbonatites of the Rufunsa Valley, Feira District: Geological Survey of Northern Rhodesia Bulletin 5, 92 p., 5 maps, 14 plates.
- Bailey, D.K., 1961, The mid-Zambezi–Luangwa Rift and related carbonatite activity: *Geological Magazine*, v. 98, p. 277–284, doi:10.1017/S0016756800060593.
- Bailey, D.K., 1966, Carbonatite volcanoes and shallow intrusions in Zambia, in Tuttle, O.F., and Gittins, J., eds., *Carbonatites*: New York, John Wiley & Sons, p. 127–154.
- Bailey, D.K., 1989, Carbonate melt from the mantle in the volcanoes of south-east Zambia: *Nature*, v. 388, p. 415–418.
- Bailey, D.K., 1990, Mantle carbonatite eruptions: Crustal context and implications, in Woolley, A.R., and Ross, M., eds., *Alkaline igneous rocks and carbonatites*: *Lithos*, v. 26, p. 37–42.
- Bailey, D.K., 1993, Carbonate magmas: *Journal of the Geological Society of London*, v. 150, p. 637–651, doi:10.1144/gsjgs.150.4.0637.
- Bailey, D.K., and Collier, J.D., 2000, Carbonatite-melilitite association in the Italian collision zone and the Ugandan rifted craton: Significant common factors: *Mineralogical Magazine*, v. 64, no. 4, p. 675–682, doi:10.1180/002646100549698.
- Bailey, D.K., Garson, M., Kearns, S., and Velasco, A.P., 2005, Carbonate volcanism in Calatrava, central Spain: A report on the initial findings: *Mineralogical Magazine*, v. 69, p. 907–915, doi:10.1180/0026461056960298.
- Bailey, K., Kearns, S., Mergoill, J., Mergoill Daniel, J., and Paterson, B., 2006, Extensive dolomitic volcanism through the Limagne Basin, central France: A new form of carbonatite activity: *Mineralogical Magazine*, v. 70, p. 1–6, doi:10.1180/0026461067020327.
- Brögger, W.C., 1921, Die Eruptivgesteine des Kristianiagebietes: IV Das Fensgeviert in Telemark Norwegen: *Videnskapsselskapets Skrifter*, 1. Mat.-Naturv. Klasse, 1920, No. 9, 408 p.
- Dixey, F., Smith, W.C., and Bisset, C.B., 1937, The Chilwa Series of Southern Nyasaland: *Geological Survey of Nyasaland Bulletin* 5, 85 p.
- Eggler, D.H., 1989, Carbonatites, primary melts, and mantle dynamics, in Bell, K., ed., *Carbonatites*: London, Unwin Hyman, p. 500–545.
- Fipke, C.E., Gurney, J.J., and Moore, R.O., 1995, Diamond Exploration Techniques Emphasising Indicator Mineral Geochemistry and Canadian Examples: *Geological Survey of Canada Bulletin* 423, 86 p.
- Foley, S.F., Yaxley, G.M., Rosenthal, A., Buhre, S., Kiseeva, E.S., Rapp, R.P., and Jacob, D.E., 2009, The composition of near-solidus melts of peridotite in the presence of CO_2 and H_2O between 40 and 60 kbar: *Lithos*, v. 112, p. 274–283, doi:10.1016/j.lithos.2009.03.020.
- Garson, M.S., 1965, Carbonatites in Southern Malawi: *Geological Survey of Malawi Bulletin* 15, 128 p.
- Harmer, R.E., and Gittins, J., 1997, The origin of dolomitic carbonatites: Field and experimental constraints: *Journal of African Earth Sciences*, v. 25, p. 5–28, doi:10.1016/S0899-5362(97)00059-6.
- Klein-Ben David, O., Logvinova, A.M., Schrauder, M., Spetius, Z.V., Weiss, Y., Hauri, E.H., Kaminsky, F.V., Sobolev, N.V., and Navon, O., 2009, High-Mg carbonatitic microinclusions in some Yakutian diamonds—A new type of diamond-forming fluid: *Lithos*, v. 112, p. 648–659, doi:10.1016/j.lithos.2009.03.015.
- Le Bas, M.J., 1999, Sovite and alvikite: Two chemically distinct calciocarbonatites C1 and C2: *South African Journal of Geology*, v. 102, p. 109–121.
- Lee, C.A., 1974, The geology of the Katete carbonatite, Rhodesia: *Geological Magazine*, v. 111, p. 133–142, doi:10.1017/S0016756800038176.
- Liyungu, A.K., 1992, Alkali Feldspar Rocks Associated with Rufunsa Carbonatites [M.Sc. thesis]: Bristol, University of Bristol, 109 p.
- Lloyd, F.E., 1985, Experimental melting and crystallisation of glassy olivine melilitites: *Contributions to Mineralogy and Petrology*, v. 90, p. 236–243, doi:10.1007/BF00378264.
- López-Ruiz, J., Cebria, J.M., Doblas, M., Oyarzun, R., Hoyos, M., and Martin, C., 1993, Cenozoic intra-plate volcanism related to extensional tectonics at Calatrava, central Iberia: *Journal of the Geological Society of London*, v. 150, p. 915–922, doi:10.1144/gsjgs.150.5.0915.
- McDonough, W.F., and Sun, S.-s., 1995, The composition of the Earth: *Chemical Geology*, v. 120, p. 223–253, doi:10.1016/0009-2541(94)00140-4.
- Nakamura, N., 1974, Determination of REE, Ba, Fe, Mg, Na and K in carbonaceous and ordinary chondrites: *Geochimica et Cosmochimica Acta*, v. 38, p. 757–775, doi:10.1016/0016-7037(74)90149-5.
- Navon, O., Hutcheon, I.D., Rossman, G.R., and Wasserburg, G.J., 1988, Mantle-derived fluids in diamond micro-inclusions: *Nature*, v. 335, p. 784–789, doi:10.1038/335784a0.
- Nelson, D.R., Chivas, A.R., Chappell, B.W., and McCulloch, M.T., 1988, Geochemical and isotopic systematics in carbonatites and implications for the evolution of ocean-island sources: *Geochimica et Cosmochimica Acta*, v. 52, p. 1–17, doi:10.1016/0016-7037(88)90051-8.
- Olafsson, M., and Eggler, D.H., 1983, Phase relations of amphibole, amphibole-carbonate, and phlogopite-carbonate peridotite: Petrologic constraints on the asthenosphere: *Earth and Planetary Science Letters*, v. 64, p. 305–315, doi:10.1016/0012-821X(83)90212-1.

- Riley, T.R., Bailey, D.K., Brewer, T., Harmer, R.E., Liebsch, H., Lloyd, F.E., and Palmer, M., 1999, Isotopic and geochemical investigation of a carbonatite-syenite-phonolite diatreme, West Eifel (Germany): *Mineralogical Magazine*, v. 63, no. 5, p. 615–631, doi:10.1180/002646199548736.
- Schrauder, M., and Navon, O., 1994, Hydrous and carbonatitic mantle fluids in fibrous diamonds from Jwaneng, Botswana: *Geochimica et Cosmochimica Acta*, v. 58, p. 761–771, doi:10.1016/0016-7037(94)90504-5.
- Schrauder, M., Koeberl, C., and Navon, O., 1996, Trace element analyses of fluid-bearing diamonds from Jwaneng, Botswana: *Geochimica et Cosmochimica Acta*, v. 60, p. 4711–4724, doi:10.1016/S0016-7037(96)00274-8.
- Stoppa, F., and Cundari, A., 1998, Origin and multiple crystallisation of the kamafugite-carbonatite association at San Venanzo–Pian di Celle, Umbria, Italy: *Mineralogical Magazine*, v. 62, p. 273–289, doi:10.1180/002646198547530.
- Sweeney, R.J., 1994, Carbonatite melt compositions in the Earth's mantle: *Earth and Planetary Science Letters*, v. 128, p. 259–270, doi:10.1016/0012-821X(94)90149-X.
- Thibault, Y., Edgar, A.D., and Lloyd, F.E., 1992, Experimental investigation of melts from a carbonated phlogopite lherzolite: Implications for metasomatism in the continental lithosphere: *The American Mineralogist*, v. 77, p. 784–794.
- Woolley, A.R., 1982, A discussion of carbonatite evolution and nomenclature and the generation of sodic and potassic fenites: *Mineralogical Magazine*, v. 46, p. 13–17, doi:10.1180/minmag.1982.046.338.03.
- Woolley, A.R., 2001, *Alkaline Rocks and Carbonatites of the World. Part 3: Africa*: London, Geological Society of London, 372 p.
- Woolley, A.R., and Church, A.A., 2005, Extrusive carbonatites: A brief review: *Lithos*, v. 85, p. 1–14, doi:10.1016/j.lithos.2005.03.018.
- Woolley, A.R., and Kempe, D.R.C., 1989, Carbonatites: Nomenclature, average chemical compositions, and element distribution, *in* Bell, K., ed., *Carbonatites*: London, Unwin Hyman, p. 1–14.
- Wyllie, P.J., and Lee, W.-J., 1999, Kimberlites, carbonatites, peridotites and silicate-carbonate liquid immiscibility explained in parts of the system $\text{CaO}-(\text{Na}_2\text{O} + \text{K}_2\text{O})-(\text{MgO} + \text{FeO})-(\text{SiO}_2 + \text{Al}_2\text{O}_3)-\text{CO}_2$, *in* Gurney J.J., Gurney, J.L., Pascoe, M.D., and Richardson, S.H., eds., *Proceedings of the VII International Kimberlite Conference, Volume 2*: Cape Town, Red Roof Design, p. 923–932.

MANUSCRIPT ACCEPTED BY THE SOCIETY 9 NOVEMBER 2010

Post-Paleozoic magmatism in Angola and Namibia: A review

P. Comin-Chiaramonti*

A. De Min

Earth Sciences Department, Trieste University, Via Weiss 8, I-34127 Trieste, Italy

V.A.V. Girardi

E. Ruberti

Instituto de Geociências, University of São Paulo, Rua do Lago 562, 05508-080 São Paulo, Brazil

ABSTRACT

Post-Paleozoic magmatism in Angola and Namibia (SW Africa) is widespread along the continental margin (flood tholeiites of the Paraná-Etendeka system), and along transverse lineaments (alkaline and alkaline-carbonatitic complexes; sodic and potassic suites). These different magmatic suites are strictly associated in space and/or time. Variable melting degrees of a veined lithospheric mantle are proposed for the most “primitive” magmas from geochemical modeling and Sr-Nd isotope systematics. A complex evolution emerges for some ultramafic rocks (cumulus processes) and for differentiated rock compositions (assimilation and fractional crystallization, AFC, magma mixing), which may also involve anatexis of the crystalline basement and emplacement of S-type granites and rhyolites. Melting of a lithospheric mantle, without an appreciable contribution of the asthenosphere (thermal input excepted), is consistent with regional thermal anomalies in the deep mantle, mapped by gravity of the geoid, seismic tomography, and paleomagnetic analysis. The Walvis Ridge and Rio Grande “hotspot tracks” are interpreted as stress response in the lithosphere during rifting. A plume-related heat source is not favored by our results.

INTRODUCTION

Angola and Namibia, on the SE margin of the South Atlantic Ocean, provide one of the best examples of a large igneous province at a continental margin, where the easternmost expression of Paraná-Etendeka magmatism predates the Early Cretaceous continental rifting. Paraná-Etendeka (more than 1.2 million km²; Piccirillo and Melfi, 1988) has been considered to be closely associated, in space and time, with continental rifting above the long-lived Tristan da Cunha mantle plume (Ewart et al., 2004a, 2004b, and references therein). On the other hand, Ernesto (2005) and Ernesto et al. (2002) demonstrated that Paraná-Etendeka

magmatism could not have been generated by the Tristan da Cunha plume, because Tristan da Cunha has never been under the region affected by the Paraná magmatism. Also, a geochemical plume signature from the Paraná tholeiites is not apparent, nor do geochemistry and age distributions allow the application of a simple hypothesis based on a plume model.

The Paraná-Etendeka tholeiites are associated with pre-, syn-, and post-tholeiite alkaline and alkaline-carbonatitic complexes that follow symmetric tectonic lineaments with respect to South America and southwestern Africa (Fig. 1; Comin-Chiaramonti and Gomes, 1996, 2005; Comin-Chiaramonti et al., 2007a, 2007b, 2007c). From these lineaments, together with the

*comin@univ.trieste.it

present-day plate motion vectors inferred from space geodesy (figure 3 in Comin-Chiaramonti and Gomes, 2005; Heflin et al., 2002), it is possible to estimate the absolute plate motions, relative motions, and the motion of the Mid-Atlantic Ridge (MAR; inset of Fig. 1 [after Fairhead and Wilson, 2005]).

This geodynamic aspect is crucial to the interpretation of active margins generally and related constraints from the geochemical scenario bearing on magma origin and distribution in time and space. Therefore, in this paper, we have endeavored to address the interplay of some the geophysical and petrological factors bearing on multiple events of magma genesis and evolution for Paran -Etendeka. Constraints on mantle source compositions are presented and discussed.

GEOLOGICAL NOTES

The tholeiitic basalt suites are represented, both in Angola and Namibia (AN, Fig. 2), by high- and low-Ti variants, interbedded with acid flows, and Chapec  and Palmas variants (Piccirillo and Melfi, 1988; Peate, 1997; Alberti et al., 1992; Marzoli et al., 1999; Ewart et al., 2004a, 2004b); the high-Ti and derivative Chapec  variants are dominant in Angola and in northern Etendeka, whereas the low-Ti and Palmas variants are dominant in southern Etendeka (Ewart et al., 2004a, 2004b). The estimated time range of this magmatism is 134–130 Ma (Renne et al., 1997; Comin-Chiaramonti et al., 2007a, 2007b).

The alkaline complexes may be subdivided, on the basis of the age of emplacement, into pre-, syn-, and post-tholeiitic basalt suites. Notably, granitic intrusions and associated rhyolitic rocks are syntholeiitic (A- and S-type) and post-tholeiitic (S-type).

Alkaline-carbonatite complexes occur mainly along the Mo amedes Arch, Angola, and along the Damara lineament, Namibia, and are Early Cretaceous in age. Late Cretaceous carbonatites occur at the Blue Hills and in the Gibeon kimberlite field (Fig. 2). An Eocene carbonatite occurs in southwestern Namibia (Dicker Willem). The general characteristics of the carbonatites from Paran -Etendeka are illustrated and discussed by Comin-Chiaramonti et al. (2007c). In this paper, we shall address the main characteristics of Angola and Namibia carbonatites, summarized here in Table 1.

The underlying basement (Hartnady et al., 1985) consists of Proterozoic rocks forming the southernmost extent of the Congo craton (Angola and Namibia; >2 Ga) and of the Damara belt (0.7–0.9 Ga), bounded to the south and to the west by the Namaqua-Natal belt (2.0–0.9 Ga; inset of Fig. 2). For the Gibeon kimberlite field, Liati et al. (2004) defined three age groups based on sensitive high-resolution ion microprobe (SHRIMP) results: 1013 ± 22 Ma, 751 ± 28 Ma, and 627 ± 24 Ma.

GEOCHEMISTRY

About 50 individual and averaged compositions were selected from more than 150 chemical analyses available in the literature (Table 1) to represent all the magmatic rock types. These are reported in the Appendix tables and summarized in Figure 3, where the subdivision between tholeiitic and alkaline compositions is illustrated.

The high-Ti suite tends to plot along a line separating the alkaline from the subalkaline fields. The alkaline rocks may be further subdivided into two main suites, potassic (transitional) and sodic (~50% and 50% of the available samples; inset of Fig. 3).

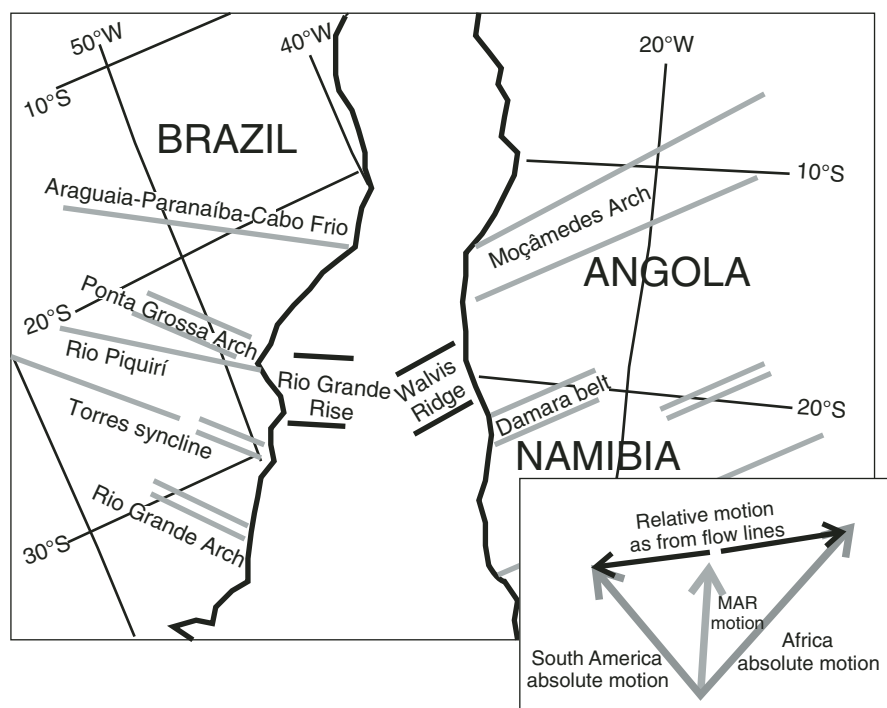


Figure 1. Main lineament in the Paran -Etendeka province (South American and African plates, western Gondwana at ca. 110 Ma; modified after Comin-Chiaramonti et al., 2007c), corresponding to the main lineaments of the alkaline and alkaline-carbonatitic complexes. Inset: Vector diagram showing relations among absolute plate motions, relative motions, and motion of the Mid-Atlantic Ridge (MAR; after Fairhead and Wilson, 2005).

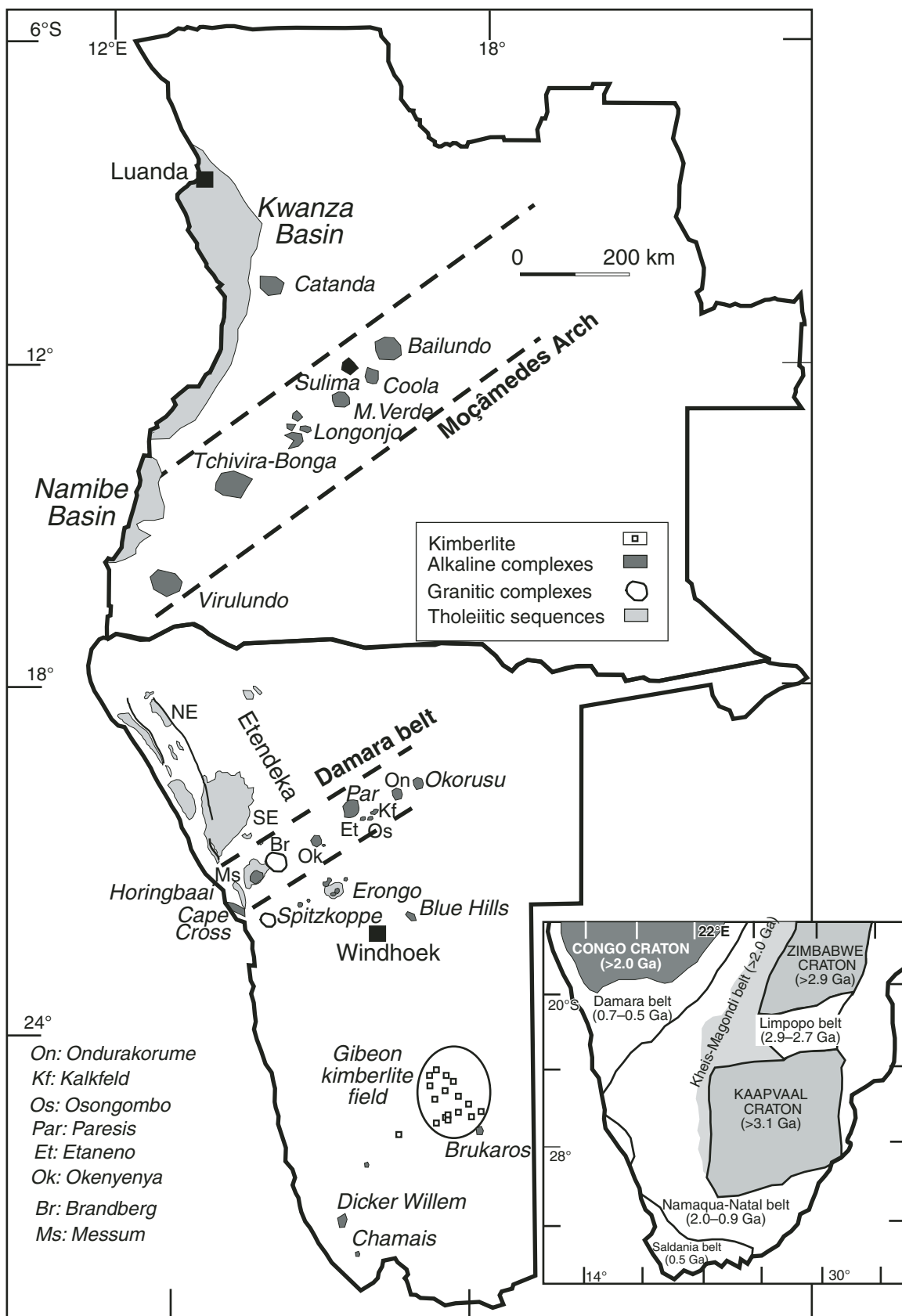


Figure 2. Generalized sketch map of the main magmatic post-Paleozoic rocks from Angola and Namibia. Data sources are in Table 1 and Google Earth (<http://earth.google.com>). Inset: Major tectonic provinces of southern Africa (after Hartnady et al., 1985).

Notably, alkaline rocks, both sodic and potassic, fall in the various alkaline fields independent of the age of emplacement. Some rock types are ultramafic with cumulus textures; carbonatites (see following) are associated both with potassic and sodic suites. Some granitic-rhyolitic bodies (Brandberg, Paresis, Spitzkoppe: field 6 of Fig. 3) show peraluminous character (Table A1). Mixed tholeiitic and alkaline affinities are also apparent from Figure 4. Different trends for low-Ti, high-Ti, and Tristan da Cunha rocks are displayed in the SiO_2 versus MgO diagram, while the sodic suite is clearly distinct from the potassic suite and Tristan da Cunha, respectively, in the SiO_2 versus $\text{Na}_2\text{O}/\text{K}_2\text{O}$ diagram. Mafic rock types of the tholeiitic basalt suites fall into the sodic field, whereas the associated acid rocks fall in the potassic field (see also Bellieni et al., 1986; Piccirillo and Melfi, 1988 [for the Paraná basin]).

Th/Yb versus Nb/Yb plots show different trends for high-Ti, low-Ti, sodic suites, and Tristan da Cunha, respectively, and strong scattering for the potassic compositions. The same scattering can be observed also for Th/Yb versus Ce and Sr (Fig. 4). This complex geochemical scenario will be further illustrated in terms of the variation of incompatible elements.

Incompatible Elements

Incompatible elements for Paraná-Etendeka and Angola-Namibia compositions with $\text{Mg}\# = 0.50\text{--}0.73$, representing the

less evolved and potentially some primary mantle source melts ($\text{Mg}\#$ around 0.7), are compared with typical compositions from the westernmost side of Paraná-Etendeka, and from Tristan da Cunha (Fig. 5).

The tholeiitic suites from Angola and Namibia are incompatible element-enriched relative to the Paraguayan analogues (westernmost Paraná-Etendeka side), which may be considered as representative of the whole Paraná-Etendeka system (Comin-Chiaromonte et al., 2007a, 2007b), but they are depleted relative to the Tristan da Cunha basanite. All tholeiites show negative Ta-Nb spikes and variable contents of large ion lithophile elements (LILEs). Positive Ba, La, Nd, and Zr spikes and a negative Ce spike are notable for the high-Ti tholeiites (Fig. 5A).

The Angola and Namibia syn- and post-tholeiitic (sodic) complexes also yielded variable LILE enrichment (Figs. 5B and 5C). However, high field strength elements (HFSE; i.e., Ta, Nb and Zr) show positive spikes, mimicking to some extent the Tristan da Cunha basanite.

A large variability is shown by the potassic alkaline rocks (Figs. 5D–5F), characterized by HFSE positive spikes, which contrast with the pattern for the Paraguayan post-tholeiitic alkaline complexes. These differences have been ascribed to different degrees of melting of a large-scale heterogeneous mantle source (i.e., 20% low-Ti and 5% high-Ti, 4%–6% sodic magmatism,

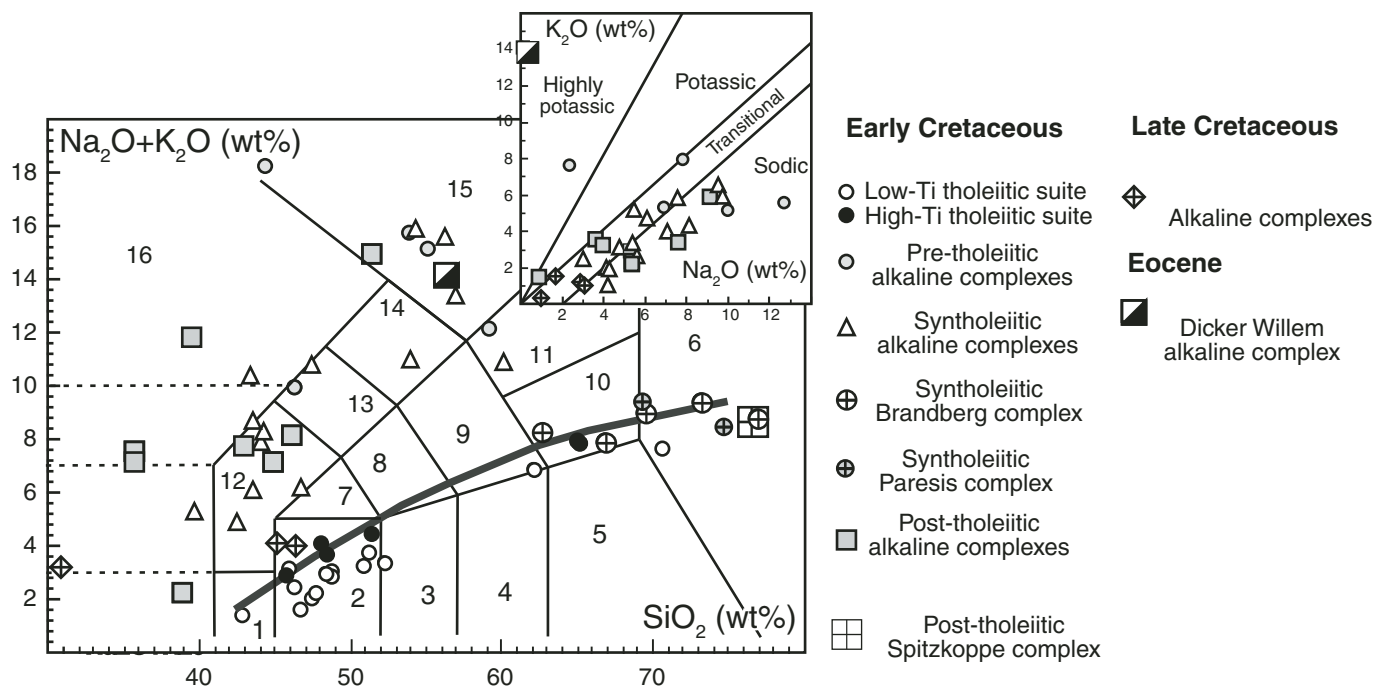


Figure 3. Total alkali-silica diagram (modified from Middlemost, 1994) for the selected analyses from Angola and Namibia. Heavy line separates alkaline and subalkaline fields (after Irvine and Baragar, 1971). Fields (volcanic-intrusive): 1—picobasalt-picrogabbro; 2—basalt-gabbro; 3—basaltic andesite-gabbrodiorite; 4—andesite-diorite; 5—dacite-granodiorite; 6—rhyolite-granite; 7—trachybasalt-monzogabbro; 8—basaltic trachyandesite-monzodiorite; 9—trachyandesite-monzonite; 10—trachydacite-quartz monzonite; 11—trachyte-syenite; 12—basanite/tephrite-foiid gabbro; 13—phonotephrite-foiid monzogabbro; 14—tephriphonolite-foiid monzosyenite; 15—phonolite-foiid syenite; 16—foiidite-foiidolite. Inset: Na_2O - K_2O diagram for alkaline rock-types (after Le Maitre, 1989).

6%–11% potassic magmatism; Piccirillo and Melfi, 1988; Comin-Chiaramonti et al., 2007a).

CARBONATITES

The Angolan carbonatites (Early Cretaceous age) show a compositional range from Ca- to Fe-carbonatites (Alberti et al., 1999; Fig. 2), while the Namibian carbonatites are Fe- and minor Ca-carbonatites of Early Cretaceous age and mainly Mg- and

Fe-carbonatites of Late Cretaceous and Eocene ages (Comin-Chiaramonti et al., 2007c; Fig. 3). Notably, the Blue-Hill carbonatite, and carbonatites from Gibeon field correspond in age to the carbonatitic plug of the Lages district (Santa Catarina State, Brazil; ca. 76 Ma; Comin-Chiaramonti and Gomes, 2005).

The silicate rocks at the contact with the carbonatite bodies are syenitic and/or trachytic-phonolitic in composition.

Large incompatible element variations were observed for the carbonatites as a group (Fig. 6), largely due to their minor phases,

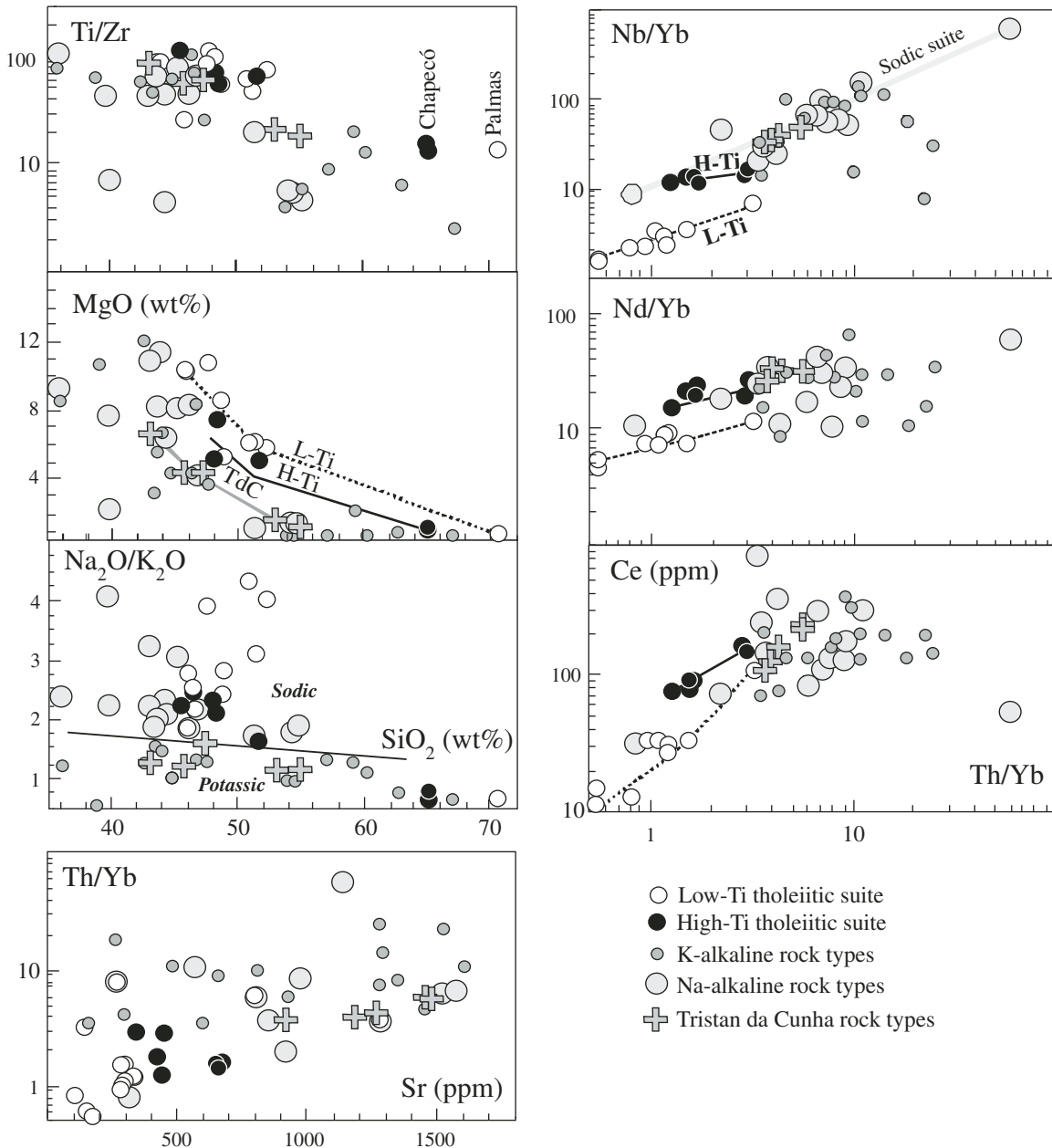


Figure 4. Diagrams showing the relationships between SiO₂ (wt%) vs. Ti/Zr, MgO (wt%), Na₂O/K₂O, and Th/Yb vs. Sr (ppm), Nb/Yb, Nd/Yb, and Ce (ppm). Sources as in Table 1. Note that granitic rocks and rhyolites are not plotted in these diagrams. TdC—Tristan da Cunha rock types.

such as apatite and monazite, pyrochlore (Nb, rare earth elements [REEs], Th, U), calzite (Ti, Zr), zirconolite (Ti, Zr, Nb), loparite (REE, Ti, Nb), and ancylite, bastnäsite, burbankite, and parisite (REE-carbonates and fluorocarbonates). Details for these phases and their stability are described by Comin-Chiaramonti et al. (2007c) and Ruberti et al. (2008). Notably, the observed incompatible element variations for carbonatites are not age-related.

KIMBERLITES

More than 70 kimberlite pipes are known from the Gibeon field (Fig. 1; age of eruption ca. 71.5 Ma, according to Davies et al., 2001). They are extremely variable in composition, imply-

ing either very heterogeneous magmas or multiple intrusions (Fig. 5G). Calculated equilibrium melts with the clinopyroxene megacrysts have REE contents comparable with those of alkali basalts (for a detailed discussion, see Davies et al., 2001). To some extent, the Gibeon field is similar in age and magmatic typology to the Lages field in Santa Catarina State, Rio Grande Rise–Uruguay lineaments (southern Brazil; Comin-Chiaramonti and Gomes, 2005). The Gibeon kimberlites are characterized by abundant mantle xenoliths (predominantly coarse-grained garnet lherzolites and subordinate harzburgites) that reflect thermal anomalies linked to the regional igneous activity, perhaps associated with thermal erosion of an originally thicker lithosphere, a short time prior to eruption (Boyd et al., 2004).

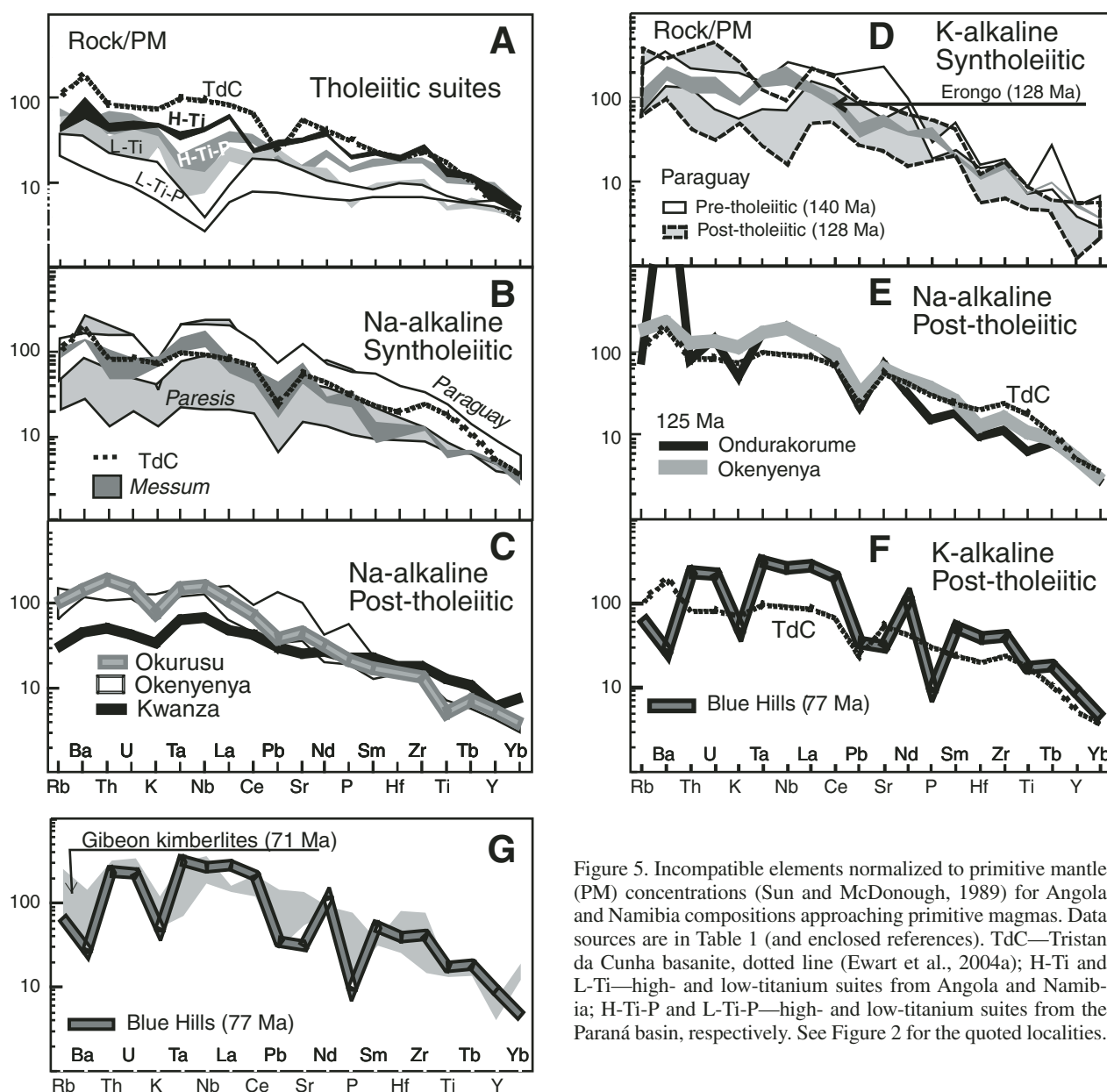


Figure 5. Incompatible elements normalized to primitive mantle (PM) concentrations (Sun and McDonough, 1989) for Angola and Namibia compositions approaching primitive magmas. Data sources are in Table 1 (and enclosed references). TdC—Tristan da Cunha basanite, dotted line (Ewart et al., 2004a); H-Ti and L-Ti—high- and low-titanium suites from Angola and Namibia; H-Ti-P and L-Ti-P—high- and low-titanium suites from the Paraná basin, respectively. See Figure 2 for the quoted localities.

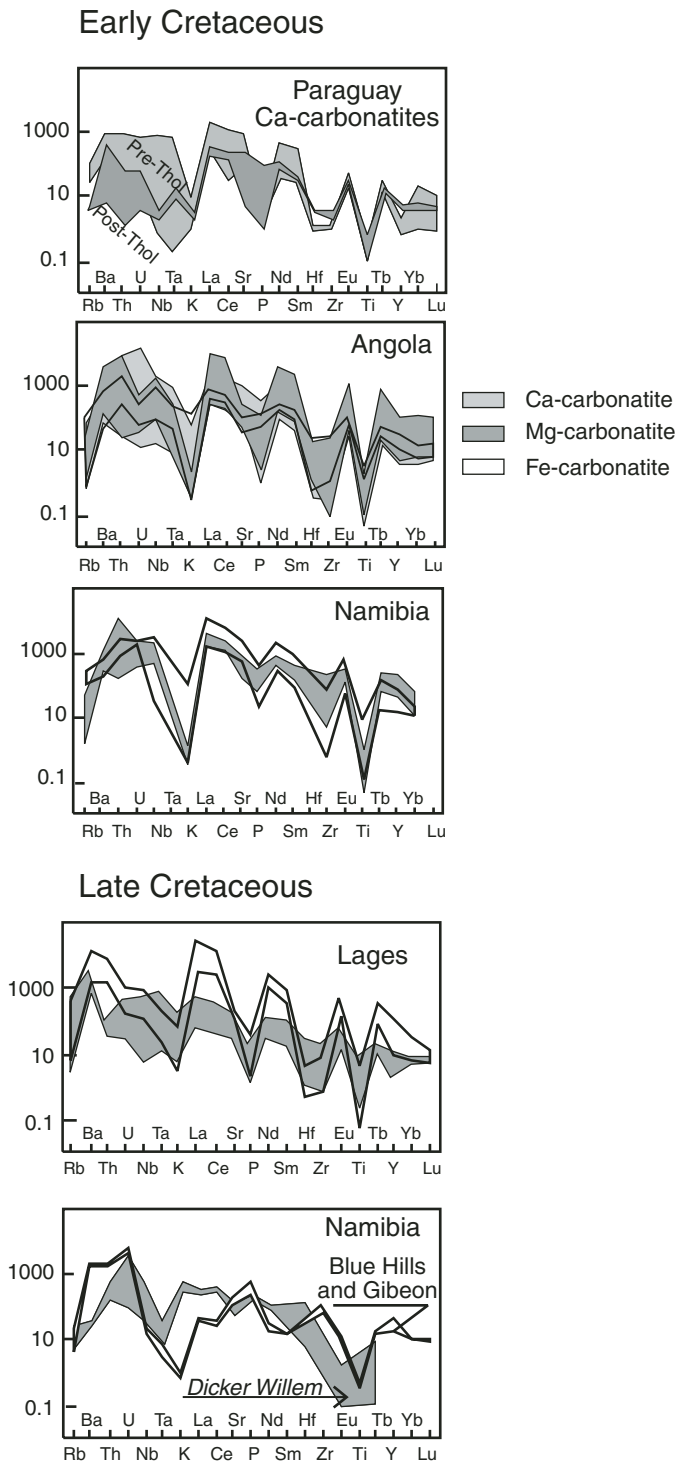


Figure 6. Incompatible elements in carbonatites normalized to primitive mantle concentrations (Sun and McDonough, 1989). Data sources are in Table 1 for Angola and Namibia and in Comin-Chiaramonti et al. (2007c) for Paraguay and Lages. Pre-Thol—pre-tholeiitic; Post-Thol—post-tholeiitic.

NAMIBIA: GRANITIC ROCKS AND RHYOLITES

Granitic rocks occur in the Damaraland, i.e., Brandberg and Spitzkoppe complexes, while rhyolitic rocks are the dominant rock types in the Paresis ring complex (Table 1; Fig. 2).

A common basaltic parent was suggested by Schmitt et al. (2000, 2002) for the rocks from the Brandberg complex, which consists of metaluminous and peralkaline suites (132–130 Ma), while leucogranitic dikes and metaluminous granites formed by evolved melts through addition of 20%–40% crustal material. The same authors envisaged parental magmas from the metaluminous suite to have generated the peralkaline rocks.

Frindt et al. (2004) suggested that the peraluminous granites of the Spitzkoppe complex (125 Ma) derived mainly from melting of a granulite metasedimentary sequence. Likewise, Early Cretaceous peraluminous rhyodacites along the Rio Grande Arch (Fig. 1) have also been interpreted in terms of partial melting of a granulitic metasedimentary sequence (Comin-Chiaramonti et al., 2009).

Prevailing peralkaline comendites and metaluminous rhyolites with subordinate syenitic rocks from the Paresis complex were interpreted to have derived from partial melting of pre-Damara quartzofeldspathic gneisses (Mingram et al., 2000).

Sr-Nd ISOTOPES

The Sr-Nd isotopic results are given in Table 2 and illustrated in Figure 7A as time-integrated data. In general, the $^{87}\text{Sr}/^{86}\text{Sr}$ (Sr_i) and $^{143}\text{Nd}/^{144}\text{Nd}$ (Nd_i) ratios of the “more primitive” Angola and Namibia rocks fall in the depleted quadrant, varying from DMM (depleted-MORB) to the EM1 (enriched mantle 1, low-Nd; cf. Faure, 2001, and references therein) mantle component, and mainly following the “Paraguay array” of Comin-Chiaramonti et al. (2007a, 2007b). Notably, the Angola and Namibia carbonatites fall in the field of the associated alkaline complexes in the depleted quadrant. The Paraná-Etendeka carbonatites usually show the same Sr_i and Nd_i values as the associated alkaline rocks, even in the late stages of fluid-rock reequilibration (Castorinal et al., 1997). However, there are substantial differences between the Angola and Namibia rocks and their American counterparts: Both pre- and post-tholeiitic carbonatites and associated alkaline complexes from Paraguay fall in the lowest Sr_i and Nd_i field of the Paraguay array, whereas the syn- and post-tholeiitic carbonatites and associated alkaline complexes from Brazil fall in the fields defined by the tholeiites (not shown in Fig. 7A; see figure 14 in Comin-Chiaramonti et al., 2007c).

Assuming that the northern Paraná and Etendeka high-Ti tholeiites are parental magmas, the ϵ_{Sr}^t – ϵ_{Nd}^t mixing curves indicate ~3%–10% of two different carbonatitic components, i.e., Brazilian-Namibian-Angolan and Paraguayan, respectively (Fig. 7B). The initial large variation of ϵ_{Sr}^t associated with the small ϵ_{Nd}^t suggests that the Sr-Nd decoupling might be related to chromatographic-like diffusion of the carbonatitic component, where high elemental Sr would be responsible for the Rb/Sr decrease (Rosset et al., 2007).

TABLE 2. REPRESENTATIVE AND AVERAGE ANALYSES OF Rb, Sr, Sm, Nd (ppm), MEASURED RATIOS OF $^{87}\text{Sr}/^{86}\text{Sr}$ AND $^{143}\text{Nd}/^{144}\text{Nd}$ (STANDARD DEVIATION IN PARENTHESES), INITIAL ISOTOPIC RATIOS, AND Nd MODEL AGES (T^{DM})

Rock type (Notional age, Ma)	SiO_2 (wt%)	Mg#	N	Rb	Sr	Sm	Nd	$(^{87}\text{Sr}/^{86}\text{Sr})_m$	$(^{143}\text{Nd}/^{144}\text{Nd})_m$	$(^{87}\text{Sr}/^{86}\text{Sr})_i$	$(^{143}\text{Nd}/^{144}\text{Nd})_i$	T^{DM} (Ma)
Early Cretaceous: Tholeiitic suites. Notional age: 130 Ma.												
Low-Ti suite												
Angola												
Picrite	42.79	0.80	3	10 (2)	269 (19)	6.4 (0.2)	23 (1)	0.70314 (20)	0.51278 (1)	0.70300	0.51268	1117
Gabbro	45.77	0.68	4	43 (2)	616 (91)	12.7 (1.8)	52 (5)	0.70502 (4)	0.51265 (4)	0.70491	0.51252	1073
Basalt	48.72	0.52	1	15	300	4.1	18	0.70489 (3)	0.51250 (5)	0.70462	0.51238	1222
Basalt	50.78	0.56	4	23 (6)	327 (70)	3.3 (0.5)	16 (1)	0.70786 (6)	0.51251 (9)	0.70748	0.51240	1038
Namibia												
Picritic gabbro	46.25	0.70	2	20.4 (0.8)	230 (6)	3.3 (0.4)	13.2 (1.6)	0.70476 (20)	0.51285 (1)	0.70428	0.51272	679
Picritic basalt	46.62	0.74	1	12	142	2.22	8.1	0.70655 (1)	0.51280 (1)	0.70609	0.51266	1007
Basalt	47.41	0.71	2	20 (12)	168 (13)	2.32 (0.10)	8.0 (0.1)	0.70538 (65)	0.51229 (3)	0.70473	0.51213	2997
Basalt	47.73	0.69	6	7 (2)	183 (28)	2.7 (0.3)	8.1 (1.9)	0.70334 (6)	0.51304 (4)	0.70313	0.51287	978
Gabbro	48.25	0.64	6	14.7 (4.5)	492 (87)	4.4 (2.4)	18.1 (11.4)	0.70909 (194)	0.51252 (5)	0.70893	0.51239	1337
Basalt	48.62	0.59	2	18 (3)	288 (53)	4.2 (0.4)	18 (3)	0.70939 (189)	0.51224 (25)	0.70905	0.51212	1781
Basalt	51.18	0.57	1	35	286	3.8	17	0.71257 (2)	0.51228 (1)	0.71194	0.51216	1583
Basaltic andesite	52.17	0.51	2	4.1 (0.8)	286 (121)	4.8 (0.2)	19.8 (0.9)	0.70831 (78)	0.51241 (0.4)	0.70823	0.51228	1560
Rhyolite	70.55	0.26	9	197 (29)	135 (40)	10.5 (1.9)	51 (10)	0.72545 (986)	0.51220 (6)	0.71752	0.51209	1534
High-Ti suite												
Angola												
Basalt	46.42	0.62	3	32 (16)	585 (157)	6.9 (0.4)	31 (5)	0.70404 (159)	0.51259 (60)	0.70384	0.51251	1015
Basalt	47.99	0.43	2	29 (4)	435 (54)	9.4 (0.8)	44 (4)	0.70524 (10)	0.51241 (11)	0.70488	0.51230	1258
Basalt	48.33	0.59	2	31 (1)	641 (98)	10.4 (0.1)	48 (1)	0.70666 (11)	0.51243 (10)	0.70640	0.51232	1250
Trachydacites	65.04	0.29	3	113 (4)	337 (55)	16.0 (1.2)	81 (5)	0.70857 (41)	0.51208 (5)	0.70675	0.51197	1638
Namibia												
Basalt	45.66	0.64	1	18	419	4.94	24.7	0.70535 (1)	0.51260 (1)	0.70512	0.51249	850
Basalt	51.31	0.48	2	29 (5)	665 (30)	10.1 (0.7)	48 (1)	0.70564 (5)	0.51234 (4)	0.70540	0.51223	1347
Trachydacites	64.94	0.27	18	141 (20)	441 (159)	15.3 (1.5)	83 (8)	0.70889 (127)	0.51231 (5)	0.70715	0.51221	1193
Early Cretaceous: Pre-tholeiitic alkaline suites												
Angola (138)												
Ijolite	46.16	0.51	1	561	1520	23	90	0.70677 (5)	0.51262 (2)	0.70467	0.51248	1195
Ne-syenite	54.93	0.19	6	150 (8)	1048 (187)	11.8 (1.3)	48 (12)	0.70631 (8)	0.51264 (2)	0.70493	0.51250	1109
Syenite	59.14	0.47	7	115 (22)	801 (126)	28.0 (3.0)	113 (28)	0.70512 (4)	0.51265 (4)	0.70431	0.51251	1106
Ca-carbonatite	5.48	8	14.2 (4.3)	10,161 (6440)	618 (423)	71.4 (33.7)	618 (423)	0.70380 (45)	0.51269 (8)	0.70379	0.51263	472
Mg-carbonatite	4.95	3	3.2 (1.6)	4353 (1747)	446 (545)	2692 (3669)	2692 (3669)	0.70456 (15)	0.51264 (25)	0.70455	0.51255	657
Namibia (137)												
Ne-syenite	53.80	0.19	4	195 (27)	2267 (1513)	4.7 (3.6)	33 (24)	0.70487 (88)	0.51258 (1)	0.70439	0.51250	656
Foidite	44.17	0.16	1	120	1134	1.8	14.6	0.70474 (1)	0.51257 (1)	0.70414	0.51250	615
Ca-carbonatite	15.85	1	145	24,686	184	1586	1586	0.70376 (2)	0.51253 (1)	0.70373	0.51247	637

(Continued)

TABLE 2. REPRESENTATIVE AND AVERAGE ANALYSES OF Rb, Sr, Sm, Nd (ppm), MEASURED RATIOS OF $^{87}\text{Sr}/^{86}\text{Sr}$ AND $^{143}\text{Nd}/^{144}\text{Nd}$ (STANDARD DEVIATION IN PARENTHESES), INITIAL ISOTOPIC RATIOS, AND Nd MODEL AGES (T^{DM}) (Continued)

Rock type (Notional age, Ma)	SiO_2 (wt%)	Mg#	N	Rb	Sr	Sm	Nd	$(^{87}\text{Sr}/^{86}\text{Sr})_m$	$(^{143}\text{Nd}/^{144}\text{Nd})_m$	$(^{87}\text{Sr}/^{86}\text{Sr})$	$(^{143}\text{Nd}/^{144}\text{Nd})$	T^{DM} (Ma)
Early Cretaceous: Syntholeiitic alkaline suites												
Angola (132)												
Tephrite	46.67	0.45	1	43	1280	11.6	65	0.70549 (3)	0.51241 (1)	0.70531	0.51232	1018
Phonolite	56.18	0.15	4	168 (5)	559 (296)	16.3 (0.8)	69 (6)	0.7551 (44)	0.51260 (2)	0.70388	0.51248	1105
Ca-carbonatite	4.72		2	0.49 (0.09)	2678 (736)	202 (58)	1223 (281)	0.70416 (1)	0.51273 (1)	0.70416	0.51264	540
Ca-carbonatite	0.48		2	0.52 (0.01)	4938 (229)	32.7 (17.3)	208 (100)	0.70396 (1)	0.51271 (1)	0.70396	0.51263	544
Mg-carbonatite	12.13		1	0.83	2461	130.5	717	0.70399 (1)	0.51272 (1)	0.70399	0.51262	605
Mg-carbonatite	9.92		1	18	1199	378.1	2450	0.70455 (1)	0.51272 (1)	0.70448	0.51264	524
Namibia (132)												
Theralite	43.54	0.65	1	52	889	3.6	34	0.70479 (2)	0.51263 (2)	0.70447	0.51257	514
Phonotephrite	44.20	0.61	2	70 (2)	1564 (106)	6.6 (2.0)	40.4 (9.8)	0.70470 (1)	0.51264 (1)	0.70446	0.51256	649
Ne-syenite	57.03	0.29	4	190 (24)	286 (223)	4.4 (2.2)	25 (12)	0.71025 (426)	0.51263 (4)	0.70664	0.51254	707
Ca-carbonatite	7.28		1	1	3629	183	1141	0.70436 (1)	0.51257 (1)	0.70436	0.51249	727
(130)												
Alkaline gabbro			5	25 (27)	646 (109)	4.5 (3.3)	19.5 (15.4)	0.70514 (39)	0.51270 (8)	0.70493	0.51258	867
Essexite			2	101 (26)	655 (20)	6.5 (0.5)	33.7 (1.1)	0.70467 (37)	0.51282 (2)	0.70385	0.51272	494
Ne-syenite			1	145	324	4.1	24.2	0.70661 (2)	0.51268 (1)	0.70422	0.51259	618
(129)												
Ne-syenite	54.03	0.32	10	157 (69)	605 (220)	18.5 (7.7)	117 (46)	0.70682 (235)	0.51250 (2)	0.70544	0.51242	806
Ca-carbonatite	3.20		2	17 (22)	10,185 (2106)	186 (35)	1270 (372)	0.70354 (2)	0.51256 (2)	0.70354	0.51256	692
Qz-monzonite	62.55	0.22	2	142 (2)	233 (11)	11.5 (0.5)	57 (6)	0.71115 (108)	0.51256 (1)	0.70789	0.51246	930
Trachydacite	66.85	0.20	2	146 (0)	201 (1)	12.5 (0.5)	63 (2)	0.71704 (10)	0.51232 (1)	0.71315	0.51222	1280
(128)												
Basanite	42.40	0.73	4	46 (3)	920 (173)	8.3 (1.2)	48 (8)	0.70468 (15)	0.51269 (1)	0.70442	0.51260	616
Tephrite	43.98	0.63	5	83 (15)	1344 (159)	9.4 (0.8)	53 (5)	0.70472 (14)	0.51267 (2)	0.70439	0.51258	658
Phonotephrite	47.35	0.56	2	124 (31)	1285 (389)	8.1 (0.0)	47 (0)	0.70488 (1)	0.51268 (1)	0.70437	0.51259	627
Foidite	43.30	0.49	1	110	1770	7.7	54	0.70478 (1)	0.51270 (1)	0.70445	0.51263	519
Nephelinite	43.50	0.58	1	80	1430	9.3	55	0.70462 (1)	0.51268 (1)	0.70433	0.51259	616
(128)												
Ankaratrite	39.60	0.63	1	49	1517	17	107	0.70433 (1)	0.51251 (1)	0.70416	0.51243	796
Phonolite	54.30	0.29	1	179	265	6	35	0.70858 (1)	0.51245 (1)	0.70502	0.51236	988
Syenite	60.13	0.17	4	112 (43)	149 (107)	15 (4)	85 (22)	0.71637 (812)	0.51213 (8)	0.71241	0.51204	1386
Early Cretaceous: Post-tholeiitic alkaline suites												
Namibia (125)												
Basalt	38.83	0.69	1	46	133	8.2	44.6	0.70373 (1)	0.51261 (1)	0.70356	0.51252	766
Nephelinite	42.90	0.73	1	67	965	7.5	44.4	0.70489 (1)	0.51252 (1)	0.70453	0.51224	825
Ca-carbonatite			2	2.5 (1.0)	1414 (102)	81 (3)	877 (32)	0.70440 (3)	0.51253 (1)	0.70439	0.51248	582
Phonotephrite (camptonite)	46.02	0.69	2	97 (4)	798 (29)	5.6 (0.1)	28.5 (1.8)	0.70451 (4)	0.51276 (1)	0.70389	0.51266	597
Nephelinite (damkjærnrite)	35.66	0.68	7	111 (26)	1280 (306)	11.5 (1.7)	64.2 (10.8)	0.70486 (29)	0.51266 (1)	0.70441	0.51257	678
Nephelinite (ainörite)	35.66	0.63	2	41 (4)	2241 (63)	10.9 (0.6)	59.6 (6.2)	0.70432 (4)	0.51270 (5)	0.70422	0.51261	636
Phonolite (tingualite)	51.24	0.40	1	206	704	3.6	20.5	0.70492 (8)	0.51273 (1)	0.70342	0.51264	570
Phonotephrite	44.70	0.52	1	281	1450	9.7	69	0.70843 (1)	0.51262 (1)	0.70743	0.51255	606

(Continued)

TABLE 2. REPRESENTATIVE AND AVERAGE ANALYSES OF Rb, Sr, Sm, Nd (ppm), MEASURED RATIOS OF $^{87}\text{Sr}/^{86}\text{Sr}$ AND $^{143}\text{Nd}/^{144}\text{Nd}$ (STANDARD DEVIATION IN PARENTHESES), INITIAL ISOTOPIC RATIOS, AND Nd MODEL AGES (T^{DM}) (Continued)

Rock type (Notional age, Ma)	SiO_2 (wt%)	Mg#	N	Rb	Sr	Sm	Nd	$(^{87}\text{Sr}/^{86}\text{Sr})_m$	$(^{143}\text{Nd}/^{144}\text{Nd})_m$	$(^{87}\text{Sr}/^{86}\text{Sr})$	$(^{143}\text{Nd}/^{144}\text{Nd})$	T^{DM} (Ma)
Late Cretaceous–Eocene alkaline suites												
Angola (93)												
Basaltite	45.11	0.61	1	49	531	10	36	0.70312 (1)	0.51279 (1)	0.70277	0.51264	1080
Namibia (77)												
Picrite	30.91	0.74	1	56	646	23.6	45	0.70455 (2)	0.51265 (2)	0.70428	0.51260	635
Ca-carbonatite	1.61	1	12	12	2327	18.9	116	0.70433 (2)	0.51264 (1)	0.70431	0.51261	648
Namibia (71)												
Kimberlite			8	135 (16)	2092 (459)	13.9 (0.3)	108 (3)	0.70480 (42)	0.51276 (6)	0.70461	0.51272	423
Kimberlite			8	60 (15)	1219 (130)	15.1 (0.8)	119 (6)	0.70391 (10)	0.51274 (9)	0.70377	0.51270	458
Namibia (49)												
Trachyte	56.15	0.04	1	164	579	13.8	50.3	0.70654 (1)	0.51263 (1)	0.70596	0.51258	1496
Foidolite	39.70	0.41	2	60 (15)	848 (261)	46 (6)	180 (49)	0.70354 (6)	0.51276 (1)	0.70340	0.51271	927
Ca-carbonatite	15.42	3	14 (4)	14 (4)	5816 (362)	41 (7)	248 (41)	0.70327 (1)	0.51274 (1)	0.70327	0.51271	528
Namibia: Granitoids and rhyolites												
Namibia (130)												
Quartz-syenite	65.00	0.46	7	139 (38)	89 (62)	10.1 (2.8)	50 (15)	0.74034 (841)	0.51255 (11)	0.73153	0.51244	947
S-granite	69.38		5	197 (12)	152 (69)	13 (1)	63 (5)	0.72002 (293)	0.51243 (1)	0.71308	0.51232	1168
S-leucogranite	76.80		1	408	14	9	47	0.81806 (2)	0.51245 (1)	0.72620	0.51235	1037
A-granite	73.19			3.7	11	95	423	0.71175 (1)	0.51261 (1)	0.70995	0.51243	1321
Comenditic rhyolite	74.50		2	434 (74)	14 (8)	27 (8)	132 (48)	0.92705 (13,451)	0.51211 (6)	0.75517	0.51200	1664
S-granite (125)												
	76.90		1	994	7	48	163	1.49968 (2)	0.51229 (1)	0.71576	0.512149	3072

Note: Sources are in Table 1 and Thompson et al. (2001). Order and localities are as in Table 1; SiO_2 (wt%) as reference; N —number of samples; italics—sodic alkaline suites; bold—carbonatites.

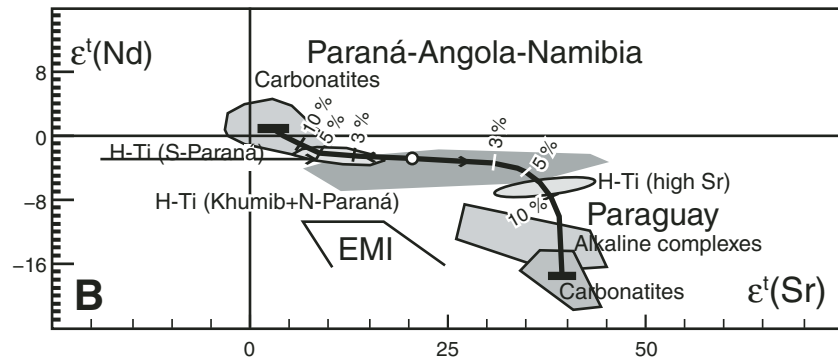
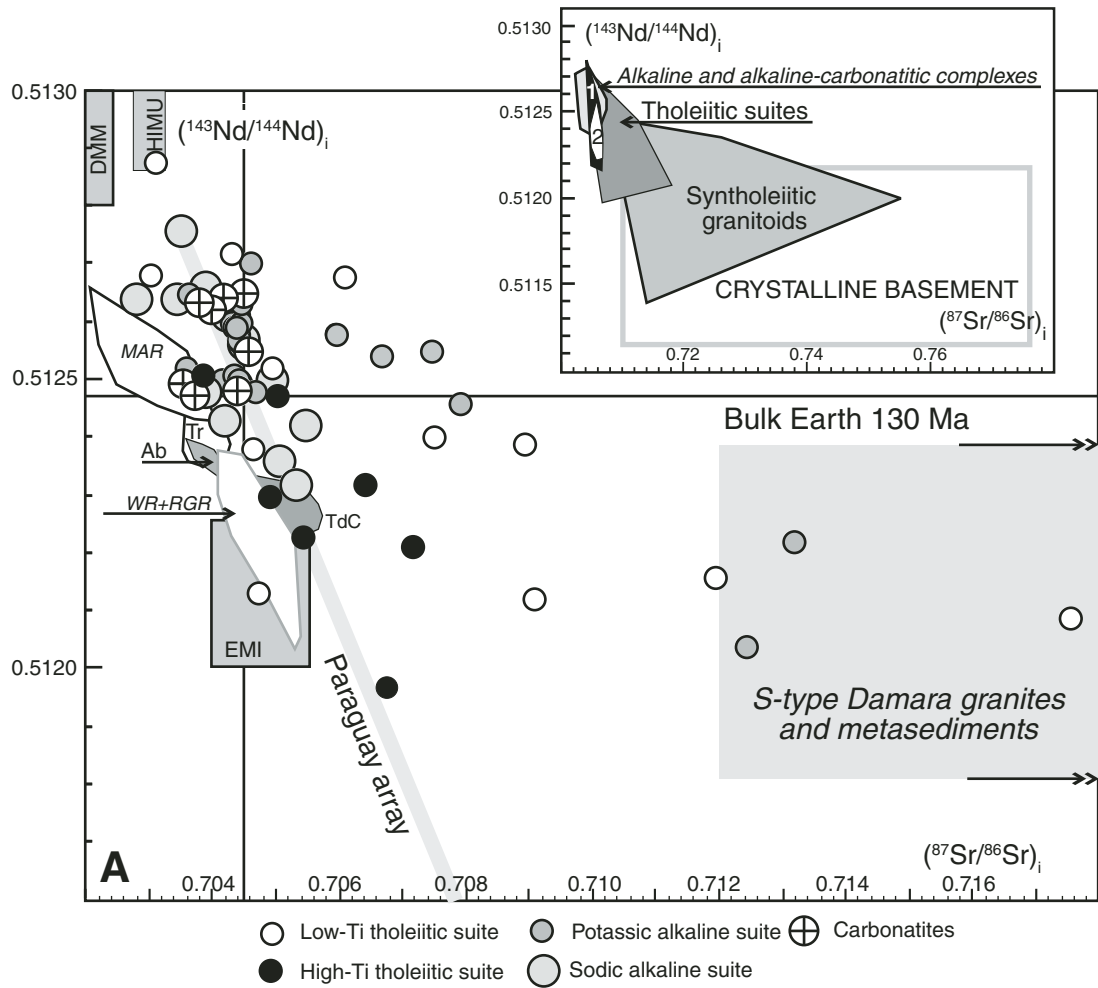


Figure 7. (A) Initial $^{87}\text{Sr}/^{86}\text{Sr}$ [$(^{87}\text{Sr}/^{86}\text{Sr})_i$] vs. initial $^{143}\text{Nd}/^{144}\text{Nd}$ [$(^{143}\text{Nd}/^{144}\text{Nd})_i$] correlation diagrams for Angola and Namibia rock. Data sources for Angola and Namibia are in Table 1; Paraguay array—Comin-Chiaramonti et al. (2007a, 2007b); Atlantic Ocean: WR+RGR—Walvis Ridge (Richardson et al., 1982) and Rio Grande Rise (Gamboa and Rabinowitz, 1984), respectively; MAR—Mid-Atlantic Ridge (Hamelin et al., 1984; Ito et al., 1987; Fontignie and Schilling, 1997); TdC—Tristan da Cunha, Inaccessible and Gough (Le Roex, 1985; Le Roex et al., 1990); Tr—Trindade (Marques et al., 1999; Siebel et al., 2000); Ab—Abrolhos (Fodor et al., 1998, and references therein). DMM (depleted mantle), HIMU (high- μ mantle), and EMI (enriched mantle I) are approximations of mantle end members taken from Hart et al. (1992). Inset: The same diagram showing also the fields of the syntholeiitic granitic rocks, the Damara basement, the South America tholeiitic suites, and the tholeiitic suites for Angola-Namibia, Low-Ti (1) and High-Ti (2), respectively. Basalts and basaltic-andesites with $\text{MgO} \geq 4 \text{ wt}\%$ and $(^{87}\text{Sr}/^{86}\text{Sr})_i \leq 0.7065$ were selected to represent compositions relatively unaffected by crustal materials (cf. Piccirillo and Melfi, 1988). (B) ϵ_t^{Sr} vs. ϵ_t^{Nd} diagram (cf. Faure, 2001, and references therein) for the Early Cretaceous magmatic rocks from Paraná-Etendeka. Mixing curves are between the mean compositions of the high-Ti tholeiites and those for the Cretaceous carbonatites from Paraná-Etendeka (Paraná-Angola-Namibia) and Paraguay, respectively. Ticks are percentages of carbonatitic component. Data sources in Rosset et al. (2007). Basalts and basaltic-andesites with $\text{MgO} \geq 4 \text{ wt}\%$ and $\text{Sri} \leq 0.7065$ were selected to represent the compositions relatively unaffected by crustal materials (cf. Piccirillo and Melfi, 1988).

Crustal-contaminated rocks, i.e., acidic Palmas and Chapecó suites (associated with low-Ti and high-Ti tholeiites, respectively; Piccirillo and Melfi, 1988), and potassic evolved rocks trend toward the fields of granitic rocks and crystalline basement (Fig. 7A and inset).

Generally, most alkaline and alkaline-carbonatite complexes, as well the Angola and Namibia and Paraná-Etendeka tholeiitic suites, appear to follow a well-defined array involving depleted (DMM or HIMU [i.e., magma source having a high $^{238}\text{U}/^{204}\text{Pb}$ ratio μ ; cf. Faure, 2001]) and enriched mantle (EMI) components: the Na-rocks (which plot close to the Bulk Earth) and the K-rocks from Paraguay, typically high in radiogenic Sr worldwide, represent the range of virtually uncontaminated Paraná-Etendeka source magmas.

Three main trends are apparent from the silica versus initial $^{87}\text{Sr}/^{86}\text{Sr}$ ratio diagram (Fig. 8): The first, with relatively low isotopic ratios, points toward the field of the Damara Precambrian granites and migmatites (Jung et al., 2003; Frindt et al., 2004), and it is consistent with the Chapecó acid rocks of the high-Ti tholeiitic suite; the second, tracking toward the Paresis rhyolites, represents the best-fitting curve for the more-evolved rocks of the potassic alkaline suite; and the third, with the highest $^{87}\text{Sr}/^{86}\text{Sr}$

ratios, trends toward anatectic granitic rocks of the pre-Damara basement (Seth et al., 1998; Frindt et al., 2004) and forms the best-fitting curve for the Palmas acid rocks of the low-Ti suite.

Assuming that the silica and Sr isotopic variations highlight multiple processes like cumulus, fractional crystallization, magma mingling, and probably AFC (see figure 16 in Bellieni et al., 1986), the presence, in time and space, of the various suites and associated carbonatites, points also to important heterogeneities in the mantle sources.

Nd Model Ages

Nd model ages (T^{DM}) have little real meaning because they do not reflect the true ages of the sources, being a function of the Sm/Nd fractionation during the melting and magma differentiation (cf. Arndt and Goldstein, 1987). Nevertheless, the T^{DM} in the Paraná-Etendeka magmatic rocks may be used, to a certain extent, to estimate the timing of a main metasomatic event in the mantle sources, as a function of the different geochemical behaviors in the different sectors of the Paraná-Etendeka.

$T^{\text{DM}}(\text{Nd})$ model ages for the whole Paraná-Angola-Namibia system from Alberti et al. (1999), Comin-Chiaramonti and Gomes (2005), and Piccirillo and Melfi (1988) suggest that

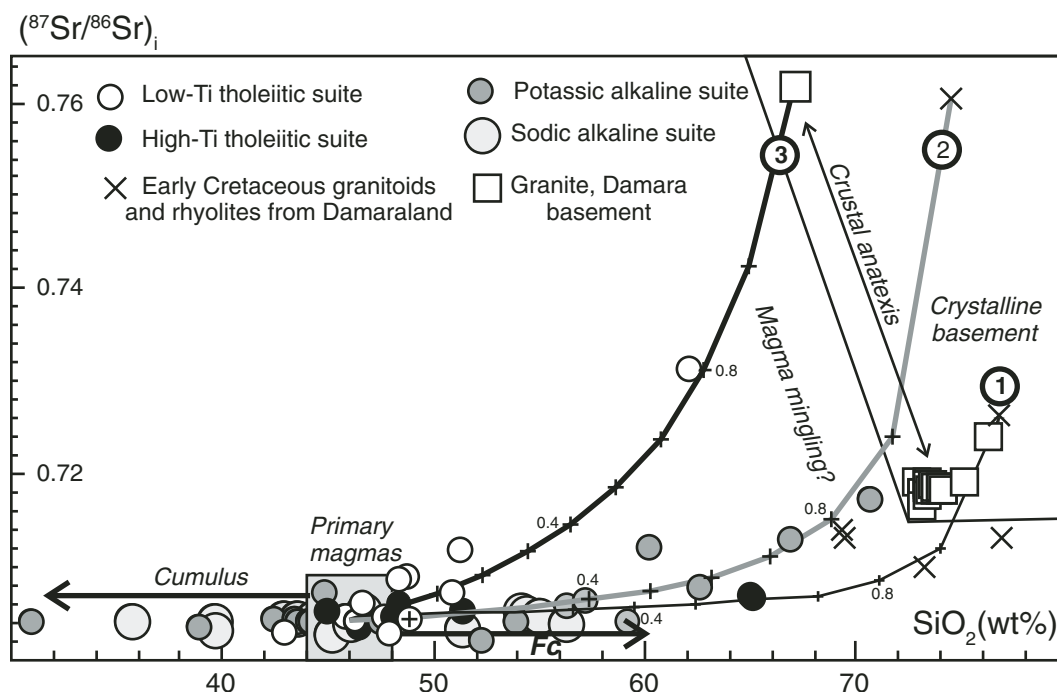


Figure 8. Mixing curves between SiO_2 and initial $^{87}\text{Sr}/^{86}\text{Sr}$ isotopic ratios. (1) "Primitive magma," high-Ti type: $\text{SiO}_2 = 48$ wt%, $\text{Sr} = 435$ ppm, $\text{Mg\#} = 0.59$, $(^{87}\text{Sr}/^{86}\text{Sr})_i = 0.70488$; end member, leucogranite: $\text{SiO}_2 = 76.8$ wt%, $\text{Sr} = 24$ ppm, $(^{87}\text{Sr}/^{86}\text{Sr})_i = 0.7260$. (2) "Primitive magma," alkaline potassic type: $\text{SiO}_2 = 44$ wt%, $\text{Sr} = 1285$ ppm, $\text{Mg\#} = 0.63$, $(^{87}\text{Sr}/^{86}\text{Sr})_i = 0.70439$; end member, comenditic rhyolite: $\text{SiO}_2 = 74.5$ wt%, $\text{Sr} = 14$ ppm, $(^{87}\text{Sr}/^{86}\text{Sr})_i = 0.76038$. (3) "Primitive magma," low-Ti type: $\text{SiO}_2 = 46$ wt%, $\text{Sr} = 230$ ppm, $\text{Mg\#} = 0.70$, $(^{87}\text{Sr}/^{86}\text{Sr})_i = 0.70428$; end member, granite: $\text{SiO}_2 = 67.5$ wt, $\text{Sr} = 30$ ppm, $(^{87}\text{Sr}/^{86}\text{Sr})_i = 0.7625$. The curves are labeled at 10% intervals. Granites from Damara basement are from Jung et al. (2003); Early Cretaceous granitoids and rhyolites from Damaraland are from Schmitt et al. (2000) and Frindt et al. (2004). Fc—fractional crystallization (cf. figure 16 in Bellieni et al., 1986).

(1) The Paraná-Angola-Namibia high-Ti flood tholeiites and dikes mainly range from 1.2 to 1.9 Ga (Angola 1.1 ± 0.2 Ga, Namibia 1.2 ± 0.1 Ga);

(2) The Paraná-Angola-Namibia low-Ti flood tholeiites range between 1.1 and 1.7 Ga (Angola 1.1 ± 0.1 Ga, Namibia 1.5 ± 0.3 Ga);

(3) The pre-tholeiitic potassic rocks and associated volcanics mainly range from 0.8 to 2.5 Ga;

(4) Early Cretaceous syn- and post-tholeiitic alkaline and carbonatitic magmatism mainly ranges from 0.4 to 0.9 Ga, excluding Paraguay (1.5 Ga) and Alto Paranaíba (1.1 Ga) carbonatites; and

(5) Late Cretaceous alkaline rocks and carbonatites span between 0.6 and 0.9 (Alberti et al., 1999; Comin-Chiaramonti and Gomes, 2005).

The variability of the model ages results delineate various Paraná-Etendeka groups and regions (Fig. 9). Notably, the model ages for Angola and Namibia are quite different from those for other Paraná-Etendeka regions. Some examples are given in Table 3.

Petrogenetic Aspects

The isotopic data indicate several possible lines of approach to the petrogenesis. They support the view that the Angola-Namibia carbonatites, mainly ranging in composition from a depleted component to the Bulk Earth, and the carbonatites and alkaline rocks from eastern Paraguay represent the end members of virtually uncontaminated source magmas from subcontinental mantle segments variously affected by metasomatic processes (Alberti et al., 1999; Comin-Chiaramonti et al., 2007a, 2007b, 2007c).

The range of model ages in the Paraná-Etendeka implies that the corresponding Cretaceous and Paleogene magmas were derived from subcontinental lithospheric mantle modified by metasomatic processes (asthenospheric components?) since Neoproterozoic to Neoproterozoic times (Comin-Chiaramonti et al., 2007a, 2007b, 2007c). Notably, the T^{DM} age relative to the clinopyroxene megacryst (Davies et al., 2001) from Gibeon kimberlites is 777 ± 70 Ma, fitting one of the three ages indicated by SHRIMP results, i.e., 1013 ± 22 Ma, 751 ± 28 Ma, and 627 ± 28 Ma. According to Liati et al. (2004), the latter ages are correlated with large-scale events in Namibia. These involve the granulite-facies metamorphism during the Namaqua collisional event and postcollisional magmatism (1000–1100 Ma), the intense magmatic activity and initial rifting stages in the Damara belt (730–770 Ma), and the early Pan-African orogeny responsible for the Damara orogen (ca. 650 Ma).

Crucial to any petrogenetic interpretation are the following points:

(1) The isotopic overlapping of different igneous rocks (i.e., tholeiites, alkaline rocks, and carbonatites), which cannot be accidental and points to sampling of different ancient reservoirs formed at the same time from the same subcontinental upper mantle;

(2) Mantle source heterogeneity induced by recycled crust in the mantle (Menzies, 1990; Weaver, 1991), or occurrence of variably veined material in the subcontinental upper mantle, or both; and

(3) Pb isotope data indicating a mantle source of ca. 2.0 Ga for the Paraná high-Ti tholeiites. Therefore, magma genesis involved ancient lithospheric mantle reset at well-defined isotopic ranges, since much of the crust in southern Brazil appears to have also been formed at ca. 2 Ga (Hawkesworth et al., 1986).

It is to be noted that the compositions of veined materials, i.e., metasomites, formed from metasomatizing melts will vary

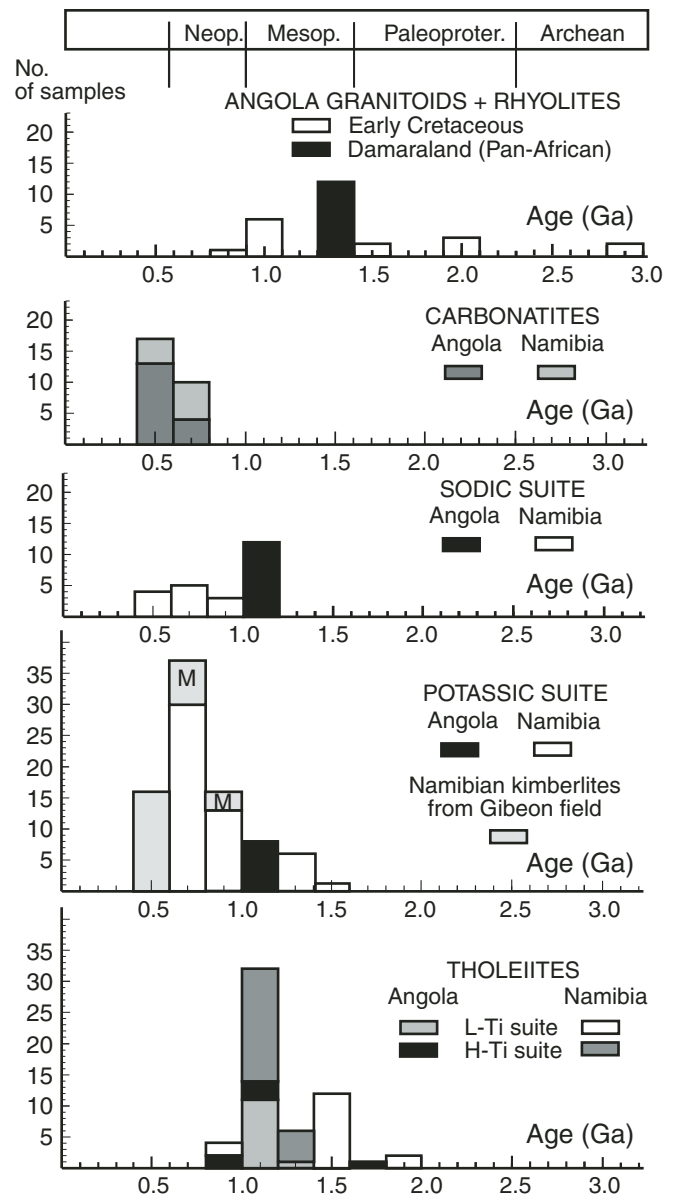


Figure 9. Histograms of model ages for the Angolan and Namibian magmatic suites (cf. Table 2). M—Megacrysts from Gibeon kimberlites (Liati et al., 2004). For comparison, model ages of S-type Mesoproterozoic granites from Damaraland are also shown.

TABLE 3. AVERAGED T^{DM} VALUES FOR ROCK FROM PARANÁ, ANGOLA, AND NAMIBIA, LOW-Ti AND HIGH-Ti THOLEIITES, RESPECTIVELY, AND FOR SOME MAGMATIC SUITES FROM THE PARANÁ-ETENDEKA SYSTEM

	Model ages (Ma)					
	Low-Ti	High-Ti	K-suites	Na-suites	Carbonatites	Kimberlites
Angola	1085 ± 83	1298 ± 257	1117 ± 31	1098 ± 26	518 ± 55	
Namibia	1577 ± 88	1208 ± 47	707 ± 94	655 ± 107	651 ± 56	470 ± 36
			1371 ± 74 (M)			777 ± 70 (M)
Southern Paraguay	1742 ± 8	1879 ± 124	1648 ± 102	822 ± 10	1500 ± 200	
Northern-central Paraguay	1303 ± 70		1642 ± 102	504 ± 45	1500 ± 200	
Alto Paranaíba			987 ± 106		1068 ± 12	928 ± 57
Whole Paraná-Etendeka	1720 ± 285	1248 ± 131	1245 ± 371	770 ± 244		

Note: M—clinopyroxene megacryst (Liati et al., 2001). Data sources are in Table 1, Comin-Chiaramonti and Gomes (1996, 2005), and Piccirillo and Melfi (1988).

with the evolution of the melt. Consequently, the veins will define mixing curves between vein and matrix (cf. α and β regression lines of Fig. 10). Therefore, a variously veined lithospheric mantle (amphibole/phlogopite-carbonate-lherzolite and amphibole-lherzolite + CO_2 -fluid type III and IV veins of Meen et al., 1989) of Proterozoic age is favored for the genesis of various magma types from the Paraná-Etendeka system (Fig. 10).

GEOPHYSICAL ASPECTS

Molina and Ussami (1999) and Ernesto et al. (2002) observed that the most important residual geoid anomalies for the South Atlantic clearly correlate with major lithospheric features, such as subtle positive anomalies along the mid-ocean ridge, negative anomalies along deep oceanic basins, thick cratons, and, above all, along the Paraná-Etendeka.

Anderson et al. (1992) observed that the upper mantle is characterized by vast domains of high temperatures rather than by small regions surrounding hotspots, and that low-velocity anomalies record previous positions of migrating ridges, tracking where the breakup of western Gondwana occurred (Tanimoto and Zhang, 1992).

Paleomagnetic data indicate that the drifting velocity was relatively high, and varied from ~23 mm/yr in the 130–80 Ma interval, to ~7 mm/yr in the 80–50 Ma time span (Ernesto, 2005). However, the path described by the South America plate implies that the regions where the alkaline magmatic activity developed were kept under significant thermal anomalies for a time interval long enough for the lithosphere to incorporate the necessary heat. Assuming that the area occupied by Paraná-Etendeka was kept under thermal anomaly for at least 50 m.y. starting in the Jurassic, then sufficient heat may have been stored in the lithosphere and magmatic activity would have occurred where tectonic conditions were favorable, like stress accommodations to the successive rotations of the plate (Ferrari and Riccomini, 1999).

In addition, the following aspects are relevant:

(1) True polar wander and paleomagnetic-paleogeographic reconstructions of the Paraná-Etendeka–Tristan da Cunha hotspot, assuming this hotspot was a fixed point of the mantle, place the Tristan da Cunha plume ~800 km south of the Paraná-Etendeka area, suggesting that plume mobility would be

required in order to maintain the Paraná-Etendeka–Tristan da Cunha relationships.

(2) Assuming that the Tristan da Cunha hotspot was located in the northern area of the Paraná-Etendeka (~20° from the present Tristan da Cunha position), the plume migrated southward from 133 to 130 Ma (main volcanic phase) to 80 Ma at a rate of ~40 mm/yr. From 80 Ma to the present, the plume has remained virtually fixed, leaving a track compatible with African plate movement. Notably, the southward migration of the plume is in opposition to the northward migration of the main Paraná-Etendeka magmatic activity (133 Ma in the south, 130 Ma in the north).

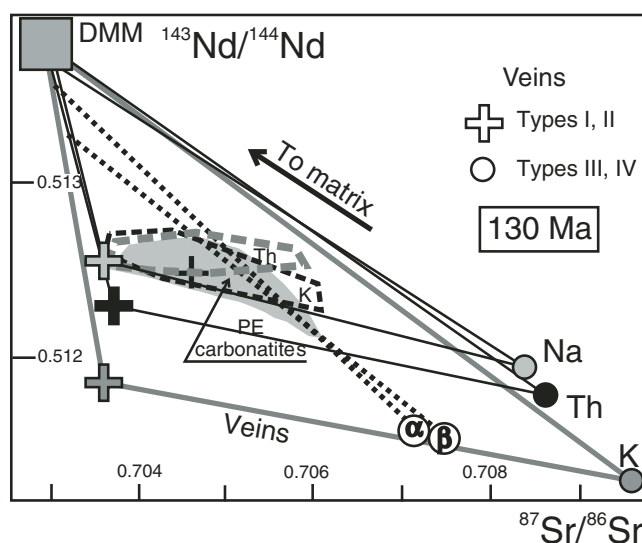


Figure 10. Calculated SCUM (subcontinental upper mantle) isotopic composition at 2.0 Ga (for a discussion, see Meen et al., 1989), projected to 130 Ma. Parental melts with various Rb/Sr and Sm/Nd ratios are assumed for K, Na (potassic and sodic rocks, respectively; from Comin-Chiaramonti et al., 2007a, 2007b, 2007c), and Th (Paraná-Etendeka [PE] tholeiitic basalts; Piccirillo and Melfi, 1988). Model DMM (depleted-MORB): Rb = 0, Sr = 0.133, Sm = 0.314, Nd = 0.628; present day bulk earth: $^{87}\text{Sr}/^{86}\text{Sr} = 0.70475$, $^{87}\text{Rb}/^{86}\text{Sr} = 0.0816$, $^{143}\text{Nd}/^{144}\text{Nd} = 0.512638$, $^{147}\text{Sm}/^{143}\text{Nd} = 0.1967$; (Rb/Sr)_{diopside}: (Rb/Sr)_{melt} ≈ 0.125, (Sm/Nd)_{diopside}: (Sm/Nd)_{melt} ≈ 1.5; K: Rb/Sr = 0.0957, Sm/Nd = 0.1344; Na: Rb/Sr = 0.0732, Sm/Nd = 0.2295; Th: Rb/Sr = 0.0733, Sm/Nd = 0.2082. For the veins, see text and Meen et al. (1989). α and β —regression lines between vein types and matrix.

(3) Regional thermal anomalies in the deep mantle, mapped by geoid and seismic tomography data, offer an alternative, plume-unrelated heat source for the generation of intracontinental magmatic provinces (figure 9 in Ernesto et al., 2002).

GEODYNAMIC SCENARIO

A factor crucial to Paraná-Etendeka magma genesis is the link with the geodynamic processes that promoted the opening of the South Atlantic. According to Nürnberg and Müller (1991), seafloor spreading in the South Atlantic (cf. Fig. 1) started ca. 125–127 Ma (chron M4). North of the Walvis–Rio Grande ridges (latitude $>28^{\circ}\text{S}$), the onset of the oceanic crust would be younger (ca. 113 Ma; Chang et al., 1988).

The Early Cretaceous alkaline-carbonatitic complexes were emplaced approximately coeval with the main flood tholeiites of the Paraná Basin and, therefore, occurred during the early stages of rifting, before continental separation. On the other hand, the Late Cretaceous analogues were emplaced during more advanced stages of Africa–South America continental separation.

The origin of the alkaline (both sodic and potassic) and alkaline-carbonatitic magmatism in terms of plate tectonics is currently debated. Various models have been proposed involving deep mantle plume/hotspots, or shallow thermal anomalies.

Whatever the temperature, size, depth of origin, and number of hotspots, the plume model fails to account for the worldwide occurrence of alkaline-carbonatite magmatism (for a discussion, see Smith and Lewis, 1999). The latter authors have also proposed an attractive model for the opening of the South Atlantic, whereby the forces acting on plates that move at differential angular velocities, and the presence of volatile-rich mantle sources (wet spot) would drive the rifting to occur parallel to the preexisting (e.g., N-S) sutures, i.e., “Adamastor Ocean” (Fig. 11).

Notably, intraplate alkaline and alkaline-carbonatite magmatism would occur where second-order “plate boundaries” (e.g., Ponta Grossa–Moçâmedes Arch, Uruguay lineament, Damara belt; cf. Fig. 1) intersect the axes of major rifting, “indicating an origin related to the erosion and cycling of continental mantle towards the ridge axis by local convection taking the form of transverse rolls” (Smith and Lewis, 1999, p. 163).

In southern Brazil, the alkaline and alkaline-carbonatite magmatism is concentrated in regions with positive geoid anomalies (Molina and Ussami, 1999) that may be related to dense, very deep materials. Moreover, the different westward angular velocities of the lithospheric fragments in the South American plate, as defined by the “second-order plate boundaries” (Unternehr et al., 1988), may have favored the decompression and melting of variously metasomatized (wet spot) portions of the lithosphere

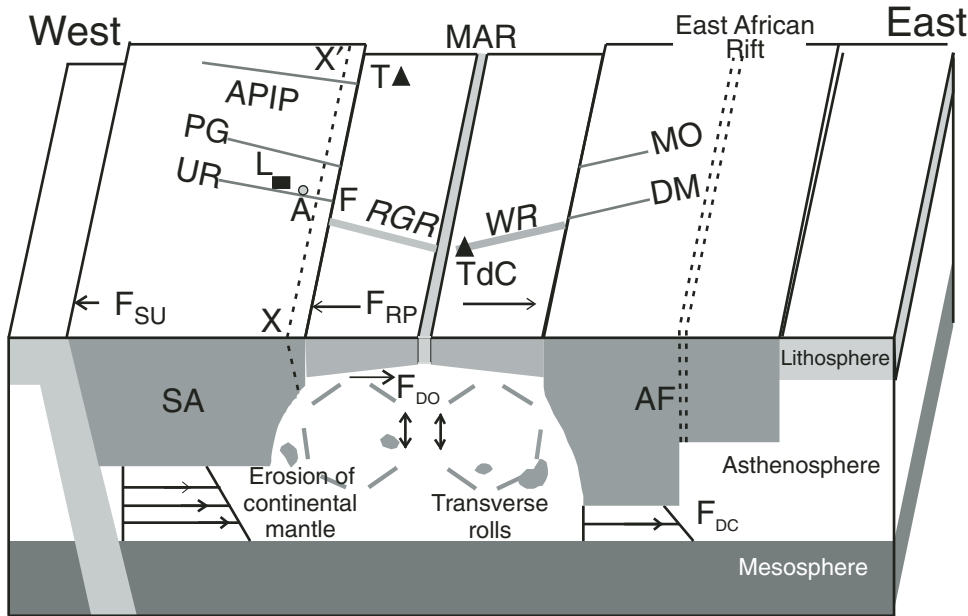


Figure 11. Forces acting on plates in rotational model illustrated for the South Atlantic Ocean (for a discussion, see Smith and Lewis, 1999). Major rifting occurs parallel to the X–X' preexisting suture (cf. Fig. 1). Intraplate volcanism is found where second-order sutures (e.g., PG–MO—Ponta Grossa–Moçâmedes Arch; UR—Uruguay lineament; DM—Damara belt) intersect the axis of rifting, indicating an origin related to erosion and cycling of continental mantle toward the ridge axis by local convection, taking the form of transverse rolls. SA—South America plate; AF—African plate; RGR—Rio Grande Rise; MAR—Mid-Atlantic Ridge; WR—Walvis Ridge; APiP—Alto Paranaíba igneous province; TdC—Tristan da Cunha; T—Trindade. Plate-moving forces (Forsyth and Uyedaf, 1975; Bott, 1992): F_{DC} , F_{DO} —continental and oceanic drag, respectively; F_{RP} —ridge push; F_{SU} —trench suction. F—Florianópolis; A—

Anitápolis; L—Lages. Note that (1) continental lithosphere is thicker than oceanic lithosphere, so continents almost always have a “keel” of lithospheric material projecting downward. As a result, the resistance to movement might be greater beneath continental plates than oceanic plates. Accordingly, continental plates might be associated with an additional continental drag force, F_{DC} , and so the resistive force acting on the base of a continental plate would be the sum of both oceanic and continental drag forces, $F_{DO} + F_{DC}$. (2) At constructive boundaries, the upwelling of hot material at ocean ridges generates a buoyant effect that produces the ocean ridge, which stands some 2–3 km above the surrounding ocean floor. Here, oceanic plates experience a force that acts away from the ridge, the so-called ridge-push force, F_{RP} , which is a result of gravity acting down the slope of the ridge. (3) Cooling of the mantle wedge against the upper surface of the subducting plate induces convection, which sucks more mantle into the wedge. This is the trench suction force, F_{SU} , which serves to pull the plate toward the trench.

mantle at different times, with variable isotopic imprinting (cf. also Comin-Chiaromonti and Gomes, 2005).

This scenario may account for Paraná-Etendeka sodic magmatism, even at the eastern Paraguay longitude, where there is evidence of active rifting structures (Asunción-Villarica graben; Comin-Chiaromonti et al., 2007a). In this case, the thermal perturbations may have been channeled along the “second order plate boundaries,” as illustrated by the hypocenters of earthquakes in South America (Comin-Chiaromonti and Gomes, 1996).

CONCLUDING REMARKS

The results of this investigation indicate that the genesis of the Paraná-Etendeka tholeiites and associated alkaline and carbonatitic suites, mainly reflects melting of heterogeneous subcontinental mantle reservoirs, without appreciable participation of plume-derived materials (Comin-Chiaromonti et al., 2007a, 2007b, 2007c). Also, these results support the view that the geochemical and isotopic signatures in the Walvis Ridge and Rio Grande Rise, believed to be the Tristan da Cunha tracks of basalt compositional variations (e.g., Turner et al., 1996), may be derived by contamination through detached continental lithospheric mantle left behind during the continental breakup processes.

In the isotopic diagrams (Figs. 7 and 10), the post-Paleozoic magmatism from Angola, Namibia, and the whole Paraná-Etendeka region appears to be related to heterogeneous mantle sources spanning from depleted mantle to enriched mantle components (EMI type). The alkaline magmatism mimics, in terms of isotopic compositions, the coeval flood tholeiites. Notably, the enriched isotopic signatures of the Early Cretaceous alkaline magmatism decrease from west (Paraguay) to east (Brazil, SE continental margin, and Namibia; Comin-Chiaromonti and Gomes, 2005). A similar decreasing isotopic shift is also observed for the age of the magmatism in Paraguay and Brazil, i.e., Early–Late Cretaceous to Tertiary (Comin-Chiaromonti et al., 2007a, 2007b, 2007c). These results suggest that the Paraná-Etendeka magmatism is related both to large- and small-scale heterogeneous mantle sources. Also, it should be noted that the isotopic signature of Trindade and Abrolhos Islands (Fig. 7A) is consistent with that of the alkaline-carbonatitic magmatism of Early Cretaceous age from Angola and Namibia, but it is quite different from that (EMI signature) of the Late Cretaceous–Tertiary analogues from the Alto Paranaíba, Ponta Grossa Arch, and Cabo Frio–Taiúva-Serra do Mar areas (Comin-Chiaromonti and Gomes, 2005). According to Thompson et al. (1998), the Alto Paranaíba would be the inland surface expression of the “dogleg” track left by the Trindade plume. However, in terms of Sr–Nd isotopes, the contribution, if any, of the asthenospheric components related to that plume is difficult to account for (Marques et al., 1999). The Tristan da Cunha (Gough and Inaccessible Islands) alkaline magmatism and the Walvis Ridge–Rio Grande Rise basalts have isotopic characteristics that are distinct or partly overlap those of the Paraná-Etendeka Early Cretaceous alkaline-carbonatitic and tholeiitic magmatism, respectively. Therefore, also in this case,

the contribution of mantle components derived from the Tristan da Cunha plume is not appreciable for Paraná-Etendeka magmatism as a whole.

Hawkesworth et al. (1986) interpreted the Etendeka (Namibia) high-TiO₂ basalts as resulting from melting of a Proterozoic lithospheric mantle, which, in the case of the Walvis Ridge (WR2 basalts of Richardson et al., 1982), was floating inside the oceanic asthenosphere during the opening of the South Atlantic. Alternatively, the elemental and isotopic signature of the high-TiO₂ basalts could be related to contamination of oceanic mantle by ancient subcontinental lithospheric mantle.

In summary, the isotopic signature of magmatic suites, in general, and of the carbonatites from the Paraná-Etendeka, in particular, reflects ancient heterogeneities preserved in the subcontinental lithospheric mantle.

Therefore, we believe, as documented also by Ernesto et al. (2002) and Ernesto (2005), that the hypothesis of asthenospheric plumes for Paraná-Etendeka magmatism is not compelling, except that it may represent a thermal perturbation.

The geochemical data show that the genesis of Paraná-Etendeka magmatism requires heterogeneous mantle sources, also in terms of radiogenic isotopes. Such heterogeneity is probably related to “metasomatic processes,” which would have occurred at ca. 0.5–1.0 Ga in Angola, Namibia, and Brazil and 1.5–1.6 Ga in eastern Paraguay (Comin-Chiaromonti and Gomes, 1996). Therefore, the contribution of asthenospheric components, derived from mantle plumes (i.e., Tristan da Cunha and Trindade), to the genesis of the Paraná-Etendeka alkaline-carbonatitic magmatism was not significant. This is consistent with the conclusions reached for the Paraná-Etendeka flood tholeiites (Ernesto et al., 2002; Ernesto, 2005; Comin-Chiaromonti et al., 2007c).

Regional thermal anomalies in the deep mantle, mapped by geoid and seismic tomography data, offer an alternative for a plume-unrelated heat source (Ernesto et al., 2002). The “hotspot tracks” of Walvis Ridge and Rio Grande Rise, as well as the Vitória-Trindade chain, might reflect the accommodation of stresses in the lithosphere during rifting rather than continuous magmatic activity induced by mantle plumes beneath the moving lithospheric plates. This model offers an alternative explanation to that described by Torsvik et al. (2009).

ACKNOWLEDGMENTS

We thank A. Marzoli for providing some unpublished analyses of rock samples from Angola. The detailed review and helpful suggestions by H.H.G.J. Ulbrich, A. Cundari, J. Gittins, and M. Gasparon are greatly appreciated. This paper resulted from the academic collaboration between the University of Trieste (Italy) and the University of São Paulo (USP, Brazil). For financial support, the Italian (MIUR-PRIN 2008, Ministero Italiano della Università e Ricerca-Progetti di Ricerca di Interesse Nazionale) and Brazilian (FAPESP, Fundação de Amparo à Pesquisa do Estado de São Paulo, and CNPq, Conselho Nacional de Pesquisa) agencies are acknowledged.

TABLE A1. REPRESENTATIVE AND AVERAGE ANALYSES (wt%) OF THE THOLEIITIC AND ALKALINE (POTASSIC AND SODIC) SUITES FROM ANGOLA AND NAMIBIA

Rock type (Locality)	N	SiO ₂	TiO ₂	Al ₂ O ₃	Fe ₂ O ₃	MnO	MgO	CaO	Na ₂ O	K ₂ O P ₂ O ₅	Mg#
EARLY CRETACEOUS: Tholeiitic suites											
L-Ti											
ANGOLA											
Picrite (Kwanza)	3	42.79	1.66	6.52	14.72	0.19	24.89	8.41	1.01	0.31	0.24 0.80
Gabbro (T. Bonga)	4	45.77	1.32	15.39	10.68	0.15	10.35	12.80	2.32	0.88	0.48 0.68
Basalt (Namibe)	1	48.72	1.04	18.99	11.23	0.15	5.36	10.39	2.62	0.42	0.22 0.52
Basalt (Kwanza)	4	50.78	1.05	16.72	11.10	0.15	6.26	9.42	2.68	0.62	0.19 0.56
NAMIBIA											
Picritic basalt (south Etendeka)	1	46.62	0.80	10.56	12.09	0.16	19.70	8.22	1.32	0.34	0.07 0.74
Basalt (south Etendeka)	2	47.41	1.03	13.19	11.97	0.16	13.56	10.59	1.69	0.30	0.10 0.71
Basalt (south Etendeka)	6	47.73	1.22	13.70	12.37	0.17	10.87	11.63	1.94	0.26	0.10 0.69
Basalt (south Etendeka)	2	48.62	1.10	14.55	11.70	0.16	8.63	9.87	2.04	0.82	0.14 0.59
Basalt (south Etendeka)	1	51.18	0.90	13.84	10.51	0.18	6.21	8.55	2.86	0.92	0.11 0.57
Basaltic andesite (north Etendeka)	2	52.17	1.54	14.52	12.84	0.20	5.86	10.61	2.70	0.67	0.18 0.51
Rhyolite (Palmas type, north Etendeka)	9	70.55	0.84	12.63	5.45	0.11	0.93	2.21	3.04	4.58	0.25 0.28
H-Ti											
ANGOLA											
Basalt (Kwanza)	3	46.42	2.05	13.86	12.54	0.19	8.44	11.75	2.84	1.15	0.44 0.60
Basalt (Kwanza)	2	47.99	2.74	13.93	15.82	0.20	5.30	9.15	3.00	1.33	0.55 0.43
Basalt (Kwanza)	2	48.33	2.61	13.83	11.78	0.16	7.49	10.54	2.82	1.35	0.40 0.59
Trachydacites (Chapécó type, Namibe)	3	65.04	1.18	13.55	6.37	0.07	1.14	1.97	3.07	4.77	0.42 0.29
NAMIBIA											
Basalt (north Etendeka)	2	51.31	3.25	12.45	12.35	0.16	5.09	8.05	2.77	1.72	0.50 0.48
Basalt (south Etendeka)	1	45.66	2.32	9.50	17.46	0.19	14.04	7.90	2.01	0.88	0.30 0.64
Trachydacites (Chapécó type, south Etendeka)	18	64.94	1.52	13.47	7.96	0.13	1.32	2.97	3.17	4.78	0.52 0.27
EARLY CRETACEOUS: Alkaline suites											
Pre-Tholeiitic											
ANGOLA											
Ijolite (T. Bonga, Coola, Sulima)	1	46.16	0.88	13.85	10.52	0.26	4.48	12.41	2.32	7.61	1.45 0.51
Ne-syenite (T. Bonga, Coola, Sulima)	6	54.93	0.38	21.72	4.41	0.21	0.42	1.91	9.92	5.20	0.18 0.19
Syenite (T. Bonga, Coola, Sulima)	7	59.14	0.78	17.80	3.98	0.19	2.25	2.24	6.89	5.31	0.30 0.56
NAMIBIA											
Ne-syenite (Kalkfeld)	4	53.80	0.90	19.45	5.64	0.19	0.53	1.05	7.77	7.96	0.09 0.19
Foidite (Kalkfeld)	1	44.17	0.05	26.48	2.98	0.07	0.23	1.41	12.76	5.48	0.05 0.16
Syntholeiitic											
ANGOLA											
Tephrite (T. Bonga)	1	46.67	1.94	17.28	12.59	0.22	4.18	9.96	4.24	1.92	0.56 0.45
Phonolite (T. Bonga)	4	56.18	0.41	19.95	4.74	0.25	0.35	1.04	9.70	5.88	0.11 0.15
NAMIBIA											
Theralite (Messum)	1	43.54	1.52	15.40	10.81	0.18	8.22	12.43	4.10	2.00	0.47 0.65
Phonotephrite (Messum)	2	44.20	1.16	17.67	9.87	0.19	6.48	9.44	5.63	2.64	0.78 0.61
Ne-syenite (Messum)	4	57.03	0.47	20.46	4.68	0.14	0.78	2.21	7.57	5.80	0.20 0.29
Ne-syenite (Etaneno)	10	54.03	0.90	18.29	7.84	0.25	1.51	4.19	7.04	3.94	0.44 0.32
Basanite (Erongo)	4	42.40	1.56	12.98	10.75	0.18	12.13	12.73	2.98	2.41	0.69 0.73
Tephrite (Erongo)	5	43.98	1.64	15.86	9.70	0.18	6.77	10.78	4.79	3.06	0.96 0.63
Phonotephrite (Erongo)	2	47.35	1.10	18.75	7.09	0.16	3.72	6.70	6.08	4.68	0.70 0.56
Foidite (Erongo)	1	43.30	1.35	19.10	13.23	0.20	3.23	7.52	8.12	4.25	0.90 0.49
Nephelinite (Erongo)	1	43.50	1.71	17.00	9.78	0.18	5.59	10.20	5.38	3.30	1.18 0.58
Ankaratrite (Paresis)	1	39.60	2.14	13.50	10.70	0.21	7.67	14.10	4.21	1.03	1.33 0.63
Phonolite (Paresis)	1	54.30	0.32	21.60	3.92	0.18	0.66	1.52	9.49	6.38	0.12 0.29
Syenite (Paresis)	4	60.13	0.97	15.93	6.81	0.20	0.56	2.63	5.48	5.13	0.33 0.17
Qz-monzonite (Brandberg)	2	62.55	1.26	14.05	12.33	0.17	1.00	3.22	4.44	3.84	0.39 0.22
Trachydacite (Brandberg)	2	66.85	0.93	13.35	6.70	0.11	0.76	2.72	3.44	4.40	0.25 0.20

(Continued)

TABLE A1. REPRESENTATIVE AND AVERAGE ANALYSES (wt%) OF THE THOLEIITIC AND ALKALINE (POTASSIC AND SODIC) SUITES FROM ANGOLA AND NAMIBIA (*Continued*)

Rock type (Locality)	<i>N</i>	SiO ₂	TiO ₂	Al ₂ O ₃	Fe ₂ O ₃	MnO	MgO	CaO	Na ₂ O	K ₂ O P ₂ O ₅	Mg#	
EARLY CRETACEOUS: Alkaline suites (<i>Continued</i>)												
Post-Tholeiitic												
NAMIBIA												
Basalt (Ondurakorume)	1	38.83	1.41	11.93	11.54	2.51	10.67	10.73	0.81	1.49	0.34	0.69
Nephelinite (<i>Okurusu</i>)	1	42.90	1.12	13.53	9.77	0.19	10.95	11.20	5.34	2.39	0.47	0.73
Phonotephrite (<i>Camptonite-Okeny.</i>)	2	46.02	1.57	15.63	9.26	0.19	8.45	8.92	5.25	2.89	0.42	0.69
Nephelinite (<i>Damkjernite-Okeny.</i>)	7	35.66	2.39	11.72	9.88	0.19	8.63	14.91	3.91	3.24	0.79	0.68
Nephelinite (<i>Alnöite-Okeny.</i>)	2	35.66	2.67	11.98	13.15	0.23	9.30	14.68	5.31	2.23	1.30	0.63
Phonolite (<i>Tinguaite</i>)	1	51.24	0.65	20.21	4.23	0.12	1.16	2.91	9.18	5.80	0.17	0.40
Phonotephrite (Spitzkoppe)	1	44.70	1.56	16.60	10.11	0.20	4.45	7.67	3.55	3.58	1.43	0.52
LATE CRETACEOUS–EOCENE: Alkaline suites												
ANGOLA												
Basalte (Kwanza)	1	45.11	2.85	13.03	13.30	0.19	8.28	12.67	3.08	1.01	0.49	0.61
NAMIBIA												
Picrite (Blue Hills)	1	30.91	3.69	5.78	16.50	0.28	18.92	17.76	1.69	1.48	0.27	0.73
Trachyte (Dicker Willem)	1	56.15	0.24	15.62	5.27	0.23	0.08	3.99	0.08	14.07	0.09	0.04
Foidolite	2	39.70	0.96	16.07	9.18	0.28	2.57	15.52	7.58	3.36	1.87	0.41
EARLY CRETACEOUS: Namibia, granitoids and rhyolites												
Syntholeiitic												
S-granite (Brandberg)	5	69.38	0.50	13.64	4.56	0.12	0.35	1.70	3.91	5.02	0.11	–
S-leucogranite (Brandberg)	1	76.80	0.14	12.30	1.48	0.03	0.15	0.52	3.62	5.17	0.01	–
A-granite (Brandberg)	1	73.19	0.22	10.23	5.57	0.08	0.03	0.09	5.06	4.36	0.02	–
Rhyolite (Paresis)	3	69.37	0.63	13.87	3.33	0.08	0.41	1.36	3.92	5.39	0.15	–
Comenditic rhyolite (Paresis)	2	74.50	0.26	11.15	4.76	0.08	0.08	0.38	3.75	4.73	0.03	–
Post-Tholeiitic												
S-Granite (Spitzkoppe)	1	76.90	0.04	12.60	1.24	0.01	0.05	0.36	3.71	4.93	0.02	–

Notes: *N*—number of samples; italicized numbers for sodic suites. Data sources as in Table 1.

Notes: *N*—number of samples; italicized numbers for sodic suites. Data sources as in Table 1.

TABLE A2. REPRESENTATIVE AND AVERAGE ANALYSES OF TRACE ELEMENTS (ppm, STANDARD DEVIATION IN PARENTHESES)

Rock type	SiO ₂	Cr	Ni	Rb	Ba	Th	U	Pb	Nb	Ta	Sr	Hf	Zr	Y	La	Ce	Nd	Sm	Eu	Gd	Yb	Eu/Eu*
EARLY CRETACEOUS: Tholeiitic suites (L-Ti and H-Ti, Low- and High Titanium suite, respectively)																						
L-Ti																						
ANGOLA Picrite	42.79	2250	926	10	183	-	-	-	30	0.4	269	0.9	132	15	24	46	23	6.4	1.02	3.98	2.04	0.58
		(75)	(51)	(2)	(13)	-	-	-	(7)	(0.1)	(19)	(0.2)	(10)	(1)	(1)	(3)	(1)	(0.2)	(0.04)	(0.24)	(0.13)	
Gabbro	45.77	407	236	43	864	-	-	-	27	0.10	616	2.1	291	22	54	102	52	12.7	2.0	5.8	3.0	0.62
		(98)	(60)	(2)	(190)	-	-	-	(1)	(0.04)	(91)	(0.2)	(12)	(2)	(2)	(8)	(5)	(1.8)	(0.6)	(0.5)	(0.3)	
Basalt	48.72	180	75	15	304	2.4	0.5	3.4	6.2	0.5	300	2.9	112	24	14	31	18	4.1	1.3	3.7	2.1	1.00
Basalt	50.78	32	34	23	231	2.1	0.5	2.2	4.4	0.6	327	2.4	99	25	12	28	16	3.3	1.11	2.6	1.77	1.12
		(8)	(12)	(6)	(6)	(0.8)	(0.3)	(1.9)	(2.8)	(0.2)	(70)	(0.2)	(6)	(3)	(2)	(6)	(1)	(0.5)	(0.05)	(0.3)	(0.22)	
NAMIBIA																						
Basaltic picrite	46.62	1472	744	12	67	1.0	0.34	1.84	3.6	0.24	142	1.5	54	15	4.9	11.7	8.1	2.2	0.69	2.45	1.29	0.90
Basalt	47.41	894	460	20	64	0.7	0.19	1.10	4.4	0.25	168	1.51	60	18	4.5	10.7	8.0	2.32	0.84	2.96	1.50	0.98
		(140)	(26)	(12)	(5)	(0.1)	(0.06)	(0.28)	(0.4)	(0.02)	(13)	(0.11)	(5)	(0.0)	(0.3)	(0.2)	(0.1)	(0.10)	(0.04)	(0.18)	(0.08)	
Basalt	47.73	586	316	7	70	0.9	0.19	1.35	6.2	0.34	183	1.79	73	22	6.0	14.0	8.1	2.7	0.93	3.23	1.83	0.96
		(21)	(38)	(2)	(11)	(0.8)	(0.08)	(0.94)	(0.8)	(0.03)	(28)	(0.22)	(9)	(2)	(1.9)	(3.7)	(1.9)	(0.3)	(0.09)	(0.20)	(0.20)	
Basalt	48.62	169	83	18	330	2.2	0.33	4.60	5.3	0.28	288	3.1	115	24	15	33	18	4.2	1.29	4.2	2.38	0.93
		(11)	(15)	(3)	(196)	(0.8)	(0.15)	(0.13)	(0.09)	(0.03)	(53)	(0.3)	(17)	(2)	(5)	(9)	(3)	(0.4)	(0.04)	(0.3)	(0.25)	
Basalt	51.18	171	82	35	313	3.4	0.63	5.6	8.0	0.42	286	3.0	111	22	16	33	17	3.8	1.11	3.4	2.24	0.93
Basaltic andesite	52.17	134	75	4.1	351	2.8	0.84	3.5	8.8	0.59	286	3.3	121	28	15	33	19.8	4.8	1.52	4.5	2.67	0.99
		(50)	(11)	(0.8)	(150)	(2.0)	(0.77)	(1.4)	(0.7)	(0.01)	(121)	(0.5)	(16)	(1)	(2)	(3)	(0.9)	(0.23)	(0.4)	(0.13)		
Rhyolite	70.55	<10	<10	197	727	14.3	4.2	20.8	31	1.8	135	8.3	361	51	51	111	51	10.5	2.1	5.0	4.48	0.78
				(29)	(92)	(1.5)	(0.9)	(4.1)	(7)	(0.2)	(40)	(1.8)	(84)	(7)	(7)	(17)	(10)	(1.9)	(0.6)	(0.5)	(0.67)	
H-Ti																						
ANGOLA Basalt	46.42	215	101	32	425	4.5	-	-	42	0.6	585	1.2	170	25	31	70	31	6.9	1.9	4.9	1.3	0.95
		(52)	(22)	(16)	(112)	(0.5)	-	-	(12)	(0.2)	(157)	(0.1)	(43)	(4)	(4)	(8)	(5)	(0.4)	(0.1)	(0.3)	(0.1)	
Basalt	47.99	152	80	29	653	3.6	1.1	5.8	35	1.7	435	5.0	229	38	39	76	44	9.4	3.2	8.9	2.88	1.05
		(110)	(18)	(4)	(135)	(0.1)	(0.2)	(0.9)	(11)	(0.2)	(54)	(0.1)	(13)	(12)	(6)	(8)	(4)	(0.8)	(0.3)	(1.1)	(0.51)	
Basalt	48.33	126	60	31	705	34	0.9	6.0	30	(1.3)	641	5.6	274	40	41	86	48	10.4	3.3	9.9	2.24	0.98
		(25)	(13)	(1)	(62)	(0.2)	(0.1)	(0.8)	(5)	(0.1)	(98)	(1.0)	(51)	(8)	(3)	(5)	(1)	(0.1)	(0.1)	(1.0)	(0.02)	
Trachydacites	65.04	<10	<10	113	1090	9.9	2.8	14.8	48	2.5	337	8.6	530	65	85	155	81	16.0	3.9	12.1	3.00	0.82
				(4)	(191)	(0.9)	(0.5)	(4.7)	(1)	(0.1)	(55)	(0.6)	(20)	(4)	(6)	(2)	(5)	(1.2)	(0.6)	(1.3)	(0.49)	
NAMIBIA																						
Basalt	45.66	412	681	18	412	2.1	0.45	3.3	13.7	0.73	419	3.1	133	18	21	46	27.7	4.94	1.49	4.58	1.17	0.94
Basalt	51.31	171	111	29	632	3.8	0.94	5.5	31.6	1.53	665	6.4	293	33	39	90	48	10.1	3.19	8.1	2.34	1.04
		(93)	(44)	(5)	(42)	(0.6)	(0.17)	(0.6)	(3.5)	(0.10)	(30)	(0.1)	(7)	(2)	(1)	(2)	(1)	(0.7)	(0.26)	(1.0)	(0.08)	
Trachydacites	64.94	19	6	141	1161	12.2	2.9	14.1	57	2.6	441	12.8	590	50	81	174	83	15.3	3.9	13.51	4.23	0.81
		(4)	(1)	(20)	(119)	(1.9)	(0.6)	(2.0)	(8)	(0.2)	(159)	(1.3)	(47)	(9)	(10)	(20)	(8)	(1.5)	(0.4)	(1.58)	(0.83)	

(Continued)

TABLE A2. REPRESENTATIVE AND AVERAGE ANALYSES OF TRACE ELEMENTS (ppm, STANDARD DEVIATION IN PARENTHESES) (Continued)

Rock type	SiO ₂	Cr	Ni	Rb	Ba	Th	U	Pb	Nb	Ta	Sr	Hf	Zr	Y	La	Ce	Nd	Sm	Eu	Gd	Yb	Eu/Eu*
EARLY CRETACEOUS: Pre-tholeiitic alkaline suites																						
ANGOLA																						
Ilolite	46.16	101	20	561	201				46	0.7	1520	0.34	48	21	108	204	90	23	6	—	5.9	—
Ne-syenite	54.93	<10	<10	150	1048	—	—	—	127	1.8	616	3.5	486	22	102	130	48	11.8	5.3	11.4	2.2	—
				(8)	(187)				(30)	(0.2)	(91)	(0.4)	(59)	(1)	(16)	(31)	(12)	(1.3)	(0.7)	(1.9)	(0.3)	
Syenite	59.14	8	22	115	1647	—	—	—	79	1.1	801	1.6	223	52	241	307	113	280	—	—	5.2	—
		(3)	(10)	(22)	(393)				(7)	(0.1)	(126)	(0.4)	(50)	(16)	(14)	(72)	(28)	(3.0)			(1.6)	
NAMIBIA																						
Ne-syenite	53.80	13	2	195	699	30	11	11	377	—	2267	19	1327	24	92	130	33	4.7	1.5	4.00	0.63	1.03
		(4)	(1)	(27)	(304)	(22)	(5)	(10)	(100)		(1513)	(15)		(23)	(92)	(127)	(24)	(3.6)	(1.1)	(3.21)	(0.51)	
Foidite	44.17	10	1	120	449	14	12	4.5	145	—	1134	1.1	65	3.5	37	53	14.6	1.81	0.49	1.25	0.16	0.95
EARLY CRETACEOUS: Syntholeiitic alkaline suites																						
ANGOLA																						
Tephrite	46.67	47	27	43	1040	7	—	—	56	—	1280	—	165	30	74	147	65	11.6	3.53	8.94	1.87	1.02
Phonolite	56.18	9	9	168	509	34	—	—	478	6.8	559	—	699	54	186	298	69	16.3	2.80	5.65	3.10	0.72
		(1)	(2)	(5)	(24)				(127)	(3.0)	(296)		(150)	(29)	(16)	(33)	(6)	(0.8)	(0.10)	(2.54)	(0.40)	
NAMIBIA																						
Theralite	43.54	265	155	52	941	4	—	3	81	—	889	—	133	24	38.7	73.4	31.2	5.75	1.87	5.20	1.84	1.03
Phonotephrite	44.20	299	148	65	1088	8.5	—	7	115	—	1386	—	133	21	60.9	109	40.4	6.62	2.17	5.34	1.30	1.08
		(55)	(16)	(5)	(133)	(0.5)		(1)	(20)		(252)		(22)	—	—	—	—	—	—	—	—	
Ne-syenite	57.03	12	4	190	740	12	—	13	96	—	286	—	308	27	44	77	25	4.43	1.16	3.91	2.84	0.83
		(8)	(2)	(24)	(368)	(8)		(4)	(48)		(223)		(194)	(19)	(19)	(34)	(12)	(2.23)	(0.25)	(2.19)	(2.03)	
Ne-syenite	54.03	14	12	157	1415	45	13	22	255	—	605	22.5	1075	87	199	358	117	18.5	3.9	15.3	10.7	0.69
		(5)	(8)	(69)	(208)	(23)	(7)	(9)	(121)		(220)	(14.2)	(675)	(43)	(73)	(137)	(46)	(7.7)	(1.1)	(6.6)	(6.0)	
Basanite	42.40	564	272	46	1102	9.9	2.4	6.2	104	5.4	920	3.3	154	22	77	137	48	8.3	2.38	5.57	1.67	1.01
		(100)	(41)	(3)	(252)	(3.6)	(0.9)	(1.7)	(29)	(1.3)	(173)	(0.2)	(5)	(1)	(23)	(41)	(8)	(1.2)	(0.37)	(0.81)	(0.09)	
Tephrite	43.98	182	90	83	1728	15	3.8	9.1	169	7.8	1344	3.9	201	25	106	187	53	9.4	2.77	6.32	1.84	1.05
		(129)	(61)	(15)	(229)	(2)	(0.5)	(2.9)	(38)	(1.5)	(159)	(0.4)	(25)	(3)	(17)	(21)	(5)	(0.8)	(0.21)	(0.41)	(0.31)	
Phonotephrite	47.35	68	33	124	1795	23	5.8	15	182	9.1	1285	3.9	245	20	122	202	47	8.1	2.36	5.5	1.61	1.02
		(37)	(18)	(31)	(290)				(21)		(389)		(20)	(2)								
Foidite	43.30	19	8	110	2060	21	5.2	12	212	10	1770	3.0	194	22	130	206	54	7.7	2.38	5.4	1.78	1.07
Nephelinite	43.50	89	57	80	1670	18	4.3	8.3	171	7.9	1430	3.8	202	26	113	202	55	9.3	2.82	7.5	1.92	1.00
Ankaratrite	39.60	675	214	49	1914	17	3.4	—	170	8.7	1517	—	299	31	162	297	107	17	4.4	6.7	2.6	1.06
Phonolite	54.30	20	8	179	635	25	5.9	—	188	1.0	265	—	345	24	84	136	35	5.6	1.1	4.3	3.3	0.66
Syenite	60.13	11	6	112	925	20	3.7	—	78	5.1	149	—	452	50	115	209	85	15	2.9	11.8	5.6	0.64
		(3)	(1)	(43)	(421)	(16)	(2.7)		(79)	(4.5)	(107)		(354)	(24)	(43)	(70)	(22)	(4)	(1.1)	(3.5)	(3.1)	
Qz-monzonite	62.55	—	—	142	808	15	4.9	13	47	3.1	233	—	382	64	62	125	57	11.5	2.9	11.5	5.8	0.76
				(2)	(86)	(1)	(0.4)	(1)	(6)	(0.1)	(11)		(13)	(4)	(8)	(13)	(6)	(0.5)	(0.8)	(0.5)	(0.4)	
Trachydacite	66.85	—	—	146	908	22	5.1	22	42	2.5	201	—	362	61	70	140	63	12.5	2.4	11.5	5.8	0.64
				(0)	(8)	(1)	(0.1)	(0)	(1)	(0.1)	(0)		(6)	(3)	(2)	(8)	(2)	(0.5)	(0.1)	(0.5)	(0.3)	

(Continued)

TABLE A2. REPRESENTATIVE AND AVERAGE ANALYSES OF TRACE ELEMENTS (ppm, STANDARD DEVIATION IN PARENTHESES) (Continued)

Rock type	SiO ₂	Cr	Ni	Rb	Ba	Th	U	Pb	Nb	Ta	Sr	Hf	Zr	Y	La	Ce	Nd	Sm	Eu	Gd	Yb	Eu/Eu*
EARLY CRETACEOUS: Post-tholeiitic alkaline suites																						
NAMIBIA																						
Basalt	38.83	784	257	46	14,222	6.5	2.9	4.1	140	—	133	—	130	25	91	133	44.6	8.24	2.44	6.27	1.42	1.00
Nephelinite	42.90	515	296	67	1034	16.3	3.2	7.1	115	—	965	—	156	24	75	131	44.4	7.51	2.14	5.38	1.89	0.98
Phonotephrite	46.02	23	9	97	932	9.5	2.5	6.4	113	—	798	—	190	21	47	84	28.5	5.6	1.70	5.61	1.60	0.92
(Camptonite)	(12)	(12)	(4)	(4)	(22)	(4)	(22)	(1)	(1)	—	(29)	—	(1)	(1)	(3)	(2)	(1.8)	(0.1)	(0.16)	(1)	(0.21)	
Nephelinite	35.66	148	111	41	1584	10.8	2.8	5.7	136	—	1280	—	181	25	88	155	64.2	11.5	2.95	7.67	1.47	0.91
(Damkjerite)	(30)	(30)	(26)	(4)	(187)	(1.5)	(0.3)	(1.7)	(16)	—	(301)	—	(61)	(3)	(21)	(31)	(10.8)	(1.7)	(0.44)	(0.84)	(0.29)	
Nephelinite	35.66	135	142	41	915	15.5	2.7	26	92	—	2241	—	145	30	112	175	59.6	10.9	4.06	8.41	1.71	1.25
(Alnöite)	(12)	(37)	(37)	(4)	(162)	(0.7)	(0.4)	(20)	(4)	—	(163)	—	(1)	(1)	(9)	(7)	(6.2)	(0.6)	(0.71)	(0.03)	(0.26)	
Phonolite	51.24	47	11	206	1176	—	—	—	152	—	704	—	189	16	56	80	20.5	3.56	1.59	2.58	1.88	1.53
(Tinguaite)										—		—										
Phonotephrite	44.70	—	—	240	1930	3	—	—	160	—	1230	—	217	22	141	234	77	11	3.5	9.2	1.6	1.04
ALKALINE SUITES: Late Cretaceous–Eocene																						
ANGOLA																						
Basalt	45.11	356	202	20	316	—	—	—	49	0.7	531	1.5	209	27	34	76	36	10.0	2.8	9.1	3.8	0.88
NAMIBIA																						
Picrite	30.91	644	313	56	267	20	4.7	—	179	12.7	646	11.9	326	41	190	372	145	23.6	6.32	—	—	2.19 0.91
Trachyte	56.15	8	3	164	2142	15	13	20	461	—	579	—	90	25	50	106	62	13.8	3.86	10.0	3.02 0.96	
Foidolite	39.70	4	<2	60	111	29	5	—	150	—	848	—	913	141	91	252	180	46	14.6	38	8 1.04	
				(15)	(33)	(3)	(1)	(49)			(261)		(465)	(66)	(9)	(6)	(49)	(6)	(2.5)	(22)	(7)	
NAMIBIA: Granitoids and rhyolites																						
Syntholeiitic																						
S-granite	69.38	—	—	197	958	21	5.9	24	48	3.3	152	—	440	63	68	142	63	13	2.72	12	6.4	0.65
				(12)	(219)	(4)	(2.4)	(3)	(4)	(0.3)	(69)	—	(56)	(5)	(5)	(16)	(5)	(1)	(0.38)	(1)	(0.5)	
S-leucogranite	76.80	—	—	408	129	45	13	29	50	5.8	19	—	212	66	67	132	47	9	0.60	9.3	8.3	0.20
A-granite	73.19	—	—	4	40	680	187	303	2270	93	11	—	16,800	1990	309	769	423	95	4.5	189	176	0.10
Rhyolite	69.37	—	—	174	1515	23	2.9	—	25	1.6	147	—	502	49	98	182	83	15	2.33	11	5.2	0.53
				(30)	(620)	(6)	(0.3)	(5)	(5)	(0.3)	(46)	—	(44)	(1)	(9)	(34)	(9)	(2)	(0.47)	(1)	(0.5)	
Comenditic rhyolite	74.50	—	—	434	81	42	16	—	163	10	14	—	1967	138	157	274	132	27	0.80	24	12	0.09
				(74)	(1)	(25)	(9)	(23)	(23)	(4)	(8)	—	(721)	(17)	(73)	(121)	(48)	(8)	(0.28)	(8)	(2)	
Post-Tholeiitic																						
S-granite	76.90	—	—	831	30	61	7	26	82	—	15	—	179	199	39	105	53	19	0.1	17	4.6	0.02

Note: Order and localities as in Table A1; SiO₂ wt%, as reference. Italicized numbers: sodic alkaline suites.

REFERENCES CITED

- Alberti, A., Piccirillo, E.M., Bellieni, G., Civetta, L., Comin-Chiaromonti, P., and Morais, E.A.A., 1992, Mesozoic acid volcanics from southern Angola: Petrology, Sr-Nd isotope characteristics and correlation with the acid stratoid volcanics suites of the Paraná basin (south-eastern Brazil): *European Journal of Mineralogy*, v. 4, p. 597–604.
- Alberti, A., Castorina, F., Censi, P., Comin-Chiaromonti, P., and Gomes, C.B., 1999, Geochemical characteristics of Cretaceous carbonatites from Angola: *Journal of African Earth Sciences*, v. 29, p. 735–759, doi:10.1016/S0899-5362(99)00127-X.
- Anderson, D.L., Tanimoto, T., and Zhang, Y.S., 1992, Plate tectonics and hotspots—The 3rd dimension: *Science*, v. 256, p. 1645–1651, doi:10.1126/science.256.5064.1645.
- Arndt, N.T., and Goldstein, S.L., 1987, Use and abuse of crust formation age: *Geology*, v. 15, p. 893–895, doi:10.1130/0091-7613(1987)15<893:UAAOCA>2.0.CO;2.
- Bellieni, G., Comin-Chiaromonti, P., Marques, L.S., Melfi, A.J., Nardy, A.J.R., Papatrechas, C., Piccirillo, E.M., Roisemberg, A., and Stofa, D., 1986, Petrogenetic aspects of acid and basaltic lavas from the Paraná Plateau (Brazil): Geological, mineralogical and petrochemical relationships: *Journal of Petrology*, v. 27, p. 915–944.
- Bott, M.H.P., 1992, The stress regime associated with continental break-up, in Storey, B.C., Alabaster, T., and Pankhurst, R.J., eds., *Magmatism and the Causes of Continental Break-Up*: Geological Society of London Special Publication 68, p. 125–136.
- Boyd, F.R., Pearson, D.G., Hoal, K.O., Nixon, P.H., Kingston, M.J., and Mertzman, S.A., 2004, Garnet lherzolites from Lowrensia, Namibia: Bulk composition and *P/T* relations: *Lithos*, v. 77, p. 573–592, doi:10.1016/j.lithos.2004.03.010.
- Boynton, W.V., 1984, Cosmochemistry of the rare earth elements: Meteorite studies, in Henderson, P., ed., *Rare Earth Element Geochemistry*: Amsterdam, Elsevier, p. 63–114.
- Bühn, B., and Rankin, A.H., 1999, Composition of natural, volatile-rich Na-Ca-REE-Sr carbonatitic fluids trapped in fluid inclusions: *Geochimica et Cosmochimica Acta*, v. 63, p. 3781–3797.
- Bühn, B., and Trumbull, R.B., 2003, Comparison of petrogenetic signatures between mantle-derived alkali silicate intrusives with and without associated carbonatite, Namibia: *Lithos*, v. 66, p. 201–221, doi:10.1016/S0024-4937(02)00220-7.
- Castorina, F., Censi, P., Comin-Chiaromonti, P.A., Gomes, C.B., Piccirillo, E.M., Alcover Neto, A., Almeida, R.T., Speziale, S., and Toledo, M.C., 1997, Geochemistry of carbonatites from eastern Paraguay and genetic relationships with potassic magmatism: C, O, Sr and Nd isotopes: *Mineralogy and Petrology*, v. 61, p. 237–260, doi:10.1007/BF01172487.
- Chang, H.K., Kowsmann, R.O., and Figueiredo, A.M.F., 1988, New concept on the development of east Brazilian margin basins: *Episodes*, v. 11, p. 194–202.
- Coltorti, M., Alberti, A., Beccaluva, L., Dos Santos, A.B., Mazzucchelli, M., Morais, E., Rivalenti, G., and Siena, F., 1993, The Tchivira Bonga alkaline-carbonatite complex (Angola): Petrological study and comparison with some Brazilian analogues: *European Journal of Mineralogy*, v. 5, p. 1001–1024.
- Comin-Chiaromonti, P., and Gomes, C.B., eds., 1996, *Alkaline Magmatism in Central-Eastern Paraguay: Relationships with Coeval Magmatism in Brazil*: São Paulo, Brazil, EDUSP (Editora da Universidade de São Paulo)/FAPESP (Fundação de Amparo à Pesquisa do Estado de São Paulo), 464 p.
- Comin-Chiaromonti, P., and Gomes, C.B., eds., 2005, *Mesozoic to Cenozoic Alkaline Magmatism in the Brazilian Platform*: São Paulo, Brazil, EDUSP (Editora da Universidade de São Paulo)/FAPESP (Fundação de Amparo à Pesquisa do Estado de São Paulo), 752 p.
- Comin-Chiaromonti, P., Marzoli, A., Gomes, C.B., Milan, A., Riccomini, C., Velázquez, V.F., Mantovani, M.M.S., Renne, P., Tassinari, C.C.G., and Vasconcelos, P.M., 2007a, Origin of Post-Paleozoic magmatism in eastern Paraguay, in Foulger, R.G., and Jurdy, D.M., eds., *Plates, Plumes, and Planetary Processes*: Geological Society of America Special Paper 430, p. 603–633.
- Comin-Chiaromonti, P., Gomes, C.B., De Min, A., Ernesto, M., Marzoli, A., and Riccomini, C., 2007b, Eastern Paraguay: An overview of the post-Paleozoic magmatism and geodynamic implications: *Rendiconti Accademia Lincei*, s. 9, v. 18, p. 139–192.
- Comin-Chiaromonti, P., Gomes, C.B., Cundari, A., Castorina, F., and Censi, P., 2007c, A review of carbonatitic magmatism in the Paraná-Angola-Namibia (PAN) system: *Periodico di Mineralogia*, v. 76, p. 25–78.
- Comin-Chiaromonti, P., Riccomini, C., Slejko, F., DeMin, A., Ruberti, E., and Gomes, C.B., 2010, Cordierite bearing lavas from Jaguarão, southern Brazil: Petrological evidence for crustal melts during early rifting of Gondwana: *Gondwana Research*, v. 18, p. 514–527.
- Cooper, A.F., and Reid, D.L., 2000, The association of potassic trachytes and carbonatites at the Dicker Willem complex, southwest Namibia: Coexisting, immiscible, but not cogenetic magmas: *Contributions to Mineralogy and Petrology*, v. 139, p. 570–583, doi:10.1007/s004100000157.
- Davies, G.R., Spriggs, A.J., and Nixon, P.H., 2001, A non-cognate origin for the Gibeon kimberlite megacryst suite, Namibia: Implications for the origin of the Namibian kimberlites: *Journal of Petrology*, v. 42, p. 159–172, doi:10.1093/petrology/42.1.159.
- Ernesto, M., 2005, Paleomagnetism of the Post-Paleozoic alkaline magmatism in the Brazilian platform: Questioning the mantle plume model, in Comin-Chiaromonti, P., and Gomes, C.B., eds., *Mesozoic to Cenozoic Alkaline Magmatism in the Brazilian Platform*: São Paulo, EDUSP (Editora da Universidade de São Paulo)/FAPESP (Fundação de Amparo à Pesquisa do Estado de São Paulo), p. 489–705.
- Ernesto, M., Marques, L.M., Piccirillo, E.M., Molina, E., Ussami, N., Comin-Chiaromonti, P., and Bellieni, G., 2002, Paraná magmatic province—Tristan da Cunha plume system: Fixed versus mobile plume, petrogenetic considerations and alternative heat sources: *Journal of Volcanology and Geothermal Research*, v. 130, p. 527–553.
- Ewart, A., Milner, S.C., Armstrong, R.A., Duncan, A.R., and Bailey, M., 2002, The Cretaceous Messum igneous complex, S.W. Etendeka, Namibia: Reinterpretation in terms of a down-sag-cauldron subsidence model: *Journal of Volcanology and Geothermal Research*, v. 114, p. 251–273, doi:10.1016/S0377-0273(01)00266-9.
- Ewart, A., Marsh, J.S., Milner, S.C., Duncan, A.R., Kamber, B.S., and Armstrong, R.A., 2004a, Petrology and geochemistry of Early Cretaceous bimodal continental flood volcanism of the NW Etendeka, Namibia. Part 1: Introduction, mafic lavas and re-evaluation of mantle source components: *Journal of Petrology*, v. 45, p. 59–105, doi:10.1093/petrology/egg083.
- Ewart, A., Marsh, J.S., Milner, S.C., Duncan, A.R., Kamber, B.S., and Armstrong, R.A., 2004b, Petrology and geochemistry of Early Cretaceous bimodal continental flood volcanism of the NW Etendeka, Namibia. Part 2: Characteristics and petrogenesis of the high-Ti latite and high-Ti and low-Ti voluminous quartz latite eruptions: *Journal of Petrology*, v. 45, p. 107–138, doi:10.1093/petrology/egg082.
- Fairhead, J.D., and Wilson, M., 2005, Plate tectonic processes in the South Atlantic Ocean: Do we need deep mantle plumes?, in Foulger, G.R., Natland, J.H., Presnall, D.C., and Anderson, D.L., eds., *Plates, Plumes, and Paradigms*: Geological Society of America Special Paper 388, p. 537–553.
- Faure, G., 2001, *Origin of Igneous Rocks: The Isotopic Evidence*: Berlin, Springer, 496 p.
- Ferrari, A.L., and Riccomini, C., 1999, Campo de esforços plio-pleistocênicos na Ilha de Trindade (Oceano Atlântico Sul, Brasil) e sua relação com a tectônica regional: *Revista Brasileira de Geociências*, v. 29, p. 195–202.
- Fodor, R.V., Mukasa, S.B., and Sial, A.N., 1998, Isotopic and trace-element indications of lithospheric and asthenospheric components in Tertiary alkalic basalts, northeastern Brazil: *Lithos*, v. 43, p. 197–217, doi:10.1016/S0024-4937(98)00012-7.
- Fontignie, D., and Schilling, J.G., 1997, Mantle heterogeneities beneath the South Atlantic: A Nd-Sr-Pb isotope study along the Mid-Atlantic Ridge (3°S–46°S): *Earth and Planetary Science Letters*, v. 146, p. 259–272.
- Forsyth, D., and Uyedaf, S., 1975, On the relative importance of the driving forces of plate motion: *Geophysical Journal of the Royal Astronomical Society*, v. 43, p. 163–200.
- Frindt, S., Trumbull, R.B., and Romer, R.L., 2004, Petrogenesis of the Gross Spitzkoppe topaz granite, central western Namibia: A geochemical and Nd-Sr-Pb isotope study: *Chemical Geology*, v. 206, p. 43–71, doi:10.1016/j.chemgeo.2004.01.015.
- Gamboa, L.A.P., and Rabinowitz, P.D., 1984, The evolution of the Rio Grande Rise in Southwest Atlantic: *Marine Geology*, v. 58, p. 35–58, doi:10.1016/0025-3227(84)90115-4.
- Hamelin, B., Dupré, B., and Allègre, C.J., 1984, Lead-strontium isotopic variations along the East Pacific Rise and Mid-Atlantic Ridge: A comparative study: *Earth and Planetary Science Letters*, v. 67, p. 340–350, doi:10.1016/0012-821X(84)90173-0.

- Harris, C., Marsh, J.S., and Milner, S.C., 1999, Petrology of the alkaline core of the Messum igneous complex, Namibia: Evidence for the progressively decreasing effect of crustal contamination: *Journal of Petrology*, v. 40, p. 1377–1397, doi:10.1093/petrology/40.9.1377.
- Hart, S.R., Hauri, E.H., Oschmann, L.A., and Whithead, J.A., 1992, Mantle plumes and entrainment: Isotopic evidence: *Science*, v. 256, p. 517–520, doi:10.1126/science.256.5056.517.
- Hartnady, C., Joubert, P., and Stowe, C., 1985, Proterozoic crustal evolution in southwestern Africa: Episodes, v. 8, p. 236–244.
- Hawkesworth, C.J., Mantovani, M.S.M., Taylor, P.N., and Palacz, Z., 1986, Evidence from the Paraná of south Brazil for a continental contribution to Dupal basalts: *Nature*, v. 322, p. 356–359, doi:10.1038/322356a0.
- Heflin, M., Argus, D., Jefferson, D., Webb, F., and Zumberge, J., 2002, Comparison of a GPS defined global reference frame with ITRF 2000: Heidelberg, Springer, GPS Solutions, v. 6, p. 72–75.
- Irvine, T.N., and Baragar, W.R.A., 1971, A guide to chemical classification of the common rocks: *Canadian Journal of Earth Sciences*, v. 8, p. 523–548.
- Issa Filho, A., Santos, A.B.R.M.D., Riffel, B.F., Lapido Loureiro, F.E.V., and McReath, I., 1991, Aspects of the geology, petrology and chemistry of some Angolan carbonatites: *Journal of Geochemical Exploration*, v. 40, p. 205–226, doi:10.1016/0375-6742(91)90039-W.
- Ito, E., White, W.M., and Göpel, C., 1987, The O, Sr, Nd and Pb isotope geochemistry of MORB: *Chemical Geology*, v. 62, p. 157–176, doi:10.1016/0009-2541(87)90083-0.
- Jung, S., Hoernes, S., and Mezger, K., 2003, Petrology of basement-dominated terranes: II. Contrasting isotopic (Sr, Nd, Pb and O) signatures of basement-derived granites and constraints on the source region of granite (Damara orogens, Namibia): *Chemical Geology*, v. 199, p. 1–28.
- Kurszlaukis, S., and Lorenz, V., 1997, Volcanological features of a low viscosity melt: The carbonatitic Gross Brückkaros volcanic field, Namibia: *Bulletin of Volcanology*, v. 58, p. 421–431, doi:10.1007/s004450050150.
- Kurszlaukis, S., Franz, L., and Lorenz, V., 1998, On the volcanology of the Gibeon kimberlite field, Namibia: *Journal of Volcanology and Geothermal Research*, v. 84, p. 257–272, doi:10.1016/S0377-0273(98)00044-4.
- Kurszlaukis, S., Franz, L., and Brey, G.P., 1999, The Blue Hill intrusive complex in southern Namibia: Relationships between carbonatites and moniticellite picrites: *Chemical Geology*, v. 160, p. 1–18, doi:10.1016/S0009-2541(99)00027-3.
- Lapido-Loureiro, F.E.V., 1973, Carbonatitos de Angola: Luanda, Instituto de Investigação Científica de Angola, 242 p.
- Le Maitre, R.W., 1989, A Classification of Igneous Rocks and Glossary of Terms: Oxford, Blackwell Scientific Publications, 193 p.
- Le Roex, A.P., 1985, Geochemistry, mineralogy and magmatic evolution of the basaltic and trachytic lavas from Gough Island, South Atlantic: *Journal of Petrology*, v. 26, p. 149–186.
- Le Roex, A.P., and Lanyon, R., 1998, Isotope and trace element geochemistry of Cretaceous Damaraland lamprophyres and carbonatites, northwestern Namibia: Evidence for plume-lithosphere interaction: *Journal of Petrology*, v. 39, p. 1117–1146, doi:10.1093/petrology/39.6.1117.
- Le Roex, A.P., Cliff, R.A., and Adair, B.J.I., 1990, Tristan da Cunha, South Atlantic: Geochemistry and petrogenesis of a basanite-phonolite lava series: *Journal of Petrology*, v. 31, p. 779–812.
- Liatí, A., Franz, L., Gebauer, D., and Fanning, C.M., 2004, The timing of mantle and crustal events in South Namibia, as defined by SHRIMP-dating of zircon domains from a garnet peridotite xenolith of the Gibeon kimberlite province: *Journal of African Earth Sciences*, v. 39, p. 147–157, doi:10.1016/j.jafrearsci.2004.07.054.
- Marques, L.S., Ulbrich, M.N.C., Ruberti, E., and Tassinari, C.G., 1999, Petrology, geochemistry and Sr-Nd isotopes of the Trindade and Martin Vaz volcanic rocks (southern Atlantic Ocean): *Journal of Volcanology and Geothermal Research*, v. 93, p. 191–216, doi:10.1016/S0377-0273(99)00111-0.
- Marzoli, A., Melluso, L., Morra, V., Renne, P.R., Sgroso, I., D'Antonio, M., Duarte Morais, L., Morais, E.A.A., and Ricci, G.M., 1999, Geochronology and petrology of Cretaceous basaltic magmatism in the Kwanza basin (western Angola), and relationships with the Paraná-Etendeka continental flood basaltic province: *Journal of Geodynamics*, v. 28, p. 341–356, doi:10.1016/S0264-3707(99)00014-9.
- Meen, J.K., Ayers, J.C., and Fregeau, E.J., 1989, A model of mantle metasomatism by carbonated alkaline melts: Trace element and isotopic compositions of mantle source regions of carbonatite and other continental igneous rocks, in Bell, K., ed., *Carbonatites, Genesis and Evolution*: London, Unwin Hyman, p. 464–499.
- Menzies, M.A., 1990, Archean, Proterozoic and Phanerozoic lithosphere, in Menzies, M.A., ed., *Continental Mantle*: Oxford, Clarendon Press, p. 67–86.
- Middlemost, E.A.K., 1994, Naming materials in the magma/igneous rock system: *Earth-Science Reviews*, v. 37, p. 215–224, doi:10.1016/0012-8252(94)90029-9.
- Milner, S.C., and Le Roex, A.P., 1996, Isotope characteristics of the Okenyanya igneous complex, northwestern Namibia: Constraints on the composition of the early Tristan plume and the origin of the EM 1 mantle component: *Earth and Planetary Science Letters*, v. 141, p. 277–291, doi:10.1016/0012-821X(96)00074-X.
- Milner, S.C., Le Roex, A.P., and O'Connor, G.M., 1995, Ages of Mesozoic igneous rocks in northwestern Namibia, and their relationship to continental breakup: *Journal of the Geological Society of London*, v. 152, p. 97–104, doi:10.1144/gsjgs.152.1.0097.
- Mingram, B., Trumbull, R.B., Littman, S., and Gerstenberger, H., 2000, A petrogenetic study of anorogenic felsic magmatism in the Cretaceous Paresis ring complex, Namibia: Evidence for mixing of crust- and mantle-derived components: *Lithos*, v. 54, p. 1–22, doi:10.1016/S0024-4937(00)00033-5.
- Molina, E.C., and Ussami, N., 1999, The geoid in southern Brazil and adjacent regions: New constraints on density distribution and thermal state on the lithosphere: *Journal of Geodynamics*, v. 28, p. 357–374, doi:10.1016/S0264-3707(99)00015-0.
- Nürnberg, D., and Müller, R.D., 1991, The tectonic evolution South Atlantic from Late Jurassic to present: *Tectonophysics*, v. 191, p. 27–53, doi:10.1016/0040-1951(91)90231-G.
- Peate, D.W., 1997, The Paraná-Etendeka Province, in Mahoney, J.J., and Coffin, M.F., eds., *Large Igneous Provinces: Continental, Oceanic and Planetary Flood Volcanism*: American Geophysical Union Geophysical Monograph 100, p. 217–245.
- Piccirillo, E.M., and Melfi, A.J., eds., 1988, *The Mesozoic Flood Volcanism from the Paraná Basin (Brazil): Petrogenetic and Geophysical Aspects*: São Paulo, Brazil, Instituto Astronômico e Geofísico, Universidade de São Paulo, 600 p.
- Prins, P., 1981, The geochemical evolution of the alkaline and carbonatite complexes of the Damaraland igneous province, south west Africa: *Annales van die Universiteit van Stellenbosch (South Africa)*, Series A1 (Geol.), v. 3, p. 145–278.
- Reid, D.L., Cooper, A.F., Rex, D.C., and Harmer, R.E., 1990, Timing of post-Karoo alkaline magmatism in southern Namibia: *Geological Magazine*, v. 127, p. 427–433, doi:10.1017/S001675680001517X.
- Renne, P.R., Ernesto, M., and Milner, S.C., 1997, Geochronology of the Paraná-Angola-Etendeka magmatic Province: *Eos (Transactions, American Geophysical Union)*, v. 78, no. 46, p. F742.
- Richardson, S.H., Erlank, A.J., Duncan, A.R., and Reid, D.L., 1982, Correlated Nd, Sr and Pb isotope variations in Walvis Ridge basalts and implications for the evolution of their mantle source: *Earth and Planetary Science Letters*, v. 59, p. 327–342, doi:10.1016/0012-821X(82)90135-2.
- Rosset, A., De Min, A., Marques, L.S., Macambira, M.J.B., Ernesto, M., Renne, P.R., and Piccirillo, E.M., 2007, Genesis and geodynamic significance of Mesoproterozoic and Early Cretaceous tholeiitic dyke swarms from the São Francisco craton (Brazil): *Journal of South American Earth Sciences*, v. 24, p. 69–92, doi:10.1016/j.jsames.2007.02.002.
- Ruberti, E., Enrich, G., Gomes, C.B., and Comin-Chiaramonti, P., 2008, Hydrothermal rare earth mineralization in the Barra do Itaipirapuã (Brazil), multiple stockwork carbonatite: *Canadian Mineralogist*, v. 46, p. 901–914, doi:10.3749/canmin.46.4.901.
- Schmitt, A.K., Emmermann, R., Trumbull, R.B., Bühn, B., and Henjes-Kunst, F., 2000, Petrogenesis and $^{40}\text{Ar}/^{39}\text{Ar}$ geochronology of the Brandberg complex, Namibia: Evidence for a major mantle contribution in metaluminous and peralkaline granites: *Journal of Petrology*, v. 41, p. 1207–1239, doi:10.1093/petrology/41.8.1207.
- Schmitt, A.K., Trumbull, R.B., Dulski, P., and Emmermann, R., 2002, Zr-Nb-REE mineralization in peralkaline granites from the Amis complex, Brandberg (Namibia): Evidence for magmatic pre-enrichment from melt inclusion: *Economic Geology and the Bulletin of the Society of Economic Geologists*, v. 97, p. 399–413.
- Seth, B., Kröner, A., Mezger, K., Nemkin, A.A., Pidgeon, R.T., and Okrush, M., 1998, Archean to Neoproterozoic magmatic events in the Kaoko belt of

- NW Namibia and their geodynamic significance: *Precambrian Research*, v. 92, p. 341–363, doi:10.1016/S0301-9268(98)00086-2.
- Siebel, W., Becchio, R., Volker, F., Hansen, M.A.F., Viramonte, J., Trumbull, R.B., Haase, G., and Zimmer, M., 2000, Trindade and Martin Vaz islands, South Atlantic: Isotopic (Sr, Nd, Pb) and trace element constraints on plume-related magmatism: *Journal of South American Earth Sciences*, v. 13, p. 79–103, doi:10.1016/S0895-9811(00)00015-8.
- Smith, A.D., and Lewis, C., 1999, The planet beyond the plume hypothesis: *Earth-Science Reviews*, v. 48, p. 135–182, doi:10.1016/S0012-8252(99)00049-5.
- Sun, S.S., and McDonough, W.F., 1989, Chemical and isotopic systematics of oceanic basalts, in Saunders, D., and Norry, M.J., eds., *Magmatism in the Ocean Basins: Geological Society of London Special Publication* 42, p. 313–345.
- Tanimoto, T., and Zhang, Y.S., 1992, Cause of low velocity anomaly along the South Atlantic hotspots: *Geophysical Research Letters*, v. 19, p. 1567–1570, doi:10.1029/92GL01225.
- Thompson, R.N., Gibson, S.A., Mitchell, J.G., Dickin, A.P., Leonardos, O.H., Brod, J.A., and Greenwood, J.C., 1998, Migrating Cretaceous-Eocene magmatism in the Serra do Mar alkaline province, SE Brazil: Melts from the deflected Trindade mantle plume?: *Journal of Petrology*, v. 39, p. 1493–1526, doi:10.1093/petrology/39.8.1493.
- Thompson, R.N., Gibson, S.A., Dickin, A.P., and Smith, P.M., 2001, Early Cretaceous basalt and picrite dykes of the southern Etendeka region, NW Namibia: Window into the role of Tristan mantle plume in Paraná-Etendeka magmatism: *Journal of Petrology*, v. 42, p. 2049–2081, doi:10.1093/petrology/42.11.2049.
- Torsvik, T.H., Rouse, S., Labails, C., and Smethurst, M.A., 2009, A new scheme for the opening of the South Atlantic Ocean and the dissection of an Aptian salt basin: *Geophysical Journal International*, v. 177, p. 1315–1333, doi:10.1111/j.1365-246X.2009.04137.x.
- Trumbull, R.B., Emmermann, R., Bühn, B., Gerstenberger, H., Mingram, B., Schmitt, A., and Volker, F., 2000, Insights on the genesis of the Cretaceous Damaraland igneous complexes in Namibia: The Nd- and Sr-isotopic perspective: *Communications of the Geological Survey of Namibia*, v. 12, p. 313–324.
- Trumbull, R.B., Bühn, B., Romer, R.L., and Volker, F., 2003, The petrology of basanite-tephrite intrusions in the Erongo complex and implications for a plume origin of Cretaceous alkaline complexes in Namibia: *Journal of Petrology*, v. 44, p. 93–112, doi:10.1093/petrology/44.1.93.
- Turner, S., Hawkesworth, C.J., Gallagher, K., Stewart, K., Peate, D., and Mantovani, M., 1996, Mantle plumes, flood basalts and thermal models for melt generation beneath continents: Assessment of conductive heating model and application to the Paraná: *Journal of Geophysical Research*, v. 101, p. 11,503–11,518, doi:10.1029/96JB00430.
- Untermeier, P., Curie, D., Olivet, J.L., Goslin, J., and Beuzart, P., 1988, South Atlantic fits and intraplate boundaries in Africa and South America: *Tectonophysics*, v. 155, p. 169–179, doi:10.1016/0040-1951(88)90264-8.
- Weaver, B.L., 1991, The origin of ocean island basalt end-member compositions: Trace element and isotopic constraints: *Earth and Planetary Science Letters*, v. 104, p. 381–397, doi:10.1016/0012-821X(91)90217-6.

MANUSCRIPT ACCEPTED BY THE SOCIETY 9 NOVEMBER 2010

Is the African cratonic lithosphere wet or dry?

Ikuo Katayama*

Department of Earth and Planetary Systems Science, Hiroshima University, Hiroshima 739-8526, Japan

Jun Korenaga

Department of Geology and Geophysics, Yale University, New Haven, Connecticut 06520, USA

ABSTRACT

Thick continental lithosphere (tectosphere) beneath African cratons has been stable for ~2.5 b.y. despite its mechanical interaction with sublithospheric mantle. Water is known to have significant influence on mechanical stiffness, and the depletion of water is often considered to be a key to preserving the thick lithosphere. Although water-rich environments indicated by the present water content of cratonic xenoliths appear to contradict this hypothesis, these water contents might have been modified at later stages due to the high diffusivity of hydrogen in minerals. Deformation microstructures such as lattice-preferred orientation indicate water-poor conditions (<200 ppm H/Si) during long-term plastic deformation in the continental lithosphere. Analysis of convective instability further constrains the water content to be less than 100 ppm H/Si. We suggest that the continental tectosphere beneath southern Africa must have a low water content, at least one order of magnitude less than oceanic upper mantle, and that the present-day water content of cratonic xenoliths most likely reflects localized metasomatism before eruption.

INTRODUCTION

Water has significant influence on the viscosity of mantle minerals (e.g., Karato et al., 1986; Mei and Kohlstedt, 2000), and consequently mantle dynamics depend strongly on the distribution of water. Continental tectosphere, which is thick mantle lithosphere lying below Archean cratons, has a thermochemical structure that differs from average suboceanic mantle (Jordan, 1975). This special kind of lithosphere is believed to have been stable and not experienced major tectonic disruptions for the last 2 b.y. or so, whereas other regions have undergone intense tectonic episodes (Richardson et al., 1984; Pearson, 1999). Although chemical buoyancy caused by the extraction of basaltic or komatiitic melts may be partly responsible for the stability of conti-

mental tectosphere (Jordan, 1975), geodynamic studies indicate that high viscosity is the most essential factor for the preservation of the thick lithosphere (Doin et al., 1997; Shapiro et al., 1999; Lenardic and Moresi, 1999; Sleep, 2003). Water is preferentially partitioned into a melt phase during partial melting (e.g., Koga et al., 2003), and a relatively low water content is expected for the residual mantle. Pollack (1986) proposed that volatile loss due to magmatic events might have increased mechanical stiffness and thus stabilized the continental tectosphere.

Cratonic mantle xenoliths, however, usually point to water-rich environments, as suggested by the common presence of hydrous minerals such as phlogopites (e.g., Pearson et al., 2003). Moreover, direct measurements of water content in cratonic xenoliths from southern Africa show a high amount of water,

*katayama@hiroshima-u.ac.jp

~800 ppm H/Si in olivine (Miller et al., 1987; Bell and Rossman, 1992; Kurosawa et al., 1997). This water content is actually higher than that in olivine from off-craton and from wedge mantle in subduction zones (Peslier and Luhr, 2006). If the mantle beneath cratons has more water than these mobile regions, then it could be very weak and easily disrupted by convection.

The origin of these “wet” signatures is a key question regarding the bulk property of continental tectosphere. Usually, these signatures are interpreted to be of a secondary origin, i.e., associated with metasomatic events prior to the kimberlite magmatism that brought those xenoliths up to the surface. That is, the wet signatures are believed to be highly localized in space and not representative of the lithospheric mantle. On the other hand, because the wet signatures are so commonly observed in cratonic xenoliths, it is also possible to regard them as representative samples and argue for wet and weak continental lithosphere (Maggi et al., 2000; Jackson, 2002). Thus, interpretation of the water contents of cratonic xenoliths has been ambiguous. They are invaluable direct samples, but we also know that they could suffer from severe sampling biases (e.g., Artemieva, 2009). The very fact that they were brought up to the surface could mean that they are fundamentally different from the rest of the continental tectosphere. A frustrating situation is that, whereas dehydrated, stiff mantle appears to be required for the long-term stability, we do not have direct samples to prove this hypothesis.

The purpose of this paper is twofold. First, we would like to point out that the deformation fabric of cratonic olivine can clearly dismiss the wet signatures of mantle xenoliths from the African lithosphere as a secondary origin and provide a direct constraint on the long-term water budget of continental tectosphere. Second, we will show such a constraint can be further tightened by a simple convective instability analysis incorporating xenolith data. We begin with a brief review on the present-day water content of cratonic olivine.

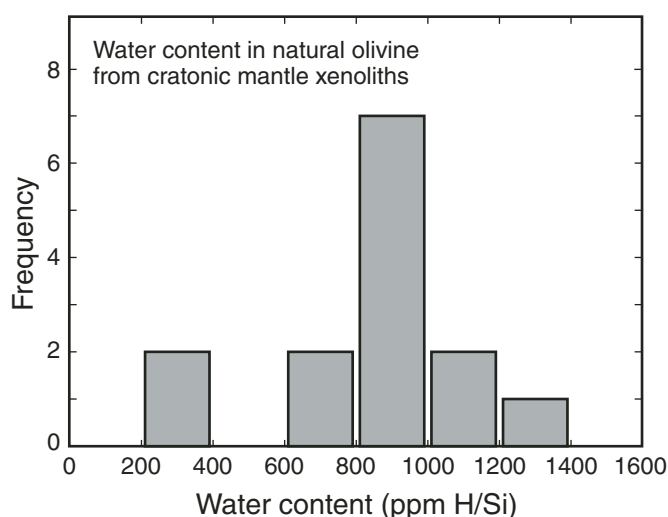


Figure 1. Water content in olivine from African cratonic xenoliths derived from deep continental lithosphere. The data are from Miller et al. (1987), Bell and Rossman (1992), and Kurosawa et al. (1997).

PRESENT WATER CONTENT IN CRATONIC OLIVINE

Trace amounts of water (hydrogen) in nominally anhydrous minerals have been widely detected by infrared spectroscopy and ion mass spectrometry (e.g., Rossman, 2006). Olivines from natural peridotites have been reported to contain ~10–1000 ppm H/Si (note that water content is expressed by atomic ratio of hydrogen and silicon, this corresponds to ~1–100 ppm H₂O by weight); olivines in garnet peridotites usually contain more water than those from spinel-peridotites (Bell and Rossman, 1992). In the cratonic xenoliths that derived from continental lithosphere, olivines show a wide range of water concentration, with an average of ~800 ppm H/Si (Fig. 1). The water contents of olivines from the cratonic lithosphere are higher than those from off-cratons (<600 ppm H/Si) and from mantle wedges (<500 ppm H/Si), both of which are tectonically active (Peslier and Luhr, 2006). Though these direct measurements provide a first clue to the water content of the continental tectosphere, it is not clear whether the present water content reflects the original value in the deep mantle because of the high diffusivity of hydrogen. The diffusion coefficient of hydrogen in olivine is more than ten orders of magnitude faster than oxygen or silicon diffusion (Mackwell and Kohlstedt, 1990), so that the water content of olivine can be easily modified; it takes days or weeks to reequilibrate a millimeter-size olivine (Fig. 2). Cratonic xenoliths are usually trapped by volatile-rich kimberlite diapirs, and this transport mechanism could easily overprint the original water content.

In fact, there are two types of geophysical data suggesting that the observed wet signatures of cratonic xenoliths are unlikely

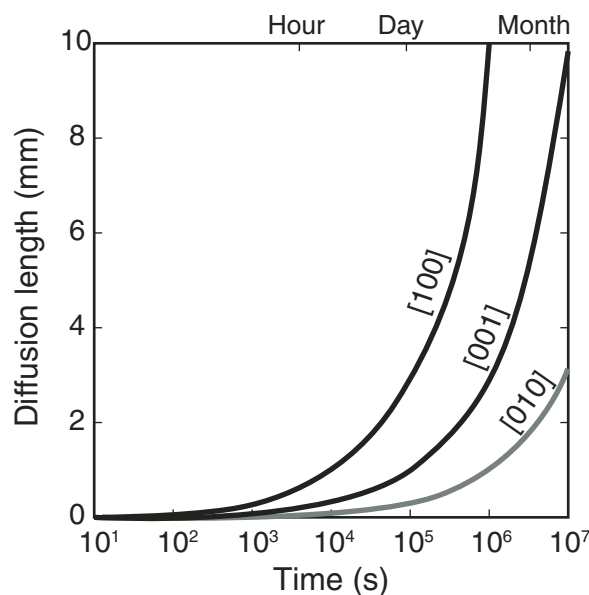


Figure 2. Diffusion length of hydrogen in olivine crystals. The diffusion coefficient is calculated at $T = 1000$ °C, from Mackwell and Kohlstedt (1990), which depends on crystallographic axis (the [100] axis is the fastest pathway of hydrogen diffusion).

to represent the bulk of tectosphere. First, by noting that mantle metasomatism also increases the content of heat-producing radiogenic elements, Rudnick et al. (1998) argued that low-heat-flow data observed over cratons preclude the possibility of a pervasively metasomatized lithosphere. Second, the lower water content of continental tectosphere is suggested by electrical conductivity (Hirth et al., 2000), though quantitative water contents are debated because electrical conductivity in olivine crystal is strongly anisotropic when hydrogen is the charge-carrying species (Yoshino et al., 2006; Wang et al., 2006).

Note that these geophysical observations are consistent with the notion of dry continental tectosphere but do not prove it, because the heat-flow argument is indirect and the interpretation of electrical conductivity is nonunique. It is not unreasonable, therefore, to hypothesize wet continental lithosphere on the basis of thermochemistry observed in cratonic xenoliths. Maggi et al. (2000), for example, argued for weak lithospheric mantle beneath continents because earthquakes in continental regions are usually confined in the crust, and they attributed the lack of strength in the mantle to its wet nature as suggested by xenoliths. It then becomes difficult to explain the stability of thick continental lithosphere, but the thickness of continental lithosphere itself has been debated for the last few decades (e.g., Anderson, 1979; Gaherty and Jordan, 1995; Gung et al., 2003; Priestley et al., 2006). Weak lithosphere would not pose any dynamic problem if continental lithosphere were not as thick as ~300 km.

How to interpret the water content of cratonic olivine is thus central to the debates surrounding the structure and dynamics of continental tectosphere. The primary water content of tectosphere, if known, could provide an important dynamical context for relevant geophysical data. In the next section, we show that such information can be extracted from the deformation microstructure of cratonic olivine.

WATER CONTENT INFERRED FROM DEFORMATION MICROSTRUCTURES

Recent laboratory experiments have shown that deformation-induced microstructures such as lattice-preferred orientation are sensitive to water content, in addition to stress and temperature (Jung and Karato, 2001; Katayama et al., 2004; Jung et al., 2006). This means that the analysis of deformation microstructures can provide a clue to water content during long-term deformation. Figure 3 shows an experimentally determined olivine fabric diagram as a function of water content and stress; the olivine [100] axis is oriented to the shear direction under water-poor conditions (A, E, and D types), whereas the [001] axis becomes parallel to the shear direction at high water concentrations (C and B types). Naturally deformed mantle peridotites show various types of olivine fabrics that correlate with their tectonic setting, i.e., peridotites from ophiolite sections commonly show A-type olivine fabric (Peselnick and Nicolas, 1978), whereas Alpine-type peridotites from subduction zones often show B- or C-type fabric (Möckel, 1969; Mizukami et al., 2004; Katayama et al.,

2005; Skemer et al., 2006). Mantle xenoliths from continental lithosphere beneath southern Africa commonly exhibit an olivine [100] axis subparallel to lineation and a (010) plane subparallel to the foliation plane (Ben Ismail and Mainprice, 1998) (see Fig. 4 for an example), which corresponds to A-type fabric. As shown in Figure 3, this type of olivine lattice-preferred orientation is found under water-poor conditions, less than ~200 ppm H/Si, so that the African cratonic lithosphere should be a dry environment during deformation.

Note that the water content in Figure 3 is based on the Paterson calibration of infrared spectroscopy data (Paterson, 1982), and if we instead apply the new calibration proposed by Bell et al. (2003), the threshold water content for the A-type fabric would be ~600 ppm H/Si. In either case, the deformation fabric indicates that the observed water contents of cratonic olivine as shown in Figure 1 do not represent the bulk water content of tectosphere. If those samples had long been as wet as observed when they were situated deep in the cratonic lithosphere, they would have been deformed more easily and should exhibit the B-, C-, or E-type fabric. Experimentally deformed olivine aggregates show a significant lattice-preferred orientation when the shear strain is larger than ~1 (Zhang et al., 2000). For a typical geological strain rate of 10^{-15} s^{-1} , it takes only ~30 m.y. to develop a significant olivine preferred orientation. Lattice-preferred orientation is difficult to modify by later-stage annealing (Heilbronner and Tullis, 2002). The fact that these samples show only the A-type fabric requires that their present-day water contents (~800–1000 ppm H/Si) must have been acquired relatively recently, and such

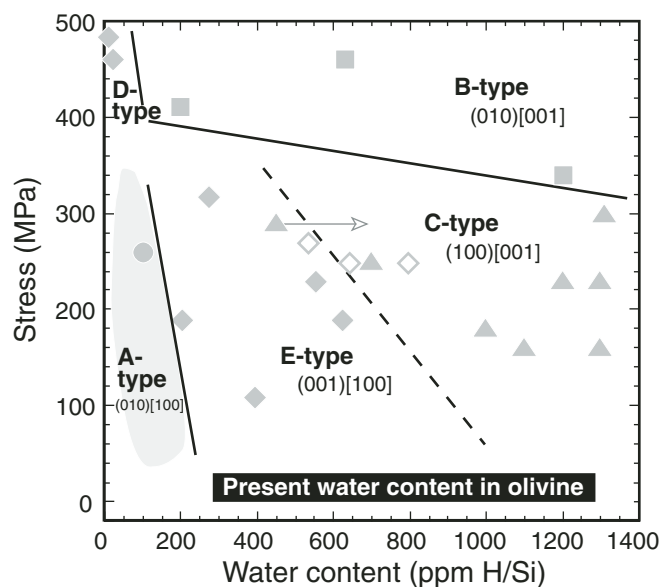


Figure 3. Olivine fabric diagram as a function of stress and water content (after Katayama et al., 2004). The present water contents in cratonic olivine are also shown in this figure, which suggests that E- or C-type olivine fabrics are dominant, whereas cratonic xenoliths commonly have the A-type fabric.

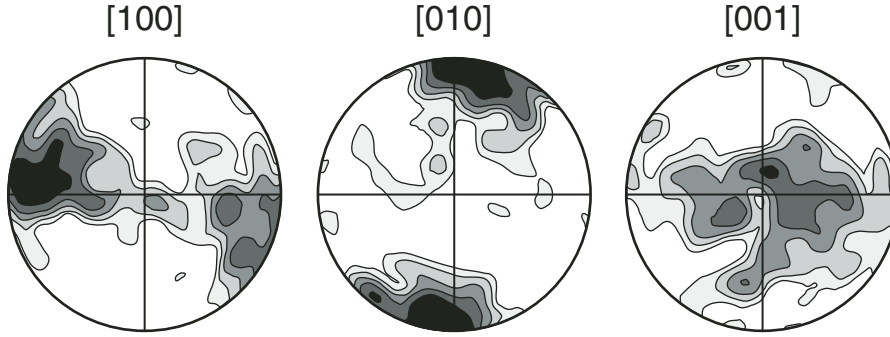


Figure 4. Lattice-preferred orientation of olivines from a kimberlite xenolith in the Kaapvaal craton (modified after Skemer and Karato, 2008). East-west direction corresponds to lineation, and north-south direction corresponds to foliation normal. The sample shows [100] maximum subparallel to lineation and [010] plane subparallel to foliation, suggesting the [100] slip and [010] plane is the dominant slip-system (A-type).

late-stage metasomatism can easily be explained by the associated volatile-rich kimberlite magmatism.

We therefore conclude that the long-term water content of continental tectosphere is lower than indicated by the present-day water content of cratonic xenoliths. The deformation fabric allows us to see through later metasomatic events in those hand samples and constrain their original water contents. As the threshold water content for the A-type fabric is still not very low to be regarded as “dry” (~200 or ~600 ppm H/Si, depending on the calibration adopted), we conducted a convective stability analysis in order to derive a tighter constraint.

CONVECTIVE STABILITY ANALYSIS

Before discussing what the nature of dry continental tectosphere must be in order to be stable over geologic time, we first need to clarify what we mean by “stable.” We can think of three different levels of stability. First, tectosphere must be stable on its own. That is, it must have enough strength to support internal density stratification, if any. Second, tectosphere should be stable against horizontal heterogeneities, such as those caused by a continent-ocean transition (Shapiro et al., 1999). Third, it must maintain its integrity over basal drag due to mantle convection (Doin et al., 1997). The last stability criterion is the most restricting and automatically tests the two other stabilities. Testing for this stability, however, involves a number of assumptions because one has to simulate the long-term behavior of mantle convection in a general way. On the other hand, the first stability, which we call the intrinsic stability, is the simplest because we can focus on tectosphere itself, and it may also be regarded as the most fundamental. If tectosphere is intrinsically unstable, it can never satisfy the second and third criteria. The notion of intrinsic stability, therefore, is useful to derive the *upper* bound on the water content of cratonic olivine.

Water-Content-Dependent Rheology

The incorporation of water increases point defects in crystal and hence significantly enhances the rate of deformation (e.g., Griggs and Blacic, 1965). A systematic correlation between water content and creep rate has been well determined for olivine

(e.g., Mei and Kohlstedt, 2000; Karato and Jung, 2003). Based on deformation microstructures of xenoliths and seismic anisotropy, the dominant deformation mechanism in continental lithosphere is likely to be dislocation creep, and the effect of water on dislocation creep is expressed as,

$$\dot{\epsilon} = AC_{OH}^r \exp\left(-\frac{E + PV}{RT}\right) \sigma^n, \quad (1)$$

where $\dot{\epsilon}$ is the strain rate, A is a scaling constant, C_{OH} is the water content, r is the water-content exponent, E is the activation energy, V is the activation volume, P is the pressure, T is the absolute temperature, R is the gas constant, σ is the differential stress, and n is the stress exponent. The parameters in this constitutive relation are summarized in Table 1. Since the water content exponent is close to 1, the strain rate changes approximately linearly with the water content. The water content in the upper mantle is estimated to be in the range of ~1–1000 ppm H/Si (e.g., Miller et al., 1987), so that the strain rate could differ up to ~3 orders of magnitude, depending on the water distribution

TABLE 1. PARAMETERS USED FOR CALCULATIONS

Crust density	2700 kg/m ³
Lithosphere density	3300 kg/m ³
Crust thickness	40 km
Surface heat flow*	51 mW/m ²
Mantle heat flow*	17 mW/m ²
Thermal diffusivity	1.0 × 10 ⁻⁶ m ² /s
Potential mantle temperature	1350 °C
Lithospheric stress	5 MPa
Flow law of dislocation creep [†]	
<i>Dry olivine</i>	
Pre-exponential constant	10 ^{6.1}
Stress exponent	3.0
Activation energy	510 kJ/mol
Activation volume	14 cm ³ /mol
<i>Wet olivine (closed system)</i>	
Pre-exponential constant	10 ^{0.56}
Stress exponent	3.0
Water content exponent	1.2
Activation energy	410 kJ/mol
Activation volume	11 cm ³ /mol

*Data from the Kaapvaal craton (Jones, 1988).

[†]Karato and Jung (2003).

in the mantle. However, when Equation 1 is extrapolated to significantly lower water content, we must take into account dry olivine rheology because wet creep and dry creep have independent mechanisms (Karato and Jung, 2003). Then, the total strain rate may be expressed (approximately) as the sum of these two creeps, i.e.,

$$\dot{\epsilon}_{\text{total}} = \dot{\epsilon}_{\text{wet}} + \dot{\epsilon}_{\text{dry}}. \quad (2)$$

The total strain rate is mostly controlled by wet rheology under water-rich conditions, and it is sensitive to water concentration, whereas the strain rate becomes less sensitive to the water content under water-poor conditions, where dry rheology controls the rate of deformation. Figure 5 shows the total strain rate of olivine calculated as a function of the water content (with $P = 5$ GPa, $T = 1000$ °C, and $\sigma = 5$ MPa), and the transition between wet and dry creeps occurs at water content of ~ 10 ppm H/Si. We used Equation 2 to estimate the viscosity of continental lithosphere.

Thermal Structure and Viscosity Profile

The thermal structure of continental lithosphere can be calculated using one-dimensional heat conduction (Turcotte and Schubert, 1982) with the present-day heat flux in the Kaapvaal craton (Jones, 1988). Internal heat generation in the lithospheric mantle was neglected in our calculations (Rudnick et al., 1998). Mantle adiabat was calculated with a potential mantle tempera-

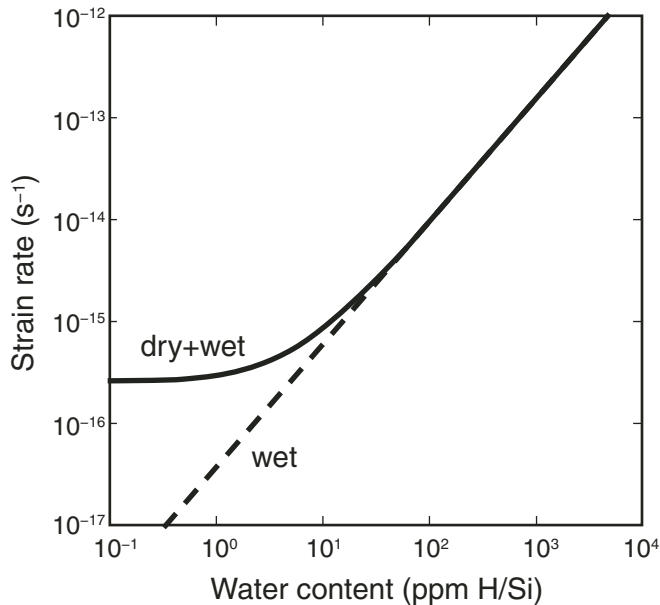


Figure 5. Strain rate of olivine aggregates as a function of water content. The dashed line was calculated using wet olivine rheology, and the solid line was calculated for sum of wet and dry rheology (parameters listed in Table 1). The deformation rate (in terms of viscosity) is sensitive to water content at water-rich conditions, whereas it will be insensitive to water when water content is less than 10 ppm H/Si.

ture of 1350 °C and a gradient of 0.5 °C/km, and the geotherm follows the mantle adiabat when they intersect. The parameters used in our calculation are summarized in Table 1. The estimated thermal structure agrees well with the pressure-temperature (P - T) conditions of kimberlite xenoliths from southern Africa (Fig. 6). Mantle xenoliths erupted in the middle Proterozoic (ca. 1.1 Ga in the Premier mine) also show similar P - T conditions to those of the Mesozoic, whereas the heat-producing elements could have been more abundant in the past. This suggests that the African cratonic lithosphere may have experienced limited changes in the thermal structure (Danchin, 1979). The effective viscosity profile can be calculated from this thermal structure and the olivine flow law (Eq. 2) as

$$\eta = \frac{\sigma}{\dot{\epsilon}}, \quad (3)$$

in which we assume a lithospheric stress of 5 MPa. This stress is based on the grain-size piezometer of cratonic xenoliths in southern Africa (Mercier, 1980). The lithospheric stress has some uncertainties due to the calibration of piezometers and the variation of grain size in the cratonic xenoliths, but this estimate is in the range of the approximate or maximum values inferred from geophysical constraints including isostatic compensation (e.g., Lambeck, 1980). Cratonic xenoliths must have deformed, probably very slowly, by dislocation creep to develop lattice-preferred orientation with the A-type fabric, and dynamic recrystallization during this dislocation creep dictates the relationship between stress and grain size. Water in the cratonic lithosphere might be heterogeneous as a result of mantle metasomatism; however, such regions could be highly localized (Katayama et al., 2009), having little impact on the bulk properties of lithosphere. In these contexts, we assumed a 300-km-thick chemically distinct lithosphere with a constant water content. The calculated viscosity structure is shown in Figure 6 for different water contents.

Water Content to Stabilize the African Cratonic Lithosphere

Based on the viscosity profile of the continental lithosphere beneath African cratons, we first calculated the differential Rayleigh number (dRa) as

$$dRa = \frac{4\alpha\rho g(z - z_0)^3}{\kappa\eta} \frac{dT}{dz} dz, \quad (4)$$

where α is the coefficient of thermal expansion, g is gravitational acceleration, ρ is the density, κ is the thermal diffusivity, and z_0 is the origin of available buoyancy (for full explanation, see Korenaga and Jordan, 2002). The local Rayleigh number (Ra) is then obtained by integrating the differential Rayleigh number from the top to the bottom of tectosphere as

$$Ra = \int dRa. \quad (5)$$

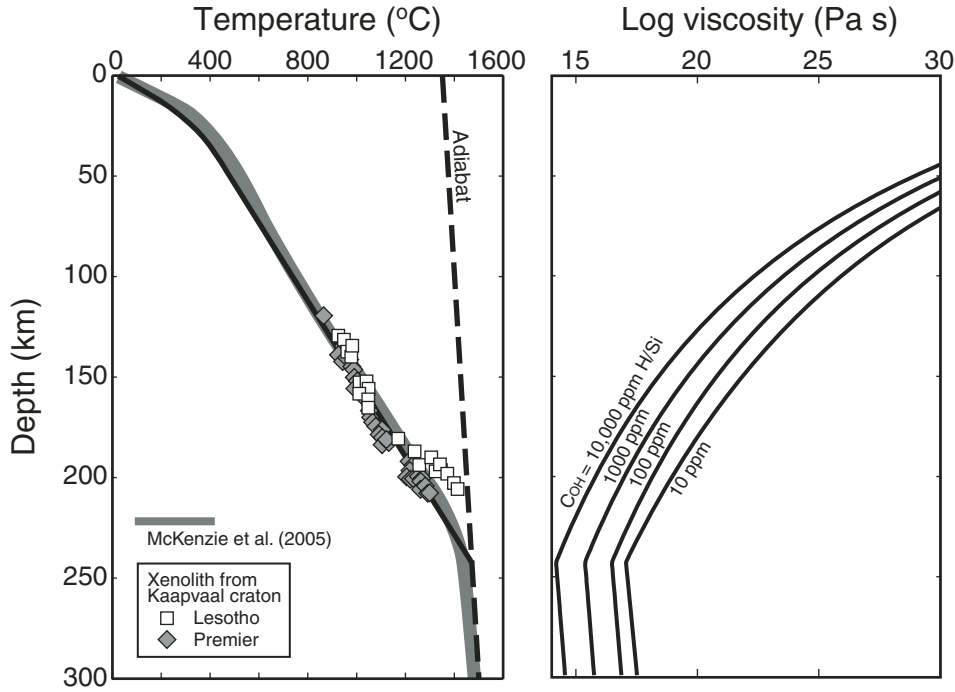


Figure 6. Thermal structure and viscosity profile of the African cratonic lithosphere. The continental geotherm was calculated from surface heat flow (Jones, 1988), and the results agree with pressure-temperature (P - T) conditions of cratonic xenoliths (Lesotho—Boyd and Nixon, 1975; Premier—Danchin, 1979). The cratonic geotherm calculated by McKenzie et al. (2005) is shown for reference. The viscosity was calculated from Equation 3 with different water contents. The detailed parameters for calculations are shown in Table 1.

We assumed no variation in compositional buoyancy within the lithosphere. The isopycnic hypothesis in the strict sense requires that density variation due to the thermal gradient be compensated by that due to the compositional gradient within the lithosphere (Jordan, 1975), but the inferred depth distribution of cratonic xenoliths does not exhibit such variation (e.g., Pearson and Nowell, 2002). Note that the compositional buoyancy of cratonic lithosphere as a whole with respect to surrounding mantle is prob-

ably partially responsible for its longevity (Shapiro et al., 1999) but is irrelevant to the intrinsic stability problem considered here.

The calculated local Ra of the African cratonic lithosphere is shown in Figure 7 as a function of the water content. The local Ra depends strongly on the water content at water-rich conditions, although it becomes less sensitive under water-poor conditions (Fig. 7). More importantly, the local Ra exceeds the critical value ($\sim 10^3$) when the water content is higher than 100 ppm H/Si. To be stable over billions of years, therefore, the water content must be lower than 100 ppm H/Si. Because we are considering the intrinsic stability only, this is the upper bound on the more likely water content. Also, these calculations are based on the present thermal structure in continental lithosphere, but the temperature of the tectosphere must have been higher in the Archean due to more abundant radiogenic elements in continental crust as well as higher mantle potential temperatures for sublithospheric mantle (e.g., Korenaga, 2006). Thus, more depletion of water would have been necessary in the Archean just to maintain the intrinsic stability. The upper bound of ~ 100 ppm H/Si is based on the rheological parameters given in Table 1, which are based on the Paterson calibration of infrared spectroscopy. We may thus summarize that, compared to the constraint required

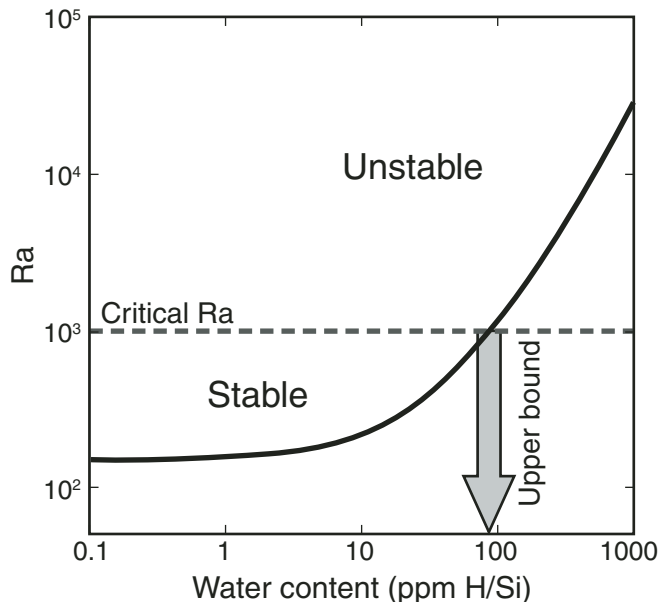


Figure 7. The calculated local Rayleigh number (Ra) is smaller than the critical Ra ($\sim 10^3$) when water content is less than 100 ppm H/Si, suggesting that continental tectosphere can be stable. However, if water content is higher than 100 ppm, the calculated Ra is higher than the critical value, and continental tectosphere might be entrained by convecting mantle.

by deformation microstructures, the consideration of intrinsic stability tightens the upper bound by a factor of two, regardless of the chosen calibration. If we instead use the calibration by Bell et al. (2003) throughout, the upper bound is ~600 ppm H/Si by the deformation fabric and reduces to ~300 ppm H/Si by requiring intrinsic stability. Given other types of instabilities, a more realistic water content should be lower than these upper bounds, and such depletion of water in the tectosphere can easily be caused by the extraction of large amounts of melts during its formation, because water is preferentially partitioned into a melt phase, as illustrated in Figure 8 ($D_{\text{H}_2\text{O}}^{\text{olivine/melt}} \sim 0.001$; Koga et al., 2003). Our stability analysis (Fig. 7), however, also indicates that values below 10 ppm H/Si would not lead to extra stability. This is because the degree of dehydration stiffening is bounded by dry dislocation creep (Fig. 5). This is also illustrated by recent experimental data, which suggest a relatively large activation volume (>10 – 15 cm³/mol; Karato, 2010). This limited effect of dehydration stiffening may be important when considering the higher levels of stability and could provide dynamic constraints on the formation and evolution of continental tectosphere.

CONCLUSIONS

The direct measurement of water in cratonic xenoliths suggests significant amounts of water in the African cratonic lithosphere similar to the oceanic upper mantle, but it has not been clear whether the present water content reflects the original value in the mantle, due to the high diffusivity of hydrogen in minerals. Here, we argue that deformation microstructures such as

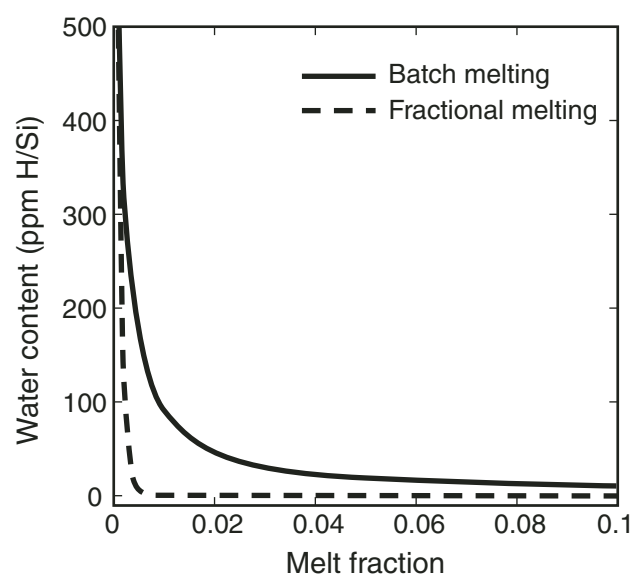


Figure 8. Water content in the residual mantle rock after partial melting calculated from partitioning coefficient of water between olivine and melt (Koga et al., 2003). Water can be removed significantly by melting process, and this results in high depletion of water in the residual lithospheric mantle.

lattice-preferred orientation from the cratonic xenoliths point to water-poor conditions ($C_{\text{OH}} < 200$ ppm H/Si) during the long-term plastic deformation. The convective stability analysis, including water-content-dependent rheology, further tightens the water content constraints by a factor of two (~100 ppm), in order to maintain the intrinsic stability of the continental tectosphere. Given other likely sources of instabilities, this water content must be regarded as the upper bound. At the same time, being very dry (e.g., <1 ppm H/Si) does not necessarily indicate very stiff tectosphere, because the effect of water content on the rheological properties of continental lithosphere is nonlinear. This nonlinear functionality must be appreciated when considering the role of water in the dynamic processes of cratonic lithosphere.

ACKNOWLEDGMENTS

We thank S. Karato for discussion. Constructive comments by I. Artemieva and P. Skemer helped to improve the manuscript. This study was supported by the Japan Society for the Promotion of Science.

REFERENCES CITED

- Anderson, D.L., 1979, Deep-structure of continents: *Journal of Geophysical Research*, v. 84, p. 7555–7560.
- Artemieva, I.M., 2009, The continental lithosphere: Reconciling thermal, seismic, and petrologic data: *Lithos*, v. 109, p. 23–46, doi:10.1016/j.lithos.2008.09.015.
- Bell, D.R., and Rossman, G.R., 1992, Water in Earth's mantle: The role of nominally anhydrous minerals: *Science*, v. 255, p. 1391–1397, doi:10.1126/science.255.5050.1391.
- Bell, D.R., Rossman, G.R., Maldener, J., Endisch, D., and Rauch, F., 2003, Hydroxide in olivine: A quantitative determination of the absolute amount and calibration of the IR spectrum: *Journal of Geophysical Research*, v. 108, 2105, doi:10.1029/2001JB000679.
- Ben Ismail, W., and Mainprice, D., 1998, An olivine fabric database: An overview of upper mantle fabrics and seismic anisotropy: *Tectonophysics*, v. 296, p. 145–157, doi:10.1016/S0040-1951(98)00141-3.
- Boyd, F.R., and Nixon, P.H., 1975, Origins of the ultramafic nodules from some kimberlites of northern Lesotho and the Monastery mine, South Africa: *Physics and Chemistry of the Earth*, v. 9, p. 431–454, doi:10.1016/0079-1946(75)90032-4.
- Danchin, R.V., 1979, Mineral and bulk chemistry of garnet lherzolite and garnet harzburgite xenoliths from the Premier mine, South Africa, in Boyd, F.R., and Meyer, H.A., eds., *The Mantle Sample: Inclusions in Kimberlites and Other Volcanics: Proceedings of the 2nd International Kimberlite Conference*: Santa Fe, American Geophysical Union, p. 104–126.
- Doin, M.-P., Fleitout, L., and Christensen, U., 1997, Mantle convection and stability of depleted and undepleted continental lithosphere: *Journal of Geophysical Research*, v. 102, p. 2771–2787, doi:10.1029/96JB03271.
- Gaherty, J.B., and Jordan, T.H., 1995, Lehman discontinuity as the base of an anisotropic layer beneath continents: *Science*, v. 268, p. 1468–1471, doi:10.1126/science.268.5216.1468.
- Griggs, D.T., and Blacic, J.D., 1965, Quartz: Anomalous weakness of synthetic crystals: *Science*, v. 147, p. 292–295, doi:10.1126/science.147.3655.292.
- Gung, Y., Panning, M.P., and Romanowicz, B., 2003, Global anisotropy and the thickness of continents: *Nature*, v. 422, p. 707–711, doi:10.1038/nature01559.
- Heilbronner, R., and Tullis, J., 2002, The effect of static annealing on microstructure and crystallographic preferred orientations of quartzites experimentally deformed in axial compression and shear, in De Meer, S., Drury, M.R., De Bresser, J.H.P., and Pennock, G., eds., *Deformation Mechanisms, Rheology and Tectonics: Current Status and Future Perspectives*: Geological Society of London Special Publication 200, p. 191–218.

- Hirth, G., Evans, R.L., and Chave, A.D., 2000, Comparison of continental and oceanic mantle electrical conductivity: Is the Archean lithosphere dry?: *Geochemistry Geophysics Geosystems*, v. 1, doi:10.1029/2000GC000048.
- Jackson, J., 2002, Faulting, flow, and the strength of the continental lithosphere: *International Geology Review*, v. 44, p. 39–61, doi:10.2747/0020-6814.44.1.39.
- Jones, M.Q.W., 1988, Heat flow in the Witwatersrand Basin and environs and its significance for the South African shield geotherm and lithosphere thickness: *Journal of Geophysical Research*, v. 93, p. 3243–3260, doi:10.1029/JB093iB04p03243.
- Jordan, T.H., 1975, The continental tectosphere: *Reviews of Geophysics and Space Physics*, v. 13, p. 1–12, doi:10.1029/RG013i003p00001.
- Jung, H., and Karato, S., 2001, Water-induced fabric transitions in olivine: *Science*, v. 293, p. 1460–1463, doi:10.1126/science.1062235.
- Jung, H., Katayama, I., Jiang, Z., Hiraga, T., and Karato, S., 2006, Effect of water and stress on the lattice preferred orientation (LPO) in olivine: *Tectonophysics*, v. 421, p. 1–22, doi:10.1016/j.tecto.2006.02.011.
- Karato, S., 2010, Rheology of the deep upper mantle and its implications for the preservation of the continental roots: A review: *Tectonophysics*, v. 481, p. 82–98, doi:10.1016/j.tecto.2009.04.011.
- Karato, S., and Jung, H., 2003, Effects of pressure on high-temperature dislocation creep in olivine: *Philosophical Magazine A*, v. 83, p. 401–414, doi:10.1080/0141861021000025829.
- Karato, S., Paterson, M.S., and FitzGerald, J.D., 1986, Rheology of synthetic olivine aggregates: Influence of grain size and water: *Journal of Geophysical Research*, v. 91, p. 8151–8176, doi:10.1029/JB091iB08p08151.
- Katayama, I., Jung, H., and Karato, S., 2004, A new type of olivine fabric from deformation experiments at modest water content and low stress: *Geology*, v. 32, p. 1045–1048, doi:10.1130/G20805.1.
- Katayama, I., Karato, S., and Brandon, M., 2005, Evidence of high water content in the deep upper mantle inferred from deformation microstructures: *Geology*, v. 33, p. 613–616, doi:10.1130/G21332.1.
- Katayama, I., Suyama, Y., Ando, J., and Komiya, T., 2009, Mineral chemistry and *P-T* condition of granular and sheared peridotite xenoliths from Kimberley, South Africa: Origin of the textural variation in the cratonic mantle: *Lithos*, v. 109, p. 333–340, doi:10.1016/j.lithos.2008.05.004.
- Koga, K., Hauri, E., Hirschmann, M., and Bell, D.R., 2003, Hydrogen concentration analyses using SIMS and FTIR: Comparison and calibration for nominally anhydrous minerals: *Geochemistry Geophysics Geosystems*, v. 4, doi:10.1029/2002GC000378.
- Korenaga, J., 2006, Archean geodynamics and the thermal evolution of the Earth, in Benn, K., Mareschal, J.C., and Condie, K.C., eds., *Archean Geodynamic Processes*: Washington D.C., American Geophysical Union, p. 7–32.
- Korenaga, J., and Jordan, T.H., 2002, Onset of convection with temperature- and depth-dependent viscosity: *Geophysical Research Letters*, v. 29, doi:10.1029/2002GL015672.
- Kurosawa, M., Yurimoto, H., and Sueno, S., 1997, Patterns in the hydrogen and trace element compositions of mantle olivines: *Physics and Chemistry of Minerals*, v. 24, p. 385–395, doi:10.1007/s002690050052.
- Lambeck, K., 1980, Estimates of stress differences in the crust from isostatic considerations: *Journal of Geophysical Research*, v. 85, p. 6397–6402, doi:10.1029/JB085iB11p06397.
- Lenardic, A., and Moresi, L., 1999, Some thoughts on the stability of cratonic lithosphere: Effects of buoyancy and viscosity: *Journal of Geophysical Research*, v. 104, p. 12,747–12,758, doi:10.1029/1999JB900035.
- Mackwell, S.J., and Kohlstedt, D.L., 1990, Diffusion of hydrogen in olivine: Implication for water in the mantle: *Journal of Geophysical Research*, v. 95, p. 5079–5088, doi:10.1029/JB095iB04p05079.
- Maggi, A., Jackson, J.A., McKenzie, D., and Priestley, K., 2000, Earthquake focal depths, effective elastic thickness, and the strength of the continental lithosphere: *Geology*, v. 28, p. 495–498, doi:10.1130/0091-7613(2000)28<495:EFDEET>2.0.CO;2.
- McKenzie, D., Jackson, J., and Priestley, K., 2005, Thermal structure of oceanic and continental lithosphere: *Earth and Planetary Science Letters*, v. 233, p. 337–349, doi:10.1016/j.epsl.2005.02.005.
- Mei, S., and Kohlstedt, D.L., 2000, Influence of water on plastic deformation of olivine aggregates 2. Dislocation creep regime: *Journal of Geophysical Research*, v. 105, p. 21,471–21,481, doi:10.1029/2000JB900180.
- Mercier, J.C., 1980, Magnitude of the continental lithospheric stresses inferred from rheomorphic petrology: *Journal of Geophysical Research*, v. 85, p. 6293–6303, doi:10.1029/JB085iB11p06293.
- Miller, G.H., Rossman, G.R., and Harlow, G.E., 1987, The natural occurrence of hydroxide in olivine: *Physics and Chemistry of Minerals*, v. 14, p. 461–472, doi:10.1007/BF00628824.
- Mizukami, T., Simon, W., and Yamamoto, J., 2004, Natural examples of olivine lattice preferred orientation patterns with a flow-normal *a*-axis maximum: *Nature*, v. 427, p. 432–436, doi:10.1038/nature02179.
- Möckel, J.R., 1969, Structural petrology of the garnet peridotite of Alpe Arami (Ticino, Switzerland): *Leidse Geologische Mededelingen*, v. 42, p. 61–130.
- Paterson, M.S., 1982, The determination of hydroxyl by infrared absorption in quartz, silicate glasses and similar materials: *Bulletin of Mineralogy*, v. 105, p. 20–29.
- Pearson, D.G., 1999, The age of continental roots: *Lithos*, v. 48, p. 171–194, doi:10.1016/S0024-4937(99)00026-2.
- Pearson, D.G., and Nowell, G.M., 2002, The continental lithospheric mantle: Characteristics and significance as a mantle reservoir: *Philosophical Transactions of the Royal Society of London, ser. A*, v. 360, p. 2383–2410, doi:10.1098/rsta.2002.1074.
- Pearson, D.G., Canil, D., and Shirey, S.G., 2003, Mantle samples included in volcanic rocks: Xenoliths and diamonds, in Carlson, R.W., ed., *Treatise on Geochemistry*, Volume 2: Oxford, Elsevier-Pergamon, p. 171–275.
- Peselnick, L., and Nicolas, A., 1978, Seismic anisotropy in an ophiolite peridotite: Application to oceanic upper mantle: *Journal of Geophysical Research*, v. 83, p. 1227–1235, doi:10.1029/JB083iB03p01227.
- Peslier, A.H., and Luhr, J.F., 2006, Hydrogen loss from olivines in mantle xenoliths from Simcoe (USA) and Mexico: Mafic alkalic magma ascent rates and water budget of the sub-continental lithosphere: *Earth and Planetary Science Letters*, v. 242, p. 302–319, doi:10.1016/j.epsl.2005.12.019.
- Pollack, H.N., 1986, Cratonization and thermal evolution of the mantle: *Earth and Planetary Science Letters*, v. 80, p. 175–182, doi:10.1016/0012-821X(86)90031-2.
- Priestley, K., McKenzie, D., and Debayle, E., 2006, The state of the upper mantle beneath southern Africa: *Tectonophysics*, v. 416, p. 101–112, doi:10.1016/j.tecto.2005.11.024.
- Richardson, S.H., Gurney, J.J., Erlank, A.J., and Harris, J.W., 1984, Origin of diamonds in old enriched mantle: *Nature*, v. 310, p. 198–202, doi:10.1038/310198a0.
- Rossman, G.R., 2006, Analytical methods for measuring water in nominally anhydrous minerals: *Reviews in Mineralogy and Geochemistry*, v. 62, p. 1–28, doi:10.2138/rmg.2006.62.1.
- Rudnick, R.L., McDonough, W.F., and O'Connell, R.J., 1998, Thermal structure, thickness and composition of the continental lithosphere: *Chemical Geology*, v. 145, p. 395–411, doi:10.1016/S0009-2541(97)00151-4.
- Shapiro, S.S., Hager, B.H., and Jordan, T.H., 1999, The continental tectosphere and Earth's long-wavelength gravity field: *Lithos*, v. 48, p. 135–152, doi:10.1016/S0024-4937(99)00027-4.
- Skemer, P., and Karato, S., 2008, Sheared lherzolite xenoliths revisited: *Journal of Geophysical Research*, v. 113, doi:10.1029/2007JB005286.
- Skemer, P., Katayama, I., and Karato, S., 2006, Deformation fabrics of the Cima di Gagnone peridotite massif, Central Alps, Switzerland: Evidence of deformation at low temperatures in the presence of water: *Contributions to Mineralogy and Petrology*, v. 152, p. 43–51, doi:10.1007/s00410-006-0093-4.
- Sleep, N.H., 2003, Survival of Archean cratonic lithosphere: *Journal of Geophysical Research*, v. 108, doi:10.1029/2001JB000169.
- Turcotte, D.L., and Schubert, G., 1982, *Geodynamics: Applications of Continuum Physics to Geological Problems*: New York, John Wiley, 450 p.
- Wang, D., Mookherjee, M., Xu, Y., and Karato, S., 2006, The effect of water on the electrical conductivity of olivine: *Nature*, v. 443, p. 977–980, doi:10.1038/nature05256.
- Yoshino, T., Matsuzaki, T., Yamashita, S., and Katsura, T., 2006, Hydrous olivine unable to account for conductivity anomaly at the top of the asthenosphere: *Nature*, v. 443, p. 973–976, doi:10.1038/nature05223.
- Zhang, S., Karato, S., Fitz Gerald, J., Faul, U.H., and Zhou, Y., 2000, Simple shear deformation of olivine aggregates: *Tectonophysics*, v. 316, p. 133–152, doi:10.1016/S0040-1951(99)00229-2.

New ^{40}Ar - ^{39}Ar ages and petrogenesis of the Massif d'Ambre volcano, northern Madagascar

C. Cucciniello

L. Melluso*

V. Morra

Dipartimento di Scienze della Terra, Università di Napoli Federico II, via Mezzocannone 8, 80134 Naples, Italy

M. Storey

*Quaternary Dating Laboratory, Department of Environmental, Social and Spatial Change,
Roskilde University, P.O. Box 260, DK-4000 Roskilde, Denmark*

I. Rocco

L. Franciosi

Dipartimento di Scienze della Terra, Università di Napoli Federico II, via Mezzocannone 8, 80134 Naples, Italy

C. Grifa

Dipartimento di Studi Geologici ed Ambientali, Università del Sannio, via dei Mulini 59a, 82100 Benevento, Italy

C.M. Petrone

Department of Earth Sciences, University of Cambridge, Downing Street, Cambridge CB2 3EQ, UK

M. Vincent

*CNIRIT (Centre National de Recherches Industrielle et Technologique),
38, Rue Rasamimanana Fiadanana 101 B.P. 6294 Antananarivo, Madagascar*

ABSTRACT

The Massif d'Ambre is the largest stratovolcano (~2500 km²) in the Cenozoic igneous province of northern Madagascar. It is broadly elongated in a N-S direction and is formed by hundreds of lava flows, plugs, spatter cones, tuff rings, pyroclastic flows, and pyroclastic fall deposits. New ^{40}Ar - ^{39}Ar age determinations for lavas of Massif d'Ambre and Bobaomby Peninsula (the northernmost tip of Madagascar) yield ages of 12.1 ± 0.2 Ma and 10.56 ± 0.09 Ma. These ages indicate that at least part of the volcanic activity of the Bobaomby Peninsula occurred later than the beginning of the activity of the Massif d'Ambre. The volcanic products of Massif d'Ambre are mildly to strongly alkaline (with sodic affinity) to tholeiitic with very limited amounts of evolved magmas. The mafic rocks have compositions similar to those of primitive

*melluso@unina.it

Cucciniello, C., Melluso, L., Morra, V., Storey, M., Rocco, I., Franciosi, L., Grifa, C., Petrone, C.M., and Vincent, M., 2011, New ^{40}Ar - ^{39}Ar ages and petrogenesis of the Massif d'Ambre volcano, northern Madagascar, in Beccaluva, L., Bianchini, G., and Wilson, M., eds., *Volcanism and Evolution of the African Lithosphere: Geological Society of America Special Paper 478*, p. 257–281, doi:10.1130/2011.2478(14). For permission to copy, contact editing@geosociety.org. © 2011 The Geological Society of America. All rights reserved.

mantle-derived magmas ($\text{MgO} > 10 \text{ wt}\%$, Cr and Ni > 400 and > 200 ppm, respectively). The strongly alkaline suite shows a liquid line of descent from basanite to phonolite, dominated by fractional crystallization of clinopyroxene and olivine. The mafic rocks (basanites, alkali basalts, transitional and tholeiitic basalts) have Zr/Nb (2.4–5.8), Ba/Nb (7–24) and La/Nb (0.7–1.1) ratios typical of incompatible element-rich within-plate basalts. The primitive mantle-normalized incompatible element patterns of the Massif d'Ambre mafic rocks are characterized by peaks at Nb and troughs at K, and are identical in shape and absolute abundances to those of the Nosy Be and Bobaomby (Cap d'Ambre) basanites. The range of $(\text{La/Yb})_n$ ratios (9–24) indicates that the Massif d'Ambre primitive compositions are the product of variable degrees of partial melting (4%–12%) of a broadly similar and slightly incompatible element-enriched mantle source. Initial $^{87}\text{Sr}/^{86}\text{Sr}$ and $^{143}\text{Nd}/^{144}\text{Nd}$ ratios of alkali basalts and basanites vary from 0.70326 to 0.70359 and 0.51279 to 0.51286, respectively. Alkali basalts and basanites have little variation in $^{206}\text{Pb}/^{204}\text{Pb}$ (19.073–19.369), $^{207}\text{Pb}/^{204}\text{Pb}$ (15.613–15.616), and $^{208}\text{Pb}/^{204}\text{Pb}$ (39.046–39.257). This range is well within that of Sr–Nd–Pb isotope values of the basanites of the Nosy Be Archipelago, thus again confirming substantially similar source compositions throughout northern Madagascar.

INTRODUCTION

During the late Cenozoic, Madagascar was affected by widespread magmatic activity in the northern and central parts of the island, with a few outcrops in the southwest (Lacroix, 1923; Besairie, 1964). In northern Madagascar, the volcanic activity is mostly represented by the Massif d'Ambre stratovolcano, volcanic complexes in the Nosy Be Archipelago, the Ankaizina district, and in the Ampasindava and Bobaomby (Cap d'Ambre) Peninsulas (Fig. 1). The geochemical characteristics of the mafic volcanic rocks of the Nosy Be Archipelago and Bobaomby Peninsula have been studied by Melluso and Morra (2000) and Melluso et al. (2007a, 2007b). Karche (1972) made a major study of the volcanic rocks of the Massif d'Ambre. A tectonic study of the area is reported in Chorowicz et al. (1997). The late Cenozoic alkaline volcanism in northernmost Madagascar is related to a roughly east-west extensional tectonic regime (Bertil and Regnault, 1998; Rakotondraompiana et al., 1999; Piqué et al., 1999; Kusky et al., 2007). The main geological structure produced by this regional extension is the Alaotra-Ankay Rift, developed in the center of Madagascar (de Wit, 2003; Kusky et al., 2007). A similar extensional tectonic regime is also observed in East Africa in recent times (Stamps et al., 2008). On the basis of a progressive eastward increase in the age of volcanism, Emerick and Duncan (1982, 1983) proposed a plume origin for the volcanism in the Comore Islands and in the northern coast of Madagascar.

In this paper, we present new ^{40}Ar – ^{39}Ar age determinations and mineral and whole-rock chemical and Sr–Nd–Pb isotope data on the volcanic rocks of Massif d'Ambre. These data allow us to better establish the age of emplacement of this volcanic complex, the roles of fractional crystallization, the nature of the mantle source, and degrees of partial melting in the formation of these rocks. The study of the Cenozoic igneous rocks of the northern Madagascar also allows us to investigate the geochemical signa-

ture of the Madagascan subcontinental mantle because: (1) the most mafic rocks have compositions akin to primitive melts (Melluso and Morra, 2000; Melluso et al., 2007b); and (2) many mafic volcanic rocks are associated with ultramafic xenoliths that provide a direct probe to the lithospheric mantle of the area (Rocco, 2009). This paper is part of an ongoing project aiming to understand the petrogenesis of Cretaceous and late Cenozoic volcanic rocks of Madagascar in their regional tectonic context.

GEOLOGICAL SETTING AND SAMPLING STRATEGY

The Cenozoic volcanic rocks cover broad areas of northern Madagascar. The Bobaomby (Cap d'Ambre) volcanic field at the northern tip of Madagascar consists of lava flows (with strongly alkaline affinity), huge spatter cones; rare, well-preserved tuff rings; and a dike swarm with the intrusions orientated either N–S or E–W (Melluso et al., 2007b). The Ankaizina sector is located on the Precambrian basement of northern Madagascar, and it consists of two volcanic fields: Mount Tsaratanana and Ambondrona. The Ampasindava province is composed of several igneous complexes having a wide range of compositions, including basalts, rhyolites, trachytes, phonolites, and intrusive rocks (gabbros to syenites and granites). The Nosy Be Archipelago, off the NW coast of Madagascar, consists of several, mostly volcanic, islands. Nosy Komba consists of an alkali gabbro–nepheline syenitic intrusion of roughly circular shape. Nosy Be island consists of Mesozoic–Cenozoic sediments that have been intruded by nepheline syenitic stocks, and subsequently covered by lava flows, scoria cones, and tuff rings of basanitic to phonotephritic composition (Melluso and Morra, 2000). Nosy Sakatia is formed by a rhyolitic lava flow crosscut by basanitic spatter cones and plugs rich in mantle xenoliths. Massif d'Ambre covers an area of $\sim 2500 \text{ km}^2$ and is the largest volcanic complex of northern Madagascar (Besairie, 1964). It is located to the south of Diego

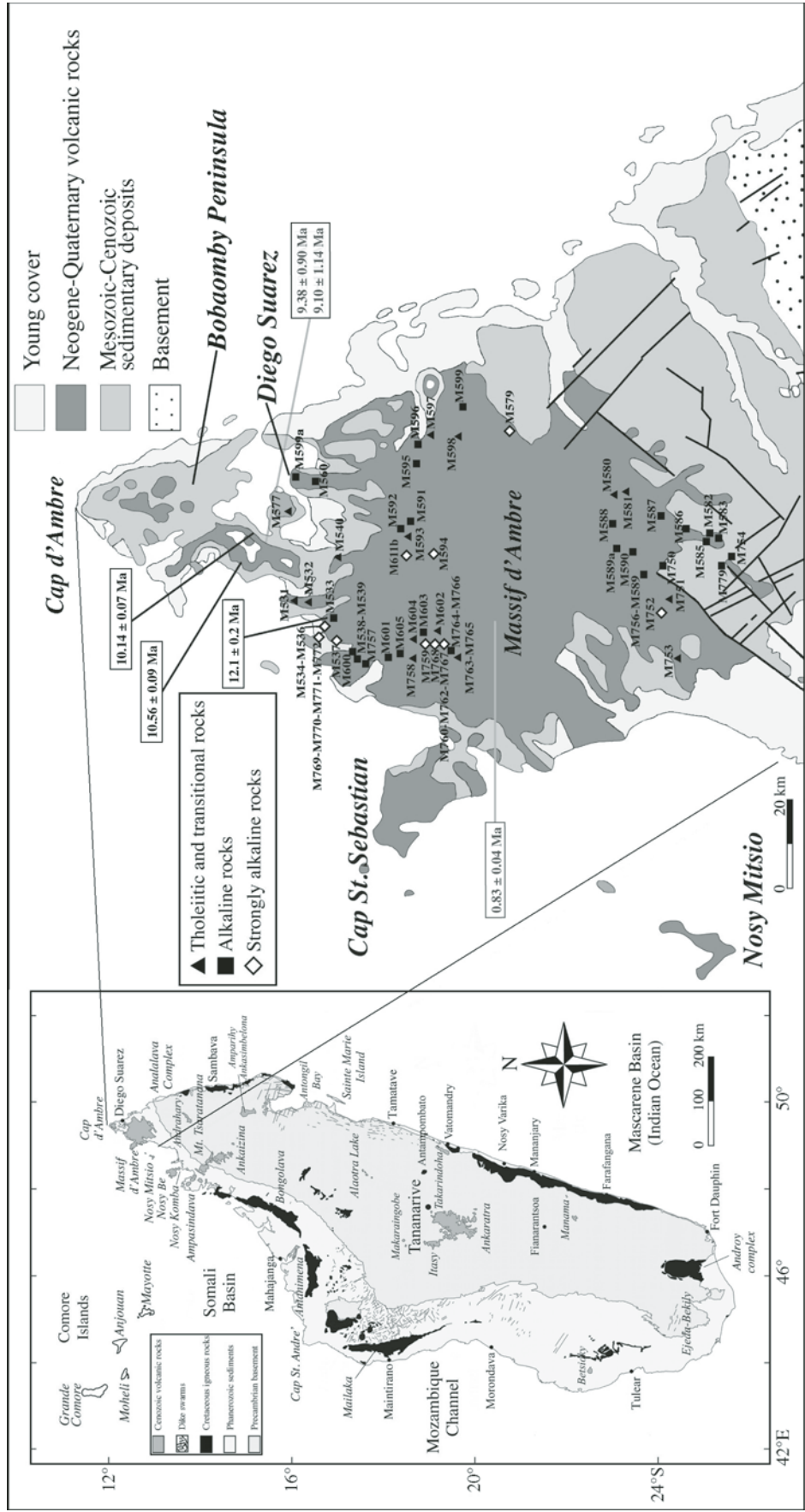


Figure 1. Geological sketch map of Massif d'Ambre area (redrawn after Besairie, 1964), and the locations of the studied samples. The global positioning system coordinates of the samples are given in Table 1. Previous K/Ar and new $^{40}\text{Ar}/^{39}\text{Ar}$ are indicated ($\pm 2\sigma$). The black lines in the sedimentary deposits and basement indicate tectonic lineaments.

Suarez and is elongated in a broadly N-S direction, corresponding to the extensional stress pattern of the area (Chorowicz et al., 1997). The Massif d'Ambre complex consists of lava flows, spatter and cinder cones, plugs, tuff rings, altered pyroclastic flows, and pyroclastic fall deposits, emplaced above the Mesozoic–Cenozoic sedimentary rocks of the Antsiranana (Diego) Basin. Spatter cones and tuff rings (the latter are often filled by lakes) are very common and represent the youngest volcanic activity of the complex. Many outcrops are rich in mantle-derived xenoliths (mostly spinel lherzolites) and xenocrysts.

Sampling of the Massif d'Ambre volcanic complex was carried out during our field trips in 2003, 2004, and 2006. We obtained samples from both western and eastern sides of the volcanic complex, with the main focus on lava flows, and additional sampling of scoria cones, welded ignimbrites, and localized plugs. Lava clasts of tuff-ring deposits (Lac Mahery) were also considered. The location of the samples (including global positioning system [GPS] coordinates) and their lithology are given in Figure 1 and Table 1.

ANALYTICAL TECHNIQUES

Sixty-three samples from Massif d'Ambre complex were studied in the present work (Table 1). They were ground in a steel jaw crusher. The rock chips were washed in distilled water and powdered in an agate mortar. Major and trace elements were analyzed by X-ray fluorescence (XRF) using first a Philips PW1400 and then an Axios Panalytical instrument at the University of Naples. Analytical uncertainties are in the order of 1%–2% for major elements and 5%–10% for trace elements. LOI (weight loss on ignition) was determined with standard gravimetric techniques, after igniting the powders at 1000 °C. Rare earth elements (REEs) and other trace elements were determined by inductively coupled plasma–mass spectrometry (ICP-MS) at ACTLABS, Ancaster, Ontario (for full details, see Melluso et al., 2007b). Mineral compositions were obtained at Centro Interdipartimentale Strumentazioni per Analisi Geomineralogiche, Naples, utilizing a JEOL JSM5310 electron microprobe. Further analytical details can be found in Melluso et al. (2009).

Ar-Ar Age Determinations and Sr-Nd-Pb Procedures

Clean plagioclase and feldspar crystals were analyzed at QUADLAB, Roskilde University. Samples were irradiated for 7 h in the Cd-shielded CLICIT (Cadmium-Lined In-Core Irradiation Tube) facility at the Oregon State University TRIGA reactor, along with Fish Canyon sanidine (28.02 Ma; Renne et al., 1998) as the neutron flux monitor. Step-heating experiments were carried out on plagioclase and alkali feldspar crystals, evenly spread as a single layer in 6 mm² sample pits, using an integrator lens and a 50 W Synrad CO₂ laser. Sample cleanup was conducted via a small-volume (450 cm³) all-metal extraction line with two water-cooled SAES GP-50 getter pumps and a cold finger at –115 °C. The argon isotopic analyses were made on a NU Instru-

ments multicollector Noblesse noble gas mass spectrometer, equipped with a faraday detector and three ion-counting electron multipliers. Analyses were carried out by measurement of ⁴⁰Ar and ³⁹Ar on the faraday detector, ³⁸Ar and ³⁷Ar on the axial electron multiplier, and ³⁶Ar on the low mass electron multiplier, with baselines being measured between each cycle. Blank measurements were made between each heating, and typical values were 1×10^{-16} moles for M/e = 40 and $<5 \times 10^{-18}$ moles for M/e = 36. Combined instrumental mass fractionation and detector intercalibration for the ⁴⁰Ar/³⁶Ar ratio (⁴⁰Ar on the faraday/³⁶Ar on the low mass electron multiplier) was corrected for by repeated measurement of 1.2×10^{-13} mole Ar aliquots from a calibrated air pipette, following similar procedures to those detailed by Brumm et al. (2010). Interference isotopes produced during irradiation were corrected using previously published values (Renne et al., 1998).

Sr and Nd isotope analyses were obtained at the Dipartimento di Scienze della Terra, University of Firenze, and the Istituto Nazionale di Geofisica e Vulcanologia (Osservatorio Vesuviano), Naples. Sample powders were dissolved in a HF-HNO₃-HCl mixture. Sr and Nd fractions were separated following standard chromatographic techniques. The total procedural blank at University of Firenze was <220 pg for Sr and <100 pg for Nd, making blank correction negligible. Mass spectrometric analyses were performed on a Thermo Finnigan Triton-Ti[®] thermal ionization mass spectrometer equipped with nine movable faraday cups. Pb isotope analyses were performed at the School of Ocean and Earth Science and Technology, University of Hawaii. Sample chips were leached with HF and dissolved successively in a HF-HNO₃-HCl mixture. Pb was then separated into both spiked and unspiked splits in a two-step elution with mixed HBr-HNO₃ solutions on 100 µl anion exchange columns. Mass spectrometric measurements were performed on a VG Sector multicollector thermal ionization mass spectrometer. Total procedural blank for Pb was <19 pg. Further details can be found in Melluso et al. (2009). The analytical procedures at the Dipartimento di Scienze della Terra (University of Firenze) and at the Osservatorio Vesuviano follow those already described by Avanzinelli et al. (2005), Melluso et al. (2009), and Di Renzo et al. (2007), respectively.

AGE DETERMINATIONS

Previous K-Ar age determinations yielded ages of 9.38 ± 0.90 Ma and 9.10 ± 1.14 Ma ($\pm 2\sigma$) for lava flows at Diego Suarez and 0.83 ± 0.04 Ma for a flow from the central part of the Massif d'Ambre (Emerick and Duncan, 1982, 1983). In addition, Emerick and Duncan (1982, 1983) reported ages of 7.32 ± 0.26 Ma for a mafic lava flow from Nosy Be and 10.15 ± 0.73 Ma for igneous rock from Nosy Komba. South of the Massif d'Ambre, ⁴⁰Ar-³⁹Ar ages on the Mount Tsaratanana volcanic rocks suggest that they were erupted from 17.5 to 16 Ma (Buchwaldt et al., 2005).

We obtained data from incremental-heating experiments on plagioclase separates of one hawaiite sample of Massif d'Ambre

TABLE 1. MAJOR (wt%) AND TRACE ELEMENT (ppm) ANALYSES AND GLOBAL POSITIONING SYSTEM COORDINATES OF THE MASSIF D'AMBRE ROCKS

Sample	Type	Lat. (°S)	Long. (°E)	SiO ₂	TiO ₂	Al ₂ O ₃	Fe ₂ O ₃	MnO	MgO	CaO	Na ₂ O	K ₂ O	P ₂ O ₅	LOI	Mg#	Sc	V	Cr	Ni	Cu	Zn	Rb	Sr	Y	Zr	Nb	Ba	
M587	Bsn	12.4926	49.1392	47.53	1.81	12.47	12.21	0.17	10.43	10.38	3.35	1.18	0.45	-0.08	66	30	246	662	257	71	95	41	500	24	152	45	371	
M766	Bsn			45.76	1.77	15.72	11.87	0.17	9.10	10.34	3.71	1.13	0.42	-0.06	63	29	233	453	262			36	509	23	145	46	384	
M767	Bsn			44.95	1.87	15.41	12.47	0.21	10.01	10.36	3.23	1.08	0.41	0.74	64	27	287	492	277			29	493	23	146	46	431	
M762	Bsn			43.89	2.32	14.72	12.35	0.20	11.19	10.21	3.15	1.33	0.65	2.14	67	30	268	449	256			43	685	30	199	57	592	
M764	Bsn			46.26	1.65	16.11	11.97	0.20	8.40	10.47	3.37	1.14	0.43	0.31	61	20	254	442	244			34	511	21	144	43	411	
M588	Bsn	12.4560	49.1191	46.27	2.50	11.71	12.95	0.20	10.07	10.43	3.46	1.58	0.82	1.19	64	27	239	371	183	55	98	62	874	35	251	75	693	
M579	Bsn	12.3462	49.2360	45.27	2.30	12.49	12.46	0.19	9.51	10.59	4.42	1.94	0.83	0.94	63	24	246	339	184	69	97	65	947	33	238	89	760	
M534	Bsn	12.1950	49.0359	44.33	2.35	12.16	12.12	0.19	9.14	10.89	4.51	1.30	0.59	2.42	63	32	288	227	91	58	93	35	820	34	276	94	730	
M768	Bsn	12.2908	49.0239	44.20	2.47	14.10	13.27	0.21	8.85	10.85	3.34	1.50	1.21	2.23	60	28	209	392	143			41	796	39	258	80	537	
M536	Bsn	12.1950	49.0359	44.98	2.48	10.96	11.65	0.17	11.03	12.59	4.03	0.61	0.40	1.10	68	43	323	779	178	94	79	29	590	27	180	60	411	
M752	Bsn	12.4955	49.0513	43.46	2.25	13.80	12.09	0.20	10.99	10.98	4.24	1.38	0.61	0.77	67	30	282	484	282			93	714	30	198	70	648	
M759	Bsn	12.2850	49.0233	44.66	1.89	14.48	12.47	0.19	10.87	10.73	3.29	1.06	0.37	0.27	66	27	239	528	313			31	461	21	138	39	387	
M760	Bsn	12.2933	49.0239	44.54	1.88	15.48	12.55	0.18	10.17	10.31	3.47	1.07	0.34	-0.23	65	28	241	499	272			36	470	24	144	44	336	
M594	Bsn	12.2857	49.1321	47.26	2.36	12.78	12.52	0.18	10.89	10.49	3.69	1.58	0.75	-0.04	66	27	231	594	284	142	92	47	771	31	219	61	530	
M770	Tph			45.55	2.37	15.09	11.98	0.21	7.04	12.33	3.44	1.37	0.62	1.74	57	33	308	336	127			40	765	26	189	66	632	
M769	Tph			46.46	2.88	16.14	13.41	0.19	5.37	8.95	3.79	2.01	0.80	1.22	47	21	176	116	88			61	865	36	266	73	577	
M538	Tph			47.87	2.30	13.07	11.98	0.18	8.25	8.35	4.24	1.89	0.66	1.21	61	23	198	397	185	61	103	65	838	35	290	75	611	
M611b	Tph	12.2099	49.0219	48.01	2.03	14.93	10.98	0.20	7.27	8.71	5.39	2.02	0.46	0.69	60	25	201	218	125	40	89	80	813	33	284	76	635	
M537	Pho-tpb	12.1963	49.0340	49.00	2.00	15.77	10.45	0.19	3.81	8.10	5.31	2.25	0.70	2.43	45	20	161	66	20	23	103	73	908	39	317	89	714	
M771	Tph-pho			53.48	1.16	19.13	7.74	0.20	2.19	4.94	6.70	4.14	0.32	4.31	39	3	135		13			142	656	28	430	102	867	
M772	Pho			59.28	0.18	19.15	5.27	0.21	0.43	1.71	7.99	5.69	0.08	2.00	16			532	285	184	242	244	39	1003	172	511		
M592	Alk bas	12.2609	49.1469	46.81	1.86	13.30	12.74	0.17	10.86	11.52	2.74	1.02	0.40	0.81	66	27	246	572	242			32	565	27	143	41	387	
M595	Alk bas	12.2679	49.2111	47.60	2.29	13.51	10.96	0.17	9.34	11.23	3.12	1.34	0.52	1.16	66	27	244	572	242			99	42	2007	26	163	41	582
M599	Alk bas	12.3105	49.2557	47.63	1.73	12.67	11.79	0.17	10.58	11.32	2.92	1.23	0.33	0.68	67	30	226	766	307	159	86	37	481	22	137	34	372	
M589	Alk bas			46.80	2.64	12.80	13.68	0.21	9.39	10.88	1.56	1.18	0.87	3.89	61	32	269	398	197	66	107	54	878	40	268	81	670	
M599a	Alk bas			48.22	1.60	13.38	13.00	0.17	11.21	10.57	2.82	0.80	0.27	0.25	66	28	229	719	356	166	95	26	412	26	118	30	439	
M560	Alk bas	12.1902	49.1689	47.03	1.61	12.83	13.33	0.18	10.89	10.25	2.77	0.74	0.37	0.46	65	28	231	574	315	62	89	25	404	22	115	28	229	
M591	Alk bas	12.2629	49.1496	45.95	1.98	12.78	12.84	0.17	10.78	11.50	2.58	0.95	0.43	1.66	65	26	249	541	292	167	93	52	573	26	148	42	351	
M603	Alk bas			48.33	1.69	13.59	11.43	0.18	10.70	9.99	3.07	0.76	0.26	1.03	68	31	213	507	243	60	97	21	437	24	125	31	269	
M590	Alk bas	12.4655	49.1138	47.31	1.72	12.86	12.82	0.18	10.63	10.12	3.03	0.91	0.42	0.04	65	30	230	675	284	74	97	34	471	21	135	36	394	
M586	Alk bas	12.5349	49.1262	47.99	1.74	13.29	11.80	0.17	9.87	10.34	3.12	1.21	0.47	0.04	65	24	217	637	247	69	83	42	521	35	152	45	503	
M582	Alk bas	12.5536	49.1194	48.05	1.82	13.18	11.83	0.17	9.78	10.50	3.00	1.20	0.47	0.16	65	27	233	630	240	72	85	43	685	40	150	43	398	
M585	Alk bas	12.5526	49.1204	48.13	1.94	13.05	11.97	0.17	9.49	10.41	3.10	1.26	0.48	0.17	64	32	246	613	224	73	88	42	518	40	161	48	453	
M583	Alk bas	12.5573	49.1156	47.85	2.11	12.94	12.03	0.17	9.44	10.95	2.83	1.09	0.58	0.94	64	29	254	575	191	80	93	32	534	28	170	52	404	
M605	Alk bas			49.55	1.70	14.19	11.68	0.18	8.63	9.59	3.54	0.71	0.23	0.64	62	28	228	398	183	44	100	24	353	24	124	26	197	

(Continued)

(Continued)

TABLE 1. MAJOR (wt%) AND TRACE ELEMENT (ppm) ANALYSES AND GLOBAL POSITIONING SYSTEM COORDINATES OF THE MASSIF D'AMBRE ROCKS (Continued)

Sample	Type	Lat. (°S)	Long. (°E)	SiO ₂	TiO ₂	Al ₂ O ₃	Fe ₂ O ₃	MnO	MgO	CaO	Na ₂ O	K ₂ O	P ₂ O ₅	LOI	Mg#	Sc	V	Cr	Ni	Cu	Zn	Rb	Sr	Y	Zr	Nb	Ba
M750	Alk bas	12.4803	49.0932	48.10	1.63	15.82	12.24	0.16	7.70	9.92	3.29	0.84	0.30	-0.40	59	26	191	354	196			22	386	22	123	29	248
M754	Alk bas	12.5743	49.0949	47.96	1.63	16.80	12.02	0.17	6.88	9.81	3.49	0.91	0.33	-0.34	56	19	216	340	190			30	395	25	126	31	273
M756	Alk bas			46.36	1.70	15.06	12.53	0.17	10.17	10.12	2.92	0.62	0.34	0.17	65	27	243	572	293			45	480	21	129	36	303
M757	Alk bas	12.2251	49.0059	46.77	1.75	14.54	12.90	0.17	9.98	10.13	2.82	0.68	0.26	0.05	64	25	222	523	257			20	377	52	112	26	430
M779	Alk bas	12.5623	49.0914	46.57	1.81	14.11	12.14	0.18	10.64	10.28	2.87	1.06	0.33	0.43	66	30	264	584	280			35	478	41	141	41	889
M589(a)	Alk bas	12.4560	49.1191	46.11	2.55	12.25	13.32	0.20	9.83	10.89	2.43	1.58	0.33	2.17	62	27	261	378	192	62	101	61	836	34	245	74	708
M600	Alk bas			47.06	1.60	14.12	12.03	0.24	10.28	10.35	3.31	0.74	0.27	0.39	66	32	236	557	274	72	91	24	357	23	119	26	246
M539	Haw			48.73	2.26	14.33	11.42	0.18	5.41	9.42	3.48	2.29	0.60	1.88	52	23	247	167	44	60	98	85	757	36	308	83	551
M601	Haw			49.87	2.52	15.45	10.73	0.19	6.20	8.13	4.17	2.09	0.66	1.54	57	22	190	128	84	39	99	79	842	34	328	81	678
M533	Haw	12.1952	49.0402	49.22	2.28	15.79	11.38	0.18	3.69	8.57	4.02	2.12	0.63	2.12	42	15	219	10	7	10	104	90	887	34	289	67	597
M540	Tho bas	12.1946	49.1127	46.35	1.52	12.26	13.59	0.18	10.36	10.05	2.07	0.52	0.23	2.88	63	24	220	598	245	61	104	15	309	21	99	22	155
M596	Tho bas	12.2734	49.2254	49.26	1.38	14.38	13.01	0.18	9.50	9.70	3.10	0.74	0.29	-0.08	62	22	200	525	247	127	94	27	380	20	114	23	210
M531	Tho bas	12.1829	49.0630	48.87	1.52	12.75	13.89	0.19	8.80	9.32	2.90	0.55	0.24	0.97	59	28	223	534	209	69	107	25	334	27	115	24	178
M597	Tho bas	12.2815	49.2346	51.70	1.67	13.94	12.78	0.18	8.72	8.63	2.85	0.88	0.23	0.29	61	25	204	465	271	156	114	44	342	45	135	26	414
M593	Tho bas	12.2582	49.1457	49.87	1.59	14.31	13.86	0.18	8.50	9.72	2.99	0.69	0.25	0.54	58	23	228	464	220	151	105	23	354	40	114	23	239
M532	Tho bas	12.1862	49.0585	49.43	1.49	13.96	13.21	0.17	7.62	9.38	3.10	0.63	0.27	0.74	56	22	219	505	206	66	113	21	360	37	120	25	270
M577	Tho bas	12.1521	49.1380	49.75	1.65	13.73	13.20	0.18	7.45	10.12	2.88	0.71	0.32	1.01	56	27	235	585	221	63	95	25	365	32	125	26	228
M581	Tho bas	12.4559	49.1564	49.20	1.29	15.47	12.55	0.17	7.43	9.98	3.15	0.53	0.25	-0.21	57	29	211	384	157	115	95	22	286	24	97	17	166
M580	Tho bas	12.4602	49.1607	49.18	1.22	15.25	13.08	0.17	7.40	9.81	3.22	0.42	0.24	-0.09	56	26	192	410	195	78	95	19	279	23	95	14	205
M598	Tho bas	12.2984	49.2369	51.41	1.63	15.14	12.95	0.17	6.42	9.91	3.10	0.77	0.19	0.03	53	24	218	311	93	149	117	32	325	36	115	21	414
M751	Tho bas	12.5041	49.0653	48.66	1.40	15.24	12.65	0.17	8.62	9.35	3.04	0.65	0.22	-0.30	61	26	195	408	255			22	314	24	108	22	182
M753	Tho bas	12.5109	49.0059	49.07	1.41	15.52	12.52	0.17	7.96	9.44	3.00	0.72	0.20	0.02	59	27	188	392	232			28	303	31	104	21	342
M758	Tho bas	12.2733	49.0153	49.33	1.51	15.88	12.22	0.17	7.37	9.35	3.26	0.68	0.22	0.08	58	24	220	341	174			18	325	24	104	22	189
M602	Rhy			76.99	0.16	13.63	1.19	0.02	0.30	0.43	2.93	4.33	0.03	1.59	36												
M604	Rhy			77.47	0.17	13.92	0.73	0.01	0.25	0.39	2.81	4.22	0.03	1.76	44	6											
M763	Rhy			77.73	0.22	13.37	0.74	0.01	0.28	0.25	1.57	5.80	0.02	3.18	46	5	26										
M765	Rhy			74.06	0.35	12.10	3.63	0.03	0.72	1.08	2.92	5.02	0.08	3.41	31	8	38										
Std	W2 meas			52.50	1.03	15.57	10.95	0.16	6.59	10.73	2.29	0.65	0.17			31.0	235.4	90.5	70.2	105.7	77.5	23.6	190.4	21.4	93.9	6.8	190.4
Std	W2 tab			52.68	1.06	15.45	10.79	0.17	6.37	10.86	2.20	0.63	0.14			35.0	262.0	93.0	70.0	103.0	77.0	20.0	194.0	24.0	94.0	7.9	182.0

Note: LOI—loss on ignition, Bsm—basanite, Tph—tephrite, Pho—phosphonite, Tph-pho—tephriphosphonite, Pho—phonolite, Alk bas—alkali basalt, Haw—hawaiite, Tho bas—tholeiitic and transitional basalt, Rhy—rhyolite. The major oxide analyses are recalculated to 100 wt% LOI-free; Mg#—molar Mg × 100/(Mg + Fe²⁺).

(M533) located close to the base of the volcanic succession in the northwestern part of the Massif d'Ambre. In addition, sanidine separates from phonolites of the Bobaomby Peninsula were also analyzed (M573, a dike from Lomoto in the central-western part of the Bobaomby Peninsula, and M559, a dike in the central-eastern part of the peninsula; see Melluso et al., 2007b; Table 2). Age spectra were examined for contiguous, concordant step ages comprising at least 40% of the gas released from the sample. Plateau ages shown in Figure 2 are the weighted mean (by variance) of three or more such concordant temperature steps and represent between 50% and 100% of the total ^{39}Ar released (Table 2). These are simple age spectra with well-defined plateaus: M533 = 12.1 ± 0.2 Ma; M559 = 10.14 ± 0.07 Ma; M573 = 10.56 ± 0.09 Ma. Isochron ages, calculated from the slope of linear regressions of $^{40}\text{Ar}/^{36}\text{Ar}$ versus $^{39}\text{Ar}/^{36}\text{Ar}$ step compositions, agree with the plateau ages, and the initial $^{40}\text{Ar}/^{36}\text{Ar}$ ratios are within error of atmosphere value of 295.5 (Table 2).

CLASSIFICATION AND PETROGRAPHY

The rocks of Massif d'Ambre are alkali basalts, tholeiitic/transitional basalts, hawaiites, basanites, tephrites, rhyolites, and phonolites, according to the total alkali-silica (TAS) diagram (Fig. 3) and CIPW norms. Alkali basalts and basanites are the dominant lithotypes. The chemical affinity of the rocks of Massif d'Ambre is sodic. Basanites and tephrites have normative nepheline contents from 5.5% to 18.2%. The alkali basalts have normative nepheline contents ranging between 0.19% and 4.96%. The tholeiitic/transitional basalts are olivine-hypersthene normative ($\text{hy} = 0.95\% - 22.02\%$). The rhyolites are peraluminous.

Most analyzed samples are very fresh, as also shown by low LOI values, ranging from -0.4% to 2.2% (Table 1), and indirectly by the tight correlation between K_2O and Rb, two highly mobile elements. Some samples show evidence of postmagmatic alteration, as indicated by the presence of calcite, zeolites, and iddingsite.

Basanites are moderately to strongly porphyritic, with phenocrysts of idiomorphic or subidiomorphic olivine. Olivine phenocrysts sometimes show an iddingsite rim. Clinopyroxene (usually showing purple Ti-rich rim) is rarer as a phenocryst, but, in some cases (e.g., sample M766), it is more abundant than olivine. Opaque oxides are found as phenocrysts or included in olivine. The groundmass is usually very fine grained and made up of clinopyroxene, plagioclase, oxides, and rare feldspathoids. Basanites often carry mantle-derived xenoliths (lherzolites, harzburgites, dunites, and wehrlites) or disrupted and kinked olivine xenocrysts.

Tephrites show phenocrysts of olivine, with rare clinopyroxene and plagioclase. Amphibole is found both as phenocryst and as microlite in the groundmass. This latter is made up also of olivine, clinopyroxene, feldspar, and opaque oxides.

Alkali basalts have olivine (with chromite inclusions) as the dominant phenocryst phase, set in a pseudo-ophitic to intersertal matrix composed of olivine, plagioclase, alkali feldspar, nepheline, sodalite, clinopyroxene, and opaque oxides. Zoned clinopyroxene sometimes occurs as phenocryst phase. Plagioclase is

the dominant feldspar and generally shows normal zoning. Large euhedral plagioclase laths often enclose subhedral or anhedral clinopyroxene crystals. Apatite is accessory. Analcime, zeolite, and calcite are secondary minerals. Sample M589a is porphyritic with phenocrysts of olivine (also as rounded xenocrysts with kink banding) and clinopyroxene set in a fine-grained or aphanitic matrix composed by dark glass, olivine, clinopyroxene, plagioclase, and opaque oxides. Sample M589 is a scoriaceous lava with phenocrysts of olivine and clinopyroxene. The groundmass is almost aphanitic and has olivine, plagioclase, clinopyroxene, opaque oxide, and glass.

Hawaiites are porphyritic and contain phenocrysts of olivine, clinopyroxene, and plagioclase. Microlites of brown mica are present in the groundmass, along with clinopyroxene, plagioclase, alkali feldspar, olivine, titanomagnetite, and apatite. Cr-rich spinel inclusions are present in olivine phenocrysts.

Tholeiitic (and transitional) basalts have subophitic to intersertal textures and contain olivine, clinopyroxene, plagioclase, and opaque oxides. Olivine is the most abundant phenocryst phase, often containing Cr-spinel inclusions. Clinopyroxene and plagioclase are rare phenocrysts but are ubiquitous as subophitic or intersertal phases in the mesostasis. Sample M597 is porphyritic, with phenocrysts of olivine, augite, and plagioclase set in a fine-grained groundmass of olivine, augite, pigeonite, plagioclase, alkali feldspar, apatite, opaque oxides, and silicic glass. Zeolites and calcite are secondary, as is iddingsite around olivine.

Tephriphonolites and phonotephrites are porphyritic, with phenocrysts of olivine, clinopyroxene, amphibole, and plagioclase. The groundmass is made up of amphibole, feldspar, clinopyroxene, and opaque oxides. Small mafic enclaves made up of plagioclase, clinopyroxene, amphibole, and magnetite are found in phonotephrites.

Phonolites are porphyritic, with phenocrysts of alkali feldspar (rarely plagioclase), opaque oxides, and deep green clinopyroxene (which was found also as an inclusion in feldspar phenocrysts). The groundmass is made up of green clinopyroxene, nepheline, alkali feldspar, and opaque oxides.

Rhyolites were found as pyroclastic rocks and more massive lithofacies (lavas and plugs). Sample M763 is aphyric with rare relicts of crystals set in glassy matrix with spherulitic texture. These spherulites are likely composed by alkali feldspar and SiO_2 polymorph. Sample M765 is a welded crystal-rich rhyolitic tuff with phenocrysts of plagioclase, clinopyroxene, and brown mica set in a glassy finely devitrified matrix composed of quartz, alkali feldspar, and brown mica. Apatite and zircon are accessories. Sample M602 is representative of a plug with well-developed columnar jointing. It is aphyric, with microlites of feldspar, brown mica, and plagioclase set in a fine-grained to cryptocrystalline groundmass rich in quartz. Monazite and xenotime are very rare accessories. Sample M604 belongs to a previously unreported twin plug (the other is represented by sample M602), and it has microlites of quartz, brown mica, alkali feldspar, and accessories, set in glassy matrix with submicroscopic intergrowths of

TABLE 2. RELATIVE Ar ISOTOPIC ABUNDANCES AND DERIVED AGES FOR SAMPLES OF MASSIF D'AMBRE AND BOBAOMBY

Lab ID	⁴⁰ Ar (moles)	³⁹ Ar (mV) ±σ	³⁸ Ar (mV) ±σ	³⁷ Ar (mV) ±σ	³⁶ Ar (mV) ±σ	% ⁴⁰ Ar*	Age (Ma) (±1σ)
Sample: M533; J = 1.832 × 10 ⁻³ ± 9.8 × 10 ⁻⁷ ; plagioclase							
1569-01A	1.75E-13	219.319 ± 0.028	6.431 ± 0.016	0.2090 ± 0.0004	30.776 ± 0.028	0.6731 ± 0.0011	11.73 ± 0.45
1569-01B	9.97E-14	124.680 ± 0.022	9.793 ± 0.015	0.1801 ± 0.0004	33.736 ± 0.025	0.3109 ± 0.0009	11.95 ± 0.16
1569-01C	1.09E-13	135.835 ± 0.021	8.631 ± 0.016	0.1721 ± 0.0004	31.908 ± 0.025	0.3578 ± 0.0008	12.47 ± 0.20
1569-01D	4.81E-14	60.119 ± 0.023	1.755 ± 0.016	0.0562 ± 0.0002	13.092 ± 0.015	0.1855 ± 0.0006	11.94 ± 0.55
1569-01E	3.34E-14	41.703 ± 0.021	0.787 ± 0.015	0.0338 ± 0.0002	9.396 ± 0.016	0.1338 ± 0.0005	12.23 ± 0.95
1569-01F	1.01E-14	12.678 ± 0.018	0.109 ± 0.014	0.0190 ± 0.0002	36.630 ± 0.400	0.0407 ± 0.0003	11.71 ± 0.39
Plateau age (steps A to F) = 12.1 ± 0.2 (±2σ), MSWD = 1.2. Isochron age = 12.1 ± 0.5 Ma, MSWD = 1, ³⁶ Ar/ ³⁹ Ar (intercept) = 295 ± 3							
Sample: M559; J = 1.835 × 10 ⁻³ ± 9.5 × 10 ⁻⁷ ; alkali feldspar							
1570-01A	2.46E-13	307.226 ± 0.027	0.342 ± 0.015	0.2018 ± 0.0004	0.772 ± 0.004	1.0445 ± 0.0008	12.26 ± 0.45
1570-01B	2.89E-13	361.422 ± 0.033	5.025 ± 0.016	0.2954 ± 0.0008	0.710 ± 0.005	1.1878 ± 0.0009	6.89 ± 0.95
1570-01C	1.43E-13	178.938 ± 0.025	21.912 ± 0.018	0.4619 ± 0.0006	2.175 ± 0.008	0.3776 ± 0.0005	37.74 ± 0.08
1570-01D	7.52E-14	93.948 ± 0.021	10.908 ± 0.015	0.2586 ± 0.0004	0.437 ± 0.004	0.2052 ± 0.0004	10.09 ± 0.09
1570-01E	7.63E-14	95.435 ± 0.022	14.709 ± 0.015	0.3159 ± 0.0005	0.525 ± 0.004	0.1703 ± 0.0004	47.30 ± 0.13
1570-01F	5.90E-14	73.733 ± 0.020	12.915 ± 0.016	0.2728 ± 0.0004	0.449 ± 0.004	0.1162 ± 0.0003	10.08 ± 0.05
1570-01G	4.04E-14	50.465 ± 0.018	8.015 ± 0.015	0.1966 ± 0.0004	0.337 ± 0.003	0.0853 ± 0.0003	50.09 ± 0.41
1570-01H	2.60E-14	32.439 ± 0.019	4.237 ± 0.015	0.0952 ± 0.0003	0.185 ± 0.003	0.0634 ± 0.0002	42.28 ± 0.68
1570-01I	2.32E-14	29.056 ± 0.020	3.570 ± 0.014	0.0736 ± 0.0002	0.212 ± 0.003	0.0596 ± 0.0002	39.46 ± 0.60
1570-01J	2.02E-14	25.248 ± 0.019	6.168 ± 0.016	0.0862 ± 0.0003	0.200 ± 0.004	0.0198 ± 0.0001	76.89 ± 0.04
Plateau age (steps C to F) = 10.1 ± 0.1 (±2σ), MSWD = 0.4. Isochron age (plateau steps) = 10.0 ± 0.2 Ma, MSWD = 0.3, ⁴⁰ Ar/ ³⁹ Ar (intercept) = 297 ± 5							
Sample: M573; J = 1.829 × 10 ⁻³ ± 9.2 × 10 ⁻⁷ ; alkali feldspar							
1573-01A	2.12E-13	265.381 ± 0.027	0.332 ± 0.016	0.1783 ± 0.0004	0.511 ± 0.004	0.8983 ± 0.0007	10.78 ± 0.35
1573-01B	1.80E-13	225.147 ± 0.025	1.775 ± 0.015	0.1704 ± 0.0004	0.543 ± 0.005	0.7525 ± 0.0012	5.25 ± 1.79
1573-01C	1.44E-13	180.289 ± 0.024	17.942 ± 0.015	0.3892 ± 0.0006	1.498 ± 0.006	0.4076 ± 0.0010	33.25 ± 0.99
1573-01D	7.43E-14	92.876 ± 0.022	11.907 ± 0.016	0.2625 ± 0.0004	0.613 ± 0.005	0.1787 ± 0.0004	43.20 ± 1.08
1573-01E	7.24E-14	90.539 ± 0.022	12.325 ± 0.026	0.3206 ± 0.0005	0.749 ± 0.004	0.1716 ± 0.0004	44.06 ± 0.65
1573-01F	8.00E-14	99.970 ± 0.022	12.364 ± 0.016	0.3252 ± 0.0008	0.600 ± 0.005	0.2038 ± 0.0004	39.81 ± 0.59
1573-01G	7.72E-14	96.504 ± 0.024	11.908 ± 0.016	0.3532 ± 0.0006	0.599 ± 0.004	0.1977 ± 0.0004	39.50 ± 0.08
1573-01H	4.07E-14	50.934 ± 0.023	3.836 ± 0.023	0.1084 ± 0.0003	0.285 ± 0.004	0.1321 ± 0.0003	23.38 ± 0.21
1573-01I	3.41E-14	42.591 ± 0.021	1.745 ± 0.014	0.0590 ± 0.0002	0.348 ± 0.003	0.1261 ± 0.0003	12.57 ± 0.09
1573-01J	2.30E-14	28.795 ± 0.019	7.193 ± 0.017	0.1006 ± 0.0003	0.559 ± 0.009	0.0146 ± 0.0001	85.21 ± 11.22
Plateau age (steps E to I) = 10.56 ± 0.09							

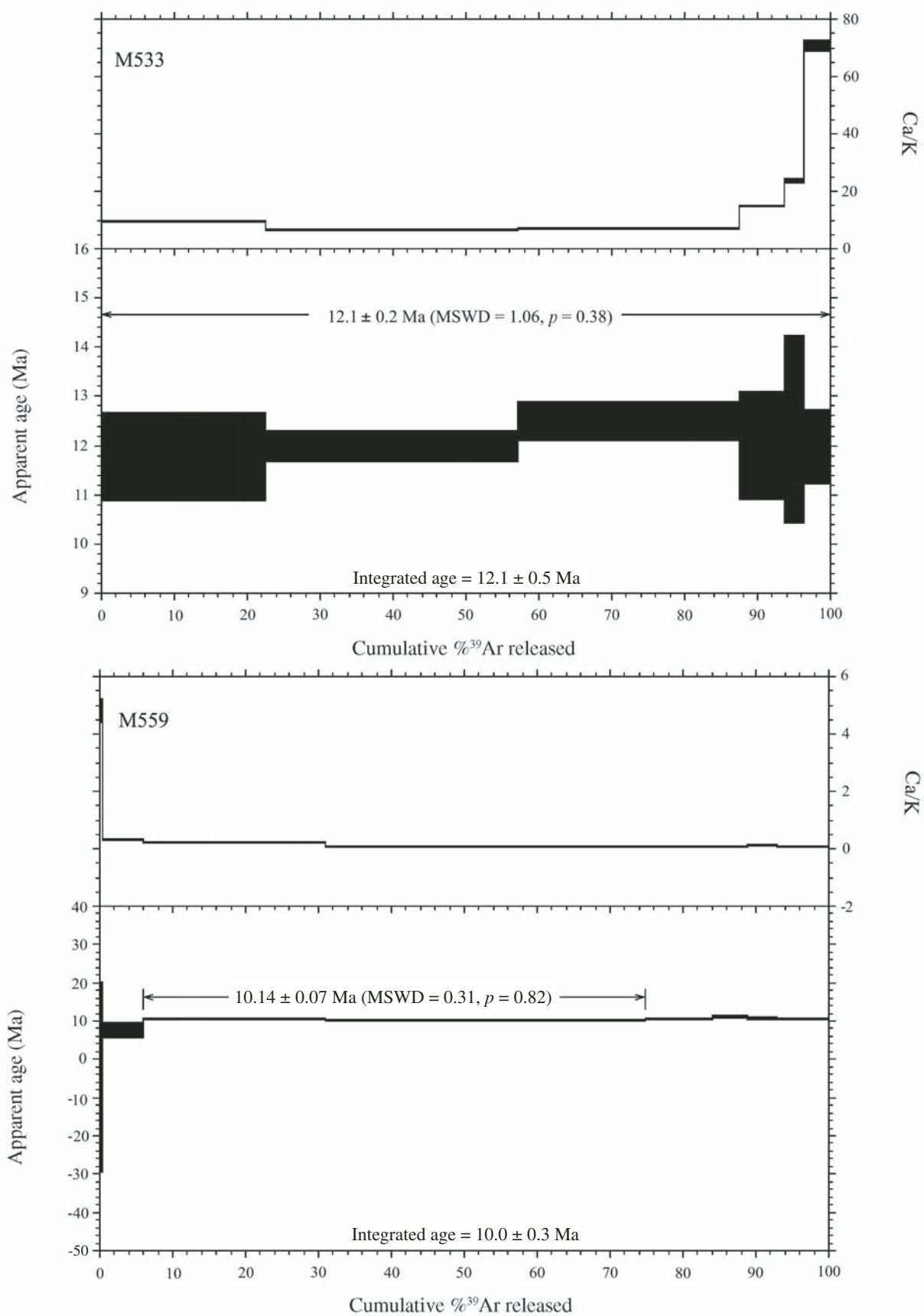


Figure 2 (Continued on following page). The ³⁹Ar release spectra for feldspar of samples M533 (Massif d'Ambre), M559, and M573 (Bobaomby). Errors on plateau (>50% ³⁹Ar released) ages are quoted as 2σ. MSWD—mean square of weighted deviates.

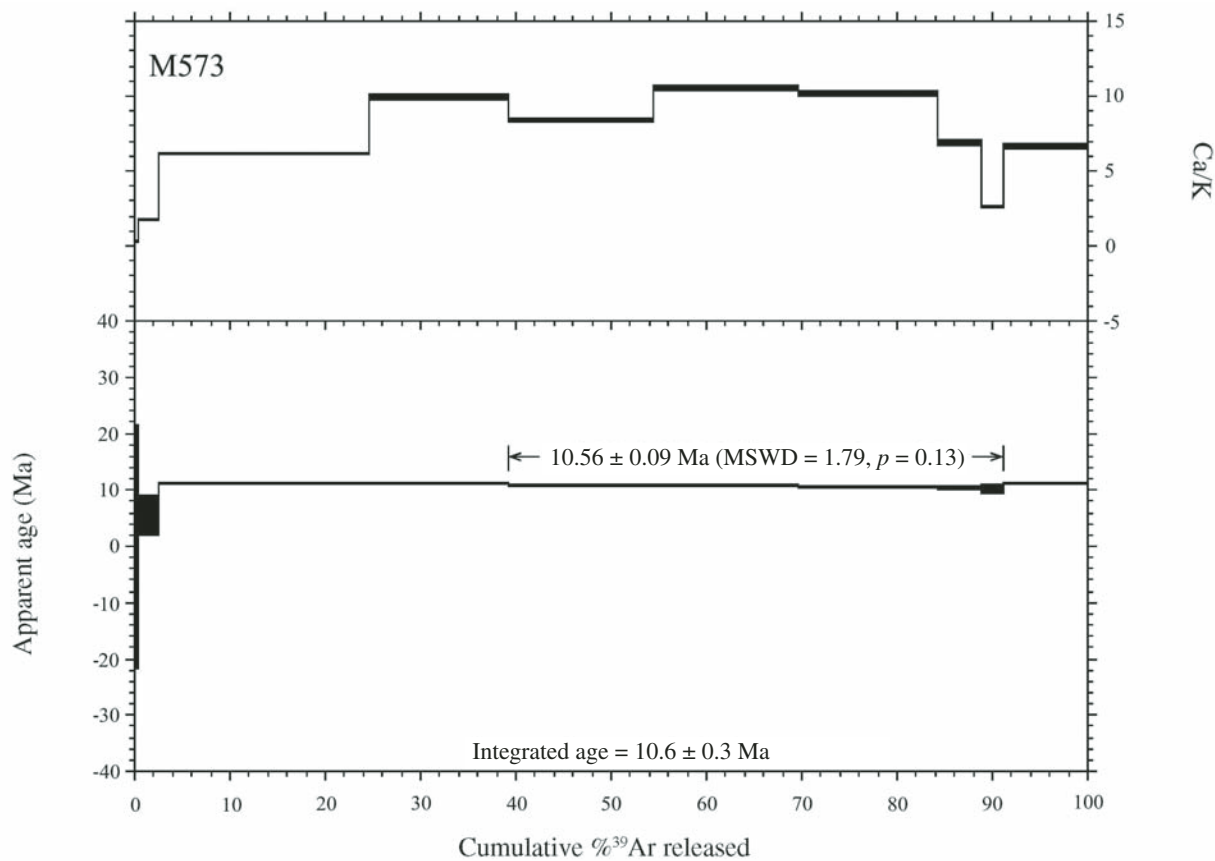


Figure 2 (Continued).

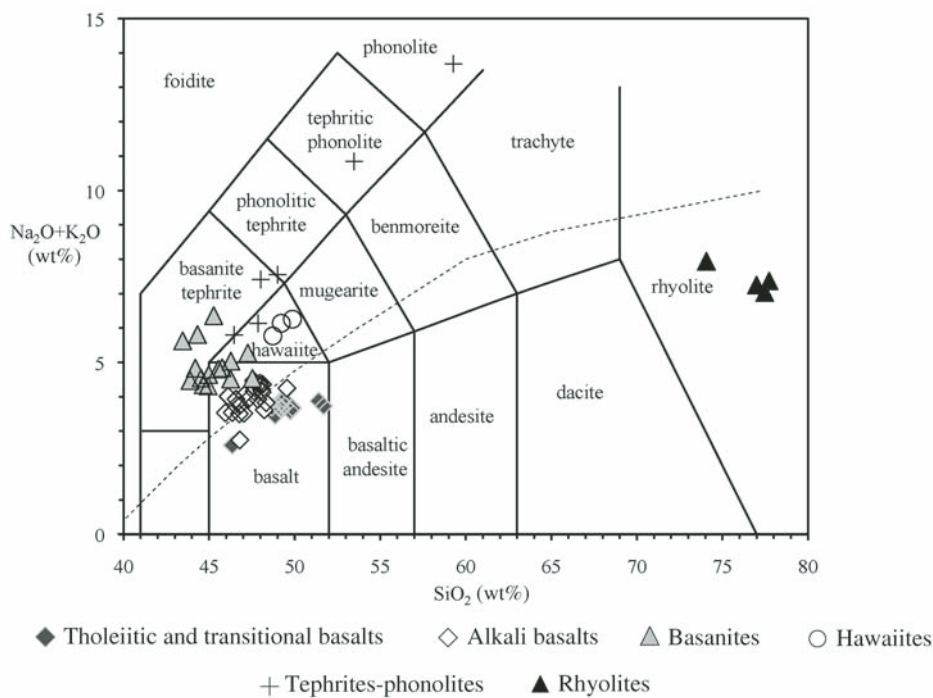


Figure 3. Total alkali-silica classification diagram (Le Bas et al., 1986) of the Massif d'Ambre rocks.

quartz and alkali feldspar. Devitrification structures (spherulites) are common.

MINERAL COMPOSITIONS

The mineral chemical data on the main lithotypes of Massif d'Ambre are reported in Tables 3–9.

Olivine

Olivine is the main phenocryst phase of the basanites and alkali basalts. The phenocrysts have a compositional range from Fo_{88} to Fo_{61} in basanites, from Fo_{86} to Fo_{49} in alkali basalts, and from Fo_{85} to Fo_{47} in tholeiitic/transitional basalts (Table 3; Fig. 4A). Similar compositional ranges have been observed also in hawaiites, tephrites, and intermediate rocks (Fo_{85} – Fo_{64}). Olivine occurs also in the groundmass of many mafic types, including tholeiitic basalts. Olivine in the groundmass of tholeiitic/transitional basalts shows a continuous range from Fo_{59} to Fo_{14} . MnO ranges from 0.01 to 1.72 wt%, and CaO ranges from 0.1 to 1.89 wt%, with the highest values found in the most Fe-rich varieties. The nickel oxide ranges from 0.03 to 0.59 wt%, with just a few phenocryst cores having more than 0.6 wt% NiO.

Pyroxene

Pyroxene of basanites, tephrites, tephritic phonolite, and phonolite ranges from diopside through Ti-salite to ferro-salite ($\text{TiO}_2 = 1.4$ – 5.3 wt%; $\text{Mg\#} = 41$ – 81 , where $\text{Mg\#} = \text{Mg} \times 100/[\text{Mg} + \text{Fe} + \text{Mn}]$), with very rare Na-pyroxene present as groundmass microlite in phonolites ($\text{Mg\#} = 0$ – 5 ; Na_2O up to 9.85 wt%). The basanites have generally more Al- and Ti-rich salite (up to 6.7 wt% Al_2O_3 and up to 3.5 wt% TiO_2 ; ~15% of $\text{CaTiAl}_2\text{O}_6$ molecule) compared to alkali basalts. Clinopyroxene of alkali basalts and hawaiites is diopside and salite, with maximum TiO_2 and Al_2O_3 contents of 4.32 and 6.19 wt%, respectively (sample M585). Augite-ferroaugite is the Ca-rich clinopyroxene of tholeiitic basalts ($\text{Ca}_{45}\text{Mg}_{39}\text{Fe}_{16}$ to $\text{Ca}_{29}\text{Mg}_{45}\text{Fe}_{29}$) and is accompanied by rare groundmass pigeonite ($\text{Ca}_8\text{Mg}_{55}\text{Fe}_{37}$

to $\text{Ca}_{18}\text{Mg}_{39}\text{Fe}_{43}$). Augite of tholeiitic-transitional magma types has the lowest Ti and Al contents (up to 1.7 wt% TiO_2 and 4.1 wt% Al_2O_3 , respectively). The clinopyroxene compositions are thus highly distinctive of the different magma types (Figs. 4B–4C). The rhyolitic ignimbrites have loose xenocrysts of titaniferous salite ($\text{Ca}_{47-48}\text{Mg}_{40-41}\text{Fe}_{11-12}$; TiO_2 from 0.9 to 1.5 wt%; $\text{Mg\#} = 77$ – 79), which are clearly fragments of mafic alkaline rocks buried in the feeding system (Table 4; Fig. 4B). No pyroxene was found in the rhyolitic plugs.

Feldspar

Plagioclase phenocrysts occur in all the studied rocks, excluding basanites. The phenocrysts are usually zoned and have a large compositional range in the tholeiitic basalts (An_{68-58}), alkali basalts and hawaiites (An_{78-17}), and tephritic phonolite (An_{75-66}). Plagioclase in the groundmass of basanites and tephrites shows a significant compositional range (An_{72-35}). Alkali feldspar is groundmass mineral in basalts, hawaiites, tephritic phonolites, and a phenocryst phase in phonolites ($\text{An}_8\text{Ab}_{79}\text{Or}_{13}$ to $\text{An}_0\text{Ab}_{51}\text{Or}_{49}$) (Table 5; Fig. 4D). The rhyolites have plagioclase (An_{47-16}) and alkali feldspar ($\text{An}_2\text{Ab}_{42}\text{Or}_{56}$ to $\text{An}_4\text{Ab}_{46}\text{Or}_{50}$).

Feldspathoids

Nepheline is present as groundmass mineral in alkaline and strongly alkaline rocks. Nepheline is Si-rich ($\text{Ne}_{76}\text{Ks}_9\text{Q}_{15}$ to $\text{Ne}_{67}\text{Ks}_{11}\text{Q}_{22}$, components in wt%), has high Na# (0.88–0.94, where $\text{Na\#} = \text{molar Na}/[\text{Na} + \text{K}]$), and has variable Sr (0.07–0.95 wt% SrO) (Table 5). Sodalite (Cl = 6.2–7.0 wt%) is present as phenocryst phase in phonolites, and as groundmass phase in tephrites and alkali basalts. It is low in K (up to 3 wt% K_2O in a tephrite) and Ca (up to 1.25 wt% CaO; Table 5).

Oxides

Chromium-rich spinel is found as inclusions in olivine phenocrysts and has a wide range of Cr# ($\text{Cr\#} = 11$ – 73 , where $\text{Cr\#} = \text{molar Cr} \times 100/[\text{Cr} + \text{Al}]$; Cr_2O_3 up to 32.3 wt%; Table 6).

TABLE 3. REPRESENTATIVE MICROPROBE ANALYSES OF OLIVINE, MASSIF D'AMBRE (wt%)

Sample				SiO_2	FeO	MnO	MgO	CaO	NiO	Sum	Fo
M579	Bsn	Pheno	Core	41.23	11.27	0.13	46.97	0.28	0.44	100.3	88.0
M534	Bsn	Rim		36.56	32.63	0.60	28.81	0.57	0.25	99.4	60.7
M770	Tph	Gndmss		36.05	34.86	0.69	26.33	0.70		98.6	56.9
M611b	Tph	Gndmss		31.85	57.70	1.59	9.36	0.70	0.01	101.2	21.9
M585	Alk bas	Gndmss		31.55	55.80	1.72	9.23	1.01		99.3	22.2
M560	Alk bas	Pheno	Core	40.56	16.10	0.01	44.01	0.28	0.34	101.3	83.0
M560	Alk bas	Pheno	Rim	36.18	43.11	0.32	23.08	0.55	0.34	103.6	85.6
M533	Haw	Pheno	Core	39.85	14.24	0.16	44.35	0.46	0.30	99.4	84.6
M751	Tho bas	Pheno	Rim	35.50	43.72	0.51	21.67	0.52	0.30	102.2	46.6
M597	Tho bas	Pheno	Core	39.71	13.32	0.07	43.37	0.24	0.81	97.5	85.2
M598	Tho bas	Gndmss		36.14	35.13	0.51	28.41	0.22	0.03	100.5	58.7
M598	Tho bas	Gndmss		30.01	61.04	1.05	5.53	0.72		98.4	13.7

Note: Fo—atomic $100 \times \text{Mg}/(\text{Mg} + \text{Fe} + \text{Mn})$. Bsn—basanite, Tph—tephrite, Alk bas—alkali basalt, Haw—hawaiite, Tho bas—tholeiitic and transitional basalt, Pheno—phenocryst, Gndmss—groundmass.

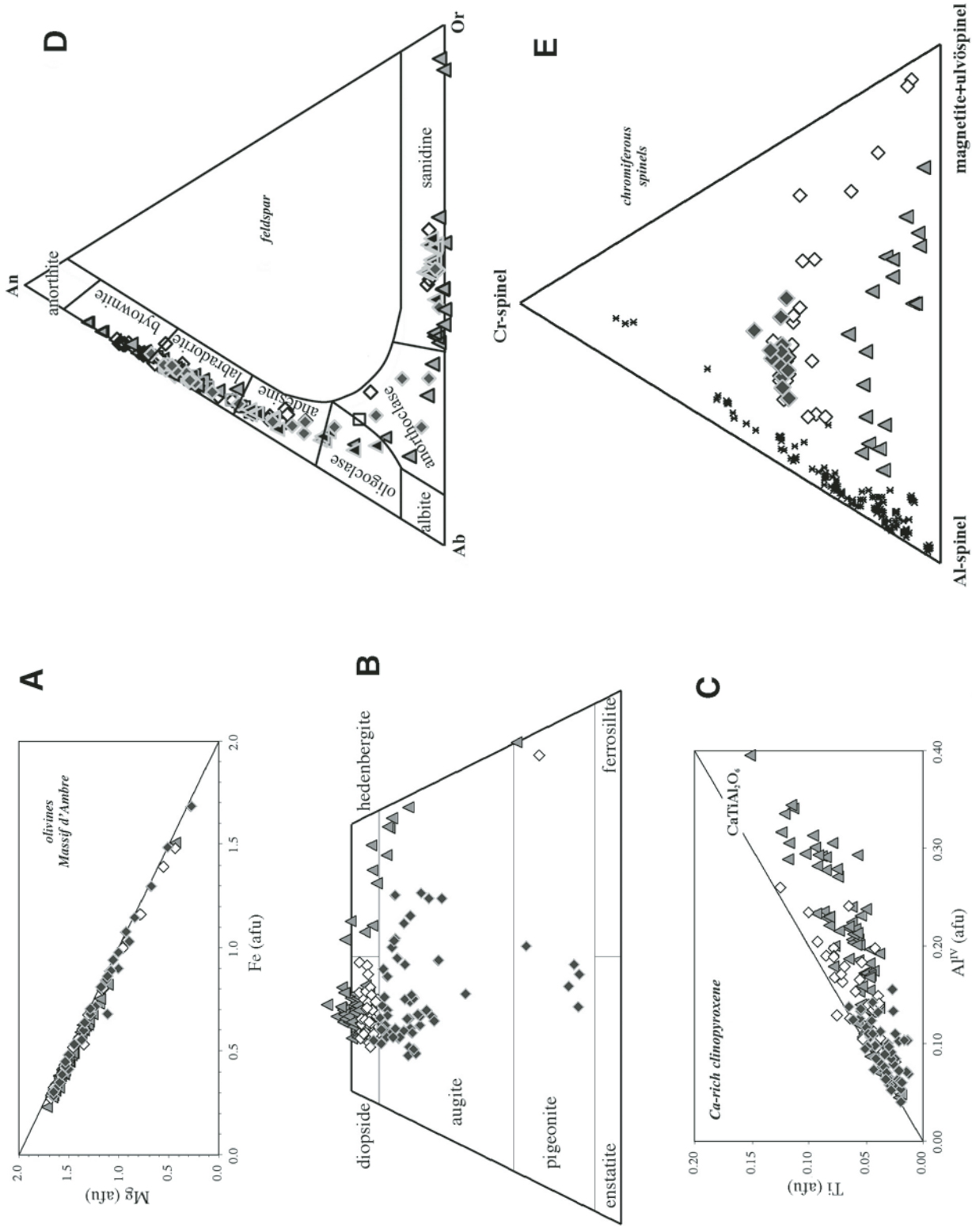


Figure 4. (A) Mg-Fe (afu, atoms per formula unit) diagram for olivine from the Massif d' Ambre rocks. (B) Composition of pyroxene in the rocks of Massif d' Ambre. Ca-poor pyroxene and two different Ca-rich pyroxene types have been found. (C) Ti-Al (afu) diagram for Ca-rich clinopyroxene of the Massif d' Ambre rocks. (D) Composition of plagioclase and alkali feldspar of Massif d' Ambre rocks. (E) Chemical variation of chromium-bearing spinels in the mafic rocks of Massif d' Ambre. The compositional range of mantle spinels of the area (Rocco, 2009) is shown for comparison.

TABLE 4. REPRESENTATIVE MICROPROBE ANALYSES OF PYROXENES, MASSIF D'AMBRE (wt%)

Sample				SiO ₂	TiO ₂	Al ₂ O ₃	FeO	MnO	MgO	CaO	Na ₂ O	Cr ₂ O ₃	Sum	Ca	Fe*	Mg	Mg#
M534	Bsn	Micropheno	Core	50.77	1.39	4.34	6.22	0.27	14.08	23.67	0.37	0.12	101.2	49.0	10.5	40.5	79.5
M534	Bsn	Micropheno	Core	47.35	1.93	3.59	16.69	0.38	6.66	20.49	1.09		98.2	47.6	30.9	21.5	41.0
M579	Bsn	Micropheno	Core	49.54	1.96	4.43	5.80	0.10	13.69	23.54	0.32	0.24	99.6	49.9	9.8	40.3	80.5
M579	Bsn	Micropheno	Core	44.48	3.61	7.96	6.92	0.13	10.99	23.24	0.61	0.34	98.3	52.8	12.5	34.7	73.5
M770	Tph	Gndmss		42.03	5.31	10.34	7.78	0.19	10.25	22.17	0.74		98.8	52.0	14.6	33.4	69.6
M771	Tph-pho	Gndmss		48.45	0.28	0.91	26.91	1.81	0.61	15.28	4.31		98.6	39.6	58.2	2.2	3.6
M772	Pho	Inclusion		51.02	0.44	1.08	27.68	0.73	0.00	5.39	9.85	0.13	96.3	19.6	80.4	0.0	0.0
M560	Alk bas	Gndmss		48.22	2.77	4.98	10.08	0.31	11.91	21.78	0.56	0.18	100.8	46.9	17.5	35.7	67.1
M585	Alk bas	Micropheno	Core	51.99	1.36	2.86	6.29	0.20	14.69	22.49	0.31	0.57	100.8	46.86	10.56	42.58	80.1
M590	Alk bas	Gndmss		51.01	1.53	3.57	6.98	0.21	13.78	22.16	0.46	0.45	100.1	47.2	12.0	40.8	77.4
M533	Haw	Pheno	Rim	48.29	2.46	4.52	9.34	0.27	11.82	21.50	0.62	0.16	99.0	47.3	16.5	36.2	68.7
M601	Haw	Gndmss		49.80	1.83	3.07	8.29	0.21	12.78	21.46	0.49	0.17	98.1	46.8	14.5	38.8	72.8
M751	Tho bas	Oikocrysts	Rim	49.86	1.39	3.95	8.92	0.31	13.74	20.47	0.22	0.56	99.4	43.8	15.4	40.8	72.6
M597	Tho bas	Gndmss		52.08	0.67	2.98	16.05	0.42	13.72	12.93	0.45		99.3	28.8	28.7	42.5	59.7
M597	Tho bas	Gndmss		51.73	0.34	0.63	22.18	0.57	19.33	3.86	0.21	0.04	98.9	8.0	36.6	55.4	60.2
M597	Tho bas	Gndmss		51.70	0.62	0.85	25.61	0.44	13.24	8.37	0.25	0.17	101.3	17.8	43.2	39.1	47.5
M597	Tho bas	Pheno	Rim	52.06	0.76	4.53	6.81	0.20	16.30	18.42	0.29	0.66	100.0	39.6	11.7	48.7	80.6
M598	Tho bas	Gndmss		47.63	0.93	1.61	24.92	0.47	6.95	16.44	0.63	0.05	99.6	35.8	43.2	21.0	32.8
M577	Tho bas	Gndmss		50.02	1.55	3.03	9.67	0.13	13.18	21.11	0.41		99.1	44.8	16.2	38.9	70.6
M765	Rhy	Pheno	Core	48.42	1.44	5.32	6.72	0.10	13.11	21.66	0.43	0.83	98.0	47.9	11.8	40.3	77.4

Note: Ca, Fe* (Fe + Mn), and Mg are in mol%; Mg# = $Mg \times 100 / (Mg + Fe + Mn)$. Bsn—basanite, Tph—tephrite, Tph-pho—tephriphonolite, Pho—phonolite, Alk bas—alkali basalt, Haw—hawaiite, Tho bas—tholeiitic and transitional basalt, Rhy—rhyolite, Micropheno—microphenocryst, Gndmss—groundmass, Pheno—phenocryst.

Alkali and tholeiitic basalts have spinels distinctly more rich in Cr than those of basanites (Fig. 4E). This feature is also noteworthy because the spinels found in the basanites systematically plot in an area believed to be forbidden due to a solvus between Fe-Ti- and Al-Cr-bearing spinels (e.g., Barnes and Roeder, 2001). At any rate, the lower Cr contents of spinels in the basanites clearly indicate different and unrelated parental magmas with respect to the less silica-undersaturated mafic rocks. These contrasting chemical compositions of spinel in differently silica-undersaturated rocks have no relationships with the Cr/Al ratios of the host rocks or with composition of mantle spinels in the area (Rocco, 2009; Fig. 4E).

The Ti-magnetite has from 7 to 87 mol% ulvöspinel and widely variable Al₂O₃ (from 0.3 to 10.7 wt%) (Table 6). Ilmenites have a limited range of solid solution toward hematite (ilmenite from 83 to 96 mol%) and have low Al₂O₃ (0.1–0.5 wt%) and variable MgO (0.3–5.9 wt%) contents. Ti-magnetite and ilmenite pairs have a large range of equilibration temperatures (from 1188 °C to 596 °C) and oxygen fugacity (from –8.4 to –21.3 log units). In the temperature-log *f*O₂ diagram, the samples plot in a wide field between the wüstite-magnetite and nickel-nickel oxide buffers.

Amphibole and Brown Mica

Amphibole is present as a phenocryst phase in tephritic phonolites. It is a kaersutite (TiO₂ = 4.8–5.6 wt%) and shows a moderate range in Mg# (48–67), and Na₂O contents (2.4–2.9 wt%). Brown mica is rare and interstitial in the alkaline rocks, and it has variable Mg# (Mg# = 18–66). The Ti content generally decreases with Mg# (TiO₂ = 5.6–7.9 wt%). Barium contents are low (<1.5 wt% BaO). Annite in the rhyolites has low Mg# (5–43) and variable Ti (1.5–5.8 wt% TiO₂) (Table 7).

Accessory Phases

Zircon crystals were found in the silicic ignimbrite M765. Rhönite microlites in the tephrite M770 have low silica (SiO₂ = 22.9–24.5 wt%), low Na₂O, and high TiO₂ contents (0.84–1.44 wt% Na₂O and 11.2–12.5 wt% TiO₂; Table 8). These compositions are very similar to those found in rhönites of the McMurdo alkaline volcanics (Kyle and Price, 1975), and they are quite different from the Kauai rhönites (Johnston and Stout, 1985). Monazite and xenotime were found in rhyolites as inclusions in brown mica. Monazite is rich in light lanthanides (6–13 wt% La₂O₃, 25–33 wt% Ce₂O₃, and 12–16 wt% Nd₂O₃). Xenotime has high yttrium and heavy lanthanides (34–35 wt% Y₂O₃, 4–5 wt% Dy₂O₃, and 3–4 wt% Yb₂O₃) (Table 9).

GEOCHEMISTRY

The mafic lavas of the Massif d'Ambre range from tholeiitic to alkaline and strongly alkaline. They have Mg# (atomic Mg × 100/[Mg + Fe²⁺]) values ranging from 67 to 71. The Cr and Ni contents (Cr = 779–443 ppm; Ni = 307–178 ppm) are within the ranges expected for mantle-derived liquids. Basanites and tephrites have SiO₂ contents from 43.5 to 48.5 wt% and have variable P₂O₅ (0.34–1.2 wt%), TiO₂ (1.9–2.9 wt%), Nb (38–75 ppm), and Sr (437–794 ppm). The alkali basalts have moderate TiO₂ (1.6–2.6 wt%) and Nb (18–41 ppm) contents. The tholeiitic and transitional basalts are characterized by a wide range of MgO (6.3–13.3 wt%) and relatively low TiO₂ (1.2–1.7 wt%), P₂O₅ (0.19–0.32 wt%), and Nb (18–29 ppm). The three main magma groups have, therefore mafic, relatively primitive rock compositions.

The mafic rocks of Massif d'Ambre are variably light lanthanide-enriched (Fig. 5; Table 10). The (La/Yb)_n ratio

(chondrite-normalized La/Yb ratio) of the mafic tholeiitic rocks ranges from 6.6 to 7.2; this ratio ranges from 10.6 to 18.6 in basanites, and from 8.5 to 15.4 in alkali basalts. The basanites have low Zr/Nb (2.6–3.4; excluding a sample with Zr/Nb = 4.1), Ba/Nb (6.7–13.1), and K/Nb ratios (107–251) and high Ti/V (41–75), whereas tholeiitic and alkali basalts have variable but higher Zr/Nb (2.4–5.8) ratios, similar K/Nb (148–365) and Ba/Nb (8.2–23.9) ratios, and moderately low Ti/V (37–48) ratios.

The tephrites have lanthanide element patterns similar to those of basanites (e.g., $(La/Yb)_n = 13–15$). No negative Eu anomalies and similar Ba/Nb and Zr/Nb (3.4–3.9 and 8.7–9.1, respectively) ratios have been found. The hawaiites have trace-element patterns very similar to those of the alkali basalts (Fig. 5).

The phonolite M772 has a concave-upward chondrite-normalized lanthanide pattern (Fig. 5) and also shows a negative Eu anomaly ($Eu/Eu^* = 0.56$, where Eu is chondrite-normalized europium and Eu^* is interpolated between chondrite-normalized Sm and Gd). The rhyolites have high SiO_2 (74.1–77.7 wt%), Rb (212–224 ppm), and Ba (681–1356 ppm) and relatively low Zr (134–209 ppm) and Sr (46–92 ppm). The rhyolite M602 has a roughly flat middle to heavy lanthanide chondrite-normalized pattern and has a marked negative Eu anomaly ($Eu/Eu^* = 0.35$).

Sr-Nd-Pb ISOTOPE DATA

Radiogenic isotope data are reported in Table 11. Basanites and alkali basalts have low initial $^{87}Sr/^{86}Sr$ (0.70326–0.70359) and relatively high $^{143}Nd/^{144}Nd$ (from 0.51279 to 0.51286; $\epsilon_{Nd}[12\text{ Ma}] = +3.1$ to $+4.6$). The basanite M579 has slightly more radiogenic $^{206}Pb/^{204}Pb = 19.369$ and $^{208}Pb/^{204}Pb = 39.257$ compared to the alkali basalt M560 ($^{206}Pb/^{204}Pb = 19.073$; $^{208}Pb/^{204}Pb = 39.046$), at similar $^{207}Pb/^{204}Pb = 15.613–15.616$. For comparison, the Nosy Be basanites range in $^{87}Sr/^{86}Sr$ from 0.70331 to 0.70366, in $^{143}Nd/^{144}Nd$ from 0.51278 to 0.51285, and in $^{206}Pb/^{204}Pb$ from 19.391 to 19.412 (Melluso and Morra, 2000).

DISCUSSION

The precise reconstruction of the volcanic stratigraphy of Massif d'Ambre is uncertain, and available radiometric ages are still very scarce. The ages so far obtained range from ca. 12.1 ± 0.2 Ma (this work) in the northwest of Massif d'Ambre to 0.83 ± 0.02 Ma (K-Ar) in the central part of the complex (Emerick and Duncan, 1982, 1983) and could indicate the presence of at least two cycles of magmatic activity. The almost identical Ar-Ar ages of the two feldspar-phyric phonolites of the Bobaomby

TABLE 5. REPRESENTATIVE MICROPROBE ANALYSES OF FELDSPARS AND FELDSPATHOIDS, MASSIF D'AMBRE (wt%)

Sample			SiO ₂	Al ₂ O ₃	FeO	CaO	Na ₂ O	K ₂ O	BaO	SrO	Cl	Sum	An	Ab	Or	Na#
Feldspars																
M534	Bsn	Gndmss	50.04	30.30	0.79	14.78	3.18	0.07	0.33	0.29		99.8	70.8	28.3	1.0	
M579	Bsn	Gndmss	56.37	25.78	0.63	7.80	5.86	1.93	1.23	1.92		101.5	35.2	52.4	12.4	
M770	Tph	Pheno	49.94	31.50	0.41	14.81	2.98	0.11	0.11	0.58		100.5	71.6	27.6	0.8	
M611b	Tph	Inclusion	54.15	28.00	1.09	11.33	4.88	0.37	0.32	0.47		100.6	54.0	43.3	2.7	
M771	Tph-pho	Pheno	49.33	31.97	0.59	15.87	2.51	0.10	0.42	1.00		101.8	74.7	24.0	1.3	
M771	Tph-pho	Pheno	49.69	29.72	0.40	13.41	3.41	0.24	0.02	0.99		97.9	65.7	32.9	1.4	
M772	Pho	Pheno	66.65	20.93	0.23	1.84	9.44	2.37	0.06	0.36		101.9	8.4	78.7	13.0	
M772	Pho	Pheno	66.69	18.45	0.41	0.00	6.16	7.83	0.00	0.21		99.8	0.0	54.7	45.3	
M560	Alk bas	Lath	62.62	22.38	0.63	4.32	7.58	2.38	0.45	0.45		100.8	20.3	65.6	14.1	
M585	Alk bas	Lath	64.05	21.93	0.21	3.69	6.23	5.01	0.09	0.85		102.1	17.2	54.8	28.0	
M590	Alk bas	Gndmss	50.94	30.12	0.75	14.26	3.46	0.18	0.00	0.67		100.4	67.6	31.4	1.0	
M533	Haw	Pheno	47.94	31.57	0.77	16.17	2.23	0.08	0.06	0.71		99.5	78.0	21.4	0.6	
M597	Tho bas	Pheno	51.03	29.14	0.60	13.61	3.57	0.16		0.29		98.4	66.7	32.4	0.9	
M597	Tho bas	Pheno	52.82	27.50	1.00	12.08	4.38	0.38	0.17	0.72		99.06	57.7	39.8	2.5	
M598	Tho bas	Gndmss	50.31	30.72	1.24	14.12	3.07	0.24	0.26	0.29		100.3	69.8	28.3	1.9	
M577	Tho bas	Gndmss	59.66	23.03	0.66	5.35	7.04	1.65	0.01	0.62		98.0	26.2	64.1	9.6	
M765	Rhy	Pheno	54.65	26.63	0.54	9.91	5.71	0.47	0.13	0.89		98.9	46.5	50.7	2.8	
M765	Rhy	Pheno	63.33	20.81	0.58	3.44	8.18	1.93		0.72		99.0	16.4	72.6	11.0	
M602	Rhy	Gndmss	66.61	19.65		0.93	5.26	8.81	0.36	0.12		101.8	4.4	45.3	50.3	
M602	Rhy	Gndmss	64.83	18.55	0.25	0.40	4.58	9.65	0.49	0.22		99.0	1.9	41.1	57.0	
Nepheline													Qz	Ne	Ks	
M579	Bsn	Gndmss	50.28	27.09	0.48	0.25	15.91	2.51	0.00	0.95		97.5	17.8	73.1	9.1	0.91
M770	Tph	Gndmss	50.03	28.83	0.89	0.96	15.43	2.31	0.05	0.35		98.8	16.6	75.2	8.2	0.91
M611b	Tph	Gndmss	50.52	28.92	0.57	0.72	16.21	2.55	0.00	0.11		99.6	15.4	75.7	8.9	0.91
M585	Alk bas	Gndmss	51.79	26.34	0.83	0.99	15.52	1.57		0.43		97.5	19.9	74.4	5.7	0.94
M585	Alk bas	Gndmss	54.13	27.57	0.83	0.51	14.19	3.02	0.15	0.13		100.5	22.4	67.2	10.5	0.88
M585	Alk bas	Gndmss	51.36	26.30	2.08	0.20	15.58	2.01	0.23	0.07		97.8	19.0	73.6	7.4	0.92
Sodalite																
M585	Alk bas	Gndmss	41.23	26.74	1.18	0.34	21.84	0.19	0.11	0.52	6.99	99.2				
M585	Alk bas	Gndmss	41.22	28.02	1.21	0.59	20.43	0.45		0.69	6.19	99.1				
M585	Alk bas	Gndmss	40.56	27.35	1.45	0.51	21.24	0.71		0.35	6.76	99.0				

Note: An, Ab, and Or in mol%; Qz, Ne, and Ks are in wt%; Na# = Na/(Na + K). Bsn—basanite, Tph—tephrite, Tph-pho—tephriphonolite, Pho—phonolite, Alk bas—alkali basalt, Haw—hawaiite, Tho bas—tholeiitic and transitional basalt, Rhy—rhyolite, Pheno—phenocryst, Gndmss—groundmass.

TABLE 6. REPRESENTATIVE MICROPROBE ANALYSES OF OXIDES (SPINEL AND ILMENITE), MASSIF D'AMBRE (wt%)

Sample			TiO ₂	Al ₂ O ₃	FeO	MnO	MgO	Cr ₂ O ₃	Sum	Cr#	Mg#
<u>Chromite</u>											
M770	Tph	Inclusion	3.90	24.41	53.74	0.43	7.06	4.70	94.2	11.4	31.6
M534	Bsn	Inclusion	1.61	32.00	29.94	0.69	15.42	15.66	95.3	24.7	66.6
M579	Bsn	Inclusion	1.60	36.15	33.23	0.25	11.70	15.45	98.4	22.3	49.8
M560	Alk bas	Inclusion	14.51	8.85	55.12	0.39	5.14	15.96	100.0	54.7	19.0
M585	Alk bas	Inclusion	1.59	27.60	29.29	0.77	9.74	30.88	99.9	42.9	42.9
M585	Alk bas	Inclusion	3.53	20.44	35.61	0.67	8.27	29.85	98.4	49.5	36.6
M598	Tho bas	Inclusion	2.48	20.64	33.86	0.96	8.48	32.29	98.7	51.2	38.3
M751	Tho bas	Inclusion	11.13	6.05	54.04	0.43	3.05	24.19	98.9	73.0	12.4
M540	Tho bas	Inclusion	1.57	24.64	33.71	0.67	8.47	30.45	99.5	45.3	38.2
<u>Magnetite</u>											
M534	Bsn	Gndmss	22.05	4.54	70.44	0.83	0.82	0.04	98.7	71.6	
M770	Tph	Gndmss	5.96	18.66	62.17	0.02	5.64	3.96	96.4	33.9	
M560	Alk bas	Gndmss	28.92	1.92	64.81	0.63	1.09		97.4	87.3	
M585	Alk bas	Gndmss	21.98	0.31	72.84	1.02	0.29	0.03	96.5	62.7	
M540	Tho bas	Gndmss	26.37	1.16	67.20	0.44	2.20	0.19	97.6	76.0	
M577	Tho bas	Gndmss	2.57	0.76	88.75	1.06	1.10		94.2	6.9	
<u>Ilmenite</u>											
M770	Tph	Gndmss	50.78	0.36	39.54	0.60	5.95	0.14	97.4		93.9
M560	Alk bas	Inclusion	50.12	0.13	47.58	1.45	1.53		100.8		92.8
M560	Alk bas	Inclusion	46.85	0.49	48.64	0.35	2.76	0.01	99.1		87.0
M751	Tho bas	Gndmss	46.81	0.33	53.12	0.61	0.27		101.1		87.1
M540	Tho bas	Gndmss	49.64	0.28	43.60	0.79	2.58	0.01	96.9		95.0
M765	Rhy	Gndmss	46.50	0.14	51.00	1.00	0.32		99.0		88.3

Note: Mg#—Mg × 100/(Mg + Fe + Mn), Cr#—Cr × 100/(Cr + Al), Ulv—ulvöspinel, Ilm—ilmenite in mol%. Tph—tephrite, Bsn—basanite, Alk bas—alkali basalt, Tho bas—tholeiitic and transitional basalt, Rhy—rhyolite, Gndmss—groundmass.

TABLE 7. REPRESENTATIVE MICROPROBE ANALYSES OF BROWN MICA AND AMPHIBOLE, MASSIF D'AMBRE (wt%)

Sample				SiO ₂	TiO ₂	Al ₂ O ₃	FeO	MnO	MgO	CaO	Na ₂ O	K ₂ O	SrO	BaO	F	Cl	Sum	Mg#
Biotite																		
M770	Tph	Gndmss		37.86	6.02	12.24	13.57	0.00	15.03	0.36	0.70	8.46	0.40	0.36	1.69	0.08	96.9	66.0
M533	Haw	Gndmss		39.40	5.58	13.22	25.70	0.41	3.22	0.56	1.90	6.92	0.63	0.00			97.5	18.0
M537	Pho-tpb	Gndmss		36.87	7.91	12.81	23.30	0.15	8.65	0.16	0.71	8.69	0.30	0.27			99.8	40.0
M765	Rhy	Micropheno	Core	34.55	5.21	12.09	24.60	0.21	10.40	0.11	0.67	7.88	0.31	0.00	4.64	0.20	100.9	43.0
M765	Rhy	Micropheno	Core	35.41	5.76	12.97	23.69	0.30	9.19	0.00	1.02	7.99	0.24	0.99	0.88	0.10	98.5	41.0
M602	Rhy	Micropheno	Core	35.01	1.67	14.95	34.32	0.61	1.03	0.15	0.65	9.23	0.03	0.11		1.49	99.3	5.0
M602	Rhy	Micropheno	Core	34.69	1.57	14.93	32.43	0.61	3.24	0.02	0.59	9.11	0.43	0.41			98.0	15.0
Amphibole																		
M771	Tph-pho	Pheno	Core	39.15	5.55	13.57	10.93	0.01	12.54	12.08	2.38	1.03		0.04	0.91	0.01	98.2	67.0
M771	Tph-pho	Pheno	Core	39.30	5.60	13.55	10.46	0.24	12.19	12.26	2.49	0.98		0.52	0.77	0.01	98.4	67.0
M771	Tph-pho	Pheno	Core	39.14	4.87	12.76	17.07	0.35	9.10	11.80	2.61	1.08			1.16	0.03	100.0	48.0
M771	Tph-pho	Pheno	Core	40.11	4.84	13.13	11.60	0.03	11.57	12.01	2.41	1.05		0.11	1.12	0.05	98.2	64.0
M771	Tph-pho	Pheno	Core	40.26	5.13	12.84	11.90	0.12	11.68	11.91	2.86	1.03		0.20	1.95	0.01	100.0	63.0

Note: Mg#—Mg × 100/(Mg + Fe + Mn). Tph—tephrite, Haw—hawaiite, Pho-tpb—phonotephrite, Rhy—rhyolite, Tph-pho—tephriphonolite, Gndmss—groundmass, Micropheno—microphenocryst, Pheno—phenocryst.

TABLE 8. REPRESENTATIVE MICROPROBE ANALYSES OF RHÖNITE AND GLASS, MASSIF D'AMBRE (wt%)

Sample			SiO ₂	TiO ₂	Al ₂ O ₃	FeO	MnO	MgO	CaO	Na ₂ O	K ₂ O	P ₂ O ₅	SrO	BaO	Cl	F	Sum
<u>Rhönite</u>																	
M770	Tph	Gndmss	23.88	11.98	15.36	21.89	0.03	10.81	11.28	1.33	0.01						97.0
M770	Tph	Gndmss	24.47	12.46	16.14	21.96		10.90	11.53	1.44							98.9
M770	Tph	Gndmss	23.83	11.82	15.41	21.09		10.66	11.05	1.14	0.04						95.4
M770	Tph	Gndmss	22.92	11.31	16.09	23.09	0.07	9.94	11.30	0.84	0.03						95.6
M770	Tph	Gndmss	23.55	11.23	15.77	23.12	0.08	9.65	11.24	1.35							96.4
<u>Glass</u>																	
M597	Tho bas		69.84	1.19	13.84	0.92		0.07	0.63	2.44	5.96	0.21	0.79	0.10	0.20	1.94	98.2
M598	Tho bas		68.63	0.92	12.46	1.76	0.24		0.45	2.63	6.82	0.35	0.44		0.27		95.0

Note: Tph—tephrite, Tho bas—tholeiitic and transitional basalt, Gndmss—groundmass.

TABLE 9. REPRESENTATIVE MICROPROBE ANALYSES OF MONAZITE, APATITE, ZIRCON, AND XENOTIME, MASSIF D'AMBRE (wt%)

Sample	SiO ₂	FeO	CaO	Na ₂ O	P ₂ O ₅	SrO	ThO ₂	UO ₂	PbO	ZrO ₂	La ₂ O ₃	Ce ₂ O ₃	Nd ₂ O ₃	Gd ₂ O ₃	Dy ₂ O ₃	Y ₂ O ₃	Ho ₂ O ₃	Tm ₂ O ₃	Yb ₂ O ₃	Cl	Sum	
Monazite																						
M602 Rhy	Core	2.68	0.62	0.38	25.00		9.52	0.12	0.23		6.21	25.35	15.65	1.65	1.08	2.83	1.99	2.56	0.66		96.5	
M602 Rhy	Core	1.14	0.03	0.52	29.50		5.28	0.08			13.25	32.91	12.08	0.72		0.83			0.44		96.8	
M604 Rhy	Core	3.80	0.03	0.96	27.04		5.05	0.30			9.53	28.20	12.92	0.46	0.56	2.56		2.97	1.05		95.6	
Xenotime																						
M602 Rhy	Core	7.55	0.03	0.42	0.33	24.96	7.91	3.81			0.52	0.58	1.92	1.71	4.39	33.99		4.08	3.53		95.7	
M602 Rhy	Core	4.31	0.50	0.72	0.07	26.81	12.42	4.13			0.06	0.96	1.59	2.22	5.29	35.41	0.61	2.59	3.84		101.5	
Apatite																						
M579 Bsn	Gndmss	1.95	0.79	53.25	0.25	42.18	1.63													0.44	100.5	
M585 Alk bas	Gndmss	2.31	0.83	53.24	0.12	41.75	1.01													0.16	99.4	
M585 Alk bas	Gndmss	4.53	0.87	51.38	0.77	40.90	1.16													0.12	99.7	
M533 Haw	Gndmss	1.62	0.39	53.68	0.21	42.74	1.03													0.41	100.1	
Zircon																						
M765 Rhy	Gndmss	30.72	0.13							67.55											98.4	
Note: Rhy—rhyolite, Bsn—basanite, Alk bas—alkali basalt, Haw—hawaiite, Micropheno—micropenocryst, Gndmss—groundmass.																						

Note: Rhy—rhyolite, Bsn—basanite, Alk bas—alkali basalt, Haw—hawaiite, Micropheno—microphenocryst, Gndmss—groundmass.

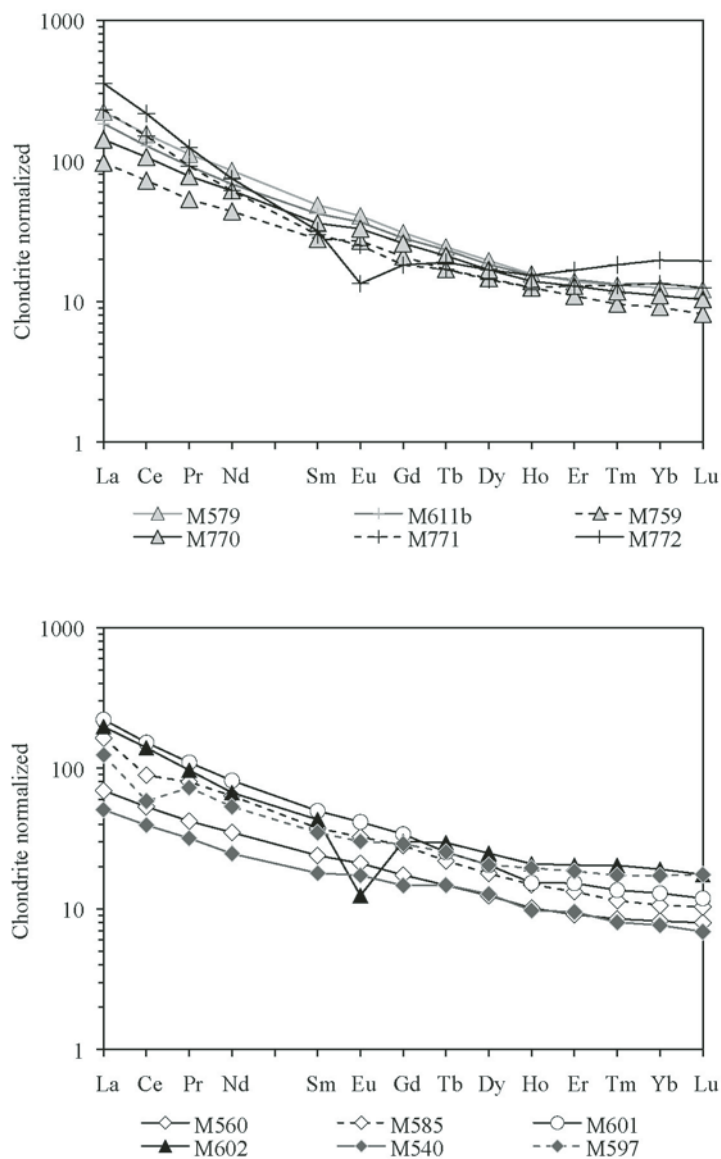


Figure 5. Chondrite-normalized lanthanide element patterns of Massif d'Ambre rocks. The chondrite values used for normalization were taken from Boynton (1984).

TABLE 10. ICP-MS ANALYZED TRACE-ELEMENT CONTENTS OF SELECTED SAMPLES (IN ppm) OF MASSIF D'AMBRE

Sample	M534	M579	M752	M759	M762	M766	M770	M769	M611B	M537	M771	M772	M560	M585	M590	M601	M533	M540	M597	M751	M602	Sid	Sid	W2-	W2-
Type	Bsn	Bsn	Bsn	Bsn	Bsn	Bsn	Tph	Tph	Tph	Pho-	Tph-	Pho	Alk	Alk	Alk	Haw	Haw	Tho	bas	Tho	bas	Rhy	bas	meas	certif
V	258	209	228	245	231	232	297	185	189	140	94	6	220	231	205	167	192	221	196	207		280	262		
Cr	205	296	390	500	400	420	310	120	180	74			496	556	589	110	23	510	370	390			90	90	
Co	48	50	50	61	48	55	47	41	40	24	14	2	63	53	58	37	25	58	48	55	1	41	43		
Ni	110	208	290	340	250	280	160	110	120	30			340	253	323	80	14	280	250	250		70	70		
Cu	64	66	60	90	60	70	60	40	50	33	20		67	79	69	40	19	60	60	60		110	110		
Zn	112	113	120	130	120	130	130	170	120	122	130	140	111	111	113	140	125	110	130	120	30	70	80		
Ga	20	20	18	19	18	20	19	22	17	23	24	27	18	20	19	20	24	18	19	18	19	17	17		
Rb	26	60	90	28	37	28	33	54	66	60	135	218	18	36	25	71	77	14	37	18	218	20	21		
Sr	744	875	724	502	709	531	783	869	760	797	641	244	381	486	438	793	779	296	321	326	57	194	190		
Y	30	31	26	22	27	22	29	31	30	32	25	32	20	37	22	30	30	17	38	21	43	21	24		
Zr	260	229	177	127	187	137	174	254	261	313	391	911	106	154	124	304	252	78	104	85	122	88	94		
Nb	87	87	69	42	56	48	67	74	75	80	90	133	28	47	36	100	62	21	24	22	48	7	8		
Cs	9.6	1.0	0.8	0.7	0.5	0.6	0.7	1.3	5.9	2.8	3.2	0.4	0.9	0.6	1.3	43.2			1.5		4.8	0.9	1		
Ba	746	780	655	440	644	436	640	647	675	731	872	510	259	485	411	704	605	182	493	218	955	177	182		
La	69.0	68.8	52.6	30.0	43.3	33.3	43.8	56.2	57.0	66.2	71.3	110.0	21.5	50.8	30.1	68.7	55.9	15.7	38.5	20.7	61.2	11.3	10		
Ce	126.2	125.0	96.6	58.5	83.6	63.7	85.8	112.0	103.0	126.2	121.0	175.0	43.0	72.0	58.4	123.0	108.0	31.8	47.2	35.6	113.0	24	23		
Pr	13.7	13.6	10.5	6.5	9.4	6.9	9.5	12.5	11.2	13.8	11.2	15.1	5.1	9.8	6.8	13.4	12.0	3.9	8.9	4.9	11.8	3.1	5.9		
Nd	50.6	51.1	40.4	26.2	37.1	27.4	36.8	49.0	40.9	50.7	36.7	44.8	21.0	38.1	26.9	49.0	45.1	14.8	32.0	18.1	40.2	12.9	13		
Sm	9.0	9.4	7.6	5.4	7.3	5.5	7.0	9.4	8.2	9.0	5.8	6.2	4.7	7.3	5.6	9.7	8.3	3.5	6.8	4.1	8.4	3.4	3.3		
Eu	2.8	3.0	2.7	2.0	2.6	2.0	2.4	3.3	2.7	2.8	1.9	1.0	1.6	2.4	1.8	3.1	2.6	1.3	2.2	1.5	0.9	1.16	1		
Gd	7.5	8.0	7.1	5.4	6.7	5.4	6.7	8.8	7.3	7.7	4.7	4.7	4.5	7.3	5.2	8.8	7.4	3.8	7.5	4.4	7.8	3.8			
Tb	1.1	1.2	1.0	0.8	1.0	0.8	1.0	1.3	1.1	1.1	0.8	0.9	0.7	1.0	0.8	1.2	1.1	0.7	1.2	0.7	1.4	0.7	0.6		
Dy	5.9	6.3	5.5	4.7	5.8	4.6	5.4	7.1	5.9	6.3	4.6	5.4	4.0	5.7	4.4	6.6	5.9	4.1	6.6	4.1	8.0	3.9	3.6		
Ho	1.1	1.1	1.0	0.9	1.0	0.9	1.0	1.3	1.1	1.2	0.9	1.1	0.7	1.1	0.8	1.1	1.1	0.7	1.4	0.8	1.5	0.8	0.8		
Er	2.8	2.9	2.6	2.3	2.8	2.3	2.7	3.4	3.0	3.1	2.7	3.5	1.9	2.8	2.0	3.2	2.9	2	3.9	2.3	4.3	2.2	2.5		
Tm	0.4	0.4	0.4	0.3	0.4	0.3	0.4	0.5	0.4	0.5	0.4	0.6	0.3	0.4	0.3	0.4	0.4	0.3	0.6	0.3	0.7	0.34	0.38		
Yb	2.5	2.6	2.2	1.9	2.3	1.9	2.3	2.9	2.8	2.9	2.8	4.1	1.7	2.2	1.8	2.7	2.6	1.6	3.6	1.8	4.0	2.1	2.1		
Lu	0.4	0.4	0.3	0.3	0.4	0.3	0.3	0.4	0.4	0.4	0.4	0.6	0.3	0.3	0.3	0.4	0.4	0.2	0.6	0.3	0.6	0.31	0.33		
Hf	5.7	5.1	4.3	3.3	4.5	3.4	4.2	6.4	5.6	6.1	7.1	15.8	2.6	3.8	3.1	7.0	5.7	2.2	2.9	2.5	4.3	2.5	2.6		
Ta	6.2	6.1	4.9	2.9	4.1	3.1	4.7	5.4	5.0	5.8	7.3	13.6	1.9	3.3	2.5	6.1	4.6	1.3	1.6	1.4	4.1	0.5	0.5		
W	1.3	0.7								1.0	2.0	1.0	0.5	0.7	0.5	2.0	1.4				4.0	3	0.3		
Pb	5.7	6.3							9.0	7.7	12.0	15.0	2.3	3.9	3.5	11.0	7.6				24.0	6	9		
Th	9.8	10.4	6.3	3.6	4.7	3.8	4.6	6.4	8.6	9.4	16.0	30.3	2.8	5.6	4.4	9.1	9.0	1.8	4.4	2.7	20.9	2.2	2.4		
U	2.2	2.2	1.4	0.9	1.1	1.0	1.1	1.6	2.1	2.4	4.4	9.3	0.6	1.1	1.0	2.2	2.0	0.4	0.9	0.6	6.0	0.5	0.5		
La/Yb _n	18.6	17.7	16.1	10.6	12.7	11.8	12.8	13.1	13.7	15.2	17.2	18.1	8.5	15.4	11.1	17.2	14.2	6.6	7.2	7.8	10.3				
Eu/Eu*	1.03	1.12	1.12	1.05	1.12	1.10	1.08	1.12	1.06	1.02	1.08	0.56	1.03	1.00	1.03	1.01	1.02	0.95	1.07	1.05	0.35				
Zr/Nb	3.0	2.6	2.6	3.0	3.3	2.9	2.6	3.4	3.5	3.9	4.3	6.8	3.8	3.3	3.5	3.0	4.1	3.7	4.3	3.9	2.5				

Note: Bsn—basanite, Tph—tephrite, Pho—tephritophenite, Tph-pho—tephritophenite, Pho—phenolite, Alk bas—alkali basalt, Haw—hawaiite, Tho bas—tholeiitic and transitional basalt, Rhy—rhyolite, Eu/Eu* = Eu_{II}/Sm_{II} × Gd_{II}^{0.5}, ICP-MS—inductively coupled plasma-mass spectrometer.

Note: Bsn—basanite, Tph—tephrite, Pho—phosphonite, Tph-pho—tephriphosphonite, Pho—phosphonite, Alk bas—alkali basalt, Haw—hawaiite, Tho bas—tholeiitic and transitional basalt, Rhy—rhyolite. Eu/Eu* = $\text{Eu}_T/(\text{Sm}_T \times \text{Gd}_T)^{0.5}$. ICP-MS—inductively coupled plasma-mass spectrometer.

Peninsula (10.56–10.14 Ma, this study) indicate that at least part of the volcanic activity of the Bobaomby Peninsula occurred later than the beginning of the activity of the Massif d'Ambre. The new data certainly indicate that the volcanism was active in the middle Miocene (Serravallian–Tortonian), at both Massif d'Ambre and Bobaomby.

Concerning spatial and temporal distribution of the three magma series of the Massif d'Ambre, the tholeiitic compositions have been found mostly in the outer parts of the volcanic complex (Fig. 1), whereas the alkaline and strongly alkaline rocks are found in the center and in the southern part of the Massif d'Ambre. It is worth noting that only strongly alkaline rocks (basanites to phonolites) have been found in the Bobaomby Peninsula, north of Massif d'Ambre (Melluso et al., 2007b). With the lack of age data on the tholeiitic rocks, and on a stratigraphic basis, we tentatively suggest that they form the base of the Massif d'Ambre, in a way similar to a shield-building stage. Tholeiitic basalts are dubitatively located in the southern part of the Ankara Massif (Lacroix, 1923), whereas alkali basalts, basanites, and their differentiates are widely scattered throughout the province.

CHARACTERISTICS OF THE MANTLE SOURCE AND MELTING PROCESSES

In the primitive mantle-normalized incompatible element patterns (Fig. 6), the mafic rocks of Massif d'Ambre have peaks at Ba and Nb, troughs at K, and smoothly decreasing normalized abundances from Nb to Lu. At roughly the same level of magmatic differentiation, there is a continuum in the enrichment level of all the incompatible elements passing from mafic tholeiitic through alkali basalts to basanites. Overall, the patterns of the different mafic rocks indicate that they can be the result of different degrees of partial melting of broadly similar mantle sources.

Assuming a very slightly incompatible element-enriched mantle (up to two times primitive mantle for the most incompatible elements and primitive mantle for heavy rare earth elements and Ti), the incompatible element pattern of primitive tholeiitic basalts (e.g., M540), alkali basalts (e.g., M560), and basanites

(e.g., M759) can be modeled by 12.5%, 5.8%, and 3.8% partial melting, respectively, of sources that started to melt in the garnet stability field and ended in the spinel field, with the highest contribution from the spinel facies given in the tholeiitic basalt generation (Fig. 7).

The Massif d'Ambre rocks are volatile-bearing, as demonstrated by the presence of amphibole, brown mica, and other volatile-bearing phases. Therefore, it is argued that they were generated from volatile-bearing mantle sources, in the lack of any major evidence of crustal contamination. The trough at potassium is noteworthy because it is present in both tholeiitic and alkaline magma types. This feature can be explained by (1) a potassium-depleted source mantle and/or (2) the presence of residual potassium-bearing phases in the source, such as amphibole or phlogopite, that hold back this element during melting.

The presence of amphibole in the source residue is currently invoked to explain troughs at potassium in the mantle-normalized patterns of alkaline lavas from Comore Archipelago (Späth et al., 1996; Class and Goldstein, 1997; Class et al., 1998) and Kenya (Späth et al., 2001), but was excluded by Melluso and Morra (2000) for the petrogenesis of the basanites of Nosy Be and by Melluso et al. (2007b) for the basanites of Bobaomby. A regression line passing close to the origin is obtained in the K versus Nb diagram of the basanites from Nosy Be, so the presence of amphibole in the source residue can be excluded. In this case, plotting the concentration of K and Nb of the most primitive samples of Massif d'Ambre, we again obtained a regression line passing very close to the origin; therefore, on the basis of the evidently similar partitioning of Nb and K during melting, we argue against the presence of a residual K-bearing phase in the source for all the primitive lavas of Massif d'Ambre. It is also difficult to postulate a K-bearing hydrous mineral in the source residue of the mafic tholeiitic rocks, given the relatively high degrees of partial melting that we calculated. It is likely that amphibole was present in the source of the northern Madagascar volcanic rocks (mantle xenoliths of Massif d'Ambre contain tiny amounts of pargasite), but it should have been exhausted very early during partial melting.

TABLE 11. Sr-Nd-Pb ISOTOPIC COMPOSITIONS OF SAMPLES OF MASSIF D'AMBRE

Sample type	M534 Bsn	M579 Bsn	M560 Alk bas	M585 Alk bas
$^{143}\text{Nd}/^{144}\text{Nd}$	0.51280	0.51287	0.51286	0.51279
$^{143}\text{Nd}/^{144}\text{Nd}_i$	0.51279	0.51286	0.51285	0.51278
$\epsilon_{\text{Nd}(12)}$	3.2	4.6	4.4	3.1
$^{87}\text{Sr}/^{86}\text{Sr}$	0.70346	0.70329	0.70339	0.70363
$^{87}\text{Sr}/^{86}\text{Sr}_i$	0.70344	0.70326	0.70336	0.70359
$^{206}\text{Pb}/^{204}\text{Pb}$		19.369	19.073	
$^{207}\text{Pb}/^{204}\text{Pb}$		15.616	15.613	
$^{208}\text{Pb}/^{204}\text{Pb}$		39.257	39.046	

Note: Isotope ratios are reported relative to 0.511850 for La Jolla Nd, to 0.71024 for NBS 987 Sr, and to the NBS 981 Pb values of Todt et al. (1996). Reproducibility for NBS 987 Sr was ± 0.00002 (2σ); for La Jolla Nd, it was ± 0.000012 ; for NBS 981 Pb, it was ± 0.011 for $^{206}\text{Pb}/^{204}\text{Pb}$ and $^{207}\text{Pb}/^{204}\text{Pb}$, and ± 0.031 for $^{208}\text{Pb}/^{204}\text{Pb}$. Within-run 2σ errors on the tabulated data were between ± 0.000014 and 0.000018 for $^{87}\text{Sr}/^{86}\text{Sr}$, ± 0.000005 and 0.000010 for $^{143}\text{Nd}/^{144}\text{Nd}$, ± 0.004 and 0.010 for $^{206}\text{Pb}/^{204}\text{Pb}$ and $^{207}\text{Pb}/^{204}\text{Pb}$, and ± 0.014 and 0.028 for $^{208}\text{Pb}/^{204}\text{Pb}$, and thus less than the external uncertainties on these standards. Total procedural blanks were negligible at <36 pg for Pb, <220 pg for Sr, and <100 pg for Nd. Measurements were made at the University of Hawaii, Firenze, and Napoli (Istituto Nazionale di Geofisica e Vulcanologia, Osservatorio Vesuviano).

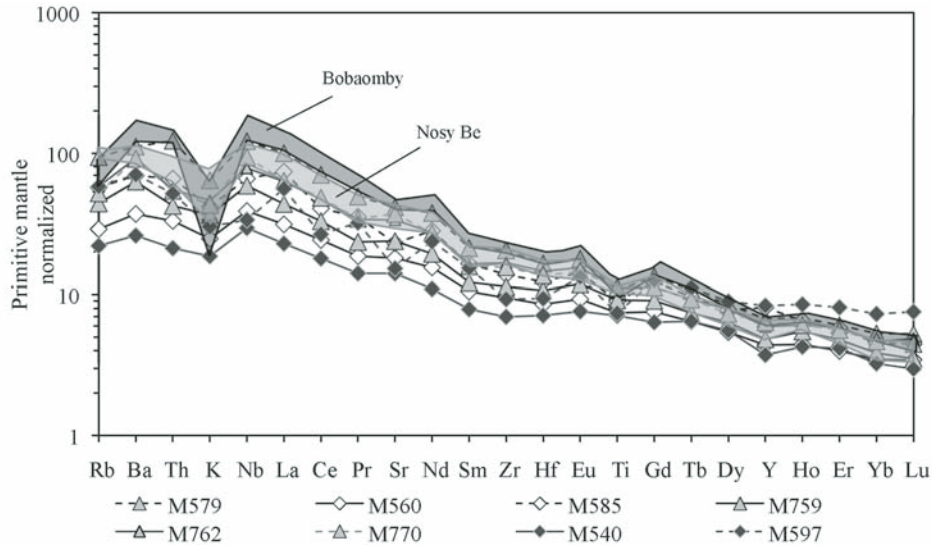


Figure 6. Primitive mantle-normalized incompatible element diagram for mafic rocks of Massif d'Ambre. Bobaomby and Nosy Be basanites are reported for comparison. Normalization values were taken from Sun and McDonough (1989).

GEOCHEMICAL SIMILARITIES OF THE MASSIF D'AMBRE MAFIC VOLCANICS WITH BOBAOMBY AND NOSY BE

The volcanic rocks of Bobaomby and Nosy Be belong to the strongly alkaline magma series, being mostly basanites and tephrites, with minor evolved samples (normative nepheline = 3%–27%; Melluso and Morra 2000; Melluso et al., 2007b). The mafic rocks have low Zr/Nb (2.7–4.1) ratios, and are strongly light (L) REE-enriched, with $(\text{La}/\text{Yb})_n$ ranging from 18 to 27. In the primitive mantle-normalized incompatible trace element patterns, the igneous rocks of Bobaomby and Nosy Be show peaks at Nb and Ta and a trough at K, similar to those observed in the mafic samples of Massif d'Ambre. Melluso and Morra (2000) and Melluso et al. (2007b) hypothesized an average degree of

partial melting of 4%–5% for the Bobaomby and Nosy Be basanites, starting from a mantle source similar to the average lithospheric mantle of McDonough (1990).

The geochemical and isotopic similarities throughout the entire province suggest a broadly similar source composition for the mafic rocks of northern Madagascar.

In the Sr-Nd diagram, basanites and alkali basalts (M534 and M585) overlap the field defined by Nosy Be Archipelago lavas, whereas the samples M560 and M579 plot close to the field defined by Comore Archipelago lavas (Fig. 8). In the $^{206}\text{Pb}/^{204}\text{Pb}$ versus $^{207}\text{Pb}/^{204}\text{Pb}$ diagram (Fig. 8), the mafic rocks of Massif d'Ambre plot above the mafic alkaline rocks of Comore Archipelago. The limited Sr, Nd, and Pb isotope data for the mafic rocks of the Massif d'Ambre exhibit little variation, suggesting derivation from a common mantle

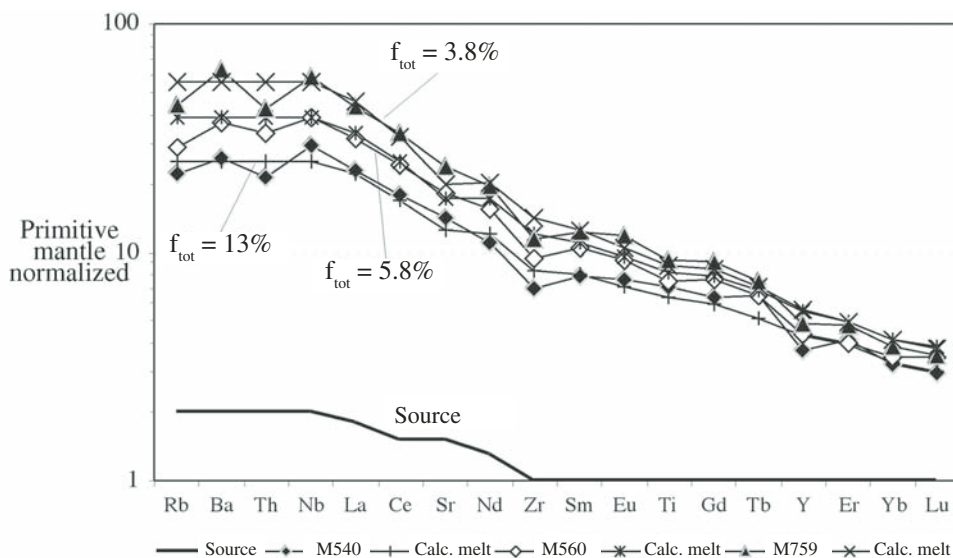


Figure 7. Comparison between observed and calculated incompatible element patterns of primitive tholeiitic basalts, alkali basalts, and basanites. The partition coefficients were taken from Niu et al. (1996), and melting models are found in Melluso et al. (2005, 2006). The primitive mantle normalization values are from Sun and McDonough (1989).

source similar to that of the mafic rocks of Nosy Be Archipelago, but distinct from the Indian Ocean mid-ocean-ridge basalt (MORB) and ocean islands (e.g., La Réunion, Mauritius). In addition, relatively high $^{206}\text{Pb}/^{204}\text{Pb}$ and low K/Nb values (Tables 1 and 11) are features noted in intraplate basalts with HIMU (High $\mu = ^{238}\text{U}/^{204}\text{Pb}$)-like isotopic composition (e.g., Späth et al., 1996). However, there is no geological evidence to suggest that the HIMU signature observed in the volcanics rocks of Massif d'Ambre can be directly related to a late Cenozoic plume.

EVOLUTION PROCESSES

The alkaline, strongly alkaline, and tholeiitic rocks of Massif d'Ambre have roughly similar compositional trends with increasing degrees of magmatic evolution (Fig. 9): SiO_2 , alkalis, Rb, and Zr increase and CaO, Sc, V, Ni, and Cr decrease with decreasing MgO (Fig. 8; Table 1), suggesting olivine and clinopyroxene control during magmatic differentiation. Al_2O_3 slightly increases with decreasing MgO, suggesting that feldspar has a subordinate role in magmatic evolution.

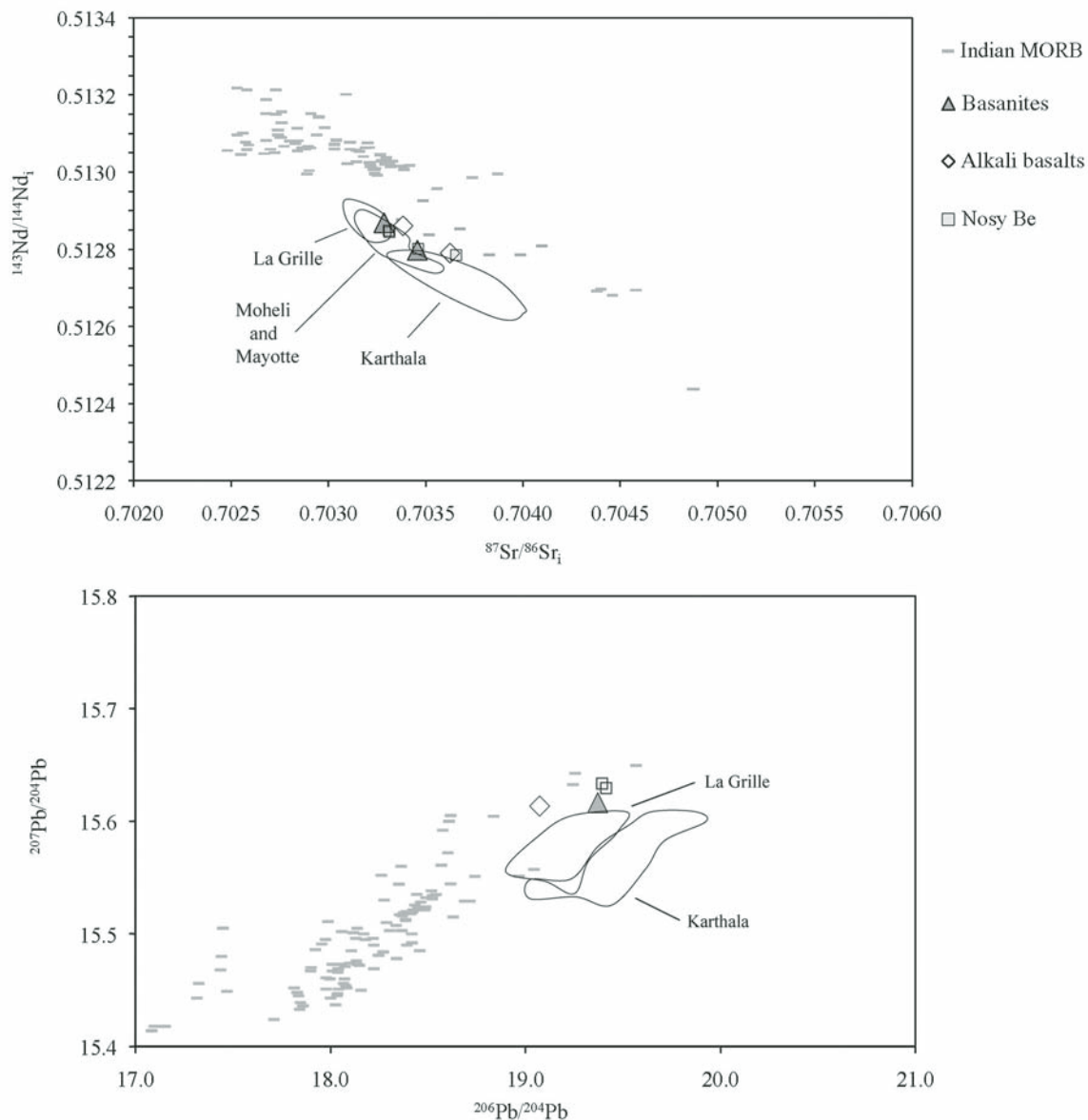


Figure 8. Pb, Sr, and Nd isotopic composition of Massif d'Ambre mafic rocks. The fields for Nosy Be and Comore Archipelago are taken from Melluso and Morra (2000); Class et al. (1997, 1998); Späth et al. (1996); and Deniel (1998). Indian mid-ocean-ridge basalt (MORB) is from Mahoney et al. (1989, 1992); Rehkämper and Hoffman (1997); and Ito et al. (1987).

The rocks of the strongly alkaline group have the widest compositional range.

The major- and trace-element variation observed in tholeiitic/transitional basalts is broadly compatible with fractional crystallization of olivine (7.6%), clinopyroxene (6.5%), and magnetite (0.4%) starting from the sample M531 to reach the chemical composition of M598. Least-squares mass balance calculations indicate that 50% fractional crystallization of olivine gabbro (27.6% olivine, 38.0% clinopyroxene, 27.3% plagioclase, and 7.1% magnetite) is required in the transition from alkali basalt

to hawaiiite. In the transition from basanite to tephrite, the cumulate removed (23%) is formed by olivine (27.4%), clinopyroxene (58.6%), magnetite (7.5%), and apatite (6.5%). The transition from tephritic phonolite to phonolite is modeled by 28% fractional crystallization of amphibole (62.8%), plagioclase (31.7%), magnetite (4.0%), and apatite (1.5%). The concave lanthanide chondrite-normalized pattern of phonolite is consistent with fractional crystallization of tiny amounts of accessory phases fractionating middle lanthanides, i.e., titanite and apatite. The results are shown in Table 12. The reasonable agreement between

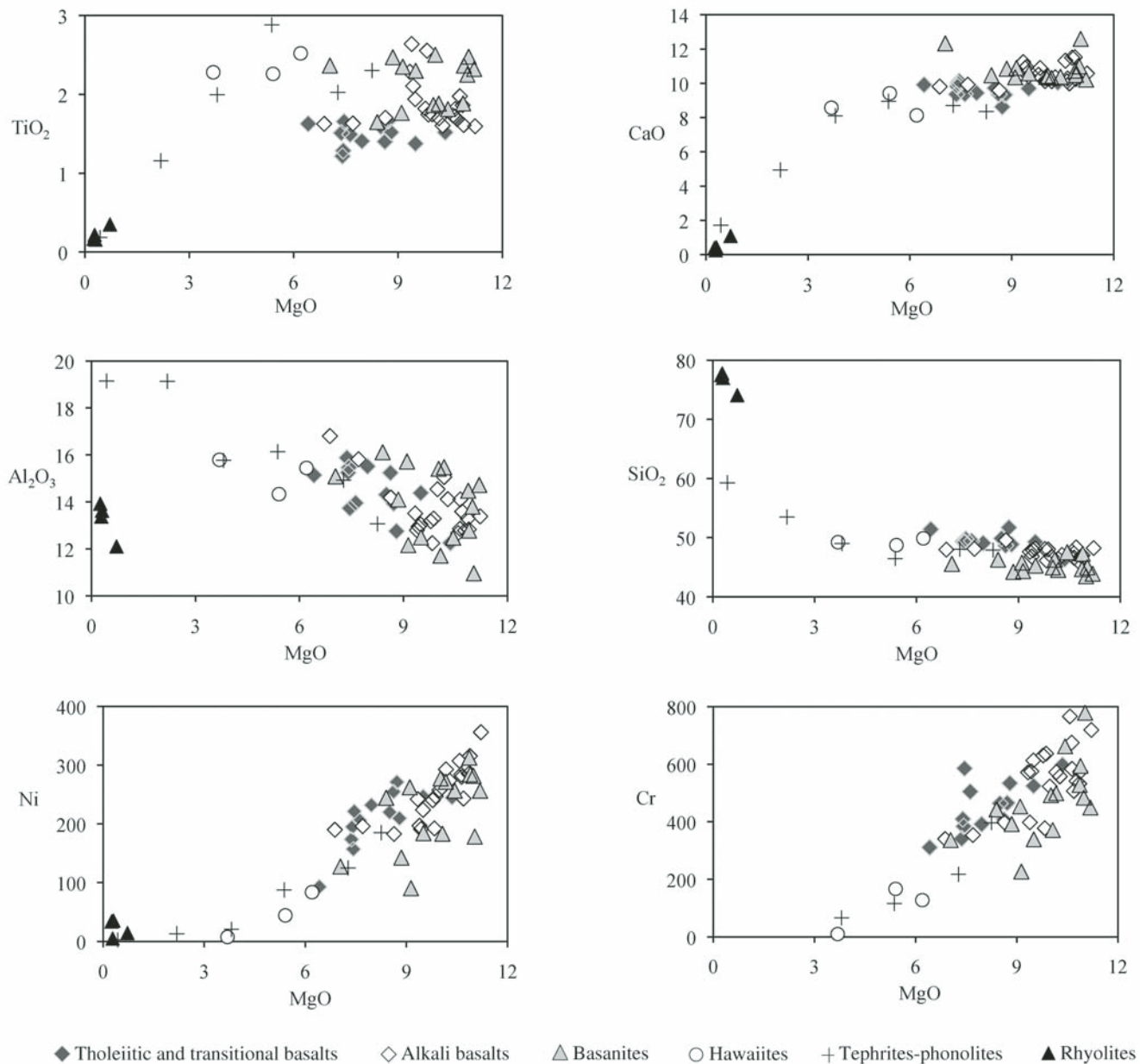


Figure 9 (Continued on following page). Major (wt%) and trace elements (ppm) of Massif d'Ambre rocks plotted versus MgO (wt%) and Zr (ppm) as differentiation indexes.

observed and calculated trace-element contents suggests that the derivation of alkaline and strongly alkaline series is broadly consistent with closed-system fractional crystallization, as already pointed out in the Bobaomby basanite-phonolite rock series (Melluso et al., 2007b).

The presence of rhyolites in the Massif d'Ambre area is interesting in the context of the late Cenozoic volcanism. Rhyolites are well known also in other areas of northern Madagascar (e.g., Nosy Be Archipelago, Ampasindava Peninsula; Lacroix, 1923), and their chemical and petrographic characteristics exclude any derivation from alkaline rocks through closed-system fractional crystallization. The peraluminous chemistry and petrographic features of the Massif d'Ambre rhyolites (such as the lack of

clinopyroxene and amphibole) likely indicate crustal contamination (e.g., Melluso et al., 2001).

CONCLUSIONS

The Massif d'Ambre stratovolcano erupted primary and evolved tholeiitic to strongly alkaline magma compositions during the middle-late Miocene, with a very large range of compositions in the associated minerals. The evolved rocks were generated after fractional crystallization of olivine, clinopyroxene, plagioclase, and magnetite, starting from mafic parental magmas. Feldspar and amphibole are the main subtracted phases in the transition from tephrite to phonolite. The rhyolites could

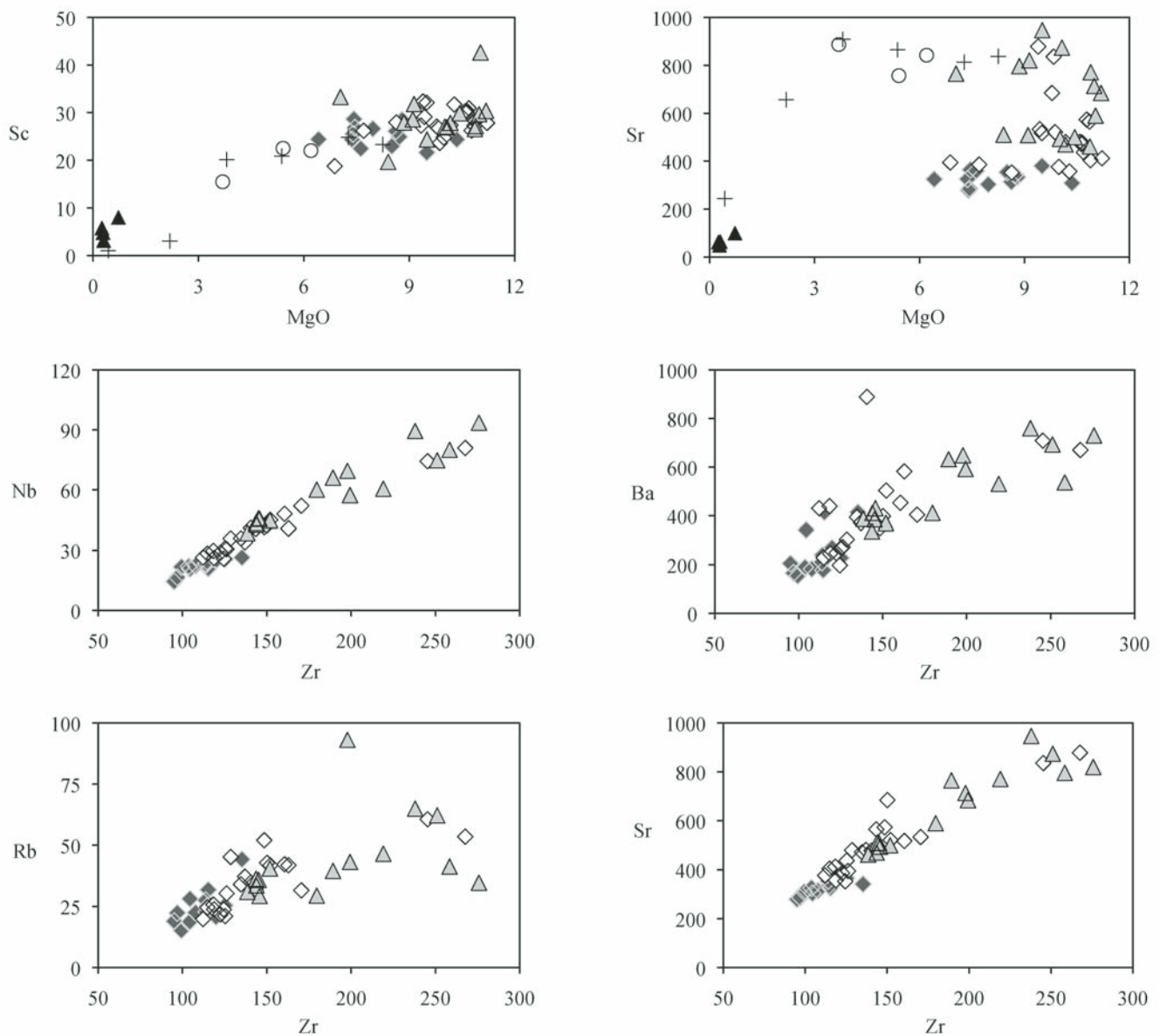


Figure 9 (Continued).

have been derived by assimilation or partial melting of continental crust or by prolonged open-system fractional crystallization of basaltic magma. Tholeiitic, alkali basalts, and basanites are increasingly enriched in all the incompatible elements, with peaks at Nb and Ta and troughs at K in the mantle-normalized diagrams. Melting models for the genesis of the mafic rocks

indicate ~4%–12% partial melting of a very slightly enriched peridotitic source located in the upper mantle close to the amphibole-spinel peridotite stability field. The geochemical and isotopic characteristics of the mafic rocks of Massif d'Ambre are similar to those observed in the basanites of Nosy Be and Bobaomby, suggesting similar source composition and

TABLE 12. MAJOR- AND TRACE-ELEMENT MASS BALANCE
CALCULATIONS BETWEEN DIFFERENT TYPES OF VOLCANIC ROCKS OF MASSIF D'AMBRE

	From	To	Chemical compositions					
	M531	M598	ol	cpx	mt		Res ²	
SiO ₂ (wt%)	50.05	51.20	37.85	49.92	0.00	%rem. sol. -14.6	0.019	
TiO ₂	1.56	1.62	0.00	0.91	16.43		0.003	
Al ₂ O ₃	13.06	15.08	0.00	5.50	1.87		0.035	
FeO _i	12.80	11.61	27.01	7.29	75.75		0.004	
MnO	0.19	0.17	0.33	0.28	0.48		0.000	
MgO	9.01	6.39	33.83	15.27	1.45		0.002	
CaO	9.55	9.87	0.27	17.03	0.00		0.001	
Na ₂ O	2.97	3.09	0.00	0.49	0.00		0.089	
K ₂ O	0.57	0.77	0.00	0.00	0.00		0.008	
P ₂ O ₅	0.24	0.19	0.00	0.00	0.00		0.006	
Fract. solid			7.7%	6.5%	3.6%	ΣRes ²	0.168	

	From	To	Chemical compositions					
	M588	M611b	ol	cpx	mt	ap	Res ²	
SiO ₂ (wt%)	46.88	48.55	37.94	50.77	0.00	1.95	%Rem. sol. -26.6	0.012
TiO ₂	2.54	2.05	0.00	1.39	25.34	0.00		0.056
Al ₂ O ₃	11.87	15.09	0.00	4.34	1.28	0.00		0.002
FeO _i	11.80	9.99	27.39	6.22	68.19	0.79		0.004
MnO	0.20	0.21	0.73	0.27	1.13	0.00		0.005
MgO	10.20	7.35	34.35	14.08	0.67	0.35		0.001
CaO	10.57	8.80	0.40	23.67	0.00	53.25		0.024
Na ₂ O	3.51	5.45	0.00	0.37	0.00	0.25		0.314
K ₂ O	1.60	2.04	0.00	0.00	0.00	0.00		0.010
P ₂ O ₅	0.83	0.46	0.00	0.00	0.00	42.18		0.053
Fract. solid			7.3%	16.5%	2.2%	0.6%	ΣRes ²	0.481

	From	To	Chemical compositions					
	M590	M533	ol	cpx	pl	mt	Res ²	
SiO ₂ (wt%)	47.93	50.88	40.70	50.43	52.22	0.00	%Rem. sol. -49.9	0.026
TiO ₂	1.74	2.36	0.00	1.82	0.00	14.09		0.081
Al ₂ O ₃	13.03	16.32	0.00	3.41	28.61	6.55		0.006
FeO _i	11.69	10.58	13.74	9.09	0.96	67.77		0.055
MnO	0.18	0.19	0.36	0.19	0.00	0.25		0.000
MgO	10.77	3.81	45.19	12.70	0.00	4.46		0.004
CaO	10.25	8.86	0.25	21.46	11.97	0.00		0.006
Na ₂ O	3.07	4.16	0.00	0.79	4.51	0.00		0.050
K ₂ O	0.92	2.19	0.00	0.00	0.36	0.00		0.052
P ₂ O ₅	0.43	0.65	0.00	0.00	0.00	0.00		0.011
Fract. solid			13.8%	18.9%	13.6%	3.5%	ΣRes ²	0.291

	Obs		Partition coefficients used				M533calc
Rb (ppm)	25.3	77.0	0.00	0.00	0.02	0.11	50.1
Sr	438	779.0	0.00	0.05	1.18	0.11	686.2
Y	22	30.5	0.01	0.72	0.02	0.64	34.4
Nb	35.5	61.8	0.01	0.07	0.01	0.01	69.4
Ba	411	605.2	0.03	0.16	0.68	0.12	684.1
La	30.1	55.9	0.00	0.03	0.14	0.15	58.7
Ce	58.4	108.0	0.00	0.02	0.02	0.02	115.3
Nd	26.9	45.1	0.00	0.80	0.02	0.03	43.2
Sm	5.6	8.3	0.01	0.46	0.11	0.02	9.6
Eu	1.8	2.6	0.03	0.31	0.73	0.03	2.9
Gd	5.2	7.4	0.00	0.84	0.07	0.02	8.2
Tb	0.8	1.1	0.03	1.12	0.06	0.02	1.2
Dy	4.4	5.9	0.03	0.71	0.31	0.30	6.7
Er	2.0	2.9	0.02	0.99	0.01	0.00	3.1
Yb	1.8	2.6	0.03	0.99	0.01	0.02	2.8
Lu	0.3	0.4	0.04	0.97	0.03	0.14	0.4

(Continued)

TABLE 12. MAJOR- AND TRACE-ELEMENT MASS BALANCE
CALCULATIONS BETWEEN DIFFERENT TYPES OF VOLCANIC ROCKS OF MASSIF D'AMBRE (*Continued*)

	From	To	Chemical compositions				%Rem. sol. -28.0	Res ²
	M771	M772	amph	pl	mt	ap		
SiO ₂ (wt%)	53.90	59.60	37.31	49.08	0.00	0.90		0.004
TiO ₂	1.17	0.19	5.35	0.00	14.08	0.00		0.004
Al ₂ O ₃	19.28	19.25	14.15	31.43	6.47	0.00		0.005
FeO _t	7.02	4.77	14.77	0.56	74.73	0.66		0.009
MnO	0.20	0.21	0.43	0.00	0.56	0.00		0.001
MgO	2.20	0.44	9.67	0.00	3.13	0.00		0.024
CaO	4.98	1.72	12.06	15.14	0.00	52.81		0.004
Na ₂ O	6.75	8.03	2.38	2.78	0.00	0.17		0.091
K ₂ O	4.18	5.72	1.31	0.08	0.00	0.00		0.034
P ₂ O ₅	0.32	0.08	0.00	0.00	0.00	42.22		0.008
Fract. solid			17.6%	8.9%	1.1%	4.1%	ΣRes²	0.185
			Obs	Partition coefficients used			M772calc	
Rb (ppm)	135.0	218.0	0.34	0.52	0.11	0.00		165.4
Sr	641	244.0	1.02	10.00	0.11	1.37		252.9
Y	25	32.0	0.41	0.02	0.64	2.91		31.1
Nb	90.0	133.0	0.08	0.01	0.01	0.00		122.8
Ba	872	510.0	0.16	9.50	0.00	0.06		436.2
La	71.3	110.0	0.06	0.09	0.15	2.50		95.6
Ce	121.0	175.0	0.10	0.09	0.02	3.23		160.6
Nd	36.7	44.8	0.44	0.02	0.03	14.00		43.4
Sm	5.8	6.2	0.91	0.11	0.02	5.68		6.4
Eu	1.9	1.0	2.00	1.53	0.03	30.00		1.3
Gd	4.7	4.7	1.19	0.03	0.02	5.13		5.0
Tb	0.8	0.9	0.87	0.04	0.12	15.40		0.9
Dy	4.6	5.4	0.78	0.02	0.30	3.90		5.3
Er	2.7	3.5	0.20	0.01	0.00	22.70		3.2
Yb	2.8	4.1	0.20	0.01	0.02	1.22		3.7
Lu	0.4	0.6	0.15	0.01	0.02	1.22		0.5

Note: ΣRes²—sum of squared residuals; partition coefficients are from Geochemical Earth Reference Model database. amph—amphibole, cpx—clinopyroxene, pl—plagioclase, mt—magnetite, ap—apatite.

mantle enrichment events throughout northern Madagascar. Further isotopic work will shed better light on the source of the northern Madagascan volcanics in space and time, especially the source relationships between tholeiitic and alkaline rocks in the Massif d'Ambre and adjoining regions.

ACKNOWLEDGMENTS

We dedicate this work to the memory of Padre Gino Lopercolo, a man who gave his life for Madagascar. We thank “la compagnie du Marteau” for the field trip of 2004 and Fosco d'Amelio for the field trip of 2003. John Mahoney is thanked for allowing isotopic work of Cucciniello and Rocco at the School of Ocean and Earth Science and Technology, University of Hawaii, and Pietro Brotzu and Andrea Marzoli are thanked for fruitful discussions. Luca del Gatto and Paola Morbidelli are thanked for their help in data elaboration and with the laboratory work. Thanks are also given to Lucia Civetta for allowing Sr-Nd analytical work at Osservatorio Vesuviano and to Hiviel Riziky (Université du Nord Madagascar) and Jean Veloson (Bureau des Mines, Antsiranana) for the necessary permits to collect samples and to bring the samples outside Madagascar. Sossio Fabio Graziano was very kind in providing precious bibliographic notes. The official reviews of Andy Saunders and an anonymous reviewer were very helpful for revising an initial

version of the manuscript. Grants for this project were provided by Ministero dell'Università e della Ricerca Scientifica e Tecnologica-Ministero dell'Istruzione, dell'Università e della Ricerca to Melluso and Morra and Fondi Regione Campania to Melluso.

REFERENCES CITED

- Avanzinelli, R., Boari, E., Conticelli, S., Francalanci, L., Guarnieri, L., Perini, G., Petrone, C.M., Ulivi, M., and Tommasini, S., 2005, High precision Sr, Nd and Pb isotopic analyses using the new generation thermal ionization mass spectrometer ThermoFinnigan Triton-Ti: *Periodico di Mineralogia*, v. 75, p. 147–166.
- Barnes, S.J., and Roeder, P.L., 2001, The range of spinel compositions in terrestrial mafic and ultramafic rocks: *Journal of Petrology*, v. 42, p. 2279–2302, doi:10.1093/petrology/42.12.2279.
- Bertil, D., and Regnault, J.M., 1998, Seismotectonics of Madagascar: *Tectonophysics*, v. 294, p. 57–74, doi:10.1016/S0040-1951(98)00088-2.
- Besairie, H., 1964, Geological Map of Madagascar: Tananarive, Service Géologique de Madagascar.
- Boynton, W.V., 1984, Cosmochemistry of the rare earth elements: *Meteorite studies*, in Henderson, P., ed., *Rare Earth Element Geochemistry*: Amsterdam, Elsevier, p. 63–114.
- Brumm, A., Jensen, G.M., van den Bergh, G.D., Morwood, M.J., Kurniawan, I., Aziz, F., and Storey, M., 2010, Hominins on Flores, Indonesia, by one million years ago: *Nature*, v. 464, p. 748–752, doi:10.1038/nature08844.
- Buchwaldt, R., Tucker, R.D., and Dymek, R.F., 2005, Geochemistry and geochronology of a Miocene volcanic suite from Mt. Tsaratanana, northern Madagascar: *Geochimica et Cosmochimica Acta*, v. 69, supp. 1, Goldschmidt Conference Abstracts 2005, p. A241.

- Chorowicz, J., Bardintzeff, J.M., Rasamimanana, G., Chotin, P., Thouin, C., and Rudant, J.P., 1997, An approach using SAR ERS images to relate extension fractures to volcanic vents: Examples from Iceland and Madagascar: *Tectonophysics*, v. 271, p. 263–283, doi:10.1016/S0040-1951(96)00250-8.
- Class, C., and Goldstein, S.L., 1997, Plume-lithosphere interactions in the ocean basins: Constraints from the source mineralogy: *Earth and Planetary Science Letters*, v. 150, p. 245–260, doi:10.1016/S0012-821X(97)00089-7.
- Class, C., Goldstein, S.L., Altherr, R., and Bachelery, P., 1998, The process of plume-lithosphere interactions in the ocean basins—The case of Grande Comore: *Journal of Petrology*, v. 39, p. 881–903, doi:10.1093/ptrology/39.5.881.
- Deniel, C., 1998, Geochemical and isotopic (Sr, Nd, Pb) evidence for plume-lithosphere interactions in the genesis of Grande Comore magmas (Indian Ocean): *Chemical Geology*, v. 144, p. 281–303, doi:10.1016/S0009-2541(97)00139-3.
- de Wit, M.J., 2003, Madagascar: Heads it's a continent, tails it's an island: *Annual Review of Earth and Planetary Sciences*, v. 31, p. 213–248, doi:10.1146/annurev.earth.31.100901.141337.
- Di Renzo, V., Di Vito, M.A., Arienzo, I., Carandente, A., Civetta, L., D'Antonio, M., Giordano, F., Orsi, G., and Tonarini, S., 2007, Magmatic history of Somma-Vesuvius on the basis of new geochemical and isotopic data from a deep borehole (Camaldoli della Torre): *Journal of Petrology*, v. 48, p. 753–784, doi:10.1093/ptrology/egl081.
- Emerick, C.M., and Duncan, R.A., 1982, Age progressive volcanism in the Comore Archipelago, western Indian Ocean, and implications for Somali plate tectonics: *Earth and Planetary Science Letters*, v. 60, p. 415–428, doi:10.1016/0012-821X(82)90077-2.
- Emerick, C.M., and Duncan, R.A., 1983, Age progressive volcanism in the Comores Archipelago, western Indian Ocean and implications for Somali plate tectonics: *Errata: Earth and Planetary Science Letters*, v. 62, p. 439–568.
- Ito, E., White, W.M., and Göpel, C., 1987, The O, Sr, Nd and Pb isotope geochemistry of MORB: *Chemical Geology*, v. 62, p. 157–176, doi:10.1016/0009-2541(87)90083-0.
- Johnston, A.D., and Stout, J.H., 1985, Compositional variation of naturally occurring rhönite: *The American Mineralogist*, v. 70, p. 1211–1216.
- Karche, J.P., 1972, Contribution à l'étude géologique de la Montagne d'Ambre et des régions voisines du Nord de Madagascar [thèse d'état]: Besançon, France, Université de Besançon, 683 p.
- Kusky, T.M., Toraman, E., and Rahamrimahefa, T., 2007, The Great Rift Valley of Madagascar: An extension of the Africa-Somali diffusive plate boundary?: *Gondwana Research*, v. 11, p. 577–579, doi:10.1016/j.gr.2006.11.009.
- Kyle, P.R., and Price, R.C., 1975, Occurrences of rhönite in alkalic lavas of the McMurdo Volcanic Group, Antarctica, and Dunedin volcano, New Zealand: *The American Mineralogist*, v. 60, p. 722–725.
- Lacroix, A., 1923, *Minéralogie de Madagascar*. 3. Lithologie Appendice—Index Géographique: Paris, Société d'Éditions Géographiques, Maritimes et Coloniales, Paris, 450 p.
- Le Bas, M.J., Le Maitre, R.W., Streckeisen, A., and Zanettin, B., 1986, A chemical classification of volcanic rocks based on the total alkali-silica diagram: *Journal of Petrology*, v. 27, p. 745–750.
- Mahoney, J.J., Natland, J.H., White, W.M., Poreda, R., Bloomer, S.H., Fisher, R.L., and Baxter, A.N., 1989, Isotopic and geochemical provinces of the Western Indian Ocean spreading centers: *Journal of Geophysical Research*, v. 94, p. 4033–4052, doi:10.1029/JB094iB04p04033.
- Mahoney, J.J., le Roex, A.P., Peng, Z.X., Fisher, R.L., and Natland, J.H., 1992, Southwestern limits of Indian Ocean ridge mantle and the origin of low- $^{206}\text{Pb}/^{204}\text{Pb}$ MORB: Isotope systematics of the central Southwest Indian Ridge (17°–50°E): *Journal of Geophysical Research*, v. 97, p. 19,771–19,790, doi:10.1029/92JB01424.
- McDonough, W.F., 1990, Constraints on the composition of the continental lithospheric mantle: *Earth and Planetary Science Letters*, v. 101, p. 1–18, doi:10.1016/0012-821X(90)90119-I.
- Melluso, L., and Morra, V., 2000, Petrogenesis of late Cenozoic mafic alkaline rocks of the Nosy Be Archipelago (northern Madagascar): Relationships with the Comorean magmatism: *Journal of Volcanology and Geothermal Research*, v. 96, p. 129–142, doi:10.1016/S0377-0273(99)00139-0.
- Melluso, L., Morra, V., Brotzu, P., and Mahoney, J.J., 2001, The Cretaceous igneous province of central-western Madagascar: Evidence for heterogeneous mantle sources, crystal fractionation and crustal contamination: *Journal of Petrology*, v. 42, p. 1249–1278, doi:10.1093/ptrology/42.7.1249.
- Melluso, L., Morra, V., Brotzu, P., Tommasini, S., Renna, M.R., Duncan, R.A., Franciosi, L., and d'Amelio, F., 2005, Geochronology and petrogenesis of the Cretaceous Antampombato-Ambatovy complex and associated dyke swarm, Madagascar: *Journal of Petrology*, v. 46, p. 1963–1996, doi:10.1093/ptrology/egi044.
- Melluso, L., Mahoney, J.J., and Dallai, L., 2006, Mantle sources and crustal input as recorded in high-Mg Deccan Trap basalts of Gujarat (India): *Lithos*, v. 89, p. 259–274, doi:10.1016/j.lithos.2005.12.007.
- Melluso, L., Morra, V., Brotzu, P., Franciosi, L., Grifa, C., Lustrino, M., Morbidelli, P., Riziky, H., and Vincent, M., 2007a, The Cenozoic alkaline magmatism in central-northern Madagascar: A brief overview: *Periodico di Mineralogia*, v. 76, p. 169–180.
- Melluso, L., Morra, V., Riziky, H., Veloson, J., Lustrino, M., Del Gatto, L., and Modeste, V., 2007b, Petrogenesis of a basanite-tephrite-phonolite volcanic suite in the Bobaomby (Cap d'Ambre) Peninsula, northern Madagascar: *Journal of African Earth Sciences*, v. 49, p. 29–42, doi:10.1016/j.jafrearsci.2007.06.002.
- Melluso, L., Sheth, H.C., Mahoney, J.J., Morra, V., Petrone, C.M., and Storey, M., 2009, Correlations between silicic volcanic rocks of the St. Mary's Islands (southwestern India) and eastern Madagascar: Implications for Late Cretaceous India-Madagascar reconstructions: *Journal of the Geological Society of London*, v. 166, p. 283–294, doi:10.1144/0016-76492007-147.
- Niu, Y., Waggoner, D.G., Sinton, J.M., and Mahoney, J.J., 1996, Mantle source heterogeneity and melting processes beneath seafloor spreading centers: The East Pacific Rise, 18°–19°S: *Journal of Geophysical Research*, v. 101, p. 27,711–27,733, doi:10.1029/96JB01923.
- Piqué, A., Laville, E., Chotin, P., Chorowicz, J., Rakotondraompiana, S., and Thouin, C., 1999, L'extension à Madagascar du Néogène à l'Actuel: Arguments structuraux et géophysiques: *Journal of African Earth Sciences*, v. 28, p. 975–983.
- Rakotondraompiana, S.A., Albouy, Y., and Piqué, A., 1999, Modèle de lithosphère pour l'île de Madagascar (Océan Indien occidental): Nouvelle interprétation des données gravimétriques: *Journal of African Earth Sciences*, v. 28, p. 961–973, doi:10.1016/S0899-5362(99)00072-X.
- Rehkämper, M., and Hofmann, A.W., 1997, Recycled ocean crust sediment in Indian Ocean MORB: *Earth and Planetary Science Letters*, v. 147, p. 93–106, doi:10.1016/S0012-821X(97)00009-5.
- Renne, P.R., Swisher, C.C., Deino, A.L., Karner, D.B., Owens, T.L., and DePaolo, D.J., 1998, Intercalibration of standards, absolute ages and uncertainties in $^{40}\text{Ar}/^{39}\text{Ar}$ dating: *Chemical Geology, Isotope Geoscience Section*, v. 145, p. 117–152.
- Rocco, I., 2009, Characteristics of the Lithospheric Mantle beneath Northern Madagascar Inferred from Ultramafic Xenoliths in Alkaline Lavas [Ph.D. thesis]: Naples, Università degli Studi di Napoli Federico II, 133 p.
- Späth, A., le Roex, A.P., and Duncan, R.A., 1996, The geochemistry of lavas from the Comores Archipelago, western Indian Ocean: Petrogenesis and mantle source region characteristics: *Journal of Petrology*, v. 37, p. 961–991, doi:10.1093/ptrology/37.4.961.
- Späth, A., le Roex, A.P., and Opiyo-Akech, N., 2001, Plume-lithosphere interaction and the origin of continental rift-related alkaline volcanism—The Chyulu Hills volcanic province, southern Kenya: *Journal of Petrology*, v. 42, p. 765–787, doi:10.1093/ptrology/42.4.765.
- Stamps, D.S., Calais, E., Saria, E., Hartnady, C., Nocquet, J.-M., Ebinger, C.J., and Fernandes, R.M., 2008, A kinematic model for the East African Rift: *Geophysical Research Letters*, v. 35, L05304, doi:10.1029/2007GL032781.
- Sun, S.s., and McDonough, W.F., 1989, Chemical and isotopic systematics of oceanic basalts: Implications for mantle composition and process, in Saunders, A.D., and Norry, M.J., eds., *Magmatism in the Ocean Basins: Geological Society of London Special Publication* 42, p. 313–345.
- Todt, W., Cliff, R.A., Hanser, A., and Hofmann, A.W., 1996, Evaluation of a ^{202}Pb - ^{203}Pb double spike for high-precision lead isotopic analyses, in Basu, A., and Hart, S.R., eds., *Earth Processes: Reading the Isotopic Code: American Geophysical Union Geophysical Monograph* 95, p. 429–437.

Metasomatism versus host magma infiltration: A case study of Sal mantle xenoliths, Cape Verde Archipelago

**Costanza Bonadiman
Massimo Coltorti
Luigi Beccaluva**

Department of Earth Sciences, University of Ferrara, Via Saragat 1, 44110 Ferrara, Italy

**William L. Griffin
Suzanne Y. O'Reilly**

*Australian Research Council (ARC), National Key Centre for Geochemical Evolution and Metallogeny of Continents (GEMOC),
Department of Earth and Planetary Sciences, Macquarie University, Sydney, NSW 2109, Australia*

Franca Siena

Department of Earth Sciences, University of Ferrara, Via Saragat 1, 44110 Ferrara, Italy

ABSTRACT

Based on phase geochemistry and Re-Os isotopic ratios, an exotic (in an oceanic setting) K-rich silicate melt, named kimberlite-type, has been claimed to be the metasomatizing agent interacting with subcontinental lithospheric mantle fragments beneath the Cape Verde Archipelago. On the basis of textural features and major- and trace-element chemistry, we constrain key geochemical indicators able to discriminate percolation at depth of this exotic melt from infiltration of the host magma in Cape Verde mantle xenoliths. Cape Verde type A lherzolites and harzburgites show evidence of dissolution of the primary phases (mainly pyroxenes) and the presence of large patches of secondary mineral (and glass) assemblages, and they do not show textural evidence of host basalt infiltration. Cape Verde type A mantle xenoliths frequently contain almost pure K-feldspar ($An_{3.8-8.8}$, Ab_{6-24} , Or_{72-89}) in the secondary mineral assemblage. They have an anomalously high K content (up to 0.49 wt%), and K/Na ratios generally >1, with respect to Cape Verde peridotites clearly affected by host basalt infiltration (type B samples). The dichotomy between Na and K observed in the two textural types suggests that the Na-alkaline host basalt ($K/Na < 1$), which infiltrated at low pressure, was able to modify the whole-rock Na content of the xenoliths (type B samples). In turn, a completely different K-rich alkaline melt, which interacted at depth with the peridotite, imposed its alkali ratio ($K/Na > 1$) on the bulk composition and formed the type A xenoliths. The kimberlite-type metasomatic agent, which reacted with the Cape Verde peridotite assemblage (mainly orthopyroxenes) in those regions where the mantle xenoliths are entrapped

in the host basalt ($P = 17$ kbar; $T = 1092$ °C), reasonably tends toward SiO_2 -saturated, K-rich basic magmas (lamproite-type?) with K-feldspars as the “liquidus” phase. Isotopic data on separate clinopyroxenes do not contribute to discrimination between metasomatism and infiltration processes but certainly concur to reinforce the hypothesis that a fragment of subcontinental lithospheric mantle domain was preserved during the opening of the Atlantic Ocean, forming K-rich undersaturated silicate melts that percolated through the peridotite matrix. Whole-rock major- and trace-element and isotopic geochemistry alone would not contribute to the interpretation of the processes occurring in the mantle xenolith. The most reliable tool would be an *in situ* mineral (and glass) study, which would be valid for Cape Verde mantle xenoliths and others. Small-melting-degree undersaturated silicate melts percolating at depth are olivine-saturated and may form, by reaction and dissolution of pyroxene, type A olivine without substantially modifying the original Fe/Mg peridotite ratio. By contrast, under low-pressure (<1.5 GPa), high-temperature regimes, olivine silicate melts infiltrating the mantle xenoliths form type B olivine, in which Fe/Mg ratios will be controlled by fractionation. Mantle diopsides interact (at depth) with undersaturated silicate melts, rearranging the most fusible elements into a new diopside composition: type A clinopyroxene. By contrast, diopsides that interact with melts at progressively lower pressure react and are locally rearranged in a new chemical structure that is able to accommodate the high diffusive elements (i.e., Fe and Ti): type B aegirine-augites. Fe^{3+} in spinel is a key element in the investigation of the processes acting on Cape Verde mantle xenoliths. As a metasomatic product, secondary chromian spinel tends toward a Fe^{3+} -buffered composition, mainly depending on pressure and chemistry of the magma. A decompression system is able to change the percolation regime from porous flow to open conduit. At this stage, the chromian spinel would be the low-pressure phase able to accommodate larger amounts of Fe^{3+} . Type A glasses have exceptionally high K_2O content, and, when associated with K-feldspars, they are buffered at ~ 9 K_2O wt%, in a silica range of 55.7–66.8 wt%. By contrast, type B glasses follow a hypothetical major-element trend toward the host basanites. In conclusion, the compositional features (in particular major elements) of minerals and glasses in relation to their chemical behavior in mantle systems are the most efficient tools to distinguish metasomatism-related (type A) from infiltration-related (type B) samples and consequently to place the mantle xenoliths in a correct genetic framework.

INTRODUCTION

Mantle xenoliths are an essential source of information about the nature, evolution, and processes of the mantle and the genesis of mafic magmas. Xenoliths can be studied by both petrographic and geochemical tools, but it is essential to discriminate between mantle events, occurring at mantle depth, and processes related to the transport of the xenoliths toward the surface. Since the pioneering studies on mantle xenoliths (e.g., Jagoutz et al., 1979; Dawson, 1984; Menzies et al., 1987), it has been recognized that superimposed textures may develop in mantle rocks by the interaction with fluids at depth before their transport to the surface (e.g., Neumann and Wulff-Pedersen, 1997; Dalton and Presnall 1998; Coltorti et al., 2000) and/or with the host magmas during their ascent (Klügel, 1998; Shaw et al., 2006; Shaw and Dingwell, 2008). The most evident effect of interaction between xenoliths and melt/fluids is the occurrence of glassy pools and patches (glass + subidiomorphic crystallites), glass films or veins, pyroxene spongy rims on pyroxenes, and sieved crystals of

pyroxene and spinel (Klügel, 1998; Arai and Abe, 1995; Yamamoto et al., 2009).

The interaction of mantle peridotites with melts at depth is the process identified as “mantle metasomatism,” which is commonly subdivided into two types (Dawson, 1984): (1) patent (modal) metasomatism characterized by the appearance of new minerals (such as amphibole, phlogopite, apatite, rutile, ilmenite, zircon) \pm glass or by the recrystallization of anhydrous preexisting peridotite minerals \pm glass; and (2) cryptic metasomatism, normally involving an enrichment in incompatible elements (e.g., K, Rb, Sr, Ba, light rare earth elements [LREEs], Ti, Nb, Zr, P, U, and Th), but in some cases also in major elements, such as Fe, Ti, and Ca, without the crystallization of new minerals. Cryptic mantle metasomatism is certainly more difficult to recognize than patent metasomatism (Neumann and Wulff-Pedersen, 1997; Dalton and Presnall, 1998; Coltorti et al., 2000; Beccaluva et al., 2001).

The most common features of metasomatized mantle xenoliths are reaction zones, i.e., spongy textures around orthopyroxene

(opx), clinopyroxene (cpx), and spinel (sp), with the recrystallization of secondary, fine-grained olivine (ol), cpx, and sp, frequently associated with glassy patches (gl). According to some authors (e.g., Shaw and Edgar, 1997; Shaw et al., 2006; Shaw and Dingwell, 2008), similar textures also can be produced through infiltration of the host basalt, modally represented by thin dark glass veins, which snake through the peridotitic matrix (e.g., Brearley and Scarfe, 1986; Shaw and Edgar, 1997; Shaw et al., 2006). These textures also have been produced experimentally (Brearley and Scarfe, 1986) and are observed in many intraplate xenolith populations worldwide, apparently independent of the nature of the transporting magma (i.e., alkali basalts, lamproitic or kimberlitic melt).

When discrete veins or glassy patches are not present, the infiltration of basaltic melts may be not revealed by the microstructure, but the primary paragenesis may be compositionally affected. For example, the high-temperature diffusive effects of the host basalt in the xenolith's minerals (Brearley and Scarfe, 1986) may be responsible for anomalous enrichment of V, Ti, and La in clinopyroxene, Ti and Fe³⁺ in spinel, and Mn in olivines, preferentially near the contact between xenolith and basalt. On the basis of major-element compositions of the phases obtained in synthetic experiments, Shaw et al. (2006) and Shaw and Dingwell (2008) doubted the efficacy of studying metasomatic textures in order to investigate the nature and evolution of the mantle; they concluded that most of the superimposed textures, including alkali-silicate glasses, are erroneously interpreted as the effects of mantle metasomatism. Instead, they are imposed by chemical and thermal effects on the xenoliths during magma transport and/or residence in a magma chamber.

The importance of finding robust distinctive criteria able to discern between these two processes is evident. In the first case, there are events occurring at mantle depth and causing an overall evolution in the mantle geochemistry both in time and space, which is ultimately responsible for the variety of volcanic activity seen at Earth's surface. In the other scenario, host basalt infiltration is the very last event affecting mantle rocks and has no bearing on mantle evolution. In order to reconstruct the original composition of the mantle, the effect of this last process has to be identified and taken into account. In order to discriminate between metasomatism and host basalt infiltration, various petrographic and geochemical criteria are proposed in this paper based on a selected well-studied suite of mantle xenoliths from Sal Island (Cape Verde Archipelago). These xenoliths are perfect samples to study because they show textural and geochemical features that clearly testify to interaction with either an exotic K-rich silicate melt at depth (metasomatism) or with basanites/nephelinites during the transport to the surface (host magma infiltration).

CAPE VERDE LITHOSPHERIC MANTLE: STATE OF THE ART

Two unrelated suites of fertile to mildly depleted lherzolites and strongly refractory harzburgites have been recognized among

“oceanic” mantle xenoliths from Cape Verde (Bonadiman et al., 2005; Simon et al., 2008). On the basis of mineral geochemistry and Re-Os isotopic systematics, the lherzolites represent a fragment of ancient subcontinental lithospheric mantle (O'Reilly and Griffin, 1996), left stranded in the oceanic lithosphere during the opening of the Atlantic Ocean (Bonadiman et al., 2005; Coltorti et al., 2010). Low-degree K-rich (kimberlite-like) melts derived from these ancient continental roots subsequently metasomatized the lherzolites and some of the harzburgites (OI2 group of Simon et al., 2008). The ultradepleted harzburgites lack any petrographic evidence of metasomatism; they contain deformed porphyroclasts of olivine and exsolved orthopyroxene (OI1 group of Simon et al., 2008) and probably represent residua of high-degree partial melting. According to Simon et al. (2008) and Neumann and Simon (2009), these residua were recycled within the deeper part of the convecting mantle and became trapped in the oceanic lithosphere before they were sampled by the ocean-island basalts. Alternatively, they can be interpreted as fragments of ancient high-MgO (low-density) cratonic mantle domains (Coltorti et al., 2010). If this is the case, the lherzolites could be the result of extensive refertilization processes, which took place after the detachment of the less-dense high-MgO mantle block (Begg et al., 2009). This “mechanical” processes would account for an independent chemical/physical evolution of the lherzolites relative to the harzburgites. However, discussion of this process is not the topic of this work.

Description of the Samples

The Sal xenoliths occur in two adjacent nephelinitic to basanitic necks (Table 1) located in the northern part of the island. Anhydrous, spinel-bearing lherzolites and harzburgites are equally represented; dunites and pyroxenites are rare. The textures are generally coarse grained and protogranular, but porphyroclastic types are also common. Deformation is only seen in rare kink-banded olivine and orthopyroxene crystals, and evidence of subsolidus re-equilibration (exsolution lamellae in pyroxenes) is only present in ultradepleted harzburgites (cpx <2%). Orthopyroxene and clinopyroxene often have distinctive secondary rims, which partially, or sometimes completely, replace the primary crystals. The replacement of primary pyroxene produces finely disseminated secondary clinopyroxene, olivine, spinel, and K-feldspar, locally associated with glassy patches (glass <5 vol%).

On the basis of a simple petrographic observation, three sets of samples were chosen for this study. The “metasomatic set” (type A) samples are composed of lherzolites and harzburgites and show all the described metasomatic textures. This set lacks evidence of veinlets crosscutting the nodule and connected with the host basalt (Figs. 1A and 1B). The “infiltrated set” (type B) samples are made up of lherzolites and harzburgites cut by veinlets, occasionally filled with plagioclase ± magnetite crystallites, connected with the host basalt (Figs. 1C and 1D). The estimated modal volume of host basalt infiltration is less than 1.5%.

TABLE 1. REPRESENTATIVE COMPOSITIONS OF CAPE VERDE XENOLITHS AND HOST LAVAS

Sample: Lithotype: Textural type:	CV43 Lh Type	CV87 Lh Type	CV98 Lh Type	CV15 Hz Type	CV76 Lh Type	CV83 Lh Type	CV23 Hz Type	CV88 Hz Type	CV34 Lh Type	CV11 Hz Type	CV32 Hz Type	CV71 Hz Type	CV8X Nephelinite	CV56X Basanite
SiO ₂	44.68	43.75	43.89	43.38	41.91	44.74	43.42	42.76	43.91	43.32	43.33	42.75	37.68	41.99
TiO ₂	0.12	0.12	0.21	0.09	0.12	0.17	0.11	0.05	0.15	0.00	0.04	0.01	3.59	3.58
Al ₂ O ₃	1.81	1.82	2.21	0.34	0.81	1.80	0.47	0.71	1.84	0.38	0.40	0.37	10.60	12.43
FeO ₁	8.34	8.28	10.08	7.68	10.71	8.07	7.56	8.18	8.36	7.84	7.72	7.89	11.28	11.70
MnO	0.13	0.13	0.14	0.12	0.13	0.13	0.12	0.12	0.13	0.12	0.12	0.12	0.17	0.16
MgO	41.81	42.39	39.19	45.52	43.60	41.37	45.07	44.92	41.79	47.25	46.82	47.60	16.59	12.75
CaO	1.52	2.13	2.79	1.35	1.45	2.59	1.46	2.40	2.52	0.57	0.79	0.58	12.77	11.59
Na ₂ O	0.33	0.12	0.23	0.26	0.26	0.26	0.26	0.01	0.08	0.01	0.01	0.01	3.47	2.36
K ₂ O	0.45	0.15	0.49	0.29	0.21	0.12	0.18	0.01	0.03	0.01	0.05	0.01	1.29	1.21
P ₂ O ₅	0.05	0.01	0.02	0.06	0.01	0.03	0.07	0.03	0.03	0.00	0.00	0.00	0.99	0.57
LOI	0.75	1.11	0.75	0.91	0.79	0.72	1.18	0.75	0.75	0.51	0.73	0.67	1.41	1.49
K/Na	1.36	1.25	2.13	1.12	0.81	0.46	0.69						0.37	0.51
V	58	66	90	37	49	83	41	47	73	40	31	28	335	343
Cr	3182	2720	2816	2542	1386	4233	3028	1687	3251	4019	2563	1995	813	641
Ni	2079	2038	1714	2414	2278	2059	2380	2438	2113	2488	2495	2548	447	257
Co	109	112	112	112	139	104	113	116	112	118	119	119	64	59
Rb	8	2	5	8	3	1	9	1	6	1	1	0	32	27
Ba	74	31	222	75	82	59	77	21	83	11	23	10	745	693
Sr	64	38	100	78	19	23	86	48	25	5	8	6	1008	774
Th	1	0	1	1	0	0	0	0	1	0	0	1	6	8
Nb	3	1	1	8	2	1	9	1	2	0	1	0	82	70
Zr	17	0	0	10	0	0	12	0	0	0	0	0	232	257
Y	3	1	1	2	1	2	2	2	2	0	1	0	28	23
La	2.46		0.76	5.08		1.11		1.68	2.00		0.93		54.4	47.5
Ce	5.9		1.9	10.0		3.5		4.2	3.6		2.4		107	91
Nd	3.07		1.47	4.78		2.48		2.11	2.19		1.56		54.7	46.9
Sm	0.86		0.43	1.08		0.83		0.50	0.70		0.61		11.8	9.7
Eu	0.220		0.136	0.235		0.265		0.130	0.190		0.155		3.48	2.82
Dy	0.490		0.430	0.570		0.610		0.320	0.410		0.240		5.91	5.03
Yb	2.29		1.71	2.01		1.78		1.57	1.62		0.93		26.0	22.4
Lu	0.180		0.150	0.140		0.180		0.170	0.160		0.070		1.57	1.5
Lu	0.035		0.035	0.020		0.035		0.030	0.030		0.015		0.25	0.25
⁸⁷ Sr/ ⁸⁶ Sr														
¹⁴³ Nd/ ¹⁴⁴ Nd														
¹⁷⁶ Hf/ ¹⁷⁷ Hf														
				0.703647	0.703958	0.703647	0.703958	0.703958	0.704582	0.703110	0.703868	0.703868	0.703868	(6)
				0.51284	0.51286	0.51284	0.51286	0.51286	0.51296	0.512952	0.512931	0.512931	0.512931	(8)
				0.28306	0.28306	0.28306	0.28306	0.28306	0.28306	0.283079	0.28304	0.28304	0.28304	(1)

Note: Major- (wt%) and trace-element (ppm) concentrations of Cape Verde mantle xenoliths and host lavas. Strontium, neodymium, and hafnium isotopic compositions were determined on separate clinopyroxenes. Numbers in parentheses are 2σ errors referring to the last significant digits. LOI—loss on ignition.

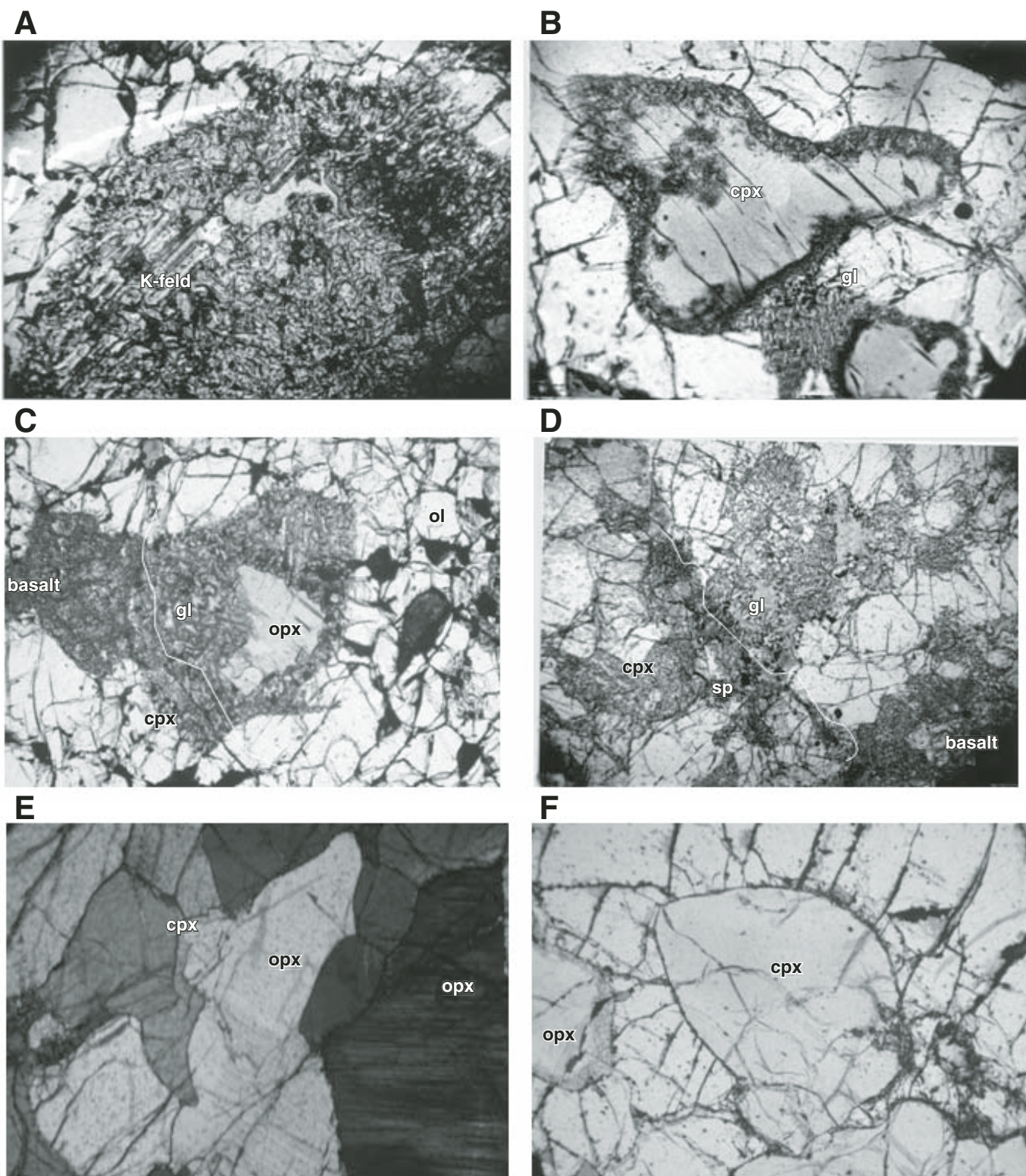


Figure 1. Textural types of Cape Verde mantle xenoliths. (A–B) Type A lherzolites; orthopyroxene (A) completely replaced by secondary metasomatic mineral assemblage (ol, cpx, sp, and K-feld) and glass; and primary clinopyroxene (B) with distinctive fine-grained secondary rims (ol + cpx + gl). (C–D) Type B harzburgites and lherzolites infiltrated by host basalt veinlets, locally inducing opx (C) melting and forming the low-pressure infiltrated secondary assemblage (D) (see text for detailed explanation). (E–F) Type C unmetasomatized harzburgites and lherzolites, respectively. Photomicrograph scale: 1.5 mm across. K-feld—K-feldspar; cpx—clinopyroxene; gl—glass; opx—orthopyroxene; ol—olivine; sp—spinel.

Small amounts of glass are present in the intergranular spaces of both groups, representing quenched alkali-silicate melts or reaction products (mainly in type A xenoliths). These glasses may contain microphenocrysts of olivine, clinopyroxene and spinel, as well as small grains of sulfides and metallic Fe-Ni alloys. Euhedral/subhedral crystals of K-feldspar, varying in size from several tens to one-hundred microns, are occasionally observed in the glass (Ryabchikov et al., 1995; Bonadiman et al., 2005; Coltorti et al., 2010; Fig. 1A). The presence of K-feldspar in mantle glassy patches is characteristic of metasomatized Cape Verde mantle xenoliths and reveals a distinctive type of the percolating metasomatic agent (kimberlite-type melt; Bonadiman et al., 2005).

Type A and type B samples were compared with a group of Cape Verde peridotites (type C) that did not show any textural evidence of secondary reactions.

Textural types A, B, and C do not unequivocally indicate metasomatic, infiltrated, and unmetasomatized samples, since films of both host basalt and metasomatic melts along the grain boundary may not be detected by simple petrographic work. Moreover, host basalt infiltration does not preclude an earlier stage of metasomatism. However, to find robust criteria to distinguish between metasomatism and infiltration of host basalt, it is important to start from petrographic evidence. The subsequent chemical criteria will confirm or deny the initial classification.

GEOCHEMICAL DATA

A large data set made up of minerals and glasses and major-, minor-, and trace-element analyses of whole rock was reported by Bonadiman et al. (2005). Details of the analytical procedures were given by Coltorti et al. (1999) and Bonadiman et al. (2005). Fe^{2+} - Fe^{3+} contents in spinels were calculated by stoichiometry after all Ti was combined with the appropriate amount of Fe, as for the ulvöspinel component (Fe_2TiO_4).

Sr-Nd-Hf isotope data for clinopyroxene separates, leached and ultrasonicated in 6 N HCl for 30 min, followed by ultrasonication in three aliquots of MQ prior to dissolution, were obtained using a Nu Plasma multicollector inductively coupled plasma-mass spectrometry system. All the analytical work concerning the isotopic measurements was carried out at the National Key Centre for Geochemical Evolution and Metallogeny of Continents (GEMOC) at Macquarie University (www.es.mq.edu.au/GEMOC/) following the techniques described by Aulbach et al. (2004).

Bulk Rock Chemistry

Major- and trace-element contents of type A, type B, and type C mantle samples and host basalts are shown in Table 1.

Regardless of the different textural types, on the whole, Cape Verde lherzolites show higher CaO and Al_2O_3 and lower MgO contents (Table 1; Fig. 2) compared to harzburgites.

Type A peridotites show an anomalously high L content (up to 0.49 wt%), compared to type B peridotites, and generally have K/Na ratios >1 . The host basalts of Sal nodules are Na-alkaline magmas with K/Na ratio <1 , similar to type B xenoliths (Table 1; Fig. 2).

Cape Verde xenoliths, irrespective of the different lithotypes and the presence of superimposed textures, show ubiquitously enriched rare earth element (REE) profiles, with $(\text{La}/\text{Yb})_n$ ranging from 5.8 to 42. This overall REE enrichment is accompanied by a pronounced positive Ba anomaly (Fig. 3). Conversely, Sr shows negative anomalies in type C samples, but it is extremely variable (from negative to strongly positive) in both type A and type B samples (Fig. 3; Table 1).

Mineral and Glass Chemistry

Based on the detailed study of the textural features of Cape Verde xenoliths, the geometrical relationships between the host basalt and mantle fragments can be decoded (type A vs. type B xenoliths). However, when the textural settings and the bulk chemistry data remain ambiguous, the compositional features (major and trace elements) of minerals and glasses become the most efficient tools for classifying mantle samples as type A or type B, and consequently assigning these samples to a correct genetic framework.

Olivine

In Cape Verde peridotites, olivine (ol) ranges from Fo 86.7 to Fo 91.5, with the highest values occurring in the harzburgites. Despite the unequivocal secondary reactions pervading type A and type B samples, no large differences were observed in terms of Fe-Mg contents between primary (ol type C) and secondary ol of type A samples. On the other hand, Ca ($\text{CaO} = 0.13\text{--}0.24$) tends to be higher and Ni ($\text{NiO} = 0.11\text{--}0.31$) lower in olivines associated with type A textures, compared to the primary grains (ol type C). In Figure 4, type A and type C olivines are plotted together with two olivine crystallites from host basalt veinlets crosscutting two xenoliths (ol type B). The latter are distinctively enriched in FeO ($\text{Fo} = 85.17\text{--}86.19$) relative to those of type A and type C assemblages.

Orthopyroxene

Orthopyroxenes (opx) only occur as a primary phase. Their Al_2O_3 content ranges from 3.65 to 6.17 wt% with Mg number ($\text{Mg\#} = \text{Mg}/[\text{Mg} + \text{Fe}] \times 100$) varying between 87.6 and 91.3 in lherzolites and between 91.3 and 93.0 in harzburgites. Despite the textural evidence of opx dissolution (especially in harzburgites, but also present in lherzolites) in both type A and type B samples, no significant variations are observed for the most fusible major elements (i.e., Al_2O_3 , FeO , CaO , and TiO_2) between the core and rim of the opx grains (Fig. 5). Orthopyroxenes in lherzolites are systematically depleted in LREE with middle (M) and heavy (H) REE contents placed around $0.7 \times \text{C1}$ chondrite; they are characterized by positive Zr and Ti anomalies. By

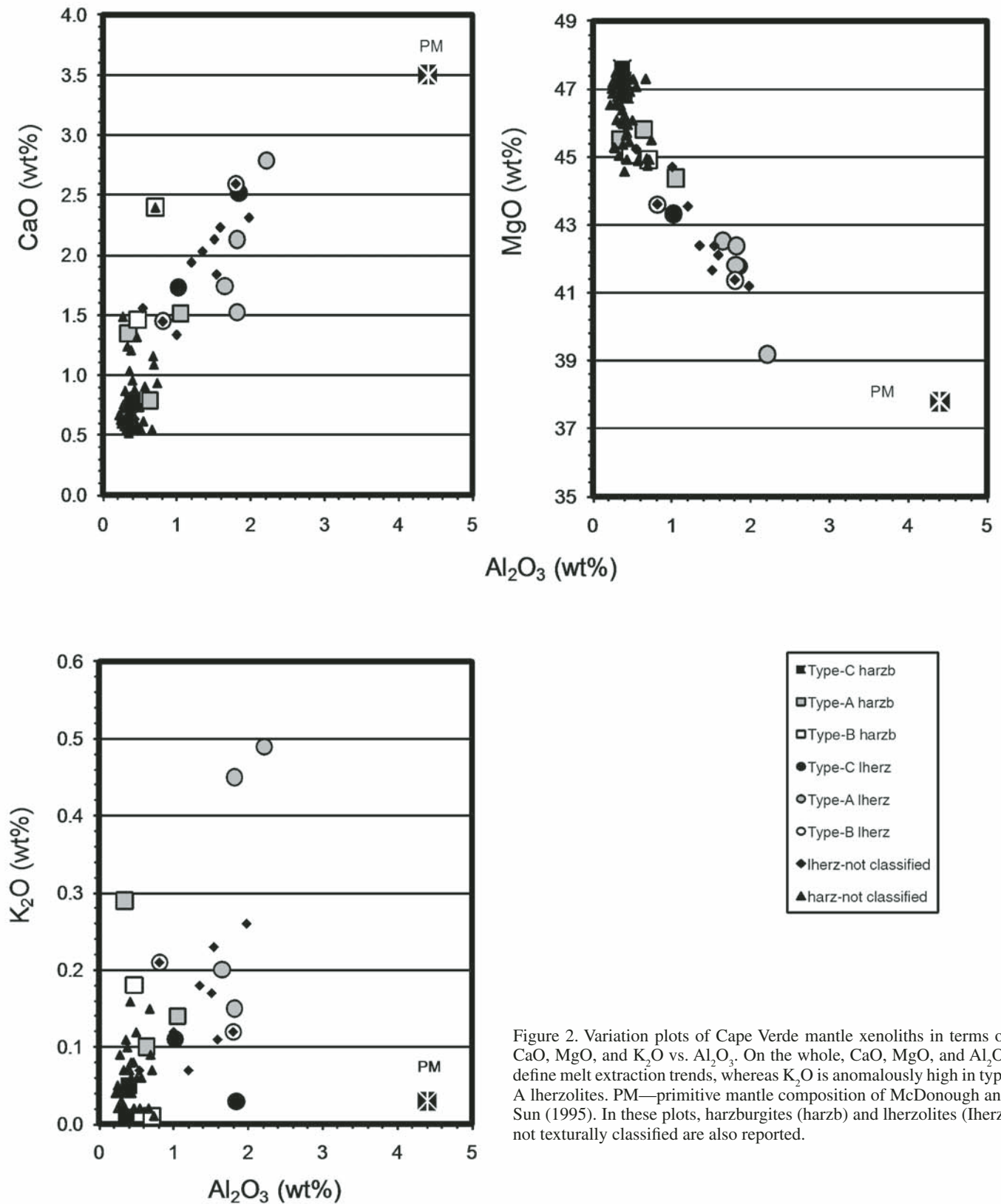


Figure 2. Variation plots of Cape Verde mantle xenoliths in terms of CaO, MgO, and K₂O vs. Al₂O₃. On the whole, CaO, MgO, and Al₂O₃ define melt extraction trends, whereas K₂O is anomalously high in type A lherzolites. PM—primitive mantle composition of McDonough and Sun (1995). In these plots, harzburgites (harzb) and lherzolites (lherz) not texturally classified are also reported.

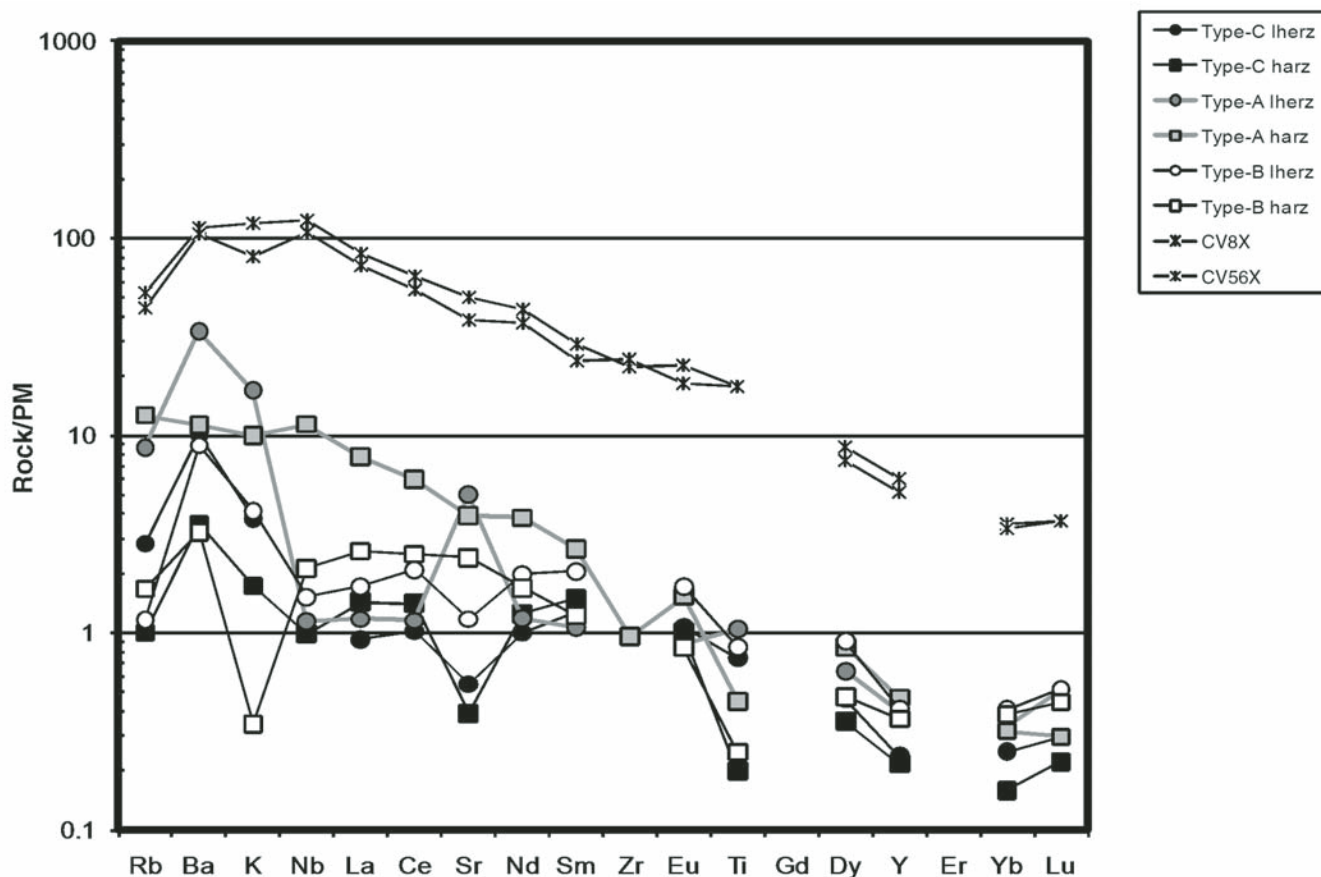


Figure 3. Abundance of trace elements in peridotites and in their host basalts (CV8X and CV56X) from Cape Verde, normalized to primitive values (PM) of McDonough and Sun (1995). harz—harzburgite, lherz—lherzolite.

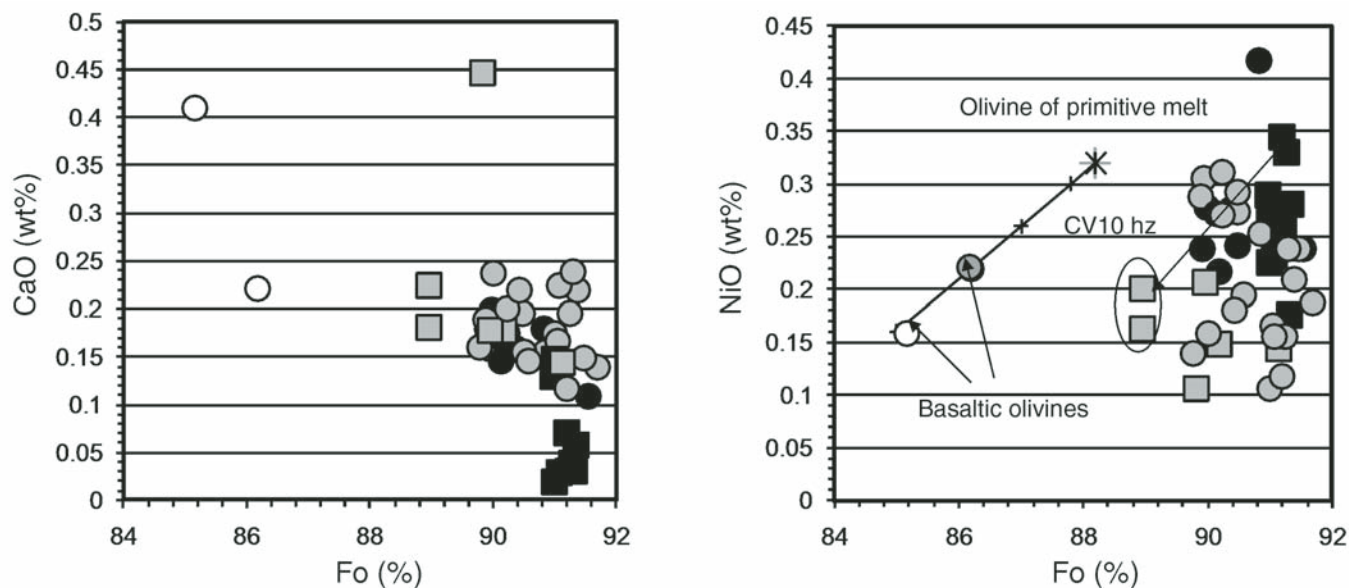


Figure 4. CaO and NiO vs. forsterite component (Fo) of Cape Verde mantle olivines. In terms of Fo component, type A olivines show almost the same composition as the primary (type C) counterparts. Conversely, they record higher Ca and lower Ni contents with respect to type C olivines. Type B olivines are represented by two crystallites of a host basalt veinlet crosscutting the nodule (lherzolite). They are distinctively enriched in iron relative to type A and type C olivines. Calculation of olivine fractionation trends used the method of Tamura et al. (2000). Symbols are as in Figure 2. hz—harzburgite.

contrast, orthopyroxene REE (plus Sr, Zr, Ti, and Y) patterns in depleted harzburgites show low concentrations in HREE, with highly (negative) fractionated M-HREE opx profiles ($[\text{Ho/Yb}]_n = 0.010\text{--}0.016$) (Fig. 6).

Clinopyroxene

Large protogranular clinopyroxenes (in type C samples) and unreacted cores of spongy grains (in both type A and type B samples) are labeled “type C cpx” and mainly occur in lherzolites. In harzburgites, type C cpx is very rare and very small in size. Type C cpx in lherzolites shows a large range of Mg# values (Mg# 86.7–92.7), anomalously low CaO (16.41–18.37 wt%), and high Cr_2O_3 (1.06–1.84 wt%) contents, com-

pared to cpx in spinel-bearing lherzolites worldwide (Pearson et al., 2003; Bonadiman et al., 2005). With respect to opx, large protogranular type C cpx shows a widespread variation in the most fusible elements (i.e., TiO_2 , Na_2O , and Al_2O_3) in both type A and type B samples. Figure 7 shows these elements plotted against FeO_t for type C, type A, and type B (as crystallites in cpx and opx spongy rims and in glassy patches) cpx, as well as cpx phenocrysts in the wall-rock basalts. It is interesting to note that the variations of such elements follow opposite trends in relation to the supposed process that affected the grain. Type A cpx associated with spongy rims of primary pyroxenes and as crystallites in glassy patches has systematically lower FeO_t , Al_2O_3 , and TiO_2 and higher CaO compared to type C cpx in lherzolites (Fig. 7). In

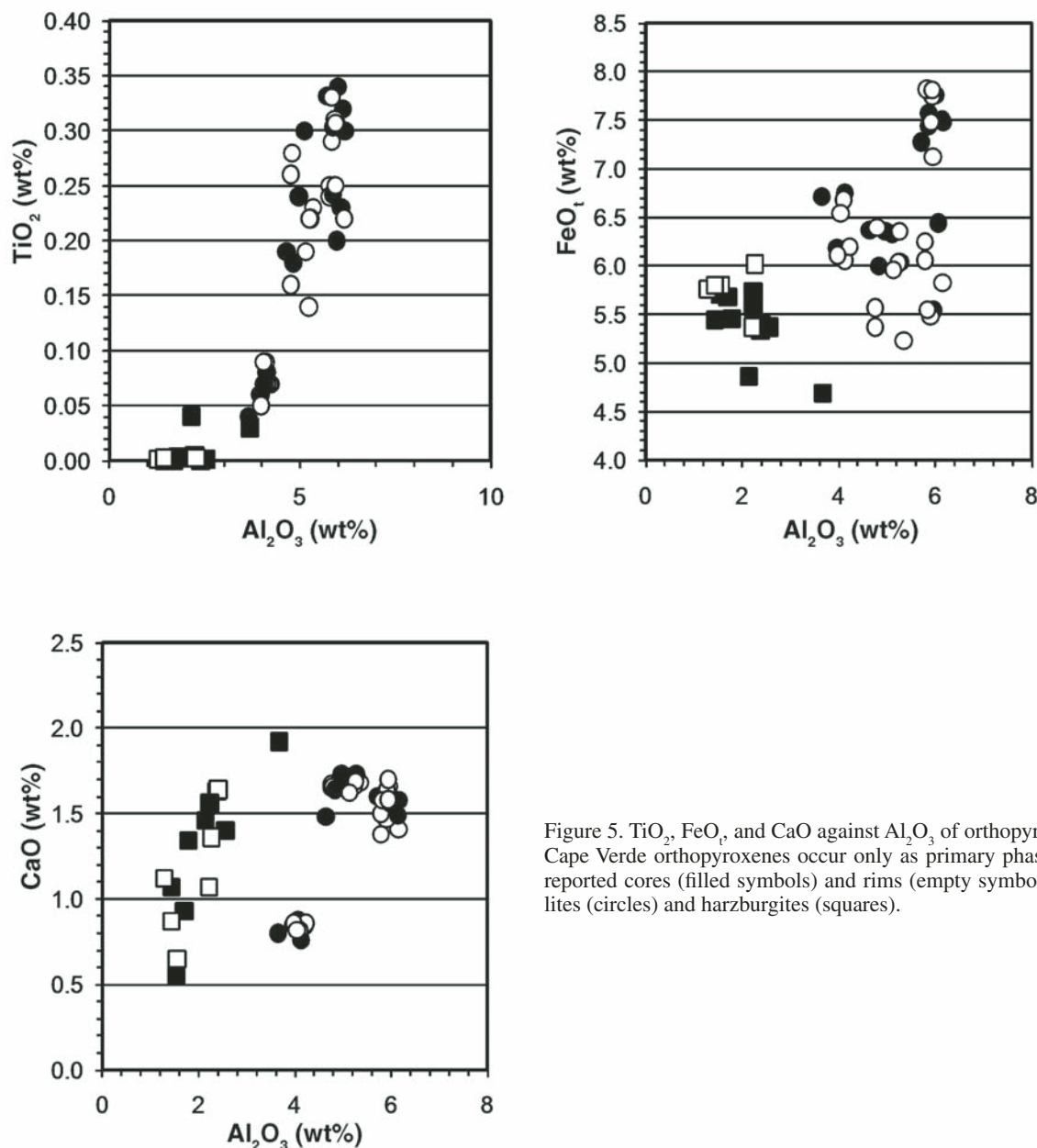


Figure 5. TiO_2 , FeO_t , and CaO against Al_2O_3 of orthopyroxenes. Since Cape Verde orthopyroxenes occur only as primary phase, these plots reported cores (filled symbols) and rims (empty symbols) for lherzolites (circles) and harzburgites (squares).

contrast, type B cpx shows higher FeO , Al_2O_3 , and TiO_2 contents comparable to those of phenocrysts in the host basalt (Fig. 7). Type A and type B both show lower Na_2O (0.25–0.78 wt%) and higher CaO (19.33–23.50 wt%) than type C cpx (Na_2O 0.24–1.8 wt%; CaO 16.41–21.14 wt%). In the Morimoto classification diagram (Morimoto et al., 1988), however, type A cpx falls into the diopside field, whereas type B cpx tends toward the augite field. In terms of trace-element contents, the unmetasomatized and/or unreacted core of spongy cpx (type C cpx) of the lherzolite suite displays convex-upward patterns with relatively high MREE relative to LREE and HREE, as well as the decoupling of Ti (almost absent) and Zr (negative) anomalies, whereas the rare cpx of harzburgites shows negative fractionated patterns (high H-MREE/LREE ratio) and negative Ti–Zr anomalies, like those commonly observed in variably depleted spinel-bearing abyssal peridotites (i.e., Hellebrand et al., 2002; Brunelli et al., 2006). Type A and type B clinopyroxenes show an overall enrichment of the entire spectrum of trace elements, defining a generally LREE-enriched trace-element profile (Fig. 8), with the highest LREE and the lowest HREE contents shown in type B cpx of CV66

harzburgite (La_n/Yb_n up to 18). The cpx trace-element profiles of both metasomatic and host infiltration types overlap the compositional ranges shown by cpx phenocrysts in equilibrium with basanites and primitive kimberlites (i.e., Francis and Minarik, 2008; Nimis et al., 2009, and reference therein).

Spinel

Primary chromian spinels (type C sp) are scarce in Cape Verde mantle xenoliths. Type C sp is homogeneous in composition within each sample and has highly variable Cr# ($\text{Cr}/[\text{Cr} + \text{Al}] \times 100$), from 14.99 to 34.10 in lherzolites and from 45.87 to 56.13 in harzburgites, without compositional overlap between the two series (Bonadiman et al., 2005; Coltorti et al., 2010), but delineating an approximate residual trend in the Cr#–Mg# space (Fig. 9). Secondary spinels (both metasomatic and infiltrated types) are small rounded inclusions in the reacted rims of primary spinel grains or in glassy patches and intergranular veinlets. Compositionally, type A sp remains chromian-spinel and shows a general tendency toward higher chromium (up to Cr# 45.9 in lherzolites; up to 79.5 in harzburgites), but it follows the general residual trend and is accompanied by a slight Ti enrichment (up to 0.16 atomic formula units [afu] in harzburgites). On the other hand, type B spinels plot off the trend toward lower Mg# (37.55–49.5) and are accompanied by remarkably high Ti (up to 0.70 afu) and Fe^{3+} (up to 0.28 afu) contents.

Glassy Patches and Related K-Feldspars

Cape Verde glasses show low totals (93%–98%), suggesting the presence of water or other volatile components. The analytical protocol used to acquire in situ analyses of the glasses hinders the alkali loss (i.e., Morgan and London, 1996). On the whole, glasses are characterized by relatively high SiO_2 (48.4–66.8 wt%), Al_2O_3 (13.9–21.4 wt %), and alkali contents (Na_2O 1.71–7.14 wt%; K_2O 3.87–8.71 wt %) (Fig. 10). Among major oxides, the best discrimination is obtained by plotting MgO, CaO, and K_2O versus SiO_2 . For reference, the values of the host lavas are also reported in all binary plots (Fig. 10). Regardless of their textural positions, type A glasses seem rather homogeneous in FeO, MgO, and, to a lesser extent, in CaO and K_2O contents. This pattern rules out the sole contribution of in situ primary phases melting during their formation, as well as a large fractionation of the percolating melt. Type A glasses are frequently associated with feldspars. Their composition falls within the range $\text{An}_{3.8-8.8}$, Ab_{6-24} , Or_{72-89} , and they show an enrichment in the orthoclase component, which is exceptional for feldspars associated with mantle metasomatism (i.e., Ionov et al., 2005). The type B glasses tend to have lower totals, SiO_2 and K_2O contents, and higher MgO and CaO than type A glasses, and they follow a trend toward the host basanites (Fig. 10). FeO , Al_2O_3 , and Na_2O contents are similar in the two groups. Thus, at least for Cape Verde mantle glasses, diagrams that consider the sum of alkalis, silica, or aluminum (i.e., alkali-silica, or the ternary plot $\text{SiO}_2/10 - \text{Al}_2\text{O}_3 - [\text{Na}_2\text{O} + \text{K}_2\text{O}]$; Shaw et al., 2006) are not useful to evaluate the conditions of mantle glass formation. Type B glasses are

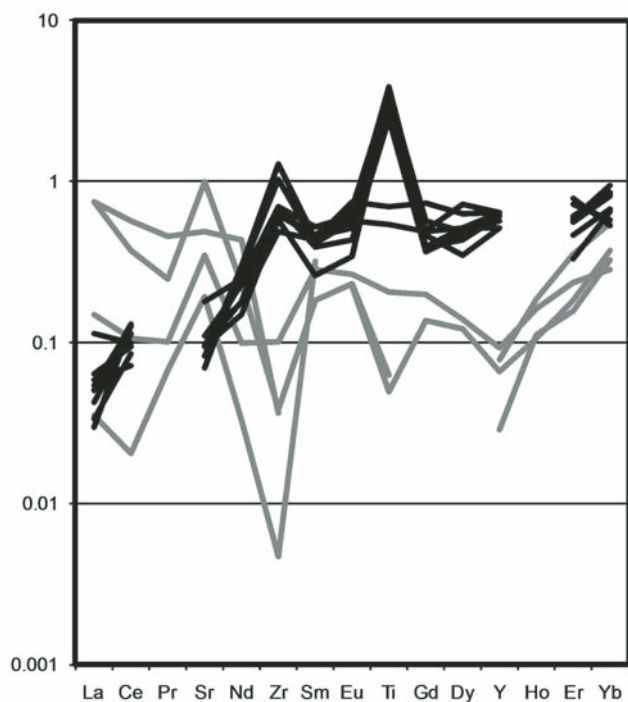


Figure 6. Abundances of rare earth elements (plus Sr, Zr, Ti, and Y) in orthopyroxenes of Cape Verde lherzolites (black lines) and harzburgites (gray lines), normalized to chondrite values of McDonough and Sun (1995). New trace-element analyses of orthopyroxenes in harzburgites were determined at the National Key Centre for Geochemical Evolution and Metallogeny of Continents (GEMOC) (www.es.mq.edu.au/GEMOC/) with a Nd:YAG ultraviolet laser system linked to an inductively coupled plasma–mass spectrometry system, and results were reduced using the GLITTER software (van Achterbergh et al., 1999). Details of the analytical procedures are available in Aulbach et al. (2004, 2007).

too small to be suitable for in situ trace-element analyses, so no comparison with type A glasses was possible. Among the latter, important distinctions are observed in relation to the different lithotypes in which they occur (Fig. 11). In lherzolites, glassy patches confined in reaction rims of cpx and opx show chondrite-normalized M-HREE profiles that mimic those of the adjacent pyroxenes; the lowest HREE contents are present in glasses associated with orthopyroxene (Yb_n 1.4–4.01). The Sr and K spikes of glasses are associated with the presence of K-feldspar (Fig. 11). In contrast, glasses in harzburgites show positively fractionated REE profiles (high LREE/M-HREE ratio), which match those of host basanites (except for the antithetic positive K anomaly), but which are richer in highly incompatible elements (Nb_n up to 1055). Glasses in both lithologies do not show significant

negative Ti and Zr anomalies, as are usually observed in mantle glasses related to alkali-silicate percolating melts (Coltorti et al., 2000, 2004; Witt-Eickschen and O'Neill, 2005).

Sr-Nd-Hf in Clinopyroxene

Isotopic analyses on separated cpx from type A and type C lherzolites reveal $^{87}\text{Sr}/^{86}\text{Sr}$ between 0.703110 (± 4) and 0.704582 (± 3), comparable to the Sr isotope compositions of the basalts in the southern islands of the archipelago (Escrib et al., 2005). The $^{143}\text{Nd}/^{144}\text{Nd}$ ratio ranges from 0.51284 (± 4) to 0.512952 (± 2) and $^{176}\text{Hf}/^{177}\text{Hf}$ ranges from 0.28304 (± 1) to 0.283079 (± 8) (Table 1). Type B samples are the most altered and were not used for isotopic measurements.

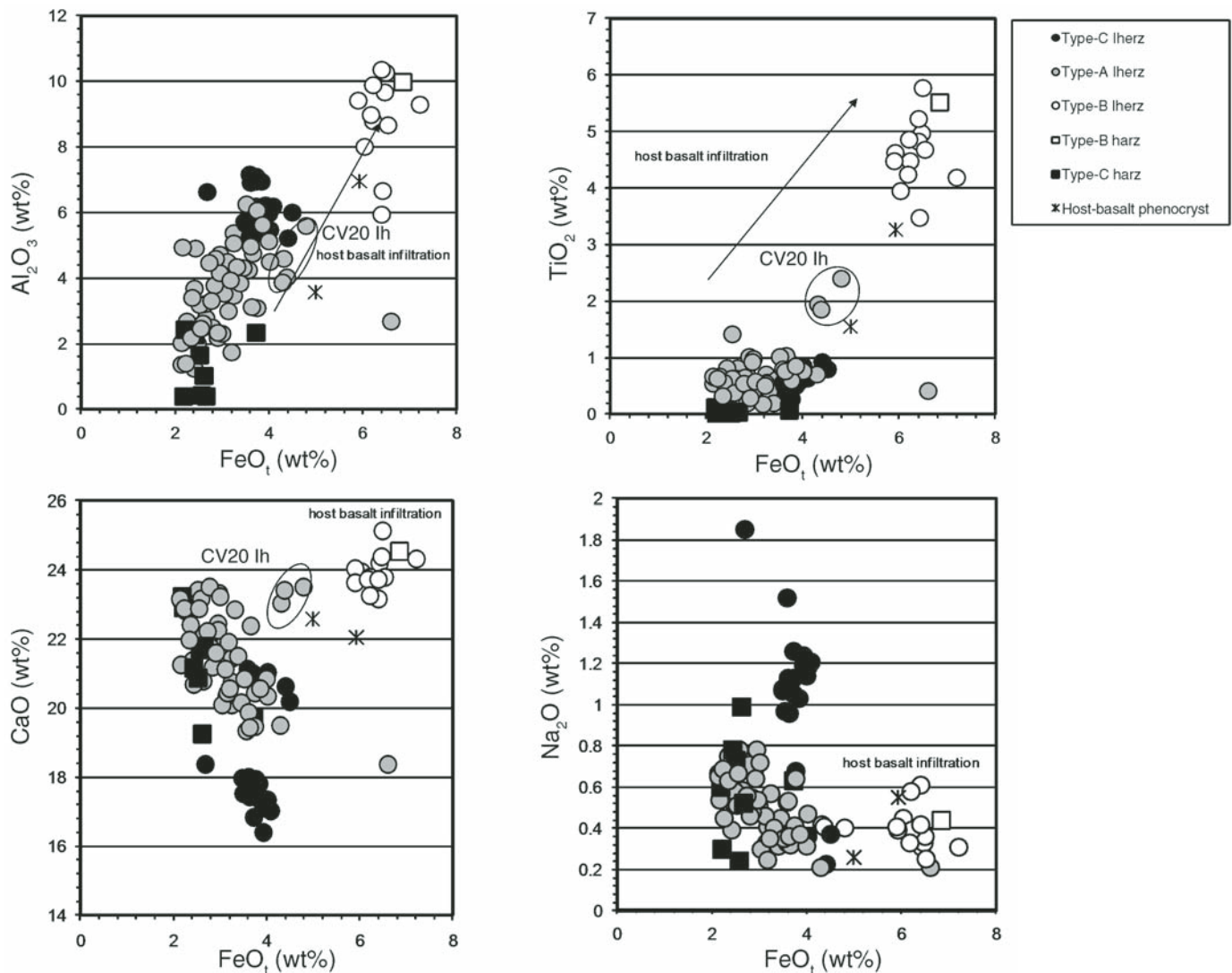


Figure 7. Al₂O₃, TiO₂, CaO, and Na₂O against FeO_t of type A, type B, and type C Cape Verde clinopyroxenes for both harzburgites (harz) and lherzolites (lherz and lh). For comparison, host basalt phenocrysts are also reported. Type B clinopyroxenes of lherzolite CV20 are actually primary clinopyroxenes embedded in infiltrated host basalt.

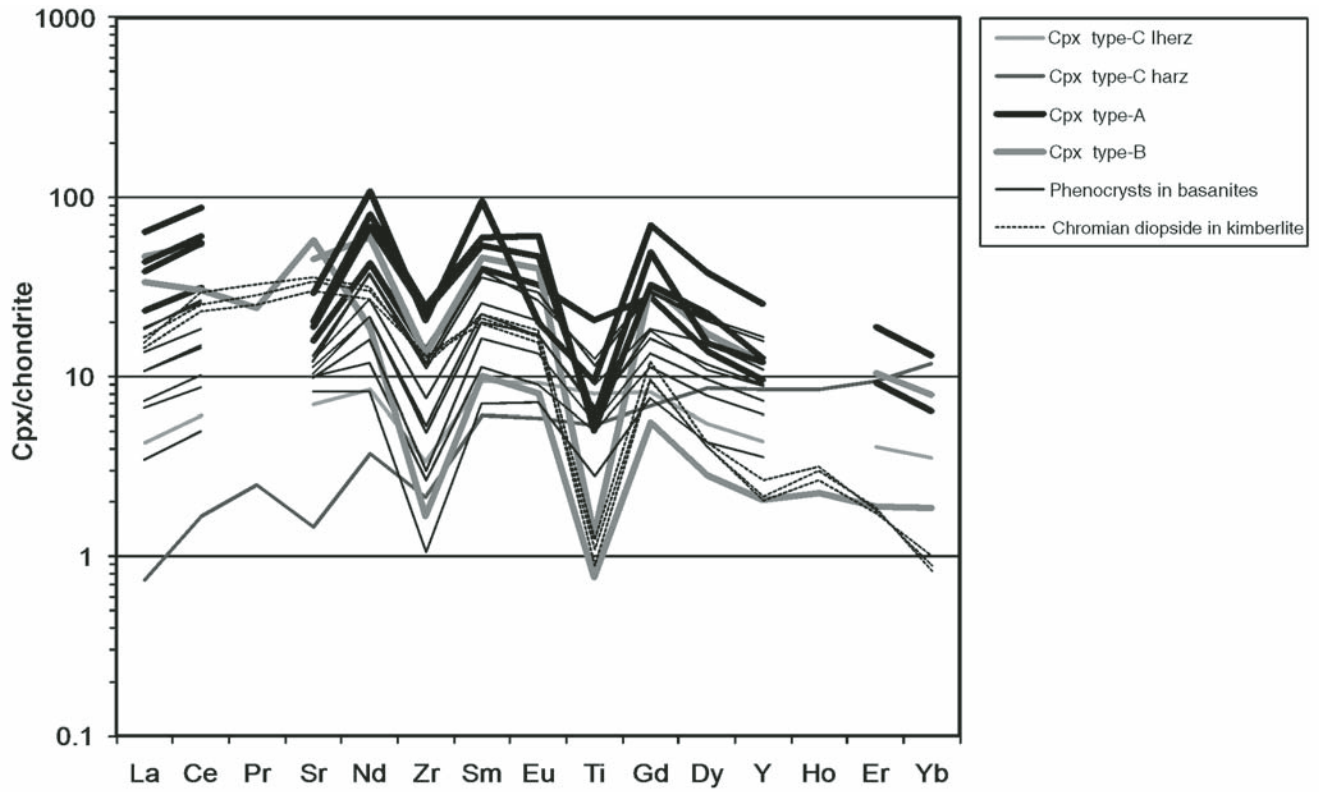


Figure 8. Abundances of rare earth elements (plus Sr, Zr, Ti, and Y) in type A and type B clinopyroxenes in Iherzolites (Iherz) and harzburgite (harz) CV66, normalized to chondrite values of McDonough and Sun (1995). Type C clinopyroxene (Cpx) in both Iherzolites and harzburgites (Bonadiman et al., 2005; Simon et al., 2008) and clinopyroxene phenocrysts in basanites (Francis and Minarik, 2008) and in kimberlites (Nimis et al., 2009) are also reported for comparison.

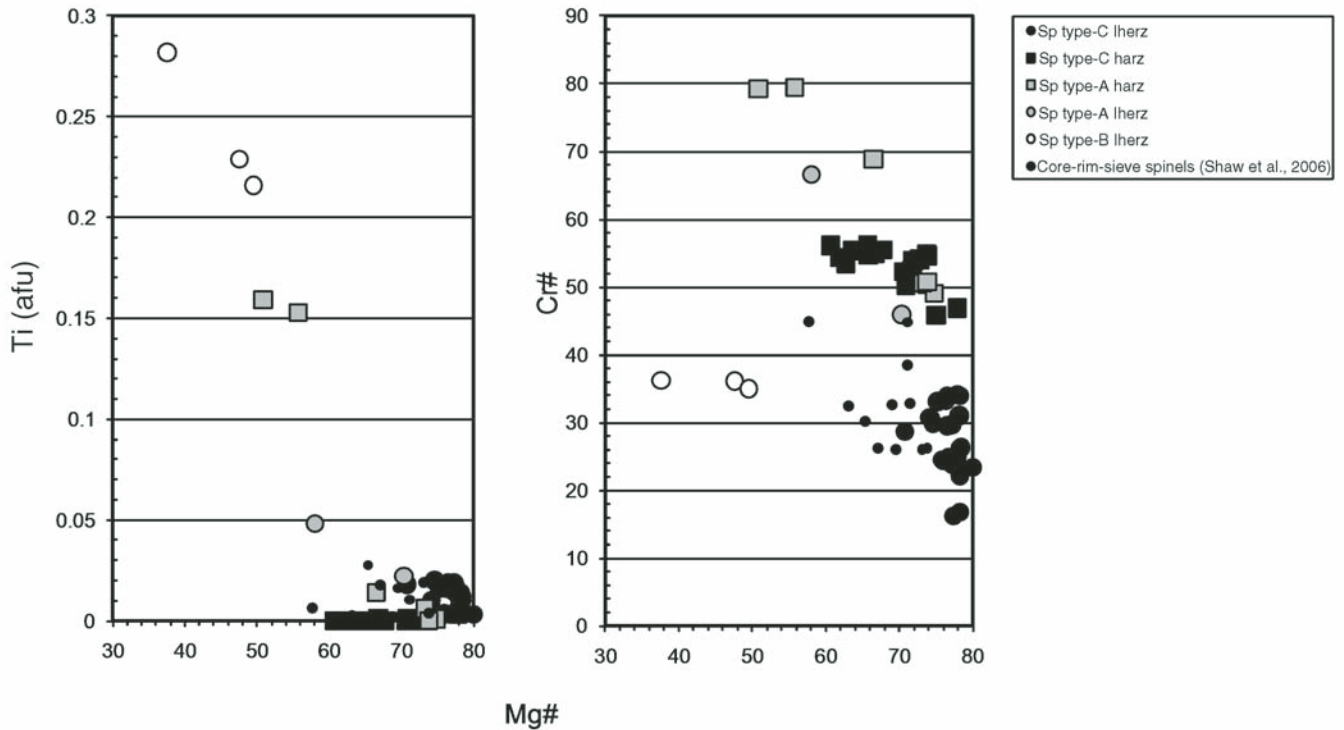


Figure 9. Ti and Cr# ($\text{Cr}/[\text{Cr} + \text{Al}]$ as afu) vs. Mg# ($\text{Mg}/[\text{Mg} + \text{Fe}]$ as afu) of type A, type B, and type C spinels (Sp). Primary spinels from a Cape Verde harzburgite (small black dots) analyzed in various textural positions by Shaw et al. (2006) are also included for comparison. afu—atomic formula units.

DISCUSSION

Whole-Rock Composition

Al_2O_3 is considered to be a robust index of partial melting of residual peridotites, because it rapidly decreases as partial melting proceeds at any depth (Herzberg, 2004) and also because postmelting processes are not efficient in modifying the Al_2O_3 in peridotites (Ionov and Hofmann, 2007). This is supported by the observation that, even in the most metasomatized (*sensu lato*) peridotites, Al_2O_3 rarely exceeds the PM (primitive mantle; McDonough and Sun, 1995) content (i.e., Lee, 2006). This does not mean that aluminum cannot be introduced by metasomatic process in a mantle peridotite (Griffin et al., 2009) but that, in terms of whole rock content, it is difficult to model Al_2O_3 in a refertilization process.

Cape Verde mantle xenoliths reflect this tendency: Postmelting processes such as “at-depth” peridotite-melt interaction (metasomatism) and/or host basalt infiltration are indistinguishable in terms of Al_2O_3 , CaO, and MgO, and no sample exceeds, in terms of “basaltic components,” the PM composition (Fig. 2). This general statement does not take into account alkalis and iron. Both type A and type B lherzolites and harzburgites show almost the same Na_2O values (Table 1), but only type A xenoliths record exceptionally high K_2O contents (Fig. 2). The dichotomy between Na and K observed in the two textural types suggests that the Na-alkaline host basalt ($\text{K}/\text{Na} < 1$), which infiltrated the xenoliths at low pressure, was able to modify the whole-rock Na content of the xenoliths. Na rapidly diffuses from an alkali basalt to the peridotite at low pressure (Lundstrom, 2003), causing the orthopyroxene to preferentially dissolve and producing type B mantle xenoliths. In turn, a completely different (K-rich) alkaline melt interacting with the peridotite at depth can produce type A Cape Verde mantle xenoliths. Whole-rock analyses of many cratonic garnet-bearing peridotites sampled by kimberlites show the same anomalous K enrichment and high K/Na ratios (Harte, 1983; Arai, 1986; Griffin et al., 2003), suggesting that they were subjected to metasomatic processes controlled by the percolation of K-rich melts. Xenoliths of this type commonly contain phlogopite and/or K-rich amphibole. The absence of such hydrous phases in the Sal xenoliths could be primarily related to different pressure-temperature (P - T) conditions of K-rich metasomatism in oceanic mantle beneath Cape Verde, compared to the P - T regime in cratonic mantle domains. The kimberlite-type metasomatic agent, reacting with the peridotite assemblage (mainly orthopyroxenes) in the region where the mantle xenoliths are entrapped in the host basalt (average $P = 17$ kbar; $T = 1092$ °C; Bonadiman et al., 2005), tends toward SiO_2 -saturated compositions. Melting experiments on SiO_2 -saturated K-rich basic magmas (lamproite-type) show that K-feldspar is a “liquidus” phase, while amphibole and phlogopite appear at higher pressures (Mitchell and Edgar, 2002).

The melting of iron (FeO) is an exception to the general rule of continuous decreases as partial melting proceeds, as observed

for other fusible major oxides. FeO_t in the residues of shallow melting (1–2 GPa) increases over 0% to ~10% melting, when both equilibrium (fixed pressure) and polybaric decompression fractional melting models are applied (Herzberg, 2004). Only at higher degrees of melting (>15%) does FeO significantly decrease (equilibrium partial melting model). Many Cape Verde mantle xenoliths show iron contents higher than PM, irrespective of the lithotype. On the whole, all the studied samples present FeO_t values higher than those calculated in melting models (at corresponding Al_2O_3 contents) with the highest FeO content in one type B sample (Fig. 12).

Experimental data show that $\text{FeO}_t \geq 8.3$ –8.5 wt% (depending on the PM model applied) cannot be obtained by partial melting of a fertile mantle ($\text{FeO}_t \sim 8\%$) at any pressure (Walter, 2003; Herzberg, 2004). Therefore, we attribute the high FeO_t of Cape Verde peridotites to postmelting enrichment processes. However, it is not straightforward to decide if this enrichment is derived from an interaction (at depth or during the ascent of the xenolith) of an Fe-rich melt as one might logically expect, since metasomatized peridotite xenoliths from intraplate worldwide localities interacting with different metasomatic agents (i.e., alkaline and carbonatitic types) show analogous Fe enrichments (Fig. 12).

Primary mantle-derived melts (from divergent and convergent environments and intraplate tectonic settings) have FeO_t contents varying from 8% to 13% (Farmer, 2003), with the highest estimated values (FeO_t , 25.7–28.7 wt%) assigned to the parental kimberlite melts (Le Roex et al., 2003; Harris et al., 2004; Kopylova et al., 2007). Subsequent interaction of mantle peridotites with any of these melts has as a consequence the addition of FeO to the peridotitic system. Some authors (Niu, 1997; Bodinier and Godard, 2003; Le Roux et al., 2007; Piccardo et al., 2007) claim that the majority of the lherzolites exposed at Earth’s surface (including off-craton mantle xenoliths) record a general refertilization of variable refractory protoliths, and all of them reflect a “generic” iron enrichment; thus, the widely observed Fe enrichment itself does not characterize the nature of the metasomatism, and it is not a useful parameter to discriminate between metasomatism and infiltration enrichments. From this viewpoint, the FeO_t and Na_2O bulk rock contents in Cape Verde mantle xenoliths have to be considered as “altered,” independent of the textural types assigned to the sample.

The selective incompatible trace-element enrichment (i.e., high field strength elements [HFSEs] vs. large ion lithophile elements [LILEs]) is frequently used to characterize the nature of the metasomatic agent, with LILE generally prevailing over HFSE in highly carbonated silicate and carbonatitic melts (i.e., Rudnick et al., 1993; Coltorti et al., 1999; Bonadiman et al., 2008). High levels of incompatible trace elements characterize almost all volcanic rocks that carry mantle xenoliths (from kimberlites to alkali basalts). The incompatible trace-element enrichment in the bulk xenoliths could be compromised by infiltration of the host magma during entrainment and eruption (Pearson et al., 2003, and reference therein). The trace-element patterns of Cape Verde xenoliths emphasize this problem, since samples without

textural evidence of host basalt infiltration (type A and type C) and samples penetrated by basaltic veinlets (type B) have similar enrichments (Fig. 3). Therefore, whole-rock geochemistry alone does not provide a straightforward way to interpret the processes that have affected mantle xenoliths.

Minerals and Glasses

Olivine

Based on olivine's crystal structure and point defect systematics and energetics (Dohmen et al., 2007), experimental studies on the diffusion rates of Fe-Mg, Ni, and Ca have demonstrated that Fe, Mg, and Ni show the same diffusion behavior (e.g., acti-

vation energy, fO_2 dependence, and, hence, diffusion mechanism) (Petry et al., 2004; Dohmen et al., 2007). On the other hand, the diffusion behavior of Ca has higher activation energies, and, consequently, the diffusion rates are much slower at most temperatures applicable to basalt/peridotite systems. Ca diffusion rates (Coogan et al., 2005) are substantially slower (by a factor of ~10, along [001]; Dohmen et al., 2007) than rates of Fe-Mg diffusion. The most important implication of this is that the Cape Verde type A olivines, which show Fe-Mg contents comparable to those of the primary counterparts (type C ol; Fig. 4), reflect the occurrence of a primary (at depth) peridotite-melt interaction well before the entrapment of the xenoliths, and at this stage, the metasomatic melt is already "buffered" in terms of Fe-Mg by the

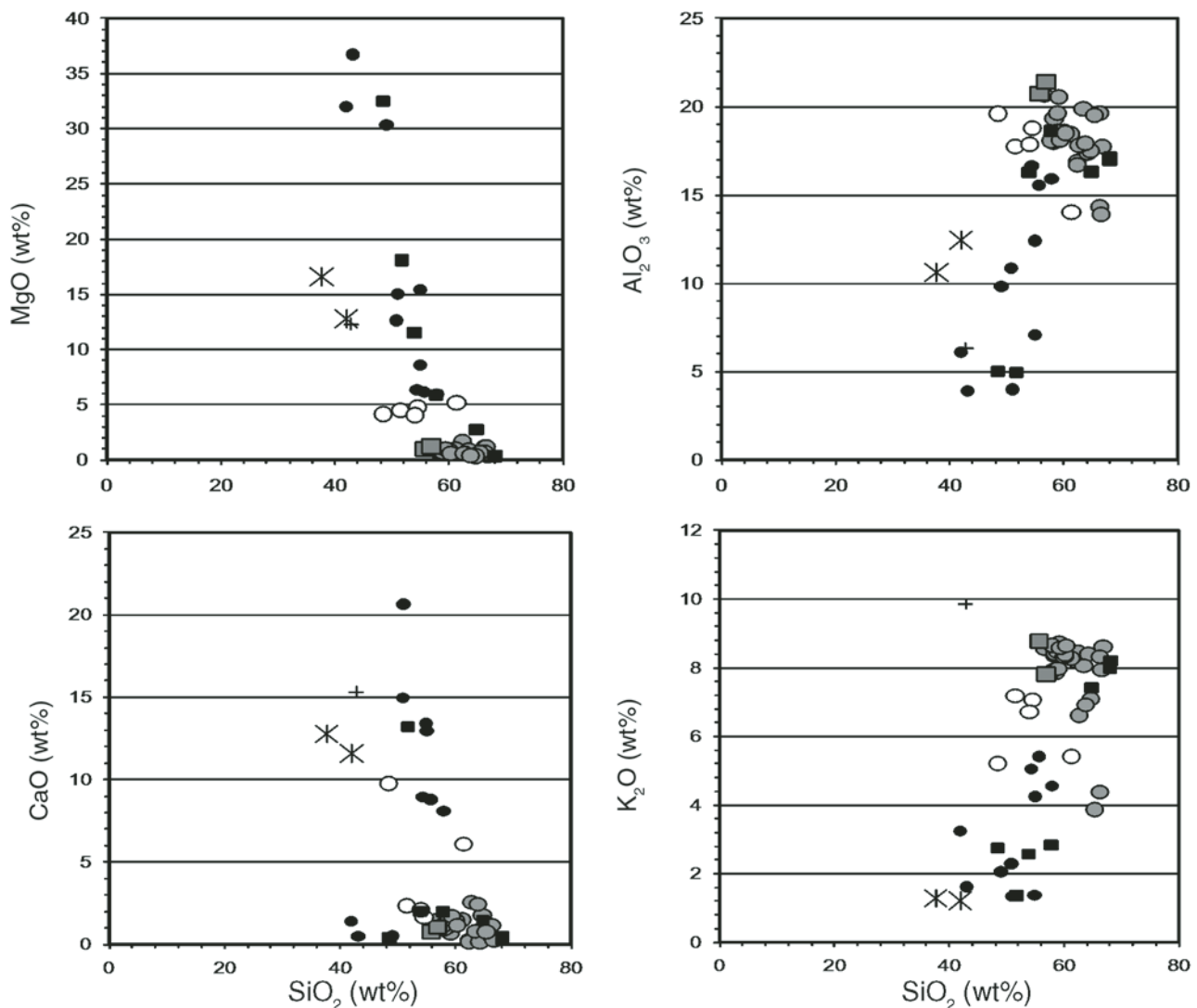


Figure 10 (Continued on following page). Major-element variation diagrams for the Cape Verde type A and type B mantle glasses and for their host basalts. Glasses associated with destabilization of orthopyroxene (black squares) and clinopyroxene (black dots) induced by host basalt infiltration in a Cape Verde harzburgite (Shaw et al., 2006) are also reported for comparison. Experimental (exp) results (cross) obtained by simulating the possible reactions that could have occurred in Cape Verde mantle xenoliths (by Shaw et al., 2006) are also included. lh—lherzolite; hz—harzburgite; cpx—clinopyroxene; opx—orthopyroxene.

peridotite system. The Ni and Ca contents in secondary olivines in both type A and type B are thus a reflection of metasomatism at depth. To test the validity of this statement, Cape Verde peridotite olivines are plotted together with two olivine crystallites present in host basalt veinlets crosscutting two nodules (Fig. 4). The latter are distinctively enriched in FeO relative to those (type A and type C) of the peridotite assemblage. Ni-Fe relationships of these crystallites are compatible with those calculated for olivine in equilibrium with a progressively fractionated melt. The fractionated trend was calculated using the method proposed by Tamura et al. (2000). Among our data set, secondary olivines from harzburgite CV10 appear to be compromised by infiltration of the host basalt, despite the lack of textural evidence, and were thus erroneously classified as type A ol (Fig. 4). Although Fe-Mg interdiffusion rates in olivine are fast (Gaetani and Watson, 2000), the homogeneous Mg# at the centimeter-scale in lherzolites and harzburgites implies melt-rock interaction times

$>10^4$ yr. Consequently, the Fe enrichment observed in olivines of harzburgite CV10 was most likely associated with fast magma flowing through intergranular films. On the whole, low-degree undersaturated silicate melts percolating at depth are olivine-saturated and may form secondary olivines by reaction and dissolution of pyroxene, without substantially modifying the original Fe/Mg of the peridotite. In contrast, in low-pressure (<1.5 GPa), high-temperature regimes, olivine silicate melts infiltrating the mantle xenoliths will produce a secondary olivine with the Fe/Mg ratio controlled by fractionation processes (Berger and Vannier, 1984; Kelemen et al., 1990).

Clinopyroxene

The exchange of iron and titanium between host basalt and Cr-rich diopsides (type C cpx) at high temperature and low pressure is rapid (i.e., Coltorti et al., 2004; Yu et al., 2006), implying high diffusion rates for these elements. However, in the cpx,

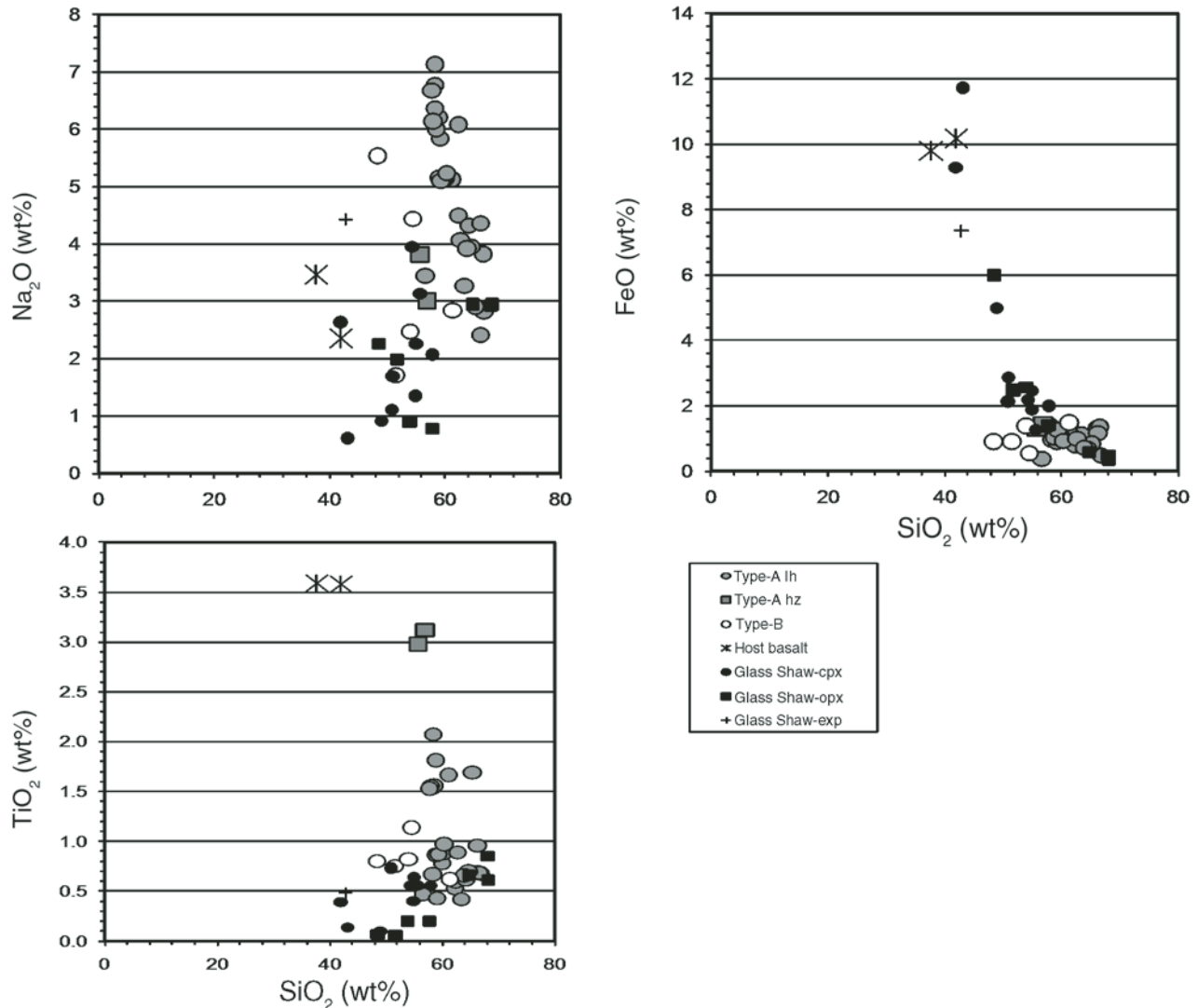


Figure 10 (Continued).

lattice Ti diffuses more rapidly than iron at low pressure. Grains of primary clinopyroxene, completely surrounded by patches of host basalt (type B cpx in Iherzolite CV20), show chemical modifications toward augite compositions in terms of Ti and Fe. In contrast, low-Ti and high-Fe contents suggest lower diffusion rate of Ti relative to iron in Cr-rich diopsides, as is typical of mantle conditions (Fig. 7).

In contrast, Al_2O_3 seems immune to high-temperature and low-pressure interactions with the host basalt (Fig. 7). In fact, even those clinopyroxenes that are clearly compromised by interactions with the host basalt (CV20 type B cpx) reflect a previous interaction with a metasomatic melt in equilibrium with peridotite diopside: Most type A clinopyroxenes have Al_2O_3 contents comparable to or lower than type C cpx. An explanation could be that the tschermakitic component in peridotitic cpx influences the thermodynamic parameters of the mixing between the two end-members $\text{CaMgSi}_2\text{O}_6$ - $\text{CaAl}_2\text{SiO}_2$, with $a_{\text{CaAl}_2\text{SiO}_6} > X_{\text{CaAl}_2\text{SiO}_6}$ in clinopyroxene solid solution, reducing the “mobility” of Al from type C to type A diopsides (Ashworth et al., 1992; Marchev et al., 2008).

The behavior of calcium is more ambiguous with respect to aluminum (Fig. 7), since the Ca content in diopside primarily depends on temperature more than pressure, but it shows the

same tendency as Al. Mantle diopsides that interact (at depth) with undersaturated silicate melts produce a new diopside composition: Type A cpx phase (Fig. 7). In contrast, peridotite diopsides that interact with infiltrated melts at progressively lower pressure tend toward a new chemical structure (i.e., aegirine, aegirine-augite), which is able to accommodate the highly diffusive elements (i.e., Fe and Ti) (Fig. 7).

As evidenced by the Cape Verde mantle data set, and as suggested by various authors (i.e., Hirose and Kawamoto, 1995; Herzberg, 2004; Griffin et al., 2009), Al_2O_3 (and to a lesser extent CaO) is confirmed as a robust parameter to investigate the melting processes occurring at depth, or the effect of (long-term?) circulation of metasomatic melts, reacting with the peridotite phases. In spinel-bearing peridotites with evident peridotite-melt reactions but without crystallization of hydrous phases, cpx is the only mineral phase able to accommodate the incompatible trace elements. The trace-element profiles of both metasomatic and infiltration types overlap the compositional ranges shown by cpx phenocrysts in equilibrium with undersaturated basaltic melts (Fig. 8). Very low degrees of partial melting (strongly undersaturated silicate melts, i.e., kimberlite-lamprophyres-melilitites-basanites-nephelinites) and

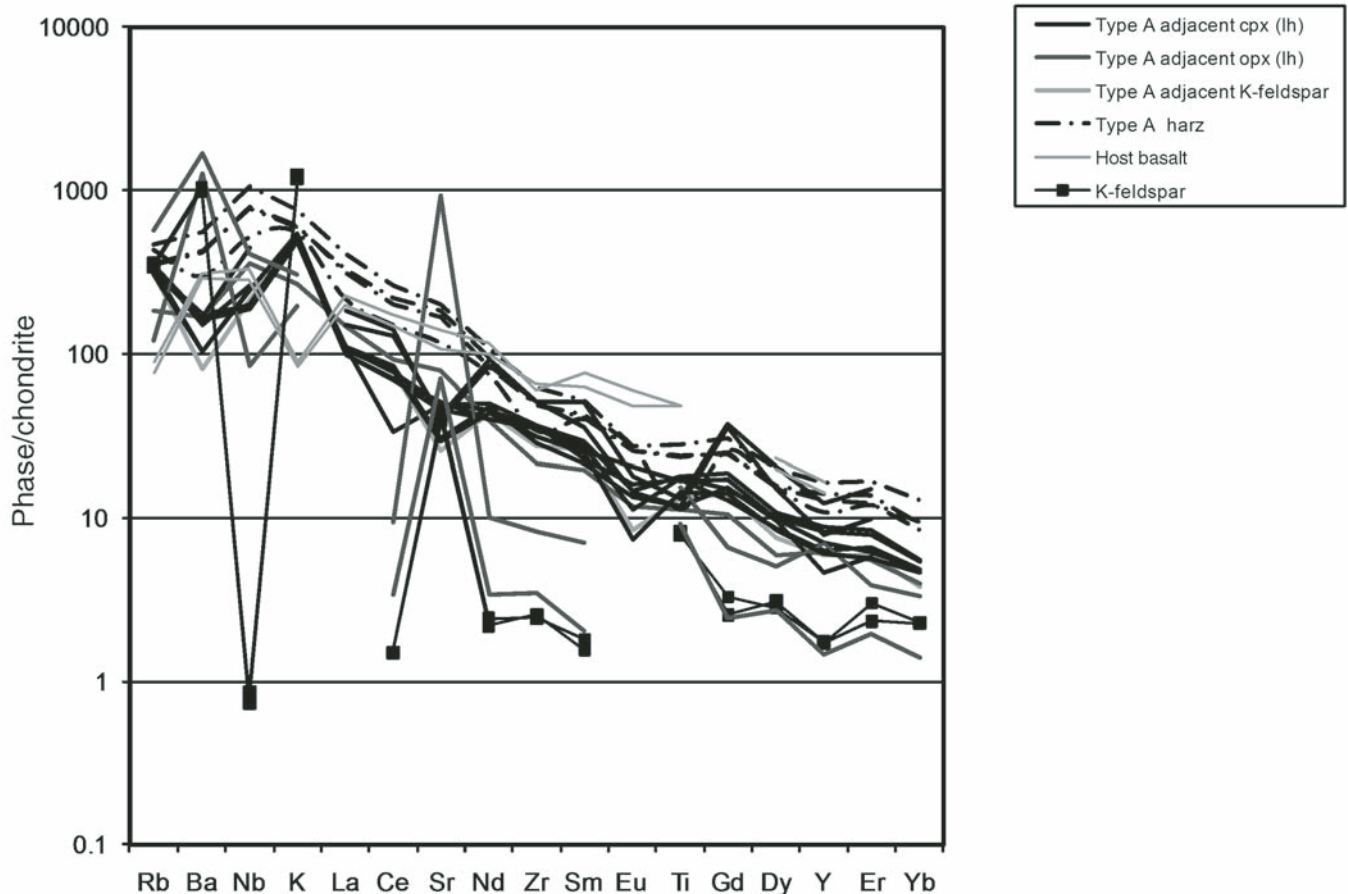


Figure 11. Chondrite-normalized patterns (values of McDonough and Sun, 1995) of Cape Verde mantle glasses and K-feldspars, compared with those of host basalts. cpx—clinopyroxene; lh—Iherzolite; opx—orthopyroxene; harz—harzburgite.

subsequently porous melt flow and diffusive exchange with the host peridotites can produce the same trace-element enrichment (mainly REE) and similar REE patterns in the newly formed cpx (Khazan and Fialko, 2005). Since REEs (and Sr) partition into the Ca sites in clinopyroxene (e.g., Wood and Blundy, 1997; Harte and Kirkley, 1997; van Westrenen et al., 1999), their abundances and distributions in recrystallized clinopyroxenes simply follow the CaO exchange between the peridotite matrix and the percolating melts, in relation to temperature conditions (Khazan and Fialko, 2005). Thus, we argue that the presence in peridotites of secondary clinopyroxenes with strong REE (and Sr) enrichment, high LREE/HREE, and La/Ce < 1 reflects the interaction with undersaturated mafic melts, but it does not discriminate among different types of melts, nor provide information as to where this interaction takes place.

Spinel

The chemistry of chromian spinel in peridotites depends on physicochemical conditions such as pressure, temperature, oxygen fugacity (fO_2), and the chemistry of the rock, and equilibrium with melt (i.e., Dick and Bullen, 1984; Shukuno and Arai, 1999). Basic magmas produced by melting of spinel-peridotite are in equilibrium with forsteritic olivine and chromian spinel under upper-mantle conditions (i.e., Lee et al., 2003; Herzberg, 2004). In the Cr-Al-Fe³⁺ ternary diagram (Fig. 13), type A sp of both lherzolites and harzburgites extend beyond the compositional field of harzburgitic type C sp toward the Cr apex.

Type A spinels are consistent with equilibrium between spinel and primary Mg-rich magmas (Shukuno and Arai, 1999). Cr content in spinels is controlled by the Al_2O_3/Cr_2O_3 ratio of the percolating Mg-rich melt in equilibrium with the mantle matrix

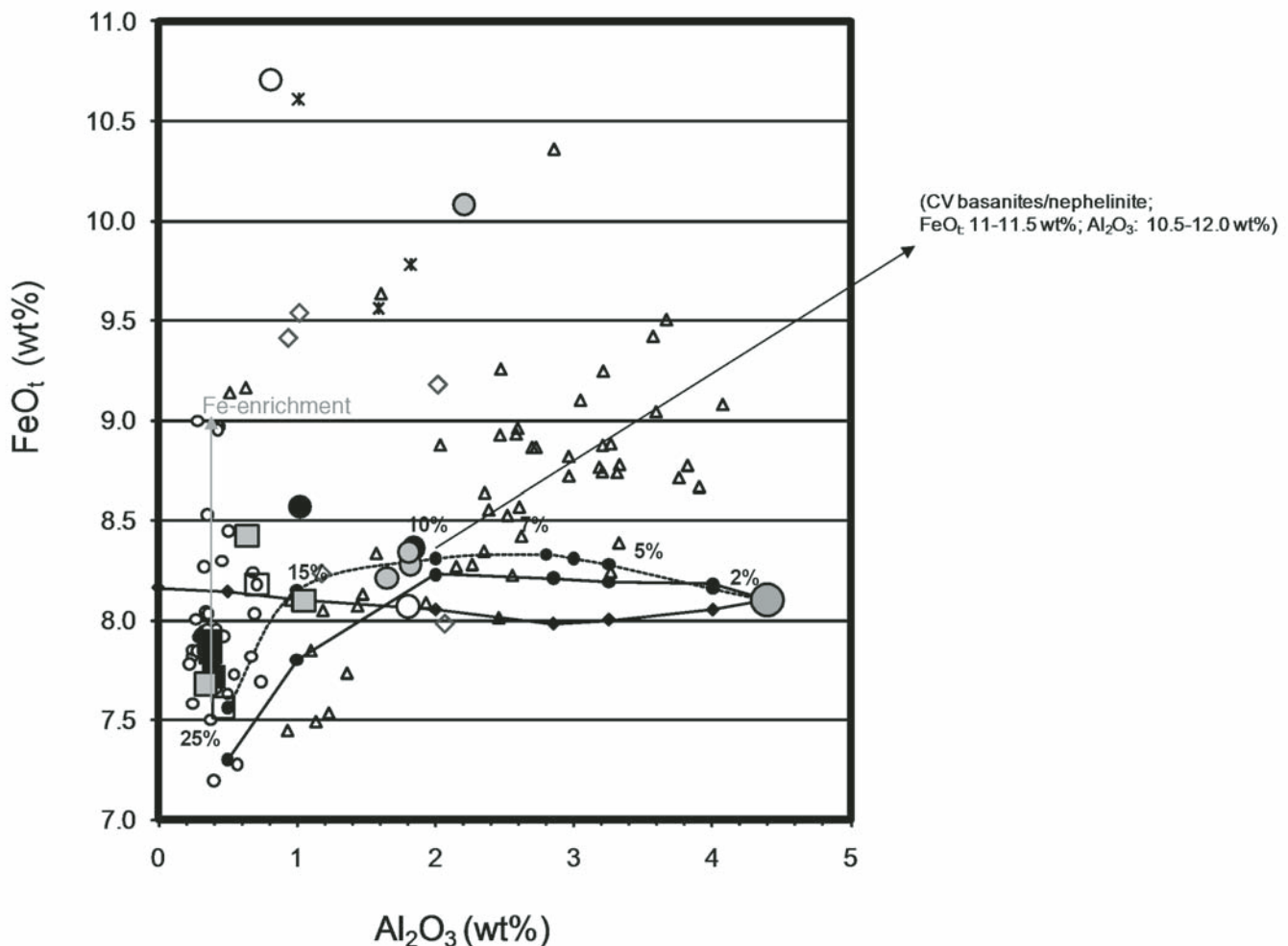


Figure 12. Whole-rock FeO_t vs. Al_2O_3 in Cape Verde type A, type B, and type C harzburgites and lherzolites; symbols are as in Figure 2. Solid and dashed curves marked by dots represent the results of equilibrium (fixed pressure) partial melting experiments at 2 GPa and 1 GPa, respectively. Solid curve marked by diamonds represents the results of polybaric (starting at 3 GPa) decompression melting experiments. The starting point (large dot) is the primitive mantle (PM) composition of McDonough and Sun (1995), and the numbers refer to melt fraction increments. Mantle xenoliths affected by intraplate alkaline silicate metasomatism (empty triangles and asterisk; Beccaluva et al., 2001; Coltorti et al., 2004) and carbonatitic metasomatism (empty diamonds; Coltorti et al., 1999) are also reported for comparison.

(Shukuno and Arai, 1999). The reaction takes place if the P - T - fO_2 conditions are confined to the high-pressure regime, and considering the high Fe^{3+} activity in Mg-rich melt (Lee et al., 2003), chromium spinel easily becomes Fe^{3+} buffered. By contrast, the type B spinels may be interpreted (as suggested by Shaw et al., 2006) as the products of low-pressure, high-temperature interaction with the host melt. The new crystallites are not chromian spinel but tend toward inverse spinel (i.e., Ti-magnetites). The primary spinels interacting with the host magma suffer the removal of the highly diffusive Al and Mg, allowing the introduction of Ti and Fe components from the host magma (type B sp) in the lattice. This general tendency, mainly due to temperature effects, is also observed in type A sp, but the Fe^{3+} component (calculated by stoichiometry) allows the discrimination between type A sp and type B sp or even primary spinel (type C) thermally disturbed by host magma (becoming type B spinel).

As already stated, chromian spinel, as a metasomatic product, tends toward a Fe^{3+} -buffered composition (Arai et al., 2003). This parameter varies significantly, depending on physicochemical conditions, mainly pressure and magma chemistry. However, it never exceeds a $Fe^{3+}/(Fe^{3+} + Al + Cr)$ atomic ratio of 0.2 (Arai et al., 2003; Wang et al., 2007, and reference therein). Cape Verde mantle spinels clearly show this: Type B sp overlap the type A sp compositional field for many components (i.e., Ti, Al, Fe), but only type B spinels record the highest Fe^{3+} contents (Figs. 9 and 13). This could be due to the condition of melt percolation; since the metasomatic melt pervades the peridotite matrix in a porous flow regime (degree of melting $<<1\%$), the Fe^{3+} activity in the melt is orders of magnitude higher than that of chromian spinels (i.e., Lee et al.,

2003; Herzberg, 2004; Canil, 2004). A decompression system (i.e., upwelling) is able to change the percolation regime from porous flow to open conduit flow (high melting degree: $>5\%$, accompanied by high temperature, and formation of veins and magma channels), and the chromian spinel is the low-pressure phase able to accommodate large amounts of Fe^{3+} . Unfortunately, this parameter was not considered by Shaw et al. (2006), when they discussed chemical variation of spinel in relation to the host magma. As Shaw and coauthors stated, the large primary spinel (core-rim and sieved) presented in the paper is definitely compromised by the host magma, but not because of the “evidence” they indicate. If they took into account the Fe^{3+} activity in spinel, their spinels would completely overlap the type B sp of this study (Fig. 13). From the data presented by Shaw et al. (2006), it is evident that the primary vermicular spinel (interdigitated with a reactive orthopyroxene) selected for their study was both preserved (i.e., compositions with $Fe^{3+} \sim 0$) and highly contaminated by the host basalt, irrespective of the textural position (core, rim, and sieve).

Glasses and Reaction Mineral Assemblage

Reaction of metasomatic melts with peridotites can modify the Al_2O_3 (and to a lesser extent CaO and TiO_2) content of pyroxenes (increasing or decreasing the original) depending on the nature of the percolating melt. For example, if the percolating melt is a volatile-bearing, high- TiO_2 silicate melt, it is able to progressively transform a primary cpx ($Al_2O_3 = 4.5$ – 5 wt%; $TiO_2 < 0.2$ wt%) into a metasomatic cpx (type A), with Al_2O_3 and TiO_2 up to 11 wt% and 4.5 wt%, respectively, before changing the original single-chain lattice to the double-chain lattice of the amphibole, if the P - T - fO_2 conditions are suitable for amphibole stability. This process has been texturally and chemically (including trace elements) well documented in peridotite xenoliths from Antarctica and Morocco (Coltorti et al., 2004; Raffone et al., 2009).

The Cape Verde metasomatizing agent was not able to form amphibole, perhaps because the melt percolation occurred at pressure and temperature conditions not suitable for the stabilization of this phase, or, more likely, because this melt is so rich in K_2O , relative to Na_2O and volatiles, that it could form a peculiar (for mantle environments) almost pure K-feldspar (Bonadiman et al., 2005). The sieved-spongy-dissolved-opx (rims or large portions of the entire crystal) can be interpreted as the product of a reaction between orthopyroxene and melt, which formed a new secondary assemblage: orthopyroxene + melt = ol2 + cpx2-O + sp2 + (K-feld)-silicate melt. Moreover, the formation of K-feldspar (K_2O up to 10.50 wt%; Bonadiman et al., 2005) as the product of in situ opx melting induced by a Na-alkaline melt (the host basalt) is almost impossible in terms of a geochemical budget.

Experimental and theoretical models indicate that low-pressure, high-temperature fractionation of intraplate basalts (alkali basalts, basanites, to olivine melilitites) is characterized by clinopyroxene, plagioclase, and olivine as liquidus phases; amphibole and spinel (ulvöspinel-magnetite) may form depending on alkali and H_2O contents (i.e., Herzberg and O'Hara, 1998; Green et al.,

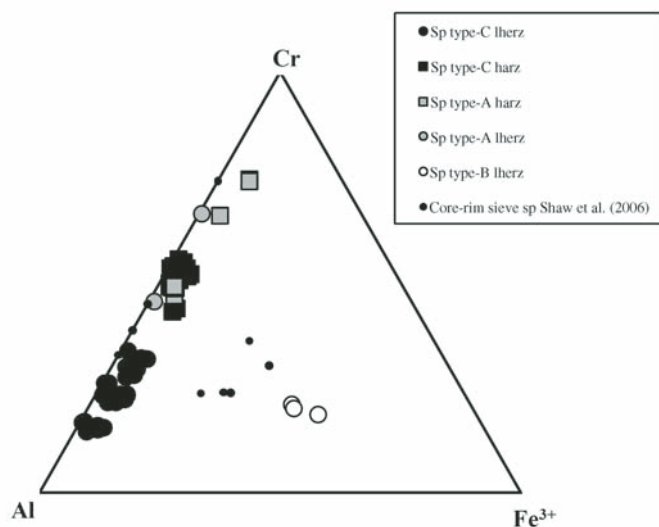


Figure 13. Plot of type A, type B, and type C spinels in terms of Al- Fe^{3+} -Cr (afu) as proposed by Arai et al. (2003) and Wang et al. (2007). Data from large primary vermicular spinel (core-rim and sieved) of a Cape Verde harzburgite (Shaw et al., 2006) are also plotted for comparison. This large spinel is either locally preserved or highly contaminated by the host basalts. Sp—spinel; lherz—lherzolite; harz—harzburgite; afu—atomic formula units.

2000; Herzberg, 2004; Pilet et al., 2005). Thus, the presence of K-feldspar in Cape Verde mantle xenoliths is difficult to explain as a reaction product between the peridotite matrix and the infiltrating (and fractionated) host basanite (Shaw et al., 2006). However, if a silica-undersaturated mafic/ultramafic melt (high K/Na: kimberlite-type melt) interacts at depth with a peridotite matrix, it would rapidly dissolve the orthopyroxene and evolve toward SiO_2 -saturated compositions (lamproite-type?). This melt will be particularly K_2O rich, higher in TiO_2 and BaO , and lower in CaO , MgO , FeO , and volatiles (H_2O , CO_2) than the primitive kimberlite-type metasomatizing agent. These geochemical characteristics perfectly correspond to those of type A Cape Verde mantle glasses and, according to the petrology of lamproites (Davis et al., 2006, and reference therein), may also account for the peculiar petrography of the Cape Verde metasomatic mineral assemblage: the coexistence of forsteritic olivine, diopsides, and K-feldspar as “liquidus phases.”

Metasomatism and Isotopic Signatures

In Sr-Nd space, the isotopic signature of cpx separated from type A and type C xenoliths varies from depleted mantle (DM) toward primitive components. These signatures are distinct with respect to the lavas from both northern and southern islands, with the cpx type A lherzolites approaching Sr-Nd (and Hf) values of the southern islands and the field of subcontinental lithospheric mantle domains as represented by group I kimberlites (Fig. 14).

On the basis of isotopic and trace-element data, the basalts of the northern islands reflect mixing between recycled oceanic crust and lower mantle with the contribution of “local” depleted material. Basalts from the southern islands, which approach the type A mantle xenolith isotopic signatures (Fig. 14), require an additional enriched component thought to be subcontinental lithospheric mantle left behind during the opening of central Atlantic, or stemming from delamination and entrainment into the Cape Verde plume (Doucelance et al., 2003; Escrig et al., 2005). Cape Verde isotopic data on separate clinopyroxenes do not help to discriminate between metasomatism and infiltration processes, but they do reinforce the hypothesis that a fragment of subcontinental lithospheric mantle domain was preserved during/after the opening of the Atlantic Ocean (Coltorti et al., 2010) and was successively able to form the K-rich undersaturated/saturated silicate melts percolating through the peridotite matrix.

Selective enrichments in incompatible trace elements (HFSE vs. LILE) are commonly used to characterize the nature of metasomatic agents, with LILE generally prevailing over HFSE in highly carbonated silicate and carbonatitic melts (Coltorti et al., 1999; Bonadiman et al., 2008). Notwithstanding these selective enrichments, high levels of incompatible elements characterize almost all volcanic rocks that carry mantle xenoliths (from kimberlites to basalt/andesites), and contents of incompatible trace elements in xenoliths could be compromised by the infiltration of the host magma during entrainment and eruption (Pearson et al., 2003, and reference therein).

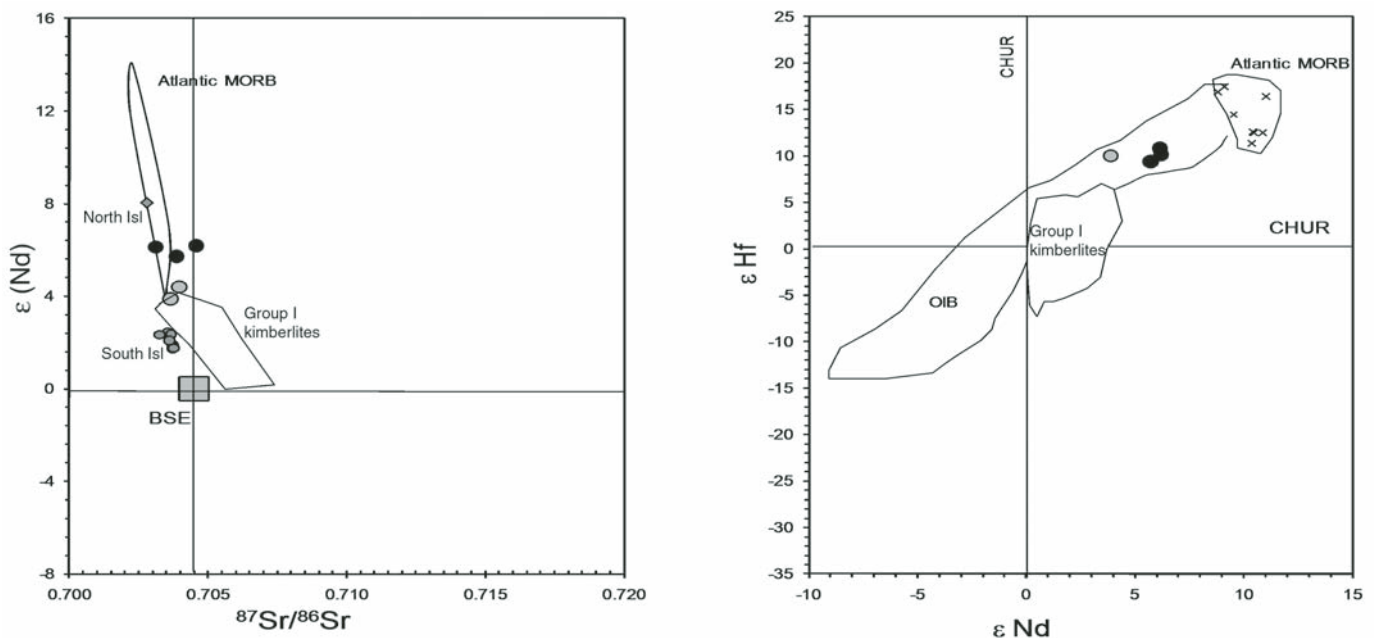


Figure 14. Isotopic compositions of separate clinopyroxenes from type A and type C Cape Verde mantle xenoliths. Symbols are as in Figure 2. Data from the basalts from the northern and southern islands (Isl) of the Cape Verde Archipelago are also reported for comparison (Gerlach et al., 1988; Doucelance et al., 2003; Escrig et al., 2005). Fields for the Atlantic mid-ocean-ridge basalt (MORB), ocean-island basalt (OIB), and group I kimberlites are drawn using literature data (Hofmann, 2003; Davis et al., 2006). BSE—Bulk Silicate Earth; CHUR—Chondrite Uniform Reservoir.

CONCLUSIONS

Based on textural features and geometrical relationships between the host basalt and mantle fragments, three textural types are recognized:

Type A consists of lherzolites and harzburgites with orthopyroxene and clinopyroxene (and spinel) partially, or sometimes completely, replaced by finely disseminated secondary clinopyroxene, olivine, or spinel (and K-feldspar), locally associated with glassy patches (glass <5 vol%) and without textural evidence of host basalt infiltration.

Type B consists of lherzolites and harzburgites clearly affected by host basalt infiltration, with veinlets crosscutting the nodule, either connected or not with the host basalt, occasionally filled with plagioclase \pm magnetite crystallites, which destabilize orthopyroxenes and/or clinopyroxenes.

Type C consists of lherzolites and harzburgites that do not show any textural evidence of either basaltic infiltration or metasomatism.

The bulk rock geochemistry alone is not enough to interpret the processes occurring in mantle xenoliths. However, in terms of bulk rock major-element contents, the dichotomy between Na and K observed in type A and type B Cape Verde xenoliths suggests that the Na-alkaline host basalt ($K/Na < 1$) is able to modify the whole-rock Na content of the xenoliths and efficiently dissolve the orthopyroxene, forming type B Cape Verde mantle xenoliths. In turn, a K-rich alkaline melt ($K/Na > 1$) interacted at depth with the peridotite system, forming type A samples, before the ascent of the xenoliths.

The Cape Verde K-rich metasomatizing agent is not able to form hydrous minerals, as commonly observed in metasomatized cratonic garnet-bearing peridotites, maybe because the melt percolation occurs at pressure and temperature conditions not suitable to stabilize these phases, or, more likely, because this melt is so rich in K_2O , with respect to Na_2O and volatiles, that it is able to form a peculiar (for mantle environments), almost pure K-feldspar (Bonadiman et al., 2005).

To interpret the processes occurring in mantle xenoliths, the most reliable results are obtained from *in situ* mineral (and glass) studies, and not only for Cape Verde mantle xenoliths. Fe/Mg in olivine is a good parameter to discriminate metasomatism from host basalt infiltration. Olivine-saturated basaltic melts percolating at depth may form secondary olivines, without substantially modifying the original Fe/Mg peridotite ratio. At low pressure (<1.5 GPa), olivine silicate melts infiltrating the mantle xenoliths form, by reaction, a secondary olivine where Fe/Mg is controlled by fractionation processes.

Al_2O_3 (and to a lesser extent CaO) is confirmed as a robust parameter to investigate the melting processes in the peridotite phases (mainly pyroxenes) occurring at depth. Mantle diopsides, which interact at depth with undersaturated silicate melts, react and rearrange the most fusible elements into a new diopside composition: type A cpx. In contrast, peridotite diopsides, which interact with melts at progressively lower pressure, react and

locally rearrange themselves into a new chemical structure (i.e., aegirine, aegirine-augite) able to accommodate the high diffusive elements (i.e., Fe and Ti): type B cpx.

The Fe^{3+} in spinel is a key element to investigate the processes acting on mantle xenoliths. As a metasomatic product, secondary chromian spinel tends toward a Fe^{3+} -buffered composition (Arai et al., 2003). This parameter varies significantly, depending on the physicochemical conditions, mainly pressure and chemistry of the magma and its percolation conditions. In a porous flow regime (degree of melting <<1%), Fe^{3+} activity in melt is various orders of magnitude higher than that of chromian spinels. When the percolation regime changes from porous flow to open conduit (high melting degree, >5%, and formation of veins and magma channels), the chromian spinel is the low-pressure phase able to accommodate large amounts of Fe^{3+} .

In conclusion, by analyzing the textural and chemical characteristics of Cape Verde xenoliths, we have decoded the geometrical and compositional relationships between host basalt and mantle fragments. As a general statement, based on the chemical behavior in the mantle system, when the textural settings remain ambiguous, a rigorous analysis of the compositional features (mainly major-element contents) of mineral and glasses (if present) is the most efficient tool to place the mantle xenoliths in the correct genetic framework.

ACKNOWLEDGMENTS

We appreciate the constructive reviews from M. Godard, E.-R. Neumann, and an anonymous reviewer, which dramatically improved the manuscript. We would like to thank Suzy Elhlou and Peter Wieland of the GEMOC Australian Research Council (ARC) National Key Centre for very helpful assistance in the laboratory and with instruments, and also Norman Pearson for his expertise and thoughtful discussions.

The analytical data were obtained using instrumentation funded by ARC Linkage Infrastructure Equipment and Facilities, and Department of Education Science and Training, Systemic Infrastructure Grants, industry partners and Macquarie University.

This is contribution 687 from the Australian Research Council National Key Centre for the Geochemical Evolution and Metallogeny of Continents (<http://www.gemoc.mq.edu.au>). This research was supported by Interlink Program (PRIN 2007) and ARC Discovery Grant to SYO'R and WLG.

REFERENCES CITED

- Arai, S., 1986, K/Na variation in phlogopite and amphibole of upper mantle peridotites due to fractionations of metasomatizing fluids: *The Journal of Geology*, v. 94, p. 436–444, doi:10.1086/629042.
- Arai, S., and Abe, N., 1995, Reaction of orthopyroxene in peridotite xenoliths with alkali-basalt melt and its implication for genesis of alpine-type chromitite: *The American Mineralogist*, v. 80, p. 1041–1047.
- Arai, S., Satoko Ishimaru, S., and Okrugin, V.M., 2003, Metasomatized harzburgite xenoliths from Avacha volcano as fragments of mantle wedge of the Kamchatka arc: Implication for the metasomatic agent: *The Island Arc*, v. 12, p. 233–246.

- Ashworth, J.R., Birdi, J.J., and Emmett, T.F., 1992, Diffusion in coronas around clinopyroxene: Modelling with local equilibrium and steady state, and a non-steady-state modification to account for zoned actinolite-hornblende: *Contributions to Mineralogy and Petrology*, v. 109, p. 307–325, doi:10.1007/BF00283321.
- Aulbach, S., Griffin, W.L., O'Reilly, S.Y., and McCandless, T.E., 2004, Genesis and evolution of the lithospheric mantle beneath the Buffalo Head terrane, Alberta (Canada): *Lithos*, v. 77, p. 413–451, doi:10.1016/j.lithos.2004.04.020.
- Aulbach, S., Pearson, N.J., O'Reilly, S.Y., and Doyle, B.J., 2007, Origins of xenolithic eclogites and pyroxenites from the Central Slave craton, Canada: *Journal of Petrology*, v. 48, p. 1843–1873, doi:10.1093/petrology/egm041.
- Beccaluva, L., Bonadiman, C., Coltorti, M., Salvini, L., and Siena, F., 2001, Depletion events, nature of metasomatizing agent and timing of enrichment processes in lithospheric mantle xenoliths from the Veneto volcanic province: *Journal of Petrology*, v. 42, p. 173–188, doi:10.1093/petrology/42.1.173.
- Begg, G.C., Griffin, W.L., Natapov, L.M., O'Reilly, S.Y., Grand, S.P., O'Neill, C.J., Hronsky, J.M.A., Poudjom Domani, Y., Swain, C.J., Deen, T., and Bowden, P., 2009, The lithospheric architecture of Africa: Seismic tomography, mantle petrology, and tectonic evolution: *Geosphere*, v. 5, p. 23–50, doi:10.1130/GES00179.1.
- Berger, E.T., and Vannier, M., 1984, Les dunites en enclaves dans les basaltes alcalins des îles océaniques: Approche pétrologique: *Bulletin Mineralogique*, v. 107, p. 649–663.
- Bodinier, J.L., and Godard, M., 2003, Orogenic, ophiolitic, and abyssal peridotites, in Carson R.W., ed., *The Mantle and Core, Volume 2: Treatise in Geochemistry*: Amsterdam, Elsevier-Pergamon, p. 103–170.
- Bonadiman, C., Beccaluva, L., Coltorti, M., and Siena, F., 2005, Kimberlite-like metasomatism and 'garnet signature' in spinel-peridotite xenoliths from Sal, Cape Verde Archipelago: Relics of a subcontinental mantle domain within the Atlantic oceanic lithosphere?: *Journal of Petrology*, v. 46, p. 2465–2493, doi:10.1093/petrology/egi061.
- Bonadiman, C., Coltorti, M., Duggen, S., Plaudetti, L., Siena, F., Thirlwall, M., and Upton, B.G.J., 2008, Palaeozoic subduction-related and kimberlite/carbonatite metasomatism in the Scottish lithospheric mantle, in Coltorti, M., and Grégoire, M., eds., *Metasomatism in Oceanic and Continental Lithospheric Mantle*: Geological Society of London Special Publication 293, p. 303–333.
- Brearely, M., and Scarfe, C.M., 1986, Dissolution rates of upper mantle minerals in an alkali basalt melt at high pressure: An experimental study and implications for ultramafic xenolith survival: *Journal of Petrology*, v. 27, p. 1157–1182.
- Brunelli, D., Seyler, M., Cipriani, A., Ottolini, L., and Bonatti, E., 2006, Discontinuous melt extraction and weak refertilization of mantle peridotites at the Vema lithospheric section (Mid-Atlantic Ridge): *Journal of Petrology*, v. 47, p. 745–771, doi:10.1093/petrology/egi092.
- Canil, D., 2004, Mildly incompatible elements in peridotites and the origins of mantle lithosphere: *Lithos*, v. 77, p. 375–393, doi:10.1016/j.lithos.2004.04.014.
- Coltorti, M., Bonadiman, C., Hinton, R.W., Siena, F., and Upton, B.G.J., 1999, Carbonatite metasomatism of the oceanic upper mantle: Evidence from clinopyroxenes and glasses in ultramafic xenoliths of Grande Comore, Indian Ocean: *Journal of Petrology*, v. 40, p. 133–165, doi:10.1093/petrology/40.1.133.
- Coltorti, M., Beccaluva, L., Bonadiman, C., Salvini, L., and Siena, F., 2000, Glasses in mantle xenoliths as geochemical indicators of metasomatic agents: *Earth and Planetary Science Letters*, v. 183, p. 303–320, doi:10.1016/S0012-821X(00)00274-0.
- Coltorti, M., Beccaluva, L., Bonadiman, C., Faccini, B., Ntafos, T., and Siena, F., 2004, Amphibole genesis via metasomatic reaction with clinopyroxene in mantle xenoliths from Victoria Land, Antarctica: *Lithos*, v. 75, p. 115–139, doi:10.1016/j.lithos.2003.12.021.
- Coltorti, M., Bonadiman, C., O'Reilly, S.Y., Griffin, W.L., and Pearson, N.J., 2010, Buoyant ancient continental mantle embedded in oceanic lithosphere (Sal Island, Cape Verde Archipelago): *Lithos*, v. 120, p. 222–233, doi:10.1016/j.lithos.2009.11.005.
- Coogan, L.A., Kasemann, S.A., and Chakraborty, S., 2005, Rates of hydrothermal cooling of new oceanic upper crust derived from lithium-geospeedometry: *Earth and Planetary Science Letters*, v. 240, p. 415–424, doi:10.1016/j.epsl.2005.09.020.
- Dalton, J.A., and Presnall, D.C., 1998, The continuum of primary carbonatitic–kimberlitic melt compositions in equilibrium with lherzolite: Data from the system $\text{CaO-MgO-Al}_2\text{O}_3\text{-SiO}_2\text{-CO}_2$ at 6 GPa: *Journal of Petrology*, v. 39, p. 1953–1964, doi:10.1093/petrology/39.11.1953.
- Davies, G.R., Stolz, A.J., Mahotkin, I.L., Nowell, G.M., and Pearson, D.G., 2006, Trace element and Sr–Pb–Nd–Hf isotope evidence for ancient, fluid-dominated enrichment of the source of Aldan Shield lamproites: *Journal of Petrology*, v. 47, p. 1119–1146.
- Dawson, J.B., 1984, Constraining types of upper mantle metasomatism, in Kornprobst, J., ed., *Kimberlites II: Mantle and Crust-Mantle Relationships*: Amsterdam, Elsevier, p. 289–294.
- Dick, H.J.B., and Bullen, T., 1984, Chromian spinel as a petrogenetic indicator in abyssal and alpine-type peridotites and spatially associated lavas: *Contributions to Mineralogy and Petrology*, v. 86, p. 54–76, doi:10.1007/BF00373711.
- Dohmen, R., Becker, H.-W., and Chakraborty, S., 2007, Fe–Mg diffusion in olivine I: Experimental determination between 700 and 1200 °C as a function of composition, crystal orientation, and oxygen fugacity: *Physics and Chemistry of Minerals*, v. 34, p. 389–407, doi:10.1007/s00269-007-0157-7.
- Doucance, R., Escrig, S., Moreira, M., Gariépy, C., and Kurz, M.D., 2003, Pb–Sr–He isotope and trace element geochemistry of the Cape Verde Archipelago: *Geochimica et Cosmochimica Acta*, v. 67, p. 3717–3733, doi:10.1016/S0016-7037(03)00161-3.
- Escrig, S., Doucance, R., Moreira, M., and Allegre, C.J., 2005, Os isotope systematics in Fogo Island: Evidence for lower continental crust fragments under the Cape Verde Southern Islands: *Chemical Geology*, v. 219, p. 93–113, doi:10.1016/j.chemgeo.2005.02.011.
- Farmer, G.L., 2003, Continental basaltic rocks, in Rudnick, R.L., ed., *The Crust, Volume 3: Treatise on Geochemistry*: Oxford, Elsevier-Pergamon, p. 85–121.
- Francis, D., and Minarik, W., 2008, Aluminum-dependent trace element partitioning in clinopyroxene: *Contributions to Mineralogy and Petrology*, v. 156, p. 439–451, doi:10.1007/s00410-008-0295-z.
- Gaetani, G.A., and Watson, E.B., 2000, Open system behavior of olivine-hosted melt inclusions: *Earth and Planetary Science Letters*, v. 183, p. 27–41, doi:10.1016/S0012-821X(00)00260-0.
- Gerlach, D.C., Cliff, R.A., Davies, G.R., Norry, M.J., and Hodgson, N., 1988, Magma sources of the Cape Verdes archipelago: Isotopic and trace element constraints: *Geochimica et Cosmochimica Acta*, v. 52, p. 2979–2992.
- Green, T.H., Blundy, J.D., Adam, J., Yaxley, G.M., 2000, SIMS determination of trace element partition coefficients between garnet, clinopyroxene and hydrous basaltic liquids at 2–7.5 GPa and 1080–1200°C: *Lithos*, v. 53, p. 165–187.
- Griffin, W.L., O'Reilly, S.Y., Abe, N., Aulbach, S., Davies, R.M., Pearson, N.J., Doyle, B.J., and Kivi, K., 2003, The origin and evolution of Archean lithospheric mantle: Precambrian Research, v. 127, p. 19–41, doi:10.1016/S0301-9268(03)00180-3.
- Griffin, W.L., O'Reilly, S.Y., Afonso, J.C., and Begg, G.C., 2009, The composition and evolution of lithospheric mantle: A re-evaluation and its tectonic implications: *Journal of Petrology*, v. 50, p. 1185–1204, doi:10.1093/petrology/egn033.
- Harris, M., le Roex, A.P., and Class, C., 2004, Geochemistry of the Uintjesberg kimberlite, South Africa: Petrogenesis of an off-craton, group I, kimberlite: *Lithos*, v. 74, p. 149–165, doi:10.1016/j.lithos.2004.02.001.
- Harte, B., 1983, Mantle peridotites and processes—The kimberlite sample, in Hawkesworth, C.J., and Norry, M.J., eds., *Continental Basalts and Mantle Xenoliths*: Nantwich, Shiva, p. 46–91.
- Harte, B., and Kirkley, M.B., 1997, Partitioning of trace elements between clinopyroxene and garnet: Data from mantle eclogites: *Chemical Geology*, v. 136, p. 1–24, doi:10.1016/S0009-2541(96)00127-1.
- Hellebrand, E., Snow, J.E., and Mühe, R., 2002, Mantle melting beneath Gakkel Ridge (Arctic Ocean): Abyssal peridotite spinel compositions: *Chemical Geology*, v. 182, p. 227–235.
- Herzberg, C., 2004, Geodynamic information in peridotite petrology: *Journal of Petrology*, v. 45, p. 2507–2530, doi:10.1093/petrology/egh039.
- Herzberg, C., and O'Hara, M.J., 1998, Phase equilibrium constraints on the origin of basalts, picrites, and komatiites: *Earth-Science Reviews*, v. 44, p. 39–79, doi:10.1016/S0012-8252(98)00021-X.
- Hirose, K., and Kawamoto T., 1995, Hydrous partial melting of lherzolite at 1 GPa: The effect of H_2O on the genesis of basaltic magmas: *Earth and Planetary Science Letters*, v. 133, p. 463–473.

- Hofmann, A.W., 2003, Sampling mantle heterogeneity through oceanic basalts: Isotopes and trace elements, in Carson, R.W., ed., *The Mantle and Core, Volume 2: Treatise in Geochemistry*: Amsterdam, Elsevier-Pergamon, p. 61–101.
- Ionov, D.A., and Hofmann, A.W., 2007, Depth of formation of subcontinental off-craton peridotites: Earth and Planetary Science Letters, v. 261, p. 620–634, doi:10.1016/j.epsl.2007.07.036.
- Ionov, D.A., Prikhodko, V.S., Bodinier, J.-L., Sobolev, A.V., and Weis, D., 2005, Lithospheric mantle beneath the south-eastern Siberian craton: Petrology of peridotite xenoliths in basalts from the Tokinsky Stanovik: Contributions to Mineralogy and Petrology, v. 149, p. 647–665, doi:10.1007/s00410-005-0672-9.
- Jagoutz, E., Palme, H., Baddenhausen, H., Blum, K., Cendales, M., Dreibus, G., Spettel, B., Lorentz, V., and Wanke, H., 1979, The abundances of major, minor and trace elements in the Earth's mantle as derived from primitive ultramafic nodules: Houston, Texas, Lunar and Planetary Institute, Proceedings of Lunar and Planetary Science Conference X, p. 2031–2050.
- Kelemen, P.B., Joyce, D.B., Webster, J.D., and Holloway, J.R., 1990, Reaction between ultramafic rock and fractionating basaltic magma: II. Experimental investigation of reaction between olivine tholeiite and harzburgite at 1150–1050 °C and 5 kb: Journal of Petrology, v. 31, p. 99–134.
- Khazan, Y., and Fialko, Y., 2005, Why do kimberlites from different provinces have similar trace element patterns?: Geochemistry Geophysics Geosystems, v. 6, Q10002, doi:10.1029/2005GC000919.
- Klügel, A., 1998, Reactions between mantle xenoliths and host magma beneath La Palma (Canary Islands): Constraints on magma ascent rates and crustal reservoirs: Contributions to Mineralogy and Petrology, v. 131, p. 237–257, doi:10.1007/s004100050391.
- Kopylova, M.G., Matveev, S., and Raudsepp, M., 2007, Searching for parental kimberlite melt: Geochimica et Cosmochimica Acta, v. 71, p. 3616–3629, doi:10.1016/j.gca.2007.05.009.
- Lee, C.-T.A., 2006, Geochemical/petrologic constraints on the origin of cratonic mantle, in *Archean Geodynamics and Environments: American Geophysical Union Geophysical Monograph* 164, p. 1–27.
- Lee, C.-T.A., Brandon, A.D., and Norman, M.D., 2003, Vanadium in peridotites as a proxy for paleo- f_{O_2} during partial melting: Prospects, limitations, and implications: Geochimica et Cosmochimica Acta, v. 67, p. 3045–3064, doi:10.1016/S0016-7037(03)00268-0.
- Le Roex, A.P., Bell, D.R., and Davis, P., 2003, Petrogenesis of Group I kimberlites from Kimberley, South Africa: Evidence from bulk rock geochemistry: Journal of Petrology, v. 44, p. 2261–2286, doi:10.1093/petrology/egg077.
- Le Roux, V., Bodinier, J.-L., Tommasi, A., Alard, O., Dautria, J.-M., Vauchez, A., and Riches, A.J.V., 2007, The Lherz spinel lherzolite: Refertilized rather than pristine mantle: Earth and Planetary Science Letters, v. 259, p. 599–612.
- Lundstrom, C.C., 2003, An experimental investigation of the diffusive infiltration of alkalis into partially molten peridotite: Implications for mantle melting processes: Geochemistry Geophysics Geosystems, v. 4, no. 8614, doi:10.1029/2001gc000224.
- Marchev, P., Arai, S., Ishida, Y., Shirasaka, M., and Downes, H., 2008, Trace element and isotopic composition of mafic and ultramafic cumulate xenoliths in alkaline basalts from the eastern Rhodopes, Bulgaria: Inferences on deep processes under the metamorphic core complexes: IOP (Institute of Physics) Conference Series: Earth and Environmental Science, v. 2, p. 1–10.
- McDonough, W.F., and Sun, S.-s., 1995, The composition of the Earth: Chemical Geology, v. 120, p. 223–253, doi:10.1016/0009-2541(94)00140-4.
- Menzies, M.A., and Hawkesworth, C.J., 1987, Upper mantle processes and composition, in Nixon, P.H., ed., *Mantle Xenoliths*: Chichester, UK, Wiley, p. 725–738.
- Mitchell, R.H., and Edgar, A.D., 2002, Melting experiment on SiO_2 -rich lamproites to 6.4 GPa and their bearing on the sources of lamproite magmas: Mineralogy and Petrology, v. 74, p. 115–128.
- Morgan, G.B., and London, D., 1996, Optimizing the electron microprobe analysis of hydrous alkali aluminosilicate glasses: The American Mineralogist, v. 81, p. 1176–1185.
- Morimoto, N., Fabries, J., Ferguson, A.K., Ginzburg, I.V., Ross, M., Seifert, F.A., Zussman, J., Aoki, K., and Gottardi, G., 1988, Nomenclature of pyroxenes: The American Mineralogist, v. 73, p. 1123–1133.
- Neumann, E.-R., and Simon, N.S.C., 2009, Ultra-refractory mantle xenoliths from ocean islands: How do they compare to peridotites retrieved from oceanic sub-arc mantle?: Lithos, Special Volume, v. 107, p. 1–16.
- Neumann, E.-R., and Wulff-Pedersen, E., 1997, The origin of highly silicic glass in mantle xenoliths from the Canary Islands: Journal of Petrology, v. 38, p. 1513–1539, doi:10.1093/petrology/38.11.1513.
- Nimis, P., Zanetti, A., Dencker, I., and Sobolev, N.V., 2009, Major and trace element composition of chromian diopsides from the Zagadochnaya kimberlite (Yakutia, Russia): Metasomatic processes, thermobarometry and diamond potential: Lithos, v. 112, p. 397–412, doi:10.1016/j.lithos.2009.03.038.
- Niu, Y., 1997, Mantle melting and melt extraction processes beneath ocean ridges: Evidence from abyssal peridotites: Journal of Petrology, v. 38, p. 1047–1074, doi:10.1093/petrology/38.8.1047.
- O'Neill, H.St.C., and Palme, H., 1997, Composition of the silicate Earth: Implications for accretion and core formation, in Jackson, I., ed., *The Earth Mantle*: Cambridge, UK, Cambridge University Press, p. 3–127.
- O'Reilly, S.Y., and Griffin, W.L., 1996, 4-D lithosphere mapping: Methodology and examples: Tectonophysics, v. 262, p. 3–18, doi:10.1016/0040-1951(96)00010-8.
- Pearson, D.G., Canil, D., and Shirey, S.B., 2003, Xenoliths and diamonds in volcanic rocks, in Carson, R.W., ed., *The Mantle and Core, Volume 2: Treatise in Geochemistry*: Amsterdam, Elsevier-Pergamon, p. 171–225.
- Petry, C., Chakraborty, S., and Palme, H., 2004, Experimental determination of Ni diffusion coefficients in olivine and their dependence on temperature, composition, oxygen fugacity, and crystallographic orientation: Geochimica et Cosmochimica Acta, v. 68, p. 4179–4188, doi:10.1016/j.gca.2004.02.024.
- Piccardo, G.B., 2008, The Jurassic Ligurian Tethys, a fossil ultra-slow spreading ocean: The mantle perspective, in Coltorti, M., and Grégoire, M., eds., *Metasomatism in Oceanic and Continental Lithospheric Mantle: Geological Society of London Special Publication* 294, p. 11–33.
- Piccardo, G.B., Zanetti, A., and Muentener, O., 2007, Melt/peridotite interaction in the Southern Lanzo peridotite: Field, textural and geochemical evidence: Lithos, v. 94, p. 181–209.
- Pilet, S., Hernandez, J., Sylvester, P., and Poujol, M., 2005, The metasomatic alternative for ocean island basalt chemical heterogeneity: Earth and Planetary Science Letters, v. 236, p. 148–166.
- Raffone, N., Chazot, G., Pin, C., Vannucci, R., and Zanetti, A., 2009, Metasomatism in the lithospheric mantle beneath Middle Atlas (Morocco) and the origin of Fe- and Mg-rich wehrlites: Journal of Petrology, v. 50, p. 197–249, doi:10.1093/petrology/egn069.
- Rudnick, R.L., McDonough, W.F., and Chappell, B.W., 1993, Carbonatite metasomatism in the northern Tanzanian mantle: Petrographic and geochemical characteristics: Earth and Planetary Science Letters, v. 114, p. 463–475, doi:10.1016/0012-821X(93)90076-L.
- Ryabchikov, J.D., Ntaflou, T., Kurat, G., and Kogarko, L.N., 1995, Glass-bearing xenoliths from Cape Verde: Evidence for a hot rising mantle jet: Mineralogy and Petrology, v. 55, p. 217–237, doi:10.1007/BF01165119.
- Shaw, C.S.J., and Dingwell, D.B., 2008, Experimental peridotite-melt reaction at one atmosphere: A textural and chemical study: Contributions to Mineralogy and Petrology, v. 155, p. 199–214, doi:10.1007/s00410-007-0237-1.
- Shaw, C.S.J., and Edgar, A.D., 1997, Post-entrainment mineral-melt reactions in spinel peridotite xenoliths from Inver, Donegal, Ireland: Geological Magazine, v. 134, p. 771–779, doi:10.1017/S001675689700784X.
- Shaw, C.S.J., Heidelberg, F., and Dingwell, D.B., 2006, Origin of reaction textures in mantle peridotite xenoliths from Sal Island, Cape Verde: The case of “metasomatism” induced by the host lava during transport: Contributions to Mineralogy and Petrology, v. 151, p. 681–697.
- Shukuno, H., and Arai, S., 1999, Olivine-chromian spinel compositional relationships of the Cenozoic alkali basalts from southwest Japan: Implications for their mantle restites: Journal of Mineralogical, Petrological, and Economic Geology, v. 94, p. 120–140, doi:10.2465/ganko.94.120.
- Simon, N.S.C., Neumann, E.-R., Bonadiman, C., Coltorti, M., Delpech, G., and Grégoire, M., 2008, Ultra-refractory domains in the oceanic mantle lithosphere sampled as mantle xenoliths at ocean islands: Journal of Petrology, v. 49, p. 1223–1251, doi:10.1093/petrology/egn023.
- Tamura, Y., Yuhara, M., and Ishii, T., 2000, Primary arc basalts from Daisen volcano, Japan: Equilibrium crystal fractionation versus disequilibrium fractionation during supercooling: Journal of Petrology, v. 41, p. 431–448.
- van Achterbergh, E., Ryan, C.G., and Griffin, W.L., 1999, Glitter: On line intensity reduction for the laser ablation inductively coupled plasma spectrometry: Houston, Texas, Lunar and Planetary Institute, 9th V.M. Goldschmidt Conference, abstract no. 7215.

- van Westrenen, W., Blundy, J.D., and Wood, B.J., 1999, Crystal chemical controls on trace element partitioning between garnet and anhydrous silicate melt: *The American Mineralogist*, v. 84, p. 838–847.
- Walter, M., 2003, Melt extraction and compositional variability in mantle lithosphere, in Carson R.W., ed., *The Mantle and Core, Volume 2: Treatise on Geochemistry*: Oxford, Elsevier-Pergamon, p. 363–394.
- Wang, J., Hattori, K.H., Kilian, R., and Stern, C.R., 2007, Metasomatism of sub-arc mantle peridotites below southernmost South America: Reduction of fO_2 by slab-melt: *Contributions to Mineralogy and Petrology*, v. 153, p. 607–624, doi:10.1007/s00410-006-0166-4.
- Witt-Eickschen, G., and O'Neill, St.C., 2005, The effect of temperature on the equilibrium distribution of trace elements between clinopyroxene, orthopyroxene in upper mantle peridotites: *Chemical Geology*, v. 221, p. 65–101, doi:10.1016/j.chemgeo.2005.04.005.
- Wood, B.J., and Blundy, J.D., 1997, A predictive model for rare earth element partitioning between clinopyroxene and anhydrous silicate melt: *Contributions to Mineralogy and Petrology*, v. 129, p. 166–181, doi:10.1007/s004100050330.
- Wood, B.J., and Fraser, G., 1977, *Elementary Thermodynamics for Geologists*: New York, Oxford University Press, 303 p.
- Yamamoto, J., Nakai, S., Nishimura, K., Kaneoka, I., Kagi, H., Sato, K., Okumura, T., Prikhod'ko, V.S., and Arai, S., 2009, Intergranular trace elements in mantle xenoliths from Russian Far East: Example for mantle metasomatism by hydrous melt: *The Island Arc*, v. 18, p. 225–241, doi:10.1111/j.1440-1738.2008.00642.x.
- Yu, J-H., O'Reilly, S.Y., Zhang, M., Griffin, W.L., and Xisheng, Xu, 2006, Roles of melting and metasomatism in the formation of the lithospheric mantle beneath the Leizhou Peninsula, South China: *Journal of Petrology*, v. 47, p. 355–383, doi:10.1093/petrology/egi078.

MANUSCRIPT ACCEPTED BY THE SOCIETY 9 NOVEMBER 2010

Magmatic evidence for African mantle propagation into the southern Tyrrhenian backarc region

Teresa Trua*

Dipartimento di Scienze della Terra, Università degli Studi di Parma, Via G.P. Usberti, 157A, I-43100 Parma, Italy

Michael P. Marani

Fabiano Gamberi

*Istituto di Scienze Marine–Consiglio Nazionale delle Ricerche,
Sezione di Geologia Marina, Via Gobetti 101, I-40129 Bologna, Italy*

ABSTRACT

Major- and trace-element and Sr-Nd-Pb isotope compositions are presented for an extensive data set of samples (44) recovered along the active ridge axis of the southern Tyrrhenian backarc basin represented by the Marsili volcano (<0.7 Ma). In addition, major and trace elements are presented for the few lavas sampled from the summit area (active at 0.4–0.1 Ma) of Vavilov volcano, located in the oceanic subbasin (i.e., Vavilov Basin) formed during the first stage of the southern Tyrrhenian backarc basin formation.

Overall, these data confirm that southern Tyrrhenian backarc basin magmatism is chemically heterogeneous, ranging from an island-arc basalt (IAB) type, prevalent throughout the backarc evolution, to an ocean-island basalt (OIB)-like magmatism that occurred later in the development of the basin. Since the lavas sampled from Vavilov volcano have been strongly altered, their isotope composition was not acquired in this study. Thus, our attempt to identify the mantle domains beneath the southern Tyrrhenian system was restricted to its youngest and active part, i.e., the Marsili backarc basin and the Aeolian arc. These new data together with previously published trace-element and Sr-Nd-Pb isotope data for Marsili volcano lavas reveal that two mantle domains are involved in their petrogenesis: One represents the southern Tyrrhenian ambient mantle from which the mid-ocean-ridge basalts (MORB) flooring the Vavilov backarc basin are derived, and the other has HIMU (high U/Pb) OIB-like character, resembling the mantle source of the nearby Ustica Na-alkaline lavas. Subduction-related signatures characterize both, although to a lesser extent in the OIB-like domain with respect to the MORB-like mantle.

The new data provide a much needed insight into the evolution of the southern Tyrrhenian backarc basin system, confirming that the HIMU OIB-like component results from the propagation of deep northern African mantle inflow around the southern tear of the subducting Ionian slab, rather than being a component that was

*teresa.trua@unipr.it

present in the mantle wedge prior to the Ionian subduction process. Furthermore, a comparison between the Marsili backarc and Aeolian arc lavas permits interpretation of the trajectories followed by the African OIB-like mantle inflow within the southern Tyrrhenian mantle wedge. In particular, mantle trajectories involve upward-directed flow from the slab edge beneath Ustica Island and Prometeo submarine lava field, slab-parallel flow beneath the Marsili backarc volcano, and arcward-directed flow affecting the western margin of the Aeolian arc, thus compositionally influencing the Alicudi basic lavas.

INTRODUCTION

The development of the southern Tyrrhenian Sea, the youngest (younger than 7 Ma) active backarc basin of the Western Mediterranean area (Kastens et al., 1988; Kastens and Mascle, 1990; Fig. 1), is coupled to the rollback of a narrow slab (the Ionian plate), sustained by tears at the northern and southern slab edges (Gvirtzman and Nur, 1999; Marani and Trua, 2002; Rosenbaum and Lister, 2004). This geodynamic setting favored the ingress of ocean-island basalt (OIB) mantle from the northern African plate into the southern Tyrrhenian mantle wedge around the edges of the subducting slab (Figs. 1 and 2), as shown from recent geophysical studies (Chiarabba et al., 2008, and references therein) and geochemical investigations of

lavas erupted at the margins of the southern Tyrrhenian backarc basin (i.e., Ustica and Prometeo—Trua et al., 2003; Stromboli—De Astis et al., 2006).

Furthermore, the active spreading center of the southern Tyrrhenian backarc basin, currently located in the southeastern sector of the basin, has a strongly elongated magmatically inflated morphology, represented by Marsili volcano (Figs. 1 and 3). The distinctive morphology of Marsili volcano indicates greater-than-normal magma production compared to typical backarc basin systems, probably related to its geodynamic setting (Marani and Trua, 2002). Moreover, the geochemical and isotope features of Marsili lavas are not fully consistent with a simple subduction setting, as indicated by a preliminary geochemical and isotope study (Trua et al., 2007). Indeed, this

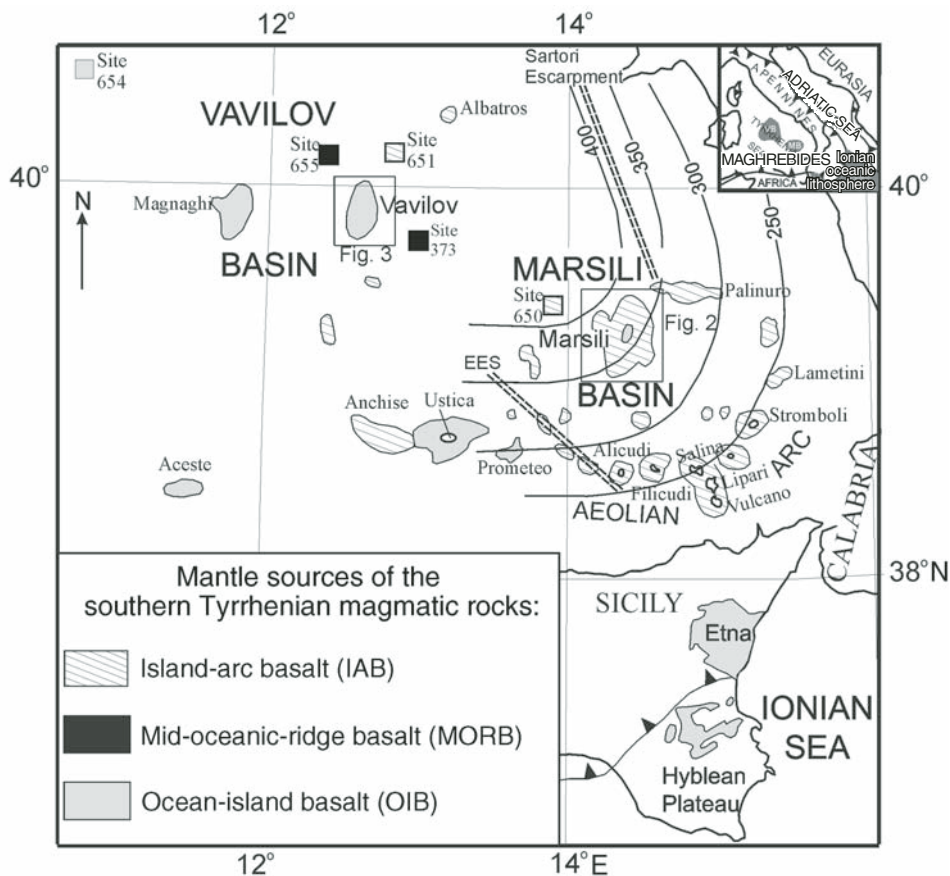


Figure 1. Schematic map of the Cenozoic magmatic rocks of the southern Tyrrhenian region according to their inferred dominant magma sources (modified after Trua et al., 2007). EES—Eolo-Enarete-Sisifo lineament.

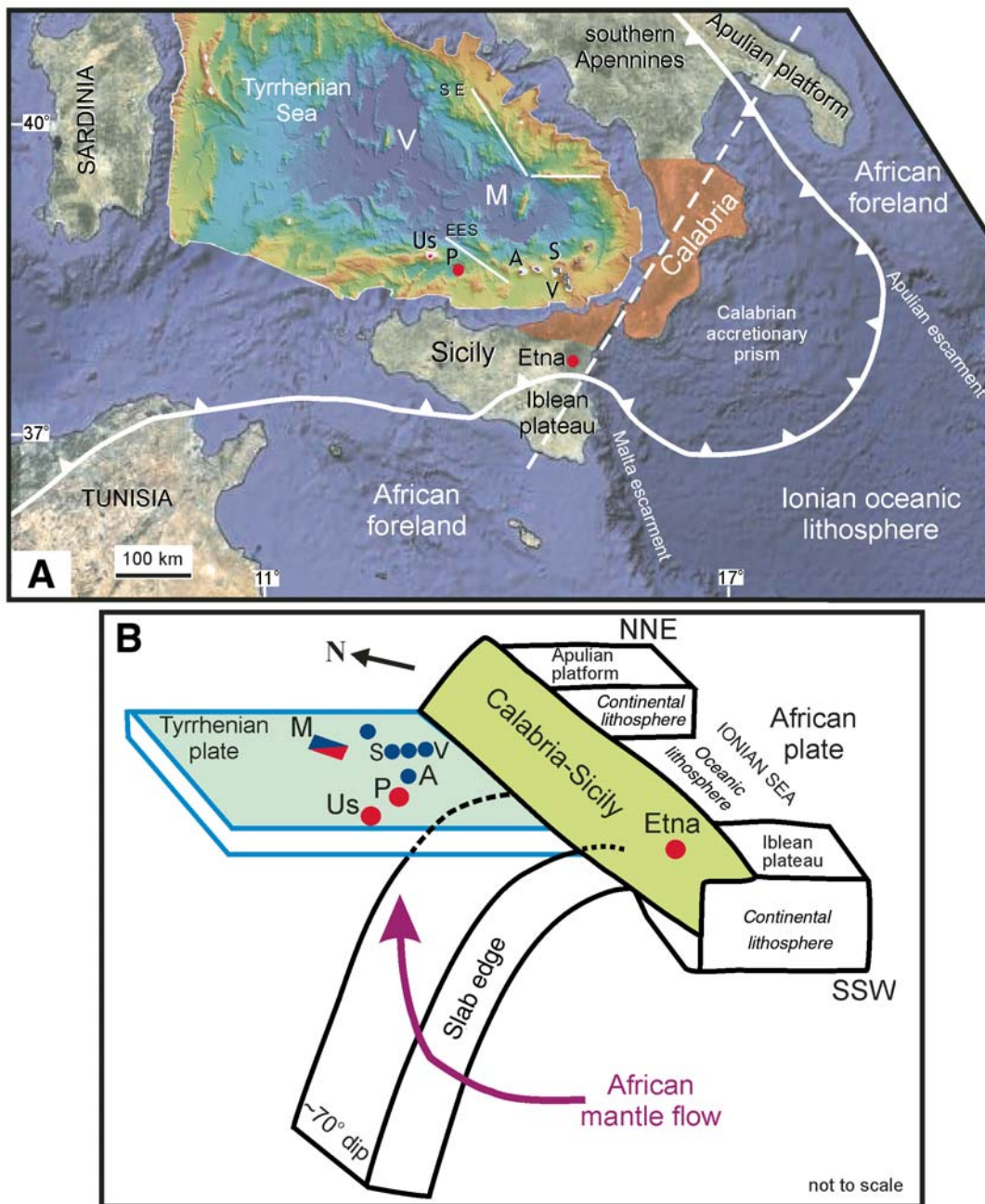
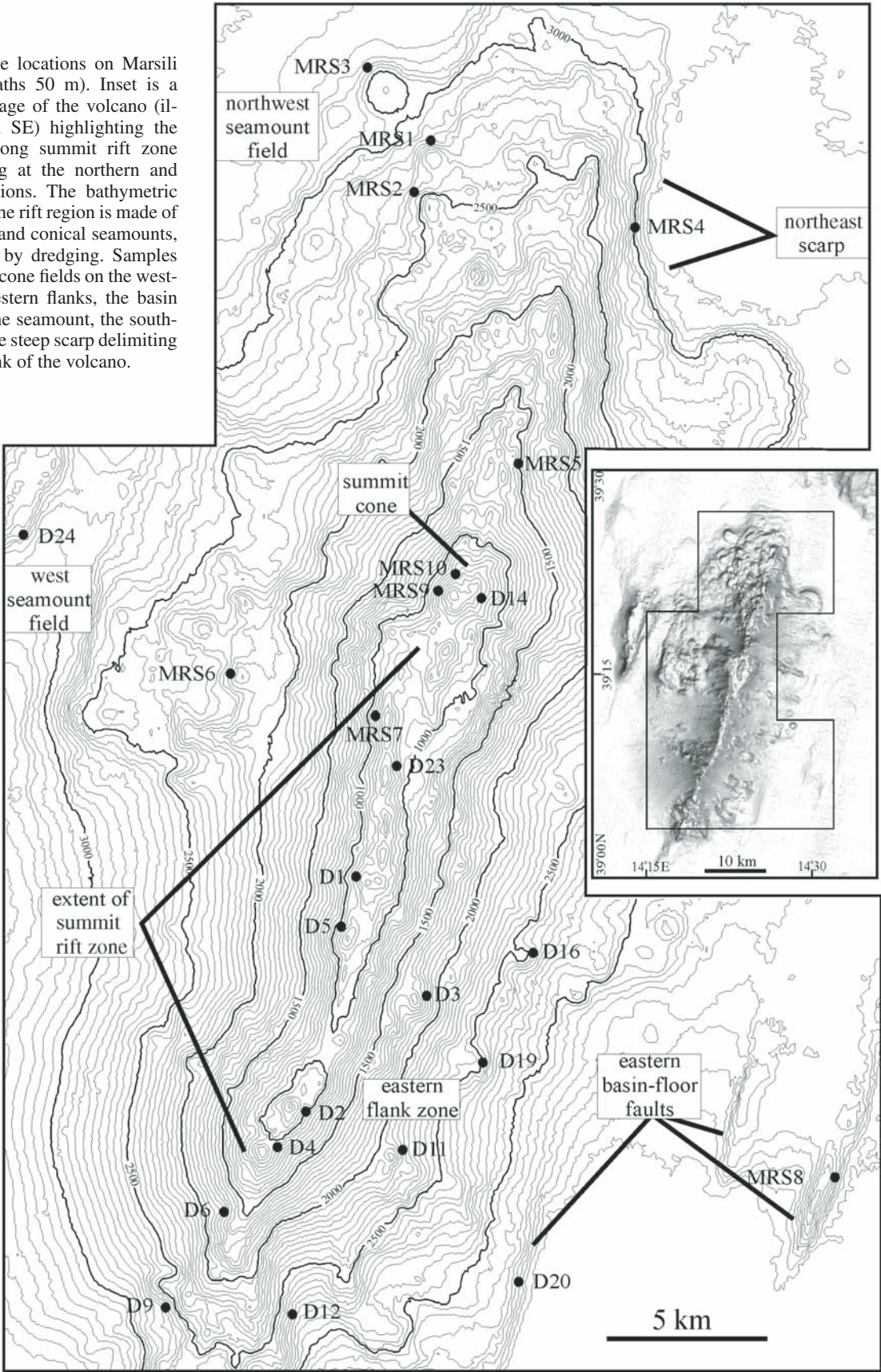


Figure 2. Regional geology and sketch of the southern Tyrrhenian subduction system. (A) Geodynamic framework showing the southern Tyrrhenian bathymetry (color-coded depth) and surrounding front (barbed white line) of the Apennine-Maghrebid fold-and-thrust belt running from the southern Apennines to northern Tunisia. The Calabria and northeastern Sicily ("Peloritani") alpine verging terrane is shown in transparent brown. African foreland units of the Iblean Plateau and Apulian platform bound the Ionian oceanic lithosphere through the offshore Malta and Apulian Escarpments, respectively. In the Tyrrhenian, the Marsili (M) and Vavilov (V) volcanoes are shown, positioned at the centers of their respective homonymous basins. Ustica Island (Us) and the submarine Prometeo lava field (P) characterized by ocean-island basalt (OIB)-like products lie to the west of the active Aeolian volcanic arc, which is represented by the islands of Alicudi (A), Salina (S), and Vulcano (V), discussed in the text. The two border faults, Sartori Escarpment (SE) and the Eolo-Enarete-Sisifo lineament (EES), approximately tracing the edges of the torn Ionian slab, are also indicated. Dashed white line refers to section in B. Source: "Tyrrhenian," 39°00'00"N, 14°00'00"E, Google Earth, 05 October 2009. (B) Sketch (not to scale) displaying the relationship between the narrow, steeply subducting Ionian slab and the surrounding African continental lithosphere subsequent to the tearing event. Docking of the compressional front against foreland units in early-mid-Pleistocene induced the lateral detachments of the old (Mesozoic) slab and ensuing sinking and rapid rollback. At the southern slab edge, African OIB-like mantle flow bypasses the slab and rises into the southern Tyrrhenian backarc basin.

Figure 3. Sample locations on Marsili Seamount (isobaths 50 m). Inset is a shaded relief image of the volcano (illumination from SE) highlighting the narrow, 20-km-long summit rift zone and its widening at the northern and southern tip regions. The bathymetric map shows that the rift region is made of small elongated and conical seamounts, several sampled by dredging. Samples also targeted the cone fields on the western and northwestern flanks, the basin faults flanking the seamount, the southeast flank, and the steep scarp delimiting the northeast flank of the volcano.



study revealed that a compositional variation occurred during the growth of Marsili volcano from dominant, island-arc basalt (IAB) magmas, geochemically and isotopically similar to the nearby Aeolian arc, to younger, but sporadic, OIB magmas, close in composition to the Na-alkaline OIB-like lavas of Ustica and Prometeo (Fig. 1). Ustica and Prometeo lavas, notwithstanding having a clear HIMU (high U/Pb) fingerprint resembling that recognized in the OIB alkaline magmas erupted on the northern African lithosphere (i.e., Hyblean Plateau; Figs. 1 and 2), have been termed OIB-like because they have some geochemical features also pointing to the involvement of small amounts of subduction-related components in their petrogenesis (Trua et al., 2003). Since a close similarity has been already observed between Marsili sample D6 and the nearby Prometeo OIB-like lavas (Trua et al., 2007), we use the term OIB-like hereafter when referring to this sample. The location of the Marsili OIB-like sample on the summit axis zone of the Marsili volcano suggests that OIB-like magmatism characterizes the late stage of Marsili volcanic activity, indicating that African mantle inflow propagated into the mantle wedge and is currently located beneath Marsili volcano (Trua et al., 2007).

Our suggestion that the OIB-like mantle component in southern Tyrrhenian backarc magmatism was provided by lateral infiltration of hot mantle from the nearby northern African plate (Trua et al., 2007) is an alternative to other models, which state that this OIB component was originally present in the mantle wedge before the addition of slab-derived components occurred (Ellam et al., 1989; Tonarini et al., 2001b; Peccerillo et al., 2004), or that it is the effect of a deep mantle plume component (Gasperini et al., 2002). The samples presented in this study focus on the effects derived from the African mantle inflow that occurred along the southern edge of the Ionian slab. Indeed, a similar mantle-flow mechanism likely also affected the northern edge of the slab, as suggested by De Astis et al. (2006). Nevertheless, further detailed petrological studies on the still poorly known Palinuro lavas, as well as on the other submarine volcanic edifices of this sector of the southern Tyrrhenian backarc basin (i.e., Albatros, Alcione, and Lametini volcanoes; Fig. 1), are required to better understand how the mantle inflow mechanism works in this part of the southern Tyrrhenian basin.

This paper reports new geochemical and Sr, Nd, and Pb isotope data for samples recovered during the MAR98 and TIR2000 cruises that complement and update earlier geochemical data available for Marsili volcano (Trua et al., 2002, 2007). Geochemical data for the few samples recovered from the Vavilov Seamount, located in the center of the nearby, but older Vavilov backarc basin (Figs. 1 and 2), are also reported. These data are then used in conjunction with published data regarding the geochemical and isotopic characteristics of southern Tyrrhenian magmatism (Trua et al., 2003; Francalanci et al., 2007, and references therein) to better explore the nature and the origin of the OIB-like mantle component involved in the magmatism of this area and the implications that it has on the tectono-magmatic evolution of the region.

SOUTHERN TYRRHENIAN BACKARC SYSTEM

The southern Tyrrhenian Sea formed during the last stage of extension occurring in the Tyrrhenian region over the past 10 m.y. (Kastens et al., 1988; Kastens and Mascle, 1990). Extension occurred behind the east-southeast-migrating Ionian subducting plate, a remnant of the African oceanic lithosphere mostly consumed during the process of convergence with the Eurasian plate, resulting in the rifting of the preexisting Alpine chain to the east of Sardinia (Rosenbaum and Lister, 2004; Beccaluva et al., 2005; Chiarabba et al., 2008).

The locus of extension moved eastward through time, in synchronism with the front of shortening. This led to the dismemberment of the Alpine orogenic chain and the east-southeastward migration of the active Apennine-Maghrebid chain and the Calabrian-Peloritani terrane (Fig. 2). According to geological and geochronological data (Kastens et al., 1988; Feraud, 1990), the progression of extension in the southern Tyrrhenian region resulted in spreading and the emplacement of oceanic crust first in the Vavilov Basin at 4.3–3.5 Ma, then in the Marsili Basin at 1.9–1.7 Ma to the southeast (Fig. 1). Furthermore, the southeastward migration of arc volcanism, from Sardinia (32–13 Ma) in the west of the southern Tyrrhenian basin to the currently active Aeolian volcanism (1.3 Ma–present; Beccaluva et al., 1985) in the south, follows the migration of backarc basin opening.

Both Vavilov and Marsili Basins have geophysical characters indicative of lithospheric stretching in a backarc environment, but only Vavilov Basin is floored by a mid-ocean-ridge basalt (MORB)-like oceanic crust as revealed by Ocean Drilling Program (ODP) Leg 107, Site 655, and Deep Sea Drilling Project (DSDP), Site 373. The emplacement of oceanic crust in the Vavilov Basin was followed by the growth of the large Magnaghi Seamount (3.0–2.7 Ma; Savelli, 1988) in the western side of the basin, and the eruption of IAB lavas in the east (ODP Leg 107, Site 651; age: 3.0–2.6 Ma; Kastens et al., 1988; Feraud, 1990). The latest magmatic activity related to the Vavilov Basin (i.e., basalts from the eastern Sardinia rifted margin, ODP Leg 107, Site 654, age: 1.8 Ma; the summit axis portion of the centrally located Vavilov Seamount, age: 0.73–0.1 Ma; Savelli, 1988; Kastens and Mascle, 1990) occurred when seafloor spreading was already active eastward, in the Marsili Basin. These latest magmatic events have geochemical fingerprints compatible with partial melting of an OIB mantle source, closely resembling the characteristics of Magnaghi Seamount lavas. Regrettably, isotopic compositions of lavas from Vavilov and Magnaghi Seamounts are lacking.

At present, the dip of the N-W-directed, subducting Ionian slab beneath the southern Tyrrhenian backarc basin and the Calabrian arc is $\sim 70^\circ$ (Fig. 2). The late spreading stage of the Marsili Basin and the growth of Marsili volcano are correlated to lateral tears that developed at the edges of the Ionian slab in early-mid-Pleistocene time, inducing a subsequent phase of rapid rollback and slab retreat (Gvirtzman and Nur, 1999; Marani and Trua, 2002). Tear faulting of the slab was generated

by the arrival at trench of the Apulian and Hyblean continental lithosphere of the African foreland, located at the margins of the subducting Ionian oceanic lithosphere (Fig. 2) (Doglioni et al., 2004; Chiarabba et al., 2008). Regional geology and geophysical data show that at the approximate time of the tearing event, in the early–mid-Pleistocene, the Apennine-Maghrebic chain underwent a marked variation in structural response to convergence. The Southern Apennines (Fig. 2), formerly undergoing NE-SW shortening, began to show belt-parallel extension and uplift (Patacca et al., 1990; Hippolyte et al., 1994; Doglioni et al., 1994; Galadini, 1999); contemporary uplift is also registered in Calabria (1 mm/yr; Westaway, 1993) and the Peloritani area in northeastern Sicily (Robertson and Grasso, 1995; Lentini et al., 1995; Butler et al., 1995). These uplift events in the Southern Apennines and Sicily are interpreted to be the effect of lithosphere rebound or lithosphere decoupling of the adjacent mountain belts in response to the release of the lateral stresses exerted by continental collision existing prior to the edge detachment of the Ionian slab (Gvirtzman and Nur, 1999; Marani and Trua, 2002; Chiarabba et al., 2008). The laterally confined deep seismicity occurring in the southern Tyrrhenian, deepening from the Calabrian terrane toward the Tyrrhenian, effectively traces the old (Mesozoic) and narrow (~200 km), subducting oceanic slab (Selvaggi and Chiarabba, 1995; Chiarabba et al., 2005).

Two important structures are suggested to represent the surface traces of the tearing process (Fig. 1): the Eastern Tyrrhenian margin fault (Marani and Trua, 2002; now Sartori Escarpment) in the northeast, and the Eolo-Enarete-Sisisfo lineament (Marani and Trua, 2002), subsequently reported as the North Sicily fault by Rosenbaum and Lister (2004), in the south. The former is a left-lateral, 100-km-long fault system, not associated with known volcanism but it delimits the regional extent of deep seismicity at the northern edge of the slab (Figs. 1 and 2). Instead, the Eolo-Enarete-Sisisfo lineament traces the deep seismicity cutoff at the southern slab edge and lies along the Ustica-Prometeo-Etna alignment, characterized by OIB-like lavas and considered to be the surface evidence of lateral mantle flow around the subducting slab edges (Fig. 2).

BACKARC VOLCANOES AND SAMPLE LOCATIONS

A brief description of the morphology of the Marsili and Vavilov volcanoes, with particular regard to the zones where the studied samples come from, is reported next.

Marsili volcano rises 3500 m from the basement level of Marsili Basin to a minimum depth of 489 m. It is elongated 60 km NNE-SSW with mean width of 20 km (Fig. 3). The seamount displays a number of characteristic volcanic elements distinguished by their location, in relation to water depth, and by their morphological expression (Marani and Trua, 2002). The sampling strategy was designed to target each of the diverse volcanic zones that make up the volcano in order to link morphology to the rock geology.

The following summary, describing the specific volcanic morphologies of the Marsili volcano that were sampled (Fig. 3), is adopted as an aid for better comprehending the underlying context of magma genesis that is developed in detail in this paper.

Samples were successfully collected from the following principal volcanic zones:

(1) The summit rift zone, a narrow (~1-km-wide), linear region of lower gradient, is approximately bounded by the 1000 m isobaths and marks the summit rift zone stretching NNE-SSW for 20 km along the central axis of the volcano. At the northern termination of the summit rift zone, a large circular cone topped by two vents marks the highest point of Marsili volcano. The summit rift zone is continuous in both the northern and southern tips of Marsili. In both these areas, the rift zone progressively widens downslope, reaching a width of ~5 km toward the base of the volcano. Steep, linear scarps bound the rift zones, separating them from the smooth, featureless flanks to the sides.

(2) The west flank seamount field is made up of seamounts that display westerly or NW-SE preferential development with more pronounced westward scarps due to their construction on the sloping flanks of Marsili volcano.

(3) The northwest flank seamount field is characterized by the development of three principal volcano morphologies: flat-top seamounts, located at the Marsili volcano base, cratered cones that developed on a 2400-m-deep bench upslope from the flat-top seamounts, and a series of stacked volcanic terraces that developed at the northern portion of the seamount field and below the crater bench.

(4) The northeast flank is represented by an 8-km-long, 700-m-high, steep scarp. It displays no small-scale morphology and is interpreted to be the result of faulting or as the headwall of a large flank failure event.

(5) The south-east flank zone, unlike the featureless southwestern flank of Marsili volcano, displays a series of small isolated volcanic constructs and flat benches on the sloping Marsili flank.

(6) Basin floor faults are represented by two sets of faults located on the Marsili Basin floor that symmetrically flank Marsili volcano to the northwest and southeast. Each is composed of two faults facing basinward and one facing the volcano, forming a horst and graben set.

Unlike Marsili volcano, Vavilov is a mature volcano that originated at the time of oceanization of the Vavilov backarc basin at ca. 3 Ma (Kastens and Mascle, 1990). The summit area has been subsequently active at 0.4–0.1 Ma (Savelli, 1988). The volcano is also elongated, having 40 km of NNE-SSW length and 15 km width. It is 2800 m high, rising from the basin floor at 3600 m depth to reach a summit at 800 m depth (Fig. 4). The overall morphology of Vavilov volcano is dominated by the strong asymmetry between its eastern and western flanks. An arcuate scar bounds the high-gradient western flank, suggesting that this portion of the volcano was affected by one or more events of flank collapse that resulted in the removal of a large volume of the preexisting edifice.

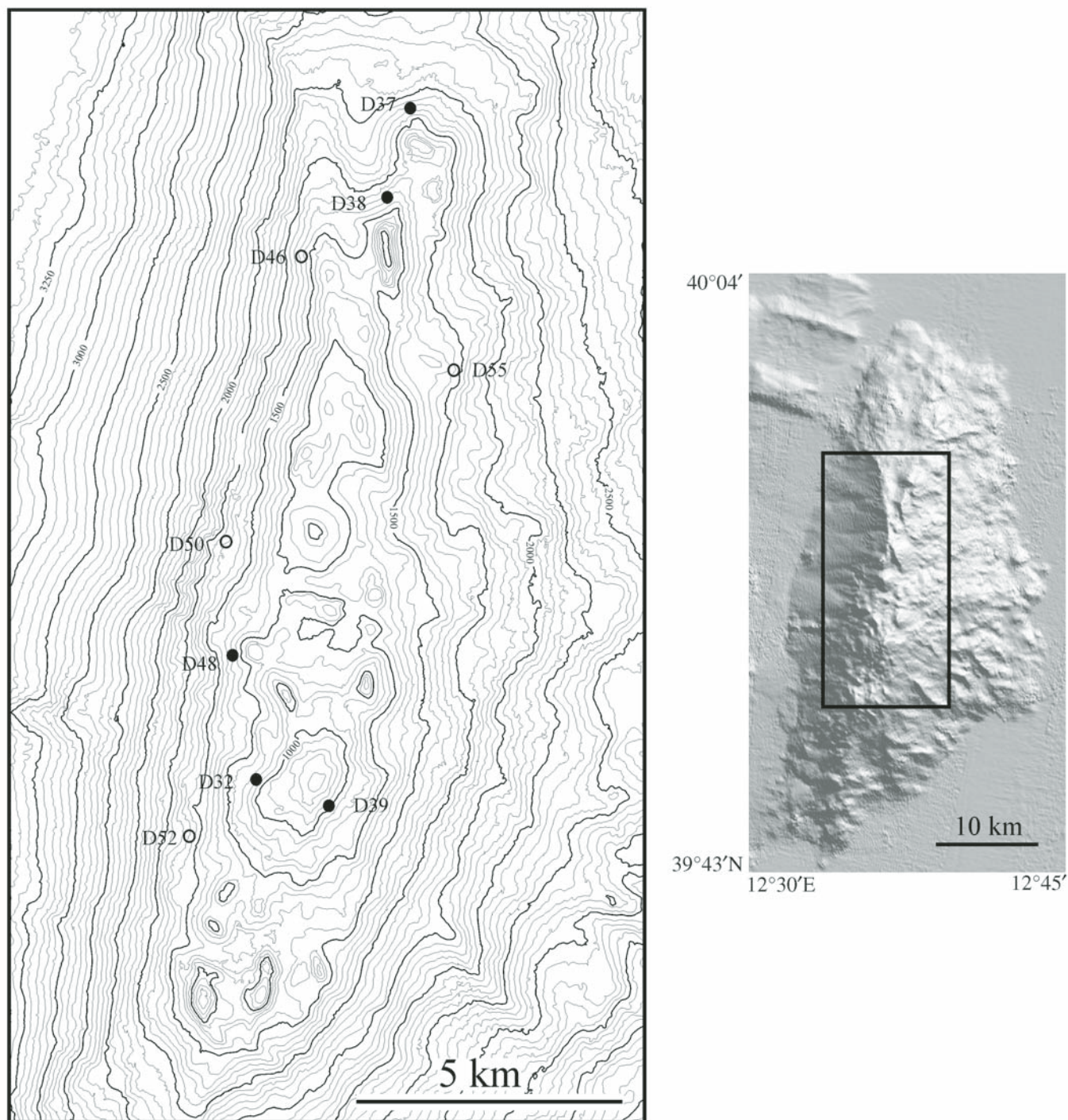


Figure 4. Sample locations on Vavilov Seamount (isobaths 50 m). Inset is a shaded relief image of the volcano (illumination from E) highlighting the steep, featureless western scarp due to sector collapse. Similar morphologically to Marsili Seamount, the older Vavilov volcano is a site of scarce sedimentation inducing the formation of hardgrounds. Samples are mostly altered (studied samples in black filled circles) and derive from the topmost portion of the volcano above 2000 m water depth.

As shown in Figure 4, the overall morphology of Vavilov volcano is analogous to that of Marsili volcano. The few samples recovered from Vavilov volcano are mostly positioned in the upper portions of the edifice at 1300, 1600, and 1900 m depth. Although reported as being significantly young, the samples from the summit region are nevertheless strongly altered.

SAMPLES AND ANALYTICAL METHODS

The studied samples represent the overall compositional spectra of the volcanic rocks dredged from the Marsili Seamount (44 samples) and the Vavilov Seamount (6 samples) during the MAR98 and TIR2000 CNR cruises (Marani et al., 1999; Gamberi et al., 2006). Concerning the Marsili data set, major elements are new for the TIR2000 samples (marked with “D”) and have been redetermined for those samples (marked with “MRS”) previously studied by Trua et al. (2002), in order to provide a data set with low comparable errors. Trace-element and isotope data are presented for the first time except for a small subset of Marsili samples (i.e., MRS1n, MRS2A, MRS3F1, D12/D2, and D6; Trua et al., 2007) and are reported in Tables 1 and 2, and are discussed in the text. The data for Vavilov lavas have not been previously published.

As formerly observed (Trua et al., 2002), the phenocryst assemblages of the Marsili basalts and basaltic andesites are of two types: in both, olivine and plagioclase are present, whereas clinopyroxene is only present in those rocks also having, at a given MgO content, higher CaO, Al_2O_3 , and pre-eruptive H_2O . The phenocryst assemblage in the Marsili andesites is made of abundant plagioclase, commonly zoned, clinopyroxene, and rare olivine. The phenocryst assemblage observed for the studied Vavilov samples is dominated by plagioclase with more scarce olivine crystals, which is petrographically similar to previously studied Vavilov lavas (Robin et al., 1987).

The samples were broken into small (<5 mm) chips, hand-picked to eliminate altered fragments, rinsed in distilled water, and then crushed to powder using an agate mill.

Major- and trace-element analyses were carried out at the Activation Laboratories Ltd. (Ontario, Canada) according to Code 4Litho package following lithium metaborate/tetraborate fusion inductively coupled plasma (ICP) and inductively coupled plasma–mass spectrometry (ICP-MS); loss on ignition (LOI) was measured according to standard gravimetric methods (<http://www.actlabs.com>).

Most of the Sr, Nd, and Pb isotopic analyses were performed at Activation Laboratories Ltd. (Ancaster, Canada). Sr, Nd, and Pb isotope compositions were analyzed on a Finnigan MAT 261 8-collector mass-spectrometer in static mode. During the period of work, the weighted average of 15 SRM-987 Sr and of 10 La Jolla Nd standard runs yielded 0.710261 ± 12 (2 σ) and 0.511850 ± 5 (2 σ) for $^{87}\text{Sr}/^{86}\text{Sr}$ and $^{143}\text{Nd}/^{144}\text{Nd}$, respectively. Nd isotopic analysis are corrected for $^{143}\text{Nd}/^{144}\text{Nd} = 0.511860$. The measured Pb isotope ratios were normalized to mass fractionation of 0.13% per atomic mass unit calculated from replicate measurements of

Pb isotope composition of NBS SRM-982 standards. External reproducibility of Pb isotope ratios are 0.1% for $^{206}\text{Pb}/^{204}\text{Pb}$, 0.15% for $^{207}\text{Pb}/^{204}\text{Pb}$, and 0.2% for $^{208}\text{Pb}/^{204}\text{Pb}$ based on repeated measurements of standard BCR-1 ($^{206}\text{Pb}/^{204}\text{Pb} = 18.800 \pm 0.010$ [2 σ]; $^{207}\text{Pb}/^{204}\text{Pb} = 15.611 \pm 0.009$ [2 σ]; $^{208}\text{Pb}/^{204}\text{Pb} = 38.647 \pm 0.024$ [2 σ]; 5 measurements). Further details of these methods can be found on Activation Laboratories Web site.

Seven rock samples were analyzed for Sr and Nd isotopes at Laboratoire Magmas et Volcans, Observatoire de Physique du Globe–CNRS (Clermont-Ferrand, France) following the same analytical procedures described in Trua et al. (2003). Four of these samples were also analyzed at the Activation Laboratories Ltd. (see previous) in order to test the interlaboratory variation of the Sr and Nd isotope ratios, which is found to be within the 2 σ error (Table 2).

RESULTS

Major and Trace Elements

The entire compositional variation of the Marsili lavas ranges from calc-alkaline basalts to basaltic andesites and high-K calc-alkaline andesites, overlapping with the range defined by the Alicudi and Filicudi lavas from the nearby Aeolian arc (Fig. 5).

One Marsili basaltic sample (i.e., sample D12D/1; Table 1), highly porphyritic (PI [porphyritic index] = 35 vol%) for phenocrysts of olivine and clinopyroxene, lies at the SiO_2 -poor end of the field defined by the Marsili lavas. All other, less porphyritic (PI <20 vol%) Marsili basalts show a large range of K_2O contents for rocks having similar SiO_2 contents; this is also observed in SiO_2 versus other major-element variation diagrams (not shown). The wide range in terms of major-element contents at a given SiO_2 (or MgO) content of these basalts has been attributed to the eruption of at least two varieties of magmas from the Marsili volcano (Trua et al., 2002): One type shows lower Al, Ca, and K and higher Fe, Na, and Ti with respect to the second type, represented by lavas having clinopyroxene as an additional phenocryst phase. Furthermore, petrological modeling (Trua et al., 2002) suggests that the major-element variations observed among Marsili lavas, from basalts to the evolved high-K andesites, can be explained by a large degree (80%) of intracrustal fractional crystallization, involving a mineralogical assemblage mainly made of olivine + clinopyroxene + plagioclase, of a melt compositionally similar to the high-Ca basalts (i.e., MRS2A sample; Table 1).

The newly dredged Vavilov samples have undergone a high degree of alteration, as evidenced by frequent veins, fractures, and vesicles filled largely with carbonates and/or zeolites, and alteration of glass and primary minerals. The alteration process caused a high degree of major-element redistribution in the Vavilov samples, as shown by comparisons of their major-element patterns with those of unaltered volcanic samples previously recovered from Vavilov volcano, for which chemical data, also reported in Table 1, were published by Serri (1990). The record of element mobility (e.g., Si, K, Na) observed in the dredged Vavilov

samples is typical of submarine seawater-dominated, low-temperature alteration of volcanic rocks (Schramm et al., 2005). Thus, we cannot assess the magmatic affinity of these samples from the SiO_2 versus K_2O diagram, but, as discussed later herein, several incompatible trace elements of these samples appear to have preserved the original magmatic contents, and thus they can be used for this aim.

Trace Elements

All Marsili basalts are light rare earth element (LREE) enriched (Fig. 6A), with sample D6 having the highest La_N/Lu_N ratio (= 18), sample D12D/1 having the lowest La_N/Lu_N ratio (= 3), and the remaining samples ranging in La_N/Lu_N from 3 to 8. Among the Marsili basalts, a correlation between heavy (H) REE

TABLE 1. GEOCHEMICAL DATA FOR VOLCANIC ROCKS FROM MARSILI (THIS STUDY) AND VAVILOV (THIS STUDY, SERRI, 1990) SEAMOUNTS

Rock type: Sample:	Marsili Seamount								
	Basalts								
	MRS1B	MRS1En	MRS1H	MRS2A	MRS2B	MRS2E	MRS3C	MRS3E2	MRS3F1
SiO_2 (wt%)	49.69	49.25	49.60	50.03	49.85	49.92	50.07	49.89	50.91
TiO_2	1.16	1.12	1.13	0.67	0.66	0.67	1.08	1.08	1.10
Al_2O_3	17.07	16.85	17.01	17.94	17.99	17.85	17.45	17.39	17.67
Fe_2O_3	9.12	9.11	9.16	6.88	6.86	6.87	7.75	7.82	7.81
MnO	0.14	0.14	0.14	0.12	0.12	0.12	0.13	0.13	0.13
MgO	7.47	8.18	8.03	7.73	7.93	7.75	7.17	7.44	6.96
CaO	9.94	9.77	9.84	12.34	12.43	12.38	9.66	9.53	9.60
Na_2O	3.46	3.34	3.39	2.32	2.30	2.39	3.52	3.35	3.42
K_2O	0.80	0.80	0.80	0.97	0.91	0.98	1.06	1.04	1.00
P_2O_5	0.20	0.19	0.20	0.17	0.16	0.18	0.29	0.28	0.28
H_2O	0.39	0.83	0.33	0.87	0.73	0.87	0.98	1.28	1.53
Total	99.44	99.58	99.63	100.04	99.94	99.98	99.16	99.23	100.41
Cs (ppm)	—	0.50	—	1.88	—	—	—	—	0.76
V	—	172	—	201	—	—	—	—	187
Cr	—	263	—	165	—	—	—	—	195
Ni	—	156	—	92	—	—	—	—	116
Rb	—	9	—	21	—	—	—	—	22
Sr	—	357	—	394	—	—	—	—	417
Y	—	20.3	—	16.4	—	—	—	—	22.5
Zr	—	84	—	50	—	—	—	—	104
Nb	—	9.4	—	5.8	—	—	—	—	16.5
Ba	—	191	—	422	—	—	—	—	362
La	—	12.6	—	14.2	—	—	—	—	23.9
Ce	—	25.6	—	28.0	—	—	—	—	44.1
Pr	—	3.1	—	3.4	—	—	—	—	5.1
Nd	—	13.0	—	13.7	—	—	—	—	19.4
Sm	—	3.0	—	3.1	—	—	—	—	4.1
Eu	—	1.09	—	0.98	—	—	—	—	1.30
Gd	—	3.50	—	3.30	—	—	—	—	3.99
Tb	—	0.59	—	0.51	—	—	—	—	0.65
Dy	—	3.50	—	2.90	—	—	—	—	3.80
Ho	—	0.73	—	0.59	—	—	—	—	0.79
Er	—	1.98	—	1.62	—	—	—	—	2.14
Tm	—	0.31	—	0.25	—	—	—	—	0.36
Yb	—	1.88	—	1.53	—	—	—	—	2.09
Lu	—	0.27	—	0.23	—	—	—	—	0.31
Hf	—	1.9	—	1.3	—	—	—	—	2.3
Ta	—	0.54	—	0.33	—	—	—	—	0.94
Pb	—	2.3	—	6.8	—	—	—	—	3.3
Th	—	2.40	—	3.90	—	—	—	—	4.45
U	—	0.69	—	1.06	—	—	—	—	1.23

(Continued)

TABLE 1. GEOCHEMICAL DATA FOR VOLCANIC ROCKS FROM MARSILI (THIS STUDY) AND VAVILOV (THIS STUDY, SERRI, 1990) SEAMOUNTS (*Continued*)

Rock type: Sample:	Marsili Seamount								
	Basalts								
	MRS4	MRS6	D1C/2	D3C	D5A	D12D/1	D16AB	D20A	D6 (OIB-like)
SiO ₂ (wt%)	49.94	49.21	51.03	49.05	51.37	46.40	49.56	47.65	49.38
TiO ₂	0.90	0.80	1.00	0.78	0.79	0.63	1.08	0.95	1.13
Al ₂ O ₃	16.71	16.29	18.47	16.82	15.69	10.95	17.48	15.69	18.41
Fe ₂ O ₃	8.11	7.13	8.84	7.77	8.21	8.84	8.47	8.43	8.30
MnO	0.13	0.13	0.15	0.14	0.15	0.15	0.14	0.14	0.14
MgO	7.44	8.90	4.42	8.85	8.23	14.23	6.15	9.39	6.53
CaO	11.53	11.59	9.15	11.10	11.26	14.82	11.26	10.05	9.63
Na ₂ O	3.19	2.47	3.42	2.58	2.58	1.50	3.63	2.91	3.70
K ₂ O	0.78	1.13	1.92	1.08	1.33	0.36	0.80	1.29	1.21
P ₂ O ₅	0.18	0.22	0.34	0.2	0.25	0.13	0.20	0.25	0.68
H ₂ O	0.65	1.56	1.32	1.43	0.49	2.38	1.27	3.96	1.16
Total	99.56	99.43	100.06	99.8	100.35	100.39	100.04	100.71	100.27
Cs (ppm)	0.37	1.35	1.89	1.14	1.35	0.24	0.50	1.25	0.51
V	196	205	290	244	242	226	189	242	232
Cr	122	360	—	316	275	770	157	284	105
Ni	97	150	39	145	105	201	64	144	116
Rb	9	25	52	28	34	6	10	32	19
Sr	450	510	543	444	452	351	391	442	945
Y	20.1	21.0	24.1	19.6	20.0	14.4	24.9	21.9	25.0
Zr	97	79	106	66	79	34	110	82	128
Nb	8.5	12.2	12.8	6.3	9.3	3.2	8.7	6.8	31.5
Ba	167	411	571	311	436	82	177	250	657
La	15.1	19.3	26.3	14.8	19.3	5.6	11.8	18.8	56.3
Ce	30.7	38.9	45.1	26.5	33.8	11.4	23.2	35.8	92.2
Pr	3.8	4.8	5.6	3.4	4.3	1.7	3.2	4.8	11.0
Nd	15.5	18.9	21.7	14.4	17.3	7.9	13.9	20.1	41.2
Sm	3.5	4.0	4.2	3.1	3.5	2.0	3.2	4.2	6.5
Eu	1.08	1.22	1.44	1.07	1.19	0.75	1.26	1.36	2.14
Gd	3.65	3.92	4.57	3.48	3.78	2.42	3.95	4.37	6.19
Tb	0.58	0.62	0.71	0.56	0.60	0.41	0.67	0.66	0.82
Dy	3.44	3.56	4.11	3.39	3.49	2.54	4.18	3.85	4.50
Ho	0.71	0.74	0.84	0.70	0.71	0.52	0.87	0.77	0.87
Er	2.00	2.02	2.33	1.95	1.97	1.39	2.41	2.17	2.42
Tm	0.33	0.32	0.35	0.29	0.30	0.22	0.38	0.32	0.36
Yb	1.84	1.83	2.34	1.95	1.94	1.33	2.35	2.08	2.31
Lu	0.28	0.27	0.35	0.29	0.29	0.19	0.36	0.31	0.33
Hf	2.2	1.8	2.6	1.9	2.1	1.1	2.7	2.1	3.0
Ta	0.50	0.81	0.81	0.41	0.59	0.17	0.56	0.47	1.98
Pb	3.3	5.7	9.1	4.8	5.9	1.6	2.7	5.7	5.1
Th	3.89	4.09	6.86	4.03	5.15	1.09	3.36	4.11	9.00
U	0.99	1.32	1.88	1.10	1.41	0.28	0.90	1.00	2.64

(Continued)

TABLE 1. GEOCHEMICAL DATA FOR VOLCANIC ROCKS FROM MARSILI (THIS STUDY) AND VAVILOV (THIS STUDY, SERRI, 1990) SEAMOUNTS (*Continued*)

Rock type: Sample:	Marsili Seamount								
	Basaltic andesites								
	MRS7A4	MRS7B	D1B	D1C/1	D2/1	D2/2	D4	D4D	D5B
SiO ₂ (wt%)	51.92	52.11	51.24	51.89	54.33	53.59	51.73	52.83	52.13
TiO ₂	0.86	0.85	0.99	1.01	1.04	1.02	0.90	0.95	0.83
Al ₂ O ₃	17.40	17.34	18.29	18.4	17.84	17.69	17.62	18.28	16.4
Fe ₂ O ₃	8.84	8.77	8.76	8.86	7.94	7.69	7.74	7.37	7.80
MnO	0.15	0.15	0.15	0.15	0.14	0.14	0.14	0.13	0.15
MgO	5.19	5.07	4.20	4.07	3.78	3.98	6.06	4.98	7.13
CaO	9.96	9.81	9.13	9.05	8.14	8.16	9.92	9.35	10.50
Na ₂ O	3.06	3.03	3.40	3.48	3.85	3.79	3.2	3.49	2.94
K ₂ O	1.42	1.45	1.98	2.04	1.95	1.98	1.73	1.41	1.59
P ₂ O ₅	0.25	0.32	0.34	0.35	0.28	0.49	0.29	0.41	0.26
H ₂ O	0.62	0.81	0.77	0.96	1.00	1.80	0.76	0.83	0.51
Total	99.67	99.71	99.25	100.26	100.29	100.33	100.09	100.03	100.24
Cs (ppm)	—	1.58	1.90	2.06	1.75	2.19	1.79	0.68	1.60
V	—	258	294	291	261	254	239	233	247
Cr	—	—	—	—	—	—	137	36	219
Ni	—	—	38	42	45	48	83	58	90
Rb	—	42	53	54	51	54	46	29	42
Sr	—	488	542	542	453	443	481	697	470
Y	—	21.8	24.3	24.4	26.2	25.9	22.2	22.3	22.0
Zr	—	76	105	107	126	132	99	112	90
Nb	—	9.6	12.5	13.0	11.8	12.4	11.5	18.8	9.8
Ba	—	466	585	588	466	470	532	466	505
La	—	24.8	26.6	26.4	23.9	24.6	23.6	33.7	20.4
Ce	—	47.1	45.0	45.0	41.1	41.2	40.9	57.3	35.8
Pr	—	5.1	5.5	5.5	5.1	5.1	5.0	6.9	4.5
Nd	—	19.6	21.9	21.9	20.7	20.4	20.0	26.6	18.2
Sm	—	4.2	4.2	4.3	4.2	4.0	3.9	4.6	3.6
Eu	—	1.42	1.43	1.42	1.40	1.34	1.32	1.52	1.22
Gd	—	4.01	4.56	4.56	4.61	4.44	4.36	4.70	3.99
Tb	—	0.70	0.70	0.72	0.74	0.72	0.66	0.67	0.62
Dy	—	3.94	4.16	4.20	4.40	4.24	3.83	3.83	3.61
Ho	—	0.79	0.85	0.84	0.92	0.89	0.79	0.78	0.74
Er	—	2.35	2.39	2.34	2.60	2.55	2.20	2.20	2.08
Tm	—	0.34	0.36	0.36	0.41	0.39	0.33	0.32	0.33
Yb	—	2.20	2.34	2.36	2.65	2.57	2.20	2.12	2.06
Lu	—	0.32	0.36	0.35	0.40	0.38	0.33	0.32	0.31
Hf	—	2.3	2.6	2.6	3.1	3.2	2.6	2.7	2.2
Ta	—	0.65	0.82	0.83	0.85	0.85	0.77	1.16	0.65
Pb	—	6.8	7.8	9.0	6.7	6.9	7.2	3.8	12.8
Th	—	6.75	6.71	6.90	8.21	7.88	6.59	6.28	5.80
U	—	1.74	1.93	1.95	2.10	2.15	1.79	1.81	1.62

(Continued)

TABLE 1. GEOCHEMICAL DATA FOR VOLCANIC ROCKS FROM MARSILI (THIS STUDY) AND VAVILOV (THIS STUDY, SERRI, 1990) SEAMOUNTS (*Continued*)

Rock type: Sample:	Marsili Seamount							
	Basaltic andesites							
	D5C	D11A	D11B	D11C	D19A	D23E	D23F	D23H
SiO ₂ (wt%)	52.76	52.86	52.31	52.18	51.91	52.69	66.01	52.63
TiO ₂	0.87	0.70	0.68	0.68	0.74	1.10	0.15	1.11
Al ₂ O ₃	17.08	18.09	18.02	17.8	18.30	16.91	12.84	16.96
Fe ₂ O ₃	6.64	6.89	6.86	6.88	5.37	10.31	2.48	10.22
MnO	0.14	0.13	0.13	0.13	0.12	0.16	0.07	0.16
MgO	5.79	6.16	6.23	6.24	6.79	4.29	1.24	4.23
CaO	9.74	10.28	10.35	10.44	11.15	8.91	1.85	8.87
Na ₂ O	3.18	2.96	2.88	2.93	2.83	3.46	5.00	3.48
K ₂ O	1.68	1.31	1.21	1.14	1.03	1.77	5.08	1.73
P ₂ O ₅	0.27	0.32	0.32	0.32	0.14	0.29	0.08	0.29
H ₂ O	1.89	1.31	1.41	1.31	1.58	0.55	5.67	0.61
Total	100.04	101.01	100.4	100.05	99.96	100.44	100.47	100.29
Cs (ppm)	1.64	0.70	0.61	0.66	1.40	1.90	15.6	1.88
V	239	206	208	207	183	358	22.67	364
Cr	140	118	112	115	125	—	—	—
Ni	63	73	74	71	63	42	—	54
Rb	46	24	25	28	20	45	256	45
Sr	493	615	622	632	402	484	156	499
Y	23.0	18.6	18.6	18.6	18.3	23.4	38.9	24.0
Zr	100	95	93	92	72	98	171	101
Nb	11.1	13.8	13.7	14.0	5.5	12.2	26.1	12.8
Ba	553	355	350	348	249	542	150	549
La	23.1	26.8	27.1	26.5	11.0	24.9	59.3	25.3
Ce	40.7	44.5	45.4	44.2	20.9	43.6	104.6	44.4
Pr	5.0	5.3	5.4	5.3	2.8	5.5	12.3	5.5
Nd	19.7	20.6	20.7	20.4	12.2	21.8	42.6	22.2
Sm	3.9	3.6	3.7	3.6	2.7	4.3	7.6	4.4
Eu	1.30	1.23	1.27	1.21	1.00	1.47	0.33	1.47
Gd	4.16	3.76	3.78	3.67	3.09	4.69	7.09	4.75
Tb	0.65	0.55	0.56	0.55	0.50	0.72	1.08	0.72
Dy	3.82	3.18	3.20	3.10	3.10	4.15	6.12	4.12
Ho	0.78	0.64	0.65	0.64	0.63	0.85	1.25	0.85
Er	2.19	1.80	1.83	1.77	1.78	2.32	3.72	2.33
Tm	0.35	0.29	0.29	0.28	0.27	0.35	0.60	0.35
Yb	2.18	1.78	1.83	1.76	1.73	2.28	4.07	2.21
Lu	0.33	0.27	0.27	0.27	0.26	0.34	0.60	0.34
Hf	2.4	2.2	2.2	2.2	1.9	2.5	6.0	2.5
Ta	0.76	0.94	0.91	0.90	0.40	0.86	2.49	0.85
Pb	7.4	4.5	4.2	4.2	5.1	8.1	29.3	8.1
Th	6.59	5.41	5.34	5.27	3.56	7.39	45.43	8.02
U	1.84	1.69	1.64	1.62	1.06	2.00	13.62	2.05

(Continued)

TABLE 1. GEOCHEMICAL DATA FOR VOLCANIC ROCKS FROM MARSILI (THIS STUDY) AND VAVILOV (THIS STUDY, SERRI, 1990) SEAMOUNTS (*Continued*)

Rock type: Sample:	Marsili Seamount								
	Andesites								
	MRS9D1	MRS9E	MRS9F	MRS10D5	MRS10G	MRS10E	D14B/1	D14B/2	D14C
SiO ₂ (wt%)	58.84	58.87	58.7	61.06	61.39	61.22	59.71	60.96	58.42
TiO ₂	0.98	0.99	0.98	0.95	0.96	0.92	0.94	0.96	0.98
Al ₂ O ₃	16.92	17.09	17.05	16.64	16.72	16.42	16.23	16.65	16.95
Fe ₂ O ₃	7.11	7.00	7.14	5.87	5.87	5.74	6.78	5.90	7.36
MnO	0.14	0.14	0.14	0.13	0.13	0.13	0.43	0.14	0.14
MgO	2.32	2.26	2.26	1.90	1.90	1.95	2.06	1.98	2.69
CaO	5.88	5.92	5.94	4.41	4.38	4.39	4.44	4.54	5.98
Na ₂ O	4.47	4.58	4.57	4.97	4.98	4.82	4.81	4.92	4.44
K ₂ O	2.35	2.33	2.35	2.91	3.04	2.97	3.12	3.25	2.37
P ₂ O ₅	0.38	0.40	0.41	0.40	0.40	0.37	0.42	0.40	0.40
H ₂ O	0.66	0.73	0.72	0.84	0.70	0.77	1.33	0.67	0.35
Total	100.05	100.31	100.26	100.08	100.47	99.7	100.27	100.37	100.08
Cs (ppm)	—	—	2.67	—	—	4.2	4.14	4.68	2.53
V	—	—	203	—	—	126	136	138	208
Cr	—	—	1	—	—	—	—	—	—
Ni	—	—	5	—	—	—	31	26	29
Rb	—	—	66	—	—	90	84	90	66
Sr	—	—	448	—	—	334	372	378	473
Y	—	—	27.0	—	—	31.0	32.8	33.4	27.8
Zr	—	—	165	—	—	198	204	212	172
Nb	—	—	27.0	—	—	23.0	25.1	26.6	25.0
Ba	—	—	827	—	—	1.110	1170	1210	846
La	—	—	45.8	—	—	46.1	43.5	45.3	43.2
Ce	—	—	81.1	—	—	83.8	72.8	76.4	71.2
Pr	—	—	8.7	—	—	8.6	8.8	9.1	8.4
Nd	—	—	30.8	—	—	30.3	33.4	34.3	31.0
Sm	—	—	5.6	—	—	5.8	6.0	6.1	5.5
Eu	—	—	1.57	—	—	1.72	1.80	1.87	1.69
Gd	—	—	5.19	—	—	5.40	6.28	6.26	5.44
Tb	—	—	0.80	—	—	0.90	0.95	0.96	0.82
Dy	—	—	4.57	—	—	5.20	5.45	5.58	4.66
Ho	—	—	0.95	—	—	1.10	1.11	1.14	0.95
Er	—	—	2.60	—	—	3.30	3.18	3.26	2.66
Tm	—	—	0.44	—	—	0.48	0.49	0.50	0.41
Yb	—	—	2.60	—	—	3.10	3.26	3.40	2.73
Lu	—	—	0.40	—	—	0.50	0.51	0.51	0.42
Hf	—	—	3.7	—	—	5.1	4.8	5.0	3.9
Ta	—	—	1.52	—	—	1.70	1.84	1.89	1.67
Pb	—	—	10.2	—	—	25.0	15.2	16.3	9.9
Th	—	—	12.73	—	—	16.2	15.38	15.99	13.04
U	—	—	3.45	—	—	4.30	4.42	4.46	3.65

(Continued)

TABLE 1. GEOCHEMICAL DATA FOR VOLCANIC ROCKS FROM MARSILI (THIS STUDY) AND VAVILOV (THIS STUDY, SERRI, 1990) SEAMOUNTS (*Continued*)

Data source: Sample:	Vavilov Seamount (basalts)						From Serri (1990)	
	This work						T-72 35-1C	T-73 34-2C
	D32B	D37A	D38A	D38B	D39A	D48A		
SiO ₂ (wt%)	32.29	31.67	25.61	28.09	30.21	32.05	48.15	48.83
TiO ₂	1.41	1.39	1.78	1.67	1.30	1.23	3.1	1.84
Al ₂ O ₃	15.08	14.62	15.50	14.50	15.19	14.77	18.26	19.85
Fe ₂ O ₃	9.53	7.49	9.15	8.36	9.72	7.67	12.55	10.23
MnO	0.12	0.10	0.11	0.09	0.11	0.11	0.17	0.16
MgO	7.17	9.27	11.89	8.35	9.88	9.60	3.82	3.95
CaO	15.90	14.43	10.44	14.92	13.58	15.88	9.57	10.3
Na ₂ O	3.03	2.99	2.79	2.91	2.80	2.55	3.44	3.7
K ₂ O	0.32	0.88	0.46	0.94	0.23	0.48	0.56	0.51
P ₂ O ₅	0.25	0.36	0.40	0.49	0.24	0.33	0.36	0.35
H ₂ O	14.21	16.12	21.29	18.57	16.24	14.12	0.02	0.3
Total	99.31	99.32	99.42	98.89	99.5	98.79	100	100.02
Cs (ppm)	—	0.14	0.14	0.34	—	—	—	—
V	173	137	160	170	162	168	346	232
Cr	—	—	—	—	—	—	33	82
Ni	70	103	72	68	102	108	33	31
Rb	1.89	11.22	7.20	10.95	1.58	4.14	10	7
Sr	409	405	328	407	377	490	343	305
Y	20.1	21.2	26.8	25.1	19.1	17.9	42	42
Zr	83	136	164	160	79	90	228	229
Nb	9.2	24.4	23.9	24.3	11.4	16.3	21	15
Ba	90	245	191	233	76	140	100	95
La	7.6	16.6	17.2	17.0	6.9	14.1	17.6	14.4
Ce	16.8	32.4	35.5	35.0	15.9	29.4	42.8	36.2
Pr	2.3	3.8	4.5	4.2	2.0	3.3	—	—
Nd	11.0	16.3	19.5	19.2	9.7	14.7	—	—
Sm	2.9	3.5	4.4	4.5	2.8	3.4	7.17	6.17
Eu	1.22	1.29	1.73	1.64	1.17	1.22	2.47	2.03
Gd	3.69	4.08	5.24	4.67	3.21	3.40	—	—
Tb	0.62	0.65	0.81	0.79	0.56	0.55	1.23	1.18
Dy	3.49	3.92	4.93	4.49	3.40	3.22	—	—
Ho	0.73	0.74	0.93	0.88	0.68	0.64	—	—
Er	2.15	2.21	2.70	2.60	1.91	1.80	—	—
Tm	0.31	0.31	0.37	0.37	0.27	0.26	—	—
Yb	1.86	1.93	2.31	2.38	1.75	1.65	3.31	3.63
Lu	0.27	0.29	0.35	0.34	0.26	0.24	0.50	0.54
Hf	2.0	2.9	3.6	3.6	1.9	2.1	—	—
Ta	0.65	1.73	1.63	1.62	0.55	1.00	—	—
Pb	10.6	15.6	12.0	—	7.4	18.5	—	—
Th	0.76	2.39	2.23	2.16	0.63	2.11	—	—
U	0.65	0.77	0.98	0.98	0.67	0.60	—	—

abundances and the degree of LREE enrichment is not always observed, and this causes the crossing in the patterns of these samples (i.e., MRS1En and MRS2A in Fig. 6A).

Overall, the mantle-normalized incompatible trace-element patterns for all, but one, Marsili basalts are typical of IAB magmas, inasmuch as they display strong depletions in Nb and Ta and enrichments in K and Pb relative to the adjacent elements (Fig. 7A). Nevertheless, the subduction signature, expressed by

the light rare earth element/high field strength element (LREE/HFSE) and large ion lithophile element/high field strength element (LILE/HFSE) ratios, is variable for rock samples having similar SiO₂ content, as illustrated by samples MRS1En and MRS2A (Fig. 7A). Indeed, the lower abundances of HFSE and REE and the higher positive Pb anomaly in sample MRS2A suggest that the mantle source supplying this magma was more depleted and had also a stronger subduction signature compared

TABLE 2. ISOTOPIC COMPOSITION FOR VOLCANIC ROCKS FROM MARSILI SEAMOUNT

	$^{87}\text{Sr}/^{86}\text{Sr}$	$^{143}\text{Nd}/^{144}\text{Nd}$	$^{206}\text{Pb}/^{204}\text{Pb}$	$^{207}\text{Pb}/^{204}\text{Pb}$	$^{208}\text{Pb}/^{204}\text{Pb}$
Basalts					
MRS1En	—	0.512879 ± 7	19.072^{\dagger}	15.635	38.931
	$0.703528 \pm 12^{*}$	$0.512889 \pm 7^{*}$	—	—	—
MRS2A	0.704940 ± 12	0.512671 ± 5	19.109^{\dagger}	15.674	39.115
	$0.704933 \pm 13^{*}$	$0.512667 \pm 7^{*}$	—	—	—
MRS3F1	0.703565 ± 11	0.512890 ± 6	19.225^{\dagger}	15.633	39.020
	$0.703580 \pm 11^{*}$	$0.512893 \pm 5^{*}$	—	—	—
MRS4	$0.703648 \pm 15^{*}$	$0.512858 \pm 18^{*}$	19.129	15.653	39.059
D3C	0.704616 ± 10	0.512789 ± 7	19.219	15.654	39.108
D5A	0.704328 ± 12	0.512775 ± 7	19.069	15.661	38.987
D12/D1	$0.704494 \pm 14^{\dagger}$	$0.512780 \pm 7^{\dagger}$	19.160^{\dagger}	15.663	39.106
D20A	0.704491 ± 11	0.512714 ± 6	19.012	15.657	39.026
D6 (OIB-like)	0.703222 ± 14	$0.512921 \pm 4^{\dagger}$	19.554^{\dagger}	15.634	39.177
	0.703205 ± 13	0.512913 ± 4	19.547	15.643	39.220
Basaltic andesites					
MRS7B	0.704437 ± 11	0.512699 ± 4	19.155	15.669	39.095
	$0.704420 \pm 14^{*}$	$0.512693 \pm 6^{*}$	—	—	—
D2/1	0.704300 ± 13	0.512796 ± 7	19.231	15.672	39.137
D19A	0.704398 ± 12	0.512767 ± 6	19.099	15.683	39.148
D23H	0.704433 ± 12	0.512709 ± 5	19.184	15.675	39.132
Andesites					
MRS9F	$0.704094 \pm 12^{*}$	$0.512797 \pm 6^{*}$	19.244	15.664	39.134
MRS10E	$0.704734 \pm 13^{*}$	$0.512759 \pm 6^{*}$	19.218	15.660	39.123

Note: 2σ error is reported for Sr and Nd isotope ratios. See text for further details of the analytical methods. OIB—ocean-island basalt.

*Sr and Nd isotopic analyses carried out at Laboratoire Magmas et Volcans, Observatoire de Physique du Globe—CNRS (Clermont-Ferrand, France); the other samples were analyzed at Activation Laboratories, Ltd. (Ancaster, Canada).

[†]Data from Trua et al. (2007).

with the source of sample MRS1En. The incompatible trace-element pattern of sample D12D/1 broadly mirrors that observed for the other Marsili basalts, but has lower trace-element concentrations (Fig. 7A), consistent with the high porphyric character of this sample. Instead, sample D6 has a pattern at places similar to the other Marsili basalts but significantly more enriched

(Fig. 7A). Indeed, it lacks the large Nb-Ta-K anomalies and has a very small Pb positive anomaly, revealing a strong trace-element similarity with the nearby OIB-like lavas of Ustica and Prometeo (Fig. 7A).

The compositional range of REE and incompatible trace elements for the Marsili basaltic andesites partially overlaps that of the Marsili basalts, extending to slightly higher abundances of these elements (Figs. 6B and 7B). Abundances reach the highest values in the Marsili andesites, which maintain REE and incompatible element patterns subparallel to those of the basalts (Figs. 6C and 7C). The overall coherence of the basalt-basaltic andesite-andesite patterns is qualitatively compatible with the previous suggestion that fractional crystallization controlled the evolution of some of the Marsili lavas (Trua et al., 2002).

The pervasive seafloor weathering suffered by the Vavilov samples does not affect the REE patterns of these samples, which exhibit a different degree of LREE enrichment ($2.8 < \text{La}_N/\text{Lu}_N < 6.3$) coupled with a weak positive Eu anomaly (Fig. 8A), indicating that plagioclase is a cumulate phase in these lavas.

The two less LREE-enriched Vavilov samples also have incompatible trace-element abundances closest to the average enriched (E) MORB, from which they are significantly different only for depletion in Rb and enrichment in U, Pb, and Sr (Fig. 8B). The other Vavilov samples have incompatible element patterns subparallel to those of the less LREE-enriched samples, with an increase in normalized values toward the left of the plot, and they also show positive, but smaller, anomalies for U and Sr. These latter Vavilov samples are geochemically similar to

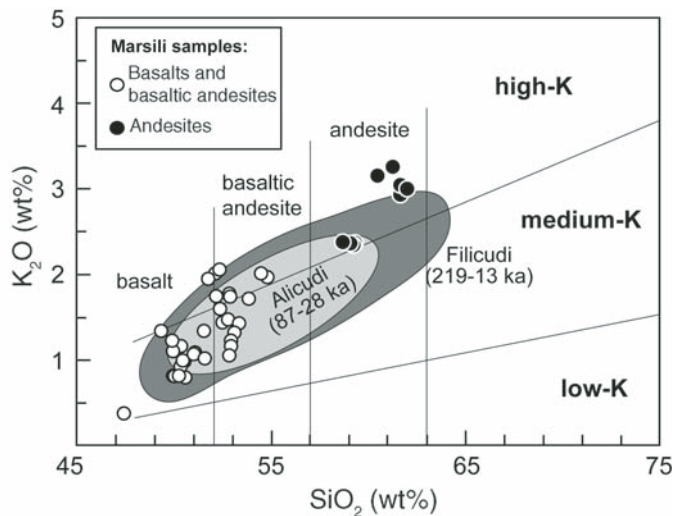


Figure 5. K_2O vs. SiO_2 (wt%) classification diagram (Le Maitre, 1989) for Marsili lavas; oxides were normalized on a water-free basis. Fields for the lavas from Alicudi and Filicudi Islands (Aeolian arc) are also reported (Francalanci et al., 2007, and references therein).

the other few basaltic samples previously recovered from the Vavilov Seamount and the nearby, but older, Magnaghi Seamount, except for those elements clearly affected by the alteration process (Fig. 8B). Since petrographic features are similar for all the Vavilov samples studied here, the REE and incompatible element patterns for the two less LREE-enriched Vavilov lavas suggest that they could have been derived from higher degrees of partial melting than the other Vavilov basic samples. Nevertheless, in the absence of the Sr-Nd-Pb isotopic compositions for the Vavilov samples, we cannot assess if these basic lavas derive from the same mantle source or not. The information that we can

obtain from the few geochemical data available on the Vavilov and Magnaghi Seamounts (this study and literature data) is that they sampled mantle sources unaffected by the subduction process, as shown by the lack of Nb-Ta and K anomalies (Fig. 8B). As previously suggested (Robin et al., 1987; Serri, 1990), geochemical features of these lavas are compatible with a derivation

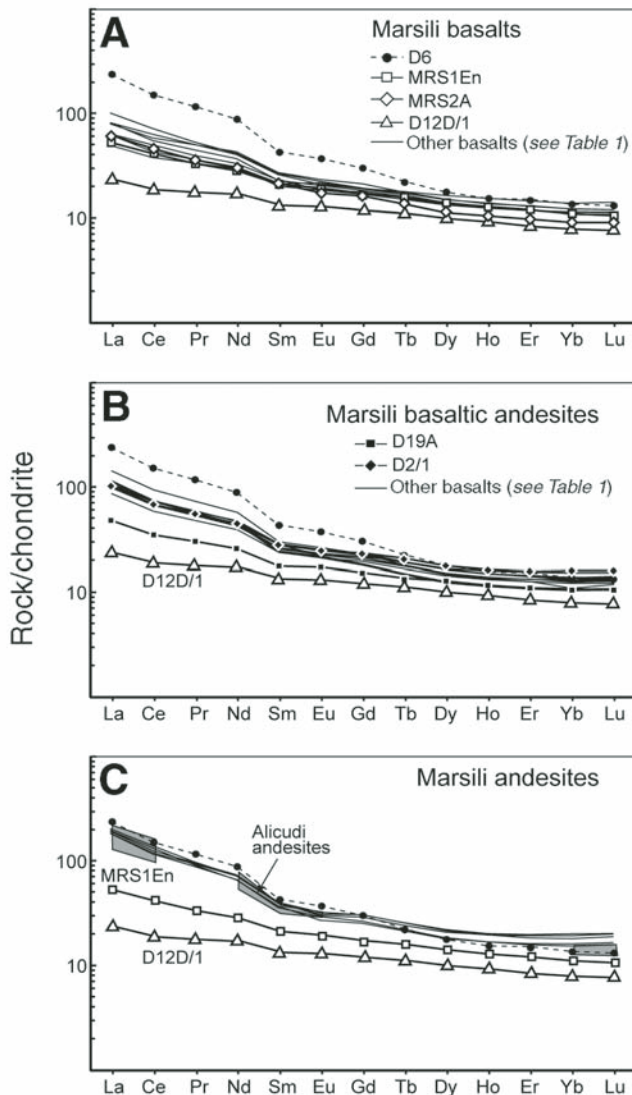


Figure 6. Chondrite-normalized rare earth element (REE; Sun and McDonough, 1989) variation diagrams. REE patterns are shown for Marsili lavas: (A) basalts; (B) basaltic andesites; and (C) andesites, compared with the range of the Alicudi andesites (Peccerillo and Wu, 1992; Peccerillo et al., 1993). In C, the pattern of Marsili basalt MRS1En is reported as a composition that can be parental to the Alicudi andesites. See text for further discussion.

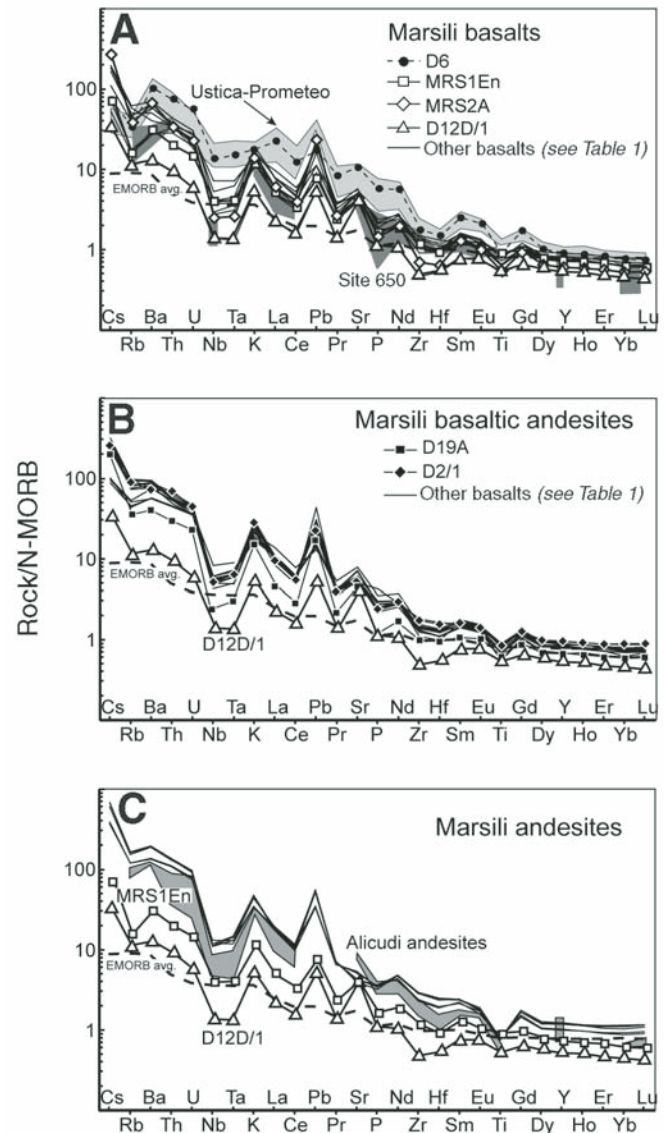


Figure 7. Normal mid-ocean-ridge basalt (N-MORB)-normalized trace-element (Sun and McDonough, 1989) variation diagrams. Trace-element patterns are shown for Marsili lavas: (A) basalts, compared with the ranges of ocean-island basalt-like Ustica and Prometeo lavas (Trua et al., 2003) and the Marsili Basin crust (Ocean Drilling Program Leg 107, Site 650; Beccaluva et al., 1990); (B) basaltic andesites; and (C) andesites, compared with the range of the Alicudi andesites (data sources are as in Fig. 6). Average enriched (E) MORB value is from Sun and McDonough (1989). In C, the pattern of Marsili basalt MRS1En is reported as a composition that can be parental to the Alicudi andesites. See text for further discussion.

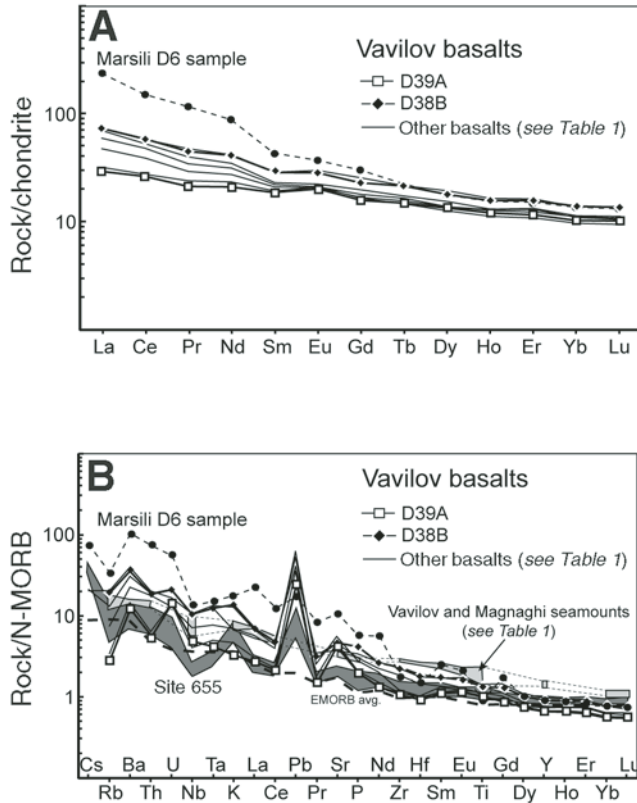


Figure 8. (A) Chondrite-normalized rare earth element and (B) normal mid-ocean-ridge basalt (N-MORB)-normalized trace element variation diagrams for Vavilov lavas (normalizing values are from Sun and McDonough, 1989). In both diagrams, the pattern for Marsili D6 sample is reported. In B, Vavilov lavas are compared with the ocean-island basalt-like lavas previously recovered from Vavilov and Magnaghi Seamounts (Serri, 1990; see also Table 1) and the Vavilov Basin oceanic crust (Ocean Drilling Program Leg 107, Site 655; Beccaluva et al., 1990; Gasperini et al., 2002). Average enriched (E) MORB is from Sun and McDonough (1989).

by partial melting of an OIB-type mantle source, but in absence of isotopic data on these samples, we cannot assess which type it is among those identified as principal end-member isotopic components in OIB magmas (i.e., HIMU, EMII [Enriched Mantle II], EMII [Enriched Mantle II]; Hart, 1988).

Isotopes

The Sr, Nd, and Pb isotope data for Marsili rocks, which include both new and the few published results (as indicated in Table 2 caption), are illustrated in Figure 9. Isotope values for

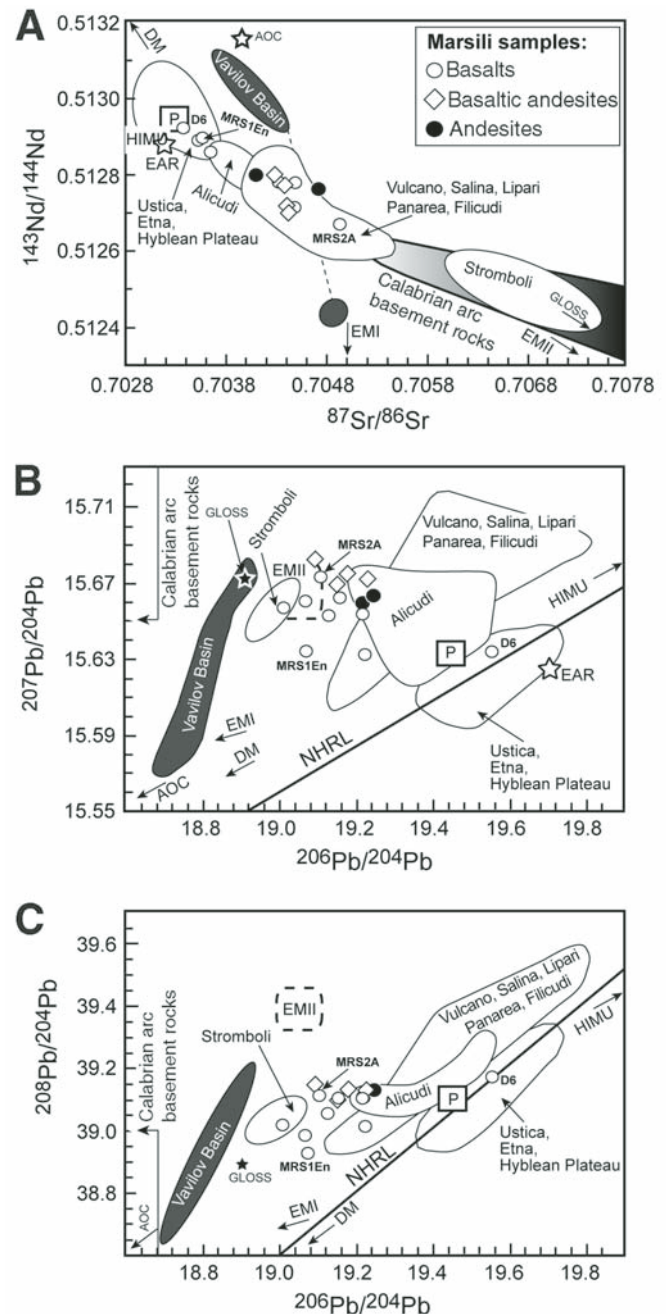


Figure 9. Diagrams of (A) $^{87}\text{Sr}/^{86}\text{Sr}$ versus $^{143}\text{Nd}/^{144}\text{Nd}$, (B) $^{207}\text{Pb}/^{204}\text{Pb}$ versus $^{206}\text{Pb}/^{204}\text{Pb}$, and (C) $^{208}\text{Pb}/^{204}\text{Pb}$ versus $^{206}\text{Pb}/^{204}\text{Pb}$ for Marsili rocks (this study) and other southern Tyrrhenian island-arc basalt (IAB) and ocean-island basalt (OIB) magmas having $\text{MgO} > 6$ wt% and $\text{SiO}_2 < 55$ wt%. P—Prometeo OIB-like lavas. Data sources are as follow: Hyblean Plateau, Ustica, and Prometeo (Trua et al., 2003); Etna (Tonarini et al., 2001a); Vavilov Basin (Ocean Drilling Program Leg 107: Sites 655 and 651, Deep Sea Drilling Project Site 373; Hamelin et al., 1979; Beccaluva et al., 1990; Gasperini et al., 2002); Stromboli, Vulcano, Salina, Lipari, Panarea, Filicudi, Alicudi (Ellam et al., 1988, 1989; Francalanci et al., 1993; De Astis et al., 2000; Calanchi et al., 2002); Calabrian arc basement (Caggianelli et al., 1991). Depleted mantle (DM), HIMU (high U/Pb), EMI (Enriched Mantle I), and EMII (Enriched Mantle II) are end-member mantle components (Zindler and Hart, 1986; Hart, 1988). EAR—European asthenospheric reservoir (Cebria and Wilson, 1995); NHRL—Northern Hemisphere reference line (Hart, 1984); GLOSS—global subducting sediment component (Plank and Langmuir, 1998); AOC—fluid from altered oceanic crust (Ishizuka et al., 2003).

mafic ($\text{MgO} > 6 \text{ wt\%}$ and $\text{SiO}_2 < 55 \text{ wt\%}$) IAB lavas from the Aeolian arc, OIB lavas from Ustica and Prometeo (Tyrrhenian lithosphere) and Etna-Hyblean Plateau (N. African lithosphere), and MORB lavas from the Vavilov backarc basin are also reported for comparison (Fig. 9), as they well represent the different sources involved in the petrogenesis of the southern Tyrrhenian magmatism.

The variations in Sr, Nd, and Pb isotopes for the Marsili samples are much greater than analytical error and reveal the following features:

(1) There is a negative correlation for $^{87}\text{Sr}/^{86}\text{Sr}$ versus $^{143}\text{Nd}/^{144}\text{Nd}$ among the Marsili basalts. These lavas collectively range from lavas closely resembling the southern Tyrrhenian OIB-like lavas (i.e., D6) to lavas isotopically more similar to the Aeolian arc lavas (i.e., MRS2A), but not extending to the most radiogenic compositions observed in the Stromboli lavas.

(2) $^{207}\text{Pb}/^{204}\text{Pb}$ and $^{208}\text{Pb}/^{204}\text{Pb}$ ratios well above the Northern Hemisphere reference line (NHRL; i.e., the best-fit line through North Atlantic and Pacific MORB and OIB; Hart, 1984) for all the Marsili samples, but one, reveal a strong Pb isotope similarity with the IAB lavas, among the Aeolian arc lavas, having relatively low $^{206}\text{Pb}/^{204}\text{Pb}$ ratio.

(3) There is an offset to a higher $^{206}\text{Pb}/^{204}\text{Pb}$ value in sample D6 that also has $^{207}\text{Pb}/^{204}\text{Pb}$ and $^{208}\text{Pb}/^{204}\text{Pb}$ ratios plotting on the NHRL. The Pb isotope compositions of this sample are consistent with the OIB-like affinity of this lava, previously derived from the Sr-Nd isotope compositions alone (Trua et al., 2007).

(4) Finally, the more evolved Marsili lavas (basaltic andesites and andesites) define a small range of Sr, Nd, and Pb isotope compositions, falling within the range defined by the Marsili basalts in the $^{87}\text{Sr}/^{86}\text{Sr}$ versus $^{143}\text{Nd}/^{144}\text{Nd}$ diagram or slightly above it in the plots of Pb isotope ratios.

DISCUSSION

Defining the nature of the upper mantle beneath the southern Tyrrhenian backarc basin would help us to understand the unusual coexistence of IAB and OIB-like magmas that characterizes this region. In the following sections, we examine the variation in the geochemical and isotope features of the Marsili lavas in order to obtain insight into the petrogenesis and evolution of the Marsili backarc basin lavas. Then, by comparing the geochemical and isotopic data of the Marsili mafic ($\text{MgO} > 6 \text{ wt\%}$ and $\text{SiO}_2 < 55 \text{ wt\%}$) lavas with coeval mafic IAB (i.e., Aeolian arc) and OIB-like (i.e., Ustica and Prometeo) lavas erupted around the Marsili backarc basin, we attempt to evaluate the extent to which the OIB-like component influences the chemistry of the southern Tyrrhenian arc/backarc lavas.

Magma Sources and Evolution of Marsili Magmas

An important advantage of working on the axis of the Marsili spreading center is that mantle melts travel through young and

thin lithosphere before their eruption, and thus their geochemical features are not affected by intracrustal assimilation processes that may occur within thicker arc crust. Indeed, Marsili volcano developed on the axis of the spreading center of the relatively young (younger than 2 Ma) ocean-crust-floored Marsili backarc basin (Marani and Trua, 2002), and thus it is likely that the geochemical signature of the Marsili basic lavas is not affected by the crustal contamination processes frequently observed at the early stages of the evolution of the nearby Aeolian arc magmas (Francalanci et al., 2007, and references therein). Marsili basic lavas thus provide an unambiguous means for constraining the nature and origin of their mantle sources.

Employing a smaller Sr-Nd-Pb database, Trua et al. (2007) proposed that the spread defined by the Marsili basic lavas derives from mixtures between two distinct mantle sources and

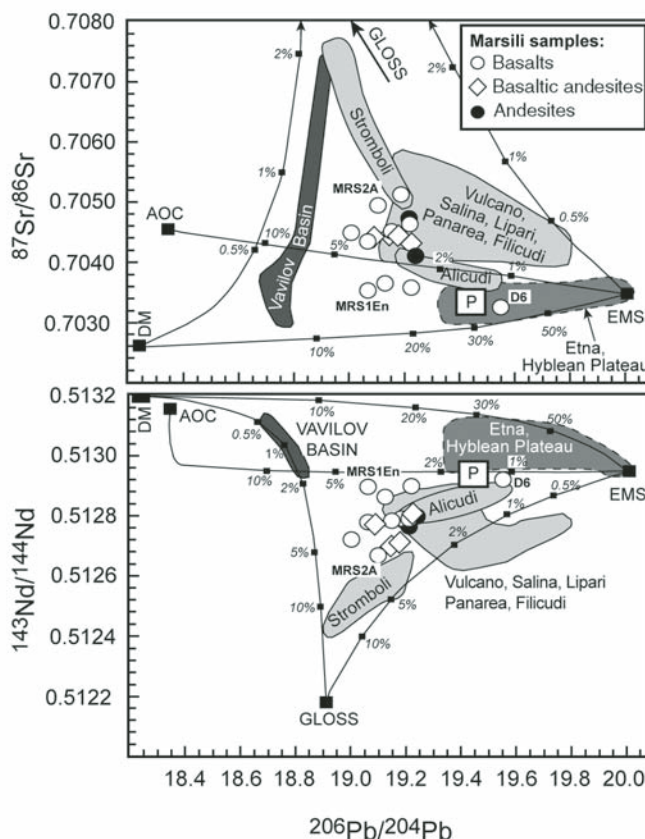


Figure 10. $^{206}\text{Pb}/^{204}\text{Pb}$ versus $^{87}\text{Sr}/^{86}\text{Sr}$ and $^{143}\text{Nd}/^{144}\text{Nd}$ diagrams for the Marsili lavas (this study) and southern Tyrrhenian island-arc basalt and ocean-island basalt mafic ($\text{MgO} > 6 \text{ wt\%}$; $\text{SiO}_2 < 55 \text{ wt\%}$) rocks (for previously published results, data sources are as in Fig. 9). The solid lines represent mixing between: a depleted mantle (DM) wedge and an enriched mantle source (EMS); the depleted mantle and EM sources and bulk sediment (GLOSS—global subducting sediment component; Plank and Langmuir, 1998); and the EM source and fluid from altered oceanic crust. Compositions of the end-member components are listed in Table 3. External errors (2 SD) of Sr, Nd, and Pb isotopic data are smaller than the symbols.

TABLE 3. END MEMBERS USED IN ISOTOPIC MODELING

	Depleted mantle (DM)	Enriched mantle source (EMS)	Altered oceanic crust (AOC) fluid	Global subducting sediment (GLOSS) composition
Sr	13.584	18	558	327
Nd	1.3416	1.2	0.148	27
Pb	0.0576	0.3	10.1	19.9
⁸⁷ Sr/ ⁸⁶ Sr	0.7026	0.7035	0.7045	0.7173
¹⁴³ Nd/ ¹⁴⁴ Nd	0.5132	0.51294	0.51315	0.51218
²⁰⁶ Pb/ ²⁰⁴ Pb	18.24	20.01	18.35	18.913

Note: Data sources: DM from Chauvel et al. (1992); EMS from Tonarini et al. (2001b), Tonarini et al. (2001a), Trua et al. (1998); AOC from Ishizuka et al. (2003); GLOSS from Plank and Langmuir (1998).

slab-derived components. The larger database acquired in this study has permitted us to better constrain the relative contributions of the various source components involved in the petrogenesis of the Marsili mafic lavas. In Figure 10, we illustrate our preferred mixing models, obtained by using the Sr-Nd-Pb isotopic relationships involving four end members (see Table 3 for details in their compositions): (1) a resident depleted mantle wedge, from which the most MORB-like lavas of the Vavilov backarc basin derived; (2) an enriched mantle source akin to that of the Ustica and Prometeo OIB-like magmas related to the African mantle source of Etna-Hyblean Plateau HIMU-OIB magmas; and two chemically distinct components derived from the subducting slab, one (3) similar to the altered oceanic crust fluid component of Ishizuka et al. (2003) and the other (4) resembling the bulk global subducted sediment (GLOSS) component of Plank and Langmuir (1998). It is noteworthy that, in the absence of isotope data on the Ionian subducted sediments, we assume that the GLOSS component represents a suitable substitute since the Marsili basalts point to it in these diagnostic isotope ratio diagrams (Fig. 10).

Calculated mixing lines show that, in terms of mantle components, the Marsili lavas derive from hybrid mantle sources resulting from a mixing of the resident depleted mantle wedge with the incoming enriched mantle source component. In detail, the amount of the enriched mantle source component was lower (<20%) in the mantle sources of the Marsili IAB lavas with respect to that required (up to 50%) in order to generate the mantle source of Marsili OIB-like lava. Overall, the Marsili hybrid mantle sources were also affected by the addition of small (<5%), but variable subduction (fluid and sediment)-related components. Indeed, mixing curves in Figure 10 show that the Marsili IAB lavas having the stronger subduction signature (i.e., MRS2A; Fig. 7A) derive from hybrid mantle sources containing similar amounts of slab-derived fluid (2%–5%) but higher amounts of the GLOSS sediment component with respect to the mantle source of the IAB lavas, which show a weaker subduction signature (i.e., MRS1En; Fig. 7A). A small addition (0.5%) of the subduction (fluid and sediment)-related components also affected the mantle source of the Marsili OIB-like lava (Fig. 10), in agreement with the weak subduction fingerprint shown by the geochemical composition of this lava (Fig. 7A).

We do not propose that the mixing model gives any more than a qualitative indication of the petrogenesis of the Marsili

mafic lavas, because, as argued by Pearce et al. (1999), Hf-Nd systematics are necessary in order to quantify the slab component from the isotope compositions of subduction-related magmas. However, it is possible to obtain a better insight into the physico-chemical characteristic of the slab-derived flux added to the mantle source by using appropriate diagrams, such as the Th/Ce and Ba/La_{ch} (ch—chondrite normalized) versus ²⁰⁶Pb/²⁰⁴Pb diagrams (Figs. 11A and 11B). The Ba/La_{ch} ratio represents an indisputable measure of hydrous fluid/melt addition to the mantle source, whereas the Th/Ce ratio is expected to show dramatic changes with the addition of subducted melt and/or fluid sediment (Ellam and Hawkesworth, 1988; Pearce et al., 1995; Elliott et al., 1997; Class et al., 2000; Ishizuka et al., 2003). In these diagrams, by comparing the Marsili backarc with Aeolian arc basic lavas, it is thus possible to document eventual arc-backarc variations in the characteristics of the slab-derived flux. The Marsili basic lavas define a scattered range that overlap at high values of Th/Ce and Ba/La_{ch} with those of Stromboli lavas. Francalanci et al. (2007) observed that the Aeolian arc lavas define a field having an unusual shape on the Th/Ce versus ²⁰⁶Pb/²⁰⁴Pb diagram (Fig. 11A), with a steeper portion ending with the Stromboli lavas and a much shallower linear trend defined by the Salina, Alicudi, and Vulcano lavas. By using U-series disequilibrium and Sr-Nd isotope data, these authors demonstrated that the steep trend of the Aeolian lava field results from the progressive addition of the sediment melt component, and it reaches its maximum value (<2%) in the Stromboli lavas, whereas the correlation defined by the Salina, Alicudi, and Vulcano lavas reflects a progressive addition to the mantle source of aqueous fluids, released from the Mesozoic oceanic Ionian crust. The higher amount of the sediment component (5%) added to the mantle sources suggested by our mixing calculations for the Marsili lavas overlapping the field of Stromboli lavas (Fig. 11A) mainly depends on the fact that we assumed bulk sediment addition, whereas Francalanci et al. (2007) used a sediment melt component. Nevertheless, admitting that the subducted sediment component was delivered in the same way to the mantle source of the Marsili and Aeolian lavas, the amount of the added sediment was more variable in the Marsili backarc basin system and able to generate the low Th/Ce ratios observed for some Marsili basic lavas (Fig. 11A).

The range of Ba/La_{ch} values for the Marsili basic lavas is also scattered compared to those of the Aeolian basic lavas;

some Marsili lavas have similar $^{206}\text{Pb}/^{204}\text{Pb}$ but lower $\text{Ba}/\text{La}_{\text{ch}}$ ratios than the Aeolian lavas (Fig. 11B). Among the Marsili lavas, those having the lowest Th/Ce ratios lie on the trend extending from the IAB lavas drilled at the Vavilov backarc basin (i.e., ODP Leg 107, Site 651; Fig. 1) to Marsili and Prometeo OIB-like lavas. This trend, which covers a wide range in the $^{206}\text{Pb}/^{204}\text{Pb}$ ratios, could be ascribed to a shift in the mantle source composition from the ambient mantle wedge to the incoming OIB-like mantle component.

The Marsili OIB-like D6 sample may also have some implications for the origin of Alicudi lavas. Indeed, in the isotope and trace-element versus isotope ratios diagrams (Figs. 9–11), one end of the Alicudi field approaches or extends into the field for the southern Tyrrhenian HIMU OIB-like lavas, thus suggesting

that the mantle source of these Aeolian lavas experienced some involvement from the OIB-like component. This observation permits us to suggest that the shift observed for the Alicudi lavas is not uniquely related to the addition of a high $^{206}\text{Pb}/^{204}\text{Pb}$ aqueous fluid component derived from the Mesozoic oceanic Ionian crust, as suggested by Francalanci et al. (2007), but also requires the involvement of an OIB-like component. Furthermore, we do not see that the OIB-like component was originally present in the mantle source of the Alicudi lavas, as previously proposed (Peccerillo et al., 2004). This aspect will be better discussed in the following sections.

Sr–Nd–Pb isotope systematics testifies that among the Marsili IAB magmas, only those showing the strongest subduction signature represent suitable parental magmas for the evolved andesites (Figs. 9 and 10). These results agree with previous petrological calculations (Trua et al., 2002), according to which the high-K andesites could be produced from a large degree of fractional crystallization of magmas having geochemical composition close to these basaltic melts (i.e., MRS2A; Fig. 7C).

By contrast, the Marsili basalts showing the least subduction signature (Fig. 7A) and Sr and Nd isotope features approaching the D6 OIB-like sample (Fig. 9) represent suitable parental magmas for the last-stage Alicudi andesites. According to Peccerillo et al. (2004), the Alicudi andesites derive their $^{87}\text{Sr}/^{86}\text{Sr}$ (0.70345–0.70364) and $^{143}\text{Nd}/^{144}\text{Nd}$ (0.51286–0.51289) ratios, less radiogenic than Alicudi basalts, from an AEC (assimilation + equilibrium crystallization) affecting the parental basaltic magmas. In our opinion, the finding among the Marsili basalts of samples such as MRS1En supplies an alternative explanation to the AEC mechanism invoked by Peccerillo et al. (2004) for the evolution of the Alicudi magmas. Indeed, the MRS1En sample shows Sr–Nd isotope compositions (Table 2) similar to those of the Alicudi andesites, thus suggesting that fractional crystallization of parental magmas isotopically similar to this Marsili lava could account for the origin of the Alicudi evolved rocks. Our hypothesis is also supported by the observation that the REE and incompatible trace-element patterns of the Alicudi andesites are parallel to those of sample MRS1En, but at higher trace-element abundances (Figs. 6C and 7C).

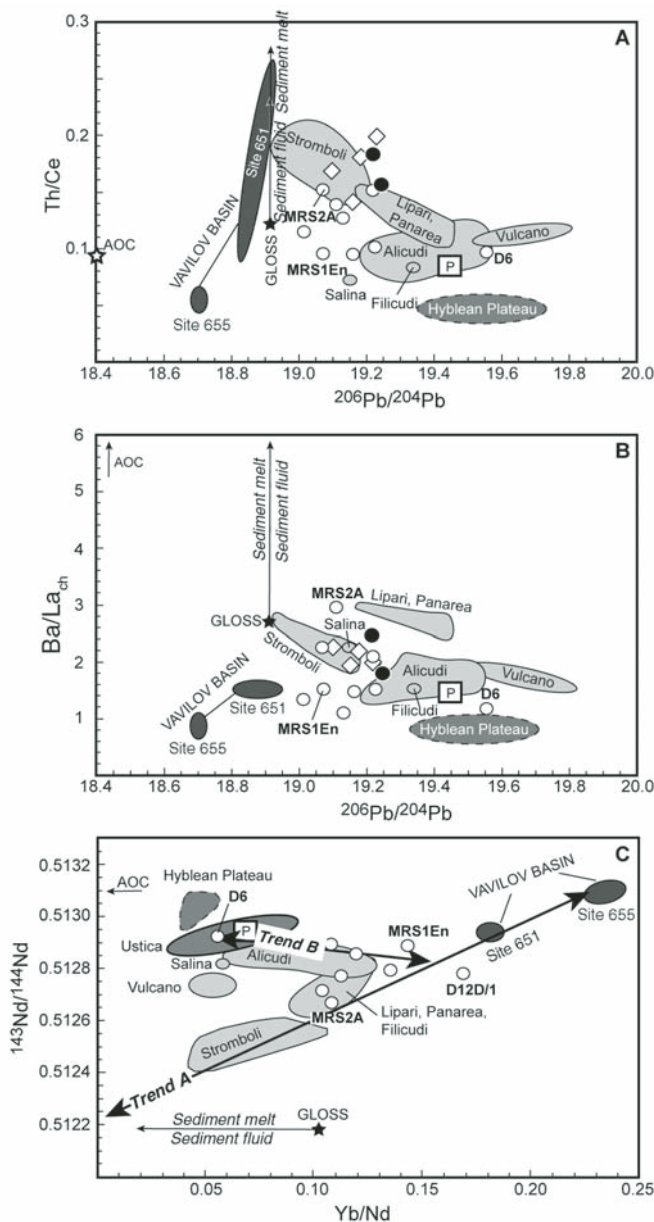


Figure 11. (A) $^{206}\text{Pb}/^{204}\text{Pb}$ versus Th/Ce diagram, (B) $^{206}\text{Pb}/^{204}\text{Pb}$ versus $\text{Ba}/\text{La}_{\text{ch}}$ (ch—chondrite normalized; normalizing factors are from Kay, 1980), and (C) $^{143}\text{Nd}/^{144}\text{Nd}$ versus Yb/Nd diagram for the Marsili lavas and the southern Tyrrhenian island-arc basalt and ocean-island basalt mafic ($\text{MgO} > 6 \text{ wt\%}$; $\text{SiO}_2 < 55 \text{ wt\%}$) rocks. The arrows from GLOSS give a qualitative indication of the effect of addition of the GLOSS component as a melt or fluid rather than as a bulk (GLOSS—global subducting sediment component; Plank and Langmuir, 1998). The trends of the GLOSS-derived arrows are parallel to the trends obtained by Ishizuka et al. (2006) for 12% melt and 2% fluid, respectively, assumed to have been equilibrated with subducted oceanic sediments. Data sources are as in Figures 9 and 10. AOC—altered oceanic crust.

Location of the “African” OIB-Like Mantle Component beneath the Southern Tyrrhenian System

Our attempt to identify the location of the “African” OIB-like mantle domain beneath the southern Tyrrhenian system is constrained by the existing samples for which the Sr-Nd-Pb isotopic compositions are known. These samples are restricted to the youngest and active part of the region, the Marsili backarc basin and the related Aeolian arc. Indeed, very few samples are available from the Vavilov backarc basin, the oldest part of the system (Fig. 1), and all of these lack the Sr-Nd-Pb isotope analyses needed for assessing the isotopic fingerprint of their mantle source.

As discussed already, the Sr-Nd-Pb isotope trend observed for the Marsili backarc lavas (Figs. 9 and 10) is clearly related to the addition of an OIB-like component to the resident MORB mantle wedge. The geochemical and isotopic similarities of the Marsili D6 OIB-like sample with the Ustica and Prometeo OIB-like lavas (Figs. 7A, 9, and 10) indicate that the mantle component involved in their petrogenesis might be similar. Furthermore, Trua et al. (2003) demonstrated that Ustica and Prometeo OIB-like lavas belong to the same mantle feeding the OIB magmas erupted on the north portion of the African plate (i.e., Etna and Hyblean Plateau lavas). As indicated by the magmas erupted from the African foreland (Hyblean Plateau) and the edge between the African and European plates (Etna), the resident mantle beneath this portion of the north African plate has an isotopic composition that is moderately OIB HIMU-like (Fig. 9), isotopically intermediate between HIMU and depleted mantle components (Trua et al., 1998; Tonarini et al., 2001a; De Astis et al., 2006; Bianchini et al., 2008).

Besides the Marsili backarc volcano, the “African” OIB-like component appears to have been also involved in the genesis of Aeolian arc magmatism, namely in the magmatism of Alicudi Island, located in the western sector of the Aeolian arc (Figs. 1 and 2). The possibility that a depleted-enriched mixed mantle source similar to that of Marsili backarc magmas may also be present beneath Alicudi Island is discussed in the following sections.

Geodynamic Implications for the Distribution of the OIB-Like Component

Petrological (Trua et al., 2003; De Astis et al., 2006), geological (Marani and Trua, 2002), and seismological (Chiarabba et al., 2008) studies suggest that the most likely mechanism for the presence of the OIB-like mantle component in southern Tyrrhenian magmatism is the channeling, across tears at the edges of the Ionian slab, of African-related mantle into the arc-basin system (Figs. 1 and 2). Close examination of the Marsili basic lavas further supports this suggestion. Indeed, the trajectories defined by the Marsili lavas on the isotope diagrams (Figs. 9 and 10) or diagrams resulting from a combination of the trace elements and isotope ratios (Figs. 11A and 11B) suggest that a gradual change

from a resident depleted mantle wedge, previously metasomatized by the subduction process, to an OIB-like mantle source, akin to that feeding the Ustica-Prometeo lavas, occurred during the growth of Marsili volcano, built up in the last 0.7 m.y.

The compositional effects of a gradual mixing between the incoming OIB-like mantle and the ambient southern Tyrrhenian mantle, contaminated by the subduction process, can be investigated in the $^{143}\text{Nd}/^{144}\text{Nd}$ versus Yb/Nd diagram (Fig. 11C). The use of Nd as the denominator of the trace-element ratio in this type of diagram means that any mixing trend must be linear. Since the element contents of the end members involved in the mixing process invoked for the genesis of southern Tyrrhenian magmatism are still poorly known, we thus prefer to use this diagram only for a qualitative investigation of the mixing-derived compositional effects. In Figure 10C, the southern Tyrrhenian basic lavas define two trends, which intersect at relatively high values of Yb/Nd, whereas they extend, at lower Yb/Nd values, toward a hypothetical sediment-derived melt component (trend A) or into the field of the Ustica OIB-like lavas (trend B). The Stromboli field falls along trend A, requiring sediment addition via a melt component to the presubduction southern Tyrrhenian MORB (i.e., Site 655) mantle wedge, in agreement with the petrogenetic model proposed by Francalanci et al. (2007) for these Aeolian arc lavas. Sediment addition also occurred in the mantle sources of the Marsili IAB lavas, but the spread of these lavas along trend A confirms that the amount of this component decreased from MRS2A to MRS1En mantle sources. Trend B represents a low-gradient inverse correlation that, to a first approximation, suggests mixing between an OIB-like component and a MORB mantle wedge, previously slightly modified by the subduction process. Indeed, the end members of trend B are the Marsili OIB-like sample (D6) and the Marsili IAB lavas (MRS1En) having the lowest subduction trace-element signature (Fig. 7A). Alicudi basic lavas also plot along the same trend, further supporting our suggestion for the involvement of an OIB-like component in their mantle sources. Finally, the position of the Vulcano and Salina lavas on Figure 10C suggests that the OIB-like component was also involved in the genesis of these Aeolian lavas, although their mantle sources prior to the OIB mixing process were already significantly affected by the subduction-related process in a similar manner to the Stromboli lavas.

If the geochemical gradients defined by the southern Tyrrhenian backarc basin magmas, and part of the Aeolian arc magmas, are caused by an incoming OIB-like mantle component and a preexisting mantle wedge, how did the invoked OIB-like mantle inflow generate the variable mantle domains observed in the southern Tyrrhenian backarc/arc system?

In our model, the development of tears at the edges of the subducting Ionian slab provides the necessary condition for inflow of African OIB-like mantle, thus originating the extreme variability of mantle domains in a relatively narrow zone (Fig. 12).

Tearing of the northern and southern edges of the subducting Ionian slab likely occurred during early-middle Pleistocene (Marani and Trua, 2002; Mattei et al., 2007), the time of

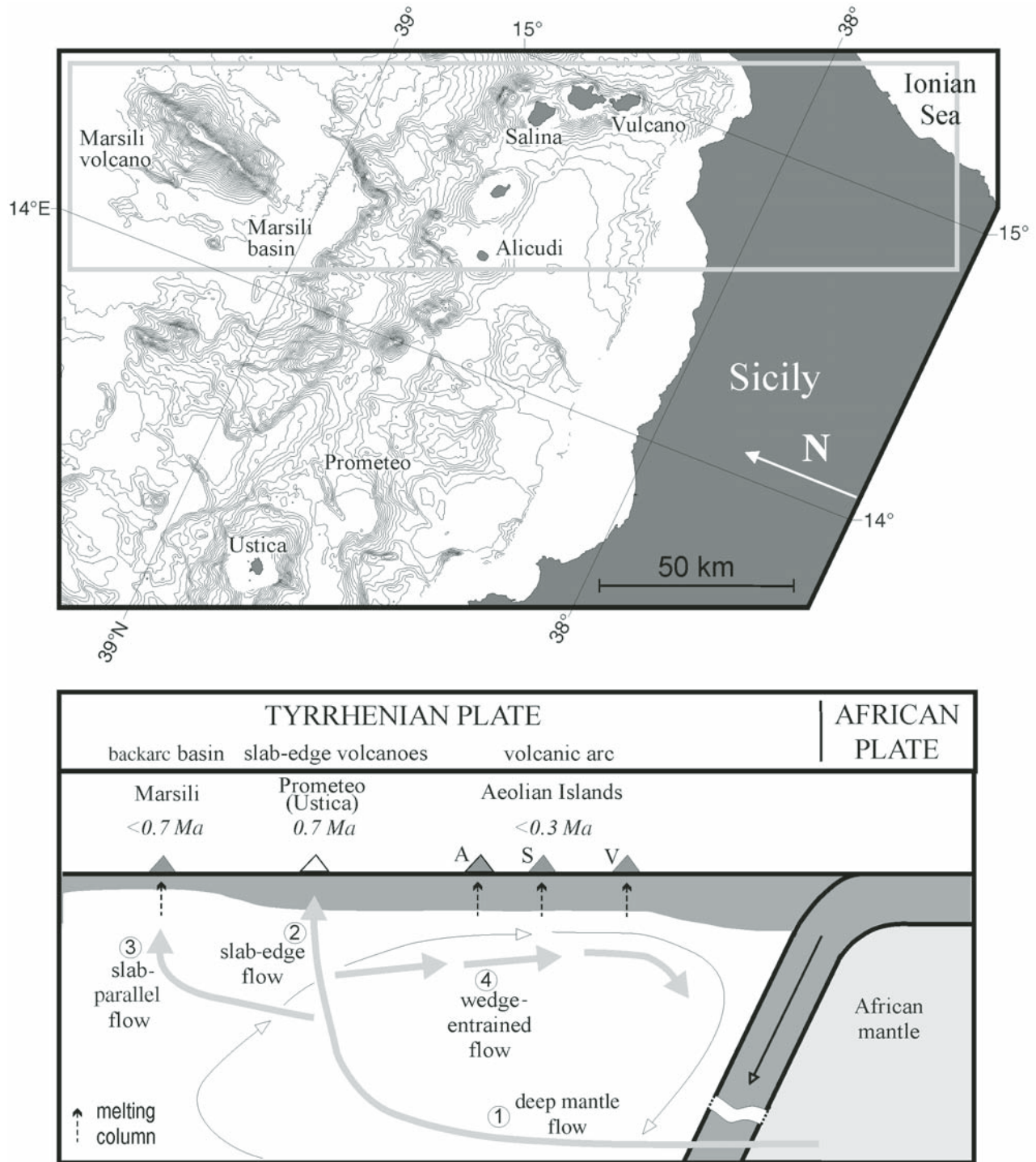


Figure 12. (A) General bathymetry of the Marsili volcano and Aeolian island arc (isobaths 100 m). Also shown are Ustica Island and the submarine Prometeo field. Gray box is the area summarized in the sketch. (B) Cross-section sketch (not to scale) of the interpreted flow paths of African ocean-island basalt (OIB)-like mantle (in thick gray arrows) in the mantle wedge (wedge flow in thin black arrows). Numbers indicate the stages of mantle propagation: 1—deep mantle flows in around the slab edges; 2—African mantle penetrates into the mantle wedge to feed the OIB-like lavas of Ustica and Prometeo, projected in the drawing; 3—a slab-parallel component of the inflowing mantle reaches the region beneath Marsili volcano, furnishing the OIB-like imprint to several of the Marsili lavas, best represented by OIB-like sample D6; and 4—an arcward-directed flow component, due to entrainment by mantle wedge flow, feeds African mantle to Alicudi Island. Salina and Vulcano Islands are also reported, although their OIB-like imprint is considered to derive from flow around the northern slab tear (De Astis et al., 2006). See text for discussion.

formation of Marsili volcano. The eruption of distinctive mafic compositions at various stages of Marsili volcano formation testifies that magma homogenization between the ambient MORB mantle wedge and the incoming OIB-like mantle component was inefficient. Since magma homogenization at asthenosphere viscosities requires a much longer period (e.g., Kellogg and Turcotte, 1990) than our interpreted age of slab tearing and the initiation of mantle inflow, it is reasonable to suppose that the contribution from the OIB-like component was extremely variable beneath the Marsili volcano, varying from sector to sector. We investigate the dynamics of African mantle flow at the southern edge of the subducting Ionian slab due to the up-to-date and exhaustive sampling density that exists only for this portion of the subduction system relative to the very scarce samples from the northern regions.

Lateral mantle flow around the southern edge of the Ionian slab injected hot African asthenosphere into the relatively cold subduction environment, leading to the ingress of African mantle into the mantle wedge, which is anomalous for a subduction system. Propagation of deep African asthenosphere into the southern Tyrrhenian mantle wedge took place by sideways flow around the tear at the southern edge of the slab (Fig. 12). An upward-directed flow from the slab edge caused decompression melting and eruption, as revealed by the OIB-like lavas of Ustica and Prometeo (Trua et al., 2003).

A second, slab parallel, trajectory of mantle flow is interpreted to have extended to Marsili volcano. Slab (trench)–parallel trajectories of the incoming mantle flow in such settings are likely, as is shown by other backarc basin examples in the Lau-Tonga (Turner and Hawkesworth, 1998; Smith et al., 2001) and in the South Sandwich backarc basins (Leat et al., 2004; Müller et al., 2008). Slab-parallel flow contributed to the observed enhanced melting beneath Marsili volcano and induced the gradual IAB-OIB mixing recorded by the Marsili mafic lavas. Indeed, increased decompression melting and the focusing of mantle streamlines are specifically effective beneath the thinned lithosphere of spreading centers (Taylor and Martinez, 2003). Furthermore, Marsili volcano is positioned close to the slab center and ~350 km above it. Laboratory models of slab thermal evolution during rollback (Kincaid and Griffiths, 2003) have shown that, after flowing around the slab edges, flow velocity and higher temperatures are focused toward the centerline of the slab. In the southern Tyrrhenian, rollback of the Ionian slab accelerated due to the development of the slab tears suggested to have taken place in early-middle Pleistocene. Thus, based on the modeling results, it is likely that from this time, the dynamics within the mantle wedge may have favored the establishment of a thermal gradient in the mantle flowing along a slab-parallel trajectory, generating a thermal maximum at the slab center where Marsili volcano is now located. The exceptional eruption of the OIB-like lava on the rift zone of Marsili volcano shows that the African asthenosphere was conveyed beneath the summit of the volcano during its most recent history.

In addition, African mantle flow likely moved arcward, within the mantle wedge, in the direction of Alicudi. This is suggested by

the OIB-like fingerprint of Alicudi basic lavas, which are isotopically similar to that of the Marsili lavas (Fig. 12), despite the very different flow paths followed by the mantle to feed the two different geodynamic regions. This observation suggests that the African mantle is able to retain a similar compositional and thermal viability within two discrete geodynamic settings, during both slab-parallel and wedge-entrained arcward flows.

Geochemical trends suggest that the OIB-like component is also involved in the central sector of the Aeolian arc (Fig. 11), beneath Salina and Vulcano Islands. However, since the invasion of the southern Tyrrhenian mantle wedge by African mantle inflow is also considered to occur from the northern edge of the subducting Ionian slab (De Astis et al., 2006), it is difficult to assess the origin of the OIB-like component involved in the genesis of the magmatism of the central Aeolian arc sector. A detailed sampling of the poorly studied submarine volcanic areas located on the northeastern side of the southern Tyrrhenian backarc basin (i.e., Palinuro, Lametini; Fig. 1) is needed in order to solve this still-unclear aspect related to the dynamics of African mantle inflow in the southern Tyrrhenian region.

ACKNOWLEDGMENTS

We are grateful to P.M. Holm and P.T. Leat for their constructive reviews that substantially improved the manuscript. This work was funded by: “Programma di Ricerca di Interesse Nazionale” of Italian Ministero dell’Università e della Ricerca and Fondi di Ateneo per la Ricerca of Parma University (to Trua); and by CNR (Consiglio Nazionale delle Ricerche), GNV (Gruppo Nazionale di Vulcanologia), and Servizi Tecnici-APAT (Agenzia per la Protezione dell’Ambiente e per i servizi Tecnici) (to Marani and Gamberi).

REFERENCES CITED

- Beccaluva, L., Gabbianelli, G., Lucchini, F., Rossi, P.L., and Savelli, C., 1985, Petrology and K/Ar ages of volcanics dredged from the Aeolian seamounts: Implications for geodynamic evolution of the Southern Tyrrhenian basin: *Earth and Planetary Science Letters*, v. 74, p. 187–208, doi:10.1016/0012-821X(85)90021-4.
- Beccaluva, L., Bonatti, E., Dupuy, C., Ferrara, G., Innocenti, F., Lucchini, F., Macera, P., Petrini, R., Rossi, P.L., Serri, G., Seyler, M., and Siena, F., 1990, Geochemistry and mineralogy of volcanic rocks from ODP Sites 650, 651, 655 and 654 in the Tyrrhenian Sea, in Kastens, K., et al., eds., *Proceedings of the Ocean Drilling Program, Scientific Results, Volume 107*: College Station, Texas, Ocean Drilling Program, p. 49–74.
- Beccaluva, L., Bianchini, G., Coltorti, M., and Verde, M., 2005, Cenozoic tectono-magmatic evolution of the Central-Western Mediterranean: Migration of an arc-interarc basin system and variations in the mode of subduction, in Finetti, I.R., ed., *CROP PROJECT—Deep Seismic Exploration of the Central Mediterranean and Italy*: Amsterdam, Elsevier, p. 623–639.
- Bianchini, G., Beccaluva, L., and Siena, F., 2008, Post-collisional and intraplate Cenozoic volcanism in the rifted Apennines/Adriatic domain, in Dostal, J., ed., *Rift-Related Magmatism: Lithos, Special Issue*, v. 101, p. 125–140.
- Butler, R.W.H., Grasso, M., and Lickorish, H., 1995, Plio-Quaternary megasequence geometry and its tectonic controls within the Maghrebian thrust belt of south-central Sicily: *Terra Nova*, v. 7, p. 171–178, doi:10.1111/j.1365-3121.1995.tb00686.x.
- Caggianelli, A., Del Moro, A., Paglionico, A., Piccaretta, G., Pinarelli, L., and Rottura, A., 1991, Lower crustal granite genesis connected with chemical

- fractionation in the continental crust of Calabria (southern Italy): *European Journal of Mineralogy*, v. 3, p. 159–180.
- Calanchi, N., Peccerillo, A., Tranne, C.A., Lucchini, F., Rossi, P.L., Kempton, P., Barbieri, M., and Wu, T.W., 2002, Petrology and geochemistry of volcanic rocks from the island of Panarea: Implications for mantle evolution beneath the Aeolian island arc (southern Tyrrhenian Sea): *Journal of Volcanology and Geothermal Research*, v. 115, p. 367–395, doi:10.1016/S0377-0273(01)00333-X.
- Cebria, J.M., and Wilson, M., 1995, Cenozoic mafic magmatism in Western/Central Europe: A common European asthenospheric reservoir?: *Terra Nova*, v. 7, p. 162.
- Chiarabba, C., Jovane, L., and DiStefano, R., 2005, A new view of Italian seismicity using 20 years of instrumental recordings: *Tectonophysics*, v. 395, p. 251–268, doi:10.1016/j.tecto.2004.09.013.
- Chiarabba, C., De Gori, P., and Speranza, F., 2008, The southern Tyrrhenian subduction zone: Deep geometry, magmatism and Plio-Pleistocene evolution: *Earth and Planetary Science Letters*, v. 268, p. 408–423, doi:10.1016/j.epsl.2008.01.036.
- Class, C., Miller, D.M., Goldstein, S.L., and Langmuir, C.H., 2000, Distinguishing melt and fluid subduction components in Umnak volcanics, Aleutian Arc: *Geochemistry Geophysics Geosystems*, v. 1, doi:10.1029/1999GC000010.
- De Astis, G., Peccerillo, A., Kempton, P., La Volpe, L., and Wu, T.W., 2000, Transition from calc-alkaline to potassium-rich magmatism in subduction environments: Geochemical and Sr, Nd, Pb isotopic constraints from the island of Vulcano (Aeolian arc): *Contributions to Mineralogy and Petrology*, v. 139, p. 684–703, doi:10.1007/s004100000172.
- De Astis, G., Kempton, P.D., Peccerillo, A., and Wu, T.W., 2006, Trace element and isotopic variations from Mt. Vulture to Campanian volcanoes: Constraints from slab detachment and mantle inflow beneath southern Italy: *Contributions to Mineralogy and Petrology*, v. 151, p. 331–351, doi:10.1007/s00410-006-0062-y.
- Doglioni, C., Mongelli, F., and Pieri, P., 1994, The Puglia uplift (SE Italy): An anomaly in the foreland of the Apennine subduction due to buckling of a thick continental lithosphere: *Tectonics*, v. 13, p. 1309–1321, doi:10.1029/94TC01501.
- Doglioni, C., Innocenti, F., Morellato, C., Procaccianti, D., and Scrocca, D., 2004, On the Tyrrhenian Sea opening, in Marani, M.P., Gamberi, F., and Monatti, E., eds., *From Seafloor to Deep Mantle: Architecture of the Tyrrhenian Backarc Basin: Memorie Descrittive Della Carta Geologica d'Italia*, v. LXIV, p. 147–164.
- Ellam, R.M., and Hawkesworth, C.J., 1988, Elemental and isotopic variations in subduction related basalts: Evidence for a three component model: *Contributions to Mineralogy and Petrology*, v. 98, p. 72–80, doi:10.1007/BF00371911.
- Ellam, R.M., Menzies, M.A., Hawkesworth, C.J., Leeman, W.P., Rosi, M., and Serri, G., 1988, The transition from calc-alkaline to potassic orogenic magmatism in the Aeolian Islands, southern Italy: *Bulletin of Volcanology*, v. 50, p. 386–398, doi:10.1007/BF01050638.
- Ellam, R.M., Hawkesworth, C.J., Menzies, M.A., and Rogers, N.W., 1989, The volcanism of southern Italy: Role of subduction and the relationship between potassic and sodic alkaline magmatism: *Journal of Geophysical Research*, v. 94, p. 4589–4601, doi:10.1029/JB094iB04p04589.
- Elliott, T., Plank, T., Zindler, A., White, W., and Bourdon, B., 1997, Element transport from slab to volcanic front at the Mariana Arc: *Journal of Geophysical Research*, v. 102, p. 14,991–15,019, doi:10.1029/97JB00788.
- Feraud, G., 1990, ^{39}Ar - ^{40}Ar analysis on basaltic lava series of Vavilov Basin, Tyrrhenian Sea (Ocean Drilling Program, Leg 107, Holes 655B and 651A), in Kastens, K., et al., eds., *Proceedings of the Ocean Drilling Program, Scientific Results, Volume 107: College Station, Texas, Ocean Drilling Program*, p. 93–97.
- Francalanci, L., Taylor, S.R., McCulloch, M.T., and Woodhead, J.D., 1993, Geochemical and isotopic variations in the calc-alkaline rocks of Aeolian arc, southern Tyrrhenian Sea, Italy: Constraints on magma genesis: *Contributions to Mineralogy and Petrology*, v. 113, p. 300–313, doi:10.1007/BF00286923.
- Francalanci, L., Avanzinelli, R., Tommasini, S., and Heuman, A., 2007, A west-east geochemical and isotopic traverse along the volcanism of the Aeolian Island arc, southern Tyrrhenian Sea: Inferences on mantle source processes, in Beccaluva, L., Bianchini, G., and Wilson, M., eds., *Cenozoic Volcanism in the Mediterranean Area: Geological Society of America Special Paper 418*, p. 235–263.
- Galadini, F., 1999, Pleistocene changes in the central Apennine fault kinematics: A key to decipher active tectonics in central Italy: *Tectonics*, v. 18, p. 877–894, doi:10.1029/1999TC900020.
- Gamberi, F., Marani, M., Landuzzi, V., Magagnoli, A., Penitenti, D., Rosi, M., Bertagnini, A., and Di Roberto, A., 2006, Sedimentologic and volcanologic investigation of the deep Tyrrhenian Sea: Preliminary results of cruise VST02: *Annals of Geophysics*, v. 49, p. 767–781.
- Gasparini, D., Blichert-Toft, J., Bosch, D., Del Moro, A., Macera, P., and Alberede, F., 2002, Upwelling of deep mantle material through a plate window: Evidence from the geochemistry of Italian basaltic volcanics: *Journal of Geophysical Research*, v. 107, no. B12, 2367, doi:10.1029/2001JB000418.
- Gvirtzman, Z., and Nur, A., 1999, The formation of Mount Etna as the consequence of slab rollback: *Nature*, v. 401, p. 782–785, doi:10.1038/44555.
- Hamelin, B., Lambret, B., Joron, J.L., Treuil, M., and Allègre, C.J., 1979, Geochemistry of basalt from the Tyrrhenian Sea: *Nature*, v. 278, p. 832–834, doi:10.1038/278832a0.
- Hart, S.R., 1984, A large-scale isotope anomaly in the Southern Hemisphere mantle: *Nature*, v. 309, p. 753–757, doi:10.1038/309753a0.
- Hart, S.R., 1988, Heterogeneous mantle domains: Signatures, genesis and mixing chronologies: *Earth and Planetary Science Letters*, v. 90, p. 273–296, doi:10.1016/0012-821X(88)90131-8.
- Hippolyte, J.C., Angelier, J., and Roure, F., 1994, A major geodynamic change revealed by Quaternary stress patterns in the Southern Apennines (Italy): *Tectonophysics*, v. 230, p. 199–210, doi:10.1016/0040-1951(94)90135-X.
- Ishizuka, O., Taylor, R.N., Milton, J.A., and Nesbitt, R.W., 2003, Fluid-mantle interaction in an intra-oceanic arc: Constraints from high-precision Pb isotopes: *Earth and Planetary Science Letters*, v. 211, p. 221–236, doi:10.1016/S0012-821X(03)00201-2.
- Ishizuka, O., Taylor, R.N., Milton, J.A., Nesbitt, R.W., Yuasa, M., and Sakamoto, I., 2006, Variation in the mantle sources of the northern Izu arc with time and space—Constraints from high-precision Pb isotopes: *Journal of Volcanology and Geothermal Research*, v. 156, p. 266–290, doi:10.1016/j.jvolgeores.2006.03.005.
- Kastens, K.A., and Mascle, J., 1990, The geological evolution of the Tyrrhenian Sea: An introduction to the scientific results of ODP Leg 107, in Kastens, K.A., et al., eds., *Proceedings of the Ocean Drilling Program, Scientific Results, Volume 107: College Station, Texas, Ocean Drilling Program*, p. 3–26.
- Kastens, K.A., Mascle, J., Aurox, C., Bonatti, E., Broglia, C., Channell, J., Curzi, P., Emeis, K.-C., Glaçon, G., Hasegawa, S., Hieke, W., Mascle, G., McCoy, F., McKenzie, J., Mendelson, J., Müller, C., Réhault, J.-P., Robertson, A., Sartori, R., Sprovieri, R., and Torii, M., 1988, ODP Leg 107 in the Tyrrhenian Sea: Insights into passive margin and back-arc basin evolution: *Geological Society of America Bulletin*, v. 100, p. 1140–1156, doi:10.1130/0016-7606(1988)100<1140:OLITTS>2.3.CO;2.
- Kay, R.W., 1980, Volcanic arc magmas: Implications of a melting mixing model for element cycling in the crust–upper mantle system: *The Journal of Geology*, v. 88, p. 497–522, doi:10.1086/628541.
- Kellogg, L.H., and Turcotte, D.L., 1990, Mixing and the distribution of heterogeneities in a chaotically convecting mantle: *Journal of Geophysical Research*, v. 95, p. 421–432, doi:10.1029/JB095iB01p00421.
- Kincaid, C., and Griffiths, R.W., 2003, Laboratory models of thermal evolution of the mantle during rollback subduction: *Nature*, v. 425, p. 58–62, doi:10.1038/nature01923.
- Leat, P.T., Pearce, J.A., Barker, P.F., Millar, I.L., Barry, T.L., and Larter, R.D., 2004, Magma genesis and mantle flow at a subducting slab edge: The South Sandwich arc-basin system: *Earth and Planetary Science Letters*, v. 227, p. 17–35, doi:10.1016/j.epsl.2004.08.016.
- Le Maitre, R.W., 1989, *A Classification of Igneous Rocks and Glossary of Terms: Recommendations of the IUGS Subcommittee on the Systematics of Igneous Rocks*: Oxford, Blackwell Scientific, 193 p.
- Lentini, F., Carbone, S., Catalano, S., Di Stefano, A., Garagano, C., Romeo, M., Straluzza, S., and Vinci, G., 1995, Sedimentary evolution of basins in mobile belts: Examples from the Tertiary terrigenous sequences of the Peloritani mountains (NE Sicily): *Terra Nova*, v. 7, p. 161–170, doi:10.1111/j.1365-3121.1995.tb00685.x.
- Marani, M.P., and Trua, T., 2002, Thermal constriction and slab tearing at the origin of a superinflated spreading ridge: Marsili volcano (Tyrrhenian Sea): *Journal of Geophysical Research*, v. 107, no. B9, 2188, doi:10.1029/2001JB000285.
- Marani, P.M., Gamberi, F., Casoni, L., Carrara, G., Landuzzi, V., Musacchio, M., Penitenti, D., Rossi, L., and Trua, T., 1999, New rock and hydrothermal

- samples from the southern Tyrrhenian Sea: The MAR-98 research cruise: *Giornale di Geologia*, v. 61, p. 3–24.
- Mattei, M., Cifelli, F., and D'Agostino, N., 2007, The evolution of the Calabrian arc: Evidence from paleomagnetic and GPS observations: *Earth and Planetary Science Letters*, v. 263, p. 259–274, doi:10.1016/j.epsl.2007.08.034.
- Müller, C., Bayer, B., Eckstaller, A., and Miller, H., 2008, Mantle flow in the South Sandwich subduction environment from source-side shear wave splitting: *Geophysical Research Letters*, v. 35, L03301, doi:10.1029/2007GL032411.
- Patacca, E., Sartori, R., and Scandone, P., 1990, Tyrrhenian and Apenninic arcs: Kinematic relations since late Tortonian times: *Memorie della Società Geologica Italiana*, v. 45, p. 425–451.
- Pearce, J.A., Baker, P.E., Harvey, P.K., and Luff, I.W., 1995, Geochemical evidence for subduction fluxes, mantle melting and fractional crystallization beneath the South Sandwich Island arc: *Journal of Petrology*, v. 36, p. 1073–1109.
- Pearce, J.A., Kempton, P.D., Nowell, G.M., and Noble, S.R., 1999, Hf–Nd element and isotope perspective on the nature and provenance of mantle and subduction components in arc-basin system: Examples from the western Pacific: *Journal of Petrology*, v. 40, p. 1579–1611, doi:10.1093/ptrology/40.11.1579.
- Peccerillo, A., and Wu, T.W., 1992, Evolution of calc-alkaline magmas in continental arc volcanoes: Evidence from Alicudi, Aeolian arc (southern Tyrrhenian Sea, Italy): *Journal of Petrology*, v. 33, p. 1295–1315.
- Peccerillo, A., Kempton, P.D., Harmon, R.S., Santo, A.P., Boyce, A.J., and Tripodo, A., 1993, Petrological and geochemical characteristics of the Alicudi volcano, Aeolian Islands, Italy: Implications for magma genesis and evolution: *Acta Vulcanologica*, v. 3, p. 235–249.
- Peccerillo, A., Dallai, L., Frezzotti, M.L., and Kempton, P., 2004, Sr–Nd–Pb–O isotopic evidence for decreasing crustal contamination with ongoing magma evolution at Alicudi volcano (Aeolian arc, Italy): Implications for style of magma–crust interaction and for mantle source compositions: *Lithos*, v. 78, p. 217–233, doi:10.1016/j.lithos.2004.04.040.
- Plank, T., and Langmuir, C.H., 1998, The chemical composition of subducting sediment and its consequences for the crust and mantle: *Chemical Geology*, v. 145, p. 325–394, doi:10.1016/S0009-2541(97)00150-2.
- Robertson, A.H.F., and Grasso, M., 1995, Overview of the Late Tertiary–Recent tectonic and palaeo-environmental development of the Mediterranean region: *Terra Nova*, v. 7, p. 114–127, doi:10.1111/j.1365-3121.1995.tb00680.x.
- Robin, C., Colantoni, P., Genesseeux, M., and Rehault, J.P., 1987, Vavilov Seamount: A mildly alkaline Quaternary volcano in the Tyrrhenian Basin: *Marine Geology*, v. 78, p. 125–136, doi:10.1016/0025-3227(87)90071-5.
- Rosenbaum, G., and Lister, G.S., 2004, Neogene and Quaternary rollback evolution of the Tyrrhenian Sea, the Apennines, and the Sicilian Maghrebides: *Tectonics*, v. 23, TC1013, doi:10.1029/2003TC001518.
- Savelli, C., 1988, Late Oligocene to Recent episodes of magmatism in and around the Tyrrhenian Sea: Implications for the processes of opening in a young inter-arc basin of intra-orogenic (Mediterranean) type: *Tectonophysics*, v. 146, p. 163–181, doi:10.1016/0040-1951(88)90089-3.
- Schramm, B., Devey, C.W., Gillis, K.M., and Lackschewitz, K., 2005, Quantitative assessment of chemical and mineralogical changes due to progressive low-temperature alteration of East Pacific Rise basalts from 0 to 9 Ma: *Chemical Geology*, v. 218, p. 281–313, doi:10.1016/j.chemgeo.2005.01.011.
- Selvaggi, G., and Chiarabba, C., 1995, Seismicity and P-wave velocity image of the southern Tyrrhenian subduction zone: *Geophysical Journal International*, v. 121, p. 818–826, doi:10.1111/j.1365-246X.1995.tb06441.x.
- Serri, G., 1990, Neogene–Quaternary magmatism of the Tyrrhenian region: Characterization of the magma sources and geodynamic implications: *Memorie della Società Geologica Italiana*, v. 41, p. 219–242.
- Smith, G.P., Wiens, D.A., Fisher, K.M., Dorman, L.M., Webb, S.C., and Hildebrand, J.A., 2001, A complex pattern of mantle flow in the Lau back-arc: *Science*, v. 292, p. 713–716, doi:10.1126/science.1058763.
- Sun, S.S., and McDonough, W.F., 1989, Chemical and isotopic systematics of oceanic basalts: Implications for mantle composition and processes, in Saunders, A.D., and Norry, M.J., eds., *Magmatism in the Ocean Basins: Geological Society of London Special Publication* 42, p. 313–345.
- Taylor, B., and Martinez, F., 2003, Back-arc basin basalt dynamics: *Earth and Planetary Science Letters*, v. 210, p. 481–497, doi:10.1016/S0012-821X(03)00167-5.
- Tonardini, S., Armienti, P., D'Orazio, M., and Innocenti, F., 2001a, Subduction-like fluids in the genesis of Mt. Etna magmas: Evidence from boron isotopes and fluid mobile elements: *Earth and Planetary Science Letters*, v. 192, p. 471–483, doi:10.1016/S0012-821X(01)00487-3.
- Tonardini, S., Leeman, W.P., and Ferrara, G., 2001b, Boron isotopic variations in lavas of the Aeolian volcanic arc, south Italy: *Journal of Volcanology and Geothermal Research*, v. 110, p. 155–170, doi:10.1016/S0377-0273(01)00203-7.
- Trua, T., Esperanca, S., and Mazzuoli, R., 1998, The evolution of the lithospheric mantle along the N. African plate: Geochemical and isotopic evidence from the tholeiitic and alkaline volcanic rocks of the Hyblean Plateau, Italy: *Contributions to Mineralogy and Petrology*, v. 131, p. 307–322, doi:10.1007/s004100050395.
- Trua, T., Serri, G., Marani, M., Renzulli, A., and Gamberi, F., 2002, Volcanological and petrological evolution of Marsili Seamount (southern Tyrrhenian Sea): *Journal of Volcanology and Geothermal Research*, v. 114, p. 441–464, doi:10.1016/S0377-0273(01)00300-6.
- Trua, T., Serri, G., and Marani, M., 2003, Lateral flow of African mantle below the nearby Tyrrhenian plate: Geochemical and isotopic evidence: *Terra Nova*, v. 15, doi:10.1046/j.1365-3121.2003.00509.x.
- Trua, T., Serri, G., and Marani, M., 2007, Geochemical features and geodynamic significance of the southern Tyrrhenian backarc basin, in Becalova, L., Bianchini, G., and Wilson, M., eds., *Cenozoic Volcanism in the Mediterranean Area: Geological Society of America Special Paper* 418, p. 221–233.
- Turner, S., and Hawkesworth, C., 1998, Using geochemistry to map mantle flow beneath the Lau Basin: *Geology*, v. 26, p. 1019–1022, doi:10.1130/0091-7613(1998)026<1019:UGTMMF>2.3.CO;2.
- Westaway, R., 1993, Quaternary uplift of southern Italy: *Journal of Geophysical Research*, v. 98, p. 21,741–21,772, doi:10.1029/93JB01566.
- Zindler, A., and Hart, S., 1986, Chemical geodynamics: *Annual Review of Earth and Planetary Sciences*, v. 14, p. 493–571, doi:10.1146/annurev.ea.14.050186.002425.

Contents

Preface and Acknowledgments

1. *Late Mesozoic to Quaternary intraplate magmatism and its relation to the Neoproterozoic lithosphere in NE Africa—New data from lower-crustal and mantle xenoliths from the Bayuda volcanic field, Sudan*
Friedrich Lucassen, Gerhard Franz, Rolf L. Romer, and Peter Dulski
2. *Holocene opening directions along the axes of the Red Sea (Afar) and Main Ethiopian Rifts: An overview*
V. Acocella, B. Abebe, and T. Korme
3. *The upper-mantle low-velocity anomaly beneath Ethiopia, Kenya, and Tanzania: Constraints on the origin of the African superswell in eastern Africa and plate versus plume models of mantle dynamics*
Andrew A. Nyblade
4. *The Ethiopia Afar Geoscientific Lithospheric Experiment (EAGLE): Probing the transition from continental rifting to incipient seafloor spreading*
Ian D. Bastow, Derek Keir, and Eve Daly
5. *Peridotite xenoliths from Ethiopia: Inferences about mantle processes from plume to rift settings*
Luigi Beccaluva, Gianluca Bianchini, Robert M. Ellam, Claudio Natali, Alessandro Santato, Franca Siena, and Finlay M. Stuart
6. *Evolution of the lithospheric mantle beneath the East African Rift in Tanzania and its potential signatures in rift magmas*
Sonja Aulbach, Roberta L. Rudnick, and William F. McDonough
7. *Petrology and geochemistry of alkaline lava series, Kilimanjaro, Tanzania: New constraints on petrogenetic processes*
Philippe Nonnotte, Mathieu Benoit, Bernard Le Gall, Christophe Hémond, Joël Rolet, Joseph Cotten, Pierre Brunet, and Edikafumeni Makoba
8. *Trace-element distribution between coexisting aqueous fumarole condensates and natrocarbonatite lavas at Oldoinyo Lengai volcano, Tanzania*
Alexander J. Teague, Jacob Hanley, Terry M. Seward, and Frederik Reutten
9. *Cameroon Line alkaline magmatism (central Africa): A reappraisal*
Emmanuel Njonfang, Alexandre Nono, Pierre Kamgang, Vincent Ngako, and Félix M. Tchoua
10. *Mineralogical and geochemical fingerprints of mantle metasomatism beneath Nyos volcano (Cameroon volcanic line)*
M.I. Teitchou, M. Grégoire, R. Temdjim, R.T. Ghogomu, C. Ngwa, and F.T. Aka
11. *Dolomitic volcanism in Zambia: Cr and K signatures and comparisons with other dolomitic melts from the mantle*
D.K. Bailey and S. Kearns
12. *Post-Paleozoic magmatism in Angola and Namibia: A review*
P. Comin-Chiaramonti, A. De Min, V.A.V. Girardi, and E. Ruberti
13. *Is the African cratonic lithosphere wet or dry?*
Ikuo Katayama and Jun Korenaga
14. *New ^{40}Ar - ^{39}Ar ages and petrogenesis of the Massif d'Ambre volcano, northern Madagascar*
C. Cucciniello, L. Melluso, V. Morra, M. Storey, I. Rocco, L. Franciosi, C. Grifa, C.M. Petrone, and M. Vincent
15. *Metasomatism versus host magma infiltration: A case study of Sal mantle xenoliths, Cape Verde Archipelago*
Costanza Bonadiman, Massimo Coltorti, Luigi Beccaluva, William L. Griffin, Suzanne Y. O'Reilly, and Franca Siena
16. *Magmatic evidence for African mantle propagation into the southern Tyrrhenian backarc region*
Teresa Trua, Michael P. Marani, and Fabiano Gamberi



THE GEOLOGICAL SOCIETY
OF AMERICA®

3300 Penrose Place ■ P.O. Box 9140
Boulder, CO 80301-9140, USA

ISBN 978-0-8137-2478-2



9 780813 724782